

به نام خدا



مرکز دانلود رایگان مهندسی متالورژی و مواد

www.Iran-mavad.com



Gernot Kostorz (Editor)

Phase Transformations in Materials



www.iran-mavad.com

Phase Transformations in Materials. Edited by Gernot Kostorz
Copyright © 2001 WILEY-VCH Verlag GmbH, Weinheim
ISBN: 3-527-30256-5

مرجع دانشجویان و مهندسين مواد

Related titles from WILEY-VCH

Eric Lifshin (Ed.)

X-ray Characterization of Materials

ISBN 3-527-29657-3

Dierk Raabe

Computational Materials Science

ISBN 3-527-29541-0

Gernot Kostorz (Ed.)

Phase Transformations in Materials



Weinheim · New York · Chichester · Brisbane · Singapore · Toronto

www.iran-mavad.com

مرجع دانشجویان و مهندسين مواد

Editor:
Prof. Gernot Kistorz
ETH Zürich
Institut für Angewandte Physik
CH-8093 Zürich
Switzerland

This book was carefully produced. Nevertheless, authors, editor and publisher do not warrant the information contained therein to be free of errors. Readers are advised to keep in mind that statements, data, illustrations, procedural details or other items may inadvertently be inaccurate.

Library of Congress Card No. applied for

British Library Cataloguing-in-Publication Data:
A catalogue record for this book is available from the British Library.

Die Deutsche Bibliothek – Cataloguing-in-Publication Data:
A catalogue record for this book is available from Die Deutsche Bibliothek
ISBN 3-527-30256-5

© WILEY-VCH Verlag GmbH, D-69469 Weinheim (Federal Republic of Germany), 2001

All rights reserved (including those of translation in other languages). No part of this book may be reproduced in any form – by photoprinting, microfilm, or any other means – nor transmitted or translated into machine language without written permission from the publishers. Registered names, trademarks, etc. used in this book, even when not specifically marked as such, are not to be considered unprotected by law.

Printed in the Federal Republic of Germany
Printed on acid-free paper.

Indexing: Borkowski & Borkowski, Schauernheim

Composition, Printing and Bookbinding: Konrad Triltsch, Print und digitale Medien GmbH, 97199 Ochsenfurt-Hohestadt

www.iran-mavad.com

مرجع دانشجویان و مهندسين مواد

*To the memory of Peter Haasen
(1927–1993)*

Preface

In 1991, the late Peter Haasen, who had set out to edit a comprehensive treatment of “Materials Science and Technology” together with Robert W. Cahn and Edward J. Kramer, a very successful series of up-to-date coverages of a broad range of materials topics, wrote the following in a Preface to Volume 5.

“Herewith we proudly present the first volume of this Series, the aim of which is to provide a comprehensive treatment of materials science and technology. The term ‘materials’ encompasses metals, ceramics, electronic and magnetic materials, polymers and composites. In many cases these materials have been developed independently within different disciplines but are now finding uses in similar technologies. Moreover, similarities found among the principles underlying these various disciplines have led to the discovery of common phenomena and mechanisms. One of these common features, phase transformations, constitutes the topic of this volume and rates among the fundamental phenomena central to the Series. A phase transformation often delivers a material into its technologically useful form and microstructure. For example, the major application of metals and alloys as mechanically strong materials relies on their multi-phase microstructure, most commonly generated by one or more phase transformations.”

Peter Haasen, who passed away in 1993, did not live to see the overwhelming success of this volume. A revised edition was planned as early as 1996 and finally, work on the individual chapters began in 1998. Almost all of the original authors agreed to update their earlier work, in many cases they arranged for the participation of younger colleagues who had made major contributions to the field. It is thus with similar pride the present editor submits the second edition of “Phase Transformations” to the scholarly public. It was with some hesitation that he assumed the task of editor, as he did not like giving the impression of plagiarizing a successful work. All the credit for the idea, the original chapter definitions and the selection of the initial authors remains with Peter Haasen. He would certainly have liked to work on a new edition himself and, assuming that he would have judged it timely to accomplish it about ten years after the first edition, this editor tried to help reaching this goal in the original spirit.

Thus, all the chapters kept their original titles. The contents have been thoroughly re-edited and updated and reflect the progress in the field up to about the middle of the year 2000. As before, the book starts with the foundations of phase transformations (“Thermodynamics and Phase Diagrams” by A. D. Pelton). The sequence of the following Chapters has been slightly modified. As most of the volume concerns the solid state, Chapter 2 (by H. Müller-Krumbhaar, W. Kurz and E. Brener) is devoted to solidification, a subject of great basic and technological relevance. Chapter 3 by G. E. Murch covers the most important ideas and methods of diffusion kinetics in solids, an indispensable ingredient to many phase transformations. Statistical theories of phase transformations are presented by K. Binder in Chapter 4, featuring phenomenological concepts and computational methods. Diffusion controlled homogeneous phase transformations are treated in Chapter 5 (“Homogeneous Sec-

ond Phase Precipitation” by R. Wagner, R. Kampmann and P. W. Voorhees) and Chapter 6 (“Spinodal Decomposition” by K. Binder and P. Fratzl), looking at the very complex kinetical aspects of the formation of new phases from the points of view of metastability and instability in an initially homogeneous system. Heterogeneous phase transformations are treated in Chapter 7 (“Transformations Involving Interfacial Diffusion” by G. R. Purdy and Y. Bréchet) while Chapter 8 by G. Inden deals with atomic ordering, mostly involving substitutional alloys and intermetallic phases. Though much progress has been made in elucidating equilibrium ordered states, kinetical aspects are still widely unexplored in this field. Finally, the numerous aspects of diffusionless transformations in the solid state are taken up by L. Delaey (Chapter 9), and a completely new Chapter on the effects of pressure on phase transformations has been provided by M. Kunz (Chapter 10).

In working on this new edition, the editor had great pleasure interacting with the authors, those of the first edition as well as those who joined for the new edition. He is grateful to all of them for their friendly and competent co-operation. Thanks are due to the publisher for expedient support and for the preparation of the subject index.

It is hoped that this book will be useful as a source of reference to active researchers and advanced students; more up-to-date and more detailed than encyclopedic articles, but not as complete and extensive as any monographs. Phase transformations are among the most complex and most versatile phenomena in solid state physics and materials science – and have considerable impact on production and processing technology. The present book should encourage the reader to enter and more deeply appreciate this challenging field.

Gernot Kostorz, Zürich

April 2001

List of Contributors

Prof. Kurt Binder
Universität Mainz
Institut für Physik
Staudinger Weg 7
D-55099 Mainz
Germany
Chapters 4 and 6

Prof. Yves J. M. Bréchet
Laboratoires de Thermodynamiques
at Physico-Chimique Métallurgiques BP75
Domaine Universitaire de Grenoble
F-38402 Saint Martin d'Herès
France
Chapter 7

Dr. Efim Brener
Institut für Festkörperforschung
Forschungszentrum Jülich
D-52425 Jülich
Germany
Chapter 2

Prof. Luc Delaey
Katholieke Universiteit Leuven
Dept. Metaalkunde en Toegepaste
Materiaalkunde
Decroylaan 2
B-3030 Heverlee-Leuven
Belgium
Chapter 9

Prof. Peter Fratzl
Institut für Metallphysik
Montan-Universität Leoben
Jahnstraße 12
A-8700 Leoben
Austria
Chapter 6

Prof. Gerhard Inden
Max-Planck-Institut für Eisenhütten-
forschung GmbH
Max-Planck-Str. 1
D-40237 Düsseldorf
Germany
Chapter 8

Dr. Reinhard Kampmann
GKSS-Forschungszentrum Geesthacht
GmbH
Institut für Werkstoffforschung
Postfach 1160
D-21494 Geesthacht
Germany
Chapter 5

Prof. Martin Kunz
ETH Zürich
Labor für Kristallographie
Sonneggstr. 5
CH-8092 Zürich
Switzerland
now at:
Naturhistorisches Museum Basel
Augustinerstr. 2
CH-4053 Basel
Switzerland
Chapter 10

Prof. Wilfried Kurz
École Polytechnique de Lausanne
DMX-G, Ecublens
CH-1015 Lausanne
Switzerland
Chapter 2

Prof. Heiner Müller-Krumbhaar
Institut für Festkörperforschung
Forschungszentrum Jülich
D-52425 Jülich
Germany
Chapter 2

Prof. Graeme E. Murch
University of Newcastle
Dept. of Chemical and Materials
Engineering
Romkin Drive
Newcastle, NSW 2308
Australia
Chapter 3

Prof. Arthur D. Pelton
École Polytechnique de Montréal
Centre de Recherche en Calcul
Thermochimique
CP 6079
Succursale A
Montréal, Québec H3C 3A7
Canada
Chapter 1

Prof. Gary R. Purdy
Dept. of Materials Science and Engineering
McMaster University
1280 Main Street
Hamilton, Ontario L8S 4L7
Canada
Chapter 7

Prof. Peter W. Voorhees
Dept. of Materials Science and Engineering
Northwestern University
2225 N. Campus Drive
Evanston, IL 60208-3108
USA
Chapter 5

Prof. Richard Wagner
Forschungszentrum Jülich
D-52425 Jülich
Germany
Chapter 5

Contents

1	Thermodynamics and Phase Diagrams of Materials	1
	<i>A. D. Pelton</i>	
2	Solidification	81
	<i>H. Müller-Krumbhaar, W. Kurz, E. Brener</i>	
3	Diffusion in Crystalline Solids	171
	<i>G. E. Murch</i>	
4	Statistical Theories of Phase Transitions	239
	<i>K. Binder</i>	
5	Homogeneous Second Phase Precipitation	309
	<i>R. Wagner, R. Kampmann, P. W. Voorhees</i>	
6	Spinodal Decomposition	409
	<i>K. Binder, P. Fratzl</i>	
7	Transformations Involving Interfacial Diffusion	481
	<i>G. R. Purdy, Y. J. M. Bréchet</i>	
8	Atomic Ordering	519
	<i>G. Inden</i>	
9	Diffusionless Transformations	583
	<i>L. Delaey</i>	
10	High Pressure Phase Transformations	655
	<i>M. Kunz</i>	
Index	697

1 Thermodynamics and Phase Diagrams of Materials

Arthur D. Pelton

Centre de Recherche en Calcul Thermochimique, École Polytechnique,
Montréal, Québec, Canada

List of Symbols and Abbreviations	3
1.1 Introduction	5
1.1.1 Notation	5
1.2 Gibbs Energy and Equilibrium	5
1.2.1 Gibbs Energy	5
1.2.2 Chemical Equilibrium	6
1.3 Predominance Diagrams	7
1.3.1 Calculation of Predominance Diagrams	7
1.3.2 Ellingham Diagrams as Predominance Diagrams	8
1.3.3 Discussion of Predominance Diagrams	9
1.4 Thermodynamics of Solutions	9
1.4.1 Gibbs Energy of Mixing	9
1.4.2 Chemical Potential	10
1.4.3 Tangent Construction	11
1.4.4 Gibbs-Duhem Equation	11
1.4.5 Relative Partial Properties	11
1.4.6 Activity	12
1.4.7 Ideal Raoultian Solutions	12
1.4.8 Excess Properties	13
1.4.9 Activity Coefficient	14
1.4.10 Multicomponent Solutions	14
1.5 Binary Phase Diagrams	14
1.5.1 Systems with Complete Solid and Liquid Miscibility	14
1.5.2 Thermodynamic Origin of Phase Diagrams	16
1.5.3 Pressure-Composition Phase Diagrams	19
1.5.4 Minima and Maxima in Two-Phase Regions	20
1.5.5 Miscibility Gaps	21
1.5.6 Simple Eutectic Systems	22
1.5.7 Regular Solution Theory	23
1.5.8 Thermodynamic Origin of Simple Phase Diagrams Illustrated by Regular Solution Theory	24
1.5.9 Immiscibility – Monotectics	26
1.5.10 Intermediate Phases	26
1.5.11 Limited Mutual Solubility – Ideal Henrian Solutions	29
1.5.12 Geometry of Binary Phase Diagrams	31

1.6	Application of Thermodynamics to Phase Diagram Analysis	34
1.6.1	Thermodynamic/Phase Diagram Optimization	34
1.6.2	Polynomial Representation of Excess Properties	34
1.6.3	Least-Squares Optimization	35
1.6.4	Calculation of Metastable Phase Boundaries	39
1.7	Ternary and Multicomponent Phase Diagrams	39
1.7.1	The Ternary Composition Triangle	39
1.7.2	Ternary Space Model	39
1.7.3	Polythermal Projections of Liquidus Surfaces	41
1.7.4	Ternary Isothermal Sections	43
1.7.4.1	Topology of Ternary Isothermal Sections	45
1.7.5	Ternary Isopleths (Constant Composition Sections)	46
1.7.5.1	Quasi-Binary Phase Diagrams	47
1.7.6	Multicomponent Phase Diagrams	47
1.7.7	Nomenclature for Invariant Reactions	49
1.7.8	Reciprocal Ternary Phase Diagrams	49
1.8	Phase Diagrams with Potentials as Axes	51
1.9	General Phase Diagram Geometry	56
1.9.1	General Geometrical Rules for All True Phase Diagram Sections	56
1.9.1.1	Zero Phase Fraction Lines	58
1.9.2	Choice of Axes and Constants of True Phase Diagrams	58
1.9.2.1	Tie-lines	60
1.9.2.2	Corresponding Phase Diagrams	60
1.9.2.3	Theoretical Considerations	60
1.9.2.4	Other Sets of Conjugate Pairs	61
1.10	Solution Models	62
1.10.1	Sublattice Models	62
1.10.1.1	All Sublattices Except One Occupied by Only One Species	62
1.10.1.2	Ionic Solutions	62
1.10.1.3	Interstitial Solutions	64
1.10.1.4	Ceramic Solutions	64
1.10.1.5	The Compound Energy Formalism	65
1.10.1.6	Non-Stoichiometric Compounds	65
1.10.2	Polymer Solutions	66
1.10.3	Calculation of Limiting Slopes of Phase Boundaries	66
1.10.4	Short-Range Ordering	68
1.10.5	Long-Range Ordering	71
1.11	Calculation of Ternary Phase Diagrams From Binary Data	72
1.12	Minimization of Gibbs Energy	74
1.12.1	Phase Diagram Calculation	76
1.13	Bibliography	76
1.13.1	Phase Diagram Compilations	76
1.13.2	Thermodynamic Compilations	77
1.13.3	General Reading	78
1.14	References	78

List of Symbols and Abbreviations

Symbol	Designation
a_i	activity of component i
C	number of components
c_p	molar heat capacity
E	electrical potential of a galvanic cell
F	degrees of freedom/variance
G	Gibbs energy in J
g	molar Gibbs energy in J/mol
g_i	partial molar Gibbs energy of i
G_i^0	standard Gibbs energy of i
g_i^0	standard molar Gibbs energy of i
Δg_i	relative partial Gibbs energy i
g^E	excess molar Gibbs energy
g_i^E	excess partial Gibbs energy of i
ΔG	Gibbs energy change
ΔG^0	standard Gibbs energy change
Δg_m	molar Gibbs energy of mixing
Δg_f^0	standard molar Gibbs energy of fusion
Δg_v^0	standard molar Gibbs energy of vaporization
H	enthalpy in J
h	molar enthalpy in J/mol
h_i	partial enthalpy of i
H_i^0	standard enthalpy of i
h_i^0	standard molar enthalpy of i
Δh_i	relative partial enthalpy of i
h^E	excess molar enthalpy
h_i^E	excess partial enthalpy of i
ΔH	enthalpy change
ΔH^0	standard enthalpy change
Δh_m	molar enthalpy of mixing
Δh_f^0	standard molar enthalpy of fusion
Δh_v^0	standard molar enthalpy of vaporization
K	equilibrium constant
k_B	Boltzmann constant
n	number of moles
n_i	number of moles of constituent i
N_i	number of particles of i
N^0	Avogadro's number
p_i	partial pressure of i
P	total pressure
P	number of phases
q_i	general extensive variable

R	gas constant
S	entropy in J/K
s	molar entropy in J/mol K
s_i	partial entropy of i
S_i^0	standard entropy of i
s_i^0	standard molar entropy of i
Δs_i^0	relative partial entropy of i
s^E	excess molar entropy
s_i^E	excess partial entropy of i
ΔS	entropy change
ΔS^0	standard entropy change
Δs_m	molar entropy of mixing
Δs_f^0	standard molar entropy of fusion
Δs_v^0	standard molar entropy of vaporization
T	temperature
T_f	temperature of fusion
T_c	critical temperature
T_E	eutectic temperature
U	internal energy
v_i	molar volume of i
v_i^0	standard molar volume of i
X_i	mole fraction of i
Z	coordination number
γ_i	activity coefficient of i
ε	bond energy
η	empirical entropy parameter
μ_i	chemical potential of i
ν	number of moles of “foreign” particles contributed by a mole of solute
ξ	molar metal ratio
σ	vibrational bond entropy
ϕ_i	generalized thermodynamic potential
ω	empirical enthalpy parameter
b.c.c.	body-centered cubic
f.c.c.	face-centered cubic
h.c.p.	hexagonal close-packed

1.1 Introduction

An understanding of thermodynamics and phase diagrams is fundamental and essential to the study of materials science. A knowledge of the equilibrium state under a given set of conditions is the starting point in the description of any phenomenon or process.

The theme of this chapter is the relationship between phase diagrams and thermodynamics. A phase diagram is a graphical representation of the values of thermodynamic variables when equilibrium is established among the phases of a system. Materials scientists are used to thinking of phase diagrams as plots of temperature versus composition. However, many other variables such as total pressure and partial pressures may be plotted on phase diagrams. In Sec. 1.3, for example, predominance diagrams will be discussed, and in Sec. 1.8 chemical potential–composition phase diagrams will be presented. General rules regarding phase diagram geometry are given in Sec. 1.9.

In recent years, a quantitative coupling of thermodynamics and phase diagrams has become possible. With the use of computers, simultaneous optimizations of thermodynamic and phase equilibrium data can be applied to the critical evaluation of binary and ternary systems as shown in Sec. 1.6. This approach often enables good estimations to be made of the thermodynamic properties and phase diagrams of multicomponent systems as discussed in Sec. 1.11. These estimates are based on structural models of solutions. Various models such as the regular solution model, the sublattice model, and models for interstitial solutions, polymeric solutions, solutions of defects, ordered solutions, etc. are discussed in Secs. 1.5 and 1.10.

The equilibrium diagram is always calculated by minimization of the Gibbs en-

ergy. General computer programs are available for the minimization of the Gibbs energy in systems of any number of phases, components and species as outlined in Sec. 1.12. When coupled to extensive databases of the thermodynamic properties of compounds and multicomponent solutions, these provide a powerful tool in the study of materials science.

1.1.1 Notation

Extensive thermodynamic properties are represented by upper case symbols. For example, G = Gibbs energy in J. Molar properties are represented by lower case symbols. For example, $g = G/n$ = molar Gibbs energy in J/mol where n is the total number of moles in the system.

1.2 Gibbs Energy and Equilibrium

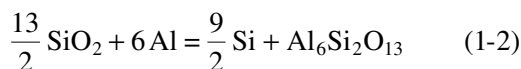
1.2.1 Gibbs Energy

The Gibbs energy of a system is defined in terms of its enthalpy, H , entropy, S , and temperature, T :

$$G = H - TS \quad (1-1)$$

A system at constant temperature and pressure will approach an equilibrium state that minimizes G .

As an example, consider the question of whether silica fibers in an aluminum matrix at 500 °C will react to form mullite, $\text{Al}_6\text{Si}_2\text{O}_{13}$



If the reaction proceeds with the formation of dn moles of mullite then, from the stoichiometry of the reaction, $dn_{\text{Si}} = (9/2) dn$, $dn_{\text{Al}} = -6 dn$, and $dn_{\text{SiO}_2} = -13/2 dn$. Since the four substances are essentially immiscible at 500 °C, we need consider only the

standard molar Gibbs energies, G_i^0 . The Gibbs energy of the system then varies as:

$$dG/dn = g_{\text{Al}_6\text{Si}_2\text{O}_{13}}^0 + \frac{9}{2} g_{\text{Si}}^0 - \frac{13}{2} g_{\text{SiO}_2}^0 - 6 g_{\text{Al}}^0 = \Delta G^0 = -830 \text{ kJ} \quad (1-3)$$

where ΔG^0 is the standard Gibbs energy change of reaction, Eq. (1-2), at 500 °C.

Since $\Delta G^0 < 0$, the formation of mullite entails a decrease in G . Hence, the reaction will proceed spontaneously so as to minimize G .

1.2.2 Chemical Equilibrium

The partial molar Gibbs energy of an ideal gas is given by:

$$g_i = g_i^0 + RT \ln p_i \quad (1-4)$$

where g_i^0 is the standard molar Gibbs energy (at 1 bar), p_i is the partial pressure in bar, and R is the gas constant. The second term in Eq. (1-4) is entropic. As a gas expands at constant T , its entropy increases.

Consider a gaseous mixture of H_2 , S_2 and H_2S with partial pressures p_{H_2} , p_{S_2} and $p_{\text{H}_2\text{S}}$. The gases can react according to



If the reaction, Eq. (1-5), proceeds to the right with the formation of $2 dn$ moles of H_2S , then the Gibbs energy of the system varies as:

$$\begin{aligned} dG/dn &= 2 g_{\text{H}_2\text{S}} - 2 g_{\text{H}_2} - g_{\text{S}_2} \\ &= (2 g_{\text{H}_2\text{S}}^0 - 2 g_{\text{H}_2}^0 - g_{\text{S}_2}^0) \\ &\quad + RT (2 \ln p_{\text{H}_2\text{S}} - 2 \ln p_{\text{H}_2} - \ln p_{\text{S}_2}) \\ &= \Delta G^0 + RT \ln (p_{\text{H}_2\text{S}}^2 p_{\text{H}_2}^{-2} p_{\text{S}_2}^{-1}) \\ &= \Delta G \end{aligned} \quad (1-6)$$

ΔG , which is the Gibbs energy change of the reaction, Eq. (1-5), is thus a function of the partial pressures. If $\Delta G < 0$, then the reaction will proceed to the right so as to minimize G . In a closed system, as the re-

action continues with the production of H_2S , $p_{\text{H}_2\text{S}}$ will increase while p_{H_2} and p_{S_2} will decrease. As a result, ΔG will become progressively less negative. Eventually an equilibrium state will be reached when $dG/dn = \Delta G = 0$.

For the equilibrium state, therefore:

$$\begin{aligned} \Delta G^0 &= -RT \ln K \\ &= -RT \ln (p_{\text{H}_2\text{S}}^2 p_{\text{H}_2}^{-2} p_{\text{S}_2}^{-1})_{\text{equilibrium}} \end{aligned} \quad (1-7)$$

where K , the “equilibrium constant” of the reaction, is the one unique value of the ratio $(p_{\text{H}_2\text{S}}^2 p_{\text{H}_2}^{-2} p_{\text{S}_2}^{-1})$ for which the system will be in equilibrium at the temperature T .

If the initial partial pressures are such that $\Delta G > 0$, then the reaction, Eq. (1-5), will proceed to the left in order to minimize G until the equilibrium condition of Eq. (1-7) is attained.

As a further example, we consider the possible precipitation of graphite from a gaseous mixture of CO and CO_2 . The reaction is:

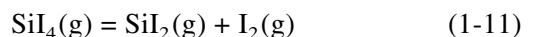
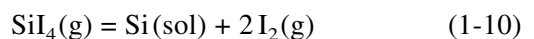


Proceeding as above, we can write:

$$\begin{aligned} dG/dn &= g_{\text{C}} + g_{\text{CO}_2} - 2 g_{\text{CO}} \\ &= (g_{\text{C}}^0 + g_{\text{CO}_2}^0 - 2 g_{\text{CO}}^0) + RT \ln (p_{\text{CO}_2}/p_{\text{CO}}^2) \\ &= \Delta G^0 + RT \ln (p_{\text{CO}_2}/p_{\text{CO}}^2) \\ &= \Delta G = -RT \ln K + RT \ln (p_{\text{CO}_2}/p_{\text{CO}}^2) \end{aligned} \quad (1-9)$$

If $(p_{\text{CO}_2}/p_{\text{CO}}^2)$ is less than the equilibrium constant K , then precipitation of graphite will occur in order to decrease G .

Real situations are, of course, generally more complex. To treat the deposition of solid Si from a vapour of SiI_4 , for example, we must consider the formation of gaseous I_2 , I and SiI_2 so that three reaction equations must be written:



The equilibrium state, however, is still that which minimizes the total Gibbs energy of the system. This is equivalent to satisfying simultaneously the equilibrium constants of the reactions, Eqs. (1-10) to (1-12), as will be shown in Section 1.12 where this example is discussed further.

1.3 Predominance Diagrams

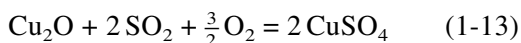
1.3.1 Calculation of Predominance Diagrams

Predominance diagrams are a particularly simple type of phase diagram which have many applications in the fields of hot corrosion, chemical vapor deposition, etc. Furthermore, their construction clearly illustrates the principles of Gibbs energy minimization and the Gibbs Phase Rule.

A predominance diagram for the Cu-S-O system at 1000 K is shown in Fig. 1-1. The axes are the logarithms of the partial pressures of SO_2 and O_2 in the gas phase. The diagram is divided into areas or domains of stability of the various

solid compounds of Cu, S and O. For example, at point Z, where $p_{\text{SO}_2} = 10^{-2}$ and $p_{\text{O}_2} = 10^{-7}$ bar, the stable phase is Cu_2O . The conditions for coexistence of two and three solid phases are indicated respectively by the lines and triple points on the diagram.

For example, along the univariant line (phase boundary) separating the Cu_2O and CuSO_4 domains the equilibrium constant $K = p_{\text{SO}_2}^{-2} p_{\text{O}_2}^{-3/2}$ of the following reaction is satisfied:



Hence, along this line:

(1-14)

$$\log K = -2 \log p_{\text{SO}_2} - \frac{3}{2} \log p_{\text{O}_2} = \text{constant}$$

This boundary is thus a straight line with a slope of $(-3/2)/2 = -3/4$.

In constructing predominance diagrams, we define a "base element", in this case Cu, which must be present in all the condensed phases. Let us further assume that there is no mutual solubility among the condensed phases.

Following the procedure of Bale et al. (1986), we formulate a reaction for the for-

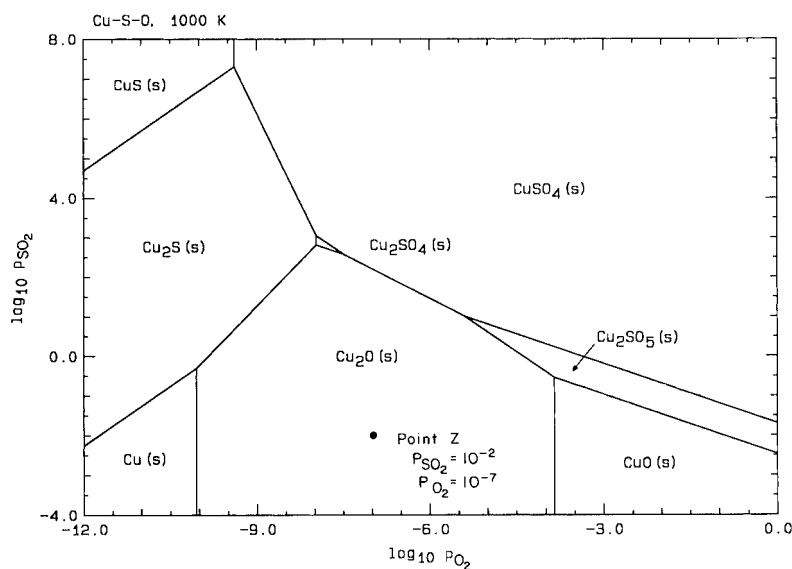
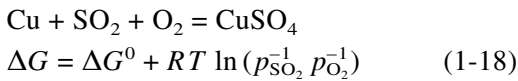
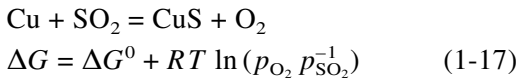
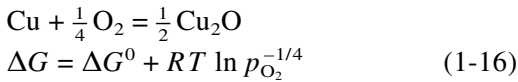
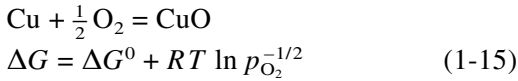


Figure 1-1. Predominance diagram. $\log p_{\text{SO}_2}$ versus $\log p_{\text{O}_2}$ (bar) at 1000 K for the Cu-S-O system (Bale et al., 1986).

mation of each solid phase, always from one mole of the base element Cu, and involving the gaseous species whose pressures are used as the axes (SO_2 and O_2 in this example):



and similarly for the formation of Cu_2S , Cu_2SO_4 and Cu_2SO_5 .

The values of ΔG^0 are obtained from tables of thermodynamic properties. For any given values of p_{SO_2} and p_{O_2} , ΔG for each formation reaction can then be calculated. The stable compound is simply the one with the most negative ΔG . If all the ΔG values are positive, then pure Cu is the stable compound.

By reformulating Eqs. (1-15) to (1-18) in terms of, for example, S_2 and O_2 rather than SO_2 and O_2 , a predominance diagram with $\ln p_{\text{S}_2}$ and $\ln p_{\text{O}_2}$ as axes can be constructed. Logarithms of ratios or products of partial pressures can also be used as axes.

1.3.2 Ellingham Diagrams as Predominance Diagrams

Rather than keeping the temperature constant, we can use it as an axis. Figure 1-2 shows a diagram for the Fe–S–O system in which $RT \ln p_{\text{O}_2}$ is plotted versus T at constant $p_{\text{SO}_2} = 1$ bar. The diagram is of the same topological type as Fig. 1-1.

A similar phase diagram of $RT \ln p_{\text{O}_2}$ versus T for the Cu–O system is shown in

Fig. 1-3. For the formation reaction:



we can write:

$$\Delta G^0 = -RT \ln K = RT \ln (p_{\text{O}_2})_{\text{equilibrium}}$$

$$= \Delta H^0 - T \Delta S^0 \quad (1-20)$$

The diagonal line in Fig. 1-3 is thus a plot of the standard Gibbs energy of formation of Cu_2O versus T . The temperatures indicated by the symbol M and $\boxed{\text{M}}$ are the melting points of Cu and Cu_2O respectively. This line is thus simply a line taken from the well-known *Ellingham Diagram* or ΔG^0 vs. T diagram for the formation of oxides. However, by drawing vertical lines at the melting points of Cu and Cu_2O as shown in Fig. 1-3, we convert the plot to a true phase diagram. Stability domains for Cu(sol), Cu(l), $\text{Cu}_2\text{O}(\text{sol})$, and $\text{Cu}_2\text{O}(\text{l})$ are shown as functions of T and of imposed p_{O_2} . The lines and triple points indicate

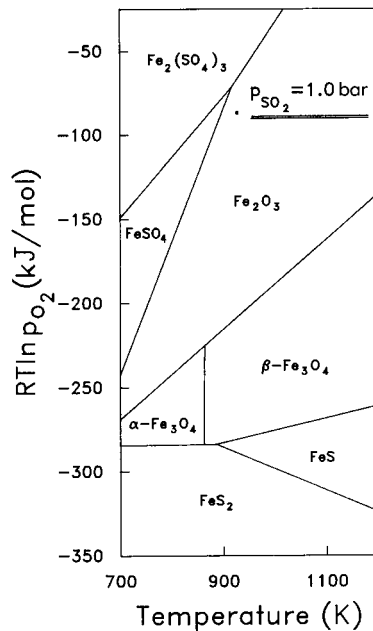


Figure 1-2. Predominance diagram. $RT \ln p_{\text{O}_2}$ versus T at $p_{\text{SO}_2} = 1.0$ bar for the Fe–S–O system.

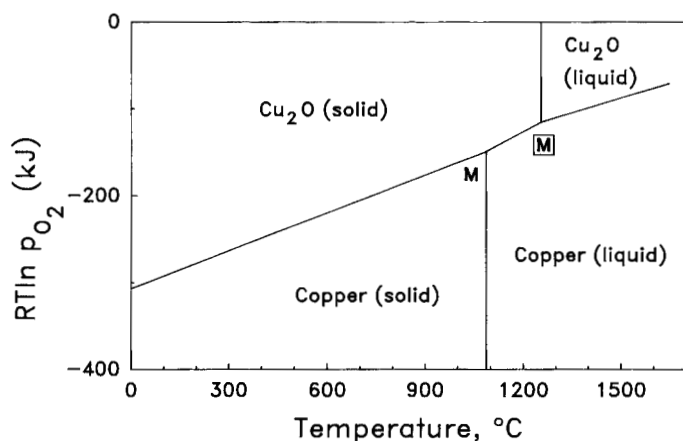


Figure 1-3. Predominance diagram (also known as a Gibbs energy-temperature diagram or Ellingham diagram) for the Cu–O system. Points M and \bar{M} represent the melting points of the metal and oxide respectively.

conditions of two- and three-phase equilibrium.

1.3.3 Discussion of Predominance Diagrams

In this section discussion is limited to the assumption that there is no mutual solubility among the condensed phases. The calculation of predominance phase diagrams in which mutual solubility is taken into account is treated in Sec. 1.9, where the general geometrical rules governing predominance diagrams and their relationship to other types of phase diagrams are discussed.

We frequently encounter predominance diagrams with domains for solid, liquid, and even gaseous compounds which have been calculated *as if* the compounds were immiscible, even though they may actually be partially or even totally miscible. The boundary lines are then no longer phase boundaries, but are lines separating regions in which one species “predominates”. The well known $E-pH$ or Pourbaix diagrams of aqueous chemistry are examples of such predominance diagrams.

Predominance diagrams may also be constructed when there are two or more base elements, as discussed by Bale (1990).

Predominance diagrams have found many applications in the fields of hot corrosion, roasting of ores, chemical vapor deposition, etc. A partial bibliography on their construction and applications includes Yokokawa (1999), Bale (1990), Bale et al. (1986), Kellogg and Basu (1960), Ingraham and Kellogg (1963), Pehlke (1973), Garrels and Christ (1965), Ingraham and Kerby (1967), Pilgrim and Ingraham (1967), Gulbransen and Jansson (1970), Pelton and Thompson (1975), Shatynski (1977), Stringer and Whittle (1975), Spencer and Barin (1979), Chu and Rahmel (1979), and Harshe and Venkatachalam (1984).

1.4 Thermodynamics of Solutions

1.4.1 Gibbs Energy of Mixing

Liquid gold and copper are completely miscible at all compositions. The Gibbs energy of one mole of liquid solution, g^l , at 1400 K is drawn in Fig. 1-4 as a function of composition expressed as *mole fraction*, X_{Cu} , of copper. Note that $X_{Au} = 1 - X_{Cu}$. The curve of g^l varies between the standard molar Gibbs energies of pure liquid Au and Cu, g_{Au}^0 and g_{Cu}^0 .

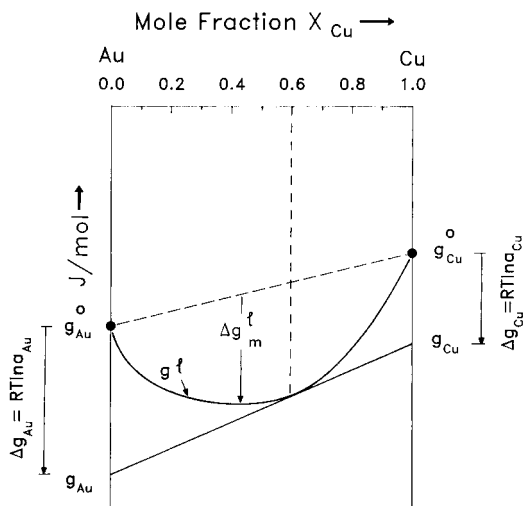
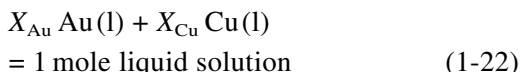


Figure 1-4. Molar Gibbs energy, g^l , of liquid Au–Cu alloys at constant temperature (1400 K) illustrating the tangent construction.

The function Δg_m^l shown on Fig. 1-4 is called the molar *Gibbs energy of mixing* of the liquid solution. It is defined as:

$$\Delta g_m^l = g^l - (X_{\text{Au}} g_{\text{Au}}^0 + X_{\text{Cu}} g_{\text{Cu}}^0) \quad (1-21)$$

It can be seen that Δg_m^l is the Gibbs energy change associated with the isothermal mixing of X_{Au} moles of pure liquid Au and X_{Cu} moles of pure liquid Cu to form one mole of solution:



Note that for the solution to be stable it is necessary that Δg_m^l be negative.

1.4.2 Chemical Potential

The *partial molar Gibbs energy* of component i , g_i , also known as the *chemical potential*, μ_i , is defined as:

$$g_i = \mu_i = (\partial G / \partial n_i)_{T, P, n_j} \quad (1-23)$$

where G is the Gibbs energy of the solution, n_i is the number of moles of compo-

nent i , and the derivative is taken with all $n_j (j \neq i)$ constant.

In the example of the Au–Cu binary liquid solution, $g_{\text{Cu}} = (\partial G^l / \partial n_{\text{Cu}})_{T, P, n_{\text{Au}}}$, where $G^l = (n_{\text{Cu}} + n_{\text{Au}}) g^l$. That is, g_{Cu} , which has units of J/mol, is the rate of change of the Gibbs energy of a solution as Cu is added. It can be seen that g_{Cu} is an intensive property of the solution which depends upon the composition and temperature but not upon the total amount of solution. That is, adding δn_{Cu} moles of copper to a solution of given composition will (in the limit as $\delta n_{\text{Cu}} \rightarrow 0$) result in a change in Gibbs energy, δG , which is independent of the total mass of the solution.

The reason that this property is called a *chemical potential* is illustrated by the following thought experiment. Imagine two systems, I and II, at the same temperature and separated by a membrane that permits only the passage of copper. The chemical potentials of copper in systems I and II are $g_{\text{Cu}}^I = \partial G^I / \partial n_{\text{Cu}}^I$ and $g_{\text{Cu}}^{\text{II}} = \partial G^{\text{II}} / \partial n_{\text{Cu}}^{\text{II}}$. Copper is transferred across the membrane, with $dn^I = -dn^{\text{II}}$. The change in the total Gibbs energy accompanying this transfer is then:

$$dG = d(G^I + G^{\text{II}}) = -(g_{\text{Cu}}^I - g_{\text{Cu}}^{\text{II}}) dn_{\text{Cu}}^{\text{II}} \quad (1-24)$$

If $g_{\text{Cu}}^I > g_{\text{Cu}}^{\text{II}}$, then $d(G^I + G^{\text{II}})$ is negative when $dn_{\text{Cu}}^{\text{II}}$ is positive. That is, the total Gibbs energy will be decreased by a transfer of Cu from system I to system II. Hence, Cu will be transferred spontaneously from a system of higher g_{Cu} to a system of lower g_{Cu} . Therefore g_{Cu} is called the chemical potential of copper.

An important principle of phase equilibrium can now be stated. *When two or more phases are in equilibrium, the chemical potential of any component is the same in all phases.*

1.4.3 Tangent Construction

An important construction is illustrated in Fig. 1-4. If a tangent is drawn to the curve of g^l at a certain composition ($X_{\text{Cu}}=0.6$ in Fig. 1-4), then the intercepts of this tangent on the axes at $X_{\text{Au}}=1$ and $X_{\text{Cu}}=1$ are equal to g_{Au} and g_{Cu} respectively at this composition.

To prove this, we first consider that the Gibbs energy of the solution at constant T and P is a function of n_{Au} and n_{Cu} . Hence:

$$\begin{aligned} dG_{T,P}^l &= \left(\frac{\partial G^l}{\partial n_{\text{Au}}} \right) dn_{\text{Au}} + \left(\frac{\partial G^l}{\partial n_{\text{Cu}}} \right) dn_{\text{Cu}} \\ &= g_{\text{Au}} dn_{\text{Au}} + g_{\text{Cu}} dn_{\text{Cu}} \end{aligned} \quad (1-25)$$

Eq. (1-25) can be integrated as follows:

$$\begin{aligned} \int_0^{G^l} dG^l &= \int_0^{n_{\text{Au}}} g_{\text{Au}} dn_{\text{Au}} + \int_0^{n_{\text{Cu}}} g_{\text{Cu}} dn_{\text{Cu}} \\ G^l &= g_{\text{Au}} n_{\text{Au}} + g_{\text{Cu}} n_{\text{Cu}} \end{aligned} \quad (1-26)$$

where the integration is performed at constant composition so that the intensive properties g_{Au} and g_{Cu} are constant. This integration can be thought of as describing a process in which a pre-mixed solution of constant composition is added to the system, which initially contains no material.

Dividing Eqs. (1-26) and (1-25) by $(n_{\text{Au}} + n_{\text{Cu}})$ we obtain expressions for the molar Gibbs energy and its derivative:

$$g^l = X_{\text{Au}} g_{\text{Au}} + X_{\text{Cu}} g_{\text{Cu}} \quad (1-27)$$

and

$$dg^l = g_{\text{Au}} dX_{\text{Au}} + g_{\text{Cu}} dX_{\text{Cu}} \quad (1-28)$$

Since $dX_{\text{Au}} = -dX_{\text{Cu}}$, it can be seen that Eqs. (1-27) and (1-28) are equivalent to the tangent construction shown in Fig. 1-4.

These equations may also be rearranged to give the following useful expression for a binary system:

$$g_i = g + (1 - X_i) dg/dX_i \quad (1-29)$$

1.4.4 Gibbs–Duhem Equation

Differentiation of Eq. (1-27) yields:

$$\begin{aligned} dg^l &= (X_{\text{Au}} dg_{\text{Au}} + X_{\text{Cu}} dg_{\text{Cu}}) \\ &\quad + (g_{\text{Au}} dX_{\text{Au}} + g_{\text{Cu}} dX_{\text{Cu}}) \end{aligned} \quad (1-30)$$

Comparison with Eq. (1-28) then gives the *Gibbs–Duhem equation* at constant T and P :

$$X_{\text{Au}} dg_{\text{Au}} + X_{\text{Cu}} dg_{\text{Cu}} = 0 \quad (1-31)$$

1.4.5 Relative Partial Properties

The difference between the partial Gibbs energy g_i of a component in solution and the partial Gibbs energy g_i^0 of the same component in a *standard state* is called the *relative partial Gibbs energy* (or *relative chemical potential*), Δg_i . It is most usual to choose as standard state the pure component in the same phase at the same temperature. *The activity a_i of the component relative to the chosen standard state* is then defined in terms of Δg_i by the following equation, as illustrated in Fig. 1-4.

$$\Delta g_i = g_i - g_i^0 = \mu_i - \mu_i^0 = RT \ln a_i \quad (1-32)$$

Note that g_i and μ_i are equivalent symbols, as are g_i^0 and μ_i^0 , see Eq. (1-23).

From Fig. 1-4, it can be seen that:

$$\begin{aligned} \Delta g_m &= X_{\text{Au}} \Delta g_{\text{Au}} + X_{\text{Cu}} \Delta g_{\text{Cu}} \\ &= RT (X_{\text{Au}} \ln a_{\text{Au}} + X_{\text{Cu}} \ln a_{\text{Cu}}) \end{aligned} \quad (1-33)$$

The Gibbs energy of mixing can be divided into enthalpy and entropy terms, as can the relative partial Gibbs energies:

$$\Delta g_m = \Delta h_m - T \Delta s_m \quad (1-34)$$

$$\Delta g_i = \Delta h_i - T \Delta s_i \quad (1-35)$$

Hence, the enthalpy and entropy of mixing may be expressed as:

$$\Delta h_m = X_{\text{Au}} \Delta h_{\text{Au}} + X_{\text{Cu}} \Delta h_{\text{Cu}} \quad (1-36)$$

$$\Delta s_m = X_{\text{Au}} \Delta s_{\text{Au}} + X_{\text{Cu}} \Delta s_{\text{Cu}} \quad (1-37)$$

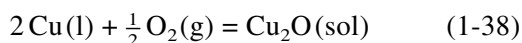
and tangent constructions similar to that of Fig. 1-4 can be used to relate the relative *partial enthalpies and entropies* Δh_i and Δs_i to the *integral molar enthalpy of mixing* Δh_m and *integral molar entropy of mixing* Δs_m respectively.

1.4.6 Activity

The activity of a component in a solution was defined by Eq. (1-32).

Since a_i varies monotonically with g_i it follows that *when two or more phases are in equilibrium the activity of any component is the same in all phases*, provided that the activity in every phase is expressed with respect to the same standard state.

The use of activities in calculations of chemical equilibrium conditions is illustrated by the following example. A liquid solution of Au and Cu at 1400 K with $X_{\text{Cu}}=0.6$ is exposed to an atmosphere in which the oxygen partial pressure is $p_{\text{O}_2}=10^{-4}$ bar. Will Cu_2O be formed? The reaction is:



where the Cu(l) is in solution. If the reaction proceeds with the formation of dn moles of Cu_2O , then $2dn$ moles of Cu are consumed, and the Gibbs energy of the Au–Cu solution changes by

$$-2(dG^1/dn_{\text{Cu}})dn$$

The total Gibbs energy then varies as:

$$\begin{aligned} dG/dn &= g_{\text{Cu}_2\text{O}} - \frac{1}{2}g_{\text{O}_2} - 2(dG^1/dn_{\text{Cu}}) \\ &= g_{\text{Cu}_2\text{O}} - \frac{1}{2}g_{\text{O}_2} - 2g_{\text{Cu}} \\ &= (g_{\text{Cu}_2\text{O}}^0 - \frac{1}{2}g_{\text{O}_2}^0 - 2g_{\text{Cu}}^0) \\ &\quad - \frac{1}{2}RT \ln p_{\text{O}_2} - 2RT \ln a_{\text{Cu}} \\ &= \Delta G^0 + RT \ln (p_{\text{O}_2}^{-1/2} a_{\text{Cu}}^2) \\ &= \Delta G \end{aligned} \quad (1-39)$$

For the reaction, Eq. (1-38), at 1400 K, $\Delta G^0 = -68.35$ kJ (Barin et al., 1977). The activity of Cu in the liquid alloy at $X_{\text{Cu}}=0.6$ is $a_{\text{Cu}}=0.43$ (Hultgren et al., 1973). Substitution into Eq. (1-39) with $p_{\text{O}_2}=10^{-4}$ bar gives:

$$dG/dn = \Delta G = -50.84 \text{ kJ}$$

Hence under these conditions the reaction entails a decrease in the total Gibbs energy and so the copper will be oxidized.

1.4.7 Ideal Raoultian Solutions

An *ideal solution* or *Raoultian solution* is usually defined as one in which the activity of a component is equal to its mole fraction:

$$a_i^{\text{ideal}} = X_i \quad (1-40)$$

(With a judicious choice of standard state, this definition can also encompass ideal Henrian solutions, as discussed in Sec. 1.5.11.)

However, this Raoultian definition of ideality is generally only useful for simple substitutional solutions. There are more useful definitions for other types of solutions such as interstitial solutions, ionic solutions, solutions of defects, polymer solutions, etc. That is, the most convenient definition of ideality depends upon the solution model. This subject will be discussed in Sec. 1.10. In the present section, Eq. (1-40) for an ideal substitutional solution will be developed with the Au–Cu solution as example.

In the ideal substitutional solution model it is assumed that Au and Cu atoms are nearly alike, with nearly identical radii and electronic structures. This being the case, there will be no change in bonding energy or volume upon mixing, so that the enthalpy of mixing is zero:

$$\Delta h_m^{\text{ideal}} = 0 \quad (1-41)$$

Furthermore, and for the same reason, the Au and Cu atoms will be randomly distributed over the lattice sites. (In the case of a liquid solution we can think of the “lattice sites” as the instantaneous atomic positions.)

For a random distribution of N_{Au} gold atoms and N_{Cu} copper atoms over $(N_{\text{Au}} + N_{\text{Cu}})$ sites, Boltzmann's equation can be used to calculate the configurational entropy of the solution. This is the entropy associated with the spatial distribution of the particles:

$$S^{\text{config}} = k_B \ln (N_{\text{Au}} + N_{\text{Cu}})! / N_{\text{Au}}! N_{\text{Cu}}! \quad (1-42)$$

where k_B is Boltzmann's constant. The configurational entropies of pure Au and Cu are zero. Hence the configurational entropy of mixing, ΔS^{config} , will be equal to S^{config} . Furthermore, because of the assumed close similarity of Au and Cu, there will be no non-configurational contribution to the entropy of mixing. Hence, the entropy of mixing will be equal to S^{config} . Applying Stirling's approximation, which states that $\ln N! = [(N \ln N) - N]$ if N is large, yields:

$$\Delta S_m^{\text{ideal}} = S^{\text{config}} = -k_B (N_{\text{Au}} + N_{\text{Cu}}) \times \left(N_{\text{Au}} \ln \frac{N_{\text{Au}}}{N_{\text{Au}} + N_{\text{Cu}}} + N_{\text{Cu}} \ln \frac{N_{\text{Cu}}}{N_{\text{Au}} + N_{\text{Cu}}} \right) \quad (1-43)$$

For one mole of solution, $(N_{\text{Au}} + N_{\text{Cu}}) = N^0$, where N^0 = Avogadro's number. We also note that $(k_B N^0)$ is equal to the ideal gas constant R . Hence:

$$\Delta S_m^{\text{ideal}} = -R (X_{\text{Au}} \ln X_{\text{Au}} + X_{\text{Cu}} \ln X_{\text{Cu}}) \quad (1-44)$$

Therefore, since the ideal enthalpy of mixing is zero:

$$\Delta g_m^{\text{ideal}} = RT (X_{\text{Au}} \ln X_{\text{Au}} + X_{\text{Cu}} \ln X_{\text{Cu}}) \quad (1-45)$$

By comparing Eqs. (1-33) and (1-45) we obtain:

$$\Delta g_i^{\text{ideal}} = RT \ln a_i^{\text{ideal}} = RT \ln X_i \quad (1-46)$$

Hence Eq. (1-40) has been demonstrated for an ideal substitutional solution.

1.4.8 Excess Properties

In reality, Au and Cu atoms are not identical, and so Au–Cu solutions are not perfectly ideal. The difference between a solution property and its value in an ideal solution is called an *excess property*. The *excess Gibbs energy*, for example, is defined as:

$$g^E = \Delta g_m - \Delta g_m^{\text{ideal}} \quad (1-47)$$

Since the ideal enthalpy of mixing is zero, the excess enthalpy is equal to the enthalpy of mixing:

$$h^E = \Delta h_m - \Delta h_m^{\text{ideal}} = \Delta h_m \quad (1-48)$$

Hence:

$$g^E = h^E - T s^E = \Delta h_m - T s^E \quad (1-49)$$

Excess partial properties are defined similarly:

$$g_i^E = \Delta g_i - \Delta g_i^{\text{ideal}} = RT \ln a_i - RT \ln X_i \quad (1-50)$$

$$s_i^E = \Delta s_i - \Delta s_i^{\text{ideal}} = \Delta s_i + R \ln X_i \quad (1-51)$$

Also:

$$g_i^E = h_i^E - T s_i^E = \Delta h_i - T s_i^E \quad (1-52)$$

Equations analogous to Eqs. (1-33), (1-36) and (1-37) relate the integral and partial excess properties. For example, in Au–Cu solutions:

$$g^E = X_{\text{Au}} g_{\text{Au}}^E + X_{\text{Cu}} g_{\text{Cu}}^E \quad (1-53)$$

$$s^E = X_{\text{Au}} s_{\text{Au}}^E + X_{\text{Cu}} s_{\text{Cu}}^E \quad (1-54)$$

Tangent constructions similar to that of Fig. 1-4 can thus also be employed for excess properties, and an equation analogous

to Eq. (1-29) can be written:

$$g_i^E = g^E + (1 - X_i) dg^E/dX_i \quad (1-55)$$

The Gibbs–Duhem equation, Eq. (1-31), also applies to excess properties:

$$X_{Au} dg_{Au}^E + X_{Cu} dg_{Cu}^E = 0 \quad (1-56)$$

In Au–Cu alloys, g^E is negative. That is, Δg_m is more negative than $\Delta g_m^{\text{ideal}}$ and so the solution is thermodynamically more stable than an ideal solution. We say that Au–Cu solutions exhibit *negative deviations from ideality*. If $g^E > 0$, then the solution is less stable than an ideal solution and is said to exhibit *positive deviations*.

1.4.9 Activity Coefficient

The *activity coefficient* of a component in a solution is defined as:

$$\gamma_i = a_i/X_i \quad (1-57)$$

From Eq. (1-50):

$$g_i^E = RT \ln \gamma_i \quad (1-58)$$

In an ideal solution $\gamma_i = 1$ and $g_i^E = 0$ for all components. If $\gamma_i < 1$, then $g_i^E < 0$ and by

Eq. (1-50), $\Delta g_i < \Delta g_i^{\text{ideal}}$. That is, the component i is more stable in the solution than it would be in an ideal solution of the same composition. If $\gamma_i > 1$, then $g_i^E > 0$ and the driving force for the component to enter into solution is less than in the case of an ideal solution.

1.4.10 Multicomponent Solutions

The equations of this section were derived with a binary solution as an example. However, the equations apply equally to systems of any number of components. For instance, in a solution of components A–B–C–D ..., Eq. (1-33) becomes:

$$\Delta g_m = X_A \Delta g_A + X_B \Delta g_B + X_C \Delta g_C + X_D \Delta g_D + \dots \quad (1-59)$$

1.5 Binary Phase Diagrams

1.5.1 Systems with Complete Solid and Liquid Miscibility

The temperature–composition (T – X) phase diagram of the CaO–MnO system is shown in Fig. 1-5 (Schenck et al., 1964; Wu, 1990). The abscissa is the composi-

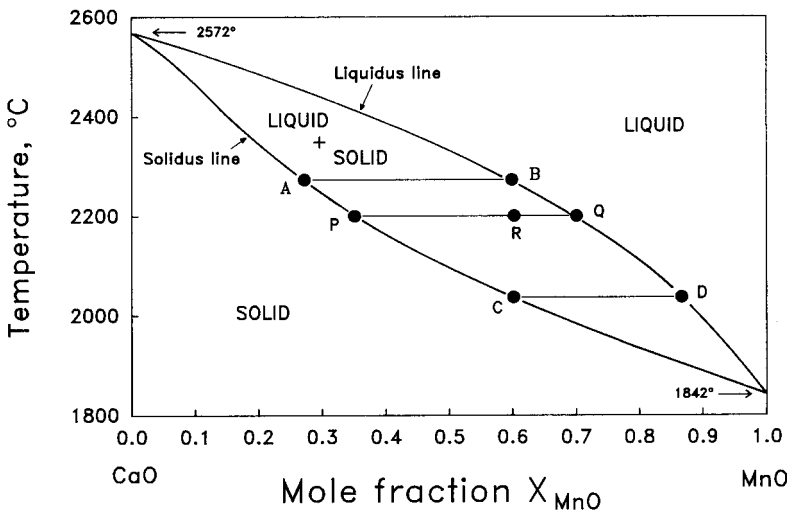


Figure 1-5. Phase diagram of the CaO–MnO system at $P = 1$ bar (after Schenck et al., 1964, and Wu, 1990).

tion, expressed as mole fraction of MnO, X_{MnO} . Note that $X_{\text{MnO}} = 1 - X_{\text{CaO}}$. Phase diagrams are also often drawn with the composition axis expressed as weight percent.

At all compositions and temperatures in the area above the line labelled liquidus, a single-phase liquid solution will be observed, while at all compositions and temperatures below the line labelled solidus, there will be a single-phase solid solution. A sample at equilibrium at a temperature and overall composition between these two curves will consist of a mixture of solid and liquid phases, the compositions of which are given by the liquidus and solidus compositions at that temperature. For example, a sample of overall composition $X_{\text{MnO}} = 0.60$ at $T = 2200^\circ\text{C}$ (at point R in Fig. 1-5) will consist, at equilibrium, of a mixture of liquid of composition $X_{\text{MnO}} = 0.70$ (point Q) and solid of composition $X_{\text{MnO}} = 0.35$ (point P).

The line PQ is called a *tie-line* or *conode*. As the overall composition is varied at 2200°C between points P and Q , the compositions of the solid and liquid phases remain fixed at P and Q , and only the relative proportions of the two phases change. From a simple mass balance, we can derive the *lever rule* for binary systems: (moles of liquid)/(moles of solid) = PR/RQ . Hence, at 2200°C a sample with overall composition $X_{\text{MnO}} = 0.60$ consists of liquid and solid phases in the molar ratio $(0.60 - 0.35)/(0.70 - 0.60) = 2.5$. Were the composition axis expressed as weight percent, then the lever rule would give the weight ratio of the two phases.

Suppose that a liquid CaO–MnO solution with composition $X_{\text{MnO}} = 0.60$ is cooled very slowly from an initial temperature of about 2500°C . When the temperature has decreased to the liquidus temperature 2270°C (point B), the first solid appears, with a composition at point A

($X_{\text{MnO}} = 0.28$). As the temperature is decreased further, solid continues to precipitate with the compositions of the two phases at any temperature being given by the liquidus and solidus compositions at that temperature and with their relative proportions being given by the lever rule. Solidification is complete at 2030°C , the last liquid to solidify having composition $X_{\text{MnO}} = 0.60$ (point C).

The process just described is known as equilibrium cooling. At any temperature during equilibrium cooling the solid phase has a uniform (homogeneous) composition. In the preceding example, the composition of the solid phase during cooling varies along the line APC . Hence, in order for the solid grains to have a uniform composition at any temperature, diffusion of CaO from the center to the surface of the growing grains must occur. Since solid-state diffusion is a relatively slow process, equilibrium cooling conditions are only approached if the temperature is decreased very slowly. If a sample of composition $X_{\text{MnO}} = 0.60$ is cooled very rapidly from the liquid, concentration gradients will be observed in the solid grains, with the concentration of MnO increasing towards the surface from a minimum of $X_{\text{MnO}} = 0.28$ (point A) at the center. Furthermore, in this case solidification will not be complete at 2030°C since at 2030°C the average concentration of MnO in the solid particles will be less than $X_{\text{MnO}} = 0.60$. These considerations are discussed more fully in Chapter 2 of this volume (Müller-Krumbhaar et al., 2001).

At $X_{\text{MnO}} = 0$ and $X_{\text{MnO}} = 1$ in Fig. 1-5 the liquidus and solidus curves meet at the equilibrium melting points, or *temperatures of fusion* of CaO and MnO, which are $T_{\text{f(CaO)}}^0 = 2572^\circ\text{C}$, $T_{\text{f(MnO)}}^0 = 1842^\circ\text{C}$.

The phase diagram is influenced by the total pressure, P . Unless otherwise stated,

T - X diagrams are usually presented for $P = \text{const.} = 1 \text{ bar}$. For equilibria involving only solid and liquid phases, the phase boundaries are typically shifted only by the order of a few hundredths of a degree per bar change in P . Hence, the effect of pressure upon the phase diagram is generally negligible unless the pressure is of the order of hundreds of bars. On the other hand, if gaseous phases are involved then the effect of pressure is very important. The effect of pressure will be discussed in Sec. 1.5.3.

1.5.2 Thermodynamic Origin of Phase Diagrams

In this section we first consider the thermodynamic origin of simple “lens-shaped” phase diagrams in binary systems with complete liquid and solid miscibility.

An example of such a diagram was given in Fig. 1-5. Another example is the Ge-Si phase diagram in the lowest panel of Fig. 1-6 (Hansen, 1958). In the upper three panels of Fig. 1-6, the molar Gibbs energies of the solid and liquid phases, g^s and g^l , at three temperatures are shown to scale. As illustrated in the top panel, g^s varies with composition between the standard molar Gibbs energies of pure solid Ge and of pure solid Si, $g_{\text{Ge}}^{0(s)}$ and $g_{\text{Si}}^{0(s)}$, while g^l varies between the standard molar Gibbs energies of the pure liquid components $g_{\text{Ge}}^{0(l)}$ and $g_{\text{Si}}^{0(l)}$.

The difference between $g_{\text{Ge}}^{0(l)}$ and $g_{\text{Si}}^{0(s)}$ is equal to the standard molar Gibbs energy of fusion (melting) of pure Si, $\Delta g_{\text{f(Si)}}^0 = (g_{\text{Si}}^{0(l)} - g_{\text{Si}}^{0(s)})$. Similarly, for Ge, $\Delta g_{\text{f(Ge)}}^0 = (g_{\text{Ge}}^{0(l)} - g_{\text{Ge}}^{0(s)})$. The Gibbs energy of fusion of a pure component may be written as:

$$\Delta g_{\text{f}}^0 = \Delta h_{\text{f}}^0 - T \Delta s_{\text{f}}^0 \quad (1-60)$$

where Δh_{f}^0 and Δs_{f}^0 are the standard molar enthalpy and entropy of fusion.

Since, to a first approximation, Δh_{f}^0 and Δs_{f}^0 are independent of T , Δg_{f}^0 is approximately a linear function of T . If $T > T_{\text{f}}^0$, then Δg_{f}^0 is negative. If $T < T_{\text{f}}^0$, then Δg_{f}^0 is positive. Hence, as seen in Fig. 1-6, as T decreases, the g^s curve descends relative to g^l . At 1500°C , $g^l < g^s$ at all compositions. Therefore, by the principle that a system always seeks the state of minimum Gibbs energy at constant T and P , the liquid phase is stable at all compositions at 1500°C .

At 1300°C , the curves of g^s and g^l cross. The line $P_1 Q_1$, which is the *common tangent* to the two curves, divides the composition range into three sections. For compositions between pure Ge and P_1 , a single-phase liquid is the state of minimum Gibbs energy. For compositions between Q_1 and pure Si, a single-phase solid solution is the stable state. Between P_1 and Q_1 , a total Gibbs energy lying on the tangent line $P_1 Q_1$ may be realized if the system adopts a state consisting of two phases with compositions at P_1 and Q_1 and with relative proportions given by the lever rule. Since the tangent line $P_1 Q_1$ lies below both g^s and g^l , this two-phase state is more stable than either phase alone. Furthermore, no other line joining any point on g^l to any point on g^s lies below the line $P_1 Q_1$. Hence, this line represents the true equilibrium state of the system, and the compositions P_1 and Q_1 are the liquidus and solidus compositions at 1300°C .

As T is decreased to 1100°C , the points of common tangency are displaced to higher concentrations of Ge. For $T < 937^\circ\text{C}$, $g^s < g^l$ at all compositions.

It was shown in Fig. 1-4 that if a tangent is drawn to a Gibbs energy curve, then the intercept of this tangent on the axis at $X_i = 1$ is equal to the partial Gibbs energy or chemical potential g_i of component i . The *common tangent construction* of Fig. 1-6 thus ensures that the chemical potentials of

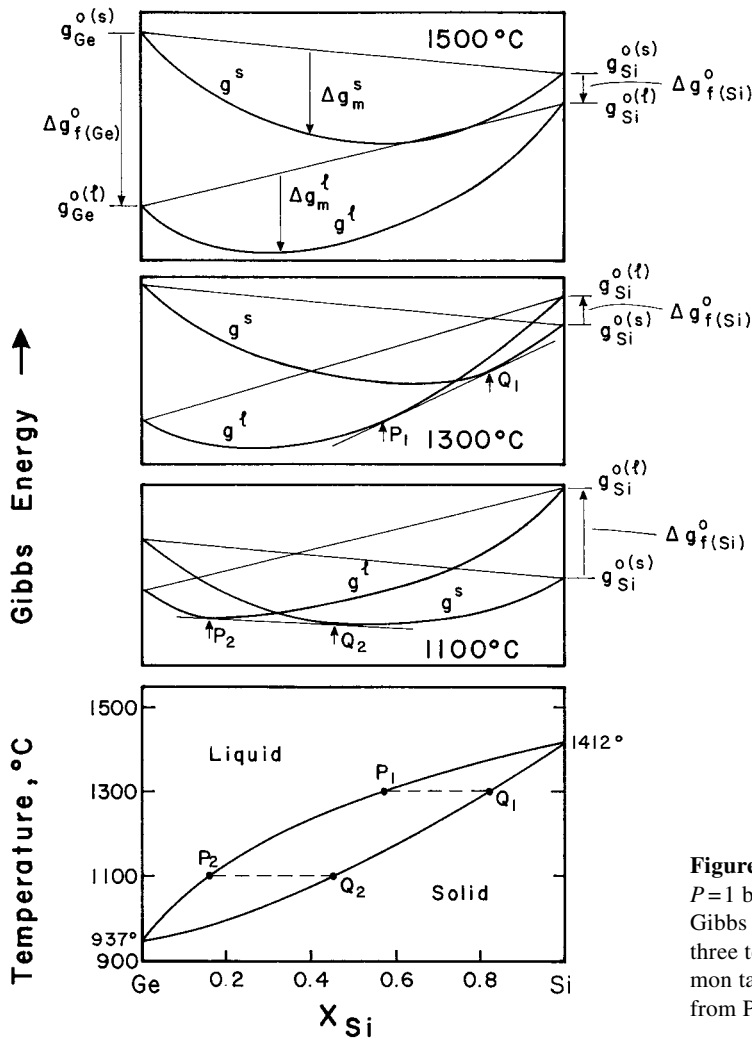


Figure 1-6. Ge–Si phase diagram at $P=1$ bar (after Hansen, 1958) and Gibbs energy composition curves at three temperatures, illustrating the common tangent construction (reprinted from Pelton, 1983).

Ge and Si are equal in the solid and liquid phases at equilibrium. That is:

$$g_{\text{Ge}}^{\text{l}} = g_{\text{Ge}}^{\text{s}} \quad (1-61)$$

$$g_{\text{Si}}^{\text{l}} = g_{\text{Si}}^{\text{s}} \quad (1-62)$$

This equality of chemical potentials was shown in Sec. 1.4.2 to be the criterion for phase equilibrium. That is, the common tangent construction simultaneously minimizes the total Gibbs energy and ensures the equality of the chemical potentials, thereby showing that these are equivalent criteria for equilibrium between phases.

If we rearrange Eq. (1-61), subtracting the Gibbs energy of fusion of pure Ge, $\Delta g_{\text{f(Ge)}}^0 = (g_{\text{Ge}}^{0(\text{l})} - g_{\text{Ge}}^{0(\text{s})})$, from each side, we get:

$$(g_{\text{Ge}}^{\text{l}} - g_{\text{Ge}}^{0(\text{l})}) - (g_{\text{Ge}}^{\text{s}} - g_{\text{Ge}}^{0(\text{s})}) = - (g_{\text{Ge}}^{0(\text{l})} - g_{\text{Ge}}^{0(\text{s})}) \quad (1-63)$$

Using Eq. (1-32), we can write Eq. (1-63) as:

$$\Delta g_{\text{Ge}}^{\text{l}} - \Delta g_{\text{Ge}}^{\text{s}} = - \Delta g_{\text{f(Ge)}}^0 \quad (1-64)$$

or

$$RT \ln a_{\text{Ge}}^{\text{l}} - RT \ln a_{\text{Ge}}^{\text{s}} = - \Delta g_{\text{f(Ge)}}^0 \quad (1-65)$$

where a_{Ge}^l is the activity of Ge (with respect to pure liquid Ge as standard state) in the liquid solution on the liquidus, and a_{Ge}^s is the activity of Ge (with respect to pure solid Ge as standard state) in the solid solution on the solidus. Starting with Eq. (1-62), we can derive a similar expression for the other component:

$$RT \ln a_{\text{Si}}^l - RT \ln a_{\text{Si}}^s = -\Delta g_{\text{f(Si)}}^0 \quad (1-66)$$

Eqs. (1-65) and (1-66) are equivalent to the common tangent construction.

It should be noted that absolute values of Gibbs energies cannot be defined. Hence, the relative positions of $g_{\text{Ge}}^{0(l)}$ and $g_{\text{Si}}^{0(l)}$ in Fig. 1-6 are completely arbitrary. However, this is immaterial for the preceding discussion, since displacing both $g_{\text{Si}}^{0(l)}$ and $g_{\text{Si}}^{0(s)}$ by the same arbitrary amount relative to $g_{\text{Ge}}^{0(l)}$ and $g_{\text{Ge}}^{0(s)}$ will not alter the compositions of the points of common tangency.

It should also be noted that in the present discussion of equilibrium phase diagrams we are assuming that the physical dimensions of the single-phase regions in the system are sufficiently large that surface (interfacial) energy contributions to the Gibbs energy can be neglected. For very fine grain sizes in the sub-micron range, however, surface energy effects can noticeably influence the phase boundaries.

The shape of the two-phase (solid + liquid) “lens” on the phase diagram is determined by the Gibbs energies of fusion, Δg_{f}^0 , of the components and by the mixing terms, Δg^s and Δg^l . In order to observe how the shape is influenced by varying Δg_{f}^0 , let us consider a hypothetical system A–B in which Δg^s and Δg^l are ideal Raoultian (Eq. (1-45)). Let $T_{\text{f(A)}}^0 = 800$ K and $T_{\text{f(B)}}^0 = 1200$ K. Furthermore, assume that the entropies of fusion of A and B are equal and temperature-independent. The enthalpies of fusion are then given from Eq. (1-60) by the expression $\Delta h_{\text{f}}^0 = T_{\text{f}}^0 \Delta s_{\text{f}}^0$ since

$\Delta g_{\text{f}}^0 = 0$ when $T = T_{\text{f}}^0$. Calculated phase diagrams for $\Delta s_{\text{f}}^0 = 3, 10$ and 30 J/mol K are shown in Fig. 1-7. A value of $\Delta s_{\text{f}}^0 \approx 10$ is typical of most metals. However, when the components are ionic compounds such as ionic oxides, halides, etc., Δs_{f}^0 can be significantly larger since there are several ions per formula unit. Hence, two-phase “lenses” in binary ionic salt or oxide phase diagrams tend to be “fatter” than those encountered in alloy systems. If we are considering vapor–liquid equilibria rather than solid–liquid equilibria, then the shape is determined by the entropy of vaporization, Δs_{v}^0 . Since Δs_{v}^0 is usually an order of magnitude larger than Δs_{f}^0 , two-phase (liquid + vapor) lenses tend to be

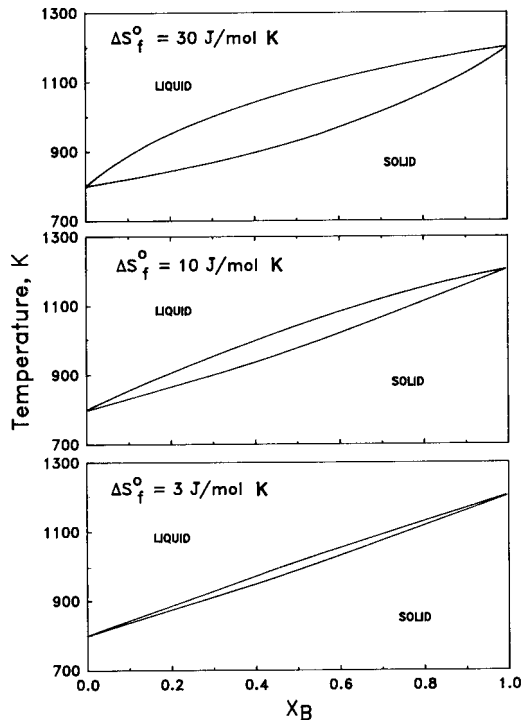


Figure 1-7. Phase diagram of a system A–B with ideal solid and liquid solutions. Melting points of A and B are 800 and 1200 K, respectively. Diagrams are calculated for entropies of fusion $\Delta s_{\text{f(A)}}^0 = \Delta s_{\text{f(B)}}^0 = 3, 10$ and 30 J/mol K.

very wide. For equilibria between two solid solutions of different crystal structure, the shape is determined by the entropy of solid–solid transformation, which is usually smaller than the entropy of fusion by approximately an order of magnitude. Therefore two-phase (solid+solid) lenses tend to be very narrow.

1.5.3 Pressure–Composition Phase Diagrams

Let us consider liquid–vapor equilibrium with complete miscibility, using as an example the Zn–Mg system. Curves of g^v and g^l can be drawn at any given T and P , as in the upper panel of Fig. 1-8, and the

common tangent construction then gives the equilibrium vapor and liquid compositions. The phase diagram depends upon the Gibbs energies of vaporization of the components $\Delta g_{v(\text{Zn})}$ and $\Delta g_{v(\text{Mg})}$ as shown in Fig. 1-8.

To generate the isothermal pressure–composition (P – X) phase diagram in the lower panel of Fig. 1-8 we require the Gibbs energies of vaporization as functions of P . Assuming monatomic ideal vapors and assuming that pressure has negligible effect upon the Gibbs energy of the liquid, we can write:

$$\Delta g_{v(i)} = \Delta g_{v(i)}^0 + RT \ln P \quad (1-67)$$

where $\Delta g_{v(i)}$ is the standard Gibbs energy of vaporization (when $P=1$ bar), which is given by:

$$\Delta g_{v(i)}^0 = \Delta h_{v(i)}^0 - T \Delta s_{v(i)}^0 \quad (1-68)$$

For example, the enthalpy of vaporization of Zn is $\Delta h_{v(\text{Zn})}^0 = 115\,300$ J/mol at its normal boiling point of 1180 K (Barin et al., 1977). Assuming that Δh_v^0 is independent of T , we calculate from Eq. (1-68) that $\Delta s_{v(\text{Zn})}^0 = 115\,300/1180 = 97.71$ J/mol K. From Eq. (1-67), $\Delta g_{v(\text{Zn})}$ at any T and P is thus given by:

$$\Delta g_{v(\text{Zn})} = (115\,300 - 97.71 T) + RT \ln P \quad (1-69)$$

A similar expression can be derived for the other component Mg.

At constant temperature, then, the curve of g^v in Fig. 1-8 descends relative to g^l as the pressure is lowered, and the P – X phase diagram is generated by the common tangent construction. The diagram at 1250 K in Fig. 1-8 was calculated under the assumption of ideal liquid and vapor mixing ($g^{E(l)} = 0$, $g^{E(v)} = 0$).

P – X phase diagrams involving liquid–solid or solid–solid equilibria can be calculated in a similar fashion through the fol-

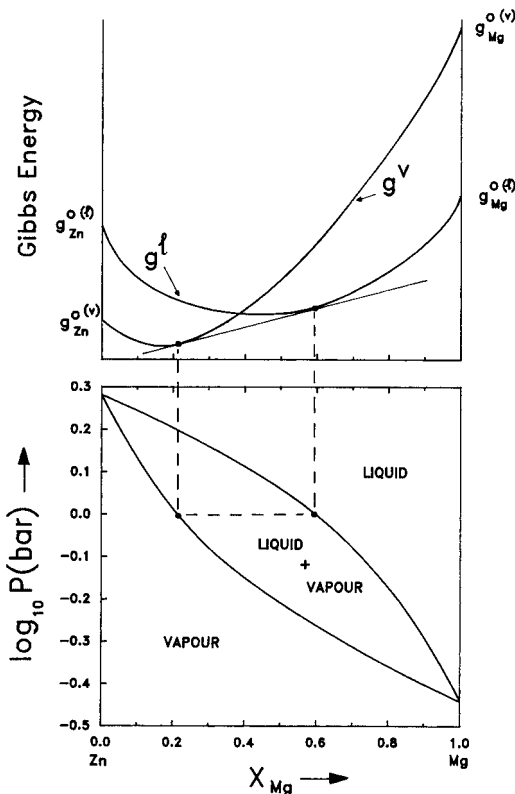


Figure 1-8. Pressure–composition phase diagram of the Zn–Mg system at 1250 K calculated for ideal vapor and liquid solutions. Upper panel illustrates common tangent construction at a constant pressure.

lowing general equation, which gives the effect of pressure upon the Gibbs energy change for the transformation of one mole of pure component i from an α -phase to a β -phase:

$$\Delta g_{\alpha \rightarrow \beta} = \Delta g_{\alpha \rightarrow \beta}^0 + \int_{P=1}^P (\nu_i^\beta - \nu_i^\alpha) dP \quad (1-70)$$

where $\Delta g_{\alpha \rightarrow \beta}^0$ is the standard ($P=1$ bar) Gibbs energy of transformation, and ν_i^β and ν_i^α are the molar volumes.

1.5.4 Minima and Maxima in Two-Phase Regions

As discussed in Sec. 1.4.8, the Gibbs energy of mixing Δg_m may be expressed as the sum of an ideal term $\Delta g_m^{\text{ideal}}$ and an excess term g^E . As has just been shown in Sec. 1.5.2, if Δg_m^s and Δg_m^l for the solid and liquid phases are both ideal, then a “lens-shaped” two-phase region always results. However in most systems even approximately ideal behavior is the exception rather than the rule.

Curves of g^s and g^l for a hypothetical system A–B are shown schematically in Fig. 1-9 at a constant temperature (below the melting points of pure A and B) such

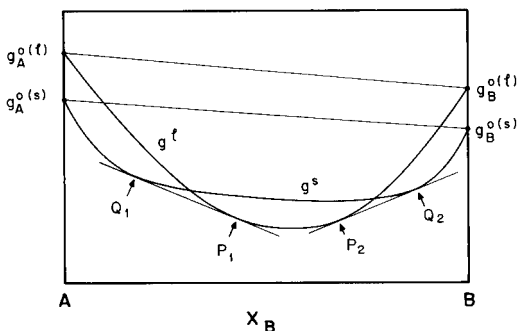


Figure 1-9. Isothermal Gibbs energy-composition curves for solid and liquid phases in a system A–B in which $g^{E(l)} > g^{E(s)}$. A phase diagram of the type of Fig. 1-10 results.

that the solid state is the stable state for both pure components. However, in this system $g^{E(l)} < g^{E(s)}$, so that g^s presents a flatter curve than does g^l and there exists a central composition region in which $g^l < g^s$. Hence, there are two common tangent lines, P_1Q_1 and P_2Q_2 . Such a situation gives rise to a phase diagram with a minimum in the two-phase region, as observed in the Na_2CO_3 – K_2CO_3 system (Dessureault et al., 1990) shown in Fig. 1-10. At a composition and temperature corresponding to the minimum point, liquid and solid of the same composition exist in equilibrium.

A two-phase region with a minimum point as in Fig. 1-10 may be thought of as a two-phase “lens” which has been “pushed down” by virtue of the fact that the liquid is relatively more stable than the solid. Thermodynamically, this relative stability is expressed as $g^{E(l)} < g^{E(s)}$.

Conversely, if $g^{E(l)} > g^{E(s)}$ to a sufficient extent, then a two-phase region with a maximum will result. Such maxima in (liquid + solid) or (solid + solid) two-phase regions are nearly always associated with the existence of an intermediate phase, as will be discussed in Sec. 1.5.10.

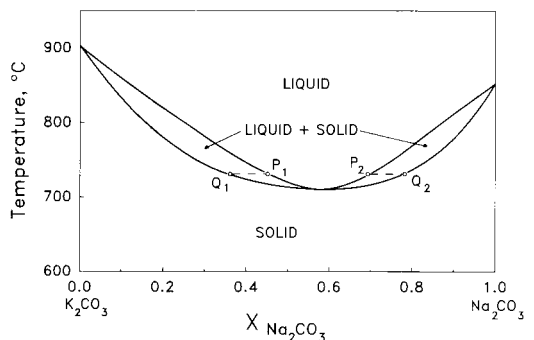


Figure 1-10. Phase diagram of the K_2CO_3 – Na_2CO_3 system at $P=1$ bar (Dessureault et al., 1990).

1.5.5 Miscibility Gaps

If $g^E > 0$, then the solution is thermodynamically less stable than an ideal solution. This can result from a large difference in size of the component atoms, ions or molecules, which will lead to a (positive) lattice strain energy, or from differences in electronic structure, or from other factors.

In the Au–Ni system, g^E is positive in the solid phase. In the top panel of Fig. 1-11, $g^{E(s)}$ is plotted at 1200 K (Hultgren et al., 1973) and the ideal Gibbs energy of mixing, $\Delta g_m^{\text{ideal}}$, is also plotted at 1200 K. The sum of these two terms is the Gibbs energy of mixing of the solid solution, Δg_m^s , which is plotted at 1200 K as well as at other temperatures in the central panel of Fig. 1-11. Now, from Eq. (1-45), $\Delta g_m^{\text{ideal}}$ is always negative and varies directly with T , whereas g^E varies less rapidly with temperature. As a result, the sum $\Delta g_m^s = \Delta g_m^{\text{ideal}} + g^E$ becomes less negative as T decreases. However, the limiting slopes to the $\Delta g_m^{\text{ideal}}$ curve at $X_{\text{Au}} = 1$ and $X_{\text{Ni}} = 1$ are both infinite, whereas the limiting slopes of g^E are always finite (Henry's Law). Hence, Δg_m^s will always be negative as $X_{\text{Au}} \rightarrow 1$ and $X_{\text{Ni}} \rightarrow 1$ no matter how low the temperature. As a result, below a certain temperature the curve of Δg_m^s will exhibit two negative “humps”. Common tangent lines P_1Q_1 , P_2Q_2 , P_3Q_3 to the two humps at different temperatures define the ends of tie-lines of a two-phase solid–solid miscibility gap in the Au–Ni phase diagram, which is shown in the lower panel in Fig. 1-11 (Hultgren et al., 1973). The peak of the gap occurs at the *critical* or *consolute* temperature and composition, T_c and X_c .

When $g^{E(s)}$ is positive for the solid phase in a system it is usually also the case that $g^{E(l)} < g^{E(s)}$ since the unfavorable factors (such as a difference in atomic dimensions) which are causing $g^{E(s)}$ to be positive will

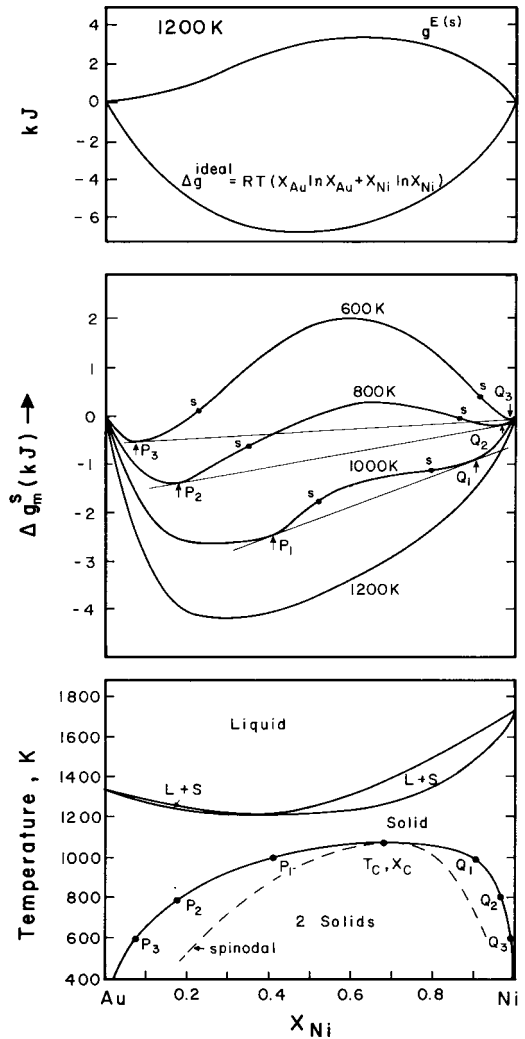


Figure 1-11. Phase diagram (after Hultgren et al., 1973) and Gibbs energy–composition curves of solid solutions for the Au–Ni system at $P = 1$ bar. Letters “s” indicate spinodal points (Reprinted from Pelton, 1983).

have less of an effect upon $g^{E(l)}$ in the liquid phase owing to the greater flexibility of the liquid structure to accommodate different atomic sizes, valencies, etc. Hence, a solid–solid miscibility gap is often associated with a minimum in the two-phase (solid + liquid) region, as is the case in the Au–Ni system.

Below the critical temperature the curve of Δg_m^s exhibits two inflection points, indicated by the letter “s” in Fig. 1-11. These are known as the *spinodal points*. On the phase diagram their locus traces out the *spinodal curve* (Fig. 1-11). The spinodal curve is not part of the equilibrium phase diagram, but it is important in the kinetics of phase separation, as discussed in Chapter 6 (Binder and Fratzl, 2001).

1.5.6 Simple Eutectic Systems

The more positive g^E is in a system, the higher is T_c and the wider is the miscibility

gap at any temperature. Suppose that $g^{E(s)}$ is so positive that T_c is higher than the minimum in the (solid + liquid) region. The result will be a phase diagram such as that of the MgO–CaO system shown in Fig. 1-12 (Doman et al., 1963; Wu, 1990).

The lower panel of Fig. 1-12 shows the Gibbs energy curves at 2450 °C. The two common tangents define two two-phase regions. As the temperature is decreased below 2450 °C, the g^s curve descends relative to g^l and the two points of tangency P_1 and P_2 approach each other until, at $T = 2374$ °C, P_1 and P_2 become coincident at the composition E. That is, at $T = 2374$ °C

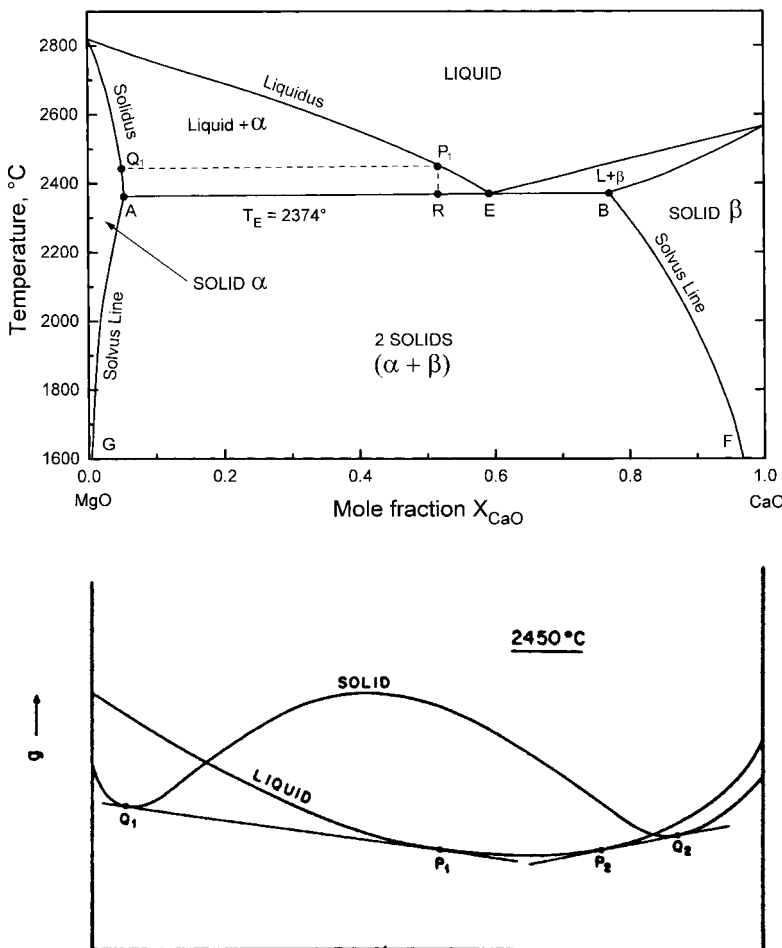


Figure 1-12. Phase diagram at $P=1$ bar (after Doman et al., 1963, and Wu, 1990) and Gibbs energy–composition curves at 2450 °C for the MgO–CaO system. Solid MgO and CaO have the same crystal structure.

there is just one common tangent line contacting the two portions of the g^s curve at compositions A and B and contacting the g^l curve at E. This temperature is known as the *eutectic temperature*, T_E , and the composition E is the *eutectic composition*. For temperatures below T_E , g^l lies completely above the common tangent to the two portions of the g^s curve and so for $T < T_E$ a solid–solid miscibility gap is observed. The phase boundaries of this two-phase region are called the *solvus* lines. The word eutectic is from the Greek for “to melt well” since the system has its lowest melting point at the eutectic composition E.

This description of the thermodynamic origin of simple eutectic phase diagrams is strictly correct only if the pure solid components A and B have the same crystal structure. Otherwise, a curve for g^s which is continuous at all compositions cannot be drawn.

Suppose a liquid MgO–CaO solution of composition $X_{\text{CaO}}=0.52$ (composition P_1) is cooled from the liquid state very slowly under equilibrium conditions. At 2450°C the first solid appears with composition Q_1 . As T decreases further, solidification continues with the liquid composition following the liquidus curve from P_1 to E and the composition of the solid phase following the solidus curve from Q_1 to A. The relative proportions of the two phases at any T are given by the lever rule. At a temperature just above T_E , two phases are observed: a solid of composition A and a liquid of composition E. At a temperature just below T_E , two solids with compositions A and B are observed. Therefore, at T_E , during cooling, the following *binary eutectic reaction* occurs:



Under equilibrium conditions the temperature will remain constant at $T = T_E$ until all

the liquid has solidified, and during the reaction the compositions of the three phases will remain fixed at A, B and E. For this reason the eutectic reaction is called an *invariant* reaction. More details on eutectic solidification may be found in Chapter 2 (Müller-Krumbhaar et al., 2001).

1.5.7 Regular Solution Theory

Many years ago Van Laar (1908) showed that the thermodynamic origin of a great many of the observed features of binary phase diagrams can be illustrated at least qualitatively by simple regular solution theory. A simple *regular solution* is one for which:

$$g^E = X_A X_B (\omega - \eta T) \quad (1-72)$$

where ω and η are parameters independent of temperature and composition. Substituting Eq. (1-72) into Eq. (1-29) yields, for the partial properties:

$$g_A^E = X_B^2 (\omega - \eta T), \quad g_B^E = X_A^2 (\omega - \eta T) \quad (1-73)$$

Several liquid and solid solutions conform approximately to regular solution behavior, particularly if g^E is small. Examples may be found for alloys, molecular solutions, and ionic solutions such as molten salts and oxides, among others. (The very low values of g^E observed for gaseous solutions generally conform very closely to Eq. (1-72).)

To understand why this should be so, we only need a very simple model. Suppose that the atoms or molecules of the components A and B mix substitutionally. If the atomic (or molecular) sizes and electronic structures of A and B are similar, then the distribution will be nearly random, and the configurational entropy will be nearly ideal. That is:

$$g^E \approx \Delta h_m - T S^E(\text{non-config}) \quad (1-74)$$

More will be said on this point in Sec. 1.10.5.

We now assume that the bond energies ϵ_{AA} , ϵ_{BB} and ϵ_{AB} of nearest-neighbor pairs are independent of temperature and composition and that the average nearest-neighbor coordination number, Z , is also constant. Finally, we assume that the enthalpy of mixing results mainly from the change in the total energy of nearest-neighbor pair bonds.

In one mole of solution there are $(N^0 Z/2)$ nearest-neighbor pair bonds, where N^0 is Avogadro's number. Since the distribution is assumed random, the probability that a given bond is an A–A bond is equal to X_A^2 . The probabilities of B–B and A–B bonds are, respectively, X_B^2 and $2X_A X_B$. The molar enthalpy of mixing is then equal to the sum of the energies of the nearest-neighbor bonds in one mole of solution, minus the energy of the A–A bonds in X_A moles of pure A and the energy of the B–B bonds in X_B moles of pure B:

$$\begin{aligned}\Delta h_m &= (N^0 Z/2) \\ &\quad \times (X_A^2 \epsilon_{AA} + X_B^2 \epsilon_{BB} + 2X_A X_B \epsilon_{AB}) \\ &\quad - (N^0 Z/2) (X_A \epsilon_{AA}) - (N^0 Z/2) (X_B \epsilon_{BB}) \\ &= (N^0 Z) [\epsilon_{AB} - (\epsilon_{AA} + \epsilon_{BB})/2] X_A X_B \\ &= \omega X_A X_B\end{aligned}\quad (1-75)$$

We now define σ_{AB} , σ_{AA} and σ_{BB} as the vibrational entropies of nearest-neighbor pair bonds. Following an identical argument to that just presented for the bond energies we obtain:

$$\begin{aligned}s^E(\text{non-config}) &\quad (1-76) \\ &= (N^0 Z) [\sigma_{AB} - (\sigma_{AA} + \sigma_{BB})/2] = \eta X_A X_B\end{aligned}$$

Eq. (1-72) has thus been derived. If A–B bonds are stronger than A–A and B–B bonds, then $(\epsilon_{AB} - \eta_{AB} T) < [(\epsilon_{AA} - \eta_{AA} T)/2 + (\epsilon_{BB} - \eta_{BB} T)/2]$. Hence, $(\omega - \eta T) < 0$ and $g^E < 0$. That is, the solution is rendered more stable. If the A–B bonds are rela-

tively weak, then the solution is rendered less stable, $(\omega - \eta T) > 0$ and $g^E > 0$.

Simple non-polar molecular solutions and ionic solutions such as molten salts often exhibit approximately regular behavior. The assumption of additivity of the energy of pair bonds is probably reasonably realistic for van der Waals or coulombic forces. For alloys, the concept of a pair bond is, at best, vague, and metallic solutions tend to exhibit larger deviations from regular behavior.

In several solutions it is found that $|\eta T| < |\omega|$ in Eq. (1-72). That is, $g^E \approx \Delta h_m = \omega X_A X_B$, and to a first approximation g^E is independent of T . This is more often the case in non-metallic solutions than in metallic solutions.

1.5.8 Thermodynamic Origin of Simple Phase Diagrams Illustrated by Regular Solution Theory

Figure 1-13 shows several phase diagrams, calculated for a hypothetical system A–B containing a solid and a liquid phase with melting points of $T_{f(A)}^0 = 800$ K and $T_{f(B)}^0 = 1200$ K and with entropies of fusion of both A and B set to 10 J/mol K, which is a typical value for metals. The solid and liquid phases are both regular with temperature-independent excess Gibbs energies

$$g^{E(s)} = \omega^s X_A X_B \quad \text{and} \quad g^{E(l)} = \omega^l X_A X_B$$

The parameters ω^s and ω^l have been varied systematically to generate the various panels of Fig. 1-13.

In panel (n) both phases are ideal. Panels (l) to (r) exhibit minima or maxima depending upon the sign and magnitude of $(g^{E(l)} - g^{E(s)})$, as has been discussed in Sec. 1.5.4. In panel (h) the liquid is ideal but positive deviations in the solid give rise to a solid–solid miscibility gap as discussed in Sec. 1.5.6. On passing from panel (h) to

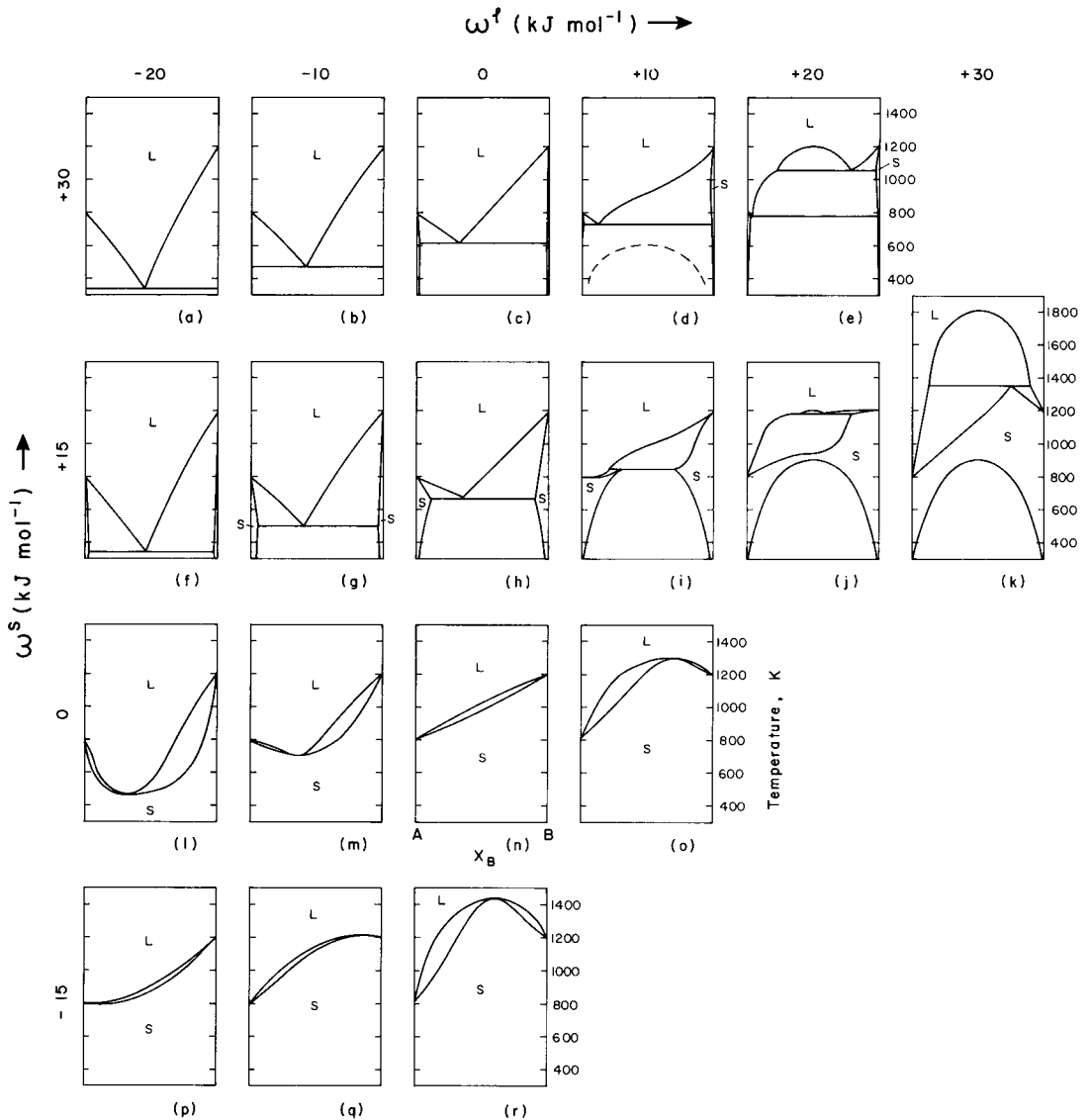


Figure 1-13. Topological changes in the phase diagram for a system A–B with regular solid and liquid phases, brought about by systematic changes in the regular solution parameters ω^s and ω^l . Melting points of pure A and B are 800 K and 1200 K. Entropies of fusion of both A and B are 10.0 J/mol K (Pelton and Thompson, 1975). The dashed curve in panel (d) is the metastable liquid miscibility gap (Reprinted from Pelton, 1983).

panel (c), an increase in $g^{E(s)}$ results in a widening of the miscibility gap so that the solubility of A in solid B and of B in solid A decreases. Panels (a) to (c) illustrate that negative deviations in the liquid cause a relative stabilization of the liquid with re-

sultant lowering of the eutectic temperature.

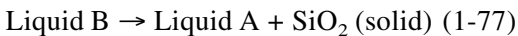
Eutectic phase diagrams are often drawn with the maximum solid solubility occurring at the eutectic temperature (as in Fig. 1-12). However, panel (d) of Fig. 1-13, in

which the maximum solubility of A in the B-rich solid solution occurs at approximately $T=950$ K, illustrates that this need not be the case even for simple regular solutions.

1.5.9 Immiscibility – Monotectics

In Fig. 1-13(e), positive deviations in the liquid have given rise to a *liquid–liquid miscibility gap*. The CaO–SiO₂ system (Wu, 1990), shown in Fig. 1-14, exhibits such a feature. Suppose that a liquid of composition $X_{\text{SiO}_2}=0.8$ is cooled slowly from high temperatures. At $T=1815^\circ\text{C}$ the miscibility gap boundary is crossed and a second liquid layer appears with a composition of $X_{\text{SiO}_2}=0.97$. As the temperature is lowered further, the composition of each liquid phase follows its respective phase boundary until, at 1692°C , the SiO₂-rich liquid has a composition of $X_{\text{SiO}_2}=0.99$ (point B), and in the CaO-rich liquid $X_{\text{SiO}_2}=0.74$ (point A). At any temperature, the relative amounts of the two phases are given by the lever rule.

At 1692°C the following invariant *binary monotectic reaction* occurs upon cooling:



The temperature remains constant at 1692°C and the compositions of the phases remain constant until all of liquid B is consumed. Cooling then continues with precipitation of solid SiO₂ with the equilibrium liquid composition following the liquidus from point A to the eutectic E.

Returning to Fig. 1-13, we see in panel (d) that the positive deviations in the liquid in this case are not large enough to produce immiscibility, but they do result in a flattening of the liquidus, which indicates a “tendency to immiscibility”. If the nucleation of the solid phases can be suppressed

by sufficiently rapid cooling, then a *metastable liquid–liquid miscibility gap* is observed as shown in Fig. 1-13(d). For example, in the Na₂O–SiO₂ system the flattened (or “S-shaped”) SiO₂ liquidus heralds the existence of a metastable miscibility gap of importance in glass technology.

1.5.10 Intermediate Phases

The phase diagram of the Ag–Mg system (Hultgren et al., 1973) is shown in Fig. 1-15(d). An *intermetallic phase*, β' , is seen centered approximately about the composition $X_{\text{Mg}}=0.5$. The Gibbs energy curve at 1050 K for such an intermetallic phase has the form shown schematically in Fig. 1-15(a). The curve $g^{\beta'}$ rises quite rapidly on either side of its minimum, which occurs near $X_{\text{Mg}}=0.5$. As a result, the β' phase appears on the phase diagram only over a limited composition range. This form of the curve $g^{\beta'}$ results from the fact that when $X_{\text{Ag}} \approx X_{\text{Mg}}$ a particularly stable crystal structure exists in which Ag and Mg atoms preferentially occupy different sites. The two common tangents P_1Q_1 and P_2Q_2 give rise to a maximum in the two-phase ($\beta' + \text{liquid}$) region of the phase diagram. (Although the maximum is observed very near $X_{\text{Mg}}=0.5$, there is no thermodynamic reason for the maximum to occur exactly at this composition.)

Another intermetallic phase, the ϵ phase, is also observed in the Ag–Mg system, Fig. 1-15. The phase is associated with a *peritectic invariant* ABC at 744 K. The Gibbs energy curves are shown schematically at the peritectic temperature in Fig. 1-15(c). One common tangent line can be drawn to g^l , $g^{\beta'}$ and g^ϵ .

Suppose that a liquid alloy of composition $X_{\text{Mg}}=0.7$ is cooled very slowly from the liquid state. At a temperature just above 744 K a liquid phase of composition C and

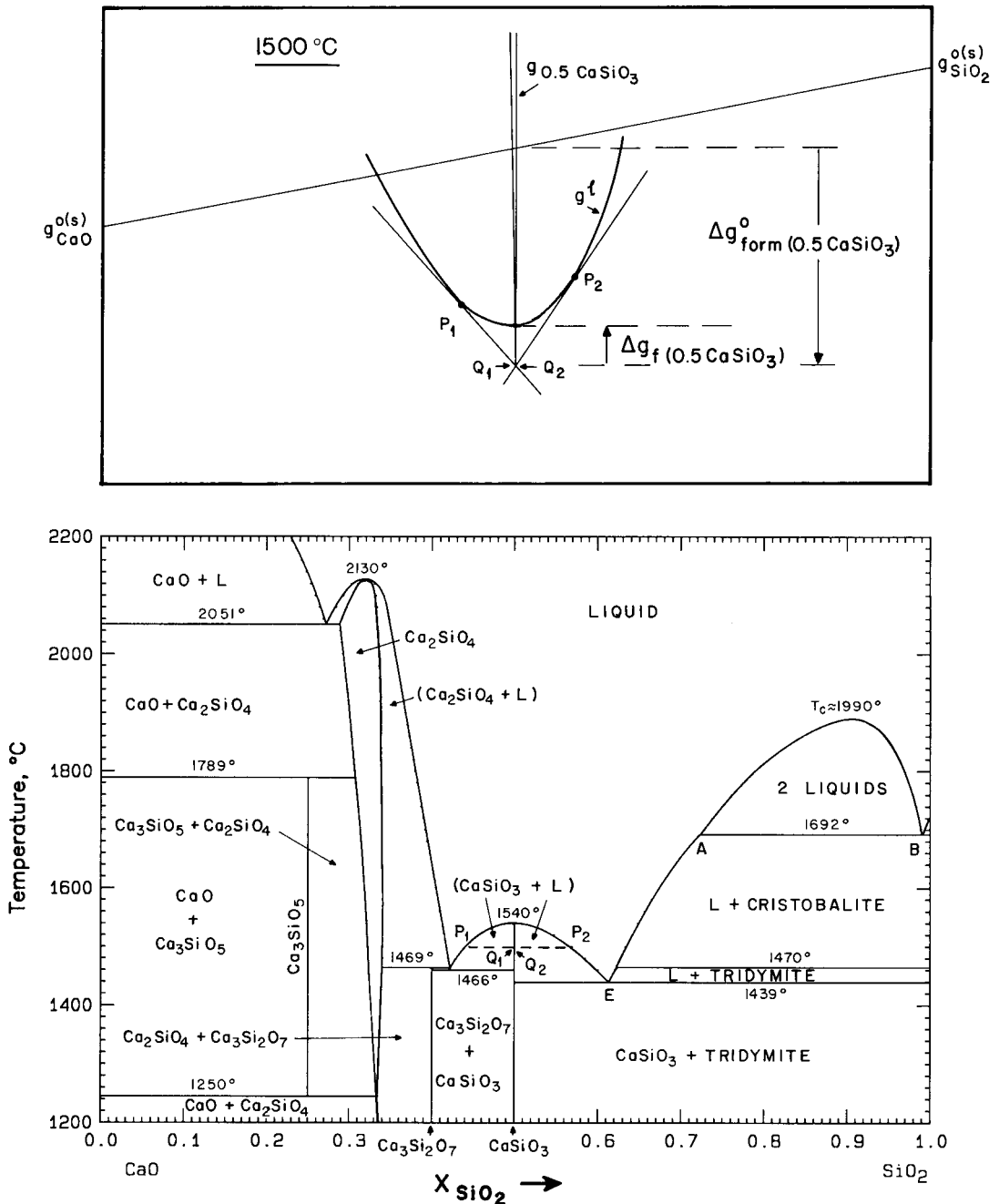


Figure 1-14. CaO–SiO₂ phase diagram at $P=1$ bar (after Wu, 1990) and Gibbs energy curves at 1500 °C illustrating Gibbs energies of fusion and formation of the stoichiometric compound CaSiO₃.

mum in Fig. 1-15(d). Because the CaSiO_3 single-phase region is so narrow, we refer to CaSiO_3 as a *stoichiometric compound*. Any deviation in composition from the stoichiometric 1:1 ratio of CaO to SiO_2 results in a very large increase in Gibbs energy.

The ϵ phase in Fig. 1-15 is based on the stoichiometry AgMg_3 . The Gibbs energy curve, Fig. 1-15(c), rises extremely rapidly on the Ag side of the minimum, but somewhat less steeply on the Mg side. As a result, Ag is virtually insoluble in AgMg_3 , while Mg is sparingly soluble. Such a phase with a narrow range of homogeneity is often called a *non-stoichiometric compound*. At low temperatures the β' phase exhibits a relatively narrow range of stoichiometry about the 1:1 AgMg composition and can properly be called a compound. However, at higher temperatures it is debatable whether a phase with such a wide range of composition should be called a "compound".

From Fig. 1-14 it can be seen that if stoichiometric CaSiO_3 is heated it will melt isothermally at 1540°C to form a liquid of the same composition. Such a compound is called *congruently melting* or simply a *congruent compound*. The compound Ca_2SiO_4 in Fig. 1-14 is congruently melting. The β' phase in Fig. 1-15 is also congruently melting at the composition of the liquidus/solidus maximum.

It should be noted with regard to the congruent melting of CaSiO_3 in Fig. 1-14 that the limiting slopes dT/dX of both branches of the liquidus at the congruent melting point (1540°C) are zero since we are really dealing with a maximum in a two-phase region.

The AgMg_3 (ϵ) compound in Fig. 1-15 is said to *melt incongruently*. If solid AgMg_3 is heated it will melt isothermally at 744 K by the reverse of the peritectic reaction,

Eq. (1-78), to form a liquid of composition C and another solid phase, β' , of composition A.

Another example of an *incongruent compound* is $\text{Ca}_3\text{Si}_2\text{O}_7$ in Fig. 1-14, which melts incongruently (or peritectically) to form liquid and Ca_2SiO_4 at the peritectic temperature of 1469°C .

An incongruent compound is always associated with a peritectic. However, the converse is not necessarily true. A peritectic is not always associated with an intermediate phase. See, for example, Fig. 1-13(i).

For purposes of phase diagram calculations involving stoichiometric compounds such as CaSiO_3 , we may, to a good approximation, consider the Gibbs energy curve, $g_{0.5(\text{CaSiO}_3)}$, to have zero width. All that is then required is the value of $g_{0.5(\text{CaSiO}_3)}$ at the minimum. This value is usually expressed in terms of the *Gibbs energy of fusion* of the compound, $\Delta g_{\text{f}(0.5 \text{ CaSiO}_3)}^0$ or the *Gibbs energy of formation* $\Delta g_{\text{form}(0.5 \text{ CaSiO}_3)}^0$ of the compound from the pure solid components CaO and SiO_2 according to the reaction: $0.5 \text{ CaO}(\text{sol}) + 0.5 \text{ SiO}_2(\text{sol}) = 0.5 \text{ CaSiO}_3(\text{sol})$. Both these quantities are interpreted graphically in Fig. 1-14.

1.5.11 Limited Mutual Solubility – Ideal Henrian Solutions

In Sec. 1.5.6, the region of two solids in the $\text{MgO}-\text{CaO}$ phase diagram of Fig. 1-12 was described as a miscibility gap. That is, only one continuous g^s curve was assumed. If, somehow, the appearance of the liquid phase could be suppressed, then the two solvus lines in Fig. 1-12, when projected upwards, would meet at a critical point above which one continuous solid solution would exist at all compositions.

Such a description is justifiable only if the pure solid components have the same crystal structure, as is the case for MgO and CaO. However, consider the Ag–Mg system, Fig. 1-15, in which the terminal (Ag) solid solution is face-centered-cubic and the terminal (Mg) solid solution is hexagonal-close-packed. In this case, one continuous curve for g^s cannot be drawn. Each solid phase must have its own separate Gibbs energy curve, as shown schematically in Fig. 1-15(b) for the h.c.p. (Mg) phase at 800 K. In this figure, $g_{\text{Mg}}^{0(\text{h.c.p.})}$ and $g_{\text{Ag}}^{0(\text{f.c.c.})}$ are the standard molar Gibbs energies of pure h.c.p. Mg and pure f.c.c. Ag, while $g_{\text{Ag}}^{0(\text{h.c.p.-Mg})}$ is the standard molar Gibbs energy of pure (hypothetical) h.c.p. Ag in the h.c.p. (Mg) phase.

Since the solubility of Ag in the h.c.p. (Mg) phase is limited we can, to a good approximation, describe it as a *Henrian ideal solution*. That is, when a solution is sufficiently dilute in one component, we can approximate $g_{\text{solute}}^E = RT \ln \gamma_{\text{solute}}$ by its value in an infinitely dilute solution. That is, if X_{solute} is small we set $\gamma_{\text{solute}} = \gamma_{\text{solute}}^0$ where γ_{solute}^0 is the *Henrian activity coefficient* at $X_{\text{solute}} = 0$. Thus, for sufficiently dilute solutions we assume that γ_{solute} is independent of composition. Physically, this means that in a very dilute solution there is negligible interaction among solute particles because they are so far apart. Hence, each additional solute particle added to the solution produces the same contribution to the excess Gibbs energy of the solution and so $g_{\text{solute}}^E = dG^E/dn_{\text{solute}} = \text{constant}$.

From the Gibbs–Duhem equation, Eq. (1-56), if $dg_{\text{solute}}^E = 0$, then $dg_{\text{solvent}}^E = 0$. Hence, in a Henrian solution γ_{solute} is also constant and equal to its value in an infinitely dilute solution. That is, $\gamma_{\text{solute}} = 1$ and the solvent behaves ideally. In summary then, for dilute solutions ($X_{\text{solvent}} \approx 1$) *Henry's Law* applies:

$$\gamma_{\text{solvent}} \approx 1$$

$$\gamma_{\text{solute}} \approx \gamma_{\text{solute}}^0 = \text{constant} \quad (1-79)$$

(Care must be exercised for solutions other than simple substitutional solutions. Henry's Law applies only if the ideal activity is defined correctly, as will be discussed in Sec. 1.10).

Treating, then, the h.c.p. (Mg) phase in the Ag–Mg system (Fig. 1-15(b)) as a Henrian solution we write:

$$\begin{aligned} g^{\text{h.c.p.}} &= (X_{\text{Ag}} g_{\text{Ag}}^{0(\text{f.c.c.})} + X_{\text{Mg}} g_{\text{Mg}}^{0(\text{h.c.p.})}) \\ &\quad + RT (X_{\text{Ag}} \ln a_{\text{Ag}} + X_{\text{Mg}} \ln a_{\text{Mg}}) \\ &= (X_{\text{Ag}} g_{\text{Ag}}^{0(\text{f.c.c.})} + X_{\text{Mg}} g_{\text{Mg}}^{0(\text{h.c.p.})}) \\ &\quad + RT (X_{\text{Ag}} \ln (\gamma_{\text{Ag}}^0 X_{\text{Ag}}) + X_{\text{Mg}} \ln X_{\text{Mg}}) \end{aligned} \quad (1-80)$$

where a_{Ag} and γ_{Ag}^0 are the activity and activity coefficient of silver with respect to pure f.c.c. silver as standard state. Let us now combine terms as follows:

$$\begin{aligned} g^{\text{h.c.p.}} &= [X_{\text{Ag}} (g_{\text{Ag}}^{0(\text{f.c.c.})} + RT \ln \gamma_{\text{Ag}}^0) \\ &\quad + X_{\text{Mg}} g_{\text{Mg}}^{0(\text{h.c.p.})}] \\ &\quad + RT (X_{\text{Ag}} \ln X_{\text{Ag}} + X_{\text{Mg}} \ln X_{\text{Mg}}) \end{aligned} \quad (1-81)$$

Since γ_{Ag}^0 is independent of composition, let us define:

$$g_{\text{Ag}}^{0(\text{h.c.p.-Mg})} = (g_{\text{Ag}}^{0(\text{f.c.c.})} + RT \ln \gamma_{\text{Ag}}^0) \quad (1-82)$$

From Eqs. (1-81) and (1-82) it can be seen that, relative to $g_{\text{Mg}}^{0(\text{h.c.p.})}$ and to the hypothetical standard state $g_{\text{Ag}}^{0(\text{h.c.p.-Mg})}$ defined in this way, the h.c.p. solution is ideal. Eqs. (1-81) and (1-82) are illustrated in Fig. 1-15(b). It can be seen that as γ_{Ag}^0 becomes larger, the point of tangency N moves to higher Mg concentrations. That is, as $(g_{\text{Ag}}^{0(\text{h.c.p.-Mg})} - g_{\text{Ag}}^{0(\text{f.c.c.})})$ becomes more positive, the solubility of Ag in h.c.p. (Mg) decreases.

It must be stressed that $g_{\text{Ag}}^{0(\text{h.c.p.-Mg})}$ as defined by Eq. (1-82) is solvent-dependent. That is, $g_{\text{Ag}}^{0(\text{h.c.p.-Mg})}$ is not the same as, say, $g_{\text{Ag}}^{0(\text{h.c.p.-Cd})}$ for Ag in dilute h.c.p. (Cd) solid solutions.

Henrian activity coefficients can usually be expressed as functions of temperature:

$$RT \ln \gamma_i^0 = a - bT \quad (1-83)$$

where a and b are constants. If data are limited, it can further be assumed that $b \approx 0$ so that $RT \ln \gamma_i^0 \approx \text{constant}$.

1.5.12 Geometry of Binary Phase Diagrams

The geometry of all types of phase diagrams of any number of components is governed by the Gibbs Phase Rule.

Consider a system with C components in which P phases are in equilibrium. The system is described by the temperature, the total pressure and the composition of each phase. In a C -component system, $(C-1)$ independent mole fractions are required to describe the composition of each phase (because $\sum X_i = 1$). Hence, the total number of variables required to describe the system is $[P(C-1) + 2]$. However, as shown in Sec. 1.4.2, the chemical potential of any component is the same in all phases ($\alpha, \beta, \gamma, \dots$) since the phases are in equilibrium. That is:

$$\begin{aligned} g_i^\alpha(T, P, X_1^\alpha, X_2^\alpha, X_3^\alpha, \dots) \\ = g_i^\beta(T, P, X_1^\beta, X_2^\beta, X_3^\beta, \dots) \\ = g_i^\gamma(T, P, X_1^\gamma, X_2^\gamma, X_3^\gamma, \dots) = \dots \end{aligned} \quad (1-84)$$

where $g_i^\alpha(T, P, X_1^\alpha, X_2^\alpha, X_3^\alpha, \dots)$ is a function of temperature, of total pressure, and of the mole fractions $X_1^\alpha, X_2^\alpha, X_3^\alpha, \dots$ in the α phase; and similarly for the other phases. Thus there are $C(P-1)$ independent equations in Eq. (1-84) relating the variables.

Let F be the differences between the number of variables and the number of equations relating them:

$$\begin{aligned} F &= P(C-1) + 2 - C(P-1) \\ F &= C - P + 2 \end{aligned} \quad (1-85)$$

This is the *Gibbs Phase Rule*. F is called the number of *degrees of freedom* or *variance* of the system and is the number of parameters which can and must be specified in order to completely specify the state of the system.

Binary temperature–composition phase diagrams are plotted at a fixed pressure, usually 1 bar. This then eliminates one degree of freedom. In a binary system, $C = 2$. Hence, for binary isobaric $T-X$ diagrams the phase rule reduces to:

$$F = 3 - P \quad (1-86)$$

Binary $T-X$ diagrams contain single-phase areas and two-phase areas. In the single-phase areas, $F = 3 - 1 = 2$. That is, temperature and composition can be specified independently. These regions are thus called *bivariant*. In two-phase regions, $F = 3 - 2 = 1$. If, say, T is specified, then the compositions of both phases are determined by the ends of the tie-lines. Two-phase regions are thus termed *univariant*. Note that the overall composition can be varied within a two-phase region at constant T , but the overall composition is not a parameter in the sense of the phase rule. Rather, it is the compositions of the individual phases at equilibrium that are the parameters to be considered in counting the number of degrees of freedom.

When three phases are at equilibrium in a binary system at constant pressure, $F = 3 - 3 = 0$. Hence, the compositions of all three phases, as well as T , are fixed. There are two general types of three-phase *invariants* in binary phase diagrams. These are the *eutectic-type* and *peritectic-type* invariants as illustrated in Fig. 1-16. Let the three phases concerned be called α, β and γ , with β as the central phase as shown in Fig. 1-16. The phases α, β and γ can be solid, liquid or gaseous. At the eutectic-type invariant, the following invariant re-

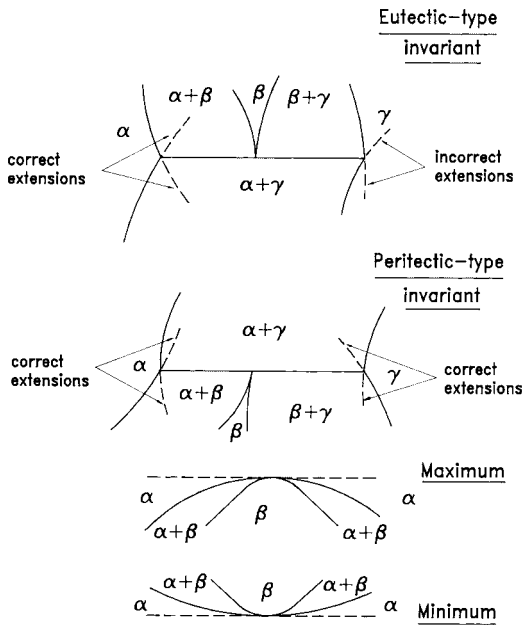


Figure 1-16. Some geometrical units of binary phase diagrams, illustrating rules of construction.

action occurs isothermally as the system is cooled:



whereas at the peritectic-type invariant the invariant reaction upon cooling is:



Some examples of eutectic-type invariants are: (i) *eutectics* (Fig. 1-12) in which $\alpha = \text{solid}_1$, $\beta = \text{liquid}$, $\gamma = \text{solid}_2$; the eutectic reaction is $l \rightarrow s_1 + s_2$; (ii) *monotectics* (Fig. 1-14) in which $\alpha = \text{liquid}_1$, $\beta = \text{liquid}_2$, $\gamma = \text{solid}$; the monotectic reaction is $l_2 \rightarrow l_1 + s$; (iii) *eutectoids* in which $\alpha = \text{solid}_1$, $\beta = \text{solid}_2$, $\gamma = \text{solid}_3$; the eutectoid reaction is $s_2 \rightarrow s_1 + s_3$; (iv) *catatectics* in which $\alpha = \text{liquid}$, $\beta = \text{solid}_1$, $\gamma = \text{solid}_2$; the catatectic reaction is $s_1 \rightarrow l + s_2$.

Some examples of peritectic-type invariants are: (i) *peritectics* (Fig. 1-15) in which $\alpha = \text{liquid}$, $\beta = \text{solid}_1$, $\gamma = \text{solid}_2$. The peri-

itectic reaction is $l + s_2 \rightarrow s_1$; (ii) *syntectics* (Fig. 1-13(k)) in which $\alpha = \text{liquid}_1$, $\beta = \text{solid}$, $\gamma = \text{liquid}_2$. The syntectic reaction is $l_1 + l_2 \rightarrow s$; (iii) *peritectoids* in which $\alpha = \text{solid}_1$, $\beta = \text{solid}_2$, $\gamma = \text{solid}_3$. The peritectoid reaction is $s_1 + s_3 \rightarrow s_2$.

An important rule of construction which applies to invariants in binary phase diagrams is illustrated in Fig. 1-16. This *extension rule* states that at an invariant the extension of a boundary of a two-phase region must pass into the adjacent two-phase region and not into a single-phase region. Examples of both correct and incorrect constructions are given in Fig. 1-16. To understand why the “incorrect extensions” shown are not right consider that the $(\alpha + \gamma)$ phase boundary line indicates the composition of the γ -phase in equilibrium with the α -phase, as determined by the common tangent to the Gibbs energy curves. Since there is no reason for the Gibbs energy curves or their derivatives to change discontinuously at the invariant temperature, the extension of the $(\alpha + \gamma)$ phase boundary also represents the stable phase boundary under equilibrium conditions. Hence, for this line to extend into a region labeled as single-phase γ is incorrect.

Two-phase regions in binary phase diagrams can terminate: (i) on the pure component axes (at $X_A = 1$ or $X_B = 1$) at a transformation point of pure A or B; (ii) at a critical point of a miscibility gap; (iii) at an invariant. Two-phase regions can also exhibit maxima or minima. In this case, both phase boundaries must pass through their maximum or minimum at the same point as shown in Fig. 1-16.

All the *geometrical units* of construction of binary phase diagrams have now been discussed. The phase diagram of a binary alloy system will usually exhibit several of these units. As an example, the Fe–Mo phase diagram (Kubaschewski, 1982) is

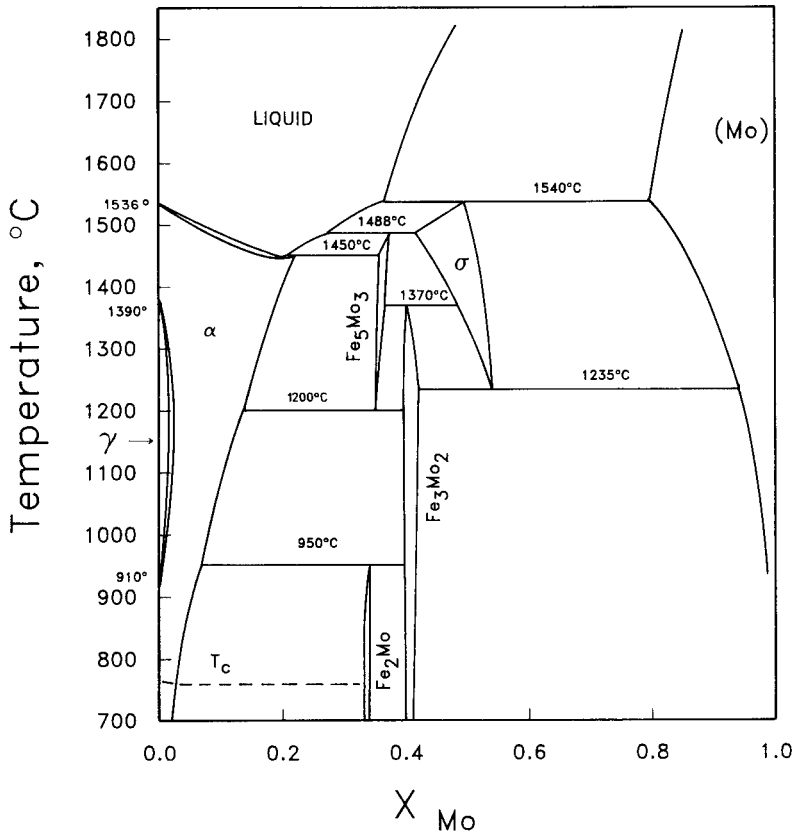


Figure 1-17. Fe–Mo phase diagram at $P=1$ bar (Kubaschewski, 1982).

shown in Fig. 1-17. The invariants in this system are peritectics at 1540, 1488 and 1450 °C; eutectoids at 1235 and 1200 °C; peritectoids at 1370 and 950 °C. The two-phase (liquid + γ) region passes through a minimum at $X_{\text{Mo}}=0.2$.

Between 910 °C and 1390 °C is a two-phase ($\alpha + \gamma$) γ -loop. Pure Fe adopts the f.c.c. γ structure between these two temperatures but exists as the b.c.c. α phase at higher and lower temperatures. Mo, however, is more soluble in the b.c.c. than in the f.c.c. structure. That is, $g_{\text{Mo}}^{0(\text{b.c.c.}-\text{Fe})} < g_{\text{Mo}}^{0(\text{f.c.c.}-\text{Fe})}$ as discussed in Sec. 1.5.11. Therefore, small additions of Mo stabilize the b.c.c. structure.

In the CaO–SiO₂ phase diagram, Fig. 1-14, we observe eutectics at 1439, 1466

and 2051 °C; a monotectic at 1692 °C; and a peritectic at 1469 °C. The compound Ca₃SiO₅ dissociates upon heating to CaO and Ca₂SiO₄ by a peritectoid reaction at 1789 °C and dissociates upon cooling to CaO and Ca₂SiO₄ by a eutectoid reaction at 1250 °C. Maxima are observed at 2130 and 1540 °C. At 1470 °C there is an invariant associated with the tridymite \rightarrow cristobalite transition of SiO₂. This is either a peritectic or a catatctic depending upon the relative solubility of CaO in tridymite and cristobalite. However, these solubilities are very small and unknown.

1.6 Application of Thermodynamics to Phase Diagram Analysis

1.6.1 Thermodynamic/Phase Diagram Optimization

In recent years the development of solution models, numerical methods and computer software has permitted a quantitative application of thermodynamics to phase diagram analysis. For a great many systems it is now possible to perform a simultaneous critical evaluation of available phase diagram measurements and of available thermodynamic data (calorimetric data, measurements of activities, etc.) with a view to obtaining optimized equations for the Gibbs energies of each phase which best represent all the data. These equations are consistent with thermodynamic principles and with theories of solution behavior.

The phase diagram can be calculated from these thermodynamic equations, and so one set of self-consistent equations describes all the thermodynamic properties and the phase diagram. This technique of analysis greatly reduces the amount of experimental data needed to fully characterize a system. All data can be tested for internal consistency. The data can be interpolated and extrapolated more accurately and metastable phase boundaries can be calculated. All the thermodynamic properties and the phase diagram can be represented and stored by means of a small set of coefficients.

Finally, and most importantly, it is often possible to estimate the thermodynamic properties and phase diagrams of ternary and higher-order systems from the assessed parameters for their binary sub-systems, as will be discussed in Sec. 1.11. The analysis of binary systems is thus the first and most

important step in the development of databases for multicomponent systems.

1.6.2 Polynomial Representation of Excess Properties

Empirical equations are required to express the excess thermodynamic properties of the solution phases as functions of composition and temperature. For many simple binary substitutional solutions, a good representation is obtained by expanding the excess enthalpy and entropy as polynomials in the mole fractions X_A and X_B of the components:

$$h^E = X_A X_B [h_0 + h_1 (X_B - X_A) + h_2 (X_B - X_A)^2 + h_3 (X_B - X_A)^3 + \dots] \quad (1-89)$$

$$s^E = X_A X_B [s_0 + s_1 (X_B - X_A) + s_2 (X_B - X_A)^2 + s_3 (X_B - X_A)^3 + \dots] \quad (1-90)$$

where the h_i and s_i are empirical coefficients. As many coefficients are used as are required to represent the data in a given system. For most systems it is a good approximation to assume that the coefficients h_i and s_i are independent of temperature.

If the series are truncated after the first term, then:

$$g^E = h^E - T s^E = X_A X_B (h_0 - T s_0) \quad (1-91)$$

This is the equation for a regular solution discussed in Sec. 1.5.7. Hence, the polynomial representation can be considered to be an extension of regular solution theory. When the expansions are written in terms of the composition variable $(X_B - X_A)$, as in Eqs. (1-89) and (1-90), they are said to be in *Redlich–Kister form*. Other equivalent polynomial expansions such as orthogonal Legendre series have been discussed by Pelton and Bale (1986).

Differentiation of Eqs. (1-89) and (1-90) and substitution into Eq. (1-55) yields the

following expansions for the partial excess enthalpies and entropies:

$$h_A^E = X_B^2 \sum_{i=0} h_i [(X_B - X_A)^i - 2i X_A (X_B - X_A)^{i-1}] \quad (1-92)$$

$$h_B^E = X_A^2 \sum_{i=0} h_i [(X_B - X_A)^i + 2i X_B (X_B - X_A)^{i-1}] \quad (1-93)$$

$$s_A^E = X_B^2 \sum_{i=0} s_i [(X_B - X_A)^i - 2i X_A (X_B - X_A)^{i-1}] \quad (1-94)$$

$$s_B^E = X_A^2 \sum_{i=0} s_i [(X_B - X_A)^i + 2i X_B (X_B - X_A)^{i-1}] \quad (1-95)$$

Partial excess Gibbs energies, g_i^E , are then given by Eq. (1-52).

Eqs. (1-89) and (1-90), being based upon regular solution theory, give an adequate representation for most simple substitutional solutions in which deviations from ideal behavior are not too great. In other cases, more sophisticated models are required, as discussed in Sec. 1.10.

1.6.3 Least-Squares Optimization

Eqs. (1-89), (1-90) and (1-92) to (1-95) are linear in terms of the coefficients. Through the use of these equations, all integral and partial excess properties (g^E , h^E , s^E , g_i^E , h_i^E , s_i^E) can be expressed by linear equations in terms of the one set of coefficients $\{h_i, s_i\}$. It is thus possible to include all available experimental data for a binary phase in one simultaneous linear least-squares optimization. Details have been discussed by Bale and Pelton (1983), Lukas et al. (1977) and Dörner et al. (1980).

The technique of coupled thermodynamic/phase diagram analysis is best illustrated by examples.

The phase diagram of the LiF–NaF system is shown in Fig. 1-18. Data points measured by Holm (1965) are shown on the diagram. The Gibbs energy of fusion of

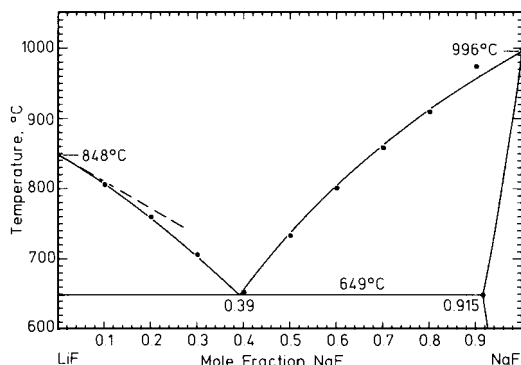


Figure 1-18. LiF–NaF phase diagram at $P=1$ bar calculated from optimized thermodynamic parameters (Sangster and Pelton, 1987). Points are experimental from Holm (1965). Dashed line is theoretical limiting liquidus slope for negligible solid solubility.

each pure component at temperature T is given by:

$$\Delta g_f^0 = \Delta h_{f(T_f)}^0 (1 - T/T_f) + \int_{T_f}^T (c_p^l - c_p^s) (1 - 1/T) dT \quad (1-96)$$

where $\Delta h_{f(T_f)}^0$ is the enthalpy of fusion at the melting point T_f , and c_p^l and c_p^s are the heat capacities of the pure liquid and solid. The following values are taken from Barin et al. (1977):

$$\begin{aligned} \Delta g_{f(\text{LiF})}^0 &= 14.518 + 128.435 T \\ &+ 8.709 \times 10^{-3} T^2 - 21.494 T \ln T \\ &- 2.65 \times 10^5 T^{-1} \quad \text{J/mol} \end{aligned} \quad (1-97)$$

$$\begin{aligned} \Delta g_{f(\text{NaF})}^0 &= 10.847 + 156.584 T \\ &+ 4.950 \times 10^{-3} T^2 - 23.978 T \ln T \\ &- 1.07 \times 10^5 T^{-1} \quad \text{J/mol} \end{aligned} \quad (1-98)$$

Thermodynamic properties along the liquidus and solidus are related by equations like Eqs. (1-64) and (1-65). Taking the ideal activities to be equal to the mole fractions:

$$\begin{aligned} RT \ln X_i^l - RT \ln X_i^s + g_i^{E(l)} - g_i^{E(s)} \\ = - \Delta g_{f(i)}^0 \end{aligned} \quad (1-99)$$

where $i = \text{LiF}$ or NaF . Along the LiF -rich liquidus, the liquid is in equilibrium with essentially pure solid LiF . Hence, $X_{\text{LiF}}^s = 1$ and $g_{\text{LiF}}^{E(s)} = 0$. Eq. (1-99) then reduces to:

$$RT \ln X_{\text{LiF}}^l + g_{\text{LiF}}^{E(l)} = -\Delta g_{f(\text{LiF})}^0 \quad (1-100)$$

From experimental values of X_{LiF}^l on the liquidus and with Eq. (1-97) for $\Delta g_{f(\text{LiF})}^0$, values of $g_{\text{LiF}}^{E(l)}$ at the measured liquidus points can be calculated from Eq. (1-100).

Along the NaF -rich solidus the solid solution is sufficiently concentrated in NaF that Henrian behavior (Sec. 1.5.11) can be assumed. That is, for the solvent, $g_{\text{NaF}}^{E(s)} = 0$. Hence, Eq. (1-99) becomes:

$$RT \ln X_{\text{NaF}}^l - RT \ln X_{\text{NaF}}^{(s)} + g_{\text{NaF}}^{E(l)} = -\Delta g_{f(\text{NaF})}^0 \quad (1-101)$$

Thus, from the experimental liquidus and solidus compositions and with the Gibbs energy of fusion from Eq. (1-98), values of $g_{\text{NaF}}^{E(l)}$ can be calculated at the measured liquidus points from Eq. (1-101).

Finally, enthalpies of mixing, h^E , in the liquid have been measured by calorimetry by Hong and Kleppa (1976).

Combining all these data in a least-squares optimization, the following expressions for the liquid were obtained by Sangster and Pelton (1987):

$$h^{E(l)} = X_{\text{LiF}} X_{\text{NaF}} \times [-7381 + 184(X_{\text{NaF}} - X_{\text{LiF}})] \text{ J/mol} \quad (1-102)$$

$$s^{E(l)} = X_{\text{LiF}} X_{\text{NaF}} \times [-2.169 - 0.562(X_{\text{NaF}} - X_{\text{LiF}})] \text{ J/mol} \quad (1-103)$$

Eqs. (1-102) and (1-103) then permit all other integral and partial properties of the liquid to be calculated.

For the NaF -rich Henrian solid solution, the solubility of LiF has been measured by Holm (1965) at the eutectic temperature where the NaF -rich solid solution is in equilibrium with pure solid LiF . That is,

$a_{\text{LiF}} = 1$ with respect to pure solid LiF as standard state. In the Henrian solution at saturation,

$$a_{\text{LiF}} = \gamma_{\text{LiF}}^0 X_{\text{LiF}} = \gamma_{\text{LiF}}^0 (1 - 0.915) = 1$$

Hence, the Henrian activity coefficient in the NaF -rich solid solution at 649°C is $\gamma_{\text{LiF}}^0 = 11.76$. Since no solubilities have been measured at other temperatures, we assume that:

$$RT \ln \gamma_{\text{LiF}}^0 = R(922) \ln(11.76) = 18900 \text{ J/mol} = \text{constant} \quad (1-104)$$

Using the notation of Eq. (1-82):

$$g_{\text{LiF}}^{0(s, \text{NaF})} = g_{\text{LiF}}^{0(s)} + 18900 \text{ J/mol} \quad (1-105)$$

where $g_{\text{LiF}}^{0(s)}$ is the standard Gibbs energy of solid LiF , and $g_{\text{LiF}}^{0(s, \text{NaF})}$ is the hypothetical standard Gibbs energy of LiF dissolved in solid NaF .

The phase diagram drawn in Fig. 1-18 was calculated from Eqs. (1-97) to (1-104). Complete details of the analysis of the LiF - NaF system are given by Sangster and Pelton (1987).

As a second example of thermodynamic/phase diagram optimization, consider the Cd - Na system. The phase diagram, with points measured by several authors (Mathewson, 1906; Kurnakow and Kusnetzow, 1907; Weeks and Davies, 1964) is shown in Fig. 1-19.

From electromotive force measurements on alloy concentration cells, several authors have measured the activity coefficient of Na in liquid alloys. The data are shown in Fig. 1-20 at 400°C . From the temperature dependence of $g_{\text{Na}}^E = RT \ln \gamma_{\text{Na}}$, the partial enthalpy of Na in the liquid was obtained via Eq. (1-52). The results are shown in Fig. 1-21. Also, h^E of the liquid has been measured by Kleinstuber (1961) by direct calorimetry. These thermodynamic data for g_{Na}^E , h_{Na}^E and h^E were

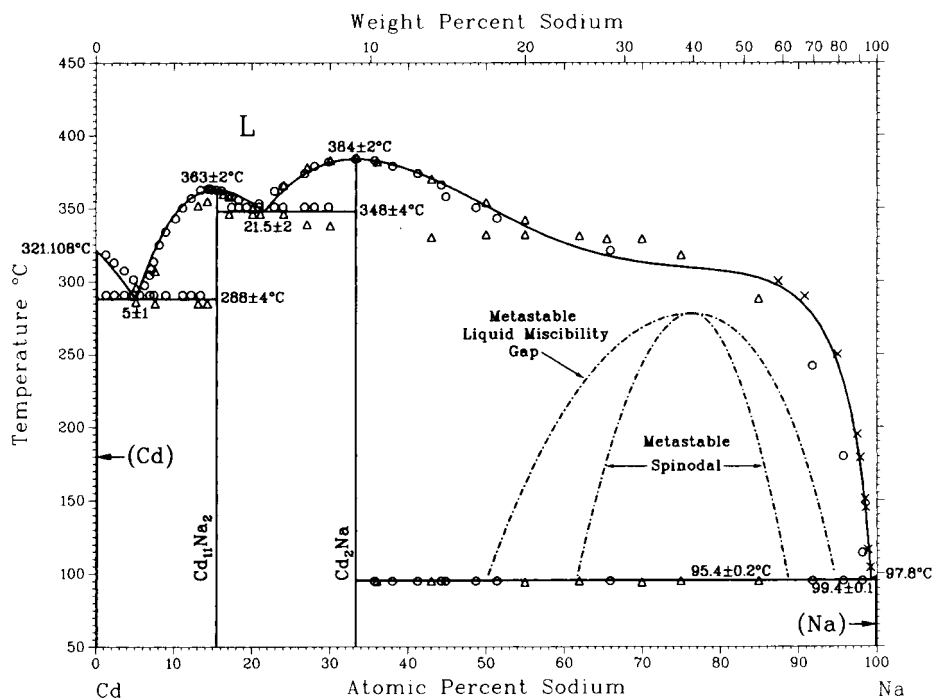


Figure 1-19. Cd–Na phase diagram at $P=1$ bar calculated from optimized thermodynamic parameters (Reprinted from Pelton, 1988a). \circ Kurnakow and Kusnetzow (1907), \triangle Mathewson (1906), \times Weeks and Davies (1964).

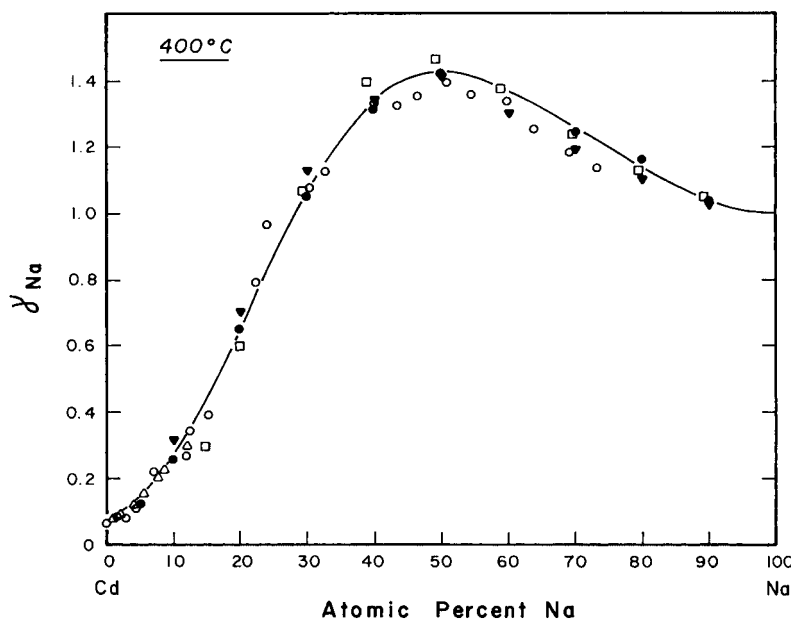


Figure 1-20. Sodium activity coefficient in liquid Cd–Na alloys at 400°C . Line is calculated from optimized thermodynamic parameters (Reprinted from Pelton, 1988a). \square Hauffe (1940), \bullet Lantratov and Mikhailova (1971), \triangle Maiorova et al. (1976), \blacktriangledown Alabyshev and Morachevskii (1957), \circ Bartlett et al. (1970).

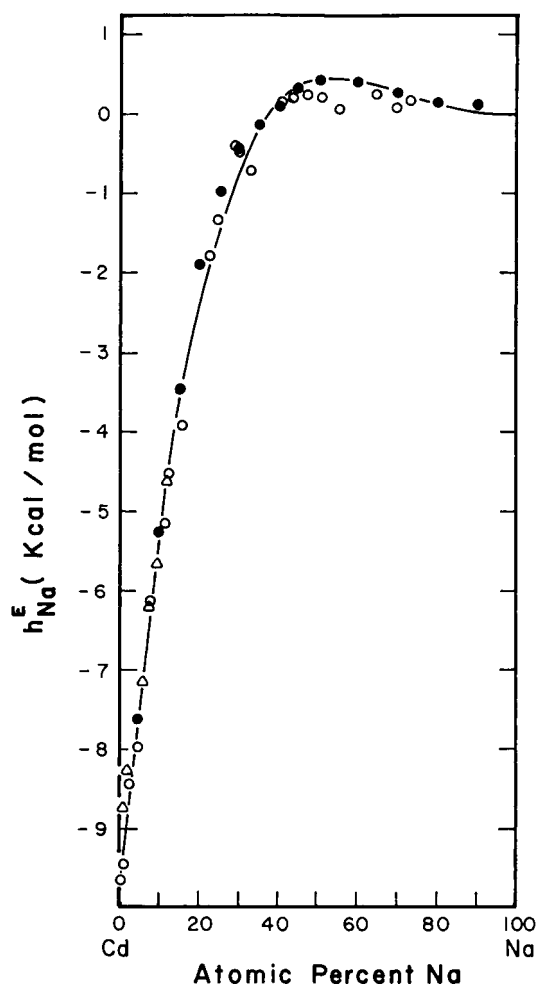


Figure 1-21. Partial excess enthalpy of sodium in liquid Cd–Na alloys. Line is calculated from optimized thermodynamic parameters (Reprinted from Pelton, 1988a). ● Lantratov and Mikhailova (1971), △ Maierova et al. (1976), ○ Bartlett et al. (1970).

optimized simultaneously (Pelton, 1988a) to obtain the following expressions for h^E and s^E of the liquid:

$$h^{E(l)} = X_{\text{Cd}} X_{\text{Na}} [-12508 + 20316 (1-106) \\ \times (X_{\text{Na}} - X_{\text{Cd}}) - 8714 (X_{\text{Na}} - X_{\text{Cd}})^2] \text{ J/mol}$$

$$s^{E(l)} = X_{\text{Cd}} X_{\text{Na}} [-15.452 + 15.186 (1-107) \\ \times (X_{\text{Na}} - X_{\text{Cd}}) - 10.062 (X_{\text{Na}} - X_{\text{Cd}})^2 \\ - 1.122 (X_{\text{Na}} - X_{\text{Cd}})^3] \text{ J/mol K}$$

Eq. (1-106) reproduces the calorimetric data within 200 J/mol^{-1} . Eqs. (1-52), (1-58), (1-93) and (1-95) can be used to calculate h_{Na}^E and γ_{Na} . The calculated curves are compared to the measured points in Figs. 1-20 and 1-21.

For the two compounds, Gibbs energies of fusion were calculated (Pelton, 1988a) so as to best reproduce the measured phase diagram:

$$\Delta g_{\text{f}(1/13 \text{ Cd}_{11}\text{Na}_2)}^0 = 6816 - 10.724 T \text{ J/g-atom} \quad (1-108)$$

$$\Delta g_{\text{f}(1/3 \text{ Cd}_2\text{Na})}^0 = 8368 - 12.737 T \text{ J/g-atom} \quad (1-109)$$

The optimized enthalpies of fusion of 6816 and 8368 J/g-atom agree within error limits with the values of 6987 and 7878 J/g-atom measured by Roos (1916). (See Fig. 1-14 for an illustration of the relation between the Gibbs energy of fusion of a compound and the phase diagram.)

The phase diagram shown in Fig. 1-19 was calculated from Eqs. (1-106) to (1-109) along with the Gibbs energies of fusion of Cd and Na taken from the literature (Chase, 1983). Complete details of the analysis of the Cd–Na system are given by Pelton (1988a).

It can thus be seen that one simple set of equations can simultaneously and self-consistently describe all the thermodynamic properties and the phase diagram of a binary system.

The exact optimization procedure will vary from system to system depending upon the type and accuracy of the available data, the number of phases present, the extent of solid solubility, etc. A large number of optimizations have been published in the *Calphad Journal* (Pergamon) since 1977.

1.6.4 Calculation of Metastable Phase Boundaries

In the Cd–Na system just discussed, the liquid exhibits positive deviations from ideal mixing. That is, $g^{E(l)} > 0$. This fact is reflected in the very flat liquidus in Fig. 1-19 as was discussed in Sec. 1.5.9.

By simply not including any solid phases in the calculation, the metastable liquid miscibility gap as well as the spinodal curve (Sec. 1.5.5) can be calculated as shown in Fig. 1-19. These curves are important in the formation of metallic glasses by rapid quenching.

Other metastable phase boundaries such as the extension of a liquidus curve below a eutectic can also be calculated thermodynamically by simply excluding one or more phases during the computations.

1.7 Ternary and Multicomponent Phase Diagrams

This section provides an introduction to ternary phase diagrams. For a more detailed treatment, see Prince (1966); Ricci (1964); Findlay (1951); or West (1965).

1.7.1 The Ternary Composition Triangle

In a ternary system with components A–B–C, the sum of the mole fractions is unity, $(X_A + X_B + X_C) = 1$. Hence, there are two independent composition variables. A representation of composition, symmetrical with respect to all three components, may be obtained with the equilateral “composition triangle” as shown in Fig. 1-22 for the Bi–Sn–Cd system. Compositions at the corners of the triangle correspond to the pure components. Along the edges of the triangle compositions corresponding to the three binary subsystems Bi–Sn, Sn–Cd

and Cd–Bi are found. Lines of constant mole fraction X_{Bi} are parallel to the Sn–Cd edge, while lines of constant X_{Sn} and X_{Cd} are parallel to the Cd–Bi and Bi–Sn edges respectively. For example, at point *a* in Fig. 1-22, $X_{Bi} = 0.05$, $X_{Sn} = 0.45$ and $X_{Cd} = 0.50$.

Similar equilateral composition triangles can be drawn with coordinates in terms of wt.% of the three components.

1.7.2 Ternary Space Model

A ternary temperature–composition “phase diagram” at constant total pressure may be plotted as a three-dimensional “space model” within a right triangular prism with the equilateral composition triangle as base and temperature as vertical axis. Such a space model for a simple eutectic ternary system A–B–C is illustrated in Fig. 1-23. On the three vertical faces of the prism we find the phase diagrams of the three binary subsystems, A–B, B–C and C–A which, in this example, are all simple eutectic binary systems. The binary eutectic points are e_1 , e_2 and e_3 . Within the prism we see three *liquidus surfaces* descending from the melting points of pure A, B and C. Compositions on these surfaces correspond to compositions of liquid in equilibrium with A-, B- and C-rich solid phases.

In a ternary system at constant pressure, the Gibbs phase rule, Eq. (1-85), becomes:

$$F = 4 - P \quad (1-110)$$

When the liquid and one solid phase are in equilibrium $P=2$. Hence $F=2$ and the system is bivariant. A ternary liquidus is thus a two-dimensional surface. We may choose two variables, say T and one composition coordinate of the liquid, but then the other liquid composition coordinate and the composition of the solid are fixed.

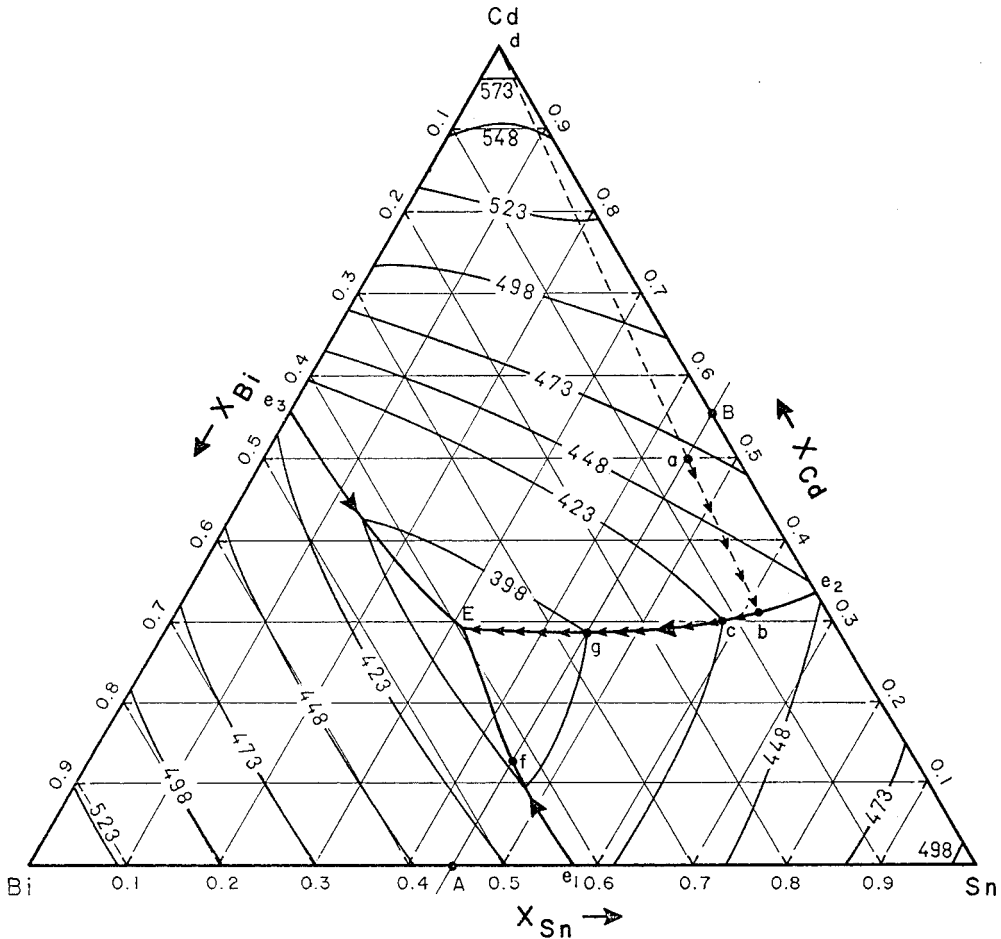


Figure 1-22. Projection of the liquidus surface of the Bi–Sn–Cd system onto the ternary composition triangle (after Bray et al., 1961–1962). Small arrows show the crystallization path of an alloy of overall composition at point *a*. (Reprinted from Pelton, 1996.)

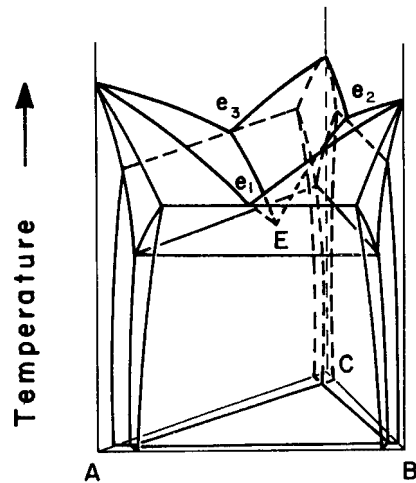


Figure 1-23. Perspective view of ternary space model of a simple eutectic ternary system. e_1 , e_2 , e_3 are the binary eutectics and E is the ternary eutectic. The base of the prism is the equilateral composition triangle. (Reprinted from Pelton, 1983.)

The A- and B-liquidus surfaces in Fig. 1-23 intersect along the line e_1E . Liquids with compositions along this line are therefore in equilibrium with A-rich and B-rich solid phases simultaneously. That is, $P=3$ and so $F=1$. Such “valleys” are thus called *univariant lines*. The three univariant lines meet at the *ternary eutectic point E* at which $P=4$ and $F=0$. This is an invariant point since the temperature and the compositions of all four phases in equilibrium are fixed.

1.7.3 Polythermal Projections of Liquidus Surfaces

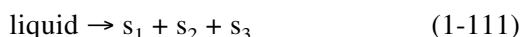
A two-dimensional representation of the ternary liquidus surface may be obtained as an orthogonal projection upon the base composition triangle. Such a *polythermal projection* of the liquidus of the Bi–Sn–Cd system (Bray et al., 1961–62) is shown in Fig. 1-22. This is a simple eutectic ternary system with a space model like that shown in Fig. 1-23. The constant temperature lines on Fig. 1-22 are called *liquidus isotherms*. The univariant valleys are shown as heavier lines. By convention, the large arrows indicate the directions of decreasing temperature along these lines.

Let us consider the sequence of events occurring during the equilibrium cooling from the liquid of an alloy of overall composition a in Fig. 1-22. Point a lies within the field of *primary crystallization* of Cd. That is, it lies within the composition region in Fig. 1-22 in which Cd-rich solid will be the first solid to precipitate upon cooling. As the liquid alloy is cooled, the Cd-liquidus surface is reached at $T \approx 465$ K (slightly below the 473 K isotherm). A solid Cd-rich phase begins to precipitate at this temperature. Now, in this particular system, Bi and Sn are nearly insoluble in solid Cd, so that the solid phase is virtually

pure Cd. (Note that this fact cannot be deduced from Fig. 1-22 alone.) Therefore, as solidification proceeds, the liquid becomes depleted in Cd, but the ratio $X_{\text{Sn}}/X_{\text{Bi}}$ in the liquid remains constant. Hence, the composition path followed by the liquid (its *crystallization path*) is a straight line passing through point a and projecting to the Cd-corner of the triangle. This crystallization path is shown on Fig. 1-22 as the line ab .

In the general case in which a solid solution rather than a pure component or stoichiometric compound is precipitating, the crystallization path will not be a straight line. However, for equilibrium cooling, a straight line joining a point on the crystallization path at any T to the overall composition point a will extend through the composition, on the solidus surface, of the solid phase in equilibrium with the liquid at that temperature.

When the composition of the liquid has reached point b in Fig. 1-22 at $T \approx 435$ K, the relative proportions of the solid Cd and liquid phases at equilibrium are given by the *lever rule* applied to the *tie-line dab*: (moles of liquid)/(moles of Cd) = da/ab . Upon further cooling, the liquid composition follows the univariant valley from b to E while Cd and Sn-rich solids coprecipitate as a binary eutectic mixture. When the liquidus composition attains the ternary eutectic composition E at $T \approx 380$ K the invariant *ternary eutectic reaction* occurs:



where s_1 , s_2 and s_3 are the three solid phases and where the compositions of all four phases (as well as T) remain fixed until all liquid is solidified.

In order to illustrate several of the features of polythermal projections of liquidus surfaces, a projection of the liquidus of a hypothetical system A–B–C is shown in Fig. 1-24. For the sake of simplicity, iso-

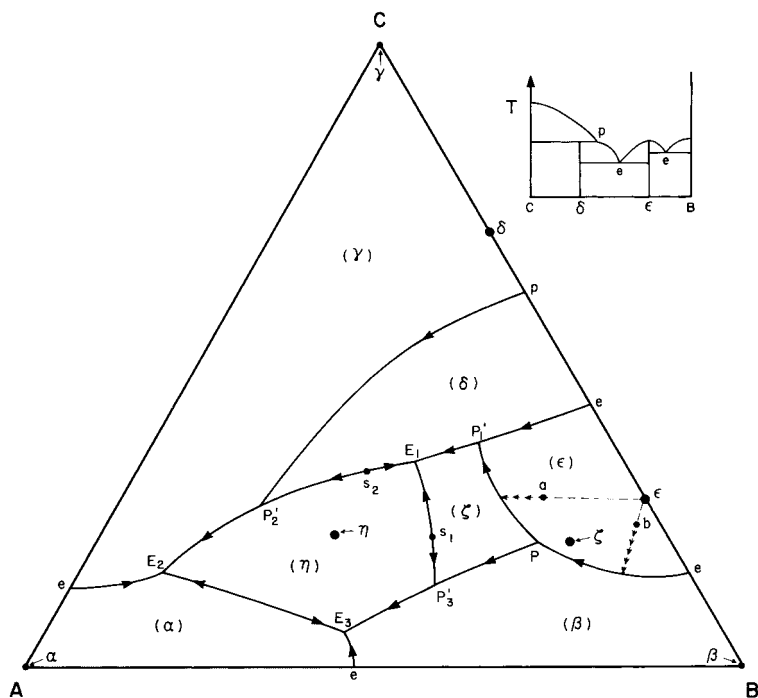


Figure 1-24. Projection of the liquidus surface of a system A–B–C. The binary subsystems A–B and C–A are simple eutectic systems. The binary phase diagram B–C is shown in the insert. All solid phases are assumed pure stoichiometric components or compounds. Small arrows show crystallization paths of alloys of compositions at points *a* and *b*. (Reprinted from Pelton, 1983.)

therms are not shown, only the univariant lines with arrows to show the directions of decreasing temperature. The binary subsystems A–B and C–A are simple eutectic systems, while the binary subsystem B–C contains one congruent binary phase, ϵ , and one incongruent binary phase, δ , as shown in the insert in Fig. 1-24. The letters *e* and *p* indicate binary eutectic and peritectic points. The ϵ and δ phases are called *binary compounds* since they have compositions within a binary subsystem. Two *ternary compounds*, η and ζ , with compositions within the ternary triangle, as indicated in Fig. 1-24, are also found in this system. All compounds, as well as pure solid A, B and C (the “ α , β and γ ” phases), are assumed to be stoichiometric (i.e., there is no solid solubility). The fields of primary crystallization of all the solids are indicated in parentheses in Fig. 1-24. The composition of the ϵ phase lies within its

field, since ϵ is a congruent compound, while the composition of the δ phase lies outside of its field since δ is incongruent. Similarly for the ternary compounds, η is a congruently melting compound while ζ is incongruent. For the congruent compound η , the highest temperature on the η liquidus occurs at the composition of η .

The univariant lines meet at a number of *ternary eutectics* *E* (three arrows converging), a *ternary peritectic* *P* (one arrow entering, two arrows leaving the point), and several *ternary quasi-peritectics* *P'* (two arrows entering, one arrow leaving). Two *saddle points* *s* are also shown. These are points of maximum *T* along the univariant line but of minimum *T* on the liquidus surface along a section joining the compositions of the two solids. For example, s_1 is at a maximum along the univariant $E_1 P'_3$, but is a minimum point on the liquidus along the straight line $\zeta s_1 \eta$.

Let us consider the events occurring during cooling from the liquid of an alloy of overall composition a in Fig. 1-24. The primary crystallization product will be the ϵ phase. Since this is a pure stoichiometric solid the crystallization path of the liquid will be along a straight line passing through a and extending to the composition of ϵ as shown in the figure.

Solidification of ϵ continues until the liquid attains a composition on the univariant valley. Thereafter the liquid composition follows the valley towards the point P'_1 in co-existence with ϵ and ζ . At point P'_1 the invariant *ternary quasi-peritectic reaction* occurs isothermally:



Since there are two reactants in a quasi-peritectic reaction, there are two possible outcomes: (i) the liquid is completely consumed before the ϵ phase; in this case, solidification will be complete at the point P'_1 ; (ii) ϵ is completely consumed before the liquid. In this case, solidification will continue with decreasing T along the univariant line P'_1E_1 with co-precipitation of δ and ζ until, at E , the liquid will solidify eutectically (liquid $\rightarrow \delta + \zeta + \eta$). To determine whether outcome (i) or (ii) occurs, we use the mass balance criterion that, for three-phase equilibrium, the overall composition a must always lie within the *tie-triangle* formed by the compositions of the three phases. Now, the triangle joining the compositions of δ , ϵ and ζ does not contain the point a , but the triangle joining the compositions of δ , ζ and liquid at P'_1 does contain the point a . Hence, outcome (ii) occurs.

An alloy of overall composition b in Fig. 1-24 solidifies with ϵ as primary crystallization product until the liquid composition contacts the univariant line. Thereafter, co-precipitation of ϵ and β occurs with the liquid composition following the

univariant valley until the liquid reaches the peritectic composition P . The invariant *ternary peritectic reaction* then occurs isothermally:



Since there are three reactants, there are three possible outcomes: (i) the liquid is consumed before either ϵ or β and solidification terminates at P ; (ii) ϵ is consumed first, solidification then continues along the path PP'_3 ; or (iii) β is consumed first and solidification continues along the path PP'_1 . Which outcome occurs depends on whether the overall composition b lies within the tie-triangle (i) $\epsilon\beta\zeta$; (ii) $\beta\zeta P$, or (iii) $\epsilon\zeta P$. In the example shown, outcome (i) will occur.

1.7.4 Ternary Isothermal Sections

Isothermal projections of the liquidus surface do not provide information on the compositions of the solid phases at equilibrium. However, this information can be presented at any one temperature on an *isothermal section* such as that shown for the Bi–Sn–Cd system at 423 K in Fig. 1-25. This phase diagram is a constant temperature slice through the space model of Fig. 1-23.

The liquidus lines bordering the one-phase liquid region of Fig. 1-25 are identical to the 423 K isotherms of the projection in Fig. 1-22. Point c in Fig. 1-25 is point c on the univariant line in Fig. 1-22. An alloy with overall composition in the one-phase liquid region of Fig. 1-25 at 423 K will consist of a single liquid phase. If the overall composition lies within one of the two-phase regions, then the compositions of the two phases are given by the ends of the *tie-line* which passes through the overall composition. For example, a sample with overall composition p in Fig. 1-25 will consist

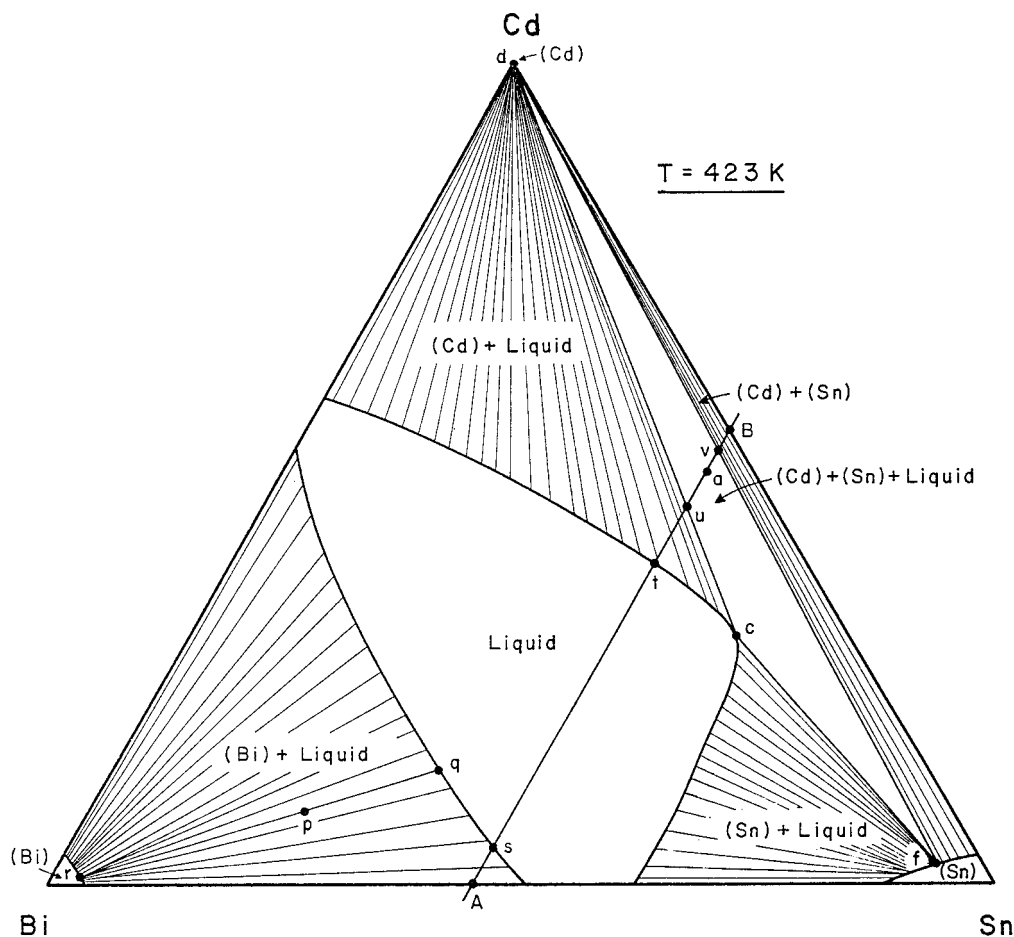


Figure 1-25. Isothermal section of the Bi–Sn–Cd system at 423 K at $P = 1$ bar (after Bray et al., 1961–1962). Extents of solid solubility in Bi and Sn have been exaggerated for clarity of presentation. (Reprinted from Pelton, 1996.)

of a liquid of composition q on the liquidus and a solid Bi-rich alloy of composition r on the solidus. The relative proportions of the two phases are given by the lever rule: (moles of liquid)/(moles of solid) = pr/pq , where pr and pq are the lengths of the tie-line segments.

In the case of solid Cd, the solid phase is nearly pure Cd, so all tie-lines of the (Cd + liquid) region converge nearly to the corner of the triangle. In the case of Bi- and Sn-rich solids, some solid solubility is observed. (The actual extent of this solubility

is somewhat exaggerated in Fig. 1-25 for the sake of clarity of presentation.) Alloys with overall compositions rich enough in Bi or Sn to lie within the single-phase (Sn) or (Bi) regions of Fig. 1-25 will consist at 423 K of single-phase solid solutions. Alloys with overall compositions at 423 K in the two-phase (Cd + Sn) region will consist of two solid phases.

Alloys with overall compositions within the three-phase triangle dcf will, at 423 K, consist of three phases: solid Cd- and Sn-rich solids with compositions at d and f and

liquid of composition c . To understand this better, consider an alloy of composition a in Fig. 1-25, which is the same composition as the point a in Fig. 1-22. In Sec. 1.7.3 we saw that when an alloy of this composition is cooled, the liquid follows the path ab in Fig. 1-22 with primary precipitation of Cd and then follows the univariant line with co-precipitation of Cd and Sn so that at 423 K the liquid is at the composition point c , and two solid phases are in equilibrium with the liquid.

1.7.4.1 Topology of Ternary Isothermal Sections

At constant temperature the Gibbs energy of each phase in a ternary system is represented as a function of composition by a surface plotted in a right triangular prism with Gibbs energy as vertical axis and the composition triangle as base. Just as the compositions of phases at equilibrium in binary systems are determined by the points of contact of a common tangent line to their isothermal Gibbs energy curves, so the compositions of phases at equilibrium in a ternary system are given by the points of contact of a common tangent plane to their isothermal Gibbs energy surfaces. A common tangent plane can contact two Gibbs energy surfaces at an infinite number of pairs of points, thereby generating an infinite number of tie-lines within a two-phase region on an isothermal section. A common tangent plane to three Gibbs energy surfaces contacts each surface at a unique point, thereby generating a three-phase tie-triangle.

Hence, the principal topological units of construction of an isothermal ternary phase diagram are three-phase ($\alpha + \beta + \gamma$) tie-triangles as in Fig. 1-26 with their accompanying two-phase and single-phase areas. Each corner of the tie-triangle contacts a

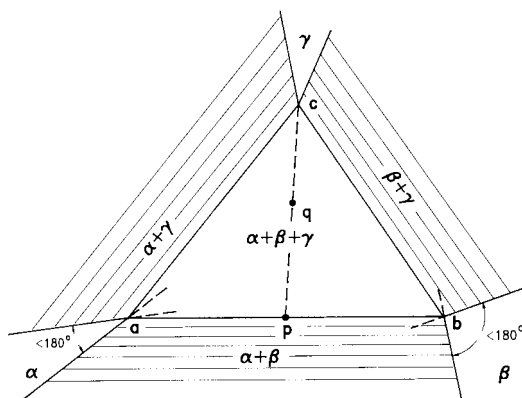


Figure 1-26. A tie-triangle in a ternary isothermal section illustrating the lever rule and the extension rule.

single-phase region, and from each edge of the triangle there extends a two-phase region. The edge of the triangle is a limiting tie-line of the two-phase region.

For overall compositions within the tie-triangle, the compositions of the three phases at equilibrium are fixed at the corners of the triangle. The relative proportions of the three phases are given by the *lever rule of tie-triangles*, which can be derived from mass balance considerations. At an overall composition q in Fig. 1-26 for example, the relative proportion of the γ phase is given by projecting a straight line from the γ corner of the triangle (point c) through the overall composition q to the opposite side of the triangle, point p . Then: (moles of γ)/(total moles) = qp/cp if compositions are expressed in mole fractions, or (weight of γ)/(total weight) = qp/cp if compositions are in weight percent.

Isothermal ternary phase diagrams are generally composed of a number of these topological units. An example for the Al–Zn–Mg system at 25 °C is shown in Fig. 1-27 (Köster and Dullenkopf, 1936). The β , γ , δ , θ , η and ζ phases are binary intermetallic compounds with small (~1 to 6%)

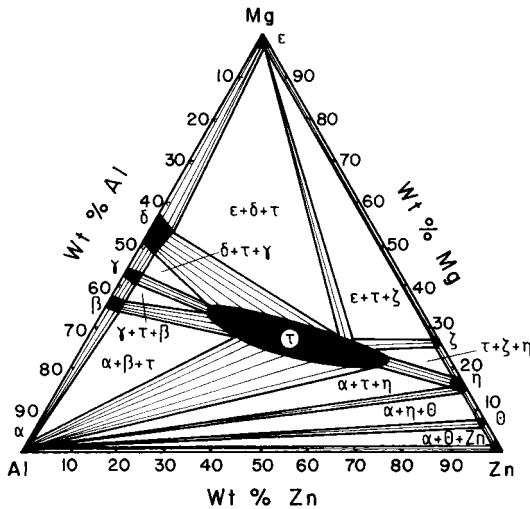


Figure 1-27. Ternary isothermal section of the Al–Zn–Mg system at 25°C at $P=1$ bar (after Köster and Dullenkopf, 1936). (Reprinted from Pelton, 1983.)

ranges of stoichiometry which can dissolve a limited amount (~ 1 to 6%) of the third component. The τ phase is a ternary phase with a single-phase region existing over a fairly extensive oval-shaped central composition range. Examination of Fig. 1-27 shows that it consists of the topological units of Fig. 1-26.

An *extension rule*, a case of *Schreinermakers' Rule* (Schreinermakers, 1915), see Sec. 1.7.5, for ternary tie-triangles is illustrated in Fig. 1-26. At each corner, the extension of the boundaries of the single-phase regions, indicated by the broken lines, must either both project into the triangle as at point a , or must both project outside the triangle as at point b . Furthermore, the angle between these extensions must be less than 180° . For a proof, see Lipson and Wilson (1940) or Pelton (1995).

Many published phase diagrams violate this rule. For example, it is violated in Fig. 1-27 at the δ -corner of the $(\epsilon + \delta + \tau)$ tie-triangle.

Another important rule of construction, whose derivation is evident, is that within any two-phase region tie-lines must never cross one another.

1.7.5 Ternary Isopleths (Constant Composition Sections)

A vertical *isopleth*, or constant composition section through the space model of the Bi–Sn–Cd system, is shown in Fig. 1-28. The section follows the line AB in Fig. 1-22.

The phase fields on Fig. 1-28 indicate which phases are present when an alloy with an overall composition on the line AB is equilibrated at any temperature. For example, consider the cooling, from the liquid state, of an alloy of composition a which is on the line AB (see Fig. 1-22). At $T \approx 465$ K, precipitation of the solid (Cd) phase begins at point a in Fig. 1-28. At $T \approx 435$ K (point b in Figs. 1-22 and 1-28) the solid (Sn) phase begins to appear. Finally, at the eutectic temperature T_E , the ternary reaction occurs, leaving solid (Cd) + (Bi) + (Sn) at lower temperatures. The intersection of the isopleth with the univariant lines on Fig. 1-22 occurs at points f and g which are also indicated on Fig. 1-28. The intersection of this isopleth with the isothermal section at 423 K is shown in Fig. 1-25. The points s , t , u and v of Fig. 1-25 are also shown on Fig. 1-28.

It is important to note that on an isopleth the tie-lines do not, in general, lie in the plane of the diagram. Therefore, the diagram provides information only on which phases are present, not on their compositions. The boundary lines on an isopleth do not in general indicate the phase compositions, only the temperature at which a phase appears or disappears for a given overall composition. The lever rule cannot be applied on an isopleth.

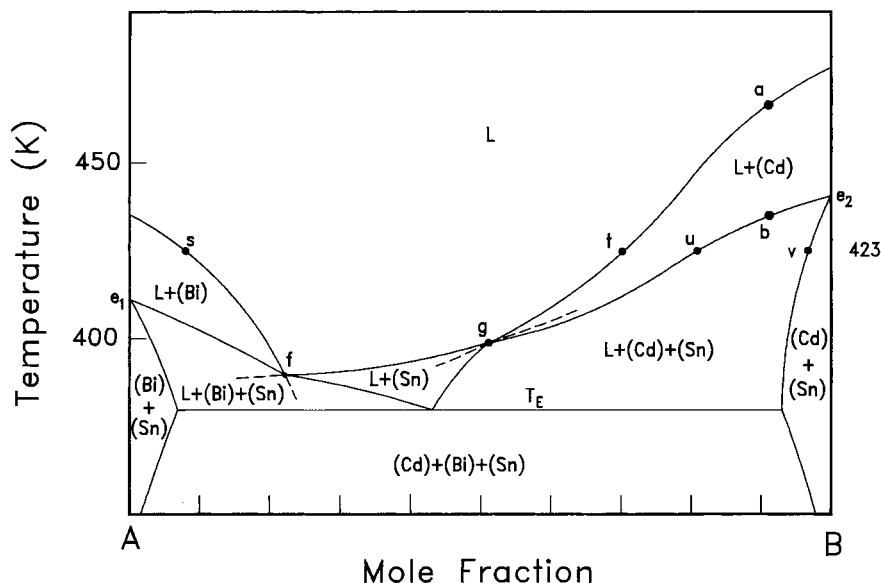


Figure 1-28. Isopleth (constant composition section) of the Bi–Sn–Cd system at $P=1$ bar following the line AB at $X_{\text{Sn}} = 0.45$ of Fig. 1-22. (Reprinted from Pelton, 1996).

Certain geometrical rules apply to isopleths. As a phase boundary line is crossed, one and only one phase either appears or disappears. This *Law of Adjoining Phase Regions* (Palatnik and Landau, 1964) is illustrated by Fig. 1-28. The only apparent exception occurs for the horizontal invariant line at T_E . However, if we consider this line to be a degenerate infinitely narrow four-phase region ($L + (Cd) + (Bi) + (Sn)$), then the law is also obeyed here.

Three or four boundary lines meet at intersection points. At an intersection point, such as point f or g , *Schreinemakers' Rule* applies. This is discussed in Sec. 1.9.

Apparent exceptions to these rules (such as, for example, five boundaries meeting at an intersection point) can occur if the section passes exactly through a node (such as a ternary eutectic point) of the space model. However, these apparent exceptions are really only limiting cases (see Prince, 1963 or 1966).

1.7.5.1 Quasi-Binary Phase Diagrams

Several of the binary phase diagrams in the preceding sections (Figs. 1-5, 1-10, 1-12, 1-14, 1-18) are actually isopleths of ternary systems. For example, Fig. 1-12 is an isopleth at constant $X_O = n_O / (n_{\text{Mg}} + n_{\text{Ca}} + n_O) = 0.5$ of the Mg–Ca–O system. However, all tie-lines lie within (or virtually within) the plane of the diagram because $X_O = 0.5$ in every phase. Therefore, the diagram is called a *quasi-binary* phase diagram.

1.7.6 Multicomponent Phase Diagrams

Only an introduction to multicomponent phase diagrams will be presented here. For more detailed treatments see Palatnik and Landau (1964), Prince (1963), Prince (1966) and Hillert (1998).

For systems of four or more components, two-dimensional sections are usually plot-

ted with one or more compositional variables held constant. Hence these sections are similar to the ternary isopleths discussed in Sec. 1.7.5. In certain cases, sections at constant chemical potential of one or more components (for example, at constant oxygen partial pressure) can be useful. These are discussed in Sec. 1.8.

Two sections of the Fe–Cr–V–C system (Lee and Lee, 1992) are shown in Figs. 1-29 and 1-30. The diagram in Fig. 1-29 is a T-composition section at constant Cr and V content, while Fig. 1-30 is a section at constant $T=850^{\circ}\text{C}$ and constant C content of 0.3 wt.%. The interpretation and topological rules of construction of these sections are the same as those for ternary isopleths, as discussed in Sec. 1.7.5. In fact, the same rules apply to a two-dimensional constant-composition section for a system of any number of components. The phase fields on the diagram indicate the phases present

at equilibrium for an overall composition lying on the section. Tie-lines do not, in general, lie in the plane of the diagram, so the diagram does not provide information on the compositions or amounts of the phases present. As a phase boundary is crossed, one and only one phase appears or disappears (Law of Adjoining Phase Regions). If temperature is an axis, as in Fig. 1-29, then horizontal invariants like the line AB in Fig. 1-29 can appear. These can be considered as degenerate infinitely narrow phase fields of $(C + 1)$ phases, where C is the number of components (for isobaric diagrams). For example in Fig. 1-29, on the line AB , five phases are present. Three or four phase boundaries meet at intersection points at which Schreinemaker's Rule applies. It is illustrated by the extrapolations in Fig. 1-29 at points a , b and c and in Fig. 1-30 at points b , c , n , i and s (see discussions in Sec. 1.9).

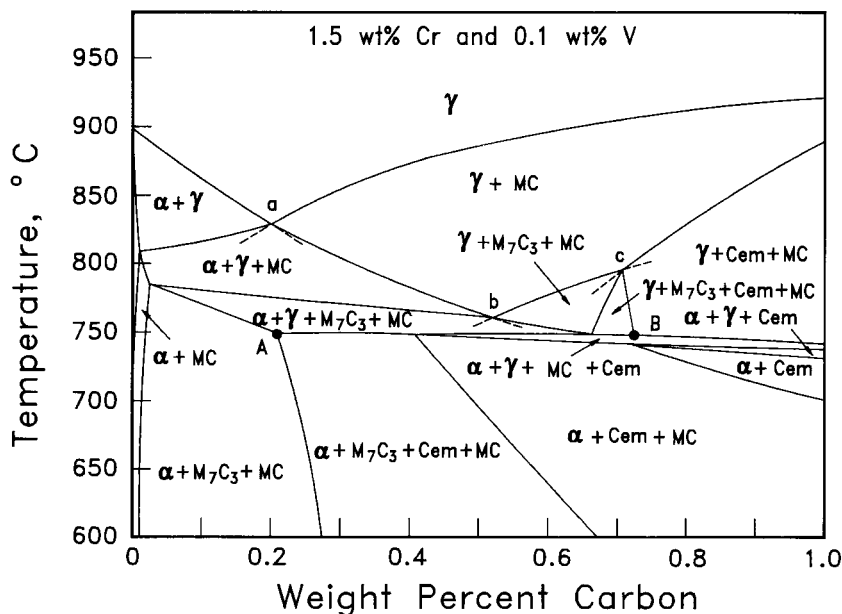


Figure 1-29. Section of the Fe–Cr–V–C system at 1.5 wt.% Cr and 0.1 wt.% V at $P=1$ bar (Lee and Lee, 1992).

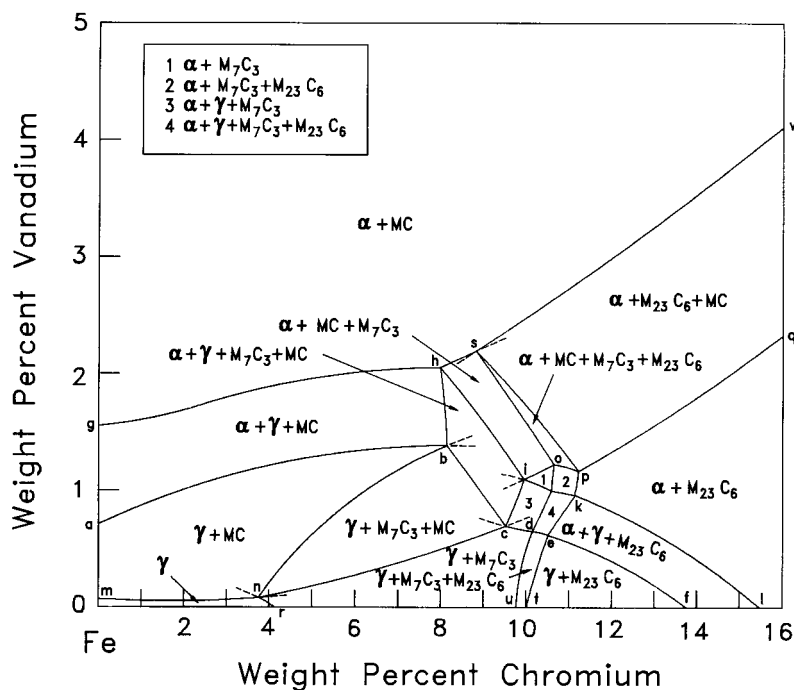


Figure 1-30. Section of the Fe–Cr–V–C system at 850°C and 0.3 wt.% C at $P = 1$ bar (Lee and Lee, 1992).

1.7.7 Nomenclature for Invariant Reactions

As discussed in Sec. 1.5.12, in a binary isobaric temperature–composition phase diagram there are two possible types of invariant reactions: “eutectic-type” ($\beta \rightarrow \alpha + \gamma$), and “peritectic type” ($\alpha + \gamma \rightarrow \beta$). In a ternary system, there are “eutectic-type” ($\alpha \rightarrow \beta + \gamma + \delta$), “peritectic-type” ($\alpha + \beta + \gamma \rightarrow \delta$), and “quasiperitectic-type” ($\alpha + \beta \rightarrow \gamma + \delta$) invariants (Sec. 1.7.3). In a system of C components, the number of types of invariant reaction is equal to C . A reaction with one reactant, such as ($\alpha \rightarrow \beta + \gamma + \delta + \epsilon$) is clearly a “eutectic-type” invariant reaction but in general there is no standard terminology. These reactions are conveniently described according to the numbers of reactants and products (in the direction which occurs upon cooling). Hence the reaction ($\alpha + \beta \rightarrow \gamma + \delta + \epsilon$) is a $2 \rightarrow 3$ reaction; the reaction ($\alpha \rightarrow \beta + \gamma$

+ δ) is a $1 \rightarrow 3$ reaction; and so on. The ternary peritectic-type $3 \rightarrow 1$ reaction ($\alpha + \beta + \gamma \rightarrow \delta$) is an invariant reaction in a ternary system, a univariant reaction in a quaternary system, a bivariant reaction in a quinary system, etc.

1.7.8 Reciprocal Ternary Phase Diagrams

A *reciprocal ternary salt system* is one consisting of two cations and two anions, such as the Na^+ , K^+/F^- , Cl^- system of Fig. 1-31. The condition of charge neutrality ($n_{\text{Na}^+} + n_{\text{K}^+} = n_{\text{F}^-} + n_{\text{Cl}^-}$) removes one degree of freedom. The system is thus *quasiter-nary* and its composition can be represented by two variables, usually chosen as the *cationic mole fraction* $X_{\text{K}} = n_{\text{K}} / (n_{\text{Na}} + n_{\text{K}})$ and the *anionic mole fraction* $X_{\text{Cl}} = n_{\text{Cl}} / (n_{\text{F}} + n_{\text{Cl}})$, where n_i = number of moles of ion i . Note that $X_{\text{Na}} = (1 - X_{\text{K}})$ and $X_{\text{F}} = (1 - X_{\text{Cl}})$.

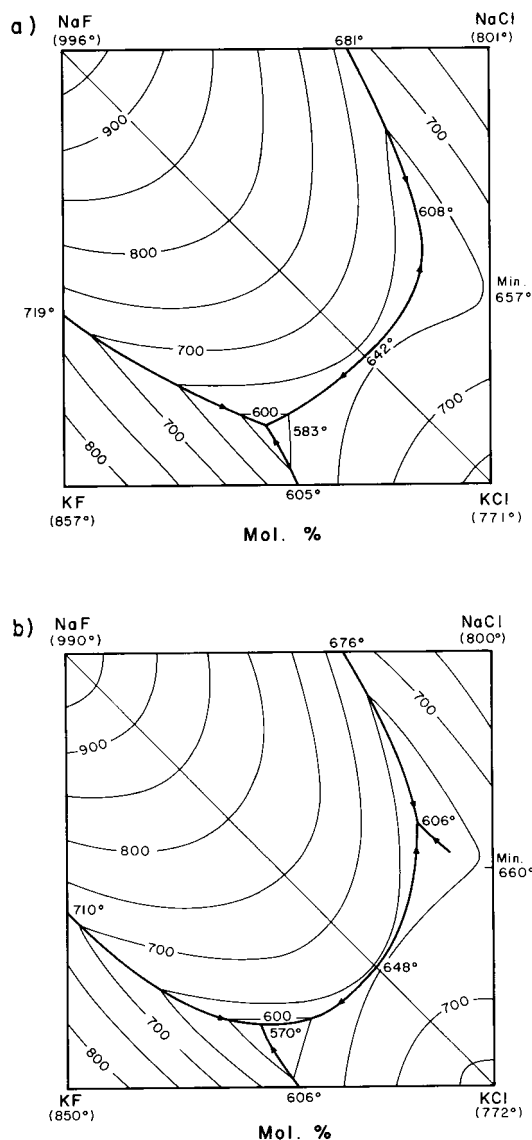


Figure 1-31. Projection of the liquidus surface of the Na⁺, K⁺/F⁻, Cl⁻ reciprocal ternary system.

- a) Calculated from optimized binary thermodynamic parameters.
 b) As reported by Polyakov (1940).

The assumption has, of course, been made that the condition ($n_{\text{Na}} + n_{\text{K}} = n_{\text{F}} + n_{\text{Cl}}$) holds exactly in every phase. If there is a deviation from this exact stoichiometry, then the phase diagram is no longer quasi-

ternary but is an isopleth of the four-component Na–K–F–Cl system, and tie-lines no longer necessarily lie in the plane of the diagram.

In Fig. 1-31 the cationic and anionic fractions are plotted as axes of a square. Compositions corresponding to the four neutral salts (KF, KCl, NaCl, NaF) are found at the corners of the square. Edges of the square correspond to the binary subsystems such as NaF–NaCl. A ternary space model (analogous to Fig. 1-23) can be constructed with temperature as vertical axis. The phase diagram of Fig. 1-31 is a polythermal projection of the liquidus surface upon the composition square.

In this system, three of the binary edges are simple eutectic systems, while the NaCl–KCl binary system exhibits a solidus/liquidus minimum. There is a ternary eutectic at 570°C in Fig. 1-31(b). The NaF–KCl diagonal contains a saddle point at 648°C in Fig. 1-31(b). This saddle point is a eutectic of the *quasibinary system* NaF–KCl. That is, a binary phase diagram NaF–KCl could be drawn with one simple eutectic at 648°C. However, the NaCl–KF system, which forms the other diagonal, is not a quasibinary system. If compositions lying on this diagonal are cooled at equilibrium from the liquid, solid phases whose compositions do not lie on this diagonal can precipitate. Hence, a simple binary phase diagram cannot be drawn for the NaCl–KF system.

For systems such as Ca²⁺, Na⁺/F⁻, SO₄²⁻ in which the ions do not all have the same charge, composition axes are conveniently expressed as equivalent ionic fractions (e.g. $Y_{\text{Ca}} = 2n_{\text{Ca}}/(2n_{\text{Ca}} + n_{\text{Na}})$), see Sec. 1.9.2.1.

The concept of reciprocal systems can be generalized beyond simple salt systems and is closely related to the sublattice model (Sec. 1.10.1).

For further discussion and references, see Pelton (1988b) and Blander (1964).

1.8 Phase Diagrams with Potentials as Axes

So far we have considered mainly isobaric temperature–composition phase diagrams. However there are many other kinds of phase diagrams of interest in materials science and technology with pressure, chemical potentials, volume, etc. as axes. These can be classified into geometrical types according to their rules of construction.

For instance, binary isothermal P – X diagrams as in Fig. 1-8 are members of the same type as binary isobaric T – X diagrams because they are both formed from the same topological units of construction. Other useful phase diagrams of this same geometrical type are isothermal chemical potential–composition diagrams for ternary systems. An example is shown in the lowest panel of Fig. 1-32 (Pelton and Thompson, 1975) for the Co–Ni–O system at $T = 1600$ K (and at a constant total hydrostatic pressure of 1 bar). Here the logarithm of the equilibrium partial pressure of O_2 is plotted versus the metal ratio $\xi = n_{Ni}/(n_{Co} + n_{Ni})$, where n_i = number of moles of i . There are two phases in this system under these conditions, a solid alloy stable at lower p_{O_2} , and a solid solution of CoO and NiO stable at higher p_{O_2} . For instance, point a gives p_{O_2} for the equilibrium between pure Co and pure CoO at 1600 K. Between the two single-phase regions is a two-phase (alloy + oxide) region. At any overall composition on the tie-line cd between points c and d , two phases will be observed, an alloy of composition d and an oxide of composition c . The lever rule applies just as for binary T – X diagrams.

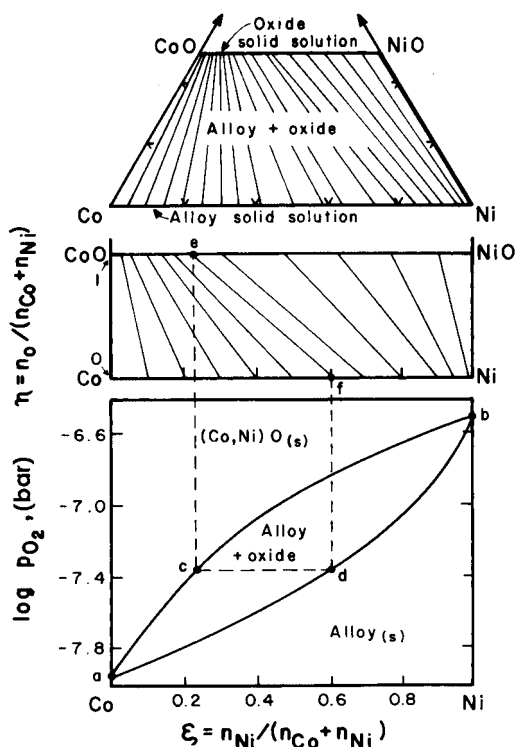


Figure 1-32. Corresponding phase diagrams for the Co–Ni–O system at 1600 K (from Pelton and Thompson, 1973).

The usual isothermal section of the ternary Co–Ni–O system at 1600 K is shown in the top panel of Fig. 1-32. There are two single-phase regions with a two-phase region between them. The single-phase areas are very narrow because oxygen is only very slightly soluble in the solid alloy and CoO and NiO are very stoichiometric oxides. In the central panel of Fig. 1-32 this same diagram is shown with the composition triangle “opened up” by putting the oxygen corner at infinity. This can be done if the vertical axis becomes $\eta = n_O / (n_{Co} + n_{Ni})$ with the horizontal axis as $\xi = n_{Ni} / (n_{Co} + n_{Ni})$. These are known as *Jänecke coordinates*. It can be seen in Fig. 1-32 that each tie-line, ef , of the isothermal section corresponds to a tie-line cd of the

$\log p_{\text{O}_2}$ – ξ diagram. This underscores the fact that every tie-line of a ternary isothermal section corresponds to a constant chemical potential of each of the components.

Another example of a $\log p_{\text{O}_2}$ – ξ diagram is shown for the Fe–Cr–O system at 1573 K in the lower panel of Fig. 1-33 (Pelton and Schmalzried, 1973). The corresponding ternary isothermal section in Jänecke coordinates is shown in the upper panel. Each of the invariant three-phase tie-triangles in the isothermal section corresponds to an invariant line in the

$\log p_{\text{O}_2}$ – ξ diagram. For example, the (spinel + (Fe, Cr)O + alloy) triangle with corners at points *a*, *b* and *c* corresponds to the “eutectic-like” or *eutecular* invariant with the same phase compositions *a*, *b* and *c* at $\log p_{\text{O}_2} \approx -10.7$. We can see that within a three-phase tie-triangle, p_{O_2} is constant.

An example of yet another kind of phase diagram of this same geometrical type is shown in Fig. 1-34. For the quaternary Fe–Cr–O₂–SO₂ system at $T = 1273$ K and at constant $p_{\text{SO}_2} = 10^{-7}$ bar, Fig. 1-34 is a plot of $\log p_{\text{O}_2}$ versus the molar metal ratio

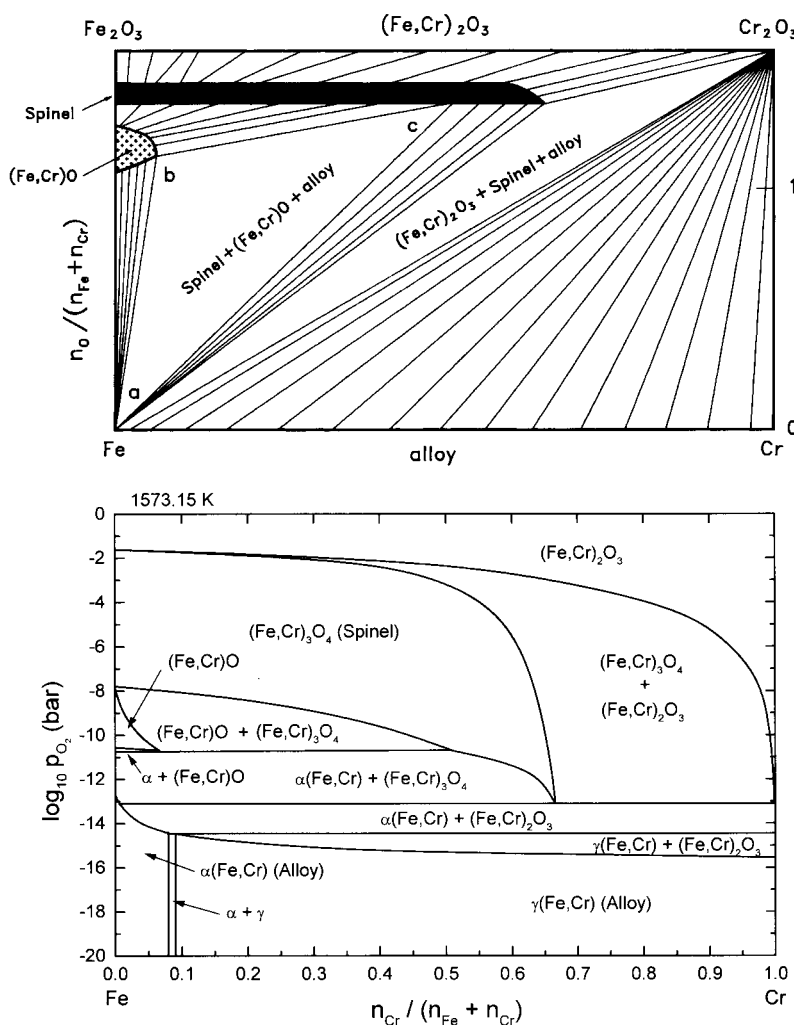


Figure 1-33. Corresponding phase diagrams for the Fe–Cr–O system at 1573 K (Pelton and Schmalzried, 1973). Experimental points from Katsura and Muan (1964).

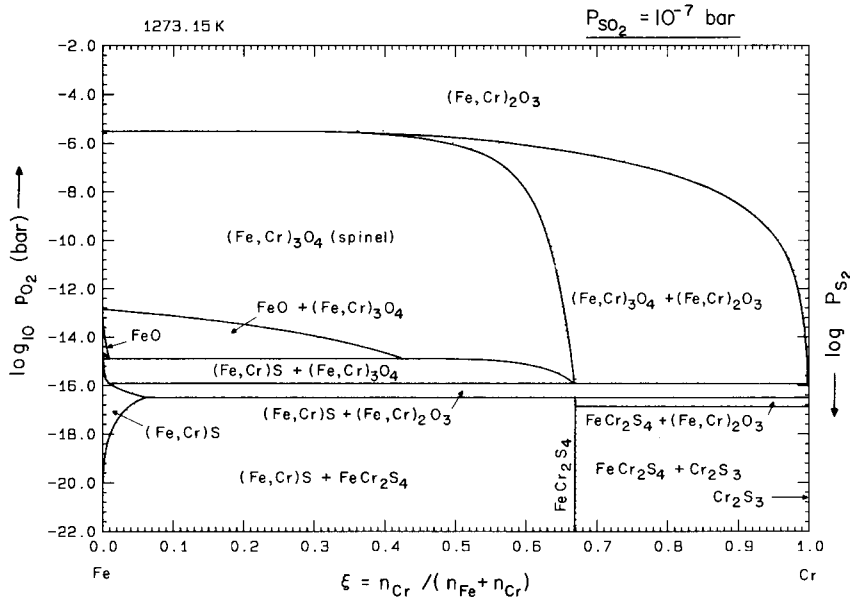


Figure 1-34. Calculated phase diagram of $\log p_{O_2}$ versus molar metal ratio at $T = 1273.15$ K and $p_{SO_2} = 10^{-7}$ bar for the Fe–Cr–SO₂–O₂ system.

ξ . Since $\log p_{O_2}$ varies as $-1/2 \log p_{S_2}$ when p_{SO_2} and T are constant, Fig. 1-34 is also a plot of $\log p_{S_2}$ versus ξ .

Plotting T versus ξ at constant p_{O_2} in the Fe–Cr–O system, or at constant p_{O_2} and p_{SO_2} in the Fe–Cr–SO₂–O₂ system, will also result in phase diagrams of this same

geometrical type. Often for ceramic systems, we encounter “binary” phase diagrams such as that for the “CaO–Fe₂O₃” system in Fig. 1-35, which has been taken from Phillips and Muan (1958). How are we to interpret such a diagram? How, for instance, do we interpret the composition

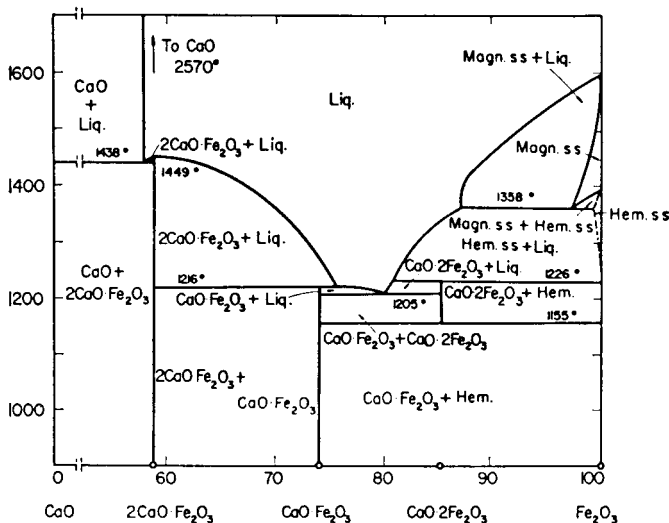


Figure 1-35. Phase diagram for the “CaO–Fe₂O₃” system in air ($p_{O_2} = 0.21$ bar) from Phillips and Muan (1958) (Reprinted by permission of the American Ceramic Society from Levin et al., 1964).

axis when applied to the magnetite phase? In light of the preceding discussion, it can be seen that such diagrams are really $T-\xi$ plots at constant p_{O_2} , where ξ is the metal ratio in any phase. The diagram will be different at different oxygen partial pressures. If p_{O_2} is not fixed, the diagram cannot be interpreted.

It can be seen that the diagrams discussed above are of the same geometrical type as binary $T-X$ diagrams because they are all composed of the same geometrical units of construction as in Fig. 1-16. Their interpretation is thus immediately clear to anyone familiar with binary $T-X$ diagrams. Chemical potential–composition

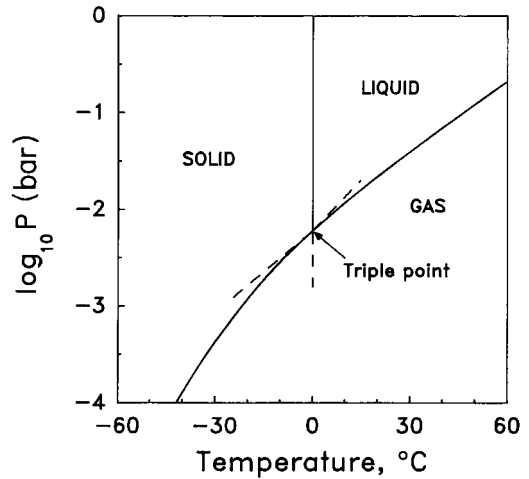


Figure 1-36. Pressure-temperature phase diagram of H_2O .

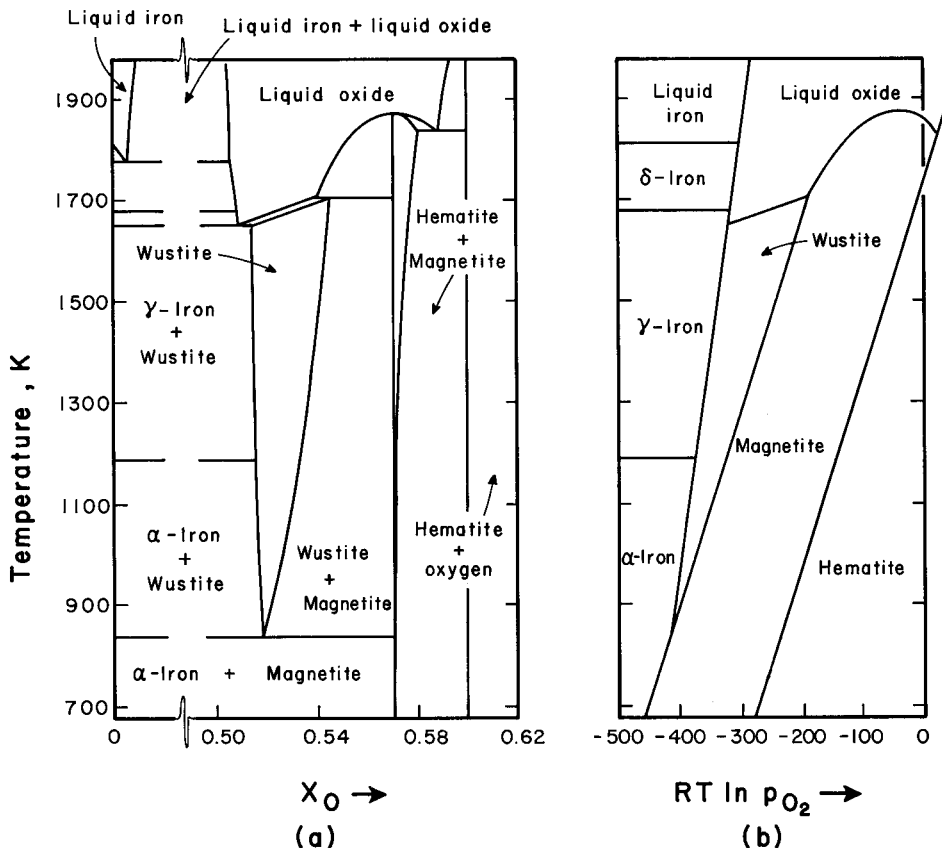


Figure 1-37. Corresponding phase diagrams for the Fe–O system at $P_{TOTAL} = 1$ bar (after Muan and Osborn, 1965).

diagrams (Figs. 1-32 to 1-34) are useful in the study of hot corrosion, metallurgical roasting processes, chemical vapor deposition, and many aspects of materials processing.

Another important geometrical type of phase diagram is exemplified by P – T phase diagrams for one-component systems, as shown for H_2O in Fig. 1-36. In such diagrams (see also Chapter 10 by Kunz (2001)) bivariant single-phase regions are indicated by areas, univariant two-phase regions by lines, and invariant three-phase regions by *triple points*. An important rule of construction is the *extension rule*, which is illustrated by the broken lines in Fig. 1-36. At a triple point, the extension of any two-phase line must pass into the single-phase region of the third phase. Clearly, the predominance diagrams

of Figs. 1-1 to 1-3 are of this same geometrical type.

As yet another example of this geometrical type of diagram, a plot of $RT \ln p_{O_2}$ versus T for the Fe–O system is shown in Fig. 1-37(b). Again, one-, two- and three-phase regions are indicated by areas, lines and triple points respectively. Fig. 1-37(a) is the binary T –composition phase diagram for the Fe–O system. The correspondence between Figs. 1-37(a) and 1-37(b) is evident. Each two-phase line of Fig. 1-37(b) “opens up” to a two-phase region of Fig. 1-37(a). Each tie-line of a two-phase region in Fig. 1-37(a) can thus be seen to correspond to a constant p_{O_2} . Triple points in Fig. 1-37(b) become horizontal invariant lines in Fig. 1-37(a).

Yet another type of phase diagram is shown in Fig. 1-38. This is an isothermal

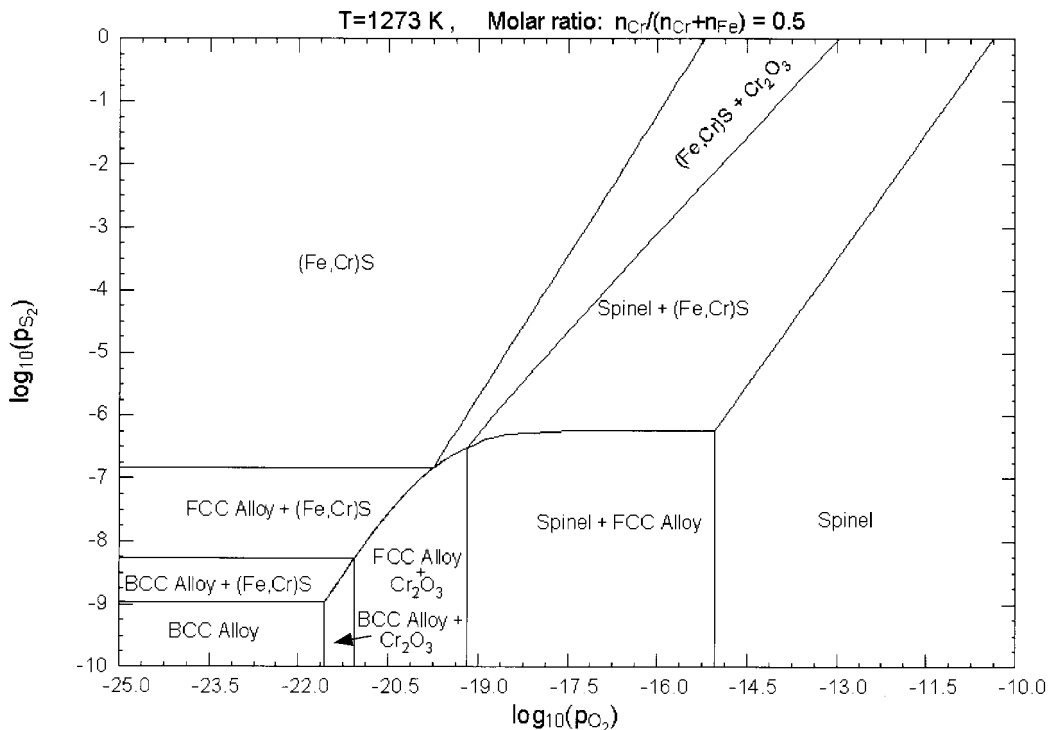


Figure 1-38. Phase diagram of $\log p_{S_2}$ versus $\log p_{O_2}$ at 1273 K and constant molar metal ratio $n_{Cr}/(n_{Fe} + n_{Cr}) = 0.5$ in the Fe–Cr–S₂–O₂ system.

section at constant molar metal ratio $n_{\text{Cr}}/(n_{\text{Fe}} + n_{\text{Cr}}) = 0.5$ for the Fe–Cr–S₂–O₂ system. This diagram was calculated thermodynamically from model parameters. The axes are the equilibrium sulfur and oxygen partial pressures. Three or four boundary lines can meet at an intersection point. Some of the boundary lines on Fig. 1-38 separate a two-phase region ($\alpha + \beta$) from another two-phase region ($\alpha + \gamma$). These lines thus represent the conditions for three-phase ($\alpha + \beta + \gamma$) equilibrium.

1.9 General Phase Diagram Geometry

Although the various phase diagrams shown in the preceding sections may appear to have quite different geometries, it can be shown that, in fact, all true phase diagram sections obey the same set of geometrical rules. Although these rules do not apply directly to phase diagram projections such as Figs. 1-22, 1-24 and 1-31, such diagrams can be considered to consist of portions of several phase diagram sections projected onto a common plane.

By “true” phase diagram we mean one in which each point of the diagram represents one unique equilibrium state. In the present section we give the general geometrical rules that apply to all true phase diagram sections, and we discuss the choices of axes and constants that ensure that the diagram is a true diagram.

We must first make some definitions. In a system of C components we can define $(C+2)$ thermodynamic potentials ϕ_i . These are T , P , μ_1 , μ_2 , ..., μ_C , where μ_i is the chemical potential defined in Eq. (1-23). For each potential there is a corresponding extensive variable q_i related by:

$$\phi_i = (\partial U / \partial q_i)_{q_j (j \neq i)} \quad (1-114)$$

Table 1-1. Corresponding pairs of potentials ϕ_i and extensive variables q_i .

ϕ_i :	T	P	μ_1	μ_2 ... μ_C
q_i :	S	$-V$	n_1	n_2 ... n_C

where U is the internal energy of the system. The corresponding potentials and extensive variables are listed in Table 1-1. It may also be noted that the corresponding pairs are found together in the terms of the general Gibbs–Duhem equation:

$$SdT - VdP + \sum n_i d\mu_i = 0 \quad (1-115)$$

1.9.1 General Geometrical Rules for All True Phase Diagram Sections

The Law of Adjoining Phase Regions applies to all true sections. As a phase boundary line is crossed, one and only one phase either appears or disappears.

If the vertical axis is a potential (T , P , μ_i), then horizontal invariant lines like the eutectic line in Fig. 1-12 or the line AB in Fig. 1-29 will be seen when the maximum number of phases permitted by the phase rule are at equilibrium. However, if these are considered to be degenerate infinitely narrow phase fields, then the Law of Adjoining Phase Regions still applies. This is illustrated schematically in Fig. 1-39 where the three-phase eutectic line has been “opened up”. Similarly, if both axes are potentials, then many phase boundaries may be degenerate infinitely narrow regions. For example, all phase boundaries on Figs. 1-1 to 1-3, 1-36 and 1-37(b) are degenerate two-phase regions which are schematically shown “opened up” on Fig. 1-40.

All phase boundary lines in a true phase diagram meet at nodes where exactly four lines converge, as in Fig. 1-41. N phases (α_1 , α_2 , ..., α_N) where $N \geq 1$ are common

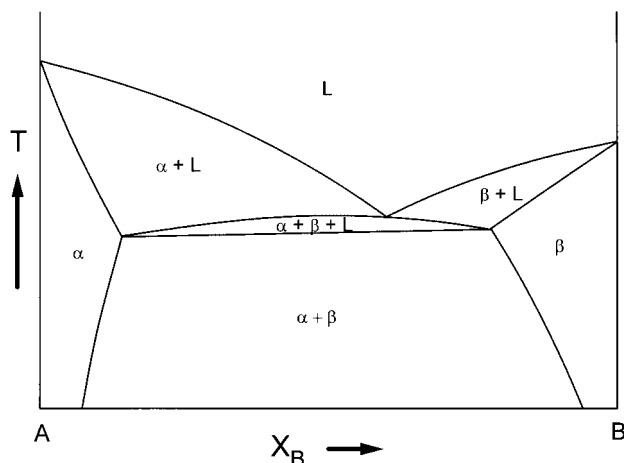


Figure 1-39. An isobaric binary T - X phase diagram (like Fig. 1-12) with the eutectic line “opened up” to illustrate that this is a degenerate 3-phase region.

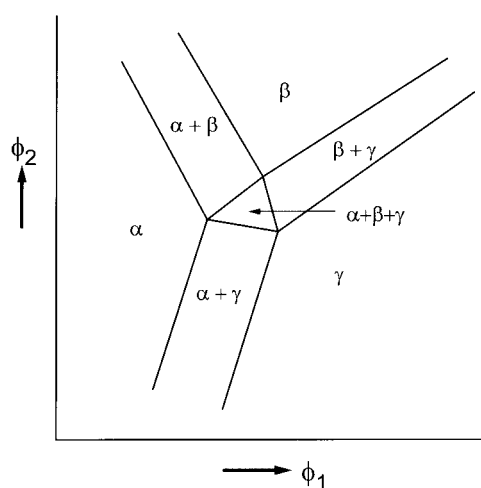


Figure 1-40. A potential–potential phase diagram (like Fig. 1-1 or Fig. 1-36) with the phase boundaries “opened up” to illustrate that they are degenerate 2-phase regions.

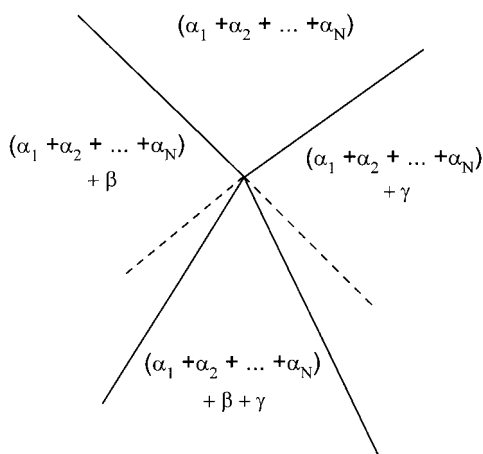


Figure 1-41. A node in a true phase diagram section.

to all four regions. *Schreinemakers' Rule* states that the extensions of the boundaries of the N -phase region must either both lie within the $(N+1)$ -phase regions as in Fig. 1-41 or they must both lie within the $(N+2)$ -phase region. This rule is illustrated by the extrapolations in Fig. 1-29 at points a , b and c and in Fig. 1-30 at points b , c , n , i and s . The applicability of Schreinemakers' Rule to systems of any number of

components was noted by Hillert (1985) and proved by Pelton (1995). In the case of degenerate phase regions, all nodes can still be considered to involve exactly four boundary lines if the degenerate boundaries are “opened up” as in Figs. 1-39 and 1-40.

An objection might be raised that a minimum or a maximum in a two-phase region in a binary temperature–composition phase diagram, as in Fig. 1-10 or in the lower panel of Fig. 1-16, represents an ex-

ception to Schreinemakers' Rule. However, the extremum in such a case is not actually a node where four phase boundaries converge, but rather a point where two boundaries touch. Such extrema in which two phase boundaries touch with zero slope may occur for a C -phase region in a phase diagram of a C -component system when one axis is a potential. For example, in an isobaric temperature–composition phase diagram of a four-component system, we may observe a maximum or a minimum in a four-phase region separating two three-phase regions. A similar maximum or minimum in a $(C-n)$ -phase region, where $n > 0$, may also occur, but only for a degenerate or special composition path. For further discussion, see Hillert (1998).

1.9.1.1 Zero Phase Fraction Lines

All phase boundaries on true phase diagram sections are *zero phase fraction (ZPF) lines*, a very useful concept introduced by Gupta et al. (1986). There are ZPF lines associated with each phase. On one side of its ZPF line the phase occurs, while on the other side it does not. For example, in Fig. 1-30 the ZPF line for the α phase is the line $abcdef$. The ZPF line for the γ phase is $ghijkl$. For the MC phase the ZPF line is $mnciopq$. The ZPF line for M_7C_3 is $rnbhspket$, and for $M_{23}C_6$ it is $udjosv$. These five ZPF lines yield the entire two-dimensional phase diagram. Phase diagram sections plotted on triangular coordinates as in Figs. 1-25 and 1-27 also consist of ZPF lines.

In the case of phase diagrams with degenerate regions, ZPF lines for two different phases may be coincident over part of their lengths. For example, in Fig. 1-12, line $CABD$ is the ZPF line of the liquid, while $CEBF$ and $DEAG$ are the ZPF lines for the α and β phases respectively. In

Fig. 1-1, all lines are actually two coincident ZPF lines.

The ZPF line concept is very useful in the development of general algorithms for the thermodynamic calculation of phase diagrams as discussed in Sec. 1-12.

1.9.2 Choice of Axes and Constants of True Phase Diagrams

In a system of C components, a two-dimensional diagram is obtained by choosing two axis variables and holding $(C-1)$ other variables constant. However, not all choices of variables will result in a true phase diagram. For example on the P – V diagram for H_2O shown schematically in Fig. 1-42, at any point in the area where the $(S+L)$ and $(L+G)$ regions overlap there are two possible equilibrium states of the system. Similarly, the diagram of carbon activity versus X_{Cr} at constant T and P in the Fe–Cr–C system in Fig. 1-43 (Hillert, 1997) exhibits a region in which there is no unique equilibrium state.

In order to be sure that a diagram is a true phase diagram, we must choose one *and only one* variable (either ϕ_i or q_i) from

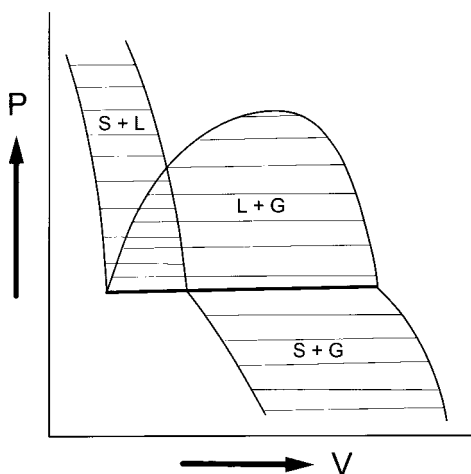


Figure 1-42. Schematic P – V diagram for H_2O . This is not a true phase diagram.

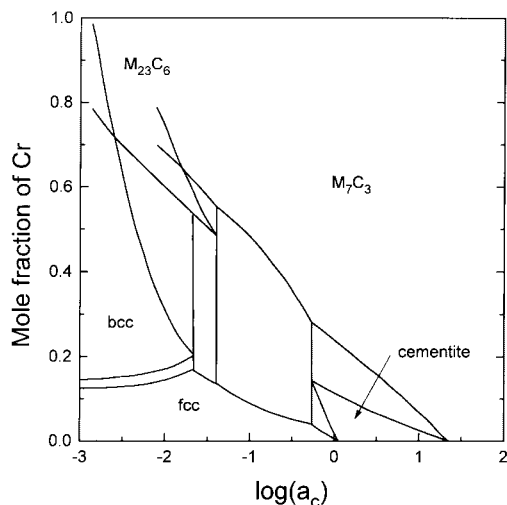


Figure 1-43. Carbon activity versus mole fraction of Cr at constant T and P in the Fe–Cr–C system. This is not a true phase diagram (from Hillert, 1997).

each of the $(C+2)$ conjugate pairs in Table 1-1. (Also, at least one of these must be an extensive variable q_i .) From among the n ($1 \leq n \leq C+2$) selected extensive variables, $(n-1)$ independent ratios are then formed. These $(n-1)$ ratios along with the $(C+2-n)$ selected potentials are the $(C+1)$ required variables. Two are chosen as axis variables and the remainder are held constant.

As a first example, consider a binary system with components A–B. The conjugate pairs are (T, S) , $(P, -V)$, (μ_A, n_A) and (μ_B, n_B) . Let us choose one variable from each pair as follows: T, P, n_A, n_B . From the selected extensive variables, n_A and n_B , we form a ratio such as $n_B/(n_A + n_B) = X_B$. The resultant phase diagram variables are T, P, X_B . Choosing any two as axes and holding the third constant will give a true phase diagram as in Fig. 1-6 or Fig. 1-8.

As a second example, consider Fig. 1-38 for the Fe–Cr–S₂–O₂ system. We choose one variable from each conjugate pair as follows: $T, P, \mu_{S_2}, \mu_{O_2}, n_{Fe}, n_{Cr}$. From the

selected extensive variables we form the ratio $n_{Fe}/(n_{Fe} + n_{Cr})$. Fig. 1-38 is a plot of μ_{S_2} versus μ_{O_2} at constant T, P and $n_{Fe}/(n_{Fe} + n_{Cr})$.

In Fig. 1-28 the selected variables are T, P, n_{Bi}, n_{Sn} and n_{Cd} , and ratios are formed from the selected extensive variables as $n_{Cd}/(n_{Cd} + n_{Bi})$ and $n_{Sn}/(n_{Cd} + n_{Bi} + n_{Sn}) = X_{Sn}$. Fig. 1-28 is a plot of T versus $n_{Cd}/(n_{Cd} + n_{Bi})$ at constant P and X_{Sn} .

Fig. 1-42, the P – V diagram for H₂O, is not a true phase diagram because P and V are members of the same conjugate pair. For the diagram shown in Fig. 1-43, we can choose one variable from each pair as follows: $T, P, \mu_C, n_{Fe}, n_{Cr}$. However the vertical axis is $X_{Cr} = n_{Cr}/(n_{Fe} + n_{Cr} + n_C)$. This ratio is not allowed because it contains n_C which is not on the list of chosen variables. That is, since we have chosen μ_C to be an axis variable, we cannot also choose n_C . Hence, Fig. 1-43 is not a true phase diagram. A permissible choice for the vertical axis would be $n_{Cr}/(n_{Fe} + n_{Cr})$ (see Fig. 1-33). Note that many regions of Figs. 1-42 and 1-43 do represent unique equilibrium states. That is, the procedure given here is a sufficient, but not necessary, condition for constructing true phase diagrams.

To apply this procedure simply, the components of the system should be formally defined to correspond to the desired axis variables or constants. For example, in Fig. 1-1 we wish to plot p_{SO_2} and $\log p_{O_2}$ as axes. Hence we define the components as Cu–SO₂–O₂ rather than Cu–S–O.

In several of the phase diagrams in this chapter, $\log p_i$ or $RT \ln p_i$ has been substituted for μ_i as axis variable or constant. From Eq. (1-32), this substitution can clearly be made if T is constant. However, even when T is an axis of the phase diagram as in Fig. 1-37(b), this substitution is still permissible since μ_i^0 is a monotonic function of T . The substitution of $\ln a_i$ for

μ_i results in a progressive expansion and displacement of the axis with increasing T that preserves the overall geometry of the diagram.

1.9.2.1 Tie-lines

If only potentials (T , P , μ_i) are held constant, then all tie-lines lie in the plane of the phase diagram section. In this case, the compositions of the individual phases at equilibrium can be read from the phase diagram, and the lever rule applies as, for example, in Figs. 1-6, 1-25, 1-33 or 1-34. However, if a ratio of extensive variables, such as a composition, is held constant as in the isopleths of Figs. 1-28 to 1-30, then in general, tie-lines do not lie in the plane.

If both axes are composition variables (ratios of n_i), and if only potentials are held constant, then it is desirable that the tie-lines (which lie in the plane) be straight lines. It can be shown (Pelton and Thompson, 1975) that this will only be the case if the denominators of the two composition variable ratios are the same. For example, in the central panel of Fig. 1-32, which is in Jänecke coordinates, the composition variables, $n_{\text{Co}}/(n_{\text{Co}} + n_{\text{Ni}})$ and $n_{\text{O}}/(n_{\text{Co}} + n_{\text{Ni}})$, have the same denominator. This same diagram can be plotted on triangular coordinates as in the upper panel of Fig. 1-32 and such a diagram can also be shown (Pelton and Thompson, 1975) to give straight tie-lines.

Similarly, in the quasiternary reciprocal phase diagram of Fig. 1-31 the vertical and horizontal axes are $n_{\text{Na}}/(n_{\text{Na}} + n_{\text{K}})$ and $n_{\text{Cl}}/(n_{\text{Cl}} + n_{\text{F}})$. To preserve charge neutrality, $(n_{\text{Na}} + n_{\text{K}}) = (n_{\text{Cl}} + n_{\text{F}})$, and so the tie-lines are straight. Generally, in quasiternary reciprocal salt phase diagrams, straight tie-lines are obtained by basing the composition on one equivalent of charge. For example, in the $\text{CaCl}_2\text{--NaCl--CaO--}$

Na_2O system we would choose as axes the *equivalent cationic and anionic fractions*, $n_{\text{Na}}/(n_{\text{Na}} + 2n_{\text{Ca}})$ and $n_{\text{Cl}}/(n_{\text{Cl}} + 2n_{\text{O}})$, whose denominators are equal because of charge neutrality.

1.9.2.2 Corresponding Phase Diagrams

When only potentials are held constant and when both axes are also potentials, then the geometry exemplified by Figs. 1-1 to 1-3, 1-26 and 1-37(b) results. Such diagrams were called “type-1 phase diagrams” by Pelton and Schmalzried (1973). If only potentials are held constant and one axis is a potential while the other is a composition variable, then the geometry exemplified by Figs. 1-8, 1-12, 1-34, 1-37(a), and the lower panel of Fig. 1-33 results. These were termed “type-2” diagrams. Finally, if only potentials are held constant and both axes are compositions, then a “type-3” diagram as in the upper panels of Figs. 1-32 and 1-33 results.

If the ϕ_i axis of a phase diagram is replaced by a composition variable that varies as its conjugate variable q_i (ex: q_i/q_j , $q_i/(q_i + q_j)$), then the new diagram and the original diagram are said to form a pair of *corresponding phase diagrams*. For instance, Figs. 1-37(a) and 1-37(b) are corresponding type-1 and type-2 phase diagrams, while Fig. 1-33 shows a corresponding pair of type-2 and type-3 diagrams. It is useful to draw corresponding diagrams beside each other as in Figs. 1-37 or 1-33 because the information contained in the two diagrams is complementary.

1.9.2.3 Theoretical Considerations

A complete rigorous proof that the procedure described in this section will always generate a true phase diagram is beyond the scope of this chapter. As an outline of the proof, we start with the generalized

stability criterion:

$$(\partial\phi_1/\partial q_1)_{\phi_2, \phi_3, \dots, q_N, q_{N+1}, q_{N+2}, \dots, q_{C+2}} \geq 0 \quad (1-116)$$

This equation states that a potential ϕ_i always increases as its conjugate variable q_i increases when either ϕ_j or q_j from every other conjugate pair is held constant. For instance, μ_i of a component always increases as that component is added to a system (that is, as n_i is increased) at constant T and P , when either the number of moles or the chemical potential of every other component is held constant. In a binary system, for example, this means that the equilibrium Gibbs energy envelope is always convex, as shown in Fig. 1-6. If the envelope were concave, then the system would be unstable and would separate into two phases, as shown in Fig. 1-11.

Consider first a phase diagram with axes ϕ_1 and ϕ_2 with $\phi_3, \phi_4, \dots, \phi_{C+1}$ and q_{C+2} constant. Such a diagram is always a true phase diagram. If the potential ϕ_1 is now replaced by q_1 , the diagram still remains a true phase diagram because of Eq. (1-116). The sequence of equilibrium states that occurs as q_1 is increased will be the same as that which occurs as ϕ_1 is increased when all the other variables (ϕ_i or q_i) are held constant.

A true phase diagram is therefore obtained if the axis variables and constants are chosen from the variables $\phi_1, \phi_2, \dots, \phi_N, q_{N+1}, q_{N+2}, \dots, q_{C+1}$ with q_{C+2} held constant. The extensive variables can be normalized as (q_i/q_{C+2}) or by any other independent and unique set of ratios.

It should be noted that at least one extensive variable, q_{C+2} , is considered to be constant across the entire diagram. In practice, this means that one of the extensive variables must be either positive or negative everywhere on the diagram. For certain formal choices of components, extensive composition variables can have negative

values. For example, in the predominance diagram of Fig. 1-1, if the components are chosen as $\text{Cu-SO}_2\text{-O}_2$, then the compound Cu_2S is written as $\text{Cu}_2(\text{SO}_2)\text{O}_{-2}$; that is $n_{\text{O}_2} = -1$. This is no problem in Fig. 1-1, since μ_{O_2} rather than n_{O_2} was chosen from the conjugate pair and is plotted as an axis variable. However, suppose we wish to plot a diagram of μ_{Cu} versus μ_{SO_2} at constant T and P in this system. In this case, the chosen variables would be $T, P, \mu_{\text{SO}_2}, n_{\text{O}_2}$. Since one of the selected extensive variables must always be positive, and since n_{O_2} is the only selected extensive variable, it is necessary that n_{O_2} be positive everywhere. For instance, a phase field for Cu_2S is not permitted. In other words, only compositions in the $\text{Cu-SO}_2\text{-O}_2$ subsystem are permitted. A different phase diagram would result if we plotted μ_{Cu} versus μ_{SO_2} in the $\text{Cu-SO}_2\text{-S}_2$ subsystem with n_{S_2} always positive. Cu_2O would then not appear, for example. That is, at a given μ_{Cu} and p_{SO_2} we could have a low p_{O_2} and a high p_{S_2} in equilibrium with, for example, Cu_2S , or we could have a high p_{O_2} and a low p_{S_2} in equilibrium with, for example, Cu_2O . Hence the diagram will not be a true diagram unless compositions are limited to the $\text{Cu-SO}_2\text{-O}_2$ or $\text{Cu-SO}_2\text{-S}_2$ triangles. As a second example, if μ_{SiO} and μ_{CO} are chosen as variables in the SiO-CO-O system, then the diagram must be limited to $n_{\text{O}} > 0$ (SiO-CO-O subsystem) or to $n_{\text{O}} < 0$ (SiO-CO-Si-C subsystem).

1.9.2.4 Other Sets of Conjugate Pairs

The set of conjugate pairs in Table 1-1 is only one of many such sets. For example, if we make the substitution ($H = TS + \sum n_i \mu_i$) in Eq. (1-115), then we obtain another form of the general Gibbs–Duhem equation:

$$-H d(1/T) - (V/T) dP + \sum n_i d(\mu_i/T) = 0 \quad (1-117)$$

This defines another set of pairs of conjugate potentials and extensive variables: $(1/T, -H)$, $(P, -V/T)$, $(\mu_i/T, n_i)$. Choosing one and only one variable from each pair, we can construct a true phase diagram by the procedure described above. However, these diagrams may be of limited practical utility. This is discussed by Hillert (1997).

1.10 Solution Models

In Sec. 1.4.7, the thermodynamic expressions for simple ideal substitutional solutions were derived and in Secs. 1.5.7 and 1.6.2, the regular solution model and polynomial extensions thereof were discussed. For other types of solutions such as ionic mixtures, interstitial solutions, polymeric solutions, etc., the most convenient definition of ideality may be different. In the present section we examine some of these solutions. We also discuss structural ordering and its effect on the phase diagram. For further discussion, see Pelton (1997).

1.10.1 Sublattice Models

The sublattice concept has proved to be very useful in thermodynamic modeling. Sublattice models, which were first developed extensively for molten salt solutions, find application in ceramic, interstitial solutions, intermetallic solutions, etc.

1.10.1.1 All Sublattices Except One Occupied by Only One Species

In the simplest limiting case, only one sublattice is occupied by more than one species. For example, liquid and solid MgO–CaO solutions can be modeled by assuming an anionic sublattice occupied only by O^{2-} ions, while Mg^{2+} and Ca^{2+} ions mix on a cationic sublattice. In this

case the model is formally the same as that of a simple substitutional solution, because the site fractions X_{Mg} and X_{Ca} of Mg^{2+} and Ca^{2+} cations on the cationic sublattice are numerically equal to the overall component mole fractions X_{MgO} and X_{CaO} . Solid and liquid MgO–CaO solutions have been shown (Wu et al., 1993) to be well represented by simple polynomial equations for g^E .

As a second example, the intermetallic ϵ -FeSb phase exhibits non-stoichiometry toward excess Fe. This phase was modeled (Pei et al., 1995) as a solution of Fe and stoichiometric FeSb by assuming two sublattices: an “Fe sublattice” occupied only by Fe atoms and an “Sb sublattice” occupied by both Fe and Sb atoms such that, per gram atom,

$$\Delta g_m = 0.5 RT (y_{Fe} \ln y_{Fe} + y_{Sb} \ln y_{Sb}) + \alpha y_{Fe} y_{Sb} \quad (1-118)$$

where $y_{Sb} = (1 - y_{Fe}) = 2X_{Sb}$ is the site fraction of Sb atoms on the “Sb sites” and α is an empirical polynomial in y_{Sb} .

1.10.1.2 Ionic Solutions

Let us take as an example a solution, solid or liquid, of NaF, KF, NaCl and KCl as introduced in Sec. 1.7.8. If the cations are assumed to mix randomly on a cationic sublattice while the anions mix randomly on an anionic sublattice, then the molar Gibbs energy of the solution can be modeled by the following equation which contains an ideal mixing term for each sublattice:

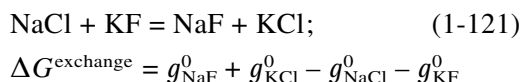
$$g = (X_{Na} X_{Cl} g_{NaCl}^0 + X_K X_F g_{KF}^0 + X_{Na} X_F g_{NaF}^0 + X_K X_{Cl} g_{KCl}^0) \quad (1-119) \\ + RT (X_{Na} \ln X_{Na} + X_K \ln X_K) \\ + RT (X_F \ln X_F + X_{Cl} \ln X_{Cl}) + g^E$$

where the factor $(X_{Na} X_{Cl})$, for example, is the probability, in a random mixture, of

finding a Na ion and a Cl ion as nearest neighbors. Differentiation of Eq. (1-119) gives the following expression for the activity of NaF:

$$RT \ln a_{\text{NaF}} = -X_{\text{K}} X_{\text{Cl}} \Delta G^{\text{exchange}} \quad (1-120) \\ + RT \ln (X_{\text{Na}} X_{\text{F}}) + g_{\text{NaF}}^{\text{E}}$$

where $\Delta G^{\text{exchange}}$ is the Gibbs energy change for the following *exchange reaction* among the pure salts:



In this example, $\Delta G^{\text{exchange}} < 0$. The salts NaF and KCl are thus said to form the *stable pair*. The first term on the right of Eq. (1-120) is positive. The members of the stable pair thus exhibit positive deviations, and in Fig. 1-31 this is reflected by the flat liquidus surfaces with widely spaced isotherms for NaF and KCl. That is, the mixing of pure NaF and KCl is unfavorable because it involves the formation of $\text{K}^+ - \text{F}^-$ and $\text{Na}^+ - \text{Cl}^-$ nearest-neighbor pairs at the expense of the energetically preferable $\text{Na}^+ - \text{F}^-$ and $\text{K}^+ - \text{Cl}^-$ pairs. If $\Delta G^{\text{exchange}}$ is sufficiently large, a miscibility gap will be formed, centered close to the *stable diagonal* joining the stable pair.

Blander (1964) proposed the following expression for g^{E} in Eq. (1-119):

$$g^{\text{E}} = X_{\text{Na}} g_{\text{NaCl-NaF}}^{\text{E}} + X_{\text{K}} g_{\text{KCl-KF}}^{\text{E}} \quad (1-122) \\ + X_{\text{F}} g_{\text{NaF-KF}}^{\text{E}} + X_{\text{Cl}} g_{\text{NaCl-KCl}}^{\text{E}} \\ - X_{\text{Na}} X_{\text{K}} X_{\text{F}} X_{\text{Cl}} (\Delta G^{\text{exchange}})^2 / ZRT$$

where, for example, $g_{\text{NaCl-NaF}}^{\text{E}}$ is the excess Gibbs energy in the NaCl–NaF binary system at the same cationic fraction X_{Na} as in the ternary, and where Z is the first coordination number. That is, g^{E} contains a contribution from each binary system. The final term in Eq. (1-122) is a first-order correction for non-random mixing which

accounts for the fact that the number of $\text{Na}^+ - \text{F}^-$ and $\text{K}^+ - \text{Cl}^-$ nearest-neighbor pairs will be higher than the number of such pairs in a random mixture. This term is usually not negligible.

The phase diagram in Fig. 1-31(a) was calculated by means of Eqs. (1-119) and (1-122) solely from optimized excess Gibbs energies of the binary systems and from compiled data for the pure salts. Agreement with the measured diagram is very good.

Eqs. (1-119) and (1-122) can easily be modified for solutions in which the numbers of sites on the two sublattices are not equal, as in $\text{MgCl}_2 - \text{MgF}_2 - \text{CaCl}_2 - \text{CaF}_2$ solutions. Also, in liquid salt solutions the ratio of the number of lattice sites on one sublattice to that on the other sublattice can vary with concentration, as in molten $\text{NaCl} - \text{MgCl}_2 - \text{NaF} - \text{MgF}_2$ solutions. In this case, it has been proposed (Sabounji and Blander, 1975) that the molar ionic fractions in all but the random mixing terms of these equations should be replaced by equivalent ionic fractions. Finally, the equations can be extended to multicomponent solutions. These extensions are all discussed by Pelton (1988b).

For solutions such as liquid NaF–KF–NaCl–KCl for which $\Delta G^{\text{exchange}}$ is not too large, these equations are often sufficient. For solutions with larger exchange Gibbs energies, however, in which liquid immiscibility appears, these equations are generally unsatisfactory. It was recognized by Sabounji and Blander (1974) that this is due to the effect of non-randomness upon the second nearest-neighbor cation–cation and anion–anion interactions. To take account of this, Blander proposed additional terms in Eq. (1-122). Dessureault and Pelton (1991) modified Eqs. (1-119) and (1-122) to account more rigorously for non-random mixing effects, with good re-

sults for several molten salt systems with miscibility gaps. See also section 1.10.4.

1.10.1.3 Interstitial Solutions

As an example of the application of the sublattice model to interstitial solutions we will take the f.c.c. phase of the Fe–V–C system. Lee and Lee (1991) have modeled this solution using two sublattices: a metallic sublattice containing Fe and V atoms, and an interstitial lattice containing C atoms and vacancies, va . The numbers of sites on each sublattice are equal. An equation identical to Eq. (1-119) can be written for the molar Gibbs energy:

$$g = (X_{Fe} X_{va} g_{Feva}^0 + X_{Fe} X_C g_{FeC}^0 + X_V X_{va} g_{Vva}^0 + X_V X_C g_{VC}^0) + RT (X_{Fe} \ln X_{Fe} + X_V \ln X_V) + RT (X_C \ln X_C + X_{va} \ln X_{va}) + g^E \quad (1-123)$$

where $X_{Fe} = (1 - X_V)$ and $X_C = (1 - X_{va})$ are the site fractions on the two sublattices and “Feva” and “Vva” are simply pure Fe and V, i.e., $g_{Feva}^0 = g_{Fe}^0$. An expression for g^E as in Eq. (1-122), although without the final non-random mixing term, was used by Lee and Lee with optimized binary g^E parameters. Their calculated Fe–V–C phase diagram is in good agreement with experimental data. The sublattice model has been similarly applied to many interstitial solutions by several authors.

1.10.1.4 Ceramic Solutions

Many ceramic solutions contain two or more cationic sublattices. As an example, consider a solution of Ti_2O_3 in $FeTiO_3$ (ilmenite) under reducing conditions. There are two cationic sublattices, the A and B sublattices. In $FeTiO_3$, Fe^{2+} ions and Ti^{4+} ions occupy the A and B sublattices, respectively. With additions of Ti_2O_3 , Ti^{3+}

ions occupy both sublattices. The solution can be represented as $(Fe_{1-x}^{2+} Ti_x^{3+})_A (Ti_{1-x}^{4+} Ti_x^{3+})_B$ where x is the overall mole fraction of Ti_2O_3 . The ions are assumed to mix randomly on each sublattice so that:

$$\Delta S^{ideal} = -2R[(1-x) \ln(1-x) + x \ln x] \quad (1-124)$$

Deviations from ideal mixing are assumed to occur due to interlattice cation–cation interactions according to

$$\begin{aligned} & (Fe_A^{2+} - Ti_B^{4+}) + (Ti_A^{3+} - Ti_B^{3+}) \\ &= (Fe_A^{2+} - Ti_B^{3+}) + (Ti_A^{3+} - Ti_B^{4+}) \\ \Delta G &= a + bT \end{aligned} \quad (1-125)$$

where a and b are the adjustable parameters of the model. The probability that an A–B pair is an $(Fe_A^{2+} - Ti_B^{3+})$ or a $(Ti_A^{3+} - Ti_B^{4+})$ pair is equal to $x(1-x)$. Hence, $g^E = x(1-x)(a + bT)$.

Similar models can be proposed for other ceramic solutions such as spinels, pseudobrookites, etc. These models can rapidly become very complex mathematically as the number of possible species on the lattices increases. For instance, in Fe_3O_4 – Co_3O_4 spinel solutions, Fe^{2+} , Fe^{3+} , Co^{2+} and Co^{3+} ions are all distributed over both the tetrahedral and octahedral sublattices. Four independent equilibrium constants are required (Pelton et al., 1979) to describe the cation distribution even for the ideal mixing approximation. This complexity has been rendered much more tractable by the “compound energy model” (Sundman and Ågren, 1981; Hillert et al., 1988). This is not actually a model, but is rather a mathematical formalism permitting the formulation of various models in terms of the Gibbs energies, g^0 , of “pseudocomponents” so that equations similar to Eq. (1-119) can be used directly.

1.10.1.5 The Compound Energy Formalism

As an example, the model for the $\text{FeTiO}_3\text{-Ti}_2\text{O}_3$ solution in Sec. 1.10.1.4 will be reformulated. By taking all combinations of an A-sublattice species and a B-sublattice species, we define two real components, $(\text{Fe}^{2+})_A(\text{Ti}^{4+})_B\text{O}_3$ and $(\text{Ti}^{3+})_A(\text{Ti}^{3+})_B\text{O}_3$, as well as two “pseudo-components”, $(\text{Fe}^{2+})_A(\text{Ti}^{3+})_B\text{O}_3^-$ and $(\text{Ti}^{3+})_A(\text{Ti}^{4+})_B\text{O}_3^+$.

Pseudocomponents, as in the present example, may be charged. Similarly to Eq. (1-119) the molar Gibbs energy can be written

$$g = (1-x)^2 g_{\text{FeTiO}_3}^0 + x^2 g_{\text{Ti}_2\text{O}_3}^0 + x(1-x) g_{\text{FeTiO}_3^-}^0 + x(1-x) g_{\text{Ti}_2\text{O}_3^+}^0 - T\Delta s^{\text{ideal}} \quad (1-126)$$

Note that charge neutrality is maintained in Eq. (1-126). The Gibbs energies of the two pseudocomponents are calculated from the equation

$$\Delta G = a + bT = g_{\text{FeTiO}_3^-}^0 + g_{\text{Ti}_2\text{O}_3^+}^0 - g_{\text{FeTiO}_3}^0 - g_{\text{Ti}_2\text{O}_3}^0 \quad (1-127)$$

where ΔG is the Gibbs energy change of Eq. (1-125) and is a parameter of the model. One of $g_{\text{FeTiO}_3^-}^0$ or $g_{\text{Ti}_2\text{O}_3^+}^0$ may be assigned an arbitrary value. The other is then given by Eq. (1-127). By substitution of Eq. (1-127) into Eq. (1-126) it may be shown that this formulation is identical to the regular solution formulation given in Sec. 1.10.1.4. Note that excess terms, g^E , could be added to Eq. (1-126), thereby giving more flexibility to the model. In the present example, however, this was not required.

The compound energy formalism is described and developed by Barry et al. (1992), who give many more examples. An advantage of formulating the sublattice model in terms of the compound energy formalism is that it is easily extended to

multicomponent solutions. It also provides a conceptual framework for treating many different phases with different structures. This facilitates the development of computer software and databases because many different types of solutions can be treated as cases of one general formalism.

1.10.1.6 Non-Stoichiometric Compounds

Non-stoichiometric compounds are generally treated by a sublattice model. Consider such a compound $A_{1-\delta}B_{1+\delta}$. The sublattices normally occupied by A and B atoms will be called, respectively, the A-sublattice and the B-sublattice. Deviations from stoichiometry (where $\delta=0$) can occur by the formation of defects such as B atoms on A sites, vacant sites, atoms occupying interstitial sites, etc. Generally, one type of defect will predominate for solutions with excess A and another type will predominate for solutions with excess B. These are called the majority defects.

Consider first a solution in which the majority defects are A atoms on B sites and B atoms on A sites: $(A_{1-x}B_x)_A(A_yB_{1-y})_B$. It follows that $\delta=(x-y)$. In the compound energy formalism we can write, for the molar Gibbs energy,

$$g = (1-x)(1-y) g_{AB}^0 + (1-x)y g_{AA}^0 + x(1-y) g_{BB}^0 + xy g_{BA}^0 + RT [x \ln x + (1-x) \ln(1-x) + y \ln y + (1-y) \ln(1-y)] \quad (1-128)$$

where g_{AB}^0 is the molar Gibbs energy of (hypothetical) defect-free stoichiometric AB. Now the defect concentrations at equilibrium are those that minimize g . Therefore, setting $(\partial g / \partial x) = (\partial g / \partial y) = 0$ at constant δ , we obtain

$$\frac{xy}{(1-x)(1-y)} = \exp \left(- (1-x-y) \frac{\Delta g_1 + \Delta g_2}{RT} \right) \quad (1-129)$$

where $\Delta g_1 = (g_{AA}^0 - g_{AB}^0)$ and $\Delta g_2 = (g_{BB}^0 - g_{AB}^0)$ are the Gibbs energies of formation of the majority defects and where g_{BA}^0 has been set equal to g_{AB}^0 . At a given composition $\delta = (x - y)$, and for given values of the parameters Δg_1 and Δg_2 , Eq. (1-129) can be solved to give x and y , which can then be substituted into Eq. (1-128) to give g . The more positive are Δg_1 and Δg_2 , the more steeply g rises on either side of its minimum, and the narrower is the range of stoichiometry of the compound.

Consider another model in which the majority defects are vacancies on the B-sublattice and B atoms on interstitial sites. We now have three sublattices with occupancies $(A)_A(B_{1-y}va_y)_B(B_xva_{1-x})_I$ where "I" indicates the interstitial sublattice. The A-sublattice is occupied exclusively by A atoms. A vacancy is indicated by va. Stoichiometric defect-free AB is represented by $(A)(B)(va)$ and $(x - y) = 2\delta/(1 - \delta)$. Per mole of $A_{1-\delta}B_{1+\delta}$, the Gibbs energy is:

$$g = (1 - \delta) \{ [(1 - x)(1 - y)g_{ABva}^0 + (1 - x)y g_{Avava}^0 + x(1 - y)g_{ABBB}^0 + xy g_{Avab}^0 + RT [x \ln x + (1 - x) \ln (1 - x) + y \ln y + (1 - y) \ln (1 - y)] \} \quad (1-130)$$

Eq. (1-130) is identical to Eq. (1-128) apart from the factor $(1 - \delta)$, and gives rise to an equilibrium constant as in Eq. (1-129). Other choices of majority defects result in very similar expressions. The model can easily be modified to account for other stoichiometries A_mB_n , for different numbers of available interstitial sites, etc., and its extension to multicomponent solutions is straightforward.

1.10.2 Polymer Solutions

For solutions of polymers in monomeric solvents, very large deviations from simple Raoultian ideal behaviour (i.e. from Eq. (1-

40)) are observed. This large discrepancy can be attributed to the fact that the individual segments of the polymer molecule have considerable freedom of movement. Flory (1941, 1942) and Huggins (1942) proposed a model in which the polymer segments are distributed on the solvent sites. A large polymer molecule can thus be oriented (i.e. bent) in many ways, thereby greatly increasing the entropy. To a first approximation the model gives an ideal mixing term with mole fractions replaced by volume fractions in Eq. (1-45):

$$\Delta g_m^{\text{ideal}} = RT \left(X_A \ln \frac{X_A v_A^0}{X_A v_A^0 + X_B v_B^0} + X_B \ln \frac{X_B v_B^0}{X_A v_A^0 + X_B v_B^0} \right) \quad (1-131)$$

Lewis and Randall (1961) have compared the Flory-Huggins equation with experimental data in several solutions. In general, the measured activities lie between those predicted by Eq. (1-131) and by the Raoultian ideal equation, Eq. (1-45). A recent review of the thermodynamics of polymer solutions is given by Trusler (1999).

1.10.3 Calculation of Limiting Slopes of Phase Boundaries

From the measured limiting slope $(dT/dX)_{X_A=1}$ of the liquidus at the melting point of a pure component A, much information about the extent of solid solubility, as well as the structure of the liquid, can be inferred. Similar information can be obtained from the limiting slopes of phase boundaries at solid-state transformation points of pure components.

Eq. (1-65) relates the activities along the liquidus and the solidus to the Gibbs energy of fusion:

$$RT \ln a_A^l - RT \ln a_A^s = -\Delta g_{f(A)}^0 \quad (1-132)$$

In the limit $X_A \rightarrow 1$, the liquidus and solidus converge at the melting point $T_{f(A)}$. Let us assume that, in the limit, Raoult's Law, Eq. (1-40), holds for both phases. That is, $a_A^l = X_A^l$ and $a_A^s = X_A^s$. Furthermore, from Eq. (1-60),

$$\Delta g_{f(A)}^0 \rightarrow \Delta h_{f(A)} (1 - T/T_{f(A)})$$

Finally, we note that

$$\lim_{X_A \rightarrow 1} (\ln X_A) = \lim_{X_A \rightarrow 1} (\ln (1 - X_B)) = -X_B$$

Substituting these various limiting values into Eq. (1-132) yields:

$$\begin{aligned} \lim_{X_A \rightarrow 1} (dX_A^l/dT - dX_A^s/dT) \\ = \Delta h_{f(A)}^0 / R (T_{f(A)})^2 \end{aligned} \quad (1-133)$$

If the limiting slope of the liquidus, $\lim_{X_A \rightarrow 1} (dX_A^l/dT)$, is known, then the limiting

slope of the solidus can be calculated, or vice versa, as long as the enthalpy of fusion is known.

For the LiF–NaF system in Fig. 1-18, the broken line is the limiting liquidus slope at $X_{LiF}=1$ calculated from Eq. (1-133) under the assumption that there is no solid solubility (that is, that $dX_A^s/dT=0$).

Agreement with the measured limiting liquidus slope is very good, thereby showing that the solid solubility of NaF in LiF is not large.

In the general case, the solute B may dissolve to form more than one “particle”. For example, in dilute solutions of Na_2SO_4 in MgSO_4 , each mole of Na_2SO_4 yields two moles of Na^+ ions which mix randomly with the Mg^{2+} ions on the cationic sublattice. Hence, the real mole fraction of solvent, X_A , is $(1 - \nu X_B)$ where ν is the number of moles of foreign “particles” contributed by one mole of solute. In the present example, $\nu=2$.

Eq. (1-133) now becomes:

$$\begin{aligned} \lim_{X_A \rightarrow 1} (dX_A^l/dT - dX_A^s/dT) \\ = \Delta h_{f(A)}^0 / \nu R (T_{f(A)})^2 \end{aligned} \quad (1-134)$$

The broken line in Fig. 1-44 is the limiting liquidus slope calculated from Eq. (1-134) under the assumption of negligible solid solubility.

It can be shown (Blander, 1964) that Eq. (1-134) applies very generally with the factor ν as defined above. For example, adding LiF to NaF introduces only one foreign

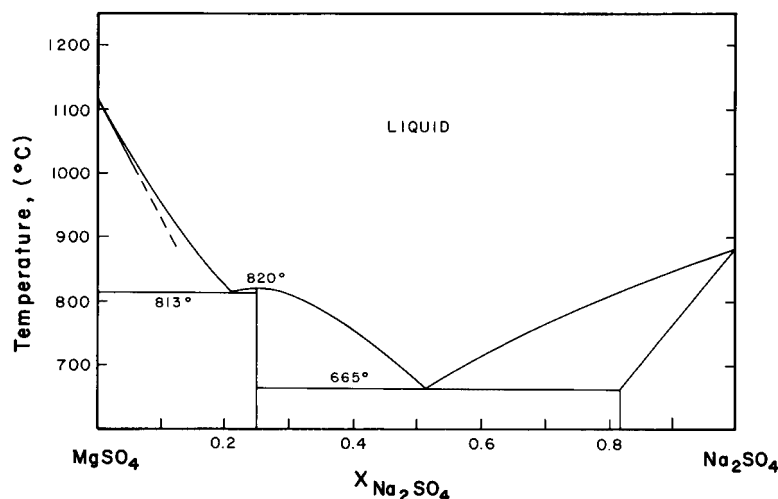


Figure 1-44. Phase diagram of the MgSO_4 – Na_2SO_4 system calculated for an ideal ionic liquid solution. Broken line is the theoretical limiting liquidus slope calculated for negligible solid solubility taking into account the ionic nature of the liquid. Agreement with the measured diagram (Ginsberg, 1909) is good.

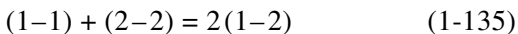
particle Li^+ . The F^- ion is not “foreign”. Hence, $\nu=1$. For additions of Na_2SO_4 to MgSO_4 , $\nu=2$ since two moles of Na^+ ions are supplied per mole of Na_2SO_4 . For CaCl_2 dissolved in water, $\nu=3$, and so on. For C dissolving interstitially in solid Fe, $\nu=1$. The fact that the solution is interstitial has no influence on the validity of Eq. (1-134). Eq. (1-134) is thus very general and very useful. It is independent of the solution model and of the excess properties, which become zero at infinite dilution.

An equation identical to Eq. (1-134) but with the enthalpy of transition, Δh_{tr}^0 , replacing the enthalpy of fusion, relates the limiting phase boundary slopes at a transformation temperature of a component.

1.10.4 Short-Range Ordering

The basic premise of the regular solution model (Sec. 1.5.7) is that random mixing occurs even when g^E is not zero. To account for non-random mixing, the regular solution model has been extended though the *quasichemical model for short-range ordering* developed by Guggenheim (1935) and Fowler and Guggenheim (1939) and modified by Pelton and Blander (1984, 1986) and Blander and Pelton (1987). The model is outlined below. For a more complete development, see the last two papers cited above, Degterov and Pelton (1996), Pelton et al. (2000) and Pelton and Chartrand (2000).

For a binary system, consider the formation of two nearest-neighbor 1–2 pairs from a 1–1 and a 2–2 pair:



Let the molar Gibbs energy change for this reaction be $(\omega - \eta T)$. Let the nearest-neighbor coordination numbers of 1 and 2 atoms or molecules be Z_1 and Z_2 . The total number of bonds emanating from an i atom

or molecule is $Z_i X_i$. Hence, mass balance equations can be written as

$$\begin{aligned} Z_1 X_1 &= 2n_{11} + n_{12} \\ Z_2 X_2 &= 2n_{22} + n_{12} \end{aligned} \quad (1-136)$$

where n_{ij} is the number of i – j bonds in one mole of solution. “Coordination equivalent fractions” may be defined as:

$$Y_1 = 1 - Y_2 = Z_1 X_1 / (Z_1 X_1 + Z_2 X_2) \quad (1-137)$$

where the total number of pairs in one mole of solution is $(Z_1 X_1 + Z_2 X_2)/2$. Letting X_{ij} be the fraction of i – j pairs in solution, Eq. (1-136) may be written as:

$$\begin{aligned} 2Y_1 &= 2X_{11} + X_{12} \\ 2Y_2 &= 2X_{22} + X_{12} \end{aligned} \quad (1-138)$$

The molar enthalpy and excess entropy of mixing are assumed to be directly related to the number of 1–2 pairs:

$$\begin{aligned} \Delta h_{\text{m}} - T s^{\text{E(non-config)}} \\ = (Z_1 X_1 + Z_2 X_2) X_{12} (\omega - \eta T) / 4 \end{aligned} \quad (1-139)$$

An approximate expression for the configurational entropy of mixing is given by a one-dimensional Ising model:

$$\begin{aligned} \Delta s_{\text{m}}^{\text{config}} &= -R(X_1 \ln X_1 + X_2 \ln X_2) \\ &\quad - \frac{R}{2} (Z_1 X_1 + Z_2 X_2) \\ &\quad \times [X_{11} \ln(X_{11}/Y_1^2) + X_{22} \ln(X_{22}/Y_2^2) \\ &\quad + X_{12} \ln(X_{12}/2Y_1 Y_2)] \end{aligned} \quad (1-140)$$

The equilibrium distribution is calculated by minimizing Δg_{m} with respect to X_{12} at constant composition. This results in a “quasichemical” equilibrium constant for the reaction, Eq. (1-135):

$$\frac{X_{12}^2}{X_{11} X_{22}} = 4 \exp \left(\frac{-(\omega - \eta T)}{RT} \right) \quad (1-141)$$

When $(\omega - \eta T) = 0$, the solution of Eqs. (1-138) and (1-141) gives a random distribu-

tion with $X_{11}=Y_1^2$, $X_{22}=Y_2^2$ and $2Y_1Y_2$, and Eq. (1-140) reduces to the ideal Raoultian entropy of mixing. When $(\omega - \eta T)$ becomes very negative, 1-2 pairs predominate. A plot of Δh_m or $s^{E(\text{non-config})}$ versus composition then becomes V-shaped and a plot of $\Delta s_m^{\text{config}}$ becomes m-shaped, with minima at $Y_1=Y_2=1/2$, which is the composition of maximum ordering, as illustrated in Fig. 1-45. When $(\omega - \eta T)$ is quite negative, the plot of g^E also has a negative V-shape.

For Fe-S liquid solutions, the activity coefficients of sulfur as measured by several authors are plotted in Fig. 1-46. It is clear in this case that the model should be applied with $Z_{\text{Fe}}=Z_{\text{S}}$. The curves shown in Fig. 1-46 were calculated from the quasi-chemical model with $(\omega - \eta T)$ expanded as

the following optimized (Kongoli et al., 1998) polynomial:

$$(1-142)$$

$$(\omega - \eta T) = -(70017 + 9T) - 74042 Y_{\text{S}} - (798 - 15T) Y_{\text{S}}^3 + 40791 Y_{\text{S}}^7 \text{ J/mol}^{-1}$$

Far fewer parameters are required than if a polynomial expansion of g^E (as in Sec. 1.6.2) were used. Furthermore, and more importantly, the model permits successful predictions of the properties of multicomponent systems as illustrated in Fig. 1-47, where measured sulfur activities in quaternary liquid Fe-Ni-Cu-S solutions are compared with activities calculated (Kongoli et al., 1998) solely from the optimized model parameters for the Fe-S, Ni-S and Cu-S binary systems. A pair exchange reaction like Eq. (1-135) was assumed for each M-S pair (M=Fe, Ni, Cu), and an optimized polynomial expansion of $(\omega_{\text{MS}} - \eta_{\text{MS}} T)$ as a function of Y_{S} , similar to Eq. (1-142), was obtained for each binary. Three equilibrium constant equations like Eq. (1-141) were written, and it was assumed that $(\omega_{\text{MS}} - \eta_{\text{MS}} T)$ in the quaternary system was constant at constant Y_{S} . No adjustable ternary or quaternary parameters were required to obtain the agreement shown in Fig. (1-47), although the model permits the inclusion of such terms if required.

Silicate slags are known to exhibit such short-range ordering. In the CaO-SiO₂ system, Δh_m has a strong negative V-shape, as in Fig. 1-45, but with the minimum at $X_{\text{SiO}_2}=1/3$ which is the composition corresponding to Ca₂SiO₄. That is, the ordering is associated with the formation of orthosilicate anions SiO₄⁴⁻. In the phase diagram, Fig. 1-14, the CaO-liquidus can be seen to descend sharply near the composition $X_{\text{SiO}_2}=1/3$. The quasichemical model has been extended by Pelton and Blander (1984) to treat silicate slags. The diagram

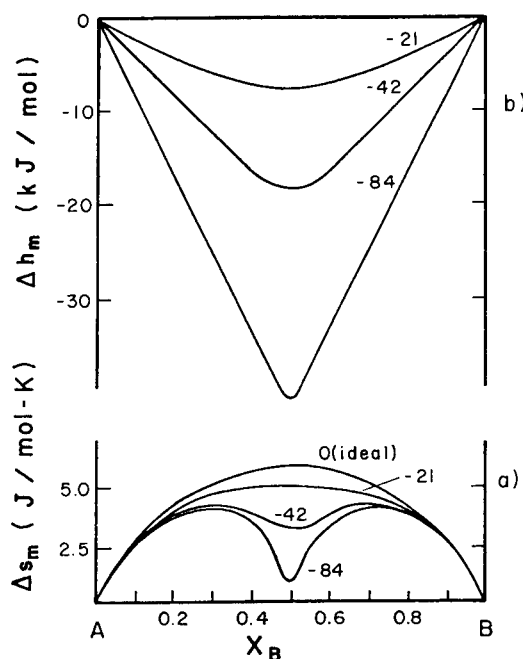


Figure 1-45. Molar enthalpy and entropy of mixing curves for a system AB calculated at 1000°C with $Z_1=Z_2=2$ from the quasichemical model for short-range ordering with $(\omega - \eta T)=0, -21, -42$, and -84 kJ.

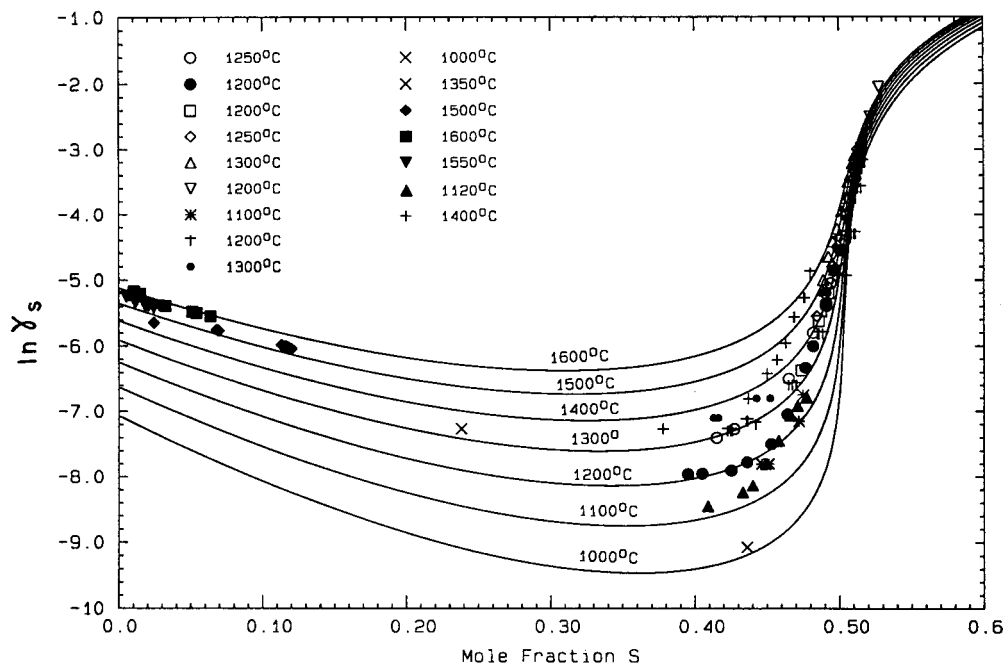


Figure 1-46. Activity coefficient of sulfur in liquid Fe-S solutions calculated from optimized quasichemical model parameters and comparison with experimental data (Kongoli et al., 1998).

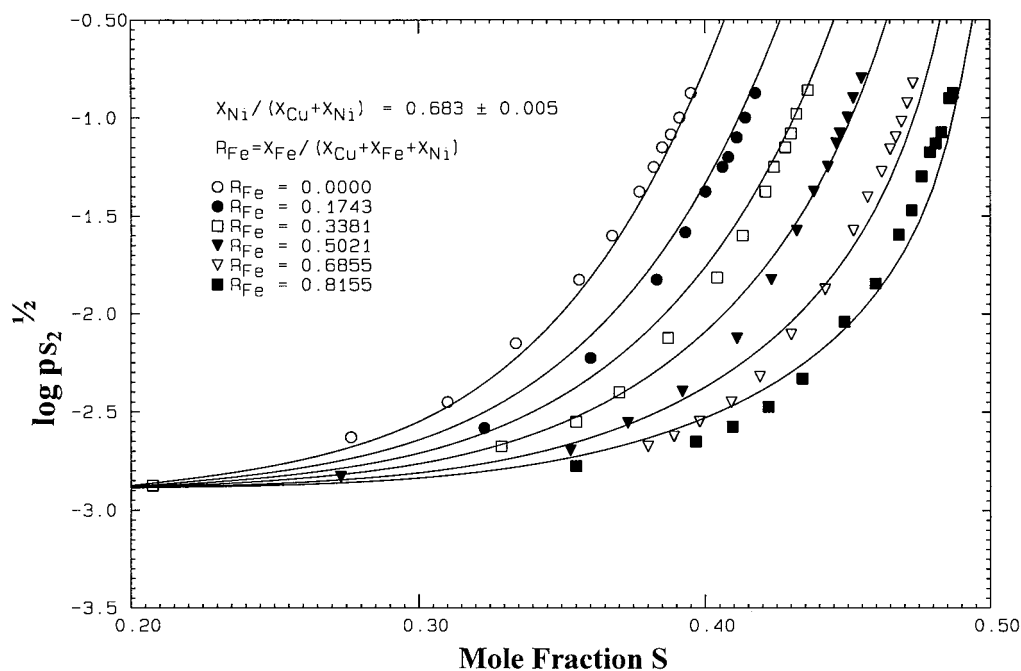


Figure 1-47. Equilibrium partial pressure of sulfur at 1200°C over Fe-Ni-Cu-S mattes predicted by the quasichemical model from binary data (Kongoli et al., 1998) and comparison with experimental data (Bale and Toguri, 1996).

shown in Fig. 1-14 is thermodynamically calculated (Wu, 1990).

Many liquid alloy solutions exhibit short-range ordering. The ordering is strongest when one component is relatively electropositive (on the left side of the periodic table) and the other is relatively electronegative. Liquid alloys such as Alk–Au (Hensel, 1979), Alk–Pb (Saboungi et al., 1985) and Alk–Bi (Petric et al., 1988a), where Alk = (Na, K, Rb, Cs), exhibit curves of Δh_m and Δs_m similar to those in Fig. 1-45 with one composition of maximum ordering. For example, in the Au–Cs system the minima occur near the composition AuCs; in Mg–Bi alloys the minima occur near the Mg_3Bi_2 composition, while in K–Pb alloys the maximum ordering is at K_4Pb .

It has also been observed that certain liquid alloys exhibit more than one composition of ordering. For example, in K–Te alloys, the “excess stability function”, which is the second derivative of Δg_m , exhibits peaks near the compositions KTe_8 , KTe and K_2Te (Petric et al., 1988b) thereby providing evidence of ordering centred on these compositions. The liquid might be considered as consisting of a series of mutually soluble “liquid intermetallic compounds”.

When $(\omega - \eta T)$ is expanded as a polynomial as in Eq. (1-142), the quasichemical model and the polynomial model of Sec. 1.6.2 become identical as $(\omega - \eta T)$ approaches zero. That is, the polynomial model is a limiting case of the quasichemical model when the assumption of ideal configurational entropy is made.

When $(\omega - \eta T)$ is positive, (1-1) and (2-2) pairs predominate. The quasichemical model can thus also treat such clustering, which accompanies positive deviations from ideality.

Recent work (Pelton et al., 2000; Pelton and Chartrand, 2000) has rendered the

model more flexible by permitting the Z_i to vary with composition and by expanding the $(\omega - \eta T)$ as polynomials in the bond fractions X_{ij} rather than the overall component fractions. A merger of the quasichemical and sublattice models has also been completed (Chartrand and Pelton, 2000), permitting nearest-neighbor and second-nearest neighbor short-range-ordering to be treated simultaneously in molten salt solutions.

1.10.5 Long-Range Ordering

In solid solutions, long-range ordering can occur as well as short-range ordering. In Fig. 1-15 for the Ag–Mg system, a transformation from an α' to an α phase is shown occurring at approximately 665 K at the composition Ag_3Mg . This is an *order–disorder* transformation. Below the transformation temperature, *long-range ordering* (superlattice formation) is observed. An *order parameter* may be defined which decreases to zero at the transformation temperature. This type of phase transformation is not a first-order transformation like those considered so far in this chapter. Unlike first-order transformations which involve a change of state (solid, liquid, gas) and also involve diffusion over distances large compared with atomic dimensions, order–disorder transformations, at least at the stoichiometric composition (Ag_3Mg in this example), occur by atomic rearrangement over distances of the order of atomic dimensions. The slope of the curve of Gibbs energy versus T is not discontinuous at the transformation temperature. Ordering and order–disorder transformations are discussed in Chapter 8 (Inden, 2001).

A type of order–disorder transformation of importance in ferrous metallurgy is the magnetic transformation. Below its *Curie temperature* of 769 °C, Fe is ferromagnetic.

Above this temperature it is not. The transformation involves a change in ordering of the atomic spins and is not first order. Additions of alloying elements will change the temperature of transformation. Magnetic transformations are treated in Chapter 4 (Binder, 2001). See also Miodownik (1982) and Inden (1982).

1.11 Calculation of Ternary Phase Diagrams From Binary Data

Among 70 metallic elements $70!/3!67! = 54\,740$ ternary systems and 916 895 quaternary systems are formed. In view of the amount of work involved in measuring even one isothermal section of a relatively simple ternary phase diagram, it is very important to have a means of estimating ternary and higher-order phase diagrams.

The most fruitful approach to such predictions is via thermodynamic methods. In recent years, great advances have been made in this area by the international Calphad group. Many key papers have been published in the *Calphad Journal*.

As a first step in the thermodynamic approach, we critically analyze the experimental phase diagrams and thermodynamic data for the three binary subsystems of the ternary system in order to obtain a set of mathematical expressions for the Gibbs energies of the binary phases, as was discussed in Sec. 1.6. Next, interpolation procedures based on solution models are used to estimate the Gibbs energies of the ternary phases from the Gibbs energies of the binary phases. Finally, the ternary phase diagram is calculated by computer from these estimated ternary Gibbs energies by means of common tangent plane or total Gibbs energy minimization algorithms.

As an example of such an estimation of a ternary phase diagram, the experimental

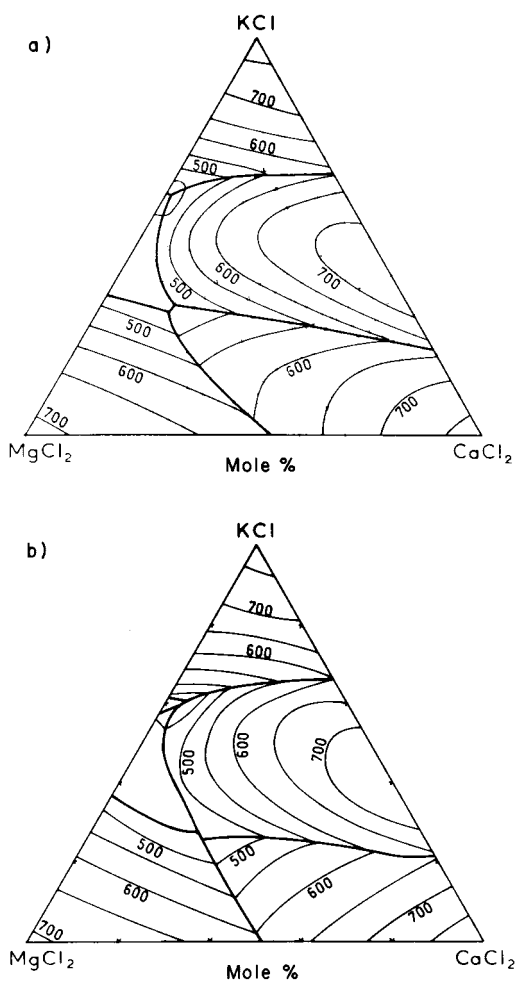


Figure 1-48. Projection of the liquidus surface of the KCl–MgCl₂–CaCl₂ system.

- a) Calculated from optimized binary thermodynamic parameters (Lin et al., 1979).
b) As reported by Ivanov (1953).

(Ivanov, 1953) and estimated (Lin et al., 1979) liquidus projections of the KCl–MgCl₂–CaCl₂ system are shown in Fig. 1-48. The estimated phase diagram was calculated from the thermodynamic properties of the three binary subsystems with the Gibbs energy of the ternary liquid approximated via the equation suggested by

Kohler (1960):

$$g^E = (1 - X_A)^2 g_{B/C}^E + (1 - X_B)^2 g_{C/A}^E + (1 - X_C)^2 g_{A/B}^E \quad (1-143)$$

In this equation, g^E is the excess molar Gibbs energy at a composition point in the ternary liquid phase and $g_{B/C}^E$, $g_{C/A}^E$ and $g_{A/B}^E$ are the excess Gibbs energies in the three binary systems at the same ratios X_B/X_C , X_C/X_A and X_A/X_B as at the ternary point. If the ternary liquid phase as well as the three binary liquid phases are all regular solutions, then Eq. (1-143) is exact. In the general case, a physical interpretation of Eq. (1-143) is that the contribution to g^E from, say, pair interactions between A and B particles is constant at a constant ratio X_A/X_B apart from the dilutive effect of the C particles, which is accounted for by the term $(1 - X_C)^2$ taken from regular solution theory.

Ternary phase diagrams estimated in this way are quite acceptable for many purposes. The agreement between the experimental and calculated diagrams can be greatly improved by the inclusion of one or two "ternary terms" with adjustable coefficients in the interpolation equations for g^E . For example, the ternary term $aX_{KCl}X_{MgCl_2}X_{CaCl_2}$, which is zero in all three binaries, could be added to Eq. (1-143) and the value of the parameter a which gives the "best" fit to the measured ternary liquidus could be determined. This, of course, requires that ternary measurements be made, but only a very few (even one or two in this example) experimental liquidus points will usually suffice rather than the larger number of measurements required for a fully experimental determination. In this way, the coupling of the thermodynamic approach with a few well chosen experimental measurements holds promise of greatly reducing the experimen-

tal effort involved in determining multi-component phase diagrams.

Reviews of various interpolation procedures and computer techniques for estimating and calculating ternary and higher-order phase diagrams are given by Ansara (1979), Spencer and Barin (1979) and Pelton (1997).

Other equations, similar to the Kohler Eq. (1-143) in that they are based on extension of regular solution theory, are used to estimate the thermodynamic properties of ternary solutions from the properties of the binary subsystems. For a discussion and references, see Hillert (1980). However, for structurally more complex solutions involving more than one sublattice or with significant structural ordering, other estimation techniques must be used. For a review, see Pelton (1997).

An example, the calculation of the phase diagram of the NaCl–KCl–NaF–KF system in Fig. 1-31, has already been presented in Sec. 1.10.1.2.

The quasichemical model for systems with short-range ordering was discussed for the case of binary systems in Sec. 1.10.4. The model has been extended to permit the estimation of ternary and multi-component phase diagrams (Pelton and Blander, 1986; Blander and Pelton, 1987; Pelton and Chartrand, 2000). Very good results have been obtained in the case of silicate systems. The liquidus surface of the SiO_2 –MgO–MnO system, estimated from optimized binary data with the quasichemical model for the liquid and under the assumption of ideal mixing for the solid $MgSiO_3$ – $MnSiO_3$ and Mg_2SiO_4 – Mn_2SiO_4 solutions, is shown in Fig. 1-49. Agreement with the measured phase diagram (Glasser and Osborn, 1960) is within experimental error limits.

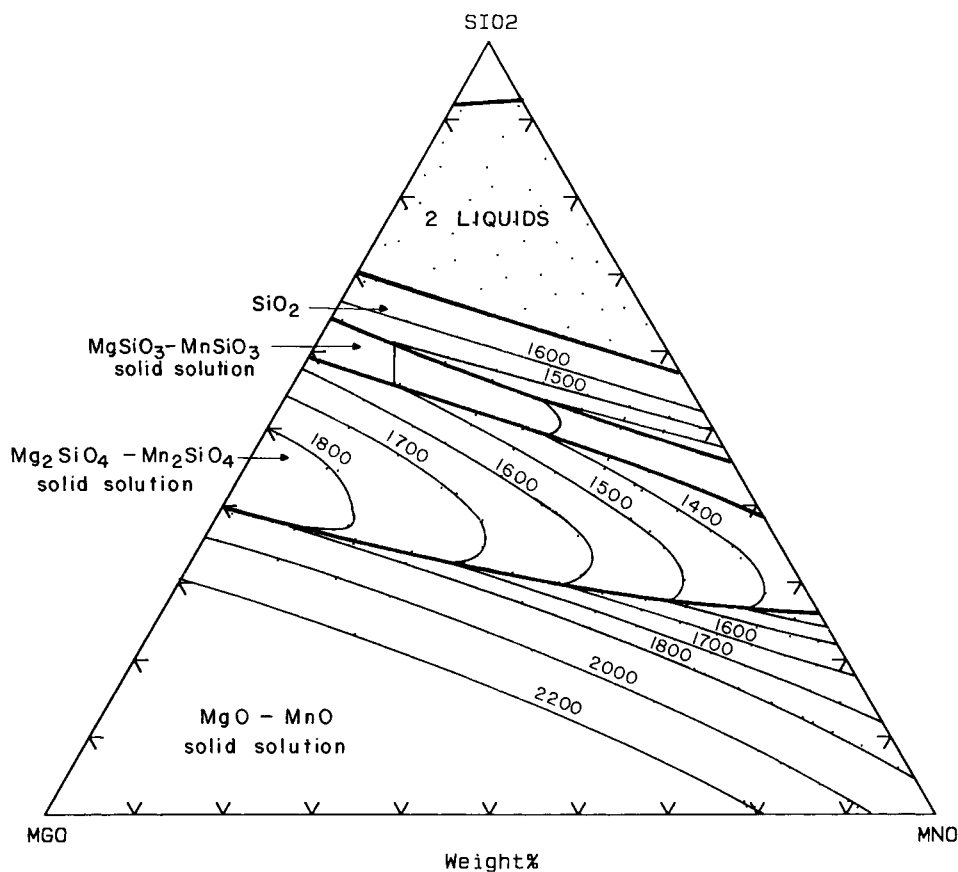


Figure 1-49. Projection of liquidus surface of the SiO_2 - MgO - MnO system calculated from optimized binary parameters with the quasichemical model for the liquid phase.

1.12 Minimization of Gibbs Energy

Throughout this chapter it has been shown that phase equilibria are calculated by Gibbs energy minimization. Computer software has been developed in recent years to perform such calculations in systems of any number of components, phases and species.

Consider a system in which several stoichiometric solid or liquid compounds A, B, C, ... could be present at equilibrium along with a number of gaseous, liquid or solid

solution phases $\alpha, \beta, \gamma, \dots$. The total Gibbs energy of the system may be written as:

$$G = (n_A g_A^0 + n_B g_B^0 + \dots) + (n_\alpha g_\alpha + n_\beta g_\beta + \dots) \quad (1-144)$$

where n_A, n_B , etc. are the number of moles of the pure solid or liquidus; g_A^0, g_B^0 , etc. are the molar Gibbs energies of the pure solids or liquids (which are functions of T and P); n_α, n_β , etc. are the total number of moles of the solution phases; g_α, g_β , etc. are the molar Gibbs energies of the solution phases (which are function of T, P and composition). For a given set of constraints

(such as fixed T , P and overall composition), the free energy minimization algorithms find the set of mole numbers n_A , n_B , etc., n_α , n_β , etc. (some may be zero) as well as the compositions of all solution phases which globally minimize G . This is the equilibrium phase assemblage. Other constraints such as constant volume or a fixed chemical potential (such as constant p_{O_2}) may be applied.

A discussion of the strategies of such algorithms is beyond the scope of the present chapter. One of the best known general Gibbs energy minimization programs is Solgasmix written by Eriksson (1975) and constantly updated.

When coupled to a large thermodynamic database, general Gibbs energy minimization programs provide a powerful tool for the calculation of phase equilibria. Several such expert database systems have been developed. They have been reviewed by Bale and Eriksson (1990).

An example of a calculation performed by the F*A*C*T (Facility for the Analysis of Chemical Thermodynamics) expert system, which the author has helped to develop, is shown in Table 1-2. The program

Table 1-2. Calculation of equilibrium state when 1 mole SiI_4 is held at 1400 K in a volume of 10^4 l. Calculations performed by minimization of the total Gibbs energy.

$SiI_4 =$		
2.9254 (0.67156	I
	+0.28415	SiI_2
	+0.24835E-01	I_2
	+0.19446E-01	SiI_4
	+0.59083E-05	SiI
	+0.23039E-07	Si
	+0.15226E-10	Si_2
	+0.21462EE-11	Si_3
	(1400.0,0.336E-01,G)	
	+0.11182	Si
	(1400.0,0.336E-01,S1, 1.0000)	

has been asked to calculate the equilibrium state when 1 mol of SiI_4 is held at 1400 K in a volume of 10^4 l. The thermodynamic properties of the possible product species have been automatically retrieved from the database and the total Gibbs energy has been minimized by the Solgasmix algorithm. At equilibrium there will be 2.9254 mol of gas of the composition shown and 0.11182 mol of solid Si will precipitate. The total pressure will be 0.0336 bar.

Although the calculation was performed by minimization of the total Gibbs energy, substitution of the results into the equilibrium constants of Eqs. (1-10) to (1-12) will show that these equilibrium constants are satisfied.

Another example is shown in Table 1-3 (Pelton et al., 1990). Here the program has been asked to calculate the equilibrium

Table 1-3. Calculation of equilibrium state when reactants shown (masses in g) are held at 1873 K at a pressure of 1 atm. Calculations performed by minimization of the total Gibbs energy.

100. Fe + 0.08 O + 0.4 Fe + 0.4 Mn + 0.3 Si + 0.08 Ar =		
0.30793 litre (99.943	vol% Ar
	+0.24987E-01	vol% Mn
	+0.24069E-01	vol% SiO_2
	+0.82057E-02	vol% Fe
	+0.79044E-07	vol% O
	+0.60192E-08	vol% Si
	+0.11200E-08	vol% O_2
	+0.35385E-15	vol% Si_2
	(1873.0, 1.00	,G)
+ 0.18501 gram (49.948	wt.% SiO_2
	+42.104	wt.% MnO
	+7.9478	wt.% FeO)
	(1873.0, 1.00	,SOLN 2)
+ 100.99 gram (99.400	wt.% Fe
	+0.33630	wt.% Mu
	+0.25426	wt.% Si
	+0.98375E-02	wt.% O_2)
	(1873.0, 1.00	,SOLN 3)

state when 100 g Fe, 0.08 g oxygen, 0.4 g Fe, 0.4 g Mn, 0.3 g Si and 0.08 g Ar are brought together at 1873 K at a total pressure of 1 bar. The database contains data for a large number of solution phases as well as for pure compounds. These data have been automatically retrieved and the total Gibbs energy has been minimized. At equilibrium there are 0.30793 l of a gas phase, 0.18501 g of a molten slag, and 100.99 g of a molten steel of the compositions shown.

The Gibbs energies of the solution phases are represented as functions of composition by various solution models (Sec. 1.10). As discussed in Sec. 1.11, these models can be used to predict the thermodynamic properties of N -component solutions from evaluated parameters for binary (and possibly ternary) subsystems stored in the database. For example, in the calculation in Table 1-3, the Gibbs energy of the molten slag phase was estimated by the quasichemical model from optimized parameters for the binary oxide solutions.

1.12.1 Phase Diagram Calculation

Gibbs energy minimization is used to calculate general phase diagram sections thermodynamically using the zero phase fraction line concept (Sec. 1.9.1.1), with data retrieved from databases of model coefficients. For example, to calculate the diagram of Fig. 1-30, the program first scans the four edges of the diagram to find the ends of the ZPF lines. Each line is then followed from beginning to end, using Gibbs energy minimization to determine the point at which a phase is just on the verge of being present. When ZPF lines for all phases have been drawn, then the diagram is complete. Because, as shown in Sec. 1.9, all true phase diagram sections obey the same geometrical rules, one algorithm suffices to

calculate all types of phase diagrams with any properly chosen variables as axes or constants.

1.13 Bibliography

1.13.1 Phase Diagram Compilations

The classic compilation in the field of binary alloy phase diagrams is that of Hansen (1958). This work was continued by Elliott (1965) and Shunk (1969). These compilations contain critical commentaries. A non-critical compilation of binary alloy phase diagrams is supplied in looseleaf form with a continual up-dating service by W.G. Moffatt of the General Electric Co., Schenectady, N.Y. An extensive non-critical compilation of binary and ternary phase diagrams of metallic systems has been edited by Ageev (1959–1978). An index to all compilations of binary alloy phase diagrams up to 1979 was prepared by Moffatt (1979). A critical compilation of binary phase diagrams involving Fe has been published by Kubaschewski (1982). Ternary alloy phase diagrams were compiled by Ageev (1959–1978).

From 1979 to the early 1990s, the American Society for Metals undertook a project to evaluate critically all binary and ternary alloy phase diagrams. All available literature on phase equilibria, crystal structures, and often thermodynamic properties were critically evaluated in detail by international experts. Many evaluations have appeared in the *Journal of Phase Equilibria* (formerly *Bulletin of Alloy Phase Diagrams*), (ASM Int'l., Materials Park, OH), which continues to publish phase diagram evaluations. Condensed critical evaluations of 4700 binary alloy phase diagrams have been published in three volumes (Massalski et al., 1990). The ternary phase

diagrams of 7380 alloy systems have also been published in a 10-volume compilation (Villars et al., 1995). Both binary and ternary compilations are available from ASM on CD-ROM. Many of the evaluations have also been published by ASM as monographs on phase diagrams involving a particular metal as a component.

Each year, MSI Services (<http://www.msiwp.com>) publishes *The Red Book*, which contains abstracts on alloy phase diagrams from all sources, notably from the extensive Russian literature. MSI also provides a CD-ROM with extensive alloy phase diagram compilations and reports.

Phase diagrams for over 9000 binary, ternary and multicomponent ceramic systems (including oxides, halides, carbonates, sulfates, etc.) have been compiled in the 12-volume series, *Phase Diagrams for Ceramists* (1964–96, Am. Ceramic Soc., Columbus, OH). Earlier volumes were non-critical compilations. However, recent volumes have included critical commentaries.

Phase diagrams of anhydrous salt systems have been compiled by Voskresenskaya (1970) and Robertson (1966).

An extensive bibliography of binary and multicomponent phase diagrams of all types of systems (metallic, ceramic, aqueous, organic, etc.) has been compiled by Wisniak (1981).

1.13.2 Thermodynamic Compilations

Several extensive compilations of thermodynamic data of pure substances of interest in materials science are available. These include the JANAF Tables (Chase et al., 1985) and the compilations of Barin et al. (1977), Barin (1989), Robie et al. (1978) and Mills (1974), as well as the series of compilations of the National Institute of Standards and Technology (Washington, D.C.).

Compilations of properties of solutions (activities, enthalpies of mixing, etc.) are much more difficult to find. Hultgren et al. (1973) present the properties of a number of binary alloy solutions. An extensive bibliography of solution properties of all types of solutions was prepared by Wisniak and Tamir (1978).

Thermodynamic/phase diagram optimization as discussed in Sec. 1.6.1 has been carried out for a large number of alloy, ceramic and other systems. Many of these evaluations have been published in the international *Calphad Journal*, published since 1977 by Pergamon Press. Several of the evaluations in the *Journal of Phase Equilibria* discussed above include thermodynamic/phase diagram optimizations, as do a number of the evaluations in Vol. 7 of *Phase Diagrams for Ceramists*.

Extensive computer databases of the thermodynamic properties of compounds and solutions (stored as coefficients of model equations) are available. These include F*A*C*T (<http://www.crct.polymtl.ca>), Thermocalc (<http://www.met.kth.se>), ChemSage (<http://gttserv.lth.rwth-aachen.de>), MTS-NPL (<http://www.npl.co.uk>), Thermodata (<http://www.grenet.fr>), HSC (<http://www.outokumpu.fi>), and MALT2 (<http://www.kagaku.com>). Gibbs energy minimization software permits the calculation of complex equilibria from the stored data as discussed in Sec. 1.12 as well as the thermodynamic calculation of phase diagram sections. A listing of these and other available databases is maintained at <http://www.crct.polymtl.ca>.

A bibliographic database known as Thermdoc, on thermodynamic properties and phase diagrams of systems of interest to materials scientists, with updates, is available through Thermodata (<http://www.grenet.fr>).

1.13.3 General Reading

The theory, measurement and applications of phase diagrams are discussed in a great many texts. Only a few can be listed here. A recent text by Hillert (1998) provides a complete thermodynamic treatment of phase equilibria as well as solution modeling and thermodynamic/phase diagram optimization.

A classical discussion of phase diagrams in metallurgy was given by Rhines (1956). Prince (1966) presents a detailed treatment of the geometry of multicomponent phase diagrams. A series of five volumes edited by Alper (1970–1978) discusses many aspects of phase diagrams in materials science. Bergeron and Risbud (1984) give an introduction of phase diagrams, with particular attention to applications in ceramic systems, see also Findlay (1951), Ricci (1964) and West (1965).

In the *Calphad Journal* and in the *Journal of Phase Equilibria* are to be found many articles on the relationships between thermodynamics and phase diagrams.

It has been beyond the scope of the present chapter to discuss experimental techniques of measuring thermodynamic properties and phase diagrams. For the measurement of thermodynamic properties, including properties of solutions, the reader is referred to Kubaschewski and Alcock (1979). For techniques of measuring phase diagrams, see Pelton (1996), Raynor (1970), MacChesney and Rosenberg (1970), Buckley (1970) and Hume-Rothery et al. (1952).

1.14 References

- Ageev, N. V. (Ed.) (1959–1978), *Phase Diagrams of Metallic Systems*, Vols. 1–22. Moscow: Acad. Sci. USSR.
- Alabyshev, A. F., Morachevskii, A. G. (1957), *Z. Neorg. Khim.* 2, 669.
- Alper, A. M. (Ed.) (1970–1978), *Phase Diagrams – Materials Science and Technology*, Vols. 1–5. New York: Academic.
- Ansara, I. (1979), *Internat. Met. Rev.* 238, No. 1, 20.
- Bale, C. W. (1990), *Canad. Metall. Quart.* 29, 263.
- Bale, C. W., Eriksson, N. G. (1990), *Canad. Metall. Quart.* 29, 105.
- Bale, C. W., Pelton, A. D. (1983), *Metall. Trans. B14*, 77.
- Bale, C. W., Toguri, J. (1996), private communication.
- Bale, C. W., Pelton, A. D., Thompson W. T. (1986), *Canad. Metall. Quart.* 25, 107.
- Barin, I. (1989), *Thermochemical Data of Pure Substances*. 2. Weinheim: VCH Verlagsgesellschaft.
- Barin, I., Knacke, O., Kubaschewski, O. (1977), *Thermochemical Properties of Inorganic Substances*. Berlin: Springer Verlag.
- Barry, T. I., Dinsdale, A. T., Gishby, J. A., Hallstedt, B., Hillert, M., Jansson, B., Jonsson, J., Sundman, B., Taylor, J. R. (1992), *J. Phase Equilib.* 13, 459.
- Bartlett, H. E., Neethling, A. J., Crowther, P. (1970), *J. Chem. Thermo.* 2, 523.
- Bergeron, C. J., Risbud, S. H. (1984), *Introduction to Phase Equilibria in Ceramics*. Columbus, Ohio: Amer. Ceramic Soc.
- Binder, K. (2001), in: *Phase Transformations in Materials*: Kosterz, G. (Ed.). Weinheim: Wiley-VCH, Chap. 4.
- Binder, K., Fratzl, P. (2001), in: *Phase Transformations in Materials*: Kosterz, G. (Ed.). Weinheim: Wiley-VCH, Chap. 6.
- Blander, M. (1964), *Molten Salt Chemistry*. New York: Interscience, Chap. 3.
- Blander, M., Pelton, A. D. (1987), *Geochim. et Cosmochim. Acta* 51, 85.
- Bray, H. F., Bell, F. D., Harris, S. J. (1961–1962), *J. Inst. Metals* 90, 24.
- Buckley, R. A. (1970), in: *Techniques of Metals Research*, Vol. IV, Part 1: Rapp, R. A. (Ed.). New York: Interscience.
- Chartrand, P., Pelton, A. D. (2000), *Metall. Mater. Trans.*, in press.
- Chase, M. W. (1983), *Bull. Alloy Phase Diag.* 4, 124.
- Chase, M. W., Davies, C. A., Downey, J. R., Frurip, D. J., McDonald, R. A., Syverud, A. N. (1985), *JANAF Thermochemical Tables*, 3rd ed. New York: Amer. Inst. Physics.
- Chu, W. F., Rahmel, A. (1979), *Rev. High-Temp. Mater.* IV, 139.
- Degterov, S., Pelton, A. D. (1996), *J. Phase Equilib.* 17, 488.
- Dessureault, Y., Pelton, A. D. (1991), *J. Chim. Phys.* 88, 1811.
- Dessureault, Y., Sangster, J., Pelton, A. D. (1990), *J. Electrochem. Soc.* 137, 2941.
- Doman, R. C., Barr, J. B., McNally, R. N., Alper, A. M. (1963), *J. Am. Ceram. Soc.* 46, 313.
- Dörner, P., Henig, E.-Th., Krieg, H., Lucas, H. L., Petzow, G. (1980), *Calphad Journal* 4, 241.

- Elliott, R. P. (1965), *Constitution of Binary Alloys*. First Supplement. New York: McGraw-Hill.
- Eriksson, N. G. (1975), *Chemical Scripta* 8, 100.
- Findlay, A. (1951), *The Phase Rule*, 9th edn., revised by Campbell, A. N., Smith, N. A. New York: Dover.
- Flory, P. J. (1941), *J. Chem. Phys.* 9, 660.
- Flory, P. J. (1942), *J. Chem. Phys.* 10, 5.
- Fowler, R. H., Guggenheim, E. A. (1939), *Statistical Thermodynamics*. Cambridge: Cambridge Univ. Press, p. 350.
- Garrels, R. M., Christ, C. L. (1965), *Solutions Minerals and Equilibria*. New York: Harper and Row.
- Ginsberg, A. S. (1909), *Z. Anorg. Chem.* 61, 130.
- Glasser, E. P., Osborn, E. F. (1960), *J. Amer. Ceram. Soc.* 43, 136.
- Guggenheim, E. A. (1935), *Proc. Roy. Soc. A* 148, 304.
- Gulbransen, E. A., Jansson, S. A. (1970), *Proc. Symp. Electrochem. Soc. Fall meeting 1969*. New York: The Electrochem. Soc., p. 3.
- Gupta, H., Morral, J. E., Nowotny, H. (1986), *Scripta Metall.* 20, 889.
- Hansen, M. (1958), *Constitution of Binary Alloys*, 2nd edn. New York: McGraw-Hill.
- Harshe, G., Venkatachalam, S. (1984), *J. Metals* 36, 34.
- Hauffe, K. (1940), *Z. Elektrochem.* 46, 348.
- Hensel, F. (1979), *Adv. Phys.* 28, 555.
- Hillert, M. (1980), *Calphad Journal* 4, 1.
- Hillert, M. (1985), *Int. Metall. Rev.* 30, 45.
- Hillert, M. (1997), *J. Phase Equilib.* 18, 249.
- Hillert, M. (1998), *Phase Equilibria, Phase Diagrams and Phase Transformations*. Cambridge: Cambridge University Press.
- Hillert, M., Jansson, B., Sundman, B. (1988), *Z. Metallk.* 79, 81.
- Holm, J. L. (1965), *Acta Chem. Scand.* 19, 638.
- Hong, K. C., Kleppa, O. J. (1976), *J. Chem. Thermodyn.* 8, 31.
- Huggins, M. L. (1942), *Ann. N.Y. Acad. Sci.* 43, 1.
- Hultgren, R., Desai, P. D., Hawkins, D. T., Gleiser, M., Kelly, K. K., Wagman, D. D. (1973), *Selected Values of the Thermodynamic Properties of the Elements and Binary Alloys*. Metals Park, Ohio: Am. Soc. of Metals.
- Hume-Rothery, W., Christian, J. W., Pearson, W. B. (1952), *Metallurgical Equilibrium Diagrams*. London: Inst. Phys.
- Inden, G. (1982), *Bull. Alloy Phase Diag.* 2, 412.
- Inden, G. (2001), in: *Phase Transformations in Materials*: G. Kostorz (Ed.). Weinheim: Wiley-VCH, Chap. 8.
- Ingraham, T. R., Kellogg, H. H. (1963), *TMS-AIME* 227, 1419.
- Ingraham, T. R., Kerby, R. (1967), *Canad. Metall. Quart.* 6, 89.
- Ivanov, A. I. (1953), *Izv. Sekt. Fiz.-Khim. Anal. Inst. Obshchei Neorg. Khim. Akad. Nauk SSSR* 23, 197.
- Katsura, T., Muan, A. (1964), *TMS-AIME* 230, 77.
- Kellogg, H. H., Basu, S. K. (1960), *TMS-AIME* 218, 70.
- Kleinstuber, T. (1961), Ph.D. Thesis, Univ. Munich, Germany.
- Kohler, F. (1960), *Monatsh. Chemie* 91, 738.
- Köster, W., Dullenkopf, W. (1936), *Z. Metallk.* 28, 309.
- Kongoli, F., Dessureault, Y., Pelton, A. D. (1998), *Metall. and Mat. Trans.* 29B, 591.
- Kubaschewski, O. (1982), *Iron-Binary Phase Diagrams*. New York: Springer Verlag.
- Kubaschewski, O., Alcock, C. B., (1979), *Metallurgical Thermochemistry*, 5th ed. New York: Pergamon Press.
- Kurnakow, N. S., Kusnetzow, A. N. (1907), *Z. Anorg. Chem.* 52, 173.
- Kunz, M. (2001), in: *Phase Transformations in Materials*: G. Kostorz (Ed.). Weinheim: Wiley-VCH, Chap. 10.
- Lantratov, M. F., Mikhailova, A. G. (1971), *Zh. Prikl. Khimii* 44, 1778.
- Lee, B.-J., Lee, D. N. (1991), *Calphad* 15, 293.
- Lee, B. J., Lee, D. N. (1992), *J. Phase Equilib.* 13, 349.
- Levin, E. M., Robbins, C. R., McMurdie, H. F. (1964), and 11 supplements to (1996), *Phase Diagrams for Ceramists*; Columbus, Ohio: Am. Ceramic Soc.
- Lewis, G. N., Randall, M. (1961), *Thermodynamics*, revised by Pittzer, K. S., Brewer, L. New York: McGraw-Hill.
- Lin, P.-L., Pelton, A. D., Bale, C. W. (1979), *J. Am. Ceram. Soc.* 62, 414.
- Lipson, H., Wilson, A. J. C. (1940), *J. Iron Steel Inst.* 142, 122.
- Lukas, H. L., Henig, E.-Th., Zimmermann, B. (1977), *Calphad Journal* 1, 225.
- MacChesney, J. B., Rosenberg, P. E. (1970), in *Phase Diagrams – Materials Science and Technology*, Vol. 1: Alper, A. M. (Ed.). New York: Academic, Ch. 3.
- Maierova, E. A., Morachevskii, A. G., Kovalenko, S. G. (1976), *Elektrokhimiya* 12, 313.
- Massalski, T. B., Okamoto, H., Subramanian, P. R., Kacprzak, L. (1990), *Binary Alloy Phase Diagrams*, 2nd ed. Metals Park, OH: Am. Soc. Metals.
- Mathewson, C. H. (1906), *Z. Ang. Chem.* 50, 180.
- Mills, K. C. (1974), *Thermodynamic Data for Inorganic Sulphides, Selenides and Tellurides*. London: Butterworths.
- Miodownik, A. P. (1982), *Bull. Alloy Phase Diag.* 2, 406.
- Moffatt, W. B. (1979), *The Index to Binary Phase Collections*, Schenectady, N.Y.: General Electric Corp.
- Muan, A., and Osborn, F. (1965), *Phase Equilibria Among Oxides in Steelmaking*. Reading, MA.: Addison Wesley.
- Müller-Krumbhaar, H., Kurz, W., Brener, E. (2001), in: *Phase Transformations in Materials*: G. Kostorz (Ed.). Weinheim: Wiley-VCH, Chap. 2.

- Palatnik, L. S., Landau, A. I. (1964), *Phase Equilibria in Multicomponent Systems*. NY: Holt, Rinehart and Winston.
- Pehlke, R. D. (1973), *Unit Processes of Extractive Metallurgy*. New York: Elsevier.
- Pei, B., Björkman, B., Sundman, B., Jansson, B. (1995), *Calphad* 19, 1.
- Pelton, A. D. (1983), in: *Physical Metallurgy*: Cahn, R. W., Haasen, P. (Eds.). Amsterdam: Elsevier, Chap. 7.
- Pelton, A. D. (1988a), *Bull. Alloy Phase Diag.* 9, 41.
- Pelton, A. D. (1988b), *Calphad Journal* 12, 127.
- Pelton, A. D. (1995), *J. Phase Equilib.* 16, 501.
- Pelton, A. D. (1996), in: *Physical Metallurgy*: Cahn, R. W., Haasen, P. (Eds.). Amsterdam, North-Holland, Chap. 6.
- Pelton, A. D. (1997), in: *Advanced Physical Chemistry for Process Metallurgy*: Sano, N., Lu, W.-K., Riboud P. (Eds.). New York, Academic, Chap. 3.
- Pelton, A. D., Bale, C. W. (1986), *Metall. Trans. A* 17, 1057.
- Pelton, A. D., Blander, M. (1984), *Proc. AIME Symp. on Molten Salts and Slags*. Warrendale, Pa.: The Metall. Soc. AIME, p. 281.
- Pelton, A. D., Blander, M. (1986), *Metall. Trans. B* 17, 805.
- Pelton, A. D., Chartrand, P. (2000), *Metall. Mater. Trans.*, in press.
- Pelton, A. D., Degterov, S. A., Eriksson, G., Robelin, C., Dessureault, Y. (2000), *Metall. Mater. Trans.*, B31, 651.
- Pelton, A. D., Schmalzried, H. (1973), *Metall. Trans.* 4, 1395.
- Pelton, A. D., Schmalzried, H., Sticher, J. (1979), *J. Phys. Chem. Solids* 40, 1103.
- Pelton, A. D., Thompson, W. T. (1975), *Prog. Solid State Chem.* 10, part 3, 119.
- Pelton, A. D., Thompson, W. T., Bale, C. W., Eriksson, N. G. (1990), *High Temp. Sci.* 26, 231.
- Petric, A., Pelton, A. D., Saboungi, M.-L. (1988a), *J. Electrochem. Soc.* 135, 2754.
- Petric, A., Pelton, A. D., Saboungi, M.-L. (1988b), *J. Chem. Phys.* 85, 5070.
- Phillips, B., Muan, A. (1958), *J. Am. Ceram. Soc.* 41, 448.
- Pilgrim, R. F., Ingraham, T. R. (1967), *Canad. Metall. Quart.* 6, 333.
- Polyakov, V. D. (1940), *Izv. Sektora Fiz.-Khim Analiza Inst. Obshchei Neorg. Khim. Akad. Nauk SSSR* 13, 308.
- Prince, A. (1963), *Metall. Rev.* 8, 213.
- Prince, A. (1966), *Alloy Phase Equilibria*. Amsterdam: Elsevier.
- Raynor, G. V. (1970), in: *Physical Metallurgy*, 2nd edn: Cahn, R. W. (Ed.). Amsterdam: North Holland, Chap. 7.
- Rhines, F. N. (1956), *Phase Diagrams in Metallurgy*. New York: McGraw-Hill.
- Ricci, J. E. (1964), in: *Molten Salt Chemistry*: Blander, M. (Ed.). New York: Interscience, Chap. 4.
- Robertson, W. D. (Ed.) (1966), *Binary Phase Diagrams of Halide Salts*, U. S. At. En. Comm. Contract AT (30-1) 2723, Washington: Clearinghouse for Federal Scientific and Techn. Info.
- Robie, R. A., Hemingway, B. S., Fisher, J. R. (1978), *Thermodynamic Properties of Minerals and Related Substances at 298.15 K and 1 Bar Pressure and at Higher Temperatures*. Washington: U.S. Government Printing Office.
- Roos, G. D. (1916), *Z. Anorg. Chem.* 94, 329.
- Saboungi, M.-L., Blander, M. (1974), *High Temp. Sci.* 6, 37.
- Saboungi, M.-L., Blander, M. (1975), *J. Am. Ceram. Soc.* 58, 1.
- Saboungi, M.-L., Herron, S. J., Kumar, R. (1985), *Ber. Bunsenges. Phys. Chem.* 89, 375.
- Sangster, J., Pelton, A. D. (1987), *J. Phys. Chem. Ref. Data* 16, 509.
- Schenk, H., Froberg, M. G., Nunninghof, R. (1964), *Arch. Eisenhütten* 35, 269.
- Schreinemakers, F. A. H. (1915), *Proc. K. Akad. Wetenschappen, Amsterdam (Section of Sciences)* 18, 116.
- Shatynski, S. R. (1977), *Oxidn. Metals* 11, 307.
- Shunk, F. A. (1969), *Constitution of Binary Alloys*. Second Supplement. New York: McGraw-Hill.
- Spencer, P. J., Barin, I. (1979), *Mater. Eng. Appl.* 1, 167.
- Stringer, J., Whittle, D. P. (1977), *Rev. Int. Htes. Temp. Réfract.* 14, 6.
- Sundman, B., Ågren, J. (1981), *J. Phys. Chem. Solids* 42, 297.
- Trusler, J. P. M. (1999), in: *Chemical Thermodynamics*: Letcher, T. (Ed.). Abingdon, Oxon, UK: Blackwell Science, Chap. 16.
- Van Laar, J. J. (1908), *Z. Phys. Chem.* 63, 216; 64, 257.
- Villars, P., Prince, A., Okamoto, H. (1995), *Handbook of Ternary Alloy Phase Diagrams*. Metals Park, OH: Am. Soc. Metals.
- Voskresenskaya, N. K. (Ed.) (1970), *Handbook of Solid-Liquid Equilibria in Systems of Anhydrous Inorganic Salts*, Vol. 1, TT69-55079/1, AEC-tr-69831/3, UC-4, Washington: U.S. At. En. Comm. and Nat'l. Sci. Foundation.
- Weeks, J. R., Davies, H. A. (1964), AEC Report, Conf. 660712-1, BNL-10372.
- West, D. R. F. (1965), *Ternary Equilibrium Diagrams*. New York: McMillan.
- Wisniak, J. (1981), *Phase Diagrams: A Literature Source Book*, Vols. 1 and 2. New York: Elsevier.
- Wisniak, J., Tamir, A. (1978), *Mixing and Excess Thermodynamic Properties: A Literature Source Book*. New York: Elsevier.
- Wu, P. (1990), Ph. D. thesis, Ecole Polytechnique, Montreal.
- Wu, P., Eriksson, G., Pelton, A. D. (1993), *J. Am. Ceram. Soc.* 76, 2065.
- Yokokawa, H. (1999), *J. Phase Equilib.* 20, 258.

10 High Pressure Phase Transformations

Martin Kunz

ETH Zürich, Labor für Kristallographie, Zürich, Switzerland

List of Symbols and Abbreviations	657
10.1 Introduction	659
10.2 Pressure-Driven Phase Transitions	660
10.2.1 Framework flexion	661
10.2.2 Increase in coordination number	663
10.2.3 Pressure-induced ordering	664
10.3 Generating High Pressure	666
10.3.1 Dynamic pressure generation	667
10.3.2 Static pressure devices	668
10.3.2.1 Large-volume presses	668
10.3.2.2 Diamond anvil cells	671
10.4 Probing Phase Transformations in Materials at High Pressure	673
10.4.1 Volumetric techniques	674
10.4.2 Spectroscopic techniques	674
10.4.2.1 Microscopy	674
10.4.2.2 Raman and infrared spectroscopy	674
10.4.2.3 Mössbauer spectroscopy	675
10.4.2.3 X-Ray absorption spectroscopy	676
10.4.2.5 NMR	676
10.4.3 Ultrasonic sound velocity	677
10.4.4 Diffraction techniques	678
10.4.4.1 X-ray diffraction	678
10.4.4.2 Neutron diffraction	679
10.5 Examples	679
10.5.1 Zincblende-type semiconductors	679
10.5.1.1 Si and Ge	680
10.5.1.2 GaAs	681
10.5.1.3 InSb	682
10.5.2 Materials in the B-C-N system	683
10.5.2.1 C	684
10.5.2.2 B-N	685
10.5.2.3 C-N	686
10.5.2.4 B-C	686
10.5.2.5 B-C-N	686
10.5.3 H ₂ O	687
10.5.3.1 Ice Ih, XI and Ic	688

10.5.3.2 Ice II 689

10.5.3.3 Ice III and Ice IX 689

10.5.3.4 Ice V, Ice IV and Ice XII 690

10.5.3.5 Ice VI, Ice VII, Ice VIII, Ice X 690

10.5.3.6 Amorphous ice at high pressure 691

10.6 Acknowledgment 692

10.7 References 692

List of Symbols and Abbreviations

a, b, c	lattice parameters
E_0	internal energy at zero pressure in shock experiment
E_H	Hugoniot internal energy in a shock experiment
G	Gibbs energy
H	enthalpy
λ	wavelength
μ	chemical potential
n	number of moles
P	pressure
P_0	ambient pressure
P_H	Hugoniot pressure
Q	heat
ρ_0	density at zero pressure
S	entropy
T	temperature
T_c	critical temperature in superconductors
T_0	temperature at zero pressure
T_H	Hugoniot temperature
U	internal energy
U_p	sample velocity
U_s	shock velocity
V	molar volume
V_0	molar volume at zero pressure
V_H	molar volume in the shocked Hugoniot state
ΔV_{dis}	difference in molar volume due to an order/disorder process
$V_{\text{disordered}}$	molar volume of the disordered state
V_{ordered}	molar volume of the ordered state
W	work
ADX	angle dispersive X-ray diffraction
AX	compound semiconductors of 1 : 1 stoichiometry
bcc	body centered cubic
ccp	cubic closest packing (= fcc)
ct	carat
DAC	diamond anvil cell
dhcp	hexagonal closest packing with doubled c-axis
EDX	energy dispersive X-ray diffraction
EXAFS	extended X-ray absorption fine structure
fcc	face centered cubic (=ccp)
hcp	hexagonal closest packing
HDA	high density amorphous phase of H_2O
HEL	Hugoniot elastic limit
HP	high pressure

HT	high temperature
IR	infrared
LDA	low-density amorphous phase of H ₂ O
NMR	nuclear magnetic resonance
RT	room temperature
XAS	X-ray absorption spectroscopy

10.1 Introduction

The understanding of condensed matter requires a knowledge of the relationship between temperature, pressure and chemical environment on the one hand and volume, bonding and electronic and magnetic structure on the other. In gases, pressure, temperature and volume largely follow a simple and universal relationship, but the situation in condensed matter is much more complicated. This is mainly due to interatomic interactions, which are much stronger in condensed material than in gases and cause structural, electronic and magnetic correlations. Pelton (2001, Chap. 1 of this book) explores the interdependence between chemical composition and temperature in great detail. In this chapter, we will mainly focus on the effects of pressure on the state of solid material.

The exploration of the physics and chemistry of material under high pressure is of a remarkably inter-disciplinary interest. This is reflected in the variety of scientific problems that are the focus of modern high-pressure research. The understanding of the interdependence between structural distortions and electronic and magnetic properties is a typical example of a physical problem that benefits from experiments performed at high pressure. Another topic within physics that relies on high-pressure experiments is the calibration and refinement of theoretical models describing the interaction of atoms. High-pressure experiments on very simple covalent systems such as solid hydrogen or helium provide valuable data, which help to formulate fundamental concepts on the nature of matter. A fascinating problem in condensed-matter chemistry is the structural change of a solid (or liquid) and its phase transitions as a reaction on an external pressure. Its understanding offers chemists vital insights into

the thermodynamics of solid or liquid material (see also the Chapter by Binder, 2001). In a more practical way, materials scientists are interested in adding pressure to the variables temperature and chemical composition in order to stabilize new materials with technically interesting properties. A prominent example of a class of materials whose synthesis and exploration depend on the application of high pressure is the family of novel abrasives and super-hard materials. In recent years, high-pressure experiments are even used in the life sciences. A popular key issue in this area is the question on the origin of life (e.g., Pedersen, 1997). A more applied interest of biology in high pressure is the search for commercially viable alternative ways of food sterilization (e.g., Ondrey and Kamiya, 2000; Thakur and Nelson, 1998; Mermelstein, 1999).

Forcing a given set of atoms into a small volume by applying high pressure increases the interatomic interaction. This in turn leads to structural phase transitions and changes in physical properties. The driving forces for high pressure-induced phase transitions are obviously linked to the need to optimize the volume occupied by the atoms for a given pressure. In Sec. 10.2, we will discuss the most important mechanisms, which are the immediate cause of pressure-driven phase transitions. Extracting information on solid or liquid material at high pressure ("high" pressure in this chapter refers to pressures in the range 0.1 – 100 GPa) is an experimental challenge and was first tackled by Percy William Bridgman in the first half of this century (e.g., Bridgman, 1946). He was awarded the Nobel Prize for physics in 1946 for his ground-breaking achievements in this important field. Since the time of Bridgman the technology necessary to perform experiments at high pressure

has experienced extensive development. Section 10.3 will briefly summarize the current state of the art of high-pressure experimentation. Although third-generation synchrotron sources produced a minor revolution in high-pressure crystallography, X-ray diffraction is by no means the only way of investigating material when subjected to pressure. In Sec. 10.4, we will review the most common probes used for physical and chemical investigations at high pressure. Section 10.5 treats in detail the high-pressure phase transitions for a selected sample of materials, which are of special interest within materials science.

10.2 Pressure-Driven Phase Transitions

The physical quantities that define the thermodynamic state of a system can be differentiated into intensive quantities (i.e., temperature T , pressure P , chemical potential μ) and extensive quantities (i.e., entropy S , volume V , number of moles n). Conjugate quantities are pairs of an intensive and an extensive variable (i.e., T , S or P , V). Their products have the dimensions of energy or a volume-normalized energy, which can be used to describe the relative stability of a given system. The thermodynamic stability is determined by the minimum of the internal energy U , which is defined as a sum of a heat term Q and a work term W ,

$$U = Q + W \quad (10-1)$$

where Q is a function of temperature and entropy and W is a function of pressure and volume. On an atomistic level, Q can be viewed as the vibrational energy of the atoms oscillating around their equilibrium position. W can be visualized as the sum of the potential energies from the inter atomic

interactions between the ensemble of constituting atoms.

The absolute value of the internal energy cannot be measured. However, the difference between two states is independent of the path and mechanism of the change of the system (Hess's law). This makes the difference in the internal energy dU a very important quantity in comparing a system at two different states:

$$dU = TdS - PdV \quad (10-2)$$

Entropy S and volume V are two independent variables that are very difficult to control in an experiment. However, two successive Legendre transformations of U transform the internal energy first into the enthalpy H

$$H = U + PV \quad (10-3)$$

and then into the Gibbs energy G

$$G = H - TS = U + PV - TS \quad (10-4)$$

The total exact differential of G yields

$$dG = -SdT + VdP \quad (10-5)$$

which has the desirable property that the independent variables T and P are easily modified and controlled in an experiment. This makes G the critical quantity, which has to be considered when comparing a system at different states. While Pelton (2001) focuses on the variation of G as a function of the chemical composition and temperature, we will here investigate the change in G upon increasing pressure.

If a system is subject to changing pressure at constant temperature, Eq. (10-5) reduces to

$$dG = VdP \quad (10-6)$$

The change in the Gibbs energy on changing pressure is thus

$$(\partial G / \partial P)_T = V \quad (10-7)$$

Equation (10-7) states an intuitive triviality, i.e., that in order to minimize the Gibbs energy upon increasing pressure, a given system will reduce its volume. Volume reduction is thus the ultimate driving force of structural change and phase transformation as a reaction on increasing pressure. However, the way a volume is reduced can be different, depending on the initial structure and configurational entropy of the system and also on the amount of pressure applied. In the following we will focus on the three most important mechanisms responsible for structural changes at high pressure. These are framework flexion, increase in coordination number and pressure-induced ordering.

10.2.1 Framework flexion

A number of technologically important oxide materials (e.g., zeolites, perovskites) can be viewed as being built of relatively rigid corner-linked polyhedra forming a rather flexible framework. These materials are known to react on changing temperature and/or pressure mainly by flexion at the polyhedral joints rather than by polyhedral compression, i.e., bond length reduction (e.g., Hazen and Finger, 1978; Velde and Besson, 1982; Hemley et al., 1994). Silica (SiO_2) can be viewed as a typical example of the behavior of framework structures under pressure. It has a rich phase diagram in P - T space. The ambient condition phase is α -quartz, which consists of interconnected spirals of corner-linked SiO_4 tetrahedra. Silica has two high-pressure polymorphs, of which only coesite can be viewed as a tetrahedral framework structure. Its framework is characterized by four-fold rings of tetrahedra connected to chains, which in turn are packed via shared tetrahedral corners to the densest known tetrahedral framework. At ambient condi-

tions (coesite can be quenched to room pressure), both structures exhibit nearly ideal Si-O-Si angles of between 143° and 144° . The phase transition is thus structurally characterized by building the tetrahedral framework in coesite more densely than in α -quartz. This can be demonstrated by looking at the oxygen surroundings in both structures: In α -quartz, each oxygen has three oxygen neighbors at $\sim 2.6 \text{ \AA}$, which represent the tetrahedral oxygen neighbors. The closest oxygen atoms from any other tetrahedron are found at a distance of $\sim 3.5 \text{ \AA}$. In coesite on the other hand, there are also three oxygen neighbors at 2.6 \AA around each O, indicating the stiff behavior of the SiO_4 tetrahedra. The next nearest oxygen neighbors in coesite, however, are observed at a distance of only $3.0\text{--}3.2 \text{ \AA}$ (room pressure). Both structure types react to applied pressure with a very large decrease in the Si-O-Si angles (Fig. 10-1), while the Si-O bond lengths remain more or less constant. Densification within the stability field of quartz is thus achieved by flexion of the framework through rigid rotations of the SiO_4 tetrahedra, resulting in a decrease of the Si-O-Si angle from 144° to 125° . If this reaches a limit, denser packing of the polyhedra is achieved by framework reconstruction. Further densification, however, eventually involves an increase in the coordination number (see Sec. 10.2.2). Thus, a pure compression at RT or a rapid (shock) compression of α -quartz leads to an amorphization involving both framework collapse and an increase in coordination number (Hemley et al., 1994). Pressure-induced amorphization seems to be a common feature of many framework structures, indicating a volume reduction by a collapse of the framework. This destroys the long-range order while still largely maintaining the short-range order of the primary building blocks. A similar

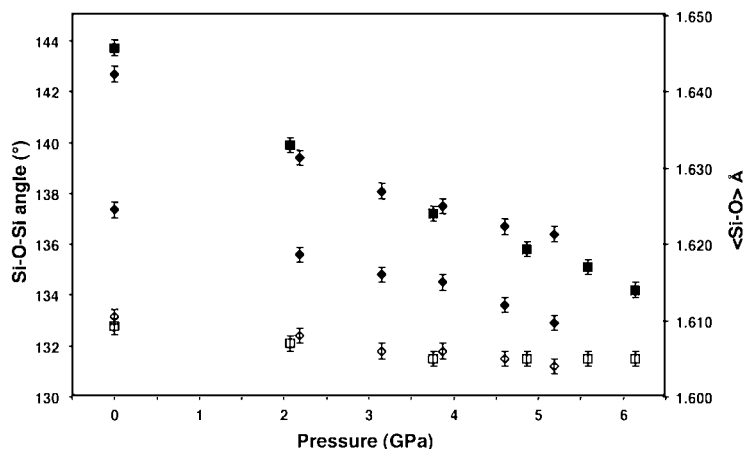


Figure 10-1. Si–O–Si angles (solid symbols) and average Si–O bond lengths (open symbols) vs. pressure for quartz (squares) and coesite (diamonds). Note the (within experimental errors) constant $\langle\text{Si–O}\rangle$ distances with increasing pressure, while the Si–O–Si angles show a significant negative correlation. This demonstrates that framework structures (such as tetrahedral SiO_2 polymorphs) adapt their volume through framework flexion. Data from Levien et al. (1980) and Levien and Prewitt (1981).

effect is also thought to be responsible for the high-density form of amorphization of ice (Mishima et al., 1984; see also Sec. 10.5.3.6).

The most open frameworks known in inorganic chemistry are adopted by the zeolite structure family. These structures exhibit some peculiar effects upon compression. Zeolite frameworks are characterized by large cages and channels, which can be occupied by extra-framework cations or molecules. As in silica, volume reduction on zeolite can be most easily achieved by a reduction of the framework channels, which is achieved through rigid body rotations of the framework tetrahedra and thus bending of the Si–O–Si angles. A study of the natural zeolite natrolite for example showed that compression leads to a continuous reduction of the unit-cell volume without any structural phase transition up to ~ 7 GPa (Belitsky et al., 1992). Above 7 GPa, the investigated samples underwent amorphization, similar to the transition observed for silica. This amorphization again indicates the collapse

of the tetrahedral framework into a glassy tetrahedral arrangement.

If the channels and holes in a framework are large enough, we can even obtain the seemingly paradox result of a negative compressibility. This happens if the molecular size of the pressure medium is small enough to be squeezed into the channels. Because the pressure medium seems to be packed more densely within the zeolite structure than in the fluid, the total volume of the system (crystal plus pressure medium) decreases. The volume of the crystal alone, however, increases with applied pressure. In a similar way, Hazen (1983) observed compressional anomalies for zeolite 4a, which exhibits different phase transitions depending on the pressure medium used. All of the observed high-pressure phases showed higher compressibilities at high pressure.

A more frequent but still unusual phenomenon observed upon compressing framework structures is a negative linear or areal compressibility. Materials with these

properties will expand in one or two dimensions upon hydrostatic compression. As shown by Baughman et al. (1998), this also implies a negative Poisson's ratio, i.e., lateral contraction upon uniaxial compression. These authors also demonstrate that properties such as a negative Poisson's ratio are in most cases linked to geometric constraints in hinged framework structures. Because such behavior can result in increasing surface area upon increasing hydrostatic pressure, it is of potential interest to material scientists. In principle it is conceivable to manufacture these compounds into porous composite material with zero or negative volume compressibilities.

Another example of a structure family whose phase transitions are characterized by framework flexion are the perovskites. This material, with the general formula ABX_3 , can be viewed as a stuffed derivative of WO_3 -type structures. WO_3 (BX_3) is built up of a three-dimensional network of corner-linked WO_6 octahedra, the W (B) cations occupying the corners of the cube-shaped unit cell. In perovskite the center of this cube is occupied by the A cations. In the ideal structure, the B–X–B angle at the connecting octahedral corners is 180° . As shown by Glazer (1972), this octahedral framework is susceptible to a number of distortions which are characterized by rigid octahedral rotations, thus pure framework flexions. These distortions can even be observed at ambient conditions depending on the nature of the A and B cations. At ambient conditions, the geometry is controlled by the relative size and thus the bonding requirements of the cations involved. In a similar way the effect of compression depends on the relative size at ambient conditions and the relative compressibilities of the A and B cations. In most cases the A cation is the more compressible unit, thus leading to increasing polyhedral tilting

(i.e., framework flexion) with increasing pressure. An example of this is the increasing orthorhombic distortion of $MgSiO_3$ with increasing pressure (Fiquet et al., 2000).

10.2.2 Increase in coordination number

Many crystal structures are best described by a closest packing of anions with some of the interstitial sites (two tetrahedra and one octahedron per anion) occupied by a cation. In this simple, but in many cases very successful picture, the large and soft anions are in contact with each other and the small, more rigid cations are isolated from each other and in contact only with their surrounding anions. The number of anions surrounding any given cation is determined by the ratio of the "sizes" of the cations and anions (for the problem of defining the "size" of an atom see e.g., Ross and Price (1997)). In such a close-packed array of anions, rigid polyhedral rotation is usually not able to accommodate a volume reduction imposed by increasing pressure. The only way to optimize the volume upon increasing pressure is through more efficient packing of the anions involved, thus reducing the anion–anion distances within the structure. This reduces the 'size' of the anions without affecting the respective size of the cations, which leads to a higher cation/anion size ratio. As a consequence, the coordination number of the cations increases. Such a coordination increase is generally accompanied by a lengthening of the cation–anion distances, which at first glance may appear a surprising effect for a high-pressure phase transition. However, the lengthening of the first coordination sphere is compensated by a shortening of the second shell. It is therefore worthwhile looking not only at the nearest neighbors of a cation. When looking at both the first and

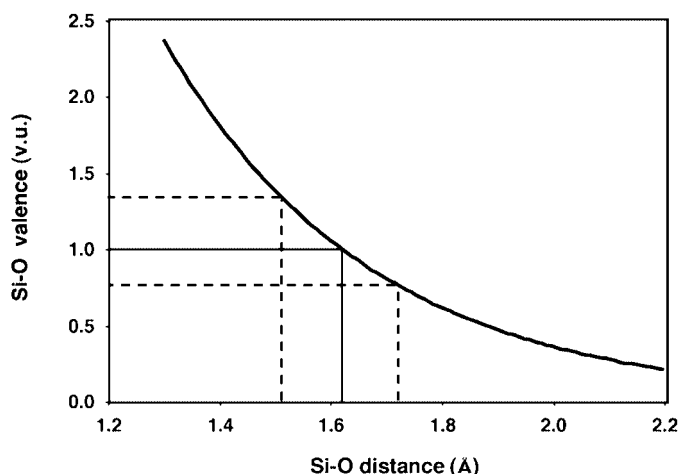


Figure 10-2. The exponential relationship between bond valence and bond length leads to more regular geometries at high pressure; High pressure tends to destabilize structures through overbonding. For a given average bond length, the average bond valence is higher (= more overbonding) the more the individual bond lengths are different from each other (= irregular geometry).

second coordination shells of a cation, a coordination increase can be visualized as making the bonding environment of a cation less distorted. Keeping this in mind, the increase in coordination number can be quantitatively rationalized by the distortion theorem (Brown, 1992). The compression of a close-packed array of anions leads first to a reduction in the anion–anion distance without rearranging the actual packing. This reduces all cation–anion distances, which leads to a strengthening of the individual bonds. In the framework of Brown’s bond valence approach, a general strengthening of cation–anion bonds around a given atom induces an ‘overbonding’ of the atoms, which in turn destabilizes the structure. Because of the exponential relationship between bond strength and bond length (Fig. 10-2), a set of equal bond lengths will have a lower bond valence sum than the same number of bonds with the same average value, but different individual bond lengths (distorted arrangement). An increase in coordination number thus reduces the overbonding of the atoms in the crystal by making the bonding environment around the atoms less distorted. A very instructive example of this effect is the aforementioned phase transition in sil-

ica (SiO_2) from coesite (4-coordinated Si, 2-coordinated O) to stishovite (6-coordinated Si, 3-coordinated O). While the coesite structure is described by a very dense packing of corner-linked SiO_4 tetrahedra, stishovite adopts the rutile structure, characterized by chains of edge-sharing SiO_6 octahedra. Other prominent examples of increasing coordination numbers at increasing pressure are the well-known phase transitions from the NaCl (6-fold) type structure to the CsCl (8-fold) structure in alkali chlorides or the high-pressure transitions from zincblende (4-fold) to NaCl or $\beta\text{-Sn}$ (6-fold) in many AX semiconductors (see Sec. 10.5.1).

10.2.3 Pressure-induced ordering

The potential effect of high pressure on order–disorder phase transitions has only recently been fully realized. The interested reader is referred to the excellent and thorough review by Hazen and Navrotsky (1996). In this section we only give a brief summary of the main features of pressure-induced order–disorder phenomena.

Atoms on a given crystallographic site can order with respect to their chemical species, exact position, magnetic moment

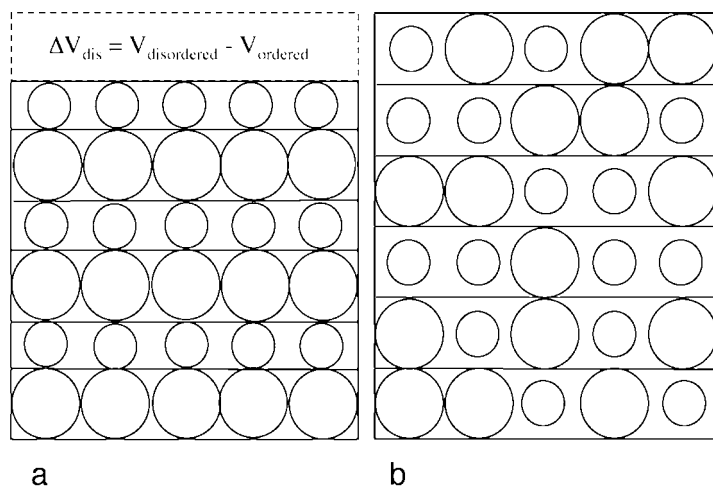


Figure 10-3. Schematic drawing to illustrate a possible mechanism of pressure-induced ordering. Two sets of balls of different sizes occupy (a) a smaller volume in an ordered arrangement than (b) the same number of balls in a disordered distribution.

or electronic state. In the following, disorder with respect to chemical species is referred to as ‘substitutional disorder’, whereas disorder on two neighboring sites is called ‘structural disorder’. Changes in any of these order parameters across a phase transition are known to have an effect on the molar volume of the material (e.g., Owen and Liu, 1947). Depending on whether the molar volume is smaller for an ordered or disordered state, pressure can thus – in principle – promote ordering or disordering effects. Nevertheless, such effects are very often hampered by reduced diffusion rates at high pressure. It is therefore fair to say that at moderate temperatures (≤ 1500 K), high pressure does not necessarily induce order–disorder transitions, but certainly supports such reactions. The fast kinetics above ~ 1500 K, however, allow rapid equilibration with respect to ordering and even in many cases inhibit quenching of an ordering pattern stable at high pressure and high temperature (Hazen and Navrotsky, 1996).

Based on present data, the volume change $\Delta V_{\text{dis}} = V_{\text{disordered}} - V_{\text{ordered}}$ of structural or substitutional disorder tends to be positive, suggesting that high pressure fa-

vors an ordered arrangement (Hazen and Navrotsky, 1996). This can be understood by the fact that an ordered arrangement of two atomic species of different ‘sizes’ leads to an alternation of ‘small’ and ‘large’ layers or rods (Fig. 10-3 a). A disordered arrangement, on the other hand, forces each of the disordered sites to have the apparent size of the largest atom sharing this site (Fig. 10-3 b). An ordering dependence of the molar volume (and therefore a pressure dependence of the ordering) can also be observed in flexible framework structures such as feldspars. At first glance, the molar volume of such structures should not be critically correlated with the size of the cations, because in these structures most of the volume change induced by ordering or pressure can be accommodated by the intra-polyhedral angles (Sec. 10.2.1). The observed volume changes, however, can be understood on the basis of the variation of intra-polyhedral angles, depending on the cation species occupying the respective polyhedra (e.g., Geisinger et al., 1985). Simple geometric considerations show that varying distributions of a given set of angles in space leads to different enclosed volumes (Fig. 10-4).

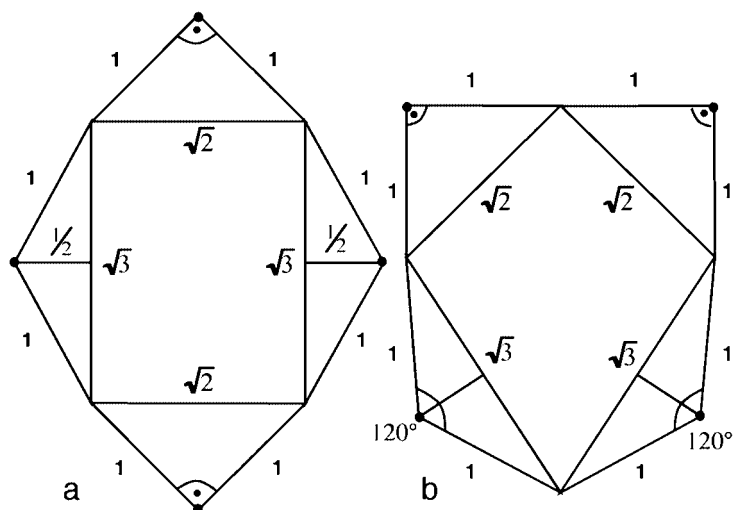


Figure 10-4. Schematic two-dimensional sketch to demonstrate how the distribution of a given set of rigid triangles (polyhedra in 3-d) affects the area (volume in 3-d) enclosed. The area between the triangles in (a) is 2.450, while the triangles in (b) enclose an area of 2.414 (after Hazen and Navrotsky, 1996).

The largest volume changes are observed for substitutional ordering processes. $A^{4+}B_2^{2+}O_4$ spinels, for example, show a difference in molar volume of up to 3.5% between the normal (fully ordered) and the inverse (disordered on the octahedral site) modifications (Hazen and Yang, 1999). The pressure behavior of the spinel family is especially interesting, because they show both pressure-induced disordering as well as pressure-induced ordering for one and the same structure type depending on the chemical species involved (Wittlinger et al., 1998; Hazen and Yang, 1999).

The rather scarce data on pressure dependence of charge distribution seems to indicate that charge ordering tends to be suppressed by high pressure. NaV_2O_5 for example shows a charge-ordering transition around 35 K at ambient pressure. This transition seems to be shifted to lower temperatures at higher pressures and disappears completely around 1 GPa (Ohwada et al., 1999). This suggests that in the case of NaV_2O_5 , high pressure induces a charge-disorder phase transition. In a similar way, the application of pressure to Sm_4Bi_3 shifts

the charge-ordering transition to lower pressures and eventually even induces an iso-structural phase transition where the mixed valence compound $Sm_3^{2+}Sm^{3+}Bi_3^{3-}$ changes to a purely 3-valent material $Sm_4^{3+}Bi_3^{4-}$ (Ochiai et al., 1985).

Another technically interesting phenomenon that is connected to the pressure dependence of ordering and correlation of charge carriers is the well-documented pressure dependence of T_c in certain ceramic superconductors (e.g., Acha et al., 1997; Han et al., 1997). Although neither the superconductivity nor its relationship to high pressure is fully understood in oxide materials, it is justified to assume that the observed strong shift in T_c with increasing pressure is connected to a subtle interplay between pressure-induced structural distortions, orbital overlaps and charge-carrier distribution.

10.3 Generating High Pressure

The technology of pressure cells compatible with *in situ* experiments for material characterization has experienced tre-

mendous development since the ground-breaking work of Bridgman. Consequently, there is a very comprehensive and vast literature on this subject to which the more committed reader is referred (Miletich et al., 2000; Holzapfel, 1997; Eremets, 1996; Ahrens, 1987). Only a brief overview will be given in this section.

There is a huge variety of different techniques for generating pressures. They can initially be divided into static methods and dynamic techniques.

10.3.1 Dynamic pressure generation

The highest pressures (10^2 – 10^3 GPa) can be obtained using dynamic shock-wave generation. This is achieved by means of explosives or by a projectile that is accelerated toward the target with a gas gun (Ahrens, 1980, 1987). The shock-wave technique was originally developed in the mid-1950s at Los Alamos, USA, in the course of the development of atomic bombs (Walsh and Christian, 1955). In its simplest case, the impact of a projectile on the target produces a uniaxial shock wave. The shock wave passes through the sample at shock velocity U_s . The sample itself is accelerated to the sample velocity U_p , and U_s and U_p , together with the temperature, are the quantities measured during a shock-wave experiment. The velocities are usually determined by measuring entrance and exit times of the shock wave. For samples of a few millimeters in length, the time to be measured is in the range of 10^{-1} to $\sim 10^1$ μ s. Ignoring the yield strength of the solid (which is justified at the high shock pressures encountered during a shock-wave experiment), the material behaves as a fluid. In such an experiment, the volume decreases from V_0 to V_H , the temperature increases from T_0 to T_H and the pressure from P_0 to P_H , while the internal

energy rises from E_0 to E_H . The Rankine–Hugoniot relations combine these quantities to (ρ_0 = density at ambient conditions):

$$V_H = V_0 (U_s - U_p)/U_s \quad (10-8)$$

$$P_H = \rho_0 U_s U_p \quad (10-9)$$

$$E_H - E_0 = (V_0 - V_H) P_H/2 \quad (10-10)$$

The measurements of U_s and U_p give the quantities on the left of Eqs. (10-8) to (10-10) for one experiment. Various experiments at different strengths of explosion or different velocities of the projectile produce different points, forming the Hugoniot curve describing the Hugoniot equations of state $V_H(P_H)$. In order to reduce the Hugoniot equations of state into an isothermal equation of state, careful thermodynamic corrections have to be applied (Poirier, 1991). A material passed by a shock wave usually displays various stages. Up to a pressure of the Hugoniot elastic limit (HEL) (0.2 to 20 GPa), the sample behaves elastically, corresponding to the propagation of the longitudinal shock wave. Above the HEL, plastic deformation of the material occurs, giving rise to the fluid-like behavior that creates the Hugoniot curves. If a material undergoes a phase transition, this is readily observed as changes of slope in the Hugoniot curves, separated by a mixed-phase regime (Fig. 10-5).

In this sense, in a shock-wave experiment the material can only be investigated by the difference in U_p and U_s , which both depend on the volume reduction of the sample. The accuracy of these measurements becomes critical once the volume reductions are small at very high pressures. Third-generation synchrotron radiation sources or even free-electron lasers of the future may offer improved possibilities. The increase in X-ray flux of these X-ray sources may allow for stroboscopic X-ray

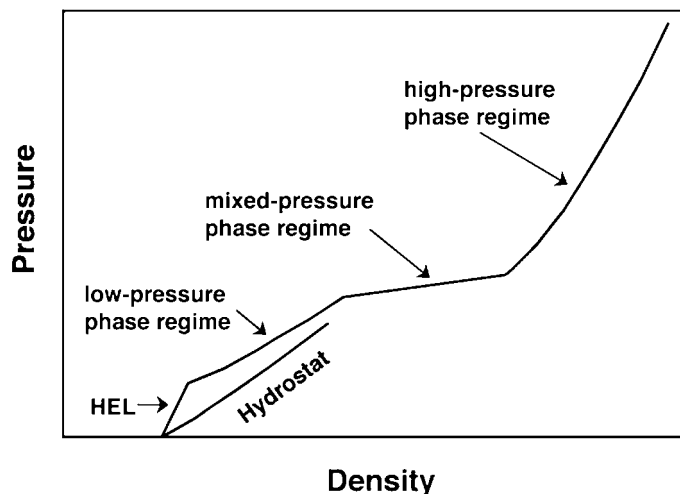


Figure 10-5. Hugoniot curve of a hypothetical material undergoing a phase transformation at high pressure. The low-pressure phase approaches its hydrostatic behavior after passing the Hugoniot elastic limit (HEL). The existence of a shock-induced high-pressure phase is seen by the onset of the mixed-phase regime. The hydrostat of the high-pressure phase can be recognized in the high-pressure phase regime (after Ahrens, 1980).

diffraction in the microsecond regime. This would enable structural information to be extracted of a material under extreme dynamic pressure. Today, shock-wave experiments are highly complementary to static high-pressure experiments. Undoubtedly, one of their most crucial roles is the creation of an equation of state up to extreme pressures without any additional pressure standard. This provides invaluable anchor points for all pressure scales currently used in static high-pressure experiments (Mao et al., 1978; Jamieson et al., 1980).

10.3.2 Static pressure devices

Devices to generate static pressures that are sustainable for an *a priori* indefinite time can be divided into 'large-volume presses' and 'diamond anvil cells'. The primary difference between these two families of devices lies in the volume of material subjected to high pressure and consequently the maximum pressure attainable. For large-volume devices the compressed volume lies between 1 mm^3 and 1 cm^3 . This allows maximum pressures of around

20 GPa to be obtained. Diamond anvil cells, in contrast, enclose a volume of $<10^{-3} \text{ mm}^3$, i.e., only a few pico-liters. These devices are capable of maximal pressures up to 200 to 500 GPa.

103.2.1 Large-volume presses

Historically, the first large-volume cells were hydraulic presses as built by Bridgman. He was able to compress fluids up to 10 GPa. In modern high-pressure research, hydraulic devices are limited to maximal pressures between 1 and 2 GPa and will therefore not be discussed any further in this chapter. Presses operating with solid pressure media up to 50 GPa are the most important tools in modern materials science for the synthesis of materials at simultaneously high pressure and high temperature. Increasingly, large-volume devices are also used for *in situ* studies in combination with synchrotron and neutron radiation.

Piston-Cylinder systems are the simplest design for compressing material. They rely on a cylinder acting as the sample chamber. The sample is compressed by a piston fitted within the cylinder. Closed-end cylin-

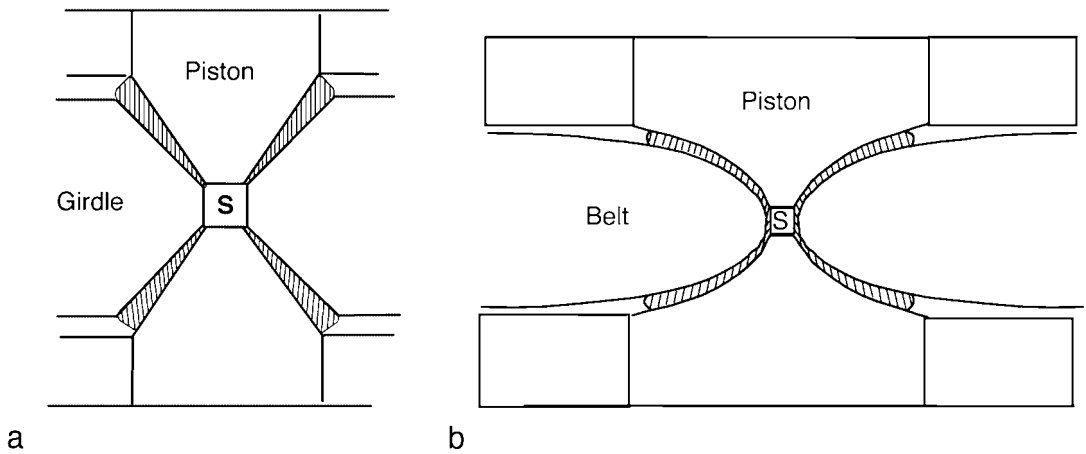


Figure 10-6. Schematic drawing of (a) a girdle-type press and (b) a belt apparatus. The shaded area corresponds to gasket material. S shows the sample position. Note how consequent cutting of stress amplifying corners on the girdle and decrease of length-to-width ratio on the piston lead from a girdle press to a belt design.

ders are closed on one side and the sample is compressed with one piston from the other side. Open-end cylinders rely on two opposite pistons. The maximal pressure of 5 GPa attained by piston-cylinder devices is generally limited by the yield strength of the cylinder. Various techniques exist to increase this yield strength. In a technique called *frettaging* the cylinder is prepared such that in its default state, the outer part retains a residual tensile stress and the inner part a compressive stress. Adding the work stress leads to a partial cancellation of these stresses, thus allowing for the application of higher loads to the sample. Pre-loading the cylinder is another way to increase the yield strength of the cylinder to higher values. Pre-load can be achieved by using a soft but incompressible material (lead) as the inner cylinder material and by initially overstraining it into its flow regime. Another method relies on the application of an external load on the cylinder simultaneously with the application of the load on the piston. Alternatively, cylinders can be reinforced by winding a strong wire under tension around the cylinder. The

most straightforward way to reinforce a cylinder is by increasing the ratio of its diameter to length. If this is pursued consequently, we arrive at two conical pistons compressing a sample contained in a girdle (Fig. 10-6a). A modification of the girdle design is obtained by optimizing the conical shape of the anvils. A cycloid shape of the pistons, as shown in Fig. 10-6b, ensures the optimal compromise ensuring sufficient cylinder support at low pressure while maintaining a reasonable stroke in the high-pressure regime. This 'belt design' is by far the most widely used high-pressure apparatus for materials synthesis and is frequently applied in industry for the synthesis of super-hard material. The maximum pressure achieved by belt devices is around 10 GPa. Such devices have also been optimized with respect to sample volume; a flat belt apparatus constructed by Fukunaga et al. (1987) was capable of compressing a sample of 125 ml up to pressures of 5 – 7 GPa.

The disadvantage of piston-cylinder assemblies is the intrinsic opacity of both piston and cylinder, thus inhibiting most *in*

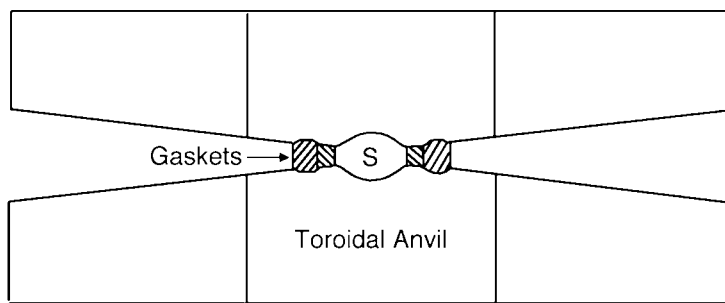


Figure 10-7. The principle of the toroidal anvil. The cut is circular symmetric around the vertical axis of the plot. The sample (S) is surrounded by a washer within a toroidal belt containing gasket material. This geometry prevents the sample from being extruded, thus creating a hydrostatic pressure despite the uniaxial force applied.

situ observations. This problem is alleviated by opposed anvil systems which operate with a gasketing system instead of a cylinder. The very first example of this type was built by Bridgman (1952). A logical extension of the Bridgman design are profiled Bridgman anvils as first proposed by Ivanov and coworkers in the 1960s (e.g., Ivanov et al., 1991) leading to toroidal anvils (Fig. 10-7). This principle was optimized most consequently in the Paris–Edinburgh cell design (Besson et al., 1992). The advantage of X-ray and neutron transparent gasketing has been exploited to the maximum in this cell. This is the reason why this cell design has advanced to the state-of-the-art model for *in situ* high-pressure neutron diffraction and is also employed for X-ray experiments. A development of the Los Alamos neutron group pushes the limits of P and T attainable with toroidal anvils up to 50 GPa and 3000 K, thus enabling *in situ* neutron studies up to these conditions.

A quite different approach to compressing large volumes up to pressures of 30 GPa was first developed by researchers in Japan using multi-anvil designs (Akimoto, 1987). A very successful product is the DIA-type cubic anvil press. In this device, six tungsten carbide (WC) or sintered diamond anvils are arranged parallel to the faces of a cube that encloses the cell assembly. A ram exerts an axial force, which

is also translated into an equatorial compression through wedges attached to the four equatorial anvils. Although initially designed for synthesis experiments, various models of this type have been used in recent years at synchrotron radiation sources for *in situ* X-ray diffraction studies in Japan (Photon factory and Spring-8), Brookhaven (NSLS) and Hamburg (DESY). This is possible because the small gaps between the individual anvils allow for entry and exit of X-rays, and the cell assembly containing the sample is made of X-ray transparent material (BN, epoxy). With tapered anvils made of sintered diamond, maximal pressures of 20 – 25 GPa at temperatures around 1000 °C can be attained.

A rather different geometry in multi-anvil technology is the split-sphere design (Liebermann and Wang, 1992) pioneered at Okayama University by Ito. It consists of a uniaxial ram applying force on a split sphere (first stage) that contains a cube-shaped cavity with the body diagonal along the axis of the ram. The cavity is occupied by a cube built of eight WC cubes with truncated corners. The truncated corners in turn form an octahedral cavity that hosts the cell assembly. The cell assembly is usually a MgO octahedron with a Pt capsule containing the sample in its center. A variation of this design is the split-cylinder design in which the sphere of the first stage is replaced by a cylinder. Multi-anvil presses

based on the split-sphere approach are also used as *in situ* devices at the 'Synchrotron Radiation Source' in Daresbury (UK) and the 'Advanced Photon Source' at Argonne National Laboratory (USA).

However, the determination of pressure is not straightforward. In principle, pressure can be calculated by dividing the force by the area on which it is acting. In practice this is not applicable, mainly because of the unpredictable friction losses and ill-defined compressibilities of the cell assembly. Therefore, pressure has to be determined through a calibration procedure. When *in situ* diffraction techniques are impossible, this can be done by determining phase transitions revealed through changes in resistivity of metals and semiconductors (e.g., Bi, Ba, ZnS, GaAs, GaP). The respective high-pressure phase transitions are determined in hydraulic pressure devices whose pressure can be directly measured by a pressure gauge. If *in situ* observation is possible, the equations of state of materials such as NaCl, Cu, Mo, Ag and Pd, which have been determined up to very high pressures through shock-wave experiments, can be applied to calibrate the press. Because the reproducibility for a given press and cell assembly is very high, pressure of subsequent experiments can be determined from the force applied on the cell assembly.

The strength of large-volume devices lies in their potential for material synthesis at simultaneously high temperature and high pressure. The relatively large size of the compressed volume ($\sim 0.1\text{--}1\text{ cm}^3$) allows inclusion of a heater (usually cylindrical graphite or LaCrO_3 resistance heaters) as well as thermocouples, which enable pressure and temperature to be combined in a very controlled way. Due to the large volume, these devices are limited to maximal pressures of 50 GPa at the very best.

10.3.2.2 Diamond anvil cells

Experiments at extreme pressures, which are of interest not only to geophysicists and planetologists, but also to physicists and chemists studying, for example, solidification and metallization of 'gases', can be achieved using diamond anvil cells (DAC). Diamond anvil cells are in principle very small opposed-anvil devices of Bridgman type. The anvils are made of diamond single crystals, shaped in the brilliant cut with the bottom tip truncated to form the anvil surface (culet). This simple design allows the special properties of diamonds to be used in two ways. First, the extreme hardness of diamonds allows very high pressure to be generated. Pressures attained depend of course on the size of the culet. Maximal pressures of 500 GPa have been reported (Xu et al., 1986) and pressures between 100 and 200 GPa can be reliably reproduced. The second advantage of using single crystalline diamonds as pressure anvils is the high transparency of diamond for almost the entire electromagnetic spectrum. This allows us not only to easily observe samples under high pressure, but also to probe them with spectroscopic methods as well as X-ray diffraction (Sec. 10.4). The strength of DACs is thus their huge range of pressure combined with the ease of performing *in situ* experiments, and this all with a device of the size of a fist, which is also easy to operate by non-specialists.

The very first DAC was constructed using a big (8 ct) gem-quality diamond (taken from smugglers by the US government and donated to the US National Bureau of Standards) in which a hole was drilled (Jamieson, 1957; Lawson and Tang, 1950). Pressure on the sample in the hole was applied via a piston (piano string) pressed on the sample. The limited pressure range obtain-

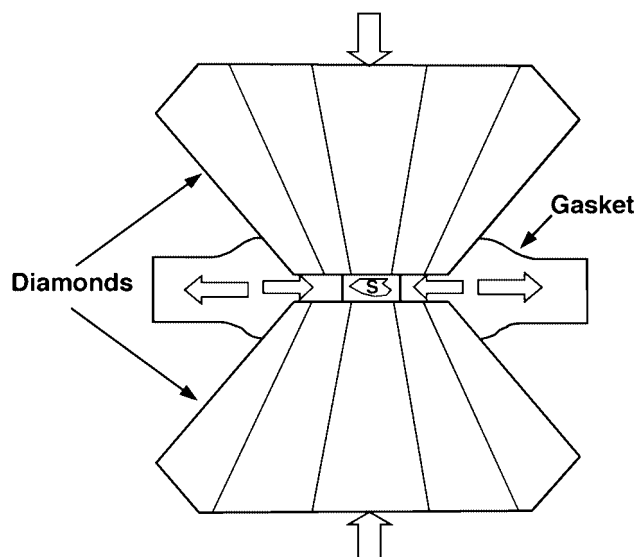


Figure 10-8. Sketch illustrating the principle of the diamond anvil cell. The axial force applied to the diamonds is partly translated into a plastic deformation of the gasket, which results in a circular symmetric equatorial force. This ensures quasi-hydrostatic conditions at the sample (S), which is embedded in a pressure medium.

able with this approach was painfully realized when the 8 ct diamond was crushed during an experiment. As a consequence, the opposed-anvil geometry was developed (Weir et al., 1959; Jamieson et al., 1959), first by simply squeezing a powdered sample between the culets of two opposed anvils and later by introducing the gasketing technique (Van Valkenburg, 1964). Its principle has remained unchanged since its invention and is as simple as it is efficient (Fig. 10-8). A hole about 100 to 200 μm in diameter is drilled in a metal foil (Fe, W, Re). This hole serves as sample chamber and is filled with the sample (powder or single crystal) and a pressure medium (alcohol, liquid gas). The pressure medium is compressed through an axial force exerted by the diamonds on the gasket. The gasket seals the sample chamber and at the same time transforms part of the axial pressure into an equatorial pressure through the plastic deformation of the gasket material. In this way the pressure medium is compressed isotropically and therefore transmits a hydrostatic pressure on the sample. This design was popularized for materials

research by Bassett (Merrill and Bassett, 1974) and Mao (Mao and Bell, 1975). Further details on the technology of DACs and also on its various modifications and developments are given in excellent reviews by Hazen and Finger (1982) and Miletich et al. (2000).

As for the large volume devices, the accurate determination of pressure in a diamond anvil cell is a difficult issue. The most accurate values are obtained by adding an internal standard to the sample whose equation of state is known with sufficient precision to relate its diffraction pattern to a pressure value (e.g., Angel et al., 1997). A very convenient and popular alternative, albeit not quite as accurate, is the exploitation of the pressure shift of fluorescence lines. The most frequently used fluorescence is the R1 line of ruby (Mao et al., 1978). This method again benefits from the transparency of the diamond high-pressure windows. A ruby, which is packed together with the sample into the gasket hole, is illuminated with a green or blue laser that induces a red fluorescence line. The wavelength of this line depends on pres-

sure ($d\lambda/dP = 0.37 \text{ nm GPa}^{-1}$) and can thus be used to determine the pressure within the sample chamber. More recent developments of this approach use different fluorescence lines with various pressure and temperature dependence in order to simultaneously determine pressure and temperature in the sample chamber (e.g., Datchi et al., 1997).

Because of the very small volumes of the sample chamber ($\sim 0.001 \text{ mm}^3$), combining pressure and temperature in a diamond anvil cell is a difficult task. In principle there are two different approaches, namely external and internal heating. With external heating, the whole sample chamber, including diamonds, is enclosed in a resistance heater (e.g., Hazen and Finger, 1982; Bassett et al., 1993) that heats the entire assembly consisting of gasket, diamond anvils and sample. Temperature is measured via thermocouples attached to the outer diamond facets, assuming that the high thermal conductivity of the diamonds allows for only a very small temperature gradient between sample and outer diamond facets. This technique has consequently been optimized by using the gasket material itself as a resistance heater, thus minimizing the heated volume and thermal gradients (Dubrovinsky et al., 1997). An alternative approach is the use of an infrared laser beam, which is focused through the (IR-laser transparent) diamonds onto the sample, where it is absorbed and thus transformed into heat. This technique was again pioneered by Bassett (e.g., Bassett and Ming, 1972) and then further developed and optimized by Boehler (Boehler and Chopelas, 1991) and Fiquet and Andrault (Fiquet et al., 1994). Measuring temperature with this technique is even more difficult because it explicitly assumes that only the sample is heated up. The only way to obtain a quantitative estimate of the sample temperature

is by measuring the black-body radiation of the glowing sample and fitting it to Planck's spectral function (e.g., Bassett and Weathers, 1987). When doing HP-HT experiments with laser heating we should bear in mind the possibility of thermal pressure, i.e., the increase of pressure in the heated area, while the pressure determined by a ruby chip outside the hot-spot remains constant (Andrault et al., 1996).

10.4 Probing Phase Transformations in Materials at High Pressure

A very important aspect when doing experiments on high-pressure phase transformations is the possibility of investigating the phase transformation *in situ* at conditions of high pressure and possibly simultaneously high temperature. As mentioned above, this is much easier to do in static experiments than with dynamic shock-wave techniques. This is mainly due to the very short time that is available in a shock-wave experiment. We will therefore focus on static experiments in the following. Among the static experiments, the transparency of the diamond pressure windows in a DAC allows for much more versatile experimental techniques compared with large-volume presses. For large-volume experiments, direct observation of the sample is limited to either transport properties (e.g., electric resistance) or, if using some sort of electromagnetic radiation as a probe, severe compromises in signal-to-background and accessible space have to be accepted. Nevertheless, the range of *in situ* techniques applicable to both DACs and large-volume devices has grown considerably and continues to expand. There is an extensive specialized literature on each of the various techniques. We will give here a brief over-

view on and introduction to the available techniques, with references to the more detailed literature. Many techniques can be used to measure different physical properties and *vice versa*. In the following we will differentiate by the technique rather than by the measured property.

10.4.1 Volumetric techniques

The first *in situ* observations in large-volume cells were pioneered by Bridgman (e.g., Bridgman, 1940) on piston-cylinder devices. He made volumetric measurements by simply measuring the stroke of the piston as a function of force (pressure) applied to the sample. This technique obviously assumes that deformation of the piston and cylinder, as well as leakage, can be neglected. The accuracy in V/V_0 obtained through this method can be fine-tuned to about 1 in 1000 (Anderson and Swenson, 1984). In general, the accuracy is limited to lower values by deformation of the piston and the cylinder. Compressibilities are therefore most often and much more accurately determined using diffraction techniques (see Sec. 10.4.4). Prior to the availability of *in situ* diffraction techniques, however, volumetric measurements were the only way of measuring compressibilities as a function of pressure, and they provided extremely valuable data.

10.4.2 Spectroscopic techniques

There are a variety of spectroscopic techniques making use of various segments of the electromagnetic spectrum. Although the transparency of diamonds makes DACs a very obvious tool for spectroscopic techniques, they are by no means limited to them, but – due to the advent of brilliant synchrotron radiation sources – are increasingly also applied in combination with large-volume presses.

10.4.2.1 Microscopy

A rather cheap, but in many cases highly efficient ‘spectroscopic’ device is the human eye. Visual observation of a sample under high pressure can be a very useful and sensitive tool for observing a phase transformation and pinpointing it in P – T space. An example of this has been described by Arlt et al. (2000), where the pressure dependence of a high-temperature phase transition in Mn-pyroxenes turned out to be difficult to determine using diffraction techniques, but could be optically observed through the discontinuous change in birefringence.

10.4.2.2 Raman and infrared spectroscopy

The most popular spectroscopic techniques applied in high-pressure studies are Raman and infrared (IR) spectroscopies. They both probe the vibrational properties of the material under investigation. Because lattice vibrations strongly depend on the topology of the chemical bonds of a substance, these spectroscopic techniques are very sensitive to phase transformations. Vibrational modes involving a dipole change can be excited by absorbing an infrared photon giving rise to an absorption band in the infrared. The energies of these lattice modes are thus of the same magnitude as the energy of the IR photons. If the photon energy is much higher, the interaction of the photon with the lattice can induce a vibrational mode, where the energy of the lattice mode is transferred from the photon to the lattice. This decreases the energy of the photon and therefore induces a wavelength shift on the scattered photons (Raman spectroscopy). Because energy can be transferred in both ways (to and from the lattice), the respective wavelength shift

can be positive or negative. By measuring the wavelength shifts of transmitted laser light of a wavelength around 500 nm, a characteristic fingerprint of the vibrational properties of a given substance is obtained. Again, this fingerprint critically depends on bond strengths and the structural configuration and is therefore ideal for detecting phase transformations. While in general Raman shifts are measured for the optical branches of the vibrational spectrum, very carefully designed experiments are able to determine the minute frequency shifts caused by the acoustic branches, too. Such Brillouin scattering experiments are very interesting, because they allow the full elastic tensor to be measured as a function of pressure (e.g., Sinogeikin and Bass, 1999). The elastic tensor is a material property that is useful in its own right. Its strong dependence on structural parameters makes it a very sensitive probe for detecting and investigating phase transformations (Carpenter and Salje, 1998). A very instructive and comprehensive overview of high-pressure specific problems and applications of IR and Raman spectroscopy is given by Gillet et al. (1998).

10.4.2.3 Mössbauer spectroscopy

Mössbauer spectroscopy has become increasingly popular in materials science to probe site-dependent distributions of charge and magnetic moment. Its application to high pressure is limited to DAC experiments (Pasternak and Taylor, 1996; McCammon, 2000). In a classical Mössbauer experiment, the radiation emitted by the γ -source lifts the sample nuclei into an excited state through an absorption event. During re-emission, a fraction of the γ -quanta is emitted without recoil on the lattice (recoil-free fraction) and can thus be reabsorbed by a nucleus in the same struc-

tural environment (resonant absorption) while lifting it into an excited state. The energy of the excited state of a given nucleus is a function of its structural environment, and therefore varies between individual substances. This energy shift (isomershift) is another characteristic fingerprint for a given structural state as well as for the electronic charge of the nucleus. The isomer shift can be measured by altering the relative energy of the γ -quanta through the Doppler effect caused by relative movements of sample and source. The γ -quanta of the most popular Mössbauer nuclei ($^{57}\text{Fe}_{26}$) are in the range of 14.4 keV and are thus strongly absorbed even by diamonds. It is for this reason that the first high-pressure Mössbauer experiments were performed using more exotic Mössbauer nuclei such as ^{153}Eu , ^{129}I and ^{170}Yb , which have higher γ -energies. These experiments helped answer some interesting questions about the physics of magnetic materials (e.g., Pasternak et al., 1986; Abd-Elmeguid et al., 1980). The development of especially miniaturized diamond anvil cells (e.g., Pasternak and Taylor, 1990, 1996) together with advances in detector technology also allowed successful Mössbauer experiments to be performed on ^{57}Fe nuclei (e.g., McCammon et al., 1998). While traditional Mössbauer experiments make use of the energy structure of the emitted γ -rays, modern synchrotron sources with their time-pulsed radiation also allow us to exploit the time structure of a Mössbauer event. As mentioned above, a Mössbauer event involves the absorption of a γ -quantum by lifting the Mössbauer nucleus in an excited state. This state lasts for a time span in the range of 100 ns before it decays and emits the scattered radiation. Because individual synchrotron X-ray bursts can be gated into a time interval in the range of 100 ps with $1\text{ }\mu\text{s}^{-1}$ repetition

rates, the actual decay event can be separated from the primary synchrotron radiation. This allows the individual decay events and their interaction with the nuclear and magnetic lattice to be investigated directly. In such a 'nuclear resonant scattering' experiment, the emitted γ -rays of the individual nuclei in the material have different wavelengths owing to the hyperfine interaction of the magnetic ^{57}Fe nucleus. The different wavelengths of radiation emitted from different nuclei cause a quantum-beat oscillation pattern, which in turn yields information on the material investigated (e.g., Smirnov, 1999). The high brilliance of synchrotron radiation sources, which are required for such experiments, also makes nuclear forward scattering much easier to apply in combination with diamond anvil cells. High-pressure experiments using nuclear forward scattering as a probe to investigate structural and magnetic phase transitions have therefore quickly become very popular (e.g., Nasu, 1996; Lubbers et al., 1999).

10.4.2.4 X-Ray absorption spectroscopy

The high X-ray brilliance of modern synchrotron radiation facilities not only revolutionized high-pressure diffraction (see Sec. 10.4.4), but also provided the opportunity to apply X-ray absorption spectroscopy (XAS) methods in high-pressure research. In particular, developments on large-volume presses (Paris–Edinburgh) which were originally built for neutron diffraction, proved to be very useful for *in situ* XAS experiments. Most popular among the high-pressure XAS techniques are the 'extended X-ray absorption fine structure' (EXAFS) experiments (i.e., Katayama et al., 1997). The principle of EXAFS is well known and has been described since the early days of quantum mechanics (see

Brown et al. (1988) for a review). If an incident X-ray photon hitting an atom in the sample has an energy equal to the energy difference between the ground state and the excited state of a core electron, it will be absorbed by the atom while lifting the core electron to an excited state. Photons at this energy have a high probability of being absorbed by the sample, which leads to characteristic absorption edges in the transmitted X-ray spectrum. Core electrons in their excited state (photoelectrons) are delocalized from their parent atom and can thus interact with the intermediate surroundings of the atom as well as with other photoelectrons, leading to an oscillatory contribution in the X-ray spectrum in the vicinity of an absorption edge. It is this oscillatory part that is extracted from an EXAFS experiment. It is dependent on the immediate surroundings of an atom and therefore contains information about the local neighborhood of an atom in a solid or a liquid. When photoelectrons are recaptured by an atom, they will emit characteristic fluorescence radiation which by itself can again be used as a probe for characterizing a material. The advantage of XAS methods in comparison with diffraction methods is their sensitivity to local and short-range effects. This makes them very powerful for the investigation of phase transformations, not only in crystalline solids but also in amorphous solids and liquids (e.g., Buontempo et al., 1998).

10.4.2.5 NMR

A final spectroscopic tool that can be applied to samples under high pressure is NMR. An NMR experiment exploits the interaction between the magnetic moment and the spin of the nucleus on the one hand and a static magnetic field disturbed by pulses of a radio frequency field on the

other. Introductory texts on NMR are available, e.g., by Akitt (1983) or Kirkpatrick (1988). The spin of a nucleus leads to a precession motion of its magnetic moment if placed in a static magnetic field. A magnetic perturbation in the radio frequency range of the static field causes a tilting of the precession axis. The time the nucleus needs to revert its precession axis into its static position depends on the nature of the nucleus itself as well as its immediate surroundings in the crystalline or amorphous host. NMR, similar to XAS techniques, is therefore a useful probe for investigating short-range phenomena. Alternatively, the analysis of NMR spin echoes also allows information on viscosity and self-diffusion rates in liquids to be extracted.

The application of NMR to high pressure is an experimental challenge because it has to deal with both the inherently small volumes encountered in high-pressure experiments and the magnetic susceptibility of most materials suitable for construction of high-pressure devices. Nevertheless, the first high-pressure NMR experiment was performed as early as 1954, in combination with a Bridgman-type press (Benedek and Purcell, 1954). The press was almost entirely made from a non-magnetic Be–Cu alloy. Combining NMR and DAC is even more difficult because of the extremely small sample volumes. However, Bertani et al. (1992) developed an NMR–DAC, again made of Be–Cu alloy. This DAC is compatible with a cylindrical cryostat and is thus able to combine high pressure and low temperature, allowing for the study of the pressure and temperature dependence of the Knight shift in solids (e.g., Kluthe et al., 1996). An NMR set-up for the investigation of gases and liquids at pressures up to 20 bar has been developed by Woelk and Bargon (1992).

10.4.3 Ultrasonic sound velocity

Measuring sound velocities at high pressure is of great interest, mainly for seismologists who use this to correlate seismic models with mineralogical models of the earth. The importance of this method for materials science is not quite so obvious although in principle, discontinuities in the change in sound velocity at high pressure can be used to detect phase transformations and to characterize them through the elastic tensor. A simple pulse-transmission or pulse-echo method can be combined with a piston-cylinder apparatus in order to measure velocities at pressures up to about 1 GPa. A more sophisticated approach is ultrasonic interferometry, which can be combined with a split-sphere apparatus. In this technique, two phase-coherent pulses, separated in time by the approximate return travel time in the sample, are applied to a cell assembly under pressure, which is attached to a buffer rod. When combining this technique with a large-volume press, the anvils are simultaneously acting as buffer rods. For two consecutive pulses, the echo of the first pulse from the far end of the sample overlaps with the echo of the second pulse from the sample–buffer interface. The interference caused by this overlap leads to a modification of the amplitude of the resultant signal. This amplitude in turn can be modified by changing the carrier frequency, causing a beat pattern as a function of frequency. The difference on the frequency scale between two successive interference extremes yields the sound velocity, if the dimensions of the sample are known. This method has an advantage over more traditional pulse-transmission techniques, in that it involves only one interface, reducing the possible coupling problems for the acoustic signals. Owing to the applied high pressure, mechanical con-

tact and thus coupling between the materials forming the interface is further enhanced. A more thorough introduction to this technique is given by Rigden et al. (1992) and Li et al. (1998). There have been recent efforts to combine ultrasonic interferometry with diamond anvil cells. In this case, however, because of the very small sample volumes, the carrier frequencies have to be in the GHz range (Shen et al., 1998).

10.4.4 Diffraction techniques

Probably the most versatile and at the same time powerful tools for characterizing phase transformations at high pressure are diffraction methods. There is a huge amount of literature on this field. Here we only briefly present the various domains of high-pressure diffraction giving appropriate references for the more interested reader.

10.4.4.1 X-ray diffraction

A comprehensive introduction to the basic principles of X-ray diffraction is given by, e.g., Stout and Jensen (1989). X-ray diffraction at high pressure has initially only been possible in combination with diamond anvil cells. Despite the high transparency of diamonds to X-rays, diffraction experiments suffer both from the small sample volume and from shielding and absorption effects from the pressure cell components. This is the reason why high-pressure experiments on sealed-tube sources are mostly restricted to single crystals, because the diffraction signal of a crystal of a size of about 100 μm is sufficiently strong to pass through the diamond anvil (Hazen and Finger, 1982; Miletich et al., 2000; Angel et al., 2000). By measuring accurate lattice parameters on single crystals (Angel, 2000a), we are able to detect and char-

acterize even subtle phase transformations (Carpenter et al., 1998; Angel, 2000b). In addition, measurements of single-crystal diffraction intensities serve to establish an accurate structural model for the observed phase transformations and are therefore of great importance to the understanding of phase transformations at high pressure.

X-ray powder diffraction is much more difficult to perform at laboratory sources (e.g., Haines et al., 1998), mainly because of the inherently small sample volumes. For this same reason even at synchrotron sources the dominating diffraction technique for investigating powdered samples has been energy-dispersive diffraction (e.g., Holzapfel, 1997), making use of the much higher flux of a white beam compared with monochromatic radiation. Energy-dispersive diffraction was initially the only method of choice for *in situ* diffraction studies in combination with large-volume presses (Yagi et al., 1987; Weidner et al., 1992; Mezouar et al., 1996). In the energy-dispersive mode, the diffraction signal is recorded on the energy scale for a fixed Bragg angle using a Ge solid-state detector. Modern synchrotron radiation sources, coupled with new two-dimensional detector technology, however, allow monochromatic powder experiments with both diamond anvil cells (e.g., Fiquet et al., 2000) and large-volume presses (Parise et al., 1998; Mezouar et al., 1999a). In this technique, the diffraction signal of a monochromatic X-ray beam is recorded as a function of the Bragg angle. In contrast to energy-dispersive data, such angle-dispersive data allow for a quantitative interpretation of the diffracted intensities in order to establish and refine a structural model. Another advantage of angle-dispersive diffraction over energy-dispersive techniques is the higher resolution achievable with monochromatic radiation.

Although synchrotron radiation can overcome the intensity problem caused by the small sample volumes in high-pressure powder diffraction experiments, the additional intensity cannot resolve the problem of inadequate powder statistics of small sample volumes. This problem can be partly alleviated using digital two-dimensional detectors such as online image-plate detectors or CCD cameras (Shimomura et al., 1992).

A further step in the use of the unique properties of synchrotron radiation has recently been made by performing inelastic X-ray scattering through a diamond anvil cell in order to determine the acoustic phonon dispersion in materials (Krisch et al., 1997). The application of this very useful technique in high-pressure research is still very new and under development.

10.4.4.2 Neutron diffraction

A very comprehensive introduction to the general principles of neutron diffraction is given by Bacon (1975). The advantage of neutron diffraction over X-ray diffraction is that neutrons are more sensitive to light elements. Furthermore, neutron diffraction is able to distinguish between a lattice of nuclei and a magnetic lattice. Neutron powder diffraction at high pressure has been carried out since the 1960s. The development of the Paris–Edinburgh press (see Sec. 10.3.2.1) dramatically increased the pressure range accessible for *in situ* neutron powder diffraction. The quest towards higher pressures is followed even more consequently with revolutionary sapphire cells (e.g., Goncharenko and Mirebeau, 1998) allowing for neutron diffraction experiments up to pressures of 50 GPa. Another remarkable development in high-pressure neutron diffraction is the possibility of performing inelastic single-crystal

neutron diffraction again in combination with the Paris–Edinburgh cell (Klotz et al., 1996; 1997). Such data complement the static picture of a given material as obtained through an elastic scattering experiment with the dynamic nature (phonons) of the crystalline material.

10.5 Examples

10.5. Zincblende-type semiconductors

Due to their pivotal role in modern electronic technology, semiconductors are probably the most intensely studied class of materials. Experiments at high pressure are crucial for the testing of theoretical models, because the application of pressure is a straightforward way of modifying the band structure of the material without changing the chemistry. It is therefore not surprising that semiconductors were among the very first materials to be investigated at high pressure (e.g., Bridgman, 1935; Miller and Taylor, 1949). Since then, theoretical as well as experimental work in this field has increased greatly.

Application of high pressure on semiconductors leads to a closing of the interatomic distances and thus of the gaps between formerly localized molecular orbitals. Increasing overlap of the orbitals leads to an increasing delocalization of the electrons, which in turn enhances electrical conductivity up to a metallization of the originally insulating or semiconducting compounds. Narrowing and closing of the gap between valence and conduction bands not only has an effect on the electrical conduction but also on the optical absorption. It is for this reason that optical spectroscopy was one of the first methods used to study phase transformations in semiconductors at high pressure (Slykhouse and

Drickamer, 1958; Paul, 1959; Goñi and Syassen, 1998).

High-pressure driven phase transformations have also been extensively studied in the past 30 to 40 years using diffraction methods. In the following only an overview of phase transformations in zincblende-type semiconductors will be given, without claiming completeness even in this limited segment of semiconductors. A most thorough and comprehensive review of this subject is given by Nelmes and McMahon (1998).

First structural diffraction studies on these materials were performed on powdered samples using energy-dispersive X-ray diffraction (EDX) (see Sec. 10.4.4). The picture emerging from these studies is a sequence of phase transitions where volume optimization is achieved by a stepwise increase in coordination number (see Sec. 10.2.2). This increase in coordination number was believed to happen through the following sequence of phase transformations: 4-fold (diamond, zincblende, wurtzite) \rightarrow 6-fold (NaCl, β -tin) \rightarrow 8-fold (simple hexagonal) \rightarrow 8-fold with six close second nearest neighbors (bcc, CsCl) or 12-fold (ccp, hcp). For a description of the structure types relevant for semiconductor crystal chemistry, see Nelmes and McMahon (1998). The availability of *in situ* angle-dispersive X-ray powder diffraction (ADX) (see Sec. 10.4.4) has changed this simple model dramatically, mainly because of the much higher resolution of the ADX technique relative to EDX. The overall picture emerging from these new experiments is that at least the change from 4-fold to 6-fold coordination is characterized by a decrease in symmetry, in contrast to the general crystal-chemical trend of increasing symmetry with increasing pressure. The new 6-coordinated phases can be structurally described as distorted derivatives of

NaCl (Cmcm, cinnabar, Imm2, Immm) or, β -tin (Imma, simple hexagonal) structures. An interesting aspect also is that a site-ordered version of the diatomic β -tin structure, which previously was believed to be of great importance in semiconductor crystal-chemistry, probably does not exist for any of the group III–V and II–VI semiconductors. A further peculiarity, which has been found in Si, Ge and GaAs, is the occurrence of different phases at a given pressure, depending whether one is on a compressional or decompressional branch of the P-path. In a similar way, InSb, HgSe and HgTe exhibit intermediate phases during their sluggish phase transitions from 4-fold to 6-fold coordination. These intermediate phases (“hidden” phases) cannot so far be isolated as single phases, but always occur together with the stable low- or high-pressure modification. Most of these peculiarities are believed to be linked to site-ordering problems (non-existence of diatomic β -tin) or to problems of achieving a true equilibrium state when compressing at room temperature („hidden“ phases). Systematic experiments at simultaneously high temperature and high pressure are therefore the next experimental step to be taken to obtain a complete understanding of semiconductor phase transformations.

In the following the phase transformations in Si, Ge, GaAs and InSb will be discussed in more detail, because they are instructive examples of most of the special features encountered in the high-pressure behavior of group IV, III–V, and II–VI, semiconductors.

10.5.1.1 Si and Ge

The phase transformations of Si and Ge are quite similar. The main differences are found in large discrepancies in the respective transformation pressures and in an ad-

ditional 'intermediate phase' in Si at high pressure. Both Si and Ge crystallize in the diamond structure at ambient conditions. The diamond structure can be viewed as the monatomic version of the zincblende structure. The zincblende structure is a cubic closest packing (ccp) of anions with half of its tetrahedral interstices occupied by the cations. The hexagonal closest packing (hcp) analog to the zincblende structure is the wurtzite structure. At 11 GPa (Si) and 10.6 GPa (Ge), the diamond-type structure transforms to the β -tin structure. The exact transition pressure is known to depend on the amount of stress in the sample. For silicon, the β -tin structure transforms into an orthorhombically distorted version of the β -tin structure at 13.2 GPa (McMahon and Nelmes, 1993). The corresponding phase transformation also occurs in Ge, but at around 75 GPa (Nelmes et al., 1996). These orthorhombic phases transform to the previously detected simple hexagonal structure at 15.6 GPa (Si) and ~ 85 GPa (Ge) (Ruoff and Li, 1995; Vohra et al., 1986). A further increase in pressure causes Si to adopt another orthorhombic (Cmca) structure (Si-VI) around 37.6 GPa (Duclos et al., 1990; Hanfland et al., 1999), where the Si atoms are 10- and 11-coordinated. A remarkable detail of the Si-VI phase is that it is iso-structural to Cs-V (Schwarz et al., 1998). Not only is the topology between these two phases identical, but also the axial ratios and free atomic coordinates have almost exactly the same values. Until now, an analogous phase has not been found for Ge. Instead, Ge is believed to transform to a hexagonal closest packed structure with a doubled c-axis (dhcp) (Vohra et al., 1986) around 100 GPa. The experimental evidence presented in favor of such a dhcp structure is, however, scarce and further experiments are required to confirm this phase. Si, in turn, is observed

to transform to a hexagonal closest packed structure (hcp) (Si-VII) around 41.8 GPa (Duclos et al., 1990) and finally to a cubic closest packed structure (ccp) around 78 GPa (Duclos et al., 1987). In hcp as well as ccp, the individual atoms are bonded to 12 nearest neighbors. The ccp structure is believed to remain stable until at least 248 GPa (Duclos et al., 1990).

On decompression, five more phases have been found for Si. Slow pressure release from Si-II (β -tin structure) leads to the Si-III phase (Besson et al., 1987). It adopts a body centered cubic structure (BC8) with 16 atoms per unit cell. The transition from Si-II to Si-III has recently been shown to occur via an intermediate rhombohedral phase (Crain et al., 1994), which represents a slight rhombohedral distortion (R8) of the BC8 structure type. Transition pressures from β -tin to R8 and R8 to BC8 are 10.1 GPa and 2 GPa, respectively. The decompressional behavior of Si is different when the rate of pressure release is very fast. In this case, Si-II (β -tin) seems to transform into two tetragonal phases, whose structures are not yet known.

Slow decompression of Ge-II (β -tin structure) leads to a phase (Ge-III) with a non-centrosymmetric, tetragonal structure (ST12) with space-group $P4_32_12$. Unexpectedly, the BC8 structure, which in Si is obtained through slow pressure release, can be grown in Ge by fast decompression from the β -tin structure.

10.5.1.2 GaAs

GaAs is the III–V analogue of Ge. It is of very great technological importance, which explains the large amount of research performed on this compound. Despite the intense scrutiny devoted to GaAs, its high-pressure phase transformations re-

mained a controversial topic for many years. GaAs has the zincblende structure at ambient conditions. A high-pressure phase transformation to a GaAs-II phase was first found through electrical measurements (Minomura and Drickamer, 1962). In the 1980s, it was recognized that the structure would most probably be of orthorhombic symmetry. However, space group as well as structural topology remained ambiguous (Shimomura et al., 1980; Baublitz and Ruoff, 1982; Weir et al., 1989) in that a proposed model (space group $Pm2m$) implied very close Ga–Ga and As–As contacts. ADX experiments again proved to be the key to resolving the puzzle, although the very similar X-ray scattering power of Ga and As created additional problems. The high resolution of the ADX patterns were, however, able to reveal small reflections, which allowed for an experimental distinction between $Pm2m$ and $Cmcm$ (which can be described as a distorted NaCl structure). Ga and As form slightly distorted NaCl-type planes parallel (001). Neighboring planes are shifted parallel to [010] by about half a Ga–As distance (Nelmes and McMahon, 1998). Upon further compression, GaAs has been reported to undergo another phase transition to a simple hexagonal structure (Weir et al., 1989). However, a diatomic compound such as GaAs, cannot adopt the simple hexagonal structure, although the topology of the atoms does have this symmetry. To adopt this structure, GaAs would have to be completely site-disordered. It can be speculated that the similar scattering power of Ga and As may make a diffraction pattern (because of limited resolution and signal-to-noise ratio) appear to have simple hexagonal symmetry, when in truth it remains of orthorhombic symmetry. This would imply that GaAs remains in $Cmcm$ structure up to the highest pressure investigated, i.e., 108 GPa.

Two more phases of GaAs have been found. The first occurs upon decompression of the GaAs-II phase. It leads to a 4-coordinated cinnabar structure (McMahon and Nelmes 1997). The other can be grown by heating the GaAs-II phase to about 450 K at a pressure of ~ 14 GPa (McMahon et al., 1998). Its structure (SC16) is the diatomic equivalent of the BC8 structure found in Ge and Si.

10.5.1.3 InSb

InSb, which at ambient conditions also adopts the zincblende structure, is probably the most impressive example of a phase diagram that has been completely rewritten in the past 5–10 years. The problem of very similar scattering powers is even more severe in InSb than in GaAs. In order to unravel the crystal chemistry of its high-pressure phases, the ADX technique had to be supported by anomalous scattering in order to distinguish between true symmetries and pseudo-symmetries caused by the similar scattering powers (Nelmes and McMahon, 1998). The peculiar feature of InSb is that two different successions of high-pressure phases as a function pressure can be observed, albeit in a reproducible way. The basic succession is from the zincblende type to a superstructure of $Cmcm$ (InSb-IV) around 3 GPa. At 9 GPa the structure transforms to an orthorhombic distorted NaCl phase (InSb-III) with space group $Immm$. The $Immm$ phase appears to be attained through an intermediate site-disordered orthorhombic phase with space group $Imma$. The transformation from $Imma$ occurs with time (a few hours) or upon slight heating. InSb-III, in turn, transforms at 17 GPa to a new phase with yet unknown structure, and upon further compression over 21 GPa, to a site-disordered body centered cubic structure. A new fea-

ture in this case is that the transition from the zincblende-type phase to InSb-IV can also be preceded by an additional phase transition around 2.1 GPa, which produces a mixture of a site-disordered β -tin phase and the InSb-II phase with orthorhombic symmetry (Immm). This mixture recrystallizes to InSb-IV when left for a few hours. Even more peculiar is the fact that if, during the presence of the mixed phase the pressure is increased to about 3 GPa within a few hours, the formation of InSb-IV is suppressed (Nelmes et al., 1993a). The InSb-II phase persists up to 9 GPa where it does not show any phase transition to InSb-III, because InSb-III already has the Immm structure.

As outlined in this brief summary of the unusual high-pressure behavior of GaAs and InSb, there seems to be a number of unusual phenomena in the structural behavior of zincblende-type semiconductors at high pressure. These phenomena may well be linked to kinetic problems as they are often encountered during phase transformations at high pressure. As shown by Leinenweber (1993) and Kunz et al. (1996), such kinetic problems can be alleviated by adding high temperature to high pressure. Very often heating a compressed sample may eventually lead to a stable phase. In a similar way, the nonexistence of a site-ordered β -tin phase could be linked to microstrain and/or kinetics. Mezouar et al. (1999b) showed that different phases can be obtained at a given pressure, depending on the microstrain and hydrostaticity present in a pressure cell. It will thus be a challenge in future high-pressure semiconductor research to combine high pressure and high temperature while simultaneously probing the sample.

10.5.2 Materials in the B–C–N system

Diamond (i.e., the high-pressure polymorph of carbon) is not only a precious and popular gem stone, it also has great technological significance owing to its extraordinary physical properties. The most prominent of these is a Mohs hardness of 10 (diamond is the hardest material known) making it a most efficient abrasive material. The reason for the extreme hardness of diamond lies in the combination of high covalency together with the smallness of the core electron shell of carbon, distinguishing it from the isomorphous compounds Si and Ge (see Sec. 10.5.1.1). Also unusual is the combination of a very high thermal conductivity coupled with a low electrical conductivity, which makes it an interesting material as a heat sink in microelectronic applications. Graphite (i.e., the low-pressure polymorph of C) also has technological importance thanks to its electrical (e.g., graphite electrodes) as well as its mechanical (steel additive, graphite composite material, nanotubes) and lubricating properties. Therefore, (pseudo-)isoelectronic systems of C have attracted much attention in the hope of obtaining materials with graphite- and diamond-like properties. There is reason to believe that ternary compounds in the B–C–N system with graphite-like structures might be semiconductors with high thermal stability or, alternatively, diamond-type phases in the B–C–N field may exhibit abrasive properties exceeding those of diamond combined again with a much higher thermal stability (Kurdyumov and Solozhenko, 1999).

Crystallographic investigations of superhard materials *in situ* at high pressure pose an additional challenge: the extreme hardness of the material causes strong deviatoric stresses when compressing a powdered sample (Weidner et al., 1994a, b).

The deviatoric strain caused by the deviatoric stress leads to anisotropic peak broadening, which in turn makes the accurate interpretation of powder patterns more difficult.

10.5.2.1 C

Carbon crystallizes in three different polymorphs (Fig. 10-9a). Graphite, the stable phase at ambient conditions, is characterized by a stacking of hexagonal layers, where the individual layers are formed by a honeycomb net of 6-membered rings formed by C. The layered structure is responsible for the very low hardness (Mohs 1–2) as well as the anisotropic electrical properties of graphite. Graphite can exist in a hexagonal (2H) and rhombohedral (3R) modification, where these polytypes differ in the stacking of the layers: ABABAB for 2H and ABCABC for 3R. If graphite is pressurized, it transforms to diamond. For kinetic reasons,

a pressure of about 8 GPa (5 GPa if a C-solution in a metal melt is used as precursor) usually has to be combined with a temperature of ~ 1000 K in order to obtain cubic diamond. The crystal structure of cubic diamond is the monatomic equivalent of the zincblende structure [see Sec. 10.5.1 and Nelmes and McMahon (1998) for detailed descriptions of these structure types]. Although the phase boundary has a positive slope and thus would extend to much lower pressures at room temperature, graphite compressed at room temperature does not readily adopt the diamond structure. Instead, pure compression of graphite at room temperature up to 12 GPa and subsequent annealing at about 1000 K leads to the formation of a hexagonal form of diamond (lonsdaleite). This transformation is reversible in the temperature range between 1000 and 1300 K. If heated above 1400 K, however, lonsdaleite converts to cubic diamond. Subsequent further changes in the P – T field do not induce any

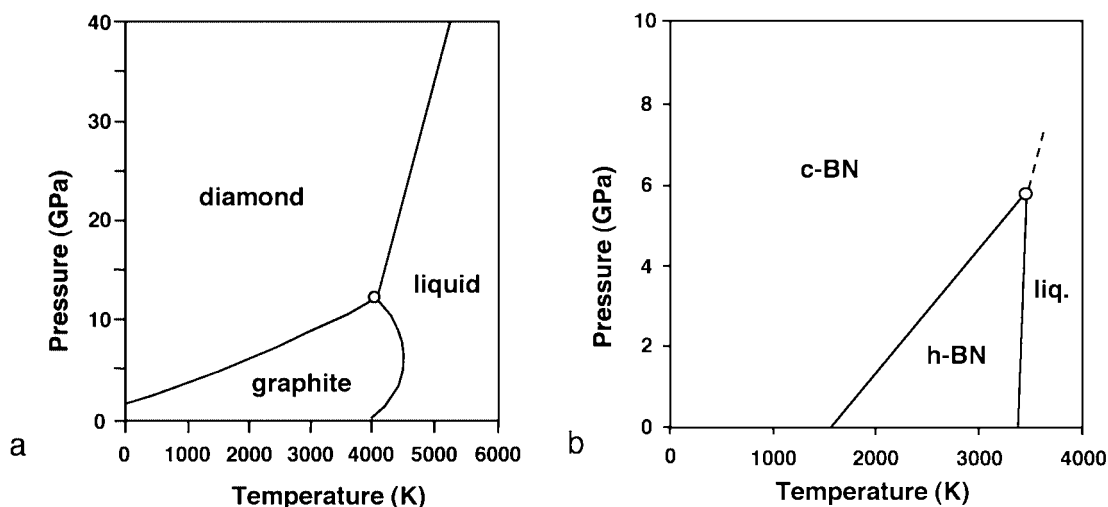


Figure 10-9. P – T phase diagrams for (a) carbon and (b) BN. Note that the two topologies are identical. (b) is different from (a) in that it is shifted to lower pressures. This causes the phase boundary between h-BN (graphite-type) and c-BN (diamond-equivalent) to cross the zero pressure line at ~ 1600 K, thus making c-BN the stable phase at ambient conditions. After Bundy (1989) and Solozhenko (1994, 1999).

further phase transformations as long as we remain above the graphite–diamond phase boundary. This implies that lonsdaleite, which crystallizes in the wurtzite structure, is metastable with respect to diamond. The stability of diamond under high pressure seems to be much higher than that of silicon or germanium (see Sec. 10.5.1.1). No phase changes have been observed up to pressures of 550 GPa (Xu et al., 1986). This is attributed to the fact that C, unlike Si and Ge, does not have any core p-electrons, which brings the valence electrons in C much closer to the nucleus and thus stabilizes the cubic high symmetry structure (Bundy, 1989).

In the B–C–N phase field, there are four important ternary phases known, namely BCN, BC₂N, BC₃N and BC₄N. In addition to these, there are numerous binary phases such as BN and several B-rich B–N solid solutions, B₄C and BC₃ along the B–C line and C₃N₄ as the only binary carbon–nitride. Many of these phases can be synthesized as graphite-like compounds through sputter deposition or chemical vapor deposition (CVD), yielding thin films suitable for abrasive protection. Because in this chapter we are mainly interested in high-pressure phase transformations, we will focus on structural transformations relevant to the synthesis of bulk samples.

10.5.2.2 B–N

The III-V analogue to carbon is BN. Owing to its industrial importance as a diamond substitute in drilling and polishing applications, a large amount of research has been done in this field. The topology of the phase diagram is very similar to that of carbon (Fig. 10-9). However, it is shifted towards lower temperatures so that the phase boundary between the graphite-type hexagonal phase (h-BN) and a zincblende-

type cubic phase (c-BN) crosses the 1 bar line at a temperature of about 1600 K. This makes the zincblende-type c-BN the stable phase at ambient conditions (Solozenko, 1994; Solozenko et al., 1999). However, the growth of c-BN at atmospheric pressure is only possible in the presence of supercritical fluids and seed crystals. Spontaneous crystallization of c-BN has not been observed at pressures below 2 GPa (Solozenko, 1994). This fact has, of course, important technological consequences, as c-BN is the phase with the desired abrasive properties. The graphite-like phase (h-BN) is the stable phase at low pressure and high temperatures. The graphite-like phase can occur as hexagonal (2H) or rhombohedral (3R) polytype (e.g., Britun et al., 1999). Like most binary and ternary phases in the B–C–N system, h-BN has a turbostratic structure. This structure can be described as a graphite structure with good in-plane ordering but random orientation of the individual planes around the layer normal. This leads to the absence of *hkl* or *h0l* reflections, while *hk0* and *00l* reflections exhibit very irregular peak shapes (e.g., Andreev and Lundström, 1994). The phase boundary between c-BN and h-BN has a positive slope and meets the liquidus in a triple point at 3480 K and 5.9 GPa (Solozenko et al., 1999). Similar to the carbon phase diagram, the BN also forms a metastable phase (w-BN) at high pressure, which crystallizes in the wurtzite structure. The transitions between the various polytypes are either martensitic or diffusional, depending on the synthesis and formation conditions (shock compression vs catalytic synthesis) as well as on the ordering degree of the precursor material (Kurdyumov, 1995). A curious but potentially very interesting BN phase has recently been synthesized by laser heating a c-BN sample up to 5000 K at pressures between 5–15 GPa

(Golberg et al., 1996). This procedure yielded multi-walled nanotubes, which did not contain any other inclusions as they are frequently obtained when producing nanotubes via a plasma-arc discharge method.

10.5.2.3 C–N

A lot of effort has been put into the synthesis of sp^3 -bonded carbon nitrides, again in the hope of creating super-hard materials. This hope has been supported by theoretical calculations predicting the stability of C_3N_4 phases whose bulk moduli were calculated to exceed the value of diamond (Sung and Sung, 1996; Liu and Cohen, 1989, 1990). These theoretical studies predict five different phases of C_3N_4 . Besides a graphite-like phase, an α - and a β -phase are expected. These would be structurally identical to the corresponding phases of Si_3N_4 . Their expected bulk moduli are 425 GPa and 451 GPa, respectively. A more recent theoretical study (Teter and Hemley, 1996) predicts two more high-pressure phases. A cubic phase should be structurally identical to the high-pressure Zn_2SiO_4 polymorph. The bulk modulus for this phase is calculated to be higher than that of diamond (496 GPa vs. 444 GPa). Nguyen et al. (1998) managed to synthesize a bulk C_3N_4 phase by laser heating a C_{60} film with liquid nitrogen in a diamond anvil cell at 2000 K and 18 GPa. The diffraction pattern of the retrieved phase is very close to the one predicted theoretically for the cubic structure by Teter and Hemley (1996). The measured compressibility, however, is much higher than predicted (249 GPa vs. 449 GPa). The phase was found to decompose upon pressure release below 14 GPa. Successful attempts at bulk synthesis of C_3N_4 have also been reported by He et al. (1998) and Dymont et al. (1999). In both cases a precursor containing C, N and H

was pressurized to about 7 GPa and temperatures between 600 and 1200 K. This procedure yielded faceted crystals of α - and β - C_3N_4 .

10.5.2.4 B–C

The crystal chemistry along the B–C axis has been well studied (Thévenot, 1990). The most important binary is B_4C . Its structure is a stuffed derivative of α -boron, where in B_4C the individual boron icosahedral chains are linked through a three-atom C–B–C chain. So far no high-pressure phases of B_4C are known. However, owing to the electron-deficient nature of the intra-icosahedral bonding, boron-rich solids such as B_4C are expected to be inverted-molecular solids, where the compressibility of the molecules is higher than that of the intermolecular links. This is unusual because in most cases the compressibility of a molecular crystal is controlled by the stiffness of the weak van der Waals bonding between the molecules, while the bonds within the molecules are rather rigid. The inverted compressibility was experimentally confirmed for B_4C (Nelmes et al., 1995). Such an inverted behavior is remarkable for a compound like B_4C in view of the very strong and covalent B bonds within the B_{12} molecules.

10.5.2.5 B–C–N

Ternary phases in the B–C–N system are rather difficult to grow, mainly because of the high stability of BN–C mixtures relative to true B–C–N phases. Nevertheless, several ternary phases have been synthesized (see Solozhenko (1997) for a review). Graphite-type phases with ternary compositions are mostly grown using CVD methods or nitration of B- and N-containing compounds in the condensed state. Investi-

gations of possible diamond-type structures in this system are difficult owing to the difficulty of distinguishing true ternary phases from a mechanical mixture of C and BN with diffraction methods. In order to create diamond-type ternary phases (exhibiting zincblende- or wurtzite-related structures), the diffusion during the high-pressure/high-temperature experiment has to be suppressed, otherwise the ternary phases decompose into c-BN and diamond. This can be understood on the basis of the significant positive deviation of $C_x(\text{BN})_{1-x}$ solid solutions from Vegard's law. It implies that ternary high-pressure phases will have a higher volume than a linear combination of the components involved and will thus, provided sufficient atomic diffusion occurs, be unstable at high pressure. The most efficient way of preventing diffusion and thus segregation is shock compression (e.g., Komatsu et al., 1996). Another possibility of transforming graphite-type C-B-N material into a diamond-type phase is by laser heating a sample in a diamond anvil cell (Knittle et al., 1995). The samples were grown at pressures between 30 and 50 GPa combined with temperatures between 2000 and 2500 K. This approach appears so far to be the only published example where a ternary phase could actually be grown from both ternary graphitic precursors and mechanical mixtures. It should be mentioned, however, that the analytical data of Knittel et al., (1995) could equally well be interpreted as resulting from mechanical mixtures of dispersed diamond and c-BN (Solozhenko, 1997).

10.5.3 H₂O

Water not only occurs as the life-sustaining liquid phase, but also has an exceptionally rich phase diagram (Fig. 10-10) in its solid state. All solid phases of water are

commonly called ice. Presently, there are 12 crystalline and two amorphous phases of ice accepted. Crystalline ice phases are labeled with Roman numerals from I to XII in the approximate sequence of their discovery. The high structural variability can be explained by a subtle interplay between enthalpic and entropic contributions. The flexible O-H...O hydrogen bond with a strong O-H bond and at least one weak O...H hydrogen bond around each hydrogen enables the formation of a large number of energetically similar topologies. In addition, the total energy of the system can be significantly altered through the entropy of a disordered distribution of the O-H...O asymmetry in the framework.

The flexibility of the hydrogen bonds is intimately linked to their asymmetric geometry. With simple bond valence and ionic radius arguments, it is possible to show that this asymmetry is a direct consequence of the fact that the closest unstrained O-O distance is longer than the sum of two relaxed O-H bonds. This would lead to an underbonding of the hydrogen atom. As outlined above (see Sec. 10.2.2), such an underbonding can be compensated for by an asymmetric coordination geometry. This model implies straight O-H...H geometries for strong hydrogen bonds, but bent (because under-constrained) O-H...O configurations for weaker hydrogen bonds (Brown, 1976, 1995). Therefore the model correctly predicts the counter-intuitive fact that high-pressure phases of ice will tend to have weaker hydrogen bonds. This is due to the requirement for a denser packing of water molecules in high-pressure phases (see Sec. 10.2.1), leading to bent and thus weakened hydrogen bonds.

The hydrogen bond is not only critical for H₂O with respect to its structural aspects, but also with respect to its electronic properties. The disordering of the hydro-

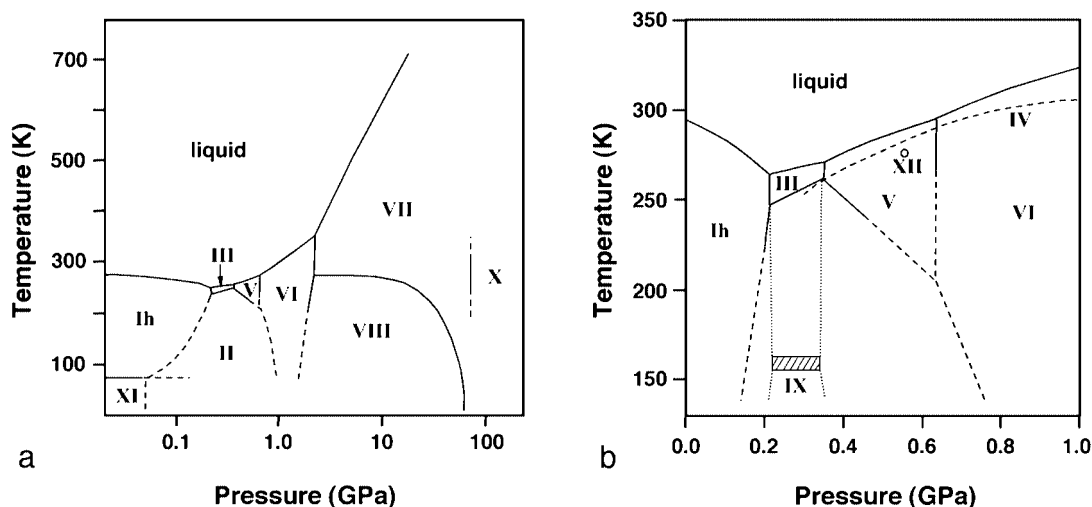


Figure 10-10. (a) P - T phase diagram for H_2O , (b) enlargement of the central section of (a). Note that in (a) the pressure scale is logarithmic. (After Petrenko and Whitworth, 1999.)

gen bonds strongly increases the polarizability and electrical conductivity of H_2O . There exists a vast literature on the structure, physics and chemistry of H_2O , including a very comprehensive and thorough review by Petrenko and Whitworth (1999).

A common feature of all ice phases is that the H_2O molecules form a three-dimensional tetrahedral framework. This, combined with the versatility of the hydrogen bonds, makes H_2O an interesting study case for understanding the possible mechanisms of a framework to reduce its volume. At low pressures, H_2O adopts rather open frameworks (see Sec. 10.5.3.1). At pressures above ca. 0.6 GPa, however, it is able to reduce the molar volume significantly by forming two interpenetrating, but unconnected frameworks (see Sec. 10.5.3.5). In the intermediate range between 0.2 and 0.6 GPa, it adjusts to the imposed volume constraint mainly by straining the individual bonds (Sec. 10.5.3.3 and Sec. 10.5.3.4), which can lead to a weakening of O...H hydrogen bonds with increasing pressure, as mentioned above. Under certain condi-

tions, lack of kinetics favors a chaotic framework collapse leading to an amorphous phase (Sec. 10.5.3.6).

10.5.3.1 Ice Ih, XI and Ic

The ice phase occurring at ambient pressure (ice Ih) has a hexagonal structure, where the oxygen atoms occupy the positions of the monatomic version of the wurtzite structure (see Sec. 10.5.1.1). The hydrogen atoms are placed asymmetrically between neighboring oxygen atoms. Each oxygen thus forms two O-H bonds and two O...H hydrogen bonds. The distribution of the O-H bonds and O...H hydrogen bonds is disordered, resulting in space group $P6_3/mmc$ (hcp space group). The local distribution of the H atoms, however, has to follow the two ice rules (Bernal and Fowler, 1933), which are valid for all other ice phases; (1) there are always two O-H bonds for each oxygen, (2) there is only one H per O-O contact. These rules follow directly out of bond-valence rules and cation-cation repulsion considerations.

The cubic analog to Ih exists as a meta-stable polymorph designated Ic (ccp space group Fd3m). It is structurally characterized by a diamond-type sub-lattice of the oxygen atoms. Ice Ic can be formed by recovering any of the high-pressure phases in liquid nitrogen and subsequently heating it to 120–170 K. There is no way of producing Ic directly from Ih, heating Ic to about 200 K on the other hand transforms it to Ih. The energetic difference between Ic and Ih is only between 13 and 50 Jmol⁻¹ (Handa et al., 1988). Hexagonal ice can in principle be transformed into an ordered polymorph around 72 K (ice XI). However, the process of collectively rearranging O-H...H bonds can only take place if there are a sufficient number of protonic point defects present, which enable the propagation of the bond reorientations. Such defects can easily be incorporated through doping with alkali hydroxides. The phase transition Ih → XI was first observed through dielectric permittivity (Kawada, 1972). The exact structure is now agreed to have the orthorhombic space group Cmc2₁, with all OH-dipoles parallel c oriented in a ferroelectric way (Line and Whitworth, 1996; Jackson et al. 1997).

A special and well known common property of all these low-pressure phases of H₂O is that their density (0.92–0.934 g cm⁻³) is somewhat lower than that of liquid water.

10.5.3.2 Ice II

The first true high-pressure phase was discovered in 1900 by Tammann. It can be formed through compression of Ih at temperatures between –35° and –70°C. Its structure is quite peculiar in two ways. First, it has a perfectly ordered arrangement of the hydrogen bond pattern. Secondly, despite the high pressure of its

stability-field, its structural topology is characterized by puckered 6-membered rings of H₂O, which are stacked along the hexagonal c-axis to form open channels, similar to the ones formed by Ih. The space group of ice II is R $\bar{3}$. The higher density of ice II relative to ice Ih is mainly achieved by the puckering of the 6-membered rings and the denser stacking of the rings by means of bending and thus weakening of the O–H...H bonds. Furthermore, the channels of ice II can be occupied by He atoms, creating a He hydrate similar to clathrate hydrates (Londono et al., 1993). Incorporation of He actually extends the stability field of ice II up to the liquidus. Heating ice II in the absence of He, however, transforms ice II to ice III.

10.5.3.3 Ice III and Ice IX

Ice III is structurally characterized by puckered 5-membered rings that are mutually linked in three dimensions to give a complicated framework of tetragonal symmetry, space group P4₁2₁2 (Kamb and Prakash, 1968). The hydrogen distribution within the stability field of ice III is highly disordered (Whalley et al., 1968). However, it can be ordered by cooling at constant pressure. If the temperature is reduced into the stability field of ice II, ice III remains metastable. Between –65 and –108°C, the ordering increases gradually, inducing the phase transformation to ice IX (the ordered variety of ice III) as revealed by measurements of electrical permittivity. Neutron diffraction, however, reveals a significant amount of residual ordering also in ice III (Londono et al., 1993, Kuhs et al., 1998). Ice III is the high-pressure polymorph of H₂O with the lowest density (1.165 g cm⁻³). However, unlike Ice Ih, its density at the liquidus is higher than the corresponding density of the liquid phase,

resulting in a positive slope of the liquidus in P - T space.

10.5.3.4 Ice V, Ice IV and Ice XII

Further compression of ice III or ice II leads to ice V. The structure of ice V is a complex framework built by 4- and 5-membered oxygen rings (Kamb et al., 1967). Each oxygen atom is tetrahedrally surrounded by four neighboring oxygen atoms. The symmetry is monoclinic with space group $A2/a$. The hydrogen atoms are distributed in a disordered arrangement between the oxygen links. In fact, the two-fold axis of this space group does not allow for any proton ordering. Proton ordering, if it occurs, would thus imply a noncentrosymmetric space group Aa .

A special feature of ice V is that in its stability field, at least two ice phases without their own stability fields have been described. Ice IV has been observed within the stability field of ice II, ice V and ice VI. Even a liquidus for ice IV, which lies within the field of these solid phases has been established (Chou and Haselton, 1998). The structure of ice IV is quite remarkable. Only slightly puckered 6-membered rings are linked together within a plane by strongly elongated 6-membered rings forming a puckered plane with trigonal symmetry. The planes are stacked in an ABABAB sequence where A- and B-planes are shifted relative to each other by the value of the hexagonal a -axis. Like-type planes (A-A and B-B, respectively) are linked together by hydrogen bonds through the regular 6-membered rings of the neighboring planes. This results in a single, self-penetrating framework with a higher density (1.436 g cm^{-3}) than ice V (1.402 g cm^{-3}).

Only recently, another new phase of ice has been described by Lobban et al. (1998)

within the stability field of ice V. The new phase can reproducibly be grown at 0.55 GPa and 260 K with slow cooling rates. Its structure consists of two symmetrically independent sets of oxygen atoms. The first one forms zig-zag chains parallel c . Neighboring chains are rotated by 90° . These chains are connected by the second type of oxygen atoms thus forming a tetrahedral framework, whose density (1.437 g cm^{-3}) is very close to that of ice IV. While in ice IV, the increase in density relative to ice V is achieved by self-penetration, ice XII compresses by additional bending. In both metastable phases, the hydrogen positions are disordered between the O-O links.

10.5.3.5 Ice VI, Ice VII, Ice VIII, Ice X

Compressing ice V beyond 0.6 GPa induces a phase transformation to ice VI. This is the first example of an ice phase, where the structure is characterized by two interpenetrating frameworks which are not linked together ('self-clathrates', Kamb, (1965)). In ice VI, the topologies of two frameworks are identical. They are symmetrically related by an inversion and shifted relative to each other by $a/2 + b/2 + c/2$. The individual frameworks can be described as chains of tetrahedra, extended along c . All tetrahedra of one framework have the same orientation. The chains of each framework are connected parallel a and b with each other, but unconnected with the chains of the other sublattice.

Ice VII has, together with ice VIII and ice X, the densest H_2O topology. Its packing is as efficient as it is simple and can be described by two interpenetrating frameworks of the cubic ice Ic. The hydrogen positions in ice VII are completely disordered (Walrafen et al., 1982; Kuhs et al., 1984). The interesting aspect of this structure is

that the oxygen atoms form a body centered cubic lattice. This implies that each oxygen atom has eight nearest neighbors. However, it forms hydrogen bonds only to four of them in tetrahedral orientation and in this way forms two interpenetrating but independent frameworks. This also implies that the O–O distances to the hydrogen-bonded oxygen neighbors are equivalent to the non-bonded O–O contacts.

The disorder–order transition from ice VII to ice VIII was first observed through dielectric measurements (Whalley et al., 1966). Although the structure crystallizes in the tetragonal space group $I4_1/amd$, the positions of the oxygen atoms deviate only little from a body centered cubic lattice, confirming the order–disorder nature of the phase transformation of ice VII to ice VIII (Kuhs et al., 1984). The ordering pattern of the O–H bonds is ferroelectric within one sub-lattice, but antiferroelectric between the two frameworks. In ice VIII, the O–D distances remain almost constant with increasing pressure (Nelmes et al., 1993b), although the O–O distances decrease significantly. This leads to a decrease in the distance between the two potential wells of the hydrogen position. Therefore, the entropy difference between the ordered and disordered state decreases gradually with increasing pressure, leading to a progressively steeper phase boundary VII–VIII, which eventually ends as a vertical slope at 62 GPa (Pruzan et al., 1993). At this point, the energy barrier between the two proton positions is sufficiently small to be crossed with the thermal energy of the protons, thus leading to a dynamic disorder. This phase thus has the average position of the hydrogen atoms in the middle between the two oxygen atoms. An identical structural configuration can be expected for a structure with a single potential minimum as is predicted for ice X at pressures exceeding 62 GPa.

In ice X, the O–O contacts are squeezed sufficiently close together that the hydrogen can sit unstrained in the center of the O–O-link. Such a symmetric O–H–O arrangement thus has no potential for disorder in the first place. Such a phase is different from a double-well phase with a dynamically disordered proton, which from a physical point of view should still be called ice VII. Ice X has been predicted by Kamb and Davis (1964). Although experimental evidence for a symmetric phase was observed from IR spectroscopic studies by the appearance of a new mode characteristic of a symmetric O–H–O configuration (Goncharov et al., 1996; Aoki et al., 1996, Pruzan et al., 1997), it should be pointed out that up to now there is no direct experimental evidence for a truly proton-ordered single-well phase of ice X. This lack of experimental evidence is due to the difficulty of performing experiments that are able to localize hydrogen or deuterium positions in the pressure range of 60 GPa and more.

10.5.3.6 Amorphous ice at high pressure

As mentioned above, there are two amorphous high-pressure phases of H_2O in the solid state. A first phase is formed by compressing ice Ih at 77 K (where slow kinetics inhibit the recrystallization of ice II) to the extrapolated liquidus of Ih. Its density in the quenched state is 1.17 g cm^{-3} . Upon heating, this high-density amorphous (HDA) phase transforms to a second amorphous phase with lower density (0.94 g cm^{-3}) at 125 K (LDA). LDA, in turn can be transformed into HDA at 77 K by compression to 0.6 GPa.

The research on the high-pressure phases of ice is far from completed. The understanding of the various amorphous phases and the theoretical and experimental quest

for ice X and beyond are just the most prominent examples of a lively topic with relevance to physical chemistry and materials science.

10.6 Acknowledgements

The author wishes to thank Vladimir Solozhenko, Richard Nelmes, Mohammed Mezouar, Guillaume Fiquet, and Denis Andrault for valuable discussions. This work received support from the 'Schweizerische Nationalfonds' (Swiss National Science Foundation) through grant # 21-052682.97.

10.7 References

- Abd-Elmeguid, M. M., Micklitz, H., Buschow, K. J. H. (1980), *J. Phys. IV, Colloque*, 41, C1.
- Acha, C., Loureiro, S. M., Chaillout, C., Tholence, J. L., Capponi, J. J., Marezio, M., Nunez-Regueiro, M. (1997), *Physica C* 282–287, 1167.
- Ahrens, T. J. (1980), *Science* 207, 1035.
- Ahrens, T. J. (1987), in: *Methods of Experimental Physics*, Vol. 24A: Sammis, C. G. Henyey, T. L. (Eds.). New York: Academic Press, p. 185.
- Akimoto, S. (1987), in: *AGU Geophysical Monograph*, Vol. 39, *Mineral Physics 2*: Manghanni, M. H., Syono, Y. (Eds.). Washington DC: American Geophysical Union, p. 1.
- Akitt, J. W. (1983), *NMR and Chemistry*. New York: Chapman and Hall.
- Anderson, M. S., Swenson C. A. (1984), *J. Appl. Phys.* 56, 2697.
- Andrault, D., Fiquet, G., Peyronneau, J., Itié, J. P., Richet, P., Gillet, Ph. (1996), in: *Proceedings of the 3rd NIRIM International Symposium on Advanced Materials (ISAM '96)*, National Institute for Research in Inorganic Materials, Tsukuba, Japan, p. 297.
- Andreev, Y. G., Lundström, T. (1994), *J. Appl. Crystallogr.* 27, 767.
- Angel, R. J. (2000a), in: *Comparative Crystal Chemistry, MSA Reviews in Mineralogy*, Vol. 40: Hazen, R. M. (Ed.). Washington DC: Mineralogical Society of America, Chapter 8, in press.
- Angel, R. J. (2000b), in: *Transformation Processes in Minerals, MSA Reviews in Mineralogy*, Vol. 39: Redfern, S., Carpenter, M., Salje E., Seifert F. (Eds.). Washington DC: Mineralogical Society of America, p. 38.
- Angel, R. J., Allan, D. R., Miletich, R., Finger, L. W. (1997), *J. Appl. Crystallogr.* 30, 461.
- Angel, R. J., Downs, R. T., Finger, L. W. (2000), in: *Comparative Crystal Chemistry, Reviews in Mineralogy*, Vol. 40: Hazen, R. M. (Ed.). Washington DC: Mineralogical Society of America, Chapter 5, in press.
- Aoki, K., Yamawaki, H., Sakashita, M., Fujihisa, H. (1996), *Phys. Rev. B* 54, 15673.
- Arlt, T., Kunz, M., Stolz, J., Armbruster, T., Angel, R. J. (2000), *Contrib. Mineral. Petr.* 138, 35.
- Bacon, G. E. (1975), *Neutron Diffraction*, 3rd edn. Oxford: Clarendon Press.
- Bassett, J. M., Ming, L.-C. (1972), *Phys. Earth Planet. Mater.* 6, 154.
- Bassett, W. A., Weathers, M. S. (1987), in: *AGU Geophysical Monograph*, Vol. 39, *Mineral Physics 2*, Manghanni, M. H., Syono, Y. (Eds.). Washington DC: American Geophysical Union, p. 129.
- Bassett, W. A., Shen, M. J., Bucknum, M. J., Ming Chou, I. (1993), *Rev. Sci. Instrum.* 64, 2340.
- Baublitz, M., Ruoff, A. L. (1982), *J. Appl. Phys.* 53, 6179.
- Baughman, R. H., Stafström, S., Cui, C., Dantas, S. O. (1998), *Science* 279, 1522.
- Belitsky, I. A., Fursenko, B. A., Gabuda, S. B., Kholdev, O. V., Seryotkin, Y. V. (1992), *Phys. Chem. Minerals* 18, 497.
- Benedek, G. B., Purcell, E. M. (1954), *J. Chem. Phys.* 22, 2003.
- Bernal, J. D., Fowler, R. H. (1933), *J. Chem. Phys.* 1, 515.
- Bertani, R., Mali, M., Roos, J., Brinkmann, D. (1992), *Rev. Sci. Instrum.* 63, 3303.
- Besson, J. M., Mokhtari, E. H., Gonzales, J., Weill, G. (1987), *Phys. Rev. Lett.* 59, 473.
- Besson, J. M., Hamel, G., Grima, T., Nelmes, R. J., Loveday, J. S., Hull, S., Häusermann, D. (1992), *High Pressure Res.* 8, 625.
- Binder, K. (2001), in: *Phase Transformations in Materials*: Kosterz, G. (Ed.). Weinheim: Wiley-VCH, Chap. 4.
- Boehler, R., Chopelas, A. (1991), *Geophys. Res. Lett.* 18, 1147.
- Bridgman, P. W. (1935), *Proc. Am. Acad. Arts Sci.* 70, 285.
- Bridgman, P. W. (1940), *Proc. Am. Acad. Arts Sci.* 74, 11.
- Bridgman, P. W. (1946), *Collected Experimental Papers of P. W. Bridgman*, Vol. VI, p. 164.
- Bridgman, P. W. (1952), *Proc. Am. Acad. Arts Sci.* 81, 167.
- Britun, V. F., Kurdyumov, A. V., Petrusha, I. A. (1999), *Mater. Lett.* 41, 83.
- Brown, G. E. Jr, Calas, G., Waychunas, G. A., Petiau, J. (1988), in: *Spectroscopy Methods, MSA Reviews in Mineralogy*, Vol. 18: Hawthorne F. C. (Ed.). Washington DC: Mineralogical Society of America, p. 431.
- Brown, I. D. (1976), *Acta Crystallogr. A* 32, 24.
- Brown, I. D. (1992), *Acta Crystallogr. B* 48, 553.

- Brown, I. D. (1995), *Can. J. Phys.* 73, 676.
- Bundy, F. P. (1989), *Physica A* 156, 169.
- Buontempo, U., Filippini, A., Farcia-Martinez, D., Postorino, P., Mezouar, M., Itié, J. P. (1998), *Phys. Rev. Lett.* 80, 1912.
- Carpenter, M. A., Salje, E. K. H. (1998), *Eur. J. Mineral.* 10, 693.
- Carpenter, M. A., Salje, E. K. H., Graeme-Barber, A. (1998), *Eur. J. Mineral.* 10, 621.
- Chou, J. M., Haselton, H. T. (1998), *Rev. High Pressure Sci. Technol.* 7, 1132.
- Crain, J., Ackland, G. J., Maclean, J. R., Piltz, R. O., Hatton, P. D., Pawley, G. S. (1994), *Phys. Rev. B* 50, 13043.
- Datchi, F., LeToullec, R., Loubeyre, P. (1997), *J. Appl. Phys.* 81, 3333.
- Dubrovinsky, L. S., Saxena, S. K., Lazor, P. (1997), *Geophys. Res. Lett.* 24, 1835.
- Duclos, S. J., Vohra, Y. K., Ruoff, A. L. (1987), *Phys. Rev. Lett.* 58, 775.
- Duclos, S. J., Vohra, Y. K., Ruoff, A. L. (1990), *Phys. Rev. B* 41, 12021.
- Dymont, V. P., Nekrashevich, E. M., Starchenko, I. M. (1999), *Solid State Commun.* 111, 443.
- Fiquet, G., Andrault, D., Itié J. P., Gillet, P., Richet, P. (1994), EGS XIX General Assembly, *Annales Geophysicae*, C6, Supplement I, Vol. 12, 24.
- Fiquet, G., Dewaele, A., Andrault, D., Kunz, M., LeBihan, T. (2000), *Geophys. Res. Lett.* 27, 1; 21.
- Fukunaga, O., Yamaoka, S., Akaishi, M., Kanda, H., Osawa, T., Shimomura, Nagashima, T., Yoshikawa, M. (1987), in: *AGU Geophysical Monograph*, Vol. 39, *Mineral Physics 2: Manghnanni*, M. H., Syono, Y. (Eds.). Washington DC: American Geophysical Union, p. 17.
- Geisinger, K. L., Gibbs, G. V., Navrotsky, A. (1985), *Phys. Chem. Minerals* 11, 266.
- Gillet, P., Hemley, R. J., McMillan, P. F. (1998), in: *Ultra-High Pressure Mineralogy, MSA Reviews in Mineralogy*, Vol. 37: Hemley, R. J. (Ed.). Washington DC: Mineralogical Society of America, p. 525.
- Glazer, A. M. (1972), *Acta Crystallogr. B* 28, 2284.
- Golberg, D., Bando, Y., Eremets, M., Takemura, K., Kurashime, K., Yusa, H. (1996), *Appl. Phys. Lett.* 69, 2045.
- Goncharenko, I. N., Mirebeau, I. (1998), *Rev. High Pressure Sci. Technol.* 7, 475.
- Goncharov, A. F., Struzhkin, V. V., Somayazulu, M. S., Hemley, R. J., Mao, H. K. (1996), *Science* 273, 218.
- Goñi, A. R., Syassen, K. (1998), *Semiconductors and Semimetals* 54, New York: Academic Press, p. 247.
- Haines, J., Leger, J. M., Chateau, C., Bini, R., Ulivi, L. (1998), *Phys. Rev. B* 58, R2909.
- Han, C. Y., Lin, W., Wu, Y. S., Yin, B., Tang, D. S. (1999), *Physica C* 282–287, 1189.
- Handa, Y. P., Klug, D. D., Whalley, E. (1988), *Can. J. Chem.* 66, 919.
- Hanfland, M., Schwarz, U., Syassen, K., Takemura, K. (1999), *Phys. Rev. Lett.* 82, 1197.
- Hazen, R. M. (1983), *Science* 219, 1065.
- Hazen, R. M., Finger, L. W. (1978), Geological Society of America, Annual Meeting 1978, Toronto; Abstracts, 10, 418.
- Hazen, R. M., Finger, L. W. (1981), *Rev. Sci. Instrum.* 52, 75.
- Hazen, R. M., Finger L. W. (1982), *Comparative Crystal Chemistry*. New York: John Wiley & Sons.
- Hazen, R. M., Navrotsky, A. (1996), *Am. Mineral.* 81, 1021.
- Hazen, R. M., Yang, H. (1999), *Am. Mineral.* 84, 1956.
- He, D. W., Zhang, F. X., Zhang, X. Y., Qin, Z. C., Zhang, M., Liu, R. P., Xu, Y. F., Wang, W. K. (1998), *J. Mater. Res.* 13(12), 3458.
- Hemley, R. J., Prewitt, C. T., Kingma, K. J. (1994) in: *Silica, MSA Reviews in Mineralogy*, Vol. 29: Heany, P. J., Prewitt, C. T. Gibbs, G. V. (Eds.). Washington DC: Mineralogical Society of America, p. 41.
- Holzappel, W. B. (1997), in: *High-Pressure Techniques in Chemistry and Physics: Holzappel, W. B., Isaacs, N. S. (Eds.)*. Oxford: Oxford University Press, p. 64.
- Ivanov, A. N., Nikolaev, N. A., Pashkin, N. V., Savchenko, B. N., Smirnov, L. S., Taran, Y. V. (1991), Institute of Theoretical and Experimental Physics. Preprint No. 91 - 76. Dubna.
- Jackson, S. M., Nield, V. M., Whitworth, R. W., Oguro, M., Wilson, C. C. (1997), *J. Phys. Chem. B* 101, 6142.
- Jamieson, J. (1957), *J. Geol.* 65, 334.
- Jamieson, J. C., Lawson, A. W., Nachtrieb N. D. (1959), *Rev. Sci. Instrum.* 30, 1016.
- Kamb, B., Davis, B. L. (1964), *Proc. Natl Acad. Sci. USA* 52, 1433.
- Kamb, B. (1965), *Science* 150, 205.
- Kamb, B., Prakash, A., Knobler, C. (1967), *Acta Crystallogr.* 22, 706.
- Kamb, B., Prakash, A. (1968), *Acta Crystallogr. B* 24, 1317.
- Katayama, Y., Mezouar, M., Itié, J. P., Besson, J. M., Syfosse, G., LeFevre, P., DiCiccio, A. (1997), *J. Phys. IV, Colloque* 7, C2.
- Kawada, S. (1972), *J. Phys. Soc. Jpn.* 32, 1442.
- Kirkpatrick, R. J. (1988), in: *Spectroscopy Methods, MSA Reviews in Mineralogy*, Vol. 18: Hawthorne F. C. (Ed.). Washington DC: Mineralogical Society of America, p. 341.
- Klotz, S., Besson, J. M., Hamel, G., Nelves, R. J., Loveday, J. S., Marshall, W. G. (1996), *High Pressure Res.* 14, 294.
- Klotz, S., Besson, J. M., Braden, M., Karch, K., Pavone, P., Strauch, D., Marshall, W. G. (1997), *Phys. Rev. Lett.* 79, 1313.
- Kluthe, S., Markendorf, R., Mali, M., Roos, J., Brinkmann, D. (1996), *Phys. Rev. B* 53, 11369.

- Knittle, E., Kaner, R. B., Jeanloz, R., Cohen, M. L. (1995), *Phys. Rev. B* 51, 12149.
- Komatsu, T., Nomura, M., Kakudate, Y., Fujiwara, S. (1996), *J. Mater. Chem.* 6, 1799.
- Krisch, M., Mermet, A., San Miguel, A., Sette, F., Masciovecchio, C., Ruocco, G., Verbeni, R. (1997), *Phys. Rev. B* 56, 8691.
- Kuhs, W. F., Finney, J. L., Vettier, C., Bliss, D. V. (1984), *J. Chem. Phys.* 81, 3612.
- Kuhs, W. F., Lobban, C., Finney, J. L. (1998), *Rev. High Pressure Sci. Technol.* 7, 1141.
- Kunz, M., Leinenweber, K., Parise, J. B., Wu, T. C., Bassett, W. A., Brister, K., Weidner, D. J., Vaughan, M. T., Wang, Y. (1996), *High Pressure Res.* 14, 311.
- Kurdyumov, A. V. (1995), *Powder Metall. Metal Ceram.* 34, 409.
- Kurdyumov, A. V., Solozhenko, V. L. (1999), *Sverkh-tverdye Materialy (J. Superhard Mater.)* 21, 3.
- Lawson, A. W., Tang, T. Y. (1950), *Rev. Sci. Instrum.* 21, 815.
- Leinenweber, K. (1993), National Synchrotron Light Source, Annual Report.
- Levien, L., Prewitt, C. T., Weidner, D. J. (1980), *Am. Mineral.* 65, 920.
- Levien, L., Prewitt, C. T. (1981), *Am. Mineral.* 66, 324.
- Li, B., Ganglin, C., Gwanmesia, G. D., Liebermann, R. C. (1998), in: *Properties of Earth and Planetary Materials at High Pressure and Temperature*. AGU Geophysical Monograph, Vol. 101: Manghnani, M. H., Yagi, T. (Eds.). Washington DC: American Geophysical Union, p. 41.
- Liebermann, R. C., Wang, Y. (1992), in: *High Pressure Research: Application to Earth and Planetary Sciences*. AGU Geophysical Monograph, Vol. 67: Syono, Y., Manghnani, M. H. (Eds.). Washington DC: American Geophysical Union, p. 19.
- Line, C. M. B., Whitworth, R. W. (1996), *J. Chem. Phys.* 104, 10008.
- Liu, A. Y., Cohen, M. L. (1989), *Science* 245, 841.
- Liu, A. Y., Cohen, M. L. (1990), *Phys. Rev.* 41, 10727.
- Lobban, C., Finney, J. L., Kuhs, W. F. (1998), *Nature* 391, 268.
- Londono, J. D., Kuhs, W. F., Finney, J. L. (1993), *J. Chem. Phys.* 98, 4878.
- Lubbers, R., Wortmann, G., Grünsteudel, H. F. (1999), *Hyperfine Interact.* 123, 529.
- Mao, H. K., Bell, P. M. (1975) Carnegie Institution Washington Year Book, 74, p. 402.
- Mao, H. K., Bell, P. M., Shaner, J. W., Steinberg, D. J. (1978), *J. Appl. Phys.* 49(6), 3276.
- McCammon, C. (2000), in: *Transformation Processes in Minerals*, Vol. 40: Redfern, S., Carpenter, M., Salje E., Seifert F. (Eds.). Washington DC: Mineralogical Society of America, p. 241.
- McCammon, C., Peyronneau, J., Poirier, J. P. (1998), *Geophys. Res. Lett.* 25, 1589.
- McMahon, M. I., Nelmes, R. J. (1993), *Phys. Rev. B* 47, 8337.
- McMahon, M. I., Nelmes, R. J. (1997), *Phys. Rev. Lett.* 78, 3697.
- McMahon, M. I., Nelmes, R. J., Allan, D. R., Belmonte, S. A., Bovornratanaraks, T. (1998), *Phys. Rev. Lett.* 80, 5564.
- Mermelstein, N. H. (1999), *Food Technol.* 53, 86.
- Merrill, L., Bassett, W. A. (1974), *Rev. Sci. Instrum.* 45, 290.
- Mezouar, M., Besson, J. M., Syfosse, G., Itié, J. P., Häusermann, D., Hanfland, M. (1996), *Phys. Status Solidi B* 198, 403.
- Mezouar, M., LeBihan, T., Libotte, H., LeGodec, Y., Häusermann, D. (1999a), *J. Synchrotron Rad.* 6, 1115.
- Mezouar, M., Libotte, H., Députier, S., LeBihan, T., Häusermann, D. (1999b), *Phys. Status Solidi B* 211, 395.
- Miletich, R., Allen, D. R., Kuhs, W. F. (2000), in: *Comparative Crystal Chemistry, MSA Reviews in Mineralogy*, Vol. 39: Hazen, R. M. (Ed.). Washington DC: Mineralogical Society of America, Chap. 2, in press.
- Miller, P. H., Taylor, J. H. (1949), *Phys. Rev.* 76, 179.
- Minomura, S., Drickamer, H. G. (1962), *J. Phys. Chem. Solids* 23, 451.
- Mishima, O. H., Calvert, L. D., Whalley, E. (1984), *Nature* 310, 393.
- Nasu, S. (1996), *High Pressure Res.* 14, 405.
- Nelmes, R. J., McMahon, M. I., Hatton, P. D., Piltz, R. O., Crain, J. (1993a), *Phys. Rev. B* 47, 35; *B* 48, 9949 (Corrigendum).
- Nelmes, R. J., Loveday, J. S., Wilson, R. M., Besson, J. M., Pruzan, Ph., Klotz, S., Hamel, G., Hull, S. (1993b), *Phys. Rev. Lett.* 71, 1192.
- Nelmes, R. J., Loveday, J. S., Wilson, R. M., Marshall, W. G., Besson, J. M., Klotz, S., Hamel, G., Aselage, T. L., Hull, S. (1995), *Phys. Rev. Lett.* 74, 2268.
- Nelmes, R. J., Liu, H., Belmonte, S. A., Loveday, J. S., McMahon, M. I., Allan, D. R., Häusermann, D., Hanfland, M. (1996), *Phys. Rev. B* 53, R2907.
- Nelmes, R. J., McMahon, M. I. (1998), *Semiconductors and Semimetals* 54. New York: Academic Press, p. 145.
- Nguyen, J. H., Caldwell, W. A., Benedetti, L. R., Kruger, M. B., Jeanloz, R. (1998), *Materials Research Society Symposium Proceedings*, Vol. 499, p. 303.
- Ochiai, A., Suzuki, T., Kasuya, T. (1985), *J. Magn. Magn. Mater.* 52, 13.
- Ohwada, K., Nakao, N., Takesu, N., Isobe, M., Ueda, Y., Fujii, Y. (1999), *IUCr XVII Glasgow '99. Congress and General Assembly. Abstract Book*, P09.OC.002, 114.
- Ondrey, G., Kamiya, T. (2000), *Chem. Eng.* 107, 26.
- Owen, E. A., Liu Y. H. (1947), *Philos. Mag.* 38, 354.

- Parise, J. B., Weidner, D. J., Chen, J., Liebermann, R. C., Chen G. (1998), *Annu. Rev. Mat. Sci.* 28, 349.
- Pasternak, M. P., Taylor, R. D. (1990), *Hyperfine Interact.* 62, 89.
- Pasternak, M. P., Taylor, R. D. (1996), in: *Mössbauer Spectroscopy applied to Magnetism and Materials Science*, Vol. 2: Long, G. J., Grandjean F. (Eds.). New York: Plenum Press, p. 167.
- Pasternak, M. P., Farrell, J. N., Taylor, R. D. (1986), *Hyperfine Interact.* 28, 837.
- Paul, W. (1959), *J. Phys. Chem. Solids* 8, 196.
- Pedersen, K. (1997), *FEMS Microbiol. Rev.* 20, 399.
- Pelton, A. D. (2001), in: *Phase Transformations in Materials*: Kostorz, G. (Ed.). Weinheim-VCH, Chap. 1.
- Petrenko, V. F., Whitworth, R. W. (1999), *The Physics of Ice*, Oxford: Oxford University Press.
- Poirier, J. P. (1991), *Introduction to the Physics of the Earth's Interior*, Cambridge: Cambridge University Press, Chap. 4.7.
- Pruzan, Ph., Chervin, J. C., Canny, B. (1993), *J. Chem. Phys.* 99, 9842.
- Pruzan, Ph., Wolanin, E., Gauthier, M., Chervin, J. C., Canny, B., Häusermann, D., Hanfland, M. (1997), *J. Phys. Chem. B* 101, 6230.
- Rigden, S. M., Gwanmesia, G., Jackson, I., Liebermann, R. C. (1992), in: *High Pressure Research: Application to Earth and Planetary Sciences*. AGU Geophysical Monograph, Vol. 67: Manghnani, M., Syono, Y. (Eds.). Washington DC, American Geophysical Union, p. 167.
- Ross, N. L., Price G. D. (1992) (Eds.), *The Stability of Minerals*, London: Chapman & Hall, Chap. 1.
- Ruoff, A. L., Li, T. (1995), *Annu. Rev. Mater. Sci.* 25, 249.
- Schwarz, U., Takemura, K., Hanfland, M., Syassen, K. (1998), *Phys. Rev. Lett.* 81, 2711.
- Shen, A. H., Reichmann, H. J., Chen, G., Angel, R. J., Bassett, W. A., Spetzler, H. (1998), in: *Properties of Earth and Planetary Materials at High Pressure and Temperature*. AGU Geophysical Monograph, Vol. 101: Manghnani, M. H., Yagi, T. (Eds.). Washington DC, American Geophysical Union, p. 71.
- Shimomura, O., Kawamura, T., Fukamachi, T., Hosoia, S., Hunter, S., Bienestock, A. (1980), in: *High Pressure Science and Technology*, Vol. 1: Vodar, B., Marteau, P. (Eds.). Oxford: Pergamon Press, p. 534.
- Shimomura, O., Takemura, K., Fujihisa, H., Fuji, Y., Ohishi, Y., Kikegawa, T., Amemiya, Y., Matsushita, T. (1992), *Rev. Sci. Instrum.* 63, 967.
- Sinogekin, S. V., Bass, J. D. (1999), *Phys. Rev. B* 59, R14141.
- Slykhouse, T. E., Drickamer, H. G. (1958), *J. Phys. Chem. Solids* 7, 207.
- Smirnov, G. V. (1999), *Hyperfine Interact.* 123/124, 31.
- Solozhenko, V. L. (1994), *Diamond Related Mater.* 4, 1.
- Solozhenko, V. L. (1997), *Eur. J. Solid State Inorg. Chem.* 34, 797.
- Solozhenko, V. L., Turkevich, V. Z., Holzapfel, W. B. (1999), *J. Phys. Chem. B* 103, 2903.
- Solozhenko, V. L. (1999), *J. Phys. Chem. B* 103, 2903.
- Stout, G. H., Jensen, L. H. (1989), *X-ray Structure Determination*. New York, John Wiley & Sons.
- Sung, C. M., Sung, M. (1996), *Mater. Chem. Phys.* 43, 1.
- Tammann, G. (1900), *Annalen der Physik, Series 4*, 2, 1.
- Teter, D. M., Hemley, R. J. (1996), *Science* 271, 53.
- Thévenot, F. (1980), *J. Europ. Ceramic Soc.* 6, 205.
- Van Valkenburg, A. (1964), *Diamond Res.* 17.
- Velde B., Besson J. M. (1982), in: *High Pressure in Research and Industry*, 8th AIRAPT Conference Proceedings, Vol. 2, p. 704.
- Vohra, Y. K., Brister, K. E., Desgreniers, S., Ruoff, A. L., Chang, K. J., Cohen, M. L. (1986), *Phys. Rev. Lett.* 56, 1944.
- Walrafen G. E., Abebe, M., Mauer, F. A., Block, S., Piermarini, G. J., Munro, R. (1982), *J. Chem. Phys.* 77, 2166.
- Walsh, J. M., Christian, R. H. (1955), *Phys. Rev.* 97, 1544.
- Weidner, D. J., Vaughan, M. T., Ko, J., Wang, Y., Liu, X., Yeganeh-Haeri, A., Pacalo, R. E., Zhao, Y. (1992), in: *High Pressure Research: Application to Earth and Planetary Sciences*. AGU Geophysical Monograph, Vol. 67: Syono, Y., Manghnani, M. H. (Eds.). Washington DC, American Geophysical Union, p. 13.
- Weidner, D. J., Wang, Y., Vaughan, M. T. (1994a), *Geophys. Res. Lett.* 21, 753.
- Weidner, D. J., Wang, Y., Vaughan, M. T. (1994b), *Science* 266, 419.
- Weir, C. E., Lippincott, E. R., Van Valkenburg, A., Bunting, E. N. (1959), *J. Res. Natl Bur. Standards USA* 63A, 55.
- Weir, S. T., Vohra, Y. K., Vanderborgh, C. A., Ruoff, A. L. (1989), *Phys. Rev. B* 39, 1280.
- Whalley, E., Davidson, D. W., Heath, J. B. R. (1966), *J. Chem. Phys.* 45, 3976.
- Whalley, E., Heath, J. B. R., Davidson, D. W. (1968), *J. Chem. Phys.* 45, 3976.
- Wittlinger, J., Werner, S., Schulz, H. (1998), *Acta Crystallogr. B* 54, 714.
- Woelk, K., Bargon, J. (1992), *Rev. Sci. Instrum.* 63, 3307.
- Xu, J. A., Mao, H. K., Bell, P. M. (1986), *Science* 232, 1404.
- Yagi, T., Akaogi, M., Shimomura, O., Tamai, H., Akimoto, S. (1987), in: *High Pressure Research in Mineral Physics*. AGU Geophysical Monograph, Vol. 39: Manghnani, M. H., Syono, Y. (Eds.). Washington DC, American Geophysical Union, p. 141.

2 Solidification

Heiner Müller-Krumbhaar

Institut für Festkörperforschung, Forschungszentrum Jülich, Germany

Wilfried Kurz

Département des Matériaux, EPFL, Lausanne, Switzerland

Efim Brener

Institut für Festkörperforschung, Forschungszentrum Jülich, Germany

List of Symbols and Abbreviations	82
2.1 Introduction	85
2.2 Basic Concepts in First-Order Phase Transitions	86
2.2.1 Nucleation	87
2.2.2 Interface Propagation	89
2.2.3 Growth of Simple Crystal Forms	91
2.2.4 Mullins–Sekerka Instability	93
2.3 Basic Experimental Techniques	95
2.3.1 Free Growth	96
2.3.2 Directional Growth	98
2.4 Free Dendritic Growth	100
2.4.1 The Needle Crystal Solution	101
2.4.2 Side-Branching Dendrites	108
2.4.3 Experimental Results on Free Dendritic Growth	115
2.5 Directional Solidification	120
2.5.1 Thermodynamics of Two-Component Systems	121
2.5.2 Scaled Model Equations	124
2.5.3 Cellular Growth	126
2.5.4 Directional Dendritic Growth	131
2.5.5 The Selection Problem of Primary Cell Spacing	135
2.5.6 Experimental Results on Directional Dendritic Growth	139
2.5.7 Extensions	149
2.6 Eutectic Growth	152
2.6.1 Basic Concepts	152
2.6.2 Experimental Results on Eutectic Growth	158
2.6.3 Other Topics	163
2.7 Summary and Outlook	164
2.8 References	165

List of Symbols and Abbreviations

a	distance
A	area
A	amplitude
\hat{A}	differential operator
a_I, a_K	constants
b	arbitrary parameter
\hat{B}	self-adjoint differential operator
ΔC	miscibility gap
C, C'	constants
C_E	eutectic concentration
C_L, C_S, C_α , etc.	concentration
c_p	specific heat at constant pressure
d	atomistic length, capillary length
D	diffusion constant
d_0	capillary length
D_i	transport coefficients, diffusion constants
D_T	thermal diffusion coefficient
$E_1(P)$	exponential integral
erfc	error function complement
F	Helmholtz energy
f	scaling function
g	Gibbs energy density
ΔG	change in Gibbs energy
\hat{G}	Gibbs energy per surface element
$G(\{\xi_i\})$	Gibbs energy
G_T	constant temperature gradient
J	probability current
K	curvature
k	segregation coefficient, wave number
k_B	Boltzmann constant
L	natural scale
l	external length, diffusion length
\tilde{l}	thickness of layer, diffusion length
L_m	latent heat of melting
m_α, m_β	liquidus or solidus slope
N_i	particle number of species i
P	pressure, Péclet number
\mathcal{P}	principal value
$P(\{\xi_i\})$	probability of configuration
q	wave number, inverse length
Q_{\min}	minimal work
r	radius of nucleus, radial distance
$R(S)$	local radius of curvature at point S

R_0	radius of curvature
r_c	critical radius
S	position on the interface, entropy
ΔS	change in entropy
T	temperature
t	time
Δt	change in time
T_0	reference temperature
T_E	eutectic temperature
T_I	interface temperature
T_m	melting temperature
u	dimensionless temperature field or concentration field
U	energy
V	speed
V_a	maximal speed, absolute stability
V_c	critical velocity
ν_R	growth rate
w	probability of fluctuation
\mathbf{x}	space coordinates
X_i, X_j	extensive variables
Y_i, Y_j	intensive variables
Z	partition function
z	space coordinate
β	interface kinetics
β_4	4-fold anisotropy of the kinetic coefficient
γ	surface tension or surface free energy
Γ	ratio of S–L interface energy to specific melting entropy
Γ_2	Green's function integral
Δ	supercooling (negative temperature field u at infinity)
δ	local concentration gap, surface tension anisotropy
ε	relative strength of anisotropy of capillary length
$\xi(x, t)$	deviation of the interface
η	coordinate
ϑ	angle of orientation relative to the crystallographic axes
Θ	function of (x, t)
$\kappa(s)$	mobility
λ	interface spacing, wavelength
$\Lambda(\sigma, \varepsilon)$	solubility function
λ_2	wavelength of side branch
λ_f	wavelength of the fastest mode
λ_s	stability length
μ	chemical potential
ν_0	effective kinetic prefactor
ξ	variable

ξ_i	position vectors
$\Delta \xi_i$	small normal displacement
ρ	Ivantsov radius
σ	scaling function
τ	variable
Ω	atomic volume, atomic area
DLA	diffusion limited aggregation
DS	directional solidification
f	faceted
l.h.s.	left-hand side
nf	non-faceted
PVA	pivalic acid
r.h.s.	right-hand side
SCN	succinonitrate
WKB	Wenzel–Kramers–Brillouin technique for singular perturbations

2.1 Introduction

This chapter on solidification discusses the basic mechanisms of the liquid–solid phase transformation. In particular, we address the phenomena of cellular and dendritic patterns formed by the interface between liquid and solid, as the interface, or solidification front, advances into the liquid during the solidification process.

The atomistic processes of the liquid–solid transformation are still not well understood, so we will use a phenomenological level of description. The processes on very large scales, such as casting or welding, depend greatly on the experimental equipment and are discussed, for example, by Flemings (1991) and Mordike (1991).

We will therefore restrict our attention to phenomena occurring on some important intermediate length scales. There is a natural scale L of the order of micrometers (or up to millimeters) that gives a measure for the microcrystalline structures formed during the solidification process. In its simplest form this natural length is the geometric mean $L \sim \sqrt{dl}$ of a microscopic intrinsic length d defined by typical material properties and an external length l defined by the macroscopic arrangement of the experimental equipment. The intrinsic correlation lengths in liquids and solids near the freezing point are rather short, of the order of atomic size, or several Ångströms, because solidification is a phase transition of first order. By contrast, the experimental equipment gives external length scales in the range of centimeters to meters, such that we consequently arrive at the mentioned scale of micrometers.

Assuming for the moment that only two lengths are important, why should we expect L to be given by the geometric mean rather than, for example, the arithmetic

mean? An intuitive argument goes as follows: the patterns formed at the solid–liquid interface and in both adjacent phases during the solidification process result from the competition of two “forces”, one being stabilizing for homogeneous structures, the other being destabilizing. The stabilizing force here clearly must be associated with the intrinsic atomistic length d , since we have argued that it is related to the length of correlation or coherence inside the material or at the interface. In contrast, we must associate the external length l with a destabilizing force. Again this is a quite natural assumption, as the phase transformation or destabilization of the nutrient phase is induced by the experimental environment.

It is now obvious that the result of such a competition of “forces” should be expressed by the product dl of the two representative quantities rather than by the sum, since the latter would change the relative importance of the two lengths when their values become very different.

Admittedly, these arguments look a little overstressed considering the many parameters controlling the details of a solidification process. Note, however, that nothing has been said so far about the precise relation of d , l and L to any specific process, nor have we defined the proportionality factor. In principle, d and l could also enter with different exponents but fortunately things are not usually that complicated right from the start.

If we are still courageous enough to make one more step on this slightly unsafe ground, we may finally assume that the external length scale l is related (destabilizing force!) to the speed V of the solidification, which gives a length when combined with a diffusion constant D for heat or matter as $l \sim D/V$. From this we immediately obtain a relation between the speed of phase change

V and the length scale L of the resulting pattern:

$$VL^2 \approx \text{constant} \quad (2-1)$$

Surprisingly enough, we have arrived at about the most celebrated equation for processes of dendritic, directional and eutectic solidification, without even defining any of these processes! Two remarks, therefore, may be in order here. First, detailed studies of the different solidification schemes in recent years have attempted to extract the common and universal aspects of these processes. Such common features indicate a common basis of rather general nature, as outlined above. Second, we have of course ignored most of the specific aspects of each individual process. In directional solidification, for example, a band of possible wavelengths for stationary patterns are found and up to now it is not clear if and how a specific wavelength from that band is finally selected. The assumption of just two independent length scales in many cases is also a rather gross simplification of the actual situation. We will therefore leave this line of general arguments and look at some concrete models that are believed to capture at least some essentials for the fascinating patterns produced during solidification.

Some remarkable progress has been achieved in the theoretical treatment of these phenomena during the recent years. In the list of references, we have concentrated our attention on recent developments since there are some good reviews on older work (for example, Langer, 1980a; Kurz and Fisher, 1998).

An experimentalist may finally wonder why we have expressed most of the equations in a non-dimensionally scaled form rather than writing all material parameters down explicitly at each step. One reason is that the equations then appear much sim-

pler than if we attempted to carry along all prefactors. The second and more important reason is that the scaled form allows for a much simpler comparison of experiments for different sets of parameters which usually appear only in some combinations in the equations, thereby leading to cancellations and compensations.

Section 2.2 gives a quick summary of the ingredients for a theory, starting at nucleation, then deriving boundary conditions for a propagating interface between two phases, and finally discussing some general aspects of the diffusion equation with a propagating boundary. This is followed by an introduction to basic experimental techniques in Sec. 2.3. In Sec. 2.4, the case of a simple solid growing in a supercooled melt is discussed in some detail, leading to the present understanding of dendritic growth. In Sec. 2.5 the technically important process of directional solidification is presented. The evolution of cellular patterns above a critical growth rate can in principle be understood without any knowledge of dendritic growth. Actually, the parameter range for simple sinusoidal cells is very narrow so that we usually operate in the range of deep cells or even dendrites, which suggests our sequence of presentation. Finally, these concepts are extended in Sec. 2.6 to alloys with a eutectic phase diagram and the resulting complex phenomena. As this field is currently in rapid theoretical development, our discussion here necessarily is somewhat preliminary. The chapter is closed by a summary with complementary remarks.

2.2 Basic Concepts in First-Order Phase Transitions

The different possible phases of a material existing in thermodynamic equilibrium

must be discriminated by some quantity in order to formulate a theory. Such quantities are called “order parameters” and should correspond to extensive thermodynamic variables. The difference between a solid and a liquid is defined by the shear modulus, which changes discontinuously at the phase transition. This definition describes the difference in long-range orientational correlations between two distant pairs of neighboring atoms. Normally, we use instead the more restrictive concept of translational order as expressed through two point correlation functions, or Bragg peaks, in scattering experiments.

Although these different order-parameter concepts pose a number of subtle questions, particularly in two dimensions where fluctuations are very important, we will simply assume in this chapter that there is some quantity which discriminates between a solid and a liquid in a unique way. Such an order parameter may be the density, for example, which usually changes during melting, or the composition in a two-component system. We would like to stress, however, that these are just auxiliary quantities that change as a consequence of the solid–liquid transition but which are not the fundamental order parameters in the sense of symmetry arguments. For a more general discussion see the Chapter by Binder (Binder, 2001) and literature on order–disorder transitions (Brazovsky, 1975; Nelson, 1983).

First-order transitions are characterized by a discontinuous change of the order parameter. All intrinsic length scales are short, typically of the size of a few atomic diameters. We may therefore assume local thermal equilibria with locally well-defined thermodynamic quantities like temperature, etc., and smooth variations in these quantities over large distances. Interfaces in such systems will represent singu-

larities or discontinuities in some of the quantities, such as the order parameter or the associated chemical potential, but they will still leave the temperature as a continuous function of the position in space.

2.2.1 Nucleation

A particular consequence of the well-defined local equilibrium is the existence of well-defined metastable states, corresponding to a local, but not global, minimum in the free energy. But so far we have neglected thermal fluctuations. The probability of a fluctuation (or deviation from the average state) of a large closed system is

$$w \sim \exp(\Delta S) \quad (2-2)$$

where ΔS is the change in entropy of the system due to the fluctuation (see, e.g., Landau and Lifshitz, 1970). Defining Q_{\min} as the minimal work necessary to create this change in thermodynamic quantities, we obtain

$$\Delta S = Q_{\min}/T_0 \quad (2-3)$$

with T_0 being the average temperature of the system. Note that this holds even for large fluctuations, as long as the change of extensive quantities in the fluctuation region is small compared with the respective quantities in the total system.

Considering this system as a metastable liquid within which a fluctuation has formed a small solid region, and assuming, furthermore, that the liquid is only slightly metastable, we arrive at the well-known result (Landau and Lifshitz, 1970) in three dimensions for a one-component system:

$$Q_{\min} = -\frac{4\pi r^3}{3\Omega} [\mu_L(P) - \mu_S(P)] + 4\pi r^2 \gamma \quad (2-4)$$

which together with Eqs. (2-2) and (2-3) gives the probability for the reversible for-

mation of a spherical solid nucleus of radius r within a slightly supercooled liquid. Here Ω is the atomic volume, P the pressure, $\mu_L > \mu_S$ are the chemical potentials of liquid and solid in a homogeneous system, and γ is the (here isotropic) surface tension, or surface free energy.

A few remarks should be made here. When deriving Eq. (2-4), we use the concept of small deviations from equilibrium, while Eqs. (2-2) and (2-3) are more generally valid (Landau and Lifshitz, 1970). In the estimation of the range of validity of Eq. (2-4), it is apparent, however, that it should be applicable to even very large supercoolings for most liquids, since the thermal transport is either independent of, or faster than, the kinetics of nucleus formation (Ohno et al., 1990). The range of validity of Eq. (2-4) is then typically limited by the approach to the “spinodal” region, where metastable states become unstable, even when fluctuations are ignored (see the Chapter by Binder and Fratzl, 2001).

Assuming, therefore that we are still in the range of well-defined metastable states, we may write Eqs. (2-2) and (2-3) as

$$w = v_0 \exp(-\Delta G/T_0) \quad (2-5)$$

identifying the change in Gibbs energy ΔG by Eq. (2-4), with an undetermined prefactor v_0 . Here we do not discriminate between surface tension and surface free energy, despite the fact that the first is a tensorial quantity, and the latter only scalar (although it may be anisotropic, which is ignored here). A difference between surface tension and surface free energy arises when the system does not equilibrate between surface and bulk so that, for example, the number of atoms in the surface layer is conserved. Throughout this chapter, we will assume perfect local equilibration in this respect, and we may then ignore the difference.

The extremal value of Eqs. (2-4) and (2-5) with respect to the variation of r gives the critical radius

$$r_c = \frac{2\gamma}{\Delta\mu} \Omega \quad (3\text{-dim}) \quad (2-6a)$$

or

$$r_c = \frac{\gamma}{\Delta\mu} \Omega \quad (2\text{-dim}) \quad (2-6b)$$

so that for $r < r_c$, the nucleus tends to shrink, while for $r > r_c$ it tends to grow and at $r = r_c$ it is in an unstable equilibrium.

The same thermal fluctuations causing such a nucleus to appear also produce deviations from the average spherical shape. This leads to power-law corrections in the prefactor of Eq. (2-5) or logarithmic corrections in the exponent (Voronkov, 1983; Langer, 1971).

So far these considerations have dealt with static aspects only. Since the fluctuations vary locally with time, Eq. (2-5) may be interpreted as the rate at which such fluctuation occurs, and, consequently, with $r = r_c$ we obtain the rate for the formation of a critical nucleus which, after appearance, is assumed to grow until the new phase fills the whole system. This is the classical nucleation theory. A very elegant formulation was given by analytic continuation into the complex plane (Langer, 1971). Further additions include the definition of the prefactor in Eq. (2-5) and a more detailed analysis of the kinetics near $r = r_c$ (Zettlemoyer, 1969, 1976).

Considering the many uncertainties entering from additional sources such as the range of atomic potentials and the change of atomic interaction in the surface, we will ignore all these effects by absorbing them into the effective kinetic prefactor v_0 in Eq. (2-5), to be determined experimentally.

2.2.2 Interface Propagation

An interface between two regions in space of different order parameters (solid vs. liquid) will be treated in this chapter as a *jump discontinuity* and as an object of infinitesimal thickness. In this section we derive a local equation of motion for the interface, which will serve as a boundary condition in the remaining part of the chapter.

For simplicity, consider a one-dimensional interface in a two-dimensional system. Ignoring the atomic structure, assume that the interface is a smooth continuous line. Marking points at equal distances a on this line, we may then define velocities of the points in the normal direction as

$$V_i = \frac{\Delta \xi_i}{\Delta t} \quad (2-7)$$

where $\Delta \xi_i$ is the small normal displacement of point i . If we assume these points to be kept at fixed positions ξ_i for the moment, a (restricted) Gibbs energy $G(\{\xi_i\})$ may be assigned to this restricted interface. The probability of this configuration is

$$P(\{\xi_i\}) = Z^{-1} \exp(-G/T) \quad (2-8)$$

with temperature T in units of $k_B K$ and Z the partition function. Since the total probability is conserved, we obtain the continuity equation

$$\frac{\partial P}{\partial t} + \text{div}_{(i)} \mathbf{J} = 0 \quad (2-9)$$

with $\mathbf{J} = \{J_i\}$ as the probability current in i -space

$$J_i = V_i P - D_i \frac{\partial P}{\partial \xi_i} \quad (2-10)$$

and the divergence taken in the same abstract space. The first term in Eq. (2-10) is a drift, the second term the constitutive relation with transport coefficients D_i , and the derivative is taken normal to the inter-

face. We now assume local equilibrium to exist on length scales a (i.e. $i \rightarrow i \pm 1$) such that the probability current is zero

$$V_i P = D_i \frac{\partial P}{\partial \xi_i} \quad (2-11)$$

and with Eqs. (2-7) and (2-8), we immediately arrive at

$$\frac{\partial \xi_i}{\partial t} = - \frac{D_i}{T} \frac{\partial G(\{\xi_i\})}{\partial \xi_i} \quad (2-12)$$

Taking the continuum limit $a \rightarrow 0$, we obtain the final form

$$\frac{\partial \xi(S)}{\partial t} = - \kappa(S) \frac{\delta \hat{G}}{\delta \xi(S)} \quad (2-13)$$

This is the time-dependent Ginzburg–Landau equation (Burkhardt et al., 1977). Here S denotes a position on the interface, $\partial \xi(S)$ is the normal displacement, $\delta/\delta \xi(S)$ the variational derivative, and $\kappa(S)$ the “mobility”, which may depend on position and orientation. \hat{G} is the Gibbs energy per surface element.

We will now make some explicit assumptions about G in order to arrive at an explicit equation of motion. Let \hat{n}_S be the normal direction on the interface, $\gamma(\hat{n}_S)$ the interface free energy, ϑ the angle of orientation relative to the crystallographic axes, $R(S)$ the local radius of curvature at point S on the interface, and $A_{L,S}$ the areas covered by liquid or solid. The Gibbs free energy of the total solid–liquid system with interface is

$$G_{\text{tot}} = \int_S dS \gamma + \int_{\text{Liquid}} dA_L g_L(\mathbf{x}) + \int_{\text{Solid}} dA_S g_S(\mathbf{x}) \quad (2-14)$$

from which the variational derivative in Eq. (2-13) is formally obtained by

$$\delta G_{\text{tot}} = \int_S dS \left[\frac{\delta \hat{G}}{\delta \xi} \right] \delta \xi(S) \quad (2-15)$$

where $\delta\xi(S)$ is a small arbitrary displacement of the interface in the normal direction. Explicitly this is written as

$$\delta G_{\text{tot}} = \int_S \{ \gamma \delta(dS) + dS \delta\gamma \} - \int_S dS \delta\xi(S) [g_L(S) - g_S(S)] \quad (2-16)$$

with Gibbs energy densities g given here per atomic "volume" (or area) Ω . As usual, we have to extract terms $\delta\xi$ out of the terms $\delta(dS)$ and $\delta\gamma$. Assuming γ to depend only on local orientation,

$$\delta\gamma(\vartheta) = \frac{d\gamma}{d\vartheta} \delta\vartheta \quad (2-17)$$

and with (2-18)

$$\delta\vartheta = \frac{d}{dS} \delta\xi; \quad \frac{d}{dS} = \frac{d\vartheta}{dS} \frac{d}{d\vartheta}; \quad \frac{d}{dS} \vartheta = -\frac{1}{R}$$

we obtain

$$\delta\gamma(\vartheta) = -\frac{d\gamma}{d\vartheta} \frac{1}{R} \frac{d}{dS} \delta\xi \quad (2-19)$$

The other term simply gives

$$\delta(dS) = \frac{1}{R} dS \delta\xi \quad (2-20)$$

Incorporating Eqs. (2-19) and (2-20) into Eq. (2-16) and integrating Eq. (2-19) by parts, we obtain through comparison with Eq. (2-15)

$$\frac{\partial\xi}{\partial t} \equiv V_{\perp} = \kappa(\vartheta) \left\{ \Delta g(S) - \frac{1}{R} \left(\gamma + \frac{d^2\gamma}{d\vartheta^2} \right) \right\} \quad (2-21)$$

as an explicit local equation for the advancement of an interface in two dimensions with normal velocity V_{\perp} , anisotropic kinetic coefficient $\kappa(\vartheta)$, surface Gibbs energy $\gamma(\vartheta)$, and jump $\Delta g = g_L - g_S$ of Gibbs energy density at position S along the interface (Burkhardt et al., 1977). Here, the Gibbs energy density g corresponds to an

infinite solid or liquid without influences from curvature terms. For a single-component system, $\mu = g\Omega$, where μ is the chemical potential of the respective phase. The generalization to three dimensions adds another curvature term into Eq. (2-21), which then corresponds to two curvatures and angles in the two principal directions (for isotropic γ , the curvature $1/R$ is simply changed to $2/R$).

Two useful observations can be made at this stage. There is a solution with $V_{\perp} = 0$ if the term $\{\dots\}$ in Eq. (2-21) is zero. For finite radius of curvature R , this corresponds precisely to the critical nucleus, Eq. (2-6b), but now with anisotropic $\gamma(\vartheta)$. This equation therefore determines the shape of the critical nucleus in agreement with the *Wulff construction* (Wulff, 1901). Second, for very large mobility $\kappa(\vartheta)$ the deviation from equilibrium $\{\dots\}$ may be very small in order to produce a desired normal velocity V_{\perp} . We will use this simplification of equilibrium at the interface

$$\Delta g \cong \frac{1}{R} (\gamma + \gamma'') \quad (2\text{-dim}) \quad (2-22)$$

wherever possible, but we will comment on the changes due to finite $\kappa(\vartheta)$. The double prime means derivatives as in Eq. (2-21). In many cases this seems to be justified by experimental conditions. On the other hand, very little is known quantitatively about $\kappa(\vartheta)$. A last point to mention here is our assumption that the interfaces are not faceted at equilibrium. If they are faceted, as crystals typically are at low temperatures in equilibrium with their vapor, the situation is considerably more complicated and not completely understood (Kashuba and Pokrovsky, 1990).

It is now generally believed that faceted surfaces undergo a kinetic roughening transition even at small driving forces, so that a rough surface is present under growth con-

ditions. The concept outlined above then generally applies in an effective fashion. Actually, facets may persist over experimentally relevant length scales, which are not covered by this analysis in the kinetic region. A summary of theoretical developments can be found in the article by Krug and Spohn (1992).

To complete this section on the basic theoretical ingredients, we will now discuss the influence of diffusive transport of heat or matter on the propagation of a solid–liquid interface (see also Langer, 1980a).

2.2.3 Growth of Simple Crystal Forms

a) Flat interface

The simplest model for a solidifying system consists of two half-spaces filled with the liquid and solid of a one-component material of invariant density and separated by a flat interface. The interface is approximately in equilibrium (Eq. (2-22)) at melting temperature T_m but advancing at a speed V in the positive z -direction into the liquid. During this freezing process, latent heat L_m has to be transported into the supercooled liquid, the solid remaining at T_m .

The equation of motion is then the thermal diffusion equation

$$\frac{\partial}{\partial t} T(\mathbf{x}, t) = D_T \nabla^2 T(\mathbf{x}, t) \quad (2-23)$$

with thermal diffusion coefficient D_T and appropriate boundary conditions. At infinity in the supercooled liquid the temperature $T_\infty < T_m$ is prescribed, and T_m is the temperature at the interface. It is now very convenient to replace the temperature field T by a dimensionless u through the transformation

$$u(\mathbf{x}, t) = \frac{T(\mathbf{x}, t) - T_m}{(L_m/c_p)} \quad (2-24)$$

where c_p is the specific heat of the liquid at constant pressure. If, instead of temperature or heat, a second chemical component is diffusing, a similar transformation to the same dimensionless equations can be made. This is described in Section 2.5.2. We would like to stress the importance of such a scaled representation as it allows us to compare at a glance experimental situations with different sets of parameters.

In this dimensionless form, the equation of motion is

$$\frac{\partial}{\partial t} u = D_T \nabla^2 u \quad (2-25)$$

and the boundary conditions are

$$u = u_\infty < 0 \quad \text{for } z \rightarrow \infty \quad (2-26a)$$

$$u = 0 \quad \text{at interface} \quad (2-26b)$$

So far we have not specified how the interface motion is coupled to the equation of motion. Obviously, the latent heat L_m generated during this freezing process at a rate proportional to V has to be carried away through the diffusion field. This requires a continuity equation at the interface

$$V = -D_T \hat{n} \cdot \nabla u \quad (2-27)$$

and since in the model here only the z -axis is important

$$V = -D_T \frac{\partial}{\partial z} u(z, t) \quad \text{at interface} \quad (2-28)$$

The growth rate is therefore proportional to the gradient of the diffusion field at the interface in the liquid. As the interface is moving, we conveniently make a coordinate transformation from $\{z, t\}$ for $\{z', t'\}$ into a frame of reference moving along with the interface at $z' = 0$:

$$\begin{aligned} z' &= z - \int_0^t V(\tau) d\tau \\ t' &= t \end{aligned} \quad (2-29)$$

Performing that transformation, we obtain the following for the diffusion equation (after having again dropped the primes for convenience):

$$\frac{1}{D_T} \frac{\partial u}{\partial t} = \nabla^2 u + \frac{2}{l} \frac{\partial u}{\partial z} \quad (2-30)$$

which defines a diffusion length

$$l \equiv 2 D_T / V \quad (2-31)$$

The interface is now always at $z=0$, which makes the boundary condition Eq. (2-26b) and the continuity Eq. (2-28) definite.

We can obtain a stationary solution by combining Eq. (2-30) with Eqs. (2-26) and (2-28) when $\partial u / \partial t = 0$:

$$u = \exp\left(-\frac{2z}{l}\right) - 1; \quad z \geq 0 \quad (2-32)$$

This equation is consistent with the assumption that $u=0$ ($T=T_m$) everywhere in the solid.

This equation describes the diffusion field ahead of the interface. It varies exponentially from its value at the interface toward the value far inside the liquid, so that the diffusion field has a typical "thickness" of l .

Note that we have not used Eq. (2-26a) as a boundary condition at infinity, but find from Eq. (2-32) that $u=-1$ implies the so-called "unit supercooling", which corresponds to

$$T(z=\infty) = T_m - (L_m/c_p) \quad (2-33)$$

This basically says that the difference in melting enthalpy L_m between liquid and solid must be compensated by a temperature difference in order to globally conserve the energy of the system during this stationary process. In other words, if Eq. (2-33) is not fulfilled by Eq. (2-26a), the process cannot run with a stationary profile of the thermal field, Eq. (2-32). On the other hand, a particular value of the growth

rate V (or l) is not specified, but seems to be arbitrary. This degeneracy is practically eliminated by other effects such as interface kinetics (Collins and Levine, 1985) or the density difference between solid and liquid (Caroli et al., 1984), so that in practice a well-defined velocity will be selected.

b) Growth of a sphere

The influence of the surface tension γ when it is incorporated through Eq. (2-21) is most easily understood by looking at a spherical crystal. This will not lead to stationary growth. In order to make the analysis simple, we will invoke the so-called "quasistationary approximation", by setting the left-hand side in Eq. (2-25) equal to zero. The physical meaning is that the diffusion field adjusts itself quickly to a change in the boundary structure which is, however, still evolving in time because the continuity equation is velocity-dependent. Of course, this approximation reproduces the stationary solutions precisely (if they exist), and in addition, it exactly identifies the instability of a stationary solution as long as it is not of the Hopf type (i.e., the critical eigenvalue is not complex). It is generally assumed that the approximation is good as long as the diffusion length is large compared with other lengths of the evolving pattern.

In a spherical coordinate system, the equation of motion then becomes

$$\frac{1}{D_T} \frac{\partial u}{\partial t} \approx 0 = \left\{ \frac{\partial^2}{\partial r^2} + \frac{2}{r} \frac{\partial}{\partial r} \right\} u \quad (2-34)$$

as a simple Laplace equation.

The interface is at radius $R_0(t)$ and is advancing with time. The continuity equation requires

$$v_R \equiv \frac{dR_0}{dt} = - D_T \left. \frac{\partial u}{\partial r} \right|_{r=R_0(t)} \quad (2-35)$$

Concerning the boundary condition, we note that for a simple substance the difference in slopes of the chemical potentials for solid and liquid at the melting point (Landau and Lifshitz, 1970) is L_m/T_m , giving

$$\Delta\mu = -L_m(T - T_m)/T_m \quad (2-36)$$

With Eqs. (2-21) and (2-24), the boundary condition in the case of isotropic γ becomes

$$u(\text{interface}) = -d_0 K - \beta V \quad (2-37)$$

with curvature

$$K = \begin{cases} 2/R, & 3\text{-dim} \\ 1/R, & 2\text{-dim} \end{cases} \quad (2-38)$$

capillary length

$$d_0 = \gamma T_m c_p / L_m^2 \quad (2-39)$$

and interface kinetics

$$\beta = \kappa^{-1} T_m c_p / L_m^2 \quad (2-40)$$

The generalization to non-isotropic γ follows from Eq. (2-21) and comments.

Note that in Eq. (2-37) both curvature and non-equilibrium occur at the boundary as opposed to the simple case in Eq. (2-26b), shown above. At infinity we finally impose

$$u_\infty = u(\infty, t) = -\Delta \quad (2-41)$$

as the now arbitrary dimensionless supercooling. This equation, together with Eq. (2-24), is the definition of Δ .

The solution to Eq. (2-34) with Eqs. (2-35), (2-37), and (2-41) in the liquid is then simply

$$u(r) = -\Delta + \frac{R_0}{r} \left(\Delta - \frac{2d_0}{R_0} \right) \bigg/ \left(1 + \frac{\beta D_T}{R_0} \right) \quad (2-42)$$

where we have used $K=2/r$ as the curvature of the spherical surface in three dimensions.

The growth rate therefore is

$$v_R \equiv \frac{dR_0}{dt} = \frac{D_T}{R_0} \left(\Delta - \frac{2d_0}{R_0} \right) \bigg/ \left(1 + \frac{\beta D_T}{R_0} \right) \quad (2-43)$$

and it is found that for large radii $R_0(t)$ the growth rate is proportional to the supercooling Δ :

$$V_R \approx \frac{D_T}{R_0} \Delta \left(1 - \beta \frac{D_T}{R_0} + \dots \right) \quad (2-44)$$

It can also be seen that the kinetic coefficient β becomes less important in the limit of large radii and correspondingly small growth rates. This in many cases justifies our previous equilibrium approximation, Eq. (2-22).

We have not discussed here the solidification of a binary mixture. As the details of the phase diagram will become important later, we will postpone this topic to the section on directional solidification. We would like to mention, however, that the representation of the diffusion field in dimensionless form, found in Eq. (2-24), has the virtue that several results can be carried over directly from the thermal case to compositional diffusion, although there are some subtleties in the boundary conditions which make the latter more difficult to analyze.

2.2.4 Mullins–Sekerka Instability

We now combine the considerations of Secs. 2.2.3a) and b) to study the question of whether an originally flat interface will remain flat during the growth process. The results indicate that a flat interface moving into a supercooled melt will become rippled (Mullins and Sekerka, 1963, 1964).

The basic equations are almost exactly the same as in the previous section a) Eqs. (2-30), (2-27), (2-26a), but instead of the boundary condition Eq. (2-26b), we now

have to consider deviations from a flat interface as we move parallel to the interface in the x -direction. This is provided by Eq. (2-37) as the boundary condition, where we set $\beta=0$ for simplicity.

Denoting the deviation of the interface from $z=0$ as $\zeta(x, t)$, we designate the curvature for small amplitudes simply as $K=-\partial^2\zeta/\partial x^2$, where, in agreement with Eq. (2-38), the sign of K allows for the curvature to be positive for a solid protrusion into liquid. We follow here the notation of Langer (1980a).

In a quasistationary approximation, for the sake of simplicity we set the l.h.s. in Eq. (2-30) equal to zero, which of course allows for the stationary solution, Eq. (2-32). It is not difficult to treat the fully time-dependent problem here, but the modifications do not change the results substantially. We now perturb that solution by making a small sinusoidal perturbation of the flat interface:

$$\zeta(x, t) = \hat{\zeta}_k \exp(ikx + \Omega_k t) \quad (2-45)$$

Similarly, a perturbation of the diffusion field is made in the liquid and in the solid

$$u(x, z, t) = \exp\left(-\frac{2z}{l}\right) - 1 \quad (2-46)$$

$$+ \hat{u}_k \exp(ikx - qz + \Omega_k t);$$

$$u'(x, z, t) = \hat{u}'_k \exp(ikx + q'z + \Omega_k t)$$

where the unprimed form is for the liquid, and the primed values are for the solid. Inserting Eq. (2-46) into Eq. (2-30) with $\partial u/\partial t=0$, we obtain

$$\begin{aligned} -2q/l + q^2 - k^2 &= 0 \\ 2q'/l' + q'^2 - k^2 &= 0 \end{aligned} \quad (2-47)$$

Replacing z in Eq. (2-46) by $\zeta(x, t)$ from Eq. (2-45), we can insert this into the boundary condition Eq. (2-37) for $\beta=0$ to obtain

$$\hat{u}'_k = -2\hat{\zeta}_k/l + \hat{u}_k = -d_0 k^2 \hat{\zeta}_k \quad (2-48)$$

where we have linearized the $\exp(\dots)$ with respect to ζ . Instead of the velocity in Eq. (2-27), we must now use $V_\zeta = 2D/l + \partial\zeta/\partial t$. With this equation and the same linearization as before

$$\Omega_k \hat{\zeta}_k = -D(2/l)^2 \hat{\zeta}_k + Dq\hat{u}_k + D'q'\hat{u}'_k \quad (2-49)$$

is obtained for the conservation law, Eq. (2-27) (and for small values of ζ , practically Eq. (2-28)). Eliminating \hat{u}_k here using Eq. (2-48) and eliminating q using Eq. (2-47) in the limit $kl \gg 1$ or $k \approx q \approx q'$, we obtain

$$\begin{aligned} \Omega_k &= V(q - 2/l) - (Dq + D'q')d_0 k^2 \\ &\approx kV[1 - \frac{1}{2}(1 + D'/D)ld_0 k^2] \end{aligned} \quad (2-50)$$

This formula describes the basic mechanism of diffusion-controlled pattern formation in crystal growth. Although in general, diffusion tends to favor homogeneous structures, in the present case it works in the opposite direction! This is easy to understand; the foremost points of a sinusoidal deformation of the interface can dissipate the latent heat of freezing by a larger space angle into the liquid than the points inside the bays. The latter points will therefore be slowed down. The tip points will be accelerated in comparison with the average rate of advancement.

The formula therefore consists of a destabilizing part leading to positive Ω_k and a stabilizing part controlled by the capillarity d_0 . The stabilization is most efficient at large k values or short wavelengths; at longer wavelengths, the destabilization due to diffusion into the supercooled liquid dominates.

The dividing line is marked by the combination of $d_0 l$, which is most conveniently expressed as

$$\lambda_S = 2\pi/k_S = 2\pi\sqrt{d_0 l} \quad (2-51)$$

assuming $D=D'$. This will be called the "stability length", which gives a measure

of the typical lengths for diffusion-generated ripples on the interface, since the fastest-growing mode has a wavelength $\lambda_f = \sqrt{3} \lambda_S$. This is the first explicit example of the fundamental scaling relation Eq. (2-1) mentioned in the introduction to this chapter.

2.3 Basic Experimental Techniques

Before discussing the various growth models, a short overview of selected experiments that have contributed to our present understanding will be given.

An exhaustive treatment of the subject is not intended here; only some of the characteristic techniques will be described. No specific reference will be given to the many solidification processes available. The main emphasis will be on growth of crystals, because direct evidence on nucleation mechanisms is generally not available. There is an exception; the original technique developed by Schumacher et al. (1998). These authors analysed quenched-in nuclei (inoculants) in glassy Al alloys in the transmission electron microscope. In this state, nucleation kinetics are very slow and *in-situ* observation of the phases and their structure, composition and crystal orientation can be measured. The reader

interested in nucleation experiments is referred to reviews by Perepezko et al. (1987, 1996).

There are two essentially different situations of solidification, or, more generally, of phase transformation (Fig. 2-1):

- i) free (undercooled or equiaxed) growth,
- ii) constrained (columnar or directional) growth.

In the first case (Fig. 2-1 a), the melt undercools, before transforming into a crystal, until nucleation sets in. The crucible that contains the melt must be less effectively catalytic to crystallization than the heterogeneous particles in the melt. The crystals then grow with an interface temperature above the temperature of the surrounding undercooled liquid. Heat is carried into the liquid. The temperature gradient at the solid–liquid interface in the liquid is therefore negative and approximately zero in the solid owing to the initially small crystal size relative to the thermal boundary layer.

In the second case of constrained growth (Fig. 2-1 b), the temperature gradient is positive in both liquid and solid, and the first solid is either formed in contact with the chill mold or is already present, as in surface treatment by lasers, for example, where growth occurs epitaxially after re-

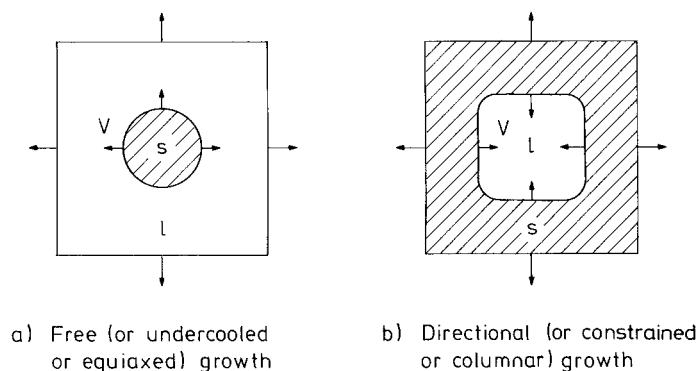


Figure 2-1. Growth in (a) undercooled melt (free growth) and (b) superheated melt (directional growth). The arrows on the outside of the mold represent the heat flux, and the arrows at the solid/liquid interface, the growth direction.

melting. In case i), nucleation is essential in controlling the microstructure (the grain size), while in case ii), nucleation is of minor importance.

Typical technical processes with respect to these two classes of solidification are as follows:

i) casting into low conductivity molds (ceramics), producing small temperature gradients, or adding inoculating agents or stirring the melt, thereby producing many heterogeneous or homogeneous nuclei;

ii) processes with high heat flux imposed through strong cooling of the solid such as continuous casting, welding, laser treatment, or through heating of the melt and cooling of the solid, such as in single crystal growth or *Bridgman type* directional solidification experiments (see also Flemings, 1991).

In free growth, the undercooling ΔT of the melt is given and controls the growth rate V and the scale (spacing λ or tip radius R) of the forming microstructure. In directional growth, the rate of advance of the isotherms is imposed by heat flux leading to an imposed growth rate (constrained growth). This, in turn, controls the interface temperature (undercooling) and the microstructural scales. These three variables (temperature, growth rate, and microstructural size) have to be measured experimentally for a quantitative comparison of theory and experiment. A number of material parameters of the alloy system have to be known, such as the solid-liquid interfacial energy with its anisotropy, the diffusion coefficient, the stable and metastable phase diagram, etc.

The experimental techniques are divided into two classes; those which produce relatively small growth rates and those which aim for high solidification rates. The corresponding experimental setup is quite dif-

ferent, and some of its important elements will be described below.

2.3.1 Free Growth

Slow growth rates

In free growth, the undercooling ΔT or the temperature of the melt $T_0 = (T_m - \Delta T)$ is imposed on the system, and the growth rate V and the microstructural scale are the dependent variables. For low undercoolings, and therefore slow growth rates, all three variables can be measured precisely if the substance is transparent. The crystallization of non-transparent metals, however, is the major issue in solidification studies relevant to technical applications.

Instead of investigating the crystallization of metallic systems directly, suitable model substances have to be found. These are generally organic "plastic crystals" which, like metals, have simple crystal structures and low melting entropies (Jackson, 1958). One of the substances which behaves very similarly to metals and also has well characterized properties is succinonitrile (SCN) (Huang and Glicksman, 1981). Numerous results have been obtained with this material by Glicksman and co-workers. Their careful experimental approach not only produced the most precise measurements known at that time but has also stimulated new ideas about possible mechanisms of structure formation through the discrepancy found between the observations and the predictions of previous theories.

Fig. 2-2 shows the experimental setup developed by Glicksman et al. (1976) to study free dendritic solidification. After zone melting, the material is introduced into the growth chamber (C), which is then slowly undercooled with the heaters (A) and (B) in order to avoid premature crystal-

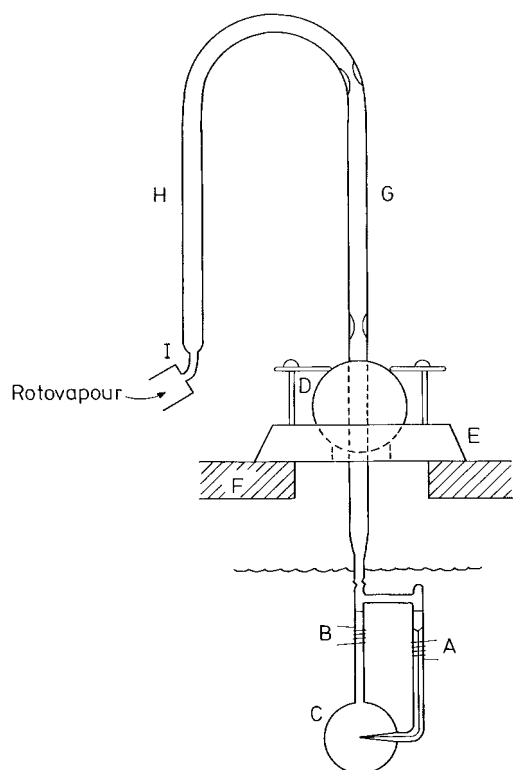


Figure 2-2. Equipment for free growth of organic dendrites (Glicksman et al., 1976). A and B, control heaters; C, growth chamber; D, tilting and rotating device; F, tank cover; G and H, zone-refining tubes.

lization. By careful adjustment of heater (A), growth starts there, and a crystal grows through the orifice in chamber (C). From then on, the dendrite can grow freely into the undercooled liquid and its shape, size and growth rate, depending on super-

cooling, are measured with the aid of photographs. In order to choose a proper projection plane of observation, the entire equipment can be translated, rotated and tilted at (D). A series of similar experiments have been performed at low temperatures with rare gases (Bilgram et al., 1989).

In this kind of experiment, it is important to avoid thermal or solutal convection, as this transport mechanism will change the results and make them difficult to compare with diffusional theory. Glicksman et al. (1988) have shown the effect of thermally driven convection on the growth morphology of pure SCN dendrites. Fig. 2-3 clearly shows a strong deviation of the growth rate at undercoolings lower than 1 K, where convection is believed to accelerate dendrite growth. Here V_0 is the dendrite tip rate of pure diffusion-controlled growth. Recent experiments on free dendritic growth of succinonitrile in space under microgravity conditions in the undercooling range of 0.064 to 1.844 K confirmed this effect clearly (Koss et al., 1999).

Another type of slow dendrite growth in undercooled media has been analyzed by Trivedi and Laorchan (1988). These authors made interesting *in situ* observations during the crystallization of glasses. Even if the driving forces in these systems are very large, growth is heavily restricted due to slow diffusion and attachment kinetics.

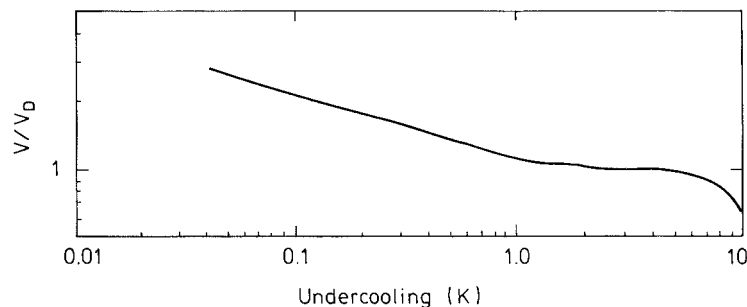


Figure 2-3. Ratio of measured growth rate, V , to predicted rate from diffusion theory, V_D , as a function of undercooling (Glicksman et al., 1988).

Fast growth rates

In order to explore solidification behavior under very large driving forces, Herlach et al. (1993) and Herlach (1994, 1997) systematically measured dendrite growth rates in a large number of highly undercooled alloys. Nucleation is avoided by levitation melting in an ultrahigh vacuum environment. Undercooling of more than 300 K leading to growth rates of up to 70 m/s has been reached. Such large undercoolings have been obtained by several authors before, but growth rates have not been measured. Interesting results in Ni–Sn alloys have also been obtained by high-speed cinematography of highly undercooled samples. These results were produced by Wu et al. (1987) by encapsulating the melt in glass. They tried to measure tip radii from the photograph. In this case, however, only the thermal images of the dendrites could be seen, their tips being controlled by solute diffusion. The radii from the thermal images are therefore believed to be much larger than the real radii.

2.3.2 Directional growth

Slow growth rates

Understanding of solidification improved in the 1950s when the need for better semiconductor materials stimulated research using directional growth techniques such as zone melting and Bridgman growth. Later, directional casting became an important topic of research for the production of single crystal turbine blades. Fig. 2-4 shows the essentials of two techniques: Bridgman type and *chill plate* directional solidification. The first of these processes (Fig. 2-4a) has the advantage of being able to produce a constant growth rate and a constant temperature gradient over a considerable length and to allow for a certain uncoupling of these two most important variables. It was this latter advantage which, early on in solidification research, provided much insight into the mechanisms of growth. With one growth rate, but varying temperature gradient (or vice versa), plane-front, cellular or dendritic morphologies could be grown, and their evolution studied. Important concepts (constitutional undercooling, cell growth,

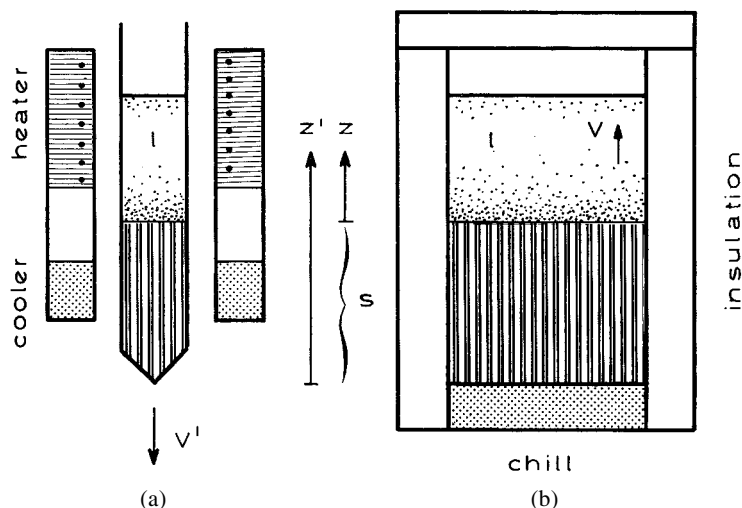


Figure 2-4. Basic methods of directional solidification; (a) Bridgman type furnace and (b) directional casting.

etc.) have been developed with the aid of observations made with the Bridgman type of equipment. The experiments by Hunt et al. (e.g., Burden and Hunt, 1974) deserve special attention, as the quality of the measurements was of a very high standard.

Furthermore, most of the work on *directional eutectics* and their growth mechanisms was performed with the aid of this technique. In eutectic solidification, the microstructure after transformation has the same size (interphase spacing λ) as that found at the growing interface and thus allows for direct conclusions to be drawn concerning the growth process. This important variable can therefore be easily determined in non-transparent metals. This, however, is not possible with the corresponding quantity of the dendrite, the tip radius R , as discussed earlier.

One disadvantage of the Bridgman experiment is the need for a small diameter due to heat flux constraints. This is avoided in the process shown in Fig. 2-4b (*directional casting*), but in this case a separation of the variables V and G is not possible. Therefore, this method is less interesting for scientific purposes. However it is used extensively for directional casting of single crystal turbine blades (Versnyder and Shank, 1970).

For *in-situ* observation of microstructure information, we can also use plastic crystals in an experimental arrangement resembling a two-dimensional Bridgman apparatus, as shown in Fig. 2-5. Two glass slides containing the organic analogue are moved over a heating and cooling device producing a constant temperature gradient G_T . This can be controlled to certain limits by the temperature difference and distance between heater and cooler (Somboonsuk and Trivedi, 1985; Trivedi and Somboonsuk, 1985; Akamatsu et al., 1995; Ginibre et al., 1997; Akamatsu and Faivre, 1998).

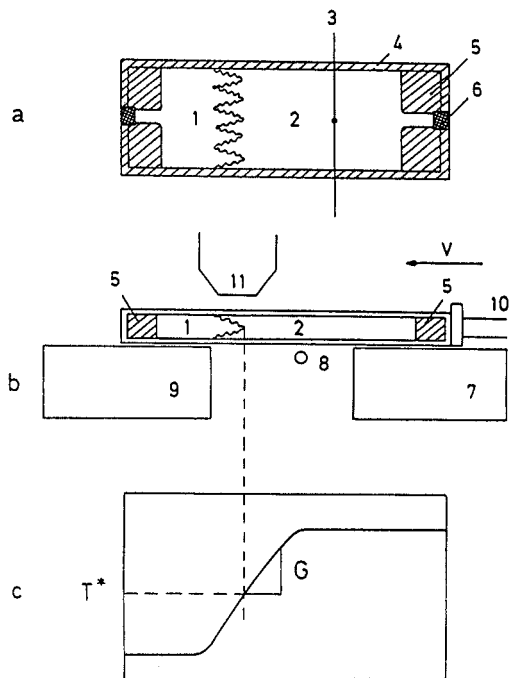


Figure 2-5. Schematic diagram of growth cell (a, b) for observation of directional solidification of transparent substances under a microscope (Esaka and Kurz, 1985). 1, solid; 2, liquid; 3, thermocouple; 4, cell; 5, low melting glass; 6, araldite seal; 7 and 8, heaters; 9, cooler; 10, drive mechanism; 11, microscope. In (c) the temperature distribution in the growth cell is shown.

A thin thermocouple incorporated into the alloy allows for measurement of interface temperature (Fig. 2-6) and temperature gradient in liquid and solid (Esaka and Kurz, 1985; Somboonsuk and Trivedi, 1985; Trivedi and Somboonsuk, 1985; Trivedi and Kurz, 1986).

Fast growth rates

There have been attempts to increase the growth rate in Bridgman type experiments. The first to reach rates of the order of several mm/s were Livingston et al. (1970). The best way to reach much higher rates is through laser resolidification using a stable

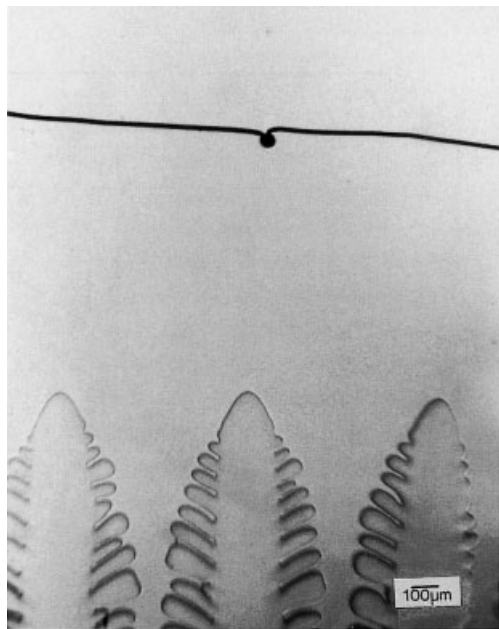


Figure 2-6. Array of dendrites approaching a fine thermocouple for measurement of the tip temperature and temperature gradient. Diameter of the bead approximately 50 μm (Esaka and Kurz, 1985).

high-powered laser. In this case, a small melt pool with very steep temperature gradients is created (for a remelted layer of 100 μm thickness, the temperature gradient G_T is of the order of 5000 K/mm). The microstructure is then constrained to follow closely the heat flow, which is perpendicular to the isotherms (Fig. 2-7). Therefore, knowing the angle θ between the direction of growth and the direction and rate of movement of the laser beam allows for the growth rate to be obtained locally, even in the electron microscope (Zimmermann et al., 1989). Note that the growth rate increases from zero at the interface with the substrate up to a maximum at the surface. The only unknown which would be extremely difficult to measure is the interface temperature.

Consequently, in the case of rapid directional growth we can determine the post-

solidification microstructure and its growth rate as well as the bath temperature and the growth rate in rapid undercooled growth. In both cases, the measurement of the interface temperature is not possible for the time being and must be evaluated through theory alone.

2.4 Free Dendritic Growth

The most popular example of dendritically (= tree-like) growing crystals is given by snowflakes. The six primary arms on each snowflake look rather similar but there is an enormous variety of forms between different snowflakes (Nakaya, 1954). From our present knowledge, the similarity of arms on the same snowflake is an indication of similar growth conditions over the arms of a snowflake, the variation of structure along each arm being an indication of a time variation of external growth conditions.

In order to formulate a theory, some specific assumptions about these environmental conditions must be made. Unfortunately, the growth of a snowflake is an extremely complicated process, involving strongly anisotropic surface tension and kinetics and the transport of heat, water vapor, and even impurities. Therefore, we will initially drastically simplify the model assumptions. In the same spirit, a number of precise experiments have been performed to identify quantitatively the most important ingredients for this mechanism.

In its simplest form, dendritic growth requires only a supercooled one-component liquid with a solid nucleus inside, so that the heat released at the solid-liquid interface during growth is transported away into the liquid. This is precisely the condition given in Sec. 2.2.3 concerning a sphere growing into the supercooled, and there-

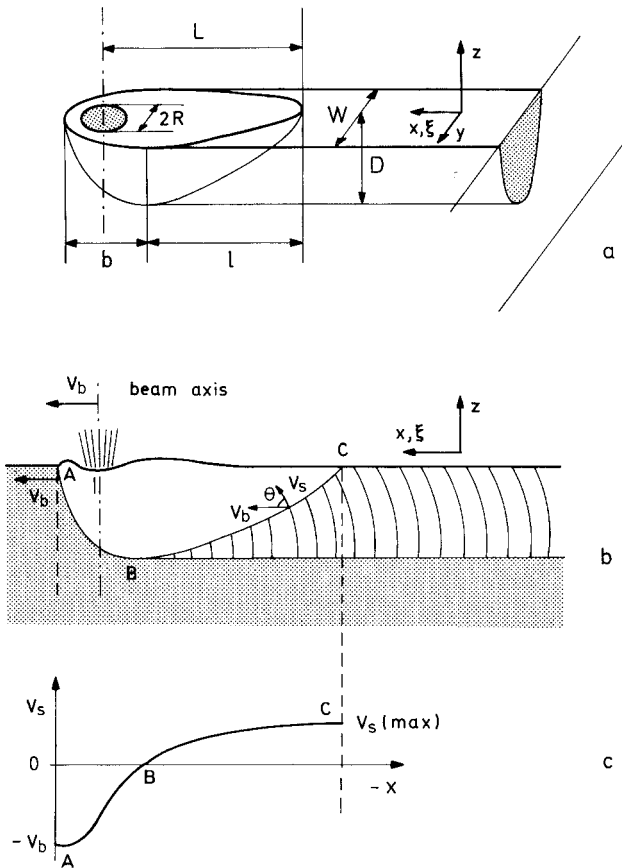


Figure 2-7. Schematic diagrams of a laser trace (a, b) and of the local interface velocity (c). V_b is the laser scanning velocity and V_s is the velocity of the solid/liquid interface which increases from zero at the bottom of the trace to a maximum at the surface. W and D are the width and depth of the trace, respectively, and θ is the angle between the growth direction and the scanning direction.

fore metastable, liquid. A relatively straightforward stability analysis (Mullins and Sekerka, 1963, 1964; Langer, 1980a) shows that the solid tends to deviate from spherical form as soon as its radius R has become larger than seven times the critical radius $R_c = 2d_0/\Delta$. A time-dependent analysis has also been carried out (Yokoyama and Kuroda, 1988). During the further evolution, these deformations evolve into essentially independent arms, the primary dendrites.

The growth of such dendrites is a very widespread phenomenon, as will become clearer in Sec. 2.5 on directional solidification. There are also close relations to processes called diffusion-limited aggregation (DLA) (for a review see Meakin, 1988; for relation to crystal growth, see Uwaha and

Saito, 1990; Xiao et al., 1988). For these processes, some specific assumptions are made about the incorporation of atoms into the advancing interface which are not easily carried over into the notion of surface tension, etc. Another line of closely related problems concerns the viscous flow of two immiscible liquids (Saffmann and Taylor, 1958; Brenner et al., 1988; Dombre and Hakim, 1987; Kessler and Levine, 1986c). We will briefly refer to this in Sec. 2.5.

2.4.1 The Needle Crystal Solution

In this subsection, we will look at an isolated, needle-shaped crystal growing under stationary conditions into a supercooled melt. A stationary condition, of course, only

holds in a frame of reference moving at velocity V in the positive z -direction. For a one-component crystal, the latent heat of freezing must be diffused away into the liquid.

The process is therefore governed by the heat diffusion Eq. (2-25)

$$0 = \nabla^2 u + \frac{2}{l} \frac{\partial u}{\partial z} \quad (2-52)$$

where we have used a dimensionless form, Eq. (2-30), for a stationary pattern together with the definition of the diffusion length, Eq. (2-31). If the diffusion constants in the crystal and the liquid are different, we would have to use two diffusion lengths. The continuity Eq. (2-27) at the interface is for normal velocity

$$V_{\perp} = -D_T \hat{n} \cdot \nabla u_L + D_T \hat{n} \cdot \nabla u_S \quad (2-53)$$

where the subscripts L and S denote gradients taken on the liquid side and on the solid side of the interface. This is known as the “two-sided” model (Langer and Turski, 1977) and, because of identical diffusion constants, as the “symmetrical” model. The generalization to different diffusion constants is simple.

The boundary condition at the interface is

$$u_I = -d_0 K - \beta V \quad (2-54)$$

and at infinity

$$u_{\infty} = -\Delta \quad (2-55)$$

as introduced before in Eqs. (2-37) and (2-41), respectively. Note that a constant like Δ may be added on the right-hand side of both equations without changing the results apart from this additive constant in the u -field, as frequently appears in the literature. The definition of Δ follows easily from Eqs. (2-24) and (2-41).

In general, the capillary length d_0 and the kinetic coefficient β are anisotropic because of the anisotropy of the crystalline

lattice, but they are not directly related (Burkhardt et al., 1977). For the moment, we will assume $\beta=0$, i.e., the interface kinetics should be infinitely fast. Even then, the curvature K in Eq. (2-54) is a complicated function of the interface profile. The simplest approximation for the moment, therefore, is to ignore both terms on the r.h.s. of the boundary condition, which corresponds to setting the surface tension to zero. The boundary condition is then simply a constant ($=0$ in our notation).

A second-order partial differential equation such as the diffusion equation can be decomposed in the typical orthogonal coordinate systems, and we therefore obtain a closed form solution for the problem with a boundary of parabolic shape: a rotational paraboloid in three dimensions and a simple parabola in two dimensions. This is the famous “Ivantsov” solution (Ivantsov, 1947).

The straightforward way to look at this problem is as a coordinate transformation from the cartesian $\{x, z\}$ frame, where z is the growth direction, to the parabolic coordinates $\{\xi, \eta\}$:

$$\xi = (r - z)/\varrho; \quad \eta = (r + z)/\varrho$$

where r is the radial distance $\sqrt{x^2 + z^2}$ from the origin, and ϱ is a constant. After transforming the differential operators in Eqs. (2-52) and (2-53) to $\{\xi, \eta\}$ (Langer and Müller-Krumbhaar, 1977, 1978), it can be seen immediately that $\eta(\xi) = \eta_S = 1$ for the interface is a solution to the problem confirming the parabolic shape of the interface, with ϱ being the radius of curvature at the tip.

This *Ivantsov radius*, ϱ , is now related to the supercooling Δ and the diffusion length l by the relation

$$\Delta = \begin{cases} P e^P E_1(P) & \text{3-dim} \\ \sqrt{\pi} P e^P \operatorname{erfc}(\sqrt{P}) & \text{2-dim} \end{cases} \quad (2-56a) \quad (2-56b)$$

which for small $\Delta \ll 1$ gives

$$\Delta \approx \begin{cases} P(-\ln P - 0.5772...) & \text{3-dim} \\ \sqrt{\pi P} & \text{2-dim} \end{cases}$$

and for $\Delta \rightarrow 1$ asymptotically

$$\Delta \approx \begin{cases} 1 - 1/P & \text{3-dim} \\ 1 - 1/2 P & \text{2-dim} \end{cases}$$

where the dimensionless *Péclet number* P is defined as the relation

$$P = \varrho/l = \varrho V/2D \quad (2-57)$$

between tip radius and growth rate. $E_1(P)$ is the exponential integral

$$E_1(P) = \int_P^{\infty} \frac{e^{-t}}{t} dt \quad (2-58)$$

and erfc is the complement of the error function.

Eq. (2-56) may be interpreted as an expression of supercooling in terms of the *Péclet number*. This explanation is important because the following considerations of surface tension give only very small corrections to the shape of the needle crystal. Therefore, Eq. (2-56) will be also valid with non-zero surface tension at typical experimental undercoolings of $\Delta \cong 10^{-1}$. An important consequence is that the scaling results derived below then become independent of the dimensionality (2 or 3), if the supercooling is expressed through the *Péclet number*.

The basic result of Eqs. (2-57) and (2-48) is that the growth rate of this parabolic needle is inversely proportional to the tip radius, but no specific velocity is selected. For experimental comparison, we make a fit of the tip shape to a parabola. The tip radius of that parabola is then compared with the Ivantsov radius ϱ . The actual tip radius will be different from the Ivantsov radius of the fit parabola, because of sur-

face tension effects. Before we consider surface tension explicitly we now give an integral formulation for the problem using *Green's functions*, which has proved to be more convenient for analytical and numerical calculations (Nash and Glicksman, 1974).

The value of a temperature field $u(\mathbf{x}, t)$ in space and time is obtained by multiplying the Green's function of the diffusion equation with the distribution for sources and sinks for heat and integrating the product over all space and time. In our case, this explicitly gives

$$u(\mathbf{x}, z, t) = \int_{-\infty}^t dt' \int d\mathbf{x}' G[\mathbf{x} - \mathbf{x}', z - \zeta(\mathbf{x}', t')] + V(t - t', t - t') \left\{ V + \frac{\partial \zeta}{\partial t'} \right\} \quad (2-59)$$

(Langer, 1987b), with the Green's function

$$G(\mathbf{x}, z, t) = \frac{1}{(4\pi Dt)^{3/2}} \exp\left(-\frac{|\mathbf{x}|^2 + z^2}{4Dt}\right) \quad (2-60)$$

for diffusion in an infinite three-dimensional medium (symmetrical case), while ζ is the z coordinate of the interface. The source term $\{\dots\}$ in this equation is obviously the interface in the frame of reference moving at velocity V in the z -direction. This equation already contains the conservation law or the continuity equation at the interface. Furthermore, it is valid everywhere in space and, in particular, at the interface $z = \zeta(\mathbf{x}, t)$, where the l.h.s. of Eq. (2-59) is then set equal to Eq. (2-54). Here u is assumed to vanish at infinity, so Δ must be added on the l.h.s.

In the two-dimensional case and for stationary conditions, this can be rewritten as

$$\Delta - \frac{d_0}{\varrho} K\{\zeta\} = P \Gamma_2\{P, x, \zeta(x)\} \quad (2-61)$$

(Langer, 1987b), with

$$\Gamma_2 \{P, x, \zeta(x)\} = \frac{1}{2\pi} \int_0^\infty \frac{dy}{y} \int_{-\infty}^{+\infty} dx' \quad (2-62)$$

$$\times \exp\left(-\frac{P}{2y} \{(x-x')^2 + [\zeta(x) - \zeta(x') + y]^2\}\right)$$

In addition, it was shown (Pelce and Poineau, 1986) that with the parabolic Ivantsov solution

$$\zeta(x) \rightarrow \zeta_{IV} = -\frac{1}{2}x^2 \quad (2-63)$$

we can obtain

$$P\Gamma_2 \{P, x, \zeta_{IV}(x)\} = \Delta$$

which is independent of x , with Δ coming from Eq. (2-56b). Note that from Eqs. (2-59) to (2-61) we have replaced x by $x\varrho$ etc., which mirrors the scaling form of Eq. (2-57).

We are now ready to consider a non-zero capillary length d_0 Eq. (2-39), which we generalize to be anisotropic:

$$d_0 \rightarrow d = d_0(1 - \varepsilon \cos 4\vartheta) \quad (2-64)$$

where ϑ is the angle between the interface-normal and the z -axis (2-dim, 4-fold anisotropy), and $\varepsilon > 0$ is the relative strength of that anisotropy. This form arises from the assumption

$$\gamma = \gamma_0(1 + \delta \cos 4\vartheta) \quad (2-65)$$

for anisotropy surface tension, which gives through Eq. (2-22) $\varepsilon = 15\delta$. Note that it is the stiffness γ'' which dominates the behavior, not γ directly. Along the Ivantsov parabola, the angle ϑ is related to x :

$$d = d_0 A(x); \quad A(x) = 1 - \varepsilon + \frac{8\varepsilon x^2}{(1 + x^2)^2} \quad (2-66)$$

and the deviation from $\zeta_{IV}(x)$ can be expressed as

$$-\frac{d}{\varrho P} K(\xi) = \Gamma_2 \{P, x, \xi\} - \Gamma_2 \{P, x, \zeta_{IV}\} \quad (2-67)$$

For convenience we combine some parameters into a dimensionless quantity σ :

$$\sigma = \frac{2Dd_0}{\varrho^2 V} = \frac{d_0}{2DP^2} V \quad (2-68)$$

so that the l.h.s. of Eq. (2-67) becomes

$$-\frac{d}{\varrho P} K = -\sigma A K \quad (2-69)$$

the curvature as usual being

$$K\{\xi\} = -\frac{\partial^2 \xi / \partial x^2}{[1 + (\partial \xi / \partial x)^2]^{3/2}} \quad (2-70)$$

It should be clear at this point that the parameter σ in Eq. (2-68) plays an important role, because it multiplies the highest derivative in Eqs. (2-61) and (2-67). More specifically, we can expect that the resulting structure $\zeta(x)$ of the interface depends on the material properties and experimental conditions only through this parameter σ (within the model assumptions), which becomes a function of P and ε

$$\sigma = \sigma(P, \varepsilon) \quad (2-71)$$

The importance of the parameter σ was recognized in an earlier stability analysis (Langer and Müller-Krumbhaar, 1978, 1980) of the isotropic case. It turned out later, however, that the anisotropy is essential in determining the precise value of σ . This is crucial as $\varepsilon \rightarrow 0$ implies $\sigma \rightarrow 0$, i.e., no stationary needle solutions exist without anisotropy.

We will now briefly describe the analysis of Eq. (2-67). The details of this singular perturbation theory are somewhat involved, and we therefore have to omit them here. The basic method was formulated by Kruskal and Segur (1985), and the first scaling relations for dendritic growth were obtained for the boundary-layer model (Ben Jacob et al., 1983, 1984). A good introduction to the mathematical aspects can

be found in the lectures by Langer (1987b), on which the following presentation is based. The most mathematically sound (nonlinear) solution seems to have been given by Ben Amar and Pomeau (1986). For convenience, we have sketched a slightly earlier linearized version here, while the nonlinear treatment leads to basically the same result.

Looking for a solution to Eq. (2-67) in linear approximation, we start by expanding to first order in

$$\zeta_1(x) = \zeta(x) - \zeta_{1V}(x) \quad (2-72)$$

In the limit of the small Péclet number, and with the substitution

$$\zeta_1(x) = (1+x^2)^{3/4} Z(x) \quad (2-73)$$

gives

$$(\hat{B} + \hat{A}) \cdot Z(x) = \sigma/(1+x^2)^{3/4} \quad (2-74)$$

where \hat{B} is a self-adjoint differential operator

$$\hat{B} = \sigma \frac{d^2}{dx^2} + \frac{(1+x^2)^{1/2}}{A(x)} + 0(\sigma) \quad (2-75)$$

and

$$\begin{aligned} \hat{A} \cdot Z(x) &= \frac{(1+x^2)^{3/4}}{2\pi A(x)} \\ &\times \mathcal{P} \int_{-\infty}^{+\infty} dx' \frac{(x+x')(1+x'^2)^{3/4}}{(x-x')[1+\frac{1}{4}(x+x')^2]} Z(x') \end{aligned} \quad (2-76)$$

with \mathcal{P} denoting the principal value.

The integral kernel in Eq. (2-76) is anti-symmetric apart from a prefactor $A(x)^{-1}$. An analytic solution to Eq. (2-74) has not yet been found. A necessary condition to be fulfilled by the present inhomogeneity is that it should be orthogonal to the null-eigenvectors $\tilde{Z}(x)$ of the adjoint homogeneous problem:

$$(\hat{B} + \hat{A}^+) \cdot Z(x) = 0 \quad (2-77)$$

such that

$$\Lambda(\sigma, \varepsilon) \equiv \int_{-\infty}^{+\infty} dx' \frac{\tilde{Z}(x)}{(1+x^2)^{3/4}} = 0 \quad (2-78)$$

In fact, this is already a sufficient condition for the solvability of the inhomogeneous equation, but it is not very simple.

A solution for $\tilde{Z}(x)$ can be found by a WKB technique, for which we refer to the literature (Kessler et al., 1987, 1988; Langer, 1987b; Caroli et al., 1986a, b). The result for the solvability condition, Eqs. (2-71) and (2-78), is that the parameter σ should depend on anisotropy ε as

$$\sigma \approx \sigma_0 \varepsilon^{7/4} \quad (2-79)$$

in the limit $P \rightarrow 0$, $\varepsilon \rightarrow 0$, with some constant prefactor σ_0 of order unity.

Eq. (2-79) is the solution for the needle-shaped crystal with capillary anisotropy $\varepsilon > 0$, together with Eq. (2-68). Note again that ε is the anisotropy of capillary length, which differs by a factor from surface-tension anisotropy Eq. (2-65). Formally, there is not just one solution but infinitely many, corresponding to slow, fat needles which are dynamically unstable. Only the fastest of these needle solutions appears to be stable against tip-splitting fluctuations and may thus represent an ‘observable’ needle crystal, as expressed by Eq. (2-79). For practical comparison, experimental data is best compared with numerical solutions of Eq. (2-61), because the applicability of Eq. (2-79) seems to be restricted to very small values of ε (Meiron, 1986; Ben Amar and Moussallam, 1987; Misbah, 1987). This will be discussed further in the next section.

Needle-crystal solution in three-dimensional dendritic growth

The theory of dendritic growth becomes extremely difficult, however, for three-di-

mensional (3D) anisotropic crystals. A simple extrapolation of the 2D case, where the surface energy is averaged in the azimuthal direction (axisymmetric approach, Ben Amar, 1998; Barbieri and Langer, 1989), is very important in order to have some qualitative predictions. But any physical anisotropy will give rise to a non-axisymmetric shape of the crystal. A numerical approach to the non-axisymmetric problem was presented by Kessler and Levine (1988) who pointed out the following aspect of the problem. In either the 2D or the axisymmetric case, selection of the growth velocity follows from the solvability condition of smoothness of the dendrite tip. In the 3D non-axisymmetric case a solvability condition must be satisfied for each of the azimuthal harmonics. Kessler and Levine made several approximations and performed only a two-mode calculation, but the crucial point of their analysis is that they found enough degrees of freedom to satisfy all solvability conditions.

More recently, an analytic theory of three-dimensional dendritic growth has been developed by Ben Amar and Brener (1993). In the framework of asymptotics beyond all orders, they derived the inner equation in the complex plane for the non-axisymmetric shape correction to the Ivantsov paraboloid. The solvability condition for this equation provides selection of both the stability parameter $\sigma \propto \varepsilon^{7/4}$ and the interface shape. The selected shape can be written as

$$z(r, \phi) = -\frac{r^2}{2} + \sum A_m r^m \cos m\phi \quad (2-80)$$

where all lengths are reduced by the tip radius of curvature ρ . Solvability theory (Ben Amar and Brener, 1993) predicts that the numbers A_m are independent of the anisotropy strength α , in the limit of small α . For example, the first non-trivial term for

cubic symmetry corresponds to $m=4$ and $A_4=1/96$ is only numerically small. Therefore, the shape correction, Eq. (2-80), in units of the tip radius of curvature, depends mostly on the crystalline symmetry and is almost independent of the material and growth parameters.

Stability theory for the 3D dendritic growth against tip-splitting modes has been developed by Brener and Mel'nikov (1995).

An important aspect of Eq. (2-80) is that the shift vector $r^m \cos m\phi$ grows at a faster rate than the underlying Ivantsov solution. This means that only the tip region, where the anisotropy correction is still small, can be described by the usual approximation (Kessler and Levine, 1988; Ben Amar and Brener, 1993), a linearization around the Ivantsov paraboloid. This is the crucial difference between the 3D non-axisymmetric case and the 2D case. In the latter, small anisotropy implies that the shape of the selected needle crystal is close to the Ivantsov parabola everywhere; in the former, strong deviations from the Ivantsov paraboloid appear for any anisotropy.

Several important questions arise. How is the tail of the dendrite to be described? Is it possible to match the non-axisymmetric shape (Eq. (2-80)) in the tip region to the asymptotic shape in the tail region? What is the final needle-crystal solution? The answers to these questions have been given by Brener (1993).

The basic idea is that the non-axisymmetric shape correction, generated in the tip region, should be used as an 'initial' condition for a time-dependent *two-dimensional* problem describing the motion of the *cross-section* of the interface in the tail region. In this reduced description, the role of time is played by the coordinate z for steady-state growth in the z direction. The deviation from the isotropic Ivantsov solution remains small only during the initial

period of the evolution. This initial deviation can be handled by a linear theory starting from a mode expansion which takes the same form as Eq. (2-80) with, in principle, arbitrary coefficients. These amplitudes then have to be chosen according to the predictions of selection theory (Ben Amar and Brener, 1993) in order to provide the matching to the tip region. As ‘time’ goes on, the deviation increases owing to the Mullins–Sekerka instability and a nonlinear theory must take over. We can guess what the long-time behavior of the system will be. Indeed, this two-dimensional problem is precisely the same as that which leads to two-dimensional dendritic structures. Four well-developed arms (for cubic symmetry) grow with a constant speed in the directions favored by the surface energy anisotropy. Each arm has a parabolic shape, its growth velocity, $v_2 = 2D P_2^2(\Delta) \times \sigma_2^*(\varepsilon)/d_0$, and the radius of curvature of its tip, $\varrho_2 = d_0/(P_2 \sigma_2^*)$, are given by 2D selection theory, where the anisotropic surface energy again plays a crucial role. The Péclet number $P_2 = \varrho_2 v_2/2D$ is related to the undercooling Δ by the 2D Ivantsov formula, which for small Δ gives

$$P_2 = (\Delta) = \Delta^2/\pi \quad (2-81)$$

The selected stability parameter $\sigma_2 = d_0/(P_2 \varrho_2)$ depends on the strength of the anisotropy ε , and $\sigma_2^*(\varepsilon) \propto \varepsilon^{7/4}$ for small ε as was explained above. Replacing t by $|z|/v$ and reducing all lengths by ϱ , we can present the shape of one-quarter of the interface (except very close to the dendritic backbone) in the form

$$x(y, z) = |z| \frac{v_2}{v} - \frac{y^2}{2} \frac{\varrho}{\varrho_2} \quad (2-82)$$

This asymptotic describes the strongly anisotropy interface shape far behind the tip and does not match, for small Δ , the shape described by Eq. (2-80). In this case an im-

portant intermediate asymptotic exists if the size of the 2D pattern is still much smaller than a diffusion length $(Dt)^{1/2}$. This 2D Laplacian problem (with a fixed flux from the outside) was solved, both numerically and analytically, by Almgren et al. (1993) who were interested in anisotropic Hele–Shaw flow. They found that after some transition time the system shows an asymptotic behavior which is independent of the initial conditions and involves the formation of four well-developed arms. The length of these arms increases in time as $t^{3/5}$ and their width increases as $t^{2/5}$. The basic idea that explains these scaling relations is that the stability parameter $\sigma_2 = 2D d_0/(\varrho_2^2 v_2)$ is supposed to be equal to $\sigma_2^*(\varepsilon)$ even though both v_2 and ϱ_2 depend on time. Moreover, the growing self-similar shape of the arms was determined. In terms of the dendritic problem it reads (Brener, 1993)

$$y(x, z) = (5|z|/3)^{2/5} \left(\frac{\sigma_2^*}{\sigma_2^*} \right)^{1/5} \left(\frac{x}{x_{\text{tip}}} \right)^{2/3} \times \int_{x/x_{\text{tip}}}^1 \frac{ds}{s^{2/3} \sqrt{1-s^4}} \quad (2-83a)$$

where the tip position x_{tip} of the arm is given by

$$x_{\text{tip}}(z) = (5|z|/3)^{3/5} (\sigma_2^*/\sigma^*)^{1/5} \quad (2-83b)$$

The ratio $\sigma_2^*(\varepsilon)/\sigma^*(\varepsilon)$ is independent of ε in the limit of small ε . This means that the shape, Eq. (2-83), in the tail region is almost independent of the material and growth parameters, as well as shape, Eq. (2-80), in the tip region (if all lengths are reduced by ϱ).

Recent experiments on 3D dendrites (Bisang and Bilgram, 1995) and numerical simulations (Karma and Rappel, 1998) are in very good agreement with these theoretical predictions.

2.4.2 Side-Branching Dendrites

This section provides a summary of the present understanding of dendritic growth. It is centered around numerical simulations of isolated side-branching dendrites in a one-component system where heat diffusion is the relevant dynamical process. Alternatively, it also describes dendritic growth from a two-component system at essentially constant temperature. In the latter case, we should also discuss the phase diagram; this will be covered later in the section on directional solidification. For many typical cases of growth from a dilute solution however, the information contained in this section should be sufficient.

We start with the definition of the model resulting from the set of Eqs. (2-52) to (2-55). The dynamics come from the conservation law, Eq. (2-53), at the interface. As in the previous section, we use here the form of dimensionless units introduced in Sec. 2.2.3 for the case of heat diffusion. The case of chemical diffusion (temperature then being assumed constant $= T_0$) can be treated by the same equations. The normalization is described in Sec. 2.5.2. For convenience, we will simply summarize here the basic formulas for both cases.

In contrast to Eqs. (2-37) and (2-54), we will now normalize the following equation to obtain $u=0$ at infinity, which results from adding the constant Δ to the field-variable u in all equations. Then, the diffusion field becomes

$$u = \begin{cases} (T - T_\infty)/(L_m c_p^{-1}) \\ \text{thermal diffusion} \\ (\mu - \mu_\infty)/(\Delta C \partial\mu/\partial C) \\ \text{chemical diffusion} \end{cases} \quad (2-84)$$

where μ is the chemical potential difference between solute and solvent and ΔC ($0 \leq \Delta C \leq 1$) is the miscibility gap at the operating temperature T_0 .

The dimensionless supercooling is given as

$$\Delta = \begin{cases} (T_m - T_\infty)/(L_m c_p^{-1}) \\ \text{thermal} \\ (\mu_{eq} - \mu_\infty)/(\Delta C \partial\mu/\partial C) \\ \text{chemical} \end{cases} \quad (2-85)$$

The capillary length is then

$$d = [\gamma(\vartheta) + \gamma''(\vartheta)] \begin{cases} T_m c_p L_m^{-2} \\ \text{thermal} \\ \Delta C^{-2} (\partial\mu/\partial C)^{-1} \\ \text{chemical} \end{cases} \quad (2-86)$$

The quantity $\partial\mu/\partial C$ is not easily measured, but for small $\Delta C \ll 1$ of a dilute solution, it can be related to the slope of the liquidus line dT/dC at $T_0 = T_m$ by

$$\frac{\partial\mu}{\partial C} \approx \frac{L_m}{T_m \Delta C} \left| \frac{dT}{dC} \right| \quad (2-87)$$

(Mullins and Sekerka, 1963, 1964; Langer, 1980a). Note that the chemical capillary length can be several orders of magnitude larger than the thermal length.

The boundary condition, Eq. (2-54), then simply changes to

$$u_1 = \Delta - dK - \beta V \quad (2-88)$$

where now the anisotropic capillary length d is used. The kinetic coefficient may also depend on concentration (Caroli et al., 1988), which we ignore here. Far away from the interface in the liquid, the boundary condition becomes

$$u_\infty = 0 \quad (2-89)$$

For the chemical case, we may practically ignore diffusion in the solid.

The diffusion Eq. (2-52) and the conservation law, Eq. (2-53), remain unchanged, and the diffusion length is defined as before as $l = 2D_T/V$, with V being the average velocity of the growing dendrite.

There are, of course, important differences between two and three dimensions, as a three-dimensional needle crystal is not necessarily rotationally symmetric around its axis. Snow crystals, for example, show large anisotropies in directions orthogonal to the growth direction of the primary dendritic needle (Yokoyama and Kuroda, 1988). In the immediate neighborhood of the tip, however, the deviation from this rotational symmetry is often small. Therefore, we may work with this two-dimensional model by using an “effective” capillary length. The scaling relations given below are expected to be insensitive to this apart from a constant prefactor of order unity in the $\sigma(\varepsilon)$ -relation (Kessler and Levine, 1986b, d; Langer, 1987a).

The numerical simulations were performed for a two-dimensional crystal–liquid

interface. In Fig. 2-8, we show a typical dendrite with side branches resulting from the time-dependent calculations (Saito et al., 1987, 1988) (compare with the experimental result by Glicksman et al. (1976) in Fig. 2-9). The profile is symmetric around the axis by definition of the calculation. An approximately parabolic tip has been formed from which side branches begin to grow further down the shaft (only the early stage of side-branch formation was considered). They have a typical distance which, however, is not strictly regular.

As a first result, the scaling relation, Eq. (2-68), was checked using the Péclet number from Eq. (2-56b). Experimentally, this requires the anisotropic capillary length and the supercooling to be varied independently. In Fig. 2-10, the scaled numerical results are shown as symbols for two dif-

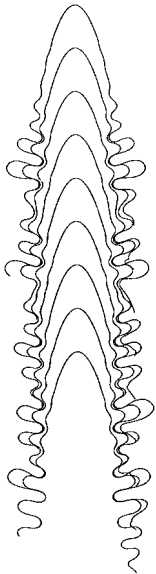


Figure 2-8. Free dendrite in stationary growth computed in quasistationary approximation for the two-dimensional case. Capillary anisotropy was $\varepsilon=0.1$ (Saito et al., 1988). The parameter-dependence of the growth rate, tip radius and sidebranch spacing is consistent with analytical scaling results from solvability theory of the needle crystal.

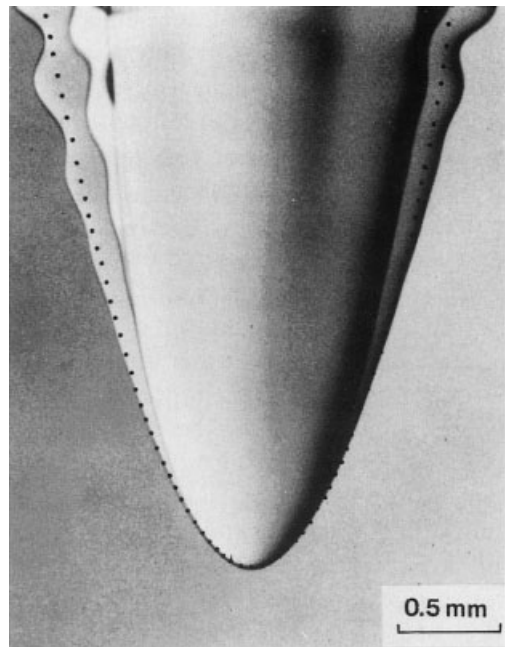


Figure 2-9. Dendrite tip in pure succinonitrile (SCN) at small undercoolings and inscribed parabola for measuring the tip radius (Huang and Glicksman, 1981).

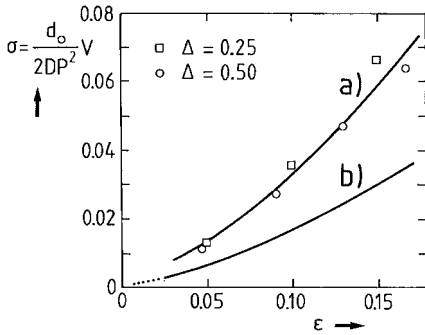


Figure 2-10. Scaling parameter $\sigma(\epsilon)$ for free dendritic growth depending on capillary anisotropy ϵ and for two-dimensional supercoolings Δ . Average capillary length is d_0 , diffusion constant D , and Péclet number P . Comparison of numerical results (circles and squares, Fig. 2-8, one-sided model) with solvability results: (a) one-sided model (Misbah, 1987), (b) two-sided model (Ben Amar and Moussallam, 1987). The agreement is excellent, the independence upon supercooling is seen to work at least up to $\Delta=0.5$.

ferent supercoolings and compared with the results (full lines) for the stationary needle crystal. The upper line corresponds to the model with diffusion in the liquid only (Misbah, 1987), as used in the numerical simulation here. The lower line corresponds to the symmetrical model with equal diffusion in liquid and solid (Ben Amar and Moussallam, 1987). Apparently, the two results look the same, apart from a factor of approximately two in σ . Note that in unscaled form (i.e., multiplying by P^2) the data for the two supercoolings would differ by about two orders of magnitude!

From an experimental point of view, it is better to use Fig. 2-10 rather than Eq. (2-79) for comparison, as the range of validity of Eq. (2-79) seems to be restricted to rather small values of ϵ . For unknown material parameters such as diffusion constant, capillary length and anisotropy, we can still check the scaling relation of the

growth rate V through the Péclet number, Eq. (2-56), depending on supercooling. Eq. (2-68) should then give a constant, although arbitrary, value of σ . This scaling result was confirmed experimentally in the 1970s, before the full theory existed (Langer and Müller-Krumbhaar, 1978, 1980). At that time, it was assumed (“marginal stability” hypothesis) that a universal value of $\sigma \approx 0.03$ was determined by a dynamic mechanism independent of anisotropy. The results for the needle crystal, together with these numerical simulations, now show that σ depends on anisotropy ϵ as shown in Fig. 2-10. Experimental tests on the ϵ -dependence (Sec. 2.4.3) are still rather sparse and do not quite fit that picture, for reasons not well understood.

So far we have only looked at the relation between growth rate, anisotropy and supercooling. We will now consider the size of the dendrite, which is approximately parabolic, and which can probably be characterized by the radius of curvature at its tip.

This is a subtle point, as the tip radius cannot easily be measured directly. As an alternative, we can try to fit a parabola to the observed dendrite in the tip region. The tip radius of this fitted parabola should be interpreted as the Ivantsov radius ϱ , which turns out to be slightly larger than the true tip radius R of the dendrite. The deviation of R for ϱ does not depend on supercooling Δ but on anisotropy ϵ . This is shown in Fig. 2-11, where a comparison is made between the dynamic numerical simulations (Saito et al., 1988) and the needle crystal solution in the limit of small Péclet number (Ben Amar and Moussallam, 1987). It can be seen that there is excellent agreement and that the actual tip radius R becomes smaller than the Ivantsov radius ϱ at increasing ϵ .

We now can relate the growth rate V and the tip radius R or the Ivantsov radius ϱ in

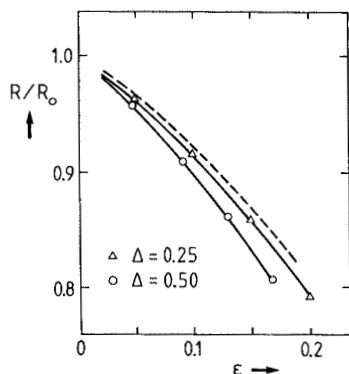


Figure 2-11. Tip radius of free dendrite over Ivantsov radius plotted versus anisotropy as a function of dimensionless supercooling. The numerical results (see also Fig. 2-8, 2-10) are consistent with the predictions from the needle solution (Ben Amar and Moussallam, 1987).

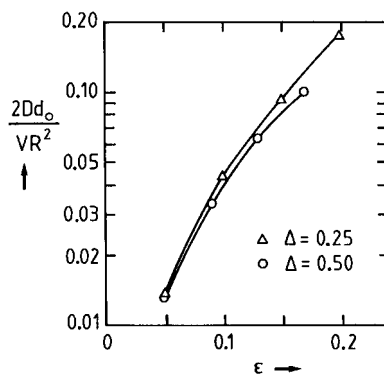


Figure 2-12. Numerical scaling result confirming $VR^2 = \text{const.}$ for free dendritic growth independent of supercooling Δ , depending on anisotropy ε only (Saito et al., 1988).

order to check the scaling form Eq. (2-68) involving the radius rather than the Péclet number. The Ivantsov parabola and its radius ϱ basically originate from a global conservation law for the quantity (heat) released at the interface, while the tip radius R is a local geometric quantity. In practical experiments, by fitting a parabola to the tip, we can interpolate between these two numbers, the result depending on how far down the shaft the fitting parabola is used. Using the actual radius R rather than the Ivantsov radius ϱ , perfect scaling can be seen in Fig. 2-12 with respect to supercooling Δ , even up to the very large value of $\Delta = 0.5$. Since for smaller supercoolings, $\Delta \leq 0.1$, the difference between ϱ and R becomes negligible, as shown in Fig. 2-11, and we may safely use Eq. (2-68) as

$$VR^2 \approx V\varrho^2 = \frac{2Dd_0}{\sigma(\varepsilon)} = \text{constant} \quad (2-90)$$

independent of supercooling Δ , to interpret experiments and to make predictions. The term “constant” here means that the product VR^2 depends on material parameters

only. This is precisely the relation, Eq. (2-1), derived from qualitative considerations in the introduction to this chapter. This relation has been confirmed by the analysis of many experiments (Huang and Glicksman, 1981).

The final point to be discussed here concerns the side branches and their origin, spacing and amplitudes. This issue is theoretically not completely resolved, because none of the available analytical approximations can correctly handle the long-wavelength limit of side-branch perturbations. Moreover, the subject is somewhat technically involved. Therefore, we will only summarize the main arguments below and refer to the above-mentioned numerical simulations (Saito et al., 1988) for comparison with experiments.

An important quantity which characterizes the stability of flat moving interface ripples is the so-called stability length

$$\lambda_S = 2\pi \sqrt{ld_0} \quad (2-91)$$

where d_0 is the capillary length, and l the diffusion length. Perturbations of wave-

lengths λ longer than λ_S will grow, while shorter wavelengths will decay with time. This quantity characterizes the competition between the destabilizing diffusion field through l against the stabilizing surface tension through d_0 . A derivation of this Mullins–Sekerka instability was given in Sec. 2.2.4.

It is natural to assume that this length scale is related to the formation of side branches. A direct estimate of the typical wavelength λ_2 of the side branches is

$$\lambda_2 \geq \lambda_S = 2\pi \sqrt{ld_0} = 2\pi \varrho \sqrt{\sigma} \quad (2-92)$$

The remarkable result of the numerical simulation is shown in Fig. 2-13. Apparently, the ratio λ_2/λ_S is a constant of approximately 2.5, which is independent of supersaturation and anisotropy. This seems to be in quite good agreement with experiments (Glicksman et al., 1976; Dougherty et al., 1987; Honjo et al., 1985; Huang and Glicksman, 1981).

The experimental comparison was made, in fact, with an older theoretical concept (Langer and Müller-Krumbhaar, 1978), which did not correctly consider anisotropy. By accident, however, the experi-

mental anisotropy of the material succinonitrile (Huang and Glicksman, 1981), $\varepsilon \approx 0.1$, gave the same σ -value as the theoretical concept, and since ε cannot be varied easily, there was no discrepancy.

To summarize these results, it appears that the scaling relation, Eq. (2-92), shown in Fig. 2-13 from the numerical solution of the model in two dimensions, is in agreement with the experimental results.

We will now give a somewhat qualitative explanation of the mechanism of side-branch formation as far as this can be deduced from the theoretical approaches. A linear stability analysis (Langer and Müller-Krumbhaar, 1978, 1980; Kessler and Levine, 1986a; Barber et al., 1987; Barbieri et al., 1987; Bensimon et al., 1987; Caroli et al., 1987; Kessler et al., 1987; Pelce and Calvin, 1987) indicates that the relevant modes for side-branch formation in the frame of reference moving with the tip consist of an almost periodic sinusoidal wave travelling from the tip down the shaft such that they are essentially stationary in the laboratory frame of reference (Langer and Müller-Krumbhaar, 1982; Deissler, 1987). The amplitude of these waves is not constant in space, but first grows exponentially in the tip region (Barbieri et al., 1987; Caroli et al., 1987). The exponential increase of that envelope in the tip region depends on the “wavelength” of the oscillatory part (Bouissou et al., 1990).

In contrast to the earlier analysis by Langer and Müller-Krumbhaar, all these modes are probably stable, so that without a triggering source of noise, they would decay, and a smooth needle crystal would result. Some driving force in the form of noise due to thermal or hydrodynamic fluctuations is needed to generate side branches, but apparently this is usually present. Estimates of the strength of these fluctuations (Langer and Müller-Krumb-

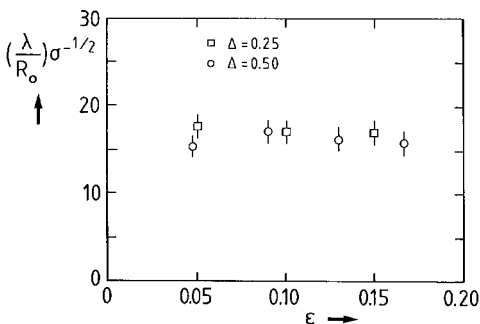


Figure 2-13. Scaled sidebranch spacing $\lambda = \lambda_2$, normalized with Ivantsov radius R_0 and $\sigma(\varepsilon)^{1/2}$, plotted versus capillary anisotropy for two supercoolings. No dependence on ε or Δ is found, as expected (Saito et al., 1988).

haar, 1982; Barbieri et al., 1987; Langer, 1987a) are still somewhat speculative.

Given such a small noise at the tip, the exponentially increasing envelope over the side branches into the direction of the tail then amplifies that noise so that the side branches become visible. This happens over a range of about two to ten side-branch spacings. The actual selected wavelength of the side branches in that tip region (assuming a white noise, triggering all modes equivalently), according to these considerations, is defined by the mode with the largest amplitude at a distance of about one "wavelength" away from the tip. This is the product of the average amplitude due to noise at the tip and the amplification factor from the envelope.

Langer (1987a) described the side-branching deformation as a small (linear) perturbation moving on a cylindrically symmetric needle crystal (Ivantsov paraboloid). The noise-induced wave packets generated in the tip region grow in amplitude, spread and stretch as they move down the sides of the dendrite producing a train of side branches. In the linear approximation, the amplitude grows exponentially and the exponent is proportional to $|z|^{1/4}$. These results are in approximate, qualitative agreement with available experimental observations (Huang and Glicksman, 1981; Dougherty et al., 1987; Bisang and Bilgram, 1995), but experimentally observed side branches have much larger amplitudes than explicable by thermal noise in the framework of the axisymmetric approach. This means that either the thermal fluctuation strength is not quite adequate to produce visible side-branching deformations, or agreement with experiment would require at least one more order of magnitude in the exponential amplification factor.

The description of the side-branching problem, which takes into account the ac-

tual non-axisymmetric shape of the needle crystal, defined by Eqs. (2-83a, b), was given by Brenner and Temkin (1995). They found that the root-mean-squared amplitude for the side branches generated by thermal fluctuations is

$$\langle \xi_l^2(Z, Y) \rangle^{1/2} \sim \bar{Q} \exp \left\{ \frac{2x^{3/2}}{3\sqrt{3}\sigma|z|^{1/2}} \right\} \quad (2-93)$$

where the function $x(z)$ is given by the underlying "needle" solution, Eq. (2-83b), and the fluctuation strength \bar{Q} is given by Langer (1987a), $\bar{Q}^2 = 2k_B T^2 c_p D / (L_m^2 \nu \varrho^4)$.

The root-mean-squared amplitude for the side branches increases with the distance from the tip, $|z|$. This amplitude grows exponentially as a function of $(|z|^{2/5}/\sigma^{1/2})$. The important result is that the amplitude of the side branches for the anisotropic needle grows faster than for the axisymmetric paraboloid shape. In the latter case $x(z) = 2|z|^{1/2}$ and the amplitude grows exponentially as a function of $(|z|^{1/4}/\sigma^{1/2})$. This effect resolves the puzzle that experimentally observed side branches have much larger amplitudes than can be explained by thermal noise in the framework of the axisymmetric approach. Agreement with experiment now is indeed very good (Bisang and Bilgram, 1995).

Far down from the tip the side-branching deformations grow out of the linear regime and eventually start to behave like dendrites themselves. It is clear that the branches start to grow as free steady-state dendrites only at distances from the tip which are of the order of the diffusion length which, in turn, is much larger than the tip radius ϱ in the limit of small P . This means that there is a large range of z , $1 \ll |z| \ll 1/P$, where the side branches already grow in the strongly nonlinear regime, but they do not yet behave as free dendrites. We can think of some fractal ob-

ject where the length and thickness of the dendrites and the distance between them increase according to some power laws with the distance $|z|$ from the tip. The dendrites in this object interact, owing to the competition in the common diffusion field. Some of them die and some continue to grow in the direction prescribed by the anisotropy. This competition leads to the coarsening of the structure in such a way that the distance between the surviving dendrites $\lambda(z)$ is adjusted to be of the same order of magnitude as the length of the dendrites, $l(z)$. The scaling arguments give $\lambda(z) \sim l(z) \sim |z|$ (Brenner and Temkin, 1995). The morphology measurements on SCN crystals yield a good quantitative agreement with this linear law (Li and Beckermann, 1998).

We now summarize the presently established findings for free dendritic growth with respect to their *experimental significance*. A discussion of additional effects such as faceting will be given in Sec. 2.5.7 in the context of directional solidification.

For a given material with fixed D , d_0 and ε , the growth rate V depends upon supercooling Δ through Eq. (2-68), and with Péclet number P taken from Eq. (2-56). The dimensionless parameter σ is given in Fig. 2-10. This is demonstrated for various materials in Fig. 2-14. The size or tip radius of the dendrite is related to its velocity by Eq. (2-90) and can be taken from Fig. 2-12. The typical wavelength of the side branches is then given by Eq. (2-92) and can be taken from Fig. 2-13. This provides all the basic information that should be valid in the tip region.

Beyond the understanding of steady-state growth of the tip, the major new concept that has emerged over the last few years is that complex pattern formation processes occurring on the much larger scale of an entire dendrite grain structure

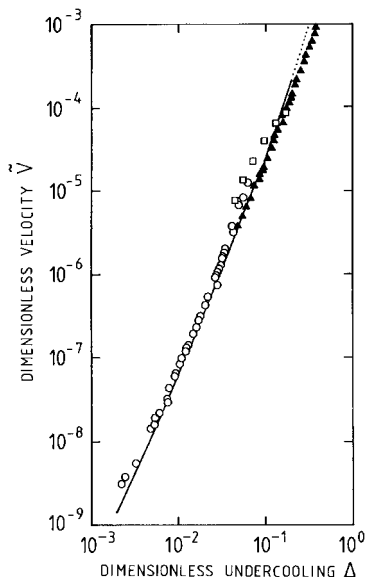


Figure 2-14. Dimensionless growth rate $\tilde{V} = Vd_0/2D$ versus dimensionless undercooling Δ . The scaling quantity for the full curve (Langer and Müller-Krumbhaar, 1977, 1978) was taken as $\sigma = 0.025$ (coincidentally in agreement with the anisotropy of succinonitrile). For references to the experimental points see Langer (1980a). Excellent agreement between theory (solid line) and experiment is found.

can be described by remarkably simple “scaling laws”. The whole dendritic structure with side-branches looks like a fractal object on a scale smaller than the diffusion length and as a compact object on a scale larger than the diffusion length (Brenner et al., 1996).

The new steady-state growth structures that have been identified are the so-called “doublons” in two dimensions (Ihle and Müller-Krumbhaar, 1994; Ben Amar and Brenner, 1995), first observed in the form of a doublet cellular structure in directional solidification (Jamgotchian et al., 1993), and the “tripylon” in three dimensions (Abel et al., 1997). Both structures have been shown to exist without crystalline anisotropy, unlike conventional dendrites. The doublon has the form of a dendrite split

into two parts about its central axis with a narrow liquid groove between the two parts, and triplons in three dimensions are split into three parts. For a finite anisotropy, however, these structures only exist above a critical undercooling (or supersaturation for the isothermal solidification of an alloy), such that standard dendrites growing along $\langle 100 \rangle$ directions are indeed the selected structures in weakly anisotropy materials at low undercoolings, in agreement with most experimental observations in organic and metallic systems. From a broad perspective, the existence of doublons and triplons is of fundamental importance because it has provided a basis on which to classify the wide range of possible growth morphologies that can form as a function of undercooling and anisotropy (Brener et al., 1996).

We have so far ignored the influence of the kinetic coefficient β in Eq. (2-88). This omission is not likely to be very important for low growth rates, but for fast growth rates, as in directional solidification, β should be taken into account. We will return to this point in Sec. 2.5.

2.4.3 Experimental Results on Free Dendritic Growth

The answer to the question of whether dendritic growth is diffusion-controlled or controlled by anisotropic attachment kinetics, was sought by Papapetrou (1935), who was probably the first to make systematic *in situ* experiments on free dendritic growth. He examined dendritic crystals of transparent salts (KCl, NaCl, NH_4Br , $\text{Pb}(\text{NO}_3)_2$, and others) under a microscope in aqueous solutions and proposed that the tip region should be close to a paraboloid of rotational symmetry.

Many years later, the extensive and systematic experiments by Glicksman and

his co-workers made an essential contribution to our understanding of dendritic growth in pure undercooled melts (Glicksman et al., 1976; Huang and Glicksman, 1981). This research was initially concerned mainly with highly purified succinonitrile (SCN). It was extended to cyclohexanol (Singh and Glicksman, 1989), water (Fujioka, 1978; Tirmizi and Gill, 1989), rare gases (Bilgram et al., 1989), and to other pure substances with a crystal anisotropy different from SCN such as pivalic acid (PVA) (Glicksman and Singh, 1989). Work on free growth of alloys includes $\text{NH}_4\text{Cl}-\text{H}_2\text{O}$ (Kahlweit, 1970; Chan et al., 1978), $\text{NH}_4\text{Br}-\text{H}_2\text{O}$ (Dougherty and Golub, 1988), SCN with acetone and argon (Glicksman et al., 1988; Chopra et al., 1988), PVA-ethanol (Dougherty, 1990), and others.

The specific merit of the work of Glicksman et al. was that the systems for which they characterized all the properties, including surface energy, diffusion coefficient, phase diagram etc., have been examined. This led to clear evidence in the mid-1970s that the theory of that time (using extremum arguments for the operating point of the tip) was not able to describe the results quantitatively.

At the same time, Müller-Krumbhaar and Langer worked on precisely the same problem and proposed a theory based on the stability of the growing dendrite tip, called the marginal stability criterion (Langer and Müller-Krumbhaar, 1977, 1978). Most of the existing experimental data could be fitted using this criterion. Despite the fact that this theory incorrectly ignored the important role of anisotropy (as we know now), it inspired a number of new experiments and also attracted the interest of other physicists.

As has been said before, today's theory is consistent with the older approximate

theory if we allow for a $\sigma(\varepsilon)$ value that varies with the anisotropy of the capillary length. The corresponding central equation for dendritic growth (Eq. (2) in Kurz and Trivedi, 1990) should therefore still apply.

Pure substances (thermal dendrites)

Fig. 2-15 shows dendrites of two different transparent materials with cubic crystal structure: face-centered cubic PVA and body-centered cubic SCN (Glicksman and Singh, 1989). Qualitatively, both dendrites look similar, but their branching behavior shows some important differences. The un-

perturbed tip of PVA is longer, with a sharper delineation of the crystallographic orientations. Glicksman and Singh (1989) found that PVA has a ten-fold larger surface energy anisotropy than SCN (see Table 2.1). The tip radii and growth rates as a function of undercooling for both substances scale well when using the values 0.22 and 0.195 for σ , respectively (Fig. 2-16). According to solvability theory, the great difference in the anisotropy constant ε should make a larger difference in $\sigma(\varepsilon)$ (compare with Fig. 2-10). The reason for this discrepancy is not known, and we have to leave this point to future research.

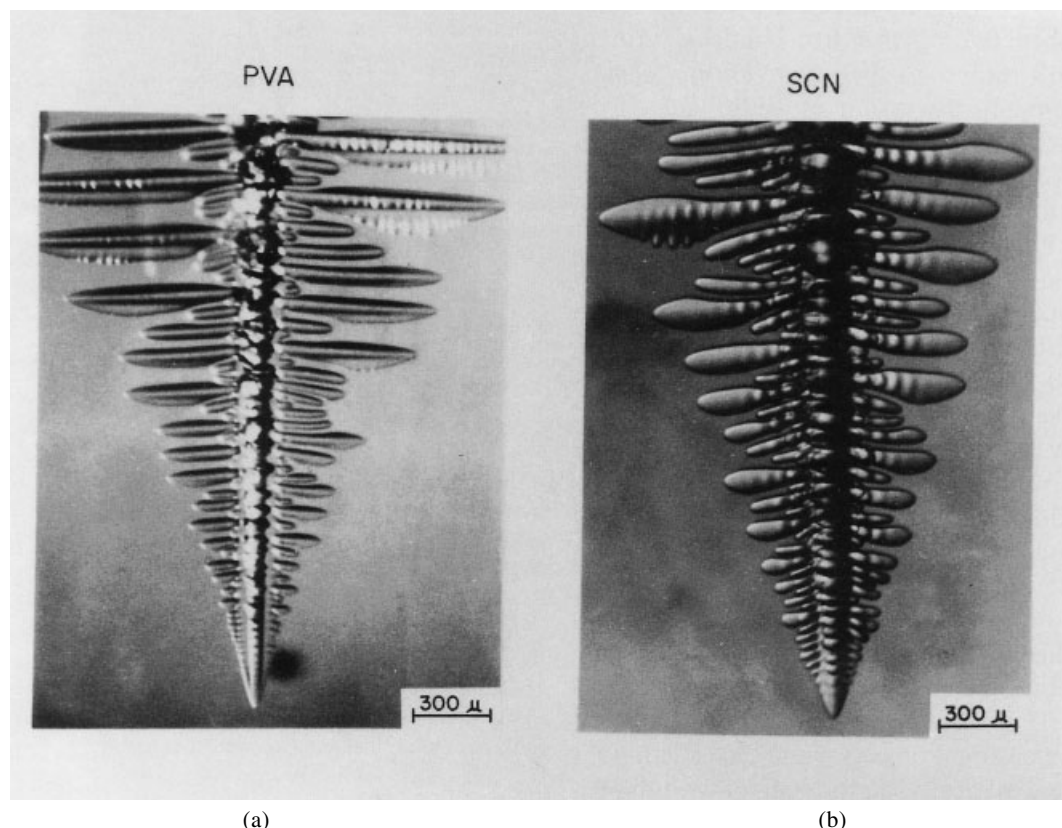


Figure 2-15. Dendrite morphologies of two transparent materials with small melting entropies and cubic crystal structures (plastic crystals); (a) pivalic acid (PVA) and (b) succinonitrile (SCN) (Glicksman and Singh, 1989).

Table 2-1. Experimentally determined dendrite tip quantities.

System	Growth type	σ^*	$R^2 V$ [$\mu\text{m}^3/\text{s}$]	λ_2/R	δ	Reference
<i>Thermal dendrites</i>						
Succinonitrile (SCN)	Pure Free	0.0195		3	0.005	Huang and Glicksman (1981)
Pivalic acid (PVA)	Free	0.022		7	0.05	Glicksman and Singh (1986, 1989)
Cyclohexanol	Free	0.027				Singh and Glicksman (1989)
<i>Solutal dendrites</i>						
NH ₄ Br–49 wt.% H ₂ O	Alloy Free	0.081 ± 0.02	18 ± 3	5.2	0.016 ± 0.004	Dougherty and Gollub (1988)
SCN–1.3 wt.% ACE	Directional	0.032*	1300	2.1 ± 0.2		Esaka and Kurz (1985)
SCN–4 wt.% ACE	Directional	0.037*	441 ± 30	2.2 ± 0.3		Somboonsuk et al. (1984)
CBr ₄ –7.9 wt.% C ₂ Cl ₆	Directional	0.044*	978 ± 8	3.18		Seetharaman et al. (1988)
C ₂ Cl ₆ –89.5 wt.% CBr ₄	Directional	0.038*	124 ± 13	3.47		Seetharaman et al. (1988)
<i>Thermal and solutal dendrites</i>						
SCN–ACE	Alloy Free	See reference				Chopra et al. (1988)
SCN–argon	Free	See reference				Chopra et al. (1988)
PVA–1 wt.% ethanol	Free	0.05 ± 0.02		6 ± 1	0.006 ± 0.002	Dougherty (1991)
PVA–2/4 vol.% ethanol	Free	0.032 ± 0.006	35	6.8		Bouissou et al. (1989)

* Due to differences in the definitions of σ^* these values, as given in the corresponding literature, are smaller by a factor of 2 with respect to the values used by Dougherty and Gollub (1988) and defined in this paper. The values given here have been obtained by multiplying the original data by a factor of 2 in order to compare with the same (one-sided) model. (See also Fig. 2-10.)

Koss et al. (1999) have shown that even in microgravity environment there is a small but significant difference between transport theory and experiment. Again this has to be left to the future.

The secondary branch formation which starts in SCN at a distance of three tip radii

behind the tip is delayed up to about seven radii in PVA. This is quite consistent with the recent calculations discussed in Sec. 2.5.4. The ratio of initial secondary arm spacing λ_2 over tip radius R is also indicated in Table 2-1.

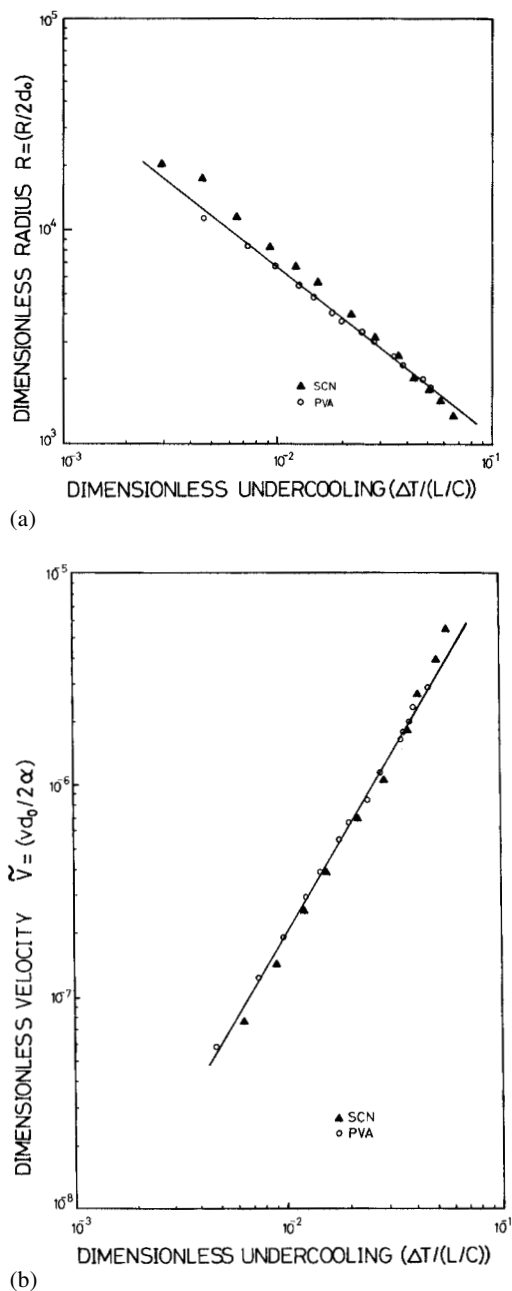


Figure 2-16. Effect of undercooling on (a) tip radius and (b) growth rate of the two organic materials shown in Fig. 2-15 ($\alpha = D$). The experimental results superimpose as they are plotted with respect to dimensionless parameters (Glicksman and Singh, 1989).

Free alloy growth (thermal and solutal dendrites)

In the free dendritic growth of alloys, an interesting observation has been made by various authors. For constant undercooling, the growth rate first increases when small amounts of a second substance are added to a pure material, then reaches a maximum, and finally drops and converges with the pure solutal case. Early experiments in this area by Fujioka and Lindemeyer were first successfully analyzed by Langer (1980c). Fig. 2-17 shows some results on SCN–ACE alloys from Chopra et al. (1988). The increase in V is accompanied by a decrease in the tip radius, which sharpens due to the effect of solute. The experimental findings can be compared to two models: Karma and Langer (1984) (broken line) and Lipton et al. (1987) (full line). Both models provide at least qualitatively good predictions of the observed behavior. In their more recent calculations, Ben Amar and Pelce (1989) concluded that the simple model by Lipton et al. (1987) is consistent with their more rigorous approach.

Table 2-1 gives a summary of representative results of *in situ* experiments concerning the dendrite tip.

Large undercoolings

Interesting experiments have also been performed with pure and alloyed systems under large driving forces, which reach values beyond unit undercooling (for example by Wu et al. (1987) and especially by Herlach et al. (1990–1999), see Table 2-2).

Some of these are reproduced in Fig. 2-18 together with predictions from IMS (Ivantsov–marginal stability) theory (Lipton et al., 1987; Trivedi et al., 1987; Boettinger et al., 1988) (with $\sigma(\epsilon) = 0.025$) and including interface attachment kinetics.

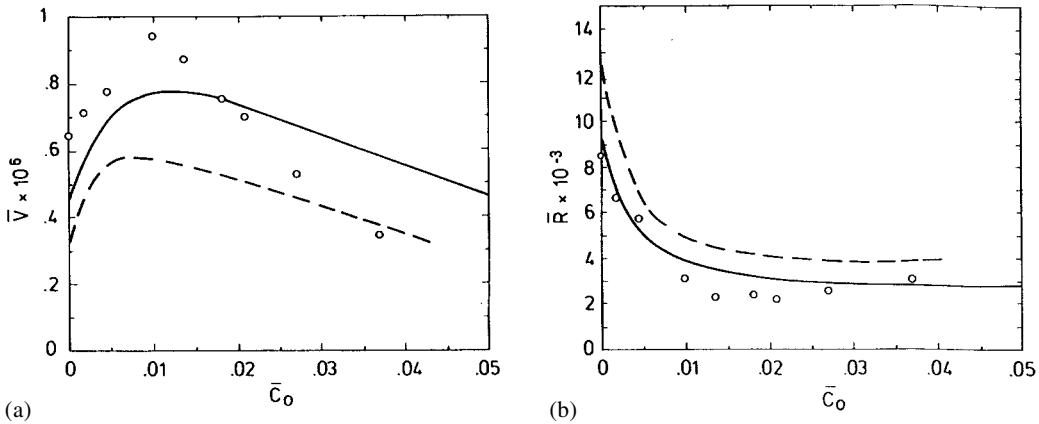


Figure 2-17. Effect of dimensionless composition at constant undercooling of 0.5 K (2.1% of unit undercooling) on (a) dimensionless growth rate and (b) on dimensionless tip radius for free dendritic growth in SCN–acetone alloys (Lipton et al., 1987). Points: experiments (Chopra et al., 1988); solid line: LGK model (Lipton et al., 1987); interrupted line: Karma and Langer (1984) model.

These results are specifically of interest because two different techniques, one for the determination of the diffusive speed and the other for the undercooling–growth rate relationship of the dendrites, have been coupled in order to make the analysis as free from adjustable parameters as possible. Up to undercoolings of 200 K there is reasonable agreement between experiment and theory using the best fit for the measured diffusive speed and the liquid diffusivity, $V_D = 26$ m/s and $D_L = 2.7 \times 10^{-9}$ m²/s (Arnold et al., 1999). The lower $V(\Delta T)$ -curve is for a constant (equilibrium) value of the distribution coefficient $k(V) = k_e$ showing the importance of the appropriate velocity dependence of the distribution coefficient.

At higher undercoolings other phenomena take over.

One example is the grain refinement beyond a certain undercooling. This structure has been explained by dendrite fragmentation due to morphological instability of the fine dendrite trunks (Schwarz et al., 1990; Karma, 1998).

Table 2-2. Dendritic growth velocity measurements in highly undercooled melts; comparison between experiment and theory (Herlach and coworkers, 1999–2000).

Metals and alloys

Co–Pd	Volkman et al. (1998)
Co–V	Tournier et al. (1997)
Cu	Li et al. (1996)
Ni	Eckler and Herlach (1994)
Ni–Al	Barth et al. (1994), Assadi et al. (1998)
Ni–B	Eckler et al. (1991 a, 1992, 1994)
Ni–C	Eckler et al. (1991 b)
Ni–Si	Cochrane et al. (1991)
Ni–Zr	Schwarz et al. (1997), Arnold et al. (1999)

Intermetallics

CoSi	Barth et al. (1995)
FeAl	Barth et al. (1997)
FeSi	Barth et al. (1995)
Ni ₃ Al	Assadi et al. (1996)
Ni _x Sn _y	Barth et al. (1997)
NiTi	Barth et al. (1997)
Ni _x Ti _y Al _z	Barth et al. (1997)

Semiconductors

Ge	Li et al. (1995 a, 1996)
Ge–Cu	Li and Herlach (1996)
Ge–Si	Li et al. (1995 b)
Ge–Sn	Li and Herlach (1996)

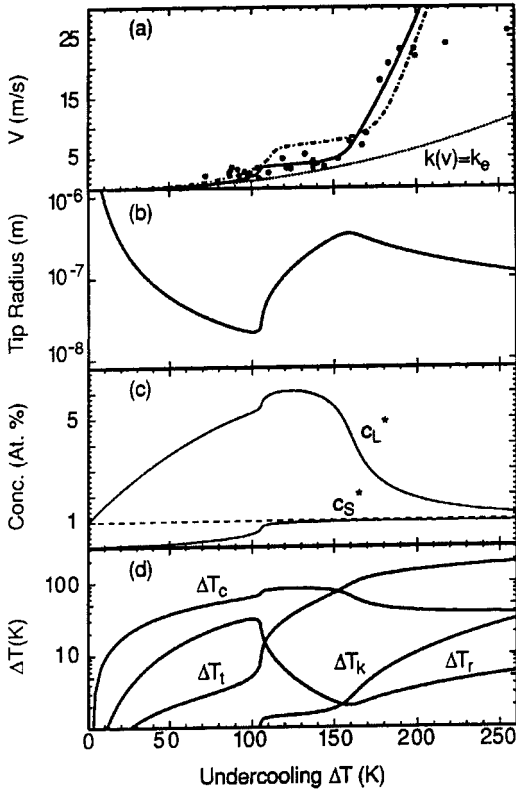


Figure 2-18. Dependence on total bath undercooling of Ni–1 wt. % Zr alloy. (a) Dendrite growth velocity, as measured (dots), and results from Ivantsov–marginal stability dendrite growth theory using the values $V_D=26$ m/s and $D_l=2.7 \times 10^{-9}$ m²/s. The lower curve in (a) is for local equilibrium partition. (b) The calculated dendrite tip radius, (c) the computed interface compositions and (d) the individual undercooling contributions: thermal undercooling ΔT_t , constitutional undercooling ΔT_c , curvature undercooling ΔT_r , and attachment kinetic undercooling ΔT_k (Arnold et al., 1999).

2.5 Directional Solidification

Directional solidification is the most frequent way in which a material changes its state from solid to liquid. The necessary removal of the latent heat of freezing usually occurs in a direction prescribed by the location of heat sinks: for a freezing lake, it

is the cold atmosphere above it, in casting iron in a foundry, it is the cold sand mold, into which the heat flow is directed.

At first, it may seem surprising to think that anything interesting should happen at the solid–liquid interface during this process. In contrast to the situation described earlier, in Secs. 2.4 and 2.2.4, the solid in a casting process is cold and the liquid is hot, so that we would expect the interface to be stable against perturbations.

However, so far we have just considered the solidification of a one-component material, while in reality a mixture of materials is almost always present, even if one of the components is rather dilute. If, therefore, we assume that material diffusion is the rate-determining (slow) mechanism, while heat diffusion is much faster, the origin of a destabilization of the flat interface can be easily understood on a qualitative basis. We may consider one of the two components of the liquid as an “impurity”, which, instead of being fully incorporated into the solid, is rejected at the interface. Such excess impurities have to be diffused away into the liquid in much the same way as latent heat has to be carried away in the case of a pure material as a rate-determining mechanism. Accordingly, precisely the same destabilization and subsequent formation of ripples and dendrites should occur.

Based on these qualitative arguments we can expect the following modification of the Mullins–Sekerka instability (Sec. 2.2.4) to occur in the present situation of directional solidification. The diffusion of material together with capillary effects produces a spectrum for the growth rates or the decay rates similar to Eq. (2-50), while the temperature field acts as a stabilizer, independent of the curvature of the interface, when a constant term (independent of V) inside the brackets of Eq. (2-50) is sub-

tracted. At low solidification rates, the flat interface is stable; above a critical speed, it becomes unstable against the formation of ripples, cells and dendrites.

In the next section, a few thermodynamic questions related to interface properties in two-component systems are considered, before describing patterns in directional solidification.

2.5.1 Thermodynamics of Two-Component Systems

There is a vast amount of literature available on the thermodynamics of solidification and on multi-component systems (for example Callen, 1960; Baker and Cahn, 1971). Despite this fact, to further the clarity of presentation, we would like to at least sketch the tools that may be used to generalize some approximations which will be made in the next sections.

The fundamental law of thermodynamics defines entropy as a total differential in relation to energy and work:

$$dU = T dS - P dV + \sum_i \mu_i dN_i \quad (2-94)$$

with energy U , entropy S , volume V , pressure P , particle numbers N_i for each species and chemical potential μ_i . The energy is a homogeneous function of the extensive variables

$$U(bS, bV, bN_i, \dots) = bU(S, V, N_i, \dots) \quad (2-95)$$

with an arbitrary scale parameter $b > 0$.

With the differentiation rule $d(XY) = XdY + YdX$, other thermodynamic potentials \tilde{U} are obtained from U by Legendre transformations

$$\tilde{U} = U - \sum_j X_j Y_j \quad (2-96)$$

where X_j are some extensive variables, and Y_j the corresponding intensive variables.

The Helmholtz energy F is then

$$F(T, V, N_i, \dots) = U - TS; \\ dF = -S dT - P dV + \sum_i \mu_i dN_i \quad (2-97)$$

and the often-used Gibbs energy G is

$$G(T, P, N_i, \dots) = U - TS + PV = \sum_i \mu_i dN_i; \\ dG = -S dT + V dP + \sum_i \mu_i dN_i \quad (2-98)$$

At atmospheric pressure in metallurgical applications, the differences between F and G often can even be neglected, but generally the Gibbs energy, Eq. (2-98), is most frequently used. It follows immediately that the chemical potentials μ_i are defined as

$$\left(\frac{\partial G}{\partial N_i} \right)_{T,P} = \mu_i \quad (2-99)$$

The thermodynamic equilibrium for a system is defined by the minimum of the respective thermodynamic potential with respect to all unconstrained internal parameters of the system. If the system consists of two subsystems α and β in contact with each other, then in thermal equilibrium the temperatures, pressures, and the chemical potentials for each particle type i must be equal:

$$T_\alpha = T_\beta, \quad P_\alpha = P_\beta, \quad \mu_{i,\alpha} = \mu_{i,\beta} \quad (2-100)$$

For the case under consideration we have a solid phase α (with assumed low concentration of B atoms) and a liquid phase β (with higher concentration of B atoms). For simplicity, we further assume that the atomic volumes of both species are the same and unchanged under the solid-liquid transformation.

For a system with a curved interface between a solid and a liquid of different compositions, the chemical potentials can be calculated as follows. Assuming that N_A particles of solvent and N_B particles of solute are given, there will be an unknown

this temperature, we first hit the liquidus line $\tilde{C}_L(T)$, and the system begins to solidify, producing a solid of very low concentration marked by the solidus line $\tilde{C}_S(T)$. When the temperature is slowly lowered, solidification becomes complete at T_0 . At lower temperatures, the whole system is solid.

The region between $\tilde{C}_S(T)$ and $\tilde{C}_L(T)$ is the two-phase region: if we prepare a system at a concentration between C_S^0 and C_L^0 at high temperatures and then quickly quench it to T_0 , the system starts to separate into a solid phase of concentration C_S^0 and a liquid phase of C_L^0 . In practice, this is a very slow process, with lengths varying with time t approximately as $t^{1/3}$ (Lifshitz and Slyozov, 1961; Wagner, 1961).

In the case of directional solidification, a thermal gradient in the system defines a direction such that the liquid is hot and the solid is cold. A flat interface may then be present at a position in space at temperature T_0 . For equilibrium between solid and liquid at that temperature, the concentration in the solid must be at $C_S^0 = C_\infty$, and in the liquid at $C_L^0 = \tilde{C}_L(T_0)$. We now assume that the liquid at infinity has concentration C_∞ . Clearly there must be a decrease in concentration as we proceed from the interface into the liquid. In order to maintain such an inhomogeneous concentration, the interface must move toward the liquid.

In other words, when the liquid of composition C_L^0 freezes, the solid will only have a concentration C_S^0 . The difference in concentrations

$$\Delta C = C_L^0 - C_S^0 \quad (2-103)$$

is not incorporated but is pushed forward by the advancing interface and must be carried away through diffusion into the liquid. This is equivalent to the latent heat generated by a pure freezing solid, discussed in Sec. 2.2.3. Therefore, we expect a spatial

concentration profile ahead of the interface which decays exponentially from C_L^0 at the interface to C_∞ far away from the interface. But why should it decay to C_∞ (or why should the interface choose a temperature position such that $C_S^0 = C_\infty$)?

The answer is quite simple, and again was given in similar form in Sec. 2.2.3, Eq. (2-33) for the pure thermal case: if C_S^0 were not identical to C_∞ , then during the solidification process there would be either a total increase (or decrease) of concentration – which clearly is impossible – or at least the concentration profile could not be stationary.

This is a rather strict condition, which we can reformulate as follows: if we impose a fixed temperature gradient $\partial T/\partial z$ and move this at fixed speed V_0 over a system of concentration C_∞ at infinity in the liquid (toward the liquid in the positive z -direction), then the interface will choose a position such that its temperature is at T_0 , the concentration in the solid will be C_S^0 (averaged parallel to the interface), and the liquid concentration at a flat interface will be at C_L^0 . This follows from global conservation of matter together with the imposed stationary solidification rate.

As a final point, we can even derive a condition for the stability of the interface. The concentration profile in the liquid will decay exponentially with distance z away from the interface as

$$C_L(z) = (C_L^0 - C_\infty) e^{-2z/l} + C_\infty \quad (2-104)$$

by analogy to Eq. (2-32). Since we assume the temperature gradient

$$G_T = \partial T/\partial z > 0 \quad (2-105)$$

to be fixed, the temperature varies linearly with distance z from the interface. This may be written (by $G_T = (T - T_0)/z$) as

$$C_L(T) = (C_L^0 - C_\infty) e^{-2(T-T_0)/(l G_T)} + C_\infty \quad (2-106)$$

and incorporated into Fig. 2-19 as a dashed-dotted line. Note that the diffusion length l is again defined as $l = 2D/V_0$, with D being the diffusion constant of solute atoms in the solvent, and V_0 the interface velocity imposed by the advancement rate of the temperature gradient.

From Eq. (2-106), it is obvious that the dashed-dotted concentration line in Fig. 2-19 converges very quickly to C_∞ for high solidification speeds V_0 . As long as that concentration line is fully in the liquid region of the phase diagram, nothing specific happens. But if the dashed-dotted line partly goes through the two-phase region between $\tilde{C}_S(T)$ and $\tilde{C}_L(T)$, the liquid in front of the interface is supercooled! This implies the possibility of an instability of the solid–liquid interface, which is completely analogous to the discussion in Sec. 2.2.4.

A sufficient condition for stability of the interface in directional solidification is therefore

$$\Delta C \frac{V}{DG_T} < \left| \frac{d\tilde{C}_L}{dT} \right| \quad (2-107)$$

so that the dashed-dotted curve remains outside the two-phase region (Mullins and Sekerka, 1963; Langer, 1980a). Here we have assumed that material diffusion in the solid can be ignored. In fact, in practical situations, violation of this condition typically means “instability” of the interface, so that cellular or dendritic patterns are formed. The reason for this latter conclusion is that the effect of stabilization due to capillarity (or surface tension) is rather weak for typical experiments at threshold.

In summary, in this section we have derived both the boundary condition – in terms of chemical potential – for a curved interface and a basic criterion for interface stability during directional solidification.

2.5.2 Scaled Model Equations

A theoretical analysis of practical situations of directional solidification suffers – among other problems – from the many relevant parameters entering the description. The usual way to proceed in such cases is to scale out as many parameters as possible, writing the problem in dimensionless variables. We have done this already in the discussion of free dendritic growth by introducing the dimensionless diffusion field u ; in hydrodynamic applications, it is common practice to use Reynolds and Rayleigh numbers (Chandrasekhar, 1961).

For our present problem, we will proceed in an analogous way. The first step is to express all experimental parameters (wherever possible) in length units (i.e., diffusion length, capillary length, etc.). For presenting results, we divide these lengths by the thermal length introduced below, as this is a macroscopic length which will approximately set the scale at the onset of the instability.

Directional solidification involves chemical diffusion of material together with heat diffusion. As heat diffusion is usually faster by several orders of magnitude, we may often assume constant temperature gradients to exist in the liquid and in the solid. Furthermore, we will also assume that there are equal thermal diffusivities in liquid and solid, which is often the case within a few percent, but this has to be checked for concrete applications. The diffusion field to be treated dynamically then corresponds to the chemical concentration.

It is clear from the discussion in the previous section that for a flat interface moving at constant speed there is a concentration jump $\Delta C = C_L^0 - C_S^0$ across the interface, while in the liquid and in the solid, the term C_∞ is approached asymptotically because of the condition of stationary

movement, together with the global conservation of matter. We therefore normalize the diffusion field in the liquid to

$$u_L = \frac{C(\text{Liquid}) - C_\infty}{\Delta C} \quad (2-108)$$

so that it varies from one to zero in the positive z -direction from the interface at $z=0$ to $z=\infty$. If the interface is not at position $z=0$ but at ξ , we must require $u_L = 1 - \xi/l_T$, because at a distance

$$l_T = \frac{\Delta C}{G_T} \left| \frac{dT}{d\tilde{C}_L} \right| \quad (2-109)$$

the liquidus concentration has reached the asymptotic value. This is the thermal length which we assume to be fixed by the thermal gradient G_T , the concentration jump ΔC , and the liquidus line $\tilde{C}(T)$, which is here assumed to be a straight line in the T vs. C diagram.

The equation of motion in quasi-stationary approximation then becomes, in analogy to Eq. (2-52) with $l = 2D_L/V$

$$\frac{1}{D_L} \partial_t u_L \approx 0 = \nabla^2 u_L + \frac{2}{l} \frac{\partial u_L}{\partial z} \quad (2-110)$$

This equation applies equivalently to the solid but with a different chemical diffusion length l' due to different chemical diffusion constants. The boundary condition in analogy to Eq. (2-88) obviously becomes

$$u_L(\xi) = 1 - dK - \xi(x, t)/l_T - \beta V_\perp \quad (2-111)$$

where we now have $\Delta=1$ as the first term on the r.h.s., with curvature K being positive for the tip of a solid nose pointing into the liquid. The capillary length d is discussed below and interface kinetics with $\beta \neq 0$ will be discussed in Sec. 2.5.4. The solid boundary condition is simply

$$u_S = k(u_L - 1) \quad (2-112)$$

with segregation coefficient k (equilibrium values assumed) defined as

$$k = \left| \frac{dT}{d\tilde{C}_L} \right| \left/ \left| \frac{dT}{d\tilde{C}_S} \right| \right. \quad (2-113)$$

through the slopes of the liquidus and solidus lines. When they intersect at $\{T_m, C=0\}$ this is equivalent to the conventional definition $k = C_S/C_L$, but in the above formulation, $k=1$ may also be true for a constant jump in concentrations, independent of temperature.

The conservation law at the interface $z = \xi$ finally becomes

$$V_\perp \{1 + (1 - k)(u_L - 1)\} = -D_L \hat{n} \cdot \nabla u_L + D_S \hat{n} \cdot \nabla u_S \quad (2-114)$$

where V_\perp is the interface velocity in direction \hat{n} normal to the interface. For $k=1$, the brackets $\{\dots\}$ give 1, corresponding to a constant concentration jump, while for $k=0$, they give u_L , since for a solid in Eq. (2-112), $u_S=0$.

This standard model for directional solidification (Saito et al., 1989) therefore consists of Eqs. (2-108) to (2-114), together with an additional diffusion equation as Eq. (2-110) inside the solid phase.

The open point is finally the relation of the capillary length d (Eq. (2-111)) with experimentally measurable material parameters. As a first step, we interpret the u -field, Eq. (2-108), as a scaled form of the chemical potential μ (see Sec. 2.5.1) near T_0

$$u_L = \frac{\mu - \mu_\infty}{\Delta C (\partial \mu / \partial \tilde{C}_L)} \quad (2-115)$$

assuming that linearizing μ around its equilibrium value at the liquidus line $\tilde{C}_L(T_0)$ is sufficient to describe its dependence upon C . By the definitions in Eq. (2-102) together with Eq. (2-111), we now obtain the capillary length in the form given in Eq. (2-86) for the chemical case. Here we have

generalized to anisotropic γ as derived in Eq. (2-21). It can finally be related to measurable quantities using the Clausius–Clapeyron equation for the latent heat L_m of freezing of a solution at T_m

$$L_m = -T_m \Delta C (d\mu/dT)_{\text{coex}} \quad (2-116)$$

where $(d\mu/dT)_{\text{coex}}$ is the slope of the coexistence line when μ is plotted against T . Together with

$$\left(\frac{d\mu}{dT}\right)_{\text{coex}} = \left(\frac{\partial\mu}{\partial C}\right) \frac{d\tilde{C}_L}{dT} + \frac{\partial\mu}{\partial T} \quad (2-117)$$

this gives for the chemical capillary length, d , in the limit of small ΔC

$$d = [\gamma + \gamma''(\vartheta)] \frac{T_m}{\Delta C L_m |\partial T / \partial \tilde{C}_L|} \quad (2-118)$$

Certain approximations used here, such as the linearization involved in Eq. (2-115) or neglecting of $\partial\mu/\partial T$ in Eqs. (2-118), may not be safe for the case of a large segregation coefficient $k \approx 1$ or when ΔC is large (Langer, 1980a). In most practical applications, however, this is a minor source of error in comparison with other experimental uncertainties. Furthermore, the concentration jump ΔC in Eq. (2-118) is kept fixed, while in reality it should correspond to the temperature-dependent difference in concentration between the liquidus and solidus lines. Both for slow and fast growth rates, however, this only gives a minor correction, and we will ignore its effect in order to facilitate comparison with free dendritic growth.

In summary, with this model we now have all the ingredients to discuss some basic features of directional solidification by analytical and numerical tools. The presentation in the scaled form may not seem at first to be the most convenient means of direct comparison with experiments. Its great advantage over an explicit incorporation of

all parameters is that qualitatively different behavior always corresponds to different ratios of length scales or time scales rather than some differences in absolute measures, and, consequently, this presentation allows for a more intuitive formulation of results.

2.5.3 Cellular Growth

A plane interface between the solid phase and the liquid phase of a two-component system tries to locate its position in a thermal gradient so that the chemical potentials of both components are continuous across the interface. Under stationary growth conditions, that position corresponds to a temperature, such that the concentration in the solid (solidus line of the phase diagram) is equal to the concentration in the distant liquid. This growth mode persists for velocities up to a critical velocity, above which the interface undergoes a Mullins–Sekerka instability toward cellular structures. A necessary condition for this instability to occur follows from Eq. (2-107), which can be written in terms of chemical diffusion length $l = 2D/V$ and thermal diffusion length l_T , Eq. (2-109), as

$$l/l_T \lesssim 2 \quad (2-119)$$

The 2 comes from the specific definition of l , and the inequality for instability is only approximate because minor surface tension effects have not yet been considered here. Incorporation of surface tension reveals that the instability first occurs for a critical wavelength λ_c larger than the stability length $\lambda_s = 2\pi\sqrt{d_l}$. Slightly above the critical pulling speed V_c , the interface makes periodic structures of finite amplitude. This was analyzed by Wollkind and Segel (1970), and for other specific cases, by Langer and Turski (1977). A more general treatment was given by Caroli et al. (1982).

The result of these investigations is that in a diagram of pulling speed V versus wavelength λ there exists a closed curve of neutral stability, Fig. 2-20. At fixed V , a small amplitude perturbation of the interface at a wavelength on that curve neither grows nor decays. Perturbations at wavelengths outside that curve decay, inside the curve they grow to some finite amplitude. This is similar to periodic roll patterns in the Rayleigh–Benard system of a fluid heated from below (Chandrasekhar, 1961), but here a maximal speed, V_a , is present, above which a flat interface is absolutely stable. For normal alloys, this speed is very high, while for liquid crystals, it is more easily accessible in controlled experiments (Bechhoefer et al., 1989). The diffusion length at V_a is of the order of the capillary length.

At low speeds, but slightly above the critical velocity, V_c sinusoidal “cells” will be formed for systems with segregation coefficients k near unity. For small segregation coefficients, however, the neutral

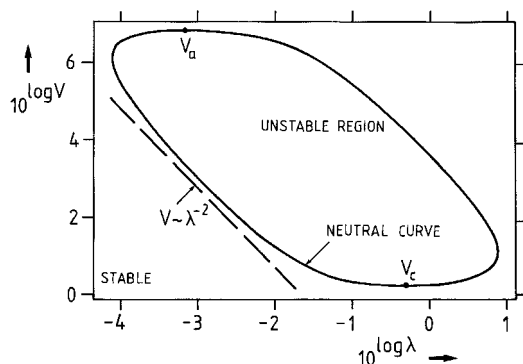


Figure 2-20. Neutral stability curve for a flat solid–liquid interface in directional solidification (schematic). The dependence of the growth rate (pulling speed) V on the wavelength λ of the interface perturbation is approximately $V \sim \lambda^{-2}$, both for the short and long wavelength part of the neutral stability curve, V_c and V_a are the lower critical velocity and upper limit of absolute stability, respectively.

curve does not define such a normal bifurcation but rather an inverse bifurcation. This means that immediately above V_c large amplitude cells with deep grooves are formed. A time sequence of the evolution of a sinusoidal perturbation into elongated cells at 1% above V_c due to inverse bifurcation is shown in Fig. 2-21. This can be understood theoretically (Wollkind and Segel, 1970; Langer and Turski, 1977; Caroli et al., 1982) by means of an amplitude equation valid near V_c :

$$\frac{\partial A}{\partial t} = \left(\frac{V - V_c}{V_c} \right) A - a_1 |A|^2 A + \dots \quad (2-120)$$

where A is the (possibly complex) amplitude of a periodic structure $\exp(ikx)$ with $k = 2\pi/l_c$. The coefficient a_1 is called the Landau coefficient. If it is positive, we have

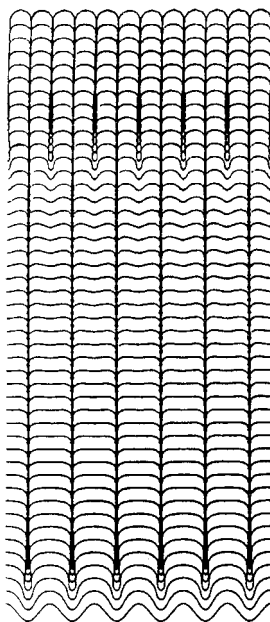


Figure 2-21. Time evolution of an interface from sinusoidal to cellular structure slightly above the critical threshold V_c for the case of inverse bifurcation. A secondary instability quickly leads to a halving of the wavelength.

a normal bifurcation with $|A| \sim \sqrt{V - V_c}$, while for $a_1 < 0$, the third order term does not stabilize the pattern but allows very large amplitudes leading to elongated cells (Fig. 2-21), which will be stabilized by some higher-order effects.

A second phenomenon is usually associated with this inverse bifurcation, namely, the splitting of the wavelength $\lambda_c \rightarrow \lambda_c/2$. Qualitatively, this is understandable from nonlinear corrections since the squaring of the original pattern $\sim \exp(ikx)$ produces terms $\sim \exp(i2kx)$. This effect has clearly been observed in experiments (de Cheveigne et al., 1986).

We will discuss some aspects of the very high speed region in Sec. 2.5.7 but devote the main part of the following discussions to the most interesting region for practical purposes, which is not too close to the upper and lower bounds of the growth rate V_a and V_c .

Approximating by straight lines the neutral curve of the logarithmic plot Fig. 2-20 in the intermediate velocity region, we find for both the small and the large λ limits the relation

$$V\lambda^2 \approx \text{constant} \quad (2-121)$$

Again we have recovered the form of Eq. (2-1) mentioned in the introduction as a scaling law where λ here is the cell spacing. This suggests that the cellular pattern formed in actual experiments would also follow this behavior. Unfortunately, this problem has not yet been settled to a satisfactory degree from a theoretical point of view. This is partly due to the difficulty of finding good analytical approximations to the cellular structures, which makes numerical calculations necessary to a large degree. We will return to this point in Sec. 2.5.5.

For small amplitude cells obtainable under normal bifurcation, some progress

has been made (Brattkus and Misbah, 1990). A phase-diffusion equation has been derived describing the temporal evolution of a pattern without complete periodic variation of the interface. The basic idea is to replace the periodic trial form $\exp(ikx)$ by a form $\exp(i\Theta(x, t))$ so that $q(x, t) = \partial\Theta/\partial x$ is now no longer a constant but is slowly varying in space along the interface and evolving with time. We can derive a nonlinear phase diffusion equation

$$\partial_t q = \partial_x \{ \tilde{D}(q) \partial_x q \} \quad (2-122)$$

with a diffusion coefficient $\tilde{D}(q)$ depending in a complicated way on q . The procedure is well known in hydrodynamics and it is associated there with the so-called Eckhaus instability (Eckhaus, 1965). This instability eventually causes an (almost) periodic spatial structure to lose or gain one "period", thereby slightly changing the average wavelength. In directional solidification, the result (Brattkus and Misbah, 1990) is shown in Fig. 2-22, where velocity is plotted against wavenumber in a small interval above the critical velocity. The full line is the neutral curve, the full triangles mark the Eckhaus boundary of phase stability. A periodic (sinusoidal) pattern is stable against phase slips only inside the region surrounded by triangles, thereby allowing for an Eckhaus band of stationary periodic solutions with a substantially reduced spread in wavenumbers as compared to the linear stability results. Note also that the results for phase stability (dashed line) from the amplitude equation only hold in an extremely small region above V_c , while only 20% above V_c , it shows no overlap with the result from the present analysis (triangles). The short-wavelength branch has a very complicated structure, while the long-wavelength branch far from the threshold scales as $\lambda_{\text{Eck}} \sim V^{-1/2}$, again like the neutral curve. This also seems to be in

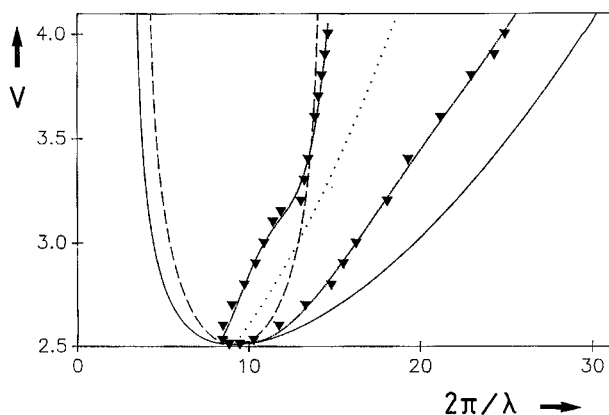


Figure 2-22. Stability diagram V vs. $2\pi/\lambda$ near the lower critical threshold for a flat moving interface in directional solidification. The solid line is the neutral stability curve Fig. 2-20, the dotted curve is the most dangerous mode, the dashed curve is the limit of the Eckhaus stability from the amplitude equation. The triangles mark the Eckhaus limit as obtained from the full nonlinear analysis (Brattkus and Misbah, 1990), with stable cellular interfaces possible only inside that region. The band width of possible wavelengths for cellular interfaces accordingly is smaller by a factor of ≈ 0.4 , as compared to the band width given by the neutral (linear) stability curve.

agreement with experimentally observed results, as discussed later (Billia et al., 1987, 1989; Somboonsuk et al., 1984; Esaka and Kurz, 1985; Eshelman and Trivedi, 1987; Faivre et al., 1989; Kurowsky, 1990).

At higher velocities, the cells quickly become elongated (Fig. 2-23) with deep grooves forming bubbles. This was first obtained through numerical calculations by Ungar and Brown (1984a, b, 1985a, b). Calculations with a dynamical code in quasi-stationary approximation (Saito et al., 1989) confirmed the stability of these structures with respect to local deformations and short-wavelength perturbations. The long-wavelength Eckhaus stability has not been investigated yet for these cells. All calculations were made in two dimensions, which are believed to be appropriate for experiments of directional solidification in a narrow gap between glass plates.

At higher velocities and wavelengths (or cell sizes) not much smaller than the diffusion length, the grooves become very

narrow, similar to Fig. 2-21 (Ungar and Brown, 1984a, b, 1985a, b, Karma, 1986, Kessler and Levine, 1989, McFadden and Coriell, 1984, Pelce and Pumir, 1985).

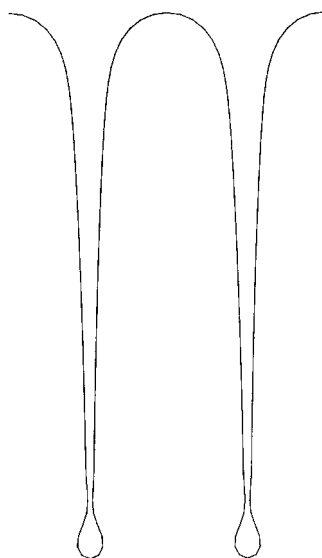


Figure 2-23. Computed example for a deep cellular interface at $V \approx 5 V_c$ with bubble formation at the bottom of the groove (Saito et al., 1990).

If the velocity is fixed and the wavelength λ is reduced significantly below the diffusion length l , the Saffmann–Taylor limit is reached (Brener et al., 1988; Dombre and Hakim, 1987; Kessler and Levine, 1986c), which is equivalent to a low-viscosity fluid being pushed into a channel of width λ filled with a high-viscosity fluid. The low-viscosity fluid forms a finger just like the solid in directional solidification. Near the tip, the width of the finger λ_f corresponds to

$$\lambda_f = \Delta \lambda$$

with cell spacing λ , where $\Delta < 1$ is the actual supercooling at the tip (remember that $\Delta = 1$ for a flat interface at $\zeta = 0$, and $\Delta = 0$ for a flat interface at $\zeta = l_T$). This serves to verify the consistency of numerical calculations (Saito et al., 1989). An even more detailed analysis was carried out by Mashaal et al. (1990).

For comparison with experiments, it is useful to draw a V vs. λ diagram (Fig. 2-24). Here the full line is again the neutral curve, the broken line is the most dangerous (or most unstable) mode, and the dotted line denotes the relation $l = \lambda$, where the diffusion length is equal to the imposed wavelength. The asterisks mark some detailed numerical investigations (Saito et al., 1989). The asterisk furthest to the left is close to the above-mentioned Saffmann–Taylor limit. At slightly higher wavelengths, where $\lambda < l$ still holds, we are in a scaling region, where the radius of curvature at the tips of the cells is about 1/5 of the cell spacing, as also found experimentally (Kurowsky, 1990). All these considerations give sufficient confidence that the numerical calculations may also provide insight into the mechanism of directional solidification for the most interesting case

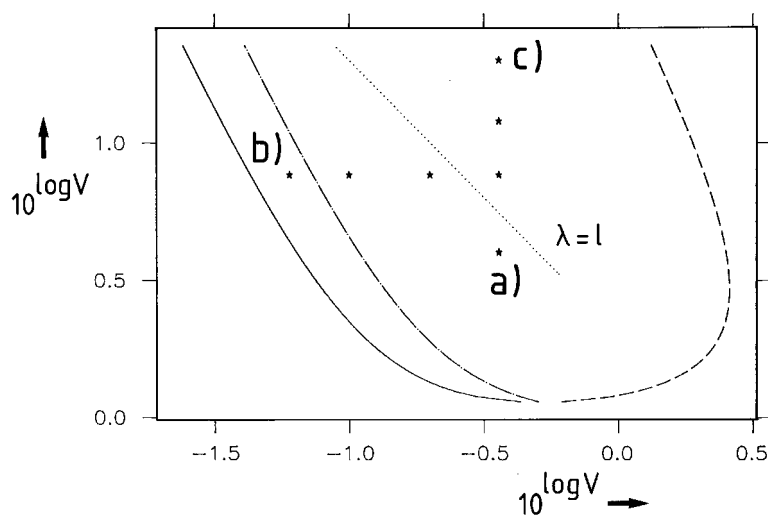


Figure 2-24. “Phase”-diagram $\log(V)$ vs. $\log(\lambda)$ for interface patterns in directional solidification. The solid and dashed curves denote the neutral stability curve, and the dashed-dotted curve the most dangerous mode. Asterisks mark fixed parameter values discussed hereafter. The lower critical threshold here is $V_c \approx 1$, $\lambda_c \approx 0.5$ for velocity and cell spacing. For other parameters see text. At low pulling speeds and high wavelengths cellular patterns with narrow grooves are found (a). At very short wavelengths and moderate speeds cellular patterns with wide grooves are found, consistent with theories for viscous fingering. At high pulling speeds, such that the cell spacing λ is significantly wider than the diffusion length l , side-branching dendritic arrays are formed (c) (Saito et al., 1990). The speeds are still much smaller than the absolute stability limit V_a .

of dendritic arrays formed at higher growth rates.

A few words on numerical methods and system parameters may be in order before we discuss the dendritic region. The numerical code is equivalent to the one used for the free dendritic case with the modification that it is necessary to integrate over several cells to arrive safely outside the diffusion length. Furthermore, in principle, diffusion has to be considered in both the liquid and the solid. Since the diffusion coefficient for material in the solid is usually much lower than it is in the liquid, it is found that diffusion in the solid alloy can usually be neglected on time scales for the formation of cells. For long durations, of course, microsegregation takes place, and solid diffusion then becomes important (Kurz and Fisher, 1998).

A more serious difficulty in directional solidification is the large number of parameters defining the system. We will concentrate here on typical parameter values used in experiments performed for some transparent materials between glass plates. Several tests and specific calculations also done for alloys, however, indicate that a large part of the results can be carried over to these more relevant situations from a metallurgical point of view without qualitative changes.

2.5.4 Directional Dendritic Growth

The diagram in Fig. 2-24 showing velocity versus λ in logarithmic form indicates that qualitatively different behavior may be expected depending on whether the diffusion length is larger or smaller than the cell spacing. In the previous section, we discussed the first case. When the diffusion length becomes smaller than the cell spacing we expect that the individual cells become more and more independent of each

other, until finally they may behave like individual isolated dendrites.

In order to test this hypothesis, a series of numerical experiments were performed at a fixed cell spacing and increasing pulling velocity (Saito et al., 1989). The numerical parameters of the model were representatively taken to correspond to steel with Cr–Ni ingredients (Lesoult, 1980). In dimensionless units, the critical velocity and wavelength for the plane-front instability were $V_c = 1.136$, $\lambda_c = 0.514$. The anisotropy of the capillarity length was not known and was taken as $\varepsilon = 0.1$ to allow for comparison with the previously mentioned calculations on the free dendritic case. The cellular wavelength was fixed to $\lambda = 0.36$, corresponding to the asterisks at increasing velocity and constant λ in Fig. 2-24.

At the lowest velocity still below the $l = \lambda$ dividing line, rounded cells were observed; the tip was not well approximated by a parabola. At higher speeds ($V = 12$) the parabolic structure of the tip became visible, Fig. 2-25, and at even higher speeds ($V = 20$) the dendritic structure with side branches was fully developed, Fig. 2-26.

We can now compare the resulting tip radius with the predictions from free dendritic growth. Note that in the present case the velocity is fixed rather than the supercooling, so that the dendrite now uses a supercooling corresponding to the given velocity. This means that the tip of the dendrite is no longer at a position in the temperature-gradient field like a flat interface, but has advanced toward the warmer liquid.

Fig. 2-27 contains the ratio of the tip radius divided by the radius from scaling, Eq. (2-68) (where the Péclet number P was used in the original form as the ratio of tip radius to diffusion length). Furthermore, this figure gives the ratio of the tip radius to the Ivantsov radius, which comes from

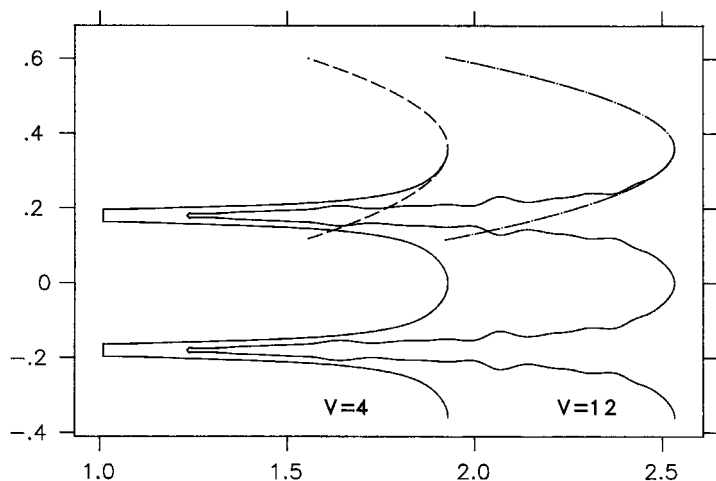


Figure 2-25. Transition from needle-shaped to dendritic cells at increasing pulling speeds. $V = 4$ is below the dotted line in Fig. 2-24, and $V = 12$ above it. Parabolas adjusted to the tip radius are not a good fit to the profiles.

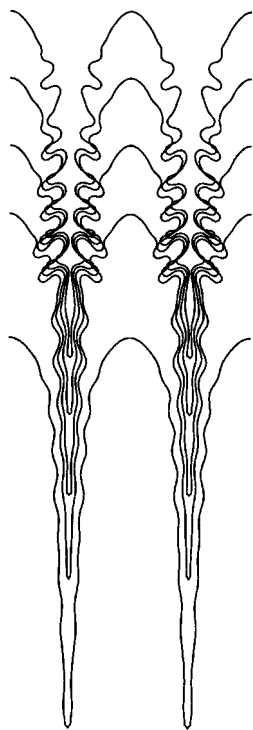


Figure 2-26. Time sequence of a dendritic array at $V = 40$, $\varepsilon = 0.1$, corresponding to point (c) in Fig. 2-24. The starting structure corresponds to $V = 12$, similar to Fig. 2-25. The cellular array quickly converges to a stationary side-branching mode of operation.

the Péclet number through the relation for the supercooling at the tip, Eq. (2-56). The data are instantaneous measurements rather than time-averaged measurements. It is obvious from Fig. 2-27 that the scaling relation, Eq. (2-68), holds very well at rather low speeds, where neighboring cells still interact substantially through the diffusion field, while the relation from the Ivantsov formula for the Péclet number only holds at higher velocities. The obvious reason for the latter deviation at low velocities is that the Ivantsov relation represents a global conservation law for an isolated parabolic structure, which is clearly not valid when several cells are within a diffusion length.

The observation that the scaling relation, Eq. (2-68), is very robust obviously has to do with the fact that it results from a solvability condition at the tip of the dendrite, which is only very weakly influenced by deformations further down the shaft.

In the same study, it was also confirmed that the side branches fulfilled precisely the same scaling relation (Fig. 2-13) as the

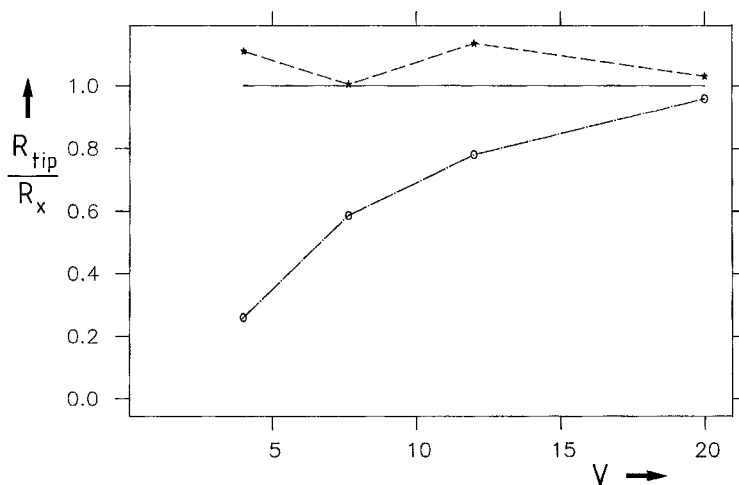


Figure 2-27. Ratios R_{tip}/R_x of tip radius computed numerically (Fig. 2-24) over two theoretical predictions, where R_x is either the Ivantsov radius (circles) or the radius from solvability theory (asterisks). See also Fig. 2-12. The result is in nearly perfect agreement with the solvability theory down to very low speeds in the cellular region. The Ivantsov radius (for free growth) is not a good approximation there, as the diffusion fields of neighboring cells strongly overlap. At high speeds, essentially free dendritic growth is confirmed (Saito et al., 1990).

free dendrites at relatively low speeds of $V=12$ shown in Fig. 2-25. In this case, the side branches are just beginning to show up, while the tip is not very noticeably parabolic.

Up to this point these investigations were done at a constant anisotropy of $\varepsilon=0.1$ of the capillarity length. In Fig. 2-28 the normalized supercooling Δ has been plotted against velocity V , where

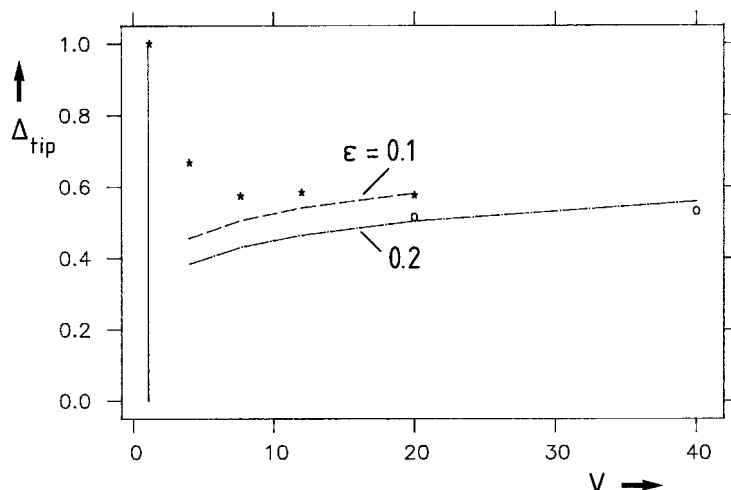


Figure 2-28. Supercooling at the tip of a cell or dendrite vs. pulling speed as obtained from numerical simulation. For a flat interface at low speeds, the global conservation law forces $\Delta = 1$, then it decreases until $l \approx \lambda$, and finally approaches the slowly increasing relation $\Delta(V)$ obtained for the free dendritic case (see also Fig. 2-40). The expected dependence on capillary anisotropy ε is also recovered.

$\Delta=1$ for a flat interface at stationary growth. Two sets of data for $\varepsilon=0.1$ and $\varepsilon=0.2$ are shown. If we increase the pulling speed above the critical value $V \approx 1$, the supercooling at the tip of the cellular patterns first decreases, because the forward bulges come into a range of higher temperature. At intermediate velocity, Δ goes through a minimum and finally approaches the broken lines corresponding to the scaling relation, Eq. (2-68), together with the Ivantsov relation, Eq. (2-56). At intermediate velocities, the supercooling Δ is above the corresponding curve meaning that the Péclet number, and therefore, the Ivantsov radius is larger than expected from the free dendritic scaling.

This is in agreement with Fig. 2-27 shown above. The minimum of the Δ versus V relation is in the range where the diffusion length is comparable to the cell spacing, as expected from Fig. 2-24.

As a final example, Fig. 2-29 shows a dendritic array at the relatively high velocity $V=40$ at anisotropy $\varepsilon=0.2$. As in free dendritic growth, the structure appears sharper than the structure in Fig. 2-26 at smaller anisotropy.

The opposite case of extremely small anisotropies has not yet been analyzed in great detail, and it is rather unclear what happens both from a theoretical and an experimental point of view. It is likely that at zero anisotropy $\varepsilon=0$, the cells will tend to split if the cell spacing becomes much larger than the diffusion length, which affords the possibility for chaotic dynamics at high speeds. However, this is still speculative.

Let us take a quick look at the kinetic coefficient β in Eq. (2-111). As can be concluded from its multiplication by V_\perp , β becomes more and more important at high growth rates. For the free dendritic case with kinetic coefficient β and 4-fold an-

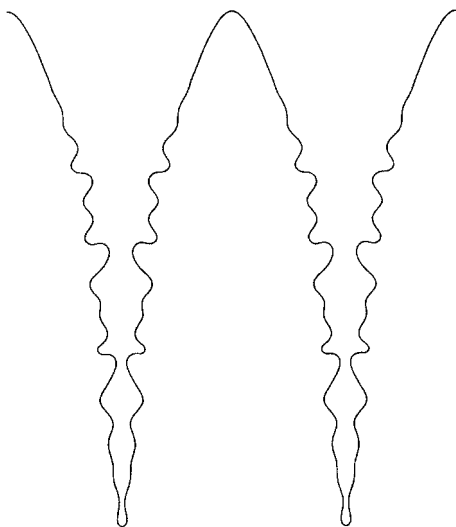


Figure 2-29. Pronounced parabolic directional dendrites at speed $V=40$, $\varepsilon=0.2$, as used in Fig. 2-28. Note that the tip-radius here is about 0.03 and the short-wavelength limit of neutral stability 0.05 in units of the cellular spacing. This is qualitatively consistent with experimental observations of large interdendritic spacings in units of tip radii. Tip splitting was only observed at much lower values of capillary anisotropy.

isotropy β_4 of the kinetic coefficient, a scaling relation similar to Eq. (2-68) was derived by Brener and Melnikov (1991):

$$\beta V = \sigma_\beta \left(\frac{2D_L \beta}{d_0} \right)^{9/2} P^{11/2} \beta_4^{7/2} \quad (2-123)$$

with a constant prefactor $\sigma_\beta \approx 5$ and with Péclet number P as used before in Eq. (2-68). The scaling relation, Eq. (2-123), consists of several non-trivial power laws; only the one with $P=R/l$ relating tip radius to velocity has been confirmed (Classen et al., 1991). With regard to the general agreement between analytical and numerical results obtained so far, however, there is little doubt that these scaling results (and others given by Brener and Melnikov, 1991) will also hold for the dendritic region $\lambda \geq l$ in directional solidification.

A final point to be kept in mind is that the tip supercooling Δ in directional solidification is not small, as required by the approximations used for the derivation of the scaling relation. On the other hand, $P=1$ corresponds to a supercooling as large as $\Delta \approx 0.75$; 0.6 for 2-dim and 3-dim, respectively, and the scaling relations can be expected to hold over a large range of velocities, as already indicated from the other free dendritic case, Fig. 2-12.

In summary, these investigations have shown that there appears to be a smooth transition from cellular to dendritic structures. The dendritic growth laws are very well represented by the scaling relations for the free dendritic case. This scaling should hold in the region

$$d_0 < R \approx l < \lambda < l_T \quad (2-124)$$

where λ is the primary cell spacing. It was proposed by Karma and Pelce (1989a, b) that the transition from cells to dendrites could occur via an oscillatory instability, for which the present investigations under quasi-stationary approximation have shown no evidence. A fully time-dependent calculation is possible in principle with Green's function methods (Strain, 1989).

2.5.5 The Selection Problem of Primary Cell Spacing

An important question from an engineering point of view appears to be the following: suppose we know all the material parameters and the experimentally controllable parameters like thermal gradient and pulling speed for a directional solidification process – can we then predict the distance between the cells and dendrites?

A positive answer to this question is desirable because the mechanical properties of the resulting alloy are improved with a decrease in the primary cell spacing (see

Kurz and Fisher (1998) and references therein).

In a rigorous sense the answer is still negative, but at least arguments can be given for the existence of some boundaries on the wavelengths (or cell spacings) which can be estimated with the use of simplifications.

The situation here shows some similarity to the formation of hydrodynamic periodic roll patterns (Newell and Whitehead, 1969; Kramer et al., 1982; Riecke and Paap, 1986). In a laterally infinite system, a whole band of parallel rolls is present above the threshold for roll formation, the so-called Eckhaus band. This was mentioned in Sec. 2.5.3 for directional solidification.

The reason for the stability of these rolls is that an infinitesimal perturbation is not sufficient to create or annihilate a roll, but a perturbation must exceed a threshold value before such an adjustment can occur.

In directional solidification, the situation is different insofar as the envelope over the tips of the cells could make a smooth deformation of very long wavelength, thereby building up enough deformation energy so that a cell could be created or annihilated at isolated points. One indication for such a process is the oscillatory instability of cells postulated by Karma and Pelce (1989) and Rappel and Brener (1992).

The only hard argument for the selection of a unique wavelength comes from an analysis of a spatially modulated thermal gradient acting on a cellular pattern of small amplitude (normal bifurcation) which imposes a *ramp* on the pattern (Misbah, 1989; Misbah et al., 1990). The idea originally proposed for the hydrodynamic case (Kramer et al., 1982) is to have a periodically varying thermal gradient parallel to the interface, which keeps the interface flat in some regions and allows

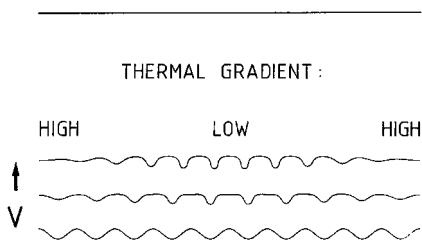


Figure 2-30. Numerical study of cellular wavelength selection at the interface by introducing a ramp in the thermal gradient field. A high thermal gradient on the side approximately normal to the interface keeps the interface flat, the smaller gradient in the center allows for cells to develop. At fixed ramp profile a unique cell spacing is selected in the center, starting from different initial conditions (Misbah, 1990, unpublished).

for the formation of cells in between (Fig. 2-30). For such a specific setup it was shown (Misbah et al., 1990) that a unique wavelength must be selected in the center of the small-gradient area. The reason for this special construction is that it allows for the formation of cells at arbitrarily small amplitudes (and therefore small pinning forces) in the region of strong thermal gradient.

In general, however, the boundary conditions on the other sides of the cells, due to the container walls, are not well specified and typically will not provide such a ramp structure (see Misbah (1989), however, for growth in a rotating vessel). For the time being, we can therefore try to at least find some boundary similar to the Eckhaus band for the limits of large and small wavelengths in the cell spacing.

It is not easy to extend the corresponding analysis of small-amplitude cells (Brattkus and Misbah, 1990) to cells with deep grooves, as these essentially infinite grooves present a kind of topological constraint on the number of longitudinal cells in a given lateral interval. The creation or

annihilation of cells is therefore likely to be a discrete process.

A natural mechanism for the local reduction of cell spacings (or creation of a new cell) is either a nucleation in one of the grooves (the liquid is supercooled), or even more likely, the formation of a new cell out of a side branch in such a groove. Alternatively, tip splitting of a cell may give the same result (Fisher and Kurz, 1978, 1980).

The opposite mechanism for the increase of cell spacing (or annihilation of an existing cell) could occur through the competition of neighboring cells for the diffusion field, such that one cell finally moves at a slightly slower speed than the neighboring cells and, consequently, will be suppressed relative to the position of the moving front.

These two mechanisms have been conjectured by many authors in the past. Some progress has been made recently by the confirmation of the scaling relations in the dendritic region. It seems, therefore, worthwhile to reformulate those conjectures with the help of these scaling relations. Let us first consider the short-wavelength λ (cell spacing) argument. Assume that we are at dendritic growth speeds, Eq. (2-124), ignoring here kinetic coefficients. The solidification front then looks like an array of individual dendrites which only weakly interact with each other through the diffusion field $l < \lambda$.

The solidification front $\xi=0$ will be understood here as a smooth envelope touching all the dendrite tips, so that deformations of the front have a smallest wavelength λ equal to the cell spacing. There are now basically two “forces” acting on deformations $\partial \xi(x, t) / \partial t$ of that front. If some of the tips are trailing a little behind the others, they will be screened through the diffusion field of the neighboring tips, as in the conventional Mullins–Sekerka instability, but now without a stabilizing

surface tension interacting between neighboring tips. Taking this into account, the destabilizing force is $F_d \approx \Omega_k^{(d)} \tilde{\xi}_k$ with $\Omega_k^{(d)} = V|k|$ for a sinusoidal perturbation of amplitude $\tilde{\xi}_k$ of a plane interface without surface tension moving at velocity V and wavenumber k . The maximum lies at $k = 2\pi/\lambda$. The actual area under this perturbation $\tilde{\xi}_k$ contained in the solid cells is smaller by a factor $\approx 2R/\lambda$. We thus arrive at a maximal destabilizing force of

$$F_d \approx \Omega^{(d)} \zeta_\lambda; \quad \Omega^{(d)} \approx 4\pi V R / \lambda^2 \quad (2-125)$$

corresponding to a depression or enhancement of every second dendrite.

On the other hand, each of these individual dendrites knows its operating point, and through the given velocity its supercooling at the tip. We approximate this by the asymptotic form of Eq. (2-56) $\Delta \approx 1 - 1/P$ since basically the variation of Δ with P enters below, even through P may not be very large compared to unity. Capillary effects do not seem to be very important in this region and are thus neglected here for simplicity. By definition, $\Delta = 1 - z_{\text{tip}}/l_T$, and the two expressions for Δ can be evaluated: $z_{\text{tip}} \approx l_T l / R$. The stabilizing force $F_s \approx \Omega^{(s)} \zeta_\lambda$ follows from the obvious relation $\Omega^{(s)} = dV_{\text{tip}}/dz_{\text{tip}}$ as

$$F_s \approx \Omega^{(s)} \zeta_\lambda; \quad \Omega^{(s)} \approx -2 \frac{V R}{l_T l} \quad (2-126)$$

As expected, the sign of this “force” is opposite to the destabilizing force, Eq. (2-125). Setting the sum of the two equal to zero, we expect an instability to occur first at cell spacings

$$\lambda \approx \sqrt{l_T l} \quad (2-127)$$

for segregation coefficients around one. We cannot say much about small segregation coefficients because the nonlinearity in Eq. (2-114) replacing Eq. (2-56) be-

comes important there. Of course, a number of rough approximations were used specifically in the treatment of the destabilizing force, but this argument should at least qualitatively capture the competition mechanism between neighboring dendrites. A more detailed analysis (Warren and Langer, 1990) is quite promising at large velocities in comparison with experiments (Somboonsuk et al., 1984) (see also Kessler and Levine, 1986c; Bechhoefer and Libchaber, 1987).

Let us now look at the large-wavelength limit λ . The initial growth conditions are assumed to be just as before, Eq. (2-124), but now at possibly large cell spacings λ . In the numerical calculations, it was found (Saito et al., 1989) that for fixed cell spacing λ at increasing velocity, a *tail instability* occurs (Fig. 2-31). A side branch in the

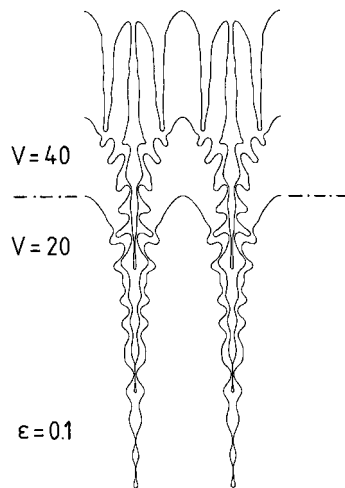


Figure 2-31. After a sudden increase in the growth rate in the dendritic region at fixed cell spacing, tail instability occurs. One of the side branches near the tip produces a protuberance in the forward direction, which then becomes a new primary cell (the imposed mirror symmetry is not present in reality of course). In accordance with the stability of dendritic cells against tip splitting (compare Fig. 2-29), this tail instability appears to be an important selection mechanism for primary cell spacing. See also Fig. 2-43.

groove between two dendrites splits off a ternary branch, which then moves so fast in the strong supersaturation in the groove that it finally becomes a new primary branch. In the plot, the imposed mirror symmetry is, of course, artificial, but it even acts opposite to this effect, making the process more plausible in reality. In fact, this is also observed experimentally (Esaka and Kurz, 1985), in particular when the solid consists of slightly misaligned regions separated by grain boundaries, so that the growth direction of two neighboring dendrites is slightly divergent. Our basic assumption now is that this tail instability occurs when the intersection of parabolic envelopes over neighboring dendrites occurs at a point $z \leq 0$, where, theoretically, $\Delta > 1$. In this case, there is no need for long-range diffusion around a side branch, for its dynamics become local. Of course, this assumption ignores geometrical competition between neighboring side branches to a certain extent, but for the moment there seems to be no better argument to hand.

Taking into account the point that neighboring parabolas with tip position at $z_{\text{tip}} > 0$ cannot intersect further down to the cold side than at $z=0$, we obtain $z_{\text{tip}} = l_T l / R$ from the two relations for Δ , just as in the previous case of small wavelengths. But now we must use the parabolic relation $z_{\text{tip}} = \lambda^2 / 8R$ for the intersection of two parabolas of radius R at $z=0$, which are a distance λ apart. The tail instability is then expected to occur for

$$\lambda \gtrsim \sqrt{l_T l} \quad (2-128)$$

again with a prefactor roughly of the order of unity. In comparison with Eq. (2-127), it can be seen that in both cases the same scaling relation results. The scaling with the inverse growth rate l follows the neutral stability curve at velocities safely in

between the two critical values and again recovers Eq. (2-1) by noting that $l \sim V^{-1}$ and therefore $V \lambda^2 \approx \text{constant}$. The results, Eqs. (2-127) and (2-128), seem to be in agreement with experiments (Somboonsuk et al., 1984; Kurowsky, 1990; Kurz and Fisher, 1981, 1998) concerning the scaling with respect to diffusion length l and thermal length l_T . The limit $k \rightarrow 0$ for the segregation coefficient as a singular point is not reliably tractable here.

The previously given relation $\lambda \sim l^{1/4}$ (Hunt, 1979; Trivedi, 1980; Kurz and Fisher, 1981) seems to be valid in an intermediate velocity region (Fig. 2-28) where Δ does not vary significantly, so that $z_{\text{tip}} / l_T \approx 1/2$ (see also Sec. 2.6.1).

A serious point is the neglect of surface tension and anisotropy in these derivations. In the experiments analyzed so far the relation $V \lambda^2 \approx \text{const.}$ seems to hold approximately, but what happens for the capillary anisotropy ε going to zero? Numerically, tip splitting occurs at lower velocities for smaller ε . In a system with anisotropy $\varepsilon = 0$ (and zero kinetic coefficient) the structures probably show chaotic dynamics at velocities where the diffusion length l is smaller than the short wavelength limit of the neutral stability curve (Fig. 2-24), but this is rather speculative (Kessler and Levine, 1986c).

In considering whether the tail instability (large λ) or the competition mechanism (small λ) will dominate in casting processes, we tend to favor the former. If the solidification front consists of groups of dendrites slightly misoriented against each other due to small-angle grain boundaries, cells will disappear at points where the local growth directions are converging and new cells will appear through the tail instability at diverging points at the front.

To summarize, the most likely scaling behavior of the primary cell spacing λ , de-

pending on pulling velocities, follows Eqs. (2-1) and (2-128) as a consequence of the arguments presented in this section. This conclusion is supported by a number of experiments (Billia et al., 1987; Somboonsuk et al., 1984; Kurowsky, 1990; Esaka and Kurz, 1985), but more work remains to be done.

2.5.6 Experimental Results on Directional Dendritic Growth

Since 1950, *in situ* experiments on directional solidification (DS) of transparent model systems have been performed (Kofler, 1950). However, it was some time before such experiments were specifically conceived to support microstructural models developed in the 1950s and early 1960s. The work of Jackson and Hunt (1966) is a milestone in this respect (see also Hunt et al., 1966). Their experimental approach to dendritic growth has been developed further by several groups: Esaka and Kurz (1985), Trivedi (1984), Somboonsuk et al. (1984), Somboonsuk and Trivedi (1985), Eshelman et al. (1988), Seetharaman and Trivedi (1988), Seetharaman et al. (1988), de Cheveigne et al. (1986), Akamatsu et al. (1995), Akamatsu and Faivre (1998), and others. Substantial progress has been made during these years, especially due to results obtained by Faivre and coworkers in very thin ($\sim 15 \mu\text{m}$) cells that constrain the patterns to two dimensions. This research is still producing interesting new insights into the dynamics of interface propagating during crystallization.

The specific interest of DS is that growth morphologies can be studied not only for dendritic growth but also for cellular and plane front growth. We will discuss these phenomena in the sequence of their appearance when the growth rate is increased from V_c , the limit of first formation of

Mullins–Sekerka (MS) instabilities (also called limit of constitutional undercooling), to rates where plane front growth again appears at velocities above V_a , the absolute stability limit.

Morphological instabilities. The onset of plane front interface instability is observed to start at defects such as grain boundaries, subgrain boundaries and dislocations, forming a more or less pronounced depression at the intersection with the solid–liquid boundary, as shown in Fig. 2-32 (Fisher and Kurz, 1978). It is inherently difficult to quantitatively observe the break-down because the growth rates are small, and a long period of time is required to reach steady state.

The amplitude and wavelength of the perturbations as a function of V developing in systems with small distribution coefficients k (of the order of 0.1) are shown in Fig. 2-33. In $\text{CBr}_4\text{--Br}_2$ (de Cheveigne et al., 1986) and SCN--ACE (Eshelman and Trivedi, 1987), the bifurcation is of a subcritical type, i.e., there are two critical growth rates, one for increasing growth rate, V_c^+ , and another lower value for decreasing growth rate, V_c^- . Therefore, a periodic interface shape with infinitesimally small amplitudes cannot form in these systems. As has been discussed in Sec. 2.5.3, only systems with k near unity will give supercritical (normal) bifurcation with a single, well-defined critical growth rate V_c . The evolution of the wavelength for two temperature gradients (70 and 120 K/cm) is shown in Fig. 2-33b. At the onset of instability the experimentally determined wavelength is smaller than the critical wavelength by a factor of 2–3 compared with linear stability analysis. Increasing the rate above the threshold leads to a decrease in the wavelength proportional to $V^{-0.4}$ (de Cheveigne et al., 1986; Kurowsky, 1990). Once stability has started, the

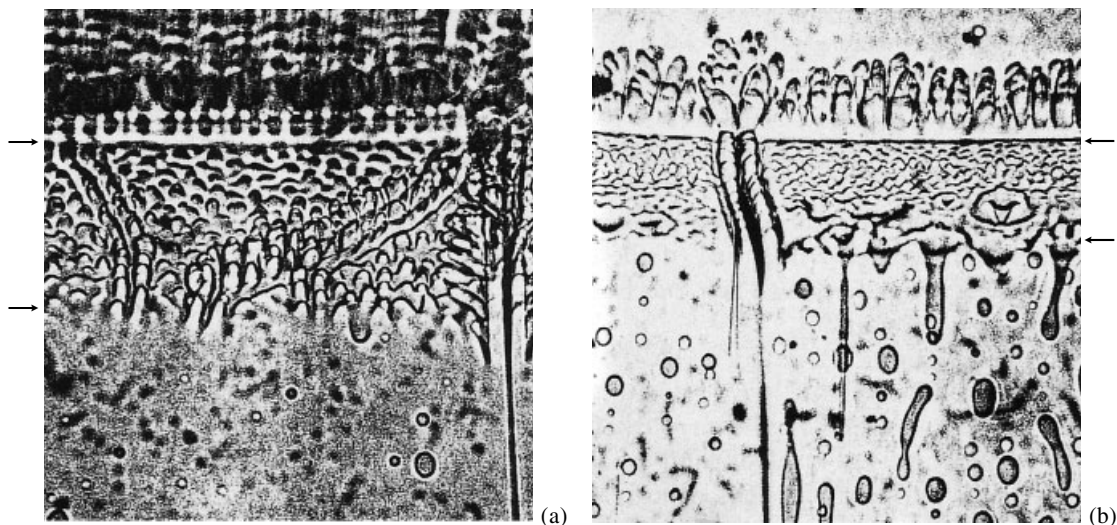


Figure 2-32. Morphological instabilities of a planar solid/liquid interface as seen on an inclined solidification front between two glass plates (arrows). Photograph (a) was taken at an earlier stage than (b). The beginning of the breakdown at defects such as dislocations, subgrain boundaries, or grain boundaries intersecting with the solid/liquid interface is evident. The widths of the photographs correspond to 100 μm .

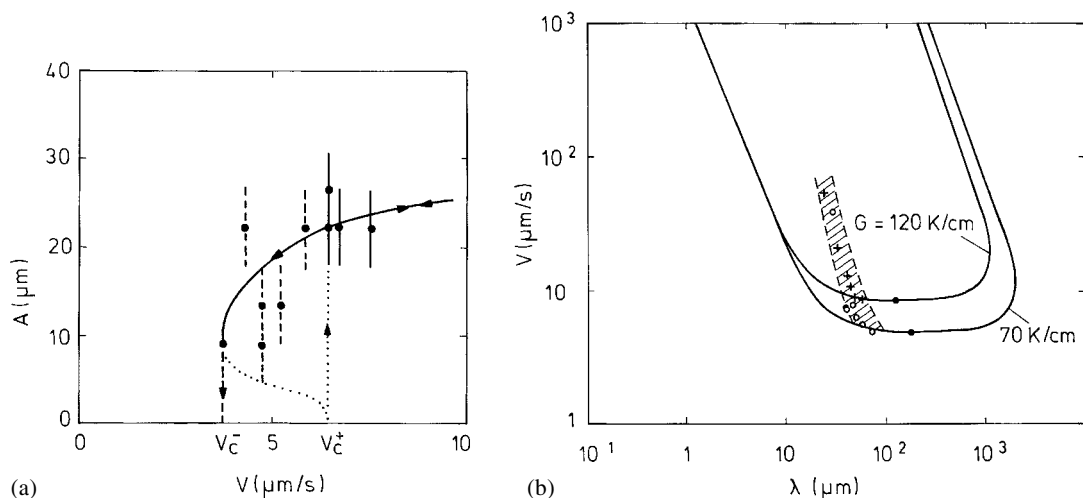


Figure 2-33. Amplitude, A , and wavelength, λ , of a periodic deformation of the solid/liquid interface of $\text{CBr}_4\text{-Br}_2$ solution versus pulling speed (de Cheveigne et al., 1986). Diagram (a) shows the hysteresis between appearance and disappearance of perturbations (typical for an inverse bifurcation) for a temperature gradient of 12 K/mm. The lines in diagram (b) represent the calculated neutral stability curves for the two gradients indicated. Open circles are experimental results for 7 K/mm, and crosses, for 12 K/mm. See also Fig. 2-21.

structure evolves to a steady-state cellular or dendritic growth mode. Which one of these structures will finally prevail is a question of the growth conditions.

Cells and dendrites. Losert et al. (1998 a) developed an interesting technique in which a spatially periodic UV laser pulse is directed onto the solidification front of the

transparent succinonitrile–coumarin system. These experiments allowed for a systematic investigation of the dynamic selection and stability of cellular structures.

Through an increase in V (or C_∞ , or a decrease in G_T), a columnar dendritic structure can be formed out of a cellular array (Fig. 2-34). All three morphologies (in-

stabilities, cells, dendrites) appear to have their own wavelength or array spacing. Owing to competition between neighboring crystals, the mean spacing of large amplitude cells seems to be always larger than that of the initial perturbations of the plane front, and the mean trunk distance (primary spacing λ) of the dendrites, larger than the

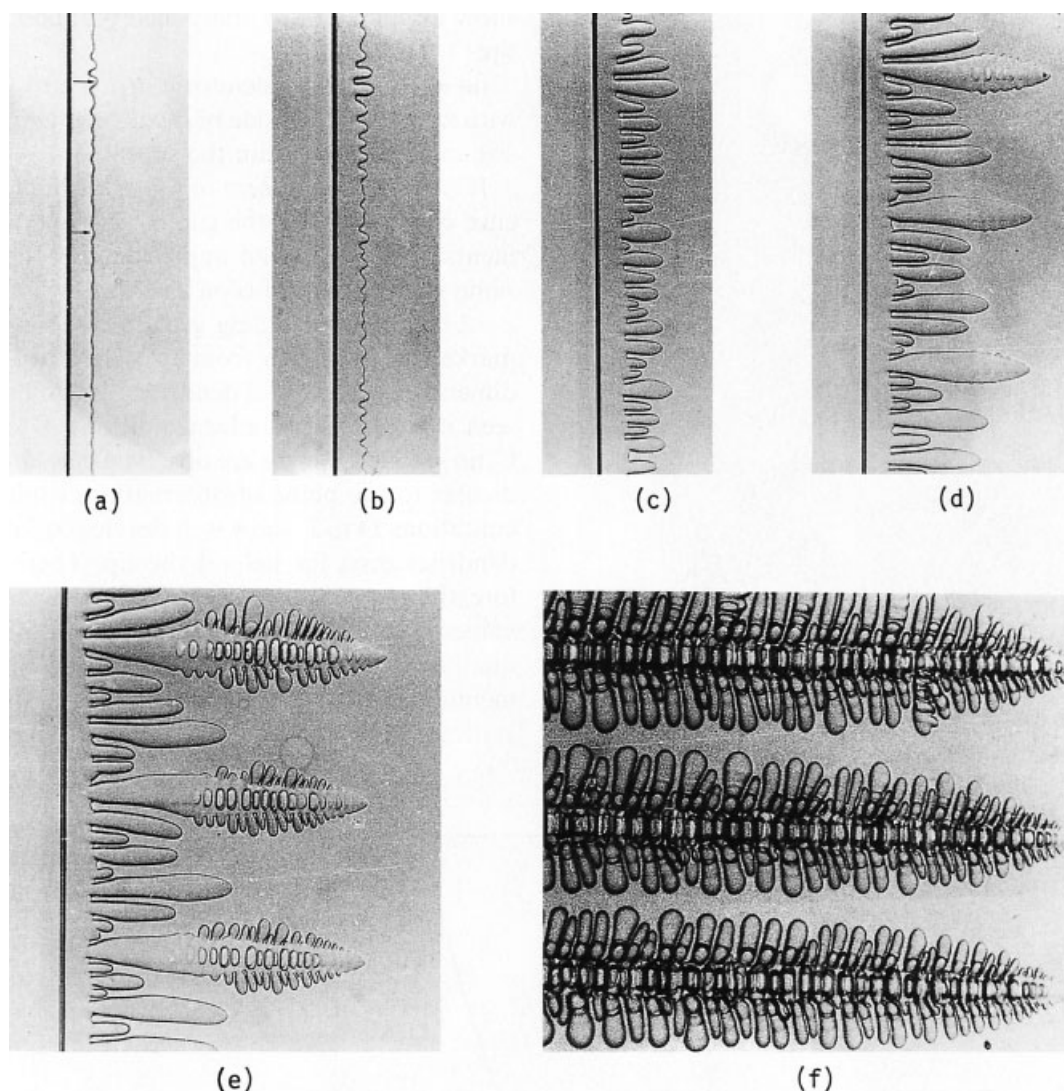
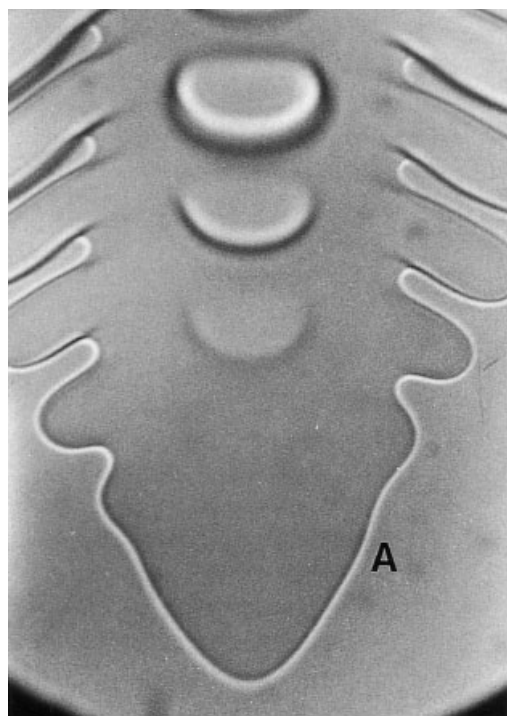
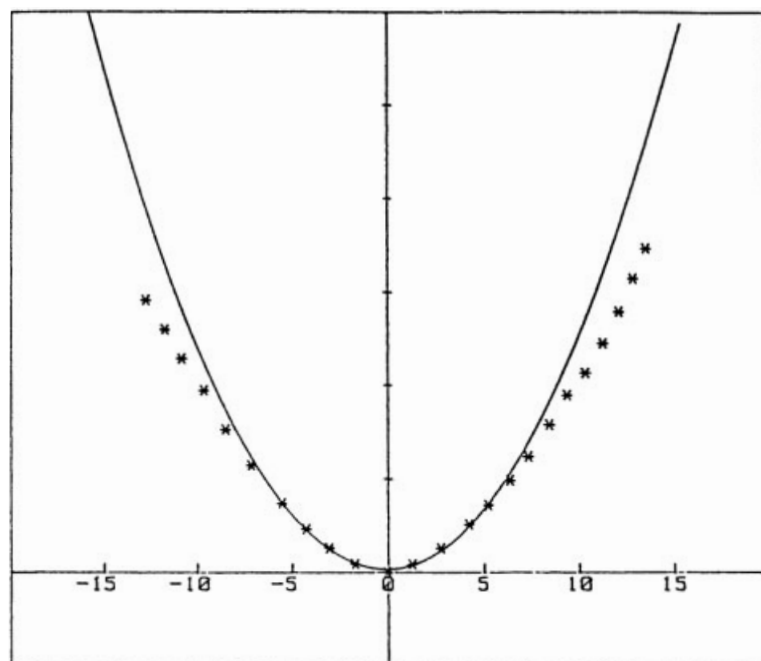


Figure 2-34. Time evolution of the solid/liquid interface morphology when accelerating the growth rate from 0 to 3.4 $\mu\text{m/s}$ at a temperature gradient of 6.7 K/mm. Magnification 41 \times . (a) 50 s, (b) 55 s, (c) 65 s, (d) 80 s, (e) 135 s, (f) 740 s (Trivedi and Somboonsuk, 1984).



(a)

10 μm



(b)

Distance (μm)

spacing between smooth cells. The reason for this change in typical spacing is not yet clear. We will come back to this subject later. Before we do so, some relevant observations on tip growth need to be discussed.

The tip is the “head” of the dendrite where most of the structural features are initiated. Fig. 2-35 shows a dendrite tip of succinonitrile (SCN) with 1.3 wt.% acetone (ACE) in an imposed temperature gradient, $G_T = 16 \text{ K/cm}$ and a growth rate, $V = 8.3 \text{ μm/s}$. The smooth tip of initially parabolic shape (Fig. 2-35b) is clearly visible. In contrast of free thermal dendrites (Fig. 2-9), in DS of alloys the secondary instabilities start forming much closer to the tip. The imposed temperature gradient also widens the dendrite along the shaft relative to a parabola fitted to the tip. This effect increases with an increasing temperature gradient (Esaka, 1986).

Figure 2-35. Dendrite tip of SCN–1.3 wt.% acetone solution in directional growth. (a) For $V = 8.3 \text{ μm/s}$ and $G = 1.6 \text{ K/mm}$; (b) parabola fitting the tip growing at $V = 33 \text{ μm/s}$ and $G = 4.4 \text{ K/mm}$ (Esaka and Kurz, 1985; Esaka, 1986).

The sequence of steady-state growth morphologies, from well-developed large amplitude cells to well-developed dendrites, is shown in Fig. 2-36. Besides the information on the form and size of the corresponding growth morphologies, this figure also contains indications specifying the diffusion length $l = 2D/V$ and the ratio of the half spacing over tip radius. The characteristic diffusion distance decreases more rapidly than the primary spacing of the dendrites (Fig. 2-36). When $l \geq \lambda$ the ratio $\lambda/2R$ of directionally solidified SCN-1 wt.% ACE alloys is between 5.5 and 6, in agreement with numerical calculations (Sec. 2.5.3).

These observations are summarized in Fig. 2-37. Three areas of growth can be differentiated for this alloy:

- i) at low speeds, cells are found showing no side branches and a non-parabolic tip;
- ii) at intermediate rates (over a factor 5 in V), cellular dendrites are formed with weakly developed secondary arms, and they show an increasingly sharpened parabolic tip;
- iii) at large rates dendritic arrays grow with well-developed side branches and a tip size much smaller than the spacing.

It is difficult at present to judge the influence of the width of the gap of the experi-

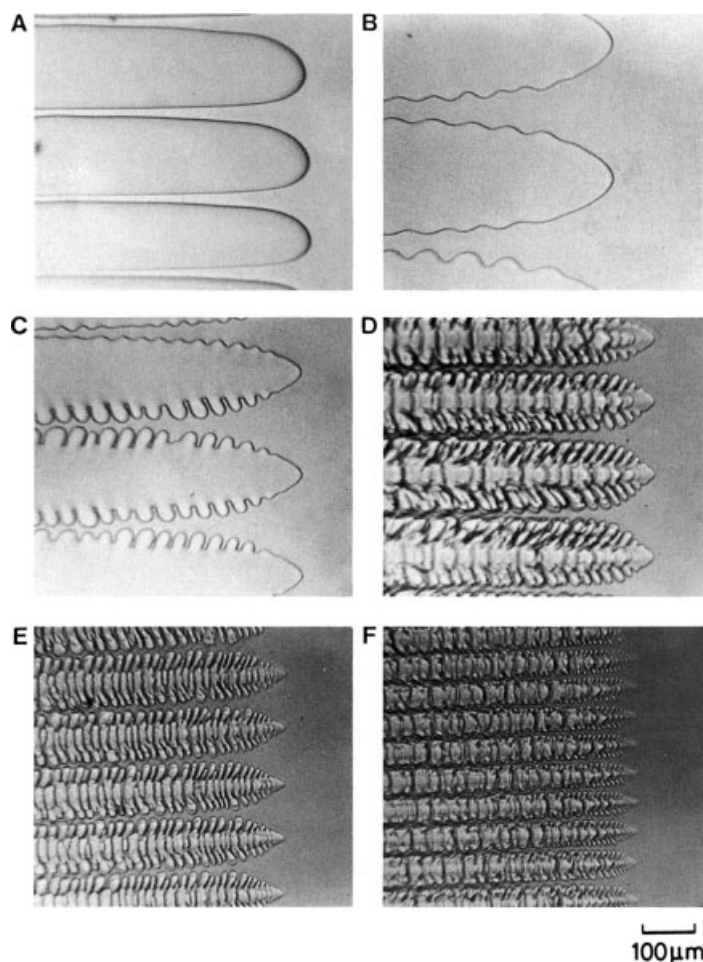


Figure 2-36. Cellular and dendritic growth morphologies in SCN-1.3 wt.% acetone; thermal gradient $8 \text{ K/mm} < G < 10.5 \text{ K/mm}$ (Esaka, 1986). The growth rate V in $\mu\text{m/s}$, the diffusion length $(2D/V)$ in mm, and the ratio of the primary trunk spacing to the tip diameter are as follows: A = 1.6, 1.6, 2.0; B = 2.5, 1.0, 2.5; C = 8.3, 0.3, 5.5; D = 16, 0.16, 6.0; E = 33, 0.08, 7.5; F = 83, 0.03, 9.0.

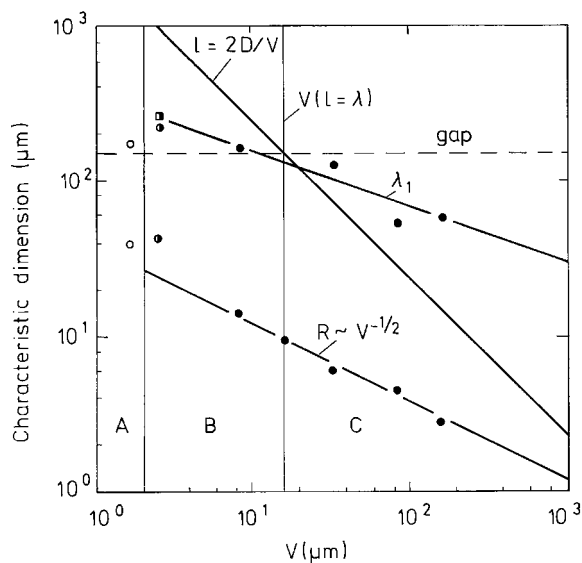


Figure 2-37. Primary trunk spacing, diffusion length and tip radius of SCN–1.3 wt.% acetone dendrites as a function of the growth rate for a temperature gradient of 9.7 K/mm. The various points correspond to the conditions and microstructures given in Fig. 2-36 (Esaka, 1986). In region A no side arms are observed and the tips are of non-parabolic shape; in B the tip becomes parabolic and some side arms appear; in C well-developed side arms and a parabolic tip are the sign of isolated tips.

mental cell, which had approximately the same size as the diffusion distance, when $\lambda = l$. The corresponding growth rate also marks the transition from two- to three-dimensional growth of dendrites, as can be seen in Fig. 2-36. Under conditions A to C, no secondary arms are observed perpendicular to the plane of observation, while conditions D to F show well-developed 3D dendrites even far behind the tip. Therefore, the gap might somewhat influence the values of the transition rates but not the qualitative behavior of the transition. As mentioned above, the theory (in quasi-stationary approximation) only indicates a very gradual change in morphology. It is interesting to compare Fig. 2-36 with Figs. 2-25 and 2-26. It can be seen that both the theoretical and the experimental approaches show qualitatively the same behavior, even if the material constants used are not the same.

The critical role of crystalline anisotropy in interface dynamics has been demonstrated experimentally in directional growth of transparent $\text{CBr}_4\text{--C}_2\text{Cl}_6$ alloys grown as single crystals in thin samples (Akamatsu

et al., 1995). With the $\langle 100 \rangle$ direction oriented along the heat flow direction, characteristic cellular/dendritic arrays such as shown in Fig. 2-36 are obtained. With other orientations, where growth is rendered “effectively isotropic” a “seaweed” structure is observed, the tips of which form what has been called on the basis of theoretical predictions a doublon (Ihle and Müller-Krumbhaar, 1994).

The formation of doublons has also been suggested to play an important role in the formation of “feathery” grains in technical aluminum alloys. Recent detailed observations with electron back-scattered diffraction (EBSD) combined with optical and scanning electron microscopy (Henry et al., 1998) have clearly shown that feathery grains are made of $\langle 110 \rangle$ columnar dendrites, whose primary trunks are aligned along and split in their center by a $\langle 111 \rangle$ coherent twin plane. The impingement of secondary $\langle 110 \rangle$ side arms gives rise to incoherent wavy twin boundaries. The switch from $\langle 100 \rangle$ to $\langle 110 \rangle$ growth direction was attributed to the small anisotropy of the solid–liquid interfacial energy of alumi-

num, which can be changed by the addition of solute (Henry et al., 1998).

The scaling of the initial side-branch spacing λ_2 with respect to the tip radius is shown in Fig. 2-38. Both quantities scale closely with $L^2 V = \text{const.}$ or $L^2 C_\infty = \text{const.}$ (where $L \sim R$ or λ_2). Fig. 2-38b also shows the quantity λ_p , the distance from the tip down the shaft, where the first signs of tip perturbations in the SCN–ACE system can be observed. Here λ_p is of the same order as λ_2 .

The ratio λ_2/R obtained by Esaka and Kurz (1985) for SCN–1.3 wt.% ACE is independent of growth rate according to the precision of the measurements and takes a value of 2.1 ± 0.2 (see Fig. 2-39 and Table 2-1). This is in good agreement with the measurement of Somboonsuk and Trivedi (1985) who found a value of 2.0 on the same system over a wide range of growth rates, compositions, and temperature gradients (Trivedi and Somboonsuk, 1984). This ratio increases with crystal anisotropy

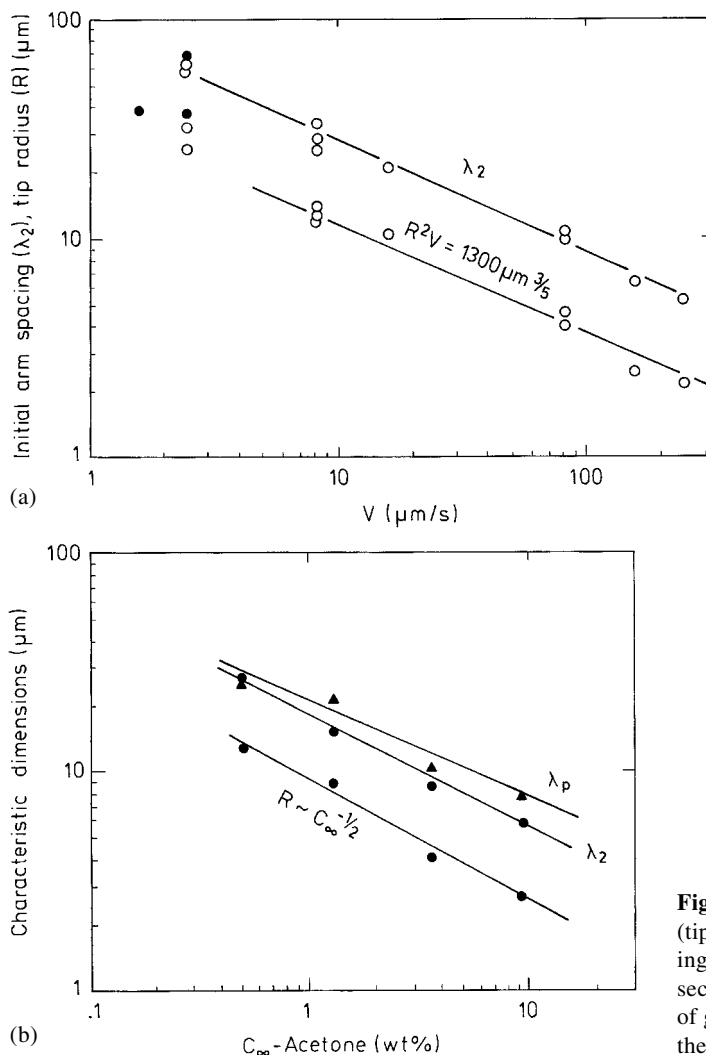


Figure 2-38. Characteristic dimensions (tip radius, R , initial secondary arm spacing, λ_2 , and distance of appearance of secondary instabilities, λ_p) as a function of growth rate (a), and as a function of the alloy concentration (b) (Esaka, 1986).

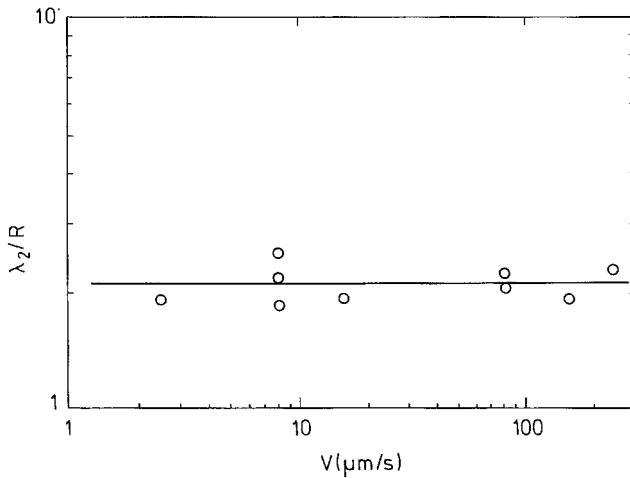


Figure 2-39. Ratio of initial arm spacing to tip radius as a function of growth rate (Esaka and Kurz, 1985).

in agreement with numerical calculations (Figs. 2-26, 2-29, 2-13) and decreases with increasing temperature gradient. On the other hand, its value is larger in the case of free dendritic growth (Table 2-1).

The tip undercooling of the dendrite is a measure of the driving force necessary for its growth at the imposed rate V . Fig. 2-40 shows the variation of the tip temperature with V , the undercooling being defined by the difference between T_m and the tip temperature. During an increase in growth rate,

the cellular growth region is characterized by a decrease in undercooling, while toward the dendritic region, the undercooling increases again (Fig. 2-28).

One of the characteristics of directional solidification of cells/dendrites is the formation of array structures with a primary trunk spacing λ . For cellular and cellular-dendritic structures the growth direction/crystal orientation relationship plays an important role in the establishment of stable or unstable array patterns with a

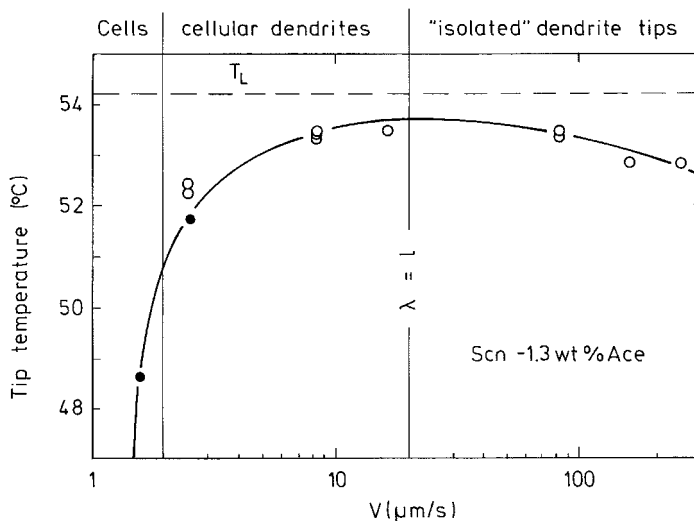


Figure 2-40. Tip temperatures of the dendrites of Fig. 2-36 as a function of growth rate (Esaka and Kurz, 1985). See also Fig. 2-28.

characteristic spacing, as has been shown by Akamatsu and Faivre (1998). The growth-rate dependence of dendritic patterns has been shown in the log-log plot of Fig. 2-37. We can see that the slope of λ vs. V is initially lower than the slope of R vs. V . If we take the three points around $V(l=\lambda)$, where the tip temperature is approximately constant, the slope is about 0.25, while a mean slope through all measurements shown gives 0.4. This is fully consistent with data by Kurowsky (1990). Furthermore, it is in agreement with our arguments in Sec. 2.5.5.

Most of the measurements give a rate exponent somewhere between the two limiting values, 0.25–0.5. Taking the lower value expressed by temperature gradient and concentration gives a relationship $\lambda \sim G_T^{-0.5} C_\infty^{0.25}$ (Hunt, 1979; Kurz and Fisher, 1981; Trivedi, 1984). Therefore, a normalized spacing $\lambda^4 G_T^2 V / k \Delta T_0$ is plotted vs. V in Fig. 2-41, showing that different materials behave similarly except for a constant factor (note that the solidus–liquidus interval of an alloy, ΔT_0 , is proportional to C_∞).

Primary spacings, however, are not uniquely defined but form a rather wide distribution. This is shown in Fig. 2-42 for one superalloy which was directionally solidified under different conditions. This behavior can be understood by examining the mechanism of wavelength (spacing) reduction through tail instability, which is a complicated process. A series of competitive processes between secondary and tertiary arms in a region behind the tip (of the order of one primary spacing) finally causes one tertiary branch to grow through and to become a new primary trunk (Esaka et al., 1988), as shown in Figs. 2-43 and 2-31. The range of stability of dendritic arrays has been analysed by Losert et al. (1998b). Hunt and Lu (1996) approached

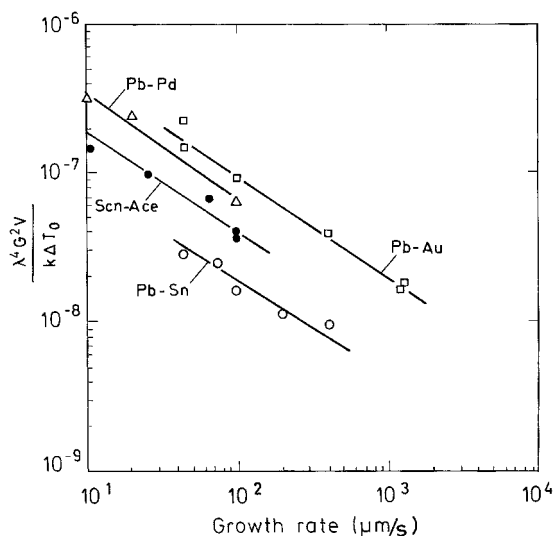


Figure 2-41. Normalized primary trunk spacing, λ , as a function of growth rate for various alloy systems (Somboonsuk et al., 1984). Note that the variation with growth rate at these high velocities is in agreement with the discussion in Sec. 2.5.5.

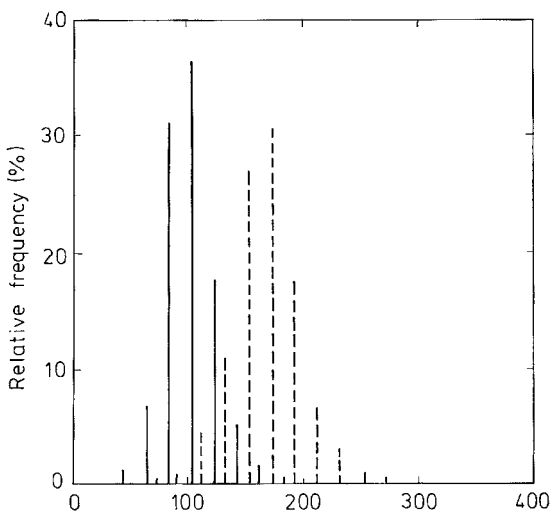


Figure 2-42. Distribution of nearest dendrite–dendrite separations (primary trunk spacings) measured on a transverse section of a directionally solidified Ni-base superalloy (Quested and McLean, 1984). Solid lines for 16.7 $\mu\text{m/s}$ and broken lines for 83.3 $\mu\text{m/s}$.

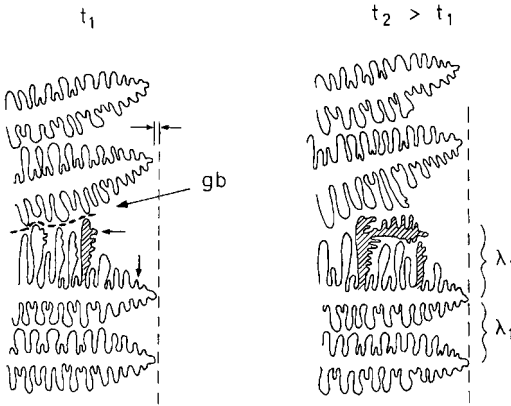


Figure 2-43. Mechanism for the formation of a new primary trunk by repeated branching of side arms at a grain boundary (gb). The increasing spacing at the gb allows a tertiary branch to develop and to compete in its growth with other secondary branches (hatched arms) (Esaka et al., 1988).

this problem by numerical modeling using a minimum undercooling criterion for the selection of the lower limit of array growth.

Effects at high growth rates

As the final topic in this section, we discuss some interesting effects which have been observed at very high growth rates. In laser experiments of the type shown in

Fig. 2-7, the interface may be driven to velocities of several m/s. Under such high rates, the structures become extremely fine. Primary spacings as small as 20 nm have been measured in Al–Fe alloys (Gremaud et al., 1990). Fig. 2-44 represents measured primary spacings (black squares), measured secondary spacings (open squares), and the calculated tip radius of the dendrites, using Ivantsov's solution and the solvability-scaling criterion (Kurz et al., 1986, 1988). λ and λ_2 vary as $V^{-0.5}$, as does the tip radius when the Péclet number of the tip is not too large. At large Péclet numbers (or small diffusion distances), capillary forces become dominant, which is the reason for the limit of absolute stability, V_a . Ludwig and Kurz (1996a) determined cell spacing and amplitude close to absolute stability in succinonitrile–argon alloys and found for both $\lambda^{3/2}V = \text{const.}$

Since the classical paper by Mullins and Sekerka (1964), it has been known that plane front growth should also be observed at interface rates where the diffusion length reaches the same order as the capillary length. This critical rate, called the limit of absolute stability, can be calculated from linear stability analysis (for temperature

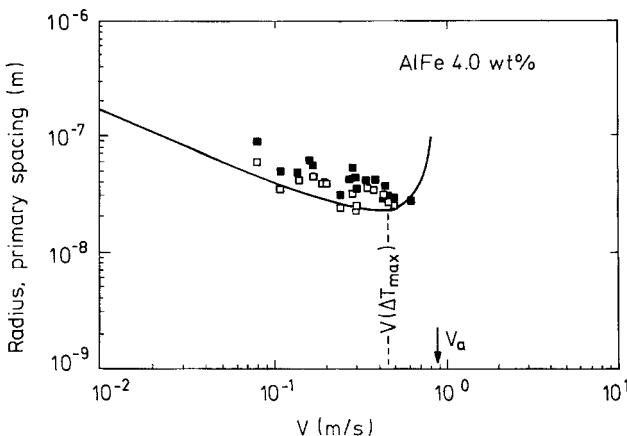


Figure 2-44. Experimentally determined primary spacings (black squares), secondary arm spacings (open squares) and calculated tip radius (line) for Al–4 wt.% Fe alloy rapidly solidified by laser treatment. The minimum in tip temperature or the maximum in undercooling is due to the decreasing curvature undercooling when the dendrite approaches the limit of absolute stability, V_a (Gremaud et al., 1990).

gradients which are not too high) approximately as

$$V_a = \Delta T_0 D / k \Gamma$$

Here Γ is the ratio of solid–liquid interface energy to specific melting entropy. Typical limits are of the order of m/s. The precise value depends also on the effect of a varying solute diffusion coefficient (due to the large undercoolings), on the variations of k and ΔT_0 with the growth rate associated with the loss of local equilibrium, and, finally, on interface kinetics, which cannot be ignored. According to an extensive study of several alloy systems, it may be stated that at V_a we generally do not observe a simple plane front growth but rather an oscillating interface, which produces bands of plane front and cellular dendritic morphology. Fig. 2-45a shows such a transition from columnar dendritic grains to bands (Carrard et al., 1992). Fig. 2-45b shows more details of the banded structure. It is visible that the dark band is cellular/dendritic and the clear band structure-less (supersaturated plane front growth). The possibility of chaotic interface motion was shown by Misbah et al. (1991), and oscillatory motion of a plane interface with time was suggested by Corriell and Sekerka (1983) and Temkin (1990). The full theoretical analysis of the banding problem has been given by Karma and Sarkissian (1993), see also Kurz and Trivedi (1996). Growth rates much higher than V_a are needed in order to definitely produce an absolutely stable plane solid–liquid interface (Fig. 2-46).

Under steady-state growth conditions using a transparent organic system, Ludwig and Kurz (1996b) observed the onset of absolute stability but no sign of banding. The latter was due to the fact that the experiments had to be undertaken with highly diluted alloys. This was necessary as one had

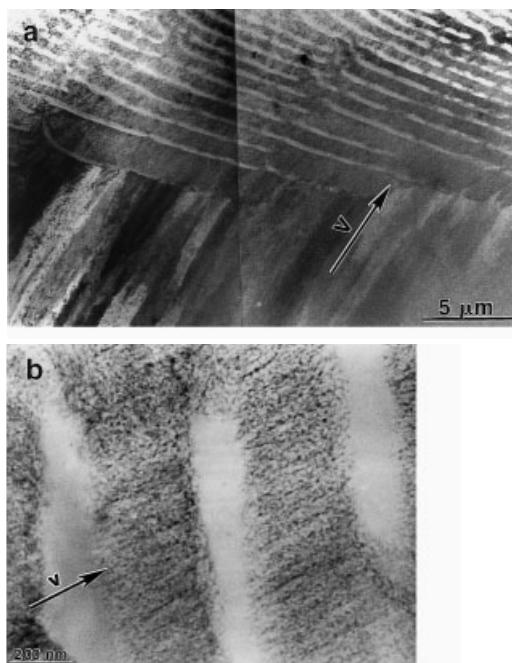


Figure 2-45. Transmission electron micrographs of the banded structure in laser-remelted alloys. (a) General view of the abrupt transition from columnar eutectic grains (lower part) to a banded structure (upper part) in a eutectic Al–33 wt.% Cu alloy with a solidification rate, $V=0.5$ m/s. (b) Enlarged view of the dark and light bands in a cellular dendritic Al–4 wt.% Fe alloy with $V=0.7$ m/s (Carrard et al., 1992).

to work under heat flow limited conditions allowing a growth rate of not more than some mm/s. In order to reach absolute stability at these low rates the composition (and ΔT_0) had to be kept very small (typically below 100 mK).

2.5.7 Extensions

In this section, we summarize a few improvements on the theory of solidification regarding various effects that are important in the practical experimental situation. They are observed when experimental parameters are outside the range of the simple models considered in this chapter, or when

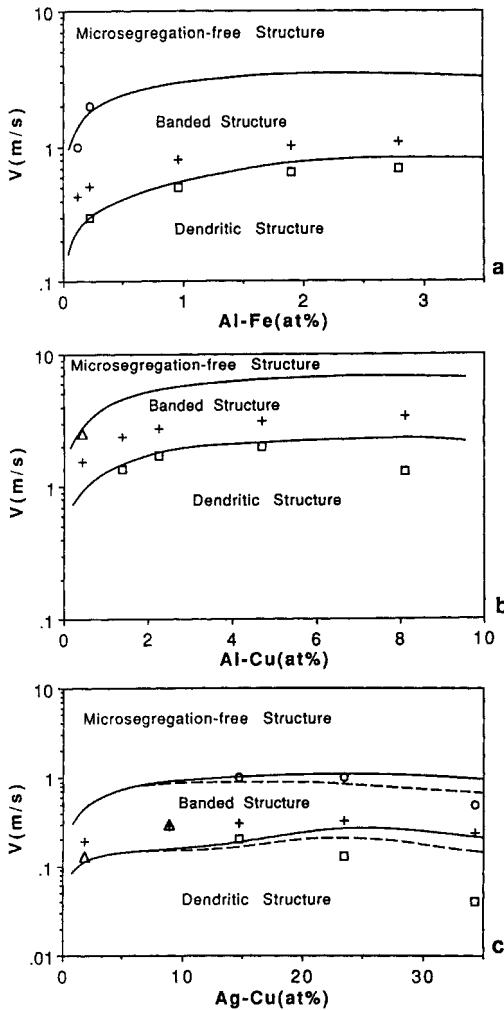


Figure 2-46. Experimental velocities at the transitions from dendrites to bands (squares) and from bands to microsegregation-free structures (circles) for the (a) Al-Fe, (b) Al-Cu and (c) Ag-Cu systems. The triangles indicate experimentally determined transitions from dendrites to microsegregation-free structure, and the crosses the values of the absolute stability limit. The full and dashed lines are the theoretical predictions of the model for dilute and concentrated solutions, respectively (Carrard et al., 1992).

additional factors influence the growth of the solid.

The models in this chapter are minimal in the sense that they were intended to capture the essence of a phenomenon with the

smallest possible number of experimental parameters. Despite this simplification, however, the results appear to be of general importance.

The discussion of free dendritic growth has been restricted so far to small Péclet numbers or low supercoolings. In directional solidification, however, we are usually at moderate or even high Péclet numbers (Ben Amar, 1990; Brener and Melnikov, 1990). It was shown by Brener and Melnikov (1990) that in this case a deviation from dendritic scaling occurs if $Pe^{1/2}$ increases approximately beyond unity. At high growth rates, furthermore, kinetic coefficients can no longer be ignored at the interface. A proposed scaling relation (Brener and Melnikov, 1991) was confirmed numerically (Classen et al., 1991), and combined anisotropy of surface tension and kinetic coefficient was treated analytically (Brener and Levine, 1991; Ben-Jacob and Garik, 1990). A general treatment of kinetic coefficients on interface stability was given by Caroli et al. (1988). For eutectic growth, this was formulated by Geilikman and Temkin (1984). For higher anisotropies than considered so far, we encounter facets on the growing crystals. This was analyzed for single dendrites (Adda Bedia and Ben Amar, 1991; Maurer et al., 1988; Raz et al., 1989; Yokoyama and Kuroda, 1988) and for directional solidification (Bowley et al., 1989).

In our treatment of directional solidification, only one diffusion field was treated explicitly, namely the compositional diffusion. If a simple material grows dendritically (thermal diffusion), small amounts of impurities may become a matter of concern. This was reconsidered by Ben Amar and Pelce (1989), confirming the previous conclusion (Karma and Langer, 1984; Karma and Kotliar, 1985; Lipton et al., 1987) that impurities may increase the dendritic growth rate.

A subject of appreciable practical importance concerns the late stages of growth, where coarsening of the side branch structures occurs together with segregation (Kurz and Fisher, 1998). If elastic forces are not of primary importance, it is now generally accepted (see Chapter 6, Sec. 6.4.1) that a relation $L^* = A + B t^{1/3}$ (Huse, 1986) is a good representation of typical length scales L^* varying with time t during diffusional coarsening processes. This confirms the classical Lifshitz–Slyozov–Wagner theory (Lifshitz and Slyozov, 1961; Wagner, 1961). The result, however, is not specific about the geometric details, for example, in directional solidification, and it also assumes constant temperature.

We have only briefly mentioned the transition from dendritic arrays back to a plane front during directional solidification at very high speeds. The importance of kinetic coefficients was demonstrated by Brenner and Temkin (1989), and recently, the possibility of chaotic dynamics in this region similar to those described in the Kuramoto–Sivashinsky equation was suggested by Misbah et al. (1991).

A richness of dynamic phenomena was obtained in a stability analysis of eutectics (Datye et al., 1981). The possibility of *tilted lamellar arrays* in eutectics was demonstrated by Caroli et al. (1990) and, similarly, for directional solidification at high speeds by Levine and Rappel (1990). This was observed in experiments on nematic liquid crystals (Bechhoefer et al., 1989) and in eutectics (Faivre et al., 1989).

Finally, the density difference between liquid and solid should have some marked influence on the growth mode (Caroli et al., 1984, 1989). For dendritic growth, forced flow was treated in some detail by Ben Amar et al. (1988), Ben Amar and Pomeau (1992), Bouissou and Pelce (1989), Bouissou et al. (1989, 1990) and Rabaud et

al. (1988). Other sources of convective instability (Corriell et al., 1980; Sahm and Keller, 1991) cannot be discussed here in any detail, as the literature is too extensive in order to be covered within this chapter.

Phase-field models

In recent years, the phase-field methodology has achieved considerable importance in modeling and numerically simulating a range of phase transitions and complex growth structures that occur during solidification. Phase-field models have been applied to a wide range of materials such as pure melts, simple binary alloys, eutectic and peritectic phase transitions and grain growth structures in situations as diverse as dendritic growth and rapid solidification.

In the phase-field formulation a mathematically sharp solid–liquid interface is smeared out or regularized and treated as a boundary layer, with its own equation of motion. The resulting formulation no longer requires front tracking and the imposition of boundary conditions, but must be related to the sharp interface model by an asymptotic analysis. In fact, there are many ways to prescribe a smoothing and dynamics of the sharp interface consistent with the original sharp-interface model. So there is no unique phase-field model, but rather a family of related models. The first phase-field model was developed by Langer (1986) in *ad hoc* manner. Subsequently, models have been placed on a more secure basis by deriving them within the framework of irreversible thermodynamics (Penrose and Fife, 1990; Wang et al., 1993). Caginalp (1989) presented for the first time the relation between phase-field models and sharp interface models or free boundary problems by considering the sharp

interface limit in which the interface thickness is allowed to tend to zero.

However, the technique also has some disadvantages. The first is related to the effective thickness of the diffuse interface of alloys (1–5 nm) which is three to four orders of magnitude smaller than the typical length scale of the microstructure. Since the interface must spread over several points of the mesh, this limits considerably the size of the simulation domain. The second problem arises from the attachment kinetics term, which plays a significant role in the phase-field equation, unlike microstructure formation of metallic alloys at low undercooling. These two factors have so far limited phase-field simulations of alloy solidification with realistic solid-state diffusivities to relatively large supersaturations. Recent mathematical and computational advances, however, are rapidly changing this picture. Some of the recent advances include: 1) a reformulated asymptotic analysis of the phase-field model for pure melts (Karma and Rappel, 1996, 1998) that has (i) lowered the range of accessible undercooling by permitting more efficient computations with a larger width of the diffuse interface region (as compared to the capillary length), and (ii) made it possible to choose the model parameters so as to make the interface kinetics vanish; 2) a method to compensate for the grid anisotropy (Bösch et al., 1995); 3) an adaptive finite element method formulation that refines the zone near the diffuse interface and that has been used in conjunction with the reformulated asymptotics to simulate 2D dendritic growth at low undercooling (Provatas et al., 1998); 4) the implementation of the method for fluid flow effects (Diepers et al., 1997; Tonhardt and Amberg, 1998; Tong et al., 1998), and 5) the extension of the technique to other solidification phenomena including eutectic (Karma, 1994;

Elder et al., 1994; Wheeler et al., 1996) and peritectic reactions (Lo et al., 2000).

2.6 Eutectic Growth

2.6.1 Basic Concepts

Eutectic growth is a mode of solidification for a two-component system. Operating near a specific point in the phase diagram, it shows some unique features (Kurz and Fisher, 1998; Lesoult, 1980; Hunt and Jackson, 1966; Elliot, 1983).

The crucial point in eutectic growth is that the solidifying two-component liquid at a concentration near C_E (Fig. 2-19) can split into two different solid phases. The first phase consists of a high concentration of A atoms and a low concentration of B atoms; the second solid phase has the opposite concentrations. These two phases appear alternatively as lamellae or as fibers of one phase in a matrix of the other phase.

One condition for the appearance of a eutectic alloy is apparently a phase diagram (as sketched in Fig. 2-19) with a temperature T_E . The two-phase regions meet at (T_E, C_E) , and the two liquidus lines intersect before they continue to exist as metastable liquidus lines (dash-dotted line) at temperatures somewhat below T_E . This is a material property of the alloy (Pb–Sn for example). The other condition is the experimental starting condition for the concentration in the high-temperature liquid. Assume that we are moving a container filled with liquid at concentration C_∞ in a thermal gradient field where the solid is cold, the liquid is hot, and the solidification front is proceeding towards the liquid in the positive z -direction. As a stationary solution, we find a similar condition to the simple directional solidification case; that is the concentration in the solid \bar{C}_S aver-

aged across the front must be equal to C_∞ to maintain global mass conservation together with a stationary concentration profile near the front.

Assume now that the liquid concentration at infinity, C_∞ , is close to C_E and the temperature at the interface is at T_E . The solid may split into two spatially alternating phases now on the equilibrium (binodal) solidus lines $\tilde{C}_S(T_I)$, one located near $C \rightarrow 0$, and one located near $C \rightarrow 1$ at $T_I < T_E$. To see what happens, let us look at the situation with the concentration in the liquid C_∞ being precisely at eutectic composition $C_\infty = C_E$. At $T_I < T_E$, there may now be alternating lamellae formed of solid concentration \tilde{C}_S^α and \tilde{C}_S^β (Fig. 2-47), the corresponding metastable liquidus concentrations being at \tilde{C}_L^α and \tilde{C}_L^β . For both solid phases now the liquid concentration $C_\infty = C_E$ is in the metastable two-phase regions at T_I : $\tilde{C}_S^\alpha < C_\infty < \tilde{C}_L^\alpha$, $\tilde{C}_L^\beta < C_\infty < \tilde{C}_S^\beta$. In principle, we have to consider the possibility of metastable solid phases (Temkin, 1985), which we ignore here for simplicity.

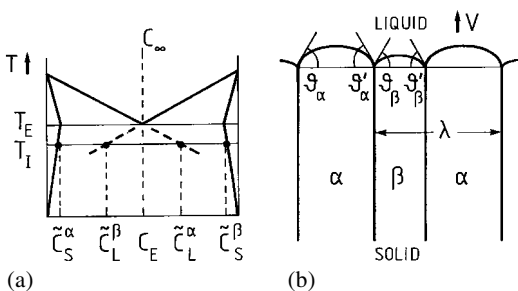


Figure 2-47. Sketch of symmetrical eutectic phase diagram (a) and eutectically growing lamellar cells (b), where α is the solid phase with concentration \tilde{C}_S^α , and β the solid phase with concentration \tilde{C}_S^β . The average temperature at the interface is around T_I below the eutectic temperature T_E . The liquid at the interface is at metastable concentrations (dashed lines in (a)). The solid-liquid interfaces in (b) are curved and they meet with α - β interfaces at three-phase coexistence points.

Diffusion of excess material not incorporated into one of the lamellae does not have to continue up to infinity but only to the neighboring lamella, which has the opposite composition relative to C_∞ . Assuming again for simplicity a symmetric phase diagram, we may write this flux balance as

$$V C_E (1-k) = D \frac{\Delta \tilde{C}}{(\lambda/2)} \quad (2-129)$$

where the left-hand side describes the flux J of material to be carried away from each lamellar interface during growth at velocity V , which then must be equal to the diffusion current (concentration gradient) over a distance $\lambda/2$ to the neighboring lamella (across the liquid, as we ignore diffusion in the solid). $\Delta \tilde{C} = \tilde{C}_L^{(\alpha)} - \tilde{C}_L^{(\beta)}$ is the concentration difference in the liquid at the interfaces of the lamellae, and $k < 1$ is the segregation coefficient.

With the help of the liquidus slopes $dT/d\tilde{C}_L$ as material parameters, we can express the undercooling $\Delta T_I = T_E - T_I$ as

$$\Delta T_I = \Delta \tilde{C} 2 \left| \frac{dT}{d\tilde{C}_L} \right| \quad (2-130)$$

(symmetrical phase diagram assumed about C_E) and thus

$$\Delta T_I = 2 \left| \frac{dT}{d\tilde{C}_L} \right| C_E (1-k) \frac{\lambda}{l} \quad (2-131)$$

Again, $l = 2 D/V$ is the diffusion length.

So far we have ignored the singular growth points on the interface where the liquid and two lamellae α and β meet (Fig. 2-47). At this triple point in real space (or three-phase junction), the condition of mechanical equilibrium requires that the surface tension forces exerted from the three interfaces separating α , β and the liquid cancel to zero. In the simplest version, this condition defines some angles ϑ_α , ϑ_β of the two

solid–liquid interfaces relative to a flat interface. Accordingly, the growth front will have local curvature. What is worse, there is no guarantee that the α – β solid–solid interfaces are really parallel to the growth direction. Making a symmetry assumption for simplicity again, we can ignore this problem for the moment. The curvature K of the growth front at each lamella is then proportional to λ^{-1} . This curvature requires, through the Gibbs–Thomson relation, Eq. (2-102), another reduction, ΔT_K , of the interface temperature below T_I :

$$\Delta T_K = T_E dK \quad (2-132)$$

where d is an effective capillary length, depending on surface tensions, with K now taken as $K \sim \lambda^{-1}$.

The total reduction of temperature below T_E during eutectic growth can thus be written as

$$\Delta T = \Delta T_I + \Delta T_K = T_E \left\{ a_I \frac{\lambda}{l} + a_K \frac{d}{\lambda} \right\} \quad (2-133)$$

with dimensionless constants a_I and a_K .

Plotting this supercooling as a function of lamellar spacing, we find a minimal supercooling $\partial \Delta T / \partial \lambda = 0$ at

$$\lambda = \sqrt{a_K / a_I} \sqrt{ld} \quad (2-134)$$

Again, this is the fundamental scaling relation conjectured in Eq. (2-1) and encountered in various places in this chapter, where the origin is a competition between driving force and stabilizing forces, most intuitively expressed in Eq. (2-133).

A more thorough theoretical analysis of eutectic growth was given in the seminal paper by Jackson and Hunt (1966), which is still a standard reference today. One basic approximation in this paper was to average the boundary conditions on flux and temperature over the interface. This led to Eq. (2-133), and it was argued that the min-

imum undercooling would serve as the operating point of the system with spacing given by Eq. (2-134).

This stationary calculation was extended by Datye and Langer (1981) to a dynamic stability analysis, where the solid–solid–liquid triple points could move parallel and perpendicular to the local direction of growth, coupled however to the normal direction of the local orientation of the front. It was found that the marginal stability coincided exactly with the point of minimum undercooling.

The basic model equations for eutectic growth in a thermal gradient field can be written in scaled form as follows (Brattkus et al., 1990; Caroli et al., 1990). Neglecting diffusion in the solid (one-sided model) and assuming a single diffusion coefficient D for solute diffusion near eutectic concentration C_E (Fig. 2-47), we assume a symmetric phase diagram about C_E for simplicity.

We define a relative (local) concentration gap as

$$\delta = \frac{\Delta C_\alpha}{\Delta C} \quad (2-135)$$

with $\Delta C_\alpha = C_E - \tilde{C}_S^\alpha(T)$, $\Delta C_\beta = \tilde{C}_S^\beta(T) - C_E$ and $\Delta C = \Delta C_\alpha + \Delta C_\beta$.

The dimensionless composition is then defined as

$$u = \frac{C - C_E}{\Delta C(T_E)} \quad (2-136)$$

and (in contrast to the previous definitions) we express lengths and times in units of a diffusion length \tilde{l} and time $\tilde{\tau}$

$$\tilde{l} = D/V, \quad \tilde{\tau} = D/V^2 \quad (2-137)$$

(Note that \tilde{l} here differs by a factor of 2 from previous definitions.) Restricting our attention to two dimensions corresponding to lamellar structures, we now define the

diffusion equation as

$$\frac{\partial u}{\partial t} = \nabla^2 u + \frac{\partial}{\partial z} u \quad (2-138)$$

The conservation law at the interface $z = \zeta(x, t)$ is

$$-\hat{n} \cdot \nabla u = \Delta(x, t) (1 + \dot{\zeta}) n_z \quad (2-139)$$

with the unit vector \hat{n} normal to the interface and

$$\Delta(x, t) = \begin{cases} \delta & \text{for } x \text{ in } \alpha/\lambda\text{-front regions} \\ \delta - 1 & \text{for } x \text{ in } \beta/\lambda\text{-front regions} \end{cases} \quad (2-140)$$

The Gibbs–Thomson relation for the boundary becomes

$$u(\zeta, t) = \begin{cases} -d_\alpha K - \frac{\zeta}{l_{T\alpha}} & \text{in } \alpha/\lambda\text{-regions} \\ -d_\beta K - \frac{\zeta}{l_{T\beta}} & \text{in } \beta/\lambda\text{-regions} \end{cases} \quad (2-141)$$

(kinetic coefficients were considered by Geilikman and Temkin (1984). Finally, and this is a new condition in comparison with the simple directional solidification, the triple point where three interfaces meet should be in mechanical equilibrium

$$\gamma_{\alpha L} + \gamma_{\beta L} + \gamma_{\alpha\beta} = 0 \quad (2-142)$$

with the surface tension vectors γ oriented so that each vector points out of the triple point and is tangent to the corresponding interface. As before, K is the local curvature of the interface, being positive for a solid bulging into the liquid. The dimensionless capillary and thermal lengths associated with the α -phase are

$$d_\alpha = \frac{1}{\tilde{l}} \frac{\gamma_{\alpha L} T_E}{m_\alpha (\Delta C) L_\alpha} \quad (2-143)$$

$$l_{T\alpha} = \frac{1}{\tilde{l}} \frac{m_\alpha (\Delta C)}{G_T} \quad (2-144)$$

and are equivalent for the β phase, with $m_\alpha = |dT/d\tilde{C}_L^\alpha|$ as the absolute liquidus slope, G_T as the fixed thermal gradient and L_α as the specific latent heat. At infinity, $z \rightarrow \infty$, the boundary condition to Eq. (2-138) is u_∞ , depending on the initial concentration in the liquid. This then forms a closed set of equations.

Ahead of the eutectic front, the diffusion field can be thought of as containing two ingredients: a diffusion layer of thickness \tilde{l} associated with global solute rejection and modulations due to the periodic structure of the solid of the extent λ ($\lambda \ll \tilde{l}$). When the amplitude of the front deformations is small compared to these lengths, the averaging approximation by Jackson and Hunt (1966) (and also by Datye and Langer, 1981) seems justified.

This point was taken up by Caroli et al. (1990), who found that the approximation is safe only in the limit of large thermal gradients

$$G_T \gg V m (\Delta C) / D. \quad (2-145)$$

This approximation appears difficult to reach experimentally, though.

In an attempt to shed some light on wavelength selection, Datye et al. (1981) and Langer (1980b) considered finite amplitude perturbations of the local wavelength (Fig. 2-48). This type of approach was used in a somewhat refined version by Brener et al. (1987). They derived an approximate potential function for wavelengths λ and argued that under finite amplitude of noise, the wavelength selected on average is defined by a balance in the creation rates and the annihilation rates of lamellae. In other words, if lamellae disappear through suppression by neighboring lamellae and appear through nucleation, then an equal rate of these processes leads to a selection of an average spacing $\bar{\lambda}$, because both depend on λ . The operating point was found in a

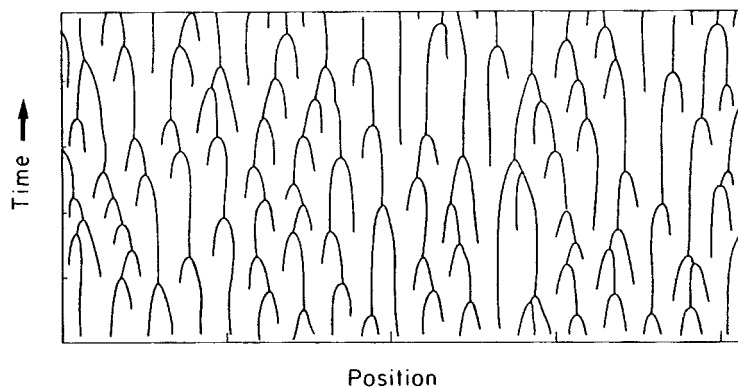


Figure 2-48. Turbulent behavior of lamellar spacings with time in a simplified model of eutectic growth (Datye et al., 1981).

limited interval near the wavelength corresponding to minimal supercooling (or maximal velocity in an isothermal process) and, accordingly, is described by Eq. (2-134).

More recent extensions of the theory (Coullet et al., 1989) gave indications that the orientation of the lamellae (under isotropic material parameters) are necessarily parallel to the growth direction of the front but may be tilted and travel sideways at some specific angles (Caroli et al., 1990; Kassner and Misbah, 1991). Finally, it was found (Kassner and Misbah, 1991b) that the standard model of eutectic solidification has an intrinsic scaling structure

$$\lambda \sim \sqrt{l_d} f(l/l_T) \quad (2-146)$$

with a scaling function f depending only on l/l_T so that $\lambda \sim V^{-1/2}$ for $2l \leq l_T$ or for high enough velocities, while at lower velocities the exponent should be smaller: $\lambda \sim V^{-0.3}$. This is in good agreement with the arguments given for ordinary directional solidification and also explains a lot of experimental data (Lesoult, 1980).

Numerical simulations of the full continuum model of eutectic growth were subsequently carried out by Kassner and Misbah (1990, 1991a, b, c). They gave a fairly complete description of the steady-state structures to be expected in the eutectic

system, revealing the similarities in the structure of solution space between eutectic and dendritic growth by showing the existence of a discrete set of solutions for each parameter set (Kassner and Misbah, 1991b). Axisymmetric solutions were shown to cease to exist beyond a certain wavelength by merging in a fold singularity. For larger wavelengths, extended tilted states appear. They were characterized in detail, both numerically (Kassner and Misbah, 1991c) and analytically (Misbah and Temkin, 1992; Valance et al., 1993). The supercritical nature of the tilt bifurcation was demonstrated and a prediction was made as to how *extended* tilted domains could be produced rather than the localized structures found so far. This prediction was borne out by subsequent experiments by the Faivre group (Faivre and Mergy, 1992a). Amplitude equations were derived that explained how a supercritical bifurcation could give rise to localized tilted domains and predicted a dynamical wavelength selection mechanism (Caroli et al., 1992; Kassner and Misbah, 1992a) as well as describing the influence of crystalline anisotropy (Kassner and Misbah, 1992a). Again, this was verified in detail experimentally (Faivre and Mergy, 1992b). A similarity equation was derived both for axisymmetric (Kassner and Misbah,

1991b) and tilted states (Kassner and Misbah, 1992b), giving the corrections to the aforementioned scaling law. Anomalous asymmetric cells bearing resemblance to asymmetric cells in experiments on dilute alloys (Jamgotchian et al., 1993) were found in the numerical solution of the eutectic growth problem and described analytically (Kassner et al., 1993).

To conclude the discussion of steady states, it was shown numerically that a number of periodicity-increasing bifurcation exist, greatly enlarging the space of possible stationary solutions (Baumann et al., 1995a). These results strongly suggest that the question of wavelength selection should be considered from a different point of view. It is known that a band of steady-state solutions exists in directional solidification beyond the instability threshold and a similar statement holds for eutectic (even though there is no threshold in this case). Moreover, careful experiments (Faivre, 1996) have clarified that the observed wavelength depends on the history of the sample. Therefore, there is no wavelength selection in the strict mathematical sense. This is at least true in the absence of noise, i.e. for the deterministic equations of motion. However, the investigations of Baumann et al. (1995a) render it plausible that a whole attractor of steady-state solutions with accumulation points exists. One of these accumulation points is the point of marginal stability. Since the temporal evolution of any structure in the vicinity of this attractor will become slow, it seems likely that observed wavelengths will correspond to points of increased density of this attractor. There have been objections (Karma and Rappel, 1994) that many of the newly found steady-state solutions are on the low-wavelength side of the point of marginal stability, hence they are unstable and therefore irrelevant for pattern formation. This

objection was countered (Baumann et al., 1995b) by pointing out that there is quite a number of steady states on the high-wavelength side of this point and that the question of irrelevance for pattern formation is a question of time-scales. Since these become slow near the accumulation point, the relevance of a density of additional states cannot be easily discarded. It should be kept in mind that tilted lamellar states are also unstable with respect to phase diffusion near the tilt bifurcation (Fauve et al., 1991). Nevertheless, they survive experimental time-scales, because phase diffusion is very slow.

The first *dynamic* simulation of the continuum model of eutectic growth (in the quasi-stationary approximation) appears to have been done by Kassner et al. (1995), but the only extensive study so far is due to Karma and Sarkissian (1996). This beautiful work was done in close collaboration with experimentalists and thus validated quantitatively. It pinpointed a number of new short-wavelength oscillatory instabilities and made quantitative predictions for the $\text{CBr}_4\text{--C}_2\text{Cl}_6$ system allowing these instabilities to be reproduced in experiments (Faivre, 1996; Ginibre et al., 1997). Therefore, a pretty complete picture exists today of the possible stationary and oscillatory patterns in lamellar eutectic growth and their stability range.

A recent development is the stability analysis of ternary eutectics by Plapp and Karma (1999), based on an extension of the Datye–Langer theory. It shows how the presence of a third component in the system leads to the formation of eutectic colonies; an effective description of the eutectic front on length scales much larger than the lamellar spacing is provided, which yields a simple means of calculating an approximate stability spectrum.

2.6.2 Experimental Results on Eutectic Growth

Eutectic growth was a subject of much interest to experimentalists in the late 1960s and early 1970s. Substantial research has been motivated by the possibility of developing new high-temperature materials. The *in situ* directional solidification of two phases of very different properties is an interesting method of producing composite materials with exceptional properties. However, since these materials could not outperform the more conventional, directionally solidified dendritic superalloys in the harsh environment of a gas turbine, the interest dropped. Therefore, most of the research on eutectics was performed before 1980 (for a review, see Kurz and Sahm, 1975; Elliott, 1983). One exception is the ongoing research concerning casting of eutectic alloys such as cast iron (Fe–C or Fe–Fe₃C eutectic) and Al–Si.

Casting alloys are generally inoculated and solidify in equiaxed form (free eutectic growth) (see Flemings, 1991). This fact, however, does not make any substantial difference to their growth behavior because growth is solute diffusion controlled in nearly all cases owing to the high concentration of the second element. The models described above therefore apply to both directional and free solidification.

The different alloys can be classified into four groups of materials (Kurz and Fisher, 1998): lamellar or fibrous systems, and non-faceted/non-faceted (nf/nf) or non-faceted/faceted (nf/f) systems.

The distinction between f and nf growth behavior can be made with the aid of the melting entropy. Small entropy differences ΔS_f between liquid and solid (typical for metals and plastic crystals such as SCN, PVA, etc.) lead to nf growth with atomically rough interfaces. Materials with large

ΔS_f values are prone to form atomically smooth interfaces, which lead to the formation of macroscopically faceted appearance.

In the case of nf/nf eutectics, volume fractions (of one eutectic phase) of less than 0.3 lead generally to fibers, while at volume fractions between 0.3 and 0.5, lamellar structures prevail. The microstructures of nf/nf eutectics (often simple metal/metal systems) are considered regular and those of nf/f eutectics (mostly the above-mentioned casting alloys) are considered irregular. Fig. 2-49 shows schematically the morphology of the growth front in both cases. It can be easily understood that growth in nf/nf eutectics is much more of a steady-state type than it is in f/nf eutectics.

Regular structures

Applying a criterion such as growth at the extremum to the solution of the capil-

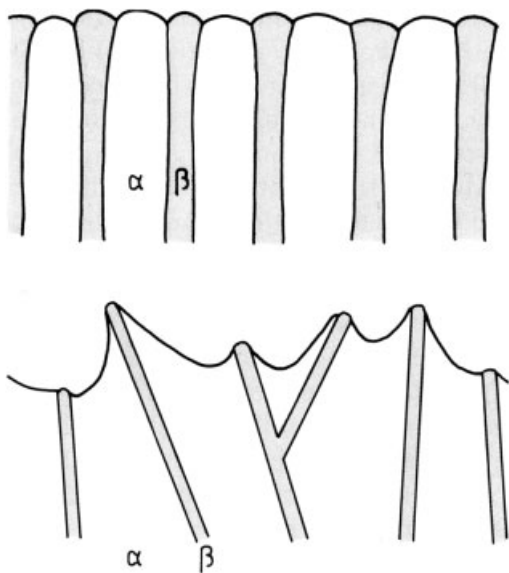


Figure 2-49. Solid/liquid interface morphologies of (a) regular (nf/nf) eutectics and of (b) irregular (nf/f) eutectics during growth.

lary-corrected diffusion equations (Jackson and Hunt, 1966), Eq. (2-133), we obtain for nf/nf eutectics the well-known relationships (Eq. (2-134))

$$\lambda^2 V = C$$

$$\Delta T^2/V = 4C'$$

where C and C' are constants. Fig. 2-50 shows that this behavior has been observed globally in many eutectic systems, some of them having been studied over five orders of magnitude in velocity. The situation is much less clear when it comes to analyzing

eutectoid systems. (Eutectoids are “eutectics” with the liquid parent phase replaced by a solid.) Often a $\lambda^3 V$ relationship is found in these systems (Fig. 2-50b) over some range of the variables (see Eq. (2-146)).

In general, it may be said that the field of eutectic growth is under-represented in materials research, and many more careful studies are needed before a clearer insight into their growth can be gained. Trivedi and coworkers began such research in the early 1990s, and some of their results are

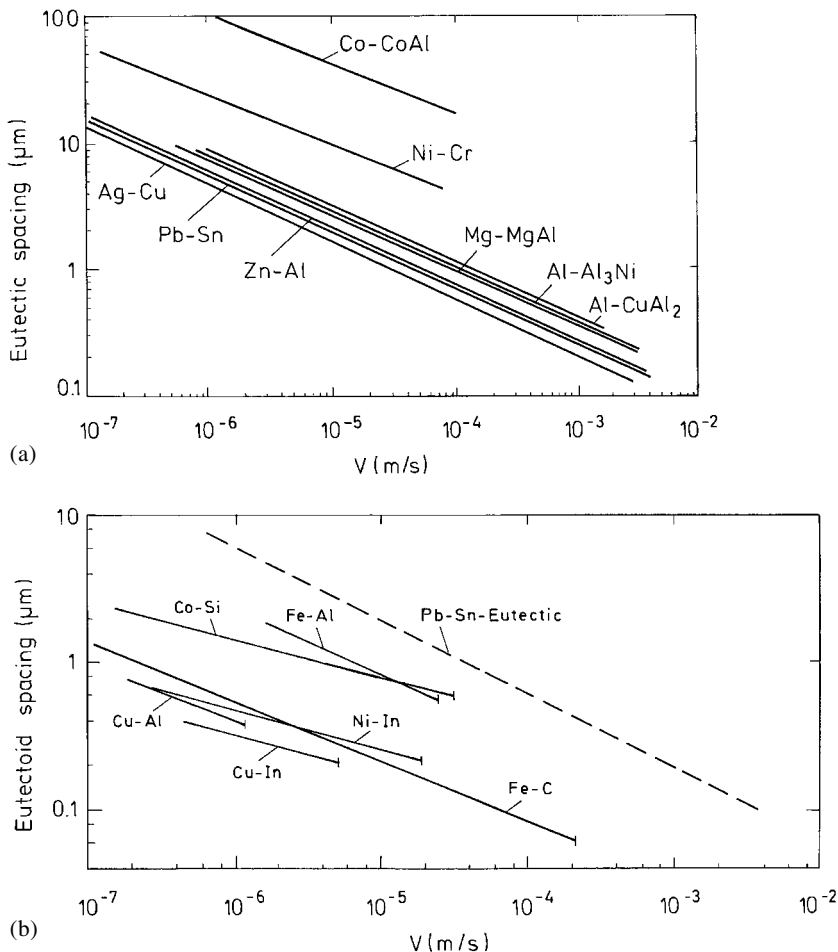


Figure 2-50. Lamellar spacings of (a) directionally solidified eutectics and (b) directionally transformed eutectoids as a function of growth rate (Kurz and Sahn, 1975).

presented here. Fig. 2-51 indicates that in eutectics the spacings are also not at all uniquely defined. There is a rather wide distribution around a mean value for each rate (Trivedi et al., 1991). The operating range of eutectics is determined by the per-

manent creation and movement of faults (see below). This process is three-dimensional and cannot be realistically simulated in two-dimensional calculations.

In Fig. 2-52, the mean spacings are plotted as points, and the limits of the distribu-

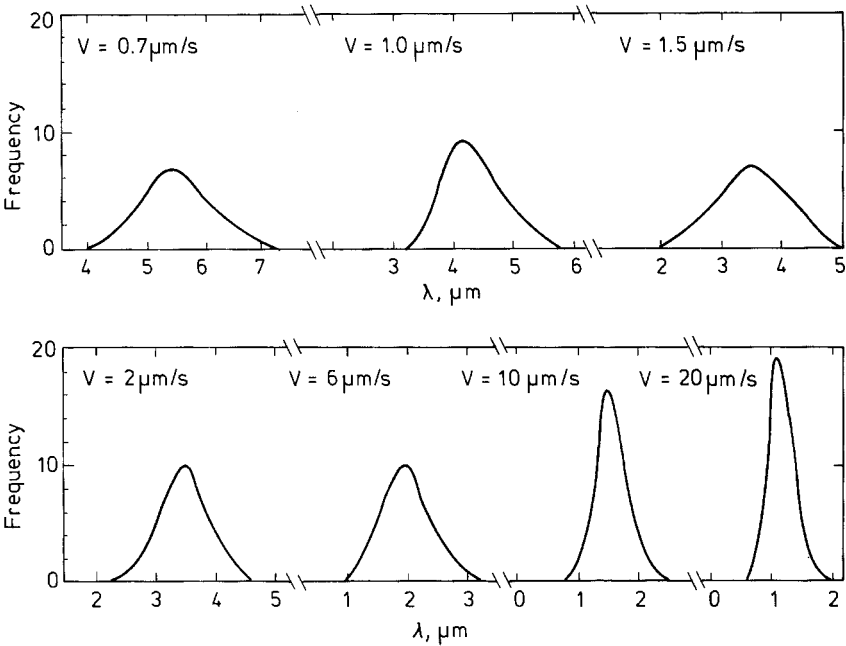


Figure 2-51. Eutectic spacing distribution curves as a function of velocity for Pb–Pd eutectics (Trivedi et al., 1991).

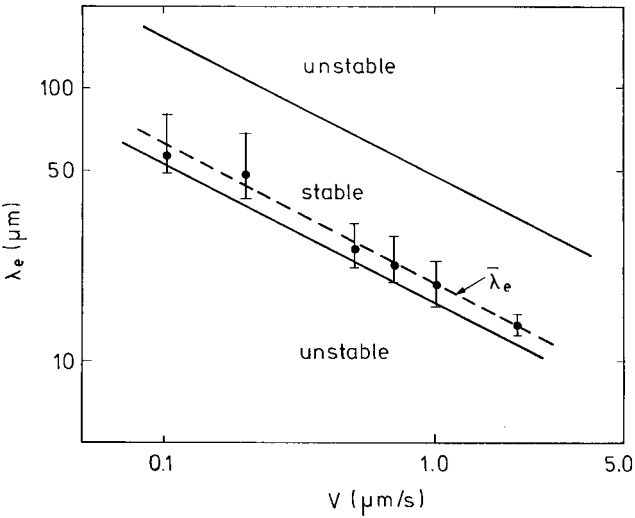


Figure 2-52. A comparison of the experimental results on the interlamellar spacing variation with velocity for CBr₄–C₂Cl₆ with the theoretical values (solid lines) for two marginally stable spacings (Seetharaman and Trivedi, 1988).

tion are given by the extension of the bars. From the calculated range of stability, which was discussed by Jackson and Hunt (1966), it can be seen that the minimum of the experimental values coincides with the theoretical prediction (see also Sec. 2.6.1). This, however, does not provide definitive proof of this prediction, due to the fact that several physical parameters of the system are not precisely known. On the other hand, it is clear that eutectic spacings do not explore the upper range of stability (catastrophic breakdown), at least not in nf/nf systems. Some other mechanism limits the spacing at its upper bound. The adjustment of spacings is a rapid process, and its rate increases when the spacing increases (Seetharaman and Trivedi, 1988).

Irregular structures

The above relationship for eutectic spacing and undercooling as a function of growth rate are also useful in the case of irregular systems such as the nf/f casting alloys Fe–C or Al–Si (Fig. 5-49b). Jones and Kurz (1981) introduced a factor, ϕ , which is equal to the ratio of the mean spacing, $\langle\lambda\rangle$, of the irregular structure to the spacing at the extremum. This leads to the following relationships:

$$\langle\lambda\rangle^2 V = \phi^2 C$$

$$\langle\Delta T\rangle^2/V = [\phi + (1/\phi)]^2 C'$$

Faults

Defects in the ideal lamellar or fibrous structure are an essential ingredient of eu-

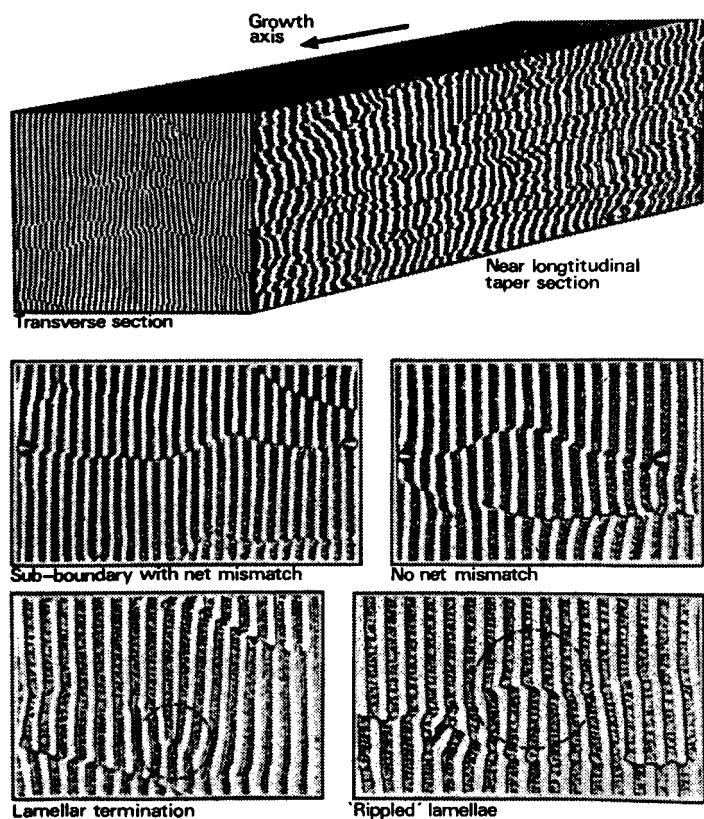


Figure 2-53. Eutectic fault structures in directionally solidified Al–CuAl₂ alloy (Double, 1973).

tectic growth. They allow the two-phase crystal to rotate into crystallographically (energetically) favorable orientations (Hogan et al., 1971) and to adapt its spacing to the local growth conditions. In lamellar systems, there are different types of faults (Double, 1973): single or extended faults, with or without net mismatch (Fig. 2-53). They mostly represent sub-boundaries of a eutectic grain and could develop through polygonization of dislocations which form because of the stresses created at the inter-phase boundaries of the composite. Fig. 2-54 shows distributions of fault spacings, Λ , for different growth rates indicated by different lamellar spacings, λ (Riquet and Durand, 1975). In the case of non-faceted fibrous structures, the faults are formed by simple fiber branches or terminations.

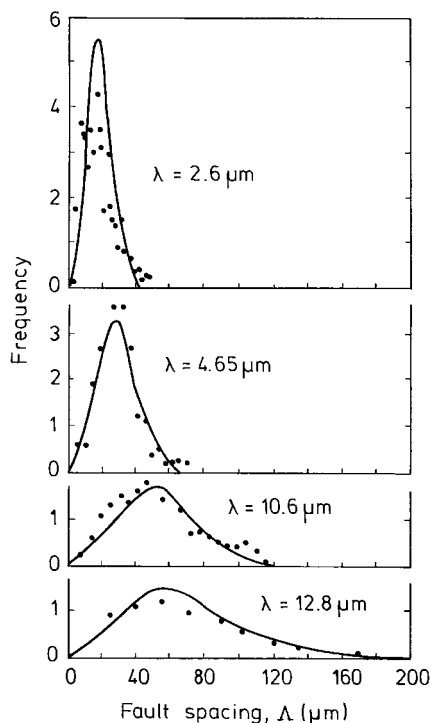
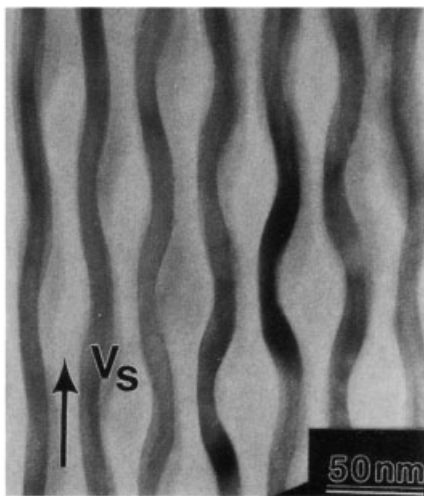


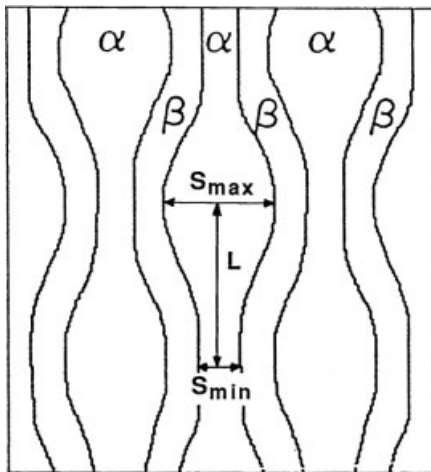
Figure 2-54. Eutectic fault spacing distribution curves for Al-CuAl₂ directionally solidified with different growth rates and spacing values as indicated (Riquet and Durand, 1975).

Oscillations

Periodic oscillations have been observed as a morphological instability in several systems grown under various conditions (Hunt, 1987; Carpay, 1972; Zimmermann et al., 1990; Gill and Kurz, 1993, 1995). These morphological instabilities form in off-eutectic alloys even at growth rates of several cm/s, as is shown in Fig. 2-55.



(a)



(b)

Figure 2-55. Periodic oscillations in hypoeutectic Al-CuAl₂ eutectic under rapid laser resolidification conditions: (a) experimental observation and (b) simulation (Zimmermann et al., 1990; Karma, 1987).

There is good correspondence of the observed structures with the results of theoretical modeling by Datye and Langer (1981) and by Karma (1987). In recent experiments a complete stability diagram for the lamellar $\text{CBr}_4\text{-C}_2\text{Cl}_6$ eutectic has been determined by Ginibre et al. (1997) (Fig. 2-56a). It shows the observed structures for the variables dimensionless spacing (Λ) and concentration (η). In the limits $1 < \Lambda < 2$ the basic state is stable, but over a decreasing composition range when $\Lambda = \lambda/\lambda_{\min}$ is increased. Outside this regime, three different states and combinations of these have been found; tilt mode (T), 1λ oscillations (period-preserving oscillatory or optical mode) and 2λ oscillations (period-doubling oscillatory mode, Fig. 2-56). These results are in good quantitative agreement with numerical results by Karma and Sarkissian (1996).

As was the case with dendrites, eutectics also form extremely fine microstructures when they are subject to rapid solidification. A value of $\lambda = 15$ nm (each phase is some 20 atoms wide) seems to be the minimum spacing that can be achieved with growth rates of the order of 0.2 m/s (Zimmermann et al., 1989). In highly undercooled alloys anomalous eutectic structures have been found which, as with dendrites, seem to be the result of the large capillary forces involved with such fine scales (Goetzinger et al., 1998).

2.6.3 Other Topics

Peritectics

A wide spectrum of microstructures can be found in peritectic alloys. Recently this has produced a great deal of interest (Kerr and Kurz, 1996). In directional solidification, when the G/V ratio is high enough, i.e., in the range of the limit of constitutional undercooling of the phase with the

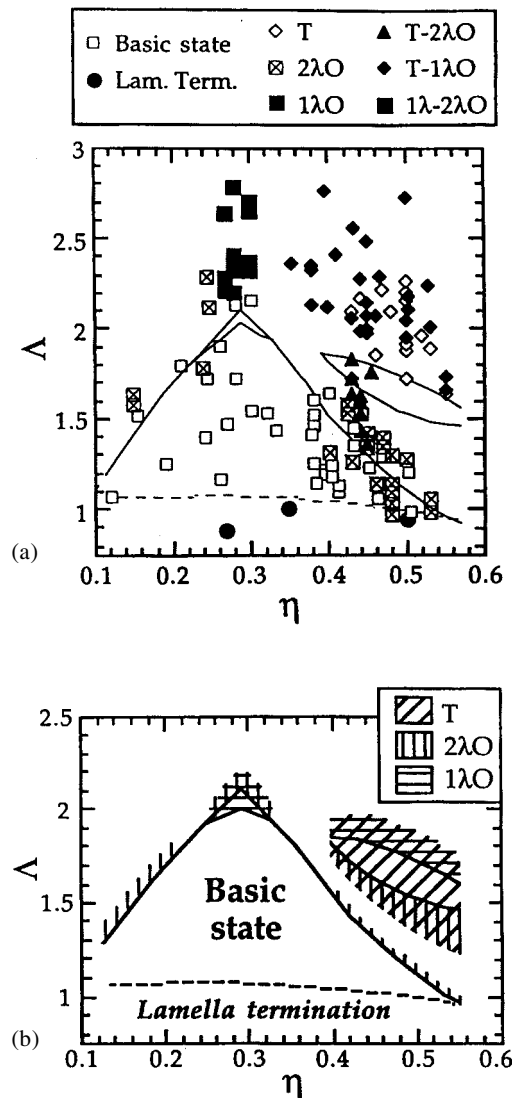


Figure 2-56. Stability diagram of directionally solidified $\text{CBr}_4\text{-C}_2\text{Cl}_6$ alloys. (a) Symbols: experimentally observed periodic patterns (Ginibre et al., 1997). Lam. Term.: lamellar termination. (b) Curves: numerically calculated diagram (Karma and Sarkissian, 1996).

smaller distribution coefficient, more complex microstructures can form in the two-phase region. New phases may appear during transient or steady-state growth via nucleation at the solidification front. The ac-

tual microstructure selection process is thus controlled by nucleation of the phases, and by growth competition between the nucleated grains and the pre-existing phase under non-steady-state conditions. In this case nucleation in the constitutionally undercooled zone ahead of the growth front has to be taken into account in order to determine the microstructure selection (Ha and Hunt, 1997; Hunziker et al., 1998). Further, new structures have been observed which are controlled by convection. More detailed discussions of this subject can be found in Karma et al. (1998), Park and Trivedi (1998), Trivedi et al. (1998), Vandyoussefi et al. (2000), Mazumder et al. (2000).

Phase/microstructure selection

Phase and microstructure selection is of utmost importance to applications of solidification theory as it controls the properties of materials. Nucleation and growth have to be modeled in order to make predictions of structures as a function of composition and the solidification variables; growth rate and temperature gradient for directional solidification, undercooling for free growth. The interested reader is referred to a recent overview by Boettinger et al. (2000) where these phenomena are discussed.

Micro/macro modeling

The last decade has experienced significant progress in numerical modeling of combined macroscopic and microscopic solidification phenomena. Nucleation and growth models have been implemented in 2D and 3D heat flow and fluid flow programs providing a substantial improvement of our analytical tools for optimized and new materials processes such as single crystal casting of superalloys for gas tur-

bines. The interested reader is referred to Rappaz (1989), Rappaz et al. (2000), Wang et al. (1995), Wang and Beckermann (1996), Beckermann and Wang (1996), Boettinger et al. (2000).

2.7 Summary and Outlook

During the recent years, very substantial improvements in our understanding of the pattern-forming processes in solidification have been achieved. Although the basic model equations have been known for several decades, it is only during recent years that the mathematical and numerical tools were extended to allow for a reliable analysis of the complicated expressions. In addition, careful experiments have been performed, mostly on model substances, which have provided an impressive amount of precise, quantitative data. This combined effort has basically solved the problem of free dendritic growth with respect to velocity selection and side branch formation.

In the process of directional solidification, a consistent picture is now emerging, relating the growth mode to free dendritic growth and, at the same time, to viscous fingering and growth in a channel. At very high growth rates that approach the limit of absolute stability, the situation is still somewhat unclear, for non-equilibrium effects like kinetic coefficients then become of central importance. These quantities are difficult to determine experimentally. Furthermore, the selection of the primary spacings of the growing array of cells and dendrites is still subject to discussion. One such point of contention, for example, is the typically observed increase in spacing when moving from cellular to dendritic structures in model substances.

In eutectic growth, the situation is even less understood, for good reason. The

three-phase junctions at the solid–liquid interface enter as additional conditions and further details of the phase diagram become important. The dynamics of the system seem to show a richer structure than ordinary directional solidification. The selection of spacings between the different solid phases in materials of practical importance occurs through three-dimensional defect formation. In addition, nucleation and faceting of the interfaces should be considered.

A number of problems common to all of these growth modes have only been touched upon so far. These problems include, for example, the redistribution of material far behind the tip regions, the treatment of elastic effects, and the interaction with hydrodynamic instabilities due to thermal and compositional gradients.

In summary, we expect the field to remain very active in the future, as it is attractive from a technological point of view. It will certainly provide some surprises and new insights into the general concepts of pattern formation in dissipative systems.

2.8 References

- Abel, T., Brener, E., Müller-Krumbhaar, H. (1997), *Phys. Rev. E* 55, 7789.
- Adda Bedia, M., Ben Amar, M. (1991), *Phys. Rev. A* 43, 5702.
- Akamatsu, S., Faivre, G. (1998), *Phys. Rev. E* 58, 3302.
- Akamatsu, S., Faivre, G., Ihle, T. (1995), *Phys. Rev. E* 51, 4751.
- Almgren, R., Dai, W.-S., Hakim, V. (1993), *Phys. Rev. Lett.* 71, 3461.
- Arnold, C. B., Aziz, M. J., Schwarz, M., Herlach, D. M. (1999), *Phys. Rev. B* 59, 334.
- Assadi, H., Barth, M., Greer, A. L., Herlach, D. M. (1996), *Mat. Sci. Forum* 215–216, 37.
- Assadi, H., Barth, M., Greer, A. L., Herlach, D. M. (1998), *Acta Mater.* 46, 491.
- Baker, J. C., Cahn, J. (1971), in: *Solidification*: Hughel, T. A., Bolling, G. F. (Eds.). Metals Park, OH, USA: American Society of Metals.
- Barber, M. N., Barbieri, A., Langer, J. S. (1987), *Phys. Rev. A* 36, 3340.
- Barbieri, A., Langer, J. S. (1989), *Phys. Rev. A* 39, 5314.
- Barbieri, A., Hong, D. C., Langer, J. S. (1987), *Phys. Rev. A* 35, 1802.
- Barth, M., Wei, B., Herlach, D. M., Feuerbacher, B. (1994), *Mater. Sci. Eng. A* 178, 305.
- Barth, M., Wei, B., Herlach, D. M. (1995), *Phys. Rev. B* 51, 3422.
- Barth, M., Wei, B., Herlach, D. M. (1997), *Mater. Sci. Eng. A* 226–228, 770.
- Baumann, R., Kassner, K., Misbah, C., Temkin, D. (1995a), *Phys. Rev. Lett.* 74, 1597.
- Baumann, R., Kassner, K., Misbah, C., Temkin, D. (1995b), *Phys. Rev. Lett.* 75, 2445.
- Bechhoefer, J., Libchaber, A. (1987), *Phys. Rev. Lett.* 58, 1393.
- Bechhoefer, J., Simon, A. J., Libchaber, A., Oswald, P. (1989), *Phys. Rev. A* 40, 3974.
- Beckermann, C., Wang, C. Y. (1996), *Metall. Mater. Trans. A* 27A, 2784.
- Ben Amar, M. (1990), *Phys. Rev. A* 41, 2080.
- Ben Amar, M. (1998), *Physica D* 111, 409.
- Ben Amar, M., Brener, E. (1993), *Phys. Rev. Lett.* 71, 589.
- Ben Amar, M., Brener, E. (1995), *Phys. Rev. Lett.* 75, 561.
- Ben Amar, M., Moussallam, B. (1987), *Physica* 25D, 155.
- Ben Amar, M., Pelce, P. (1989), *Phys. Rev. A* 39, 4263.
- Ben Amar, M., Pomeau, Y. (1968), *Europhys. Lett.* 2, 307.
- Ben Amar, M., Pomeau, Y. (1992), in: *Solids Far from Equilibrium*: Godreche, C. (Ed.). Cambridge: Cambridge University Press.
- Ben Amar, M., Bouissou, Ph., Pelce, P. (1988), *J. Crystal Growth* 92, 97.
- Ben Jacob, E., Garik, P. (1990), *Nature* 343, 523.
- Ben Jacob, E., Goldenfeld, N., Langer, J. S., Schön, G. (1983), *Phys. Rev. Lett.* 51, 1930.
- Ben Jacob, E., Goldenfeld, N., Langer, J. S., Schön, G. (1984), *Phys. Rev. A* 29, 330.
- Bensimon, D., Pelce, P., Shraiman, B. I. (1987), *J. Phys. France* 48, 2081.
- Bilgram, J. H., Firmann, M., Hürlimann, E. (1989), *J. Crystal Growth* 96, 175.
- Billia, B., Jamgotchian, H., Capella, L. (1987), *J. Crystal Growth* 82, 747.
- Billia, B., Jamgotchian, H., Capella, L. (1989), *J. Crystal Growth* 94, 987.
- Binder, K. (2001), in: *Phase Transformations in Materials*: Kostorz, G. (Ed.), Weinheim: Wiley-VCH, Chap. 4.
- Binder, K., Fratzl, P. (2001), in: *Phase Transformations in Materials*: Kostorz, G. (Ed.), Weinheim: Wiley-VCH, Chap. 6.
- Bisang, U., Bilgram, J. H. (1995), *Phys. Rev. Lett.* 75, 3898.

- Boettinger, W. J., Coriell, S. R., Trivedi, R. (1988), in: *Rapid Solidification Processing: Principles and Technologies IV*: Mehrabian, R., Parrish, P. A. (Eds.), Baton Rouge, LA: Claitor's, p. 13.
- Boettinger, W. J., Coriell, S. R., Greer, A. L., Karma, A., Kurz, W., Rappaz, M., Trivedi, R. (2000), *Acta Mater.* 48, 43.
- Bösch, A., Shochet, O., Müller-Krumbhaar, H. (1995), *Z. Physik B97*, 367.
- Bouissou, Ph., Pelce, P. (1989), *Phys. Rev. A* 40, 6673.
- Bouissou, Ph., Perrin, B., Tabeling, P. (1989), *Phys. Rev. A* 40, 509.
- Bouissou, Ph., Chiffaudel, A., Perrin, B., Tabeling, P. (1990), *Europhys. Lett.* 13, 89.
- Bowley, R., Caroli, B., Caroli, C., Graner, P., Nozieres, P., Roulet, B. (1989), *J. Phys. France* 50, 1377.
- Brattkus, K., Misbah, C. (1990), *Phys. Rev. Lett.* 64, 1935.
- Brattkus, K., Caroli, B., Caroli, C., Roulet, B. (1990), *J. Phys. France* 51, 1847.
- Brazovsky, S. (1975), *Sov. Phys. JETP* 41, 85.
- Brener, E. (1993), *Phys. Rev. Lett.* 71, 3653.
- Brener, E. A., Levine, H. (1991), *Phys. Rev. A* 43, 883.
- Brener, E. A., Melnikov, V. I. (1990), *J. Phys. France* 51, 157.
- Brener, E. A., Melnikov, V. I. (1991), *Adv. Phys.* 40, 53.
- Brener, E. A., Temkin, D. E. (1989), *Europhys. Lett.* 10, 171.
- Brener, E. A., Temkin, D. (1995), *Phys. Rev. E* 51, 351.
- Brener, E. A., Geilikman, M. B., Temkin, D. E. (1987), *Sov. Phys. JETP* 65, 93.
- Brener, E. A., Geilikman, M. B., Temkin, D. E. (1988), *Sov. Phys. JETP* 67, 1002.
- Brener, E. A., Müller-Krumbhaar, H., Temkin, D. (1996), *Phys. Rev. E* 54, 2714.
- Burden, M. H., Hunt, J. D. (1974), *J. Crystal Growth* 22, 99.
- Burkhardt, T., Kroll, D., Müller-Krumbhaar, H. (1977), *J. Crystal Growth* 38, 13.
- Caginalp, G., (1989), *Phys. Rev. A* 39, 5887.
- Callen, H. B. (1960), *Thermodynamics*. New York: Wiley.
- Caroli, B., Caroli, C., Roulet, B. (1982), *J. Phys. France* 43, 1767.
- Caroli, B., Caroli, C., Roulet, B. (1984), *J. Crystal Growth* 66, 575.
- Caroli, B., Caroli, C., Roulet, B., Langer, J. S. (1986a), *Phys. Rev. A* 33, 442.
- Caroli, B., Caroli, C., Misbah, C., Roulet, B. (1986b), *J. Phys. France* 47, 1623.
- Caroli, B., Caroli, C., Roulet, B. (1987), *J. Phys. France* 48, 1423.
- Caroli, B., Caroli, C., Roulet, B. (1988), in: *Solid State Phenomena*: Kubin, L. P., Martin, G. (Eds.). Aedermannsdorf, CH: Trans. Tech. Publ.
- Caroli, B., Caroli, C., Roulet, B., Faivre, G. (1989), *J. Crystal Growth* 94, 253.
- Caroli, B., Caroli, C., Roulet, B., Brattkus, K. (1990), *J. Phys. France* 51, 1865.
- Caroli, B., Caroli, C., Fauve, S. (1992), *J. Phys. I (Paris)* 2, 281.
- Carpay, F. M. A. (1972), in: *Handbuch der Mikroskopie in der Technik*, Vol. VI: Freund, H. (Ed.). Frankfurt: Umschau, p. 355.
- Carrard, M., Gremaud, M., Zimmermann, M., Kurz, W. (1992), *Acta Metall. Mater.* 40, 983.
- Chan, S.-K., Reimer, H.-H., Kahlweit, M. (1978), *J. Crystal Growth* 43, 229.
- Chandrasekhar, C. (1961), *Hydrodynamics and Hydrodynamic Stability*. Oxford: Clarendon.
- de Cheveigne, S., Guthman, C., Lebrun, M. M. (1986), *J. Physique* 47, 2095.
- Chopra, M. A., Glicksman, M. E. Singh, N. B. (1988), *Metall. Trans.* 19A, 3087.
- Classen, A., Misbah, C., Müller-Krumbhaar, H. (1991), *Phys. Rev. A* 43, 6920.
- Cochrane, R. F., Greer, A. L., Eckler, K., Herlach, D. M. (1991), *Mater. Sci. Eng. A* 133, 698.
- Collins, J. B., Levine, H. (1985), *Phys. Rev. B* 31, 6119.
- Corriell, S., Sekerka, R. F. (1983), *J. Crystal Growth* 61, 499.
- Corriell, S., Cordes, M., Boettinger, M., Sekerka, R. (1980), *J. Crystal Growth* 49, 13.
- Coullet, P., Goldstein, R. E., Gunaratne, G. H. (1989), *Phys. Rev. Lett.* 63, 1954.
- Datye, V., Langer, J. S. (1981), *Phys. Rev. B* 24, 4155.
- Datye, V., Mathur, R., Langer, J. S. (1981), *J. Stat. Phys.* 29, 1.
- Deissler, R. J. (1987), *Physica* 22D, 233.
- Diepers, H.-J., Beckermann, C., Steinbach, I. (1997), in: *Solidification Processing 1997*: Beech, J., Jones H. (Eds.), Sheffield, UK: University, p. 426.
- Dombre, T., Hakim, V. (1987), *Phys. Rev. A* 36, 2811.
- Double, D. D. (1973), *Mater. Sci. Eng.* 11, 325.
- Dougherty, A. (1991), *J. Crystal Growth* 110, 501.
- Dougherty, A., Gollub, J. P. (1988), *Phys. Rev. A* 38, 3043.
- Dougherty, A., Kaplan, P. D., Gollub, J. P. (1987), *Phys. Rev. Lett.* 58, 1652.
- Eckhaus, W. (1965), *Studies in Nonlinear Stability Theory; Springer Tracts in Natural Philosophy* 6. Berlin: Springer.
- Eckler, K., Cochrane, R. F., Herlach, D. M., Feuerbacher, B. (1991a), *Mater. Sci. Eng. A* 133, 702.
- Eckler, K., Herlach, D. M., Hamerton, R. G., Greer, A. L. (1991b), *Mater. Sci. Eng. A* 133, 730.
- Eckler, K., Cochrane, R. F., Herlach, D. M., Feuerbacher, B., Jurisch, M. (1992), *Phys. Rev. B* 45, 5019.
- Eckler, K., Herlach, D. M. (1994), *Mater. Sci. Eng. A* 178, 159.
- Eckler, K., Herlach, D. M., Aziz, M. J. (1994), *Acta Metall. Mater.* 42, 975.

- Elliot, R. (1983), *Eutectic Solidification Processing – Crystalline and Glassy Alloys*. London: Butterworths.
- Esaka, H. (1986), Sc.D. thesis, EPFL, Lausanne, CH.
- Esaka, H., Kurz, W. (1985), *J. Crystal Growth* 72, 578.
- Esaka, H. Kurz, W., Trivedi, R. (1988), in: *Solidification Processing 1987*. London: The Institute of Metals, p. 198.
- Eshelman, M. A., Trivedi, R. (1987), *Acta Metall.* 35, 2443.
- Eshelman, M., Seetharaman, V., Trivedi, R. (1988), *Acta Metall.* 36, 1165.
- Faivre, G. (1996), *J. Crystal Growth* 166, 29.
- Faivre, G., Mergy, J. (1992a), *Phys. Rev. A* 45, 7320.
- Faivre, G., Mergy, J. (1992b), *Phys. Rev. A* 46, 963.
- Faivre, G., de Cheveigne, S., Guthmann, C., Kurowsky, P. (1989), *Europhys. Lett.* 9, 779.
- Fauve, S., Douady, S., Thual, O. (1991), *J. Phys. II* 1, 311.
- Fisher, D. J., Kurz, W. (1978), unpublished.
- Fisher, D. J., Kurz, W. (1980), *Acta Metall.* 28, 777.
- Flemings, M. C. (1991), in: *Materials Science and Technology Vol. 15, Processing of Metals and Alloys*: Cahn, R. W. (Ed.). Weinheim: VCH Verlagsgesellschaft, p. 1.
- Fujioka, T. (1978), Ph.D. Thesis, Carnegie-Mellon Univ. Pittsburgh (unpublished).
- Geilikman, M. B., Temkin, D. (1984), *J. Crystal Growth* 67, 607.
- Gill, S., Kurz, W. (1993), *Acta Metall. Mater.* 41, 3563.
- Gill, S., Kurz, W. (1995), *Acta Metall. Mater.* 43, 139.
- Ginibre, M., Akamatsu, S., Faivre, G. (1997), *Phys. Rev. E* 56, 780.
- Glickman, M. E., Singh, N. B. (1986), in: *Rapidly Solidified Powder Alloys*: Fine, M. E. Stark, E. A. (Eds.). Philadelphia: ASTM, p. 44.
- Glickman, M. E., Singh, N. B. (1989), *J. Crystal Growth* 98, 277.
- Glicksman, M., Shafer, R. J., Ayers, J. D. (1976), *Metall. Trans. A* 7, 1747.
- Glickman, M. E., Singh, N. B., Chopra, M. (1988), *J. Crystal Growth* 92, 543.
- Goetzinger, R., Barth, M., Herlach, D. M. (1998), *Acta Mater.* 46, 1647.
- Gremaud, M., Carrard, M., Kurz, W. (1990), *Acta Metall. Mater.* 39, 1431.
- Ha, H. P., Hunt, J. D. (1997), in: *Proc. 4th Dec. Int. Conf. on Solidification Proc. (SP'97)* Beech, J., Jones, H. (Eds.), Sheffield, UK: University, p. 444.
- Henry, S., Minghetti, T., Rappaz, M. (1998), *Acta Mater.* 46, 6431.
- Herlach, D. M. (1994), *Mater. Sci. Eng. A* 179–180, 147.
- Herlach, D. M. (1997), *Mater. Sci. Eng. A* 226–228, 348.
- Herlach, D. M., Cochrane, R. F., Egry, I., Fecht, H. J., Greer, A. L. (1993), *Intern. Mater. Rev.* 38, 273.
- Hogan, L. M., Kraft, R. W., Lemkey, F. D. (1971), *Adv. Mater. Res.* 5, 83.
- Honjo, H., Ohta, S., Sawada, Y. (1985), *Phys. Rev. Lett.* 55, 841.
- Huang, S. C., Glicksman, M. E. (1981), *Acta Metall.* 29, 701; 717.
- Hunt, J. D. (1979), in: *Solidification and Casting of Metals*. London: TMS, p. 1.
- Hunt, J. D. (1987), private communication.
- Hunt, J. D., Jackson, K. A. (1966), *Trans. Metall. Soc. AIME* 236, 843.
- Hunt, J. D., Jackson, K. A., Brown, H. (1966), *Rev. Sci. Instr.* 37, 805.
- Hunt, J. D., Lu, S.-Z. (1996), *Metall. Mater. Trans.* 27A, 611.
- Hunziker, O., Vandyoussefi, M., Kurz, W. (1998), *Acta Mater.* 46, 6325.
- Huse, D. (1986), *Phys. Rev. B* 34, 7845.
- Ihle, T., Müller-Krumbhaar, H. (1994), *Phys. Rev. E* 49, 2972.
- Ivantsov, G. P. (1947), *Dokl. Akad. Nauk SSSR* 58, 567.
- Jackson, K. A. (1958), in: *Liquid Metals and Solidification*. Cleveland: ASM, p. 174.
- Jackson, K. A., Hunt, J. D. (1966), *Trans. Metall. Soc. AIME* 236, 1129.
- Jamgotchian, H., Trivedi, R., Billia, B. (1993), *Phys. Rev. E* 47, 4313.
- Jones, H., Kurz, W. (1981), *Z. Metallkunde* 72, 792.
- Kahlweit, M. (1970), *J. Crystal Growth* 6, 125.
- Karma, A. (1986), *Phys. Rev. Lett.* 57, 858.
- Karma, A. (1987), *Phys. Rev. Lett.* 59, 71.
- Karma, A. (1994), *Phys. Rev. E* 49, 2245.
- Karma, A. (1998), *Intern. J. Non-Equilib. Process.* 11, 201.
- Karma, A., Langer, J. S. (1984), *Phys. Rev. A* 30, 3147.
- Karma, A., Kotliar, B. G. (1985), *Phys. Rev. A* 31, 3266.
- Karma, A., Pelce, P. (1989a), *Phys. Rev. A* 39, 4162.
- Karma, A., Pelce, P. (1989b), *Europhys. Lett.* 9, 713.
- Karma, A., Rappel, W.-J. (1994), *Phys. Rev. Lett.* 75, 2444.
- Karma, A., Rappel, W.-J. (1996), *Phys. Rev. E* 53, 3017.
- Karma, A., Rappel, W.-J. (1998), *Phys. Rev. E* 57, 4323.
- Karma, A., Sarkissian, A. (1993), *Phys. Rev. E* 47, 513A.
- Karma, A., Sarkissian, A. (1996), *Metall. Trans.* 27, 635.
- Karma, A., Rappel, W. J., Fuh, B. C., Trivedi, R. (1998), *Metall. Trans.* 29A, 1457.
- Kashuba, A., Pokrovsky, V. (1990), *Z. Physik* 78, 289.
- Kassner, K., Misbah, C. (1990), *Phys. Rev. Lett.* 65, 1458.
- Kassner, K., Misbah, C. (1991a), *Phys. Rev. Lett.* 66, 445.
- Kassner, K., Misbah, C. (1991b), *Phys. Rev. Lett.* A 44, 6513.

- Kassner, K., Misbah, C. (1991c), *Phys. Rev. A* 44, 6533.
- Kassner, K., Misbah, C. (1992a), *Phys. Rev. A* 45, 7372.
- Kassner, K., Misbah, C. (1992b), *J. Phys. Rev. A* 25, 3213.
- Kassner, K., Valance, A., Misbah, C., Temkin, D. (1993), *Phys. Rev. E* 48, 1091.
- Kassner, K., Misbah, C., Baumann, R. (1995), *Phys. Rev. E* 51, 2751.
- Kerr, H. W., Kurz, W. (1996), *Int. Mater. Rev.* 41, 129.
- Kessler, D., Levine, H. (1986a), *Phys. Rev. Lett.* 57, 3069.
- Kessler, D., Levine, H. (1986b), *Phys. Rev. A* 33, 3352.
- Kessler, D., Levine, H. (1986c), *Phys. Rev. A* 33, 3325.
- Kessler, D., Levine, H. (1986d), *Phys. Rev. A* 36, 4123.
- Kessler, D., Levine, H. (1988), *Acta Metall.* 36, 2693.
- Kessler, D., Levine, H. (1989), *Phys. Rev. A* 39, 3041.
- Kessler, D., Koplik, J., Levine, H. (1987), in: *Pattern, Defects and Microstructures in Nonequilibrium Systems*: Walgraef, D. (Ed.). Dordrecht: Martinus Nijhoff.
- Kessler, D., Koplik, J., Levine, H. (1988), *Adv. Phys.* 37, 255.
- Kofler, A. (1950), *Z. Metallkunde* 41, 221.
- Koss, M. B., La Combe, J. C., Tennenhouse, L. A., Glicksman, M. E., Winsa, E. A. (1999), *Metall. Mater. Trans.* 30A, 3177.
- Kramer, L., Ben Jacob, E., Brand, H., Cross, M. (1982), *Phys. Rev. Lett.* 49, 1891.
- Krug, J., Spohn, H. (1992), in: *Solids Far from Equilibrium: Growth, Morphology and Defects*: Godechete, C. (Ed.). Cambridge: Cambridge University Press, p. 479.
- Kruskal, M., Segur, H. (1985), *Asymptotics Beyond All Orders in a Model of Dendritic Crystals*, A.R.A.P. Tech. Memo.
- Kurowsky, P. (1990), Thesis, GPS-Univ. Paris VII.
- Kurz, W., Fisher, D. J. (1981), *Acta Metall.* 29, 11.
- Kurz, W., Fisher, D. J. (1998), *Fundamentals of Solidification*. Aedermannsdorf, CH: Trans. Tech. Publ.
- Kurz, W., Trivedi, R. (1990), *Acta Metall. Mater.* 38, 1.
- Kurz, W., Trivedi, R. (1991), *Metall. Trans.* 22A, 3051.
- Kurz, W., Trivedi, R. (1996), *Metall. Mater. Trans.* 27A, 625.
- Kurz, W., Sahm, P. R. (1975), *Gerichtet erstarrte eutektische Werkstoffe*. Berlin: Springer Verlag.
- Kurz, W., Giovanola, B., Trivedi, R. (1986), *Acta Metall.* 34, 823.
- Kurz, W., Giovanola, B., Trivedi, R. (1988), *J. Crystal Growth* 91, 123.
- Landau, L. D., Lifshitz, E. M. (1970), *Statistische Physik*, Berlin: Akademie-Verlag.
- Langer, J. S. (1971), *Ann. Phys.* 65, 53.
- Langer, J. S. (1980a), *Rev. Mod. Phys.* 52, 1.
- Langer, J. S. (1980b), *Phys. Rev. Lett.* 44, 1023.
- Langer, J. S. (1980c), *Physico-Chem. Hydrodyn.* 1, 41.
- Langer, J. S. (1986, in: *Directions in Condensed Matter*. Grinstein, G., Mazenko, G. (Eds.). Singapore: World Scientific, p. 164.
- Langer, J. S. (1987a), *Phys. Rev. Lett.* A 36, 3350.
- Langer, J. S. (1987b), in: *Le hasard et la matiere/ Chance and matter*: Souletie, J., Vannimenus, J., Stora, R. (Eds.). Amsterdam: Elsevier Science Publ.
- Langer, J. S., Müller-Krumbhaar, H. (1977), *J. Crystal Growth* 42, 11.
- Langer, J. S., Müller-Krumbhaar, H. (1978), *Acta Metall.* 26, 1681; 1689; 1697.
- Langer, J. S., Müller-Krumbhaar, H. (1980), *Acta Metall.* 29, 145.
- Langer, J. S., Müller-Krumbhaar, H. (1982), *Phys. Rev. A* 27, 499.
- Langer, J. S., Turski, L. A. (1977), *Acta Metall.* 25, 1113.
- Lesoult, G. (1980), *Ann. Chim. Fr.* 5, 154.
- Lesoult, G. (1990), private communication.
- Levine, H., Rappel, W. (1990), unpublished.
- Li, D., Eckler, K., Herlach, D. M. (1995b), *Europhys. Lett.* 32, 223.
- Li, D., Eckler, K., Herlach, D. M. (1996), *J. Crystal Growth* 160, 59.
- Li, D., Herlach, D. M. (1996), *Phys. Rev. Lett.* 77, 1801.
- Li, D., Volkman, T., Eckler, K., Herlach, D. M. (1995a), *J. Crystal Growth* 152, 101.
- Li, Q., Beckermann, C. (1998), *Phys. Rev. E* 57, 1.
- Lifshitz, I. M., Slyozov, V. V. (1961), *J. Phys. Chem. Solids* 19, 35.
- Lipton, J., Glicksman, M. E., Kurz, W. (1987), *Metall. Trans.* 18A, 341.
- Lipton, J., Kurz, W., Trivedi, R. (1987a), *Acta Metall.* 35, 957.
- Livingston, J. D., Cline, H. E., Koch, E. F., Russel, R. R. (1970), *Acta Metall.* 18, 399.
- Lo, T. S., Karma, A., Plapp, M. (2001), *Phys. Rev. E* 63, 1504.
- Losert, W., Mesquita, O. N., Figueiredo, J. M. A., Cummins, H. Z. (1998b), *Phys. Rev. Lett.* 81, 409.
- Losert, W., Stillman, D. A., Cummins, H. Z., Kopczynski, P., Rappel, W.-J., Karma, A. (1998a), *Phys. Rev. E* 58, 7492.
- Ludwig, A., Kurz, W. (1996a), *Scripta Mater.* 35, 1217.
- Ludwig, A., Kurz, W. (1996b), *Acta Mater.* 44, 3643.
- Mashaal, M., Ben Amar, M., Hakim, V. (1990), *Phys. Rev. A* 41, 4421.
- Maurer, J., Bouissou, P., Perrin, B., Tabeling, P. (1988), *Europhys. Lett.* 8, 67.

- Mazumder, P., Trivedi, R., Karma, A. (2000), *Metall. Mater. Trans. A31*, 1233.
- McFadden, G. B., Coriell, S. R. (1984), *Physica 12D*, 253.
- Meakin, P. (1988), in: *Phase Transitions and Critical Phenomena*, Vol. 12: Domb, C., Lebowitz, J. (Eds.). London: Academic, p. 336.
- Meiron, D. I. (1986), *Phys. Rev. A33*, 2704.
- Misbah, C. (1987), *J. Phys. France 48*, 1265.
- Misbah, C. (1989), *J. Phys. France 50*, 971.
- Misbah, C., Temkin, D. (1992), *Phys. Rev. A 46*, 4497.
- Misbah, C., Müller-Krumbhaar, H., Saito, Y. (1990), *J. Crystal Growth 99*, 156.
- Misbah, C., Müller-Krumbhaar, H., Temkin, D. E. (1991), *J. Physique II*, 585.
- Mordike, B. L. (1991), in: *Materials Science and Technology Vol. 15, Processing of Metals and Alloys*: Cahn, R. W. (Ed.). Weinheim: VCH Verlagsgesellschaft, p. 111.
- Mullins, W. Sekerka, R. (1963), *J. Appl. Phys. 34*, 323.
- Mullins, W. Sekerka, R. (1964), *J. Appl. Phys. 35*, 444.
- Nakaya, U. (1954), *Snow Crystals*. Cambridge: Harvard Univ. Press.
- Nash, G. E., Glicksman, M. (1974), *Acta Metall. 22*, 1283.
- Nelson, D. (1983), in: *Phase Transitions and Critical Phenomena*: Domb, C., Lebowitz, J. (Eds.). New York: Academic Publ.
- Newell, A. C., Whitehead, J. A. (1969), *J. Fluid. Mech. 38*, 279.
- Ohno, K., Trinkaus, H., Müller-Krumbhaar, H. (1990), *J. Crystal Growth 99*, 68.
- Papapetrou, A. Z. (1935), *Z. f. Kristallograph. 92*, 89.
- Park, J. S., Trivedi, R. (1998), *J. Crystal Growth 187*, 511.
- Pelce, P., Clavin, P. (1987), *Europhys. Lett. 3*, 907.
- Pelce, P., Pomeau, Y. (1986), *Studies Appl. Math. 74*, 1283.
- Pelce, P., Pumir, A. (1985), *J. Crystal Growth 73*, 357.
- Penrose, O., Fife, P. G. (1990), *Physica D43*, 44.
- Perepezko, J. H., Uttormark, M. J. (1996), *Metall. Mater. Trans. 27A*, 533.
- Perepezko, J. H., Mueller, B. A., Ohsaka, K. (1987), in: *Undercooled Alloy Phases*: Collings, E. W., Koch, C. C. (Eds.). Warrendale: TMS, p. 289.
- Plapp, M., Karma, A. (1999), *Phys. Rev. E60*, 6865.
- Provatas, N., Goldenfeld, N., Dantzig, J. (1998), *Phys. Rev. Lett. 80*, 3308.
- Quested, P. N., McLean, M. (1984), *Mater. Science Eng. 65*, 171.
- Rabaud, M., Couder, Y., Gerard, N. (1988), *Phys. Rev. A37*, 935.
- Rappaz, M. (1989), *Inter. Mater. Rev. 34*, 93.
- Rappaz, M., Desbiolles, J.-L., Gandin, C.-A., Henry, S., Smoroz, A. (2000), *Mater. Sci. Forum 329–330*, 389.
- Rappel, W.-J., Brener, E. A. (1992), *J. Phys. I France 2*, 1779.
- Raz, E., Lipson, S. G., Polturak, E. (1989), *Phys. Rev. A40*, 1088.
- Riecke, H., Paap, H. G. (1986), *Phys. Rev. A33*, 547.
- Riquet, J. P., Durant, F. (1975), *Mat. Res. Bull. 10*, 399.
- Saffmann, P. G., Taylor, G. I. (1958), *Proc. R. Soc. London Ser. A254*, 312.
- Sahm, P. R., Keller, M. H. (1991), in: *Materials Science and Technology*, Vol. 15, Processing of Metals and Alloys. Weinheim: VCH Verlagsgesellschaft, p. 539.
- Saito, Y., Goldbeck-Wood, G. Müller-Krumbhaar, H. (1987), *Phys. Rev. Lett. 58*, 1541.
- Saito, Y., Goldbeck-Wood, G. Müller-Krumbhaar, H. (1988), *Phys. Rev. Lett. A38*, 2148.
- Saito, Y., Misbah, C., Müller-Krumbhaar, H. (1989), *Phys. Rev. Lett. 63*, 2377.
- Schumacher, P., Greer, A. L., Worth, J., Evans, P. V., Kearns, M. A., Fisher, P., Green, A. H. (1998), *Mater. Sci. Technol. 14*, 394.
- Schwarz, M., Arnold, C. B., Aziz, M. J., Herlach, D. M. (1997), *Mater. Sci. Eng. A226–228*, 420.
- Schwarz, M., Karma, A., Eckler, K., Herlach, D. M. (1990), *Phys. Rev. Lett. 56*, 324.
- Seetharaman, V., Trivedi, R. (1988), *Metall. Trans. 19A*, 2955.
- Seetharaman, V., Eshelman, M., Trivedi, R. (1988), *Acta Metall. 36*, 1175.
- Singh, N. B., Glicksman, M. E. (1989), *J. Crystal Growth 98*, 534.
- Somboonsuk, K., Trivedi, R. (1985), *Acta Metall. 33*, 1051.
- Somboonsuk, K., Mason, J. T., Trivedi, R. (1984), *Metall. Trans. A15*, 967.
- Strain, J. (1989), *J. Comput. Phys. 85*, 342.
- Temkin, D. E. (1985), *Kristallografia 30*, 1055.
- Temkin, D. E. (1990), unpublished.
- Tirmizi, S. H., Gill, W. N. (1989), *J. Crystal Growth 96*, 277.
- Tong, X., Beckermann, C., Karma, A. (1998), in: *Modeling of Casting, Welding, and Advanced Solidification Conference VIII*: Thomas, B. G., Beckermann, C. (Eds.), Warrendale, PA: TMS, p. 613.
- Tonhardt, R., Amberg, G. (1998), *J. Crystal Growth 194*, 406.
- Tournier, S., Barth, M., Herlach, D. M., Vinet B. (1997), *Acta Mater. 45*, 191.
- Trivedi, R. (1980), *J. Crystal Growth 49*, 219.
- Trivedi, R. (1984), *Metall. Trans. 15A*, 977.
- Trivedi, R., Karma, A., Lo, T. S., Mazumder, P., Plapp, M., Park, J. S. (1998), in: *Zermatt Workshop on "Solidification Microstructures"*, CD, Swiss Federal Institute of Technology Lausanne, 1015 Lausanne EPFL, Switzerland. This CD (PC format) may be obtained from the Laboratory of Physical Metallurgy, EPFL through: arlette.blatti@epfl.ch

- Trivedi, R., Kurz, W. (1986), *Acta Metall.* 34, 1663.
- Trivedi, R., Laorchan, V. (1988), *Acta Metall.* 39, 1941; 1951.
- Trivedi, R., Lipton, J., Kurz, W. (1987), *Acta Metall.* 35, 965.
- Trivedi, R., Mason, J. T., Verhoeven, J. D., Kurz, W. (1991), *Metall. Trans.* 22A, 2523.
- Trivedi, R., Somboonsuk, K. (1984), *Mater. Sci. Eng.* 65, 65.
- Trivedi, R., Somboonsuk, K. (1985), *Acta Metall.* 33, 1061.
- Ungar, L. H., Brown, R. A. (1984a), *Phys. Rev. B* 29, 1367.
- Ungar, L. H., Brown, R. A. (1984b), *Phys. Rev. B* 30, 3993.
- Ungar, L. H., Brown, R. A. (1985a), *Phys. Rev. B* 31, 1367.
- Ungar, L. H., Brown, R. A. (1985b), *Phys. Rev. B* 31, 5931.
- Uwaha, M., Saito, Y. (1990), *J. Crystal Growth* 99, 175.
- Valance, A., Misbah, C., Temkin, D., Kassner, K. (1993), *Phys. Rev. E* 48, 1924.
- Vandyousseifi, M., Kerr, H. W., Kurz, W. (2000), *Acta Mater.* 48, 2297.
- Versnyder, F. L., Shank, M. E. (1970), *Mater. Sci. Eng.* 6, 213.
- Volkman, T., Wilde, G., Willnecker, R., Herlach, D. M. (1998), *J. Appl. Phys.* 83, 3028.
- Voronkov, V. V. (1983), in: *Modern Theory of Crystal Growth*: Chernov, A. A., Müller-Krumbhaar, H. (Eds.). Heidelberg: Springer Verlag. p. 75.
- Wagner, C. (1961), *Z. Elektrochem.* 65, 581.
- Wang, C. Y., Beckermann, C. (1996), *Metall. Mater. Trans.* 27A, 2765.
- Wang, C. Y., Ahuja, S., Beckermann, C., de Groh III, H. C. (1995), *Metall. Trans.* 26B, 111.
- Wang, S.-L., Sekerka, R. F., Wheeler, A. A., Murray, B. T., Corriel, S. R., Braun, R. J., McFadden, G. B. (1993), *Physica D* 69, 189.
- Wheeler, A. A., McFadden, G. B., Boettinger, W. J. (1996), *Proc. Royal Soc. London A* 452, 495.
- Warren, J. A., Langer, J. S. (1990), *Phys. Rev. A* 42, 3518.
- Wollkind, D., Segel, L. (1970), *Philos. Trans. R. Soc. London* 268, 351.
- Wu, Y., Piccone, T. J., Shiohara, Y., Flemings, M. C. (1987), *Metall. Trans.* 18, 915; 925.
- Wulff, G. (1901), *Z. Kristallogr. Mineral.* 34, 449.
- Xiao, R. F., Alexander, J. I. D., Rosenberger, F. (1988), *Phys. Rev. A* 38, 2447.
- Yokoyama, E., Kuroda, T. (1988), in: *Dynamics of Ordering Processes in Condensed Matter*: Komura, S., Furukawa, H. (Eds.). New York: Plenum Publ., p. 95.
- Zettlemoyer, A. (Ed.) (1969), *Nucleation I*. New York: Dekker.
- Zettlemoyer, A. (Ed.) (1976), *Nucleation II*. New York: Dekker.
- Zimmermann, M., Carrard, M., Kurz, W. (1989), *Acta Metall.* 37, 3305.
- Zimmermann, M., Karma, A., Carrard, M. (1990), *Phys. Rev. B* 42, 833.

3 Diffusion Kinetics in Solids

Graeme E. Murch

Department of Mechanical Engineering, University of Newcastle, N.S.W. 2308, Australia

List of Symbols and Abbreviations	173
3.1 Introduction	175
3.2 Macroscopic Diffusion	175
3.2.1 Fick's Law	175
3.2.2 Types of Diffusion Coefficients	178
3.2.2.1 Tracer or Self-Diffusion	178
3.2.2.2 Impurity and Solute Diffusion	178
3.2.2.3 Chemical or Interdiffusion	178
3.2.2.4 Intrinsic or Partial Diffusion Coefficients	179
3.2.2.5 Surface Diffusion Coefficients	180
3.2.3 Phenomenological Equations of Irreversible Thermodynamics	181
3.2.3.1 Tracer Diffusion	182
3.2.3.2 Chemical Diffusion	184
3.2.3.3 Einsteinian Expressions for the Phenomenological Coefficients	185
3.2.3.4 Relating Phenomenological Coefficients to Tracer Diffusion Coefficients	185
3.2.4 Short-Circuit Diffusion	186
3.3 Microscopic Diffusion	189
3.3.1 Random Walk Theory	189
3.3.1.1 Mechanisms of Diffusion	189
3.3.1.2 The Einstein Equation	192
3.3.1.3 Tracer Correlation Factor	193
3.3.1.4 Impurity Correlation Factor	196
3.3.1.5 Correlation Factors for Concentrated Alloy Systems	199
3.3.1.6 Correlation Factors for Highly Defective Systems	201
3.3.1.7 The Physical or Conductivity Correlation Factor	204
3.3.1.8 Correlation Functions (Collective Correlation Factors)	206
3.3.2 The Nernst–Einstein Equation and the Haven Ratio	211
3.3.3 The Isotope Effect in Diffusion	213
3.3.4 The Jump Frequency	216
3.3.4.1 The Exchange Frequency	217
3.3.4.2 Vacancy Concentration	218
3.4 Diffusion in Materials	219
3.4.1 Diffusion in Metals	220
3.4.1.1 Self-Diffusion	220
3.4.1.2 Impurity Diffusion	220
3.4.2 Diffusion in Dilute Alloys	221

3.4.2.1	Substitutional Alloys	221
3.4.2.2	Interstitial Alloys	224
3.4.3	Diffusion in Concentrated Binary Substitutional Alloys	226
3.4.4	Diffusion in Ionic Crystals	227
3.4.4.1	Defects in Ionic Crystals	227
3.4.4.2	Diffusion Theory in Ionic Crystals	228
3.5	Experimental Methods for Measuring Diffusion Coefficients	231
3.5.1	Tracer Diffusion Methods	231
3.5.2	Chemical Diffusion Methods	232
3.5.3	Diffusion Coefficients by Indirect Methods	233
3.5.3.1	Relaxation Methods	233
3.5.3.2	Nuclear Methods	234
3.5.4	Surface Diffusion Methods	234
3.6	Acknowledgements	235
3.7	References	235

List of Symbols and Abbreviations

a	lattice parameter
b_1, b_2	solvent enhancement factors
B_1, B_2	solute enhancement factors
C, C_i	concentration: particles per unit volume of species i
c_A, c_B, c_i, c_v, c_p	mole fractions of metal A, B, species i , vacancies, paired interstitials
D	diffusion coefficient (in $\text{m}^2 \text{s}^{-1}$)
D'	short-circuit diffusion coefficient
\tilde{D}	collective diffusion coefficient or interdiffusion coefficient
D^*	tracer diffusion coefficient
D_A^I, D_B^I , etc.	intrinsic or partial diffusion coefficient of metal A, B, etc.
D_l	lattice diffusion coefficient
D_σ	diffusion coefficient derived from the ionic conductivity
D^0	pre-exponential factor
e	electronic charge
E_v^f	energy of vacancy formation
E_b, E_B	binding energy of impurity to dislocation (impurity-vacancy binding energy)
$f, f_I(f_c)$	tracer correlation factor, physical correlation factor
F_v^f	Helmholtz free energy for vacancy formation
g	coordination
G^m	Gibbs free energy of migration
H_v^f	enthalpy of vacancy formation
H^m	enthalpy of migration
H_R	Haven ratio
J	flux of atoms
k	Boltzmann constant
K	equilibrium constant
L	phenomenological coefficients
l	spacing between grain boundaries (average grain diameter)
l	distance between dislocation pinning points
m	mass
\bar{P}_{AV}	vacancy availability factor
Q	activation energy for diffusion
R	vector displacement
ΔR_i	total displacement of species i
r, r_q	jump distance of atom, of charge q
S_v^f	entropy of vacancy formation
S^m	entropy of migration
t	time
T	temperature
$T_{M.Pt.}$	temperature of melting point
u	mobility
$\langle v \rangle$	average drift velocity
V	volume

x	distance, coordinate
X_i, X_v	driving force on species i , vacancies
Z_i	number of charges on i
γ	activity coefficient
$\Gamma, \Gamma_q, \Gamma_i$	jump frequency (of charge q ; of species i)
μ	chemical potential
ν	vibration frequency
σ	ionic conductivity
ω	exchange frequency
CASCADE	computer code
DEVIL	computer code
erf	Gaussian error function
PPM	path probability method
SIMS	secondary ion mass spectrometry

“The elementary diffusion process is so very fundamental and ubiquitous in the art and science of dealing with matter in its condensed phase that it never ceases to be useful but, at the same time, is a problem which is never really solved. It remains important by any measure.”

D. Lazarus, 1984

3.1 Introduction

Many phenomena in materials science depend in some way on diffusion. Common examples are sintering, oxidation, creep, precipitation, solid-state chemical reactions, phase transformations, and crystal growth. Even thermodynamic properties and structure are sometimes dependent on diffusion, or rather the lack of it. Many of these phenomena are the subjects of other contributions in this series. This contribution is concerned with the fundamentals of the diffusion process itself.

The depth of subject matter is generally introductory, and no prior knowledge of solid-state diffusion is assumed. Where possible, the reader is directed to more detailed texts, reviews, and data compilations.

3.2 Macroscopic Diffusion

3.2.1 Fick's Laws

Although diffusion of atoms, or atomic migration, is always occurring in solids at temperatures above absolute zero, for macroscopically *measurable* diffusion a gradient of concentration is required. In the presence of such a concentration gradient $\partial C/\partial x$ (where C is the concentration in, say, particles per unit volume and x is the dis-

tance) in one direction of a certain species of atom, a flux J of atoms of the same species is established down the concentration gradient. The law relating flux and concentration gradient is Fick's First Law, which, for an isotropic medium or cubic crystal can be expressed as

$$J = -D \frac{\partial C}{\partial x} \quad (3-1)$$

The proportionality factor or “coefficient” of $\partial C/\partial x$ is termed the “diffusion coefficient” or less commonly the “diffusivity”. The recommended SI units for D are $\text{m}^2 \text{s}^{-1}$ but much of the literature is still in the older c.g.s. units $\text{cm}^2 \text{s}^{-1}$. The negative sign in Eq. (3-1) arises because the flux is in the opposite direction to the concentration gradient. This negative sign could, of course, have been absorbed into D , but it is more convenient for D to be a positive quantity.

When an external force such as an electric field also acts on the system a more general expression can be given:

$$J = -D \frac{\partial C}{\partial x} + \langle v \rangle C \quad (3-2)$$

where $\langle v \rangle$ is the average velocity of the center of mass arising from the external force on the particles. The first term in Eq. (3-2) is thus the diffusive term, and the second term is the drift term. Note the independence of these terms. The external force here is assumed to be applied gradually so that the system moves through a series of equilibrium states. When the force is suddenly applied the system can be thrown out of equilibrium. These matters and the types of external force are considered by Flynn (1972) in a general consideration of diffusion under stress.

By itself, Fick's First Law (Eq. (3-1)) is not particularly useful for diffusion measurements in the solid state since it is virtu-

ally impossible to measure an atomic flux unless steady state is reached. Further, because solid-state diffusivities are generally small, the attainment of steady state in a macroscopic specimen can take a very long time. In a few cases, where the solid-state diffusivity is high, for example carbon diffusion in austenite (Smith, 1953), the steady-state flux and the concentration gradient can be measured and the diffusivity obtained directly from Eq. (3-1).

In order to produce a basis for measuring the diffusion coefficient, Eq. (3-1) is usually combined with the equation of continuity:

$$\frac{\partial J}{\partial x} = -\frac{\partial C}{\partial t} \quad (3-3)$$

to give Fick's Second Law:

$$\frac{\partial C}{\partial t} = \frac{\partial}{\partial x} \left(D \frac{\partial C}{\partial x} \right) \quad (3-4)$$

If the diffusion coefficient is independent of concentration and therefore position, then Eq. (3-4) reduces to

$$\frac{\partial C}{\partial t} = D \frac{\partial^2 C}{\partial x^2} \quad (3-5)$$

The second-order partial differential equation Eq. (3-5) (or (3-4)) is sometimes called the "diffusion equation". Eq. (3-2) can also be developed in the same way to give

$$\frac{\partial C}{\partial t} = \frac{\partial}{\partial x} \left(D \frac{\partial C}{\partial x} \right) - \frac{\partial}{\partial x} (\langle v \rangle C) \quad (3-6)$$

and, if $\langle v \rangle$ and D are independent of C , then

$$\frac{\partial C}{\partial t} = D \frac{\partial^2 C}{\partial x^2} - \langle v \rangle \frac{\partial C}{\partial x} \quad (3-7)$$

In order to obtain a solution to the diffusion equation, it is necessary to establish the initial and boundary conditions. Once a

solution, $C(x, t)$, of the diffusion equation has been established, the diffusion coefficient itself is obtained as a parameter by fitting the experimental $C(x, t)$ to the analytical $C(x, t)$. In the following we shall focus on some analytical solutions for some well-known initial and boundary conditions used in experimental diffusion studies.

Let us first examine some solutions for Eq. (3-5). In a very common experimental arrangement for "self" and impurity diffusion a very thin deposit of amount M of radioactive isotope is deposited as a sandwich layer between two identical samples of "infinite" thickness. After diffusion for a time t the concentration is described by

$$C(x, t) = \frac{M}{2\sqrt{\pi Dt}} \exp(-x^2/4Dt) \quad (3-8)$$

which is illustrated in Fig. 3-1. If the deposit is left as a surface layer rather than a sandwich, $C(x, t)$ is doubled.

In another experimental arrangement, the surface concentration C_s of the diffusing species is maintained constant for time t , perhaps by being exposed to an atmosphere of it. Again, the substrate is thick or mathematically infinite. The solution of the diffusion equation is

$$\frac{C(x, t) - C_s}{C_0 - C_s} = \operatorname{erf}(x/2\sqrt{Dt}) \quad (3-9)$$

where C_0 is the initial or background concentration of the diffusing species in the substrate and erf is the Gaussian error function defined by

$$\operatorname{erf} z = \frac{2}{\sqrt{\pi}} \int_0^z \exp(-u^2) du \quad (3-10)$$

This function is now frequently available as a scientific library function on most modern computers. Accurate series expan-

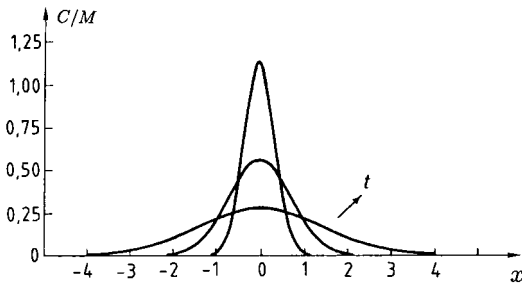


Figure 3-1. Time evolution of Eq. (3-8).

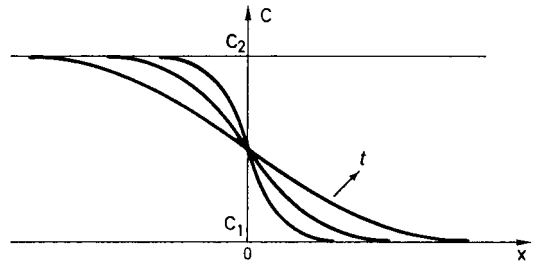


Figure 3-2. Time evolution of Eq. (3-12).

sions can be found in mathematical function handbooks.

The total amount of diffusant S taken up (or, in fact, lost, depending on the relative values of C_s and $C(x, t)$) from the substrate is given by

$$S(t) = [2/C_0 - C_s]/A(Dt/\pi)^{1/2} \quad (3-11)$$

where A is the surface area of the sample.

A further common experimental arrangement is the juxtaposition of two “infinite” samples, one of which has a uniform concentration C_0 and the other a concentration C_1 of the diffusing species. After time t the solution is

$$\frac{C(x, t) - C_0}{C_1 - C_0} = \frac{1}{2} [1 - \operatorname{erf}(x/2\sqrt{Dt})] \quad (3-12)$$

This gives a time evolution of the concentration profile as shown in Fig. 3-2.

On many occasions where this experimental arrangement is used, we are concerned with diffusion in a chemical composition gradient. The relevant diffusion coefficient (see Sec. 3.2.2.3) is frequently dependent on concentration, so Eq. (3-12) is then inappropriate, and a solution to Eq. (3-4) where $D=D(C)$ must be sought. A wellknown technique for this is the graphical integration method, usually called the Boltzmann–Matano analysis. The general solution for the concentration-dependent

diffusion coefficient can be expressed as (Boltzmann, 1894; Matano, 1933)

$$D(C') = -\frac{1}{2t} \left(\frac{\partial x}{\partial C} \right)_{C'} \int_{C_1}^{C'} x dC \quad (3-13)$$

where

$$\int_{C_1}^{C_0} x dC = 0 \quad (3-14)$$

A very detailed description of the use of this analysis is given by Borg and Dienes (1988).

In many practical situations of interdiffusion the relevant phase diagram traversed will ensure that diphasic regions or new phases will appear. This does not imply incidentally that *all* equilibrium phases will thus appear. The Boltzmann–Matano analysis can still be applied within single phase regions of the concentration profile. The growth of a new phase, provided it is diffusion controlled, can usually be described by a parabolic time law. These matters are dealt with in detail by Philibert (1991).

The solutions of the diffusion equation given here are among the more commonly encountered ones in solid-state diffusion studies. Numerous others have been given by Carslaw and Jaeger (1959) and Crank (1975).

3.2.2 Types of Diffusion Coefficients

For the non-specialist, the meaning and significance of the various diffusion coefficients used can be confusing because of inconsistent terminology in the literature. An attempt will be made here to clarify the situation as much as possible.

3.2.2.1 Tracer or Self-Diffusion

Consider a well-annealed sample of a pure metal. Although atoms are diffusing about in the sample at a rate depending on temperature, from a macroscopic point of view nothing appears to be happening. In order to *observe* diffusion macroscopically we must impose a concentration gradient. For the case of a pure metal, a radioactive tracer of the same metal is used. The resulting diffusion coefficient is termed the *tracer diffusion coefficient* with the symbol D^* . Because the tracer is chemically the same as the host, this diffusion coefficient is also termed the *self-diffusion coefficient*, although sometimes this terminology is reserved for the tracer diffusion coefficient divided by the tracer correlation factor, f (see Sec. 3.3.1.3). The same idea is readily extended to alloys and compounds. However, care must always be taken that a chemical composition gradient is not unwittingly imposed. For example, in order to measure the oxygen self-diffusion coefficient in a nonstoichiometric compound such as UO_{2+x} , we can permit ^{18}O (a stable isotope that can be probed later by nuclear analysis or Secondary Ion Mass Spectrometry) to diffuse in from the gas phase, *provided* that the partial pressure of oxygen is already in chemical equilibrium with the composition of the sample. Alternatively, a layer of $\text{U}^{18}\text{O}_{2+x}$ can be deposited on the surface of a sample of UO_{2+x} provided that it has exactly the same chemical composition as the substrate.

3.2.2.2 Impurity and Solute Diffusion

In order to measure the *impurity diffusion coefficient*, the tracer is now the impurity and is different chemically from the host. However, the concentration of impurity must be sufficiently low that there is not a chemical composition gradient. Strictly, of course, the tracer impurity should be permitted to diffuse into the sample already containing the same concentration of impurity. In practice, the concentration of tracer impurity is normally kept extremely low, thereby making this step unnecessary. Because the impurity is always in stable solid solution (unless implanted), is often termed the solute and the impurity diffusion coefficient is sometimes also termed the solute diffusion coefficient at infinite dilution. However, the terminology *solute diffusion coefficient* is often “reserved” for dilute alloys, where, in addition, we often measure the solvent diffusion coefficient. In the context of those experiments both solute and solvent diffusion coefficients frequently depend on solute content (see Sec. 3.4.2). In all of these experiments, as in self-diffusion, the *chemical* composition of the sample must remain essentially unchanged by the diffusion process, otherwise it is a chemical diffusion experiment.

3.2.2.3 Chemical or Interdiffusion

So far, we have discussed diffusion coefficients which are measured in the *absence* of chemical composition gradients. Chemical diffusion is the process where diffusion takes place in the presence of a chemical composition gradient. It is the diffusion coefficients describing this process which generate the greatest amount of confusion. It is helpful to look at several examples.

Consider first diffusion in a pseudo-one-component system. One example is the diffusion of an adsorbed monolayer onto a

clean section of surface. Another is the diffusion between two metal samples differing only in their relative concentrations of a highly mobile interstitial species such as H. A further example is diffusion between two nonstoichiometric compounds, e.g., $\text{Fe}_{1-\delta}\text{O}$ and $\text{Fe}_{1-\delta'}\text{O}$. In all of these cases only *one* species of atom is involved in the diffusion process which brings the system to a common composition (which is why it can be considered a pseudo-one-component system). Often the process can be pictured as the interdiffusion of vacant sites and atoms. The diffusion coefficient describing this process is usually called the *chemical diffusion coefficient*, sometimes the *interdiffusion coefficient*, and occasionally, the *collective diffusion coefficient*. Generally the symbol used is \tilde{D} . For these pseudo-one-component systems, the preferred name is *chemical diffusion coefficient*. In general, the chemical diffusion coefficient does not equal the self-diffusion coefficient because of effects arising from the gradient of chemical composition, see Eq. (3-99).

Chemical diffusion in *binary* substitutional solid solutions is frequently called *interdiffusion*. In a typical case pure metal A is bonded to pure metal B and diffusion is permitted at high temperature. Although *both* A and B atoms move, only one concentration profile, say of A, is established (the profile from B contains no new information). The resulting diffusion coefficient which is extracted from the profile, by the Boltzmann–Matano analysis (e.g., see Sec. 3.2.1) is termed the *interdiffusion coefficient* and is given the symbol \tilde{D} . Not infrequently, the diffusion coefficient for this situation is loosely called the chemical diffusion coefficient or the mutual diffusion coefficient. This single diffusion coefficient is sufficient to describe the concentration profile changes of the couple. Because

of its practical significance the interdiffusion coefficient is the one often quoted in metal property data books (Brandes, 1983; Mehrer, 1990; Beke 1998, 1999). See also the following section for further discussion of \tilde{D} .

3.2.2.4 Intrinsic or Partial Diffusion Coefficients

In contrast to the pseudo-one-component systems described above where the diffusion rates of the atoms and vacant sites are necessarily equal, in the substitutional binary alloy the individual diffusion rates of A and B are not generally equal since the corresponding self-diffusion coefficients are not. In the interdiffusion experiment this implies that there is a *net* flux of atoms across any lattice plane normal to the diffusion direction. If the number of lattice sites is conserved, each plane in the diffusion region must then shift to compensate. This shift with respect to parts of the sample *outside* the diffusion zone, say the ends of the sample, is called the *Kirkendall effect*. This effect can be measured by observing the migration of inert markers, usually fine insoluble wires which have been incorporated into the sample before the experiment. The assumption is that the wires follow the motion of the lattice in their vicinity.

The *intrinsic diffusion coefficients* of A and B, D_A^I and D_B^I , are defined with reference to the fluxes of A and B relative to the *local* lattice planes:

$$J_A' = -D_A^I \frac{\partial C_A}{\partial x} \quad (3-15)$$

and

$$J_B' = -D_B^I \frac{\partial C_B}{\partial x} \quad (3-16)$$

The diffusion coefficients are sometimes also termed *partial diffusion coefficients*.

If v is the velocity (Kirkendall velocity) of the lattice plane measured with respect to parts of the sample outside the diffusion zone then the fluxes with respect to it are

$$J_A = J'_A + v C_A \quad (3-17)$$

and

$$J_B = J'_B + v C_B \quad (3-18)$$

where C_A and C_B are the concentrations at the lattice planes. It should be noted that the interdiffusion coefficient is measured in this frame of reference. Since $\partial C_A / \partial x = -\partial C_B / \partial x$, we easily deduce that

$$v = (D_A^I - D_B^I) \frac{\partial C_A}{\partial x} \quad (3-19)$$

and

$$J_A = -(c_A D_B^I + c_B D_A^I) \frac{\partial C_A}{\partial x} \quad (3-20)$$

where c_A and c_B are the mole fractions of A and B. The term in parentheses in Eq. (3-20) is the interdiffusion coefficient \tilde{D} :

$$\tilde{D} = c_A D_B^I + c_B D_A^I \quad (3-21)$$

The interdiffusion coefficient is seen to be a weighted average of the individual (intrinsic) diffusion coefficients of A and B. With the aid of Eqs. (3-19) and (3-21) the intrinsic diffusion coefficients can be determined if \tilde{D} and v are known. The composition they refer to is the composition at the inert marker. Note that if there is *no* marker shift, Eq. (3-19) implies that the intrinsic coefficients are equal. The relationship of the intrinsic diffusion coefficient to the tracer (self) diffusion coefficient is explored in Sec. 3.2.3.2.

From the form of Eq. (3-21) when $c_A \rightarrow 0$, it can be seen that $\tilde{D} \rightarrow D_A^I$. It should also be noted that in this limit D_A^I reduces to the impurity diffusion coefficient of A in B.

3.2.2.5 Surface Diffusion Coefficients

Surface diffusion refers to the motion of atoms, sometimes molecules, over the surface of some substrate. The diffusing species can be adsorbed atoms, e.g. impurity metal atoms on a metal substrate (this is normally referred to as hetero-diffusion) or of the same species as the substrate (this is usually referred to as self-diffusion).

As a field, surface diffusion has evolved somewhat separately from solid-state diffusion, perhaps because of the very different techniques employed. This separateness has resulted in some inconsistencies in nomenclature between the two fields. It is appropriate here to discuss these briefly. For both self- and hetero-diffusion it is usual to refer to the motion of atoms for short distances, where there is one type of site, as “intrinsic diffusion”. When the concentration of diffusion species is very low the relevant diffusion coefficient is called a “tracer” diffusion coefficient. This is *not* in fact the diffusion coefficient obtained with radioactive tracers but a single particle diffusion coefficient. (A single particle can be followed or traced.) At higher concentrations, the relevant diffusion coefficient is called a chemical diffusion coefficient. Thus “intrinsic” diffusion is formally the same as diffusion in the pseudo-one-component system, as described in Sec. 3.2.2.3.

When the surface motion of atoms extends over long distances, and many types of site are encountered (this is macroscopic diffusion in contrast with the microscopic or “intrinsic” diffusion discussed above) the relevant diffusion coefficient is called a mass transfer diffusion coefficient. Further discussion of these and relationships among these diffusion coefficients are reviewed by Bonzel (1990).

3.2.3 Phenomenological Equations of Irreversible Thermodynamics

An implication of Fick's First Law (Eq. (3-1)) is that once the concentration gradient for species i reaches zero, all net flow for species i stops. Although frequently correct, this is rather too restrictive as a condition for equilibrium. In general, net flow for species i can cease only when all direct or indirect forces on species i are zero. This is conveniently handled by postulating linear relations between each flux and all the driving forces. We have for flux i in a system with k components

$$J_i = \sum_k L_{ik} X_k + L_{iq} X_q \quad (3-22)$$

where the L s are called phenomenological coefficients and X_i is the driving force on component i and is written as $-\text{grad } \mu_i$, where μ_i is the chemical potential of species i . X_i can also result from an external driving force such as an electric field. In this case $X_i = Z_i e E$, where Z_i is the number of changes on i , e is the electronic charge, and E is the electric field. For *ionic* conductors Z_i is the actual ionic valence. For alloys Z_i is an "effective" valence which is usually designated by the symbol Z_i^* . Z_i^* consists of two parts, the first, Z_i^{el} , represents the direct electrostatic force on the moving ion (Z_i^{el} is expected to be the ion's nominal valence), and the second, Z_i^{wd} , accounts for the momentum transfer between the electron current and the diffusing atom. A comprehensive review of all aspects of Z_i^* and the area of electromigration has been given by Huntington (1975). X_q is a driving force resulting from a temperature gradient (if present). X_q is given by $-T^{-1} \text{grad } T$. When referring to diffusion in a temperature gradient it is usual to let L_{iq} be expressed as

$$L_{iq} = \sum_{k=1}^n Q_k^* L_{ik}$$

where Q_k^* is called the "heat of transport" for species k (Manning, 1968). This can be further related to the heat of transport derived from the *actual* heat flow. This subject is dealt with further by Manning (1968) and Philibert (1991). Sometimes it is convenient to discuss the flux in an electric field occurring simultaneously with diffusion in a chemical potential gradient. A simple example would be diffusion from a tracer source in an electric field – the so-called Chemla experiment (Chemla, 1956). In such a case, we write X_i as

$$X_i = -\text{grad } \mu_i + Z_i e E \quad (3-23)$$

Now the phenomenological coefficient L_{iq} (Eq. (3-22)) describes the phenomenon of thermal diffusion, i.e., the atom flow resulting from the action of the X_q , i.e., the temperature gradient (Soret effect). There is also an equation analogous to Eq. (3-22) for the heat flow itself:

$$J_q = \sum_k L_{qk} X_k + L_{qq} X_q \quad (3-24)$$

L_{qk} is a heat flow phenomenological coefficient, i.e., the heat flow which accompanies an atom flow (the Dufour effect). L_{qq} refers directly to the thermal conductivity.

The other phenomenological coefficients, L_{ik} in Eq. (3-22), are concerned with the atomic transport process itself. The off-diagonal coefficients are concerned with "interference" between the atoms of different types. This may arise from interactions between A and B atoms and/or the competition of A and B atoms for the defect responsible for diffusion, see Sec. 3.3.1.8. A most important property of the phenomenological coefficients is that they are *independent of driving force*. Further, the matrix of L coefficients is symmetric: this is sometimes called Onsager's theorem or the reciprocity condition. That is,

$$L_{ij} = L_{ji} \quad (3-25)$$

The set of equations represented by Eq. (3-22) are normally called the “phenomenological equations” or Onsager equations and were postulated as a central part of the theory of irreversible processes. Details of the theory as it applies to diffusion can be found in many places but see especially the reviews by Howard and Lidiard (1964), Adda and Philibert (1966), and Allnatt and Lidiard (1993).

The phenomenological coefficients are sometimes said to have a “wider meaning” than quantities such as the diffusion coefficients or the ionic conductivity. The wider meaning comes about because the phenomenological coefficients do not depend on driving force but only on temperature and composition. In principle, armed with a full knowledge of the L_s , the technologist would have the power, if not to control the diffusive behavior of the material, at least to predict the diffusive behavior no matter what thermodynamic force or forces or combination thereof were acting.

Unfortunately, the experimental determination of the L_s is most difficult in the solid state. This is in contrast, incidentally, to liquids, where, by use of selectively permeable membranes, measurement of the L_s is possible. The reader might well ask then why the L_s were introduced in the first place when they are essentially not amenable to measurement! There are several reasons for this. First, relations can be derived between the L_s and the (measurable) tracer diffusion coefficients – we will discuss this further in Sec. 3.2.3.4. Further, the Onsager equations provide a kind of accounting formalism wherein an analysis using this formalism ensures that once the components and driving forces have all been identified nothing is overlooked, and that the whole is consistent; this will be discussed in Secs. 3.2.3.1 and 3.2.3.2. Finally, many “correlations” in diffusion,

e.g., the tracer correlation factor and the vacancy-wind effect, can be conveniently expressed in terms of the L_s . This can sometimes aid in understanding the nature of these complex correlations. A most important contribution to this was made by Allnatt (1982), who related the L_s directly to the microscopic behavior – see Sec. 3.3.1.8.

In the next sections we shall restrict ourselves to isothermal diffusion and focus on the relations which can be derived among the L_s and various experimentally accessible transport quantities.

3.2.3.1 Tracer Diffusion

Let us first consider tracer diffusion in a pure crystal. The general strategy is (1) to describe the flux of the tracer with the Onsager equations (Eq. (3-22)) and (2) to describe the flux with Fick’s First Law (Eq. (3-1)) and then equate the two fluxes to find expressions between the diffusion coefficient and the phenomenological coefficients. We shall deal with this in detail to show the typical procedure (see, for example, Le Claire (1975)). We can identify two components, A and its tracer A^* . We write for the fluxes of the host and tracer atoms, respectively,

$$J_A = L_{AA} X_A + L_{AA^*} X_{A^*} \quad (3-26)$$

and

$$J_{A^*} = L_{A^*A^*} X_{A^*} + L_{A^*A} X_A \quad (3-27)$$

Strictly, the vacancies should enter as a component but it is unnecessary here because of the lack of a vacancy gradient.

Since the tracer atoms and host atoms mix ideally (they are chemically identical), it can easily be shown that the driving forces are

$$X_A = -\frac{kT}{c_A} \frac{\partial c_A}{\partial x} \quad (3-28)$$

and

$$X_{A^*} = - \frac{kT}{c_{A^*}} \frac{\partial c_{A^*}}{\partial x} \quad (3-29)$$

where c_i is the mole fraction. This leads immediately to

$$J_{A^*} = -L_{A^*A^*} \frac{kT}{c_{A^*}} \frac{\partial c_{A^*}}{\partial x} - L_{A^*A} \frac{kT}{c_A} \frac{\partial c_A}{\partial x} \quad (3-30)$$

It is convenient to introduce the quantity $C_i (=Nc_i/V)$ which is the number of atoms of type i per unit volume and N is the number of entities ($A + A^*$), and V is the volume. Since there must be a symmetry condition $\partial c_A / \partial x = -\partial c_{A^*} / \partial x$, we now find that

$$J_{A^*} = \frac{\partial C_{A^*}}{\partial x} \frac{kTV}{N} \left(\frac{L_{A^*A}}{c_A} - \frac{L_{A^*A^*}}{c_{A^*}} \right) \quad (3-31)$$

However, Fick's First Law, Eq. (3-1), states that

$$J_{A^*} = -D_{A^*} \frac{\partial C_{A^*}}{\partial x} \quad (3-32)$$

and so the tracer diffusion coefficient is given by

$$D_{A^*} = \frac{kTV}{N} \left(\frac{L_{A^*A}}{c_{A^*}} - \frac{L_{A^*A^*}}{c_A} \right) \quad (3-33)$$

When $c_{A^*} \rightarrow 0$, which is the usual situation when tracers are used experimentally, we find that

$$D_{A^*} = kTV L_{A^*A} / c_{A^*} N \quad c_{A^*} \rightarrow 0 \quad (3-34)$$

Since the fluxes J_A and J_{A^*} are always equal but opposite in sign, then going through the above procedure, but now for J_A , leads to the relation

$$\frac{L_{AA} + L_{A^*A}}{c_A} = \frac{L_{AA^*} + L_{A^*A^*}}{c_{A^*}} \quad (3-35)$$

Now let us relate the diffusion coefficient to the ionic conductivity in order to obtain

an expression for the Haven ratio H_R (see also Sec. 3.3.2).

We consider the system of A and A^* in an electric field. We will assume that the A and A^* are already mixed. We will now let $X_A = X_{A^*} = ZeE$, where Z is the number of charges carried by each atom. From Eq. (3-27) the flux of A^* is

$$J_{A^*} = Z_{A^*} e E (L_{A^*A^*} + L_{A^*A}) \quad (3-36)$$

The drift mobility u_{A^*} is related to the flux by

$$J_{A^*} = C_{A^*} u_{A^*} E \quad (3-37)$$

and so

$$u_{A^*} = \frac{Z_{A^*} e V}{N} \left(\frac{L_{A^*A^*} + L_{A^*A}}{c_{A^*}} \right) \quad (3-38)$$

The mobility u_A is equal to u_{A^*} since A and A^* are chemically identical.

By means of the so-called Nernst-Einstein equation (Eq. (3-130)), the mobility can be converted to a dimensionally correct diffusivity, D_σ , i.e.,

$$D_\sigma = \frac{kTV}{N c_{A^*}} (L_{A^*A^*} + L_{A^*A}) \quad (3-39)$$

As is discussed in detail in Sec. 3.3.2, D_σ does not have a meaning in the sense of Fick's First Law (Eq. (3-1)). Its meaning is the diffusion coefficient of the *assembly* of ions as if the assembly itself acts like a single (hypothetical) particle. It is conventionally related to the tracer diffusion coefficient by the Haven ratio H_R which is defined as:

$$H_R \equiv \frac{D_{A^*}}{D_\sigma} \quad (3-40)$$

Using the equation for D_{A^*} we find, after letting $c_{A^*} \rightarrow 0$, that

$$H_R = \frac{L_{A^*A^*}}{L_{A^*A^*} + L_{A^*A}} \quad (3-41)$$

For a pure crystal and where the vacancy concentration is very low, H_R can be identified directly with the tracer correlation factor f (see Sec. 3.3.2) and

$$H_R = f = \frac{L_{A^*A^*}}{L_{A^*A^*} + L_{A^*A}} \quad (3-42)$$

Note that if $L_{A^*A} = 0$, i.e., there is no interference between tracer and host, then $H_R = 1$. More generally, when the defect concentration is high and there are correlations in the ionic conductivity (see Sec. 3.3.1.7), we find that

$$H_R = f/f_1 = \frac{L_{A^*A^*}}{L_{A^*A^*} + L_{A^*A}} \quad (3-43)$$

and f_1 is the physical correlation factor.

3.2.3.2 Chemical Diffusion

For chemical diffusion between A and B when, say, the vacancy mechanism is operating (see Sec. 3.3.1.1), the Onsager equations are written as (Howard and Lidiard, 1964)

$$J_A = L_{AA} X_A + L_{AB} X_B \quad (3-44)$$

$$J_B = L_{BB} X_B + L_{BA} X_A \quad (3-45)$$

Strictly, the vacancies should enter here as another species, so that we would write

$$J_A = L_{AA} X_A + L_{AB} X_B + L_{AV} X_V \quad (3-46)$$

$$J_B = L_{BB} X_B + L_{BA} X_A + L_{BV} X_V \quad (3-47)$$

and, because of conservation of lattice sites,

$$J_V = -(J_A + J_B) \quad (3-48)$$

The usual assumption is that the vacancies are always at equilibrium and $X_V = 0$. For this to happen the sources and sinks for vacancies, i.e., the free surface, dislocations, or grain boundaries, must be effective and sufficiently numerous.

Following the same kind of procedure as before (see Sec. 3.2.3.1), but recognizing that generally A and B do *not* ideally mix, we find that rather than by Eq. (3-28), X_i is now given by

$$X_i = -\frac{kT}{c_i} \frac{\partial c_i}{\partial x} \left(1 + \frac{\partial \ln \gamma}{\partial \ln c} \right) \quad (3-49)$$

where γ is the activity coefficient of either A or B. We find that the diffusion coefficient of, say A, actually an *intrinsic* diffusion coefficient (see Sec. 3.2.2.4), is given by

$$D_A^I = \frac{kTV}{N} \left(\frac{L_{AA}}{c_A} - \frac{L_{AB}}{c_B} \right) \left(1 + \frac{\partial \ln \gamma}{\partial \ln c} \right) \quad (3-50)$$

If we want to find a relation between D_A^I and the tracer diffusion coefficient, say D_{A^*} , we would need to introduce A^* formally into the phenomenological equations which would now become (Stark, 1976; Howard and Lidiard, 1964)

$$J_A = L_{AA} X_A + L_{AA^*} X_{A^*} + L_{AB} X_B \quad (3-51)$$

$$J_{A^*} = L_{A^*A^*} X_{A^*} + L_{A^*A} X_A + L_{A^*B} X_B \quad (3-52)$$

$$J_B = L_{BB} X_B + L_{BA} X_A + L_{BA^*} X_{A^*} \quad (3-53)$$

These equations can be developed to give

$$D_{A^*} = \frac{kTV}{N} \left(\frac{L_{A^*A^*}}{c_{A^*}} - \frac{L_{A^*A}}{c_A} \right) \quad (3-54)$$

and

$$D_A^I = \frac{kTV}{N} \left(\frac{L_{AA} + L_{A^*A}}{c_A} - \frac{L_{AB} + L_{A^*B}}{c_B} \right) \times \left(1 + \frac{\partial \ln \gamma}{\partial \ln c} \right) \quad (3-55)$$

When these two equations are combined we find that

$$D_A^I = D_{A^*} \left(1 + \frac{\partial \ln \gamma}{\partial \ln c} \right) \times \left[1 + \frac{c_{A^*}}{L_{A^*A^*} c_A} \left(\frac{L_{A^*A}}{c_{A^*}} - \frac{L_{AB}}{c_B} \right) \right] \quad (3-56)$$

This is in fact the so-called Darken equation (Darken, 1948), relating the intrinsic diffusion coefficient to the tracer diffusion coefficient *but with the addition of the term in brackets*. This term is sometimes called the “vacancy-wind-term” and does not vary much from unity. Note that it results from non-zero cross terms L_{A^*A} and L_{AB} . The approach from the phenomenological equations has told us only of the formal existence of this term, but an evaluation of it requires consideration of the detailed microscopic processes which generate the correlations contained in the cross terms. This is considered in Sec. 3.3.1.8.

These examples suffice to show how the phenomenological equations are useful in presenting a consistent and unified picture of the diffusion process, no matter how complex. For further information on the subject, the reader is directed to the classic review by Howard and Lidiard (1964) and also many other treatises, such as those by Adda and Philibert (1966), Le Claire (1975), Stark (1976), Kirkaldy and Young (1987), Philibert (1991), and Allnatt and Lidiard (1993).

3.2.3.3 Einsteinian Expressions for the Phenomenological Coefficients

An important development in the area of solid-state diffusion was the fact that the phenomenological coefficients can be expressed *directly* in terms of *atomistic* Einsteinian formulae (Allnatt, 1982).

$$L_{ij} = \lim_{V \rightarrow \infty} \lim_{t \rightarrow \infty} (6V k T t)^{-1} \times \langle \Delta \mathbf{R}^{(i)}(t) \cdot \Delta \mathbf{R}^{(j)}(t) \rangle \quad (3-57)$$

where $\Delta \mathbf{R}^{(i)}(t)$ is the total displacement of species i in time t , V is the volume, and the Dirac brackets denote a thermal average A . It is important to note that $\Delta \mathbf{R}^{(i)}$ is the sum of the displacements of the individual particles of type i . In effect, $\Delta \mathbf{R}^{(i)}$ is the dis-

placement of the system of species i as if that system were a particle itself. The diagonal phenomenological coefficients derive from correlations of the system of species i with itself, i.e., self-correlations. This does *not* mean tracer correlations here: they are correlations in the random walk of an atom. The correlations here are in the random walk of the *system* “particle”. The off-diagonal terms derive from interference of the system of species i with the system of species j . In effect it is mathematically equivalent to two systems i and j being treated like two interfering “particles”.

Eq. (3-57) has been very useful for calculating the L_{ij} by means of computer simulation – see the pioneering calculations by Allnatt and Allnatt (1984). Much of that material has been reviewed by Murch and Dyre (1989). A brief discussion is given in Sec. 3.3.1.8.

3.2.3.4 Relating Phenomenological Coefficients to Tracer Diffusion Coefficients

For the case of multi-component alloys, Manning (1968, 1970, 1971) derived expressions relating the phenomenological coefficients to tracer diffusion coefficients. The expressions were developed for a particular model for concentrated alloys, the so-called random alloy model. In this model the atomic components are randomly distributed over the available sites, the vacancy mechanism is assumed and the exchange frequencies of the atomic components with the vacancies depend only on the nature of the atomic components and not on their environment.

For a binary system the relations are

$$L_{AA} = \frac{N}{kT} c_A D_A^* \left[1 + \frac{(1-f_0)}{f_0} \frac{c_A D_A^*}{(c_A D_A^* + c_B D_B^*)} \right] \quad (3-58)$$

$$L_{AB} = \frac{N}{kT} \frac{(1-f_0)}{f_0} \frac{c_A D_A^* c_B D_B^*}{(c_A D_A^* + c_B D_B^*)} \quad (3-59)$$

where f_0 is the tracer correlation factor in the lattice of either pure component, see Sec. 3.3.1.3. The relation for L_{BB} is obtained from L_{AA} by interchanging B with A.

Lidiard (1986) showed that Eqs. (3-58) and (3-59) can in fact be obtained without recourse to the random alloy model, on the basis of two microscopic assumptions which, although intuitive in nature, are independent of any microscopic model except for the inclusion of the tracer correlation factor in the pure lattice f_0 , which is dependent on mechanism and structure. Lidiard's findings immediately suggested that Eqs. (3-58) and (3-59) are probably appropriate for a much wider range of alloys than are reasonably represented by the random alloy model itself. Bocquet (1987) also found relations of the same form for the random alloy when interstitial mechanisms are operating. With Monte Carlo computer simulation, Zhang et al. (1989a) and Allnatt and Allnatt (1991) explored the validity of Eqs. (3-58) and (3-59) in the context of the interacting binary alloy model described in Sec. 3.3.1.5. It was found that Eqs. (3-58) and (3-59) apply very well except, perhaps surprisingly, at compositions approaching impurity levels. The breakdown there is readily traced to the fact that these equations have built into them the requirement that $\omega_4 = \omega_0$ (see Sec. 3.3.1.4 for the impurity frequency notation). For many cases ω_3 also equals ω_0 and so this is equivalent to a condition of no vacancy-impurity binding. This is not surprising given that the equations originated with the random alloy model where this requirement is automatically fulfilled.

Eqs. (3-58) and (3-59) have also been derived for B1 and B2 ordered alloys (Belova and Murch, 1997).

A most important consequence of Eqs. (3-58) and (3-59) is the Darken–Manning expression which relates the interdiffusion coefficient \tilde{D} , the tracer diffusion coefficients D_A^* and D_B^* and the thermodynamic factor $(1 + \partial \ln \gamma / \partial c)$:

$$\tilde{D} = (c_B D_A^* + c_A D_B^*) \left(1 + \frac{\partial \ln \gamma}{\partial c} \right) S \quad (3-60)$$

where the vacancy wind factor S is given by

$$S = 1 + \frac{(1-f_0) c_A c_B (D_A^* - D_B^*)^2}{f_0 (c_A D_A^* + c_B D_B^*) (c_B D_A^* + c_A D_B^*)} \quad (3-60a)$$

Eq. (3-60) is not only appropriate for random alloys, but also for ordered alloys/intermetallic compounds with B1 and B2 structures. Recent computer simulations have also shown that Eq. (3-60) is a good approximation for ordered alloys/intermetallic compounds with $L1_2$, $D0_3$, and $A15$ structures (Murch and Belova, 1998).

Further discussion on relations between phenomenological coefficients and tracer diffusion coefficients, and impurity diffusion coefficients, can be found in the reviews by Howard and Lidiard (1964), Le Claire (1975), and Allnatt and Lidiard (1987, 1993).

3.2.4 Short-Circuit Diffusion

It is generally recognized that the rate at which atoms migrate along grain boundaries and dislocations is higher than that through the lattice. From an atomistic point of view it is very difficult to discuss, in a precise way, the diffusion events in such complex and variable situations. Much of the understanding has been gained from computer simulations using the Molecular Dynamics and Lattice Statics methods; see, for example, Kwok et al. (1984) and Mishin (1997). In this section we shall dis-

cuss short-circuit diffusion from a phenomenological point of view.

Fisher (1951) was probably the first to introduce a distinct diffusion coefficient for material migrating along the short-circuit path. For grain boundaries, each one is conceived as a slab of width δ for which the *average* diffusion coefficient is D' . For dislocations, each one is conceived as a pipe of diameter $2a$ for which the *average* diffusion coefficient is D' .

For conventional diffusion experiments it has been usual to distinguish three distinct regimes, depending on the magnitude of the *lattice* diffusion length $\sqrt{D_l t}$, where D_l is the lattice diffusion coefficient and t is time (Harrison, 1961).

Regime A: $\sqrt{D_l t}$ is much larger than the spacing l between the short-circuit paths. For grain boundaries l is the average diameter of the grains and for dislocations l is the distance between dislocation pinning points. Diffusion from adjacent short circuits overlap extensively. This condition is met for small-grained materials or very long diffusion times. Hart (1975) proposed that an *effective* diffusion coefficient D_{eff} can be introduced which still satisfies solutions to Fick's Second Law and can be written as

$$D_{\text{eff}} = \mathfrak{F} D' + (1 - \mathfrak{F}) D_l \quad (3-61)$$

where \mathfrak{F} is the fraction of all sites which belong to the short-circuit paths. Eq. (3-61) is usually called the Hart Equation. Le Claire (1975) has given a rough calculation using Eq. (3-61). For typical dislocation densities in metals, $\mathfrak{F} = 10^{-8}$. The *dislocation contribution* to a measured or effective D will then exceed 1% when $D'/D > 10^6$. Because the activation energy for lattice diffusion in metals is about $34 T_{\text{M.Pt.}}$, where $T_{\text{M.Pt.}}$ is the melting temperature and the activation energy for short-circuit diffusion is generally about half that of

volume diffusion, then this condition $D'/D > 10^6$ is usual for temperatures below about half the melting temperature. This is why experiments where lattice diffusion only is of interest tend to be made at temperatures *above* about half the melting temperature.

Impurities are often bound to short-circuit paths, in which case the Hart Equation (Eq. (3-60)) is written as

$$D' = \mathfrak{F} D' \exp(E_b/kT) + (1 - \mathfrak{F}) D_l \quad (3-62)$$

where E_b is the binding energy of the impurity and the diffusion coefficients refer to impurities. The Hart Equation can be shown to be fairly accurately followed when $l/\sqrt{D_l t} \leq 0.3$ and also for $l/\sqrt{D_l t} \geq 100$ (this corresponds to Regime C – see the next paragraph) (Murch and Rothman, 1985; Gupta et al., 1978).

Regime C: It is convenient to discuss the other limit out of sequence. When $\sqrt{D_l t}$ is much smaller than the distances l between the short-circuit paths, we have Regime C kinetics. In this instance, all material comes down the short-circuit paths and the measured diffusion coefficient is given entirely by D' .

Regime B: In this intermediate case, it is assumed that $\sqrt{D_l t}$ is comparable to l so that material which is transported down a short-circuit path and which diffuses out into the lattice is unlikely to reach another short-circuit path.

There are various solutions of Fick's Second Law available to cope with tracer diffusion in the presence of short-circuit paths, but space prevents us from dealing with these in any detail: they are discussed at length by Kaur, Mishin and Gust (1995). Suzuoka (1961) and Le Claire (1963) have given a solution for the grain boundary problem for the usual case when there is a finite amount of tracer originally at the surface, see Eq. (3-8). It is found, among other

things, that

$$\left(\frac{d \ln C}{dx^{6/5}}\right)^{5/3} = \left(\frac{4D_l}{t}\right)^{1/2} (D'\delta)^{-1} 0.66 \quad (3-63)$$

Hence the product $D'\delta$ can be found by determining the slope of the *linear* region (penetrations reached by grain boundary diffusion) in a plot of $\ln C$ versus $x^{6/5}$ (not the usual x^2) and also with a knowledge of D_l itself. It can be difficult, however, to obtain the two diffusion coefficients in one experiment; the practicalities of this and alternatives are discussed by Rothman (1984). An example of a tracer penetration plot with a clear contribution from grain boundary diffusion ($x^{6/5}$ dependence) is shown in Fig. 3-3.

Le Claire and Rabinovitch (1984) have addressed the dislocation pipe problem

and provided near-exact solutions to Fick's Second Law for both an isolated dislocation pipe and arrays of dislocation pipes. The profiles generally are not unlike the grain boundary ones except that a linear region in a plot of $\ln C$ versus x is now found, i.e.,

$$\frac{d \ln C}{dx} = - \frac{A(a)}{[(D'/D_l - 1)a^2]^{1/2}} \quad (3-64)$$

where A is a slowly varying function of $a/(Dt)^{1/2}$. An example of such a tracer penetration plot with a clear contribution from dislocation pipe diffusion (x dependence) is shown in Fig. 3-4.

For further details on grain boundary diffusion we refer to reviews by Peterson (1983), Mohan Rao and Ranganathan (1984), Balluffi (1984), Philibert (1991),

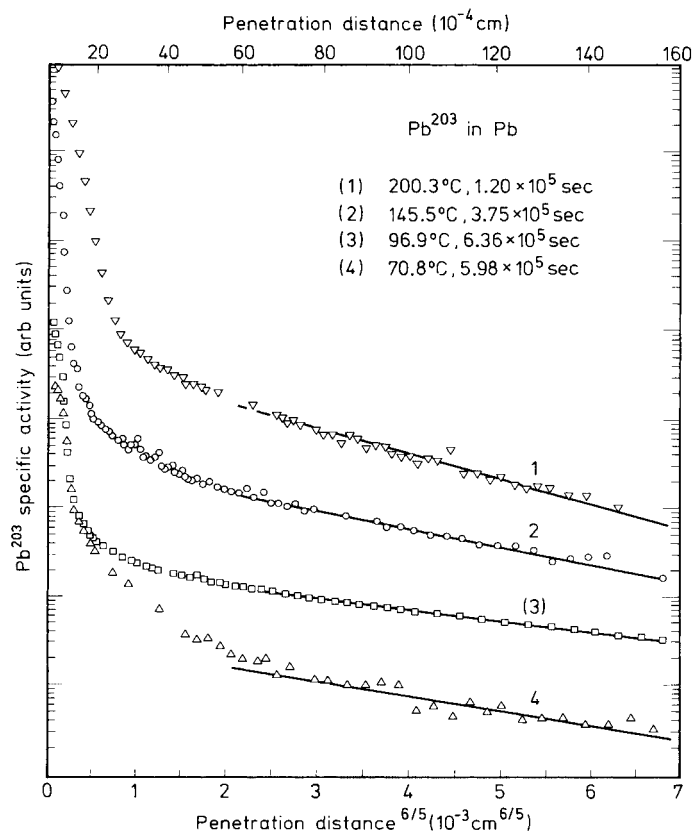


Figure 3-3. Tracer concentration profiles of ^{203}Pb into polycrystalline Pb showing a contribution from grain boundaries (Gupta and Oberschmidt, 1984).

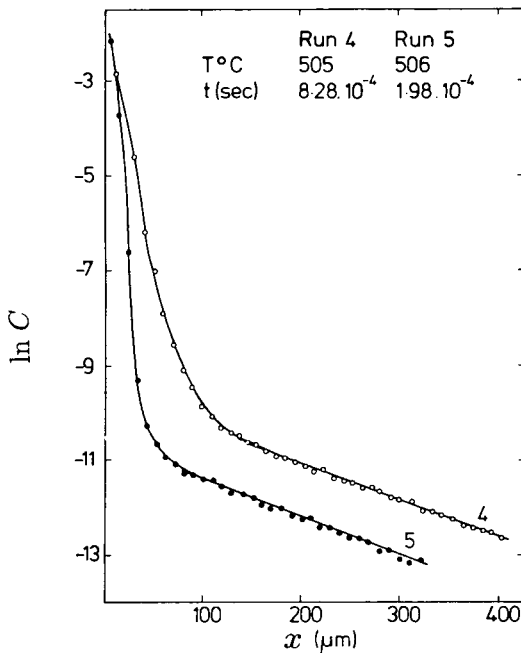


Figure 3-4. Tracer concentration profiles of ^{22}Na into single crystal NaCl showing a contribution from dislocations (Ho, 1982).

Kaur et al. (1995), Mishin et al. (1997). For dislocation pipe diffusion we refer to Le Claire and Rabinovitch (1984) and Philibert (1991).

3.3 Microscopic Diffusion

3.3.1 Random Walk Theory

We have already seen in Sec. 3.2 that the phenomenological or continuum theory of diffusion is set up in terms of quantities such as the diffusion coefficients, the ionic conductivities, or more generally, the phenomenological coefficients, L_{ij} . For the materials technologist this theory provides a perfectly suitable formalism to describe the macroscopic features arising from the diffusion of atoms in solids. By its very nature, this macroscopic theory makes no ref-

erence to the discrete atomic events which give rise to macroscopically observable diffusion. To describe the atomic events, a wholly separate theory, termed “Random Walk Theory” has been formulated. This theory is based on the premise that macroscopic diffusion is the net result of many individual atomic *jumps*. The theory attempts to relate the quantities such as the diffusion coefficients, the ionic conductivities, or, more generally, the L_{ij} , in terms of lattice and atomic characteristics, notably jump frequencies. Although originally quite precise in use (Howard, 1966), the term “Random Walk Theory” is now used rather loosely to describe any mathematical approach that focuses on the sequence of jumps of atoms in the solid state. Inextricably linked with this theory is the existence of *correlated* random walks of atoms, in other words, walks where there is an apparent memory between jump directions. Much of random walk theory is concerned with describing such correlations.

3.3.1.1 Mechanisms of Diffusion

As a prelude to a discussion of random walk theory, in this section we will briefly discuss the common mechanisms of solid-state diffusion.

Interstitial Mechanism

In the interstitial mechanism, see Fig. 3-5, sometimes called the direct interstitial mechanism, the atoms jump from one interstice to another without directly involving the remainder of the lattice. Since the interstitial atom does not need to “wait” to be neighboring to a defect in order to jump (in a sense it is always next to a vacancy), diffusion coefficients for atoms migrating with this mechanism tend to be fairly high. As would be expected, atoms

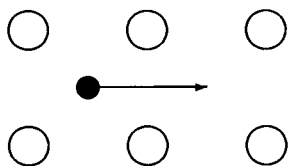


Figure 3-5. Interstitial diffusion mechanism.

such as H, N, O, and C diffuse in this way in metals. It should also be noted that without the defect being required to affect the jump, no defect concentration term and therefore defect formation energy enters the activation energy for diffusion; see Sec. 3.3.4.

Interstitialcy Mechanism

In the interstitialcy mechanism, see Fig. 3-6, sometimes called the indirect interstitial mechanism, two atoms, one an interstitial and the other an atom on a regular lattice site, move in unison. The interstitial atom moves to a regular site, whereas the regular site atom moves to an interstice. Collinear and non-collinear versions are possible depending on constraints imposed by the lattice.

Because the interstitial formation energy is generally very high in metals, the equilibrium concentration of interstitials is very

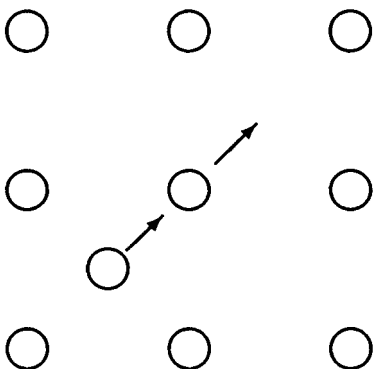


Figure 3-6. Interstitialcy diffusion mechanism.

small and their contribution to diffusion is unimportant in most cases. However, for plastically deformed or irradiated metals the concentration of interstitials (besides vacancies) can be appreciable. It should be noted that the interstitial thus formed is not located on an interstice, but in a dumbbell split configuration. The migration possibilities of dumbbells have been discussed by Schilling (1978).

As a result of measurements of the Haven ratio (see Sec. 3.3.2), the interstitialcy mechanism appears to be highly likely for silver diffusion in AgBr (Friauf, 1957). Note that with the interstitialcy mechanism, say the collinear version, a tracer atom moves a distance r whereas the charge apparently moves a distance $2r$. This needs to be taken into account in the interpretation of the Haven ratio. The interstitialcy mechanism probably occurs relatively frequently in ionic materials, especially those with open lattices such as the anion lattice in the fluorite structure or those which are highly defective. Nonetheless, there is often so much attendant local relaxation around the interstitial that far more complex quasi-interstitialcy mechanisms could well operate. An example is oxygen diffusion in UO_{2+x} , where the excess oxygen is located as di-interstitials with relaxation of two oxygen atoms from regular sites to form two new interstitials and two new vacancies. The actual mechanism of oxygen transport is not known but a quasi-interstitialcy mechanism is undoubtedly responsible (Murch and Catlow, 1987).

We should also mention that the interstitialcy mechanism appears to be very important in self-diffusion in silicon and possibly certain substitutional solutes in silicon are also transported via this mechanism (Frank et al., 1984).

Vacancy Mechanism

The most important diffusion mechanism of all is undoubtedly the vacancy mechanism, shown in Fig. 3-7. A substitutional solute atom or an atom of the solvent diffuses simply by exchanging places with the vacancy. There can be attractive or repulsive interactions of the solute with the vacancy, which can have a profound influence on the diffusion coefficient of the solute and to a lesser extent the solvent by way of correlation effects. This is discussed in Secs. 3.3.1.4 and 3.4.2. The vacancy mechanism is definitely the preferred mechanism for metals and alloys for both host and substitutional solutes. In most other materials the vacancy appears to play the major diffusion role except when the concentration of interstitials produced by nonstoichiometry or doping (in oxides) or irradiation (in metals) is so high that contributions from interstitialcy or similar mechanisms become dominant.

Aggregates of vacancies such as the divacancy or trivacancy can also contribute to diffusion. These appear to be important at high temperatures in metals where their contribution has been largely inferred from curvatures of the Arrhenius plot ($\log D$ vs. $1/T$); see, for example, the f.c.c. metals (Peterson, 1978) (see Sec. 3.4.1.1). Bound vacancy pairs, i.e., a cation vacancy bound to an anion vacancy, are important contrib-

utors to tracer diffusion in alkali halides (Bénière et al., 1976).

Interstitial-Substitutional Mechanism

On occasion, solute atoms may dissolve interstitially and substitutionally. These solute atoms may diffuse by way of the *dissociative mechanism* (Frank and Turnbull, 1956) and/or the *kickout mechanism* (Gösele et al., 1980). In *both* mechanisms the interstitial solute diffuses rapidly by the interstitial mechanism. In the *dissociative* mechanism the interstitial combines with a vacancy to form a substitutional solute. At a later time this substitutional can dissociate to form a vacancy and an interstitial solute (really a Frenkel defect). The anomalously fast diffusion of certain solutes, e.g., Cu, Ag, Au, Ni, Zr, and Pd in Pb, appears to have a contribution from the dissociative mechanism (Warburton and Turnbull, 1975; Bocquet et al., 1996). In the *kickout* mechanism, on the other hand, the solute interstitial uses the interstitialcy mechanism to involve the regular site lattice. In the process a host interstitial is formed and the interstitial solute then occupies a substitutional site. This process can be reversed at a later stage. The kickout mechanism appears to operate for rapid diffusion of certain foreign atoms, such as Au in Si (Frank et al., 1984).

Exchange Mechanism

The exchange mechanism, in which two neighboring atoms exchange places, has in the past been postulated as a possible diffusion mechanism. The existence of the Kirkendall effect in many alloy interdiffusion experiments (this implies that the respective intrinsic diffusion coefficients are unequal, which is not possible with the exchange mechanism, see Sec. 3.2.2.4) and the very high theoretical activation ener-

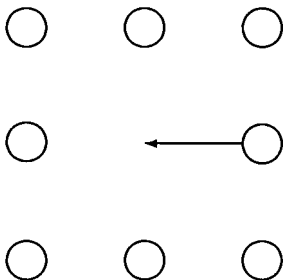


Figure 3-7. Vacancy mechanism.

gies in close-packed solids suggest that this mechanism is unlikely. It may, however, occur in liquids and in quenched-liquids such as amorphous alloys (Jain and Gupta, 1994). Ring versions of the exchange mechanism certainly have lower theoretical activation energies but require substantial cooperation among the atoms, which seems unlikely.

Surface Diffusion Mechanisms

A number of mechanisms for surface diffusion on metals (by far the most studied class of material) have been postulated. They include activated hopping of adsorbed atoms from one surface site to another, where the jump distance is simply the distance between sites. Similarly, a vacancy in a terrace, i.e., surface vacancy, can also move in the same sort of way within the terrace. At low temperatures and rough surfaces, exchange between an adsorbed atom and an atom in the substrate is predominant. At high temperatures non-localized diffusion and surface melting are also possible. The mechanisms for surface diffusion are discussed further in the book edited by Vu Thien Binh (1983) and in the reviews by Rhead (1989) and Bonzel (1990).

3.3.1.2 The Einstein Equation

Let us consider atoms (of one chemical type) diffusing in their concentration gradient in the x direction. It can readily be shown (see, for example, Adda and Philibert, 1966; Manning, 1968; Le Claire, 1975) that the *net* flux of atoms across a given plane x_0 is given by

$$J_x = C(x_0) \frac{\langle X \rangle}{t} - \frac{\partial C}{\partial x} \frac{\langle X^2 \rangle}{2t} - C(x_0) \frac{\partial C}{\partial x} \frac{\partial}{\partial C} \frac{\langle X^2 \rangle}{2t} \quad (3-65)$$

plus higher order terms. In Eq. (3-65), $C(x_0)$ is the concentration of the diffusing atoms at x_0 , $\langle X \rangle$ is the mean displacement or drift, and $\langle X^2 \rangle$ is the mean squared displacement. The Dirac brackets $\langle \rangle$ denote an average over all possible paths taken in time t .

In a situation where diffusion properties do *not* depend on position, e.g., diffusion of tracer atoms in a *chemically* homogeneous system, the third term in Eq. (3-65) is zero. The term containing the drift $\langle X \rangle$ is also zero because in a chemically homogeneous system the probability that, say, a tracer atom migrates some distance $+X$ in time t (starting from x_0) equals the probability that an atom migrates a distance $-X$. Similarly, other odd moments are zero. Provided that other higher-order terms can be neglected, Eq. (3-65) reduces to

$$J_x = \frac{\partial C}{\partial x} \frac{\langle X^2 \rangle}{2t} \quad (3-66)$$

By comparison with Fick's First Law, Eq. (3-1), Eq. (3-66) immediately gives

$$D_x^* = \frac{\langle X^2 \rangle}{2t} \quad (3-67)$$

Eq. (3-67) is called the Einstein Equation, probably the single most important equation in the theory of diffusion kinetics. The superscript $*$ indicates that the diffusion coefficient refers to tracer atom diffusion in a chemically homogeneous system. Equations for D_y^* and D_z^* have the same form as Eq. (3-67). For three-dimensional isotropic crystals the tracer diffusion coefficient is the same in every direction and

$$D^* = \frac{\langle R^2 \rangle}{6t} \quad (3-68)$$

where \mathbf{R} is the vector displacement of an atom in time t . For two-dimensional situations the factor 6 in Eq. (3-68) is replaced by 4.

3.3.1.3 Tracer Correlation Factor

Either Eq. (3-67) or (3-68) can provide the starting point for a discussion of correlation effects in the diffusion walk. For convenience we shall use Eq. (3-68). Let us consider the atomistic meaning of the displacement \mathbf{R} . It is simply the sum of n successive jump vectors, $\mathbf{r}_1, \mathbf{r}_2, \mathbf{r}_3, \dots, \mathbf{r}_n$

$$\mathbf{R} = \sum_{i=1}^n \mathbf{r}_i \quad (3-69)$$

The squared displacement \mathbf{R}^2 is then simply

$$\mathbf{R}^2 = \sum_{i=1}^n \mathbf{r}_i^2 + 2 \sum_{i=1}^{n-1} \sum_{j=1}^{n-i} \mathbf{r}_i \cdot \mathbf{r}_{i+j} \quad (3-70)$$

The average of the squared displacement $\langle \mathbf{R}^2 \rangle$ equals of course the sum of the averages and we have

$$\langle \mathbf{R}^2 \rangle = \sum_{i=1}^n \langle \mathbf{r}_i^2 \rangle + 2 \sum_{i=1}^{n-1} \sum_{j=1}^{n-i} \langle \mathbf{r}_i \cdot \mathbf{r}_{i+j} \rangle \quad (3-71)$$

For a *complete* random walk, i.e., where each direction is unrelated to the previous one, the second term in Eq. (3-71) is zero because for any product $\mathbf{r}_i \cdot \mathbf{r}_{i+j}$ there will always be another of opposite sign. We now have

$$\langle \mathbf{R}^2 \rangle = \sum_{i=1}^n \langle \mathbf{r}_i^2 \rangle \quad (3-72)$$

Because in most cases atoms require the assistance of point defects in order to move about (see Sec. 3.3.1.1), there is generally an unavoidable memory or correlation effect between jump directions. In order to appreciate this, let us focus on Fig. 3-8a where the vacancy mechanism is shown. In this figure one atom symbol is shown filled to indicate that it is a tracer and can be followed. Let us assume that the tracer and the vacancy have just exchanged places. Because the vacancy is still neighboring to the tracer the *next jump of the tracer* is quite likely to cancel out the previous jump. The

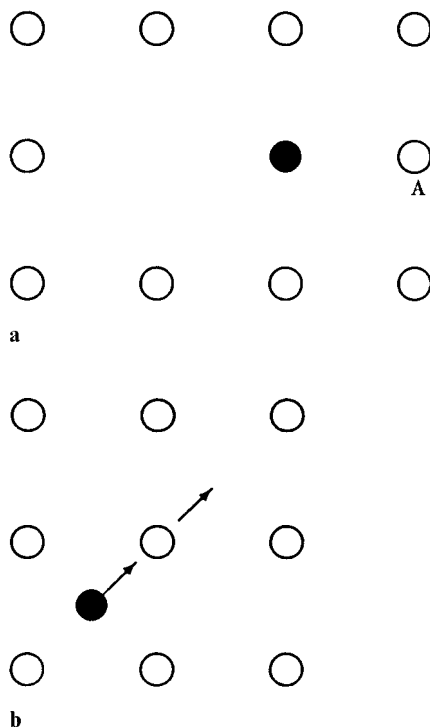


Figure 3-8. (a) Correlation effects arising from the vacancy mechanism – see text. (b) Correlation effects arising from the interstitialcy mechanism (see text).

probability of doing this is in fact exactly $2/g$ where g is the lattice coordination (Kelly and Sholl, 1987). On the other hand, the tracer has a *reduced* probability of continuing in the direction of the first jump, since this requires the vacancy to migrate to point A. In other words, there is a memory or correlation between directions of tracer jumps. In no way does this imply that the vacancy somehow favors the tracer atom. In fact, in this example atoms surrounding the vacancy jump randomly with the vacancy so that the vacancy itself moves on an uncorrelated random walk with no memory or correlation whatsoever between its jump directions. It should be noted that weaker correlations in the tracer jumps also come about as long as the va-

cancy remains in the vicinity of the tracer and can approach the tracer from a non-random direction.

Let us consider Fig. 3-8b, where the col-linear interstitialcy mechanism is assumed. Let us assume that the tracer is in the interstitial position. The first jump (a pair of atoms move) will take the tracer immediately to a regular lattice site and a new atom, formerly at a regular lattice site, takes up a position as the interstitial. The pair of atoms which next moves possibly again involves the tracer atom and in doing so will cancel out the previous tracer jump. Like the vacancy mechanism, the memory or correlation between successive tracer atom jump directions comes about purely because of the proximity of the defect. Unlike the vacancy diffusion mechanism, however, in this case the correlation comes about *only* for consecutive pairs of tracer jumps of the type interstitial site \rightarrow regular lattice site \rightarrow interstitial site.

In the presence of correlation between jump directions, the sum of the dot products $\langle \mathbf{r}_i \cdot \mathbf{r}_{i+j} \rangle$ no longer averages out to zero. A convenient way of expressing these correlations quantitatively is to form the ratio of the *actual* $\langle \mathbf{R}^2 \rangle$ to the $\langle \mathbf{R}^2 \rangle$ resulting from a complete random walk, i.e., $\langle \mathbf{R}^2 \rangle_{\text{random}}$:

$$f = \frac{\langle \mathbf{R}^2 \rangle}{\langle \mathbf{R}^2_{\text{random}} \rangle} \quad (3-73)$$

where the quantity f is called the tracer correlation factor or simply the correlation factor. Sometimes the terminology "correlation coefficient" is used, but this is to be discouraged. With Eqs. (3-71) and (3-72) we have

$$f = \lim_{n \rightarrow \infty} 1 + \frac{2 \sum_{i=1}^{n-1} \sum_{j=1}^{n-i} \langle \mathbf{r}_i \cdot \mathbf{r}_{i+j} \rangle}{\sum_{i=1}^n \langle \mathbf{r}_i^2 \rangle} \quad (3-74)$$

It should be noted that the limit $n \rightarrow \infty$ is applied to Eq. (3-74) to ensure that all possible correlations are included.

There have been numerous publications concerned with the calculation of the tracer correlation factor. The earlier work has been reviewed in detail by Le Claire (1970), more recent work has been covered by Allnatt and Lidiard (1993). Table 3-1 gives some values of f for various mechanisms and lattices. It should be noted from Table 3-1 that the correlation factor for the interstitial mechanism is unity. For this mechanism the interstitials, which are considered to be present at a vanishingly small concentration, move on an uncorrelated random walk, very much like the vacancy in the vacancy-assisted diffusion mechanism. Accordingly, the second term in Eq. (3-71) drops out and $f=1$. If the interstitial concentration is increased, the interstitials impede one another and correlations are introduced; as a result, the tracer correlation factor decreases from unity. In fact, it continues to decrease until only one interstice is left vacant. The situation now is identical to that for vacancy-assisted diffusion. The variation of f with vacancy (or vacant interstice) concentration in the f.c.c. lattice is shown in Fig. 3-9. Of course, in the unphysical situation where the interstitials do not "see" one another, i.e., multiple occupancy of a site is permitted, the interstitials continue to move on a complete random walk at all concentrations, and f always equals unity.

For cubic lattices all the jumps are of the same length. Then we have that $|\mathbf{r}_i| = r$:

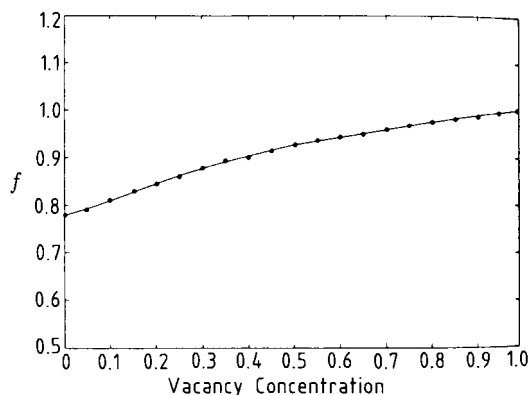
$$\sum_{i=1}^n \langle \mathbf{r}_i^2 \rangle = n r^2 \quad (3-75)$$

Then we have, with Eqs. (3-68), (3-71), and (3-75)

$$D^* = \frac{n r^2 f}{6t} = \frac{\Gamma r^2 f}{6} \quad (3-76)$$

Table 3-1. Some correlation factors (at infinitely low defect concentrations) from Le Claire (1970), Manning (1968), and Murch (1982d).

Lattice	Mechanism	f
Honeycomb	Vacancy	1/3
Square planar	Vacancy	$1/(\pi - 1)$
Triangular	Vacancy	0.56006
Diamond	Vacancy	1/2
B.c.c.	Vacancy	0.72714
Simple cubic	Vacancy	0.65311
F.c.c.	Vacancy	0.78146
F.c.c.	Divacancy	0.4579 ± 0.0005
All lattices	Interstitial	1
NaCl structure	Collinear interstitialcy	2/3
CaF ₂ structure (F)	Non-collinear interstitialcy	0.9855
CaF ₂ structure (Ca)	Collinear interstitialcy	4/5
CaF ₂ structure (Ca)	Non-collinear interstitialcy	1

**Figure 3-9.** Tracer correlation factor vs. vacancy concentration for non-interacting vacancies in the f.c.c. lattice; after Murch (1975).

where Γ is the jump frequency. The jump frequency is further discussed in Sec. 3.3.4. This partitioning of the diffusion coefficient into its uncorrelated ($\Gamma r^2/6$) and correlated (f) parts is very basic to random walk theory. Other partitionings are certainly possible, e.g., only jumps which are not immediately cancelled contribute to the jump frequency, i.e., an “effective jump” frequency, but the partitioning here seems to be the most natural.

The tracer correlation factor itself can be expressed as

$$f = \lim_{n \rightarrow \infty} \frac{\langle R^2 \rangle}{nr^2} \quad (3-77)$$

This equation has been very useful for direct computer simulation calculations of f ; see the review by Murch (1984a).

We see that f normally acts to decrease the tracer diffusion coefficient from its random walk ($f=1$) value. The inclusion of f in the expression for D^* is necessary for a complete description of the atomic diffusion process. From Table 3-1, however, it can be seen that for many 3D lattices f really only decreases D^* by some 20–30%. This is not much more than the precision routinely obtainable in measurements of the tracer diffusion coefficient (Rothman, 1984) and, given the difficulty in calculating the jump frequency Γ (see Sec. 3.3.4), may not appear to be particularly significant. There are, however, many reasons why a study of correlation effects in diffusion is sufficiently important that it has consumed the energies of many researchers over almost a 40-year period.

First, as can be seen from Table 3-1, the tracer correlation factor is quite sensitive to the mechanism of diffusion operating. Although f , *by itself*, is not measurable, measurements of the Haven ratio (see Sec. 3.3.2) and the isotope effect (see Sec. 3.3.3) (which are closely related to f) in favorable cases can throw considerable light on the mechanism(s) of diffusion that are operating. Identification of the diffusion mechanism is surely the most important ingredient in understanding the way atoms migrate in solids and how it can be controlled.

Much of our discussion so far has been concerned with pure solids with few defects. There are, however, a large number of solids where the apparent defect concentration can be fairly high, e.g., highly non-stoichiometric compounds, fast ion conductors, and certain concentrated interstitial solid solutions. In such cases the defects interact and correlation effects tend to be magnified and become highly temperature dependent. Then the apparent activation energy for tracer diffusion includes an important contribution directly from the correlation factor. Clearly, an understanding of f is a very important part of the understanding of the diffusion process in such materials. We shall deal further with this subject in Sec. 3.3.1.6. In ordered binary alloys, the correlation factor can become very small since atoms which make a jump from the “right” lattice to the “wrong” lattice tend to reverse, i.e., cancel that jump. As a result, the tracer diffusion coefficient can become abnormally small, largely because of this strong memory effect. We shall deal further with this subject in Sec. 3.3.1.5.

Another important case of correlation effects is impurity diffusion. The correlation factor for the impurity is highly dependent on the relative jump frequencies of the impurity and host atoms in the vicinity of the

impurity. We shall deal with this subject in the following section.

3.3.1.4 Impurity Correlation Factor

We first consider that the impurity concentration is sufficiently dilute that there is not a composition-dependent impurity diffusion coefficient. Accordingly, each impurity atom is considered to diffuse in pure host. The jump frequency of the impurity is given by ω_2 whereas the jump frequency of the host atoms is given by ω_0 . The significance of the subscripts will be apparent later. The vacancy mechanism is assumed.

The “tracer” now is the impurity. The result for the impurity correlation factor f_2 in the f.c.c. lattice as a function of ω_2/ω_0 is shown in Fig. 3-10. When $\omega_2 < \omega_0$ (upper curve), the impurity motion becomes considerably *decorrelated* since, after an impurity/vacancy exchange, the vacancy does not tend to remain in the vicinity of the impurity. When the impurity is next

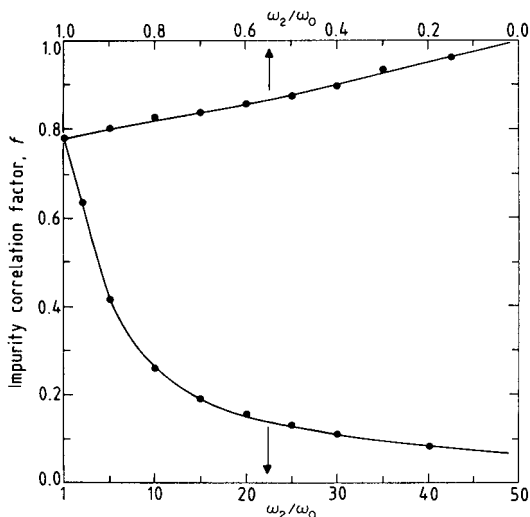


Figure 3-10. Impurity correlation factor in the f.c.c. lattice as a function of ω_2/ω_0 ; points by computer simulation (Murch and Thorn, 1978), solid lines from the formalism of Manning (1964); after Murch and Thorn (1978).

approached by the vacancy, it will tend to be from a random direction, with the result that the impurity correlation factor $f_2 \rightarrow 1.0$, thereby signifying a less correlated random walk.

Conversely, when $\omega_2 > \omega_0$ (lower curve), the impurity and vacancy tend to continue exchanging places in a particular configuration. Many impurity jumps are thereby effectively cancelled and $f_2 \rightarrow 0.0$, i.e., the jumps are more correlated. Of course, when $\omega_2 = \omega_0$ the “impurity” is now a tracer in the host, and in effect it can be considered to have a different “color” from the host. The impurity correlation factor now is the tracer correlation factor, which in this example is 0.78146 (see Table 3-1).

The diffusion coefficient can be considered to be the product of an uncorrelated and a correlated part (Eq. (3-76)). In this example, when $\omega_2 > \omega_0$, the reduced impurity correlation factor acts to *reduce* the impurity diffusion coefficient from that expected on the basis of ω_2 alone. Similarly, when $\omega_2 < \omega_0$ the raised impurity correlation factor acts to increase the impurity diffusion coefficient from that expected on the basis of ω_2 alone.

In general, the presence of the impurity atom in the host also influences the host jump frequencies in the vicinity of the impurity so that they differ from ω_0 . For the f.c.c. lattice the usual model adopted is the so-called five-frequency model and is depicted in Fig. 3-11. The frequency ω_1 is the host frequency for host atom/vacancy jumps that are *both* nearest neighbors to the impurity. This jump is often called the “rotational jump” because in effect the host can *rotate* around the impurity. The frequency ω_3 refers to a “dissociative” jump, i.e., a host atom jump which takes the vacancy *away from* the impurity. Finally ω_4 (not shown) is the “associative” jump, which is a host jump that brings the vacancy to the

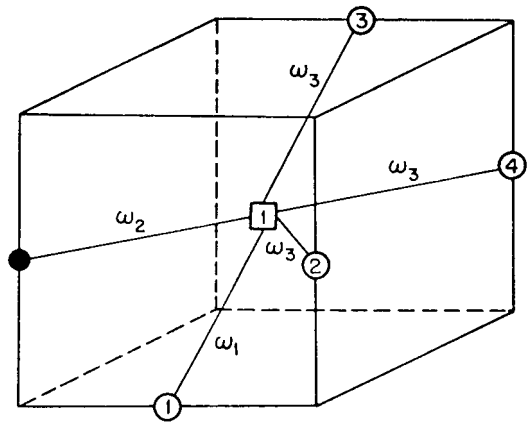


Figure 3-11. Five-frequency model for impurity diffusion in the f.c.c. lattice (see text), figure taken from Murch and Thorn (1978).

nearest neighbor position of the impurity, i.e., the reverse of ω_3 . All other host jumps occur with the frequency ω_0 .

We have mentioned “associative” and “dissociative” jumps of the vacancy. These are directly related to the impurity–vacancy binding energy E_B at the first nearest neighbor separation by

$$\omega_4/\omega_3 = \exp(-E_B/kT) \quad (3-78)$$

Note that E_B is negative for attraction between the impurity and the vacancy.

Manning (1964) has shown that the impurity correlation factor f_2 is given rigorously for the five-frequency model by

$$f_2 = (2\omega_1 + 7F\omega_3)/(2\omega_2 + 2\omega_1 + 7F\omega_3) \quad (3-79)$$

where F is the fraction of dissociating vacancies that are permanently lost from a site and are uncompensated for by returning vacancies. F is given to a very good approximation by

$$7F = 7 \quad (3-80)$$

$$- \left[\frac{10\alpha^4 + 180.5\alpha^3 + 927\alpha^2 + 1341\alpha}{2\alpha^4 + 40.2\alpha^3 + 254\alpha^2 + 597\alpha + 436} \right]$$

and $\alpha = \omega_4/\omega_0$.

Other more accurate expressions for F have been reviewed by Allnatt and Lidiard (1987, 1993). For many practical purposes the extra rigor is probably unwarranted. Extension to the case where there are vacancy-impurity interactions at second nearest neighbors has been considered by Manning (1964).

In the b.c.c. lattice the second nearest neighbor is close to the nearest neighbor (within 15% in fact). In a formal sense we need to consider *dissociative* jumps for a vacancy, jumping from the first to the second, third (not the fourth), and fifth nearest neighbors: these are denoted by ω_3 , ω'_3 , and ω''_3 .

The corresponding reverse *associative* jumps are ω_4 , ω'_4 , and ω''_4 . We also need to consider dissociative jumps from the second nearest neighbor to the fourth (ω_5) and the reverse of this (ω_6). There is no rotational, i.e., ω_1 , jump.

The binding energy E_{B1} between the impurity and the vacancy at first nearest neighbor is expressible as (see, for example, Bocquet et al., 1996)

$$\omega'_4/\omega'_3 = \omega''_4/\omega''_3 = \exp(-E_{B1}/kT) \quad (3-81)$$

The binding energy E_{B2} between the impurity and the vacancy at second nearest neighbors can be expressed as

$$\omega_6/\omega_5 = \exp(-E_{B2}/kT) \quad (3-82)$$

We also have that

$$\omega_4 \omega_4/\omega_5 \omega_3 = \omega'_4/\omega'_3 \quad (3-83)$$

In order to proceed it has been usual to reduce the large number of jump frequencies by making certain assumptions. There are two basic models. In the first, usually called Model I, it is assumed that $\omega_6 = \omega_0 = \omega'_4 = \omega''_4$. This implies that $\omega'_3 = \omega''_3$ and $\omega_3 \omega_5 = \omega'_3 \omega_4$. In the second, Model II, on the other hand, the impurity-vacancy interaction is in effect restricted to the first

nearest neighbor by means of the assumptions $\omega_3 = \omega'_3 = \omega''_3$ and $\omega_5 = \omega_6 = \omega_0$. This also implies that $\omega_4 = \omega'_4 = \omega''_4$.

Model I leads to the expression (Manning, 1964; Le Claire, 1970)

$$f_2 = \frac{7\omega'_3 F}{2\omega_2 + 7\omega'_3 F} \quad (3-84)$$

with F given by

$$7F = \frac{2\alpha^2 + 5.1817\alpha + 2.476}{\alpha + 0.8106} \quad (3-85)$$

and $\alpha = \omega_3/\omega'_4$.

Model II leads to the expression

$$f_2 = \frac{7\omega_3 F}{2\omega_2 + 7\omega_3 F} \quad (3-86)$$

where F is given by (3-87)

$$7F = \frac{3\alpha^3 + 33.43\alpha^2 + 97.38\alpha + 66.06}{\alpha^3 + 8.68\alpha^2 + 18.35\alpha + 9.433}$$

and $\alpha = \omega_4/\omega_0$.

Correlation factors for impurity diffusion via vacancies in the simple cubic lattice (Manning, personal communication, cited by Murch, 1982a) and the diamond structure have also been calculated (see Manning, 1964), as well as the h.c.p. structure (see Huntington and Ghate (1962) and Ghate (1964)). Correlation factors for impurity diffusion by interstitialcy jumps have also been reported for the f.c.c. lattice and the AgCl structure (Manning, 1959).

In many cases of impurity diffusion the expression for the impurity correlation factor is of the form

$$f_2 = \frac{u}{\omega_2 + u} \quad (3-88)$$

where u contains *only* the host frequencies; e.g., for vacancy diffusion in the f.c.c. lattice u is given by

$$u = \omega_1 + \frac{\omega_3}{2} F(\omega_4/\omega_0) \quad (3-89)$$

This form for the impurity correlation factor is especially relevant to the isotope effect in diffusion (see Sec. 3.3.3) where for self-diffusion the isotopes are tracers of the host but, being isotopes, actually have slightly different jump frequencies from the host and can be classified as “impurities”. We might also mention that for impurity diffusion experiments the isotopes can additionally be of the impurity.

As a closing remark for this section, it should be remembered that because of its mathematical form, the impurity correlation factor will be temperature dependent. Over a fairly small temperature range the temperature dependence can frequently be approximated by an Arrhenius-like expression, i.e.,

$$f_2 \approx f_2^0 \exp(-Q'/kT) \quad (3-90)$$

where Q' is some activation energy for the correlation process (this has no particular physical meaning), k is the Boltzmann constant, and f_2^0 is a “constant”. It should be noted that Q' will be unavoidably included in the activation energy for the entire impurity diffusion process and is not necessarily unimportant.

3.3.1.5 Correlation Factors for Concentrated Alloy Systems

The impurity correlation factors discussed in the previous section are probably appropriate for impurity concentrations up to about 1 at.%. At higher concentrations the impurities can no longer be considered independent in the sense that the correlation events themselves are independent. This presents a special difficulty because there is no easy way of extending, say, the five-frequency model into the concentrated regime without rapidly increasing the number of jump frequencies to an unworkable number. As a result, models have been in-

troduced which limit the number of jump frequencies but only as a result of some loss of realism.

The first of these is the “random alloy” model introduced by Manning (1968, 1970, 1971). The random alloy is of considerable interest because, despite its simplicity, it seems to describe fairly well the diffusion behavior of a large number of alloys. The atomic components (two or more) are assumed to be ideally mixed and the vacancy concentration is assumed to be very low. The atomic jump frequencies, e.g., ω_A and ω_B , in a binary alloy are explicitly specified and neither changes with composition or environment. In the very dilute limit this model formally corresponds, of course, to specifying a host jump frequency ω_0 and an impurity jump frequency ω_2 with all other host jump frequencies equal to ω_0 . However, it should be appreciated for this model that physically, although not mathematically, the jump frequencies ω_A and ω_B are *conceived* to be “average” jump frequencies. The average jump frequency of the vacancy, ω_v , was postulated to be given by

$$\omega_v = c_A \omega_A + c_B \omega_B \quad (3-91)$$

where c_A and c_B are the atomic fractions of A and B. Manning (1968, 1970, 1971) finds that

$$f_A = \frac{S + (2 - 3x_0 + c_B) \omega_B / \omega_A + (c_A - x_0)}{2 \{S + (1 - x_0) \omega_B / \omega_A + x_0\}} \quad (3-92)$$

where

$$S = \{[(c_B - x_0) \omega_B / \omega_A + (c_A - x_0)]^2 + 4x_0(1 - x_0) \omega_B / \omega_A\}^{1/2} \quad (3-92a)$$

and

$$x_0 = 1 - f \quad (3-92b)$$

and f is the correlation factor for vacancy diffusion in the pure metal A or B.

Early Monte Carlo calculations indicated that Eq. (3-92) was a very good approximation over a wide range of ω_A/ω_B but more recently it has been found that this was largely illusory (Belova and Murch, 2000). Eq. (3-92) is actually only a reasonable approximation when the exchange frequency ratio is within about an order of magnitude of unity. A much better approximation to the problem is that given by Moleko et al. (1989), but unfortunately the equations are much more cumbersome to use.

A different approach to diffusion in concentrated systems has been taken by Kikuchi and Sato (1969, 1970, 1972). They developed their Path Probability Method (PPM) to cope specifically with the problems of diffusion in concentrated systems. The method can be considered to be a time-dependent statistical mechanical approach. They started with the so-called binary alloy analogue of the Ising antiferromagnet model. In this model, sometimes called the “bond” model, interactions E_{AA} , E_{BB} , and E_{AB} are introduced between nearest neighbor components of the type A-A, B-B, and A-B, respectively. Equilibrium properties of this model are well known; see for example, Sato (1970). It is convenient to focus on the ordering energy E defined by

$$E = E_{AA} + E_{BB} - 2E_{AB} \quad (3-93)$$

(note that in the literature there are other definitions of the ordering energy which differ from this one by either a negative sign or a factor of 2). When $E > 0$, there is an ordered region in the b.c.c. and s.c. lattices (the f.c.c. lattice is more complicated but has not been investigated by the PPM). The ordered region is symmetrically placed about $c_A = 0.5$. When $E < 0$, there is a two-phase region at lower temperatures (this side has not been investigated by the PPM). The exchange frequencies ω_A and ω_B are

not given explicitly as in the random alloy model but are expressed in the following way in terms of the interaction energies (bonds) for a given atom in a given configuration:

$$\begin{aligned} \omega_i &= \nu_i \exp(-U_i/kT) \\ &\times \exp[(g_i E_{ii} + g_j E_{jj})/kT], \quad (3-94) \\ i &= A, B \quad i \neq j \end{aligned}$$

where $E_{ij} < 0$, ν_i is the lattice vibration frequency, U_i is the reference saddle point energy in the absence of interactions, g_i is the number of atoms of the same type which are nearest neighbors of the given atom and g_j is the number of atoms of the *other* type which are nearest neighbors of the given atom. Other forms of ω_i are also possible but have not been developed in this context.

In the PPM a path probability function is formulated and maximized, a process which is said to be analogous to minimizing the free energy in equilibrium statistical mechanics. The first calculations were made using what was called a time-averaged conversion. The results were in poor agreement with later Monte Carlo computer simulation results. Subsequently, substantial improvements were made (Sato, 1984) and the PPM results are now in fairly good agreement with computer simulation results. A typical comparison of the earlier results with Monte Carlo results from Bakker et al. (1976) is shown in Fig. 3-12. Note the bend at the order/disorder transition. The lower values of the correlation factors on the ordered side can be ascribed generally to the higher probability of jump reversals as an atom which jumps from the “right” sublattice to the “wrong” sublattice tends to reverse the jump while the vacancy is still present. This cancellation of jumps obviously leads to small values of f .

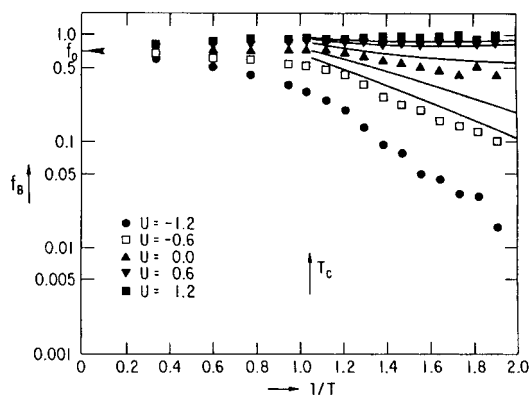


Figure 3-12. Arrhenius plot of the tracer correlation factor for B in the alloy $A_{0.6}B_{0.4}$ for various values of $U = (E_{AA} - E_{BB})/E$. Points from Bakker et al. (1976), lines from Kikuchi and Sato (1969, 1970, 1972); after Murch (1984a). The abscissa is in units of E/k .

Although there is no particular reason for assuming that the correlation factor should follow an Arrhenius behavior, e.g., Eq. (3-90), these results nonetheless show it quite well. The contribution to the total activation energy is difficult to determine directly because U_i is a “spectator quantity” in these calculations and the vacancy formation energy has not been calculated in the same work, although the latter can be determined separately in this model (Lim et al., 1990). In a recent application of this model to self-diffusion in β -CuZn (Belova and Murch, 1998), the contribution to the *total* activation energy for, say, Cu tracer diffusion was variously estimated at 22–40%. It is clear that for a complete analysis of diffusion in such materials the assessment of the contribution of the tracer correlation factor to the activation energy is essential.

We have mentioned that cancellation of jumps leads to small values of f . There are, however, special sequences of jumps in the ordered structure which lead to effective diffusion. The most important of these sequences is the so-called six-jump cycle

mechanism, which we shall now briefly discuss. This sequence is interspersed, of course, with jump reversals.

It became clear at an early stage that diffusion in fully ordered structures poses certain difficulties. A purely random walk of the vacancy will lead to large amounts of disorder and inevitably to a great increase in the lattice energy of the solid. Huntington (see Elcock and McCombie, 1958) seems to have been the first to suggest that net migration of atoms in, say, the B2 structure could occur by way of a specific sequence of six vacancy jumps with only a relatively slight increase in energy. This sequence is illustrated in Fig. 3-13a for the ordered square lattice (Bakker, 1984), and schematic energy changes for the sequence are shown in Fig. 3-13b. The starting and finishing configurations have the same energy but there has been a net migration of atoms.

The correlation factor for the six-jump cycle sequence alone has been calculated by Arita et al. (1989). The six-jump cycle sequence is contained in the earlier path probability method calculations and the Monte Carlo computer simulations (Bakker, 1984). The correlation factors calculated in those calculations are statistical averages over all possible sequences in addition to the jump reversals which tend to predominate.

Further detailed discussion of the correlation factors in concentrated alloy systems can be found in the detailed reviews by Bakker (1984), Mehrer (1998), Murch and Belova (1998).

3.3.1.6 Correlation Factors for Highly Defective Systems

Many solids, such as nonstoichiometric compounds, intercalation compounds, and fast ion conductors, appear to have a very high concentration of defects. Manning

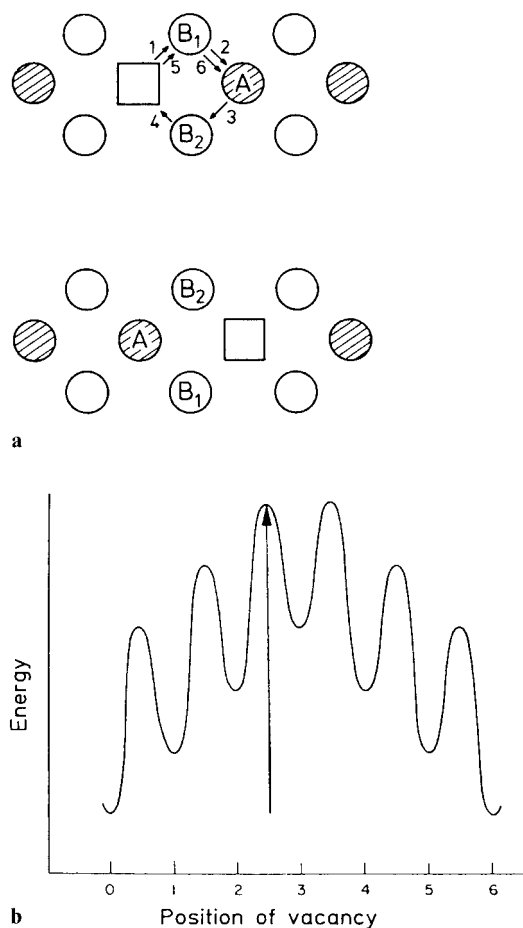


Figure 3-13. (a) Six-jump cycle in the ordered square lattice: the upper figure shows the path of the vacancy, the lower figure shows the displacements resulting from the complete cycle, after Bakker (1984). (b) Schematic representation of energy changes during the six-jump vacancy cycle, after Bakker (1984).

(1968) was probably the first to note that the correlation factor could increase if more vacancies are present. In effect, the extra vacancies *decorrelate* the reverse jump of a tracer atom; see the discussion in Sec. 3.3.1.3. As more vacancies are added we reach the limit of a single atom remaining (for convenience, the tracer) and the correlation factor is unity as befitting a complete random walk of an interstitial. Between the

extremes, provided the vacancies are randomly distributed, roughly linear behavior of the correlation factor is found (Fig. 3-9).

When the vacancies are *not* randomly distributed, which is usually the case because of atom–atom repulsion, the behavior of the correlation factor becomes more complicated. The calculations that have been performed are for the so-called lattice gas model. In this, the atoms occupy discrete sites of a rigid lattice, typically a nearest neighbor interaction being specified between the atoms. For nearest neighbor *attractive* interactions, at low temperatures a two-phase region develops symmetrically about the concentration 0.5. Conversely, with nearest neighbor repulsion an ordered region centered about a concentration 0.5 develops for the simple lattices such as honeycomb, square planar, or simple cubic. The face centered cubic and triangular lattices are rather more complicated, but have not been investigated. We shall focus on repulsion here because it is the most likely. In a manner similar to that for the concentrated alloy, the exchange frequency of a given atom with a vacancy is written for a given configuration as

$$\omega = \nu \exp(-U/kT) \exp(g_{nn} \phi_{nn}/kT) \quad (3-95)$$

where g_{nn} is the number of atoms which are nearest neighbors to the given atom, U is the activation energy for diffusion of an isolated atom, ν is the vibration frequency, and ϕ_{nn} is the atom–atom interaction energy. It can be seen that nearest-neighbor repulsion between atoms works to diminish the activation energy. Other forms of the exchange frequency are also possible, but most calculations have used this one.

Obviously lattice gas models cannot generally be very realistic in their diffusion behavior. The interest in them comes about primarily because they exhibit behavior which is rich in physics and likely to occur

to a greater or lesser extent in real materials. Surprisingly, some materials such as interstitial solid solutions are described fairly well by the lattice gas model even with only nearest neighbor interactions. This must be a result of short-range interactions being by far the most important.

Sato and Kikuchi (1971) have employed the PPM to good effect in the lattice gas model. Extensive calculations have been made, especially for the honeycomb lattice. Equally extensive Monte Carlo calculations have also been made both for this lattice and many others; see the review by Murch (1984a). A typical result is shown in Fig. 3-14. The pronounced minimum in the correlation factor is due to the effects of the ordered structure. This ordered structure consists of atoms and vacant sites arranged alternately. The wide composition variability of the ordered structure at this temperature (indicated by the arrows) is accommodated by vacant sites or "interstitials" as appropriate. When an atom jumps

from the right lattice to the wrong lattice it tends to reverse that jump, thereby giving low values of the correlation factor. As in the ordered alloy, there are sequences of jumps which lead to long-range diffusion. By and large these sequences are based around interstitialcy progressions, but rather than two atoms moving in unison as in the actual interstitialcy mechanism, here they are separated in time.

The temperature dependence of f in the lattice gas, like the alloy, is fairly strong. Again, it is usual to write f in an Arrhenius fashion, e.g., Eq. (3-90), but there is no known physical reason for assuming that f must really take this form. Fig. 3-15 shows the behavior in the square planar lattice gas. The Arrhenius plot is in fact curved above and below the order/disorder temperature, though in an experimental study this would be overlooked because of a much smaller temperature range. This activation energy will be included in the experimental tracer diffusion activation energy. This is likely to be a significant contribution which (like in the ordered alloy) cannot be ignored.

The subject of tracer correlation effects in defective materials with high defect con-

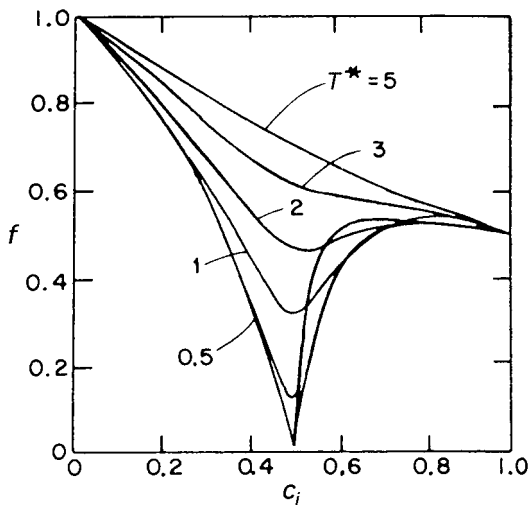


Figure 3-14. PPM results for the dependence of the tracer correlation factor on ion site fraction c_i in the honeycomb lattice with nearest neighbor repulsion. $T^* = kT/\phi_{nn}$; after Murch (1982d).

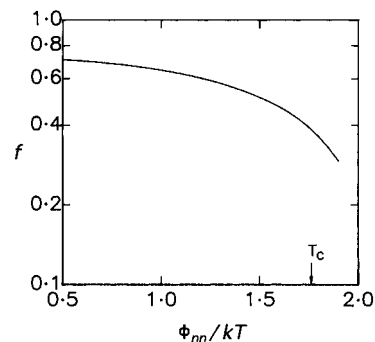


Figure 3-15. Arrhenius plot of the tracer correlation factor gained from Monte Carlo simulation of a square planar lattice gas with 50% particles and 50% vacant sites (Zhang and Murch, 1990).

tent is dealt with at length in a number of places; see, for example, Murch (1984a) and Sato (1989).

3.3.1.7 The Physical or Conductivity Correlation Factor

In Sec. 3.3.1.3 we have seen that tracer correlation effects are conventionally embodied in the so-called tracer correlation factor. In this way the correlation factor appears as a correction factor in the random walk expression for the tracer diffusion coefficient Eq. (3-76).

In 1971 Sato and Kikuchi showed that the *ionic conductivity* should also include a correlation factor, now called the physical or conductivity correlation factor and given the symbol f_I , sometimes f_c . In the usual hopping model expression for the d.c. conductivity $\sigma(0)$, we have

$$\sigma(0) = C(Ze)^2 \Gamma_q r_q^2 f_I / 6kT \quad (3-96)$$

where C is the concentration of charge carriers per unit volume, Z is the number of charges, e is the electronic charge, Γ_q is the jump frequency, r_q is the jump distance of the charge, k is the Boltzmann constant, and T is the absolute temperature.

It should be noted that f_I does not become nontrivial, i.e., $\neq 1$, until a relatively high defect concentration is present *and* ion-ion interactions and/or trapping sites are present. A model containing these was explored by Sato and Kikuchi (1971) in their pioneering work. Their results for f_I in the lattice gas model of nearest neighbor interacting atoms diffusing on a honeycomb lattice with inequivalent sites arranged alternately are shown in Fig. 3-16.

This work was the starting point for the development of the new area of correlation effects in ionic conductivity. This area has been reviewed by Murch and Dyre (1989).

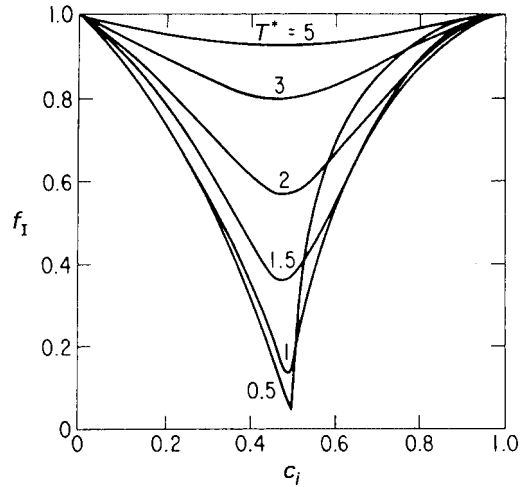


Figure 3-16. PPM results for the dependence of the physical correlation factor on ion site fraction c_i in the honeycomb lattice with nearest neighbor repulsion and site inequivalence. $T^* = kT/\phi_{nn}$ and the site difference *a priori* is $5\phi_{nn}$; after Murch (1982d).

Historically, the atomistic meaning of f_I has taken quite some time to determine, principally because the calculations (path probability and Monte Carlo methods) were based on the calculation of a flow of charge.

It is now known that the physical correlation factor can be expressed as

$$f_I = \lim_{n \rightarrow \infty} \langle \Delta \mathbf{R}^2 \rangle / nr^2 \quad (3-97)$$

where $\Delta \mathbf{R}$ is the total displacement of the system after a total of n jumps in time t . This differs from Eq. (3-77) *only* in the important points that $\Delta \mathbf{R}$ refers to the displacement of the entire system and *not* a single particle. $\Delta \mathbf{R}$ is simply the sum of the individual particle displacements \mathbf{R} occurring in time t :

$$\Delta \mathbf{R} = \sum_{\text{all particle}} \mathbf{R}_i \quad (3-98)$$

We can now see that whereas f encompasses correlation effects of a single (tracer)

particle, f_I encompasses correlation effects of the entire system in a collective sense. The correlation factor f_I of the system is manifested in the d.c. ionic conductivity, Eq. (3-96). It is also manifested in chemical diffusion (see below), but *not* in tracer diffusion.

What is sufficient to make $f_I \neq 1$? First, a relatively high concentration of defects is required (see Fig. 3-16). Next, inequality of lattice sites (and therefore a variable jump frequency), or mutual interactions among the ions, or differences in accessibilities of ions: all are sufficient, with a high concentration of defects, to give a nontrivial value for f_I .

The importance of f_I in materials with high defect concentrations cannot be overstated. For example, in a calculation of f_I in a model for CeO_2 doped with Y_2O_3 (to obtain a high concentration of anion vacancies), it was found that at 455 K f_I changed from unity at low Y^{3+} content to only 0.05 at high Y^{3+} content, corresponding to 14% of the anion sites being vacant (Murray et al., 1986). This very low value of f_I came about primarily because of the trapping effects of the Y^{3+} ions. The physical correlation factor is also temperature dependent, but there is no known physical reason why f_I should take an Arrhenius form. Fig. 3-17 shows a typical result for a lattice gas above and below the order/disorder transition. Both regions are slightly curved in fact, although this could be overlooked in an experiment over a small temperature range. The activation energy associated with f_I will be included in the overall activation energy for d.c. ionic conduction. This contribution cannot be ignored. In the model for CeO_2 doped with Y_2O_3 , the contribution is of the order of 30% very high Y^{3+} contents.

Most of the contributions to the application of f_I have centered around ionic con-

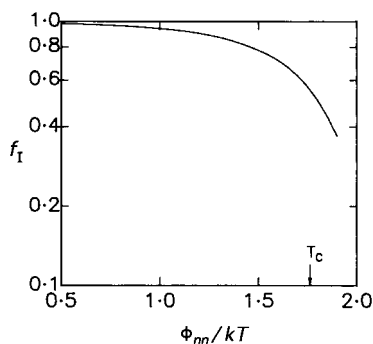


Figure 3-17. Arrhenius plot of the physical correlation factor gained from Monte Carlo simulation of a square planar lattice gas with 50% particles and 50% vacant sites (Zhang and Murch, 1990).

duction. However, f_I also occurs in the expression for the chemical diffusion coefficient in the one-component system, i.e.,

$$\tilde{D} = \Gamma r^2 f_I (1 + \partial \ln \gamma / \partial \ln c) / 6 \quad (3-99)$$

or, with Eq. (3-76)

$$= \frac{D^*}{f} f_I \left(1 + \frac{\partial \ln \gamma}{\partial \ln c} \right)$$

where γ is the activity coefficient of the particles with the term in parentheses becoming the “thermodynamic factor”. This equation applies to interstitial solid solutions and intercalation compounds such as TiS_2 intercalated with Li where the atomic mobility on the defective lattice is rate determining. It does *not* apply to ionic conductors, however, since – for charge balance reasons – *compositional* changes are controlled by atomic mobility or hole-electron hopping on another lattice. For example, in the oxygen ion conductor calcia stabilized zirconia, compositional changes of the oxygen ion vacancy concentration are probably controlled by the dopant calcium ion mobility on the cation lattice.

3.3.1.8 Correlation Functions (Collective Correlation Factors)

There are a number of other correlation phenomena in diffusion. In order to discuss these in a unified fashion, say for a binary system, it is convenient first to introduce correlation functions or collective correlation factors. They represent the correlated parts of the phenomenological coefficients (see Sec. 3.4). For the diagonal coefficients we write (Allnatt and Allnatt, 1984)

$$L_{ii} = L_{ii}^0 f_{ii} \quad i = A, B \quad (3-100)$$

where L_{ii}^0 is the uncorrelated part of L_{ii} , i.e.,

$$L_{ii}^{(0)} = C_i \Gamma_i r^2 / 6kT \quad i = A, B \quad (3-101)$$

where C_i is the number of species i per unit volume, Γ_i is the jump frequency of species i , and r is the jump distance, k is the Boltzmann constant, and T is the absolute temperature. For the off-diagonal terms (we note the Onsager condition $L_{AB} = L_{BA}$), we write

$$L_{AB} = L_{AA}^{(0)} f_{AB}^{(A)} = L_{BB}^{(0)} f_{AB}^{(B)} \quad (3-102)$$

This partitioning of the L_{ij} into these parts might appear arbitrary. The choice comes about largely by analogy with the tracer diffusion coefficient which is partitioned as a product of an uncorrelated part, containing the jump frequency etc., and a correlated part, containing the tracer correlation factor (see Eq. (3-76) and associated discussion).

Some physical understanding of the f_{ij} is appropriate here. There are two equivalent expressions for the f_{ij} . First, Allnatt (1982) and Allnatt and Allnatt (1984) showed that the f_{ij} have Einsteinian forms reminiscent of the expression for the tracer correlation factor (see Eq. (3-76)). Thus they write for a binary system A, B

$$f_{AA} = \langle \Delta \mathbf{R}_A^2 \rangle / n_A r^2 \quad (3-103)$$

where $\Delta \mathbf{R}_A$ is the displacement of the system of particles of type A, i.e., $\Delta \mathbf{R}_A$ is the vector sum of the displacements of all the atoms of type A and n_A is the total number of jumps of the species A. Thus the group of particles of type A in the system is treated *itself* like a (hypothetical) particle, and f_{AA} is its correlation factor.

Similarly,

$$f_{AB}^{(i)} = \langle \Delta \mathbf{R}_A \cdot \Delta \mathbf{R}_B \rangle / n_A r^2 \quad i = A, B \quad (3-104)$$

Thus $f_{AB}^{(i)}$ expresses correlations between the vector sum of the displacements of all the atoms of type A with the corresponding quantity for atoms of type B.

An alternative way of looking at the f_{ij} is in terms of the drifts in a driving force. Let us consider a "thought experiment" for a binary system AB where an external driving force F_d is directly felt *only* by the A atoms. It is straightforward to show (Murch, 1982a) that f_{AA} is given by

$$f_{AA} = \frac{2kT \langle X_A \rangle}{F_d n_A r^2} \quad (3-105)$$

where $\langle X_A \rangle$ is the average drift distance of the A atoms in the driving force and n_A is the number of jumps of a given A atom in time t . However, although only the A atoms feel the force directly, the B atoms feel it *indirectly* because they are competing for the same vacancies as the A atoms. Accordingly, there is also a drift of the B atoms, smaller than the drift of the A atoms. The correlation function $f_{AB}^{(i)}$ is related to this drift by

$$f_{AB}^{(i)} = \frac{2kT \langle X_B \rangle}{F_d \Gamma_i t r^2} \quad (3-106)$$

where $\langle X_B \rangle$ is the average drift distance of the B atoms.

Calculation of the Correlation Functions

Calculations have been made for various impurity models, the random alloy model and interacting or (bond) models for alloys. For impurity systems, the area has been reviewed exhaustively by Allnatt and Lidiard (1987, 1993). Here we shall restrict ourselves to a discussion of the results for the five-frequency impurity model in the f.c.c. lattice; see Fig. 3-11 and associated text for details of the model.

Inspection of Eq. (3-103) indicates that when the A atoms (say) are the infinitely dilute impurities in B, i.e., $c_A \rightarrow 0$, the system of atoms of type A reduces to a single A atom. Accordingly the diagonal correlation function f_{AA} reduces to the impurity correlation factor, f_A . We have already given Manning's (1964) expression for f_A for the five-frequency model in the f.c.c. lattice (see Eq. (3-78)). Manning (1968) showed that the cross correlation function $f_{AB}^{(A)}$ can be calculated by a careful analysis of the various impurity jump trajectories in a field. He found that $f_{AB}^{(A)}$ is given by

$$f_{AB}^{(A)} = 2 f_A \quad (3-107)$$

$$\times \frac{\omega_3 [3 - 7(1 - F)(\omega_4 - \omega_0)\omega_4^{-1}] - 2\omega_1}{2\omega_1 + 7F\omega_3}$$

where F is the fraction of dissociating vacancies that are permanently lost from a site and are uncompensated for by returning vacancies and is given by Eq. (3-80).

Let us move on to the binary random alloy model described in detail in Sec. 3.3.1.5; explicit expressions have been derived by Manning (1968). He found that f_{AA} is given by

$$f_{AA} = f_A \left[1 + 2c_A \omega_A f_A \left(M_0 \sum_{k=A,B} c_k \omega_k f_k \right) \right] \quad (3-108)$$

and

$$f_{AB}^{(A)} = 2c_A c_B \omega_A \omega_B f_A f_B \quad (3-109)$$

$$\times \left(c_A \omega_A M_0 \sum_{k=A,B} c_k \omega_k f_k \right)^{-1}$$

where $M_0 = 2f(1-f)$ and f is the tracer correlation factor in the pure lattice of either component.

The correlation functions have also been calculated in interacting bond models (see Sec. 3.3.1.5), especially with the PPM and by computer simulation. Some results of the latter are shown in Figs. 3-18 and 3-19 for the simple cubic lattice with ordering between A and B.

A brief discussion of the behavior of these quantities is appropriate here. First, with respect to f_{AA} , as $c_A \rightarrow 0$, the A atoms behave like impurities in the B matrix, and f_{AA} does in fact reduce to the impurity correlation factor f_A . At $c_A \approx 0.5$, the minima are further manifestations of the preponderance of jump reversals in the diffusion process in the ordered alloy. As $c_A \rightarrow 1$, all curves converge on unity and the correla-

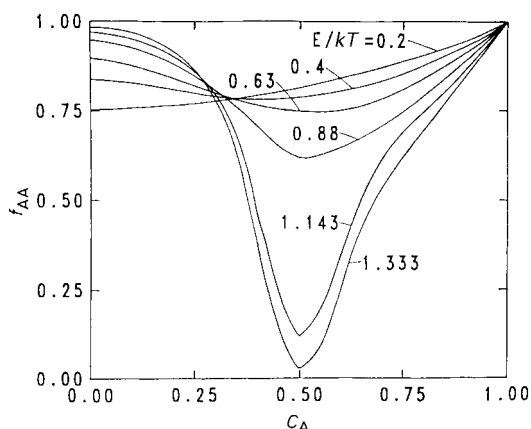


Figure 3-18. Monte Carlo results for the diagonal correlation factor f_{AA} in the simple cubic alloy as a function of c_A at various values of the ordering energy; after Zhang et al. (1989a).

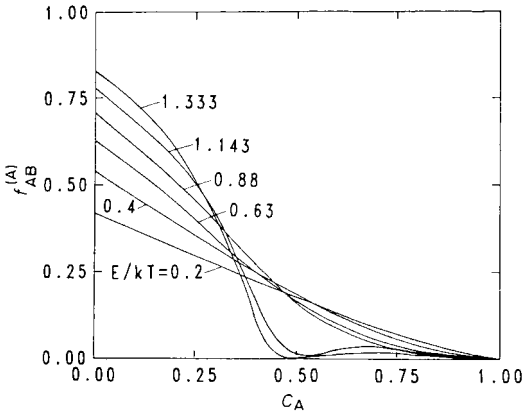


Figure 3-19. Monte Carlo results for the off-diagonal correlation factor $f_{AB}^{(A)}$ in the simple cubic alloy as a function of c_A at various values of the ordering energy; after Zhang et al. (1989a).

tion effects contained in f_{AA} disappear entirely. Next, let us discuss $f_{AB}^{(A)}$. As $c_A \rightarrow 0$, again A behaves like an impurity in B. The physical meaning of $f_{AB}^{(A)}$ has been discussed earlier, see Eq. (3-106). At this limit the B atoms have maximum interference on A. Similar to f_{AA} , minima develop at $c_A \approx 0.5$ as a result of jump cancellations. As $c_A \rightarrow 1$, all curves converge on zero as the B atoms, now in the minority, no longer have much effect on the diffusion of A.

With the correlation functions in hand, we can form the various correlation terms that commonly occur in ionic conductivity and chemical diffusion. We shall restrict ourselves to binary systems. Unary systems are dealt with in Sec. 3.3.1.7, where it is seen that the physical correlation factor is really a correlation function for a one-component system.

Correlations in Ionic Conductivity (Binary Systems)

When ionic conductivity occurs in a material where two or more ionic species sharing the same sublattice (and therefore competing for the same defects) carry the

current there are correlations or interference between the two ionic conductivities. When there are two ionic species and the vacancy mechanism is operating, the expressions for the d.c. ionic conductivities are (Murch and Dyre, 1989)

$$\sigma_A = \frac{e^2 Z_A^2 C_A \Gamma_A r^2}{6kT} \left(f_{AA} + \frac{Z_B}{Z_A} f_{AB}^{(A)} \right) \quad (3-110)$$

and

$$\sigma_B = \frac{e^2 Z_B^2 C_B \Gamma_B r^2}{6kT} \left(f_{BB} + \frac{Z_A}{Z_B} f_{AB}^{(B)} \right) \quad (3-111)$$

where e is the electronic charge, $Z_{A(B)}$ is the number of charges on A(B), $C_{A(B)}$ is the concentration of A(B), $\Gamma_{A(B)}$ is the jump frequency of A(B) and r is the jump distance.

Sometimes the bracketed terms are called the binary conductivity correlation factors; they are, in fact, formally binary analogues of f_I in Eq. (3-96). Eqs. (3-110) and (3-111) become

$$\sigma_A = e^2 Z_A^2 C_A \Gamma_A r^2 f_{IA} / 6kT \quad (3-112)$$

$$\sigma_B = e^2 Z_B^2 C_B \Gamma_B r^2 f_{IB} / 6kT \quad (3-113)$$

For those readers familiar with Manning's (1968) treatment of impurity ionic conductivity, f_{IA} (where A is the impurity in B) is expressed as

$$f_{IA} = f_A \left(1 + \frac{Z_B}{Z_A} \langle n_p \rangle \right) \quad (3-114)$$

where f_A is the impurity correlation factor and $\langle n_p \rangle$ is a complex kinetic parameter introduced by Manning. Eq. (3-114) as envisaged by Manning (1968) applies only to situations where the vacancy concentration is very low. Often the term in parentheses in Eq. (3-114) is loosely called a vacancy-wind factor, although this terminology is frequently applied to the whole of f_{IA} . In the special case where the impurity is a

tracer of the host and where, of course, $Z_A = Z_B$, the term in parentheses reduces to f_A^{-1} with the result that $f_{IA} = 1$ and there are no correlations in the ionic conductivity. However, it is emphasized that this result applies *only* where the defect concentration is very low. For high concentrations of defects which in general cannot be randomly distributed there are still residual correlations arising from non-ideal effects. These are encompassed in f_I (see Eq. (3-96)).

For the five-frequency model, see Sec. 3.3.1.4, for certain combinations of the jump frequencies it is possible to make f_{IA} (Eq. (3-114)) negative. Specifically this can occur when the vacancy and impurity are tightly bound together, i.e., when $\omega_4 > \omega_3$. Vacancies that are bound to impurities can be transported around the impurity by the host atom flux. The probability of the impurity moving upfield can then be larger than the probability of moving downfield. The impurity may then actually move upfield, opposite to its “expected” direction. For further details, see Manning (1975). It is also possible in the five-frequency model to make f_{IA} for the impurity exceed unity, even when $Z_B = Z_A$.

For concentrated interacting systems, the calculation of the f_{IA} (and f_{IB}) is of some interest, especially in the case of mixed fast ion conductors such as Na,K β -alumina. An example of the results of calculation of f_{IA} and f_{IB} , by way of the PPM, is shown in Fig. 3-20. This lattice gas model contains two species A and B ($Z_A = Z_B$) with 20% vacancies on a honeycomb lattice. The model approximates the fast ion conductor Na,K β -alumina, although it is probably also a reasonable description of some silicate glasses. Note the minima in f_{IA} and f_{IB} . These are caused by what is called a “percolation difficulty” in the flow created by ordered arrangements. Physically, many jumps are reversed. This effect seems

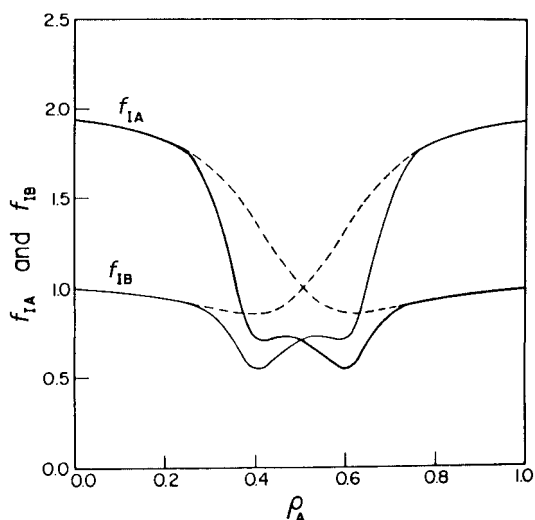


Figure 3-20. PPM results for the quantities f_{IA} and f_{IB} as a function of concentration ρ_A in the two-component conductor with 20% vacancies at half the order-disorder temperature. The dashed line shows the case where the development of long-range order is artificially suppressed; after Murch and Dyre (1989).

stronger as the dimensionality is lowered (in fact all correlation effects do), and may be a major contributor to the so-called mixed-alkali effect. This effect is characterized by a substantial decrease in the d.c. ionic conductivity at intermediate mixed compositions without any obvious physical cause. This subject is dealt with further by Murch and Dyre (1989) and Sato (1989).

Correlations in Chemical Diffusion (Binary Systems)

The usual equation of practical interest for chemical diffusion in a binary system is the Darken equation. This equation relates the intrinsic diffusion coefficient of a particular component to its tracer diffusion coefficient. The original Darken equation (which neglects correlations) is written as

$$D_A^I = D_{A^*} \left(1 + \frac{\partial \ln \gamma_A}{\partial \ln c_A} \right) \quad (3-115)$$

where γ_A is the activity coefficient of A. However, it is straightforward to show that the rigorous equation is Eq. (3-56) which can be rewritten in terms of the correlation functions (Le Claire, 1975; Murch, 1982a; Stark, 1976):

$$D_A^I = D_{A^*} \left(1 + \frac{\partial \ln \gamma_A}{\partial \ln c_A} \right) \times \left[\left(f_{AA} - f_{AB}^{(A)} \frac{c_A}{c_B} \right) / f_A \right] \quad (3-116)$$

The f_A in the denominator is the correlation factor for the actual composition of the alloy and not some impurity limit. In the literature the term derived from correlations [] is sometimes called a vacancy-wind factor and is given the symbol r_A . As it turns out, however, this term cannot vary much from unity since the original Darken equation is reasonably well obeyed. The behavior of r_A is not especially transparent. The vacancy flux in chemical diffusion is always in the same direction as that of the slower moving species (and opposite to that of the faster moving species). The vacancy-wind effect always tends to provide a given atom with an enhanced probability of flowing in a direction opposite to that of the vacancy flow. When A is less mobile than B, the vacancy-wind factor r_A effectively makes D_A^I even smaller. Conversely, when A is more mobile than B, the vacancy-wind factor r_A effectively makes D_A^I even larger. But how much? This can be partially answered in the following.

Although we have given Manning's (1968) expressions for the individual f_{ij} and the correlation factor f_A for the random alloy (Eqs. (3-108) and (3-109)), it may not be immediately obvious that r_A is in fact given in this model by (see also Sec. 3.2.3.4)

$$r_A = \frac{f D_{B^*} + c_A (D_{A^*} - D_{B^*})}{f (c_A D_{A^*} + c_B D_{B^*})} \quad (3-117)$$

where f is the tracer correlation factor for diffusion in the *pure* crystal, i.e., pure A or pure B. It turns out that the maximum in r_A in this model occurs when $c_A \rightarrow 1$. In the extreme case when the jump frequency of A is much larger than that of B, then $r_A \rightarrow f_0^{-1}$. Therefore, when $f_0 = 0.78146$ (vacancy diffusion on the f.c.c. lattice, see Table 3-1), r_A can only enhance chemical diffusion by a factor of 1.28.

Manning's equation (Eq. (3-117)) seems to have more general significance than application to the random alloy. Murch (1982a) showed that this equation performs very well indeed for an interacting alloy model that can exhibit short and long-range order. This suggests that this equation can be used almost with impunity. This subject arises again in the "Manning relations" which relate the phenomenological coefficients to the tracer diffusion coefficients (see Sec. 3.2.3.4).

The subject of the experimental check of r_A has been discussed by Bocquet et al. (1996). They pointed out that in most cases the Manning formulation for r_A and r_B (Eq. (3-117)) improves the agreement between experimental and calculated values of the Kirkendall shift and the ratio of the intrinsic diffusion coefficients D_A^I/D_B^I . However, the individual experimental values of D_A^I and D_B^I often tend to be quite a bit higher than the calculated values. The experimental Kirkendall shift also has a tendency to be higher than the calculated value. Carlson (1978) points out that the problem could be due to the random alloy assumption in the Manning formulation. However, the success of the Manning formulation for the interacting alloy model mentioned above seems to vindicate the random alloy assumption and so the reason for the discrepancy probably should be sought elsewhere.

3.3.2 The Nernst–Einstein Equation and the Haven Ratio

The Nernst–Einstein equation relates the d.c. ionic conductivity to a diffusion coefficient. Probably no other equation in diffusion has generated more misunderstanding than this one. Let us consider the standard derivation (see, for example, Batchelor (1976)), and discuss its implications in detail.

We consider a pseudo-one-component system in a situation where the flux resulting from an applied force on the particles (which are completely noninteracting) exactly counterbalances the flux due to diffusion. That is, from Eq. (3-2)

$$\langle v \rangle C = \tilde{D} \frac{dC}{dx} \quad (3-118)$$

It is important to note that the diffusion coefficient here refers to a chemical composition gradient and is most definitely conceived as a chemical diffusion coefficient, *not* a tracer or self-diffusion coefficient. Lack of appreciation of this fact leads to misunderstandings and inconsistencies.

The external force F_d is a result of a potential so that

$$F_d = - \frac{d\phi}{dx} \quad (3-119)$$

At equilibrium the distribution of *completely noninteracting* particles follows a Boltzmann distribution such that

$$C(x) = C_0 \exp[-\phi(x)/kT] \quad (3-120)$$

Eq. (3-120) must be the solution of Eq. (3-120) at steady state. We then have that

$$\frac{dC}{dx} = - \frac{C}{kT} \frac{d\phi}{dC} = \frac{CF_d}{kT} \quad (3-121)$$

With Eq. (3-118) we find that

$$\frac{\langle v \rangle}{\tilde{D}} = \frac{F_d}{kT} \quad (3-122)$$

When the external force is the result of an electric field E we have

$$F_d = ZeE \quad (3-123)$$

where Z is the number of charges (ionic valence) and e is the electronic charge.

The mobility u is defined as the velocity per unit field and so we have

$$\frac{u}{\tilde{D}} = \frac{Ze}{kT} \quad (3-124)$$

In the solid-state diffusion literature Eq. (3-124) is generally called the Nernst–Einstein relation. Because the d.c. ionic conductivity is related to the mobility by $\sigma = CZeu$, Eq. (3-124) can be rewritten as

$$\frac{\sigma}{\tilde{D}} = \frac{CZ^2e^2}{kT} \quad (3-125)$$

More generally, interactions are present between the particles and it can be shown that the *general* form of the Nernst–Einstein equation is in fact (Murch, 1982b)

$$\frac{\sigma}{\tilde{D}} = \frac{CZ^2e^2}{kT} \left(\frac{\partial \ln c}{\partial \mu} \right) \quad (3-126)$$

where μ is the chemical potential of the particles and c is the site fraction.

Now let us discuss this equation in detail by exploring some particular cases. When the distribution of particles is completely ideal, meaning that the particles do not feel one another, not even site blocking, the thermodynamic factor drops out of Eq. (3-126) and σ/\tilde{D} reduces to Eq. (3-125). In this very special case, and only in this case, the tracer diffusion coefficient D^* equals \tilde{D} , so that

$$\frac{\sigma}{D^*} = \frac{CZ^2e^2}{kT} \quad (3-127)$$

When the particles are ideally distributed but subject to the condition that no more than one particle can occupy one site, then

the thermodynamic factor in Eq. (3-126) equals $(1-c)^{-1}$. However, for this situation the tracer diffusion coefficient is related to \tilde{D} by (see, for example, Murch (1982c))

$$D^* = \tilde{D}(1-c)f \quad (3-128)$$

where f is the tracer correlation factor, so that

$$\frac{\sigma}{D^*} = \frac{CZ^2e^2}{kTf} \quad (3-129)$$

Ionic solids having virtually a perfect lattice of particles (charge carriers) fall into this category and Eq. (3-129) is appropriate to such solids. Similarly, when the particles are extremely dilute, Eq. (3-129) is again appropriate.

In the solid-state diffusion literature we very often see Eq. (3-125) used directly to calculate another diffusion coefficient, sometimes called the “charge” diffusion coefficient and given the symbol D_σ . Thus we encounter the following equation, which is also called the Nernst–Einstein equation

$$\frac{\sigma}{D_\sigma} = \frac{CZ^2e^2}{kT} \quad (3-130)$$

D_σ is dimensionally correct but it does *not* correspond to any diffusion coefficient that can actually be measured by way of Fick’s laws for a solid system. Recall that the identical Eq. (3-125) requires that the particles are completely noninteracting for it to be meaningful. We frequently then see the following equation relating D^* and D_σ

$$D^* = fD_\sigma \quad (3-131)$$

with D_σ often being called a self-diffusion coefficient or the diffusion coefficient of the (random walking) charge carriers. Eq. (3-131) is generally given as if it is self-evident or similar to Eq. (3-73). Eqs. (3-130) and (3-131) are then combined to give

$$\frac{\sigma}{D^*} = \frac{CZ^2e^2}{kTf} \quad (3-132)$$

i.e., formally the same as Eq. (3-129). This route to Eq. (3-132) is clearly a case of two wrongs ending up making a right. However, the real danger lies in the fact that Eq. (3-132) obtained in this way blinds us to its limitations, limitations which are clearly stated in the derivation of Eq. (3-129).

In practice, Eq. (3-132) has often been used to describe situations where the particles are interacting and many sites are vacant, such as in fast ion conductors. In such cases, we cannot necessarily expect a meaningful interpretation. What is the correct way to proceed? We already have the Nernst–Einstein equation to cover the situation of interacting particles (Eq. (3-126)). However, this normally cannot be applied to real materials because local charge neutrality prevents composition gradients being set up in ionic conductors *by the conducting ions themselves*. What can be done is to return once again to Eq. (3-130) and use it purely as a *definition* of D_σ , recognizing at the same time that D_σ has no Fickian meaning. Eq. (3-129) is then being used purely as a means of changing σ to a quantity which has the dimensions of a diffusion coefficient. It is clear that it would be inappropriate *in these circumstances* to call this equation the Nernst–Einstein equation.

We can now define the Haven ratio, which is simply the ratio of D^* to D_σ :

$$H_R \equiv \frac{D^*}{D_\sigma} \quad (3-133)$$

In view of what has been said above about D_σ , it is appropriate to ask whether H_R has any physical meaning. This can be partially answered by examining hopping models for conduction. It can be shown quite generally for hopping models using the vacancy mechanism that

$$H_R = \frac{f}{f_1} = \frac{f}{f + cg} \quad (3-134)$$

where f_I is the physical or conductivity correlation factor and g is a two-particle correlation factor (see Sec. 3.3.1.7). For specific models of interacting particles $f_I \leq 1$ (see Murch and Dyre (1989) for a detailed review). At the limits of an almost full or empty lattice of charge carriers, $f_I \rightarrow 1$ and $H_R = f$. This is compatible, of course, with Eq. (3-131) for these conditions.

Accordingly, a measurement of the Haven ratio (obtained by measuring σ and D^* , preferably in the same sample) can in some cases give f alone and therefore the mechanism of diffusion can be exposed. However, the interstitialcy mechanism adds a minor complication because the "charge" moves two jump distances whereas the tracer moves only one (see Fig. 3-6). This is easily taken care of in the analysis so that H_R is now written generally as (see for example, Murch (1982d))

$$H_R = \frac{f}{f_I} \left(\frac{r}{r_q} \right)^2 \quad (3-135)$$

where r and r_q are the distances moved by the tracer and charge respectively. Provided we focus on cases where $f_I = 1$ (either almost empty or full lattice of charge carriers), then H_R still has a unique value for each mechanism. The classic example of the value of H_R in identifying the mechanism is Ag motion in AgBr (Friauf, 1957). It was found that H_R varied from 0.5 at low temperature to 0.65 at high temperature. Frenkel defects (see Sec. 3.4.4) are expected and therefore a temperature dependence of H_R . But H_R is not consistent with a combination of vacancy and direct interstitial jumps. This would require that H_R varies from 0.78 to unity. The lower values of H_R obtained require a contribution from interstitialcy jumps. It was found that both collinear and noncollinear interstitialcy jumps were required to fit the behavior of H_R .

Much less satisfactorily interpreted are fast ion conductors where the defect concentration is high and f_I must be included in the analysis of H_R . A review of H_R for such materials has been provided by Murch (1982d). Further comments on the subject can be found in the review on correlation effects in ionic conductivity by Murch and Dyre (1989). An introduction to the subject may be found in the book by Philibert (1991).

3.3.3 The Isotope Effect in Diffusion

The isotope effect, sometimes called the mass effect, is of considerable importance in diffusion because it provides one of the two experimental means of gaining access to the tracer correlation factor, f (the other is the Haven ratio; see Sec. 3.3.2). Since f depends on mechanism (see Sec. 3.3.1.3), a measurement of the isotope effect can, in principle, throw light on the diffusion mechanism operating.

The measurement of the isotope effect depends on accurately measuring a small difference between the diffusion coefficients of two tracers α and β (Peterson, 1975). This small difference can be related to f in the following way. For isotropic tracer and impurity diffusion, the diffusion coefficients of α and β can be written as

$$D_\alpha = A \omega_\alpha f_\alpha \quad (3-136)$$

$$D_\beta = A \omega_\beta f_\beta \quad (3-137)$$

where A contains geometrical terms and defect concentrations which do not depend on the atom/defect exchange frequency ω .

The correlation factors f_α and f_β have the mathematical form of *impurity* correlation factors because the tracers (i.e. isotopes) in real experiments are formally impurities in the sense that their jump frequencies differ from the host atoms. Most impurity correlation factors for impurity diffusion in oth-

erwise pure and nearly perfect crystals have the mathematical form

$$f_\alpha = u/(\omega_\alpha + u) \quad (3-138)$$

$$f_\beta = u/(\omega_\beta + u) \quad (3-139)$$

where u contains exchange frequencies other than the tracer. After taking the ratio of Eqs. (3-136) and (3-137) and eliminating u and f_β (say) from Eqs. (3-136), (3-138), and (3-139), we find that

$$(D_\alpha - D_\beta)/D_\beta = f[(\omega_\alpha - \omega_\beta)/\omega_\beta] \quad (3-140)$$

At this point, the formal distinction between f_α , f_β and the tracer correlation factor f , the latter referring to a hypothetical tracer with the same jump frequency as the host, can be dropped since they are very similar in numerical value. Knowledge of the experimental jump frequencies, ω_α and ω_β , is usually not available, of course. Accordingly, they are expressed in terms of quantities which are known, such as the masses of the tracers.

Application of classical statistical mechanics to describe the dynamics of the jumping process leads to the result

$$(\omega_\alpha - \omega_\beta)/\omega_\beta = \Delta K \left[\left(\frac{m_\beta}{m_\alpha} \right)^{1/2} - 1 \right] \quad (3-141)$$

where m_α and m_β are the masses of the tracers α and β , ΔK is the fraction of the total kinetic energy, associated with the whole motion in the jump direction at the saddle point of a jump, that actually belongs to the diffusing atom. The conversion of jump frequencies to masses has unfortunately led to the introduction of this new quantity ΔK , about which detailed information is difficult to obtain. If the remainder of the lattice is not involved in the jump, $\Delta K=1$ (this is the upper limit for ΔK). More usually, there is a certain amount of coupling between the diffusing atom and the remainder of the lattice and $\Delta K < 1$.

From Eqs. (3-140) and (3-141), we find that

$$f \Delta K = \frac{(D_\alpha - D_\beta)/D_\beta}{(m_\beta/m_\alpha)^{1/2} - 1} \quad (3-142)$$

Eq. (3-142) refers to a process where only one atom jumps. The more general case of n atoms jumping simultaneously, e.g., the interstitialcy mechanism (where $n=2$) (see Fig. 3-6), is described by

$$f \Delta K = \frac{[(D_\alpha - D_\beta)/D_\beta]}{[(m_\beta + (n-1)m_0)/(m_\alpha + (n-1)m_0)]^{1/2} - 1} \quad (3-143)$$

where m_0 is the average mass of the non-tracers. It is common to refer to $f \Delta K$ in Eqs. (3-142), (3-143) as the "isotope effect" $E(n)$. Because f and ΔK are ≤ 1 then this also applies to $E(n)$. Accordingly, although a measurement of the isotope effect may not uniquely determine the mechanism, it can be invaluable in showing which mechanisms (through their values of f and n) are not consistent.

There are some mechanisms for which the appropriate correlation factor does not have the simple form of Eq. (3-136), for example a mechanism which has several jump frequencies. Nonetheless, it is always possible to derive equations equivalent to Eqs. (3-142), (3-143) for such cases (see the review by Le Claire (1970) for details).

In the discussion above, there has perhaps been the implication that the theory described here applies only to tracer diffusion in "simple" materials, e.g., pure metals, and alkali metal halides. Certainly the theory was originally developed with these cases in mind, but it can be used, *with caution*, in other more complex situations. One of the earliest of these was application to impurity diffusion. In this case the tracers α and β now refer to isotopes of an impurity which is chemically different from the host. When the mechanism is not in any

doubt, and frequently it is not to the experienced researcher in the field, a measurement of the isotope effect for self-diffusion yields ΔK . If the impurity is substitutional, and provided that ΔK is assumed to be the same as for self-diffusion, then an isotope measurement for the impurity can give the correlation factor for impurity diffusion. Since the impurity correlation factor is a function of local jump frequencies, e.g., the five-frequency model in the f.c.c. lattice (see Fig. 3-11), then a knowledge of f combined with other knowledge of the same jump frequencies can lead to a knowledge of some of their ratios (see, for example, Rothman and Peterson (1967), Bocquet (1972), and Chen and Peterson (1972, 1973)).

The “impurity form” of the tracer correlation factor is also implied for Manning’s theory for vacancy diffusion in the random alloy model (see Sec. 3.3.1.5). Therefore, isotope effect measurements in concentrated alloys which are reasonably well described thermodynamically by the random alloy model can be interpreted along traditional lines. Similarly, it has been shown by Monte Carlo computer simulation that the impurity form of f is also valid for vacancy diffusion in a lattice containing a high concentration of randomly distributed vacancies, up to 50% in fact (Murch, 1984b).

When order is increased among the components, the impurity form for f even for vacancy diffusion is increasingly not followed. For example, in the stoichiometric binary alloy AB with order, the correlation factor, forced to follow the impurity form, diverges from the actual f below the order/disorder temperature (Zhang et al., 1989b) (see Fig. 3-21). A very similar situation arises for the case of ordered atoms diffusing by the vacancy mechanism on a highly defective lattice such as is often en-

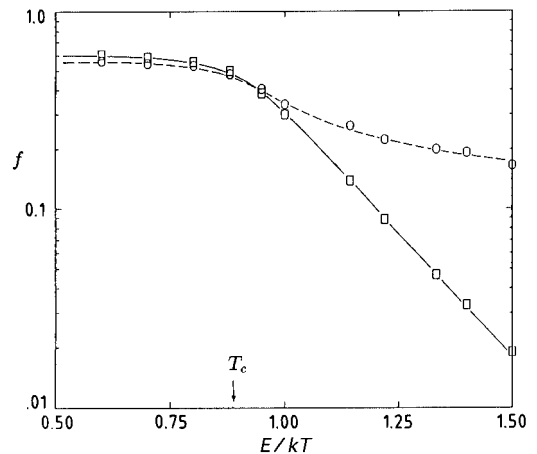


Figure 3-21. Arrhenius plot of Monte Carlo results for the tracer correlation factor in the simple cubic lattice. \square represents the actual tracer correlation factor; \circ represents the tracer correlation factor forced to follow the impurity form; after Zhang et al. (1989b).

countered at low temperature in fast ion conductors (Zhang and Murch, 1997). The implication of these and other findings is that the isotope effect measured in ordered materials does not contain the usual tracer correlation factor but some other correlation factor defined *only* by way of the impurity form, Eq. (3-136). This does not mean that isotope effect measurements in ordered materials are intrinsically without meaning, but simply that they cannot be easily interpreted.

The actual measurement of the isotope effect in diffusion requires the very accurate measurement of $(D_\alpha - D_\beta)/D_\beta$. This quantity typically lies between 0.0 and 0.05. Because of the inaccuracies in measurements of D it is not feasible to measure D_α and D_β in separate experiments. Normally the isotopes α and β are co-deposited in a very thin layer and permitted to diffuse simultaneously into a thick sample. The geometry of the experiment permits Eq. (3-8) to be used for each isotope.

With a little manipulation it is soon found that

$$\ln \left(\frac{C_\alpha}{C_\beta} \right) = \text{const.} - \ln C_\alpha [(D_\alpha - D_\beta)/D_\beta] \quad (3-144)$$

This means that by plotting $\ln(C_\alpha/C_\beta)$ vs. $\ln C_\alpha, (D_\alpha - D_\beta)/D_\beta$ can in fact be obtained very accurately, avoiding errors due to time and temperature of the diffusion anneal and errors in sectioning. The separation of the isotopes is normally achieved by half-life, energy spectroscopy, or the use of different kinds of radiation. Details of how to carry out careful experiments in this area can be found in the very comprehensive review of experimental techniques in diffusion by Rothman (1984). A more detailed review of the isotope effect in diffusion has been provided by Peterson (1975); see also Le Claire (1970).

3.3.4 The Jump Frequency

In Sec. 3.3.1.2 we showed that a tracer diffusion coefficient is, in essence, a product of an uncorrelated part containing the jump frequency and a correlated part containing the correlation factor, see Eq. (3-76). The Arrhenius temperature dependence of the diffusion coefficient arises largely from the jump frequency, although some temperature dependence of the correlation factor in some situations, e.g., alloys, cannot be ignored (see Secs. 3.3.1.4 to 3.3.1.6). In this section we will study the make-up of the atomic jump frequency.

First, for an atom to jump from one site to another, the defect necessary to provide the means for the jump must be available. For the interstitial diffusion mechanism there is essentially always a vacancy (really a vacant interstice) available except at high interstitial concentrations. For other mechanisms, however, the atom has to

“wait” until a defect arrives. The probability of a defect, say a vacancy, arriving at a particular neighboring site to a given atom is simply the fractional vacancy concentration c_v . However, in certain situations such as alloys showing order, or fast ion conductors showing relatively high defect ordering, the availability of vacancies to the atoms can be enhanced or depressed from the random mixing value which c_v signifies. This topic is discussed further in Secs. 3.4.2 and 3.4.3.

The probability of a given atom being next to a vacancy is thus gc_v where g is the coordination number. The jump frequency Γ can be decomposed to

$$\Gamma = g c_v \omega \quad (3-145)$$

where ω is usually called the “exchange” frequency to signify the exchange between an atom and a neighboring vacant site and to distinguish it from the actual jump frequency Γ . It is permissible at low defect concentrations to call ω the defect jump frequency, since the defect does not have to “wait” for an atom.

In, say, f.c.c. crystals where the jump distance r is given by $a/\sqrt{2}$, where a is the lattice parameter and $g=12$, the tracer diffusion coefficient from Eq. (3-76) can now be written as

$$D^* = 12 c_v \omega (a^2/2) f/6 = c_v \omega a^2 f \quad (3-146)$$

The same equation is also valid for b.c.c. crystals. Other examples have been given by Le Claire (1975).

In many solids, such as metals, alloys and ionic crystals, c_v is said to be “intrinsic” with an Arrhenius temperature dependence. The vacancy formation enthalpy is contained in the measured activation enthalpy for the tracer diffusion process (see Eq. (3-149)). In some solids, notably ionic crystals and certain intermetallic compounds, apart from the inevitable tempera-

ture-dependent intrinsic concentration, the vacancy concentration can also be manipulated by doping or by changing the degree of nonstoichiometry. In such cases this vacancy concentration is sometimes said to be “extrinsic”, and this contribution to the total vacancy concentration can easily swamp the intrinsic vacancy contribution. The extrinsic vacancy concentration is independent of temperature. However, in the case of a change in stoichiometry, temperature independence of c_v requires adjustment of the external partial pressure (see Sec. 3.4.4).

3.3.4.1 The Exchange Frequency

With the defect immediately available, the atom can jump when it acquires sufficient thermal energy from the lattice for it to pass over the energy barrier between its present site and the neighboring site. The probability of the atom having this thermal energy is given by the Boltzmann probability $\exp(-G^m/kT)$, where G^m (a Gibbs energy) is the barrier height, k is the Boltzmann constant, and T is the absolute temperature. The attempt frequency, i.e., the number of times per second the atom on its site is moving in the direction of the neighboring site, is the mean vibrational frequency $\bar{\nu}$. Accordingly, the “jump rate”, i.e., number of jumps per second, ω , is given by

$$\omega = \bar{\nu} \exp(-G^m/kT) \quad (3-147)$$

Because G^m is a Gibbs energy, the exchange frequency can be partitioned as

$$\omega = \bar{\nu} \exp(S^m/k) \exp(-H^m/kT) \quad (3-148)$$

where S^m is the entropy of migration and H^m is the enthalpy of migration. H^m is sometimes loosely called the “activation” enthalpy, but this can lead to misunderstandings, as we shall now see.

In Sec. 3.3.4.2 we show that the defect concentration in many cases depends on temperature in an Arrhenius fashion (Eq. (3-159)). In such cases, the atomic jump frequency Γ , being the product of ω , the defect concentration, and the coordination number, is written as from Eq. (3-145)

$$\Gamma = g \bar{\nu} \exp[(S^m + S_v^f)/k] \times \exp[-(H^m + H_v^f)/kT] \quad (3-149)$$

The sum of H^m and H^f is more accurately called the activation enthalpy. We emphasize again that the activation enthalpy measured in a diffusion experiment can, for some solids such as ordered alloys, contain other contributions such as from correlation effects or defect availability terms.

The enthalpy of migration and the enthalpy of defect formation are now routinely calculated by Lattice or Molecular Statics methods; see Mishin (1997) and references therein for examples of such calculations in grain boundaries.

Although it is straightforward to couch the argument above concerning ω in statistical mechanical terms, this would still be inadequate because we have neglected the participation of the remainder of the lattice, especially the neighbors of the jumping atom, in the jump process. A more satisfactory treatment has been provided by Vineyard (1957). This puts $\bar{\nu}$ on a sounder basis and gives physical significance to the entropy of migration S^m .

Vineyard (1957) took a classical statistical mechanical approach by considering the phase space of the system comprising all of its N atoms and one vacancy. Each point in this phase space represents an atomic configuration of the system. All possible configurations are represented. We are concerned with two neighboring energy minima in this phase space. These minima are centered on two points, P and Q. Point P is the phase space point repre-

senting an atom adjacent to a vacancy; all atoms are in their equilibrium positions. Point Q is the corresponding point *after* the atom–vacancy exchange. Between the points P and Q there is a potential energy barrier. In order to jump, the atom must pass over this barrier at its lowest point, a saddle point.

Vineyard (1957) was able to calculate the jump rate, i.e., the number of crossings per unit time at the “harmonic approximation”. This entailed expanding the potential energy at point P and also at the saddle point in a Taylor series to second order to give for ω

$$\omega = \left(\frac{\prod_{i=1}^N \nu_i}{\prod_{i=1}^N \nu'_i} \right) \exp(-U/kT) \quad (3-150)$$

where the ν_i are normal frequencies for vibration of the system at point P, ν'_i are the normal frequencies at the saddle point and U is the difference in potential energy between the saddle point and the equilibrium configuration point, P.

It is possible to transform Eq. (3-150) into the form of Eq. (3-148) by writing

$$\frac{\prod_{i=1}^N \nu_i}{\prod_{i=1}^N \nu'_i} = \bar{\nu} \exp(S^m/kT) \quad (3-151)$$

where the entropy of migration can be identified with

$$S^m = k \sum_{i=2}^{3N} \ln(\nu_i^0/\nu'_i) \quad (3-152)$$

and

$$\bar{\nu} = \frac{\prod_{i=1}^{3N} \nu_i}{\prod_{i=2}^{3N} \nu_i^0} \quad (3-153)$$

where ν_i^0 is the frequency of the i th normal mode with the system constrained to move normal to the direction joining point P to the saddle point.

There have been many further considerations of the detailed dynamics of the jump process, the most notable of these being the work carried out by Jacucci, Flynn and co-workers (see reviews by Jacucci (1984) and Pontikis (1990)).

For general purposes it is often sufficient to focus on Eq. (3-148) and to note that the Debye frequency is an adequate representation of the mean vibration frequency $\bar{\nu}$.

3.3.4.2 Vacancy Concentration

The change in Helmholtz energy F_V^f associated with the formation of one vacancy is given by

$$F_V^f = E_V^f - T S_V^f \quad (3-154)$$

where E_V^f and S_V^f are the energy and entropy of formation, respectively. The formation process itself is conceived to be the removal of an atom from the interior of the crystal to the surface. The entropy part has two contributions: a vibrational or thermal part S_{vib}^f arising from the fact that atoms close to the vacancy have a different vibrational frequency from those far from the vacancy, and a configurational part S_{config}^f which is usually thought to be an ideal mixing entropy, at least for pure metals – but it is rather more complicated for alloys. The configurational part for pure metals is easily found from elementary classical statistical mechanics (see, for example, Peterson (1978)). The number of different ways Ω of putting n vacancies and N atoms on $N+n$ sites assuming indistinguishability within each group is

$$\Omega = \frac{(N+n)!}{N! n!} \quad (3-155)$$

The configurational entropy is given by

$$S_{\text{config}}^f = k \ln \Omega = k \ln \left[\frac{(N+n)!}{N!n!} \right] \quad (3-156)$$

which, with Stirling's approximation $\ln N! = N \ln N - N$ for large N , results in

$$S_{\text{config}}^f = -k \left(N \ln \left[\frac{N}{N+n} \right] + n \ln \left[\frac{n}{N+n} \right] \right) \quad (3-157)$$

The total change in free energy when n vacancies are produced is

$$nF_V^f = nE_V^f - T(nS_{\text{config}}^f) \quad (3-158)$$

After substitution of Eq. (3-157) and putting the derivative $\partial F / \partial n = 0$ to obtain the equilibrium number of vacancies, we soon find that

$$\frac{n}{N+n} = c_v = \exp(S_{\text{vib}}^f/k) \exp(-E_V^f/kT) \quad (3-159)$$

where c_v is the site fraction of vacancies. Note that the configurational term has disappeared. The vibrational contribution S_{vib}^f is considered to be small and the leading term in Eq. (3-159) is usually ignored, and

$$c_v = \exp(-E_V^f/kT) \quad (3-160)$$

For low pressures we can also assume (not always safely) that the energy of formation E_V^f can be approximated by the enthalpy of formation H_V^f .

Divacancies are handled in a similar way (see, for example, Peterson (1978)). Frenkel and Schottky defects in ionic crystals (see Sec. 3.4.4) can also be analysed along similar lines (Kofstad, 1972). Alloys, however, present a special problem because of uncertainties about reference states including the typical surface site where an atom is to be symbolically placed (see, for example, Lim et al. (1990) and Foiles and Daw (1987)).

Calculations of defect formation energies are frequently handled by lattice relax-

ation techniques with computer codes such as DEVIL and CASCADE (these techniques are described in the book edited by Catlow and Mackrodt, 1982) and lattice dynamics and Monte Carlo methods (see, for example, Jacucci, 1984).

Vacancy concentrations in metals are conventionally measured by quenching, dilatometry, and positron annihilation. An introduction to these techniques has been provided by Borg and Dienes (1988), and a detailed review is also available (Siegel, 1978).

3.4 Diffusion in Materials

Probably every type of solid has, at one time, been investigated for its diffusion behavior. It is impossible in the space here to cover even the major findings. In this section we propose to discuss, at an introductory level, diffusion in metals and alloys, and, as an example of ionic crystals, oxides. Our emphasis here is on the usual theoretical framework for a description of diffusion in these materials rather than on data compilations or reviews. Diffusion data compilations for metals and alloys can be found in the Smithells Metals Reference Book (Brandes, 1983) and in the extensive compilations in Landolt-Börnstein (Mehrer, 1990). The older tracer diffusion data up to 1970 on metals and oxides has been collected by Askil (1970) and data on oxides up to 1970 on metals and oxides has been collected by Askil (1970) and data on oxides up to 1980 by Freer (1980). Extensive compilations of diffusion data in nonmetallic solids have been published in Landolt-Börnstein (Beke, 1998 1999). The journal *Defect and Diffusion Form*, formerly *Diffusion and Defect Data*, regularly publishes abstracts of all diffusion-related papers and extensive indices are regularly provided.

3.4.1 Diffusion in Metals

3.4.1.1 Self-Diffusion

We have seen (Sec. 3.3.4) that the tracer diffusion coefficient in solids normally follows an Arrhenius form. This is usually written empirically as

$$D = D^0 \exp(-Q/RT) \quad (3-161)$$

where D^0 is called the pre-exponential factor, or sometimes the “frequency factor”, Q is the activation energy for diffusion, R is the ideal gas constant, and T is the absolute temperature. In most pure metals self-diffusion is characterized by a pre-exponential D^0 which falls in the range 10^{-3} to $5 \times 10^{-6} \text{ m}^2 \text{ s}^{-1}$. This corresponds to activation entropies which are positive and of the order of k , the Boltzmann constant. The activation energy Q is given fairly closely ($\pm \approx 10\%$) by $Q = 34 T_{\text{M.P.}}$, where $T_{\text{M.P.}}$ is the melting point. These values lead to a value of the self-diffusion coefficient at the melting point of about $10^{-12} \text{ m}^2 \text{ s}^{-1}$.

Careful dilatometric and quenching experiments on a large number of f.c.c. metals indicate the vacancy as being the defect responsible for “normal” diffusion in f.c.c. metals. For vacancy diffusion the tracer diffusion coefficient is written for cubic lattices as

$$D^* = g c_v \omega r^2 f / 6 \quad (3-162)$$

where g is the coordination, c_v is the vacancy concentration, ω is the vacancy-atom exchange frequency, r is the jump distance, and f is the tracer correlation factor. The decomposition of c_v into its enthalpy/entropy parts is given by Eq. (3-159). The decomposition of ω is given in Eq. (3-148). The tracer correlation factor is discussed in Sec. 3.3.1.3.

For some f.c.c. metals, e.g., silver (Rothman et al., 1970; Lam et al., 1973), where

diffusion measurements have been made over a very wide temperature range, there is a slight curvature in the Arrhenius plots. This has been variously attributed to a contribution to diffusion from divacancies (see, for example, Peterson (1978)), or from vacancy double jumps (Jacucci, 1984). Because of the high activation energy, however, the latter is really only a candidate for explaining curvature very close to melting temperature and not over a wide temperature range.

There is still controversy over the cause of the curvature in Ag and other f.c.c. metals, with one view favoring a temperature-dependent activation energy and diffusion by single vacancies (see the review by Mundy (1992)), and the other tending to favor, in part, a contribution from divacancies at high temperatures (Seeger, 1997). The behavior of self-diffusion in b.c.c. metals is quite varied. Some b.c.c. metals such as Cr show linear Arrhenius plots. The alkali metals show slightly curved plots. Finally, there is a large group of “anomalous” metals including β -Zr, β -Hf, β -Ti, γ -U, and ϵ -Pu, which show a strong curvature and show values of D_0 and Q both of which are anomalously low. There has been considerable controversy here also. Again, the monovacancy mechanism and a temperature-dependent activation energy have been strongly supported (Mundy, 1992) but this view alone does not seem to be entirely consistent with the nature of the curvature. Other processes such as ring mechanisms and Frenkel pair formation/recombination may be operative (Seeger, 1997).

3.4.1.2 Impurity Diffusion

The appropriate diffusion coefficient for an impurity A (at infinite dilution) in a host of B when the vacancy mechanism is oper-

ating is (for cubic lattices)

$$D_A = g p_{AV} \omega_A r^2 f_A / 6$$

$$= D_A^0 \exp(-Q_A/RT) \quad (3-163)$$

where g is the coordination, p_{AV} is the vacancy availability factor to the impurity, ω_A is the impurity–vacancy exchange frequency, r is the jump distance, and f_A is the impurity correlation factor (for details see Sec. 3.3.1.4). Again, as for self-diffusion in metals, in many cases we can discern “normal” behavior wherein the Arrhenius plots are linear and D_A^0 and Q_A do not differ greatly from the self-diffusion values. As pointed out by Le Claire (1975, 1978), the relative values are determined principally by $\Delta Q = Q_A - Q_B$, where Q_B is the self-diffusion activation energy for the host. When $D_A > D_B$, the impurity is a fast diffuser and ΔQ is negative. It is often found that this is correlated to a situation where the valence of the impurity is greater than that of the host. The converse is true when $D_A < D_B$.

The similarity between impurity and host diffusivities suggest the vacancy mechanism for both. For this mechanism it can easily be shown that (see, for example, Le Claire, 1978)

$$\Delta Q = (H_A^m - H_B^m) + E_B - Q' \quad (3-164)$$

where H_A^m , H_B^m are the activation enthalpies of migration for the impurity and host, E_B is the vacancy–impurity binding enthalpy, and Q' is the activation enthalpy arising from the temperature dependence of f_A (see Eq. (3-90)). This is normally a fairly small contribution.

There are “anomalous” impurity diffusers which have diffusion coefficients much higher than the host. Well-known examples are the diffusion of noble metals in Pb. As has been discussed in conjunction with the substitutional-vacancy diffusion mechanism, the impurities probably exist partly as

interstitials and partly as substitutionals (see Sec. 3.3.1.1). For a full discussion of all aspects of impurity diffusion we refer to Le Claire (1978).

3.4.2 Diffusion in Dilute Alloys

3.4.2.1 Substitutional Alloys

Alloys containing something less than about 1–2% solute concentrations are considered to be sufficiently dilute that the diffusion of solute atoms can be considered in terms of isolated atoms or isolated groupings of atoms such as pairs. For many binary dilute alloys, measurements of the solute diffusion coefficient D_2 (measured as a tracer diffusion coefficient) have been made as a function of solute concentration (we use the subscript 2 to denote the solute and 0 to denote the solvent). It is usual to represent the solute diffusion coefficient empirically as

$$D_2(c_2) = D_2(0) (1 + B_1 c_2 + B_2 c_2^2 \dots) \quad (3-165)$$

where $D_2(0)$ is the solute diffusion coefficient for $c_2 \rightarrow 0$, c_2 is the atomic fraction of solute and B_1 , B_2 , ... are termed *solute enhancement factors*. $D_2(0)$ is also called the impurity diffusion coefficient (at infinite dilution) depending on the context of the experiment.

Similarly, solvent diffusion coefficients D_0 , also measured as tracer diffusion coefficients, are represented as

$$D_0(c_2) = D_0(0) (1 + b_1 c_2 + b_2 c_2^2 \dots) \quad (3-166)$$

and b_1 , b_2 , ... are termed *solvent enhancement factors*.

Of interest are the solute and solvent enhancement factors. Naturally, also of interest is the composition (a) of values of the solute and solvent diffusion coefficients and (b) of values of their respective activation energies.

In Eq. (3-166) $D_2(0)$ arises from isolated solute atoms, while the term containing B_1 arises from pairs of solute atoms which are sufficiently close that the solute jump frequency differs from the isolated solute–vacancy exchange frequency ω_2 . B_2 arises from triplets of solute atoms.

The *solute* enhancement factor B_1 has been calculated for the f.c.c. lattice by extending the five-frequency model (see Sec. 3.3.1.4) to include three new frequencies. These frequencies describe solute jumps which create, i.e., associate, a new solute pair (ω_{23}), dissociate a solute pair (ω_{24}), and reorient an existing pair (ω_{21}). Pairs of solute atoms do not occur randomly when solute atoms interact. When an interaction energy E_{22} between solute atoms is defined it is straightforward to show that

$$\omega_{24} \exp(-E_{22}/kT) = \omega_{23} \exp(-E_{2B}/kT)$$

where E_{2B} is the impurity–vacancy binding energy. If it is assumed that the impurity correlation factor does not depend on solute concentration (Stark, 1972, 1974), then B_1 is given by (Bocquet, 1972; Le Claire, 1978)

$$B_1 = -[6 + 12 \exp(-E_{22}/kT)] - \exp(-E_{2B}/kT) \times \left[4 \frac{\omega_{21}}{\omega_2} \exp(-E_{22}/kT) - 14 \frac{\omega_{23}}{\omega_2} \right] \quad (3-167)$$

If it is assumed that $E_{22}=0$ and that $\omega_{21}=\omega_{23}=\omega_2$ then B_1 is reduced to

$$B_1 = 18 [\exp(-E_{2B}/kT) - 1] \quad (3-167a)$$

There have been no calculations along similar lines of B_2 .

The *solvent* enhancement factor b_1 can be calculated by noting the number of jump frequencies close to the solute. For instance, in the five-frequency model for the f.c.c. lattice we need to count the number of solvent frequencies which differ from

ω_0 , the solvent exchange frequency far from the solute. For the f.c.c. lattice the result for b_1 is (Howard and Manning, 1967)

$$b_1 = -18 + \frac{\omega_4}{\omega_0} \left[4 \frac{\chi_1}{f_0} \frac{\omega_1}{\omega_3} + 14 \frac{\chi_2}{f_0} \right] \quad (3-168)$$

where χ_1 and χ_2 are termed partial correlation factors and are known functions of the ratios ω_2/ω_1 , ω_1/ω_3 and ω_4/ω_0 , and f_0 is the correlation factor in the pure lattice.

Eq. (3-168) can be re-expressed as

$$b_1 = -18 + \left[4 \frac{\chi_1}{f} \frac{\omega_1}{\omega_0} + 14 \frac{\chi_2}{f_0} \frac{\omega_3}{\omega_0} \right] \times \exp(-E_{2B}/kT) \quad (3-169)$$

thereby showing the effect of an altered vacancy concentration near a solute by virtue of the solute–vacancy binding energy E_{2B} .

There are similar relations for the b.c.c. lattice. For the impurity model described in Sec. 3.3.1.4 (Model I), b_1 is given by (Jones and Le Claire, 1972)

$$b_1 = -20 + 14 \frac{u_1}{f} + 6 \frac{\omega_3}{\omega_0} \frac{v_1}{f} \exp(-E_{2B}/kT) \quad (3-170)$$

and for Model II (see Sec. 3.3.1.4)

$$b_1 = -20 + 6 \frac{u_2}{f} + 14 \frac{\omega_3}{\omega_0} \frac{v_2}{f} \exp(-E_{2B}/kT) \quad (3-171)$$

where u_1 , v_1 (ω_2/ω'_3 , ω_3/ω'_3) and u_2 , v_2 (ω_2/ω_3 , ω_4/ω_0) are called mean partial correlation factors and are known functions of the frequencies given.

It is possible to express b_1 in terms of the *ratio* of the solute and solvent diffusion coefficients. This aids in the discussion of the numerical values taken by the enhancement factors. For the f.c.c. lattice, b_1 is given by Le Claire (1978).

$$b_1 = -18 + \frac{4f_0}{1-f_2} \frac{D_2}{D_0} \left[\frac{4\chi_1(\omega_1/\omega_3) + 14\chi_2}{f_0(4\omega_1/\omega_3) + 14F} \right] \quad (3-172)$$

where F has been given in Sec. 3.3.1.4 (see Eq. (3-80)) and f_0 is the tracer correlation factor in the pure lattice. The term in brackets is roughly unity and the impurity correlation factor f_2 is about 0.5. The greater the solute diffusion coefficient is compared with the solvent diffusion coefficient, then the more likely it is that b_1 is greater than zero. On the other hand, for slow solute diffusers b_1 will probably be negative but not less than -18 . A few examples taken from Le Claire (1978) are given in Table 3-2.

The solvent enhancement factor b_2 results from the change in the solvent jump frequencies in the vicinity of *pairs* of solute atoms. Expressions for b_2 for the f.c.c. lattice have been given by Bocquet (1972).

As noted by Le Claire (1978), the expressions for b_1 and B_1 are similar in form. Provided that the frequency ratios in one equation do not greatly differ from the other, as might be expected from relatively weak perturbations caused by the solute, then b_1 and B_1 tend to have the same sign and roughly comparable magnitudes, apart from the $\exp(-E_{22}/kT)$ term in the expres-

sion for B_1 . These comments are borne out by the data in Table 3-2.

The relative values of the diffusion coefficients of solute and solvent are dictated largely by the difference in activation energies for solute and solvent diffusion rather than by differences in the pre-exponential factors. The difference $\Delta Q = Q_2 - Q_0$ (where Q_2 and Q_0 are the activation energies for solute and solvent respectively) often seems to be closely related to the difference in valencies of solute and solvent, Z_2 and Z_0 . When ΔQ is negative (fast solute diffusion), $Z_2 > Z_0$. On the other hand, when ΔQ is positive $Z_2 < Z_0$. These matters are discussed further in a detailed review by Le Claire (1978). The reader is also directed to a recent commentary (Le Claire, 1992).

An approximate approach which acts as a transition between the models described above and the concentrated alloy models of Sec. 3.4.3 is the complex model initiated first by Dorn and Mitchell (1966) and developed by Faupel and Hehenkamp (1986, 1987). When impurities (B) have a positive excess charge, vacancy-impurity complexes of one vacancy and i impurity atoms are likely to form. Assuming that the binding free energy ($-G_{Bi}$) is independent of the configuration of the impurity atoms, Dorn and Mitchell (1966) wrote for the

Table 3-2. Some values of solute and solvent enhancement factors, from Le Claire (1978).

Alloy system (Solvent-solute)	Lattice	D_2/D_0	b_1	B_1	$T(^{\circ}\text{C})$
Ag-Pd	f.c.c.	0.04	-8.2	-7.5	730
Ag-Au	f.c.c.	3.7	7.0	5.5	730
Ag-Cd	f.c.c.	5.3	13.0	8.5	730
Ag-In	f.c.c.	8.4	37	30	730
Ag-Tl	f.c.c.	0.26	-1.2	-0.56	730
β -Ti-V	b.c.c.	1.26	-4.3	-2.5	1400
V-Ti	b.c.c.	1.66	16	27	1400
α -Fe-Si	b.c.c.	1.64	20.4	12.4	1427

mole fraction of vacancies in the i th complex c_{vi}

$$c_{vi} = c_v(0) \binom{g}{0} c_0^{g-i} c_2^i \exp(G_{Bi}/kT) \quad (3-173)$$

where $c_v(0)$ is the mole fraction of vacancies in the pure metal (A) and c_0 and c_2 are the mole fractions of solvent (A) and solute (B) respectively, and g is the coordination. Bérces and Kovács (1983) modified Eq. (3-173) to take into account possible *configurations* of the complexes.

Within this complex model framework Faupel and Hehenkamp (1986, 1987) have introduced *average* effective jump frequencies per solvent (A) atom $\langle \omega_{\text{eff}}^A \rangle_i$ and average effective jump frequencies per solute (B) atom $\langle \omega_{\text{eff}}^B \rangle_i$ in the i th complex (the latter specifically includes correlation effects – which are always important for the solute). The normalized solvent diffusion coefficient can now be written as

$$\frac{D_0(c_2)}{D_0(0)} = c_0^{g-1} - \sum_{i=1}^{g-1} \frac{\langle \omega_{\text{eff}}^A \rangle_i}{f_0 \omega_0} \binom{g-1}{i} \times c_0^{g-1-i} c_2^i \exp(G_{Bi}/kT) \quad (3-174)$$

Similarly, the normalized solute diffusion coefficient can be written as

$$\frac{D_0(c_2)}{D_0(0)} = c_0^{g-1} - \sum_{i=2}^g \frac{i}{g} \frac{\langle \omega_{\text{eff}}^B \rangle_i}{f_2 \omega_2} \binom{g}{i} \times c_0^{g-1} c_2^{i-1} \exp[(G_{Bi} - G_{B1})/kT] \quad (3-175)$$

These equations for the normalized solute and solvent diffusion coefficients can be expanded in terms of c_2 to give explicit expressions for the various solute and solvent enhancement factors by way of comparison with Eqs. (3-165) and (3-166); see Le Claire (1992).

It has been found, in a number of careful studies in f.c.c. systems (Ag–Sb, Ag–Sn) where the impurities have excess positive charge, that solvent diffusion on alloying is

enhanced in a nonlinear way (Hehenkamp et al., 1980; Hehenkamp and Faupel, 1983). Moreover, independent measurements of the vacancy concentration on alloying have shown a *linear* dependence between normalized vacancy concentration and the normalized solvent diffusion coefficient (Hehenkamp et al., 1980; Hehenkamp and Faupel, 1983). The nonlinear enhancement of solvent diffusion upon alloying is thus apparently due to a corresponding nonlinear increase in the vacancy concentration on alloying. These findings are very nicely described by the complex model.

Despite its obvious limitations, the complex model can be useful quantitatively up to 5 at.% of solute and qualitatively even higher; see Le Claire (1992).

3.4.2.2 Interstitial Alloys

Elements such as H, N, O, and C dissolve interstitially in metals and diffuse by the interstitial mechanism. The diffusion coefficients here are often measured by relaxation techniques or outgassing. Tracer diffusion is difficult to measure in the case of N and O because of the lack of suitable radioisotope; however, other techniques are available (see Sec. 3.5.1).

For interstitials at infinite dilution, the interstitials move independently (by the interstitial mechanism, see Fig. 3-5). The vacancy concentration (vacant interstice) is unity, the correlation factor is unity (a complete random walk), and the tracer diffusion coefficient is given simply by (from Eqs. (3-76) and (3-145))

$$D^* = g \omega_0 r^2/6 \quad (3-176)$$

where ω_0 is the interstitial/vacant interstice “exchange” frequency.

In a number of cases the interstitial concentration can become sufficiently high for the interstitials to interfere with one an-

other and this interference may have an important effect on diffusion. An example is C in austenite where the carbon interstitials can fill roughly 8% of the octahedral voids. The two theoretical approaches taken to cope with the problem are reminiscent of the situation found in the modeling of substitutional alloys (see Sec. 3.4.2.1). In the first, the exchange frequencies for the solute are specified. In the second, the exchange frequencies are specified indirectly by way of interaction energies.

For the first approach, McKee (1980a, b) and Le Claire (1981) conceived a four-frequency model for interstitial solute diffusion in the f.c.c. lattice (the octahedral voids of the f.c.c. lattice). Two distinct species are considered: the isolated interstitial with a jump frequency of k_0 , and paired interstitials, which rotate with frequency u_1 , dissociate with frequency u_3 , and associate with frequency u_4 . The following expression for the tracer diffusion coefficient of the interstitial solute can then be derived (Le Claire (1981) using Howard's (1966) random walk method)

$$D^* = 4r^2 \left[k_0 + \frac{c_p}{6c} \left(4u_1 + 14u_3 - \frac{(2u_1 - 3u_3)^2}{(2u_1 + 7u_3)} - 12k_0 - 7k_0 \frac{u_3}{u_4} \right) \right] \quad (3-177)$$

where c_p is the site fraction concentration of paired interstitials and c is the site fraction of interstitials. Using the pair association method, McKee (1980a, b) derived a similar result valid for weak binding of the paired interstitials. Explicit expressions for the tracer correlation factor can be found in the original papers.

It was also possible to determine an expression for the chemical diffusion coefficient, \tilde{D} , relating to diffusion of the solute in its own concentration gradient. In the weak binding limit the expression for \tilde{D} is

(McKee, 1981)

$$\tilde{D} = \frac{1}{3} r^2 [12k_0 + 12u_4/u_3] \times [4u_1 + 7u_3 - 12k_0 + 7(u_4 - k_0)u_3/u_4] \times c \{1 + c[1 + 12(1 - u_4/u_3)]\} \quad (3-178)$$

where r is the jump distance. Eq. (3-178) contains a thermodynamic factor.

The above model, where the frequencies are specified explicitly, is probably only valid for 1–2% of interstices occupied. At higher concentrations many more frequencies are required with the result that this approach becomes unwieldy. For the second approach a lattice gas model is used to represent the solute interstitials and their lattice of interstices. High concentrations of interstitials can in principle be handled with this model. In this *rigid* model the atoms are localized at sites and pairwise interactions among atoms are specified. The exchange frequency of a solute atom to a neighboring site can be written as (Sato and Kikuchi, 1971)

$$\omega = \nu \exp(g_{nn} \phi_{nn}/kT) \exp(-U/kT) \quad (3-179)$$

although many other choices are possible. In Eq. (3-179) ν is the vibration frequency, g_{nn} is the number of *occupied* interstices that are nearest neighbors to a solute, ϕ_{nn} is the solute–solute “binding” energy (positive or negative), and U is the migration energy for an *isolated* solute atom. In effect the solute neighbors can assist or impede the diffusion process depending on the sign of ϕ_{nn} .

By its nature this model requires a statistical mechanical approach for its analysis. One method used is the PPM (Sato and Kikuchi, 1971; Sato, 1989, see also Sec. 3.3.1.5); another is the Monte Carlo computer simulation method (Murch, 1984a). It is convenient to decompose the tracer diffusion coefficient into

$$D^* = g r^2 V W f \exp(-U/kT)/6 \quad (3-180)$$

where V is the vacancy availability factor (the average availability of neighboring vacant interstices to an interstitial solute atom, and is a more general quantity than c_v), and W represents the effect of the environment on the jump frequency. It is in effect the statistical average of the first term in Eq. (3-179). The same lattice gas model has also been applied extensively to fast ion conductors (see, for example, Murch (1984a)).

Chemical diffusion can readily be expressed along similar lines (Murch, 1982c) as

$$\tilde{D} = g r^2 V W v f_1 \times \exp(-U/kT) (\partial \mu / kT / \partial \ln c) / 6 \quad (3-181)$$

where μ is the chemical potential of the solute and f_1 is the physical correlation factor (see Sec. 3.3.1.7). The physics for f_1 are not contained in the first approach (Eq. (3-178)).

These approaches seem to describe C tracer and chemical diffusion in γ -Fe fairly well (McKee, 1980a, b, 1981; Murch and Thorn, 1979) but other applications have not been made because of the lack of suitable data, especially for D^* .

Quantum effects are an important ingredient in the description of H diffusion in metals; see the reviews by Völkl and Alefeld (1975), Fukai and Sugimoto (1985), and Hempelmann (1984).

3.4.3 Diffusion in Concentrated Binary Substitutional Alloys

Dilute alloy models, see Sec. 3.4.2.1, cannot be extended very far into the concentrated regime without rapidly increasing the number of jump frequencies to an unworkable level. As a result, models have been introduced which limit the number of jump frequencies but only as a result of

some loss of realism. The first of these is the random alloy model introduced by Manning (1968, 1970, 1971). The second is the interacting bond model which has been extensively developed by Kikuchi and Sato (1969, 1970, 1972).

In the random alloy model, the atomic components are assumed to be mixed randomly and the vacancy mechanism is assumed. The atomic jump frequencies ω_A and ω_B for the two components A and B are specified and these do not change with composition or environment. The tracer diffusion coefficient of, say, A is given by

$$D_A^* = g \omega_A r^2 c_v f_A / 6 \quad (3-182)$$

where g is the coordination, r is the jump distance, and c_v is the vacancy site fraction (see Sec. 3.3.4.2). The only theoretical requirement here is to calculate the tracer correlation factor f_A ; this has been described in Sec. 3.3.1.5 on correlation effects in diffusion. The random alloy model performs very well in describing the diffusion behavior of many alloy systems which are fairly well disordered. This subject is discussed extensively in the review by Bakker (1984) to which we refer. A much more accurate method for dealing with f_A has been given by Moleko et al. (1989).

For alloys which exhibit order, Manning's theory, based on the random alloy model, still performs reasonably well in describing certain aspects of diffusion behavior, notably correlation effects which can be expressed in terms of the tracer diffusion coefficients, see Sec. 3.3.1.8 and the review by Murch and Belova (1998). A wholly different approach pioneered by Kikuchi and Sato (1969) is the PPM (see Sec. 3.3.1.5) in which the tracer diffusion coefficient is expressed in terms of quantities which are statistically averaged over the atomic configurations encountered in the alloy. The tracer diffusion coefficient

of, say, A is now written as

$$D_A^* = g \bar{\omega}_A r^2 \bar{p}_{Av} \bar{f}_A / 6 \quad (3-183)$$

where $\bar{\omega}_A$ is an averaged exchange frequency which includes the effect of the environment on the jump frequency, \bar{p}_{Av} is the vacancy availability factor, i.e., the probability of finding a vacancy next to an A atom (see below), and \bar{f}_A is the tracer correlation factor. We have discussed the correlation factor \bar{f}_A in Sec. 3.3.1.5, to which we refer. The quantity $\bar{\omega}_A$ is the average of the exchange frequency for an A atom with a vacancy in particular configuration:

$$\omega_A = \nu_A \exp(-U_A/kT) \times \exp[(g_A E_{AA} + g_B E_{AB})/kT] \quad (3-184)$$

where ν_A is the vibration frequency, U_A is the migration energy (referred to some reference) for a jump, g_A is the number of A atoms that are nearest neighbors to a given A atom (itself next to a vacancy), g_B is the number of B atoms which are likewise nearest neighbors to the A atom, and E_{AA} and E_{AB} are nearest neighbor interactions (assumed negative here). This equation is essentially the binary analogue of Eq. (3-179). We see that the neighbors of the atom A can increase or decrease the apparent migration energy.

The use of c_v alone in the expression for D_A^* in Eq. (3-182) implies that either component “sees” the vacancy equally. This obviously cannot generally be true. The introduction of the quantity \bar{p}_{Av} in Eq. (3-183) (and \bar{p}_{Bv}) is a recognition that vacancies are somewhat apportioned between the two atomic components. This is not a small effect, particularly in alloys which show separate sublattices.

The overall activation energy for diffusion is now rather complicated. Apart from the usual contribution from the vacancy formation energy and reference migration energy, we have a complicated contribution

from $\bar{\omega}_A$ because the configurations change with temperature. We also have contributions from \bar{p}_{Av} and the tracer correlation factor. In order to make sense of the experimental activation energies, we need to model the system in question; there seems to be no alternative. Few detailed applications of this model have yet been made. One detailed application has been made to β -CuZn (Belova and Murch, 1998). Further details can be found in the review by Bakker (1984), see also the review by Murch and Belova (1998).

Interdiffusion in binary concentrated alloys has been dealt with largely in Secs. 3.2.3.2 and 3.3.1.8. Some recent calculations (which use the “bond model” described above) have been performed by Zhang et al. (1988) and Wang and Akbar (1993), see also the review by Murch and Belova (1998).

3.4.4 Diffusion in Ionic Crystals

In this section diffusion in ionic crystals (exemplified here by oxides) will be briefly discussed. A more detailed discussion has been provided by Kofstad (1972) and Schmalzried (1995). Diffusion in other ionic crystals, especially alkali metal halides and silver halides, has been reviewed by, for example, Fredericks (1975), Laskar (1990, 1992), Monty (1992).

3.4.4.1 Defects in Ionic Crystals

In order to discuss diffusion in ionic crystals, we need first to discuss at an elementary level the types of defects which arise. Of almost overriding concern in ionic crystals is the requirement of charge neutrality.

Let us first consider *stoichiometric* crystals, say the oxide MO, and “intrinsic” defect production. The Schottky defect (actu-

ally a pair of defects) consists of a vacant anion site and a vacant cation site. It arises as a result of thermal activation and *not* through interaction with the atmosphere. The Schottky defect generation is written as a chemical reaction, i.e.,



where 0 refers to a perfect crystal, V_M'' is a vacant (V) metal (M) site, the primes refer to effective negative charges (with respect to the perfect crystal), $V_O^{\bullet\bullet}$ is a vacant (V) oxygen (O) site and the dots refer to effective positive charges. This is the Kröger-Vink defect notation (see, for example, Kofstad (1972)).

We can write an equilibrium constant K_s for the reaction in the following form, valid for low defect concentrations:

$$K_s = [V_M''] [V_O^{\bullet\bullet}] \quad (3-186)$$

where the brackets $[\]$ indicate concentrations. Eq. (3-186) is usually called the Schottky product. K_s can be expressed in the usual way

$$K_s = \exp(-G_s^f/kT) \quad (3-187)$$

where G_s^f is the Gibbs energy of formation of the Schottky defect, which can be partitioned into its enthalpy H_s^f and entropy S_s^f parts.

The other type of defect occurring in the stoichiometric ionic crystal is the Frenkel defect. The Frenkel defect (actually a pair of defects) consists of a cation interstitial and cation vacancy or an anion interstitial and anion vacancy. In the latter case it has also been called an anti-Frenkel defect, although this nomenclature is now relatively uncommon. Like the Schottky defect, the Frenkel defect is thermally activated. The Frenkel defect generation is also written as a chemical reaction, for example for cationic disorder:



where M_M is a metal atom (M) on a metal site (M), $M_i^{\bullet\bullet}$ is an *effectively* doubly positively charged metal ion on interstitial i site and V_M'' is an *effectively* doubly negatively charged metal ion vacancy. We have assumed double charges here purely for illustrative purposes.

The equilibrium constant for the Frenkel defect reaction can be written as

$$K_F = [M_i^{\bullet\bullet}] [V_M''] \quad (3-189)$$

provided that the defect concentration is low. This equation is often called the Frenkel product. Again, the equilibrium constant K_F can be expressed as $\exp(-G_F^f/kT)$ where G_F^f is the Gibbs energy of formation of the Frenkel defect, which again can be partitioned into its enthalpy H_F^f and entropy S_F^f parts.

3.4.4.2 Diffusion Theory in Ionic Crystals

In most mechanisms of diffusion except the interstitial mechanism, an atom must “wait” for a defect to arrive at a nearest neighbor site before a jump is possible (see Sec. 3.3.4). Thus the jump frequency includes a defect concentration term, e.g., c_v , the vacancy concentration. Let us examine an example for diffusion involving the Frenkel defect. Although both an interstitial and a vacancy are formed, in oxides one of them is likely to be much more mobile, i.e., to have a lower migration energy, than the other. (In the case of stoichiometric UO_2 , for example, theoretical calculation of migration energies suggests a much lower migration energy for the oxygen vacancy than for the interstitial (by either interstitial or interstitialcy mechanisms) (Catlow, 1977).) At the stoichiometric composition,

$$[M_i^{\bullet\bullet}] = [V_M''] \quad (3-190)$$

so that the cation vacancy concentration is given by

$$[V_M''] = c_v = \exp(-G_F^f/2kT) \quad (3-191)$$

$$= \exp(-H_F^f/2kT) \exp(S_F^f/2k) \quad (3-192)$$

The measured activation enthalpy for diffusion will be the migration enthalpy plus *half* the Frenkel defect formation enthalpy. The reader might well ask how we know we are dealing with a Frenkel defect and not a Schottky defect, and if we do know it is the Frenkel defect then how do we know it is the vacancy mechanism that is operating and not the interstitialcy mechanism? In general, we have to rely on independent information, principally computer calculations of defect formation and migration enthalpies, but structural information such as is provided by neutron diffraction and thermodynamic information is also useful.

Another process of interest here is the intrinsic “ionization” process whereby an electron is promoted from the valence band to the conduction band leaving behind a hole in the valence band. In the Kröger-Vink notation, we write for the intrinsic ionization process (the electrons and holes may be localized on the metal atoms)



All ionic crystals are capable, in principle, of becoming nonstoichiometric. The limit of nonstoichiometry is largely dictated by the ease with which the metal ion can change its valence and the ability of the structure to “absorb” defects without reverting to some other structure and thereby changing phase. Nonstoichiometry can be achieved by either 1) an anion deficiency, which is accommodated by either anion vacancies, e.g., UO_{2-x} , or metal interstitials, e.g., $Nb_{1+y}O_2$ or 2) an anion excess, which is accommodated by either anion interstitials, e.g., UO_{2+x} or metal vacancies, e.g.,

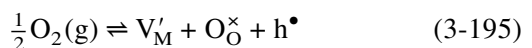
$Mn_{1-y}O$. As an example we will deal with an anion excess accommodated by metal vacancies.

The degree of nonstoichiometry and therefore the defect concentration accompanying it are functions of temperature and partial pressure of the components. The defects produced in this way are sometimes said to be “extrinsic”, but this terminology is probably to be discouraged since they are still strictly intrinsic to the material. In an oxide it is usual, at the temperatures of interest, to consider only the partial pressure of oxygen since it is by far the more volatile of two components. In carbides, where the temperatures of diffusion of interest are much higher, the metal partial pressure can be comparable to the carbon partial pressure and either can be manipulated externally.

The simplest chemical reaction generating nonstoichiometry is



where O_O^\times is a neutral (\times) oxygen ion on an oxygen site and V_M^\times is a neutral metal vacancy. Physically, this corresponds to oxygen being adsorbed on the surface to form ions and more lattice sites, thereby effectively making metal vacancies. These vacancies diffuse in by cation–vacancy exchange until the entire crystal is in equilibrium with the atmosphere. Excess oxygen nonstoichiometry corresponds also to oxidation of the metal ions. Here in this example, the holes produced are conceived to be associated very closely with the metal vacancies. The holes can be liberated, in which case the reaction can now be written



If the hole is then localized at a metal ion, we can consider this as the chemical equivalent of having M^{3+} ions formally present in the sublattice of M^{2+} ions.

Assuming reaction Eq. (3-194) is the preferred one, we find that the equilibrium constant for this reaction is

$$K_1 = \frac{[V_M^\times]}{p_{O_2}^{1/2}} \quad (3-196)$$

thereby immediately showing that the *metal vacancy concentration depends on the partial pressure of oxygen* in the following way:

$$[V_M^\times] = K_1 p_{O_2}^{1/2} \quad (3-197)$$

Accordingly, the metal vacancy concentration is directly proportional to $p_{O_2}^{1/2}$.

Assuming that the reaction in Eq. (3-195) is the preferred one, we find that the equilibrium constant for this reaction is

$$K_2 = \frac{[h^\bullet][O_O^\times][V_M']}{p_{O_2}^{1/2}} \quad (3-198)$$

The concentration of $[O_O^\times]$ is essentially constant and is usually absorbed into K_2 . The condition of electrical neutrality requires that

$$[h^\bullet] = [V_M'] \quad (3-199)$$

thereby showing that the metal vacancy concentration *depends on the partial pressure of oxygen* in the following way:

$$[V_M'] = K_2^{1/2} p_2^{1/4} \quad (3-200)$$

Accordingly, the metal vacancy concentration is directly proportional to $p_{O_2}^{1/4}$.

Let us assume that the migration of metal ions will principally be via vacancies in the nonstoichiometric region, since they are the predominant defect. Since the tracer diffusion coefficient of the metal ions depends directly on vacancy concentration (see Sec. 3.3.4), then the tracer diffusion coefficient will depend on oxygen partial pressure in the same way that either $[V_M^\times]$ or $[V_M']$ does. A measurement of the tracer diffusion coefficient as a function of oxy-

gen partial pressure will expose the actual charge state of the vacancy, i.e., V_M^\times or V_M' .

In practice, this kind of differentiation between charge states and even defect types does not often occur unambiguously. The result of plotting $\log D^*$ versus $\log p_{O_2}$ often does not show precisely one slope and often there is also some curvature. These effects can sometimes be associated with contributions to the diffusion from the three types of vacancy, V_M^\times , V_M' , and V_M'' , e.g., $Co_{1-\delta}O$ (Dieckmann, 1977). Probably the most successful and convincing application of this mass-action law approach has made the defect types in $Ni_{1-\delta}O$ compatible with data from tracer diffusion, electrical conductivity, chemical diffusion, and deviation from stoichiometry/partial pressure (Peterson, 1984).

At higher partial pressures of oxygen, which in some cases such as $Co_{1-\delta}O$, $Mn_{1-\delta}O$, and $Fe_{1-\delta}O$ can result in large deviations from stoichiometry, we can logically expect that defect interactions could play an important role. First, the concentrations in the mass-action equations should be replaced by activities. This so greatly complicates the analysis that progress has been fairly slow. The retention of concentrations rather than activities may be permissible, however, because there is some evidence that non-ideal effects tend to cancel in a $\log D/\log p_{O_2}$ plot (Murch, 1981). At high defect concentrations, defect clustering to form complex defects which themselves might move or act as sources and sinks for more mobile defects, is possible. Two very well-known examples, identified by neutron scattering, are the Koch-Cohen clusters in $Fe_{1-\delta}O$ (Koch and Cohen, 1969) and the Willis cluster in UO_{2+x} (Willis, 1978). Although attempts have been made to incorporate such defects into mass-action equations, it is probably fair to say that the number of adjustable pa-

rameters thereby resulting and the lack of any precise independent information on the mobility or lifetime of the defect complexes make any conclusions reached rather speculative. New statistical mechanical approaches have considerable promise, however (see the review by Murch (1995)).

Somewhat analogous to changing the defect concentration, i.e., deviation from stoichiometry by changing the oxygen partial pressure, is the doping of ionic crystals with ions of a different valence from the host metal ion in order to produce defects. As an example, consider the solubility of an oxide $\mathcal{M}_2\text{O}_3$ in an oxide MO_2 . The implication in the stoichiometry $\mathcal{M}_2\text{O}_3$ is that the \mathcal{M} ions have a valence of +3, compared with +4 for M in the oxide MO_2 . For charge neutrality reasons the doped oxide adopts either oxygen vacancies, metal interstitials, or some electronic defect, the choice being dictated by energetics. Let us consider the first of these:



where \mathcal{M}'_{M} is a \mathcal{M} ion on a M site. The site fraction of oxygen vacant sites is not quite directly proportional to the dopant site fraction because extra normal oxygen sites are created in the process. The diffusion coefficient of oxygen here is proportional to the concentration of vacant oxygen sites.

For very large deviations from stoichiometry, or high dopant concentrations, those extrinsic defects greatly outnumber the intrinsic defects. However, at low dopant concentrations (or small deviations from stoichiometry), all the various mass-action laws must be combined. This complicates the analysis, and space prevents us from dealing with it here. For a more detailed discussion of this and the foregoing, we refer to Kofstad (1972) and Schmalzried (1995).

Generally, cation diffusion in the oxides of the transition metals (which show non-

stoichiometry (cation vacancies) in the cation sublattice) is generally well understood except at large deviations from stoichiometry (see the review by Peterson (1984)). Other oxides such as MgO and Al_2O_3 , although apparently simple, are less well understood because of the low intrinsic defect population and the presence of extrinsic defects coming from impurities (Subbarao, 1985). An understanding of oxygen diffusion in oxides has been hampered by the lack of suitable radioisotopes, but methods using ^{18}O and secondary ion mass spectrometry (SIMS) have rapidly changed the situation (Rothman, 1990). Ionic conductivity (where possible) (see Sec. 3.3.2 for the relation to diffusion) has traditionally been the measurement which has given much more information on oxygen movement; see, for example, the review by Nowick (1984).

3.5 Experimental Methods for Measuring Diffusion Coefficients

In this section we briefly discuss the more frequently used methods of measuring diffusion coefficients.

3.5.1 Tracer Diffusion Methods

By far the most popular and, if performed carefully, the most reliable of the experimental methods for determining “self” and impurity diffusion coefficients is the thin-layer method. Here, a very thin layer of radiotracer of the diffusant is deposited at the surface of the sample. The deposition can be done by evaporation, electrochemical methods, decomposition of a salt, sputtering, etc. The diffusant is permitted to diffuse for a certain time t at high temperature, “high” being a relative term here. If the thickness of the layer de-

posited is much smaller than \sqrt{Dt} , then Eq. (3-8) describes the time evolution of the concentration–depth profile. After diffusion, the concentration–depth profile in the sample is established by sectioning and counting the radioactivity in each section. A number of techniques are available for sectioning. For thick sections $\geq 3 \mu\text{m}$, mechanical grinding is the standard method. Microtomes can be used for sections of about $1 \mu\text{m}$, electrochemical methods for $\geq 5 \text{ nm}$, and sputtering for $\geq 1 \text{ nm}$. The diffusion coefficient is obtained from the slope of the $\ln C(x, t)$ versus x^2 plot (see Eq. (3-8)). Fig. 3-22 shows an exemplary tracer concentration profile of this type (Mundy et al., 1971).

A variant of the method is the “residual activity” or “Gruzin (1952) method”. Rather than counting the activity in each section, the activity remaining in the sample is determined. This requires an integration of Eq. (3-8) and a knowledge of the radiation absorption characteristics of the material. At the limits of very soft or very

hard radiation the method can give comparable accuracy to the counting of sections.

A few elements do not have convenient radioisotopes. The diffusion part of the experiment is still performed in much the same way but now with stable isotopes. In some cases, e.g., ^{18}O , the diffusant source is in the gas phase, although a thin source of oxide containing ^{18}O can be deposited in some cases. After diffusion, nuclear reaction analysis of ^{18}O can be used (see, for example, the review by Lanford et al. (1984)), in order to establish the concentration profile. Much more popular recently, especially for oxygen, is SIMS (see, for example, the reviews by Petuskey (1984), Kilner (1986) and Manning et al. (1996)).

Excellent detailed (and entertaining) expositions and critiques of all methods available for measuring tracer diffusion coefficients in solids have been provided by Rothman (1984, 1990).

3.5.2 Chemical Diffusion Methods

The chemical or interdiffusion coefficient can be determined in a variety of ways. For binary alloys, the traditional method has been to bond together two samples of different concentrations. Interdiffusion is then permitted to occur for a time t and at high temperature. The concentration profile can be established by sectioning and chemical analysis, but since about the late 1960s the use of an electron microprobe has been the usual procedure for obtaining the concentration profile directly. If the compositions of the starting samples are relatively close, and the interdiffusion coefficient is not highly dependent on composition, then analysis of the profile with Eq. (3-12) can lead directly to the interdiffusion coefficient \tilde{D} at the average composition. The more usual procedure is to use

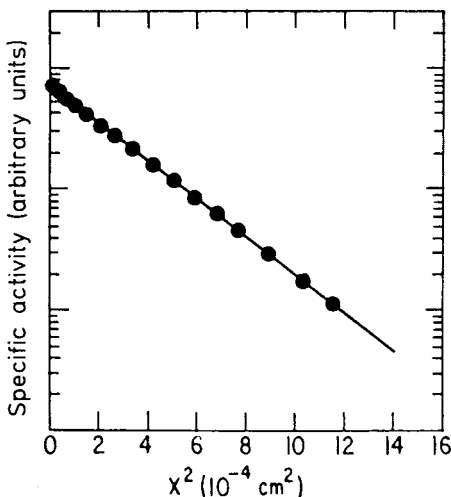


Figure 3-22. A tracer concentration profile for self-diffusion in potassium at 35.5°C (Mundy et al., 1971).

the Boltzmann–Matano graphical integration analysis (see Eqs. (3-13) and (3-14)) to obtain the interdiffusion coefficient and its composition dependence. If fine insoluble wires (to act as a marker) are also incorporated at the interface of the two samples, then the marker shift or Kirkendall shift with respect to the original interface can be measured. This shift, in association with the interdiffusion coefficient, can be used to determine the intrinsic diffusion coefficients of both alloy components *at the composition of the marker* (see Sec. 3.2.2.4).

The rate of absorption or desorption of material from the sample can also be used to determine the chemical diffusion coefficient. This method is useful only where one component is fairly volatile, such as oxygen in some nonstoichiometric oxides and hydrogen in metals. The surface composition is normally assumed to be held constant. The concentration profile can be determined by sectioning or electron microprobe analysis and can be analysed with the aid of Eq. (3-9) to yield the interdiffusion coefficient. The Boltzmann–Matano analysis can be used if there is a composition dependence.

The amount of material absorbed or desorbed from the couple, e.g., weight change, can be used with Eq. (3-11) to yield the interdiffusion coefficient. Eqs. (3-9) and (3-11) refer to situations when \sqrt{Dt} is very small compared with the geometry of the sample, i.e., diffusion into an infinite sample is assumed. When the sample must be assumed to be finite, e.g., fine particles, other, generally more complex, solutions are required; see Crank (1975). A closely related experiment can be performed where the gas phase is *chemically* in equilibrium with the solid, but is dosed with a stable isotope. An example is ^{18}O , a stable isotope of oxygen. The absorption by the solid

of ^{18}O (exchanging with ^{16}O) can be monitored in the gas phase with a mass spectrometer in order to lead to the *tracer* diffusion coefficient of oxygen (see, for example, Auskern and Belle (1961)). A drawback of methods which do not rely on sectioning is the necessary assumption of rapid gas/surface reactions.

3.5.3 Diffusion Coefficients by Indirect Methods

There are a number of methods for obtaining diffusion coefficients that do not depend on solutions of Fick's Second Law. Unfortunately space does not permit a detailed discussion of these. We shall mention them here for completeness and direct the reader to the appropriate sources. Often these methods extend the accessible temperature range for diffusion measurements. In all cases specific *atomic* models need to be introduced in order to extract a diffusion coefficient. Inasmuch as there are inevitably approximations in a model, the resulting diffusion coefficients may not be as reliable as those obtained from a concentration profile. In some cases additional correlation information can be extracted, e.g., nuclear methods. The diffusion coefficients found from these methods are essentially "self" diffusion coefficients but chemical diffusion coefficients for interstitial solutes are obtained from the Gorsky effect.

3.5.3.1 Relaxation Methods

In the relaxation methods net atomic migration is due to external causes such as stress or magnetic field (Nowick and Berry, 1972). The best known phenomena are (a) the Gorsky effect (Gorsky, 1935); for a review see Alefeld et al. (1970) and for an introduction see Borg and Dienes (1988); (b) the Snoek effect (Snoek, 1939); for an ex-

position see Wert (1970) and for an introduction see Borg and Dienes (1988); and (c) the Zener effect (Zener, 1947, 1951); for an introduction see Bocquet et al. (1996).

3.5.3.2 Nuclear Methods

A number of nuclear methods have become of increasing importance for determining diffusion coefficients in solids. The first of these is quasielastic neutron scattering (QNS), which has often been used for situations where the diffusion coefficients are larger than about $10^{-11} \text{ m}^2 \text{ s}^{-1}$ and the diffusing species exhibits a reasonably high scattering cross-section. Most of the applications have been to hydrogen (protonic) in metals (see, for example, Janot et al., 1986). For a detailed introduction to the subject see Lechner (1983) and Zabel (1984). The second method is nuclear magnetic resonance (NMR). NMR is especially sensitive to interactions of the nuclear moments with fields produced by their local environments. Diffusion of a nuclear moment can cause variations in these fields and can significantly affect the observed resonance. In particular, diffusion affects a number of relaxation times in NMR. In favorable cases diffusion coefficients between 10^{-18} and $10^{-10} \text{ m}^2 \text{ s}^{-1}$ are accessible. For a detailed introduction to the subject see Stokes (1984) and Heitjans and Schirmer (1998). We make special mention of pulsed field gradient (PFG) NMR, which has been found to be especially useful for studying anomalous diffusion (Kärger et al., 1998). Finally, we mention Mössbauer spectroscopy (MBS), which shows considerable promise for understanding diffusion processes in solids. The general requirement is that the diffusion coefficient of Mössbauer active isotope should be larger than about $10^{-13} \text{ m}^2 \text{ s}^{-1}$.

Most applications have been to solids incorporating the rather ideal isotope ^{57}Fe . See Mullen (1984) for a detailed discussion of MBS and Vogl and Feldwisch (1998) for several recent examples of applications.

3.5.4 Surface Diffusion Methods

The techniques for measuring surface diffusion are generally quite different from solid-state techniques. For short distance, microscopic or “intrinsic” diffusion (see Sec. 3.2.2.5), the method of choice is the field ion microscope. Much elegant work has been carried out with this technique by Erlich and co-workers; see for example Erlich and Stott (1980) and Erlich (1980). With this method *single* atoms can be imaged and followed. Another method, this time using the field electron microscope (Lifshin, 1992), correlates fluctuations of an emission current from a very small area with density fluctuations arising from surface diffusion in and out of the probe area (Chen and Gomer, 1979). Other methods include quasi-elastic scattering of low energy He atoms (formally analogous to quasi-elastic neutron scattering) and relaxation measurements, making use of deposition of the adsorbate in a non-equilibrium configuration, followed by annealing which permits relaxation to equilibrium. Techniques useful for following the relaxation process at this microscopic level include pulsed molecular beam combined with fast scanning IR interferometry (Reutt-Robey et al., 1988) and work function measurements (Schrammen and Hölzl, 1983).

Many methods exist for long distance or macroscopic diffusion. When the diffusing species is deposited as a source and the appropriate geometries are known then scanning for the concentration profile followed

by processing with the appropriate solution to Fick's Second Law (the Diffusion Equation) Eq. (3-5) will give the mass transfer diffusion coefficient. Radioactive tracers can certainly be used for this (Gjostein, 1970). The concentration profile (in the case of hetero-diffusion) can also be determined using scanning SIMS, local XPS, scanning Auger, scanning EM and scanning STM (Bonzel, 1990). Of interest when the atoms are weakly adsorbed is laser induced thermal desorption (LITD) (Viswanathan et al., 1982). The field electron microscope can be used to image the diffusion front of adatoms migrating into a region of clean surface (Gomer, 1958). Finally, the "capillary method", probably the best known of the macroscopic methods, starts with a perturbed surface, usually in a periodic way, say by sinusoidal grooving. There is now a driving force to minimize the surface Gibbs energy. The time dependence of the decreasing amplitude of, say, the sinusoidal profile, can be processed to give the mass transfer diffusion coefficient; see Bonzel (1990).

The reader is referred to a number of the fine reviews in the area, e.g., Rhead (1989), Bonzel (1990), and the book edited by Vu Thien Binh (1983). The first of these relates surface diffusion to a number of technologically important processes such as thin film growth, sintering, and catalysis. The second is a comprehensive compilation of surface diffusion data on metals and a detailed survey of experimental methods.

3.6 Acknowledgements

I thank my colleagues in diffusion from whom I have learnt so much. This work was supported by the Australian Research Council.

3.7 References

- Adda, Y., Philibert, J. (1966), *La Diffusion dans les Solides*. Paris: Presses Universitaires de France.
- Alefeld, G. J., Völkl, J., Schaumann, G. (1970), *Phys. Status Solidi* 37, 337.
- Allnatt, A. R. (1982), *J. Phys. C15*, 5605.
- Allnatt, A. R., Allnatt, E. L. (1984), *Phil. Mag.* A49, 625.
- Allnatt, A. R., Allnatt, E. L. (1991), *Phil. Mag.* A64, 341.
- Allnatt, A. R., Lidiard, A. B. (1987), *Rep. Prog. Phys.* 50, 373.
- Allnatt, A. R., Lidiard, A. B. (1993), *Atomic Transport in Solids*. Cambridge: Cambridge University Press.
- Arita, M., Koiwa, M., Ishioka, S. (1989), *Acta Metall.* 37, 1363.
- Askil, J. (1970), *Tracer Diffusion Data for Metals, Alloys, and Simple Oxides*. New York: IFI/Plenum.
- Auskern, A. B., Belle, J. (1961), *J. Nucl. Mater.* 3, 267.
- Bakker, H. (1984), in: *Diffusion in Crystalline Solids*: Murch, G. E., Nowick, A. S. (Eds.). New York: Academic, p. 189.
- Bakker, H., Stolwijk, N. A., van der Meij, L., Zuurendonk, T. J. (1976), *Nucl. Metall.* 20, 96.
- Balluffi, R. W. (1984), in: *Diffusion in Crystalline Solids*: Murch, G. E., Nowick, A. S. (Eds.). New York: Academic, p. 320.
- Batchelor, G. K. (1976), *J. Fluid Mech.* 74, 1.
- Beke, D. L. (Ed.) (1998), *Diffusion in Semiconductors and in Non-Metallic Solids*, Vol. 33 (Sub-volume A: Diffusion in Semiconductors), Landolt-Börnstein New Series, Berlin: Springer.
- Beke, D. L. (Ed.) (1999), *Diffusion in Semiconductors and in Non-Metallic Solids*, Vol. 33 (Sub-volume B: Diffusion in Non-Metallic Solids), Landolt-Börnstein New Series, Berlin: Springer.
- Belova, I. V., Murch, G. E. (1997), *Phil. Mag.* A75, 1715.
- Belova, I. V., Murch, G. E. (1998), *Acta Mater.* 46, 849.
- Belova, I. V., Murch, G. E. (2000), *Phil. Mag.* A80, 1469.
- Bénière, M., Chelma, M., Bénière, F. (1976), *J. Phys. Chem. Solids* 37, 525.
- Bérces, G., Kovács, I. (1983), *Phil. Mag.* A48, 883.
- Binh, Vu Thien (Ed.) (1983), *Surface Mobilities on Solid Materials*, NATO-ASI Series B, Vol. 86. New York: Plenum Press.
- Bocquet, J. L. (1972), *Rep. CEA-R-4292*. Saclay (France): Commissariat à l'Energie Atomique.
- Bocquet, J. L. (1987), *Res. Mech.* 22, 1.
- Bocquet, J. L., Brébec, G., Limoge, Y. (1996), in: *Physical Metallurgy*, 4th edn.: Cahn, R. W., Haasen, P. (Eds.). Amsterdam: North Holland, p. 535.
- Boltzmann, L. (1894), *Ann. Phys.* 53, 960.

- Bonzel, H. P. (1990), Diffusion in Metals and Alloys, in: *Landolt-Börnstein*, Vol. 13: Mehrer, H. (Ed.). Berlin: Springer-Verlag.
- Borg, R. J., Dienes, G. J. (1988), *An Introduction to Solid State Diffusion*. New York: Academic.
- Brandes, E. A. (Ed.) (1983), *Smithells Metal Reference Book*, 6th edn. London: Butterworths.
- Carlson, P. T. (1978), *Met. Trans.* A9, 1287.
- Carslaw, H. S., Jaeger, J. C. (1959), *Conduction of Heat in Solids*. New York: Oxford University Press.
- Catlow, C. R. A. (1977), *Proc. Roy. Soc. London, Ser. A* 353, 533.
- Catlow, C. R. A., Mackrodt, W. C. (1982), *Computer Simulation of Solids (Lecture Notes in Physics, Vol. 166)*. Berlin: Springer.
- Chemla, M. (1956), *Ann. Phys. Paris* 13, 959.
- Chen, J. R., Gomer, R. (1979), *Surface Science* 79, 413.
- Chen, W. K., Peterson, N. L. (1972), *J. Phys. Chem. Solids* 33, 881.
- Chen, W. K., Peterson, N. L. (1973), *J. Phys. (Paris)* 34, C9.
- Crank, J. (1975), *The Mathematics of Diffusion*. New York: Oxford University Press.
- Darken, L. S. (1948), *Trans. AIME* 175, 184.
- De Bruin, H. J., Murch, G. E., Bakker, H., Van der Meij, L. P. (1975), *Thin Solid Films* 25, 47.
- Dieckmann, R. (1977), *Z. Phys. Chem. N. F.* 107, 189.
- Dorn, J. E., Mitchell, J. B. (1966), *Acta Metall.* 14, 70.
- Elcock, E. W., McCombie, C. W. (1958), *Phys. Rev.* 109, 605.
- Erlich, G. (1980), *J. Vac. Sci. Technol.* 17, 9.
- Erlich, G., Stott, K. (1980), *Ann. Rev. Phys. Chem.* 31, 603.
- Faupel, F., Hehenkamp, Th. (1986), *Phys. Rev. B* 34, 2116.
- Faupel, F., Hehenkamp, Th. (1987), *Acta Metall.* 35, 771.
- Fisher, J. C. (1951), *J. Appl. Phys.* 22, 74.
- Flynn, C. P. (1972), *Point Defects and Diffusion*. Oxford: Clarendon Press.
- Foiles, S. M., Daw, M. S. (1987), *J. Mater. Res.* 2, 5.
- Frank, F. C., Turnbull, D. (1956), *Phys. Rev.* 104, 617.
- Frank, W., Gösele, U., Mehrer, H., Seeger, A. (1984), in: *Diffusion in Crystalline Solids*: Murch, G. E., Nowick, A. S. (Eds.). New York: Academic, p. 64.
- Fredericks, W. J. (1975), in: *Diffusion in Solids: Recent Developments*: Nowick, A. S., Burton, J. J. (Eds.). New York: Academic, p. 381.
- Freer, R. (1980), *J. Mater. Sci.* 15, 803.
- Friauf, R. J. (1957), *Phys. Rev.* 105, 843.
- Fukai, Y., Sugimoto, H. (1985), *Adv. Phys.* 34, 263.
- Ghate, P. B. (1964), *Phys. Rev. A* 113, 1167.
- Gjostein, N. A. (1970), in: *Techniques of Metals Research*, Vol. IV, Part 2: Bunshah, R. F. (Ed.). New York: Wiley, p. 405.
- Gomer, R. (1958), *Discussions Faraday Soc.* 28, 23.
- Gorsky, W. S. (1935), *Z. Phys. Sowjetunion* 8, 457.
- Gösele, U., Frank, W., Seeger, A. (1980), *Appl. Phys.* 23, 361.
- Gruzin, P. L. (1952), *Dokl. Acad. Nauk. SSSR* 86, 289.
- Gupta, D., Oberschmidt, J. (1984), in: *Diffusion in Solids: Recent Developments*: Dayananda, M. A., Murch, G. E. (Eds.). Warrendale: TMS/AIME, p. 121.
- Gupta, D., Campbell, D. R., Ho, P. S. (1978), In: *Thin Films – Interdiffusion and Reactions*: Poates, J. M., Tu, K. N., Mayer, J. W. (Eds.). New York: Wiley, p. 61.
- Harrison, L. G. (1961), *Trans. Faraday Soc.* 57, 1191.
- Hart, E. W. (1957), *Acta Metall.* 5, 597.
- Hehenkamp, Th., Faupel, F. (1983), *Acta Metall.* 31, 691.
- Hehenkamp, Th., Schmidt, W., Schlett, V. (1980), *Acta Metall.* 28, 1715.
- Heitjans, P., Schirmer, A. (1998), in: *Diffusion in Condensed Matter*: Kärger, J., Heitjans, P., Haberlandt, R. (Eds.). Wiesbaden: Vieweg, p. 116.
- Hempelmann, R. (1984), *J. Less-Common Met.* 101, 69.
- Ho, Y. K. (1982), *Thesis*. London: Imperial College.
- Howard, R. E. (1966), *Phys. Rev.* 144, 650.
- Howard, R. E., Lidiard, A. B. (1964), *Rep. Prog. Phys.* 27, 161.
- Howard, R. E., Manning, J. R. (1967), *Phys. Rev.* 154, 561.
- Huntington, H. B. (1975), in: *Diffusion in Solids: Recent Developments*: Nowick, A. S., Burton, J. J. (Eds.). New York: Academic, p. 303.
- Huntington, H. B., Ghate, P. B. (1962), *Phys. Rev. Lett.* 8, 421.
- Jacucci, G. (1984), in: *Diffusion in Crystalline Solids*: Murch, G. E., Nowick, A. S. (Eds.). New York: Academic, p. 431.
- Jain, H., Gupta, D. (Eds.) (1994), *Diffusion in Amorphous Materials*. Warrendale: TMS.
- Janot, C., Petry, W., Richter, D., Springer, T. (Eds.) (1986), *Atomic Transport and Defects in Materials by Neutron Scattering*. Berlin: Springer-Verlag.
- Jones, M. J., Le Claire, A. D. (1972), *Phil. Mag.* 26, 1191.
- Kaur, I., Mishin, Y., Gust, W. (1995), *Fundamentals of Grain and Interphase Boundary Diffusion*. Chichester: Wiley.
- Kärger, J., Fleischer, G., Roland, U. (1998), in: *Diffusion in Condensed Matter*: Kärger, J., Heitjans, P., Haberlandt, R. (Eds.). Wiesbaden: Vieweg, p. 40.
- Kelly, S. W., Scholl, C. A. (1987), *J. Phys. C* 20, 5293.
- Kikuchi, R., Sato, H. (1969), *J. Chem. Phys.* 51, 161.
- Kikuchi, R., Sato, H. (1970), *J. Chem. Phys.* 53, 2707.
- Kikuchi, R., Sato, H. (1972), *J. Chem. Phys.* 57, 4962.

- Kilner, J. A. (1986), *Mat. Sci. Forum* 7, 205.
- Kirkaldy, J. S., Young, D. J. (1987), *Diffusional in the Condensed State*. Brookfield: The Institute of Metals.
- Koch, F., Cohen, J. B. (1969), *Acta Crystallogr., Sect. B* 25, 275.
- Kofstad, P. (1972), *Nonstoichiometry, Diffusion and Electrical Conductivity in Binary Metal Oxides*. New York: Wiley.
- Kwok, T., Ho, P. S., Yip, S. (1984), *Phys. Rev. B* 29, 5363.
- Lam, N. Q., Rothman, S. J., Mehrer, H., Nowicki, L. J. (1973), *Phys. Status Solidi B* 57, 225.
- Lanford, W. A., Benenson, R., Burman, C., Wielunski, L. (1984), in: *Nontraditional Methods in Diffusion*: Murch, G. E., Birnbaum, H. K., Cost, J. R. (Eds.). Warrendale: TMS/AIME, p. 155.
- Laskar, A. L. (1990), in: *Diffusion in Materials*: Laskar, A. L., Bocquet, J. L., Brébec, G., Monty, C. (Eds.). Dordrecht: Kluwer, Academic, p. 459.
- Laskar, A. L. (1992), in: *Diffusion in Solids: Unsolved Problems*: Murch, G. E. (Ed.). Zürich: Trans. Tech. Publications, p. 207.
- Lechner, R. E. (1983), in: *Mass Transport in Solids*: Bénére, F., Catlow, C. R. A. (Eds.). London: Plenum, p. 169.
- Le Claire, A. D. (1963), *Br. J. Appl. Phys.* 14, 351.
- Le Claire, A. D. (1970), in: *Physical Chemistry – An Advanced Treatise*, Vol. 10: Eyring, H., Henderson, D., Jost, W. (Eds.). New York: Academic, p. 261.
- Le Claire, A. D. (1975), in: *Treatise in Solid State Chemistry*, Vol. 4, Reactivity of Solids: Hannay, N. B. (Ed.). New York: Plenum, p. 1.
- Le Claire, A. D. (1978), *J. Nucl. Mater.* 69/70, 70.
- Le Claire, A. D. (1981), *Phil. Mag.* A 43, 911.
- Le Claire, A. D. (1992), in: *Diffusion in Solids: Unsolved Problems*: Murch, G. E. (Ed.). Zürich: Trans. Tech. Publications, p. 19.
- Le Claire, A. D., Rabinovitch, A. (1984), in: *Diffusion in Crystalline Solids*: Murch, G. E., Nowick, A. S. (Eds.). New York: Academic, p. 259.
- Lidiard, A. B. (1986), *Acta Metall* 34, 1487.
- Lifshin, E. (1992), *Characterization of Materials, Part I, Materials Science and Technology*: R. W. Cahn, P. Haasen, E. J. Kramer (Eds.), Vol. 2A. Weinheim: VCH.
- Lim, S. H., Murch, G. E., Oates, W. A. (1990), *Phil. Mag.* B 61, 337.
- Manning, J. R. (1959), *Phys. Rev.* 113, 1445.
- Manning, J. R. (1964), *Phys. Rev.* 136, 1758.
- Manning, J. R. (1968), *Diffusion Kinetics for Atoms in Crystals*. Princeton: Van Nostrand.
- Manning, J. R. (1970), *Met. Trans.* 1, 499.
- Manning, J. R. (1971), *Phys. Rev.* B 4, 1111.
- Manning, J. R. (1975), in: *Mass Transport in Ceramics*: Cooper, A. R., Heuer, A. H. (Eds.). New York: Plenum, p. 75.
- Manning, P. S., Sirman, J. D., Kilner, J. A. (1996), *Solid State Ionics* 93, 125.
- Matano, C. (1933), *Jpn. Phys.* 8, 109.
- McKee, R. A. (1980a), *Phys. Rev. B* 21, 4269.
- McKee, R. A. (1980b), *Phys. Rev. B* 22, 2649.
- McKee, R. A. (1981), *Phys. Rev. B* 23, 1609.
- Mehrer, H. (1990), *Diffusion in Metals and Alloys, Landolt-Börnstein New Series*, Berlin: Springer.
- Mehrer, H. (1998), in: *Diffusion in Condensed Matter*: Kärger, J., Heitjans, P., Haberlandt, R. (Eds.). Wiesbaden: Vieweg, p. 1.
- Mishin, Y. (1997), *Defect Diffusion Forum* 143–147, 1357.
- Mishin, Y., Herzig, C., Bernardini, J., Gust, W. (1997), *Int. Mat. Reviews* 42, 155.
- Mohan Rao, M., Ranganathan, S. (1984), *Mat. Sci. Forum* 1, 43.
- Moleko, L. K., Allnatt, A. R., Allnatt, E. L. (1989), *Phil. Mag.* A 59, 141.
- Monty, C. (1992), in: *Diffusion in Solids: Unsolved Problems*: Murch, G. E. (Ed.). Zürich: Trans. Tech. Publications, p. 259.
- Mullen, J. G. (1984), in: *Nontraditional Methods in Diffusion*, Murch, G. E., Birnbaum, H. K., Cost, J. R. (Eds.). Warrendale: TMS/AIME, p. 59.
- Mundy, J. N. (1992), in: *Diffusion in Solids: Unsolved Problems*: Murch, G. E. (Ed.). Zürich: Trans. Tech. Publications, p. 1.
- Mundy, J. N., Miller, T. E., Porte, R. J. (1971), *Phys. Rev. B* 3, 2445.
- Murch, G. E. (1975), *J. Nucl. Mater.* 57, 239.
- Murch, G. E. (1981), *J. Phys. Chem. Solids* 42, 227.
- Murch, G. E. (1982a), *Phil. Mag.* A 46, 575.
- Murch, G. E. (1982b), *Phil. Mag.* A 45, 685.
- Murch, G. E. (1982c), *Solid State Ionics* 6, 295.
- Murch, G. E. (1982d), *Solid State Ionics* 7, 177.
- Murch, G. E. (1984a), in: *Diffusion in Crystalline Solids*: Murch, G. E., Nowick, A. S. (Eds.). New York: Academic, p. 379.
- Murch, G. E. (1984b), *Phil. Mag.* A 49, 21.
- Murch, G. E. (1995), *Rad. Effects and Defects in Solids* 134, 1.
- Murch, G. E., Belova, I. V. (1998), in: *Diffusion Mechanisms in Crystalline Materials*: Mishin, Y., Vogl, G., Cowern, N., Catlow, R., Farkas, D. (Eds.). MRS Symposium Proceedings 527. Warrendale: MRS, p. 135.
- Murch, G. E., Catlow, C. R. A. (1987), *J. Chem. Soc., Faraday Trans. II* 83, 1157.
- Murch, G. E., Dyre, J. C. (1989), *CRC Crit. Rev. Solid State Mat. Sci.* 15, 345.
- Murch, G. E., Rothman, S. J. (1979), *Phil. Mag.* A 43, 229.
- Murch, G. E., Rothman, S. J. (1985), *Diffusion Defect Data* 42, 17.
- Murch, G. E., Thorn, R. J. (1978), *Phil. Mag.* A 38, 125.
- Murch, G. E., Thorn, R. J. (1979), *J. Phys. Chem. Solids* 40, 389.
- Murray, A. D., Murch, G. E., Catlow, C. R. A. (1986), *Solid State Ionics* 18/19, 196.

- Nowick, A. S. (1984), in: *Diffusion in Crystalline Solids*: Murch, G. E., Nowick, A. S. (Eds.). New York: Academic, p. 143.
- Nowick, A. S., Berry, B. S. (1972), *Anelastic Relaxation in Crystalline Solids*. New York: Academic.
- Peterson, N. L. (1975), in: *Diffusion in Solids: Recent Developments*: Nowick, A. S., Burton, J. J. (Eds.). New York: Academic, p. 116.
- Peterson, N. L. (1978), *J. Nucl. Mater.* 69/70, 3.
- Peterson, N. L. (1983), *Int. Met. Rev.* 28, 65.
- Peterson, N. L. (1984), *Mater. Sci. Forum* 1, 85.
- Petuskey, W. T. (1984), in: *Nontraditional Methods in Diffusion*: Murch, G. E., Birnbaum, H. K., Cost, J. R. (Eds.). Warrendale: TMS/AIME, p. 179.
- Philibert, J. (1991), *Atom Movements: Diffusion and Mass Transport in Solids*, Paris: Les Editions de Physique.
- Pontikis, V. (1990), in: *Diffusion in Materials*: Laskar, A. L., Bocquet, J. L., Brébec, G., Monty, C. (Eds.). Dordrecht: Kluwer, Academic, p. 37.
- Reutt-Robey, J. E., Doren, D. J., Chabel, Y. J., Christman, S. B. (1988), *Phys. Rev. Lett* 61, 2778.
- Rhead, G. E. (1989), *Int. Materials Reviews* 34, 261.
- Rothman, S. J. (1984), in: *Diffusion in Crystalline Solids*: Murch, G. E., Nowick, A. S. (Eds.). New York: Academic, p. 1.
- Rothman, S. J. (1990), in: *Diffusion in Materials*: Laskar, A. L., Bocquet, J. L., Brébec, G., Monty, C. (Eds.). Dordrecht: Kluwer, Academic, p. 269.
- Rothman, S. J., Peterson, N. L. (1967), *Phys. Rev.* 154, 552.
- Rothman, S. J., Peterson, N. L., Robinson, J. T. (1970), *Phys. Status Solidi* 39, 635.
- Sato, H. (1970), in: *Physical Chemistry – An Advanced Treatise*, Vol. 10: Eyring, H., Henderson, D., Jost, W. (Eds.). New York: Academic, p. 579.
- Sato, H. (1970), in: *Nontraditional Methods in Diffusion*, Murch, G. E., Birnbaum, H. K., Cost, J. R. (Eds.). Warrendale: TMS/AIME, p. 203.
- Sato, H. (1989), in: *Superionic Conductors*: Laskar, A. R., Chandra, S. (Eds.). New York: Academic, p. 439.
- Sato, H., Kikuchi, K. (1971), *J. Chem. Phys.* 55, 677/702.
- Schilling, W. (1978), *J. Nucl. Mater.* 69/60, 465.
- Schmalzried, H. (1995), *Chemical Kinetics of Solids*, Weinheim: VCH.
- Schrammen, P., Hölzl, J. (1983), *Surface Science* 130, 203.
- Seeger, A. (1997), *Defect Diffusion Forum* 143–147, 21.
- Siegel, W. (1978), *J. Nucl. Mater.* 69/70, 117.
- Smith, R. P. (1953), *Acta Metall.* 1, 578.
- Snoek, J. L. (1939), *Physica* 6, 591.
- Stark, J. P. (1972), *J. Appl. Phys.* 43, 4404.
- Stark, J. P. (1974), *Acta Metall.* 22, 1349.
- Stark, J. P. (1976), *Solid State Diffusion*. New York: Wiley.
- Stokes, H. T. (1984), in: *Nontraditional Methods in Diffusion*, Murch, G. E., Birnbaum, H. K., Cost, J. R. (Eds.). Warrendale: TMS/AIME, p. 39.
- SubbaRao, E. C. (1985), *Diffusion Defect Data* 41, 1.
- Suzuoka, T. (1961), *Trans. Jpn. Inst. Met.* 2, 25.
- Vineyard, G. H. (1957), *J. Phys. Chem. Solids* 3, 121.
- Viswanathan, R., Burgess, Jr., D. R., Stair, P. C., Weitz, E. (1982), *J. Vac. Sci. Technol.* 20, 605.
- Vogl, G., Feldwisch, R. (1998), in: *Diffusion in Condensed Matter*: Kärger, J., Heitjans, P., Haberlandt, R. (Eds.), Wiesbaden: Vieweg, p. 144.
- Völkl, J., Alefeld, G. (1975), in: *Diffusion in Solids: Recent Developments*: Nowick, A. S., Burton, J. J. (Eds.). New York: Academic, p. 231.
- Wang, C. C., Akbar, S. A. (1993), *Acta Metall. Mater.* 41, 2807.
- Warburton, W. K., Turnbull, D. (1975), in: *Diffusion in Solids: Recent Developments*: Nowick, A. S., Burton, J. J. (Eds.). New York: Academic, p. 171.
- Wert, C. A. (1970), *J. Phys. Chem. Solids* 31, 1771.
- Willis, B. T. M. (1978), *Acta Crystallogr., Sect. A* 34, 88.
- Zabel, H. (1984), in: *Nontraditional Methods in Diffusion*, Murch, G. E., Birnbaum, H. K., Cost, J. R. (Eds.). Warrendale: TMS/AIME, p. 1.
- Zener, C. (1947), *Phys. Rev.* 71, 34.
- Zener, C. (1951), *J. Appl. Phys.* 22, 372.
- Zhang, L., Oates, W. A., Murch, G. E. (1988), *Phil. Mag.* A58, 937.
- Zhang, L., Oates, W. A., Murch, G. E. (1989a), *Phil. Mag.* B60, 277.
- Zhang, L., Oates, W. A., Murch, G. E. (1989b), *Phil. Mag.* A59, 171.
- Zhang, L., Murch, G. E. (1997), *Defect Diffusion Forum.* 141, 59.

4 Statistical Theories of Phase Transitions

Kurt Binder

Institut für Physik, Johannes Gutenberg-Universität Mainz,
Mainz, Federal Republic of Germany

List of Symbols and Abbreviations	240
4.1 Introduction	245
4.2 Phenomenological Concepts	246
4.2.1 Order Parameters and the Landau Symmetry Classification	246
4.2.2 Second-Order Transitions and Concepts about Critical Phenomena (Critical Exponents, Scaling Laws, etc.)	260
4.2.3 Second-Order Versus First-Order Transitions; Tricritical and Other Multicritical Phenomena	269
4.2.4 Dynamics of Fluctuations at Phase Transitions	277
4.2.5 Effects of Surfaces and of Quenched Disorder on Phase Transitions: a Brief Overview	279
4.3 Computational Methods Dealing with the Statistical Mechanics of Phase Transitions and Phase Diagrams	283
4.3.1 Models for Order–Disorder Phenomena in Alloys	283
4.3.2 Molecular Field Theory and its Generalization (Cluster Variation Method, etc.)	288
4.3.3 Computer Simulation Techniques	293
4.4 Concepts About Metastability	298
4.5 Discussion	303
4.6 References	304

List of Symbols and Abbreviations

A	prefactor of Friedel interaction
a	lattice spacing
a_i	nearest-neighbor distance
\hat{A}, \hat{A}'	critical amplitude of specific heats
B	critical amplitude of the order parameter
c	concentration
C	specific heat
C	phenomenological coefficient
c	lattice spacing in z -direction
c	cluster of geometric configuration
Δc	concentration difference
\hat{C}, \hat{C}'	critical amplitudes of ordering susceptibilities
c_{coex}	concentration at coexistence curve
c_i	concentration of lattice site i
$c_{ijk} \dots$	elastic constants
d	dimensionality
\hat{D}	critical amplitude at the critical isotherm
d^*	marginal dimensionality
E	electric field
\mathbf{e}_i	random vectors
$\mathbf{e}_l(k, x)$	phonon polarization vector
$F[\Phi(x)]$	Helmholtz energy function in operator form
f	factor of order unity
F	Helmholtz energy
ΔF^*	Helmholtz energy barrier
$F(\varphi)$	Helmholtz energy functional
\tilde{F}	scaling function of the Helmholtz energy
f, f^I, \dots, f^{IV}, f	coefficients
F_0	background Helmholtz energy of disordered phase
f_{cg}	coarse-grained Helmholtz energy
$f_{\mu\nu}$	quadrupole moment tensor
F_{reg}	background term of the Helmholtz energy
g	constant factor in the structure function
\mathbf{G}	reciprocal lattice vector
$G(x)$	order parameter correlation function
$\tilde{G}(x/\xi)$	scaling function of the correlation function
\hat{G}	critical amplitude of the correlation function
$G(x, \xi)$	order parameter correlation function
g_{nc}	multispin correlation function
H	ordering field
H	magnetic field
\mathcal{H}	Hamiltonian
\tilde{H}	scaled ordering field

h, h_c	uniform magnetic field, critical value
H_R	random field (due to impurities)
i	number and index for different lattice sites
J	energy gained when two like atoms occupy neighboring sites
J	exchange interaction
\tilde{J}	Fourier transform of the exchange interaction
J_{ij}	exchange interaction between spins at sites i and j (in cases where it is random)
J_m	strength of the magnetic interaction
J_{nn}	nearest-neighbor interaction
J_{nnn}	next-nearest-neighbor interaction
\mathbf{k}	wavevector of phonon
K_1, K_2	phenomenological coefficients
k_B	Boltzmann constant
k_F	Fermi wavenumber
L	coarse-graining length
\mathcal{L}	Lagrangian
M	period (in Fig. 4-10)
M	magnetization
M_l	mass of an atom
m_μ	sublattice magnetization
M_s	spontaneous magnetization
N	degree of polymerization
n_α	lattice sites in state α
p	pressure
P	polarization
p	dielectric polarization
$P(J)$	statistical distribution of random variable J
$P(\{S_i\})$	probability that a configuration $\{S_i\}$ occurs
p_+	probability for spin up
p_-	probability for spin down
p_b	parameter in Landau equation (bicritical points)
Q	normal coordinate
\mathbf{q}_α	primitive vectors of the reciprocal lattice
q_{\max}	value of q where $\chi(q)$ is at a maximum
q^*	nonzero wavenumber
q_{EA}	ordering parameter for the Ising spin glass
r	phenomenological coefficient in the Landau expansion
R	effective range of interaction
R	ratio of J_{nn} and J_{nnn}
R^*	critical radius of a droplet
R_i^l	site of atom l in unit cell i
r, r'	coefficient in the Landau equation
r_c	radius of polymer coil
S	entropy

$S(\mathbf{q})$	structure factor
$S(\mathbf{q}, \omega)$	scattering function
$\mathbf{S}_i, \mathbf{S}_j$	unit vectors in direction of the magnetic moment
t	time
t	reduced temperature $1 - T/T_0$ (in Sec. 4.2.2)
T_0	temperature where r changes sign
T_1	temperature where metastable ordered phase vanishes
T_b	bicritical point
T_c	critical temperature
t_{cr}	reduced temperature at crossover
T_L	Lifshitz point
$T_\lambda(x)$	transition temperature of superfluid ^4He
T_t	temperature of tricritical point
u	phenomenological coefficient
u	coefficient in Landau equation
U	enthalpy
\mathbf{u}_l	displacement vector
U_d	surface of a d -dimensional sphere
v	coefficient in the Landau equation
$v(x)$	Friedel potential
V	total volume of the thermodynamic system
$V(x_i - x_j)$	pairwise interaction of two particles
V_{ab}	interaction between atoms A and B
w	coefficient in the Landau equation
W	action in classical mechanics
$x, x_\nu, x_\mu, x_\alpha$	position vector and its components
z	dynamical critical exponent
z	coordinate (of position vector)
z	coordination number
Z	partition function
δ	scaling variable

α_{1m}, α_2	notation for phases in phase diagram
α_m	magnetic phase
α_n	nonmagnetic phase
$\alpha(x)$	short-range order parameter for metal alloys
α, α'	critical exponents related to specific heat
β	exponent related to the order parameter
$\hat{\Gamma}$	critical amplitude of the susceptibility
γ, γ'	critical exponents related to the susceptibility
Γ_0	phenomenological rate factor
δ	critical exponent at the critical isotherm
$\delta_{\mu\nu}$	Kronecker symbol
ε	binding energy of a particle

ε_{ik}	strain tensor
η	exponent related to the decay of correlations at T_c
λ	wavelength
λ	label of the phonon branch
Λ	factor changing the length scale
μ	chemical potential
μ	magnetic moment per spin
$\Delta\mu$	chemical potential difference
μ_{coex}	chemical potential at phase coexistence
ν	exponent related to the correlation length
ξ	correlation length
ξ_i	concentration difference (Eq. (4-126))
ρ	density
$\varrho(x)$	charge density distribution function
τ	characteristic time
φ	phase shift in Friedel potential
Φ	order parameter
$\Phi(x)$	order parameter density
Φ_i	concentration difference between two sublattices
Φ_{ms}	order parameter of metastable state
Φ_s	spinodal curve
$\chi(q)$	wavevector-dependent susceptibility
χ_{el}	dielectric tensor
χ_T	response function of the order parameter
χ_T	isothermal susceptibility
χ_T	staggered susceptibility
ψ	concentration difference between two sublattices
$\psi^{\text{I,II}}$	ordering parameter for D0_3 structure
ψ_α	amplitude of mass density waves
ω	characteristic frequency (for fluctuations)
$\tilde{\omega}$	scaling function

AF	antiferromagnetic
cg	coarse-grained (as index)
coex	coexistent (as index)
CV	cluster variation method
DAG	dysprosium aluminum garnet
ESR	electron spin resonance
f.c.c.	face-centered cubic
LRO	long-range order
MC	Monte Carlo (method)
MD	molecular dynamics
MFA	mean field approximation
MFA	molecular field approximation

ms	metastable state (as index)
NMR	nuclear magnetic resonance
P	paramagnetic
sc	simple cubic
SRO	short-range order

4.1 Introduction

This chapter deals with the general theoretical concepts of phase transitions of materials and their basis in statistical thermodynamics. This field has seen extensive scientific research over many decades, and a vast amount of literature exists, e.g., the statistical theory of critical point phenomena fills a series of monographs that so far consists of 17 volumes (Domb and Green, 1972–1976; Domb and Lebowitz, 1983–1997). Introductory texts require whole books (Stanley, 1971; Ma, 1976; Patashinskii and Pokrovskii, 1979; Yeomans, 1992), and so does a comprehensive account of the Landau theory of phase transitions (Tolédano and Tolédano, 1987).

This chapter therefore cannot give an exhaustive description of the subject; instead what is intended is a tutorial overview, which gives the flavor of the main ideas, methods, and results, with emphasis on the aspects which are particularly relevant for materials science, and hence may provide a useful background for other chapters in this book. Hence this chapter will contain hardly anything new for the specialist; for the non-specialist it will give an initial orientation and a guide for further reading. To create a coherent and understandable text, a necessarily arbitrary selection of material has been made which reflects the author's interests and knowledge. Reviews containing complementary material have been written by De Fontaine (1979), who emphasizes the configurational thermodynamics of solid solutions, and by Khachaturyan (1983), who emphasizes the theory of structural transformations in solids (which, from a different perspective, are discussed by Bruce and Cowley, 1981). There are also many texts which either concentrate on phase transformations of particular types of materials, such as alloys

(Tsakalakos, 1984; Gonis and Stocks, 1989; Turchi and Gonis, 1994), magnetic materials (De Jongh and Miedema, 1974; Ausloos and Elliott, 1983), ferroelectrics (Blinic and Zeks, 1974; Jona and Shirane, 1962), liquid crystals (Pershan, 1988; De Gennes, 1974; Chandrasekhar, 1992), polymeric materials (Flory, 1953; De Gennes, 1979; Riste and Sherrington, 1989; Binder, 1994; Baus et al., 1995), etc., or on particular types of phase transitions, such as commensurate–incommensurate transitions (Blinic and Levanyuk, 1986; Fujimoto, 1997), multicritical transitions (Pynn and Skjeltorp, 1983), first-order transitions (Binder, 1987a), martensitic transformations (Nishiyama, 1979; Salje, 1990), glass transitions (Jäckle, 1986; Angell and Goldstein, 1986; Cusack, 1987; Zallen, 1983; Zarzycki, 1991), percolation transitions (Stauffer and Aharony, 1992), melting (Baus, 1987), wetting transitions (Dietrich, 1988; Sullivan and Telo da Gama, 1985), metal–insulator transitions (Mott, 1974; Friedmann and Tunstall, 1978), etc. Other approaches focus on particular ways of studying phase transitions: from the random-phase approximation (Brout, 1965) and the effective-field theory (Smart, 1966) to advanced techniques such as field-theoretical (Amit, 1984) or real space renormalization (Burkhardt and van Leeuwen, 1982), and computer simulation studies of phase transitions applying Monte Carlo methods (Binder, 1979, 1984a; Mouritsen 1984; Binder and Heermann, 1988; Binder and Ciccotti, 1996) or the molecular dynamics techniques (Ciccotti et al., 1987; Hockney and Eastwood, 1988; Hoover, 1987; Binder and Ciccotti, 1996), etc. For particular models of statistical mechanics, exact descriptions of their phase transitions are available (Baxter, 1982). Of particular interest also are the dynamics of critical phenomena (Enz, 1979) and the dynamics

of first-order phase transitions (Gunton et al., 1983; Koch, 1984; Binder, 1984b, 1989; Haasen et al., 1984; Zettlemoyer, 1969; Abraham, 1974; Gunton and Droz, 1983; Herrmann et al., 1992). The latter subject is treated in two other chapters in this book (see the Chapters by Wagner et al. (2001) and Binder and Fratzl (2001)) and will not be considered here.

In this chapter, we shall briefly discuss the statistical thermodynamics of phase transitions on a phenomenological macroscopic level (Sec. 4.2), i.e., the Landau theory of first- and second-order transitions, critical and multicritical phenomena, and also the dynamics of fluctuations at phase transitions, and the effects of quenched disorder in solids. The second part (Sec. 4.3) is devoted to the complementary “microscopic” approach, where we start from “model Hamiltonians” for the system under consideration. The statistical mechanics of such models naturally leads to the consideration of some computational methods, i.e., methods based on the molecular field theory and its generalizations, and methods based on computer simulation techniques. Since in solid materials metastable phases

are ubiquitous, e.g., diamond is the meta-stable modification of solid carbon whereas graphite is the stable phase, some comments about the statistical mechanics of metastability are made in Sec. 4.4.

4.2 Phenomenological Concepts

In this section, the main facts of the theory of phase transitions are summarized, and the appropriate terminology introduced. Rather than aiming at completeness, examples which illustrate the spirit of the main approaches will be discussed, including a discussion of critical phenomena and scaling laws.

4.2.1 Order Parameters and the Landau Symmetry Classification

Table 4-1 lists condensed matter systems that can exist in several phases, depending on external thermodynamics parameters such as pressure, p , temperature, T , electric or magnetic fields (E, H). We assume that an extensive thermodynamic variable can be identified (i.e., one that is proportional

Table 4-1. Order parameters for phase transitions in various systems.

System	Transition	Order parameter
Liquid–gas	Condensation/evaporation	Density difference $\Delta \varrho = \varrho_l - \varrho_g$
Binary liquid mixture	Unmixing	Composition difference $\Delta c = c_{\text{coex}}^{(2)} - c_{\text{coex}}^{(1)}$
Nematic liquid	Orientational ordering	$\frac{1}{2} \langle 3 (\cos^2 \theta) - 1 \rangle$
Quantum liquid	Normal fluid \rightleftharpoons suprafluid	$\langle \psi \rangle$ (ψ : wavefunction)
Liquid–solid	Melting/crystallization	ϱ_G (G = reciprocal lattice vector)
Magnetic solid	Ferromagnetic (T_c)	Spontaneous magnetization M
	Antiferromagnetic (T_N)	Sublattice magnetization M_s
Solid binary mixture	Unmixing	$\Delta c = c_{\text{coex}}^{(2)} - c_{\text{coex}}^{(1)}$
AB	Sublattice ordering	$\psi = (\Delta c^{\text{II}} - \Delta c^{\text{I}})/2$
Dielectric solid	Ferroelectric (T_c)	Polarization P
	Antiferroelectric (T_N)	Sublattice polarization P_s
Molecular crystal	Orientational ordering	$Y_{lm}(\vartheta, \varphi)$

to the volume of the system) which distinguishes between these phases (examples are also given in Table 4-1), called the “order parameter”. We shall denote the order parameter as Φ , and the conjugate thermodynamic variable, the “ordering field”, as H . Using the thermodynamic potential, F , which has as “natural variables” a field, H (which is an “intensive” thermodynamic variable, i.e., independent of the volume), and the temperature, T , we have

$$\Phi = -(\partial F / \partial H)_T \quad (4-1)$$

the other derivative being the entropy,

$$S = -(\partial F / \partial T)_H \quad (4-2)$$

As examples, consider a ferromagnet, where the order parameter is the magnetization, M , or a ferroelectric, where the order parameter is the dielectric polarization, P ,

$$M = -(\partial F / \partial H)_T \quad (4-3a)$$

$$P = -(\partial F / \partial E)_T \quad (4-3b)$$

It is clear that such thermodynamic relations can be written for any material, but a quantity qualifies as an “order parameter” when a particular value of the “ordering field” exists where the order parameter exhibits a jump singularity between two distinct values (Fig. 4-1). This means that for these values of the ordering field a first-order phase transition occurs, where a first derivative of the thermodynamic potential F exhibits a singularity. At this transition, two phases can coexist; e.g., at the liquid–gas transition for a chemical potential $\mu = \mu_{\text{coex}}(T)$, two phases with different density coexist; and in a ferromagnet at zero magnetic field, phases with opposite sign of spontaneous magnetization can coexist. Although the fluid-magnet analogy (Fig. 4-1) goes further, since the first-order lines in the (μ, T) or (H, T) plane in both cases end in critical points which may even

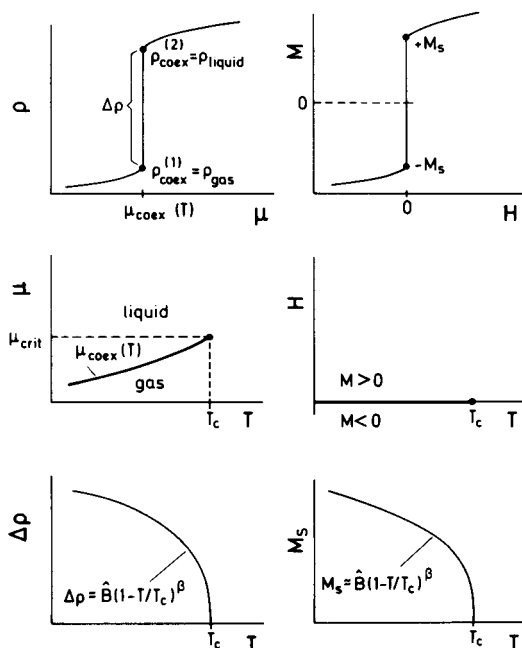


Figure 4-1. The fluid-magnet analogy. On varying the chemical potential μ at $\mu_{\text{coex}}^{(T)}$, the density ρ jumps from the value at the gas branch of the gas–liquid coexistence curve ($\rho_{\text{gas}} = \rho_{\text{coex}}^{(1)}$) to the value at the liquid branch of the coexistence curve ($\rho_{\text{liquid}} = \rho_{\text{coex}}^{(2)}$) (top left). Similarly, on varying the (internal) magnetic field H , the magnetization M jumps from the negative value of the spontaneous magnetization ($-M_s$) to its positive value (top right). While this first-order liquid–gas transition occurs at a curve $\mu_{\text{coex}}(T)$ in the μ – T -plane ending in a critical point (μ_c, T_c) where the transition is then of second order, the curve where phases with positive and negative spontaneous magnetization can coexist simply is $H=0$ ($T < T_c$) (middle). The order parameter (density difference $\Delta\rho$, or spontaneous magnetization M_s) vanishes according to a power law near T_c (bottom).

be characterized by the same critical exponents (see below), there is also an important distinction that in the magnetic problem, the Hamiltonian possesses a symmetry with respect to the change of sign of the magnetic field; reversing this sign and also reversing the sign of the magnetization leave the Hamiltonian invariant. Because of this symmetry, the transition line must occur at $H=0$. Conversely, if the system

at $H=0$ is in a monodomain state with either positive or negative spontaneous magnetization, this symmetry is violated; this is described as “spontaneous symmetry breaking”. No such obvious symmetry, on the other hand, is identified for the liquid–gas transition of fluids. Consequently, the curve $\mu_{\text{coex}}(T)$ is a nontrivial function in the $\mu-T$ -plane, and no simple symmetry operation acting on the gas phase atoms exists that would transform this phase into a liquid, or vice versa. Similar lack of symmetry between the phases is noted for unmixing transitions in binary fluid or solid mixtures, where the order parameter is a concentration difference, $\Delta c = c_{\text{coex}}^{(2)} - c_{\text{coex}}^{(1)}$, cf. Table 4-1, whereas solid binary mixtures which exhibit sublattice ordering do possess a symmetry. The order parameter in an alloy such as brass (β -CuZn) is the difference between the relative concentration of the two sublattices, $\psi = (\Delta c^{\text{II}} - \Delta c^{\text{I}})/2$. However, the two sublattices physically are completely equivalent; therefore, the Hamiltonian possesses a symmetry against the interchange of the two sublattices, which implies that ψ changes sign, just as the (idealized!) ferromagnet does for $H=0$ (Fig. 4-1). In this example of an alloy which undergoes an order–disorder transition where the permutation symmetry between the two sublattices is spontaneously broken, the “ordering field” conjugate to the order parameter is a chemical potential difference between the two sublattices, and hence this ordering field is not directly obtainable in the laboratory. The situation is comparable to the case of simple antiferromagnets, the order parameter being the “staggered magnetization” (=magnetization difference between the sublattices), and the conjugate ordering field would change sign from one sublattice to the other (“staggered field”). Although the action of such fields usually

cannot be measured directly, they nevertheless provide a useful conceptual framework.

Another problem which obscures the analogy between different phase transitions is the fact that we do not always wish to work with the corresponding statistical ensembles. For a liquid–gas transition, we can control the chemical potential via the fluid pressure, and thus a grand-canonical ensemble description makes sense. However, for the binary mixture (AB), the ordering field would be a chemical potential difference $\Delta\mu = \mu_A - \mu_B$ between the species. In an ensemble where $\Delta\mu$ is the externally controlled variable A atoms could transform into B, and vice versa. Experimentally, of course, we do not usually have mixtures in contact with a reservoir with which they can exchange particles freely, instead mixtures are kept at a fixed relative concentration c . (Such an equilibrium with a gas reservoir can only be realized for interstitial alloys such as metal hydrides or oxides.) Thus the experiment is described by a canonical ensemble description, with (T, c) being the independent variables, although the grand-canonical ensemble of mixtures is still useful for analytical theories and computer simulation. Now, as is obvious from Fig. 4-1, in a canonical ensemble description of a fluid, the first-order transition shows up as a two-phase coexistence region. Here, at a given density, ρ , with $\rho_{\text{gas}} < \rho < \rho_{\text{liquid}}$, the relative amounts of the two coexisting phases are given by the lever rule if interfacial contributions to the thermodynamic potential can be neglected. The same is true for a binary mixture with concentration c inside the two-phase coexistence region, $c_{\text{coex}}^{(1)} < c < c_{\text{coex}}^{(2)}$. These different statistical ensembles also have pronounced consequences on the dynamic properties of the considered systems: in binary mixtures at constant con-

centration, and also in fluids at constant density, the order parameter is a conserved quantity, whereas for a fluid at constant chemical potential, the order parameter is not conserved. The latter situation occurs, for instance, for fluid–gas transitions in physisorbed monolayers at surfaces, which can exchange molecules with the surrounding gas phase which is in equilibrium with this adsorbed layer.

An important distinction to which we turn next is the order of a phase transition. In the examples shown in the upper part of Fig. 4-1, a first derivative of the appropriate thermodynamic potential has a jump singularity and therefore such transitions are called *first-order transitions*. However, if we cool a ferromagnet down from the paramagnetic phase in zero magnetic field, the spontaneous magnetization sets in continuously at the critical temperature T_c (lower part of Fig. 4-1). Similarly, on cooling the alloy β -CuZn from the state where it is a disordered solid solution (in the body-centered cubic phase), sublattice ordering sets in continuously at the critical temperature ($T_c = 741$ K, see Als-Nielsen (1976)). Whereas the first derivatives of the thermodynamic potential at these continuous phase transitions are smooth, the second derivatives are singular, and therefore these transitions are also called *second-order transitions*. For example, in a ferromagnet the isothermal susceptibility χ_T and the specific heat typically have power law singularities (Fig. 4-2)

$$\chi_T \equiv -(\partial^2 F / \partial H^2)_T$$

$$\underset{T \rightarrow T_c}{=} \begin{cases} \hat{C}(T/T_c - 1)^{-\gamma}, & T > T_c \\ \hat{C}'(1 - T/T_c)^{-\gamma'}, & T < T_c \end{cases} \quad (4-4)$$

$$C_H \equiv -T(\partial^2 F / \partial T^2)_{H=0}$$

$$\underset{T \rightarrow T_c}{=} \begin{cases} \hat{A}(T/T_c - 1)^{-\alpha}, & T > T_c \\ \hat{A}'(1 - T/T_c)^{-\alpha'}, & T < T_c \end{cases} \quad (4-5)$$

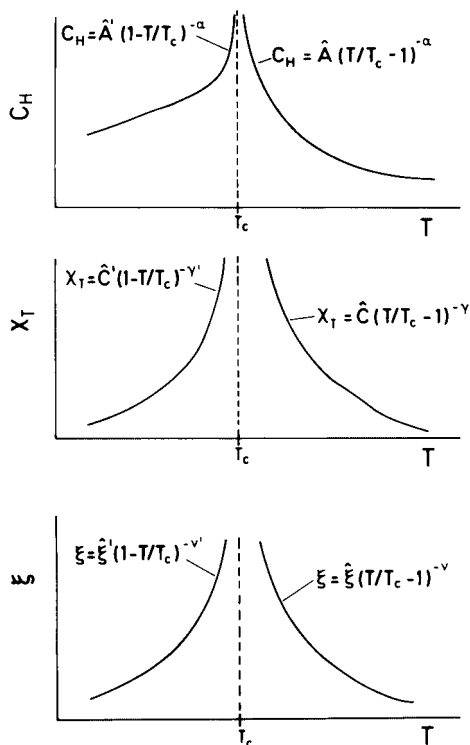


Figure 4-2. Schematic variation with temperature T plotted for several quantities near a critical point T_c : specific heat C_H (top), ordering “susceptibility” χ_T (middle part), and correlation length ξ of order parameter fluctuations (bottom). The power laws which hold asymptotically in the close vicinity of T_c are indicated.

In this context (see also Fig. 4-1), α , α' , β , γ , and γ' are critical exponents, while \hat{A} , \hat{A}' , \hat{B} , \hat{C} , and \hat{C}' are called critical amplitudes. Note that \hat{B} and β refer to the spontaneous magnetization, the order parameter (Fig. 4-1)

$$M_s \underset{T \rightarrow T_c}{=} \hat{B}(1 - T/T_c)^\beta \quad (4-6)$$

Behavior of the specific heat such as described by Eq. (4-5) immediately carries over to systems other than ferromagnets such as antiferromagnets, the liquid–gas system near its critical point, and brass near its order–disorder transition; we must remember, however, that H then means the

appropriate ordering field. In fact, this is also true for Eq. (4-4), but then the physical significance of χ_T changes. For a two-sublattice antiferromagnet, the ordering field is a “staggered field”, which changes sign between the two sublattices, and hence is thermodynamically conjugate to the order parameter of the antiferromagnet. Although such a field normally cannot be applied in the laboratory, the second derivative, χ_T (in this case it is called “staggered susceptibility”) is experimentally accessible via diffuse magnetic neutron scattering, as will be discussed below. Similarly, for the ordering alloy β -CuZn, H stands for a chemical potential difference between the two sublattices; the response function χ_T is again physically meaningful and measures the peak intensity of the diffuse scattering of X-rays or neutrons. (This scattering peak occurs at the superlattice Bragg spot characteristic of the sublattice ordering considered.) Finally, in the gas–liquid transition considered in Fig. 4-1, H is the chemical potential and χ_T the isothermal compressibility of the system.

As will be discussed in more detail in Sec. 4.2.2, the divergences of second derivatives of the thermodynamic potential at a critical point (Eqs. (4-4), (4-5), Fig. 4-2) are linked to a diverging correlation length of order-parameter fluctuations (Fig. 4-2). Hence any discussion of phase transitions must start with a discussion of the order parameter. The Landau theory (Tolédano and Tolédano, 1987) which attempts to expand the thermodynamic potential in powers of the order parameter, gives a first clue to the question of whether a transition is of second or first order (see Sec. 4.2.3).

We first identify the possible types of order parameters, since this will distinctly affect the nature of the Landau expansion. In Eqs. (4-1) and (4-4) to (4-6) we have treated the ordering field H and the order

parameter Φ as scalar quantities; although this is correct for the gas–fluid transition and for the unmixing transition of binary mixtures, the uniaxial ferro- or antiferromagnets, uniaxial ferro- or antiferroelectrics, etc., and for order–disorder transitions in alloys or mixed crystals (solid solutions), when only two sublattices need to be considered, there are also cases where the order parameter must have a vector or tensor character. Obviously, for an isotropic ferromagnet or isotropic ferroelectric the order parameter in the three-dimensional space is a three-component vector (see Eq. (4-3)). It also makes sense to consider systems where a planar anisotropy is present, such that \mathbf{M} or \mathbf{E} (Eq. (4-3)) must lie in a plane and hence a two-component vector applies as an order parameter. However, for describing antiferromagnetic ordering and for order–disorder transitions with many sublattices multicomponent order parameters are also needed, and the number of components of the order parameter, the so-called “order parameter dimensionality”, is dictated by the complexity of the structure, and has nothing to do with the spatial dimension. This is best understood by considering specific examples. Consider, for example, the ordering of Fe–Al alloys (Fig. 4-3): whereas in the disordered A2 phase Fe and Al atoms are randomly distributed over the available lattice sites, consistent with the considered concentration (although there may be some short-range order), in the ordered B2 phase (the FeAl structure) the bcc lattice is split into two inter-penetrating simple cubic (sc) sublattices, one taken preferentially by Fe, the other by Al atoms. This is the same (one-component) ordering as in β -CuZn. What is of interest here is the further “symmetry breaking” which occurs for the D0₃ structure (realized in the Fe₃Al phase): here four face-centered cubic (f.c.c.) sub-

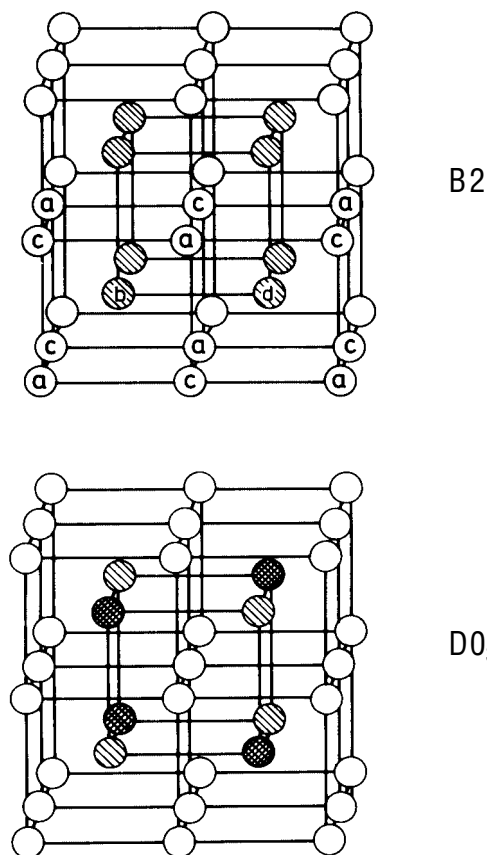


Figure 4-3. Body-centered cubic lattice showing the B2 structure (top) and D0₃ structure (bottom). The top part shows assignments of four sublattices, a, b, c, and d. In the A2 structure, the average concentrations of A and B atoms are identical on all four sublattices whereas in the B2 structure the concentrations at the b and d sublattices are the same (example: stoichiometric FeAl, with Fe on sublattices a and c; Al on sublattices b and d). In the D0₃ structure, the concentrations at the a and c sublattice are still the same, whereas the concentration at sublattice b differs from the concentration at sublattice d (example: stoichiometric Fe₃Al, with Al on sublattice b; all other sublattices taken by Fe). From Dünweg and Binder (1987).

lattices a, b, c, d must be distinguished. Although the concentrations on sublattices a and c are still equivalent, a further symmetry breaking occurs between the sublattices b and d, such that only one sublattice (e.g.,

d) is preferentially occupied by Al, all other sublattices being preferentially occupied by iron. However, the role of the sublattices (a, c) and (b, d) can be interchanged; hence a two-component order parameter is needed to describe the structure, namely (see for example, Dünweg and Binder (1987))

$$\psi^I = m_a - m_c + m_b - m_d$$

$$\psi^{II} = -m_a + m_c + m_b - m_d$$

$$m_\mu \equiv (1/N) \sum_{i \in \mu} (2c_i - 1) \quad (4-7)$$

where c_i is the concentration of lattice site i and m_μ the sublattice “magnetization” in pseudo-spin language. As can be seen as an example of an ordering with $m=8$ components, we can consider the f.c.c. antiferromagnet MnO: as Fig. 4-4 shows, the magnetic structure consists of an antiferromagnet arrangement of ferromagnetically ordered planes. If the ordering were uniaxially anisotropic, we

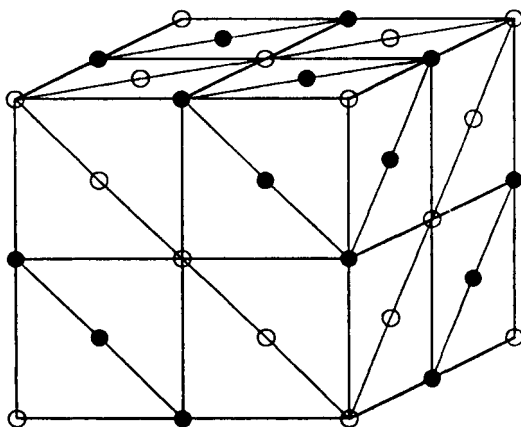


Figure 4-4. Schematic view of the MnO structure, showing the decomposition of the fcc lattice into two ferromagnetic sublattices with opposite orientation of the magnetization (indicated by full and open circles, respectively). Each sublattice is a stack of parallel close-packed planes (atoms form a triangular lattice in each plane). Note that there are four equivalent ways in which these planes can be oriented in an fcc crystal.

would have $m=4$ because of the four possible ways of orienting the planes (and there could be eight kinds of different domains coexisting in the system). Since for MnO the order parameter can take any orientation is a plane, it has two independent components, and hence the total number of order parameter components is $m=8$ (Mukamel and Krinsky, 1976). An even larger number of components is needed to describe the ordering of solid ^3He . In view of this, it is clear that even $m \rightarrow \infty$, which is also called the spherical model (Berlin and Kac, 1952; Joyce, 1972) is a useful limit to consider from the theoretical point of view.

Apart from this m -vector model for the order parameter, Table 4-1 illustrates the need to consider order parameters of tensorial character. This happens in molecular crystals such as para- H_2 (Fig. 4-5), N_2 , O_2 and KCN, in addition to liquid crystals. Whereas the atomic degrees of freedom considered for ferro- or antiferromagnetic order are magnetic dipole moments, for ferro- or antiferroelectric order electric dipole moments, the degree of freedom of the molecules in Fig. 4-5 which now matters is their electric quadrupole moment tensor:

$$f_{\mu\nu} = \int d\mathbf{x} \varrho(\mathbf{x}) \left(x_\mu x_\nu - \frac{1}{3} \sum_{\lambda=1}^3 x_\lambda^2 \delta_{\mu\nu} \right) \quad (4-8)$$

where $\varrho(\mathbf{x})$ is the charge density distribution function of a molecule, $\mathbf{x} = (x_1, x_2, x_3)$, and $\delta_{\mu\nu}$ is the Kronecker symbol.

Proper identification of the order parameter of a particular system therefore needs a detailed physical insight, and often is complicated because of coupling between different degrees of freedom, e.g., a ferromagnetic material which is cubic in the paramagnetic phase may become tetragonal as the spontaneous magnetization develops, owing to magnetostrictive couplings (for a more detailed discussion of this situation,

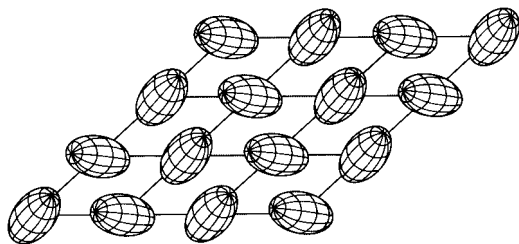


Figure 4-5. Schematic view of a lattice plane of a para- H_2 crystal, indicating the orientational order of the ellipsoid H_2 molecules.

see Grazhdankina (1969)). In this example it is clear that the spontaneous magnetization, \mathbf{M} , is the “primary order parameter” whereas the tetragonal distortion ($c/a-1$), where c is the lattice spacing in the lattice direction where the magnetization direction occurs and a is the lattice spacing perpendicular to it, is a “secondary order parameter”. For purely structural phase transitions where all considered degrees of freedom are atomic displacements, the proper distinction between primary and secondary order parameters is much more subtle (Tolédano and Tolédano, 1987).

We first formulate Landau’s theory for the simplest case, a scalar order parameter density $\Phi(\mathbf{x})$. This density is assumed to be small near the phase transition and slowly varying in space. It can be obtained by averaging a microscopic variable over a suitable coarse-graining volume L^d in d -dimensional space. For example, in an anisotropic ferromagnet the microscopic variable is the spin variable $\Phi_i = \pm 1$ pointing in the direction of the magnetic moment at lattice site i ; in an ordering alloy such as β -CuZn the microscopic variable is the difference in concentration of Cu between the two sublattices I and II in unit cell i , $\Phi_i = c_i^{\text{II}} - c_i^{\text{I}}$; and in an unmixing alloy such as Al–Zn, the microscopic variable is the concentration difference between the local Al concentration at lattice site i ($c_i=1$ if it

is taken by A_1 and $c_i=0$ otherwise) and the critical concentration, $\Phi_i=c_i-c_{\text{crit}}$. In all of these cases $\Phi(\mathbf{x})$ is considered to be an order parameter field defined in continuum space:

$$\Phi(\mathbf{x}) = \sum_{i \in L^d} \Phi_i / L^d \quad (4-9)$$

\mathbf{x} being the center of gravity of the “volume” L^d . The appropriate magnitude of the linear dimension L of the coarse-graining cell will be discussed later; obviously it must be much larger than the lattice spacing in order for the continuum description to make sense. Then a Helmholtz energy functional $F[\Phi(\mathbf{x})]$ is assumed:

$$\begin{aligned} \frac{1}{k_B T} F[\Phi(\mathbf{x})] = & \frac{F_0}{k_B T} \\ & + \int d\mathbf{x} \left\{ \frac{1}{2} r \Phi^2(\mathbf{x}) + \frac{1}{4} u \Phi^4(\mathbf{x}) \right. \\ & \left. - \frac{H}{k_B T} \Phi(\mathbf{x}) + \frac{1}{2d} [R \nabla \Phi(\mathbf{x})]^2 \right\} \end{aligned} \quad (4-10)$$

where F_0 is the background Helmholtz energy of the disordered phase, and r , u , and R are phenomenological constants. (In fact, R can be interpreted as the effective range of interaction between the atomic degrees of freedom Φ_i , as will be seen below.) Obviously, Eq. (4-10) is the Taylor series-type expansion of $F[\Phi(\mathbf{x})]$ in powers of $\Phi(\mathbf{x})$ and $\nabla \Phi(\mathbf{x})$, where just the lowest order terms were kept. This makes sense if both the coefficients u and R^2 are positive constants at T_c , whereas the essential *assumption* which defines Φ as playing the role of an order parameter of a second-order phase transition is that the coefficient r changes its sign at the transition as the variable of interest (the temperature in the present case) is varied,

$$k_B T r = r' (T - T_c) \quad (4-11)$$

Note also that in Eq. (4-10) we have *assumed* a symmetry in the problem against

the change of sign of the order parameter for $H=0$ and thus odd powers such as $\Phi^3(\mathbf{x})$ do not occur; this is true for magnets (no direction of the magnetization is preferred without magnetic field in a ferromagnet) and for sublattice ordering of alloys such as β -CuZn (since whether the Cu atoms preferentially occupy sublattices a, c in Fig. 4-3 or sublattices b, d is equivalent), but it is not true in general (e.g., third-order terms do occur in the description of the Cu_3Au structure, or in the ordering of rare gas monolayers adsorbed on graphite in the $\sqrt{3}$ structure, as will be discussed below).

In order to understand the meaning and use of Eq. (4-10), consider first the fully homogeneous case, $\nabla \Phi(\mathbf{x}) \equiv 0$, $\Phi(\mathbf{x}) \equiv \Phi_0$; then $F[\Phi]$ is the standard Helmholtz energy function of thermodynamics, which needs to be minimized with respect to Φ in order to determine the thermal equilibrium state, and $\int d\mathbf{x} = V$ the total volume of the system. Thus,

$$\frac{1}{k_B T V} \left(\frac{\partial F}{\partial \Phi_0} \right) \bigg|_{T=H=0} = r \Phi_0 + u \Phi_0^3 = 0 \quad (4-12)$$

which is solved by

$$\begin{aligned} \Phi_0 &= 0, & T > T_c \\ \Phi_0 &= \pm (-r/u)^{1/2} & (4-13) \\ &= \pm (r'/k_B u)^{1/2} (T_c/T - 1)^{1/2}, & T < T_c \end{aligned}$$

Hence Eqs. (4-10) and (4-12) indeed yield a second-order transition as T is lowered through T_c . For $T < T_c$, a first-order transition as a function of H occurs, since Φ_0 jumps from $(-r/u)^{1/2}$ to $-(-r/u)^{1/2}$ as H changes sign. This behavior is exactly that shown schematically in Fig. 4-1, with $\beta=1/2$, $\hat{B}=(r'/k_B u)^{1/2}$ and $\Phi_0(H=0)=M_S$.

If $u < 0$ in Eq. (4-10), however, we must not stop the expansion at fourth order but rather must include a term $\frac{1}{6} v \Phi^6(\mathbf{x})$ (assuming now $v > 0$). Whereas in the second-

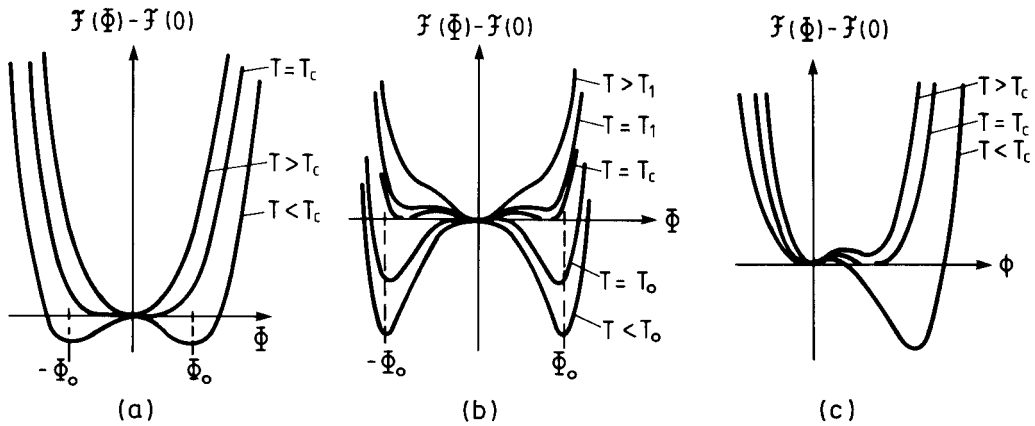


Figure 4-6. Schematic variation of the Helmholtz energy in the Landau model at transitions of (a) second order and (b) first order as a function of the (scalar) order parameter Φ . Cases (a) and (b) assume a symmetry around $\Phi=0$, whereas case (c) allows a cubic term.

order case $F(\Phi)$ has two minima for $T < T_c$ which continuously merge as $T \rightarrow T_c$ and only one minimum at $\Phi=0$ remains for $T > T_c$ (Fig. 4-6a) $F[\Phi]$ now has three minima for $T_0 < T < T_c$, and the temperature T_0 where r changes sign ($r = r'(T - T_0)$ now) differs from the phase transition temperature T_c where the order parameter jumps discontinuously from zero for $T > T_c$ to $(\Phi_0)_{T_c} = \pm(3u/4v)^{1/2}$, see Fig. 4-6b.

These results are found by analogy with Eq. (4-12) from

$$\frac{1}{k_B T V} \left(\frac{\partial F}{\partial \Phi_0} \right) \bigg|_{T=H=0} = \Phi_0 (r + u\Phi_0^2 + v\Phi_0^4) = 0 \quad (4-14)$$

which is solved by

$$\Phi_0^2 = -u/(2v) + \sqrt{(u/2v)^2 - r/v}$$

(choosing the minus sign of the square root would yield the maxima rather than the minima in Fig. 4-6b). On the other hand, we know that $[F - F(0)]/(V k_B T) = 0$ in the disordered phase, and T_c can be found (Fig. 4-6b) from the requirement that the free energy of the ordered phase then is equal to

this value, i.e.,

$$\begin{aligned} & [F(\Phi_0) - F(0)]/(V k_B T) \\ &= \Phi_0^2 \left(\frac{r}{2} + \frac{u}{4} \Phi_0^2 + \frac{v}{6} \Phi_0^4 \right) \bigg|_{T=T_c} = 0 \end{aligned} \quad (4-15)$$

With some simple algebra Eqs. (4-14) and (4-15) yield

$$T_c = T_0 + 3u^2/(32r'v) \quad (4-16)$$

and the “stability limit”, where the minimum describing the metastable ordered phase in the disordered phase above T_c disappears, is given by

$$T_1 = T_0 + u^2/(8r'v) \quad (4-17)$$

The significance of such metastable states as described by the Landau theory for first-order transitions and the associated stability limits T_0 (for the disordered phase at $T < T_c$) and T_1 will be discussed further in Sec. 4.4.

The alternative mechanism by which a first-order transition arises in the Landau theory with a scalar order parameter is the lack of symmetry of F against a sign change of Φ . Then we may add a term $\frac{1}{3}w\Phi^3$ to Eq. (4-10), with another pheno-

menological coefficient, w . For $u > 0$, $F(\Phi)$ may have two minima (Fig. 4-6c); again the transition occurs when the minima are equally deep. For $r = r'(T - T_0)$ this happens when

$$T_c = T_0 + 8w^2/(81ur') \quad (4-18)$$

the order parameter jumping there from $\Phi_0 = -9r/w$ to $\Phi_0 = 0$. Again a stability limit of ordered state in the disordered phase occurs, i.e.

$$T_1 = T_0 + w^2/(4ur') \quad (4-19)$$

At this point, an important caveat should be emphasized: free energy curves involving several minima and maxima as drawn in Fig. 4-6 are used so often in the literature that many researchers believe these concepts to be essentially rigorous. However, general principles of thermodynamics indicate that in thermal equilibrium the thermodynamic potentials are convex functions of their variables. In fact, $F(\Phi_0)$ should thus be convex as a function of Φ_0 , which excludes multiple minima! For Fig. 4-6a and b this means that for $T < T_c$ in states with $-\Phi_0 < \Phi < \Phi_0$ (where Φ_0 is the solution of Eqs. (4-13) or (4-14), respectively) the *thermal equilibrium state* is not a pure homogeneous phase: rather, the minimum free energy state is given by the double-tangent construction to $F(\Phi)$ and this corresponds to a *mixed phase state* (the relative amounts of the coexisting phases are given by the well known lever rule). Now it is standard practice, dating back to van der Waals' interpretation of this equation of state for fluids, to interpret the part of $F(\Phi)$ in Fig. 4-6 which lies above the $F(\Phi)$ given by the double-tangent construction as a metastable state provided that $\chi_T = (\partial^2 F / \partial \Phi^2)_T < 0$, whereas states with $\chi_T < 0$ are considered as intrinsically unstable states. As will be seen in Sec. 4.4, this notion is intrinsically a concept valid

only in mean-field theory, but lacks any fundamental justification in statistical mechanics. Schemes such as those shown in Fig. 4-6 make sense for a local "*coarse-grained free energy function*" only (which depends on the length scale L introduced in Eq. (4-9)), see Sec. 4.2.2, but not for the global free energy.

After this digression we return to the generalization of the Landau expansion, Eq. (4-10), the case where the order parameter has vector or tensor character. How can we find which kinds of term appear in the expansion?

Basically, there are two answers to this question. A general method, which follows below, is a symmetry classification based on group theory techniques (Landau and Lifshitz, 1958; Tolédano and Tolédano, 1987). A very straightforward alternative approach is possible if we consider a particular model Hamiltonian \mathcal{H} (for a brief discussion of some of the most useful models of statistical mechanics for studying phase transitions, see Sec. 4.3.1). We can then formulate a microscopic mean-field approximation (MFA), such as the effective field approximation of magnetism (Smart, 1966) or the Bragg-Williams approximation for order-disorder phenomena in alloys (De Fontaine, 1979), where we then expand the MFA Helmholtz energy directly.

As an example of this approach, we consider a specific model of a ternary alloy where each lattice site i may be taken by either an A, a B, or a C atom, assuming concentrations $c_A = c_B = c_C = 1/3$, and assuming that an energy J is achieved if two neighboring sites are taken by the same kind of atom. This is a special case of the q -state Potts model (Potts, 1952; Wu, 1982), the Hamiltonian being

$$\mathcal{H}_{\text{Potts}} = - \sum_{\langle ij \rangle} J \delta_{S_i, S_j}, \quad S_i = \{1, 2, \dots, q\} \quad (4-20)$$

The states 1, 2, and 3 of the Potts spin stand for the three kinds of atomic species A, B, and C here and $\langle ij \rangle$ denotes a sum over nearest neighbor pairs in the lattice. In the MFA, we construct the Helmholtz energy $F = U - TS$ simply by expressing both enthalpy U and entropy S in terms of the fractions n_α of lattice sites in states α . The entropy is simply the entropy of randomly mixing these species, and, using Stirlings equation, this yields the standard expression (see elementary textbooks on statistical thermodynamics):

$$S = -V \sum_{\alpha=1}^3 n_\alpha \ln n_\alpha \quad (4-21)$$

In the enthalpy term, MFA neglects correlations in the occupation probability of neighboring sites. Hence the probability of finding a nearest neighbor pair in α state is simply n_α^2 , and in a lattice with coordination number z there are $z/2$ pairs per site. Hence

$$U = -\frac{zJV}{2} \sum_{\alpha=1}^3 n_\alpha^2 \quad (4-22)$$

and thus

$$\frac{F}{Vk_B T} = -\frac{zJ}{2k_B T} \sum_{\alpha=1}^3 n_\alpha^2 + \sum_{\alpha=1}^3 n_\alpha \ln n_\alpha \quad (4-23)$$

We could directly minimize F with respect to n_α , subject to the constraint $\sum_{\alpha=1}^3 n_\alpha = 1$, since each site should be occupied. In order to make contact with the Landau expansion, however, we rather expand F in terms of the two order parameter components $\Phi_1 = n_1 - 1/3$ and $\Phi_2 = n_2 - 1/3$ (note that all $n_i = 1/3$ in the disordered phase). Hence we recognize that the model has a two-component order parameter and there is no symmetry between Φ_i and $-\Phi_i$. So cubic terms in the expansion of F are expected and do occur, whereas for a properly defined order parameter, there cannot be any linear term

in the expansion:

$$\begin{aligned} \frac{F}{Vk_B T} = & -\frac{zJ}{6k_B T} - \ln 3 \\ & + 3 \left(1 - \frac{zJ}{3k_B T} \right) (\Phi_1^2 + \Phi_2^2 + \Phi_1 \Phi_2) \\ & + \frac{9}{2} (\Phi_1^2 \Phi_2 + \Phi_1 \Phi_2^2) + \dots \quad (4-24) \end{aligned}$$

As expected, there is a temperature T_0 ($= zJ/3k_B$) where the coefficient of the quadratic term changes sign.

Of course, for many phase transitions a specific model description is not available, and even if a description in terms of a model Hamiltonian is possible, for complicated models the approach analogous to Eqs. (4-20) and (4-24) requires tedious calculation. Clearly the elegant but abstract Landau approach based on symmetry principles is preferable when constructing the Landau expansion. This approach starts from the observation that usually the disordered phase at high temperatures is more “symmetric” than the ordered phase(s) occurring at lower temperature. Recalling the example described in Fig. 4-3, referring to Fe–Al alloys: in the high temperature A2 phase, all four sublattices a, b, c, and d are completely equivalent. This permutation symmetry among sublattices is broken in the B2 phase (FeAl structure) where the concentration on sublattices a, c differs from the concentration on sublattices b, d. A further symmetry breaking occurs when we go from the B2 phase to the DO₃ phase (Fe₃Al structure), where the concentration on sublattice b differs from that on sublattice d. In such cases the appropriate structure of the Landau expansion for F in terms of the order parameter Φ is found from the principle that F must be invariant against all symmetry operations of the symmetry group G_0 describing the disordered phase. In the ordered phase, some symmetry ele-

ments of G_0 fall away (spontaneously broken symmetry); the remaining symmetry elements form a subgroup G of G_0 . Now the invariance of F must hold separately for terms Φ^k of any order k and this requirements fixes the character of the terms that may be present.

Rather than formulating this approach systematically, which would require a lengthy and very mathematical exposition (Tolédano and Tolédano, 1987), we rather illustrate it with a simple example. Suppose a cubic crystal exhibits a transition from a para-electric to a ferroelectric phase, where a spontaneous polarization $\mathbf{P} = (P_1, \dots, P_n)$, $n=3$, appears. F is then given as follows:

$$\begin{aligned} \frac{F[\mathbf{P}(x)]}{k_B T} &= \frac{F_0}{k_B T} + \int d\mathbf{x} \left[\frac{1}{2} \chi_{\text{el}}^{-1} \mathbf{P}^2 \right. \\ &\quad + \frac{1}{4} \left(u \sum_{\mu=1}^n P_{\mu}^4 + u' \sum_{\mu < j=1}^n P_{\mu}^2 P_j^2 \right) + \dots \\ &\quad \left. + \frac{R^2}{2d} \sum_{\mu=1}^n (\nabla P_{\mu})^2 + \dots \right] \quad (4-25) \end{aligned}$$

Whereas the quadratic term of a general dielectric medium would involve the inverse of the dielectric tensor, $\sum_{ij} (\chi_{\text{el}}^{-1})_{ij} P_i P_j$, this term is completely isotropic for cubic crystals. Inversion symmetry requires invariance against $\mathbf{P} \rightarrow -\mathbf{P}$ and hence no third-order term occurs. The fourth-order term now contains the two “cubic invariants” $\sum_i P_i^4$ and $\left(\sum_i P_i^2 \right)^2$. Here we invoke the principle that all terms allowed by symmetry will actually occur. Now Eq. (4-25) leads, in the framework of the Landau theory, to a second-order transition if both

$$u > 0 \quad \text{and} \quad u + u' > 0 \quad (4-26)$$

whereas otherwise we have a first-order transition (then terms of sixth order are needed in Eq. (4-25) to ensure stability).

This approach also carries over to cases where the order parameter is a tensor. For example, for elastic phase transitions (Cowley, 1976; Folk et al., 1976) the order parameter is the strain tensor $\{\varepsilon_{ik}\}$. Applying the summation convention (indices occurring twice in an expression are summed over), the Landau expansion is

$$\begin{aligned} F[\varepsilon_{ik}(\mathbf{x})] &= F_0 + \int d\mathbf{x} \left(\frac{1}{2} c_{iklm} \varepsilon_{ik} \varepsilon_{lm} \right. \\ &\quad + \frac{1}{3} c_{iklmrs}^{(3)} \varepsilon_{ik} \varepsilon_{lm} \varepsilon_{rs} \\ &\quad + \frac{1}{4} c_{iklmrsuv}^{(4)} \varepsilon_{ik} \varepsilon_{lm} \varepsilon_{rs} \varepsilon_{uv} \\ &\quad \left. + \dots + \text{gradient terms} \right) \quad (4-27) \end{aligned}$$

Here the c_{iklm} are elastic constants and $c_{iklmrs}^{(3)}$ and $c_{iklmrsuv}^{(4)}$ analogous coefficients of higher order (“anharmonic”) terms. For most elastic transitions symmetry permits some nonzero $c_{iklmrs}^{(3)}$ and hence leads to first-order transitions. Examples of such systems are the “martensitic transitions” in Nb_3Sn and V_3Si ; there the elastic distortion jumps at the transition from zero to a very small value ($\varepsilon_{ik} \approx 10^{-4}$) and a Landau expansion makes sense. Note that the Landau theory is not very useful quantitatively for transitions which are very strongly first order, since in that case high-order terms in the Taylor expansion are not negligible. More about martensitic phase transformations can be found in the Chapter by Delaey (2001).

Just as in a ferromagnetic transition the inverse magnetic susceptibility χ^{-1} vanishes at T_c (Eq. (4-4)) and in a ferroelectric transition the inverse dielectric susceptibility χ_{el}^{-1} vanishes at T_c (Eq. (4-25)), in a “ferroelastic” transition one of the elastic constants c_{iklm} vanishes at T_0 . For example, in KCN such a softening is observed for the elastic constant c_{44} . Note that this material has already been mentioned as an example of a phase transition where the order parameter is the electric quadrupole moment tensor (Eq. (4-8)), describing the orienta-

tion of the dumbbell-shaped CN^- ions: at the same time, it can be considered as an example for an elastic transition, where the order parameter is the strain tensor ($\varepsilon_{\mu\nu}(\mathbf{x})$)! Such an ambiguity is typical of many first-order transitions, because various dynamical variables (such as a local dielectric polarization $\mathbf{P}(\mathbf{x})$, a local quadrupole moment $f_{\mu\nu}(\mathbf{x})$ and the strain $\varepsilon_{\mu\nu}(\mathbf{x})$) may occur simultaneously in a crystal and are coupled together. In a Landau expansion, such couplings are typically of the bi-quadratic energy–energy coupling type, i.e., various types of mixed fourth-order terms occur, such as $\mathbf{P}^2(\mathbf{x}) \varepsilon_{\mu\nu} \varepsilon_{\mu'\nu'} u_{\mu\nu\mu'\nu'}$. Although this is also true for second-order transitions, there the “primary order parameter” is distinct from the fact that the associate inverse response function χ_T^{-1} vanishes at T_c . For the “secondary order parameters” the corresponding inverse response function stays finite. With first-order transitions, the inverse response function of the primary order parameter would vanish at the hypothetical temperature T_0 (stability limit of the disordered phase), which, however, cannot normally be reached in a real experiment, see Sec. 4.4. K^+CN^- is a good example of such a complicated situation with three local order parameters coupled together, since the CN^- ion also has a dipole moment. After the first-order transition at $T=110$ K from the cubic “plastic crystal” phase (where there is no long-range orientational order, the CN^- dumbbells can rotate) to the tetragonally distorted, orientationally ordered phase, a second first-order transition occurs at $T=80$ K to an antiferroelectric phase where the dipole moments order. In this system, only a microscopic theory (Michel and Naudts, 1977, 1978; De Raedt et al., 1981; Lynden-Bell and Michel, 1994) could clarify that the elastic interaction between the quadrupole moments $f_{\mu\nu}(\mathbf{x})$

(mediated via acoustic phonons) is more important than their direct electric quadrupole–quadrupole interaction. The elastic character of the phase transition is therefore an intrinsic phenomenon for this material.

We briefly discuss the appropriate construction of the order parameter (components) for order–disorder transitions. Fig. 4-3 (and Eq. (4-7)) illustrated how we can visualize the ordered structure in real space, and apply suitable symmetry operators of the point group. However, it is often more convenient to carry through a corresponding discussion of the ordering in reciprocal space rather than in real space (remember that the ordering shows up in superlattice Bragg spots appearing in the reciprocal lattice in addition to the Bragg spots of the disordered phase). For example, consider rare gas monolayers adsorbed on graphite: at low temperatures and pressures, the adatoms form a $\sqrt{3}$ structure commensurate with the graphite lattice. This $\sqrt{3}$ structure can be viewed as a triangular lattice decomposed into three sublattices, such that the adatoms preferentially occupy one sublattice. Mass density waves are taken as an order parameter (Bak et al., 1979; Schick, 1981):

$$\rho(\mathbf{x}) = \sum_{\alpha=1}^3 [\psi_{\alpha} \exp(i\mathbf{q}_{\alpha} \cdot \mathbf{x}) + \psi_{-\alpha} \exp(-i\mathbf{q}_{\alpha} \cdot \mathbf{x})] \quad (4-28)$$

Here the \mathbf{q}_{α} are the three primitive vectors associated with the reciprocal lattice of the rare gas monolayer (a being the lattice spacing of the triangular lattice)

$$\begin{aligned} \mathbf{q}_1 &= \frac{2\pi}{a} \left(0, \frac{1}{\sqrt{3}} \right) \\ \mathbf{q}_2 &= \frac{2\pi}{a} \left(-\frac{1}{2}, -\frac{1}{2\sqrt{3}} \right) \\ \mathbf{q}_3 &= \frac{2\pi}{a} \left(\frac{1}{2}, -\frac{1}{2\sqrt{3}} \right) \end{aligned} \quad (4-29)$$

and ψ_α and $\psi_{-\alpha}$ are the (complex!) order parameter amplitudes. In constructing the free energy expansion with the help of Eq. (4-28), note that the periodicity of the underlying graphite lattice allows invariant “umklapp” terms (the phase factors of third-order terms add up to a reciprocal lattice vector of the graphite lattice). Keeping only those terms in the Landau expansion, and which are nonzero in the $\sqrt{3}$ structure, with the real order parameter components ($i=\sqrt{-1}$)

$$\begin{aligned}\Phi_1 &= \sum_{\alpha=1}^3 (\psi_\alpha - \psi_{-\alpha}) / (2\sqrt{3}) \\ \Phi_2 &= \sum_{\alpha=1}^3 (\psi_\alpha - \psi_{-\alpha}) / (2i\sqrt{3})\end{aligned}\quad (4-30)$$

the expression

$$\begin{aligned}\frac{F}{Vk_B T} &= -\frac{1}{2} r(\Phi_1^2 + \Phi_2^2) \\ &+ \frac{1}{3} w(\Phi_1^3 - 3\Phi_1\Phi_2^2) + \frac{1}{4} u(\Phi_1^2 + \Phi_2^2)^2\end{aligned}\quad (4-31)$$

is obtained. This is equivalent to the result for the three-state Potts model, Eq. (4-24) (Alexander, 1975), after the quadratic form is diagonalized. A three-dimensional analog of this order (where the planes exhibiting $\sqrt{3}$ structure are stacked together to form a hexagonal lattice) occurs in the intercalated compound C_6Li (Guerard and Herold, 1975; Bak and Domany, 1979).

Similarly to the description of the density modulation in the superstructure of adsorbed layers (in two dimensions) or interstitial compounds (in three dimensions) in terms of mass density waves of the adsorbate (or interstitial, respectively), the superstructure ordering in binary alloys can be described in terms of concentration waves (Khachaturyan, 1962, 1963, 1973, 1983; De Fontaine, 1975, 1979). The same concept was used even earlier to describe the magnetic ordering of helimagnetic spin

structures in terms of “*spin density waves*” (Villain, 1959; Kaplan, 1959). We shall outline the connection between this approach and the MFA, generalizing the approach of Eqs. (4-21)–(4-23) slightly, in Sec. 4.3. Here we only mention that these concepts are closely related to the description of structural transitions in solids, where the order parameter can often be considered as a “frozen phonon”, i.e., a displacement vector wave (Bruce and Cowley, 1981). Note also that the approach of concentration waves is not restricted to solids, but can also be used to describe mesophases in fluid block-copolymer melts (Leibler, 1980; Fredrickson and Helfand, 1987; Fredrickson and Binder, 1989; Binder, 1994), see Fig. 4-7, in liquid crystalline polymers, etc.

As a final remark in this section we mention that *not for all phase transitions in solids* there does exist a group–subgroup relationship between the two groups G_1 and G_2 describing the symmetry of the phases coexisting at the transition. These phases cannot be distinguished by an order parameter which is zero in one phase and becomes nonzero in the other. Such transitions must be of first order. Examples of this situation are well known for structural phase transitions, e.g., the tetragonal–orthorhombic transition of $BaTiO_3$ or the “reconstructive” transition from calcite to aragonite (Guymont, 1981). For the so-called “non-disruptive transitions” (Guymont, 1981), the new structure can still be described in the framework of the old structure (i.e., its symmetry elements can be specified, the Wyckoff positions can be located, etc.). Landau-type symmetry arguments still yield information on the *domain structures* arising in such phase transitions (Guymont, 1978, 1981). The tetragonal–orthorhombic transition of $BaTiO_3$ is considered to be an example of such a *non-disruptive transi-*

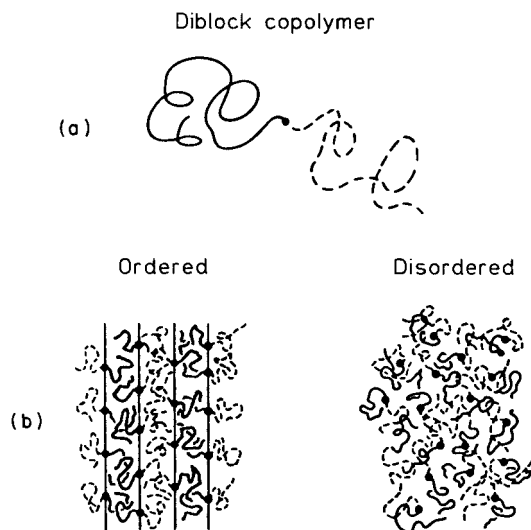


Figure 4-7. (a) Chemical architecture of a diblock copolymer. A diblock copolymer consists of a polymerized sequence of A monomers (A-block) covalently attached to a similar sequence of B monomers. (b) The microphase separation transition occurs when a compositionally disordered melt of copolymers, which are in random coil configurations (right) transforms to a spatially periodic, compositionally inhomogeneous phase (left) on lowering the temperature. For nearly symmetric copolymers the ordered phase has the lamellar structure shown. Since the wavelength of the concentration wave here is of the order of the coil gyration radius, which may be of the order of 100 Å for high molecular weight, the ordering occurs on a “mesoscopic” rather than microscopic scale (Å) and hence such phases are called “mesophases”. From Fredrickson and Binder (1989).

tion, while “reconstructive transitions” and martensitic transformations of the type of the f.c.c.–b.c.t. transition in Fe are “*disruptive*” (see the Chapter by Delaey (2001)). We shall not go into detail about such problems here, however.

4.2.2 Second-Order Transitions and Concepts about Critical Phenomena (Critical Exponents, Scaling Laws, etc.)

We now return to the case where at a critical point the order parameter of a sec-

ond-order transition vanishes continuously (Fig. 4-1). We consider the accompanying critical singularities (Fig. 4-2), in the framework of Landau theory (Eq. (4-10)). For a proper understanding of the critical fluctuations of the order parameter, we must no longer restrict the treatment to the homogeneous case $\nabla\Phi(\mathbf{x}) \equiv 0$ as was done in Eqs. (4-12) and (4-13); we now wish to consider, for example, the response to an inhomogeneous, wavevector-dependent ordering field $H(\mathbf{x})$:

$$H(\mathbf{x}) = H_q \exp(i\mathbf{q} \cdot \mathbf{x}) \quad (4-32)$$

Although for a magnetic transition such a field cannot be directly applied in the laboratory, the action of such fields can be indirectly probed by appropriate scattering measurements, e.g., magnetic neutron scattering. This is because the scattering can be viewed as being due to the inhomogeneous (dipolar) field that the magnetic moment of the neutron exerts on the probe. Therefore, the scattering intensity for a scattering vector \mathbf{q} is related to the wavevector-dependent susceptibility (see Kittel (1967)). Similarly, by the scattering of X-rays the wavevector-dependent response function to the sublattice ordering field can be measured in ordering alloys such as β -CuZn (see Als-Nielsen (1976) for a discussion of such scattering experiments in various systems).

Hence in order to deal with Eq. (4-10) we now have to minimize a functional rather than a simple function as was done in Eq. (4-12). In order to do so, we note that the problem of minimizing $\int d\mathbf{x} f(\psi, \nabla\psi)$ in Eq. (4-10) is analogous to the problem of minimizing the action in classical mechanics, $W = \int dt \mathcal{L}(x, \dot{x})$, where \mathcal{L} is the Lagrangian and $\dot{x} = dx/dt$, the velocity of a particle at point x (t =time). Just as in classical mechanics, where this problem

is solved in terms of the Euler–Lagrange equation

$$(\partial \mathcal{L} / \partial x) - \frac{d}{dt} [\partial \mathcal{L} / \partial (dx/dt)] = 0$$

we conclude here that

$$(\partial f / \partial \psi) - \nabla [\partial f / \partial (\nabla \psi)] = 0$$

in order that the Helmholtz energy functional is a minimum. Eq. (4-10) thus yields

$$r\Phi(\mathbf{x}) + u\Phi^3(\mathbf{x}) + v\Phi^5(\mathbf{x}) - \frac{R^2}{d} \nabla^2 \Phi(\mathbf{x}) = \frac{H(\mathbf{x})}{k_B T} \quad (4-33)$$

Using

$$\Phi(\mathbf{x}) = \Phi_0 + \Delta\Phi(\mathbf{x}) = \Phi_0 + \Delta\Phi_q \exp(i\mathbf{q} \cdot \mathbf{x})$$

Eqs. (4-32) and (4-33) yield, on linearizing in $\Delta\Phi_q$ for small H_q , the wavevector-dependent susceptibility

$$\begin{aligned} \chi(\mathbf{q}) &\equiv \frac{\Delta\Phi_q}{H_q} \\ &= \frac{1}{k_B T} \left[r + 3u\Phi_0^2 + 5v\Phi_0^4 + \frac{R^2}{d} q^2 \right]^{-1} \\ &= \frac{\chi_T}{1 + \xi^2 q^2} \end{aligned} \quad (4-34)$$

From Eq. (4-34) we can simply read off the temperature dependence of the susceptibility χ_T (Eq. (4-4)) and the correlation length ξ of order parameter fluctuations, which is generally expected to behave as

$$\xi = \begin{cases} \hat{\xi}(T/T_c - 1)^{-\nu}, & T > T_c \\ \hat{\xi}'(1 - T_c/T)^{-\nu'}, & T < T_c \end{cases} \quad (4-35)$$

Above T_c , the terms $3u\Phi_0^2 + 5v\Phi_0^4 = 0$, hence

$$\chi_T = \frac{1}{k_B T r} = \frac{1}{r'(T - T_c)} \quad (4-36)$$

$$\xi = \sqrt{R^2/(rd)} = (R/\sqrt{r'd})(T_c - T)^{-1/2}$$

For $T < T_c$, using Eq. (4-13) the term $5v\Phi_0^4$ near T_c is still negligible, and hence

$$\chi_T = \frac{-1}{2k_B T r} = \frac{1}{2r'(T_c - T)} \quad (4-37)$$

$$\xi = \sqrt{R^2/(-2rd)} = (R/\sqrt{2r'd})(T - T_c)^{-1/2}$$

Eqs. (4-36) and (4-37) simply imply the well known Curie–Weiss law, i.e., the exponents γ, γ' , defined in Eq. (4-4), are, in the framework of the Landau theory,

$$\gamma = \gamma' = 1 \quad (4-38)$$

Comparing Eqs. (4-35) and (4-37) we also conclude that

$$\nu = \nu' = 1/2 \quad (4-39)$$

The physical meaning of the correlation length ξ is easily recognized if the well known fluctuation relationship

$$\begin{aligned} \chi(\mathbf{q}) &= \frac{1}{k_B T} \sum_{\mathbf{x}} \exp(i\mathbf{q} \cdot \mathbf{x}) \\ &\quad \times [\langle \Phi(0) \Phi(\mathbf{x}) \rangle - \Phi_0^2] \end{aligned} \quad (4-40)$$

is expanded to second order in \mathbf{q} as

$$\begin{aligned} \chi(\mathbf{q}) &\approx \frac{1}{k_B T} \left\{ \sum_{\mathbf{x}} [\langle \Phi(0) \Phi(\mathbf{x}) \rangle - \Phi_0^2] \right. \\ &\quad \left. - \frac{1}{2} \sum_{\mathbf{x}} (\mathbf{q} \cdot \mathbf{x})^2 [\langle \Phi(0) \Phi(\mathbf{x}) \rangle - \Phi_0^2] \right\} \end{aligned} \quad (4-41)$$

which can be written as

$$\begin{aligned} \chi(\mathbf{q}) &= \frac{1}{k_B T} \sum_{\mathbf{x}} [\langle \Phi(0) \Phi(\mathbf{x}) \rangle - \Phi_0^2] \\ &\quad \times \left\{ 1 - \frac{q^2}{2d} \sum_{\mathbf{x}} x^2 [\langle \Phi(0) \Phi(\mathbf{x}) \rangle - \Phi_0^2] \right. \\ &\quad \left. / \sum_{\mathbf{x}} [\langle \Phi(0) \Phi(\mathbf{x}) \rangle - \Phi_0^2] \right\} \end{aligned} \quad (4-42)$$

Comparing Eqs. (4-34) and (4-42), we find that in terms of the order parameter correlation function $G(\mathbf{x})$,

$$G(\mathbf{x}) = \langle \Phi(0) \Phi(\mathbf{x}) \rangle - \Phi_0^2 \quad (4-43)$$

and χ_T and ξ^2 are related to the zeroth and second moment of the correlation function:

$$\chi_T = \frac{1}{k_B T} \sum_x G(x) \quad (4-44)$$

$$\xi^2 = \frac{1}{2d} \sum_x x^2 G(x) / \sum_x G(x) \quad (4-45)$$

Eq. (4-44) clearly shows that the critical divergence of χ_T occurs because the correlations $G(x)$ become long ranged: whereas off T_c the correlation function for large $|x|$ decays exponentially,

$$\ln G(x) \rightarrow -|x|/\xi, \quad |x| \rightarrow \infty \quad (4-46)$$

at T_c we have a power-law decay of the correlation function:

$$G(x) = \hat{G}|x|^{-(d-2+\eta)}, \quad T = T_c \quad (4-47)$$

The exponent describing this critical decay has been defined such that

$$\eta = 0 \quad (4-48)$$

in the Landau theory, whereas in general $\eta \neq 0$, as will be discussed below.

In order to make our collection of critical exponents complete, we also consider the critical isotherm

$$\Phi_0 = \hat{D}H^{1/\delta}, \quad T = T_c \quad (4-49)$$

Using Eq. (4-33) for a uniform field we conclude that

$$\Phi_0 = (k_B T u)^{-1/3} H^{1/3} \quad (4-50)$$

$$\text{i.e., } \hat{D} = (k_B T u)^{-1/3} \text{ and}$$

$$\delta = 1/3 \quad (4-51)$$

in the framework of the Landau theory. Finally, we turn to the specific heat, Eq. (4-5), which behaves rather pathologically in the Landau theory: for $T > T_c$ and $H = 0$, Eq. (4-10) just implies $F = F_0$, i.e., the specific heat associated with the ordering described by Φ is identically zero above

T_c . For $T < T_c$, we have instead, from Eqs. (4-10) and (4-13)

$$\begin{aligned} \frac{F - F_0}{k_B T V} &= \Phi_0^2 \left(\frac{r}{2} + \frac{u}{4} \Phi_0^2 \right) \\ &= \frac{-r^2}{4u} \approx -r'^2 \frac{(1 - T/T_c)^2}{4k_B^2 u} \end{aligned} \quad (4-52)$$

which implies $C = r'^2 (T/T_c) / (4k_B u)$ for $T < T_c$. This jump singularity of the specific heat at T_c instead of the power law in Eq. (4-5) is formally associated with vanishing critical exponents:

$$\alpha = \alpha' = 0 \quad (4-53)$$

The question must now be asked whether this description of critical phenomena is accurate in terms of the Landau theory. The free energy functional $F[\Phi(x)]$ in Eq. (4-10) should be considered as an effective Hamiltonian from which a partition function Z can be obtained so that the true Helmholtz energy becomes:

$$\begin{aligned} F &= -k_B T \ln Z \\ &= -k_B T \ln \int d[\Phi(x)] \exp \{-F[\Phi(x)]/k_B T\} \end{aligned} \quad (4-54)$$

It is natural to expect that the main contribution to the functional integral comes from the region where the integrand is largest, i.e., the vicinity of the point where $F[\Phi(x)]/k_B T$ has its minimum. If we assume that the distribution over which the average in Eq. (4-54) is a delta function at the value Φ_0 yielding the minimum, i.e., we assume that fluctuations of the order parameter make a negligible contribution to the functional integral, then the minimum of F is equivalent to the minimum of $F(\Phi)$. In general, however, this is not true, as the effects of fluctuations modify the critical behavior drastically, and the Landau theory does not hold for systems such as β -CuZn.

A first hint of the conditions for which the Landau theory is valid can be obtained

by considering the effect of fluctuations within the context of the Landau theory itself. The criterion Ginzburg (1960) suggests is that the Landau theory is valid if the mean-square fluctuation of the order parameter in a correlation volume is small in comparison with the order parameter square itself:

$$\langle [\Phi(\mathbf{x}) - \Phi_0]^2 \rangle_{L=\xi} \ll \Phi_0^2 \quad (4-55)$$

Here L is the *coarse-graining length* introduced in Eq. (4-9) in order to transform the microscopic lattice description of ordering phenomena in solids to a continuum description. On the lattice level, the local order parameter Φ_i shows a rapid variation from one lattice site to the next, and the mean-square fluctuation is very large. For example, for an Ising model of an anisotropic ferromagnet,

$$\mathcal{H}_{\text{Ising}} = -J \sum_{\langle i,j \rangle} S_i S_j - H \sum_i S_i, \quad S_i = \pm 1 \quad (4-56)$$

Where J is the exchange interaction, the sum $\langle i,j \rangle$ extends once over all nearest neighbor pairs, and S_i points in the direction of the local magnetic moment at lattice site i , we have $\Phi_i = S_i$, i.e., $\Phi_i^2 \equiv 1$. In this case $\langle [\Phi_i - \langle \Phi_i \rangle]^2 \rangle = 1 - M_s^2$ is never small in comparison with the square of the spontaneous magnetization M_s^2 near T_c . Carrying out the local averaging defined in Eq. (4-9) reduces this local fluctuation in a “volume” L^d . This averaging should, in principle, be carried out over a length scale L that is much larger than the lattice spacing a but much smaller than the correlation length ξ ,

$$a \ll L \ll \xi \quad (4-57)$$

Whereas for a study of critical phenomena it is permissible to average out local effects on the scale of a lattice spacing, relevant spatial variations do occur on the scale of ξ , as we have seen in Eqs. (4-34) and

(4-46). Replacing the right inequality in Eq. (4-57) by the equality, $L = \xi$, as done in Eq. (4-55), gives therefore the maximum permissible choice for L , for which the fluctuations in Eq. (4-55) are smallest. Even then, however, it turns out that Eq. (4-55) typically is not fulfilled for T close to T_c . In order to see this, we write Eq. (4-55) in terms of the local variable Φ_i and denote the number of lattice sites i contained L^d for the choice $L = \xi$ as $N(t)$, where $t \equiv 1 - T/T_c$. Then Eq. (4-55) becomes

$$\left\langle \left[\sum_{i \in V_\xi(\mathbf{x})} \Phi_i - \langle \Phi_i \rangle \right]^2 \right\rangle \ll \left\langle \sum_{i \in V_\xi(\mathbf{x})} \Phi_i \right\rangle^2 \quad (4-58)$$

where we have denoted the volume of size $L = \xi$ centered at \mathbf{x} as $V_\xi(\mathbf{x})$. Making use of the translational invariance of correlation functions and $\langle \Phi_i \rangle = M_s(t)$, the spontaneous order parameter which is independent of i , Eq. (4-58) becomes

$$N(t) \sum_{i \in V_\xi(\mathbf{x})} [\langle \Phi_{i=0} \Phi_i \rangle - M_s^2(t)] \ll N^2(t) M_s^2(t) \quad (4-59)$$

If the sum over correlations in Eq. (4-59) were to extend over all space, it would simply be the “susceptibility” $k_B T \chi(t)$ (see Eq. (4-42)). Since the sum does contain just the volume region over which the Φ_i s are strongly correlated with each other, the sum clearly is of the order of $f k_B T \chi(T)$, where $f < 1$ is a factor of order unity, which should have no critical (vanishing or divergent) temperature dependence as $T \rightarrow T_c$. Hence in the inequality Eq. (4-59) this factor may also be omitted, and we conclude (Als-Nielsen and Laursen, 1980) that

$$\chi(t) \ll N(t) \ll M_s^2(t) \quad (4-60a)$$

Making use of $N(t) = [\xi(t)/a]^d$, a being the lattice spacing, we obtain:

$$\text{const.} \ll [\xi(t)]^d M_s^2(t) \chi^{-1}(t) \quad (4-60b)$$

where in suitable units the constant on the left-hand side of the equality is of order unity. Using Eqs. (4-4), (4-6), and (4-35) we obtain (anticipating $\gamma = \gamma'$ and $\nu = \nu'$)

$$\text{const.} \ll t^{-\nu d + 2\beta + \gamma} \quad (4-61)$$

Inserting the Landau values for the critical exponents $\beta = 1/2$, $\nu = 1/2$, $\gamma = 1$ and knowing the critical amplitude of $\xi \sim R$, the interaction range, Eq. (4-60) implies

$$\text{const.} \ll (R/a)^d t^{(d-4)/2} \quad (4-62)$$

This condition for the validity of the Landau theory for $d < 4$ always breaks down as $t \rightarrow 0$ ($T \rightarrow T_c$). In fact, for $d < 4$ close enough to T_c a regime occurs where fluctuations dominate the functional integral (Eq. (4-54)). The “crossover” from the mean-field regime (where the Landau description is essentially appropriate) to the non-mean-field regime occurs at a reduced temperature distance $t = t_{cr}$, where Eq. (4-62) is treated as an equality: for $d = 3$,

$$t_{cr} \sim (R/a)^{-6} \quad (4-63)$$

Hence systems with a large but finite range of interaction behave in an essentially Landau-like manner. An example of such a behavior is the unmixing critical point in polymer fluid mixtures with a high degree of polymerization N : since each coil has a radius $r_c \sim N^{1/2}$, the monomer density inside the sphere taken by a polymer coil is only of order $\varrho \sim N/r_c^3 \sim N^{-1/2}$, which implies that each coil interacts with $N^{1/2}$ neighbor coils, and the effective interaction volume $(R/a)^d$ in Eqs. (4-62) and (4-63) should be taken as $N^{1/2}$, i.e., $t_{cr} \sim N^{-1}$ (De Gennes, 1979; Binder 1984c, 1994).

At this point, we emphasize that using $N(t) = [\xi(t)/a]^d$ in Eq. (4-60) is not valid in systems with long-range anisotropic interactions, such as uniaxial dipolar magnets. For a system such as LiTbF_4 (Als-Nielsen

and Laursen, 1980), the essential part of the magnetic Hamiltonian is a magneto-static dipole-dipole interaction,

$$\mathcal{H} = -\mu^2 \sum_{i \neq j} \frac{3z^2 - \mathbf{x}^2}{|\mathbf{x}|^5} S_i S_j, \quad S_i = \pm 1 \quad (4-64)$$

where μ is the magnetic moment per spin and z the coordinate of \mathbf{x} in the direction of the uniaxial anisotropy. Unlike the isotropic Ising Hamiltonian in Eq. (4-56), here the sign of the interaction depends on the direction in the lattice. Therefore, fluctuations display an essential anisotropy: instead of the isotropic result (Eq. (4-34)) of the well known Ornstein-Zernike type, the wavevector-dependent susceptibility $\chi(\mathbf{q}) = S(\mathbf{q})/k_B T$ ($S(\mathbf{q})$ = structure factor) becomes anisotropic:

$$S(\mathbf{q}) \sim [\xi^{-2} + q^2 + g(q_z/q)^2]^{-1} \quad (4-65a)$$

where q_z is the z -component of \mathbf{q} and g is a constant. Whereas Eq. (4-32) implies that $S(q, \xi=1) = S(q=0)/2$, the equation $q\xi=1$ which for Eq. (4-32) defines a sphere of radius ξ^{-1} in \mathbf{q} -space now defines an anisotropic surface. From

$$\xi^{-2} = q^2 + g(q_z/q)^2 \quad (4-65b)$$

we obtain an object having the shape of a flat disc, with radius $1/\xi$ in the $q_x - q_y$ plane but maximum extension of order $1/\xi^2$ in the q_z direction. This object, defined by $S(\mathbf{q}) = \frac{1}{2} \max \{S(\mathbf{q})\}$, can be interpreted as the Fourier transform of the correlation volume. This implies that the correlation volume in real space is a long ellipsoid, with linear dimensions ξ in the q_x, q_y direction but with linear dimension ξ^2 in the q_z direction. In d -dimensions, this argument suggests for uniaxial dipolar systems:

$$N(t) = [\xi(t)/a]^{d+1} \quad (4-66)$$

which yields in Eq. (4-60)

$$\text{const.} \ll t^{-\nu(d+1)+2\beta+\gamma} = t^{-(d-3)/2} \quad (4-67)$$

where in the last equality, the Landau exponents have been used. Comparing Eqs. (4-61) and (4-67) shows that d -dimensional uniaxial dipolar systems somehow correspond to $(d+1)$ -dimensional systems with isotropic short-range forces. Therefore the marginal dimension d^* , above which the Landau theory predicts the values of critical exponents correctly, is $d^*=3$ for uniaxial dipolar systems, unlike the standard isotropic short-range case where $d^*=4$.

For elastic phase transitions in cubic crystals where the combination of elastic constants $c_{11}-c_{12}$ softens as the critical point is approached, such as the system PrAlO_3 , the structure factor $S(\mathbf{q})$ has the form:

$$S(\mathbf{q}) \sim [\xi^{-2} + q^2 + A(q_z/q)^2 + B(q_\perp/q)^2]^{-1} \quad (4-68)$$

where $\mathbf{q}=(q_z, \mathbf{q}_\perp)$ and A and B are constants. In this case the correlation volume defined from the condition $S(\mathbf{q}) = \frac{1}{2} \max \{S(\mathbf{q})\}$ in real space is a flat disk with radius ξ^2 and diameter ξ , i.e., for elastic systems:

$$N(t) = [\xi(t)/a]^{d+2} \quad (4-69)$$

In this case, the Ginzburg criterion, Eq. (4-60), yields

$$\text{const.} \ll t^{-\nu(d+2)+2\beta+\gamma} = t^{-(d-2)/2} \quad (4-70)$$

instead of Eqs. (4-62) or (4-67), respectively. Since the marginal dimensionality for such systems is $d^*=2$, three-dimensional systems should be accurately described by the Landau theory, and this is what is found experimentally for PrAlO_3 . Examples for elastic phase transitions which are of second order are scarce, as is understandable from the symmetry considerations which lead to first-order transitions in most cases (Cowley, 1976; Folk et al., 1976). However, for many first-order ferroelastic transitions the Landau description also fits the experimental data very

well over a wide temperature range (Salje, 1990).

For all other systems we do not expect the Landau critical exponents to be an accurate description of the critical singularities. This is borne out well by the exact solution for the two-dimensional Ising model (Onsager, 1944; McCoy and Wu, 1973), where the critical exponents have the values

$$\alpha = 0 \text{ (log)}, \quad \beta = 1/8, \quad \gamma = 7/4, \\ \delta = 15, \quad \nu = 1, \quad \eta = 1/4 \quad (4-71)$$

Obviously, these numbers are a long way from the predictions of the Landau theory. Note that $\alpha = 0$ in Eq. (4-71) has the meaning $C \sim |\log |t||$, unlike the jump singularity of the Landau theory.

Even in the marginal case of uniaxial dipolar ferromagnets (or uniaxial ferroelectrics; see, e.g., Binder et al. (1976) for a discussion), the Landau theory is not completely correct; it turns out (Larkin and Khmel'nitskii, 1969; Aharony, 1976) that the power laws have the Landau form but are modified with logarithmic correction factors:

$$\chi_T = \hat{F}_\pm t^{-1} |\ln t|^{1/3}, \quad t \rightarrow 0 \quad (4-72a)$$

$$C = \hat{A}_\pm |\ln t|^{1/3}, \quad t \rightarrow 0 \quad (4-72b)$$

$$M_s = \hat{B}(-t)^{1/2} |\ln(-t)|^{1/3}, \quad t \rightarrow 0 \quad (4-72c)$$

$$M_s|_{T_c} = \hat{D} H^{1/3} |\ln H|^{1/3}, \quad H \rightarrow 0 \quad (4-72d)$$

Although for uniaxial ferroelectrics the experimental evidence in favor of Eq. (4-72) is still scarce, convincing experimental evidence does exist for dipolar ferromagnets such as LiTbF_4 (see, e.g., Als-Nielsen and Laursen (1980) for a review).

Eq. (4-72) results from including fluctuation contributions to the functional integral in Eq. (4-54) systematically, which can be done in a most powerful way by renormalization group theory (Aharony, 1973, 1976; Fisher, 1974; Wilson and Kogut,

1974; Ma, 1976; Amit, 1984; Yeomans, 1992). A description of this theory is beyond the scope of this chapter; we only mention that it is this method which yields highly accurate approximations for the values of critical exponents of three-dimensional systems. For example, for the uniaxial magnets (as described by the Ising Hamiltonian, Eq. (4-56), experimental examples being the antiferromagnets MnF_2 or FeF_2) or the ordering alloy β -brass, the exponents are predicted to be (LeGuillou and Zinn-Justin, 1980):

$$\alpha \approx 0.110, \quad \beta \approx 0.325, \quad \gamma \approx 1.240, \\ \delta \approx 4.82, \quad \nu \approx 0.63, \quad \eta \approx 0.032 \quad (4-73)$$

Whereas within the Landau theory the “order parameter dimensionality” n does not matter, as far as the values of the critical exponents are concerned, n does matter if we go beyond the Landau theory. For example, for isotropic magnets as described by the well known Heisenberg model of magnetism,

$$\mathcal{H}_{\text{Heis}} = - \sum_{i \neq j} J_{ij} \mathbf{S}_i \cdot \mathbf{S}_j - \mu H \sum \mathbf{S}_i^z \quad (4-74)$$

\mathbf{S}_i being a unit vector in the direction of the magnetic moment at lattice site i , we have (LeGuillou and Zinn-Justin, 1980):

$$\alpha \approx -0.116, \quad \beta \approx 0.365, \quad \gamma \approx 1.391, \\ \delta \approx 4.82, \quad \nu \approx 0.707, \quad \eta \approx 0.034 \quad (4-75)$$

Again these results are in fair agreement with available experimental data, such as the isotropic antiferromagnet RbMnF_3 (see Als-Nielsen (1976) for a review of experiments on critical point phenomena). Note that the negative value of α in Eq. (4-75) implies that the specific heat has a cusp of finite height at T_c .

The renormalization group theory also provides a unifying framework and justification for two important concepts about critical phenomena, namely “scaling” and

“universality”. Again we wish to convey only the flavor of the idea to the reader, rather than to present a thorough discussion. Consider, for example, the decay of the correlation function of order parameter fluctuations at the critical point, Eq. (4-47): changing the length scale from r to $r' = \Lambda r$ would change the prefactor \hat{G} but leave the power-law invariant. The physical interpretation of this fact is the “fractal structure” of critical correlations (Mandelbrot, 1982): just as a fractal geometric object looks the same on every length scale, the pattern of critical fluctuations looks the same, irrespective of the scale. Slightly off T_c , then, there should be only one relevant length scale in the problem, the correlation length ξ , which diverges as $T \rightarrow T_c$, and details such as the precise behavior of the correlation functions for interatomic distances should not matter. As a result, it is plausible that the correlation function $G(x, \xi)$ should depend only on the ratio of the two lengths x and ξ , apart from a scale factor:

$$G(x, \xi) = \hat{G} x^{-(d-2+\eta)} \tilde{G}(x/\xi) \quad (4-76)$$

Obviously, the condition $\tilde{G}(0)=1$ for the “scaling function” $\tilde{G}(x/\xi)$ ensures that Eq. (4-76) crosses over smoothly to Eq. (4-47) as $T \rightarrow T_c$, where $\xi \rightarrow \infty$.

From the “scaling hypothesis” in Eq. (4-76) we immediately derive a “scaling law” relating the exponents γ , ν and η . Using Eq. (4-44) and denoting the surface of a d -dimensional unit sphere as U_d ($U_d = 4\pi$ in $d=3$) we obtain

$$\chi_T = \frac{1}{k_B T} \sum_x G(x) \approx \frac{\tilde{G}}{k_B T_c} \int G(x, \xi) dx \\ = \frac{U_d \hat{G}}{k_B T_c} \int_0^\infty x^{1-\eta} \tilde{G}(x/\xi) dx \\ = \xi^{2-\eta} \frac{U_d \hat{G}}{k_B T_c} \int_0^\infty \delta^{1-\eta} \tilde{G}(\delta) d\delta \quad (4-77)$$

Since the integral over $\beta = x/\xi$ in Eq. (4-77) yields a constant, we conclude

$$\chi_T \sim \xi^{(2-\eta)} \sim |t|^{-\nu(2-\eta)} \sim |t|^{-\gamma}$$

cf. Eqs. (4-4) and (4-35). Thus the scaling relation results in

$$\gamma = \nu(2 - \eta) \quad (4-78)$$

Eq. (4-76) indicates that $G(x, \xi)$ depends on the two variables x and ξ in a rather special form, namely, it is a homogeneous function. A similar homogeneity assumption is also true for the singular part of the free energy,

$$F = F_{\text{reg}} + t^{2-\alpha} \tilde{F}(\tilde{H}), \quad \tilde{H} = H \hat{\Gamma} t^{-\gamma-\beta/\hat{B}} \quad (4-79)$$

where the singular temperature dependence for $\tilde{H}=0$ is chosen to be compatible with Eq. (4-5), F_{reg} is a background term which is analytic in both T and H even for $T=T_c$, while $\tilde{F}(\tilde{H})$ is another “scaling function”. At this point, we present Eq. (4-79) as a postulate, but it should be emphasized that both Eqs. (4-76) and (4-79) can be justified from Eq. (4-54) by the renormalization group approach.

Combining Eqs. (4-1) and (4-79) we obtain:

$$\Phi = -(\partial F / \partial H)_T = -\frac{\hat{\Gamma}}{\hat{B}} t^{(2-\alpha-\gamma-\beta)} \tilde{F}'(\tilde{H}) \quad (4-80)$$

Defining $-(\hat{\Gamma}/\hat{B}) \tilde{F}'(\tilde{H}) \equiv \hat{B} \tilde{M}(\tilde{H})$ with $\tilde{M}(0)=1$, we obtain:

$$\Phi = \hat{B} t^\beta \tilde{M}(\tilde{H}), \quad \beta = 2 - \alpha - \gamma - \beta \quad (4-81)$$

since for $\tilde{H}=0$, Eq. (4-80) must reduce to Eq. (4-6). Taking one more derivative we find

$$\chi_T = (\partial \Phi / \partial H)_T = \hat{\Gamma} t^{-\gamma} \tilde{M}'(\tilde{H}) \quad (4-82)$$

hence Eq. (4-79) is compatible with Eq. (4-4), as it should be. The condition that Eq. (4-81) reduces to the critical isotherm for $t \rightarrow 0$ requires that $\tilde{M}(\tilde{H} \rightarrow \infty) \sim \tilde{H}^{\beta/(\gamma+\beta)}$, in order that the powers of t

cancel out. On the other hand, this also yields

$$\Phi|_{T=T_c} \sim H^{1/(1+\gamma/\beta)} = H^{1/\delta},$$

$$\text{i.e., } \delta = 1 + \gamma/\beta \quad (4-83)$$

The scaling assumptions also imply that exponents above and below T_c are equal, i.e., $\alpha = \alpha'$, $\gamma = \gamma'$, and $\nu = \nu'$. Now there is still another scaling law which results from considering all degrees of freedom inside a correlation volume ξ^d to be highly correlated with each other, while different correlation volumes can be considered as essentially independent: this argument suggests that the singular part of the Helmholtz energy per degree of freedom can be written as $F_{\text{sing}} \approx [1/N_s(t)] \times \text{const.}$, since independent degrees of freedom do not contribute any singular free energy. Since

$$N_s(t) \sim \xi^d \sim |t|^{-d\nu}$$

we conclude, by comparison with Eq. (4-79), that

$$d\nu = 2 - \alpha \quad (4-84)$$

Note that this so-called “hyperscaling relation” with the Landau-theory exponents is only true at the marginal dimension $d^*=4$, whereas the other scaling relationships obviously are fulfilled by Landau exponents independent of the system dimensionality. However, all scaling relationships (including Eq. (4-84)) are satisfied for the two- and three-dimensional Ising model (Eqs. (4-71) and (4-73)) and the three-dimensional Heisenberg model, Eq. (4-75).

Let us consider the two-dimensional Heisenberg model. For this model the effects of statistical fluctuations are so strong that they destabilize the ordering altogether: no spontaneous ordering exists in $d=2$ for any system with order parameter dimensionality $n \geq 2$, and a critical point occurs only at zero temperature, $T_c=0$, for

$n > 2$. Thus $d=2$ is the “lower critical dimensionality” d_1 for $n \geq 2$, whereas for $n=1$ we have $d_1=1$: quasi-one-dimensional orderings are always unstable. The case $n=2, d=2$ is very special: a phase transition still occurs at a nonzero T_c , the so-called “Kosterlitz–Thouless” transition (Kosterlitz and Thouless, 1973); for $T < T_c$ we have $M_s(T) \equiv 0$ while at the same time $\xi(T) = \infty$, and the correlation function shows an algebraic decay, Eq. (4-47), with a temperature-dependent exponent η . At first sight, this behavior may appear fairly esoteric, but in fact it is closely related to the “roughening transition” of crystal surfaces (Weeks, 1980). Such roughening transitions have been observed for high-index crystal faces of various metals (Salanon et al., 1988). The power-law decay of correlations, Eq. (4-47), can be related to the behavior of the height–height correlation function of a crystal surface in the rough state (Weeks, 1980). As is well known, the roughness or flatness of crystal surfaces has a profound effect on their adsorption behavior, crystal growth kinetics, etc. (Müller-Krumbhaar, 1977).

The other important concept about critical phenomena is “universality”: since the only important length scale near a critical point is provided by the correlation length which is much larger than all “microscopic” lengths such as lattice spacing and interaction range, it is plausible that “details” on the atomic scale do not matter, and systems near a critical point behave in the same way provided that they fall in the same “universality class”. It turns out that universality classes (for systems with short-range interactions!) are determined by both spatial dimensionality d and order parameter dimensionality n , and in addition, the symmetry properties of the problem: e.g., Eq. (4-25) for $n=3$ and $u'=0$ falls in the same class as the Heisenberg

model of magnetism, Eq. (4-74), since the ferroelectric ordering would also be truly isotropic. However, in the presence of a nonvanishing “cubic anisotropy”, $u' \neq 0$, in general a different universality class results. The effect of such higher order invariants in the Landau expansion are particularly drastic again in systems with reduced dimensionality; e.g., the model with $n=2$ but cubic anisotropy no longer exhibits a Kosterlitz–Thouless transition, but rather a nonzero order parameter is stabilized again. Owing to the “marginal” character of the cubic anisotropy in $d=2$, however, the behavior is not Ising-like but rather the pathological case of a “universality class” with “nonuniversal” critical exponents occurs. The latter then do depend on “microscopic” details, such as the ratio of the interaction strengths between nearest and next nearest neighbors in the lattice (Krinisky and Mukamel, 1977; Domany et al., 1978; Swendsen and Krinsky, 1979; Landau and Binder, 1985). Again such problems are not purely academic, but relevant for order–disorder transitions in chemisorbed layers on metal surfaces, such as O on W (110) (see Binder and Landau (1989) for a review of the theoretical modeling of such systems).

One important consequence of universality is that all gas–fluid critical points in three-dimensional systems, all critical points associated with unmixing of fluid or solid binary mixtures, and all order–disorder critical points involving a single-component order parameter (such as β -brass) belong to the same universality class as the three-dimensional Ising model. All these systems not only have the same critical exponents, but also the scaling functions $\tilde{M}(\tilde{H})$, $\tilde{G}(\beta)$ etc. are all universal. Also, critical amplitude ratios are universal, such as \hat{C}/\hat{C}^+ , (Eq. (4-4), \hat{A}/\hat{A}' (Eq. (4-5)), or more complicated quantities such as

$\hat{D} \hat{\Gamma} \hat{B}^{\delta-1}$. The theoretical calculation and experimental estimation of such critical amplitude ratios are discussed by Privman et al. (1991).

An interesting problem concerns the critical singularities associated with nonordering “fields”. These singularities occur because the ordering field $\Phi(\mathbf{x})$ considered only in Eqs. (4-10) and (4-54) couples to another quantity: e.g., for an antiferromagnet in a magnetic field the order parameter Φ (the sublattice magnetization) couples to the uniform magnetization M , to the lattice parameters, to the electron density, etc. Since the Hamiltonian is invariant against interchange of the sublattices which implies a sign change of Φ , this coupling is quadratic in Φ^2 . Whereas in mean field theory the resulting critical behavior of the nonordering “field” is then proportional to $\langle \Phi \rangle^2 \sim t^{2\beta}$, taking fluctuations into account, the actual critical behavior is proportional to $\langle \Phi^2 \rangle \sim t^{(1-\alpha)}$, i.e., an energy-like singularity. Such energy-like singularities are predicted for the electrical resistivity ρ_{el} at various phase transitions (Fisher and Langer, 1968; Binder and Stauffer, 1976a), for the refractive index n_r (Gehring and Gehring, 1975; Gehring, 1977), etc. Looking for anomalies in the temperature derivative $d\rho_{el}(T)/dT$, $dn_r(T)/dT$ etc., which should exhibit specific-heat-like singularities, is often a more convenient tool for locating such phase transitions than measurements of the specific heat itself.

An important phenomenon occurs when a nonordering field which is coupled to the order parameter in this way, such as the magnetization in an antiferromagnet in an external field, is held fixed. Suppose we first study the approach to criticality by letting the uniform magnetic field h tend to its critical value $h_c(T)$: we then have the law $\Phi \sim [h_c(T) - h]^\beta$ for the order parameter and $M - M_c(T) \sim [h_c(T) - h]^{1-\alpha}$ for the mag-

netization (due to the coupling $\Phi^2(\mathbf{x}) M(\mathbf{x})$ in the Hamiltonian, as mentioned above). However, if we now consider the variation of Φ with M , combining both laws we get (assuming $\alpha > 0$)

$$\Phi \sim [M_c(T) - M]^{\beta/(1-\alpha)} \quad (4-85)$$

Considering now the phase transition in the space of $\{M, T\}$ as independent thermodynamic parameters, we then find that on crossing the critical line $M_c(T)$ the exponent describing the vanishing of the order parameter is $\beta/(1-\alpha)$ rather than β . This effect generally occurs when the critical line depends on extensive (rather than intensive) thermodynamic variables and is called “Fisher renormalization” (Fisher, 1968). This is very common for order-disorder phenomena in adsorbed layers at fixed coverage, or in alloys at fixed concentration, for unmixing critical points in ternary mixtures, etc. Other exponents also become “renormalized” similarly, e.g., γ is replaced by $\gamma/(1-\alpha)$, etc. A detailed analysis (Fisher, 1968) shows that no such “renormalization” of critical exponents occurs for systems with a fixed concentration c if the slope of the critical line vanishes, $dT_c(c)/dc = 0$, for the considered concentration. This is approximately true for β -brass, for instance.

4.2.3 Second-Order Versus First-Order Transitions; Tricritical and Other Multicritical Phenomena

An important question for any phase transition is deciding *a priori* whether it should be a second- or first-order transition; general principles are sought in answering this question, such that there would be no need for specific experimental data.

In the Landau theory, general symmetry conditions exist which allow second-

order transitions (Lifshitz, 1942). We here merely state them, without even attempting to explain the group-theoretical language (see, e.g., Tolédano and Tolédano, 1987, for a thorough treatment):

- (i) The order parameters Φ transform as a basis of a *single irreducible representation* X of the group G_0 characterizing the symmetry properties of the disordered phase.
- (ii) The symmetric part of the representation X^3 should not contain the unit representation.
- (iii) If the antisymmetric part of X^2 has a representation, the wavevector q associated with X is *not* determined by symmetry. In this case q is expected to vary continuously in the ordered phase.

If these conditions are met, a transition can nevertheless be first order, because a fourth-order term can be negative (see Sec. 4.2.1). If they are not met, the transition must be first order, according to the Landau rules.

The first of these rules essentially says that if in the ordered phase two quantities essentially independent of each other (not related by any symmetry operation, etc.) play the role of order parameter components Φ_1, Φ_2 , there is no reason why in the quadratic term $r_1(T)\Phi_1^2 + r_2(T)\Phi_2^2$ of the Landau expansion the coefficients $r_1(T), r_2(T)$ should change their sign at the same temperature. Thus, if Φ_1, Φ_2 are “primary” order parameter components, they should appear via a first-order transition.

The second condition essentially implies the absence of third-order terms (Φ^3) in the Landau expansion. It turns out, however, that in $d=2$ dimensions there are well-known counter-examples to these rules, namely the Potts model (Potts, 1952) with $q=3$ and $q=4$ (see Eq. (4-20)); as shown

by Baxter (1973), these models have second-order transitions. The critical exponents for these models are now believed to be known exactly, e.g., ($q=3$) $\alpha=1/3$, $\beta=1/9$, $\gamma=13/9$ and ($q=4$) $\alpha=2/3$, $\beta=1/12$, $\gamma=7/6$ (Den Nijs, 1979; Nienhuis et al., 1980). As mentioned in Sec. 4.2.1, an experimental example for the three-state Potts model is the $\sqrt{3}$ superstructure of various adsorbates on graphite. Convincing experimental evidence for a specific heat divergence of He^4 on grafoil described by $\alpha=1/3$ was presented by Bretz (1977). The system O on Ru (001) in the $p(2 \times 2)$ structure (Piercy and Pfnür, 1987) falls into the class of the four-state Potts models and again the data are in reasonable agreement with the predicted critical exponents.

In $d=3$ dimensions, however, the three-states Potts model has a weak first-order transition (Blöte and Swendsen, 1979) so that the Landau rule (ii) is not violated. This is of relevance for metallurgical systems such as the CuAu ordering (Fig. 4-8) on the f.c.c. lattice, which, according to Domany et al. (1982), belongs to the class of the three-states Potts model, while the Cu_3Au structure belongs to the class of the four-state Potts model. Another example of the three-state Potts model is the structural transition of SrTiO_3 stressed in the [111] direction (Bruce and Aharony, 1975). The order-disorder transition for all systems described by these types of ordering are always of first order, so there is no contradiction with this Landau rule, except for the transition to a charge density wave state in 2H-TaSe_2 (Moncton et al., 1977) which apparently is second order although there is a third-order invariant (Bak and Mukamel, 1979). It is possible, of course, that the transition is very weakly first order so that experimentally it could not be distinguished from second order. This remark also holds for other examples of apparent

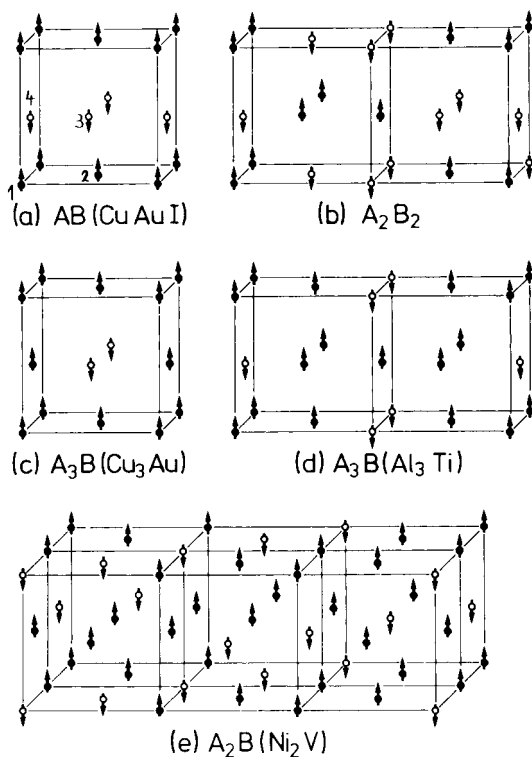


Figure 4-8. Five crystallographic superstructures on the face-centered cubic (fcc) lattice and their equivalent antiferromagnetic superstructures if in a binary alloy A-atoms (full circles) are represented as “spin up” and B atoms (open circles) are represented as “spin down”. Case (a) refers to the CuAuI structure, (b) to the A_2B_2 structure, (c) to the A_3B structure of Cu_3Au type, (d) to the A_3B structure of Al_3Ti type, and (e) the A_2B structure as it occurs in Ni_2V or Ni_2Cr . In case (a) the labels 1, 2, 3, and 4 indicate the decomposition of the fcc lattice into four interpenetrating simple cubic (sc) sublattices.

violations of the Landau rules discussed by Tolédano and Pascoli (1980), Tolédano (1981), and Tolédano and Tolédano (1987).

There are many transitions which the above Landau symmetry criteria would permit to be of second order but which are actually observed to be first order. Examples are type I or type II antiferromagnetic structures, consisting of ferromagnetic (100) or (111) sheets, respectively, with an

alternating magnetic moment direction between adjacent sheets (cf. Figs. 4-4 and 4-8a). Experimentally first-order transitions are known for FeO (Roth, 1958), TbP (Kötzler et al., 1979) (these systems have order parameter dimensionality $n=4$), UO_2 (Frazer et al., 1965; this is an example with $n=6$), MnO (Bloch and Mauri, 1973), NiO (Kleemann et al., 1980) (examples with $n=8$), etc. The standard phenomenological understanding of first-order transitions in these materials invoked magnetostrictive couplings (Bean and Rodbell, 1962) or crystal field effects (in the case of UO_2 ; see Blume, 1966), which make the coefficient u in Eq. (4-10) negative and thus produce a free energy of the type shown in Fig. 4-6b.

It has been suggested that the first-order character of the phase transition in these materials is a fundamental property due to the large number n of order-parameter components and the symmetry of the Hamiltonian: renormalization group expansions discussed by Mukamel et al. (1976a, b) and others suggested that all such transitions are “*fluctuation-induced first-order transitions*”, i.e., all antiferromagnets with $n \geq 4$ order parameters must have first-order transitions. However, there seem to be many counter-examples of cubic $n \geq 4$ antiferromagnets with phase transitions of apparently second order, such as BiTb (Kötzler, 1984), GdTb ($n=4$; Hulliger and Siegrist, 1979), and GdSb ($n=8$; McGuire et al., 1969). The reasons for this discrepancy between renormalization group predictions and experiments are not clear.

There are various other cases where “*fluctuation-induced first-order transitions*” occur, as reviewed in detail by Binder (1987a). Here we mention only the example of the phase transition from disordered block copolymer melts to the lamellar mesophase (Fig. 4-7b). For this system the

free-energy functional does not attain its minimum at wavevector $\mathbf{q}=0$ in reciprocal space but on a surface given by the equation $|\mathbf{q}|=q^*=2\pi/\lambda$, λ being the wavelength of the lamellar pattern. This reflects the degeneracy that there is no preferred direction and hence the lamellae may be oriented in any direction. Owing to the large “phase space” in \mathbf{q} -space where the inverse of the wavevector-dependent susceptibility goes “soft” ($\chi^{-1}(|\mathbf{q}|=q^*) \rightarrow 0$ as $T \rightarrow T_c$), the mean-square amplitude of the local fluctuation of the order parameter $\langle \Phi^2 \rangle - \langle \Phi \rangle^2$ would diverge as $T \rightarrow T_c$, which is physically impossible. It can be shown that this difficulty is avoided because the strong local order parameter fluctuations turn u negative near T_c (Brazovskii, 1975; Fredrickson and Helfand, 1987; Fredrickson and Binder, 1989), producing a free energy, as shown in Fig. 4-6b, for the case of “symmetric” diblock copolymers where mean field theory would predict a second-order transition. Experiments seem to confirm the first-order character of the transition (Bates et al., 1988).

For certain systems, for which $u > 0$ and thus a second-order transition occurs, it is possible by variation of a non-ordering field to change the sign of the coefficient u at a particular point. This temperature T_t , where u vanishes in Eq. (4-14), is called a *tricritical point*. From Eq. (4-14) we then immediately find

$$\Phi_0 = (-r/v)^{1/4} = (r'/v)^{1/4} (T_t/T - 1)^{1/4} \quad (4-86)$$

Hence the tricritical order parameter exponent $\beta_t = 1/4$, while Eqs. (4-32) to (4-48) remain unchanged and thus $\gamma_t = 1$, $\nu_t = 1/2$, $\eta_t = 0$. The critical isotherm, however, becomes $\nu \Phi_0^5 = H/k_B T$, i.e., $\delta_t = 5$. From Eq. (4-15) we finally find

$$\frac{F(\Phi_0) - F(0)}{V k_B T} = -\frac{t}{3} \left(\frac{-t}{v} \right)^{1/2} \quad (4-87)$$

which implies a specific heat divergence $C \sim (-t)^{-1/2}$, i.e., $\alpha_t = 1/2$. We note that this set of exponents also satisfies the scaling laws in Eqs. (4-78), (4-81), (4-83), and (4-84). Moreover, using this set of exponents in the Ginzburg criterion, Eqs. (4-58) to (4-61), we find that, with the Landau exponents for a tricritical point, this condition is marginally fulfilled, unlike the case of ordinary critical points (Eq. (4-62)). It turns out that $d^* = 3$ is the marginal dimension for tricritical points, and the mean-field power laws are modified by logarithmic correction terms similar to those noted for dipolar systems (Eq. (4-72)). Experimental examples for tricritical points include strongly anisotropic antiferromagnets in a uniform magnetic field (e.g., FeCl_2 , (Dillon et al., 1978), and dysprosium aluminum garnet (DAG) (Giordano and Wolf, 1975), see Fig. 4-9 for schematic phase diagrams), systems undergoing structural phase transitions under suitable applied pressure, such as NH_4Cl which has a tricritical point at $T_t = 250$ K and $p_t = 128$ bar (Yelon et al., 1974) or the ferroelectric KDP at $T_t = 113$ K and $p_t = 2.4$ kbar (Schmidt, 1978), etc. A model system which has been particularly carefully studied is $\text{He}^3\text{-He}^4$ mixtures: the transition temperature $T_\lambda(x)$ of the normal fluid–superfluid He^4 is depressed with increasing relative concentration x until, at a tricritical point $T_t = T_\lambda(x_t)$, the transition becomes first order. This then implies a phase separation between a superfluid phase with a lower He^3 content and a normal fluid He^3 -rich phase. Most common, of course, are tricritical phenomena in fluid binary mixtures arising from the competition of gas–liquid transitions and fluid–fluid phase separations in these systems (Scott, 1987).

Just as the vanishing coefficient u in Eq. (4-10) leads to a multicritical point, the tricritical point, another multicritical point is associated with the vanishing of the coeffi-

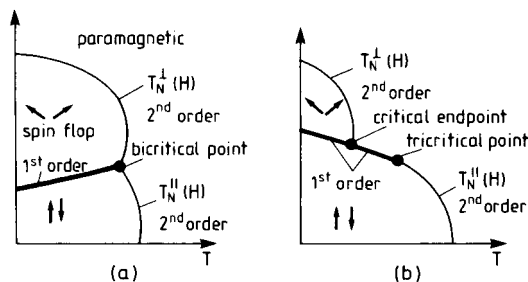


Figure 4-9. Schematic phase diagrams of antiferromagnets with uniaxial anisotropy in an applied uniform magnetic field H_{\parallel} applied parallel to the easy axis: Case (a) shows the case of weak anisotropy, case (b) the case of intermediate anisotropy, where in addition to the antiferromagnetic ordering of the spin components in the direction of the easy axis, a spin-flop ordering of the transverse components also occurs. In case (a) both transitions $T_{\parallel}(H_{\parallel})$ and $T_{\perp}(H_{\parallel})$ are of second order and meet in a bicritical point. For intermediate strength of the anisotropy the line $T_{\perp}(H_{\parallel})$ does not end at the bicritical point, but rather in a critical end-point at the first-order transition line. Then a tricritical point also appears where the anti-ferromagnetic transition $T_{\parallel}(H_{\parallel})$ becomes first order. For very strong anisotropy, the spin-flop phase disappears altogether.

cient of the $[\nabla\Phi(\mathbf{x})]^2$ term; since this term was also introduced as the lowest-order term of a systematic expansion, higher-order terms such as $[\nabla^2\Phi(\mathbf{x})]^2$ must then be included in Eq. (4-10). This problem is most conveniently discussed in the framework of the wavevector-dependent susceptibility $\chi(\mathbf{q})$, Eq. (4-34), which including the contribution resulting from a term $[\nabla^2\Phi(\mathbf{x})]^2$ can be written as ($t_0 = 1 - T_L/T$)

$$\chi(\mathbf{q}) = \frac{\hat{F}_0}{t_0 + K_1 q^2 + K_2 q^4} \quad (4-88)$$

where K_1 and K_2 are phenomenological coefficients. If $K_1 < 0$, the divergence of $\chi(\mathbf{q})$ does not occur for $t_0 = 0$, $\mathbf{q} = 0$ but at a value q_{\max} found from:

$$\begin{aligned} \frac{d}{dq} (t_0 + K_1 q^2 + K_2 q^4) &= 0 \\ \Rightarrow q_{\max} &= (-K_1/2K_2)^{1/2} \end{aligned} \quad (4-89)$$

The peak height of $\chi(\mathbf{q})$ for $|\mathbf{q}| = q_{\max}$ is then described by

$$\chi(q_{\max}) = \frac{\hat{F}}{t_0 - K_1^2/(4K_2)} \quad (4-90)$$

which implies that the actual critical point occurs at $T_c = T_L [1 + K_1^2/(4K_2)]$. An example of such an ordering characterized by a nonzero wavenumber $q^* = q_{\max}$ is the meso-phase formation in block copolymer melts (Fig. 4-7) (see Leibler (1980)). Related phenomena also occur in crystals exhibiting “incommensurate superstructures”. Usually $\chi(\mathbf{q})$ is then not isotropic in \mathbf{q} -space; in uniaxial systems, Eqs. (4-88) to (4-90) then apply only if \mathbf{q} is parallel to this preferred direction. The superstructure described by the wavelength $\lambda = 2\pi/q_{\max}$ is determined by the coefficients K_1 and K_2 and thus in general it is not a simple multiple of the lattice spacing a , but (λ/a) is an *irrational number*. This is what is meant by the term incommensurate. Examples of such incommensurate structures are “helimagnetic structures” such as VF_2 , MnAu_2 , Eu , Ho and Dy (Tolédano and Tolédano, 1987). Note that in these systems the reason for the incommensurate structure is not the existence of a negative coefficient in front of the $[\nabla\Phi(\mathbf{x})]^2$ term but the existence of

terms such as $\left(\Phi^+ \frac{\partial \Phi^-}{\partial z} - \Phi^- \frac{\partial \Phi^+}{\partial z} \right)$, where

$\Phi^+ = \Phi_0 \cos(\pi z/c)$, $\Phi^- = \Phi_0 \sin(\pi z/c)$, c being the lattice spacing in the z -direction. Such terms involving linear terms in $\nabla\Phi(\mathbf{x})$ are allowed by symmetry in certain space groups and are called “Lifshitz invariants”. Moving from lattice plane to lattice plane in the z -direction in such a helimagnetic spin structure, the spin vector (pointing perpendicular to z) describes a spiral structure like a spiral staircase. Of course, such incommensurate superstructures (also called “modulated phases”) are not restrict-

ed to magnetic systems, and many examples of dielectric incommensurate phases have been identified (e.g., NaNO_2 (Tani-saki, 1961), Rb_2ZnCl_4 , BaMnF_4 , thiourea [$\text{SC}(\text{NH}_2)_2$], see Tolédano and Tolédano (1987)). Whereas Rb_2ZnCl_4 and BaMnF_4 also involve the existence of Lifshitz invariants, thiourea is an example of the case discussed in Eqs. (4-88) to (4-90). Various examples of modulated superstructures exist in metallic alloys; see Selke (1988, 1989, 1992) and De Fontaine and Kulik (1985) for reviews of the pertinent theory and experimental examples such as Al_3Ti (Loiseau et al., 1985) and Cu_3Pd (Broddin et al., 1986).

Whereas for $T \leq T_c$ the ordering of the incommensurate phase can be described in terms of a sinusoidal variation of the local order parameter density $\Phi(x)$, the nonlinear terms present in Eq. (4-10) at lower temperatures imply that higher-order harmonics become increasingly important. Rather than a sinusoidal variation, the structure is then better described in terms of a periodic pattern of domain walls (or “solitons”), and we talk about a “*multi-soliton lattice*” or “*soliton staircase*”. Another important fact about modulated phases is that the wavevector characterizing the modulation period is not fixed at q_{max} , but varies with temperature or other parameters of the problem. This is expected from the third of the general Landau rules formulated at the beginning of Sec. 4.2.3. Usually this variation of q stops at some commensurate value where a “lock-in transition” of the incommensurate structures occurs. In the incommensurate regime rational values of the modulation (“long-period superstructures”) may have an extended regime of stability, leading to an irregular staircase-like behavior of the modulation wavelength λ as a function of temperature (or other control parameters

such as pressure, magnetic field (for magnetic structures), concentration (for alloys; see Fig. 4-10), etc.). Theoretically under certain conditions even a staircase with an infinite number (mostly extremely small!) of steps can be expected (“devil’s staircase”, see Selke (1988, 1989, 1992) for a discussion and further references). We also emphasize that the modulation need not involve only one direction in space (one wavevector), but can involve several wave-

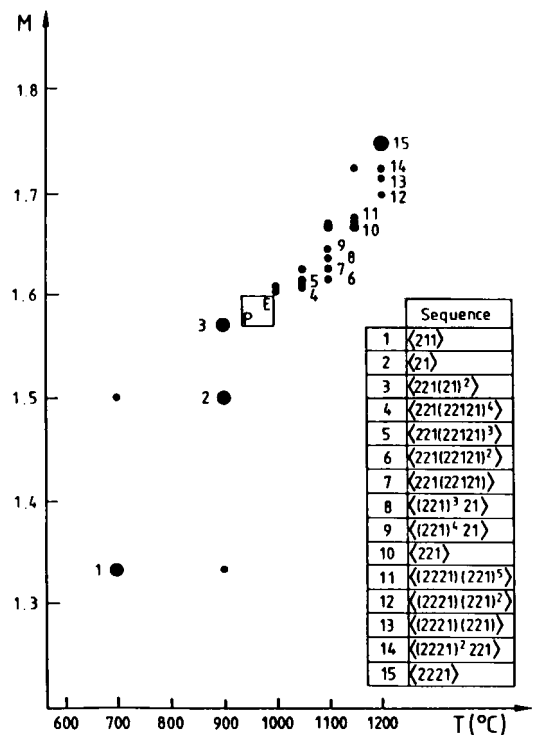


Figure 4-10. Period M (in units of the lattice spacing in the modulation direction) for the alloy $\text{Al}_{3-x}\text{Ti}_{1+x}$ as a function of the annealing temperature, as obtained from visual inspection of high-resolution electron microscopic images. Each of the fifteen different commensurate superlattices observed is composed of antiphase domains of length one or two (1-bands or 2-bands, as indicated by sequences $\langle 211 \rangle$, $\langle 21 \rangle$ etc.) based on the L1_2 structure. Very long annealing times were needed to produce these long-period superstructures supposedly at equilibrium. From Loiseau et al. (1985).

vectors. An example of the case of a two-rather than one-dimensional modulation is LiKSO_4 (Pimenta et al., 1989).

Here we discuss only the special case of Eqs. (4-88)–(4-90) briefly where, by changing external control parameters, it is possible to reach a multicritical point where K_1 vanishes, the so-called “Lifshitz point” (Hornreich et al., 1975). From Eq. (4-88) we then find that for $T = T_c (= T_L)$ we have $\chi(\mathbf{q}) \sim q^{-4}$, and comparing this with the result following from a Fourier transformation of Eq. (4-47), $\chi(q)_{T_c} \sim q^{-2+\eta}$, we conclude that $\eta_L = -2$ for the Lifshitz point, whereas for $T > T_c$ we still have $\chi(\mathbf{q}=0) = \hat{F}_0 t_0^{-1}$, i.e., $\gamma_L = 1$. Since for $K_1 = 0$ Eq. (4-88) can be rewritten as

$$\chi(\mathbf{q}) = \hat{F}_0 (1 - T_L/T)^{-1} / [1 + \xi^4 q^4] \\ \xi = [K_2 / (1 - T_L/T)]^{1/4} \quad (4-91)$$

we conclude that $\nu_L = 1/4$ for the correlation length exponent at the Lifshitz point.

Also for the Lifshitz point we can ask whether the Landau description presented here is accurate, and whether or not statistical fluctuations modify the picture. The result is that the critical fluctuations are very important. A marginal dimensionality $d^* = 8$ results in the case of an “isotropic Lifshitz point”, where in

$$K_{1x}(\partial\Phi/\partial x)^2 + K_{1y}(\partial\Phi/\partial y)^2 + K_{1z}(\partial\Phi/\partial z)^2$$

we have simultaneous vanishing of all coefficients K_{1x} , K_{1y} , and K_{1z} . Note that the more common case is the “uniaxial Lifshitz point”, where only K_{1z} vanishes while K_{1x} and K_{1y} remain nonzero. In this case the multicritical behavior is anisotropic, and we must distinguish between the correlation length ξ_{\parallel} describing the correlation function decay in the z -direction and the correlation length ξ_{\perp} in the other directions. Eq. (4-91) then holds for ξ_{\parallel} only, whereas Eq. (4-39) still holds for ξ_{\perp} .

While experimental examples for Lifshitz points are extremely scarce, e.g., the structural transition in RbCaF_3 under (100) stress (Buzaré et al., 1979), more common multicritical points are *bicritical points* where two different second-order transition lines meet. Consider, for example, the generalization of Eq. (4-10) to an n -component order-parameter field, but with different coefficient r_i for each order-parameter component Φ_i :

$$\frac{1}{k_B T} \mathcal{F}[\Phi(\mathbf{x})] = \frac{F_0}{k_B T} \quad (4-92) \\ + \int d\mathbf{x} \left\{ \frac{1}{2} r_1 \Phi_1^2(\mathbf{x}) + \frac{1}{2} r_2 \Phi_2^2(\mathbf{x}) + \dots \right. \\ \left. + \frac{1}{2} r_n \Phi_n^2(\mathbf{x}) + \frac{u}{4} [\Phi^2(\mathbf{x})]^2 \right. \\ \left. + \frac{R^2}{2d} [(\nabla \Phi_1)^2 + \dots + (\nabla \Phi_n)^2] \right\}$$

For simplicity, the fourth-order term has been taken as fully isotropic. If $r_1 = r_2 = \dots = r_n$, we would have the isotropic n -vector model discussed in Secs. 4.2.2 and 4.2.3. We now consider the case where some of these coefficients differ from each other, but a parameter p exists on which these coefficients depend in addition to the temperature. The nature of the ordering will be determined by the term $r_i \Phi_i^2$, for which the coefficient r_i changes sign at the highest temperature. Suppose this is the case where $i=1$ for $p < p_b$, then we have a one-component Ising-type transition at $T_{c1}(p)$ given by $r_1(p, T) = 0$ (the other components Φ_i being “secondary order parameters” in this phase). If, however, for $p > p_b$ the coefficient $r_2(p, T) = 0$ at the highest temperature $T_{c2}(p)$, it is the component Φ_2 which drives the transition as the primary order parameter. The point $p = p_b$, $T_{c1}(p) = T_{c2}(p) = T_b$ is then called a bicritical point.

An example of this behavior is found for weakly uniaxial antiferromagnets in a uni-

form magnetic field $H_{||}$ (Fig. 4-9). A model Hamiltonian for such a system can be written as

$$\mathcal{H} = - \sum_{\langle i,j \rangle} \{ J(1-\Delta) [S_i^x S_j^x + S_i^y S_j^y] + J S_i^z S_j^z \} - H_{||} \sum_i S_i^z \quad (4-93)$$

where we assume $J < 0$ (antiferromagnetism) and for $\Delta > 0$ the easy axis is the z -axis. For small $H_{||}$, we have a uniaxial antiferromagnetic structure and the order parameter is the z -component of the staggered magnetization M_s^z . For stronger fields $H_{||}$, however, we have a transition to a spin-flop structure (two-component

order parameter, due to the perpendicular components M_s^x and M_s^y of the staggered magnetization). In the framework of Eq. (4-92), this would mean $n=3$ and $r_2 \equiv r_3 \neq r_1$, with $H_{||}$ being the parameter p . Both lines $T_N^{\parallel}(H_{||})$ and $T_N^{\perp}(H_{||})$ and the first-order line between the two antiferromagnetic structures join in a bicritical point. A well known example of such a behavior is GdAlO_3 with $T_b = 3.1242$ K (Rohrer, 1975). Another example, in our opinion, is the Fe–Al system where the ferro-paramagnetic critical line joins the second-order A2–B2 transition (Fig. 4-11). In the metallurgical literature, the magnetic tran-

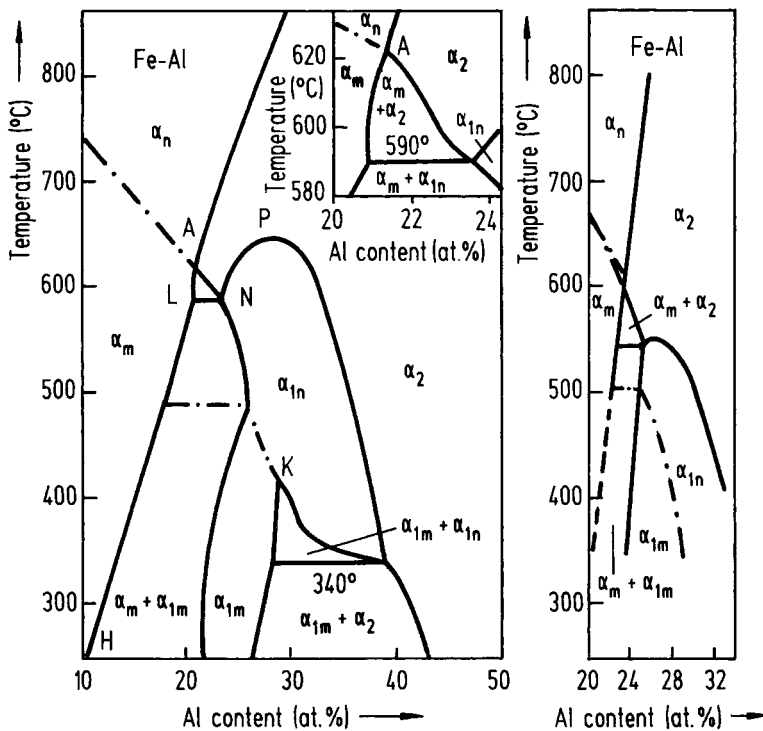


Figure 4-11. The Fe–Al phase diagram, as obtained from a mean-field calculation by Semenovskaya (1974) (left), and experimentally by Swann et al. (1972) (right). The ferro-paramagnetic transition is shown by the dash-dotted line. The crystallographically disordered (A2) phase is denoted as α_n in the nonmagnetic and α_m in the ferromagnetic state. The ordered FeAl phase having the B2 structure (Fig. 4-3) is denoted as α_2 , and the ordered Fe_3Al phase having the D_{03} structure (Fig. 4-3) is denoted as α_{1n} or α_{1m} , depending on whether it is nonmagnetic or ferromagnetically ordered, respectively. Note that first-order transitions in this phase diagram are associated with two-phase regions, since the abscissa variable is the density of an extensive variable, unlike the ordinate variable in Fig. 4-9. From Semenovskaya (1974).

sition of Fe–Al alloys is often disregarded and then the multicritical point where the A2–B2 transitions change from second to first order is interpreted as a tricritical point. Bicritical phenomena for structural phase transitions are also known, such as SrTiO_3 under stress in the [001] direction (Müller and Berlinger, 1975).

The structure of the phase diagram near bicritical points has been analyzed in detail by renormalization group methods (Fisher and Nelson, 1974; Fisher, 1975a, b; Mukamel et al., 1976a, b), experiment (Rohrer and Gerber, 1977) and Monte Carlo simulations (Landau and Binder, 1978). Apart from the fact that the exponents introduced so far take different values as $T \rightarrow T_b$, there is one additional exponent, the “crossover exponent” Φ , describing the singular approach of phase-transition lines towards the multicritical point. This behavior, and also other more complicated phenomena (tetracritical points, tricritical Lifshitz points, etc.) are beyond the scope of this chapter. For an excellent introduction to the field of multicritical phenomena we refer to Gebhardt and Krey (1979) and for a comprehensive review to Pynn and Skjeltorp (1983).

4.2.4 Dynamics of Fluctuations at Phase Transitions

Second-order phase transitions also show up in the “critical slowing down” of the critical fluctuations. In structural phase transitions, we speak about “soft phonon modes”; in isotropic magnets magnon modes soften as T approaches T_c from below; near the critical point of mixtures the interdiffusion is slowed down; etc. This critical behavior of the dynamics of fluctuations is again characterized by a dynamic critical exponent z ; we expect there to be

some characteristic time τ which diverges as $T \rightarrow T_c$:

$$\tau \sim \xi^z \sim |1 - T/T_c|^{-\nu z} \quad (4-94)$$

Many of the concepts developed for static critical phenomena (scaling laws, universality, etc.) can be carried over to dynamic critical phenomena: “dynamic scaling” (Halperin and Hohenberg, 1967; Ferrell et al., 1967; Hohenberg and Halperin, 1977), “dynamic universality classes” (Halperin et al., 1974, 1976; Hohenberg and Halperin, 1977), etc. However, the situation is much more complicated because the static universality classes are split up in the dynamic case, depending on the nature of the *conservation laws*, mode coupling terms in the basic dynamic equations, etc. For example, we have emphasized that anisotropic magnets such as RbMnF_3 , ordering alloys such as CuZn, unmixing solid mixtures such as Al–Zn, unmixing fluid mixtures such as lutidine–water, and the gas–fluid critical point all belong to the same Ising-like static universality class, but each of these examples belongs to a different dynamic universality class! Thus, in the anisotropic antiferromagnet, no conservation law needs to be considered, whereas the conservation of concentration matters for all mixtures (where it means the *order parameter is conserved*) and for ordering alloys (where the order parameter is not conserved but coupled to a conserved “nonordering density”). Whereas in solid mixtures the local concentration relaxes simply by diffusion, in fluid mixtures hydrodynamic flow effects matter, and also play a role at the liquid–gas critical point. In the latter instance, conservation of energy needs to be considered; it does not play a role for phase transitions in solid mixtures, of course, where the phonons act as a “heat bath” to the considered configurational degrees of freedom.

We do not give a detailed account of critical dynamics here, but discuss only the simplest phenomenological approach (van Hove, 1954) for non-conserved order parameters. We consider a deviation of the order parameter $\Delta\Phi(\mathbf{x}, t)$ from equilibrium at space \mathbf{x} and time t , and ask how this deviation decays back to equilibrium. The standard assumption of irreversible thermodynamics is a relaxation assumption; we put

$$\frac{\partial}{\partial t} \Delta\Phi(\mathbf{x}, t) = -\Gamma_0 \frac{\partial \mathcal{F}}{\partial \Delta\Phi(\mathbf{x})} \quad (4-95)$$

where Γ_0 is a phenomenological rate factor. Using Eq. (4-10) and linearizing $\Phi(\mathbf{x}, t) = \Phi_0 + \Delta\Phi(\mathbf{x}, t)$ around Φ_0 yields

$$\begin{aligned} \frac{\partial}{\partial t} \Delta\Phi(\mathbf{x}, t) = & -\Gamma_0 \left\{ (r + 3u\Phi_0^2) \Delta\Phi(\mathbf{x}, t) \right. \\ & \left. - \frac{R^2}{d} \nabla^2 [\Delta\Phi(\mathbf{x}, t)] \right\} \end{aligned} \quad (4-96)$$

Assuming that $\Delta\Phi(\mathbf{x}, t)$ is produced by a field $H(\mathbf{x}) = H_q \exp(i\mathbf{q} \cdot \mathbf{x})$ which is switched off at time $t=0$, we obtain (see also Sec. 4.2.2)

$$\frac{\Delta\Phi_q(t)}{\Delta\Phi_q(0)} = \exp[-\omega(q)t], \quad \omega(q) = \Gamma_0/\chi(q) \quad (4-97)$$

where Eq. (4-34) has been used. Since $\chi(q)$ diverges for $q=0$, $T \rightarrow T_c$, the characteristic frequency $\omega(q=0) \equiv \tau^{-1}$ vanishes as $\omega(q=0) \sim \chi_T^{-1} \sim \xi^{-\gamma/\nu} = \xi^{-(2-\eta)}$, and by comparison with Eq. (4-94) the result of the “conventional theory” is obtained:

$$z = 2 - \eta \quad (4-98)$$

Although Eq. (4-98) suggests that there is a scaling relationship linking the dynamic to the static exponents, this is not true in general if effects due to critical fluctuations are taken into account. In fact, for nonconserved systems, z slightly exceeds $2 - \eta$ and extensive Monte Carlo studies were needed

to establish its precise value (Wansleben and Landau, 1987).

It is important to realize that *not all fluctuations slow down* as a critical point is approached, but only those associated with long-wavelength order parameter variations. This clearly expressed in terms of the dynamic scaling relationship of the characteristic frequency:

$$\omega(\mathbf{q}) = q^z \tilde{\omega}(\beta), \quad \beta = q\xi \quad (4-99)$$

where $\tilde{\omega}(\beta)$ is a scaling function with the properties $\tilde{\omega}(\infty) = \text{const.}$ and $\tilde{\omega}(\beta \ll 1) \sim \beta^{-z}$, and, hence, is consistent with Eq. (4-94).

Most experimental evidence on dynamic critical phenomena comes from methods such as inelastic scattering of neutrons or light, NMR or ESR spectroscopy, and ultrasonic attenuation. Although the overall agreement between theory and experiment is satisfactory, only a small fraction of the various theoretical predictions have been thoroughly tested so far. For reviews, see Hohenberg and Halperin (1977) and Enz (1979).

Finally, we also draw attention to nonlinear critical relaxation. Consider, for example, an ordering alloy which is held well below T_c in the ordered phase and assume that it is suddenly heated to $T = T_c$. The order parameter is then expected to decay towards zero with time in a singular fashion, $\Phi(t) \sim t^{-\beta/\nu z}$ (Fisher and Racz, 1976). Similarly, if the alloy is quenched from a temperature $T > T_c$ to $T = T_c$, the superstructure peak appears and grows in a singular fashion with the time t after the quench, $S(\mathbf{q}, t) \sim t^{\gamma/\nu z}$ (Sadiq and Binder, 1984). Related predictions also exist for the nonlinear relaxation of other quantities (ordering energy, electrical resistivity) (Binder and Stauffer, 1976a; Sadiq and Binder, 1984).

A very important topic is the dynamics of first-order phase transitions, which will not be discussed here because it is dis-

cussed elsewhere in this book (see Chapters by Binder and Fratzl (2001) and by Wagner et al. (2001)).

4.2.5 Effects of Surfaces and of Quenched Disorder on Phase Transitions: A Brief Overview

If a system contains some impurity atoms which are mobile, we refer to “annealed disorder” (Brout, 1959). From the point of view of statistical thermodynamics, such mobile impurities act like additional components constituting the system under consideration. For a second-order transition, small fractions of such additional components have rather minor effects: the transition point may be slightly shifted relative to that of the pure material, and as the concentration of these impurities is normally strictly conserved, in principle the so-called “Fisher renormalization” (Fisher, 1968) of critical exponents is expected, as discussed in Sec. 4.2.2. For small impurity contents, the region around the transition point where this happens is extremely narrow, and hence this effect is not important.

The effect of such impurities on first-order transitions is usually more important, e.g., for a pure one-component system, the melting transition occurs at one well-defined melting temperature, whereas in the presence of mobile impurities this transition splits up into two points, corresponding to the “solidus line” and “liquidus line” in the phase diagram of a two-component system. This splitting for small impurity contents is simply proportional to the concentration of the impurities of a given type. In practice, where a material may contain various impurities of different chemical natures and different concentrations which often are not known, these splittings of the transition line in a high-dimensional pa-

rameter space of the corresponding multi-component system show up like a rounding of the first-order transition.

In solids, however, diffusion of impurity atoms is often negligibly small and such a disorder due to frozen-in, immobile impurities is called “quenched disorder” (Brout, 1959). Other examples of quenched disorder in solids are due to vacancies, in addition to extended defects such as dislocations, grain boundaries, and external surfaces. Quenched disorder has a drastic effect on phase transitions, as will be seen below.

Since the disorder in a system is usually assumed to be random (irregular arrangement of frozen-in impurities, for example), we wish to take an average of this random disorder. We denote this averaging over the disorder variables, which we formally denote here as the set $\{x_\alpha\}$, by the symbol $[\dots]_{\text{av}}$ in order to distinguish it from the thermal averaging $\langle \dots \rangle_T$ implied by statistical mechanics. Thus the average free energy which needs to be calculated in the presence of quenched disorder is

$$F = -k_B T [\ln Z \{x_\alpha\}]_{\text{av}} \quad (4-100)$$

$$= -k_B T \left[\ln \left(\text{tr}_{\{\Phi_i\}} \exp(-\mathcal{H} \{x_\alpha, \Phi_i\} / k_B T) \right) \right]_{\text{av}}$$

whereas in the case of annealed disorder it would be the partition function rather than the free energy which is averaged over the disorder:

$$F_{\text{ann}} = -k_B T \ln [Z \{x_\alpha\}]_{\text{av}} \quad (4-101)$$

$$= -k_B T \ln \left(\text{tr}_{\{\Phi_i\}} [\exp(-\mathcal{H} \{x_\alpha, \Phi_i\} / k_B T)]_{\text{av}} \right)$$

$$= -k_B T \ln \left(\text{tr}_{\{\Phi_i, x_\alpha\}} \exp(-\mathcal{H} \{x_\alpha, \Phi_i\} / k_B T) \right)$$

Eq. (4-101) again shows that annealed disorder just means that we enlarge the space of microscopic variables which need to be included in the statistical mechanics treatment, whereas the nature of quenched averaging (Eq. (4-100)) is different.

Experiments can be carried out with just one probe crystal and no averaging over many samples as is implied by Eq. (4-100) needs to be performed. This is because we can think about the parts of a macroscopic sample as subsystems over which such an average as written in Eq. (4-100) is actually performed. This “self-averaging” property of macroscopically large systems means that the average [...] over the set $\{x_\alpha\}$ could also be omitted: it need only be kept for mathematical convenience.

We first discuss the physical effects of randomly quenched impurities (point-like defects!) on phase transitions, assuming the concentrations of these defects to be very small. Various cases need to be distinguished, depending on the nature of the local coupling between the defect and the local order parameter. This coupling may be linear (“random field”), bilinear (“random bond”) or quadratic (“random anisotropy”). As an example, let us consider magnetic phase transitions described by the n -vector model of magnetism, with an exchange interaction depending on the distance between lattice points \mathbf{a}_i and \mathbf{a}_j :

$$\mathcal{H} = - \sum_{i \neq j} J(\mathbf{a}_i - \mathbf{a}_j) \mathbf{S}_i \cdot \mathbf{S}_j - \sum_i H_i S_i^z \quad (4-102)$$

In Eq. (4-102) we have assumed that impurities produce a random field H_i which has the properties

$$[H_i]_{\text{av}} = 0, \quad [H_i^2]_{\text{av}} = H_R^2 \quad (4-103)$$

and \mathbf{S}_i is an n -component unit vector in the direction of the local order parameter. Now we can show that for $n \geq 2$ arbitrary small amplitudes of the random field H_R (which physically is equivalent to arbitrary small impurity concentration) can destroy uniform long-range order (Imry and Ma, 1975): the system is broken into an irregular arrangement of domains. The mean size of the domains is larger as H_R (or the

impurity concentration, respectively) is smaller. Since no ideal long-range order is established at the critical point, this corresponds to a rounding of the phase transition.

In the case $n=1$ and $d=3$ dimensions, very weak random fields do not destroy uniform long-range order (Imbrie, 1984; Nattermann, 1998), although long-range order is destroyed if H_R exceeds a certain threshold value $H_R^c(T)$ which vanishes as $T \rightarrow T_c$. But the random field drastically changes the nature of both static and dynamic phenomena (Villain, 1985; Grinstein, 1985). In $d=2$ dimensions, arbitrary weak random fields destroy even Ising-like ($n=1$) order, producing domains of size ξ_D with $\ln \xi_D \sim (J/H_R)^2$ (see Binder, 1983a).

We now turn briefly to the physical realization of “random fields”. For symmetry reasons, no such defects are expected for ferromagnets, but they may be induced indirectly by a uniform field acting on an antiferromagnet (Fishman and Aharony, 1979; Belanger, 1998). Since antiferromagnets in a field can be “translated” into models for order–disorder phenomena in alloys (the magnetization of the antiferromagnet “translates” into the concentration of the alloy, see Sec. 4.3.1) or (in $d=2$ dimensions) in adsorbed layers (the magnetization then “translates” into the coverage of the layer), random-field effects are important for ordering alloys or order–disorder transitions in monolayers, also. A nice experimental example was provided by Wiechert and Arlt (1993) who showed that the transition of CO monolayers on graphite near 5 K to a ferroelectric phase is rounded by small dilution with N_2 molecules, in accord with the theory of random-field effects. Furthermore, random fields act on many structural phase transitions owing to impurity effects: ions at low-sym-

metry, off-center positions may produce both a random electric field and a random strain field. Also, symmetry generally permits random fields to act on tensorial order parameters in diluted molecular crystals (Harris and Meyer, 1985). For diluted molecular crystals (such as N_2 diluted with Ar, or KCN diluted with KBr, etc.) it is still unclear whether the resulting “orientational glass” phase is due to these random fields or to random bonds (for reviews, see Loidl (1989); Höchli et al. (1990); Binder and Reger (1992); Binder (1998)).

The “random bond” Hamiltonian differs from Eq. (4-102) by the introduction of disorder into the exchange terms rather than the “Zeeman energy”-type term,

$$\mathcal{H} = - \sum_{i \neq j} J_{ij} \mathbf{S}_i \cdot \mathbf{S}_j - H \sum_i S_i^z \quad (4-104)$$

Whereas in Eq. (4-102) we have assumed the pairwise energy to be translationally invariant (the exchange energy J depends only on the distance $\mathbf{a}_i - \mathbf{a}_j$ between the spins but not on their lattice vectors \mathbf{a}_i and \mathbf{a}_j separately), we now assume J_{ij} to be a random variable, e.g., distributed according to a Gaussian distribution

$$P(J_{ij}) \propto \exp[-(J_{ij} - \bar{J})^2 / 2(\Delta J)^2] \quad (4-105)$$

or according to a two-delta function distribution

$$P(J_{ij}) = p \delta(J_{ij} - J) + (1 - p) \delta(J_{ij}) \quad (4-106)$$

If $\bar{J} \gg \Delta J$ (Eq. (4-105)) or if $1 - p \ll 1$ (Eq. (4-106)), the ferromagnetic order occurring for Eq. (4-104) if $J > 0$ or $\bar{J} > 0$ is only weakly disturbed, both for $d=3$ and for $d=2$ dimensions. Following an argument presented by Harris (1974), we can see that the critical behavior of the system remains unaltered in the presence of such impurities provided that the specific heat exponent $\alpha < 0$, whereas a new type of critical behavior occurs for $\alpha \geq 0$ (see Grinstein (1985)

for a review). Of course, the impurities will always produce some shift of the critical temperature, which decreases as p in Eq. (4-106) decreases. When p becomes smaller than a critical threshold value p_c , only finite clusters of spins are still mutually connected by nonzero exchange bonds $J > 0$, and long-range order is no longer possible. The phase transition at $T=0$ produced by variation of p in Eq. (4-106) can hence be interpreted purely geometrically in terms of the connectivity of finite clusters or an infinite “percolating” network of spins (Stauffer and Aharony, 1992). This transition is again described by a completely different set of exponents.

For the case where $|\bar{J}| \ll \Delta J$ in Eq. (4-105), a new type of ordering occurs, which is not possible in systems without quenched disorder; a transition occurs to a state without conventional ferro- or antiferromagnetic long-range order but to a “spin glass phase” where the spins are frozen-in in a random direction (Binder and Young, 1986; Young, 1998). The order parameter of the Ising spin glass was introduced by Edwards and Anderson (1975) as

$$q_{EA} = [\langle S_i^2 \rangle_T]_{av} \quad (4-107)$$

The nature of the phase transition in spin glasses and the properties of the ordered phase have been the subject of intense research (Binder and Young, 1986). This great interest in spin glasses can be understood because many different systems show spin glass behavior: transition metals with a small content x of magnetic impurities such as $Au_{1-x}Fe_x$ and $Cu_{1-x}Mn_x$, diluted insulating magnets such as $Eu_xSr_{1-x}S$, various amorphous alloys, and also mixed dielectric materials such as mixtures of RbH_2PO_4 and $NH_4H_2PO_4$, where the spin represents an electric rather than magnetic dipole moment. A related random ordering of quadrupole moments rather than dipole

moments if found in “quadrupolar glasses” (also called “orientational glasses”) such as $\text{K(CN)}_{1-x}\text{Br}_x$ and $(\text{N}_2)_x\text{Ar}_{1-x}$, (Loidl, 1989; Höchli et al., 1990; Binder and Reger, 1992; Binder, 1998). However, it is still debated (Franz and Parisi, 1998) whether or not concepts appropriate for the description of spin glasses are also useful for the structural glass transition of under-cooled liquids (Jäckle, 1986).

Finally we mention systems with random anisotropic axes which can be modeled by the following Hamiltonian (Harris et al., 1973):

$$\mathcal{H} = - \sum_{i \neq j} J(\mathbf{a}_i - \mathbf{a}_j) \mathbf{S}_i \cdot \mathbf{S}_j - \sum_i (\mathbf{e}_i \cdot \mathbf{S}_i)^2 \quad (4-108)$$

where the \mathbf{e}_i are vectors whose components are independent random variables with a Gaussian distribution. This model is also believed to exhibit destruction of long-range order due to break-up in domains similar to the random field systems. It is also suggested that spin glass phases may occur in these systems. Again Eq. (4-108) is expected to be relevant, not only for disordered magnetic materials but also for dielectrics where the spin represents electric dipole moments, or displacement vectors of atoms at structural phase transitions, etc.

Very small fractions of quenched impurities which do not yet have an appreciable effect on the static critical properties of a second-order phase transition can already affect the critical dynamics drastically. An example of this behavior is the occurrence of impurity-induced “central peaks” for structural phase transitions in the scattering function $S(\mathbf{q}, \omega)$ at frequency $\omega=0$ in addition to the (damped) soft phonon peaks (Halperin and Varma, 1976). In the above systems where the impurities disrupt the conventional ordering more drastically (such as random field systems and spin

glasses) the critical dynamics again have a very different character, and dynamics characteristic of thermally activated processes with a broad spectrum of relaxation times are often observed.

It is also interesting to discuss the effect of quenched impurities on first-order transitions (Imry and Wortis, 1979). It is found that typically “precursor phenomena” near the first-order transition are induced, and the latent heat associated with the transition in the pure systems can be significantly reduced. It is also possible that such impurity effects may completely remove the latent heat discontinuity and lead to a rounding of the phase transition.

Such rounding effects on phase transitions also occur when extended defects such as grain boundaries and surfaces are considered. These disrupt long-range order because the system is then approximately homogeneous and ideal (i.e., defect-free) only over a finite region in space. While the description of the rounding and shifting of phase transitions due to finite size effects has been elaborated theoretically in detail (Privman, 1990), only a few cases exist where the theory has been tested experimentally, such as the normal fluid–superfluid transitions of He^4 confined to pores, or the melting transition of oxygen monolayers adsorbed on grafoil where the substrate is homogeneous over linear dimension L of the order of 100 \AA (see Marx, 1989). While at critical points, a rounding and shifting of the transition normally set in when the linear dimension L and the correlation length ξ are comparable (Fisher, 1971; Binder, 1987b), at first-order transitions the temperature region ΔT over which the transition is rounded and shifted is inversely proportional to the volume of the system (Imry, 1980; Challa et al., 1986).

An important effect of extended defects such as grain boundaries and surfaces is

that they often induce precursor effects to phase transitions, e.g., the “wetting transition” (Dietrich, 1988; Sullivan and Telo da Gama, 1985) where a fluid layer condensing at a surface is a precursor phenomenon to gas–fluid condensation in the three-dimensional bulk volume. Similarly “surface melting” and “grain-boundary melting” phenomena can be interpreted as the intrusion of a precursor fluid layer at a surface (or grain boundary) of a crystal (Di Tolla et al., 1996). Similarly, at surfaces of ordering alloys such as Cu_3Au , the effect of the “missing neighbors” may destabilize the ordering to the extent that “surface-induced disordering” occurs when the system approaches the transition temperature of the bulk (Lipowsky, 1984). Finally, we draw attention to the fact that the local critical behavior at surfaces differs significantly from the critical behavior in the bulk (Binder, 1983b). Such effects are outside the scope of this chapter.

4.3 Computational Methods Dealing with the Statistical Mechanics of Phase Transitions and Phase Diagrams

While the phenomenological theories in Sec. 4.2 yield a qualitative insight into phase transitions, the quantitative description of real materials needs a more detailed analysis. In this section, we complement the phenomenological theory by a more microscopic approach. In the first step, the essential degrees of freedom for a particular transition are identified and an appropriate model is constructed. In the second step, the statistical mechanics of the model are treated by suitable approximate or numerical methods.

Fig. 4-12 illustrates the modeling of order–disorder phase transitions in solids.

Transitions occur where the basic degree of freedom is the (thermally activated) diffusion process of atoms between various lattice sites. This happens for unmixing alloys such as Al–Zn or for ordering alloys such as $\beta\text{-CuZn}$ or the Cu–Au system. The modeling of such systems will be discussed in Sec. 4.3.1. Many structural transitions are of a very different nature: we encounter periodic lattice distortions where atomic displacements are comparable to those of lattice vibrations. Short wavelength distortions may give rise to “antiferrodistortive” and “antiferroelectric” ordering, as exemplified by the perovskites SrTiO_3 , PbZrO_3 , etc. Long wavelength distortions corresponding to acoustic phonons give rise to “ferroelastic” ordering. Sec. 4.3.2 will deal with the mean field treatment of such phase transitions where the order parameter is a phonon normal coordinate, and Sec. 4.3.3 is devoted to numerical methods going beyond mean-field theory.

4.3.1 Models for Order–Disorder Phenomena in Alloys

Since the diffusive motion of atoms in substitutional alloys (Fig. 4-12) is so much slower than other degrees of freedom (such as lattice vibrations), we may describe the configurational statistics of a substitutional binary alloy, to which we restrict attention for simplicity, by local occupation variables $\{c_i\}$. If lattice site i is taken by an atom of species B, $c_i = 1$, if it is taken by an atom of species A, $c_i = 0$.

Neglecting the coupling between these variables and other degrees of freedom, the Hamiltonian is then:

$$\mathcal{H} = \mathcal{H}_0 + \sum_{i \neq j} [c_i c_j v_{\text{BB}}(\mathbf{x}_i - \mathbf{x}_j) + 2c_i(1 - c_j) v_{\text{AB}}(\mathbf{x}_i - \mathbf{x}_j) + (1 - c_i)(1 - c_j) v_{\text{AA}}(\mathbf{x}_i - \mathbf{x}_j)] + \dots \quad (4-109)$$

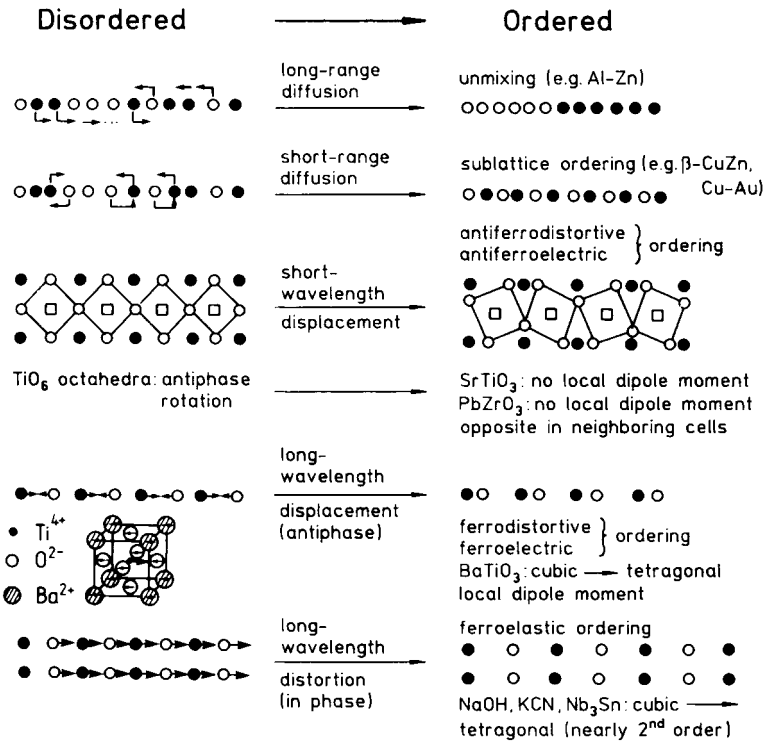


Figure 4-12. Degree of freedom essential for the description of various order–disorder transitions in solids. For further explanations, see text.

where v_{AA} , v_{AB} , and v_{BB} are interactions between pairs of AA, AB, and BB atoms. In fact, terms involving three- and four-body interactions may also occur, but are not considered here. Also, effects due to vacancies may easily be included but are neglected here.

As is well known, Eq. (4-109) can be reduced to the Ising model, Eq. (4-56), by the transformation $S_i = 1 - 2c_i = \pm 1$, apart from a constant term which is of no interest to us here. The “exchange interaction” J_{ij} between spins i and j and “magnetic field” H in Eq. (4-56) are related to the interaction parameters of Eq. (4-109) by

$$J(\mathbf{x}_i - \mathbf{x}_j) \equiv J_{ij} = [2v_{AB}(\mathbf{x}_i - \mathbf{x}_j) - v_{AA}(\mathbf{x}_i - \mathbf{x}_j) - v_{BB}(\mathbf{x}_i - \mathbf{x}_j)]/4 \quad (4-110)$$

$$H = \frac{1}{2} \left(\sum_{j(\neq i)} [v_{AA}(\mathbf{x}_i - \mathbf{x}_j) - v_{BB}(\mathbf{x}_i - \mathbf{x}_j)] \right) - \Delta\mu \quad (4-111)$$

where $\Delta\mu$ is the chemical potential difference between the two species.

The same mapping applies for the lattice-gas model of fluids, which at the same time can be considered as a model of adsorbed layers on crystalline surface substrates (in $d=2$ dimensions) (see Binder and Landau (1989) for a review) or as a model of interstitial alloys, such as hydrogen or light atoms such as C, N and O in metals (Alefeld, 1969; Wagner and Horner, 1974; Alefeld and Völkl, 1978). If we interpret B in Eqs. (4-109)–(4-111) as an occupied site and A as a vacant site, then usually $v_{AB} = v_{AA} = 0$, such that

$$\mathcal{H} = \mathcal{H}_0 + \sum_{i \neq j} c_i c_j v(\mathbf{x}_i - \mathbf{x}_j) + \varepsilon \sum_i c_i \quad (4-112)$$

ε being the binding energy which a particle feels at lattice site i (for adsorbates at surfaces, this is a binding to the substrate, and a similar enthalpy term is expected when

an interstitial is dissolved in a metal, whereas for modeling of an ordinary gas–liquid transition we would put $\varepsilon=0$). The relationships analogous to Eqs. (4-110) and (4-111) are then:

$$H = - \left[(\varepsilon + \mu)/2 + \sum_{j(\neq i)} v(\mathbf{x}_i - \mathbf{x}_j)/4 \right] \quad (4-113)$$

$$J_{ij} = -v(\mathbf{x}_i - \mathbf{x}_j)/4 \quad (4-114)$$

where μ is the chemical potential and $v(\mathbf{x}_i - \mathbf{x}_j)$ the pairwise interaction of particles at lattice sites \mathbf{x}_i and \mathbf{x}_j .

Of course, it is straightforward to generalize this approach to binary (A–B) alloys including as a third option that a lattice site is vacant (V) or to ternary alloys; then more complicated models result, e.g., the Potts (1952) model, Eq. (4-20), or the model of Blume et al. (1971). Another generalization occurs if one species (B) of a binary alloy is magnetic, e.g., Fe in Fe–Al alloys (see Dünweg and Binder (1987)). In the latter case, the Hamiltonian is (the true magnetic spin variable is now denoted as σ_i)

$$\begin{aligned} \mathcal{H} = & \mathcal{H}_0 \quad (4-115) \\ & + \sum_{i \neq j} \{ c_i c_j [v_{BB}(\mathbf{x}_i - \mathbf{x}_j) - J_m(\mathbf{x}_i - \mathbf{x}_j) \sigma_i \cdot \sigma_j] \\ & + 2c_i(1 - c_j) v_{AB}(\mathbf{x}_i - \mathbf{x}_j) \\ & + (1 - c_i)(1 - c_j) v_{AA}(\mathbf{x}_i - \mathbf{x}_j) \} + \dots \end{aligned}$$

where $J_m(\mathbf{x}_i - \mathbf{x}_j)$ denotes the strength of the magnetic interaction, which we have assumed to be of the same type as used in the Heisenberg model (Eq. (4-102)) with $n=3$ and $H_i=0$.

We will not go further into the classification of the various models here, but note one general property of both models in Eqs. (4-109) and (4-112) which becomes evident when mapping the Ising Hamiltonian Eq. (4-56): for $H=0$, this Hamiltonian is invariant against a change of sign of all spins. For $H \neq 0$, it is invariant against the

transformation $\{S_i, H\} \rightarrow \{-S_i, -H\}$. This implies a particle–hole symmetry of the phase diagram of the lattice gas model, or a symmetry against interchange of A and B in the phase diagram of the binary alloy model. Even in very ideal cases, where both partners A and B of a binary alloy crystallize in the same structure and have similar lattice spacings, the phase diagram is in reality not symmetric around the line $\langle c_i \rangle = 1/2$ (see the Cu–Au phase diagram reproduced in Fig. 4-13 as an experimental example). There are various conceivable reasons for this asymmetry of real phase diagrams: (i) the assumption of strictly pairwise potentials (Eq. (4-109)) fails, and terms such as $c_i c_j c_k$, $c_i c_j c_k c_l$ need to be included in the effective Hamiltonian; and (ii) the potentials v_{AA} , v_{AB} , and v_{BB} in Eq. (4-109) are not strictly constant but depend

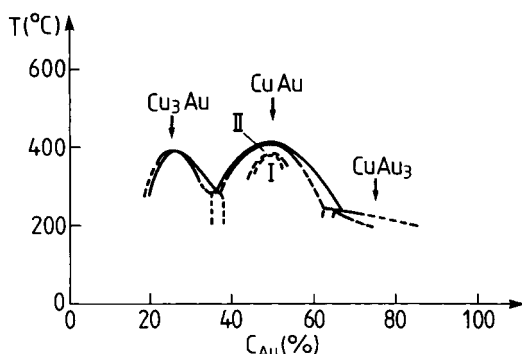


Figure 4-13. Partial phase diagram of copper–gold alloys in the temperature–concentration plane indicating the existence regions of the three ordered phases Cu_3Au , CuAu , and CuAu_3 (cf. Fig. 4-8a and c). These phases are separated from each other (and from the disordered phase occurring at higher temperatures) by two-phase coexistence regions. The boundaries of these regions are indicated by full and broken lines. Region II is a long-period modulated version of the simple CuAu structure occurring in region I. Note that for strictly pairwise constant interactions (of arbitrary range!) in a model such as Eq. (4-109) the phase diagram should have mirror symmetry around the line $c_{\text{Au}}=50\%$. From Hansen (1958).

on the average concentration $\langle c \rangle$ of the alloy, since the effective lattice parameter a and the Fermi wavenumber k_F and other physical characteristics entering the effective potential of the alloy also depend on concentration $\langle c \rangle$. In fact, both reasons probably contribute to some extent in real alloys – the first-principles derivation of model Hamiltonians such as Eq. (4-109) from the electronic structure theory for solids is a challenging problem (Bieber and Gautier 1984a,b; Zunger, 1994). Since the effective interaction typically is oscillatory in sign (Fig. 4-14) according to the Friedel form

$$v(|\mathbf{x}|) = A \cos(2|\mathbf{k}_F||\mathbf{x}| + \varphi)/|\mathbf{x}|^3 \quad (4-116)$$

where A and φ are constants, small changes in $|\mathbf{k}_F|$ and/or the distances lead to relatively large changes in $v(|\mathbf{x}|)$ for distant neighbors. Whereas the interaction Eq. (4-116) results from the scattering of conduction electrons at concentration inhomogeneities, in other cases such as H in metals the effective interactions are due to the elastic distortions produced by these interstitials in their environment. The resulting elastic interaction is also of long range (Wagner and Horner, 1974).

Since the effective interactions that should be used in Eqs. (4-109) to (4-115) often cannot be predicted theoretically in a reliable way, it may be desirable to extract them from suitable experimental data. For metallic alloys, such suitable experimental data are the Cowley (1950) short-range order parameters $\alpha(\mathbf{x}) \equiv \alpha(\mathbf{x}_i - \mathbf{x}_j)$ which describe the normalized concentration correlation function, $c \equiv \langle c_i \rangle = (1 - M)/2$, $M \equiv \langle S_i \rangle$

$$\alpha(\mathbf{x}_i - \mathbf{x}_j) \equiv \frac{\langle c_i c_j \rangle - c^2}{c(1 - c)} = \frac{\langle S_i S_j \rangle - M^2}{1 - M^2} \quad (4-117)$$

which correspond to the normalized spin correlation functions in the Ising spin rep-

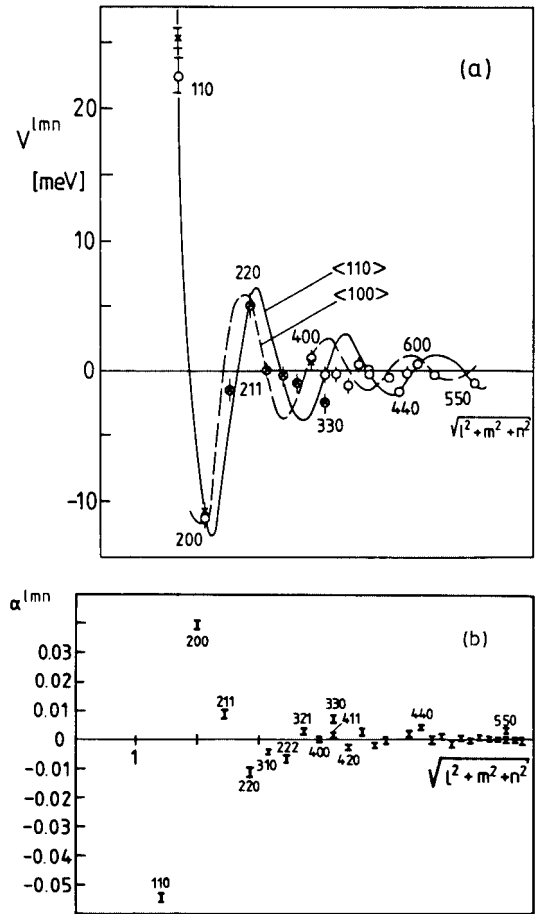


Figure 4-14. (a) Interaction potential $V^{lmn} = -2J(\mathbf{x})$ (note that $\mathbf{x} = (l, m, n) \frac{a}{2}$, a being the lattice spacing) vs. distance $|\mathbf{x}|$ (measured as $\sqrt{l^2 + m^2 + n^2}$) for $\text{NiCr}_{0.11}$ at $T = 560^\circ\text{C}$, as deduced from (b) short-range order parameters $\alpha(\mathbf{x})$ measured by diffuse neutron scattering. The circles show the results of the high-temperature approximation, Eq. (4-121), and crosses the result of the inverse Monte Carlo method. Full and broken curves represent a potential function of the Friedel form, Eq. (4-116), with different choices of the Fermi wavevector \mathbf{k}_F for $\langle 100 \rangle$ and $\langle 110 \rangle$ directions, amplitude A and phase Φ being treated as fitting parameters. From Schweika and Hauboldt (1986).

resentation (Eq. (4-117) for a ferromagnet is equivalent to the phenomenological Eq. (4-43)). In the disordered phase of an Ising spin system, it is straightforward to obtain the wavevector-dependent response func-

tion $\chi(\mathbf{q})$ describing the response to a wavevector-dependent field (cf. Eqs. (4-32), (4-34), and (4-40)), if we apply the molecular field approximation (see the next subsection). The result is (Brout, 1965):

$$S(\mathbf{q}) = k_B T \chi(\mathbf{q}) = \frac{1 - M^2}{1 - [\tilde{J}(\mathbf{q})/k_B T](1 - M^2)} \quad (4-118)$$

where $\tilde{J}(\mathbf{q})$ is the Fourier transform of the “exchange interaction” $J(\mathbf{x})$,

$$\tilde{J}(\mathbf{q}) = \sum_{j(\neq i)} J(\mathbf{x}_i - \mathbf{x}_j) \exp[i\mathbf{q} \cdot (\mathbf{x}_i - \mathbf{x}_j)] \quad (4-119)$$

In Eq. (4-118), we have once again invoked that there is a “fluctuation relation” (= static limit of the so-called “fluctuation-dissipation theorem”) relating $\chi(\mathbf{q})$ to the structure factor $S(\mathbf{q})$ which is just the Fourier transform of the correlations appearing in Eq. (4-117):

$$S(\mathbf{q}) = \sum_{j(\neq i)} \exp[i\mathbf{q} \cdot (\mathbf{r}_i - \mathbf{r}_j)] (\langle S_i S_j \rangle - M^2) \quad (4-120)$$

Combining now Eqs. (4-118) and (4-120) we see that the reciprocal of this diffuse scattering intensity $S(\mathbf{q})$ in \mathbf{q} -space is simply related to the Fourier transformation of the interactions as

$$\frac{4c(1-c)}{S(\mathbf{q})} = 1 - \frac{4\tilde{J}(\mathbf{q})}{k_B T} c(1-c) \quad (4-121)$$

For the model defined in Eqs. (4-109) to (4-111), this expression even is exact in an expansion of $1/S(\mathbf{q})$ in a power series in $1/T$ to leading order in $1/T$, and is one of the standard tools for inferring information on interactions in alloys from diffuse scattering data (Clapp and Moss, 1966, 1968; Moss and Clapp, 1968; Krivoglaz, 1969; Schweika, 1994). An example is shown in Fig. 4-14. Close to the order–disorder phase transition, we expect corrections to the molecular field expression Eq. (4-121) due to the effects of statistical fluctuations

(cf. Sec. 4.2.2); a more accurate procedure to deduce $J(\mathbf{x})$ from experimental data on $\alpha(\mathbf{x})$ is the “inverse Monte Carlo method” (Gerold and Kern, 1986, 1987; Schweika, 1989), but this method also relies on the assumption that an Ising model description as written in Eq. (4-109) is appropriate. On the level of the molecular field approximation (for alloys this is usually referred to as the Bragg–Williams (1934) approximation) or the Bethe (1935) approximation, it is possible to avoid models of the type of Eq. (4-109) and include the configurational degrees of freedom in an electronic structure calculation (Kittler and Falicov, 1978, 1979). Although such an approach sounds very attractive in principle, the results are not so encouraging in practice, as shown in Fig. 4-15. The results of this method for Cu_3Au are compared with Monte Carlo data of a nearest neighbor Ising model (Binder, 1980), with the cluster-variation treatment of the same model (Golosov et al., 1973) and with experimental data (Keating and Warren, 1951; Moss, 1964; Orr, 1960).

The conclusion of this subsection is that the development of microscopic models for the description of order–disorder phenomena in alloys is still an active area of research, and is a complicated matter, because the validity of the models can only be judged by comparing results drawn from the models with experimental data. However, these results also depend on the approximation involved in the statistical-mechanical treatment of the models (e.g., the full and broken curves in Fig. 4-15 refer to the *same* nearest-neighbor Ising model, whereas the dash-dotted curve refers to a different model). In the next subsections, we consider various sophistications of the statistical mechanics as applied to various models for phase-transition phenomena. More details about all these problems can be found in the Chapter by Inden (2001).

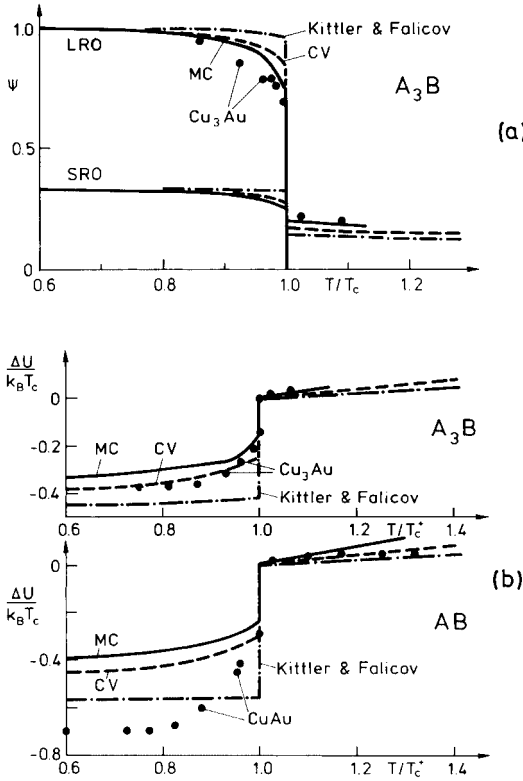


Figure 4-15. (a) Order parameters for the A_3B structure (Fig. 4-8c) on the fcc lattice: Long-range order parameter Ψ (LRO) and short-range order parameter $-\alpha_1$ for the nearest-neighbor distance (SRO) vs. temperature, according to the Monte Carlo method (Binder, 1980), the cluster variation (CV) method in the tetrahedron approximation (Goloso et al., 1973), and the Kittler–Falicov (1978, 1979) theory. Data for Cu_3Au after Keating and Warren (1951) (LRO) and after Moss (1964) (SRO). (b) Ordering energy ΔU (normalized to zero at T_c in the disordered state) vs. temperature for the fcc A_3B alloy (top) and the fcc AB alloy (bottom). Theoretical curves are from the same sources as in (a); experimental data were taken from Orr (1960) and Orr et al. (1960).

We have concentrated in this subsection on alloys, but a similar discussion could have also been presented for order–disorder phenomena in adsorbed monolayers (see for example, Binder and Landau (1981, 1989), where the modeling of systems such as H adsorbed on Pd(100) surfaces in terms

of lattice gas models is discussed), for magnetic transitions (De Jongh and Miedema, 1974), etc. Usually only the source of experimental data used to extract the interaction parameters is different: e.g., for ferromagnets such as EuS, rather than using diffuse magnetic neutron scattering in analogy with Eq. (4-118) it is more convenient to extract $\tilde{J}(q)$ from the measurements of spin wave dispersion curves found from inelastic neutron scattering (Bohn et al., 1980).

4.3.2 Molecular Field Theory and its Generalization (Cluster Variation Method, etc.)

The molecular field approximation (MFA) is the simplest theory for the description of phase transition in materials; despite its shortcomings, it still finds widespread application and has been described in great detail in various textbooks (Brout, 1965; Smart, 1966). Therefore we do not treat the MFA in full detail here, but rather indicate only the spirit of the approach.

We start with the Ising ferromagnet, Eq. (4-56). The exact Helmholtz energy can be found formally from the minimum of the functional (Morita, 1972)

$$\mathcal{F} = \sum_{\{S_i = \pm 1\}} \mathcal{H}_{\text{Ising}}(\{S_i\}) P(\{S_i\}) + k_B T \sum_{\{S_i = \pm 1\}} P(\{S_i\}) \ln(P\{S_i\}) \quad (4-122)$$

where the sums extend over all configurations of the spins in the system and $P(\{S_i\})$ is the probability that a configuration $\{S_i\}$ occurs. Eq. (4-122) thus corresponds to the thermodynamic relation $F = U - TS$ where the entropy S is written in its statistical interpretation. Minimizing Eq. (4-122) formally with respect to P yields the canonical distribution

$$P_{\text{eq}}(\{S_i\}) \sim \exp[-\mathcal{H}_{\text{Ising}}(\{S_i\})/k_B T]$$

as desired.

The MFA can now be defined by factorizing the probability $P(\{S_i\})$ of a spin configuration of the whole lattice into a product of single-site probabilities p_i which can take two values: $p_+ = (1+M)/2$ is the probability that the spin at site i is up and $p_- = (1-M)/2$ is the probability that it is down, $p_+ - p_- = M$ is the magnetization. Now the expression $J_{ij}S_iS_jp_ip_j$ (cf. Eq. (4-56)) summed over the possible values p_+ and p_- simply yields $J_{ij}M^2$, and hence Eq. (4-122) reduces to, using Eq. (4-119)

$$\frac{1}{N} \mathcal{F}^{\text{MFA}} = \frac{1}{2} \tilde{J}(q=0)M^2 - HM \quad (4-123)$$

$$+ k_B T \left[\frac{1+M}{2} \ln \left(\frac{1+M}{2} \right) + \frac{1-M}{2} \ln \left(\frac{1-M}{2} \right) \right]$$

Minimizing \mathcal{F}^{MFA} with respect to M now yields the elementary self-consistency equation:

$$M = \tanh \frac{1}{k_B T} [\tilde{J}(q=0)M + H] \quad (4-124)$$

As is well known, Eq. (4-124) implies a second-order transition at $T_c \equiv \tilde{J}(q=0)/k_B$ with the same exponents as in the Landau theory.

Clearly, in factorizing $P(\{S_i\})$ into a product of single-site probabilities and solving only an effective single-site problem, we have disregarded correlation in the probabilities of different sites. A systematic improvement is obtained if we approximate the probability of configurations not just by single-point probabilities but by using “cluster probabilities”. We consider probabilities $p_{nc}(k, i)$ that a configuration k of the n spins in a cluster of geometric configuration c occurs (c may be a nearest-neighbor pair, or a triangle, tetrahedron, etc.). Note $k=1, \dots, 2^n$ for Ising spins whereas $k=1, \dots, q^n$ for the q -state Potts model.

These probabilities can be expressed in terms of the multi-spin correlation functions $g_{nc}(i) \equiv \langle S_i S_{j_1} \dots S_{j_n} \rangle$, where the set of vectors $\mathbf{x}_{j_1} - \mathbf{x}_i, \dots, \mathbf{x}_{j_n} - \mathbf{x}_i$ defines the n -point cluster of type c located at lattice site i . The Helmholtz energy functional to be minimized in this cluster variation method (Kikuchi, 1951; Sanchez and De Fontaine, 1980, 1982; Finel, 1994) is a more complicated approximation of Eq. (4-122) than Eq. (4-123). If the largest cluster considered exceeds the interaction range, the energy term in $F = U - TS$ is treated exactly; unlike Eq. (4-123), the entropy is approximated. We find

$$\mathcal{F} = \frac{1}{2} \sum_i \sum_j J_{ij} g_{2,r_j}(i) + k_B T \sum_i \sum_{n,c} \gamma_{nc} \times \sum_{k=1}^{2^n} p_{n,c}(k, i) \quad (4-125)$$

where the coefficients γ_{nc} are combinatorial factors depending on the lattice geometry and the clusters included in the approximation (Kikuchi, 1951), e.g., in the tetrahedron approximation for the f.c.c. lattice, the sum over c in Eq. (4-125) includes the (nearest-neighbor) tetrahedron, the nearest-neighbor triangle, the nearest-neighbor pair, and the single site.

Assuming the ordered structure to be known, the symmetry operations of the associated group can be applied to reduce the number of variational parameters in Eq. (4-125). In the MFA, there is a single non-linear self-consistent equation (Eq. (4-124)) or a set of equations involving the order-parameter components if a problem more complicated than the Ising ferromagnet is considered. In the CV method, a much larger set of coupled non-linear equations involving the short-range order parameters $g_{nc}(i)$ is obtained when we minimize Eq. (4-125). Therefore, whereas the simple MFA is still manageable for a wide

variety of systems (Brout, 1965; Smart, 1966), the CV method is essentially restricted to Ising-type problems relevant for phase transitions in metallic alloys (De Fontaine, 1979; Finel, 1994). We discuss the merits of the various approaches in the next section.

At this point, we return to the formulation of the MFA for the case of an arbitrary type of ordering, rather than the simple transition from paramagnetic to ferromagnetic considered in the above treatment (Eqs. (4-123) and (4-124)) of the Ising model (Eq. (4-56)). Hence Eq. (4-123) can obviously be generalized as follows (see also De Fontaine, 1975):

$$\mathcal{F}^{\text{MFA}} = -2 \sum_{i \neq j} J(\mathbf{x}_i - \mathbf{x}_j) \xi_i \xi_j \quad (4-126)$$

$$+ k_B T \sum_i [c_i \ln c_i + (1 - c_i) \ln (1 - c_i)]$$

where $\xi_i = c_i - c = (M - S_i)/2$, and constant terms have been omitted. Expanding Eq. (4-126) in terms of ξ_i yields, again omitting a constant term,

$$\Delta \mathcal{F}^{\text{MFA}} = \frac{1}{2} \sum_{i,j} f_0''(\mathbf{x}_i - \mathbf{x}_j) \xi_i \xi_j \quad (4-127)$$

$$+ \frac{1}{3!} f_0''' \sum_i \xi_i^3 + \frac{1}{4!} f_0^{\text{IV}} \sum_i \xi_i^4$$

with the coefficients

$$f_0''(\mathbf{x} \neq 0) = -4J(\mathbf{x}_i - \mathbf{x}_j)$$

$$f_0''(\mathbf{x} = 0) = k_B T / [c(1 - c)] \quad (4-128)$$

and

$$f_0''' = -k_B T (2c - 1) / [c(1 - c)]^2 \quad (4-129)$$

$$f_0^{\text{IV}} = 2k_B T [3c^2 - 3c + 1] / [c(1 - c)]^3$$

If we group the ξ_i s properly into the sublattices reflecting the (known or assumed) state, Eq. (4-127) essentially yields the Landau expansion in terms of the order-parameter components, as discussed in Sec. 4.2.1. Rather than defining sublattices a

priori, it is often convenient to introduce Fourier transformations

$$X(\mathbf{q}) = \frac{1}{N} \sum_i \xi_i \exp[-i\mathbf{q} \cdot \mathbf{x}_i] \quad (4-130)$$

which yield:

$$\Delta \mathcal{F}^{\text{MFA}} = \frac{N}{2} \sum_{\mathbf{q}} \tilde{f}''(\mathbf{q}) |X(\mathbf{q})|^2$$

$$+ \frac{N}{3!} f_0''' \sum_{\mathbf{q}, \mathbf{q}', \mathbf{q}''} X(\mathbf{q}) X(\mathbf{q}') X(\mathbf{q}'')$$

$$\times \delta(\mathbf{q} + \mathbf{q}' + \mathbf{q}'' - \mathbf{G})$$

$$+ \frac{N}{4!} f_0^{\text{IV}} \sum_{\mathbf{q}, \mathbf{q}', \mathbf{q}'', \mathbf{q}'''} X(\mathbf{q}) X(\mathbf{q}') X(\mathbf{q}'') X(\mathbf{q}''')$$

$$\times \delta(\mathbf{q} + \mathbf{q}' + \mathbf{q}'' + \mathbf{q}''' - \mathbf{G}) \quad (4-131)$$

where \mathbf{G} is a reciprocal lattice vector and $\tilde{f}''(\mathbf{q})$ can be written as

$$\tilde{f}''(\mathbf{q}) = -4\tilde{J}(\mathbf{q}) + k_B T / [c(1 - c)] \quad (4-132)$$

Comparing Eqs. (4-121) and (4-132), we realize that the inverse structure factor (or inverse “susceptibility”, $\chi^{-1}(\mathbf{q})$) is simply proportional to $\tilde{f}''(\mathbf{q})$, as it should be, since $X(\mathbf{q})$ and $H(\mathbf{q})$ (apart from constants) are canonically conjugate thermodynamic variables. Of special importance now are the points \mathbf{q}_c where $\tilde{J}(\mathbf{q})$ has its maximum and correspondingly $\tilde{f}''(\mathbf{q})$ has a minimum, because for these wavevectors a sign change of $\tilde{f}''(\mathbf{q})$ in Eq. (4-131) occurs first (at the highest temperature). Hence a stability limit of the disordered phase is predicted as

$$k_B T_c = 4\tilde{J}(\mathbf{q}_c) c(1 - c) \quad (4-133)$$

If at this temperature a second-order transition occurs, it should actually be described by a “concentration wave” $X(\mathbf{q}_c)$ as an order parameter (see also the discussion following Eq. (4-31)). In many cases the maxima of $\tilde{J}(\mathbf{q})$ occur at special symmetry points of the Brillouin zone, and symmetry considerations in reciprocal space are useful for discussing the resulting or-

dered structures (De Fontaine, 1975, 1979; Khachaturyan, 1973, 1983).

This formulation of order–disorder transitions in alloys is analogous to the treatment of structural transitions, for which a model Hamiltonian similar to Eq. (4-127) can be written: rather than concentration deviations ξ_i we now have displacement vectors $\mathbf{u}_l(\mathbf{x})$ associated with a lattice vector \mathbf{x} for the l th atomic species in the unit cell. Just as it is useful to relate ξ_i to the Fourier transform $X(\mathbf{q})$ of the concentration deviation, it is useful to relate $\mathbf{u}_l(\mathbf{x})$ to the phonon normal coordinate $Q_{\mathbf{k},\lambda}$, defined as

$$\mathbf{u}_l(\mathbf{x}) = \frac{1}{\sqrt{NM_l}} \sum_{\mathbf{k},\lambda} \exp(i\mathbf{k} \cdot \mathbf{x}) \mathbf{e}_l(\mathbf{k},\lambda) Q_{\mathbf{k},\lambda} \quad (4-134)$$

where M_l is the mass of the atom of type l at site \mathbf{R}_l^i in the i th unit cell, $\mathbf{e}_l(\mathbf{k},\lambda)$ is a phonon polarization vector, λ labels the phonon branch and \mathbf{k} its wavevector (Fig. 4-16). In this case, $\langle Q_{\mathbf{k}_0,\lambda_0} \rangle_T$ plays the role

of an order-parameter component for the transition: in mean-field theory, the associate eigenfrequency vanishes at a temperature T_c (“soft phonon”). If this happens for a phonon with wavevector \mathbf{k}_0 at the Brillouin zone edge, we have an antiferroelectric order, provided that the phonon is polar, i.e., it produces a local dipole moment. For non-polar phonons, such as for the transition in SrTiO_3 at $T_c = 106$ K where $\mathbf{k}_0 = \pi(\frac{1}{2}, \frac{1}{2}, \frac{1}{2})/a$ (the soft phonon there physically corresponds to an antiphase rotation of neighboring TiO_6 octahedra, as indicated schematically in Fig. 4-12), the transition leads to “antiferrodistortive” order. Long-wavelength distortions corresponding to optical phonons give rise to ferroelectric ordering (an example is $\text{Pb}_5\text{Ge}_3\text{O}_{11}$, where $\mathbf{k}_0 = 0$ and $T_c = 450$ K (Gebhardt and Krey, 1979)). There are also paraelectric–ferroelectric transitions of first order, e.g., the cubic–tetragonal transition of BaTiO_3 , such that no soft mode occurs.

Just as the “macroscopic” ferroelectric ordering can be associated with the normal coordinate $Q_{\mathbf{k}_0=0,\lambda}$ of the associate optical phonon as a microscopic order parameter characterizing the displacements on the atomic scale, the “macroscopic” ferroelastic orderings, where in the phenomenological theory, Eq. (4-27), a component of the strain tensor $\varepsilon_{\mu\nu}$ is used as an order parameter, can be related to acoustical phonons. Examples are the martensitic material In-25 at.% Tl where the combination $c_{11} - c_{12}$ of the elastic constants nearly softens at $T_c = 195$ K, and $\text{LaP}_5\text{O}_{14}$ where c_{55} softens at $T_c = 400$ K and the structure changes from orthorhombic to monoclinic (Gebhardt and Krey, 1979). Of course, this correspondence between the microscopic description of displacements in crystals in terms of phonons and the phenomenological macroscopic description in terms of po-

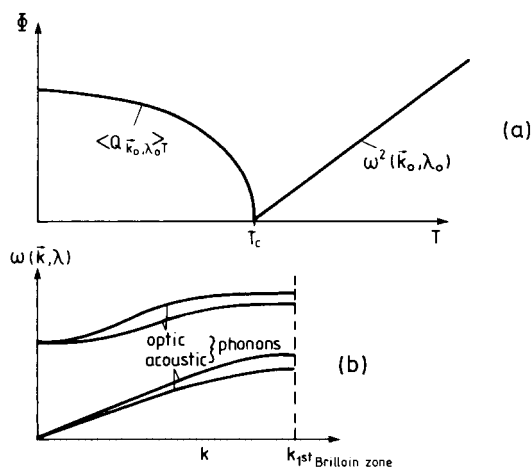


Figure 4-16. (a) Schematic temperature variation of order parameter $\Phi = \langle Q_{\mathbf{k}_0,\lambda_0} \rangle_T$ and square of the “soft-mode” frequency $\omega^2(\mathbf{k}_0, \lambda_0)$ at a displacive structural transition. (b) Schematic phonon spectrum of the solid at $T > T_c$. Note that either optical or acoustic phonons may go soft, and for optical phonons a softening may often occur at the boundary of the first Brillouin zone rather than at its center.

larization fields, strain fields, etc., is a well-known feature of condensed-matter theory (Kittel, 1967).

As is well known, the $Q_{k,\lambda}$ are defined such that the Hamiltonian of the crystal in the quasi-harmonic approximation is diagonalized (Born and Huang, 1954):

$$\begin{aligned}\mathcal{H} &= U_0 + \frac{1}{2} \sum_{i,j,l,l',\alpha,\beta} [\partial^2 U / (\partial \mathbf{x}_i^l)_\alpha (\partial \mathbf{x}_j^{l'})_\beta] \\ &\quad \times u_i^\alpha(\mathbf{x}_i) u_j^\beta(\mathbf{x}_j) \\ &= U_0 + \frac{1}{2} \sum_{k,\lambda} \omega^2(\mathbf{k}, \lambda) |Q_{k,\lambda}|^2\end{aligned}\quad (4-135)$$

Eq. (4-135) corresponds precisely to Eqs. (4-127) and (4-131) if only the “harmonic terms” (i.e., quadratic terms in the expansion with respect to the ξ_i s) are retained. The vanishing of a soft mode, $\omega^2(k_0, \lambda_0) \sim (T - T_c)$, is again equivalent to the vanishing of a coefficient $r \sim (T - T_c)$ of a quadratic term in a Landau expansion. Of course, as in the Landau theory, higher-order “anharmonic” terms in Q are crucial for the description of the ordered phase in terms of a stable order parameter $\langle Q_{k_0, \lambda_0} \rangle$ for $T < T_c$.

These anharmonic terms thoroughly modify the picture of the transition as obtained from MFA, as they lead to a coupling of the soft mode Q_{k_0, λ_0} with other noncritical modes. This coupling among modes gives rise to a damping of the soft mode. In fact, under certain circumstances even an overdamped soft mode and the appearance of a central peak are expected (Gebhardt and Krey, 1979; Bruce and Cowley, 1981).

A treatment of the anharmonic higher-order terms of a Landau-like expansion in reciprocal space is cumbersome, as Eq. (4-131) demonstrates. Denoting the amplitude of the displacement vector produced by the soft mode Q_{k_0, λ_0} in the unit cell i as Φ_i , we may formulate a model for a one-

component structural transition as follows (Bruce and Cowley, 1981):

$$\begin{aligned}\mathcal{H}_{\Phi^4} &= \sum_i \left[\frac{1}{2} r \Phi_i^2 + \frac{1}{4} u \Phi_i^4 \right] \\ &\quad + \sum_{\langle i,j \rangle} \frac{1}{2} C (\Phi_i - \Phi_j)^2\end{aligned}\quad (4-136)$$

where r , u and C are phenomenological coefficients. The last term corresponds to the harmonic interaction between displacements in neighboring lattice cells, while the anharmonicity has been restricted to the “single-site Hamiltonian” $[r \Phi_i^2/2 + u \Phi_i^4/4]$. Note that Eq. (4-136) is fully equivalent to the “Hamiltonian” $\Delta \mathcal{F}^{\text{MFA}}$ in Eq. (4-127) if $f_0''' = 0$ is chosen, since $(\Phi_i - \Phi_j)^2 = \Phi_i^2 + \Phi_j^2 - 2 \Phi_i \Phi_j$, and the coefficient C is thus equivalent to $f_0''(\mathbf{x}_i - \mathbf{x}_j)$ where $\mathbf{x}_i - \mathbf{x}_j$ is a nearest-neighbor distance, a . On the other hand, the “ Φ^4 -model” in Eq. (4-136) can be thought of as a lattice analog of the Helmholtz energy functional Eq. (4-10), putting $(\Phi_i - \Phi_j) \approx a \cdot \nabla \Phi_i$ (see Milchev et al. (1986) for a discussion).

An interesting distinction concerns this effective single-site Hamiltonian felt by the atoms undergoing the distortion. We have assumed that the ordered structure is doubly degenerate; the atoms below T_c can sit in the right or the left minimum of a double-well potential. If the single-site potential above T_c is essentially of the same type, and only the distribution of the atoms over the minima is more or less random, the transition is called “order–disorder type”. This occurs, for example, for hydrogen-bonded ferroelectrics and is analogous to the sublattice ordering described above for alloys. On the other hand, if the single-site potential itself changes above T_c to a single-well form, the transition is called “displacive”. Whereas it was often thought that displacive structural transitions exhibit well-defined soft phonons right up to their transition temperature T_c , it has now be-

come clear that all these structural transitions with a one-component order parameter acquire characteristics of order–disorder transitions close to T_c , as expected from the “universality principle”, and therefore the distinction between the character of a structural transition as being “order–disorder” or “displacive” is not a sharp one (Bruce and Cowley, 1981).

It should also be noted that the softening of $\omega(\mathbf{k}_0, \lambda_0)$ near T_c does not mean that displacements $\mathbf{u}_l(\mathbf{x})$ become very large. In fact, the mean square displacement of an atom at a structural transition is only expected to have an energy-like singularity (Meißner and Binder, 1975)

$$\langle \mathbf{u}_l^2 \rangle_T - \langle \mathbf{u}_l^2 \rangle_{T_c} \sim (T/T_c - 1)^{1-\alpha} \quad (4-137)$$

where α is the specific heat exponent. This is important because $\langle \mathbf{u}_l^2 \rangle_T$ is easily deduced experimentally from the Mössbauer effect, from the Debye–Waller factor describing the temperature variation of Bragg peaks in X-ray or neutron scattering, etc.

We end this subsection with a comment on the theory of first-order structural transitions. The common approach is to restrict the analysis entirely to the framework of the quasi-harmonic approximation, in which the Helmholtz energy at volume V and temperature T is written as

$$\begin{aligned} F(T, V) &= U - TS \\ &= U_0(V) + \frac{1}{2} \sum_{\mathbf{k}, \lambda} \hbar \omega_V(\mathbf{k}, \lambda) \\ &\quad + k_B T \sum_{\mathbf{k}, \lambda} \ln [1 - \exp(-\hbar \omega_V(\mathbf{k}, \lambda)/k_B T)] \end{aligned} \quad (4-138)$$

Therefore, if the effective potentials specifying the dynamical matrix $\partial^2 U/[(\partial \mathbf{x}_i^\alpha/\partial \mathbf{x}_j^\beta)]$ in Eq. (4-135) are known, the phonon frequencies $\omega_V(\mathbf{k}, \lambda)$ for a given volume and the free energy $F(T, V)$ are obtained. Of course in this approach, knowledge of the structure of the material is assumed. First-order transitions between

different structures can be handled by performing this calculation for both phases and identifying the temperature T_c where the free energy branches of the two phases cross. Since the quasi-harmonic theory is a calculation of the mean-field type, as pointed out above, first order transitions also show up via stability limits of the phases, where the soft modes vanish; thus we are not locating T_c but rather temperatures T_0 or T_1 (cf. Fig. 4-6b), which are often not very far from the actual transition temperature. This quasi-harmonic approach to structural phase transitions has been tried for many materials. Typical examples include RbCaF_3 (Boyer and Hardy, 1981) and the systems CaF_2 and SrF_2 (Boyer, 1980, 1981 a, b), which show phase transitions to a superionic conducting state.

4.3.3 Computer Simulation Techniques

In a computer simulation, we consider a finite system (e.g., a cubic box of size L^3 with periodic boundary conditions to avoid surface effects) and obtain information on the thermodynamic properties, correlation functions, etc. of the system (as specified by its model Hamiltonian) which is exact, apart from statistical errors. However, this approach is restricted to classical statistical mechanics (including quasi-classical models such as Ising or Potts models), although remarkable progress on application to quantum problems has been made (Kalos, 1985; Kalos and Schmidt, 1984; De Raedt and Lagendijk, 1985; Suzuki, 1992; Ceperley, 1995). The principal approaches of this type are the molecular dynamics (MD) technique and the Monte Carlo (MC) technique (for reviews of MD, see Ciccotti et al., 1987; Hoover, 1987; Hockney and Eastwood, 1988; Binder and Ciccotti, 1996; of MC, see Binder, 1979, 1984a; Mouritsen, 1984; Binder and Heermann,

1988; Binder and Ciccotti 1996). In the MD method, we numerically integrate Newton's equation of motion which follows from the chosen Hamiltonian, assuming ergodic behavior, and the quantities of interest are obtained as time averages from the simulation. This method requires that the relevant physical time scales involved in the problem are not too different from each other. The MD approach has often been applied successfully to liquid–solid transitions. It would not be suitable to study order–disorder phenomena in solid alloys, since the time step in the MD method for a solid must be much less than a phonon frequency, and this time scale is orders of magnitude smaller than the time between diffusive hops of atoms to neighboring vacant sites, which is the process relevant to equilibration of configurational degrees of freedom (Fig. 4-12).

For problems of the latter type, the MC method clearly is to be preferred. In the MC method, random numbers are used to construct a random walk through the configuration space of the model system. Using the Hamiltonian, transition probabilities between configurations are adjusted such that configurations are visited according to their proper statistical weight (Binder, 1979, 1984a; Binder and Ciccotti, 1996). Again averages are obtained as “pseudo-time averages” along the trajectory of the system in phase space, the only difference from the MD method being that the trajectory is now stochastic rather than deterministic. Both methods have been extensively reviewed (see the references quoted above); therefore, we do not give any details here, but only briefly mention the difficulties encountered when phase transitions are studied, and discuss a few typical examples of their application.

One principal difficulty is the finite-size rounding and shifting of the transition. In

principle, this problem is well understood (Fisher 1971; Challa et al., 1986; Binder, 1987b; Privman, 1990). In practice, this makes it difficult to distinguish between second-order and weakly first-order transitions. For example, extensive MD work was necessary to obtain evidence that the melting transition of two-dimensional solids with pure Lennard–Jones interaction is first order (Abraham, 1983, 1984; Bakker et al., 1984), and that the suggested two continuous transitions involving the hexatic phase do not occur in these systems (Nelson and Halperin, 1979). However, this conclusion has been called into question by recent simulations for hard-disk fluids (Jaster, 1998) providing evidence for continuous two-dimensional melting.

Another difficulty is that the periodic boundary condition (for a chosen shape of the box) prefers certain structures of a solid and suppresses others which do not “fit”: this is particularly cumbersome for incommensurate modulated structures (Selke, 1988, 1989; 1992) and for off-lattice systems, such as studies of the fluid–solid transition or phase transitions between different lattice symmetries. For example, particles interacting with a screened Coulomb potential (this is a model for colloidal suspensions or colloidal crystals (see Alexander et al., 1984)) may exhibit a fluid phase in addition to an f.c.c. and a b.c.c. crystal, and the determination of a complete phase diagram is correspondingly difficult (Kremer et al., 1986, 1987; Robbins et al., 1988). The traditional approach to dealing with such problems is to repeat the calculation for different box shapes and compare the free energies of the different phases. An interesting alternative method has been proposed by Parrinello and Rahman (1980) and Parrinello et al. (1983), who generalized the MD method by including the linear dimensions of the box as separate dynamic variables.

Another severe problem is the occurrence of metastability and hysteresis; the system may become trapped in a metastable state, the lifetime of which is longer than the observation time of the simulation. The distinction of such long-lived metastable states from true equilibrium states is difficult and may require computation of the Helmholtz energies of the phases in question.

These problems must be considered when first-order transitions are studied by computer simulation so that suitable box sizes and observation times are chosen and the initial state is prepared accordingly. Then, employing sufficient effort in computing time, and performing a careful analysis of all the possible pitfalls mentioned above, very reliable and useful results can be obtained which are superior in most cases to any of the other methods that have been discussed so far (see Fig. 4-15 for a comparison in the case of f.c.c. alloys). Misjudgements of the problems mentioned above have also led to erroneous conclusions: in the f.c.c. Ising antiferromagnet with nearest interaction J , the triple point between the AB and A_3B structures (Fig. 4-8a, c) was suggested to occur at $T=0$ (Binder, 1980) while later a nonzero T at low temperature was found, $k_B T/|J| \sim 1.0$ (Gahn, 1986; Diep et al., 1986; Kämmerer et al., 1996). Unlike in the other methods, such problems can always be clarified by substantially increasing the computational effort and carrying out more detailed analyses of the simulation "data".

A significant advantage of such a "computer experiment" is that interaction parameters of a model can be varied systematically. As an example, Fig. 4-17 shows the temperature dependence of the long-range order parameters and some short-range order parameters of an f.c.c model of an A_3B alloy with nearest-neighbor repul-

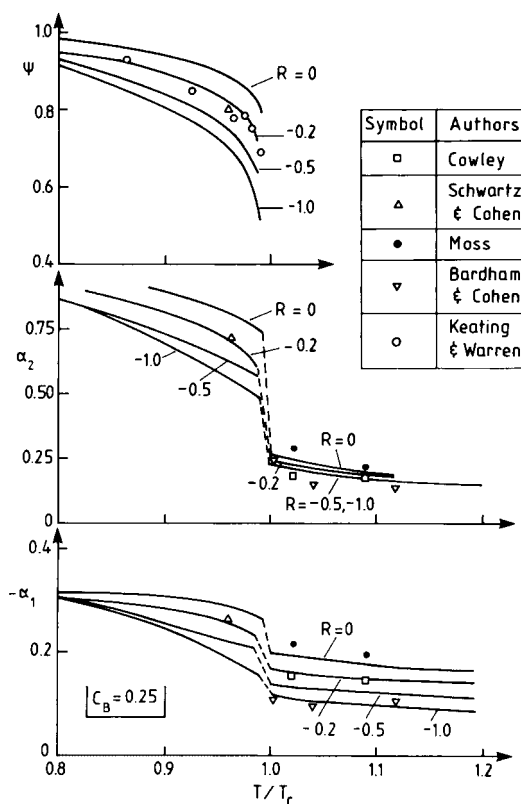


Figure 4-17. Temperature dependence of the long-range order parameter Ψ of the Cu_3Au structure and of the nearest- and next-nearest-neighbor short-range order parameter α_1 and α_2 . Curves are Monte Carlo results of Binder (1986). Points show experimental data of Cowley (1950), Schwartz and Cohen (1965), Moss (1964), Bardham and Cohen (1976), and Keating and Warren (1951). From Binder (1986).

sive (J_{nn}) and next-nearest-neighbor attractive interaction J_{nnn} (Eq. (4-110)), for various choices of their ratio $R = J_{nnn}/J_{nn}$. The comparison with experimental data shows that a reasonable description of Cu_3Au is obtained for $R = -0.2$, for $T < T_c$, whereas better experimental data for $T > T_c$ are needed before a more refined fit of effective interaction parameters can be performed.

As an example showing that the MC method can deal with very complex phase

diagrams, we consider the model in Eq. (4-115) for alloys with one magnetic component. However, in order to facilitate comparison with the MFA and CV methods, the magnetic interaction is chosen to be of Ising rather than Heisenberg type (Dünweg and Binder, 1987). Fig. 4-18 shows the resulting phase diagrams for the choice of interaction parameters $J_{nnn}/J_{nn}=0.5$ and $J_m/|J_{nn}|=0.7$. In this case, the MFA predicts a wrong phase diagram “topology” (e.g., a direct transition between paramagnetic DO_3 and A2 phases never occurs, there is always a B2 phase in between), and it also grossly overestimates the transition temperatures. In contrast, the CV method yields the phase diagram “topology” correctly, and it overestimates the transition temperature by only a few per cent. Although the CV method does not always perform so well (see Fig. 4-15, and Binder (1980) and Diep et al. (1986) for a discussion in the case of f.c.c. alloys), it is always much superior to the simple MFA, which in many cases fails dramatically.

One great advantage of the MC method over the CV method is that it can also be applied straightforwardly to models with continuous degrees of freedom, for which the CV method would be cumbersome to work out. As examples, Figs. 4-19 and 4-20 show the phase diagrams of the model in Eqs. (4-93) and (4-136), namely the anisotropic classical Heisenberg antiferromagnet in a uniform field $H_{||}$ along the easy axis and the Φ^4 model on the square lattice. Note that in the latter case the result of the MFA would be off-scale in this figure (e.g., $K_c^{-1}=4$ in the Ising limit). Finally, Fig. 4-21 shows the phase diagram of a model for $\text{Eu}_x\text{Sr}_{1-x}\text{S}$ (Binder et al., 1979):

$$\mathcal{H} = -\frac{1}{2} \sum_{i \neq j} J_{ij} x_i x_j \mathbf{S}_i \cdot \mathbf{S}_j \quad (4-139)$$

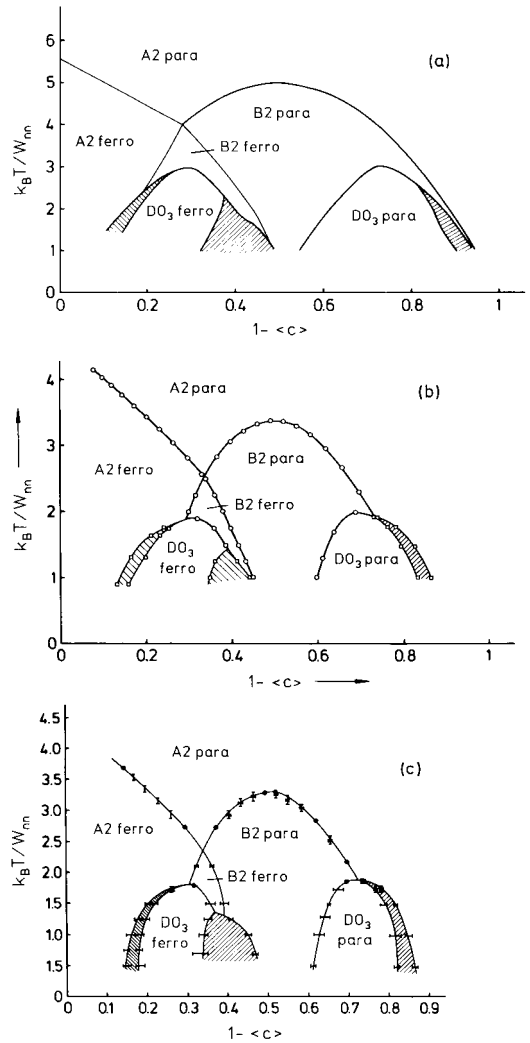


Figure 4-18. Phase diagram of the body-centered cubic binary alloy model with nearest and next nearest neighbor crystallographic interactions J_{nn} and J_{nnn} (both being “antiferromagnetic” if Ising-model terminology is used) and a ferromagnetic nearest-neighbor interaction J_m between one species, for $J_{nnn}/J_{nn}=0.5$, $J_m/|J_{nn}|=0.7$; c denotes the concentration of the magnetic species. (a) Result of the MFA (Bragg–Williams approximation); (b) result of the CV method in the tetrahedron approximation, and part (c) the MC result. The A2 phase is the crystallographically disordered phase, the orderings of the B2 and DO_3 phases are shown in Fig. 4-3. Two-phase coexistence regions are shaded. The magnetic ordering of the phases is indicated as para(-magnetic) and ferro(-magnetic), respectively. From Dünweg and Binder (1987).

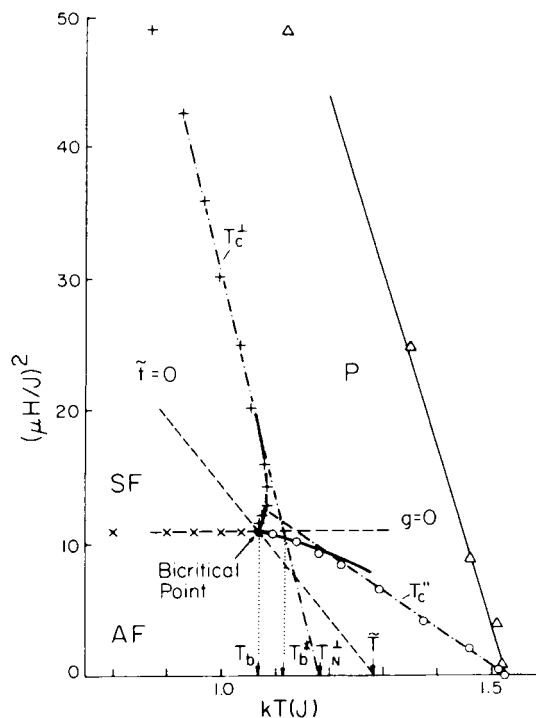


Figure 4-19. Phase diagram of a uniaxial classical Heisenberg antiferromagnet on the simple cubic lattice, as a function of temperature T and field H_{\parallel} applied in the direction of the easy axis. The anisotropy parameter Δ in the Hamiltonian Eq. (4-93) is chosen as $\Delta=0.2$. Both Monte Carlo results (crosses, circles, full curves) and the Landau theory fitted to the phase diagram in the region off the true bicritical point is shown (dash-dotted straight line). The Landau theory would overestimate the location of the bicritical temperature T_b ($T_b^* > T_b$), and fails to yield the singular umbilicus shape of the phase diagram lines T_c^\perp , T_c^\parallel near the bicritical point. The broken straight lines denote the appropriate choices of “scaling axes” for a crossover scaling analysis near T_b . The triangles show another phase diagram, namely when the field is oriented in the perpendicular direction to the easy axis. The nature of the phases is denoted as AF (antiferromagnetic), SF (spin-flop) and P (paramagnetic). See Fig. 4-9a for a schematic explanation of this phase diagram. From Landau and Binder (1978).

where S_i are unit vectors in the direction of the Eu magnetic moment, and from spin wave measurements (Bohn et al., 1980) it is known that EuS essentially exhibits superexchange between nearest and next-

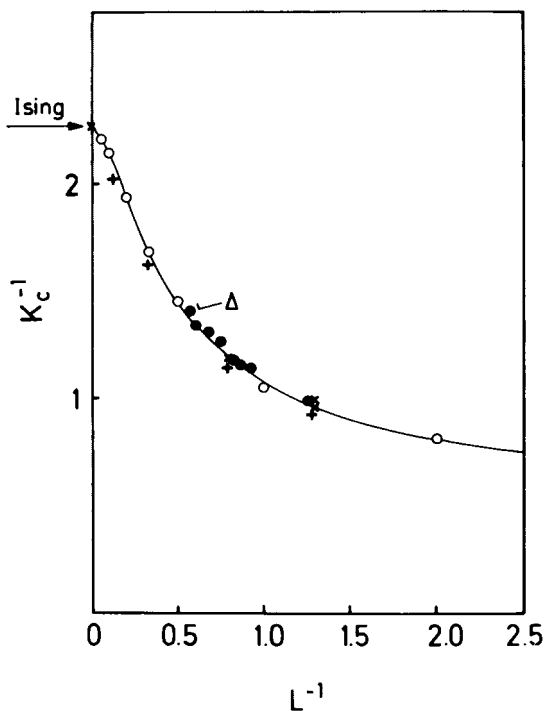


Figure 4-20. Critical line K_c^{-1} of the Φ^4 model (Eq. (4-136)) on the square lattice, shown in the space of couplings K^{-1} , L^{-1} defined as $K=-rC/u$, $L=r(r+4C)/(4u)$. Note that for $L^{-1}=0$, and K finite, the square Ising model results, the transition temperature of which is exactly known (Onsager, 1944; arrow). (●) Monte Carlo simulation of Milchev et al. (1986); (+) MD results of Schneider and Stoll (1976); (○, ×) from a real space renormalization group calculation of Burkhardt and Kinzel (1979). The disordered phase occurs above the critical line. From Milchev et al. (1986).

nearest neighbors only, further-neighbor interactions being negligibly small, with $J_{nnn}/J_{nn}=-1/2$. Thus Fig. 4-21 exhibits a remarkable agreement between computer simulation and experiment (Maletta and Felsch, 1979); there are no adjustable parameters involved whatsoever. Note that analytical methods for such problems with quenched disorder would be notoriously difficult to apply.

To conclude this subsection, we state that computer simulation techniques are

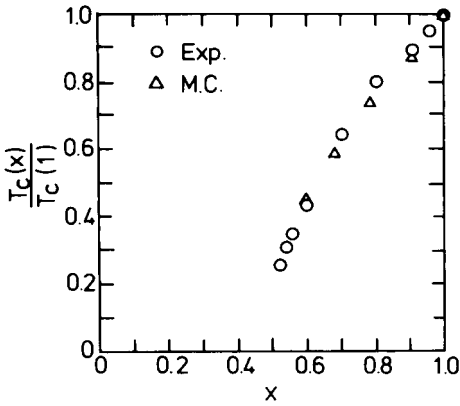


Figure 4-21. Ferromagnetic critical temperature of the model Eq. (4-139) of $\text{Eu}_x\text{Sr}_{1-x}\text{S}$ vs. concentration x of magnetic atoms. Circles denote experimental data due to Maletta and Felsch (1979), triangles the MC results for the diluted classical Heisenberg fcc ferromagnet with nearest (J_{nn}) and next-nearest (J_{nnn}) exchange, $J_{nnn} = -\frac{1}{2}J_{nn}$. From Binder et al. (1979).

well suited for studying the phase diagrams of various systems, magnetic systems, metallic alloys, structural transitions, adsorbed layers at surfaces, etc. provided that a suitable model Hamiltonian is known. Apart from the phase diagram, detailed information on long- and short-range order is also accessible. Also, for certain problems, the kinetics of phase transitions can be studied, in particular for alloys where the Monte Carlo process can directly model the atomic jump processes on the crystal lattice (Binder, 1979, 1984a; Kehr et al., 1989). Of course, there is also interest in clarifying the phase diagrams of materials in their fluid states. Computer simulations can now obtain accurate gas–liquid phase diagrams (Wilding, 1997), liquid binary mixtures (Wilding et al., 1998) and surfactants (Schmid, 1999).

4.4 Concepts About Metastability

Metastable phases are very common in nature, and, for many practical purposes, not at all distinct from stable phases (remember that diamond is only a metastable modification of graphite!). Also, approximate theories of first-order phase transitions easily yield Helmholtz energy branches that do not correspond to the thermal equilibrium states of minimum Helmholtz energy, and hence are commonly interpreted as metastable or unstable states (cf. Figs. 4-6 and 4-22). From the analog of Eq. (4-12) for $H \neq 0$,

$$\frac{1}{k_B T V} \left(\frac{\partial F}{\partial \Phi} \right)_T = r \Phi + u \Phi^3 - \frac{H}{k_B T} = 0 \quad (4-140)$$

the limit of metastability where $\chi_T = (\partial \Phi / \partial H)_T$ diverges as follows:

$$\begin{aligned} r + 3u \Phi_s^2 &= \frac{1}{k_B T} \frac{1}{\chi_T} = 0 \\ \Phi_s &= \sqrt{-r/3u} = \Phi_0 / \sqrt{3} \\ H_c &= -\frac{2r}{3} \sqrt{\frac{-r}{3u}} \end{aligned} \quad (4-141)$$

Since in the metastable states

$$\chi_T = (3 k_B T u)^{-1} (\Phi^2 - \Phi_s^2)^{-1}$$

we see that $\chi_T \rightarrow \infty$ as $\Phi \rightarrow \Phi_s$; in the (T, Φ) plane, the spinodal curve $\Phi = \Phi_s(T)$ plays the part of a line of critical points.

Similar behavior also occurs in many other theories: for example, the van der Waals equation of state describing gas–liquid condensation exhibits an analogous loop of one-phase states in the two-phase coexistence region.

Unfortunately, although the description of metastability in the framework of the MFA seems straightforward, this is not so if more accurate methods of statistical thermodynamics are used. A heuristic compu-

tational approach, discussed in Sec. 4.3.2, is the CV method where we systematically improve upon the MFA by taking more and more short-range correlations into account, the larger the cluster is chosen. Computing the equation of state for a nearest-neighbor Ising ferromagnet in this way (Kikuchi, 1967), it is found that the stable branch is nicely convergent, whereas the metastable loop becomes flatter and flatter the larger the cluster, i.e., the critical field H_c (Eq. (4-141)) converges towards zero. An exact calculation of the equation of state yields the magnetization jump from Φ_0 to $-\Phi_0$ as H changes from 0^+ to 0^- in Fig. 4-22, but does not yield any metastable state! This is not surprising, however, because statistical mechanics is constructed to yield information only on thermal equilibrium states. The partition function is dominated by the system configurations in the vicinity of the minimum of the Helmholtz energy. In a magnet with $H < 0$, states with negative magnetization have lower Helmholtz energy than those with positive magnetization. Hence the latter do not result from the partition function in the thermodynamic limit. Similar conclusions emerge from a rigorous treatment of the gas–fluid transition in systems with long-range interactions (Lebowitz and Penrose, 1966).

Two concepts emerged for the description of metastable states (for a more detailed discussion see Binder (1987a)). One concept (Binder, 1973) suggests the definition of metastability be based on the consideration of *kinetics*: starting with the system in a state of stable equilibrium, the system is brought out of equilibrium by a sudden change of external parameters (temperature, pressure, fields, etc.). For example, in the Ising-type ferromagnet of Fig. 4-22, at times $t < 0$ we may assume we have a state at $H = 0^+$, $\Phi = \Phi_0 > 0$; at $t = 0$, the field is switched to a negative value: then the

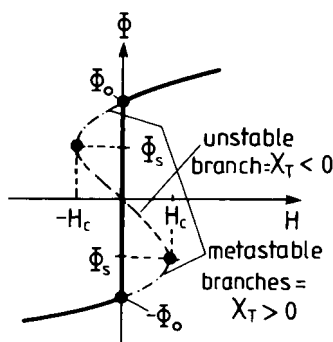


Figure 4-22. Order parameter Φ vs. conjugate field H according to the phenomenological Landau theory for system at a temperature T less than the critical temperature T_c of a second-order phase transition (schematic). At $H = 0$, a first-order transition from Φ_0 to $-\Phi_0$ occurs (thick straight line). The metastable branches (dash-dotted) end at the “limit of metastability” or “spinodal point” ($\Phi_s, -H_s$), respectively, and are characterized by a positive-order parameter susceptibility $\chi_T > 0$, whereas for the unstable branch (broken curve) $\chi_T < 0$.

magnetization in equilibrium is negative, but in the course of the nonequilibrium relaxation process from the initial state at Φ_0 a metastable state may occur with $\Phi_{ms} > 0$, although $H < 0$, which exists only over a finite lifetime τ_{ms} . In order that Φ_{ms} can clearly be identified in this dynamic process where the time-dependent order parameter $\Phi(t)$ relaxes from $\Phi(t=0) = \Phi_0$ to the negative equilibrium value $\Phi(t \rightarrow \infty)$, it is necessary that τ_{ms} is much larger than any intrinsic relaxation time. Then the time τ_{ms} for the decay of the metastable state far exceeds the time needed for the system to relax from the initial state towards the metastable state, and, in the “nonequilibrium relaxation function” $\Phi(t)$ the metastable state shows up as a long-lived flat part where $\Phi(t) \approx \Phi_{ms}$. The second concept tries to define a metastable state in the framework of equilibrium statistical mechanics by constraining the phase space so as to forbid the two-phase configurations

that otherwise dominate the partition function. Langer (1974) suggested that phase separation into two phases with order parameters $-\Phi_0$ and $+\Phi_0$ coexisting at the first-order transition at $H=0$ in Fig. 4-1 and Fig. 4-22 is suppressed if we consider a system (a) at fixed Φ between $-\Phi_0$ and $+\Phi_0$ but (b) constrain the system and divide it into cells of size L^d , and (c) require that the order parameter is not only globally fixed at Φ but also inside each cell. If L is small enough, namely $a \ll L \ll \xi_{\text{coex}}$ (this is the same condition as noted for the construction of a continuum model from the microscopic Hamiltonian, see Sec. 4.2.2, and Eqs. (4-9) and (4-57)), phase separation inside a cell cannot occur, and hence a coarse-grained Helmholtz energy density $f_{\text{cg}}(\Phi)$ of states with uniform order parameter Φ is obtained, which has exactly the double-well shape of the Landau theory (Fig. 4-6a). Since $f_{\text{cg}}(\Phi)$ then necessarily depends on this coarse-grained length scale L , it is clear that the metastable states of $f_{\text{cg}}(\Phi)$ are not precisely those observed in experiments, unlike the dynamic definition. While $f_{\text{cg}}(\Phi)$ defines a “limit of metastability” or “spinodal curve” Φ_s where $(\partial^2 f_{\text{cg}}(\Phi)/\partial \Phi^2)_T = \chi_T^{-1}$ vanishes and changes sign, this limit of metastability also depends on L and hence is not related to any physical limit of metastability. In the context of spinodal decomposition of mixtures, the problem of the extent to which a spinodal curve is relevant also arises and is discussed in detail in the chapter by Binder and Fratzl (2001).

In some systems where a mean-field description is appropriate, the lifetime of metastable states can be extremely long, and then the mean-field concept of a limit of metastability may be very useful. This fact can again be understood in terms of the Ginzburg criterion concept as outlined in Sec. 4.2.2. Since the spinodal curve

$\Phi = \Phi_s(T)$ acts like a line of critical points, as discussed above, we require (cf. Eq. (4-58))

$$\langle [\Phi(\mathbf{x}) - \Phi]^2 \rangle_{T,L} \ll [\Phi - \Phi_s(T)]^2 \quad (4-142)$$

i.e., the mean-square fluctuations in a volume L^d must be much smaller than the squared distance of the order parameter from its value at criticality, which in this case is the value at the spinodal. Now, the maximum permissible value for L is the correlation length ξ in the metastable state, which becomes

$$\xi = \{R/[6du \Phi_s(T)]^{1/2}\} [\Phi - \Phi_s(T)]^{-1/2} \quad (4-143)$$

Eq. (4-143) exhibits the critical singularity of ξ at $\Phi_s(T)$, corresponding to that of χ_T noted above. With a little algebra we find from Eqs. (4-142) and (4-143) (Binder, 1984c)

$$\begin{aligned} 1 &\ll R^2 \xi^{d-2} [\Phi - \Phi_s(T)]^2 \\ &\sim R^d [\Phi_s(T)]^{(2-d)/2} [\Phi - \Phi_s(T)]^{(6-d)/2} \\ &\sim R^d (H_c - H)^{(6-d)/4} \end{aligned} \quad (4-144)$$

This condition can only be fulfilled if the interaction range is very large. Even then for $d=3$ this inequality is not fulfilled very close to the spinodal curve.

In order to elucidate the physical significance of this condition further and to discuss the problem of the lifetime of metastable states, we briefly discuss the mean field theory of nucleation phenomena. In practice, for solid materials, heterogeneous nucleation (nucleation at surfaces, grain boundaries, dislocations, etc.) will dominate; and this may restrict the existence of metastable states much more than expected from Eq. (4-144). However, we consider here only the idealized case that homogeneous nucleation (formation of “droplets” of the stable phase due to statistical fluctuations) is the mechanism by which the metastable state decays. Since there is no

mechanism by which this process can be suppressed, metastable states cannot exist in a region where strong homogeneous nucleation occurs. *Therefore we estimate the intrinsic and ultimate limit of metastability by the condition that the Helmholtz energy barrier against homogeneous nucleation decreases to the order of the thermal energy $k_B T$* (Binder and Stauffer, 1976b).

As is well known, the nucleation barrier arises from competition between the favorable volume energy of a droplet of the new phase and the (unfavorable) surface Helmholtz energy between the droplet and the surrounding metastable background phase. In order to calculate this Helmholtz energy barrier in the framework of the Landau theory, we can still use Eqs. (4-10) and (4-33). Putting $H(x)=0$ in Eq. (4-33) and considering the situation that $\Phi(z \rightarrow \infty) = \Phi_0$, $\Phi(z \rightarrow -\infty) = -\Phi_0$ and solving for the concentration profile $\Phi(z)$ (Cahn and Hilliard, 1958), we can obtain the interface Helmholtz energy associated with a planar (infinitely extended) interface perpendicular to the z -direction (Fig. 4-23a). In the “classical theory of nucleation” (Zettlemoyer, 1969), this Helmholtz energy is then used to estimate the Helmholtz energy barrier. However, this “classical theory of nucleation” is expected to be reliable only for metastable states near the coexistence curve, where the radius R^* of a critical droplet (corresponding to a droplet Helmholtz energy exactly at the Helmholtz energy barrier ΔF^*) is much larger than the width of the interfacial profile (which then is also of the same order as the correlation length ξ_{coex} at the coexistence curve, cf. Figs. 4-23a, b). Therefore it cannot be used close to the limit of metastability. Cahn and Hilliard (1959) have extended the Landau theory to this problem, solving Eq. (4-33) for a spherical geometry, where only a radial variation of $\Phi(\rho)$ with radius ρ is

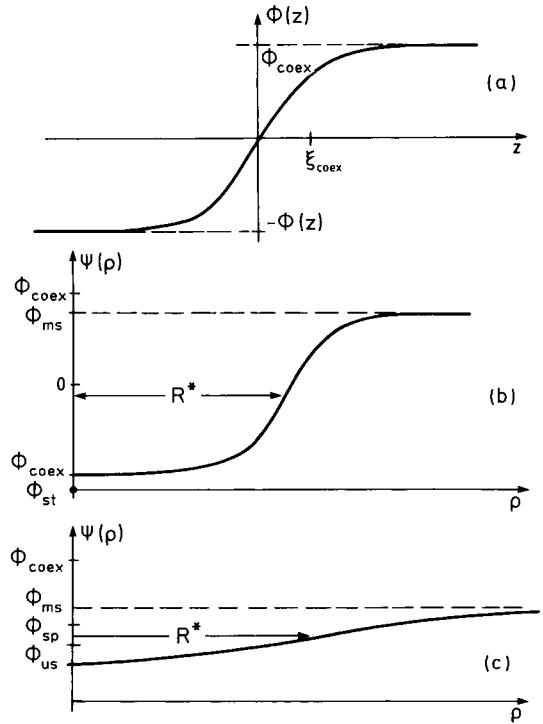


Figure 4-23. Order-parameter profile $\Phi(z)$ across an interface between two coexisting phases $\pm \Phi_{\text{coex}}$, the interface being oriented perpendicular to the z -direction (a) and the radial order-parameter profile for a marginally stable droplet in a metastable state which is close to the coexistence curve (b) or close to the spinodal curve (c). In (a) and (b) the intrinsic “thickness” of the interface is of the order of the correlation length at coexistence ξ_{coex} , whereas in (c) it is of the same order as the critical radius R^* . From Binder (1984c).

permitted, and a boundary condition $\Phi(\rho \rightarrow \infty) = \Phi_{\text{ms}}$ is imposed (Fig. 4-23b, c). Whereas for Φ_{ms} near $\Phi_{\text{coex}} = \Phi_0$ this treatment agrees with the “classical theory of nucleation”, it differs significantly from it for Φ near $\Phi_s(T)$: then the critical droplet radius R^* is of the same order as the (nearly divergent!) correlation length ξ (Eq. (4-143)), and the profile is extremely flat, $\Phi(\rho)$ reaches in the droplet center only a value slightly below Φ_s rather than the other branch of the coexistence curve. Calculating the Helmholtz energy

barrier ΔF^* , we obtain for T near T_c (Binder, 1984c; Klein and Unger, 1983)

$$\frac{\Delta F^*}{k_B T_c} \sim R^d \left(1 - \frac{T}{T_c}\right)^{(4-d)/2} \left(\frac{\Phi - \Phi_s}{\Phi_{\text{coex}}}\right)^{(6-d)/2} \quad (4-145)$$

whereas near the coexistence curve the result is

$$\frac{\Delta F^*}{k_B T_c} \sim R^d \left(1 - \frac{T}{T_c}\right)^{(4-d)/2} \left(\frac{\Phi_{\text{coex}} - \Phi}{\Phi_{\text{coex}}}\right)^{-(d-1)} \quad (4-146)$$

where all prefactors of order unity are omitted. In a system with a large range R of interaction, the nucleation barrier is very high in the mean-field critical region, in which $R^d(1 - T/T_c)^{(4-d)/2} \gg 1$ (cf. Eq. (4-62)); this factor, which controls the Ginzburg criterion, also controls the scale of the nucleation barrier as a prefactor (see Fig. 4-24). In this region the condition for the limit of metastability, $\Delta F^*/k_B T \approx 1$, is located very close to the mean-field spinodal. Then the description of nucleation phenomena in terms of the diffuse droplets described by Fig. 4-23c near the spinodal curve is meaningful ("spinodal nucleation"). On the other hand, for a system with short-range interactions where R (measured in units of the lattice spacing in Eqs. (4-145) and (4-146)) is unity, the Helmholtz energy barrier becomes of order unity long before the spinodal curve is reached. The singularity at the spinodal then completely lacks any physical significance, as the metastable state decays to the stable phase long before the spinodal is reached.

It is instructive to compare the condition $\Delta F^*/k_B T \ll 1$ with Eq. (4-144): this shows that these conditions are essentially identical! This is not surprising: the MFA is essentially correct as long as effects of statistical fluctuations are very small: the "heterophase fluctuations" (droplets of the

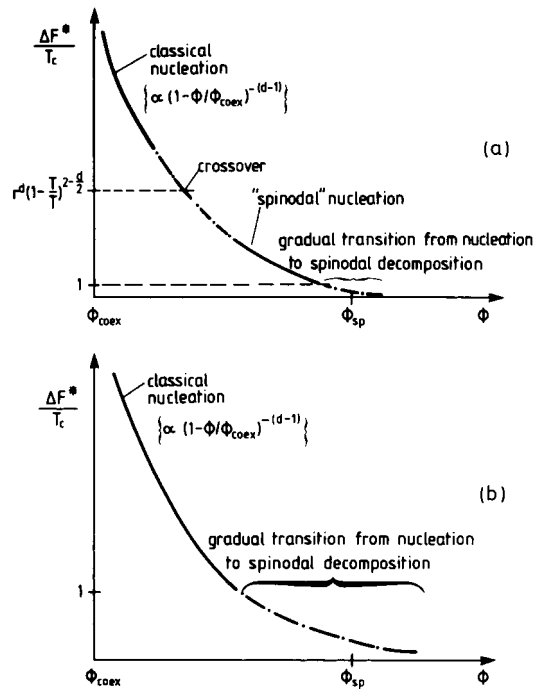


Figure 4-24. Schematic plots of the Helmholtz energy barrier for (a) the mean field critical region, i.e., $R^d(1 - T/T_c)^{(4-d)/2} \gg 1$, and (b) the non-mean field critical region i.e., $R^d(1 - T/T_c)^{(4-d)/2} \ll 1$. Note that owing to large prefactors to the nucleation rate, the constant of order unity where the gradual transition from nucleation to spinodal decomposition occurs is about 10^1 rather than 10^0 . From Binder (1984c).

new phase) are also extremely rare, and the Helmholtz energy cost to form them should be very high, as implied by Eqs. (4-145) and (4-146).

These concepts have been tested by Monte Carlo simulations on simple-cubic Ising models with various choices of the range of the interaction (Fig. 4-25, Heermann et al., 1982). For the case of nearest-neighbor interaction (each spin interacts with $q=6$ neighbors) it is seen that χ_T^{-1} differs considerably from the MFA result, and the range of fields over which metastable states can be observed is not very large. With an increase in the number of neighbors q ,

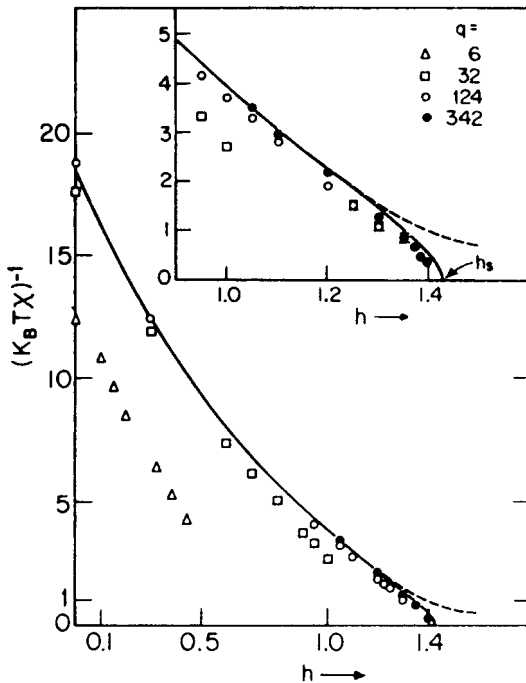


Figure 4-25. Inverse susceptibility of Ising ferromagnets plotted against $h = -H/k_B T$ at $T/T_c^{\text{MFA}} = 4/9$ for various ranges of the exchange interaction; each spin interacts with equal strength with q neighbors. The full curve is the MFA, the broken curve a fit to a droplet model description. From Heermann et al. (1982).

this range increases, the value of χ_T^{-1} at the field where nucleation becomes appreciable falls also, and the χ_T^{-1} vs. H curve quickly converges towards the MFA prediction, except in the immediate neighborhood of the limit of metastability H_c .

It is expected that the ideas sketched here will carry over to more realistic systems.

4.5 Discussion

There are many different kinds of phase transitions in materials, and the fact that a material can exist in several phases may

have a strong influence on certain physical properties. The approach of statistical mechanics tries to provide general concepts for dealing with such phenomena: classification methods are developed which also try to clarify which aspects of a phase transition are specific for a particular material and which are general ("universal"). At the same time, theoretical descriptions are available both on a phenomenological level, where thermodynamic potentials are expanded in terms of suitable order parameters and the expansion coefficients are undetermined, and can only be adjusted to experimental data, and on a microscopic level, where we start from a model Hamiltonian which is treated either by molecular field approximations or variants thereof or by computer simulation techniques.

This chapter has not given full details of all these approaches, but rather tried to give a discussion which shows what these methods can achieve, and to give the reader a guide to more detailed literature on the subject. An attempt has been made to summarize the main ideas and concepts in the field and to describe the general facts that have been established, while actual materials and their phase transitions are mentioned as illustrative examples only, with no attempt at completeness being made. Although the statistical thermodynamics of phase transitions has provided much physical insight and the merits and limitations of the various theoretical approaches are now well understood generally, the detailed understanding of many materials is still rudimentary in many cases; often there are not enough experimental data on the ordering phenomenon in question, or the data are not precise enough; a microscopic model Hamiltonian describing the interaction relevant for the considered ordering is often not explicitly known, or is so complicated that a detailed theory based on

such a model Hamiltonian does not exist. Many of the more sophisticated methods (CV method, computer simulation, etc.) are restricted in practice to relatively simple models. Hence, there still remains a lot to be done to improve our understanding of phase transitions.

4.6 References

- Abraham, F. F. (1974), *Homogeneous Nucleation Theory*. New York: Academic.
- Abraham, F. F. (1983), *Phys. Rev. Lett.* 50, 978.
- Abraham, F. F. (1984), *Phys. Rev. B* 29, 2606.
- Aharony, A. (1973), *Phys. Rev. B* 8, 1973.
- Aharony, A. (1976), in: *Phase Transitions and Critical Phenomena*, Vol. 6: Domb, C., Green, M. S. (Eds.). London: Academic, p. 358.
- Alefeld, G. (1969), *Phys. Stat. Sol.* 32, 67.
- Alefeld, G., Völkl, J. (Eds.) (1978), *Hydrogen in Metals I, II*. Berlin: Springer Verlag (Topics in Appl. Physics, Vols. 28, 29).
- Alexander, S. (1975), *Phys. Lett.* 54 A, 353.
- Alexander, S., Chaikin, P. M., Grant, P., Morales, G. J., Pincus, P., Hone, D. (1984), *J. Chem. Phys.* 80, 5776.
- Als-Nielsen, J. (1976), in: *Phase Transitions and Critical Phenomena*, Vol. 5A: Domb, C., Green, M. S. (Eds.). New York: Academic, p. 88.
- Als-Nielsen, J., Laursen, I. (1980), in: *Ordering of Strongly Fluctuating Condensed Matter Systems*: Riste, T. (Ed.). New York: Plenum Press, p. 39.
- Amit, D. J. (1984), *Field Theory, the Renormalization Group and Critical Phenomena*. Singapore: World Scientific.
- Angell, C. A., Goldstein, M. (Eds.) (1986), *Dynamic Aspects of Structure Change in Liquids and Glasses*. New York: N.Y. Acad. of Sciences.
- Ausloos, M., Elliott, R. J. (1983), *Magnetic Phase Transitions*. Berlin: Springer Verlag.
- Bak, P., Domany, E. (1979), *Phys. Rev. B* 20, 2818.
- Bak, P., Mukamel, D. (1979), *Phys. Rev. B* 19, 1604.
- Bak, P., Mukamel, D., Villain, J., Wentowska, K. (1979), *Phys. Rev. B* 19, 1610.
- Bakker, A. F., Bruin, C., Hilhorst, H. J. (1984), *Phys. Rev. Lett.* 52, 449.
- Bardham, P., Cohen, J. B. (1976), *Acta Cryst.* A32, 597.
- Bates, S. F., Rosedale, J. H., Fredrickson, G. H., Glinka, C. J. (1988), *Phys. Rev. Lett.* 61, 229.
- Baus, M. (1987), *J. Stat. Phys.* 48, 1129.
- Baus, M., Rull, L. F., Ryckaert, J. P. (Eds.) (1995), *Observation, Prediction and Simulation of Phase Transitions in Complex Fluids*. Dordrecht: Kluwer Acad. Publ.
- Baxter, R. J. (1973), *J. Phys. C* 6, L445.
- Baxter, R. J. (1982), *Exactly Solved Models in Statistical Mechanics*. London: Academic.
- Bean, C. P., Rodbell, D. S. (1962), *Phys. Rev.* 126, 104.
- Belanger, D. P. (1998), in: *Spin Glasses and Random Fields*: Young, A. P. (Ed.). Singapore: World Scientific, p. 251.
- Berlin, T. H., Kac, M. (1952), *Phys. Rev.* 86, 821.
- Bethe, H. (1935), *Proc. Roy. Soc. A* 150, 552.
- Bieber, A., Gautier, F. (1984a), *J. Phys. Soc. Japan* 53, 2061.
- Bieber, A., Gautier, F. (1984b), *Z. Phys.* B57, 335.
- Binder, K. (1973), *Phys. Rev. B* 8, 3423.
- Binder, K. (Ed.) (1979), *Monte Carlo Methods in Statistical Physics*. Berlin: Springer.
- Binder, K. (1980), *Phys. Rev. Lett.* 45, 811.
- Binder, K. (1983a), *Z. Physik* B50, 343.
- Binder, K. (1983b), in: *Phase Transitions and Critical Phenomena*, Vol. 8: Domb, C., Green, M. S. (Eds.). London: Academic Press, p. 1.
- Binder, K. (1984a), *Applications of the Monte Carlo Method in Statistical Physics*. Berlin: Springer Verlag.
- Binder, K. (1984b), in: *Condensed Matter Research Using Neutrons*: Lovesey, S. W., Scherm, R. (Eds.). New York: Plenum Press, p. 1.
- Binder, K. (1984c), *Phys. Rev. A* 29, 341.
- Binder, K. (1986), in: *Atomic Transport and Defects in Metals by Neutron Scattering*: Janot, C., Petry, T., Richter, D., Springer, T. (Eds.). Berlin: Springer, p. 12.
- Binder, K. (1987a), *Rep. Progr. Phys.* 50, 783.
- Binder, K. (1987b), *Ferroelectrics* 73, 43.
- Binder, K. (1989), in: *Alloy Phase Stability*: Gonis, A., Stocks, L. M. (Eds.). Dordrecht: Kluwer Acad. Publ., p. 232.
- Binder, K. (1994), *Adv. Polymer Sci.* 112, 181.
- Binder, K. (1998), in: *Spin Glasses and Random Fields*: Young, A. P. (Ed.). Singapore: World Scientific, p. 99.
- Binder, K., Fratzl, P. (2001), in: *Phase Transformations in Materials*: Kosterz, G. (Ed.). Weinheim: Wiley-VCH, Chap. 6.
- Binder, K., Heermann, D. W. (1988), *Monte Carlo Simulation in Statistical Physics: An Introduction*. Berlin: Springer.
- Binder, K., Landau, D. P. (1981), *Surface Sci.* 108, 503.
- Binder, K., Landau, D. P. (1989), in: *Molecule-Surface Interactions*: Lawley, K. P. (Ed.). New York: Wiley & Sons, p. 91.
- Binder, K., Stauffer, D. (1976a), *Z. Phys.* B24, 407.
- Binder, K., Stauffer, D. (1976b), *Adv. Phys.* 25, 343.
- Binder, K., Young, A. P. (1986), *Rev. Mod. Phys.* 58, 801.
- Binder, K., Meißner, G., Mais, H. (1976), *Phys. Rev. B* 15, 267.
- Binder, K., Kinzel, W., Stauffer, D. (1979), *Z. Phys.* B36, 162.
- Binder, K., Reger, J. D. (1992), *Adv. Phys.* 41, 547.

- Binder, K., Ciccotti, G. (Eds.) (1996), *Monte Carlo and Molecular Dynamics of Condensed Matter*. Bologna: Società Italiana di Fisica.
- Blinic, R., Levanyuk, A. P. (1986), *Incommensurate Phases in Dielectrics*, Vols. 1, 2. Amsterdam: North-Holland.
- Blinic, R., Zeks, B. (1974), *Soft Modes in Ferroelectrics and Antiferroelectrics*. Amsterdam: North-Holland.
- Bloch, D., Mauri, R. (1973), *Phys. Rev. B* 7, 4883.
- Blöte, H. W., Swendsen, R. H. (1979), *Phys. Rev. Lett.* 43, 799.
- Blume, M. (1966), *Phys. Rev.* 141, 517.
- Blume, M., Emery, V., Griffiths, R. B (1971), *Phys. Rev. A* 4, 1971.
- Bohn, H. G., Zinn, W., Dorner, B., Kollmar, A. (1980), *Phys. Rev. B* 22, 5447.
- Born, M., Huang, K. (1954), *Dynamical Theory of Crystal Lattices*. Oxford: Oxford Univ. Press.
- Boyer, L. L. (1980), *Phys. Rev. Lett.* 45, 1858.
- Boyer, L. L. (1981 a), *Phys. Rev. Lett.* 56, 1172.
- Boyer, L. L. (1981 b), *Ferroelectrics* 35, 83.
- Boyer, L. L., Hardy, J. R. (1981), *Phys. Rev. B* 24, 2577.
- Bragg, W. L., Williams, E. J (1934), *Proc. Roy. Soc. A* 145, 699.
- Brazovskii, S. A. (1975), *Soviet Phys. JETP* 41, 85.
- Bretz, M. (1977), *Phys. Rev. Lett.* 38, 501.
- Broddin, D., Van Tendeloo, G., Van Landuyt, J., Amelinckx, S., Portier, R., Guymont, M., Loiseau, A. (1986), *Phil. Mag.* A54, 395.
- Brout, R. (1959), *Phys. Rev.* 115, 824.
- Brout, R. (1965), *Phase Transitions*. New York: Benjamin Press.
- Bruce, A. D., Aharony, A. (1975), *Phys. Rev. B* 11, 478.
- Bruce, A. D., Cowley, R. A. (1981), *Structural Phase Transitions*. London: Taylor and Francis.
- Burkhardt, T. W., Kinzel, W. (1979), *Phys. Rev. B* 20, 4730.
- Burkhardt, T. W., van Leeuwen, J. M. J. (Eds.) (1982), *Real-Space Renormalization*. Berlin: Springer.
- Buzaré, J. Y., Fayet, J. C., Berlinger, W., Müller, K. A. (1979), *Phys. Rev. Lett.* 42, 465.
- Cahn, J. W., Hilliard, J. E. (1958), *J. Chem. Phys.* 28, 258.
- Cahn, J. W., Hilliard, J. E. (1959), *J. Chem. Phys.* 31, 688.
- Ceperley, D. M. (1995), *Rev. Mod. Phys.* 67, 279.
- Challa, M. S. S., Binder, K., Landau, D. P. (1986), *Phys. Rev. B* 34, 1841.
- Chandrasekhar, S. (1992), *Liquid Crystals*. Cambridge: Cambridge University Press.
- Ciccotti, G., Frenkel, D., McDonald, I. R. (Eds.) (1987), *Simulations of Liquids and Solids*. Amsterdam: North-Holland.
- Clapp, P. C., Moss, S. C. (1966), *Phys. Rev.* 142, 418.
- Clapp, P. C., Moss, S. C. (1968), *Phys. Rev.* 171, 754.
- Cowley, J. M. (1950), *Phys. Rev.* 77, 669.
- Cowley, J. M. (1976), *Phys. Rev. B* 13, 4877.
- Cusack, N. E. (1987), *The Physics of Structurally Disordered Matter: An Introduction*. Bristol: Adam Hilger.
- De Fontaine, D. (1975), *Acta Met.* 23, 553.
- De Fontaine, D. (1979), in: *Solid State Physics*, Vol. 34: Ehrenreich, H., Seitz, F., Turnbull, D. (Eds.). London: Academic, p. 73.
- De Fontaine, D., Kulik, J. (1985), *Acta Metall.* 33, 145.
- De Gennes, P. G. (1974), *The Physics of Liquid Crystals*. Oxford: Clarendon Press.
- De Gennes, P. G. (1979), *Scaling Concepts in Polymer Physics*. Ithaca: Cornell University Press.
- De Jongh, J. L., Miedema, A. R. (1974), *Adv. Phys.* 23, 1.
- Delacy, L. (2001), in: *Phase Transformations in Materials*: Kostorz, G. (Ed.). Weinheim: Wiley-VCH, Chap. 9.
- Den Nijs, M. P. M. (1979), *J. Phys. A* 12, 1857.
- De Raedt, H., Lagendijk, A. (1985), *Phys. Repts.* 127, 235.
- De Raedt, B., Binder, K., Michel, K. H. (1981), *J. Chem. Phys.* 75, 2977.
- Diep, H. T., Ghazali, A., Berge, B., Lallemand, P. (1986), *Europhys. Lett.* 2, 603.
- Dietrich, S. (1988), in: *Phase Transitions and Critical Phenomena*, Vol. 12: Domb, C., Lebowitz, J. L. (Eds.). New York: Academic, p. 1.
- Dillon, J. F., Chen, E. Y., Guggenheim, H. J. (1978), *Phys. Rev. B* 18, 377.
- Di Tolla, D. F., Tosatti, E., Ercolessi, F. (1996), in: *Monte Carlo and Molecular Dynamics of Condensed Matter Systems*: Binder, K., Ciccotti, G. (Eds.). Bologna: Società Italiana di Fisica, p. 345.
- Domany, E., Schick, M., Walker, J. S., Griffiths, R. B. (1978), *Phys. Rev. B* 18, 2209.
- Domany, E., Shnidman, Y., Mukamel, D. (1982), *J. Phys. C* 15, L495.
- Domb, C., Green, M. S. (Eds.) (1972–1976), *Phase Transitions and Critical Phenomena*, Vols. 1–6. New York: Academic.
- Domb, C., Green, M. S. (Eds.) (1983–1997), *Phase Transitions and Critical Phenomena*, Vols. 6–17. New York: Academic.
- Dünweg, B., Binder, K. (1987), *Phys. Rev. B* 36, 6935.
- Edwards, S. F., Anderson, P. W. (1975), *J. Phys. F* 5, 965.
- Enz, C. P. (Ed.) (1979), *Dynamic Critical Phenomena and Related Topics. Proceedings*. Berlin: Springer Verlag (Springer Lecture Notes in Physics, Vol. 104).
- Ferrell, R. A., Menyhard, N., Schmidt, H., Schwabl, F., Szeplafusy, P. (1967), *Phys. Rev. Lett.* 18, 891.
- Finel, A. (1994), in: *Static and Dynamics of Alloy Phase Transformations*: Turchi, P. E. A., Gonis, A. (Eds.). New York: Plenum Press, p. 495.
- Fisher, M. E. (1968), *Phys. Rev.* 176, 257.
- Fisher, M. E. (1971), in: *Critical Phenomena*: Green, M. S. (Ed.). London: Academic, p. 1.
- Fisher, M. E. (1974), *Rev. Mod. Phys.* 46, 587.
- Fisher, M. E. (1975 a), *AIP Conf. Proc.* 24, 273.

- Fisher, M. E. (1975b), *Phys. Rev. Lett.* **34**, 1634.
- Fisher, M. E., Langer, J. S. (1968), *Phys. Rev. Lett.* **20**, 665.
- Fisher, M. E., Nelson, D. R. (1974), *Phys. Rev. Lett.* **32**, 1350.
- Fisher, M. E., Racz, Z. (1976), *Phys. Rev. B* **13**, 5039.
- Fishman, S., Aharony, A. (1979), *J. Phys. C* **12**, L729.
- Flory, P. J. (1953), *Principles of Polymer Chemistry*. Ithaca: Cornell University Press.
- Folk, R., Iro, H., Schwabl, F. (1976), *Z. Phys. B* **25**, 69.
- Franz, S., Parisi, G. (1998), *Physica A* **261**, 317.
- Frazer, B. C., Shirane, G., Cox, D. E. (1965), *Phys. Rev.* **140A**, 1448.
- Fredrickson, G. H., Binder, K. (1989), *J. Chem. Phys.* **91**, 7265.
- Fredrickson, G. H., Helfand, E. (1987), *J. Chem. Phys.* **87**, 697.
- Friedmann, L. F., Tunstall, D. P., (Eds.) (1978), *The Metal-Non Metal Transition in Disordered Systems*. Edinburgh: SUSSP.
- Fujimoto, M. (1997), *The Physics of Structural Phase Transitions*. Berlin: Springer.
- Gahn, U. (1986), *J. Phys. Chem. Solids* **47**, 1153.
- Gebhardt, W., Krey, U. (1979), *Phasenübergänge und kritische Phänomene – Eine Einführung*. Braunschweig: Vieweg.
- Gehring, G. A. (1977), *J. Phys. C* **10**, 531.
- Gehring, G. A., Gehring, K. A. (1975), *Rep. Progr. Phys.* **38**, 1.
- Gerold, V., Kern, J. (1986), in: *Atomic Transport and Defects in Metals by Neutron Scattering*: Janot, C., Petry, T., Richter, D., Springer, T. (Eds.). Berlin: Springer Verlag, p. 17.
- Gerold, V., Kern, J. (1987), *Acta Met.* **35**, 393.
- Ginzburg, V. L. (1960), *Sov. Phys.-Solid State* **2**, 1824.
- Giordano, N., Wolf, W. P. (1975), *Phys. Rev. Lett.* **35**, 799.
- Golosov, N. S., Popov, L. E., Rudan, L. Y. (1973), *J. Phys. Chem. Solids* **34**, 1149–1159.
- Gonis, A., Stocks, L. M. (Eds.) (1989), *Alloy Phase Stability*. Dordrecht: Kluwer Acad. Publ.
- Grazhdankina, N. P. (1969), *Sov. Phys.-Usp.* **11**, 727; *Usp. Fiz. Nauk.* **96**, 291.
- Grinstein, G. (1985), in: *Fundamental Problems in Statistical Mechanics, VI*: Cohen, E. G. D. (Ed.). Amsterdam, North-Holland, p. 147.
- Guerard, D., Herold, A. (1975), *Carbon* **13**, 337.
- Gunton, J. D., Droz, M. (1983), *Introduction to the Theory of Metastable and Unstable States*. Berlin: Springer.
- Gunton, J. D., San Miguel, M., Sahni, P. S. (1983), in: *Phase Transitions and Critical Phenomena*, Vol. 8: Domb, C., Lebowitz, J. L. (Eds.). London: Academic, p. 267.
- Guymont, M. (1978), *Phys. Rev. B* **18**, 5385.
- Guymont, M. (1981), *Phys. Rev. B* **24**, 2647.
- Haasen, P., Gerold, V., Wagner, R., Ashby, M. F. (Eds.) (1984), *Decomposition of Alloys: The Early Stages*. New York: Pergamon Press.
- Halperin, B. I., Hohenberg, P. C. (1967), *Phys. Rev. Lett.* **19**, 700.
- Halperin, B. I., Varma, C. (1976), *Phys. Rev. B* **14**, 4030.
- Halperin, B. I., Hohenberg, P. C., Ma, S. K. (1974), *Phys. Rev. B* **10**, 139.
- Halperin, B. I., Hohenberg, P. C., Siggia, E. (1976), *Phys. Rev. B* **13**, 4119.
- Hansen, M. (1958), *Constitution of Binary Alloys*. New York: McGraw Hill.
- Harris, A. B. (1974), *J. Phys. C* **7**, 1671.
- Harris, A. B., Meyer, H. (1985), *Can. J. Phys.* **63**, 3.
- Harris, R., Plischke, M., Zuckermann, M. J. (1973), *Phys. Rev. Lett.* **31**, 160.
- Heermann, D. W., Klein, W., Stauffer, D. (1982), *Phys. Rev. Lett.* **49**, 1262.
- Herrmann, H. J., Janke, W., Karsch, F. (Eds.) (1992), *Dynamic of First Order Phase Transitions*. Singapore: World Scientific.
- Hockney, R. W., Eastwood, J. W. (1988), *Computer Simulation Using Particles*. Bristol: Adam Hilger.
- Höchli, U. T., Knorr, K., Loidl, A. (1990), *Adv. Phys.* **39**, 405.
- Hohenberg, P. C., Halperin, B. I. (1977), *Rev. Mod. Phys.* **49**, 435.
- Hoover, W. G. (1987), *Molecular Dynamics*. Berlin: Springer.
- Hornreich, R. M., Luban, M., Shtrikman, S. (1975), *Phys. Rev. Lett.* **35**, 1678.
- Hulliger, F., Siegrist, T. (1979), *Z. Phys. B* **35**, 81.
- Imbrie, J. Z. (1984), *Phys. Rev. Lett.* **53**, 1747.
- Imry, Y. (1980), *Phys. Rev. B* **21**, 2042.
- Imry, Y., Ma, S. K. (1975), *Phys. Rev. Lett.* **35**, 1399.
- Imry, Y., Wortis, M. (1979), *Phys. Rev. B* **19**, 3580.
- Inden, G. (2001), in: *Phase Transformations in Materials*: Kosterz, G. (Ed.). Weinheim: Wiley-VCH, Chap. 8.
- Jäckle, J. (1986), *Rep. Progr. Phys.* **49**, 171.
- Jaster, A. (1998), *Europhys. Lett.* **42**, 277.
- Jona, F., Shirane, G. (1962), *Ferroelectric Crystals*. New York: Pergamon Press.
- Joyce, J. S. (1972), in: *Phase Transitions and Critical Phenomena*, Vol. 2: Domb, C., Green, M. S. (Eds.). New York: Academic, Chapter X.
- Kämmerer, S., Dünweg, B., Binder, K., D'Onorio De Meo, M. (1996), *Phys. Rev. B* **53**, 2345.
- Kalos, M. H. (Ed.) (1985), *Monte Carlo Methods in Quantum Problems*. Dordrecht: Kluwer Acad. Publ.
- Kalos, M. H., Schmidt, K. E. (1984), in: *Applications of the Monte Carlo Method in Statistical Physics*: Binder, K. (Ed.). Berlin: Springer Verlag, p. 125.
- Kaplan, T. A. (1959), *Phys. Rev.* **116**, 888.
- Keating, D. T., Warren, B. E. (1951), *J. Appl. Phys.* **22**, 286.
- Kehr, K. W., Binder, K., Reulein, S. M. (1989), *Phys. Rev. B* **39**, 4891.
- Khachaturyan, A. G. (1962), *Fiz. Metallov i Metallovedenie* **13**, 493.
- Khachaturyan, A. G. (1963), *Fiz. tverd. Tela* **5**, 26; *ibid* **5**, 750.
- Khachaturyan, A. G. (1973), *Phys. stat. sol. (b)* **60**, 9.

- Khachaturyan, A. G. (1983), *Theory of Structural Transformation in Solids*. New York: J. Wiley & Sons.
- Kikuchi, R. (1951), *Phys. Rev.* 81, 998.
- Kikuchi, R. (1967), *J. Chem. Phys.* 47, 1664.
- Kittel, C. (1967), *Quantum Theory of Solids*. New York: J. Wiley & Sons.
- Kittler, R. C., Falicov, L. M. (1978), *J. Phys. B* 18, 2506.
- Kittler, R. C., Falicov, L. M. (1979), *Phys. Rev. B* 19, 291.
- Kleemann, W., Schäfer, F. J., Tannhäuser, D. S. (1980), *J. Magn. Magnet. Mater.* 15–18, 415.
- Klein, W., Unger, C. (1983), *Phys. Rev. B* 28, 445.
- Koch, S. W. (1984), *Dynamics of First-Ordered Phase Transitions in Equilibrium and Nonequilibrium*. Berlin: Springer.
- Kötzler, J. (1984), *Z. Phys. B* 55, 119.
- Kötzler, J., Raffius, G., Loidl, A., Zeyen, C. M. E. (1979), *Z. Phys. B* 35, 125.
- Kosterlitz, J. M., Thouless, D. J. (1973), *J. Phys. C* 6, 1181.
- Kremer, K., Robbins, M. O., Grest, G. S. (1986), *Phys. Rev. Lett.* 57, 2694.
- Kremer, K., Grest, G. S., Robbins, O. (1987), *J. Phys. A* 20, L181.
- Krinsky, S., Mukamel, D. (1977), *Phys. Rev. B* 16, 2313.
- Krivoglaz, M. A. (1969), *Theory of X-Ray and Thermal Neutron Scattering by Real Crystals*. New York: Plenum Press.
- Landau, D. P., Binder, K. (1978), *Phys. Rev. B* 17, 2328.
- Landau, D. P., Binder, K. (1985), *Phys. Rev. B* 31, 5946.
- Landau, L. D., Lifshitz, E. M. (1958), *Statistical Physics*. Oxford: Pergamon Press.
- Langer, J. S. (1974), *Physica* 73, 61.
- Larkin, A. I., Khmel'nitskii, D. E. (1969), *Zh. Eksp. Fiz.* 56, 2087; *Sov. Phys. JETP* 29, 1123.
- Lebowitz, J. L., Penrose, O. (1966), *J. Math. Phys.* 7, 98.
- LeGuillou, J. C., Zinn-Justin, J. (1980), *Phys. Rev. B* 21, 3976.
- Leibler, L. (1980), *Macromolecules* 13, 1602.
- Lifshitz, E. M. (1942), *J. Physique* 6, 61.
- Lipowsky, R. (1984), *J. Appl. Phys.* 55, 213.
- Loidl, A. (1989), *Ann. Rev. Phys. Chem.* 40, 29.
- Loiseau, A., Van Tendeloo, G., Portier, R., Ducastelle, F. (1985), *J. Physique* 46, 595.
- Lynden-Bell, R. M., Michel, K. H. (1994), *Rev. Mod. Phys.* 66, 721.
- Ma, S.-K. (1976), *Modern Theory of Phase Transitions*. Reading: Benjamin Press.
- Maletta, H., Felsch, W. (1979), *Phys. Rev. B* 20, 1079.
- Mandelbrot, B. B. (1982), *The Fractal Geometry of Nature*. San Francisco: Freeman.
- Marx, R. (1989), *Phys. Rev. B* 40, 2585.
- McCoy, B. M., Wu, T. T. (1973), *The Two-Dimensional Ising Model*. Cambridge, Mass: Harvard University Press.
- McGuire, T. R., Gambino, R. J., Pickart, S. J., Alperin, H. A. (1969), *J. Appl. Phys.* 40, 1009.
- Meißner, G., Binder, K. (1975), *Phys. Rev. B* 12, 3948.
- Michel, K. H., Naudts, J. (1977), *J. Chem. Phys.* 67, 547.
- Michel, K. H., Naudts, J. (1978), *J. Chem. Phys.* 68, 216.
- Milchev, A., Heermann, D. W., Binder, K. (1986), *J. Stat. Phys.* 44, 749.
- Moncton, D. E., Axe, J. D., Di Salvo, F. J. (1977), *Phys. Rev. B* 16, 801.
- Morita, T. (1972), *J. Math. Phys.* 13, 115.
- Moss, S. C. (1964), *J. Appl. Phys.* 35, 3547.
- Moss, S. C., Clapp, P. C. (1968), *Phys. Rev.* 171, 764.
- Mott, N. F. (1974), *Metal-Insulator Transitions*. London: Taylor and Francis.
- Mouritsen, O. G. (1984), *Computer Studies of Phase Transitions and Critical Phenomena*. Berlin: Springer.
- Müller, K. A., Berlinger, W. (1975), *Phys. Rev. Lett.* 22, 1547.
- Müller-Krumbhaar, H. (1977), in: *Crystal Growth and Materials*: Kaldis, E. (Ed.). Amsterdam: North-Holland, p. 79.
- Mukamel, D., Krinsky, S. (1976), *Phys. Rev. B* 13, 5065.
- Mukamel, D., Fisher, M. E., Domany, E. (1976a), *Phys. Rev. Lett.* 37, 565.
- Mukamel, D., Krinsky, S., Bak, P. (1976b), *AIP Conf. Proc.* 29, 474.
- Nattermann, T. (1998), in: *Spin Classes and Random Fields*: Young, A. P. (Ed.). Singapore: World Scientific, p. 277.
- Nelson, D. R., Halperin, B. I. (1979), *Phys. Rev. B* 19, 2457.
- Nienhuis, B., Riedel, E. K., Schick, M. (1980), *J. Phys. A* 13, L189.
- Nishiyama, Z. (1979), *Martensitic Transformation*. New York: Academic.
- Onsager, L. (1944), *Phys. Rev.* 65, 117.
- Orr, R. L. (1960), *Acta Met.* 8, 489.
- Orr, R. L., Luciat-Labry, J., Hultgren, R. (1960), *Acta Met.* 8, 431.
- Parrinello, M., Rahman, A. (1980), *Phys. Rev. Lett.* 45, 1196.
- Parrinello, M., Rahman, A., Vashishta, P. (1983), *Phys. Rev. Lett.* 50, 1073.
- Patashinskii, A. Z., Pokrovskii, V. I. (1979), *Fluctuation Theory of Phase Transitions*. Oxford: Pergamon Press.
- Pershan, P. S. (1988), *Structure of Liquid Crystal Phases*. Singapore: World Scientific.
- Piercy, P., Pfnür, H. (1987), *Phys. Rev. Lett.* 59, 1124.
- Pimenta, M. A., Echegut, P., Luspín, Y., Hauset, G., Gervais, F., Abélard, P. (1989), *Phys. Rev. B* 39, 3361.
- Potts, R. B. (1952), *Proc. Camb. Phil. Soc.* 48, 106.
- Privman, V. (Ed.) (1990), *Finite Size Scaling and Numerical Simulation*. Singapore: World Scientific.
- Privman, V., Hohenberg, P. C., Aharony, A. (1991), in: *Phase Transitions and Critical Phenomena*, Vol. 14: Domb, C., Lebowitz, J. L. (Eds.). London: Academic Press, Chapter 1.

- Pynn, T., Skjeltorp, A. (Eds.) (1983), *Multicritical Phenomena*. New York: Plenum Press.
- Riste, T., Sherrington, D. (Eds.) (1989), *Phase Transitions in Soft Condensed Matter*. New York: Plenum Press.
- Robbins, M. O., Kremer, K., Grest, G. S. (1988), *J. Chem. Phys.* 88, 3286.
- Rohrer, H. (1975), *Phys. Rev. Lett.* 34, 1638.
- Rohrer, H., Gerber, Ch. (1977), *Phys. Rev. Lett.* 38, 909.
- Roth, W. L. (1958), *Phys. Rev.* 110, 1333.
- Sadiq, A., Binder, K. (1984), *J. Stat. Phys.* 35, 517.
- Salanon, B., Fabre, F., Lapoujoulade, J., Selke, W. (1988), *Phys. Rev. B* 38, 7385.
- Salje, E. (1990), *Phase Transitions in Ferroelastic and Co-elastic Crystals*. Cambridge: Cambridge Univ. Press.
- Sanchez, J. M., De Fontaine, D. (1980), *Phys. Rev. B* 21, 216.
- Sanchez, J. M., De Fontaine, D. (1982), *Phys. Rev. B* 25, 1759.
- Schick, M. (1981), *Progr. Surf. Sci.* 11, 245.
- Schmid, F. (1999), in: *Computational Methods in Colloid and Interface Science*: Borowko, M. (Ed.). New York: M. Dekker, Chapter 10.
- Schmidt, V. H. (1978), in: *High Pressure and Low Temperature Physics*: Chu, C. W., Wollam, J. A. (Eds.). New York: Plenum Press, p. 237.
- Schneider, L., Stoll, E. (1976), *Phys. Rev. B* 13, 1216.
- Schwartz, T. H., Cohen, J. B. (1965), *J. Appl. Phys.* 36, 598.
- Schweika, W. (1989), in: *Alloy Phase Stability*: Stocks, G. M., Gonis, A. (Eds.). Dordrecht: Kluwer, p. 137.
- Schweika, W. (1994), in: *Statics and Dynamics of Alloy Phase Transformations*: Turchi, P. E. A., Gonis, A. (Eds.). New York: Plenum Press, p. 103.
- Schweika, W., Hauboldt, H.-G. (1986), in: *Atomic Transport and Defects in Metals by Neutron Scattering*: Janot, C., Petry, T., Richter, D., Springer, T. (Eds.). Berlin: Springer Verlag, p. 22.
- Scott, J. F. (1987), in: *Phase Transitions and Critical Phenomena*: Domb, C., Lebowitz, J. L. (Eds.). London: Academic Press, Chapter 2.
- Selke, W. (1988), *Phys. Repts.* 170, 213.
- Selke, W. (1989), in: *Alloy Phase Stability*: Gonis, A., Stocks, L. M. (Eds.). Dordrecht: Kluwer Akad. Publ.
- Selke, W. (1992), in: *Phase Transitions and Critical Phenomena*, Vol. 15: Domb, C., Lebowitz, J. L. (Eds.). London: Academic Press, p. 1.
- Semenovskaya, S. V. (1974), *Phys. Stat. Sol. (b)* 64, 291.
- Smart, J. S. (1966), *Effective Field Theories of Magnetism*. New York: W. B. Saunders.
- Stanley, H. E. (1971), *Introduction to Phase Transitions and Critical Phenomena*. Oxford: Oxford University Press.
- Stauffer, D., Aharony, A. (1992), *An Introduction to Percolation Theory*. London: Taylor and Francis.
- Sullivan, D. E., Telo da Gama, M. M. (1985), in: *Fluid Interfacial Phenomena*: Croxton, C. A. (Ed.). New York: J. Wiley and Sons, p. 45.
- Suzuki, M. (Ed.) (1992), *Quantum Monte Carlo Methods in Condensed Matter Physics*. Singapore: World Scientific.
- Swann, P. S., Duff, W. R., Fisher, R. M. (1972), *Metallurg. Trans.* 3, 409.
- Swendsen, R. H., Krinsky, S. (1979), *Phys. Rev. Lett.* 43, 177.
- Tanisaki, S. (1961), *Phys. Soc. Japan* 16, 579.
- Tolédano, J. C. (1981), *Ferroelectrics* 35, 31.
- Tolédano, P., Pascoli, G. (1980), *Ferroelectrics* 25, 427.
- Tolédano, J. C., Tolédano, P. (1987), *The Landau Theory of Phase Transitions*. Singapore: World Scientific.
- Tsakalakos, T. (1984), *Phase Transformations in Solids*. Amsterdam: North-Holland.
- Turchi, P. E. A., Gonis, A. (Eds.) (1994), *Statics and Dynamics of Alloy Phase Transformations*. New York: Plenum Press.
- van Hove, L. (1954), *Phys. Rev.* 93, 1374.
- Villain, J. (1959), *J. Phys. Chem. Solids* 11, 303.
- Villain, J. (1985), in: *Scaling Phenomena in Disordered Systems*: Pynn, R., Skjeltorp, A. (Eds.). New York: Plenum Press, p. 423.
- Wagner, H., Horner, H. (1974), *Adv. Phys.* 23, 587.
- Wagner, R., Kampmann, R., Vorhees, P. W. (2001), in: *Phase Transformations in Materials*: Kostorz, G. (Ed.). Weinheim: Wiley-VCH, Chap. 5.
- Wansleben, S., Landau, D. P. (1987), *J. Appl. Phys.* 61, 3968.
- Weeks, J. D. (1980), in: *Ordering in Strongly Fluctuating Condensed Matter Systems*: Riste, T. (Ed.). New York: Plenum Press, p. 293.
- Wiechert, H., Arlt, S. A. (1993), *Phys. Rev. Lett.* 71, 2090.
- Wilding, N. B. (1997), *J. Phys.: Condens. Matter* 9, 585.
- Wilding, N. B., Schmid, F., Nielaba, P. (1998), *Phys. Rev. E* 58, 2201.
- Wilson, K. G., Kogut, J. (1974), *Phys. Repts.* 12 C, 75.
- Wu, F. Y. (1982), *Rev. Mod. Phys.* 54, 235.
- Yelon, W. B., Cox, D. E., Kortmann, P. J. (1974), *Phys. Rev. B* 9, 4843.
- Yeomans, J. (1992), *Statistical Mechanics of Phase Transitions*. Oxford: Clarendon Press.
- Young, A. F. (Ed.) (1998), *Spin Glasses and Random Fields*. Singapore: World Scientific.
- Zallen, T. (1983), *The Physics of Amorphous Solids*. New York: J. Wiley and Sons.
- Zarzycki, J. (Ed.) (1991), *Glasses and Amorphous Materials (Materials Science and Technology, Vol. 9)*. Weinheim: VCH.
- Zettlemoyer, A. C. (Ed.) (1969), *Nucleation*. New York: Marcel Dekker.
- Zunger, A. (1994), in: *Statics and Dynamics of Alloy Phase Transformations*: Turchi, P. E. A., Gonis, A. (Eds.). New York: Plenum Press, p. 361.

5 Homogeneous Second-Phase Precipitation

Richard Wagner

Forschungszentrum Jülich GmbH, Jülich, Germany

Reinhard Kampmann

Institut für Werkstofforschung, GKSS-Forschungszentrum GmbH, Geesthacht, Germany

Peter W. Voorhees

Department of Materials Science and Engineering, Northwestern University, Evanston, Ill., USA

List of Symbols and Abbreviations	311
5.1 Introduction	314
5.2 General Considerations	315
5.2.1 General Course of an Isothermal Precipitation Reaction	315
5.2.2 Thermodynamic Considerations – Metastability and Instability	317
5.2.3 Decomposition Mechanisms: Nucleation and Growth versus Spinodal Decomposition	319
5.2.4 Thermodynamic Driving Forces for Phase Separation	322
5.3 Experimental Techniques for Studying Decomposition Kinetics	326
5.3.1 Microanalytical Tools	326
5.3.1.1 Direct Imaging Techniques	326
5.3.1.2 Scattering Techniques	328
5.3.2 Experimental Problems	330
5.3.2.1 Influence of Quenching Rate on Kinetics	330
5.3.2.2 Distinction of the Mode of Decomposition	332
5.4 Precipitate Morphologies	334
5.4.1 Experimental Results	334
5.4.2 Factors Controlling the Shapes and Morphologies of Precipitates	336
5.5 Early Stage Decomposition Kinetics	339
5.5.1 Cluster-Kinetics Approach	340
5.5.1.1 Classical Nucleation – Sharp Interface Model	340
5.5.1.2 Time-Dependent Nucleation Rate	343
5.5.1.3 Experimental Assessment of Classical Nucleation Theory	345
5.5.1.4 Non-Classical Nucleation – Diffuse Interface Model	347
5.5.1.5 Distinction Between Classical and Non-Classical Nucleation	349
5.5.2 Diffusion-Controlled Growth of Nuclei from the Supersaturated Matrix	350

www.iran-mavad.com

5.5.3	The Cluster-Dynamics Approach to Generalized Nucleation Theory	352
5.5.4	Spinodal Theories	356
5.5.5	The Philosophy of Defining of 'Spinodal Alloy' – Morphologies of 'Spinodal Alloys'	363
5.5.6	Monte Carlo Studies	367
5.6	Coarsening of Precipitates	370
5.6.1	General Remarks	370
5.6.2	The LSW Theory of Coarsening	370
5.6.3	Extensions of the Coarsening Theory to Finite Precipitate Volume Fractions	373
5.6.4	Other Approaches Towards Coarsening	377
5.6.5	Influence of Coherency Strains on the Mechanism and Kinetics of Coarsening – Particle Splitting	377
5.7	Numerical Approaches Treating Nucleation, Growth and Coarsening as Concomitant Processes	381
5.7.1	General Remarks on the Interpretation of Experimental Kinetic Data of Early Decomposition Stages	381
5.7.2	The Langer and Schwartz Theory (LS Model) and its Modification by Kampmann and Wagner (MLS Model)	383
5.7.3	The Numerical Modell (N Model) of Kampmann and Wagner (KW)	385
5.7.4	Decomposition of a Homogeneous Solid Solution	385
5.7.4.1	General Course of Decomposition	385
5.7.4.2	Comparison Between the MLS Model and the N Model	387
5.7.4.3	The Appearance and Experimental Identification of the Growth and Coarsening Stages	387
5.7.4.4	Extraction of the Interfacial Energy and the Diffusion Constant from Experimental Data	389
5.7.5	Decomposition Kinetics in Alloys Pre-Decomposed During Quenching . .	391
5.7.6	Influence of the Loss of Particle Coherency on the Precipitation Kinetics .	392
5.7.7	Combined Cluster-Dynamic and Deterministic Description of Decomposition Kinetics	394
5.8	Self-Similarity, Dynamical Scaling and Power-Law Approximations . .	395
5.8.1	Dynamical Scaling	395
5.8.2	Power-Law Approximations	398
5.9	Non-Isothermal Precipitation Reactions	401
5.10	Acknowledgements	402
5.11	References	402

List of Symbols and Abbreviations

a	lattice parameter
A	solvent atoms
$a_i^j(c)$	activity of atomic species i in phase j at composition c
B	solute atoms
c	composition
c_A	atomic fraction of A
c_0	initial composition
\bar{c}	mean composition
Δc	supersaturation or composition difference
c_α^e	equilibrium composition of matrix phase α
$c_\alpha'^e$	composition of matrix α in metastable equilibrium with coherent precipitates
c_β^e	equilibrium composition of precipitate phase β
c_p	composition of incoherent particles
c_p'	composition of coherent particles
c_{ij}	elastic constant
c_R	composition of matrix at the matrix/particle interface
$C(i)$	equilibrium cluster distribution
D	diffusion constant
\bar{D}	mean diameter of precipitated particles
E	Young's modulus
$f(R)$	size distribution function of precipitates with radii R
$F(c), f(c)$	Helmholtz energy or energy density
$F'(c), f'(c)$	Helmholtz constraint energy or constraint energy density
ΔF^*	nucleation barrier
ΔF_{el}	elastic free energy
$\Delta F_{\alpha/\beta}$	interfacial free energy
$\Delta F_{ch}(c)$	chemical driving force
f_p	precipitated volume fraction
$\tilde{F}(x)$	time-independent scaling function
G	Gibbs energy
$G(\mathbf{r}-\mathbf{r}_0)$	two-point correlation function at spatial positions \mathbf{r}, \mathbf{r}_0
H	enthalpy
i, i^*	number of atoms in a cluster or in a cluster of critical size
J^s, J^*	steady state and time-dependent nucleation rate
K	aspect ratio of an ellipsoid of revolution
K^*	gradient energy coefficient in the CH spinodal theory
K_R^{LSW}	coarsening rate according to the LSW theory
k	Boltzmann constant
L	ratio of elastic to interfacial energy
M	atomic mobility
N_v	number density of precipitates
n_v	number of atoms per unit volume

p	pressure
R	radius of precipitates
\bar{R}	mean radius of precipitates
R^*	radius of a critical nucleus or a particle being in unstable equilibrium with the matrix
R_g	molar gas constant
$R(\kappa); R(\lambda)$	amplification factor in the CH spinodal theory
S	entropy
$S(\kappa)$	structure function
$S_m = S(\kappa_m)$	maximum of structure function
T	temperature
T_A	annealing temperature
T_H	homogenization temperature
t	aging time
U	internal energy
V	volume
V_α, V_β	molar volume of α or β phase
Z	Zeldovich factor
α, α'	matrix phase
β	equilibrium precipitated phase
β'	metastable precipitated phase; transition phase
γ	shear strain
δ	misfit parameter
$\eta = (1/a_0) (\partial a / \partial c)$	atomic size factor
κ, κ	scattering vector and its magnitude
κ_m	wavenumber of the maximum of the structure function $S(\kappa)$
λ	wavelength
μ	shear modulus
μ_i^j	chemical potential of component i in phase j
ν	Poisson's ratio
Ω	atomic volume
$\sigma_{\alpha\beta}$	specific interfacial energy
τ	incubation period or scaled time in the MLS and KW models
AEM	analytical transmission electron microscopy
AFIM	analytical field ion microscopy (atom probe field ion microscope)
CH	Cahn–Hilliard spinodal theory
CHC	Cahn–Hilliard–Cook spinodal theory
CTEM	conventional transmission electron microscopy
EDX	energy-dispersive X-ray analysis
EELS	electron energy loss spectroscopy
FIM	field ion microscopy
HREM	high resolution electron microscopy
KW	Kampmann–Wagner model

LBM	Langer–Bar-On–Miller non-linear spinodal theory
LS	Langer–Schwartz theory
LSW	Lifshitz–Slyozov–Wagner theory
MCS	Monte Carlo simulation
MLS	modified Langer–Schwartz model
n.g.	nucleation and growth
SAXS	small angle X-ray scattering
SANS	small angle neutron scattering
s.d.	spinodal decomposition
TAP	tomographic atom probe

5.1 Introduction

Many technologically important properties of alloys, such as their mechanical strength and toughness, creep and corrosion resistance, and magnetic and superconducting properties, are essentially controlled by the presence of precipitated particles of a second phase. This commonly results from the decomposition of a solid solution during cooling. A fundamental understanding of the thermodynamics, the mechanism and the kinetics of precipitation reactions in metallic solids, leading to a well-defined microstructure, is therefore of great interest in materials science.

As is reflected by the schematic binary phase diagram of Fig. 5-1, for reasons of entropy the single-phase state α of a solid solution with composition c_0 is thermodynamically stable only at elevated temperatures. At lower temperatures the free energy of the system is lowered through unmixing ('decomposition' or 'phase separation') of α into two phases, α' and β .

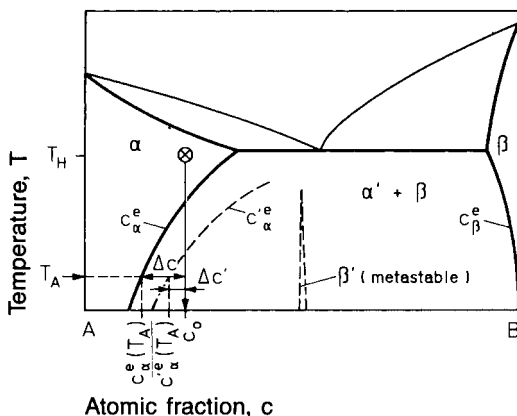


Figure 5-1. Schematic phase diagram of a binary alloy displaying a miscibility gap. Dashed lines show the metastable coherent solvus line and a possible metastable intermetallic phase β' . The long arrow indicates the quenching process.

In order to initiate a precipitation reaction, the alloy is first homogenized in the single-phase region at T_H and then either

- cooled down slowly into the two-phase region $\alpha' + \beta$, or
- quenched into brine prior to isothermal aging at a temperature T_A within the two-phase region (Fig. 5-1).

In both cases, thermodynamic equilibrium is reached if the supersaturation Δc , defined as

$$\Delta c(t) = \bar{c} - c_{\alpha}^e \quad (5-1)$$

becomes zero. (Here $\bar{c}(t)$ is the mean matrix composition at time t with $\bar{c}(t=0) \equiv c_0$.)

For case a), which frequently prevails during industrial processing, the aging temperature and the associated equilibrium solubility limit $c_{\alpha}^e(T)$ decrease continuously. Equilibrium can only be reached if the cooling rate is sufficiently low within a temperature range where the diffusion of the solute atoms is still adequately high. The precipitated volume fraction (f_p) and the dispersion of the particles of the second phase can thus be controlled via the cooling rate.

Procedure b) is frequently used for studies of decomposition kinetics under conditions which are easier to control and describe theoretically ($T = T_A = \text{const.}$; $D = \text{const.}$) than for case a). This leads to precipitate microstructures whose volume fraction and particle dispersion depend on $\Delta c(T)$ and the aging time t .

Decomposition reactions involve diffusion of the atomic species via the vacancy and/or the interstitial mechanism. Hence, the precipitate microstructure proceeding towards thermodynamic equilibrium evolves as a function of both time and temperature. In practice, a metallurgist is often requested to tailor an alloy with a specific precipitation microstructure. For this pur-

pose it would be desirable to have a theoretical concept, preferentially available as a computer algorithm, that allows suitable processing parameters to be derived for establishing the specific microstructure on grounds of the given thermodynamics of the alloy. This less empirical approach to alloy design, however, would require a comprehensive theory of precipitation kinetics, which has not yet been developed to a satisfactory level, despite recent efforts and progress made in elucidating the kinetics of first-order phase transitions in solids. Furthermore, in materials science it is frequently desirable to predict the kinetic evolution of an originally optimized precipitate microstructure under service conditions, e.g., for high-temperature applications in two-phase materials, where the precipitate distribution might undergo changes because of coarsening. Even though the kinetics of coarsening are of great practical importance, a completely satisfactory coarsening theory has so far only been developed in the limit of zero precipitated volume fraction (see Sec. 5.6). This limit, however, is never realized in technical alloys, where the volume fraction of the minor phase frequently exceeds 30%.

In the present chapter recent theoretical and experimental studies on the kinetics of phase separation in solids are reviewed from the point of view of the experimentalist. Special emphasis is placed on the questions to what extent the theoretical results can be verified experimentally and to what extent they might be of practical use to the physical metallurgist. We confine ourselves to dealing only with homogeneous and continuous phase separation mechanisms. Heterogeneous nucleation at crystal defects, and discontinuous precipitation reactions at moving interfaces, as well as unmixing in solids under irradiation are treated separately, in the chapter by Purdy and Bréchet (2001).

5.2 General Considerations

5.2.1 General Course of an Isothermal Precipitation Reaction

As illustrated for a Ni-37 at.% Cu-8 at.% Al alloy (Fig. 5-2 and 5-3), an isothermal precipitation reaction (the kinetics of which will be dealt with in more detail in Secs. 5.5, 5.6 and 5.7) is qualitatively characterized by an early stage during which an increasing number density

$$N_v(t) = \int f(R) dR \quad (5-2)$$

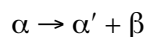
of more or less spherical solute-rich clusters ('particles') with a size distribution $f[R(t)]$ and a mean radius

$$\bar{R} = \frac{\int R f(R) dR}{\int f(R) dR} \quad (5-3)$$

are formed. In common with all homogeneous precipitation reactions studied so far, in the earliest stages of the reaction the parent phase α and the precipitate phase β share a common crystal lattice, i.e., the two phases are coherent. As inferred from the field ion micrographs of Fig. 5.2a-c and from the quantitative data of Fig. 5-3, during the early stages \bar{R} increases somewhat and the supersaturation, Δc , decreases slowly. This small reduction in Δc , however, is sufficient to terminate the nucleation of new particles, as indicated by the maximum of $N_v(t)$.

Beyond this maximum the precipitate number density decreases (Fig. 5-3) due to the onset of the coarsening reaction, during which the smaller particles redissolve, thus enabling the larger ones to grow (see Sec. 5.6). During this coarsening process the supersaturation Δc decreases asymptotically towards zero.

As mentioned previously, within the miscibility gap, the solid solution α becomes unstable and decomposes into the stable solid solution α' and the precipitated phase β :



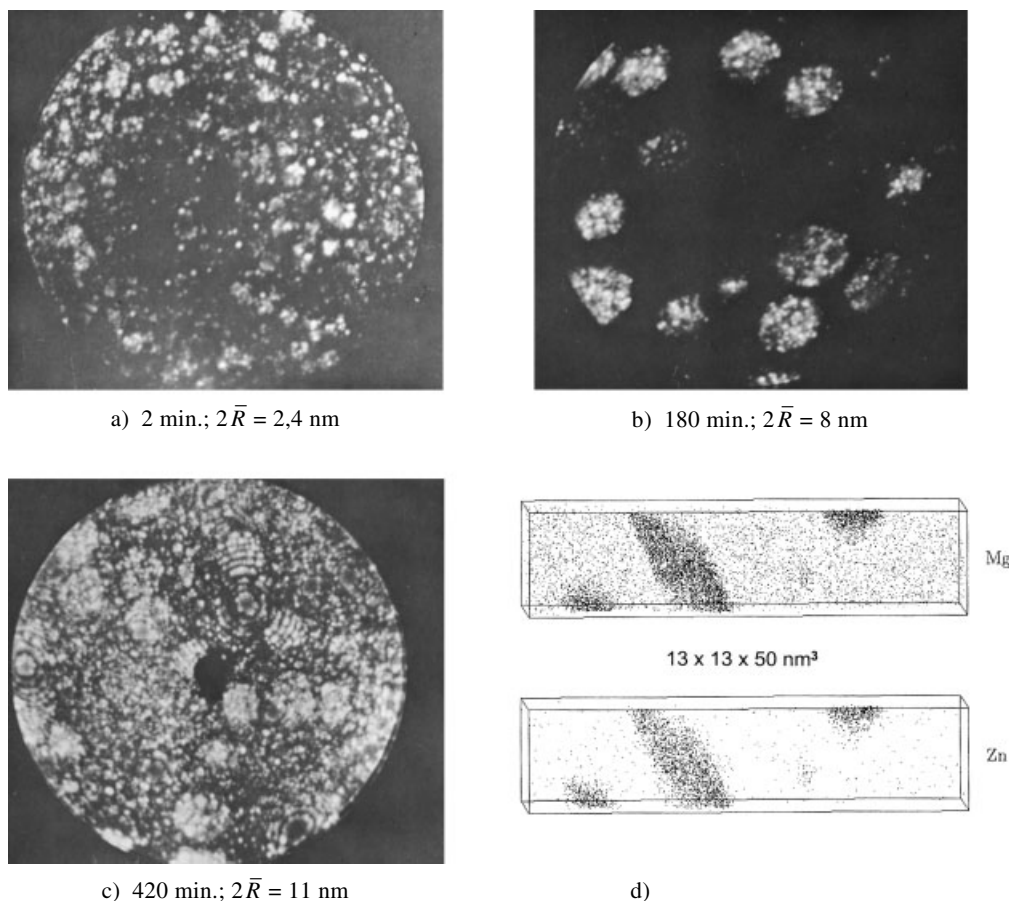


Figure 5-2. a)–c) Neon field ion image of γ' -precipitates (bright images in dark matrix) in Ni–36.8 at.% Cu–8 at.% Al aged for the given times at 580 °C (Liu and Wagner, 1984). d) Three-dimensional distribution of Mg and Zn atoms in a commercial Al–5.5 at.% Mg–1.35 at.% Zn alloy analyzed with the tomographic atom probe. Each point represents an atom. The T' precipitates are enriched in Mg and Zn (Bigot et al., 1997).

The terminal solute concentration of the solvent (A)-rich matrix α' is given by the equilibrium solubility limit $c_{\alpha}^e(T)$; the terminal composition c_p of the precipitated phase is given by the solubility at T_A at the B-rich side of the phase diagram (Fig. 5-1). Frequently, the interfacial energy $\sigma_{\alpha\beta}$ (J/m^2) between the matrix and the equilibrium precipitate is rather high, particularly if the width of the miscibility gap is large (see Sec. 5.7.4.4). In this case, the decomposition of α proceeds via the sequence $\alpha \rightarrow \alpha'' + \beta' \rightarrow \alpha' + \beta$

During the first step of the precipitation sequence a metastable precipitate (transition phase β') is formed, frequently with large associated coherency strains and a small interfacial energy $\sigma_{\alpha\beta}$. Often the metastable phase β' is an intermetallic compound with a lower solute concentration ($c_{\beta'}^e \equiv c_p'$) than the equilibrium precipitate (c_p). Because of the large coherency strains, the metastable ('coherent') solvus line (dashed line in Fig. 5-1) is shifted towards higher solute concentrations. This leads to a reduction of the supersaturation

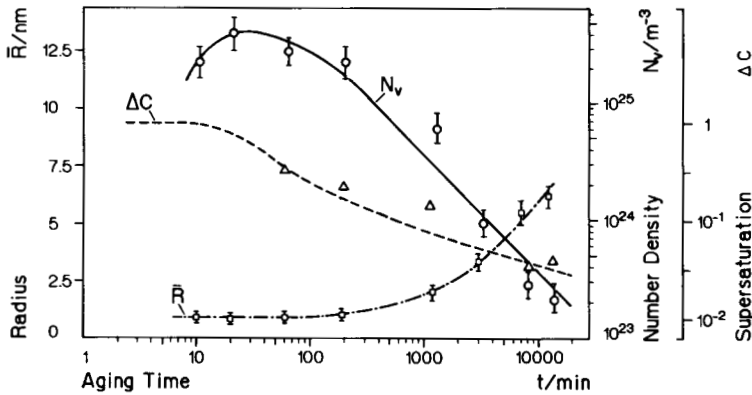


Figure 5-3. Time evolution of the mean radius \bar{R} , the number density N_v , and the supersaturation Δc of γ' -precipitates in Ni-36 at.% Cu-9 at.% Al during aging at 500°C (Liu and Wagner, 1984).

with respect to the (incoherent) equilibrium solvus line (Fig. 5-1), and, hence, to a reduction of the driving force for precipitation (see Sec. 5.2.4). Often only after extended aging do the metastable phases α'' and β' transform further to the final equilibrium phases α' and β . The crystal structure of the equilibrium phase β finally precipitated is different from that of the parent phase, leading to either a coherent, a semi-coherent or a fully incoherent α'/β interface boundary (Gleiter, 1983). The atomic structure of the latter resembles that of a high-energy, high-angle grain boundary and, thus, is associated with a rather large interfacial energy and small elastic strain energies.

The decomposition of Cu-Ti alloys with Ti contents between ≈ 1 at.% and 5 at.% serves as an example of such a complex precipitation sequence (Wagner et al., 1988):

α -Cu-(1...5 at.%) Ti

1st step $T \approx 350^\circ\text{C}$

α'' -Cu-Ti (f.c.c. solid solution) +
 β' -Cu₄Ti (metastable, coherent, body-centered-tetragonal structure, large coherency strains, small interfacial energy, $\sigma_{\alpha\beta} = 0.067 \text{ J/m}^2$)

2nd step extended aging at $T > 350^\circ\text{C}$

α' -Cu-Ti (f.c.c. solid solution) +
 β -Cu₃Ti (stable, hexagonal structure, incoherent, small strain, large interfacial energy, $\sigma_{\alpha\beta} > 0.6 \text{ J/m}^2$)

5.2.2 Thermodynamic Considerations – Metastability and Instability

Let us consider a binary alloy consisting of N_A solvent atoms A and N_B solute atoms B with $N_A + N_B = N$, or, in terms of atomic fractions, $c_A = N_A/N$ and $c_B = N_B/N$, with $c_A + c_B = 1$. (The concentrations of atoms A and B are then given as $c_A n_v$ and $c_B n_v$, where n_v is the number of atoms per unit volume.) As only one independent variable remains, we can refer to the composition of the alloy as $c \equiv c_B$ ($0 \leq c \leq 1$).

Decomposition of a supersaturated single-phase alloy into a two-phase state commonly occurs at constant temperature T and pressure p , and is thus prompted by a possible reduction in Gibbs energy (Gaskell, 1983)

$$G = H - TS \quad (5-4)$$

with the enthalpy

$$H = U + pV \quad (5-5)$$

Thermodynamic equilibrium is attained when G has reached a minimum, i.e.,

$$\delta G_{T,p} = dU + p dV - T dS = 0 \quad (5-6)$$

For phase separation in solids the term $p dV$ can usually be neglected with respect to the others in Eq. (5-6). Thus a good approximation for G is given by the Helmholtz energy

$$F = U - TS \quad (5-7)$$

which will be used in the following sections as the relevant thermodynamic function. Equilibrium is achieved if F or the corresponding Helmholtz energy density (F per unit volume or per mole) are minimized. Unmixing only takes place if the transition from the single-phase state lowers the Helmholtz energy, i.e., by convention if $\Delta F < 0$.

For a given temperature, volume and solute concentration of a heterogeneous binary alloy, equilibrium between the two phases α and β can only be achieved if the concentrations of A and B in the two phases have been established such that

$$\left(\frac{\partial F^\alpha}{\partial n_i} \right)_{T,V,n_j} = \left(\frac{\partial F^\beta}{\partial n_i} \right)_{T,V,n_j} \quad (5-8)$$

In other words, at equilibrium the chemical potentials $\mu_i^\alpha = \frac{\partial F^\alpha}{\partial n_i}$ and $\mu_i^\beta = \frac{\partial F^\beta}{\partial n_i}$ of the component i (either A or B) in the two phases are identical and the two phases have a common tangent to the associated free energy curves. This fact is illustrated in Fig. 5-4 for a supersaturated solid solution of composition c_0 , which decomposes into a B-depleted phases α' and a B-rich phase β of composition c_α^e and c_β^e , respectively. c_α^e and c_β^e are fixed by the common

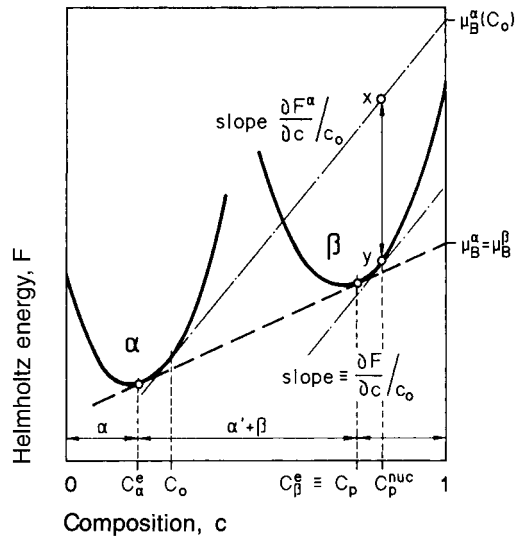


Figure 5-4. Helmholtz energy F as a function of composition for a binary alloy with a miscibility gap. The changes in F and the resulting driving forces for unmixing are illustrated.

tangent to the Helmholtz energy curves of the α - and β -phases; thus $c_\beta^e - c_\alpha^e$ represents the width of the miscibility gap at a given temperature (cf. Fig. 5.4).

Fig. 5-5a shows schematically the phase diagram of a binary alloy with a two-phase region at lower temperatures for $T = T_1$; the associated Helmholtz energy versus composition curve, $F(c)$, is shown in Fig. 5-5b. In the single-phase field α , F initially decreases with increasing solute concentration due to the growing entropy of mixing (Eq. (5-7)). In the thermodynamically equilibrated two-phase region, F varies linearly with c (bold straight line satisfying the equilibrium condition $\mu_i^\alpha = \mu_i^\beta$).

The *mean field theories* (see Secs. 5.5.1 and 5.5.4) dealing with the unmixing kinetics of solid solutions quenched into the miscibility gap are now based on the (questionable) assumption that the quenched-in single-phase states within the two-phase region can be described by a ‘constraint’ Helmholtz energy $F'(c) > F(c)$, e.g., as is

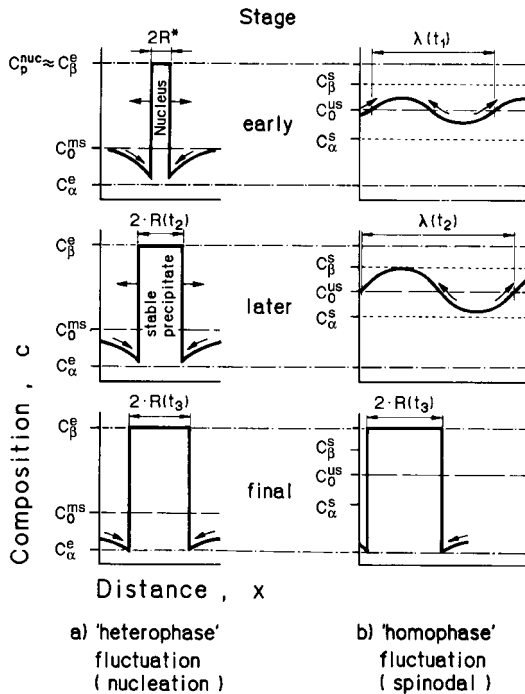


Figure 5-6. Spatial variation in solute distribution $c(r = (x, y, z))$ during a) a nucleation and growth reaction, and b) a continuous spinodal reaction at the beginning (time t_1) and towards the end (t_3) of the unmixing reaction. The notation of the compositions refers to Fig. 5-5; c_0^{ms} and c_0^{us} are the nominal compositions of the quenched-in metastable and unstable solid solutions, respectively; R^* is the critical radius of the nuclei and λ the wavelength of the composition fluctuations. The direction of the solute flux is indicated by the arrows. After an extended reaction time (e.g., after t_3), the transformation products are similar and do not allow any conclusions to be drawn with respect to the early decomposition mode.

As will be outlined in Sec. 5.5.1, the decay of a metastable solid solution via nucleation and growth has frequently been described in terms of cluster kinetics models. The cluster kinetics approaches are essentially based on the Becker–Döring theory (Becker and Döring, 1935) of the dynamics of solute cluster formation. There it is assumed that the non-equilibrium system consists of non-interacting solute-rich clusters of various size embedded in the matrix.

The time evolution of the cluster size distribution and, hence, the dynamics of the decay of the metastable alloy, are assumed to proceed via the condensation or evaporation of single solute atoms at each cluster.

In case ii, the non-equilibrium solid solution with an initial composition $c_0 > c_\alpha^s$, (Fig. 5-5 b) is unstable with respect to the formation of non-localized, spatially extended thermal composition fluctuations with small amplitudes. Hence, the unmixing reaction of an unstable solid solution, which is termed *spinodal decomposition*, is initiated via the spontaneous formation and subsequent growth of coherent ('homophase') composition fluctuations (Fig. 5-6b).

The dynamic behavior of an unstable alloy proceeding towards equilibrium has often been theoretically approached in terms of spinodal theories (see Sec. 5.5.4 and Chapter 6), amongst which the most well-known linear theory is due to Cahn (1966) and the most elaborate non-linear one is due to Langer et al. (1975). As discussed in Sec. 5.2.2, the spinodal theories are based on the assumption that in each stage of the decomposition reaction the Helmholtz energy of the non-equilibrium solid solution, which contains compositional fluctuations, can be defined. As in the cluster kinetics models, the driving force for phase separation is again provided by lowering the Helmholtz energy of the alloy. If the form of the 'constraint' Helmholtz energy $F'(c)$ of the non-uniform system is properly chosen, the composition profile with associated minimum Helmholtz energy can be determined (in principle!) at any instant of the phase transformation.

The existence of a unique spinodal curve within the framework of the mean field theories (Cahn, 1966; Cook, 1970; Skripov and Skripov, 1979) has led to the idea (still

widespread in the community of metallurgists) that there is a discontinuity of the mechanism and, in particular, of the decomposition kinetics at the boundary between the metastable and unstable regions. Therefore, many experiments have been carried out in order to determine the spinodal curve and to search for a kinetic distinction between metastable and unstable states (see Sec. 5.5.5).

In reality, there is no need to develop dynamical concepts which are confined to either the metastable *nucleation and growth regime* (case i) or to the *unstable spinodal regime* (case ii). In fact, the cluster-kinetics models and the spinodal theories can be seen as two different approaches used to describe phase separation, the dynamics of which are controlled by the same mechanism, i.e. diffusion of solvent and solute atoms driven by the gradient of the chemical potential (Martin, 1978).

This fact is reflected in the attempts to develop ‘*unified theories*’ which comprise spinodal decomposition as well as nucleation and growth. Langer et al. (1975) tried to develop such a theory on the basis of a non-linear spinodal theory (see Sec. 5.5.4), whereas Binder and coworkers (Binder et al., 1978; Mirolid and Binder, 1977) chose the cluster kinetics approach by treating spinodal decomposition in the form of a generalized nucleation theory (see Sec. 5.5.3). These theories involve several assumptions whose validity is difficult to assess a priori. The quality of all spinodal or cluster kinetics concepts, however, can be scrutinized by Monte Carlo simulations of the unmixing kinetics of binary ‘model’ alloys. These are quenched into either a metastable or an unstable state (see Sec. 5.5.6) and can be described in terms of an Ising model (Kalos et al., 1978; Penrose et al., 1978).

Although both the ‘unified theories’ and the Monte Carlo simulations only provide

qualitative insight into early-stage unmixing behavior of a binary alloy, they have revealed that there is no discontinuity in the decomposition kinetics to be expected during crossing of the mean-field spinodal curve by either increasing the concentration of the alloy and keeping the reaction temperature (T_A) constant or by lowering the reaction temperature and keeping the composition (c_0) constant. On the other hand, the mean-field description is strictly valid only for systems with infinitely long-range interaction forces (Gunton, 1984) and, hence, in general does not apply to metallic alloys (polymer mixtures might be close to the mean-field limit: Binder, 1983, 1984; Izumitani and Hashimoto, 1985; see Sec. 5.5.4). Therefore, numerous experiments that have been designed by metallurgists in order to determine a unique spinodal curve simply by searching for drastic changes in the dynamic behavior of an alloy quenched into the vicinity of the mean-field spinodal must be considered with some reservations.

In principle, the above-mentioned theories and, in particular, the Monte Carlo simulations deal mainly with the dynamic evolution of a two-phase mixture in its early stages. They frequently do not account for a further evolution of the precipitate or cluster size distribution with aging time (i.e., coarsening; see Sec. 5.6) once the precipitated volume fraction is close to its equilibrium value. On the other hand, the time evolution of the precipitate microstructure beyond its initial clustering stages has been the subject of many experimental studies and is of major interest in practical metallurgy. For this purpose, numerical approaches have been devised (Langer and Schwartz, 1980; Kampmann and Wagner, 1984) which treat nucleation, growth and coarsening as concomitant processes and thus allow the dynamic evolution of the

two-phase microstructure to be computed during the entire course of a precipitation reaction (see Sec. 5.7).

As was pointed out in Sec 5.2.1, the reaction path of a supersaturated solid solution can be rather complex, sometimes involving the formation of one or more intermediate non-equilibrium phases prior to reaching the equilibrium two-phase microstructure. Unlike in the 'early stage theories' mentioned above, these complications, which are of practical relevance, can be taken into consideration in numerical approaches. Even though they still contain a few shortcomings, numerical approaches lead to a practical description of the kinetic course of a precipitation reaction which lies closest to reality.

There are several comprehensive review articles and books dealing in a more general manner with the kinetics of first-order phase transitions (Gunton and Droz, 1984; Gunton et al., 1983; Binder, 1987; Gunton, 1984; Penrose and Lebowitz, 1979). Phase separation in solids (crystalline and amorphous alloys, polymer blends, oxides and oxide glasses) via homogeneous nucleation and growth or via spinodal decomposition represents only one aspect among many others (Gunton and Droz, 1984). Apart from the above-mentioned numerical approaches, the comprehensive articles by Martin (1978) and by de Fontaine (1982) cover most of the theoretical developments relevant to the kinetics of (homogeneous) phase separation in metallic systems. A general overview of the broad field of diffusive phase transformations in materials science including heterogeneous nucleation and discontinuous precipitation not covered in the present chapter, can be found in the article by Doherty (1983) or, as an introduction to this field, in the book by Christian (1975), see also chapter by Purdy and Bréchet (2001).

5.2.4 Thermodynamic Driving Forces for Phase Separation

Even in the single-phase equilibrium state, the mobility of the solvent and solute atoms at elevated temperatures permits the formation of composition fluctuations which grow and decay again reversibly with time. If the solid solution is quenched into the miscibility gap the two-phase mixture is the more stable state and, thus, some of these fluctuations grow irreversibly owing to the associated reduction in Helmholtz energy. The reduction in Helmholtz energy during the transformation from the initial to the final state provides the driving force ΔF . As we shall see in Sec. 5.5.1, it is possible to calculate the formation rate and the size of stable composition fluctuations ('nuclei' of the second phase) by means of the cluster kinetics approach once ΔF is known. It should, however, be emphasized at this point that for most alloys it is rather difficult to calculate ΔF with sufficient accuracy. This is seen as one of the major hindrances to performing a quantitative comparison between theory and experiment.

The driving force for precipitation is made up of two different contributions:

i) the gain in chemical Helmholtz energy, $\Delta F_{\text{ch}} < 0$, associated with the formation of a unit volume of the precipitating phase β , and

ii) the expenditure of distortion Helmholtz energy, $\Delta F_{\text{el}} > 0$, accounting for the coherency strains which result from a likely variation of the lattice parameter with the spatial composition fluctuations.

i) Chemical contribution, ΔF_{ch} . According to the tangent rule and referring to Fig. 5-4, the chemical driving force for precipitation of the equilibrium β phase out of a solid solution with composition c_0 is given by the numerical value of \overline{xy} . Assuming the

precipitating phase β already has the final bulk composition $c_\beta^e \equiv c_p$ rather than c_p^{nuc} (which is only a reasonable assumption if the supersaturation is not too large (Cahn and Hilliard, 1959 a, b)), ΔF_{ch} has been derived for a unit volume of β phase with molar volume V_β as (Aaronson et al., 1970 a, b):

$$\Delta F_{\text{ch}} = -\frac{R_g T}{V_\beta} \times \left[c_\beta^e \ln \frac{a_B(c_0)}{a_B(c_\alpha^e)} + (1 - c_\beta^e) \ln \frac{a_A(c_0)}{a_A(c_\alpha^e)} \right] \quad (5-9)$$

where $a_i(c)$ is the activity of the solvent ($i = A$) or solute component ($i = B$) in the parent phase α for the given composition.

For most alloy systems the activity data required for a computation of ΔF_{ch} by means of Eq. (5-9) are not available. In principle, they can be derived from a computation of the thermodynamic functions by means of the CALPHAD method. Originally this method was developed for the calculation of phase diagrams by Kaufman and coworkers (Kaufman and Bernstein, 1970) on the basis of a few accurately measured thermodynamic data to which suitable expressions for the thermodynamic functions had been fitted. For the sake of a simplified mathematical description, the stable solid solutions of the particular alloy system are frequently described in terms of the regular solution model, whereas the phase fields of the intermetallic compounds are approximated by line compounds. The thermodynamic functions obtained thereby are then used to reconstruct the phase diagram (or part of it). The degree of self-consistency between the reconstructed and the experimentally determined phase diagram (or the agreement between the measured thermodynamic data and the derived data) serves as a measure of the accuracy of the thermodynamic functions.

Hence, if, for example, $F(c, T)$ is known for the stable solid solution, this value can readily be extrapolated into the adjacent two-phase region to yield $F'(c)$ (see Fig. 5-5) of the supersaturated homogeneous solid solution or the related chemical potentials and activities. Of course, physically this is only meaningful if we assume (as, in fact is done for the derivation of Eq. (5-9)) that the free energy of the non-equilibrium solid solution can be properly defined within the miscibility gap.

For many binary alloys and for some ternary alloys of technological significance, the thermodynamic functions have been evaluated by means of the CALPHAD method and are compiled in volumes of the CALPHAD series (Kaufman, 1977).

Hitherto, due to the lack of available activity data, the activities entering Eq. (5-9) were frequently replaced by concentrations, i.e.,

$$\Delta F_{\text{ch}} = -\frac{R_g T}{V_\beta} \times \left[c_\beta^e \ln \frac{c_0}{c_\alpha^e} + (1 - c_\beta^e) \ln \left(\frac{1 - c_0}{1 - c_\alpha^e} \right) \right] \quad (5-10)$$

If β is almost pure B, then $c_\beta^e \approx 1$ and the chemical driving force is approximated as

$$\Delta F_{\text{ch}} \approx -\frac{R_g T}{V_\beta} \ln \frac{c_0}{c_\alpha^e} \quad (5-11)$$

For many alloys the condition $c_\beta^e \approx 1$ is *not* met. Nevertheless, it has been used for computation of ΔF . As discussed by Aaronson et al. (1970 a), the resulting error can be rather large. If the nucleating phase is a solvent-rich intermetallic compound (e.g., Ni_3Al or Cu_4Ti), the computation of ΔF_{ch} is particularly difficult, since up to now the corresponding activities are neither known nor furnished by the CALPHAD method, and Eqs. (5-10) and (5-11) are no longer valid.

ii) Reduction of the driving force by the elastic strain energy, ΔF_{el} . The formation of a composition fluctuation is associated with the expenditure of elastic strain Helmholtz energy, ΔF_{el} , if the solvent and the solute atoms have different atomic radii. According to Cahn (1962), the Helmholtz energy of a system containing homophase fluctuations is raised by

$$\Delta F_{el} = \eta^2 \Delta c^2 Y \quad (5-12)$$

where $\eta = (1/a_0) (\partial a / \partial c)$ denotes the change in lattice parameter (a_0 for the homogeneous solid solution of composition c_0) with composition, and Δc the composition amplitude. Y is a combination of elastic constants and depends on the crystallographic direction of the composition modulation. It reduces to $E/(1 - \nu)$, E and ν being Young's modulus and Poisson's ratio, respectively, if the elastic anisotropy $A \equiv 2c_{44} + c_{12} - c_{11}$ is zero; otherwise, in order to minimize ΔF_{el} , the composition fluctuations are expected to grow along the elastically soft directions, which for cubic crystals and $A > 0$ are the $\langle 100 \rangle$ directions.

In the context of heterophase fluctuations, the barrier against nucleation of the new phase is dominated by the matrix/ nucleus interfacial energy (see Sec. 5.5.1). Since coherent interfaces have a lower energy than incoherent ones, a precipitate is usually coherent (or at least semi-coherent) during the early stages of nucleation and growth. Often its lattice parameter, a_β , is slightly different from that of the parent phase, a_α . The resulting misfit between the (unstrained) matrix and the (unstrained) precipitate:

$$\delta = 2 \frac{a_\alpha - a_\beta}{a_\alpha + a_\beta} \quad (5-13)$$

can be accommodated by an elastic strain if both δ and the particles are sufficiently small; this is commonly the case during the early stages of nucleation and growth.

The problem of calculating ΔF_{el} for coherent inclusions is rather complex. It has generally been treated within the framework of isotropic elastic theory for ellipsoidal precipitates with varying axial ratios, e.g. Eshelby (1957), and has been extended to the anisotropic case (Lee and Johnson, 1982). Basically, these treatments show that the strain energy depends on the particular shape of the new phase. Only if the transformation strains are purely dilatational and if α and β have about the same elastic constants will ΔF_{el} become independent of the shape. It is then given as (Eshelby, 1957):

$$\Delta F_{el} = 2\gamma \left(\frac{1+\nu}{1-\nu} \right) \delta^2 \quad (5-14)$$

with γ being the shear modulus.

As is shown schematically in Fig. 5-7, with respect to the Helmholtz energy of the *incoherent* equilibrium phase β , the Helmholtz energy of the *coherent* phase β' is raised by the elastic energy to match the two lattices. The driving force $\Delta F^{inc} \equiv \bar{xy}$

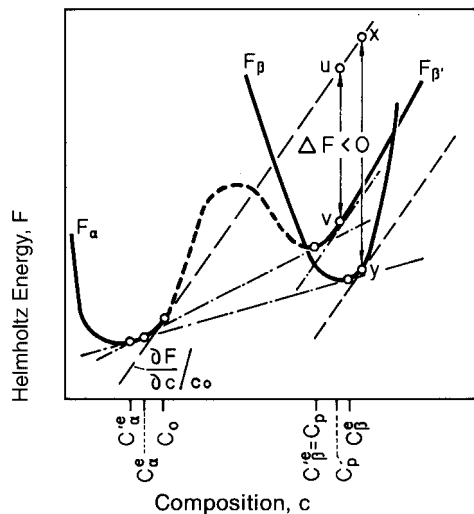


Figure 5-7. Helmholtz energy curves and associated driving forces for precipitates of the coherent metastable ($F_{\beta'}$) and incoherent equilibrium (F_{β}) phases.

is reduced to the value of $\Delta F^{\text{coh}} \equiv \overline{uv}$, and the solubility limit in the α phase increases from c_{α}^e to $c_{\alpha}^{\prime e}$.

Hence, if we refer to the resulting coherent phase diagram (cf. Fig. 5-1), the total driving force, ΔF , for coherent unmixing, implicitly already containing the elastic contribution, is obtained by replacing, e.g., in Eq. (5-11), the composition c_{α}^e of the incoherent phase by the composition $c_{\alpha}^{\prime e}$ of the coherent one:

$$\Delta F = - \frac{R_g T}{V_{\beta'}} \ln \frac{c_0}{c_{\alpha}^{\prime e}} \quad (5-15)$$

As an example, for metastable iron-rich f.c.c. precipitates ($c_{\beta}^e \approx 99.9$ at.%) with $\delta = -8 \times 10^{-3}$ formed at 500 °C in a supersaturated Cu–1.15 at.% Fe alloy ($c_0 = 1.15$ at.%, ($c_{\alpha}^e \approx 0.05$ at.%; Kampmann and Wagner, 1986), Eq. (5-12) yields $\Delta F_{\text{el}} \approx 0.13$ kJ/mol. This value is negligibly small with respect to the rather large chemical driving force (≈ 20 kJ/mol). Since, however, ΔF_{ch} decreases markedly with increasing temperature (or decreasing supersaturation), whereas ΔF_{el} does not, coherent nucleation commonly occurs at larger undercoolings or supersaturations, whereas nucleation of incoherent precipitates takes place at smaller ones. This is in fact observed in the Cu–Ti (see Sec. 5.2.1) and Al–Cu (Hornbogen, 1967) systems.

As will be shown in Sec. 5.5.1.1, the barrier ΔF^* against formation of the new phase, and hence the nucleation rate, is not only a function of the driving force but is rather sensitive to the nucleus/matrix interface energy $\sigma_{\alpha\beta}$. Therefore, the phase nucleating first will not necessarily be the equilibrium phase with the lowest Helmholtz energy but that with the lowest ΔF^* , e.g. a coherent metastable phase with a low value of $\sigma_{\alpha\beta}$. This explains the likely formation of a series of metastable phases (see Sec. 5.2.1) in various decomposing al-

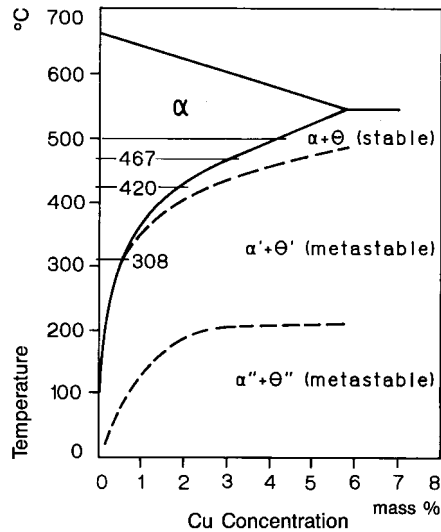


Figure 5-8. Solubility limits of Cu in Al in the presence of the metastable θ'' and θ' phases (dashed) and the stable θ phase, as a function of temperature (after Hornbogen, 1967).

loys, amongst which Al–Cu ($c_0 \leq 2.5$ at.% Cu) is probably the best known. There the stable phase (θ -CuAl₂) is incoherent, with a high associated $\sigma_{\alpha\beta}$ (≈ 1 J/m²) (Hornbogen, 1967). This inhibits homogeneous nucleation and θ is found to form only at small undercoolings, preferentially at grain boundaries (see Fig. 5-8). At larger undercoolings, a series of metastable copper-rich precipitates is formed in the order: GPI zones \rightarrow GPII zones (θ'') \rightarrow θ' with different crystal structures (see Fig. 5-8). Guinier–Preston zones of type I (GPI) and type II (GPII or θ'') are coherent and nucleate homogeneously, whereas θ' is semi-coherent and nucleates preferentially at dislocations.

Al–Mg–Si alloys represent an important group of age-hardenable structural materials heavily used by industry in both cast and wrought form. Hence, control and optimization of the precipitate microstructure during cooling and heat treatment is of par-

amount interest for optimum mechanical properties (Bratland et al., 1997). However, due to its inherent complexity, the precipitation sequence of these commercial alloys is still a matter of controversy (Dutta and Allen, 1991; Gupta and Lloyd, 1992; Edwards et al., 1998).

5.3 Experimental Techniques for Studying Decomposition Kinetics

5.3.1 Microanalytical Tools

In general, the course of a decomposition reaction, including the early stages (during which composition fluctuations and second-phase nuclei are formed, see Sec. 5.2.1) and the coarsening stages, cannot be followed continuously by any one microanalytical technique. The progress of the reaction is usually reconstructed from the microstructure that develops at various stages of the phase transformation. Thus it is necessary to analyze the spatial extension and the amplitude of composition fluctuations of incipient second-phase particles, as well as the morphology, number density, size and chemical composition of individual precipitates at various stages of the phase transformation. For this purpose microanalytical tools are required that are capable of resolving very small (typically a few nm) solute clusters, and which allow (frequently simultaneously) an analysis of their chemical composition to be made.

The tools that, in principle, meet these requirements can be subdivided into two groups: *direct imaging techniques* and *scattering techniques*.

It is beyond the scope of this chapter to discuss any one of the techniques belonging to either group in any detail. We shall only briefly summarize the merits and the shortcomings of the various techniques

with respect to both the detection limit and the spatial resolution of microanalysis.

5.3.1.1 Direct Imaging Techniques

Field ion microscopy (FIM) (Wagner, 1982) as well as conventional (CTEM) (Hobbs et al., 1986) and *high resolution* (HREM) transmission electron microscopy (Smith, 1983) allow for direct imaging of the second-phase particles, provided the contrast between precipitate and matrix is sufficient.

In CTEM both the bright field and the dark field contrast of particles less than ≈ 5 nm in diameter are often either too weak or too blurred for an accurate quantitative determination of the relevant structural precipitate parameters. Hence, CTEM does not provide access to an experimental investigation of the early stages of decomposition but remains a technique for studying the later stages. In contrast, HREM allows solute clusters of less than 1 nm diameter to be imaged, as was demonstrated for Ni_3Al precipitates in Ni-12 at.% (Si-Qun Xiao, 1989) and for silver-rich particles in Al-1 at.% Ag (Ernst and Haasen, 1988; Ernst et al., 1987). As is shown in Fig. 5-9 for the latter alloy, the particles are not ideally spherical but show some irregularities which, however, are small in comparison with their overall dimensions. Hence, describing their shapes by spheres of radius R is still a rather good approximation.

Prior to measuring the particle sizes directly from the HREM micrographs, it must be established via computer image simulations that there exists a one-to-one correspondence between the width of the precipitate contrast (dark area in Fig. 5-9) and its true size. This was verified for the HREM imaging conditions used in Fig. 5.9. The evolution of the size distribution in Al-1 at.% Ag with aging time at 413 K

as derived from HREM micrographs is shown in Fig. 5-10.

The HREM lattice imaging technique has also been employed to determine the spacings of adjacent lattice planes in various alloys undergoing phase separation (Sinclair and Thomas, 1974; Gronsky et al., 1975). The smooth variations observed were attributed to variations in lattice parameter caused by composition modulations such as we would expect from spinodal decomposition (e.g. Fig. 5-6b at t_1 or t_2). Subsequent model calculations of high-resolution images, however, showed that the spatial modulation of the lattice fringes observed on the HREM image can be significantly different from the spatial modulation of the lattice plane spacings in the specimen (Cockayne and Gronsky, 1981). In practice, it does not appear possible to derive reliable information on composition modulations from modulations of lattice fringe spacings in HREM images.

The composition of the imaged particles can, in principle, be obtained from analytical electron microscopy (AEM), which is routinely based on energy dispersive X-ray analysis (EDX) or, less frequently, on electron energy loss spectroscopy (EELS) (Williams and Carter, 1996). Due to beam spreading by electron beam/specimen interaction, the spatial resolution for routine EDX microanalysis is limited to ≥ 10 nm. This value is rather large and confines EDX microanalysis of unmixing alloys to the later stages of precipitation. The more interesting early stages of decomposition, however, where composition changes of either extended or localized solute fluctuations are expected to occur, are not amenable to EDX microanalysis.

The spatial resolution of EELS may, with difficulty, reach 1 nm (Williams and Carter, 1996), but so far, EELS has not been employed for a systematic microanal-

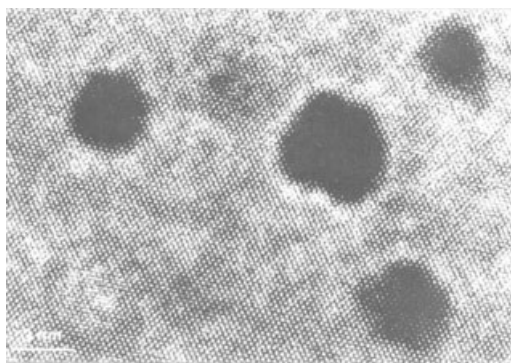


Figure 5-9. HREM lattice fringe image of Al-1 at.% Ag aged for 92 h at 413 K with silver-rich precipitates (dark areas). For imaging the Al matrix a rather large defocus (~ 280 nm) had to be chosen, which gives rise to the bright Fresnel fringes surrounding the particles (reproduced by courtesy of F. Ernst (Ernst and Haasen, 1988)).

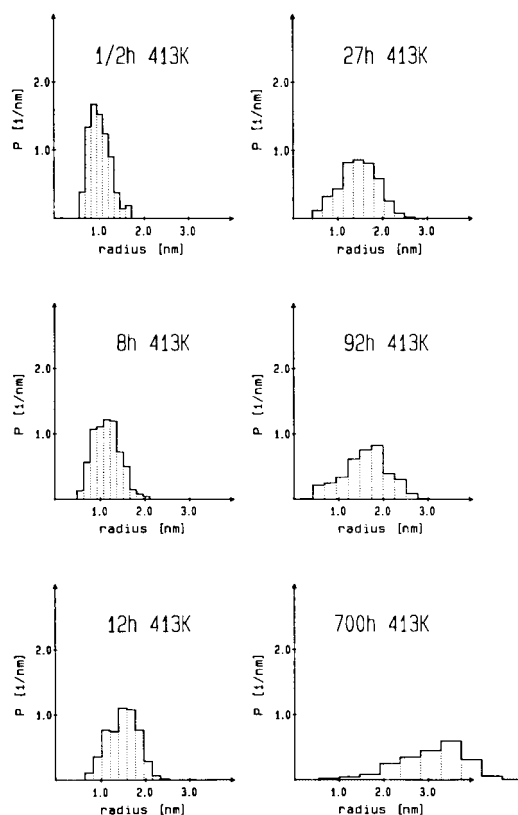


Figure 5-10. Time evolution of the particle size distribution in Al-1 at.% Ag during aging at 413 K (after Ernst and Haasen, 1988).

ysis of composition fluctuations during early-stage decomposition.

Analytical field ion microscopy (AFIM) (Wagner, 1982; Miller et al., 1996) can favorably be applied for an analysis of ultra-fine solute clusters in the early stages of decomposition, as both the imaging resolution of the FIM (see Fig. 5-2) and the spatial resolution of microanalysis of the integrated time-of-flight spectrometer ('atom probe') are sufficient, i.e., <1 nm and ≈ 2 nm, respectively. (Although the atom probe detects single atoms from the probed volume, the requirement for the analysis to be statistically significant confines the microanalytical spatial resolution to ≥ 2 nm.) As is shown in Figs. 5-2a–c and 5-19c, both the morphologies of small particles and their three-dimensional arrangements can also be determined in the FIM, at least for precipitates with sufficient contrast.

The volume sampled during an atom probe FIM analysis is rather small (typically about 200 nm^3). Hence, in order to obtain statistically significant data concerning the average size (\bar{R}) and the number density (N_v) of the precipitates, the latter ought to exceed 10^{23} m^{-3} . Since after the early stages of precipitation N_v decrease with time (see Sec. 5.2.1), AFIM shows its full potential as a microanalytical tool in studies of the early stages of precipitation, during which \bar{R} is commonly small and N_v sufficiently large (Haasen and Wagner, 1985).

With respect to analyses of the spatial arrangement and the composition of precipitated phases, the versatility of the AFIM was considerably improved by the development of the *tomographic atom probe* (TAP) (Blavette et al., 1993, 1998; Miller et al., 1996). This instrument allows for the three-dimensional reconstruction of a small volume of the microscopically heterogeneous material on a sub-nanometric

scale (Fig. 5-2d). The spatial distribution of each chemical species can be directly observed with a spatial resolution better than 0.5 nm (Auger et al., 1995; Pareige et al., 1999; Al-Kassab et al., 1997). The volume typically sampled is about $15 \times 15 \times 100 \text{ nm}^3$ and, thus, about a hundred times larger than the volume analyzed with the AFIM.

5.3.1.2 Scattering Techniques

The time evolution of the structure of supersaturated alloys, as well as of oxides and polymer blends undergoing phase separation, can be analyzed by means of small angle scattering of X-rays (SAXS), neutrons (SANS), and light. Light scattering is of course confined to transparent specimens, in which the domain sizes of the evolving second phase must be of the order of $\approx 1 \text{ }\mu\text{m}$. It has been successfully applied in studies of decomposition, e.g., of a polymer mixture of polyvinyl methyl ether (PVME) and polystyrene (PS) (Snyder and Meakin 1983a, b, 1985), and of various glass-forming oxide systems (Goldstein, 1965; Rindtone, 1975).

In principle, SAXS (Glatter, 1982) and SANS (Kostorz, 1979; Sequeira et al., 1995) provide access to a structural analysis of unmixing alloys, in both the early stages where the composition fluctuations can be small in spatial extension and in amplitude, as well as in the later stages of decomposition where \bar{R} and N_v may have attained values which are quite unfavorable for a quantitative analysis by TEM or FIM. In addition, evaluation of the Laue scattering allows the remaining supersaturation of solute atoms in the matrix to be determined.

The metallurgist is left with the problem of extracting in a quantitative manner all the structural data contained in scattering

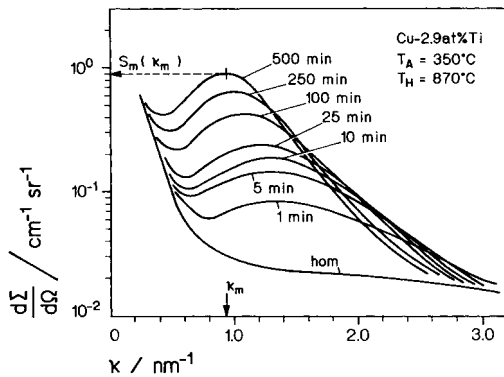


Figure 5-11. SANS curves of Cu-2.9 at.% Ti single crystals aged for the given times at 350°C. Note that even the homogenized and quenched ('hom') specimen yields SANS intensity, indicating that phase separation has occurred during quenching (Eckerlebe et al., 1986).

curves such as are shown in Fig. 5-11. This is often not trivial (Glatter, 1982), in particular for concentrated alloys (i.e., for most technical two-phase alloys). Here the scattering curve reveals a maximum (at position κ_m and with height $S_m(\kappa_m)$ in Fig. 5-11) which results from an interparticle interference of the scattered waves (Kosiorz, 1979). In general, the interparticle interference function is not known, thus impeding a straightforward quantitative analysis. Moreover, the composition and morphology of the fluctuations are required in order to perform such an analysis. For many alloys this information can only be obtained from AFIM or AEM. These complicating factors often demand the above-mentioned microanalytical tools to be employed jointly, rendering experimental studies of decomposition rather difficult and tedious.

The small angle scattering intensity is proportional to the structure function $S(\kappa, t)$; κ is the scattering vector with $\kappa \equiv |\kappa| = 4\pi \sin(\theta/2)/\lambda$; λ is the wavelength of the X-rays or neutrons and θ the scattering an-

gle. For binary alloys $S(\kappa, t)$ is the Fourier transform of the two-point correlation function at time t (Langer, 1975):

$$(5-16)$$

$$G(|\mathbf{r}-\mathbf{r}_0|, t) = \langle [c(\mathbf{r}, t) - c_0][c(\mathbf{r}_0, t) - c_0] \rangle$$

The right-hand side in Eq. (5-16) denotes the non-equilibrium average of the product of the composition amplitudes at two different spatial positions, \mathbf{r} and \mathbf{r}_0 , in the alloy with average composition c_0 .

$S(\kappa, t)$ contains all the structural information on the phase-separating system. Many theories and computer simulations dealing with phase separation yield the evolution of $S(\kappa, t)$ and predict the shift of κ_m (which is a measure of the average spacing of solute clusters) and the growth of $S_m(\kappa_m)$ with time (Langer et al., 1975; Marro et al., 1975, 1977; Binder et al., 1978).

Hence, SAXS and SANS curves measured after different aging times can be directly compared with the predictions from various theoretical kinetic concepts (see Secs. 5.5.4, 5.5.6 and 5.8.1).

In ternary systems the situation is much more complicated. For a substitutional ternary alloy, there are three linearly independent pair correlation functions with three related partial structure functions (de Fontaine, 1971, 1973), which linearly combine to the measured SAS intensity. An unambiguous characterization of the kinetics of phase separation in *ternary substitutional* alloys requires the three partial structure functions to be determined separately. This has been attempted by employing the 'anomalous small angle X-ray scattering' technique for investigations of phase separation in Al-Zn-Ag (Hoyt et al., 1987), Cu-Ni-Fe (Lyon and Simon, 1987, 1988) and Fe-Cr-Co (Simon and Lyon, 1989).

Unlike for X-rays, for thermal neutrons the atomic nuclear scattering length is not

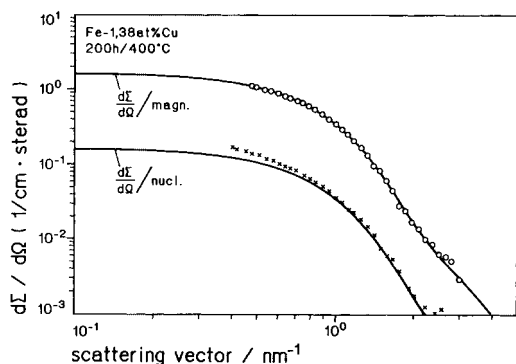


Figure 5-12. Nuclear and magnetic SANS curves of Fe-1.4 at.% Cu aged for 200 h at 400°C. From the ratio of magnetic and nuclear scattering intensities, the composition of the copper-rich clusters can be derived. Theoretical curves are shown as full lines (Kampmann and Wagner, 1986).

monotonically dependent on the atomic number (Kostorz, 1979). For this reason use of SANS is more universal and is frequently superior to SAXS for decomposition studies of binary alloys with mainly transition metal constituents having similar atomic numbers. Consequently, SAXS has only been used extensively for studies of the unmixing kinetics in Al-Zn where the difference (this, in fact, controls the contrast in SAS) in atomic scattering lengths for X-rays is sufficiently large (Rundman and Hilliard, 1967; Hennion et al., 1982; Forouhi and de Fontaine, 1987).

Furthermore, if the two phases differ not only in composition but also in magnetization, both nuclear and magnetic SANS curves can be recorded (see Fig. 5-12). These two independently measurable SANS curves sometimes even allow the composition of the scattering centers to be determined, e.g., for Fe-Cu, where diamagnetic copper-rich particles precipitate in the ferromagnetic α -Fe matrix (Kampmann and Wagner, 1986), or for phase-separated amorphous Fe₄₀Ni₄₀P₂₀ (Gerling et al., 1988).

Due to relatively simple calibration procedures in SANS experiments, the scattered intensity which is expressed in terms of the coherent (nuclear or magnetic) scattering cross-section per unit volume, $d\Sigma(\mathbf{r}, t)/d\Omega$, can be measured in absolute units. This is directly related to the structure function $S(\mathbf{r}, t)$ via (Hennion et al., 1982):

$$\frac{d\Sigma}{d\Omega}(\mathbf{r}, t) = \frac{1}{\bar{\Omega}^2} (\bar{b}_M - \bar{b}_p)^2 S(\mathbf{r}, t) \quad (5-17)$$

where \bar{b}_M and \bar{b}_p are the locally averaged (nuclear or magnetic) scattering lengths of the matrix and of the solute-rich clusters, respectively, and $\bar{\Omega}$ is the mean atomic volume.

5.3.2 Experimental Problems

5.3.2.1 Influence of Quenching Rate on Kinetics

For studies on decomposition kinetics the alloy is commonly homogenized in the single-phase region at T_H (Fig. 5-1), quenched into brine and subsequently isothermally aged at T_A . In order to capture the initial stages of the decay of the supersaturated solid solution, both the quenching and the heating rate to T_A are required to be sufficiently high in order to avoid phase separation prior to isothermal aging. This can be comfortably achieved in alloys with small supersaturations. It is, however, often a problem (or even impossible) for alloys with large supersaturations and/or small interfacial energies, where the nucleation barriers are small (see Secs. 5.2.3 and 5.5.1) and, hence, the nucleation rates large.

The driving force for unmixing in Al-1 at.% Ag at 140°C is rather small (≈ 0.5 kJ/mol). Nevertheless, because of the extremely small interfacial energy of only

$\approx 0.01 \text{ J/m}^2$ (Le Goues et al., 1984c), the barrier to nucleation is so low that precipitation commences instantaneously almost as soon as the solvus line is crossed. Thus, except for extremely high quenching rates, the non-equilibrium single-phase state cannot be frozen in and the as-quenched microstructure already contains a large number of small GP zones (Fig. 5-13).

The accessible quenching rates have been found to be insufficient for a suppression of phase separation during quenching of homogenized Cu-Ti alloys with Ti concentrations exceeding $\approx 2.5 \text{ at.}\%$. This is discernible from the SANS curve of the as-quenched specimen (Fig. 5-11) (see Sec. 5.7.5).

Further problems result from the fact that the decomposition kinetics at T_A are strongly influenced by the concentration of quenched-in excess vacancies. This depends strongly on the chosen homogenization temperature and quenching rate.

Fig. 5-14 shows SANS curves from specimens that were solution-treated at the given homogenization temperature T_H . Following quenching, each specimen was

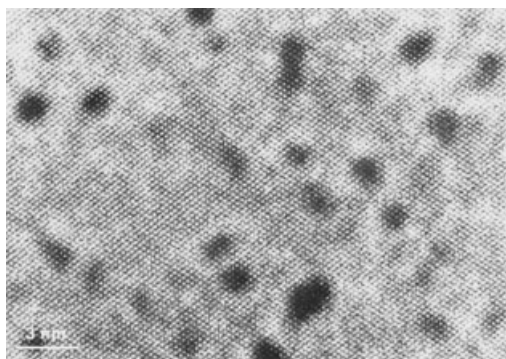


Figure 5-13. HREM micrograph of GP zones formed during quenching of Al-1 at.% Ag. The smallest GP zones have diameters of only $\sim 1 \text{ nm}$ (reproduced by courtesy of P. Wilbrandt (Ernst et al., 1987)).

aged for 10 min at 350°C . The maximum in the SANS curves is found to be higher, and its position lower, the higher the homogenization temperature. This indicates that phase separation in the early stages progresses the faster the higher the homogenization temperature is chosen. Obviously, in Cu-Ti, the concentration of quenched-in excess vacancies is correlated to T_H and significantly influences the decomposition

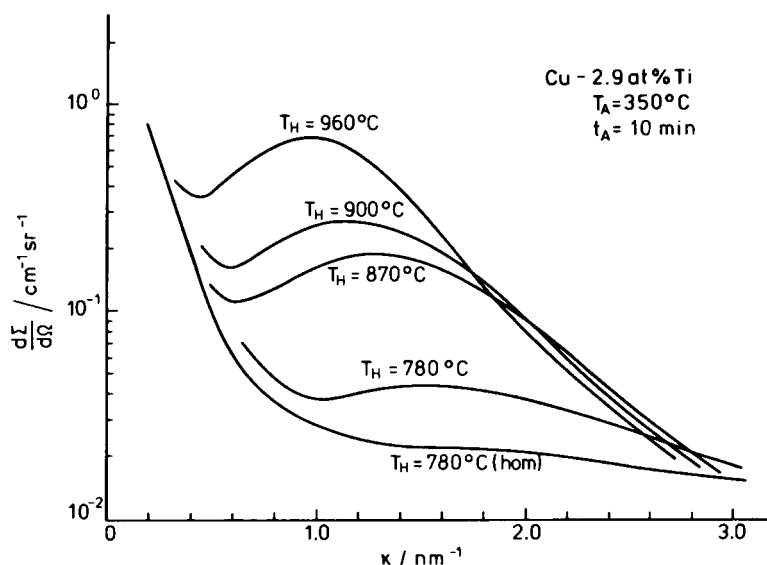


Figure 5-14. SANS curves of Cu-2.9 at.% Ti quenched from the given homogenization temperatures T_H , and (apart from the bottom curve) subsequently aged for 10 min at 350°C (Eckerlebe et al. 1986).

kinetics. This effect may be minimized if the alloy is first solution-treated at high T_H and subsequently equilibrated at a homogenization temperature slightly above the solvus temperature prior to quenching.

The inconsistency in the exact mode and kinetics of decomposition in Al–22 at.% Zn, investigated by different authors (Rundman and Hilliard, 1967; Gerold and Merz, 1967), has been explained by the presence of different quenching rates which unavoidably lead to different states of solute clustering in the as-quenched specimens (Agarwal and Herman, 1973; Bartel and Rundman, 1975).

The problems stated above make experiments devised for examination of the various spinodal theories particularly difficult.

5.3.2.2 Distinction of the Mode of Decomposition

The criterion that must be satisfied in order to distinguish spinodal decomposition (s.d.) from a nucleation and growth (n.g.) reaction is to prove by any microanalytical technique that the amplitude of the composition modulations of an alloy deeply quenched into the miscibility gap increases with time during the initial stages of phase separation (see Sec. 5.2.2 and Fig. 5-6). Even apart from the problem outlined in the preceding section, this is a rather difficult task, since the cluster diameters or the modulation wavelengths in most of the more concentrated alloys investigated so far have been found to range below the resolution limit of composition analysis, e.g. ≈ 2 nm for AFIM. Figure 5-15 reveals that the compositions of the solute clusters in Ni–36 at.% Cu–9 at.% Al (Liu and Wagner, 1984) and in a hard-magnetic Fe–29 at.% Cr–24 at.% Co (Zhu et al., 1986) alloy have reached their equilibrium values and, hence, remain constant once

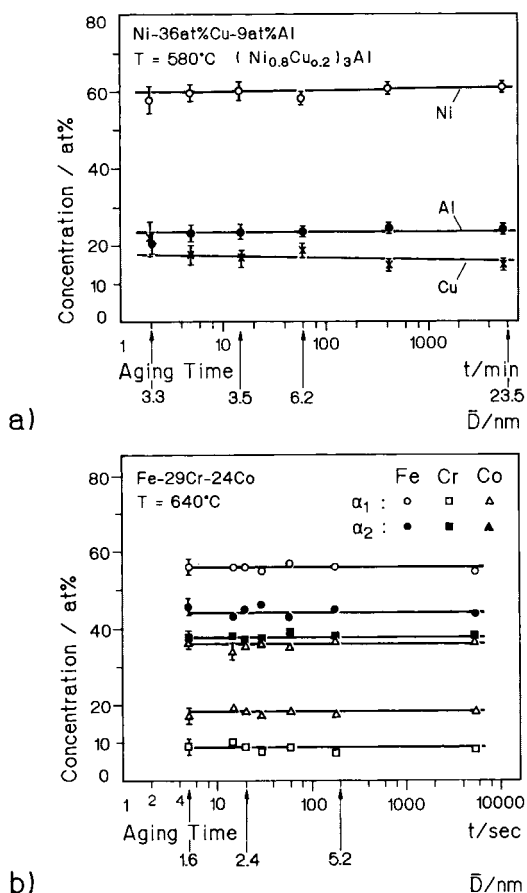


Figure 5-15. a) Composition and diameter \bar{D} , of γ' -precipitates in Ni–36 at.% Cu–9 at.% Al as a function of aging time at 580°C . The corresponding precipitate microstructure is shown in Fig. 5-2a–c (Liu and Wagner, 1984). b) Composition and diameter \bar{D} of the α_1 (matrix) and α_2 (precipitate) phases in Fe–29 at.% Cr–24 at.% Co as a function of aging time at 640°C (Zhu et al., 1986).

the clusters have attained sizes that are accessible to chemical analysis by AFIM (3 nm and 1.8 nm, respectively). (In fact both ternary alloys may be regarded as pseudobinary. Thus the thermodynamic considerations of Sec. 5.2.2 still apply.) The observed features suggest the reaction in both alloys to be of the n.g. type. However, it cannot be ruled out that these clus-

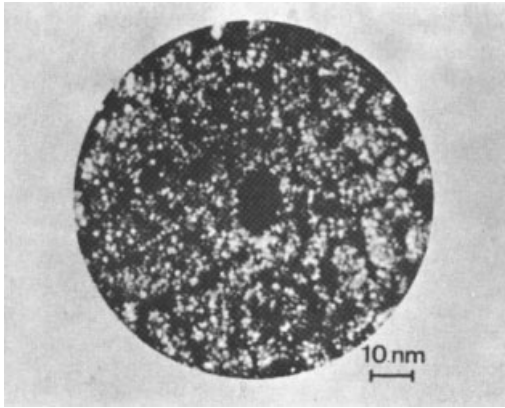


Figure 5-16. Field ion image of Fe-29 Cr-14 Co-2 Al-0.15 Zr (at.%) aged into its optimum magnetic state (Zhu et al., 1986).

ters result from a s.d. reaction which was terminated after even shorter aging times than could be covered in these studies.

Fig. 5-16 shows the interconnected precipitate microstructure of another hard-magnetic alloy, Fe-29 at.% Cr-14 at.% Co-21 at.% Al-0.15 at.% Zr, aged to yield its optimum magnetic properties. In order to characterize the decomposition process with respect to the distribution of Cr between the two phases, atom probe microanalysis was performed.

The measured Cr concentration of the darkly imaging precipitating α_2 -phase as a function of aging time at $T = 525^\circ\text{C}$ and $T = 600^\circ\text{C}$ is shown in Fig. 5-17a. During aging at 600°C for less than 5 min it increases continuously before it attains its constant equilibrium value. This behavior indicates unequivocally a spinodal decomposition mechanism. At the lower aging temperature of $T_A = 525^\circ\text{C}$, the Cr amplitude grows more slowly deeper within the miscibility gap due to the slower diffusion, but ultimately reaches higher equilibrium concentrations in the α_2 -precipitates, thus showing the spinodal behavior even more clearly. The observed increase in Cr con-

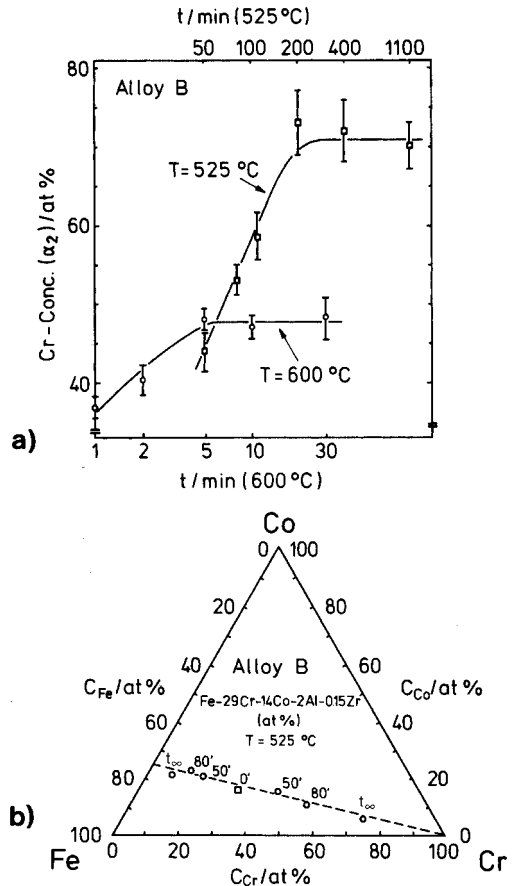


Figure 5-17. a) Evolution of the Cr concentration at 525°C and 600°C in the Cr-rich α_2 -phase as a function of aging time. b) Composition of the Fe-rich (α_1) and Cr-rich (α_2) phase after aging at 525°C for the given times (in minutes). The dashed line corresponds to the tie-line with a Fe/Co ratio of 3/1 (Zhu et al., 1986).

centration in the α_2 -phase with decreasing aging temperature is due to the widening of the miscibility gap. As the Cr concentration in the α_2 -phase increases, the proportions of Co and Fe are reduced in this phase and are correspondingly increased in the α_1 -phase. Atom probe analysis yields a Fe/Co ratio of 3:1 for both the α_1 - and α_2 -phases. This ratio corresponds to the tie-line in the ternary system along which

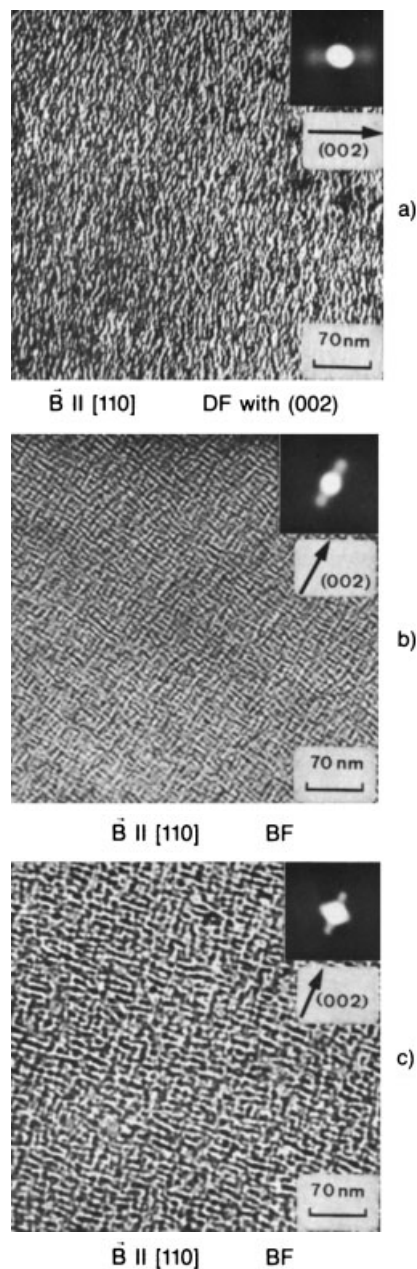


Figure 5-18. TEM micrographs of Cu-48 at.% Ni-8 at.% Fe aged for a) 8 h, b) 23 h, and c) 65 h at 500 °C. Each insert shows two satellites around the bright (002) matrix reflections. The distance between the satellites and the fundamental reflection is inversely proportional to the wavelength of composition modulations or to the precipitate spacing in modulated structures (reproduced by courtesy of R. P. Wahi (Wahi and Stajer, 1984)).

spinodal decomposition proceeds. Fig. 5-17b shows the compositions of the iron-rich and chromium-rich phases for various aging times at 525 °C and the tie-line corresponding to an Fe/Co ratio of 3 : 1.

This study is one of the very rare ones on metallic alloys to have identified a decomposition reaction unequivocally to be of the spinodal type.

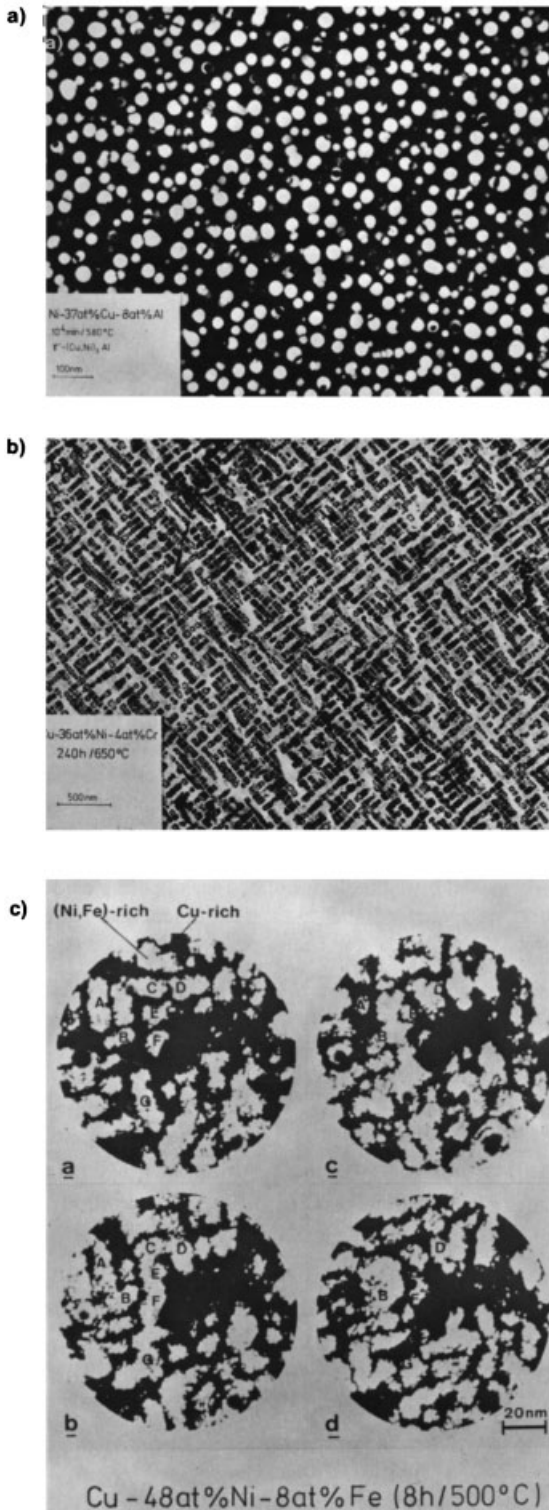
Frequently, the occurrence of either quasi-periodically aligned precipitates which give rise to side-bands in X-ray or TEM diffraction patterns (Fig. 5-18) or of a precipitated phase with a high degree of interconnectivity (e.g., Fig. 5-16) has been employed as a unique criterion by which to define an alloy as spinodal. However, as will be pointed out in Secs. 5.4.1 and 5.5.5, morphology alone cannot be used to unambiguously distinguish spinodal decomposition from a nucleation and growth reaction (Cahn and Charles, 1965).

5.4 Precipitate Morphologies

5.4.1 Experimental Results

There is a wide variety of different shapes in individual precipitates and of morphologies in precipitate microstructures. This is illustrated in Fig. 5-19 for three different Cu-Ni-based alloys with ternary additions of Al, Cr or Fe, the precipitated volume fraction (f_p) of which is rather large, e.g., f_p (CuNiAl) \approx 0.20, f_p (CuNiCr) \approx 0.19, and f_p (CuNiFe) \approx 0.37.

Aging of Ni-37 at.% Cu-8 at.% Al for 167 h at 580 °C yields randomly distributed spherical particles with $\bar{R} \approx 11$ nm and a number density of $\approx 3.6 \times 10^{22} \text{ m}^{-3}$ (Fig. 5-19a). In contrast, TEM of Cu-36 at.% Ni-4 at.% Cr aged for 240 h at 650 °C reveals a modulated precipitate structure with cuboidal particles aligned along the



three $\langle 100 \rangle$ directions (Fig. 5-19 b). Replacing Al or Cr by Fe leads to a mottled ('sponge-like') precipitate microstructure in Cu-48 at.% Ni-8 at.% Fe aged for 8 h at 500 °C. The three-dimensional interconnectivity of the mottled structure becomes discernible by a reconstruction of a sequence of FIM images which were taken at various distances underneath the original surface of the FIM specimen (Fig. 5-19 c).

Modulated structures have been predicted (Cahn, 1965; Hilliard, 1970) to evolve from spinodal decomposition in elastically anisotropic cubic matrices, owing to the tendency to minimize the coherency strain energy (see Sec. 5.2.4, Eq. (5-12)). Furthermore, in material which is either isotropic or for which the elastic energy (see Eq. (5-12)) is negligibly small, spinodal decomposition is predicted to generate an interconnected mottled precipitate morphology. Computer simulations of the latter case, which were based on a superposition of randomly oriented sinusoidal composition fluctuations of fixed wavelength, random phase shifts and a Gaussian distribution of amplitudes,

Figure 5-19. a) TEM dark field image of γ' -precipitates in Ni-37 at.% Cu-8 at.% Al aged for 167 h at 580 °C (Wagner et al. 1988). b) TEM bright field image of Cu-36 at.% Ni-4 at.% Cr aged for 240 h at 650 °C displaying particle alignment along the $\langle 100 \rangle$ matrix directions (Wagner et al., 1988). c) FIM micrographs of Cu-48 at.% Ni-8 at.% Fe aged for 8 h at 500 °C. Between each FIM micrograph 2 nm of the specimen surface were removed ('field evaporated' (Wagner, 1982)) in order to reveal the three-dimensional arrangement of the brightly imaged (Ni, Fe)-rich precipitated phase. In **a** the precipitates C, D, E, F, G are apparently isolated; after having removed 2 nm, they have merged into one large extended particle (**b**). At still greater depth (**d**; 6 nm) 'particle' C appears again to be isolated from the others by the darkly imaged matrix (reproduced by courtesy of W. Wagner (Piller et al., 1984)).

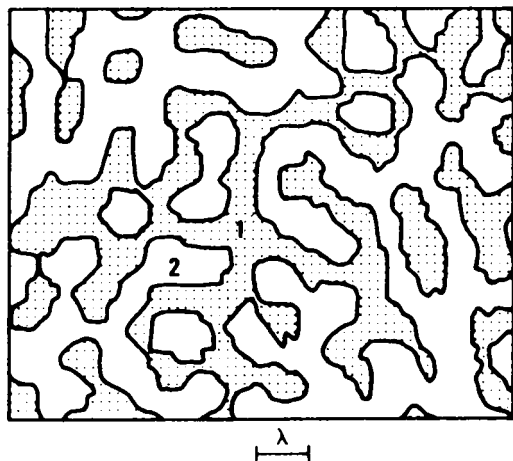


Figure 5-20. Computer-simulated cross-section of a spinodal structure in an isotropic solid displaying the interconnectivity of the two incipient phases 1 and 2 with equal volume fraction. (After Cahn, 1965).

yielded an interconnectivity of the two conjugate phases for volume fractions ranging from ≈ 0.15 to ≈ 0.85 (Cahn, 1965). The simulated morphological pattern (Fig. 5-20) resembles the FIM images shown in Figs. 5-16 and 5-19c remarkably well.

This has made it quite tempting to define these alloys and, more generally, all alloys displaying interconnected or quasi-periodical morphologies, as spinodal alloys. In general, however, in more concentrated alloys where the number density of clusters of the new phase is large and, hence, the intercluster spacing small, interconnectivity and quasi-periodicity in the late-stage microstructure may result from other mechanisms. Examples of such mechanisms are coalescence of neighboring particles (e.g., in the BaO–SiO₂ system) or selective coarsening of elastically favorably oriented particles (e.g., in Ni–Al (Ardell and Nicholson, 1966; Doi et al., 1988)). Hence, in essence, the distinction between a spinodal reaction and nucleation and growth *cannot* be based solely on any specific morphological features but requires a

complete study of the evolution of the new phase with aging time (see Sec. 5.5.5).

5.4.2 Factors Controlling the Shapes and Morphologies of Precipitates

In the case of homogeneous nucleation, the precipitating particles are commonly coherent with the matrix. Their shape is controlled by the rather complex interplay of various factors, such as the magnitude and anisotropy of the interfacial energy, the difference in the elastic constants between matrix and precipitate, and the crystal structure of the latter (Khachaturyan, 1983).

The complexity of the situation is illustrated in Fig. 5-21a (Lee et al., 1977). There the anisotropic elastic strain energy $\Delta F_{el}/\delta^2$ of an ellipsoidal Ag-rich particle with different orientational relationships with respect to a Cu or Al matrix is plotted as a function of the aspect ratio $K \equiv T/R$, where T and R denote the two axes of an ellipsoid of revolution.

Assuming the interfacial energy to be isotropic, Fig. 5-21a reveals that the minimum strain energy is obtained for platelet-shaped particles ($K \ll 1$), the cubic directions of which lie parallel to those of the Al or Cu matrices.

More generally, theory predicts (Lee et al., 1977) platelets to have the minimum and spheres to have the maximum strain energy if the precipitated phase is elastically softer than the matrix, regardless of the orientation relationship and elastic anisotropy. For the reverse situation of a hard particle embedded in a softer matrix, the sphere represents the minimum strain energy shape.

However, the elastic constants of the precipitating phase are often not available, rendering the computation of the shape with minimum strain energy difficult. In

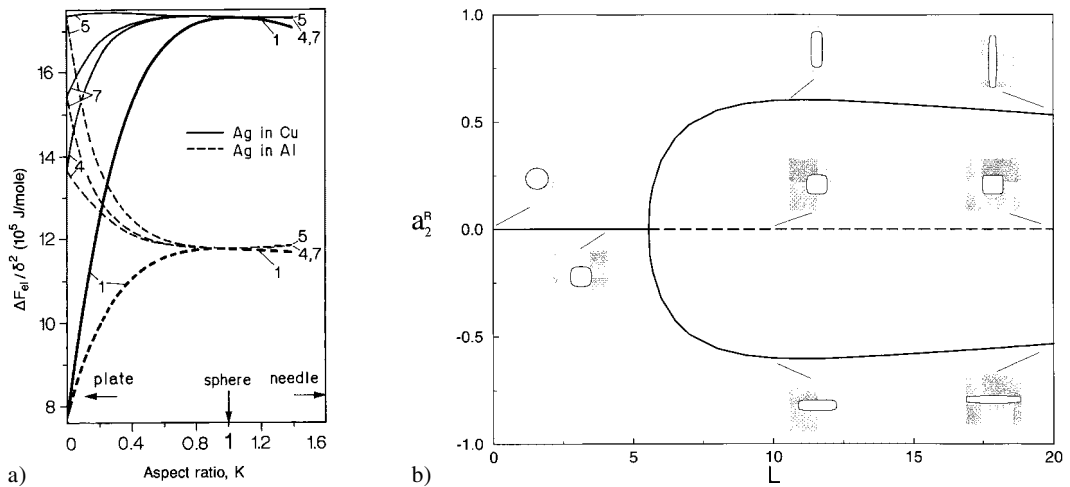


Figure 5-21. a) Strain energy vs. aspect ratio of an Ag precipitate in Cu and Al matrices. The numbers 1, 4, 5 and 7 designate different orientation relationships between matrix and precipitate. The lowest strain energy is obtained if the cubic directions of both particle and matrix are parallel to each other (curves 1), δ is the linear misfit. After Lee et al. (1977). b) The variation in a parameter, a_2^R , as a function of L . a_2^R is used to characterize the symmetry of a given family of equilibrium shapes: it is zero if the shape is four-fold symmetric and non-zero if it is two-fold symmetric (Thompson et al., 1994).

particular, this holds true if the nucleating phase is a metastable transition phase.

In essence, however, the adopted shape is determined by the balance between the interfacial Helmholtz energy $\Delta F_{\alpha\beta}$ and the elastic Helmholtz energy ΔF_{el} . $\Delta F_{\alpha\beta}$ is minimized for particles with spherical or faceted shape (e.g., Figs. 5-9 and 5-19) whereas ΔF_{el} , which is related to the particle volume, commonly prefers a platelet-like morphology (e.g., Fig. 5-21 a). Thus, during the early stages of precipitation, $\Delta F_{\alpha\beta}$ is the dominating term, whereas ΔF_{el} prevails in the limit of large particles.

The nature of this elastic stress-induced precipitate–shape transition has been investigated by Johnson and Cahn (1984) using bifurcation theory. Assuming an elastically isotropic inhomogeneous system and by restraining the morphology of the particle to be ellipsoidal it was possible to address analytically the structure of the shape bifurcation. For example, in two dimen-

sions they found that at a critical size the shape of a circular precipitate will change to an ellipse in a smooth manner as the size of the precipitate is increased; the shape bifurcation is supercritical. A supercritical bifurcation is analogous to the change in the order parameter on passing through a second-order phase transition. In contrast, in three dimensions, transcritical bifurcations (first-order transitions) are possible. Such a bifurcation implies that discontinuous changes in particle shape will occur as the particle increases its size.

The work of Johnson and Cahn clearly showed the importance of particle shape bifurcations in understanding microstructural evolution in systems with misfitting particles. Their study, however, was restricted to ellipsoidal particle shapes. This was remedied in the work of Thompson and Voorhees (1999) where the equilibrium shape of a particle in an elastically anisotropic homogeneous system with isotropic

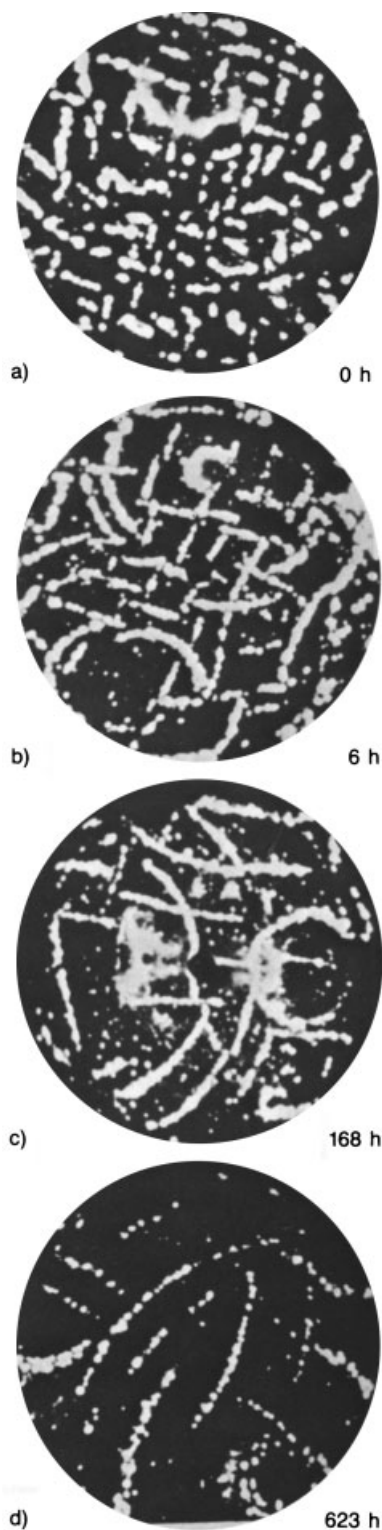
interfacial energy was determined numerically, see Fig. 5-21 b. Here the equilibrium shapes were found as a function of the dimensionless parameter $L = \delta^2 C_{44} l / \sigma_{\alpha\beta}$ where C_{44} is an elastic constant in a system with cubic elastic anisotropy, and l is the size of a particle, e.g., $l = 3V^{1/3}/4\pi$ where V is the volume of a precipitate, L is the ratio of the characteristic elastic to interfacial energy. When the particle is small, interfacial energy is the dominant factor in setting the particle shape and as L increases, the effects of elastic stress become important. When L is small and the equilibrium shape has a fourfold symmetry, a cube-like morphology with rounded corners and rounded sides will result. As L increases, at a critical size there is a supercritical bifurcation to one of two plate-like shapes oriented along the elastically soft directions. However, due to the presence of interfacial energy, the equilibrium shapes above the bifurcation point are not plates for any finite L . In the limit of infinite L the equilibrium shape is an infinitely long plate of zero thickness (Khachaturyan, 1983). The location of the bifurcation point is a function of both the elastic anisotropy and the difference in elastic constants between the phases (Schmidt and Gross, 1997). Three-dimensional calculations have also been performed where the particles are not constrained to be of a simple geometric shape (Mueller and Gross, 1998, Lee, 1997; Thompson and Voorhees, 1999).

Another qualitative difference between the possible equilibrium shapes of a particle in the presence of stress and that in the absence of stress is that the morphology of misfitting particles can be non-convex. In the absence of stress, regardless of the type of interfacial energy anisotropy, the equilibrium shape must be convex. In contrast, Thompson and Voorhees (1999) found metastable non-convex shapes in an elasti-

cally anisotropic system with a tetragonal misfit, and Schmidt and Gross (1997) found strongly non-convex global energy minimizing, pincushion-like shapes when the particle is sufficiently soft in an elastically anisotropic system. Similar pincushion-like precipitates have been observed experimentally, but in a system with a much smaller difference in elastic constants (Maheshwari and Ardell, 1992). Emphasizing the difficulty in obtaining true equilibrium shapes experimentally, Wang and Khachaturyan (1995) have suggested, however, that the shapes observed by Maheshwari and Ardell are kinetic in origin.

In an internally nitrided Fe 3 at. % Mo alloy, $(\text{Fe, Mo})_{16}\text{N}_2$ -type precipitates were found to nucleate as thin platelets with $K \approx 0.1$ and with an undistorted $\{100\}_{\alpha\text{-Fe}}$ plane common to both the α -matrix and the nitrides. The observed morphology, as well as the $\{100\}_{\alpha\text{-Fe}}$ habit planes, have been accurately predicted by applying macroscopic linear elastic theory to tetragonal Fe_{16}N_2 precipitates in ferritic iron, and assuming the interfacial energy to be isotropic (Khachaturyan, 1983). The latter assumption, however, is debatable, since during aging at 600°C $(\text{Fe, Mo})_{16}\text{N}_2$ platelets only grow markedly in diameter; their thickness remains almost constant (Fig. 5-22). This has been interpreted in terms of the large difference between the interfacial energy of the habit plane ($\approx 0.05 \text{ J/m}^2$) and that of the peripheral plane ($\approx 0.3 \text{ J/m}^2$) (Wagner and Brenner, 1978).

Under certain conditions, the elastic or magnetic interaction of precipitates with external stress fields or magnetic fields allows for the generation of anisotropic, highly oriented precipitate microstructures which are sometimes of technological importance. If the transformation strain is non-spherical, such as for Fe_{16}N_2 in ferritic Fe-N, the particles may interact with an



externally applied stress field. The resulting elastic interaction energy depends on the particular orientation of the particle with respect to this field. During aging, this causes a selective coarsening of favorably oriented particles at the expense of the energetically less favorably oriented ones. For instance, if the originally isotropically distributed Fe_{16}N_2 platelets undergo coarsening in the presence of an external tensile stress applied along [001], a highly oriented (anisotropic) precipitate structure will result (Ferguson and Jack, 1984, 1985), with the habit planes of all particles being parallel to each other and perpendicular to [001]. In addition, these platelets show a strong uniaxial magnetic anisotropy with the direction of easy magnetization parallel to the plate normal. This magnetic property can also be used for completely orienting the platelets during aging in an external magnetic field (Sauthoff and Pitsch, 1987).

5.5 Early Stage Decomposition Kinetics

As outlined in Sec. 5.2.3, the early stages of unmixing of a solid solution quenched into the miscibility gap are triggered by the growth and the decay of concentration fluctuations. Basically, the objective of any theory dealing with the kinetics of early stage decomposition is the prediction of the particular shape, ampli-

Figure 5-22. FIM micrographs of $(\text{Fe}, \text{Mo})_{16}\text{N}_2$ platelets (bright) in an α -iron matrix (dark). During coarsening at 600°C for the given times, the aspect ratio decreases from ~ 0.1 ($t = 0$) to ~ 0.04 (623 h), whereas the platelet thickness increases only from ~ 0.7 nm to ~ 1.0 nm. The platelets intersect the surface of the semi-spherical field ion tip and thus appear to be curved (Wagner and Brenner, 1978).

tude and spatial extension (or number of atoms) of a solute fluctuation which becomes critical and, hence, stable against decay. Once formed, the critical fluctuations render the supersaturated alloy unstable with respect to further unmixing.

According to Sec. 5.2.4 and referring to Fig. 5-6a, *nucleation theories* consider the formation rate of stable nuclei, the latter representing spatially localized solute-rich clusters ('particles' or 'droplets') with large concentration amplitudes. In this context, a distinction is made between *classical* (Sec. 5.5.1.1) and *non-classical* nucleation theory (Sec. 5.5.1.4) depending on how the Helmholtz energy of the non-uniform solid solution containing the cluster distribution is evaluated. Once the Helmholtz energy has been specified, the equilibrium distribution of heterophase fluctuations and the nucleation barrier (Sec. 5.2.3) can be calculated. The nucleation rate is then obtained as the transfer rate at which smaller clusters attain the critical size.

A 'composition wave' picture rather than a 'discrete droplet' formalism is employed in the spinodal theories (Sec. 5.5.4) which, as another approach, describe the early-stage decomposition kinetics in terms of the time evolution of the amplitude and the wavelength of certain stable 'homophase' fluctuations (Fig. 5-6b).

There are several papers dealing with the early-stage unmixing kinetics. Russel (1980) and Aaronson and Russel (1982) consider both classical and non-classical nucleation phenomena from a more metallurgical point of view; the formulation of a microscopic cluster theory of nucleation can be found in the article by Binder and Stauffer (1976). The comprehensive articles by Martin (1978) and by Gunton and Droz (1984) disclose developments of both nucleation and spinodal concepts not only to the theoretician but also to the materials

scientist. For more recent developments, see the chapter by Binder and Fratzl (2001).

5.5.1 Cluster-Kinetics Approach

5.5.1.1 Classical Nucleation – Sharp Interface Model

Suppose the homogenized solid solution is quenched not too deeply into the metastable regime of the miscibility gap (e.g., to point 1 in Fig. 5-5a). There it is isothermally aged at a temperature sufficiently high for solute diffusion. After a certain time, a distribution of *microclusters* containing i atoms (i -mers) will form in the matrix.

Generally, classical nucleation is now based on both a *static* and a *dynamic* part. In the static part the changes of Helmholtz energy associated with the formation of an i -mer and the cluster distribution $f(i)$ must be evaluated. In the dynamic part the kinetics of the decay of the solid solution which now is described by the given distribution of non-interacting microclusters, are calculated in terms of the time evolution of $f(i)$; ultimately this will furnish the formation rate of stable clusters, i.e. the nucleation rate.

Classical nucleation theory treats the solute fluctuations as droplets which were cut from the equilibrium precipitate phase β and embedded into the α matrix; in this *capillarity* or *droplet model* the interface between α and β is assumed to be sharp, e.g., Fig. 5-6a. In essence, the approximation reduces the number of independent variables which characterize a cluster, and which may vary during the nucleation process (e.g., the solute concentration, the atomic distribution within the cluster, its shape, the composition profile across the interface, etc.) and, hence, determine the Helmholtz energy of the system, to virtually a single one. That is the number i of

atoms contained in the cluster or, in terms of a more macroscopic picture, the radius R of the droplet; $(4\pi/3)R^3 = i\Omega_\beta$ if Ω_β denotes the atomic volume in the droplet.

Once the small nucleus containing only a few atoms is treated as a droplet of the new phase β having bulk properties (which, in fact, is a rather debatable approximation), the interfacial Helmholtz energy and the Helmholtz energy are also considered to be entirely macroscopic in nature.

The formation of a coherent droplet with radius R which gives rise to some elastic coherency strains, leads to a change of Helmholtz energy,

$$\Delta F(R) = (\Delta f_{ch} + \Delta f_{el}) \frac{4\pi}{3} R^3 + 4\pi R^2 \sigma_{\alpha\beta} \quad (5-18)$$

where, according to Sec. 5.2.4, $(\Delta f_{ch} + \Delta f_{el})$ is the driving force per unit volume and $\sigma_{\alpha\beta}$ the specific interfacial energy.

The first term in Eq. (5-18) which scales with R^3 accounts for the gain of Helmholtz energy on forming the droplet (i.e., it is negative). The second term which scales with R^2 has to be expanded on forming the interphase boundary and hence is a positive contribution to $\Delta F(R)$.

Fig. 5-23 shows the dependence of the two contributions in Eq. (5-18) on the droplet radius. The resulting droplet formation energy $\Delta F(R)$ passes through a maximum at $R \equiv R^*$ or $i \equiv i^*$ with

$$R^* = \frac{2\sigma_{\alpha\beta}}{-(\Delta f_{chem} + \Delta f_{el})} \quad \text{or} \quad i^* = \frac{4\pi}{3\Omega_\beta} \left[\frac{2\sigma_{\alpha\beta}}{-(\Delta f_{chem} + \Delta f_{el})} \right]^3 \quad (5-19)$$

Accordingly, clusters with $R = R^*$ are in unstable equilibrium with the solid solution, i.e., the Helmholtz energy of the system is lower if it contains clusters with sizes below or beyond R^* or i^* . Therefore, only clusters with radii that exceed the ra-

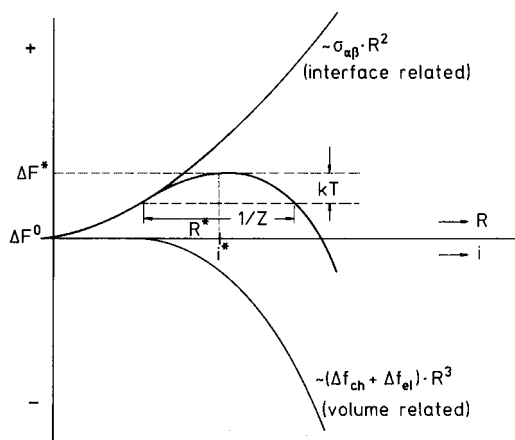


Figure 5-23. Schematic representation of Helmholtz energy changes associated with cluster formation as a function of cluster radius (R) or number i of atoms in the cluster. ΔF^0 is the Helmholtz energy of the homogeneous solid solution, Z the Zeldovich factor.

dius R^* of the *critical nucleus* are predicted to grow continuously. This requires a fluctuation to become a critical nucleus, first to overcome the activation barrier for nucleation, or the nucleation energy,

$$\Delta F(R^*) \equiv \Delta F^* = \frac{16\pi}{3} \frac{\sigma_{\alpha\beta}^3}{(\Delta f_{chem} + \Delta f_{el})^2} \quad (5-20)$$

As outlined in Sec. 5.2.4, Δf_{chem} decreases strongly with decreasing supersaturation, or, for a given concentration, with increasing aging temperature (Fig. 5-1). Correspondingly, since $\sigma_{\alpha\beta}$ and Δf_{el} are only weakly dependent on temperature, both R^* and ΔF^* increase strongly with decreasing supersaturation. Hence, the droplet model ought to approximate the energetics of an unmixing alloy better the smaller the supersaturation.

Once we have specified the free energy of formation of a droplet in terms of its size R or i (Eq. 5-18), the Helmholtz energy of the system containing a number of $f(i, t)$ of non-interacting clusters of size i per unit volume at time t is given as (Frenkel, 1939;

Russell, 1980):

$$F = \sum_1^n \Delta F(i) f(i, t) - T S_{\text{mix}} \quad (5-21)$$

The entropy of mixing S_{mix} arises from distributing the clusters on the available N_0 lattice sites per unit volume of the crystal.

The kinetics of early-stage unmixing are governed by the change in the cluster size distribution function $f(i, t)$ with aging time. Microscopically, this may occur via different processes.

Volmer and Weber (1926), Becker and Döring (1935) and Zeldovich (1943), the works which most nucleation theories are based on, assume the transitions between size classes in an assembly of non-interacting droplets to occur via the condensation or evaporation of *single* solute atoms. Hence, since only a transition between size classes i and $i + 1$ is allowed, its flux, J_i is given as (Russell, 1980):

$$J_i = \beta(i) f(i, t) - \alpha(i+1) f(i+1, t) \quad (5-22)$$

where $\beta(i)$ is the condensation rate and $\alpha(i+1)$ the evaporation rate of a single atom to a cluster of size i or from a cluster of size $(i + 1)$, respectively.

In equilibrium, the fluxes J_i must vanish and $f(i, t)$ becomes identical with the equilibrium cluster size distribution $C(i)$ for which F in Eq. (5-21) attains a minimum:

$$C(i) = N_0 \exp [-\Delta F(i)/kT] \quad (5-23)$$

It is worth noting that in this case the number of critical nuclei $C^* \equiv C(i \equiv i^*)$ is proportional to $\exp (-\Delta F^*/kT)$. Then, according to Eq. (5-22), the condensation rate and evaporation rate are related to each other via

$$\alpha(i+1) = \beta(i) \frac{C(i)}{C(i+1)} \quad (5-24)$$

In the conventional nucleation theory it is now assumed that the evaporation rate

$\alpha(i + 1)$ derived for the equilibrium situation ('principle of detailed balance') is still valid for the non-equilibrated system where $f(i, t) \neq C(i)$ and $J_i \neq 0$. Under such an assumption, which becomes reasonable when i -mers are able to relax internally between atomic condensation or evaporation, the flux of clusters between size classes i and $i + 1$ is obtained from Eqs. (5-22) and (5-23) (Russell, 1980):

$$J_i = \beta(i) C(i) \left[\frac{f(i+1, t)}{C(i+1)} - \frac{f(i, t)}{C(i)} \right] \\ \approx -\beta(i) C(i) \left[\frac{\partial f(i, t)/C(i)}{\partial i} \right] \quad (5-25)$$

In the earliest theory on nucleation (Volmer and Weber; VW, 1926) it is assumed that $f(i, t) \equiv 0$ for clusters with $i > i^*$ (or $R > R^*$), and that clusters with $R > R^*$ decay artificially into monomers, thus keeping the matrix supersaturation about constant. The resulting quasi-steady-state distribution of cluster sizes is obtained from Eq. (5-23) and shown in Fig. 5-24). In this theory the *steady-state nucleation* rate J_{VW}^s is obtained as the product of the number C^* of critical nuclei and the rate β at which a single solute atom impinges on the critical nucleus rendering it supercritical, i.e.:

$$J_{\text{VW}}^s = \beta C^* = \beta N_0 \exp (-\Delta F^*/kT) \quad (5-26)$$

One of the shortcomings of the VW theory is that supercritical droplets with $i > i^*$ are assumed *not* to belong to the cluster size distribution. This was cleared up by the theory of Becker and Döring (1935). In their theory (BD) the non-equilibrium *steady-state* distribution of small clusters with $i \ll i^*$ is identical with that of VW but unlike in the latter theory, clusters with $i^* \leq i \leq i_c$ (i_c is a somewhat arbitrarily chosen cut-off size) are considered to belong to the size distribution (Fig. 5-24).

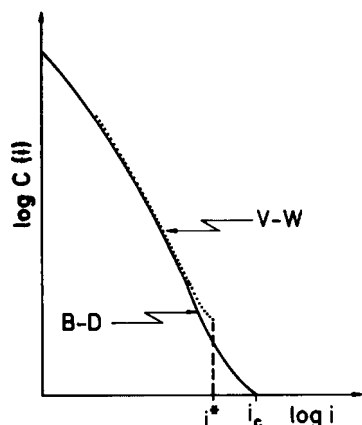


Figure 5-24. Quasi-stationary cluster size distributions of the Volmer-Weber (V-W) and Becker-Döring (B-D) theory.

Hence, according to Eq. (5-22) a decay or dissolution of supercritical droplets with $i > i^*$ becomes a likely process in the BD theory and is accounted for by the *Zeldovich factor* Z . With the assumption that the rate $\beta \equiv \beta^*$ at which a solute atom impinges on a *critical* droplet is proportional to its surface area, integration of the cluster flux equation (Eq. (5-25)) yields the *steady-state nucleation rate* J_{BD}^S of the BD theory as (Russell, 1980):

$$J_{BD}^S = Z \beta^* N_0 \exp(-\Delta F^*/kT) \quad (5-27)$$

with

$$Z = \left[\frac{-1}{2\pi kT} \frac{\partial^2 \Delta F}{\partial i^2} \bigg|_{i=i^*} \right]^{1/2} \quad (5-28)$$

According to Eq. (5-27), nucleation is a thermally activated process with an activation energy identical to that (ΔF^*) of forming a critical nucleus of size i^* or R^* . Furthermore, like the thermodynamic model that yields the number of critical nuclei proportional to $\exp(-\Delta F^*/kT)$ (Eq. (5-23)), the kinetic treatment predicts the steady-state nucleation rate also to be proportional to the same exponential factor.

The Zeldovich factor Z is of the order of $1/20$ to $1/40$; graphically, its reciprocal value corresponds approximately to the width of the potential barrier, $\Delta F(R)$ or $\Delta F(i)$, at a distance kT below the maximum (Fig. 5-23).

5.5.1.2 Time-Dependent Nucleation Rate

It must be pointed out that the above given steady-state nucleation theories do not provide any information on the momentary cluster size distribution or on the nucleation rate prior to reaching steady-state conditions, i.e., the time-dependent nucleation rate $J^*(t)$. Commonly the latter is considered in terms of the steady-state nucleation rate J^S and an *incubation period* τ via:

$$J^*(t) = J^S \exp(-\tau/t) \quad (5-29)$$

Steady-state will be achieved once the clusters have attained sizes for which the probability of redissolution is negligibly small. Referring to Fig. 5-23 and recalling the physical meaning of the Zeldovich factor Z , this will be the case for clusters with $i > i^* + 1/2 Z$ (Feder et al., 1966). As the gradient of $\Delta F(i)$ within the region $1/Z$ is rather small, the clusters will move across this region predominantly by random walk with the jump frequency β^* . The time

$$\tau = \frac{1}{2\beta^* Z} \quad (5-30)$$

to cover the distance $1/Z$ by random walk is identified with the incubation period.

So far it has been assumed that during nucleation the supersaturation and, hence, the driving force remains unchanged. At its best this may be valid for extremely low nucleation rates: in this case ΔF^* , Z and τ may be considered time-independent quantities. Russell (1980) proposed the nuclea-

tion process to terminate itself under steady-state conditions if the incubation time τ is shorter than some critical time t_c . If, however, $\tau > t_c$, phase separation will be completed without steady-state ever having been achieved. This situation, which in fact is met in most decomposing alloys studied up to now (see Sec. 5.7.4.1), is referred to as *catastrophic nucleation*; under such conditions ΔF^* , Z and τ become time dependent. Assuming that nucleation ceases once the diffusion fields and around precipitates with radius R and composition c_β^e embedded in a matrix with initial composition c_0 begin to overlap (Fig. 5-6 a), and furthermore that nucleation becomes unlikely within a region R/ε ($\varepsilon \approx 1/10$) around the particle where the solute content has decreased below $(1 - \varepsilon) c_0$, the critical time t_c is estimated to be:

$$t_c = \left[\varepsilon^6 \left(\frac{c_\beta^e}{c_0} \right)^3 \frac{1}{(2D)^3} \frac{1}{J s^2} \right]^{1/5} \quad (5-31)$$

where D is the solute diffusion coefficient.

For a quantitative assessment of classical nucleation theory, the atomic impingement rate β^* in Eq. (5-27) must be known. For spherical nuclei it was evaluated to be (Russell, 1970):

$$\beta^* = \frac{4\pi R^{*2} D c_0}{a^4} \quad (5-32)$$

where a is the lattice parameter. β^* is proportional to the nucleus surface, as was assumed in the original Becker–Döring theory.

According to Sec. 5.4.2 the nucleus shape with minimum energy may deviate from the spherical one due to different energies of the interfaces (some may be coherent, some semi- or incoherent, Sec. 5.2.1) bounding the nucleus in different crystallographic directions. It has been shown (Chan et al., 1978) that in this case

the expressions for ΔF^* , Z , β^* and τ given above for spherical clusters, have merely to be multiplied with numerical factors but otherwise remain unchanged. The magnitude of these numerical factors depends on the particular equilibrium shape of the nucleus. Ignoring volume strain energy, the equilibrium shape of the nucleus can be determined by means of the Wulff construction on a three-dimensional $\sigma_{\alpha\beta}$ -plot (Herring, 1953). The latter is obtained from a radial plot of different vectors in every direction e.g., v_1 , v_2 , v_3 in Fig. 5-25), the length of which is proportional to the energy of the interface perpendicular to the particular vector. The surface connecting the tips of all vectors represents the polar $\sigma_{\alpha\beta}$ -plot, wherein the cusps indicate interfaces with good atomic matching, i.e., low interfacial energies. Subsequently planes

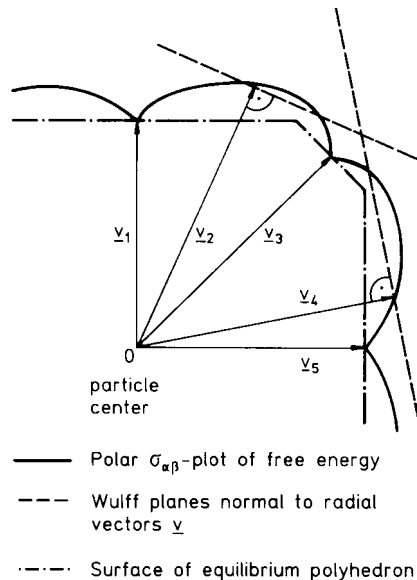


Figure 5-25. Polar $\sigma_{\alpha\beta}$ -plot for particles with anisotropic interfacial energies $\sigma_{\alpha\beta}$. The normals drawn at the tip of each vector v are the Wulff planes, the inner envelope of which gives the equilibrium shape of the precipitate. If the $\sigma_{\alpha\beta}$ -plot displays deep cusps (e.g., for v_1 , v_3 , and v_5) the Wulff construction yields a faceted polyhedron.

are drawn (the so-called *Wulff planes*) perpendicular to the vectors ν_1 , ν_2 , ν_3 , etc. which intersect the $\sigma_{\alpha\beta}$ -plot (Fig. 5-25). The inner envelope of the Wulff planes yields the equilibrium shape of the nucleus with facets at the cusps of the $\sigma_{\alpha\beta}$ -plot (Martin and Doherty, 1976).

LeGoues et al. (1982) employed a nearest-neighbor interaction, regular solution model for a computation of the $\sigma_{\alpha\beta}$ -plot as a function of T/T_c (T_c is the critical temperature) within the miscibility gap of an f.c.c. solid solution. At low temperatures they found the nucleus shape to be fully faceted by $\{100\}$ and $\{111\}$ planes whereas at $0.5 T_c$ and near-zero supersaturation, the nucleus shape can be rather well approximated by a sphere. They furthermore showed that beyond $T \approx 0.4 T_c$ the parameters ΔF^* , Z , τ , and β^* which enter the time-dependent (classical) nucleation rate (Eqs. (5-27) and (5-29)) need no longer be corrected for deviations from spherical shape.

Recently the question of to what extent the energy of the coherent interphase boundary depends on its crystallographic orientation and on temperature has been addressed by employing the cluster variation method (CVM) with effective cluster interaction parameters (Sluiter and Kawazoe, 1996; Asta, 1996). The latter are specific for the particular two-phase alloy system under consideration. They can be derived from the results of *ab initio* total energy calculations as was demonstrated by computing the thermodynamic properties of interphase boundaries between disordered f.c.c. matrices and ordered ($L1_2$ type) precipitates in Al–Li (Sluiter and Kawazoe, 1996) and Al–Sc (Asta et al., 1998) as well as disordered GP zones (cf. Fig. 5-13) in Al–Ag alloys (Asta and Hoyt, 1999). Between T_c and $T = 0.5 T_c$ the CVM-calculated energies for the cube $\{100\}$ and octahedral $\{111\}$ orientations of the flat inter-

face between Al-rich matrix and Ag-rich GP zones are found to be equal within 5%, and to increase from zero to about 30 mJ/m^2 if the temperature is lowered from T_c to $\sim 0.5 T_c$. This result is compatible with the spherical particle morphology resolved in the HREM micrographs (Figs. 5-9 and 5-13).

5.5.1.3 Experimental Assessment of Classical Nucleation Theory

A quantitative assessment of classical nucleation theory in solids is inherently difficult and thus has prompted only a few studies. First of all, the range of supercooling (or supersaturation) has to be chosen such that nucleation is homogeneous and the nucleation rates are neither unmeasurably slow nor beyond the limits of catastrophic nucleation. Secondly, the quenching rate must be sufficiently high in order to avoid phase separation during the quench but also sufficiently low in order to avoid excess vacancies to be quenched in.

Servi and Turnbull (1966) studied in a well-designed experiment homogeneous nucleation kinetics of coherent Co-rich precipitates in Cu–1 ... 2.7 wt.% Co alloys. By using electrical resistivity measurements, they could determine rather accurately the precipitated volume fraction. Assuming that the growth is diffusion-controlled (Sec. 5.5.2), from the latter the particle density at the end of the precipitation process could be derived as a function of aging temperature and composition. The thus indirectly obtained number density of Co-rich particles, which was later corroborated by CTM studies, agreed within one order of magnitude with the value predicted by classical nucleation theory if the interfacial energy was taken as $\approx 0.19 \text{ J/m}^2$; this value was derived from discrete lattice calculations (Shiflet et al., 1981).

The validity of classical nucleation theory, as proven by the Servi–Turnbull study on Cu–Co alloys, was later challenged by LeGoues and Aaronson (1984). They argued that the supersaturation employed in the Servi–Turnbull investigations was probably too high to avoid phase separation during quenching and also probably too high to avoid concomitant coarsening during the precipitation reaction. Employing a discrete lattice point model, which incorporates coherency strain energy, LeGoues and Aaronson first evaluated the ‘window’ of temperatures ($\Delta T \approx 50^\circ\text{C}$) and compositions (0.5 to 1.0 at.% Co) at which homogeneous nucleation kinetics would be neither too sluggish nor too fast, and at which no interference with coarsening would be expected. Prior to CTEM analyses, the isothermally nucleated particles had to be subjected to diffusion-controlled growth in order to increase their radius beyond a certain size ($R \approx 5$ nm) at which the Co-rich particles became easily discernible in the CTEM. The experimental results were interpreted in terms of classical nucleation theory (Eq. (5-29)). The agreement between the experimentally obtained nucleation rates and the theoretically predicted ones was again rather good, thus providing further support for the validity of classical nucleation theory. Furthermore, as is shown in Fig. 5-26, for smaller supersaturations the nucleation energies ΔF^* and the critical radii R^* as evaluated from classical nucleation theory are almost identical to the corresponding quantities calculated from either the non-classical nucleation theory (cf. Sec. 5.5.1.4, Eq. (5-37)) or a discrete lattice point theory. Hence, at least for smaller supersaturation, the classical theory predicts the nucleation rates about as well as the two more sophisticated theories.

In another attempt to assess classical nucleation theory, Kirkwood and coworkers

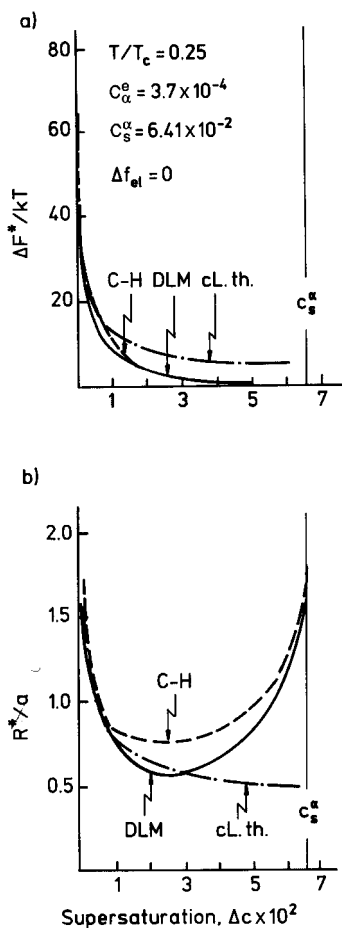


Figure 5-26. Nucleation barrier ΔF^* (a) and critical radius R^* (b) as a function of supersaturation at $T = 0.25 T_c$ according to classical theory (cl. th.), non-classical Cahn–Hilliard continuum model (C–H) and discrete lattice model (DLM). R^* is determined such that it corresponds to $(c_0 + c_c)/2$ where c_c is the composition of the nucleus at its center. (After Le Goues et al., 1984a).

(Kirkwood, 1970; West and Kirkwood, 1976; Hirata and Kirkwood, 1977) studied early-stage precipitation of γ' -Ni₃Al in Ni–Al alloys, also using CTEM. They found the γ' -Ni₃Al precipitate number density to decrease instantaneously upon aging, which is indicative of an extremely fast nucleation process and the observation

of a coarsening process rather than a nucleation event. By making certain assumptions they attempted to infer the steady-state nucleation rate from the particle density observed during coarsening. The observed lack of agreement between the experimentally derived nucleation rates and the theoretically predicted ones may be seen to result from these experimental difficulties.

5.5.1.4 Non-Classical Nucleation – Diffuse Interface Model

In the droplet model that classical nucleation is based on, it is assumed that the composition of the nucleus is more or less constant throughout its volume and that its interface is sharp. This made it possible to take the change of volume Helmholtz energy and the interfacial Helmholtz energy separately into account (Eq. (5-18)). In *non-classical nucleation theory*, developed by Cahn and Hilliard (1959a, b), the inhomogeneous solid solution in its metastable state is considered to contain homophase fluctuations with *diffuse interfaces* and a composition which varies with position throughout the cluster (Fig. 5-6b). Hence, unlike in the droplet model a critical fluctuation has now to be characterized by at least two parameters, its spatial extension or wavelength λ and its spatial composition variation. The necessary Helmholtz energy formalism, which no longer treats volume energy and surface energy separately, was elaborated by Cahn and Hilliard (1958). They wrote the Helmholtz energy change associated with the transfer from the homogeneous system with composition c_0 ,

$$F_0 = \int_V f(c_0) dV \quad (5-33a)$$

to that of the inhomogeneous system with

$$F = \int_V [f(c) + K^* (\nabla c)^2] dV \quad (5-33b)$$

as:

$$\Delta F = (F - F_0) \quad (5-33c)$$

$$= \int_V [f(c) - f(c_0) + K^* (\nabla c)^2] dV$$

The basic idea behind these expressions is to subdivide the solid with volume V into many small volume elements dV , a procedure which is often referred to as '*coarse graining*' (Langer, 1971). The free energy of each volume element is taken as $f(c) dV$, $f(c)$ is considered to be the Helmholtz energy per unit volume of the bulk material with composition c which is equal to the mean composition $c(\mathbf{r})$ within dV located at position \mathbf{r} . In essence, coarse graining requires the number of atoms within each volume element to be sufficiently large such that $c(\mathbf{r})$, as well as $f(c)$, can be specified as continuous functions. On the other hand, the number of atoms within dV must be small enough in order to avoid phase separation within the individual volume element. For the non-uniform system with composition fluctuations, Cahn and Hilliard (1958, 1959a, b) assumed that the local Helmholtz energy contains further terms depending on the composition gradient (∇c) . They finally showed that the non-uniform environment of atoms in a composition gradient may be accounted for by adding to the local Helmholtz energy a single *gradient energy* term which is proportional to $(\nabla c)^2$. Hence, the resulting Helmholtz energy of a volume element dV is expressed as $f(c) + K^* (\nabla c)^2$ where the constant K^* denotes the gradient energy coefficient. Summing up all contributions from the various volume elements yields Eq. (5-33c).

The continuum model is based on the assumption that the Helmholtz energy $f(c)$ varies smoothly with composition, i.e. the wavelength of the fluctuations must be large compared with the interatomic spac-

ing. Furthermore, for a continuum model its is required that the two evolving phases are fully coherent with each other and thus have the same crystal structure with similar lattice parameters. If the lattice parameter changes with composition, which is commonly the case in crystalline solids, the requirement for coherency leads to coherency strains which according to Eq. (5-12) are accounted for by an elastic energy term

$$f_{el}(c) = \eta^2 Y (c - c_0)^2 \quad (5-34)$$

Combining Eqs. (5-34) and (5-33c) yields

$$\Delta F = \int_V [f(c) - f(c_0) + K^* (\nabla c)^2 + \eta^2 Y (c - c_0)^2] dV \quad (5-35)$$

This expression may be interpreted in similar terms as for classical nucleation [Eq. (5-18)]: neglecting the elastic energy term, the positive contribution of the gradient energy as a barrier to nucleation acts like the surface Helmholtz energy in the droplet model and is finally overcome by the gain in chemical Helmholtz energy once the composition difference between the fluctuation and the homogeneous matrix has become sufficiently large.

Assuming isotropy, the composition profile $c(r)$ of a spherical fluctuation (r is the radial distance from the fluctuation center) is obtained from a numerical integration of (Cahn and Hilliard, 1959 a, b):

$$2K^* \frac{d^2 c}{dr^2} + 4 \frac{K^*}{r} \frac{dc}{dr} = \left. \frac{\partial f}{\partial c} \right|_c - \left. \frac{\partial f}{\partial c} \right|_{c_0} \quad (5-36)$$

with the boundary conditions $dc/dr = 0$ at the nucleus center ($r \approx 0$) and far away from it ($r \rightarrow \infty$) where $c \equiv c_0$. The critical nucleus is then determined as the fluctuation which, like a critical droplet, is in unstable equilibrium (Eq. (5-35)) with the matrix. Its composition is established such that the nucleation barrier (e.g., de Fontaine,

1982),

$$\Delta F [c^*(r)] \equiv \Delta F^* \quad (5-37)$$

$$= 4\pi \int_0^\infty \left[\Delta f(c^*) + K^* \left(\frac{dc}{dr} \right)^2 \right] r^2 dr$$

attains a minimum. Like in classical nucleation, Δf^* is the vertical distance from the tangent at c_0 to the Helmholtz energy curve at c^* (cf. Fig. 5-5b). Suppose ΔF^* is known; the nucleation rate is then obtained from Eq. (5-27) or (5-29). Provided the constraint free energy is known, the composition profile of a critical nucleus in a solid solution with composition c_0 and gradient energy coefficient K^* (K^* is of the order 10 to 100 J m⁻¹ (at. fract.)⁻²) can be obtained from integrating Eq. (5-36). Fig. 5-27 shows the composition profiles of nuclei in supersaturated solid solutions with different solute concentrations c_0 quenched to $T/T_c = 0.25$, where T_c is the critical temperature (LeGoues et al., 1984b); these calculations are based on the regular solution model for $f(c)$ (cf. Sec. 5.2.4). For *small supersaturation* ($c_0 = 2 \times 10^{-3}$) the composition within the nucleus is constant and corresponds to c_β^e of the equilibrium β -phase. The interface is almost sharp, similar to that assumed in the classical droplet model. Correspondingly, the free energy of formation of the nucleus (ΔF^*) and its size (R^*) as evaluated from either classical or non-classical theory are almost identical (Fig. 5-26) and tend to infinity as c_0 approaches c_α^e . With increasing supersaturation the composition profile becomes increasingly diffuse and the solute concentration at the nucleus center decreases (Fig. 5-27); this situation is no longer accounted for by the droplet model. Furthermore, as the initial composition (c_0) approaches the spinodal one (c_s^α), unlike the droplet model, non-classical theory predicts ΔF^* to go to zero (Fig. 5-26a), and the spatial

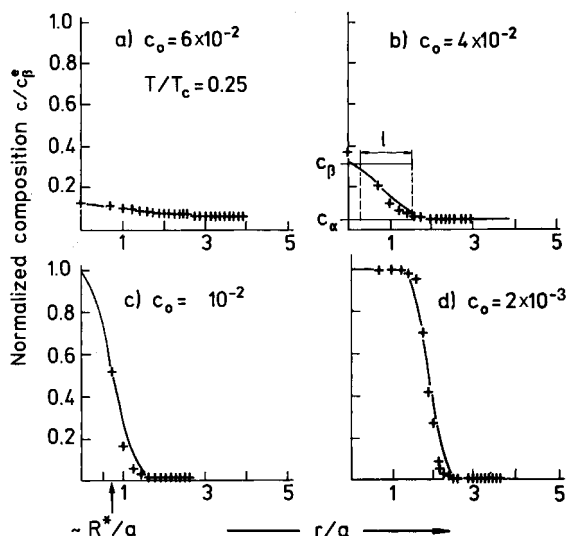


Figure 5-27. Composition profile of a spherical nucleus (center at $r = 0$) in four different metastable solid solutions with composition c_0 quenched to $T = 0.25 T_c$ into the miscibility gap. The continuous line was calculated from the Cahn–Hilliard continuum model (Eq. (5-36)), the crosses represent calculations based on the discrete lattice point model (after LeGoues et al., 1984a). The computations are based on a regular solution model with the solubility limit $c_s^\alpha = 0.37 \times 10^{-3}$ and the spinodal composition $c_s^\alpha = 6.41 \times 10^{-2}$, a is the lattice parameter of an assumed f.c.c. lattice and l the interfacial width.

extent of the critical fluctuations (or R^*) to increase again; at $c_0 \equiv c_s^\alpha$, R^* finally becomes infinite (Fig. 5-26b) suggesting a discontinuity of the decomposition mechanism at the spinodal line (cf. Sec. 5.2.3).

This *apparent discontinuity* at the spinodal results from the assumption that the decomposition path is controlled by the minimum height of the nucleation barrier, i.e., by ΔF^* , which close to the spinodal is in the order of a few kT (Fig. 5-26a) and, hence, rather low. As pointed out by de Fontaine (1969), in a system close to the spinodal many fluctuations exist, the spatial extent of which is *much smaller* than that of the critical fluctuation; neverthe-

less, their formation energies are only slightly higher than ΔF^* . In this case, the probability of the alloy decaying via the formation of those ‘short-wavelength’ fluctuations requiring a slightly higher activation energy is much higher than for a decay via the formation of critical ‘long-wavelength’ fluctuations.

5.5.1.5 Distinction Between Classical and Non-Classical Nucleation

For a practical application of non-classical nucleation theory to experimental studies of unmixing, the total constraint free energy $f'(c)$ rather far away from equilibrium, as well as K^* , have to be known in order to calculate the composition profile [Eq. (5-36)] and the nucleation energy [Eq. (5-37)]. This is the case only for simple alloy systems and, hitherto, has inhibited the application of the non-classical theory to either scientifically or industrially important alloy systems. Furthermore, so far it has been assumed that a nucleus is in equilibrium with the infinite matrix and that the nuclei do *not* interact during the nucleation stage. This may be a valid approximation as long as the supersaturation is small, i.e., where according to Figs. 5-26 and 5-27 classical nucleation theory applies. It ought to become, however, a poor approximation for more concentrated alloys where non-classical nucleation applies. In this case the nucleation rate is high (then the steady-state nucleation regime will not be observed) and, hence, the nucleus density large. These complications in non-classical nucleation make it desirable to provide the experimentalist with a criterion for the applicability of classical nucleation theory which is much easier to handle. Cahn and Hilliard (1959a,b) suggest classical theory will apply if the width l of the (diffuse) interface is considerably smaller than the

core of the nucleus where the composition is about constant (Fig. 5-27).

If we assume that a perceptible nucleation rate is obtained for $\Delta F^* \leq 25 kT$ (in the literature, $\Delta F^* \approx 60 kT$ is frequently stated for the maximum barrier at which nucleation becomes measurable; this value, however, is much too high for homogeneous nucleation to occur in solids) and employs Eqs. (5-19) and (5-20), classical nucleation theory may be applied if (Cahn and Hilliard, 1959a, b):

$$l^2 \frac{4\pi\sigma_{\alpha\beta}}{75 kT} \ll 1 \quad (5-38)$$

For Cu-Ti ($\sigma_{\alpha\beta} = 0.067 \text{ J/m}^2$; $T = 623 \text{ K}$), Fe-Cu ($\sigma_{\alpha\beta} = 0.25 \text{ J/m}^2$; $T = 773 \text{ K}$), and Cu-Co ($\sigma_{\alpha\beta} = 0.17 \text{ J/m}^2$; $T = 893 \text{ K}$) this means that the interfacial width has to be smaller than $\approx 0.56, 0.33$, and 0.42 nm , respectively, and, hence, has to be rather sharp. So far it has not been possible to measure the composition profile across a *nucleus*/matrix interface. However, analytical field ion microscopy of Cu-1.9 at.% Ti aged at 350°C for 150 s revealed the Ti concentration of particles with radii of *only* $\approx 1 \text{ nm}$ to decrease from 20 at.% (corresponding to Cu_4Ti , cf. Sec. 5.2.1) to that of the matrix within one to two atomic (111)-layers (von Alvensleben und Wagner, 1984). For the chosen aging conditions nucleation was evaluated to terminate within about 60 s (Kampmann and Wagner, 1984), thus after aging for 150 s the analyzed particles must have already experienced some growth beyond the original size of the nucleus. Nevertheless, these results provide rather good evidence that during nucleation the Cu_4Ti clusters may be considered droplets with sharp interfaces rather than spatially extended (long-wavelength) fluctuations with diffuse interfaces, even though ΔF^* is only about $10 kT$.

Although some caution is advisable in treating these tiny particles (critical nuclei in solid-state transformation are tens to hundreds of atoms in size) in terms of a continuum theory¹, and assigning them a macroscopic surface and thermodynamic bulk properties, classical nucleation theory seems to be appropriate for an estimation of the nucleation rate. This conclusion will be corroborated in Sec. 5.7.4.

5.5.2 Diffusion-Controlled Growth of Nuclei from the Supersaturated Matrix

Suppose that after nucleation the *stable nucleus* is embedded in a still supersaturated matrix. As is illustrated in Fig. 5-28, the particle will then be surrounded by a concentration gradient which provides the driving force for solute diffusion, and thus gives rise to its growth.

The growth rate can be controlled either by the rate at which atoms are supplied to the particle/matrix interface by diffusion or by the rate at which they cross the interface (Tien et al., 1973). It may be rationalized that for small particles the interface reaction is likely to be the rate-controlling step since the diffusion distances are rather short; once the particles have grown to a certain size, the matrix will be depleted from solute atoms and the associated reduction of the driving force makes diffusion likely to be the slower and, thus, rate-controlling step (Shewmon, 1965). The transition from one step to the other depends upon the relative magnitudes of solute diffusion and interface mobility.

After termination of nucleation it is commonly assumed that the mobility of the interface is sufficiently high in order to al-

¹ Many FIM studies of two-phase alloys (e.g., Cu-1 at.% Fe) revealed the shapes of even tiny clusters with as little as about twenty atoms to be already compact rather than ramified (Wagner, 1982).

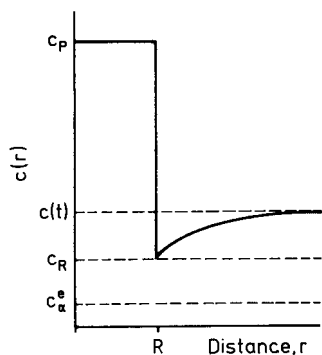


Figure 5-28. Schematic concentration field in the matrix surrounding a nucleus with radius R and composition c_p .

low the solute concentration c_R at the curved interface to achieve local equilibrium (Doherty, 1983). In this case diffusion is the rate-controlling step for the growth of *stable* coherent nuclei in a homogeneous precipitation reaction. An analytical solution of the adequate field equation,

$$D \nabla^2 c(r, t) = \frac{\partial c(r, t)}{\partial t} \quad (5-39)$$

requires certain approximations (Zener, 1949). These were critically examined and compared by Aaron et al. (1970) for the diffusion-controlled growth of spherical and platelet-shaped particles. Regardless of the particular approximation used, both the radius R of a spherical precipitate and the half-thickness T of a platelet grow with time according to a *parabolic growth law* as:

$$R = \lambda_i (Dt)^{1/2} \quad (5-40)$$

and

$$T = \lambda_j (Dt)^{1/2} \quad (5-41)$$

respectively. The rate constants λ_i and λ_j increase with increasing supersaturation, or, more specifically, with an increase in the factor

$$k^* = 2 \frac{\bar{c}(t) - c_R}{c_p - c_R} \quad (5-42)$$

in a manner which, in particular for larger values of k^* , depends upon the approximation assumed (Aaron et al., 1970). For precipitating intermetallic compounds, k^* is one or two orders of magnitude larger (e.g., ≈ 0.3 for γ' -Ni₃Al in Ni-Al and ≈ 0.2 for β' -Cu₄Ti in Cu-Ti) than for precipitating phases with $c_p \approx 1$ such as Fe-Cu, Cu-Fe and Cu-Co.

For small supersaturations, $c(r, t)$ in Eq. (5-39) may be approximated as being time-independent. In this case, an isolated spherical particle with radius R surrounded by the concentration field illustrated in Fig. 5-28 will grow at a rate

$$\frac{dR}{dt} \equiv v(R) = \frac{\bar{c}(t) - c_R}{c_p - c_R} \frac{D}{R} \quad (5-43)$$

where D (assumed to be independent of composition) is the volume diffusion coefficient in the matrix. According to the Gibbs-Thomson equation, the composition c_R of the matrix phase at a curved interface is different from that of a flat interface, the latter being in equilibrium with the equilibrium solute concentration c_α^e of the α -matrix phase, and varies with the precipitate radius as (Martin and Doherty, 1976)

$$\ln \frac{c_R(R)}{c_\alpha^e} = \frac{1 - c_\alpha^e}{c_p - c_\alpha^e} \left(\frac{2 \sigma_{\alpha\beta}}{R_g T} \frac{V_\beta}{R} \right) - \ln \frac{\gamma_\alpha(c_R)}{\gamma_\alpha(c_\alpha^e)} \quad (5-44)$$

with $\gamma_\alpha(c_R)$ and $\gamma_\alpha(c_\alpha^e)$ being the activity coefficients of the solute atoms in the α -phase at the concentration c_R and c_α^e , respectively. If the solid solution shows regular solution behavior (γ_α then becomes independent of c), Eq. (5-44) yields the well-known Gibbs-Thomson equation:

$$c_R(R) = c_\alpha^e \exp \left(\frac{2 \sigma_{\alpha\beta}}{R_g T} \frac{V_\beta}{R} \right) \quad (5-45)$$

or for larger radii in its linearized version,

$$c_R(R) = c_\alpha^e \left(1 + \frac{2 \sigma_{\alpha\beta}}{R_g T} \frac{V_\beta}{R} \right) \quad (5-46)$$

By assuming a monodispersive particle distribution and $c_R \approx \bar{c} (t \rightarrow \infty) = c_\alpha^e$ (or $c_\alpha'^e$), and $\bar{c}(t) \approx c_0$, integration of Eq. (5-43) yields

$$R(t) = \left(2 \frac{c_0 - c_\alpha^e}{c_p - c_\alpha^e} \right)^{1/2} (Dt)^{1/2} \quad (5-47)$$

It should, however, be pointed out that, so far, there is little experimental evidence for the existence of a precipitation regime during which particle growth strictly follows Eq. (5-47) (Kampmann and Wagner, 1984). In Sec. 5.7.4.3 the reason for this lack of experimental evidence will be provided, as well as a guideline to the design of experiments that allow a verification of the existence of diffusion-controlled particle growth with the predicted kinetics to be made. Most quantitative experimental observations of growth rates which yielded good agreement with the diffusion-controlled models outlined above, were confined to large particles, frequently with sizes in the micrometer range (Aaronson et al., 1970a, b; Doherty, 1982).

5.5.3 The Cluster-Dynamics Approach to Generalized Nucleation Theory

As has been pointed out in Sec. 5.5.1.1, the cluster-dynamics approach chosen by Becker and Döring (1935) is based on the assumption that the equilibrium cluster distribution function can be specified by Eqs. (5-23) and (5-18). Even though the resulting predictions of classical nucleation theory ought to become valid asymptotically for large droplets at small supersaturations, there remain some inherent deficits (Binder, 1980; Gunton et al., 1983).

For instance, for small clusters the surface energy entering Eq. (5-18) should contain size-dependent corrections to the macroscopic equilibrium energy of a flat interface. Furthermore, the separation of the droplet formation Helmholtz energy

into a bulk and a surface term appears rather debatable. To avoid some of these deficits, there have been several attempts to develop more accurate descriptions of clusters, taking into account their different sizes and shapes (e.g., Binder and Stauffer, 1976; Stauffer, 1979), and to derive an equilibrium distribution of clusters which is more realistic than the one given by Eq. (5-23). As in the classical nucleation theory, the latter is an important quantity for a computation of the cluster formation rate in terms of the more recently elaborated theories of cluster dynamics which, in essence, are extensions of the Becker–Döring theory (Binder and Stauffer, 1976; Penrose and Lebowitz, 1979; cf. Gunton et al., 1983 and the chapter by Binder and Fratzl (2001) for a general discussion of the various developments).

Unlike Becker and Döring, however, who confined the microscopic mechanism of cluster growth or shrinkage to the condensation or evaporation of monomers (Sec. 5.5.1.1), in their *generalized nucleation theory* Binder and coworkers consider the time evolution of the cluster size distribution function $f(i, t)$ more generally in terms of a *cluster coagulation* or *cluster splitting mechanism*, i.e., in a single cluster reaction step i -mers ($i = 2, 3, \dots$) are also allowed to be added or separated from an existing cluster (e.g., Binder, 1977; Mirolid and Binder, 1977). Thus, the related kinetic equation for the time evolution of $f(i, t)$ (Binder, 1977),

$$\begin{aligned} \frac{d}{dt} f(i, t) = & \sum_{i'=1}^{\infty} \alpha_{i+i', i'} f(i+i', t) \quad (5-48) \\ & - \frac{1}{2} \sum_{i'=1}^{i-1} \alpha_{i, i'} f(i, t) + \frac{1}{2} \sum_{i'=1}^{i-1} \beta_{i-i', i'} \\ & \times f(i', t) f(i-i', t) - \sum_{i'=1}^{\infty} \beta_{i, i'} f(i, t) f(i', t) \end{aligned}$$

contains four different terms. The first accounts for an increase of i -mers due to

splitting reactions $(i + i') \rightarrow (i, i')$ which are assumed to be proportional to the momentary number $f(i + i', t)$ of clusters of size $(i + i')$, where the proportionality coefficient $\alpha_{i+i', i'}$ is the rate constant. The second term describes the decrease of i -mers because of splitting reactions $i \rightarrow (i - i', i')$; as a reverse process, coagulation of clusters with sizes $(i - i')$ and i' contributes to a further increase of i -mers (third term), some of which are lost again by coagulation reactions between i -mers and i' -mers to yield $(i + i')$ -mers (fourth term). Evidently, for $i' = 1$ the monomer evaporation and condensation process, assumed to be the rate controlling step in the Becker–Döring theory, is contained in Eq. (5-48).

If, again as in classical nucleation (Sec. 5.5.1.1, Eq. (5-24)), detailed balance conditions are assumed to apply between splitting and coagulation, then the rates α and β in Eq. (5-48) can be replaced by a single reaction rate W , e.g.,

$$(5-49)$$

$$W(i, i') \equiv \alpha_{i+i', i'} C(i + i') = \beta_{i, i'} C(i) C(i')$$

Here, $C(i)$ again denotes the cluster concentration which is in thermal equilibrium with the metastable matrix.

Numerical integration of Eq. (5-48) with Eq. (5-49) provides the time evolution of the cluster concentration. This requires, however, a knowledge of the initial cluster distribution $f(i, t = 0)$, the reaction rates such as $W(i, i')$, and of $C(i)$. These quantities are not commonly available for alloys undergoing phase separation; this has so far impeded a quantitative comparison between the predictions of the generalized nucleation theory and experimental results on nucleation kinetics.

However, the solution of the kinetic equations with plausible assumptions for the missing quantities (Mirolid and Binder, 1977, see also the chapter by Binder and Fratzl (2001) has provided a profound,

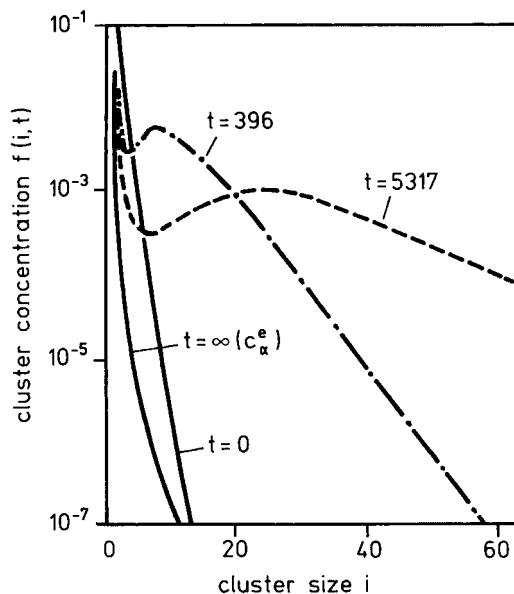


Figure 5-29. Cluster size distribution at different aging times (arbitrary units) as obtained from a numerical solution of Eqs. (5-48) and (5-49). (After Binder and Stauffer, 1976.)

though basically qualitative, insight into the dynamics of cluster formation and growth. As is shown in Fig. 5-29, the initially ($t = 0$) monotonically decreasing cluster size distribution attains for intermediate times a minimum at a size that corresponds to about that of the critical nucleus in classical nucleation theory.

The broad maximum of $f(i, t)$ (which, in fact, does not appear in the corresponding curve of the Becker–Döring nucleation theory (cf. Fig. 5-24), and its shift to larger sizes with increasing time is due to those particles which have nucleated at earlier times and, hence, have already experienced growth. At $t \rightarrow \infty$ equilibrium is reached. In this case large clusters ($i \rightarrow \infty$) of the precipitated equilibrium phase with composition c_β^e are embedded in a matrix (with composition c_α^e) which then still contains *small* clusters with the equilibrium size distribution shown in Fig. 5-29.

The qualitative features of the $f(i, t)$ -curves emerging from the generalized nucleation theory and displayed in Fig. 5-29 are corroborated by computer simulations (cf. Sec. 5.5.6). They are indicative of the occurrence of nucleation and growth as concomitant processes during the early stages of unmixing. For most solids undergoing phase separation, therefore, it is not possible to investigate experimentally nucleation and growth as individual processes proceeding subsequently on the time scale. Apart from well designed experiments, it is thus usually impossible to verify experimentally the kinetics predicted by classical or non-classical nucleation theory (Secs. 5.5.1.1 to 5.5.1.3) or predicted by growth theories (Sec. 5.5.2). This will be substantiated in more detail in Sec. 5.7.4.

The *generalizing character* of the nucleation theory of Binder and coworkers is founded on the fact that, in the sense of Sec. 5.2.3, it comprises nucleation in the metastable regime as well as the transition to spinodal decomposition in the unstable regime of the two-phase region. Consequently, the artificial divergency of both the critical radius R^* of the nucleus and the wavelength λ^* of a critical fluctuation, inherent to the Cahn–Hilliard theories of non-classical nucleation (Sec. 5.5.1.4) and spinodal decomposition (Sec. 5.5.4), is no longer discernible on approaching the spinodal line either from the metastable ('nucleation') or from the unstable ('spinodal') regime of the two-phase region (Fig. 5-30). On crossing the spinodal curves the size of a critical cluster decreases steadily until it becomes comparable to the correlation length of typical thermal fluctuations (Binder et al., 1978). Thus, no discontinuity of the mechanism or of the decomposition kinetics is expected to occur on crossing the border between the metastable and unstable regions.

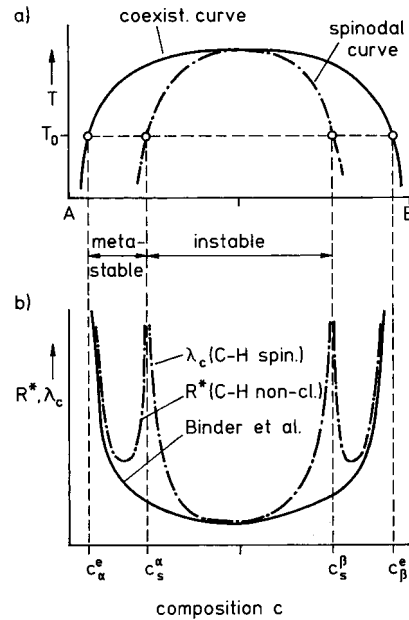


Figure 5-30. a) Schematic phase diagram of a binary alloy (components A and B) with a symmetrical miscibility gap.

b) Variation of the critical radius R^* of a nucleus and of the wavelength λ_c of a critical fluctuation with composition of the alloy at T_0 according to the non-classical Cahn–Hilliard nucleation theory (C–H non-cl.) and the Cahn–Hilliard spinodal theory (C–H spin.). Approaching the spinodal composition c_s^α from either the metastable or the unstable region causes R^* and, respectively, to diverge. In contrast, the generalized nucleation theory of Binder and coworkers yields the size of the critical cluster to decrease steadily until it becomes comparable to the correlation length of typical thermal fluctuations. There is no peculiarity on crossing the spinodal curve.

From the experimental point of view it is rather difficult and tedious to obtain *statistically significant* information from direct imaging techniques (FIM, HREM) on the time evolution of the cluster size distribution during the earliest stages of unmixing. Attempts were made by Si-Qun Xiao and Haasen (1991) who employed HREM to binary Ni–Al alloys. This information, however, is implicitly contained in the structure function $S(k, t)$ from small angle

scattering techniques, e.g., SAXS or SANS (Sec. 5.3.1.2). Binder et al. (1978) computed the time evolution of $S(\kappa, t)$ on grounds of their cluster dynamics model. For this purpose, rather crude approximations and simple assumptions had to be made concerning the originally complex shape of the size distribution function of the clusters, their shapes and their composition profiles. Hence, the resulting $S(\kappa, t)$ is only *qualitative* in nature and cannot be used for a quantitative comparison with experimentally obtained structure functions.

As is shown in Fig. 5-31a, $S(\kappa, t)$ is predicted to develop a peak the height $S_m \equiv S(\kappa_m)$ of which increases with time due to the increasing cluster volume fraction, while the peak position is shifted towards smaller values of κ , reflecting the coarsening of the cluster size distribution with time. Fig. 5-31b shows the variation of both the peak height $S_m(\kappa \equiv \kappa_m)$ and the peak position κ_m with time. On a double-logarithmic plot both curves display some curvature, though the shift of κ_m may be reasonably well represented as a power law, $\kappa_m(t) \propto t^{-1/6}$ (5-50) during the 'aging period' covered in Fig. 5-31a and 5-31b.

Even though it is not feasible to convert the scaled times shown in Fig. 5-31a and 5-31b to real times, experimental SANS curves (Fig. 5-32a) and the related $S_m(t) \propto dS^m(t)/d\Omega$ (cf. Eq. 5-17)) and $\kappa_m(t)$ -curves (Fig. 5-32b) from Cu-2.9 at.% Ti homogenized at T_H , quenched and isothermally aged at 350°C (Eckerlebe et al., 1986) display the characteristic features qualitatively predicted by the generalized nucleation theory.

Kampmann et al. (1992) developed a generic cluster-dynamics model that can be used for the quantitative interpretation of experimental kinetic data.

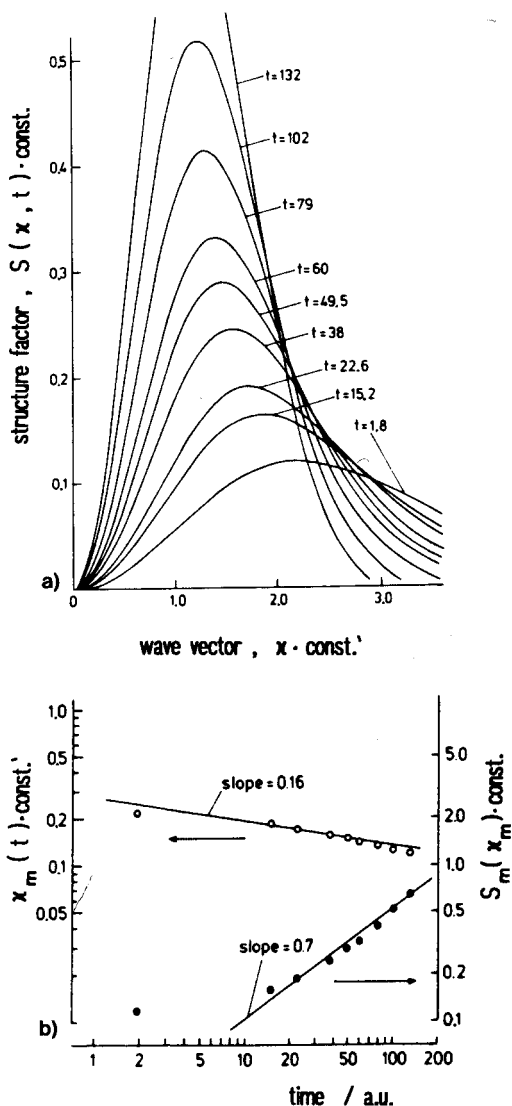


Figure 5-31. a) Time evolution of the structure function $S(\kappa, t)$, and b) of its peak height S_m and peak position κ_m as predicted by the generalized nucleation theory of Binder and coworkers for a 3-dimensional Ising model ($c_0 = 0.1$, $T/T_c = 0.6$). After Binder et al. (1978), see also the chapter by Binder and Fratzl (2001).

Unlike previous models, in this model a distinction can be made between the clustering phase being a disordered solid solution, e.g., Cu-Co with a positive pair exchange energy, or an ordered phase, e.g.,

Ni_3Al in the Ni–Al system with a negative pair exchange energy (Staron and Kampmann, 2000a, b). In the latter case the continuation of the atomic order must be accounted for when computing the growth probability of the long-range ordered Ni_3Al cluster, the growth of which is assumed to proceed via diffusional incorporation of a solute monomer (cf. Sec. 5.7.7).

5.5.4 Spinodal Theories

As has been pointed out in Sec. 5.2.3 the evolution of non-localized, spatially extended solute-enriched fluctuations into stable second phase particles is treated in terms of spinodal theories. The general concepts of the spinodal theories, including more recent extensions, are comprehensively discussed by Binder and Fratzl (2001) in Chapter 6 of this volume. We will therefore restrict ourselves to a summary of the essential predictions of those theories which may be examined by experimental studies. Although often not justified, in materials science some of these predictions are frequently employed as sufficient criteria to distinguish a spinodal reaction from an unmixing reaction via nucleation and growth.

In their continuum model for spinodal decomposition, which is based on the free energy formalism of a non-uniform binary alloy outlined in Sec. 5.5.1.4 (Eq. (5-35)), Cahn and Hilliard (1959a, b) derived the following (linearized) diffusion equation:

$$\frac{\partial c(\mathbf{r}, t)}{\partial t} = \frac{M}{n_v} \nabla^2 \left[\left(\frac{\partial^2 f}{\partial c^2} \right)_{c_0} + 2\eta^2 Y \right] \times c(\mathbf{r}, t) - 2K * \nabla^4 c(\mathbf{r}, t) \quad (5-51)$$

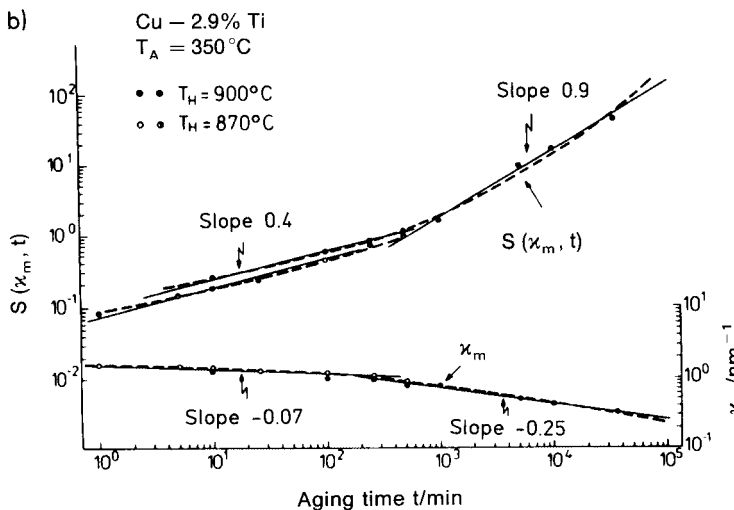
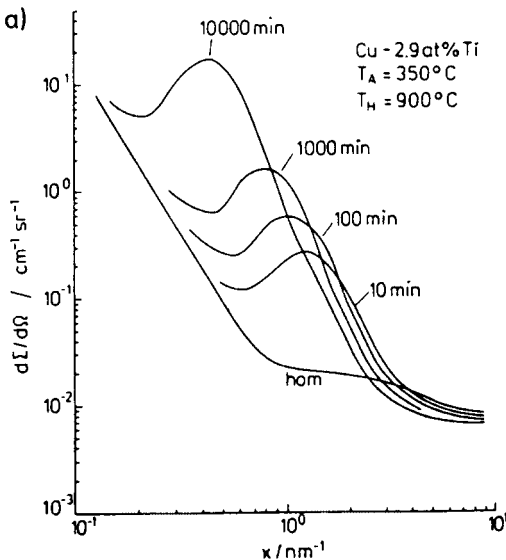


Figure 5-32. a) Time evolution of the structure function (SANS experiments) of a Cu–2.9 at.% Ti single crystal aged at 350 °C for the given times. b) Time evolution of the peak height $S_m \propto d\Sigma^m/d\Omega$ and the peak position x_m . (After Eckerlebe et al., 1986.)

for the time dependence of the composition $c(\mathbf{r}, t)$ at position \mathbf{r} . As the number of atoms per unit volume, n_v , accounts for the fact that the derivative has to be taken with respect to the concentration of component B , M is the atomic mobility and is related to the interdiffusion coefficient \tilde{D} via

$$M \equiv \tilde{D} n_v \left/ \frac{\partial^2 f}{\partial c^2} \right|_{c_0} \quad (5-52)$$

The other symbols in Eq. (5-51) were defined in Sec. 5.5.1.4.

As M is always positive, \tilde{D} takes the sign of $\partial^2 f / \partial c^2$ and so is negative inside the spinodal regime (Sec. 5.2.2), giving rise to an ‘uphill diffusion’ flux of solute atoms (cf. Fig. 5-6b).

The linearized version of the more general nonlinear diffusion equation holds if the amplitude $c(\mathbf{r}) - c_0$ of the composition fluctuation is rather small and both M and $(\partial^2 f / \partial c^2)|_{c_0}$ are independent of composition. These approximations inherently confine the Cahn–Hilliard theory (CH theory) to the earliest stages of phase separation.

By expanding the atomic distribution $c(\mathbf{r}, t)$ into a Fourier series, Eq. (5-51) can be written as

$$\frac{\partial A(\boldsymbol{\kappa})}{\partial t} = R(\boldsymbol{\kappa}) A(\boldsymbol{\kappa}) \quad (5-53)$$

with the amplitude

$$A(\boldsymbol{\kappa}) = \int [c(\mathbf{r}) - c_0] \exp(i \boldsymbol{\kappa} \cdot \mathbf{r}) d\mathbf{r} \quad (5-54)$$

of a Fourier component with wavenumber $\boldsymbol{\kappa} = 2\pi/\lambda$ if λ denotes the wavelength of the composition fluctuation. Eq. (5-51) has a solution for every $A(\boldsymbol{\kappa}, t)$ with

$$A(\boldsymbol{\kappa}, t) = A(\boldsymbol{\kappa}, 0) \exp[R(\boldsymbol{\kappa}) t] \quad (5-55)$$

where $A(\boldsymbol{\kappa}, 0)$ is the initial amplitude of the Fourier component with wavenumber $\boldsymbol{\kappa}$. The so-called *amplification factor* $R(\boldsymbol{\kappa})$

is defined as: (5-56)

$$R(\boldsymbol{\kappa}) = -\frac{M}{n_v} \left[\frac{\partial^2 f}{\partial c^2} \right]_{c_0} + 2\eta^2 Y + 2K^* \boldsymbol{\kappa}^2 \boldsymbol{\kappa}^2$$

With reference to Eqs. (5-16), (5-54) and (5-55), the structure function $S(\boldsymbol{\kappa}, t)$ or the related small angle scattering intensity (Eq. (5-17)) at time t is obtained as

$$S(\boldsymbol{\kappa}, t) = S(\boldsymbol{\kappa}, 0) \exp[2R(\boldsymbol{\kappa}) t] \quad (5-57)$$

where $S(\boldsymbol{\kappa}, 0)$ denotes the equal-time structure function of the system equilibrated at the homogenization temperature.

Inside the spinodal region $(\partial^2 f / \partial c^2)|_{c_0}$ is negative. Thus for a given negative value of the latter, $R(\boldsymbol{\kappa})$ becomes positive for all wavenumbers $\boldsymbol{\kappa}$ satisfying

$$\boldsymbol{\kappa}^2 < \boldsymbol{\kappa}_c^2 = \left(\frac{\partial^2 f}{\partial c^2} \right)_{c_0} / -2\eta^2 Y \quad (5-58a)$$

or, correspondingly, for all fluctuation wavelengths λ larger than λ_c with

$$\lambda_c^2 = 4\pi K^* / \left(\frac{\partial^2 f}{\partial c^2} \right)_{c_0} - 2\eta^2 Y \quad (5-58b)$$

Long wavelength fluctuations with $\lambda > \lambda_c$ thus will be amplified exponentially whereas short wavelength fluctuations will decay with aging time. For $\lambda_m \equiv \sqrt{2} \lambda_c$, $R(\lambda)$ attains a maximum giving rise to fastest growth of fluctuations with wavelength λ_m . On approaching the coherent spinodal curve where the denominator in Eq. (5-58b) becomes zero (cf. Sec. 5.5.3), the critical wavelength λ_c diverges in a similar manner as does the critical radius R^* (Fig. 5-30). Thus both the linear theory on spinodal decomposition and the non-classical nucleation theory (Sec. 5.5.1.4) predict abrupt changes in the decomposition kinetics on crossing the spinodal line from either side. This has prompted several experimental studies to determine the spino-

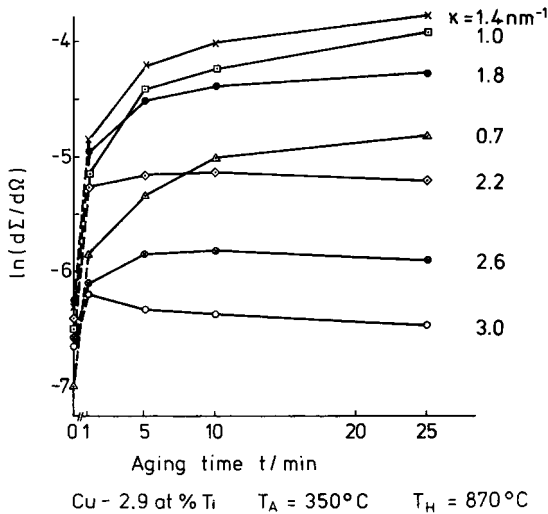


Figure 5-33. Time evolution of $d\Sigma/d\Omega$ for Cu-2.9 at.% Ti aged at 350°C for various constant wave-numbers κ (Eckerlebe et al., 1986).

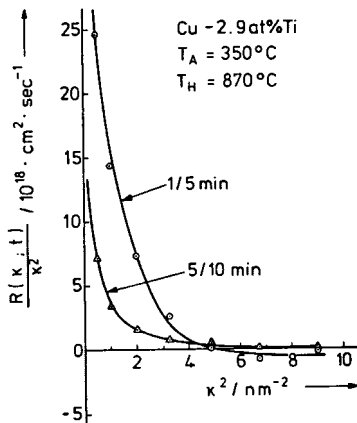


Figure 5-34. Variation of $R(\kappa, t)/\kappa^2$ with κ^2 as determined for two different time intervals (Eckerlebe et al., 1986).

dal curve on grounds of a kinetic distinction between metastable and unstable states.

In terms of the time evolution of the structure function [Eq. (5-57); now assumed to be isotropic] or the small angle scattering intensity, $S(\kappa, t)$ should increase exponentially for $\kappa < \kappa_c$ with a peak at the *time-independent* position $\kappa_m = \kappa_c / \sqrt{2}$. Furthermore, all $S(\kappa)$

curves taken at various times should cross at a *common cross-over point*, at κ_c .

Most SAXS or SANS studies of binary alloys, oxides or glasses that were deeply quenched into the miscibility gap failed to corroborate the predictions of the linearized CH theory. This is exemplified by Cu-2.9 at.% Ti isothermally aged at 350°C. As illustrated in Fig. 5-32b, the peak position of the structure function, which is frequently identified with the mean cluster spacing \bar{l} ($\bar{l} \approx 2\pi/\kappa_m = \lambda_m$), is *not* found to be time-independent but is rather shifted towards smaller values of κ owing to spontaneous coarsening of the clustering system. Furthermore, *no* common cross-over point at any κ_c (Fig. 5-32a) exists nor does $S(\kappa, t)$ grow exponentially for any value of κ (Fig. 5-33).

According to Eqs. (5-56) and (5-57), a plot of

$$R(\kappa)/\kappa^2 = (1/2\kappa^2) \frac{\partial}{\partial t} \ln [S(\kappa, t)/S(\kappa, 0)] \quad (5-59)$$

versus κ^2 should yield a straight line with $R(\kappa) \equiv 0$ at κ_c , whereas a pronounced curvature at larger values of κ has been observed experimentally in alloys (e.g., Fig. 5-34) and glass systems (Neilson, 1969). Cook (1970) attributed this curvature to random thermal composition fluctuations which were not accounted for in the original CH theory. Even with the incorporation of the thermal fluctuations into the linearized theory, at its best the resulting Cahn-Hilliard-Cook (CHC) spinodal theory is seen (Langer, 1973; Gunton, 1984) to be valid only for the earliest stages of decomposition in systems for which the range of the interaction force is considerably larger than the nearest-neighbor distance, i.e., in systems which are almost mean-field-like in nature. This is not the case for metallic alloys, oxides and glasses, but is for polymer blends. In fact, results

from kinetic studies of decomposition in various polymer mixtures, some of which are cited in Table 5-1 (for reviews, cf. Gunton et al., 1983; Binder and Fratzl (2001), Chapter 6 of this volume), were found to be consistent with the predictions of the linearized spinodal CHC theory (e.g., Okada and Han, 1986). In contrast, apart from a SANS study on the kinetics of phase separation in Mn-33 at.% Cu (Gaulin et al., 1987), *none* of the scattering experiments on metallic alloys or oxides which are listed in Table 5-1 and which probably had been quenched into the unstable region of the miscibility gap, corroborated the predictions of the CHC theory. SANS curves taken from Mn-33 at.% Cu during short-term aging (between 65 s and 210 s at 450°C) could be fitted to the CHC structure function with κ_m being time-independent during this period. Thus, it was concluded that phase separation in Mn-33 at.% Cu is of the spinodal type and the kinetics follow the CHC predictions (Gaulin et al., 1987). The $S(\kappa)$ curve of the as-quenched state already revealed a peak, in fact, at a smaller value of κ_m than for the aged samples. This is indicative of the fact that phase separation occurred during the quench owing to a finite quench rate. In this case, as has been extensively discussed by Hoyt et al. (1989), κ_m may indeed become initially time-independent, thus pretending an experimental confirmation of the CHC linear approximation.

In the framework of the mean-field theories the spinodal curve is well defined as the locus where $\partial^2 f / \partial c^2$ vanishes (Sec. 5.2.2). It can then be easily evaluated, e.g., from an extrapolation of the thermodynamic data which are known for the single-phase solid solution, into the ('mean-field') spinodal regime (Hilliard, 1970). Since, however, neither metallic alloys nor glass or oxide mixtures behave as mean-field-like systems, *no uniquely defined* spinodal

curve exists for these solid mixtures (cf. Binder and Fratzl (2001), Sec. 6.2.5, this volume). Thus in general, it is currently not feasible to predict on theoretical grounds whether a metallic, glass or oxide solid mixture has been quenched into the metastable or unstable region of the miscibility gap. In this context, it remains debatable whether each of the metallic, glass or oxide mixtures that were studied by means of SAXS or SANS, and which have been reported to undergo spinodal decomposition (Table 5-1), were truly quenched into and aged within the spinodal region of the phase diagram. Nevertheless, extensive experimental SAXS or SANS studies, in particular on Al-Zn alloys and Fe-Cr (Table 5-1), did not reveal any evidence for a drastic change in the time evolution of the $S(\kappa, t)$ curves with a change in the initial supersaturation. For the Al-Zn systems in particular, it was shown (Simon et al., 1984) that the clustering rate increases rapidly with increasing supersaturation, i.e. both κ_m and S_m are larger the deeper the quench.

Extensions of the Cahn-Hilliard theory of spinodal decomposition to ternary or multicomponent systems have been elaborated by de Fontaine (1972, 1973) and Moral and Calm (1971). However, to our knowledge the kinetic predictions from these extensions have not yet been compared with experimental results, probably because of difficulties in determining the partial structure functions of ternary alloys (cf. Sec. 5.3.1.2).

As has been pointed out in Sec. 5.2.3, the formulation of a 'unified theory' comprising both nucleation and growth as well as spinodal decomposition can also be attacked on grounds of a spinodal theory. This has been attempted in the statistical model of Langer, Bar-On and Miller (1975), which takes into account thermal fluctuations and nonlinear terms which are

Table 5-1. Some small angle scattering experiments – sometimes jointly employed with other microanalytical tools for studying the morphology – primarily designed for an investigation of spinodal decomposition. If not otherwise stated the concentrations are in at.% (N.d.: not determined.)

Decomposing solid	Experimental technique	Morphology of two-phase microstructure	Authors
<i>Metallic alloys</i>			
Al-4 wt.% Cu	SAXS	Modulated structure	Naudon et al. (1976)
Al-22% Zn	SAXS		Gerold and Merz (1967)
Al-22% Zn	SAXS, TEM	Modulated structure	Agarwal and Herman (1973)
Al-20.7 ... 49.1% Zn	SAXS		Bonfiglioli and Guinier (1966)
Al-5.3 ... 6.8% Zn	SANS	GP-zones	Hennion et al. (1982)
Al-5.3 ... 12.1% Zn	SANS, TEM		Guyot and Simon (1981) Simon et al. (1984)
Al-22% Zn-0.1 Mg	SAXS, TEM	Interconnected spherical clusters at early times; regularly spaced platelets at later stages	Forouhi and de Fontaine (1987)
Al-12 ... 32 Zn	SAXS (synchrotron radiation)		Hoyt et al. (1987, 1989)
Al-2.4% Zn-1.3 Mg	SANS		Blaschko et al. (1982, 1983)
Al-3.8 ... 9% Li with additions of Cu, Mn	SANS	N.d.	Pike et al. (1989)
Au-60% Pt	SANS		Singhal et al. (1978)
Fe-28% Cr-10% Co	SANS, TEM, AFIM	'Sponge-like' structure	Miller et al. (1984)
Fe-34% Cr	SANS	N.d.	Katano and Iizumi (1984)
Fe-30 ... 50% Cr	SANS	N.d.	Ujihara and Osamura (2000)
Fe-29.5% Cr-12.5% Co	Anomalous SAXS (synchrotron source)	N.d.	Simon and Lyon (1989)
Fe-52% Cr	SANS	N.d.	La Salle and Schwartz (1984)
Fe-20 ... 60% Cr	SANS	N.d.	Furusaka et al. (1986)
Cu-2.9% Ti	SANS, TEM	Modulated structure	Eckerlebe et al. (1986)
CuNiFe	SANS	Modulated structure	Aalders et al. (1984)
CuNiFe	SANS, TEM, AFIM	Mottled structure	Wagner et al. (1984)
CuNiFe	Anomalous SAXS (synchrotron source)	N.d.	Lyon and Simon (1987)
Cu-2% Co	SANS	N.d.	Steiner et al. (1983)
Mn-25 ... 52% Cu	SANS (analysis of integrated intensity)	N.d.	Vintaikin et al. (1979)
Mn-33% Cu	SANS	N.d.	Gaulin et al. (1987)
Ni-13% Al	SANS	Anisotropic clustering	Beddoe et al. (1984)
Ni-12.5% Si	SANS, SAXS, TEM ('side bands')	Modulated structure	Polat et al. (1986, 1989)
Ni-11.5% Ti	SANS, TEM	Modulated structures	Cerri et al. (1987, 1990)

Table 5-1. Cont.

Decomposing solid	Experimental technique	Morphology of two-phase microstructure	Authors
<i>Glasses, oxides^a</i>			
B ₂ O ₃ –(15 wt.% PbO –5 wt.% Al ₂ O ₃) (quasi-binary system)	SAXS		Craievich (1975) Acuña and Craievich (1979) Craievich and Olivieri (1981)
B ₂ O ₃ –(27 wt.% PbO –9 wt.% Al ₂ O ₃) Vycor glass	SAXS (synchrotron source) SANS		Craievich et al. (1986)
		'Sponge-like' structure consisting of a SiO ₂ -rich and a B ₂ O ₃ -alkali oxide-rich phase	Wiltzius et al. (1987)
SiO ₂ –13 mole% Na ₂ O	SAXS, TEM	'Sponge-like' structure	Neilson (1969)
TiO ₂ –(20–80 mole%) SnO ₂	SAXS, TEM, X-ray diffraction ('side band' analysis)	Lamellar modulations along [001] (Fig. 5-38)	Park et al. (1976)
<i>Polymer mixtures</i>			
Critical mixture of per- deuterated and protonated 1,4-polybutadiene polybutadiene and styrene–butadiene copolymer mixtures	Light scattering		Wiltzius et al. (1988) Bates and Wiltzius (1989) Izumitani and Hashimoto (1985)
polystyrene–polyvinyl- methylether (PS–PVME)	Light scattering		Sato and Han (1988) Sato et al. (1989) Snyder et al. (1983a, b) Hashimoto et al. (1986a, b) Okada and Han (1986)

^a For a comprehensive survey on oxides and glasses up to 1978, see Jantzen and Herman (1978).

neglected in the CH theory. The LBM non-linear theory of spinodal decomposition also accounts for the later stages of phase separation, though *not* for the coarsening regime. If coherency strains are neglected it approximates the kinetic evolution of the structure function as

$$\begin{aligned}
 \frac{dS(\kappa, t)}{dt} = & -2 \frac{M}{n_v} \kappa^2 \\
 & \times \left[\left(K^* \kappa^2 + \frac{\partial^2 f}{\partial c^2} \bigg|_{c_0} \right) S(\kappa) + A^*(t) \right] \\
 & + 2 \frac{M}{n_v} kT \kappa^2
 \end{aligned} \quad (5-60)$$

With certain approximations, nonlinear effects and thermal fluctuations are contained in the term $A^*(t)$ and in the last term, respectively. Setting $A^*(t) \equiv 0$ reproduces the corresponding equation of motion of the CHC theory, and, if the fluctuation term is also omitted, Eq. (5-57) of the original linear CH theory is regained. Langer et al. (1975) proposed a computational technique for solving Eq. (5-60). This required several approximations to be made, e.g., on $f(c)$ and on M , which inherently leaves the LBM approach with some fundamental shortcomings. Nevertheless, with respect to the features displayed in the

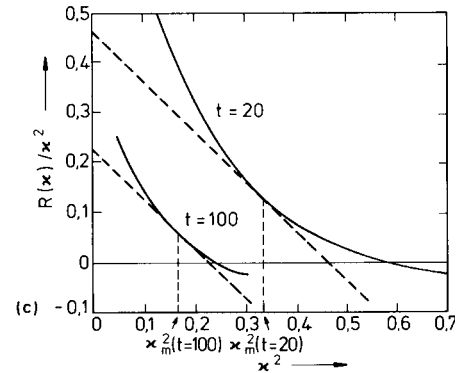
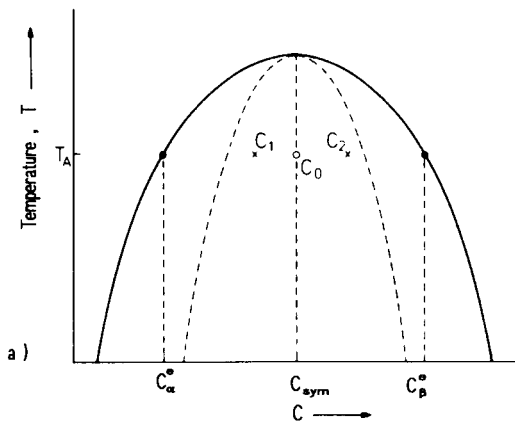


Figure 5-35. a) Phase diagram of a binary alloy with a symmetric miscibility gap centered at c_{sym} .

b) Time evolution of the structure function of an alloy with $c_0 = c_{\text{sym}}$ quenched and aged at T_A . The insert shows the distribution function of composition configurations at two different times. At $t = 80$ the evolving two-phase structure with compositions c_1 and c_2 or y_1 and y_2 , respectively, with

$$y_1 = \frac{c_1 - c_{\text{sym}}}{c_{\alpha}^e - c_{\text{sym}}} \quad \text{and} \quad y_2 = \frac{c_2 - c_{\text{sym}}}{c_{\beta}^e - c_{\text{sym}}}$$

already becomes discernible. All units are dimensionless.

c) LBM predictions on the variation of $R(x, t)/x^2$ with x^2 as determined from b) according to Eq. (5-59). Qualitatively there is good agreement with the LBM predictions and experimental results, e.g., displayed in Fig. 5-34. (After Langer et al., 1975.)

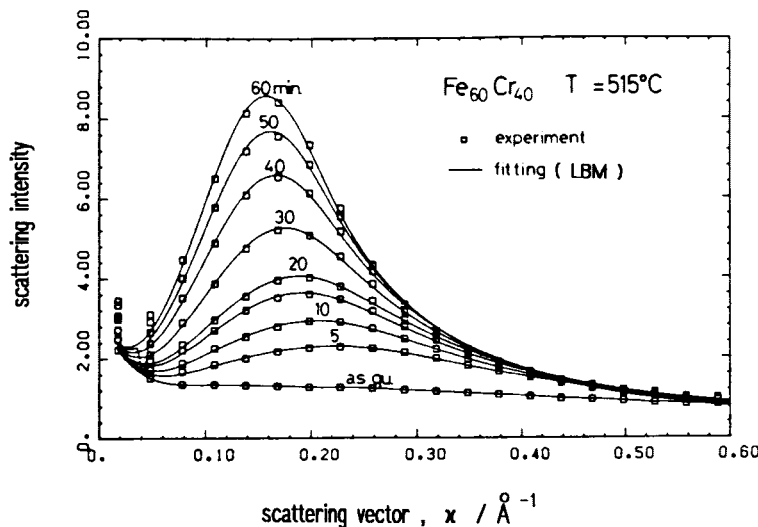
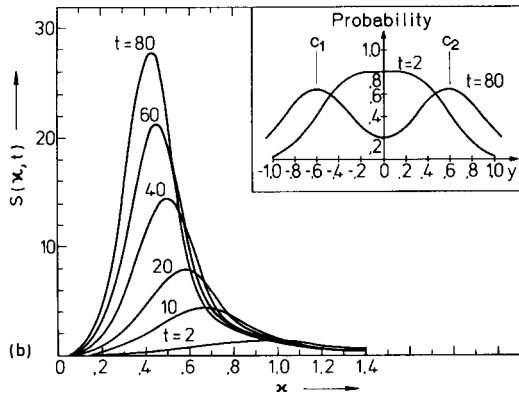


Figure 5-36. Time evolution of the structure function (SANS intensity) of Fe-40 at.% Cr aged at 515°C for the given times. Full lines are calculated from the LBM theory with three free fitting parameters. (After Furusaka et al. 1986.)

time evolution of $S(x, t)$, the predictions of the LBM theory (Fig. 5-35) are in rather good agreement with both experimental studies (e.g., Fig. 5-32 a and 5-34) and Monte Carlo studies (Sec. 5.5.6, Fig. 5-41).

In their study of phase separation in Fe-(20, 30, 40 and 60) at.% Cr alloys, Furusaka et al. (1986) compared the experimental $S(x, t)$ curves with Eq. (5-60) of the LBM theory. For shorter aging times at 515°C, the experimental data points taken from Fe-40 at.% Cr could well be fitted by Eq. (5-60) (Fig. 5-36) if kT/K^* , MK^* , and A^*/K^* were employed as three independent fitting parameters. On the grounds of the agreement with the spinodal theory of LBM, and additionally, as this particular alloy was evaluated to lie within the (mean-field) spinodal region, it has been concluded that Fe-40 at.% Cr is a 'spinodal alloy'.

Based on a similar LBM analysis of SANS data from Fe-30 ... 50 at.% Cr, Ujihara and Osamura (2000) corroborated this conclusion recently.

The nonlinear theory of spinodal decomposition developed by Langer (1971) for binary alloys has also been extended to ternary substitutional systems (Hoyt, 1989) by deriving the time-dependent behavior of the three linearly independent partial structure functions (cf. Sec. 5.3.1.2). An experimental examination of the kinetic predictions, however, is still lacking.

5.5.5 The Philosophy of Defining a 'Spinodal Alloy' – Morphologies of 'Spinodal Alloys'

Referring to the previous section it is rather difficult or even impossible to assess on a thermodynamic basis whether an alloy, glass or oxide system was truly quenched into and aged within the spinodal

region of the miscibility gap. Furthermore, the various spinodal theories are difficult to handle and many parameters in the resulting kinetic equations are often not available for most solid mixtures. Hence, like the non-classical nucleation theory, the various elegant theories that describe the kinetics of phase separation of a 'spinodal alloy' are of little use for the practical metallurgist.

Because of these problems, materials scientists have up to now employed *morphological criteria* for the definition of a 'spinodal alloy'. These are simply related to the predictions of the linear spinodal CH theory concerning the morphological evolution of a solid mixture undergoing spinodal decomposition.

Most crystalline solid solutions show a variation of lattice parameter with composition leading to coherency strains. The associated strain energy $f_{el} = \eta^2 Y (c - c_0)^2$ (Eq. (5-34)), which is accounted for in Eq. (5-51), reduces the driving force for phase separation. This effect shifts the locus of the original *chemical* (mean field) spinodal to lower temperatures, yielding the *coherent* spinodal curve (Eq. (5-58)). If the parameter Y (cf. Sec. 5.2.4), which is a combination of various elastic constants, depends on the crystallographic direction, f_{el} also becomes anisotropic. Therefore, the locus of the coherent spinodal may also vary with the crystallographic direction. This becomes particularly discernible for the tetragonal $\text{TiO}_2\text{-SnO}_2$ oxide system (Park et al., 1975, 1976), where f_{el} attains a minimum for composition waves along [001] and is larger for waves along [100] and [010]. Hence, the coherent spinodal splits up into a [001], a $\langle 101 \rangle$, and a $\langle 100 \rangle$ branch (Fig. 5-37). As a consequence the SnO_2 -rich modulations form preferentially along [001], giving rise to a lamellar structure at later aging stages (Fig. 5-38). For

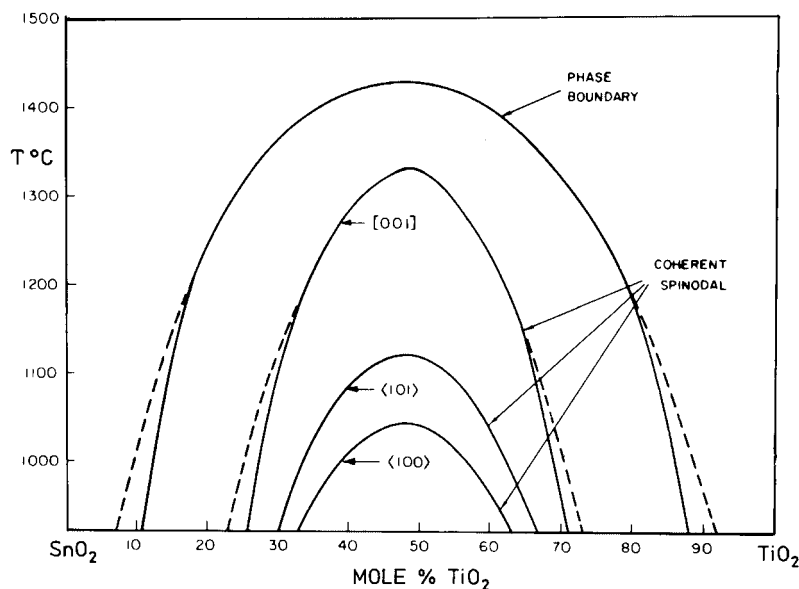


Figure 5-37. The phase diagram and the spinodal curves for composition waves along $[001]$, $\langle 101 \rangle$, and $\langle 100 \rangle$ directions for elastically anisotropic tetragonal $\text{TiO}_2\text{-SnO}_2$. The spinodals were calculated on the basis of the regular solution model. (From Park et al., 1976.)

most cubic metallic systems the elastic anisotropy parameter A (Sec. 5.2.4ii) is positive, rendering the minimum f_{el} along the elastically soft $\langle 100 \rangle$ directions. According to the CH theory the growth rate will thus be highest along the three $\langle 100 \rangle$ directions, giving rise to the frequently observed modulated precipitate microstructures (Table 5-2, Figs. 5-18, 5-19b). In isotropic materials such as polymers, glasses, or, for instance, Fe-Cr and Fe-Cr-Co alloys, the modulations do not grow along any preferential directions. The resulting two-phase microstructure is of the 'sponge-like' type and sometimes referred to as a 'mottled' or 'interconnected' precipitate microstructure (e.g., Fig. 5-16, 5-19c, 5-20). Based on these considerations, two-phase alloys displaying either *lamellar*, *modulated* or *interconnected* precipitate microstructures are commonly termed '*spinodal alloys*' by metallurgists. Furthermore, the morphology of a two-phase material is sometimes employed to derive the locus of the spinodal. This is illustrated in Fig. 5-39 for the Cr-rich ferrite phase of a cast duplex stain-

less steel that undergoes phase separation during tempering between 350°C and 450°C with an associated embrittlement (Auger et al., 1989). Increasing the Cr content of the ferritic Fe-Ni-Cr solid solution leads to the formation of Cr-rich α' -precipitates during tempering. As the α' -phase is discernible as individual particles by CTEM, it is concluded that phase separation occurred via nucleation and growth. A further increase in the Cr content, to about 25 wt.%, yielded a 'sponge-like' microstructure after tempering below 400°C . This was attributed to a spinodal mechanism. Thus the spinodal is drawn as the line that separates the two morphologies (Fig. 5-39).

It must be pointed out, however, that interconnected or modulated structures represent two-phase microstructures in the *later* stages of the reaction (e.g., Fig. 5-18). Even though they are widely believed to result from spinodal decomposition in the sense of the CH theory, their formation might be of a rather different origin. For instance, a strong elastic interaction of a high

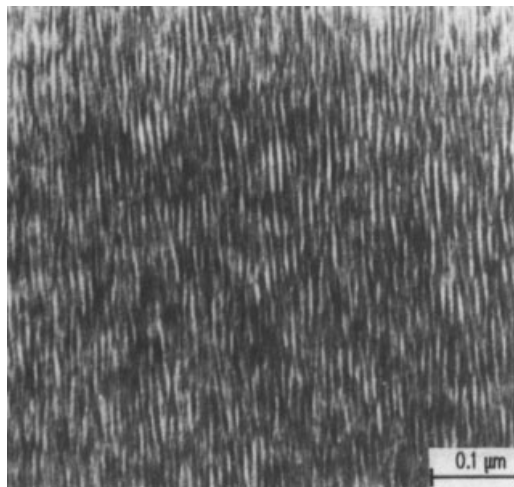


Figure 5-38. CTEM micrograph of equimolar TiO_2 - SnO_2 displaying a lamellar structure consisting of alternating TiO_2 - and SnO_2 -rich layers formed after aging at 900°C for 60 min. From Park et al. (1976).

number density of individual nuclei, each of which is surrounded by a solute-depleted zone in which no further nucleation can occur, may also lead to regularly arranged precipitates, i.e., modulated structures (Ardell et al., 1966; Doi et al., 1984, 1988; Doi and Miyazaki, 1986). On the other hand, initially interconnected microstructures in Cu-Ni-Fe alloys were found to break up into isolated plates (Piller et al., 1984). The later-stage microstructure is thus neither sufficient to draw any conclusions on the early-stage decomposition mode nor for a definition of a 'spinodal alloy'. We are therefore still left with the question as to what really is a spinodal alloy? To answer this question unequivocally, we must verify by any microanalytical technique that the amplitude of the composition waves increases gradually with time until the evolving second phase has finally reached its equilibrium composition. Such an experimental verification is a difficult task and, to our knowledge, was

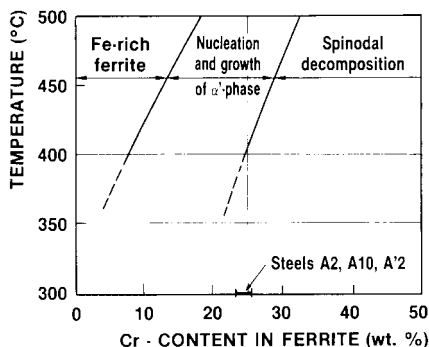


Figure 5-39. Variation of the phase boundaries in the Fe-Ni-Cr ferrite phase with chromium content as derived from microstructural observations. (After Auger et al., 1989.)

only shown for decomposing Fe-Co-Cr (Figs. 5-16 and 5-17), AlNiCo permanent magnetic materials (Hütten and Haasen, 1986) and Fe-Cr (Brenner et al., 1984) by means of AFIM, and for a phase separating polystyrene-polyvinylmethylether polymer mixture employing nuclear magnetic resonance methods (Nishi et al., 1975).

As has been outlined in Sec. 5.2.3, regardless of whether phase separation occurs via nucleation and growth or via spinodal decomposition, the underlying microscopic mechanism is diffusion of the solvent and solute atoms. In this sense there is thus no need to distinguish between the two different decomposition modes and the term 'spinodal alloy' is simply *semantic* in nature. This is also reflected in the various attempts to develop 'unified theories' comprising either mode.

From the practical point of view the microstructure of virtually all technical two-phase alloys corresponds to that of the later stages. Hence, the practical metallurgist worries little about the initial stages of unmixing but is instead interested in predicting the growth and coarsening behavior of precipitate microstructures in the later stages. This will be the subject of Secs. 5-6 and 5-7.

Table 5-2. TEM and AFIM studies on phase separating solids that revealed ‘spinodal precipitate microstructures’. If not otherwise stated the concentrations are in at.%.

Decomposing solid	Experimental technique	Morphology of two-phase microstructure	Authors
<i>Metallic alloys</i>			
Al-4 wt.% Cu	TEM (‘side-bands’)	Modulated structure	Rioja and Laughlin (1977)
Al-(2.4–3%) Li	HREM, X-ray diffraction		Radmilovic et al. (1989)
Cu ₃₋₄ Mn _x Al	TEM (‘side-bands’)	Modulated structure; at later stages Cu ₂ MnAl + Cu ₃ Al-plates	Bouchard and Thomas (1975)
Cu-(1.5–5.2 wt.%) Ti	TEM (‘satellite analysis’)	Modulated structure	Laughlin and Cahn (1975)
Cu-2.7% Ti	AFIM	Modulated structure	Biehl and Wagner (1982)
Ni-12% Ti	AFIM	Modulated structure	Grüne (1988)
Ni-29% Cu-21% Pd	TEM	Modulated structure	Murata and Iwama (1981)
Ni-base superalloys	AFIM	Short wavelength (≈2.5 nm) Cr fluctuation in γ-phase	Bouchon et al. (1990)
Nimonic 80 A	TEM (‘side-bands’)	Modulated structure	Wood et al. (1979)
Fe-25% Be	AFIM	Modulated structure	Miller et al. (1984, 1986)
CuNiFe	AFIM	Interconnected percolated structure (cf. Fig. 5-19c)	Piller et al. (1984)
CuNiFe	TEM (‘side-bands’)	Modulated structure (cf. Fig. 5-18)	Wahi and Stager (1984) Livak and Thomas (1974)
Co-10% Ti	FIM	Modulated structure	Davies and Ralph (1972)
Co-3 wt.% Ti	TEM (‘side-bands’)	Modulated structure	Singh et al. (1980)
-1 ... 2 wt.% Fe			
Mn-30 wt.% Cu	TEM, magnetic susceptibility	Interconnected structure	Yin et al. (2000)
<i>Steels</i>			
Cast Duplex stainless	TEM, AFIM	After decomposition original ferritic Fe-Cr-Ni shows ‘sponge-like’ structure	Auger et al. (1989)
Ferrous martensite			
Fe-15 wt.% Ni-1 wt.% C	TEM	Tweed structure	Taylor (1985)
Fe-25 wt.% Ni -0.4 wt.% C	TEM	Tweed structure	Taylor (1985)
Fe-13 ... 20 wt.% Mn	X-ray diffraction (‘side-bands’), TEM	Modulated structure at early times; isolated Fe ₂ Mo particles at later stages	Miyazaki et al. (1982)
<i>Amorphous alloys</i>			
Ti ₅₀ Be ₄₀ Zr ₁₀	AFIM	Wavy composition profile	Grüne et al. (1985)

Table 5-2. Cont.

Decomposing solid	Experimental technique	Morphology of two-phase microstructure	Authors
<i>Glasses, oxides</i>			
TiO ₂ -60 mole% SnO ₂	TEM	Tetragonal system with lamellar modulations along [001]	Stubican and Schultz (1970)
TiO ₂ -50 mole% SnO ₂	HREM	Tetragonal system with lamellar modulations along [001]	Horiuchi et al. (1984)
SiC-(50-75 mole%) AlN	TEM ('satellites')	Modulated structure	Kuo and Virkar (1987)

5.5.6 Monte Carlo Studies

The basic features of early stage decomposition as a stochastic process, without artificial distinction between nucleation, growth and coarsening regimes, have been extensively studied in model alloys by means of Monte Carlo (MC) computer simulations, mainly by Lebowitz, Kalos and coworkers (Lebowitz and Kalos, 1976; Binder et al., 1979; Marro et al., 1975, 1977; Penrose et al., 1978; Lebowitz et al., 1982; see also Binder and Fratzl, 2001; Chapter 6 of this volume). The binary model alloys are usually described in terms of a three-dimensional Ising model with pairwise nearest-neighbor interactions on a simple rigid cubic lattice the sites of which are occupied by either A or B atoms, and a phase diagram which displays a symmetrical miscibility gap centered at 50 at.% solute concentration (Fig. 5-40). The microscopic dynamics of this system have commonly been described by the Kawasaki model (Kawasaki, 1972). There a nearest-neighbor pair of lattice sites is chosen at random, then the atoms on those sites may be interchanged with a probability that depends on the energies of the configuration before and after the exchange in such a way that detailed balancing holds (Penrose, 1978). Monte

Carlo techniques are then employed to carry out this stochastic process.

The Kawasaki dynamics employed for MC simulations are far from being representative of a real binary alloy system as

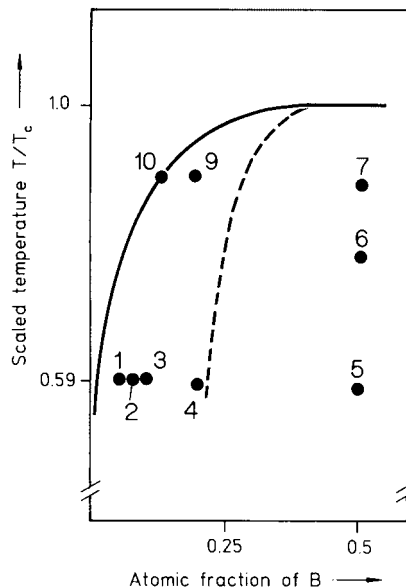


Figure 5-40. Phase diagram of the 3-dimensional Ising model approximating a binary model alloy. In terms of the mean field theory (Sec. 5.2.2) 'alloys' #1 to #4 are quenched into the metastable regime, 'alloys' #5 to #7 beyond the classical spinodal line are quenched into the unstable region of the phase diagram. (After Lebowitz et al., 1982.)

the atomic exchange is assumed to occur directly rather than indirectly via the vacancy mechanism. Nevertheless, MC simulations based on Kawasaki dynamics on an atomic scale yielded the time evolution of the cluster configuration and the structure function $S(\kappa, t)$ of model alloys quenched into any region below the solubility line (Fig. 5-40) without worrying about complicating factors, such as an insufficient quenching rate, excess vacancies, or lattice defects, which we commonly face when investigating real alloys (Sec. 5.3.2). Furthermore, MC simulations have allowed a critical examination of the various theoretical approaches in terms of cluster dynamics models or spinodal models to be made. For practical computational limitations, however, the maximum size of the model alloy has commonly been restricted to about $50 \times 50 \times 50$ lattice sites. Because of the size limitation, in general MC kinetic experiments can only cover the earlier stages of a precipitation reaction in alloys where the supersaturation is sufficiently high for the formation of a large number density of clusters or nuclei, and where the cluster sizes are still considerably smaller than the linear dimension of the model system. This is frequently not the case in real alloys.

In essence, the results from MC simulations based on Kawasaki dynamics have recovered the predictions both from the generalized nucleation theory of Binder and coworkers (Sec. 5.5.3) and from the non-linear spinodal LBM approach. In particular, the time evolution of the structure function in the kinetic Ising model displays qualitatively the same features as the corresponding ones obtained from the latter theories (cf. Figs. 5-31 and 5-35b) or from experiment (e.g., Fig. 5.32a).

For instance, $S(k, t)$ of 'alloy' # 4 (Fig. 5-41b), which according to Fig. 5-40 lies

close to the spinodal line within the metastable regime, evolves similarly to that of 'alloy' # 5 quenched into the center of the spinodal region (Fig. 5-41c). Thus, in agreement with the generalized nucleation theory and the LBM spinodal approach, but unlike the predictions of linearized CH theory of spinodal decomposition, MC simulations again reveal i) *no* evidence for any *abrupt change* of the decomposition kinetics on crossing the spinodal curve, ii) *no common cross-over* point of the $S(k)$ curves taken after different aging times, iii) *no exponential growth* of the scattering intensity for a certain time-independent wave vector in any time regime, and, furthermore, iv) the peak position of $S(\kappa, t)$ at κ_m is *not* found to be *time-independent* but is shifted towards smaller values of κ indicating the immediate growth of clusters.

Frequently, the MC data for the time evolution of the peak position (κ_m) and the peak height (S_m) of the structure function have been fitted to simple power laws (cf. Sec. 5.8.2), such as $\kappa_m(t) \propto t^{-a}$ and $S_m(t) \sim t^b$; a and b were estimated to range from 0.16 to 0.25 and 0.41 to 0.74, respectively, depending on the initial supersaturation of the 'alloy' (Marro et al., 1975, 1977; Sur et al., 1977). Lebowitz et al. (1982) pointed out, however, that due to the finite (small) size of the system it is difficult to extract from computer simulations precise and reliable information about the analytical form of $\kappa_m(t)$, for example and that it is possible to fit the same MC data with other functional forms than the power laws given above. (In Sec. 5.8.2 we will show, in fact, that apart from the late stages of coarsening, it is usually not feasible to interpret experimental kinetic data *over an extended aging period* in terms of a power-law behavior with a time-independent exponent.)

The Kawasaki dynamics are based on an unrealistic exchange mechanism between

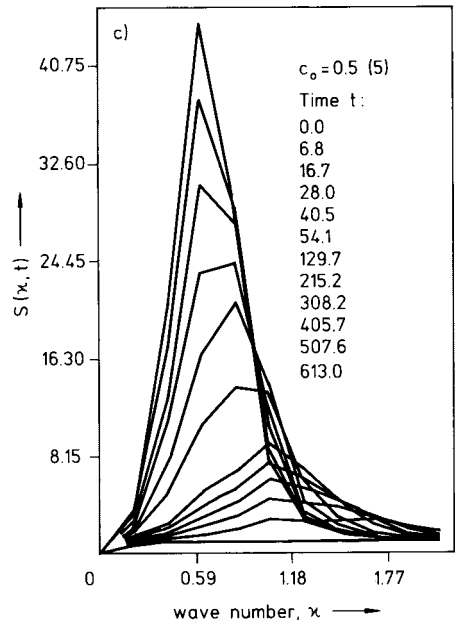
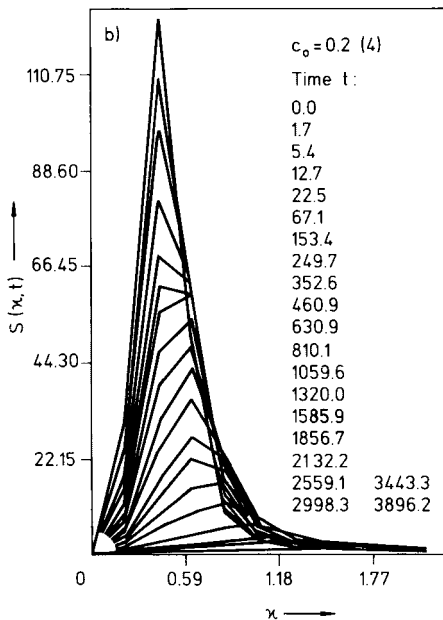
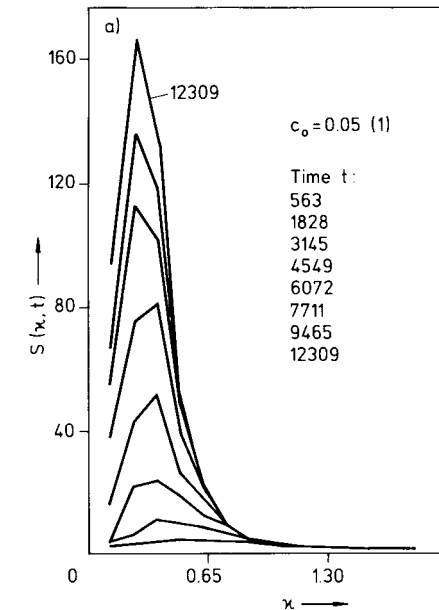


Figure 5-41. Time evolution of the structure function at $T/T_c = 0.59$ as obtained from MC computer simulations. With reference to Fig. 5-40:

a) for 'alloy' #1 with $c_0 = 0.05$ (after Lebowitz et al., 1982),

b) for 'alloy' #4 with $c_0 = 0.2$ (after Sur et al., 1977) and

c) for 'alloy' #5 with $c_0 = 0.5$ (after Marro et al., 1975). The given times are in units of a Monte Carlo step, i.e., the average time interval between two attempts at exchanging the occupancy of a specific site. The numerical results for $S(x, t)$ at the discrete values of x were connected by straight lines.

neighboring atoms. In order to account for the more realistic case of atomic diffusion being based on the vacancy mechanism, the Ising model was more recently extended to binary alloys comprising vacancies (Yaldram and Binder, 1991 a,b; Fratzl

and Penrose, 1994). Comparing the growth rates of clusters in the Ising model of a two-dimensional model alloy showed that the asymptotic regime of cluster coarsening ($\bar{R} \sim t^{1/3}$; cf. Sec. 5.6.2) is approached much faster with vacancy dynamics than

with Kawasaki dynamics, in particular at larger supersaturations; the cluster shapes are found not to depend on the particular dynamics model (Fratzl and Penrose, 1994).

In a first attempt to interpret experimental data with kinetic data obtained from MC simulations, Soisson et al. (1996) simulated phase separation in a Fe–1.34 at.% Cu alloy. The alloy was modeled as a rigid b.c.c. crystal with $2 \times L^3$ lattice sites (L varying from 32 to 64) containing one single vacancy; the energetics and the parameters of the atomistic kinetic model were adjusted to the thermodynamic and diffusion data of the Fe–Cu system. The MC results confirmed earlier results from magnetic SANS studies (Beaven et al., 1986) that the precipitating clusters are pure copper; furthermore the time evolution of the precipitated volume fraction agreed quite well with the one experimentally determined from resistivity measurements (Lê et al., 1992). In the later stages dynamical scaling behavior was shown to hold, indicating that the cluster pattern remains similar as aging time increases (cf. Sec. 5.8.1).

5.6 Coarsening of Precipitates

5.6.1 General Remarks

For most two-phase alloys, the simple model of diffusional growth of isolated non-interacting particles with uniform size, on which Eq. (5-47) is based, frequently does not give a realistic description of the further dynamic evolution of the precipitate microstructure beyond its nucleation stage. In reality, towards the end of the nucleation period a more or less broad particle size distribution $f(R)$ is established (Fig. 5-10 and 5-29). According to the Gibbs–Thomson equation (5-45), the solu-

bility $c_R(R)$ in the presence of *small* particles with a large ratio of surface area to volume is larger than that for *larger* ones. With reference to Eq. (5-43), this leads to a size-dependent growth rate, which is positive for larger particles with $\bar{c} > c_R$ and negative for smaller ones with $\bar{c} < c_R$. The growth rate becomes zero for particles with $\bar{c} = c_R$ which are in unstable equilibrium with the matrix. Their radius R^* is derived from Eq. (5-46) as

(5-61)

$$R^* \approx \frac{2\sigma_{\alpha\beta} V_\beta}{R_g T} \frac{1}{\ln(\bar{c}/c_\alpha^e)} \equiv K' \sigma_{\alpha\beta} \frac{1}{\ln(\bar{c}/c_\alpha^e)}$$

Hence, driven by the release of excess interfacial energy, larger precipitates will grow at the expense of smaller ones which dissolve again given rise to a change in the precipitate size distribution. This process, which is commonly referred to as *coarsening* or *Ostwald ripening*², frequently reduces the precipitate number density from $\approx 10^{25} \text{ m}^{-3}$ to less than 10^{19} m^{-3} in typical two-phase alloys during aging (cf. Fig. 5-3). Usually, the coarsening process is considered to be confined to the latest stages of a precipitation reaction. However, as will be shown in Sec. 5-7, coarsening may accompany the growth process outlined in Sec. 5.5.2, or may even start while the system is still in its nucleation period, depending on the initial supersaturation of the solid solution.

5.6.2 The LSW Theory of Coarsening

In essence, the coarsening of randomly dispersed second-phase particles is a multi-particle diffusion problem which is difficult to handle theoretically. In their classic LSW coarsening theory, Lifshitz and Slyo-

² In its original meaning, Ostwald ripening is confined to a coarsening reaction where the second-phase particles act as the only sinks or sources of solute atoms.

zov (1961), and Wagner (1961) calculated the time evolution of $f(R, t)$ which satisfies the continuity equation:

$$\frac{\partial f}{\partial t} + \frac{\partial}{\partial R} \left[f \frac{dR}{dt} \right] = 0 \quad (5-62)$$

On the basis of the continuity equation and of Eq. (5-43), the time evolution of the mean particle radius $\bar{R}(t)$ and the precipitate number density $N_v(t)$ are derived. Certain approximations, however, had to be made in order to solve the equations of motion analytically:

- Both terminal phases α and β are dilute solutions; their thermodynamics can be described by a dilute solution and the linearized version (Eq. 5-46) of the Gibbs–Thomson equation may be used.
- The precipitated volume fraction $f_p = (4\pi/3) \bar{R}^3 N_v$ is close to zero. In such a dilute system interparticle diffusional interactions such as those occurring in more concentrated alloys (cf. Sec. 5.6.3) can be neglected, and a particle only interacts with the infinite matrix.
- $f_p \approx \text{const.}$, i.e., the decomposition is close to completion with the supersaturation $\Delta c \approx 0$. This inherently confines the LSW theory to the late stages of a precipitation reaction.

With these assumptions the LSW theory yields in the asymptotic limit $\Delta c(t) \rightarrow 0$ temporal power laws

$$\bar{R}^3(t) = K_R^{\text{LSW}} t \quad (5-63a)$$

$$N_v(t) = K_N^{\text{LSW}} t^{-1} \quad (5-63b)$$

$$\Delta c(t) = K_C^{\text{LSW}} t^{-1/3} \quad (5-63c)$$

for the time evolution of the average particle radius, the particle density and the supersaturation, respectively, and a particle size distribution $f_{\text{LSW}}(R/\bar{R})$, the shape of which is time invariant under the scaling of the average particle size \bar{R} (Fig. 5-42). It

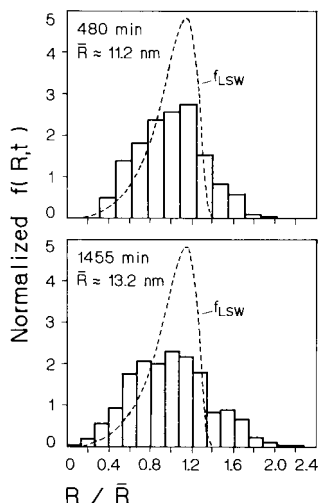


Figure 5-42. CTEM analyses of the normalized γ' -particle size distribution in Ni–8.74 wt.% Ti after aging at 692 °C for the given times. For comparison, the shape-invariant distribution function f_{LSW} of the LSW theory is included. (After Ardell, 1970.)

must be emphasized that these predictions hold only in the limit t approaching infinity, since the particle size distribution that is present at the beginning of coarsening can be quite different from the time-invariant form.

Extensions of the LSW theory to binary systems with non-zero solubilities and non-ideal solution thermodynamics, and adequate modification of the Gibbs–Thomson equation, have reproduced the temporal power laws (Eq. 5-63). The corresponding rate constants for this more realistic case were derived as (Schmitz and Haasen, 1992; Calderon et al., 1994):

$$K_R = \frac{8D V_\beta \sigma_{\alpha\beta}}{9(c_\beta^e - c_\alpha^e)^2 G_\alpha''} \quad (5-64a)$$

$$K_N = \frac{3 f_p}{4\pi} \frac{1}{K_R f_3} \quad (5-64b)$$

$$K_C = \frac{9(c_\beta^e - c_\alpha^e)}{4D} K_R^{2/3} \quad (5-64c)$$

G''_{α} is the second derivative of the molar Helmholtz energy of the α phase; f_3 is the third moment of the time-independent scaled particle radius distribution function $f(R/\bar{R})$ which in the zero volume fraction limit (i.e. $f = f_{\text{LSW}}$; see Sec. 5.6.3) is 1.129.

For an ideal solution and the dilute solution limit (i.e. $c_{\alpha}^e \ll 1$, $c_{\beta}^e \approx 1$) the rate constant K_R (Eq. 5-64a) adopts the form

$$K_R^{\text{LSW}} = \frac{8D V_{\beta} c_{\alpha}^e \sigma_{\alpha\beta}}{9R_g T} \quad (5-65)$$

of the original LSW theory (Calderon et al., 1994).

Numerous experimental studies on a wide variety of two-phase alloys attempted to examine the coarsening kinetics predicted by the LSW theory. Regardless of the particular alloy system and the micro-analytical technique employed (e.g., CTEM on Ni–Al, Ni–Ti: Ardell, 1967, 1968, 1970; and on Ni–Si: Cho and Ardell, 1997; AFIM on Ni–Al: Wendt and Haasen, 1983; SANS on Fe–Cu: Kampmann and Wagner, 1986), these studies frequently revealed the experimental size distribution function to be considerably broader than $f_{\text{LSW}}(R/\bar{R})$ (Fig. 5-42), whereas a plot of \bar{R}^3 or N_v^{-1} vs. t yielded more or less straight lines (due to limited statistics, the error bars are usually rather large). From the slopes of these *LWS plots* the product $\sigma_{\alpha\beta} D$ can be derived with c_{α}^e usually taken from the known phase diagram. Frequently Δc was also measured and plotted versus $t^{-1/3}$ (Eq. (5-63c)) in order to determine $D/\sigma_{\alpha\beta}^2$ (e.g., Ardell, 1967, 1968, 1995; Wendt and Haasen, 1983). Thus apparently absolute values for both $\sigma_{\alpha\beta}$ and D have been determined from values of $\sigma_{\alpha\beta} D$ and $D/\sigma_{\alpha\beta}^2$. However, the rate constants K_R^{LSW} and K_C^{LSW} in Eq. (5-63) were derived with the assumption c): $\Delta c \approx 0$ or $f_p = \text{const.}$ Once this condition is fulfilled, it is no

longer feasible to follow minor changes of Δc with time quantitatively by any of the experimental techniques frequently employed, such as CTEM, AFIM, SAXS or SANS (Sec. 5.3.1); in the asymptotic limit $\Delta c \rightarrow 0$, it even appears difficult to measure $\Delta c(t)$ in alloys containing a ferromagnetic phase with magnetic techniques (Ardell, 1967, 1968), though these direct methods are certainly more sensitive than CTEM, AFIM or SAS. On the other hand, in those earlier decomposition stages, where $\Delta c(t)$ is experimentally accessible, an LSW analysis *cannot* be performed, and, in particular, the rate constant K_R^{LSW} (Eq. (5-65)) is no longer valid (see Sec. 5.7.4.3). Thus, in practice, an LSW analysis based on Eqs. (5-63) and (5-65), at its best, can be performed only in dilute systems and yields only a value for the *product* $D\sigma_{\alpha\beta}$. This fact was ignored in most LSW analyses based on the independent measurement of both $\bar{R}(t^{1/3})$ and $\Delta c(t^{-1/3})$; hence, the values of D and $\sigma_{\alpha\beta}$ derived from this type of analysis must be regarded with some reservation. However, frequently the interfacial energy was derived exclusively from Eq. (5-65) under the assumption that the effective diffusivity D is identical with that obtained from an extrapolation of available high-temperature data to the aging temperature, thus neglecting the influence of quenched-in vacancies (Sec. 5.3.2.1). (In Sec. 5.7.4.4 two different methods will be discussed which allow a separate derivation of $\sigma_{\alpha\beta}$ and D to be made from experimental data, one method without even knowing $\Delta c(t)$.)

For non-ideal solid solutions, $\sigma_{\alpha\beta}$ must be derived from Eq. (5-64a). Apart from knowing D , this requires detailed information on the thermodynamics of the α matrix phase in order to derive G''_{α} . For many binary alloys the necessary thermodynamic functions have become available via the

CALPHAD method (Sec. 5.2.4). If not available, they must be derived from more or less adequate solution models, with the regular solution model being the less sophisticated one. For the case of a binary model alloy with a miscibility gap and regular solution behavior, Calderon et al. (1994) demonstrated that depending on aging temperature, $\sigma_{\alpha\beta}$ may be significantly different if assessed from the correct form of the rate constant for a regular solution or from the original LSW form, i.e. Eq. (5-65).

5.6.3 Extensions of the Coarsening Theory to Finite Precipitate Volume Fractions

There have been many efforts to extend the LSW theory to the more realistic case of a finite precipitated volume fraction and to investigate its influence on the shape of the distribution function and the coarsening kinetics (Ardell, 1972). The central challenge is to determine the effects of interparticle diffusional interactions on the growth rate of a particle of a given size. Theories accounting for these diffusional interactions fall into two broad categories: effective medium theories, and statistical theories that are based upon a solution to the diffusion field in this multiparticle system. All theories are in agreement that the presence of a non-zero volume fraction does not change the exponents of the temporal power laws given by LSW (Eq. (5-63)) or the existence of a time-independent scaled particle size distribution. The presence of a non-zero volume fraction, however, does change the amplitudes of the temporal power laws and the shape of the scaled distribution functions. The rate constant K_R^{LSW} increases with the volume fraction (Fig. 5-43) and the time-independent distribution function becomes broader and

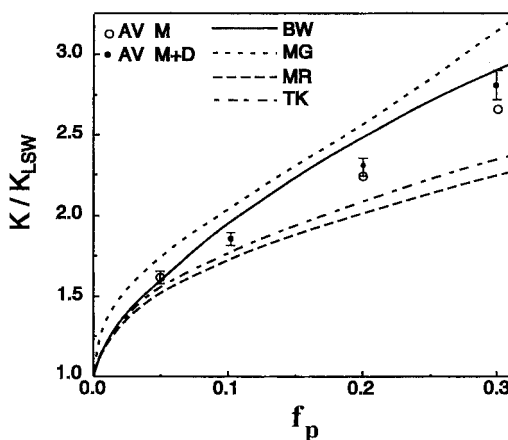


Figure 5-43. The rate constant K , relative to that of LSW, K_{LSW} , as a function of the volume fraction f_p . Shown on the figure are the predictions of Brailsford and Wynblatt (BW), Marsh and Glicksman (MG), Marqusee and Ross (MR), Tokoyama and Kawasaki (TK) and the simulations of Akaiwa and Voorhees (AV) where \circ denote the use of the monopole approximation of the diffusion field and \bullet denote monopole and dipole approximations to the diffusion field.

more symmetric as the volume fraction increases (Fig. 5-44). The reason for the increase in the rate constant is clear: as the volume fraction increases, shrinking particles move closer to growing particles and thus the concentration gradients are larger, and the rate of growth and shrinkage increases.

The effective medium theories determine the growth or shrinkage rate of a particle of a given size using a medium that is constructed, presumably, to give the statistically averaged growth rate of particles of a certain size. Examples of such theories are due to Tsumuraya and Miyata (1983), Brailsford and Wynblatt (1979) and, more recently, Marsh and Glicksman (1996). While the effective medium employed by Brailsford and Wynblatt has been shown analytically to be consistent with a solution to the multiparticle diffusion equation, this

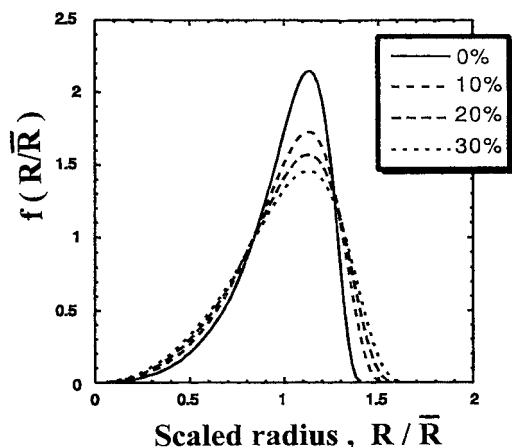


Figure 5-44. Steady-state (time-invariant) precipitate size distributions at various volume fractions. For comparison the corresponding LSW distribution for zero volume fraction is also shown. (After Tokuyama and Kawasaki, 1984.)

has not been done with the other theories. This, then, is the major disadvantage of these theories. A significant advantage, however, is that they are simple to apply and make predictions over a wide range of volume fractions, even as high as 0.95. In addition, both the Brailsford and Wynblatt and Marsh and Glicksman theories correspond reasonably well with the first-principles statistical theories for volume fractions below 0.3. Above 0.3, these are the only theories that make predictions on the rate constants and particle size distributions.

The statistical theories are based upon a solution to the multiparticle diffusion problem. The particles are assumed to be spherical and the concentration in the matrix at the interface of each particle is given by the Gibbs–Thompson equation, (5-45). For volume fractions below 0.1 the solution to the diffusion equation is represented as a monopole source or sink of solute in the center of each particle (Weins and Cahn, 1973). At higher volume fractions dipolar

terms must be included (Akaiwa and Voorhees, 1994). Given, then, a spatial distribution of particles and a particle size distribution, it is possible to determine the coarsening rate of each particle. The more challenging step is to determine from this information the statistically averaged growth rate of a particle of a given size. This can be done analytically (Marqusee and Ross, 1984; Tokuyama and Kawasaki, 1984; Yao et al., 1993), or numerically by placing a large number of particles in a box and determining their coarsening rate (Voorhees and Glicksman, 1984; Akaiwa and Voorhees, 1994; Mandyam et al., 1998). Although all of these theories begin with the same solution to the diffusion equation, none of the predictions for the rate constants and particle size distributions are in agreement, illustrating the difficulty in performing the statistical averaging.

Nevertheless, a number of qualitative effects of a finite volume fraction become clear after examining the predictions of these theories. (a) The growth rate of a particle of a given size is a function of its surrounding particles. For example, if a particle of size R_1 is surrounded by particles of radii $R < R_1$, this particle will grow, but if this particle is surrounded by particles with radii $R > R_1$, it will shrink. Thus, unlike in the LSW theory the growth rate of a particle is not solely a function of its size. (b) The local diffusional interactions give rise to spatial correlations between particles that are not random. For example, the average interparticle separation for a system undergoing coarsening is larger than that for a random spatial distribution. This is because the probability of finding a small and large particle almost touching, which can occur in a system with a random spatial distribution, is low, as the strong diffusional interactions that occur when a large and a small particle are located close to

each other causes this small particle to disappear. At larger interparticle separation distances, however, large particles tend to be surrounded by small particles as they are feeding solute to the growing large particles (Akaiwa and Voorhees, 1994). Thus, there are both spatial and particle size correlations (Marder, 1987). Information on the spatial correlations between particles is needed to determine the structure function that is measured using small angle scattering. The agreement between the predictions of Akaiwa and Voorhees (1994) for the structure function and the experimentally measured structure function in Al–Li alloys is reasonable (Che et al., 1997). (c) Another effect of interparticle diffusional interactions is that the center of mass of the particles is not fixed, but moves in a manner consistent with the concentration gradients in the system. This particle motion has been determined theoretically (Marder, 1987; Akaiwa and Voorhees, 1994), and has been observed in experiments on coarsening in transparent solid–liquid mixtures (Voorhees and Schaefer, 1987).

Experiments in which the coarsening kinetics of solid particles in a liquid (Fig. 5-45) have been measured show clearly that the coarsening rate increases with volume fraction (Hardy and Voorhees, 1988, and references therein). In two-phase solid systems, however, there are reports that the rate constant is independent of the volume fraction (Cho and Ardell, 1997). The reason for these contradictory results may be the elastic stress that is present in the two-phase solid systems. Although the predicted particle size distributions of the non-zero volume fraction theories are broader than those of LSW, nearly all experimentally measured particle size distributions are broader than the predictions of the non-zero volume fraction theories. Until recently there have been no experiments per-

formed in a system wherein the materials parameters, such as the interfacial energy and diffusion coefficient, are known (independent of a coarsening experiment) and where this system satisfies all the assumptions of theory. Therefore, it is unclear if the disagreement between theory and experiments is due to an artifact of the system employed in the experiments or a defect in the theories. Recent experiments that employ a system in which the materials parameters are known and satisfy all the assumptions of theory have been performed using solid Sn-rich particles in a Pb-rich eutectic liquid (Alkemper et al., 1999). There was no convective motion of the particles because the experiments were performed in the microgravity environment of the Space Shuttle. These experiments show that there can be very long transients associated with the coarsening process. In particular, during the course of the experiment the initially broad particle size distribution evolved slowly towards that predicted by theory. Even with a factor of four change in the average particle size the distribution never reached the steady-state distribution predicted by theory. This may be the reason why the experimentally measured particle size distributions (measured using other systems) rarely agree with theory. Nevertheless, the evolution of the distribution was found to correspond quite well with the predictions of two theories for transient Ostwald ripening.

Coarsening of two-phase alloys with *modulated* microstructures consisting of large volume fractions ($f_p \geq 30\%$) of *isolated* coherently misfitting particles, e.g., Cu–Ni–Fe and Cu–Ni–Cr (Fig. 5.19), Cu–Ni–Si (Yoshida et al., 1987), or modulated Co–Cu (Miyazaki et al., 1986), was reported to be rather sluggish. The time exponent a of the coarsening rate, defined by $\bar{R} \propto t^a$, of these alloys was consistently

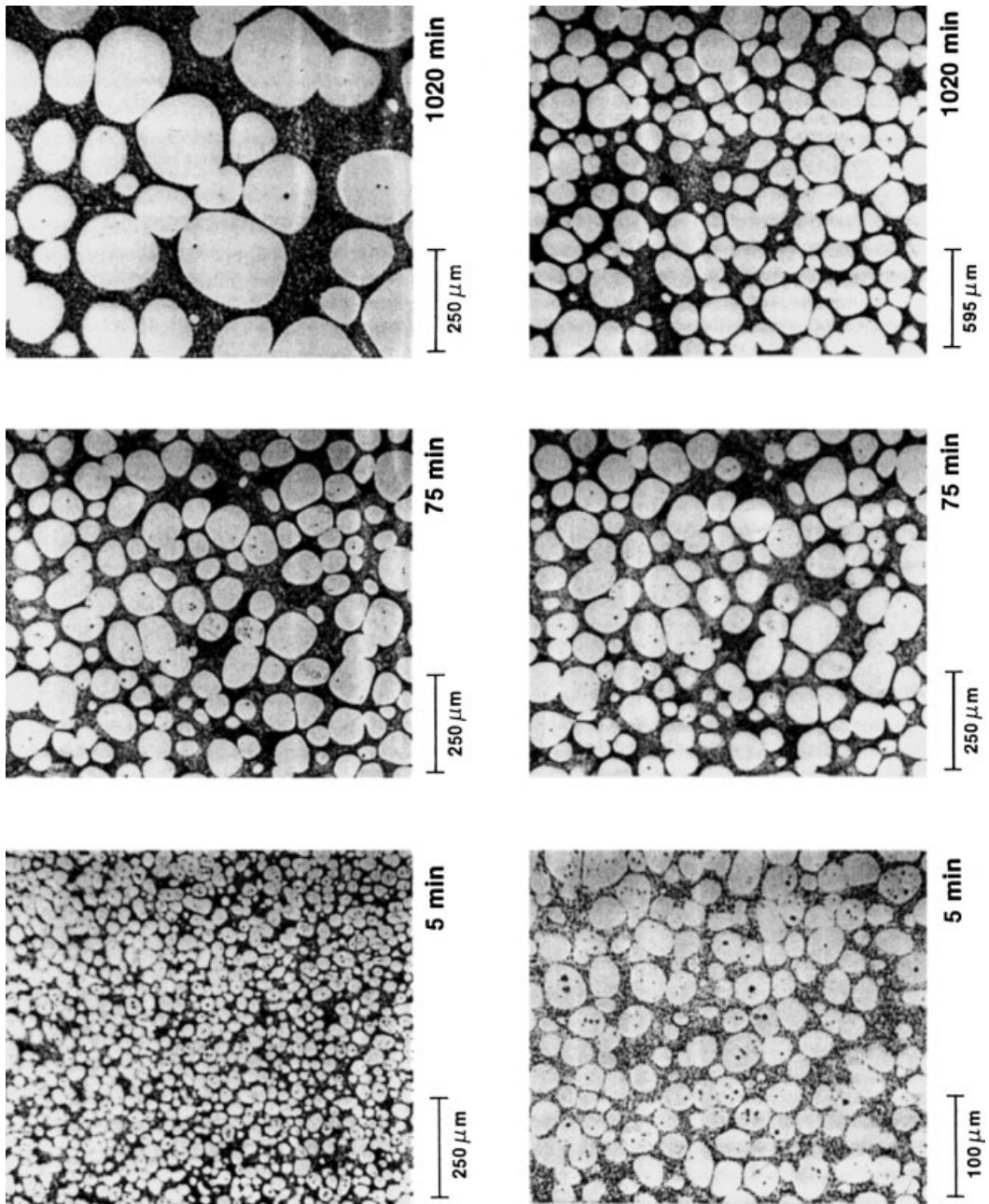


Figure 5-45. Evolution of Sn-rich particles with $f_p = 0.64$ in a liquid Pb–Sn matrix during coarsening at 185°C. The top row is at constant magnification and illustrates a typical coarsening process. For scaling the absolute size of the microstructure, in the bottom row the magnification has been multiplied by the ratio of the average intercept length \bar{L} at time t to \bar{L} at $t = 75$ min. (From Hardy and Voorhees, 1988.)

found to be less than $1/3$, the value expected from conventional coarsening theory on the basis of Ostwald ripening. Furthermore, it was shown that coarsening of a $\langle 100 \rangle$ modulated structure in *less concentrated* Co–Cu alloys (≤ 20 at.% Cu; $f_p \approx 20\%$) still follows the $t^{1/3}$ kinetics, whereas the coarsening rate becomes extremely small in a Co–50 at.% Cu alloy ($f_p \approx 50\%$), as indicated by the small time exponent $a < 1/50$ (Miyazaki et al., 1986).

As was pointed out in Sec. 5.5.5 “mottled structures” or “interconnected microstructures” can result from spinodal decomposition of alloys with *vanishing* coherency strains. Unlike for modulated structures, elastic interactions can therefore be ruled out as a likely reason for the stability of interconnected microstructures against coarsening. Nevertheless, the coarsening rate of interconnected phases is frequently *also* found *not* to follow the $t^{1/3}$ kinetics. Experimental studies on the coarsening kinetics of interconnected phases in hard magnet materials such as Fe–Cr–Co (Zhu et al., 1986), Al–Ni–Co (Hütten and Haasen, 1986; Katano and Iizumi, 1982) instead yielded time exponents a between $1/4$ and $1/10$. Evidently, an adequate theoretical description of the coarsening kinetics of both modulated and mottled microstructures has to go beyond the mere modeling of diffusional interaction between an ensemble of isolated *spherical* particles.

5.6.4 Other Approaches Towards Coarsening

In addition to the LSW-type coarsening mechanism, which is based on the evaporation and condensation of *single* atoms from dissolving and growing precipitates, Binder and Heermann (1985) also considered a *cluster-diffusion-coagulation mechanism* likely to become operative dur-

ing the *intermediate* stages of coarsening. Depending on the specific (local) microscopic diffusional mechanism which is assumed to contribute to the shift of the center of gravity of the particles and their likely coagulation, the time exponents a for the related coarsening rate were evaluated between $a = 1/6$ and $a = 1/4$ and hence are smaller than predicted by the LSW theory ($a = 1/3$).

According to Fig. 5-32b the position of the SANS peak intensity at κ_m varies in proportion to $t^{-0.25}$. This might, in fact, be interpreted in terms of a cluster-diffusion-coagulation mechanism being dominant prior to LSW-type coarsening. In Sec. 5.8.2 it will be shown, however, that even if single atom evaporation or condensation in the LSW sense is assumed to be the only microscopic mechanism contributing to particle growth, the time exponent a already displays a strong time dependence. Depending on the initial supersaturation of the alloy, $a(t)$ may then vary between almost zero and 0.5 during the course of a precipitation reaction. The question of whether a even reaches its asymptotic value $1/3$ depends on whether the experiment spans a sufficiently long range of aging times.

From the experimental point of view it thus does not appear feasible to decide merely on grounds of the measured time exponent whether the cluster-diffusion-coagulation mechanism influences the growth or coarsening kinetics of a precipitate microstructure.

5.6.5 Influence of Coherency Strains on the Mechanism and Kinetics of Coarsening – Particle Splitting

The LSW theory, as well as the extensions to finite volume fractions, assume that the coarsening process is driven entirely by the associated release of interfa-

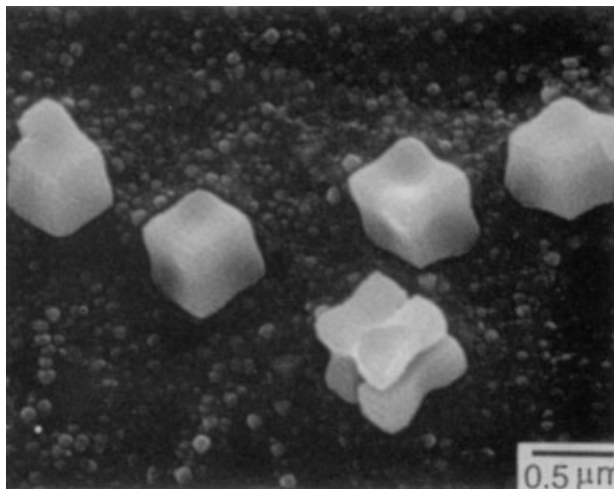


Figure 5-46. High-magnification scanning electron micrograph of concave γ' -precipitates in an aged Ni-23.4Co-4.7Cr-4Al-4.3Ti (wt.%) superalloy prior to splitting. (Reproduced by courtesy of D. Y. Yoon (Yoo et al., 1995).)

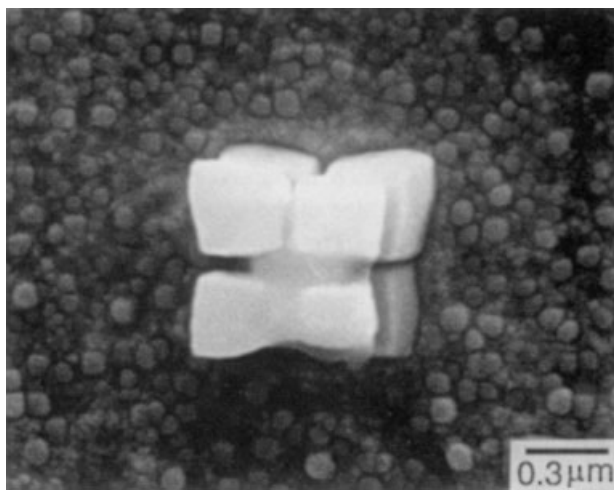


Figure 5-47. As in Fig. 5-46, showing a split γ' -precipitate.

cial energy. In the presence of elastic stresses, however, such as those induced by coherency strains, the coarsening process can be driven by the release of both the interfacial and elastic energy. The elastic energy can be decomposed into an elastic self-energy, the elastic energy of an isolated particle in an infinite medium, and an interaction energy that is due to the presence of other particles in the system. The elastic self-energy is a strong function of the shape of a particle and is responsible for the shape bifurcations mentioned in Sec. 5.4.2. Moreover, the elastic interac-

tion energy is also a function of the shape of the particles, the importance of which has been emphasized by Onuki and Nishimori (1991).

In the presence of misfit strains, inter-particle elastic interactions can give rise to pronounced spatial correlations between the precipitates. Ardell et al. (1966) proposed that the elastic interactions between γ' -Ni₃Al particles are responsible for the alignment of the particles along the elastically soft directions of the crystal during coarsening. The resulting structure of many nickel-based alloys reveals that the

γ' -type precipitates are rather uniformly distributed (Fig. 5-19b), which is sometimes reminiscent of modulated structures. These strong spatial correlations develop by two basic mechanisms. The first is that particles aligned as stringers along the elastically soft directions will grow at the expense of particles not so aligned (Ardell et al., 1966). The second is that alignment will occur by particles migrating through the matrix (Voorhees and Johnson, 1988). This migration is a result of the elastic interactions inducing a non-uniform interfacial concentration and, hence, non-uniform concentration gradients along the particle interface.

It has been observed (Miyazaki et al., 1982; Doi et al., 1984; Kaufmann et al., 1989) that during coarsening, individual γ' -type precipitates can split into groups of two or eight smaller cuboidal particles. Using a deep etching technique and a scanning electron microscope, the recent experiments of Yoo et al. (1995) have illustrated clearly the three-dimensional morphology of the particles undergoing the splitting process (Figs. 5-46 and 5-47). Such a splitting process clearly cannot be driven by a reduction in interfacial energy and thus the cause of the splitting has been ascribed to a decrease in the elastic energy. Although the elastic self-energy does not change on splitting, *assuming that the particle morphologies are the same before and after splitting*, if the elastic interaction energy is negative, e.g., as is the case for particles aligned along the elastically soft directions of an elastically anisotropic crystal, the total elastic energy will decrease upon splitting (Khachaturyan and Airapetyan, 1974; Khachaturyan et al., 1988; Johnson and Cahn, 1984; Miyazaki et al., 1982). However, constraining the morphology of the particles to be invariant upon splitting neglects the effects of the elastic interaction

on the morphology of the particles and hence on the magnitude of the elastic interaction energy itself. In fact, two-dimensional calculations (Thompson et al., 1994) wherein the morphology of a particle was not constrained found that a misfitting fourfold symmetric particle in an elastically anisotropic homogeneous crystal was stable with respect to interfacial perturbations at least up to $L = 26$ (cf. Sec. 5.4.2). Thus the conclusion reached on the basis of elastic energy considerations that splitting is possible appears to be due to the assumption that the morphology of the precipitate is invariant upon splitting. Miyazaki et al. (1982) proposed that the splitting process begins with the formation of the matrix phase in the middle of the precipitate. This idea was verified through the diffuse interface calculations of Wang et al. (1991). However, the experimental results of Yoo et al. (1995) confirmed the hypothesis of Kaufmann et al. (1989) that the splitting process is initiated via the amplification of perturbations along the precipitate-matrix interface and not by the formation of the matrix phase in the center of the particle. Thus, the cause of the splitting remains, at this point, unexplained. However, the stability of a cuboidal shaped particle in three dimensions has not been examined, and the effects of elastic inhomogeneity are still to be explored fully. Recent work by Lee (2000) has shown that splitting is possible for certain differences in elastic constants between particle and matrix.

In addition to inducing particle migration and selective coarsening, elastic interactions may alter the kinetics of the coarsening process. Calculations employing fixed (spherical or circular) particle morphologies have shown that in a two-particle system inverse coarsening is possible, wherein a small particle will grow at the expense of a large particle (Johnson, 1984;

Miyazaki et al., 1986; Johnson et al., 1990). However, similar calculations of the evolution of two precipitates in an elastically anisotropic homogeneous system wherein the morphology is not fixed have shown that inverse coarsening does not occur (Su and Voorhees, 1996). The difference between these two results is due to the strong shape dependence of the elastic interaction energy; the particle morphology must be allowed to change in a manner that is consistent with the elastic and diffusion fields in the system. Inverse coarsening can still occur, however, when more than two particles interact elastically (Su and Voorhees, 1996; Wang et al., 1992). If, however, L is sufficiently large and the system is both elastically anisotropic and inhomogeneous, Schmidt et al. (1998) have shown that two arbitrarily shaped particles can indeed be stable with respect to coarsening. These two results imply that it is essential not to constrain the morphology of the precipitates when computing the evolution of the microstructure and that elastic inhomogeneity can be an important factor in determining the stability of the system with respect to coarsening. Paris et al. (1995) have also emphasized the importance of elastic inhomogeneity in determining the stability of a system with respect to coarsening. This implies that determining the evolution of a system during coarsening with a large number, sufficient to provide accurate statistical information, of arbitrarily shaped particles is a very challenging problem. Nevertheless, some attempts have been made. For example, Onuki and Nishimori (1991) have found through diffuse interface calculations that when the precipitates are softer than the matrix, stabilization of the system with respect to coarsening may be possible. Although the size of the system examined is small, the exponent of the temporal power law for the average

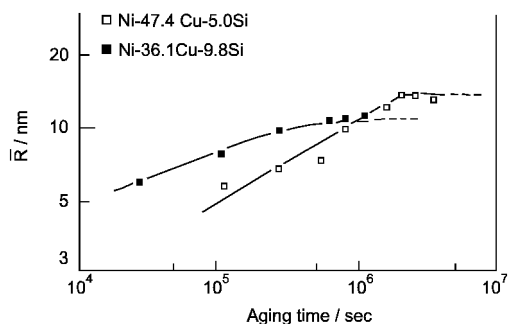


Figure 5-48. Variation of the mean radius \bar{R} of γ' -particles with aging time in two different Ni-Cu-Si alloys with $f_p = 0.18$ (Ni-47.4 Cu-5Si) and $f_p = 0.5$ (Ni-35.1 Cu-9.8 Si), numbers indicate at.%. (After Miyazaki and Doi, 1989.)

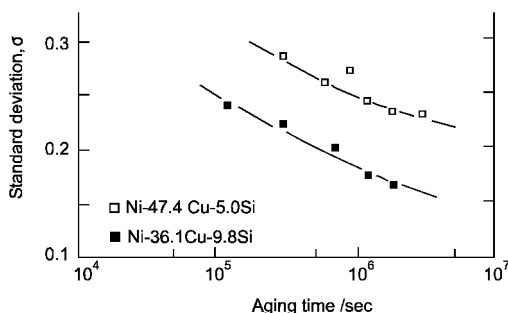


Figure 5-49. Variation of the standard deviation σ of the γ' -particle size distribution with aging time for the same alloys as in Fig. 5-48. (After Miyazaki and Doi, 1989.)

particle size is time dependent and, at the very least, much less than the classical value of $1/3$ predicted by the LSW theory. In contrast, Ising model simulations (Fratzl and Penrose, 1996) and diffuse interface calculations (Nishimori and Onuki, 1990) in an elastically anisotropic homogeneous system do not show stabilization with respect to coarsening, again indicating the importance of elastic inhomogeneity. By assuming that the systems are statistically invariant, Leo et al. (1990) have shown that the exponent for the average size scale of the precipitates can be altered by the presence of elastic stress, in this case attaining

a value of $1/2$. This result does not contradict Onuki's, as the onset of stabilization clearly violates the statistically time invariant assumption of Leo et al.

There have been many investigations of the kinetics of coarsening in elastically stressed solids. Experiments performed in Ni–Cu–Si alloys by Yoshida et al. (1987), and Miyazaki and Doi (1989) show a clear departure from the classical $t^{1/3}$ predictions for the average particle radius with the growth rate of the average particle radius and the width of the particle size distribution decreasing in time (Figs. 5-48 and 5-49). A similar departure from the $t^{1/3}$ function has also been observed in the Ti–Mo system by Langmayr et al. (1994). In contrast, in Ni–Al (Ardell, 1990), Ni–Mo–Al (Fährmann et al., 1995) and Ni–Si (Cho and Ardell, 1997) alloys the exponent for the average particle size appears to be $1/3$. The rate constant, however, appears to be independent of the volume fraction of precipitate. Although it has been speculated that elastic interactions are responsible for this result, this has not been confirmed due to the difficulty of performing calculations in systems that are sufficiently large to yield accurate statistical information.

5.7 Numerical Approaches Treating Nucleation, Growth and Coarsening as Concomitant Processes

5.7.1 General Remarks on the Interpretation of Experimental Kinetic Data of Early Decomposition Stages

In this section we turn our attention to decomposition studies of alloys with sufficiently high nucleation barriers ($\Delta F^*/kT \gtrsim 7$) decomposing via nuclea-

tion, growth and coarsening. In contrast to the considerations of the preceding sections we now ask how experimental kinetic data can be interpreted if they refer to very early decomposition stages which include *nucleation, growth and coarsening* as concomitant rather than consecutive processes on the time scale. In attempting such interpretations we have to recall that these early decomposition stages especially are characterized by dramatic changes in supersaturation and, thus, in the driving forces for nucleation and growth processes. Furthermore, during these early stages the size distribution function evolves and is subjected to drastic alterations with rather short aging periods where nucleation, growth and coarsening must be seen as competing and overlapping processes. Evidently these rather complicated phenomena are not properly accounted for by splitting the course of decomposition into a nucleation regime, a growth regime, and a coarsening regime. Moreover, the kinetic theories developed for either regime (Secs. 5.5.1, 5.5.2 and 5.6, respectively) are based on idealized assumptions which are frequently not expected to be close to reality. This holds true for the classical nucleation theories of Volmer and Weber and Becker and Döring (Sec. 5.5.1). In these theories the supersaturation is assumed to be constant. This may only be fulfilled – if at all – during the *earliest* nucleation stage. Furthermore, these theories are based on artificial assumptions of the cluster size distribution in the vicinity of the critical radius (Fig. 5-24), which are not consistent with the fact that during the nucleation process, many growing precipitates slightly larger than the critical size are formed. The theory of diffusional growth by Zener and Ham (Sec. 5.5.2) describes only the time evolution of precipitates with *uniform* size. However, towards the end of nucleation as well as at the be-

gining of the LSW coarsening regime we certainly have to deal with a *polydispersed* precipitate microstructure. Thus, even if nucleation and LSW coarsening were to be well separated on the time scale, in between these two regimes the Zener–Ham theory cannot be expected to correctly predict the measured growth kinetics quantitatively. Finally, the coarsening theories of Lifshitz, Slyozov and Wagner are based on the linearized version of the Gibbs–Thomson equation (Eq. (5-46)) and on the assumption that the supersaturation is close to zero. These restrictions also hold for the more recent theories (Sec. 5.6.3) which take into account finite precipitated volume fractions and overlapping concentration profiles between precipitates.

Thus, any theory for the kinetics of precipitation that can be employed either for a more realistic interpretation of experimental data or for a prediction of the dynamic evolution of a second-phase microstructure under elevated temperature service conditions, has to treat nucleation, growth and coarsening as concomitant processes. This was accounted for in the cluster dynamics theories of Binder and coworkers (Secs. 5.5.3, 5.6.4 and Binder and Fratzl (2001), Chapter 6 of this volume). However, as was pointed out by these authors (Binder et al., 1978; Miold and Binder, 1977), the theory developed yields a reasonable *qualitative* prediction of the features of experimentally observable quantities but does not attempt their *quantitative* interpretation.

A further decomposition theory treating nucleation, growth, and coarsening as concomitant processes was developed by Langer and Schwartz (LS model; Langer and Schwartz, 1980). This theory was formulated for describing droplet formation and growth in near-critical fluids. It was later modified by Wendt and Haasen (1983) and further improved by Kamp-

mann and Wagner (MLS model; 1984) in such a way that it could be applied for the description of the kinetics of precipitate formation and growth in metastable alloys of rather high degrees of supersaturation. The MLS model is still based on the same assumptions as the original LS theory. In particular, the explicit form of the size distribution is not accounted for and the long-time coarsening behavior is assumed to match the LSW results, i.e., is described by Eqs. (5-63 a, 5-65). A priori, it is not possible to foresee the influence of these assumptions on the precipitation kinetics.

Therefore, Kampmann and Wagner (KW; 1984) have devised an algorithm that accurately describes the entire course of precipitation within the framework of classical nucleation and growth theories. This algorithm is accurate in the sense that, unlike the LS and the MLS theories, it contains no simplifying assumption; in particular, in this algorithm, termed the *Numerical model (N model)*, the time evolution of the size distribution is computed without any approximations. From a comparison of the N model with experimental data it is possible to determine some crucial precipitation parameters of the particular alloy system as well as to scrutinize the existing nucleation and growth theories with respect to their applicability to decomposition reactions in real materials. Furthermore, the N model allows an evaluation to be made of how realistic the various approximations are which occur in both the LWS theory and the MLS model.

In this section we briefly introduce the MLS and the N models. An attempt is made to demonstrate their ability to describe the entire course of the decomposition reaction; we will also show how some essential parameters of the decomposing alloy, such as the diffusion constant and the specific interfacial energy, can be evalu-

ated by fitting the theoretically predicted curves $\bar{R}(t)$ and $N_v(t)$ to the corresponding experimental data. Furthermore, on the grounds of the N model, it is possible to examine whether certain time intervals exist during the course of a precipitation reaction in which the kinetic evolution is predicted by either the growth or the coarsening theory with sufficient accuracy.

5.7.2 The Langer and Schwartz Theory (LS Model) and its Modification by Kampmann and Wagner (MLS Model)

In the LS theory it is assumed that the system contains N_{LS} droplets per unit volume of uniform size \bar{R}_{LS} . In order to account for coarsening, the continuous distribution function $f(R, t)$ and the number of particles of critical size, i.e., $f(R^*, t) dR^*$, must be known. However, in the LS theory this is not the case. LS, therefore, introduced an apparent density $f_a(R^*, t)$ (Fig. 5-50) which is given as:

$$f_a(R^*, t) = N_{LS} \frac{b}{\bar{R}_{LS} - R^*} \quad (5-66)$$

$f_a(R^*, t)$ is thus proportional to N_{LS} and inversely proportional to the width of $f(R, t)$. The constant $b = 0.317$ is chosen in such a way that for $t \rightarrow \infty$ the coarsening rate $d\bar{R}_{LS}/dt$ is identical to K_R^{LSW} (Eq. (5-65)). Unlike the LSW theory, where $\bar{R} = R^*$, in the LS theory only particles with $R > R^*$ are counted as belonging to $f(R, t)$, i.e.

$$\bar{R}_{LS} = \frac{1}{N_{LS}} \int_{R^*}^{\infty} f(R, t) R dR \quad (5-67)$$

Thus, $\bar{R}_{LS} > R^*$ at all stages of decomposition, keeping $f_a(R^*, t)$ in Eq. (5-66) finite. Due to nucleation at a rate J and dissolution, N_{LS} changes with time according to:

$$\frac{dN_{LS}}{dt} = J - f_a(R^*, t) \frac{dR^*}{dt} \quad (5-68)$$

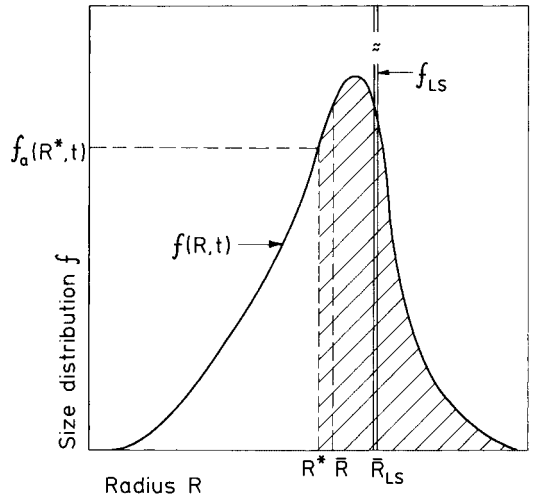


Figure 5-50. Relationship between the 'true' continuous size distribution function $f(R, t)$ yielding the mean radius \bar{R} and the related parameters of the LS model. LS assumed a monodisperse distribution, f_{LS} , of particles with radius \bar{R}_{LS} . $f_a(R^*, t) dR^*$ is the apparent number density of particles with radii between R^* and $R^* + dR^*$. In the LS theory, only particles in the hatched region belong to the precipitated phase.

The growth of particles of mean size \bar{R}_{LS} is given as:

$$\begin{aligned} \frac{d\bar{R}_{LS}}{dt} = & v(\bar{R}_{LS}) \\ & + (\bar{R}_{LS} - R^*) \frac{f_a(R^*, t)}{N_{LS}} \frac{dR^*}{dt} \\ & + \frac{1}{N_{LS}} J[R^*(t)] (R^* + \delta R^* - \bar{R}_{LS}) \end{aligned} \quad (5-69)$$

The term $v(\bar{R}_{LS})$ is given by Eq. (5-43) and accounts for the growth rate of the particles in the supersaturated matrix. The second term accounts for the change in the true distribution function caused by the dissolution of $f_a(R^*, t) dR^*$ particles with radii between R^* and $R^* + dR^*$. The third term describes the change in $f(R, t)$ caused by the nucleation of particles which must be slightly larger than those of critical size,

i.e., $R = R^* + \delta R^*$ and $\delta R^* \ll R^*$. Together with the continuity equation³,

$$(c_p - \bar{c}) \frac{4\pi}{3} \bar{R}_{LS}^3 N_{LS} = (c_0 - \bar{c}) \quad (5-70)$$

and Eq. (5-66), Eqs. (5-68) and (5-69) are the rate equations which describe the *entire* course of precipitation in the LS model. After proper scaling, these equations were numerically integrated in conjunction with steady state nucleation theory (Eq. (5-27)).

The *LS model* is based on the assumption that the equilibrium solubility of small clusters can be determined from the linearized version of the Gibbs–Thomson equation, i.e. Eq. (5-46). This linearization, however, generally does not hold for small clusters in metallic alloys (cf. Sec. 5.6.2). This becomes immediately evident for the Cu–1.9 at.% Ti system isothermally aged at 350°C. At $t=0$, R^* is 0.48 nm or 0.13 nm, depending on whether R^* is computed ($\sigma_{\alpha\beta}=0.067$ J/m², see Sec. 5.7.4.4) from the non-linearized or from the linearized version of Eq. (5-46). This example clearly demonstrates that Eq. (5-46) must be used in its *non-linearized* version, particularly for systems with large values of $\sigma_{\alpha\beta}$ and/or large supersaturations.

The *MLS model* is based on the *non-linearized* Gibbs–Thomson equation (Eq. (5-45)). Thus, the growth rate in the MLS model is:

$$\frac{dR_{LS}}{dt} = v(R_{LS}) = \frac{1}{c_p - c_\alpha^e} \frac{D}{R_{LS}} \times \left[\bar{c} - c_\alpha^e \exp \left(\frac{2\sigma_{ab} V_m}{R_g T} \frac{1}{R_{LS}} \right) \right] \quad (5-71)$$

In order to write the rate equations (5-68) to (5-70) in a properly scaled version, we introduce the following parameters:

$$R_N = \frac{2 V_m \sigma_0}{R_g T}; \quad k_\sigma = \sigma_{\alpha\beta} / \sigma_0; \quad \xi_0 = c_0 / c_\alpha^e;$$

$$\xi = \bar{c} / c_\alpha^e; \quad \xi_p = c_p / c_\alpha^e; \quad \varrho = \bar{R}_{LS} / R_N;$$

$$\varrho^* = R^* / R_N; \quad \delta\varrho^* = \delta R^* / R_N;$$

$$n = N_{LS} \frac{4\pi}{3} R_N^3; \quad \tau = \frac{D}{R_N^2} t; \quad \tilde{J} = J \frac{dn}{dN} \frac{dt}{d\tau} \quad (5-72)$$

Apart from R_N , all parameters are dimensionless; unlike in both the original LS model and the study of Wendt and Haasen (1983), in the MLS model R_N rather than the correlation length is used as the scaling length. By straightforward scaling of Eqs. (5-27), (5-61) and (5-71) we obtain the scaled version of the equations of motion (5-68) and (5-69). From these, the number density n of particles is eliminated by virtue of the scaled continuity equation

$$n = \frac{1}{\varrho^3} \frac{\xi_0 - \xi}{\xi_p - 1} \quad (5-73)$$

We finally obtain

$$\frac{d\varrho}{d\tau} + \frac{\varrho}{3} \left(\frac{1}{\xi_0 - \xi} + \frac{b k_\sigma}{\varrho \ln \xi - k_\sigma} \frac{1}{\xi \ln \xi} \right) \frac{d\xi}{d\tau} = -\tilde{J} \frac{\varrho^4}{3} \frac{\xi_p - \xi}{\xi_0 - \xi} \quad (5-74)$$

$$\begin{aligned} \frac{d\varrho}{d\tau} + \frac{b k_\sigma}{\xi (\ln \xi)^2} \frac{d\xi}{d\tau} &= \frac{1}{\xi_p - 1} \frac{1}{\varrho} [\xi - \exp(k_\sigma/\varrho)] \\ &+ \varrho^3 \frac{\xi_p - 1}{\xi_0 - \xi} \tilde{J} \left(\frac{k_\sigma}{\ln \xi} + \delta\varrho^* - \varrho \right) \end{aligned} \quad (5-75)$$

Eqs. (5-74) and (5-75) are the basic equations of the MLS model and are numerically integrated with $\sigma_0 = 0.1$ J/m²; values of $\delta\varrho^*/\varrho^*$ (ξ_0) used by Kampmann and Wagner (1984) ranged from 0.05 to 0.2.

In the LS theory only the steady-state nucleation rate has been used; in contrast,

³ Note that particles with $R = R^*$ are not contained in Eq. (5-70); we therefore call these particles ‘apparent’.

in Eqs. (5-74) and (5-75) of the MLS model, KW employed the time-dependent nucleation rate J^* (Eq. (5-29)), which involves the incubation time. In the scaled version the latter (τ_w) was evaluated from:

$$\tau_w(\xi) = \frac{1}{2} \frac{\xi_p - 1}{\xi - 1} Q^{*2} c_w^2 \equiv \tau_{w, \min} c_w^2 \quad (5-76)$$

When deriving this equation, it was assumed that the minimum time ($\tau_{w, \min}$) for a particle to reach the critical size Q^* is given by Eq. (5-47). However, for subcritical nuclei c_R is considerably larger than c_α^e , and the probability of their redissolution is rather large; hence, Eq. (5-47) overestimates the growth rate significantly. This fact is counterbalanced by the introduction of the parameter c_w . For each particular alloy system, c_w is determined in such a way that after a period τ_w the first particles become 'observable' with a reasonable number density. For all alloy systems investigated so far, c_w ranges from 1.4 to 3.5. Hence, because of the stochastic nature of cluster growth and dissolution, on average it takes about two to twelve times longer for a cluster to attain a size $R > R^*$ beyond which its further growth may be evaluated in a deterministic manner on the basis of Eq. (5-47).

5.7.3 The Numerical Model (N Model) of Kampmann and Wagner (KW)

Unlike the MLS model, in the N model the time evolution of $f(R, t)$ – or $f(Q, \tau)$ if we stick to the same nomenclature – is computed. For this purpose $f(Q, \tau)$ is subdivided into intervals $[Q_{j+1}, Q_j]$ with $|Q_j - Q_{j+1}|/Q_j \ll 1$ and n_j particles in the j -th interval. In contrast to the MLS model, dissolving particles with $Q < Q^*$ are assumed to belong to the precipitating phase, i.e.

$$n = \sum_{j=1}^{j_0} n_j \quad \text{and} \quad \bar{Q} = \frac{1}{n} \sum_{j=1}^{j_0} n_j \bar{Q}_j$$

$$\text{with } \bar{Q}_j = \frac{1}{2} (Q_j + Q_{j+1}) \quad (5-77)$$

The continuity equation in the N model then reads:

$$(\xi_p - 1) \sum_{j=1}^{j_0} \bar{Q}_j^3 n_j = \xi_0 - \xi \quad (5-78)$$

Thus the continuous time evolution of $f(Q, t)$ is split into a sequence of individual decomposition steps; these steps are chosen in such a way that within each corresponding time interval $\Delta\tau_i$ the changes of all radii Q_j , (τ_i) and of the supersaturation $\xi(\tau_i)$ remain sufficiently small. Then, both the nucleation and the growth rates can be considered as being constant during $\Delta\tau_i$ and the change of $f(Q, \tau)$ and of ξ can be reliably computed. The N model of KW contains some algorithms which ensure a rather high accuracy of the numerical calculation; it amounts to $\approx 0.5\%$ in the case of the growth rate of Q .

5.7.4 Decomposition of a Homogeneous Solid Solution

5.7.4.1 General Course of Decomposition

KW discussed the decomposition reaction of an ideally quenched alloy with $c_\alpha^e = 0.22$ at.%, $c_p = 0.20$ at.%, $c_0 = 1.9$ at.% and $\sigma_{\alpha\beta} = 0.067$ J/m². Just on the basis of these input data, the decomposition reaction can be calculated within the framework of the MLS and N models. Fig. 5-51 shows the predictions from both the MLS (full lines) and the N models (discrete symbols) for the time evolution of the radii $\bar{Q}(\tau)$ and $Q^*(\tau)$, the number density $n(\tau)$, the supersaturation $\xi(\tau)$, and the nucleation rate $\tilde{J}(\tau)$. The chosen values of $\xi_0 = 8.7$, c_α^e , σ and D correspond to those for Cu–1.9 at.% Ti aged at 350°C (see Secs. 5.7.4.3 and 5.7.4.4). Surprisingly, both models yield qualitatively similar results.

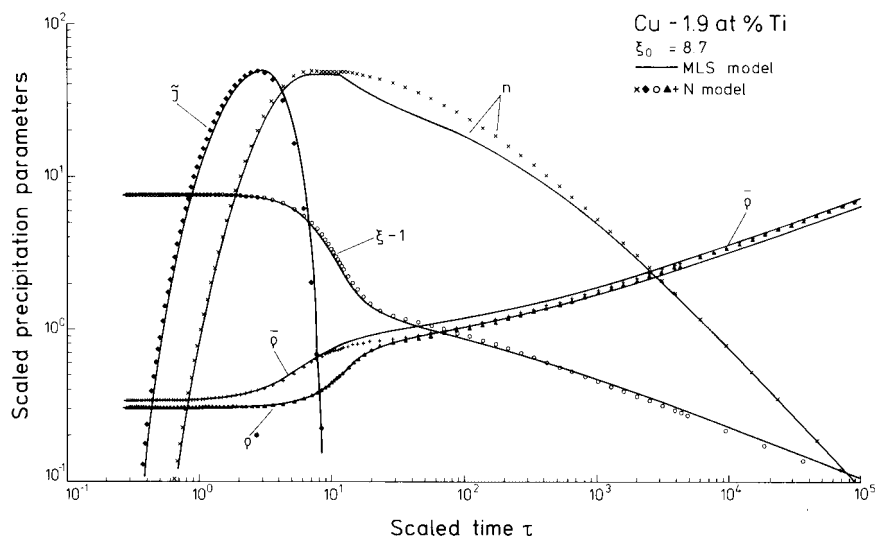


Figure 5-51. Evolution of various scaled precipitation parameters with scaled aging time τ according to both the N model and the MLS model. The chosen values of ξ_0 , $\sigma_{\alpha\beta}$ correspond to those for Cu-1.9 at.% Ti aged at 350°C.

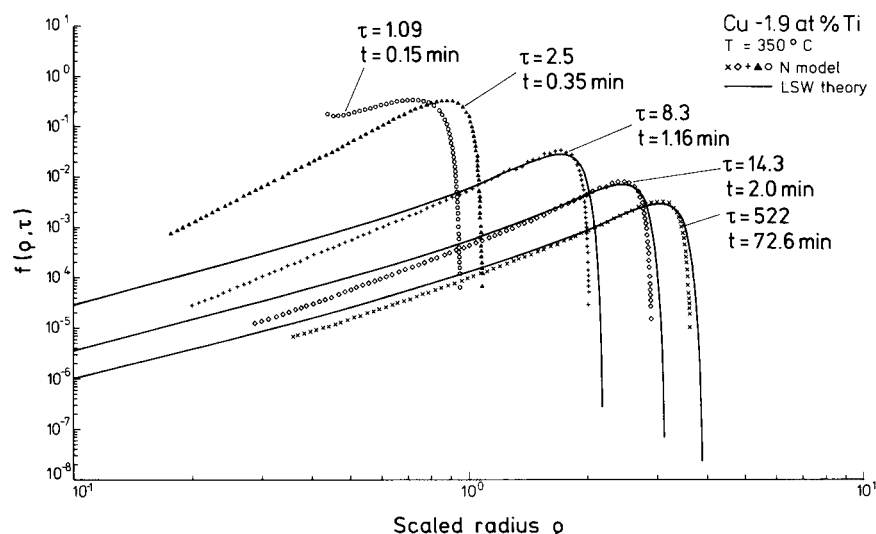


Figure 5-52. Evolution of the scaled size distribution function in Cu-1.9 at.% Ti with aging times as computed with the N model. For comparison, the distribution functions $f_{\text{LSW}}(q, \tau)$ of the LSW theory with the known values of $N_v(t)$ and $\bar{R}(t)$ are also shown. $D = 2.5 \times 10^{-15} \text{ cm}^2/\text{sec}$.

During the early nucleation period ($\tau \leq 1$) both \bar{J} and n increase, whereas ξ and, hence, q^* remain roughly constant. At this stage, the N model gives a rather narrow size distribution function $f(q, t)$ (Fig. 5-52). Since c_R is still close to $\bar{c} \approx c_0$, the

growth rate of nucleated precipitates is also close to zero, i.e., \bar{q} remains about constant. After ($\tau \geq 1$), those precipitates nucleated first become considerably larger than q^* and $f(q, t)$ becomes much broader. This is the beginning of the growth period

which is characterized by (i) the highest growth rate ever observed during the course of precipitation; (ii) a ratio $\bar{\rho}/\rho^*$ which becomes significantly larger than 1; (iii) the maximum number density (n_{\max} , $N_{v,\max}$) of particles which remains about constant; (iv) a stronger decrease of ξ ; and, consequently, (v) a decrease of \tilde{J} from its maximum value; in this particular case, \tilde{J} never reaches its steady-state value. At the end of the growth regime ($\tau \approx 15$) the supersaturation has dropped significantly and the growth rate becomes small. This effect causes ρ^* to converge towards $\bar{\rho}$ and makes $dn/d\tau < 0$ (Eq. (5-68)). During the subsequent transition period ($\tau \approx 15$), the growth rate of $\bar{\rho}$ is primarily controlled by the dissolution of particles with $\rho < \rho^*$ and only to a lesser extent by the uptake of solute atoms from the matrix, the supersaturation of which is still about 20%. During the transition period, the true distribution function $f(\rho, t)$ continuously approaches the one predicted by LSW (Fig. 5-52). At this stage, however, f_{LSW} is still a rather poor approximation for $f(\rho, t)$. This simply reflects the influence of the linearization of the Gibbs–Thomson equation (Eq. (5-46)) on which the LSW theory is based. For $\tau \rightarrow \infty$, $d\bar{\rho}^3/d\tau$ approaches asymptotically a constant value, i.e., the reaction is within the asymptotic limit of *coarsening* where the supersaturation is almost zero. At this stage $f(\rho, \tau)$ is well approximated by f_{LSW} with only minor deviations for small particle radii.

5.7.4.2 Comparison Between the MLS Model and the N Model

The precipitation reaction starts with an identical nucleation rate and identical particle sizes in both the MLS and the N models. Therefore, both models are expected to yield identical results which, in fact, is ob-

served in Fig. 5-51. During the later growth period, dissolution of particles with $\rho < \rho^*$ commences. At this stage, the MLS model only counts particles with $\rho > \rho^*$ as belonging to the second phase (Eq. (5-67)), and, furthermore, assumes $f_a(\rho = \rho^*)$ to be proportional to $1/(\bar{\rho} - \rho^*)$ (Eq. (5-66)). At this stage, this is a rather poor approximation because the N model yields a steep slope for $f(\rho \rightarrow \rho^*, \tau)$ with a rather small density $n(\rho = \rho^*)$. These facts make the MLS model predict considerably larger rate constants for the decrease of the particle number density and, hence, for the growth of $\bar{\rho}$ at the end of the growth period ($\tau \approx 15$).

Depending on the particular choice of b (Eq. (5-66)), the coarsening rate of the MLS model approaches asymptotically the value K_R^{LSW} (Eq. (5-65)) from the LSW theory. In this asymptotic limit the mean radii from both models and, hence, their coarsening rates become identical. At this stage the N model yields $\bar{\rho} \cong \rho^*$ as predicted by LSW, whereas the MLS model yields $\bar{\rho} - \rho^* = \text{const.}$, i.e., $\bar{R}_{\text{LS}} > R^*$, as required by Eq. (5-67).

We can conclude that the MLS model, which requires much less computing time than the N model, provides a good survey of the general course of precipitation. However, due to the simplifying assumptions made, it does not predict the precipitation kinetics with the same accuracy as the N model. This is particularly evident for those precipitation stages where the shape of $f(\rho, \tau)$ is extreme, as, for instance, during the later growth stages in the example discussed above.

5.7.4.3 The Appearance and Experimental Identification of the Growth and Coarsening Stages

In the following, the results from the MLS and the N models are compared with

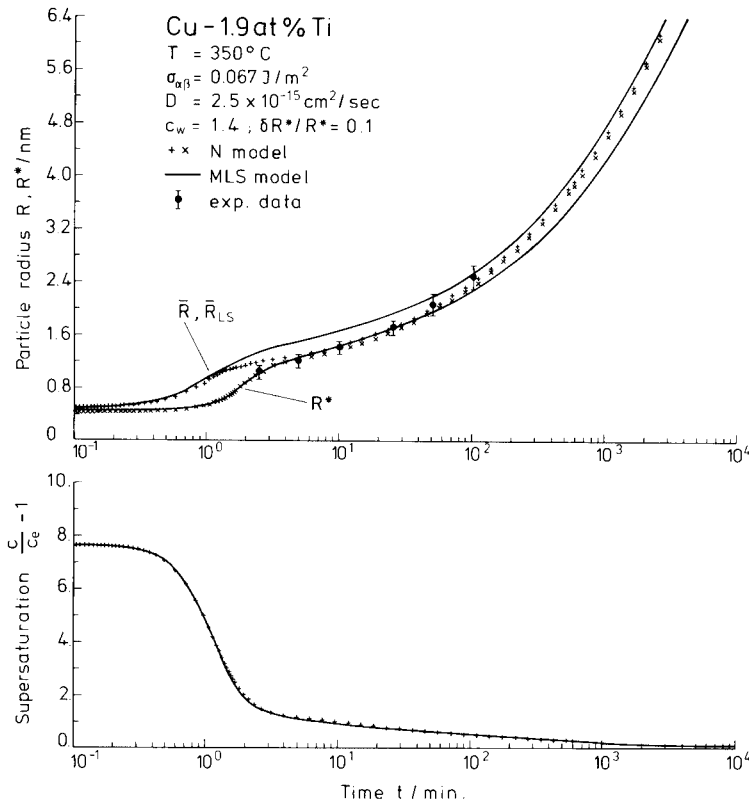


Figure 5-53. Variation of \bar{R} , R^* , \bar{R}_{LS} and of the relative supersaturation with aging time for Cu-1.9 at.% Ti as computed with the N model and the MLS model for the given set of thermodynamics data; also shown are the experimental data for $\bar{R}(t)$ from von Alvensleben and Wagner (1984).

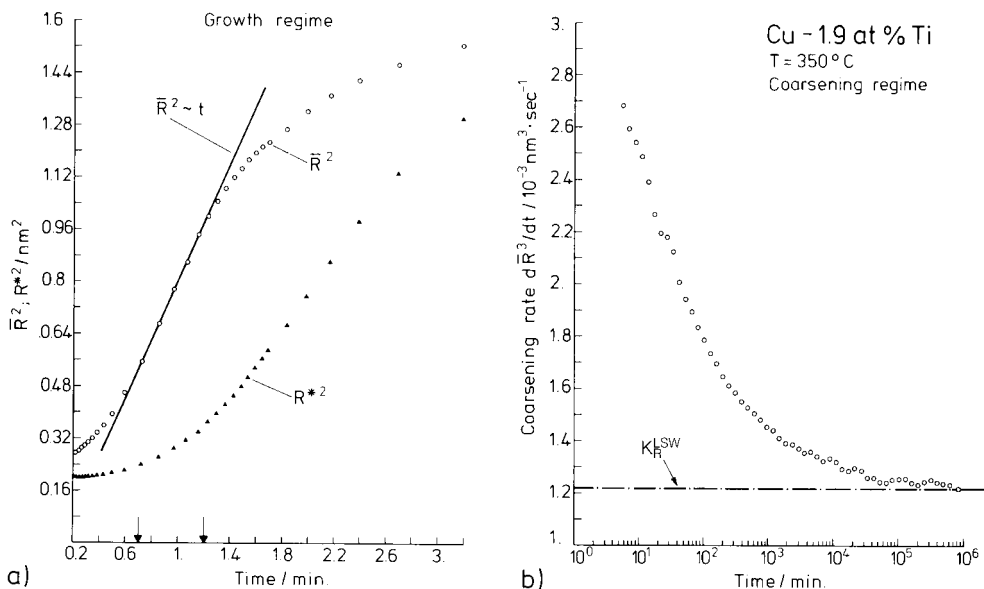


Figure 5-54. Variation of R^2 and R^{*2} with time during the growth regime for Cu-1.9 at.% Ti. During the period marked by the two arrows the kinetics follow the power-law $\bar{R} \sim t^{1/2}$. b) Variation of the coarsening rate $d\bar{R}^3/dt$ with aging time; K_R^{LSW} is the value predicted by the LSW theory, Eq. (5-65).

experimental data obtained from a FIM atom probe study of early-stage precipitation in Cu–1.9 at.% Ti at 350°C (von Alvensleben and Wagner, 1984).

Fig. 5-53 shows the time evolution of R^* and or \bar{R} in physical units. Again these experimental data points are well described by the N model. Fig. 5-53 also reveals that the experimental data cover neither the early nucleation period nor the growth regime, but rather start ($t = 2.5$ min) at the end of the latter region. From Fig. 5-54a, where \bar{R}^2 is plotted as a function of t , it is recognized that during the period $t \approx 0.7$ min to 1.2 min, \bar{R}^2 varies linearly with t as suggested by Eq. (5-40). Since this time period extends only over 0.5 min, KW concluded that for Cu–1.9 at.% Ti the time window is too short for revealing the $\bar{R} \sim t^{1/2}$ kinetics experimentally; in fact, the same holds true for many other alloy systems analyzed by KW using the N model. Furthermore, from Fig. 5-54a the slope of the straight line has been evaluated to be $0.88 \text{ nm}^2/\text{min}$, whereas the corresponding growth rate from Eq. (5-47) is computed ($c_\alpha^e = 0.22 \text{ at.}\%$, $c_p = 20 \text{ at.}\%$, $D = 2.5 \times 10^{-15} \text{ cm}^2/\text{sec}$) to be $2.5 \text{ nm}^2/\text{min}$. This result clearly demonstrates that no growth regime exists which is adequately accounted for by Eq. (5-47). In other words, the idealizations made in the derivation of Eq. (5-47) do not approximate the true situation in Cu–1.9 at.% Ti. However, if $\bar{c}(t)$ and c_R in Eq. (5-43) are replaced by their mean values respectively, during the period for which $\bar{R} \sim t^{1/2}$ holds, then Eqs. (5-40 and 5-42) with $\lambda_i = \sqrt{k^*}$ yield a value for the growth rate ($0.104 \text{ nm}^2/\text{min}$) which is only 16% higher than the true value.

In Fig. 5-54b the rate constant $d\bar{R}^3/dt$ for coarsening is plotted versus t . It is evident that for Cu–1.9 at.% Ti the rate constant $K_R^{\text{LSW}} = 1.2 \times 10^{-24} \text{ cm}^3/\text{sec}$ from the LSW

theory (Eq. (5-65)) is only reached for aging times beyond $\approx 10^4 \text{ min}$! At this stage \bar{R} has already grown to $\approx 6.4 \text{ nm}$. From this result, which reflects the influence of the linearization of Eq. (5-46), KW inferred that the LSW theory predicts the correct coarsening rate once

$$\bar{R} \geq 13 \frac{V_m \sigma_{\alpha\beta}}{R_g T} \quad (5-79)$$

If this relation holds, $f(R, t)$ is almost identical to f_{LSW} (Fig. 5-52) and $\bar{c}/c_\alpha^e \approx 1$.

According to the results from the N model, during the early coarsening stages the precipitation kinetics deviate significantly from those predicted by the LSW theory (e.g., Fig. 5-54b). Thus the widely used LSW analyses resulting in a determination of D and $\sigma_{\alpha\beta}$ on the basis of Eq. (5-63a) and Eq. (5-63c) should not be applied to early coarsening stages during which the relation does not hold.

5.7.4.4 Extraction of the Interfacial Energy and the Diffusion Constant from Experimental Data

KW determined $\sigma_{\alpha\beta}$ and D separately by fitting $\bar{R}(t)$ and $N_v(t)$ as obtained from the N model to the corresponding experimental data. Fig. 5-55 shows the variation of N_v and J^* with aging time as computed with the N and the MLS models, together with the corresponding experimental data. The peak number density $N_{v,\text{max}}$ of particles in a precipitation reaction is essentially governed by the value of ΔF^* via the nucleation rate equation (5-27). Since $\Delta F^* \sim \sigma_{\alpha\beta}^3$ (Eq. (5-20)), $N_{v,\text{max}}$ depends sensitively on the value of the interfacial energy $\sigma_{\alpha\beta}$. The very strong dependence of $N_{v,\text{max}}$ on $\sigma_{\alpha\beta}$ is clearly revealed by Fig. 5-55, showing a good fit of $N_v(t)$ for $\sigma_{\alpha\beta} = 0.067 \text{ J/m}^2$ and only poor agreement for $\sigma_{\alpha\beta} = 0.071 \text{ J/m}^2$. On the other hand, a variation in D mani-

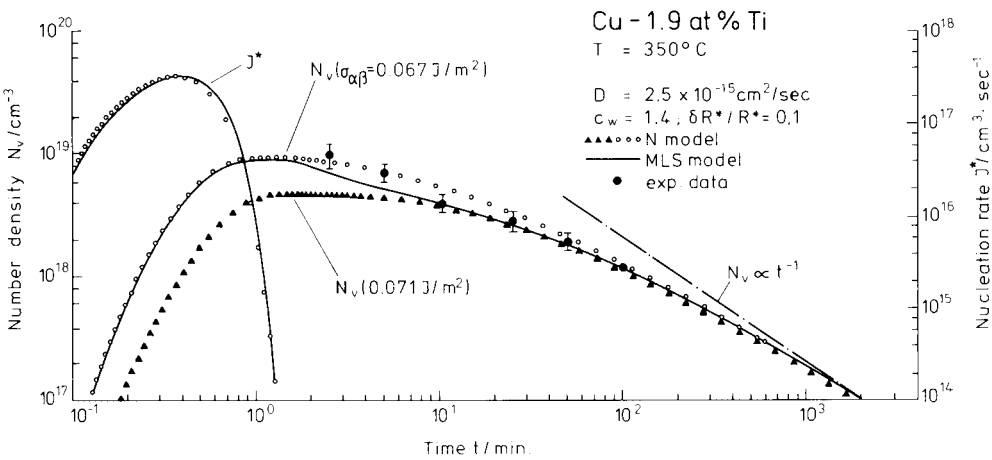


Figure 5-55. Variation of N_v and J^* with aging time for Cu-1.9 at.% Ti as computed with the N model and the MLS model for $\sigma_{\alpha\beta} = 0.067 \text{ J/m}^2$; for this value of $\sigma_{\alpha\beta}$ the computed $N_v(t)$ curve agrees well with the experimental data; poor agreement is obtained for $\sigma_{\alpha\beta} = 0.071 \text{ J/m}^2$.

Table 5-3. Correlation between the width of the miscibility gap and the coherent interfacial energies $\sigma_{\alpha\beta}$ for various two-phase alloys as determined from a fit of the N model to experimental kinetic data.

Alloy		Aging temperature	Composition/type of precipitates	Width of coherent miscibility gap	Coherent interfacial energy
at. %		°C		at. %	$\sigma_{\alpha\beta}$ J/m ²
Ni–14 Al	1	550	γ' -Ni ₃ Al	≈ 15	≈ 0.016
Ni–26 Cu–9 Al	2	550	γ' -(Cu, Ni) ₃ Al	≈ 20	≈ 0.052
		540	Not determined	≈ 20	≈ 0.050
		580	Not determined	≈ 20	≈ 0.052
Cu–1.9 Ti	3	350	β' -Cu ₄ Ti	≈ 20	≈ 0.067
Cu–2.7 Ti	4	350	β' -Cu ₄ Ti	≈ 20	≈ 0.067
Cu–1.5 Co	5	500	>95 at. % Co	≈ 95	≈ 0.171
Fe–1.4 Cu	6	400, 500	>98 at. % Cu	≈ 100	≈ 0.250
Fe–0.64 Cu	6	400	>98 at. % Cu	≈ 100	≈ 0.250

1 Wendt and Haasen (1983) (AFIM)
2 Liu and Wagner (1984) (AFIM)
3 Alvensleben and Wagner (1984) (AFIM, CTEM)
4 Eckerlebe et al. (1986) (SANS)
5 Gust (1986), unpublished (magnetic measurements)
6 Kampmann and Wagner (1986) (SANS)

festes itself in a parallel shift of the entire curve on the time scale. Thus, a fit of $\bar{R}(t)$ and of $N_v(t)$ as obtained from the N model to the experimental curves allows both $\sigma_{\alpha\beta}$ and D to be determined quite accurately.

From a variety of different two-phase alloys, the available kinetic data have been interpreted in terms of the N model. Table 5-3 presents the interfacial energies $\sigma_{\alpha\beta}$ together with the width of the (coherent) mis-

cibility gap for each given alloy. It is evident that there is a pronounced correlation between $\sigma_{\alpha\beta}$ and the compositional width, i.e., the broader the gap, the larger is $\sigma_{\alpha\beta}$. This is consistent with various theoretical predictions on the interfacial energy (see Lee and Aaronson, 1980, for a comprehensive discussion of this aspect).

5.7.5 Decomposition Kinetics in Alloys Pre-Decomposed During Quenching

The versatility of the N model is further illustrated by its ability to predict the precipitation kinetics in alloys which have experienced some phase separation during quenching. This is exemplified for Cu–2.9 at.% Ti, the decomposition reaction of which was studied by Kampmann et al. (1987) by means of SANS. They found that the cooling rate of their specimen was not sufficient to suppress the formation of Cu_4Ti precipitates during the quench; in fact, as is shown in Fig. 5-56, the solute concentration decreased from $c_0 = 2.9$ at.% Ti during the quench. With further aging, the supersaturation decreased continuously through the formation of additional clusters and the growth of existing

ones. After aging for ≈ 100 min at 350°C the metastable β' -solvus line is nearly reached at $c_\alpha^e \approx 0.22$ at.% Ti (cf. Sec. 5.2.1).

The experimentally determined kinetic behavior of the precipitate number density, of their mean radius, and of the supersaturation are displayed in Fig. 5-57a–c and compared with the predictions of the N model. For the computations, the result from the SANS evaluation was taken into account, which yielded the homogenized sample to already contain $\approx 2 \times 10^{25}$ clusters/ m^3 with $\bar{R} \approx 0.7$ nm. These could immediately grow by further depleting the matrix from solute atoms. Moreover, at $t = 0$ the supersaturation was still large enough for nucleating new clusters with smaller radii at a nucleation rate J^* (Fig. 5-57a). Thus, during the first minutes of aging, the cluster number density increased. At this stage, the alloy contained a sort of bimodal cluster distribution: the larger ones formed at a smaller supersaturation during quenching, and the smaller ones resulted from nucleation at 350°C . Due to both nucleation of new clusters and growth of pre-existing ones, the supersaturation and, hence, the nucleation rate decreased rapidly; after aging for ≈ 3 min, nu-

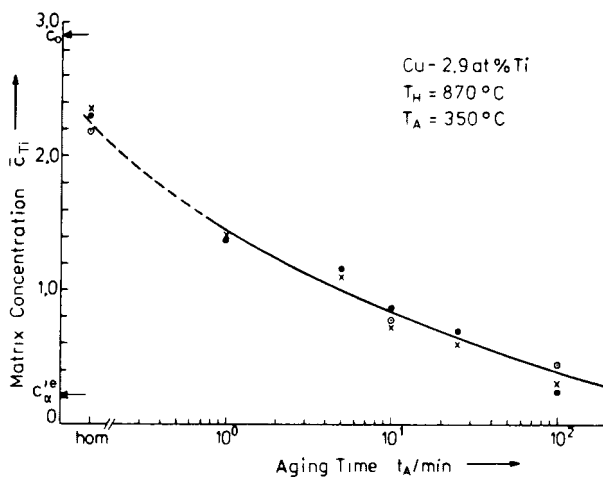


Figure 5-56. Decrease in the solute concentration in the matrix with aging time, as determined from Laue scattering (\odot), from the integrated intensity (\times), and the Guinier approximation (\bullet) of SANS curves.

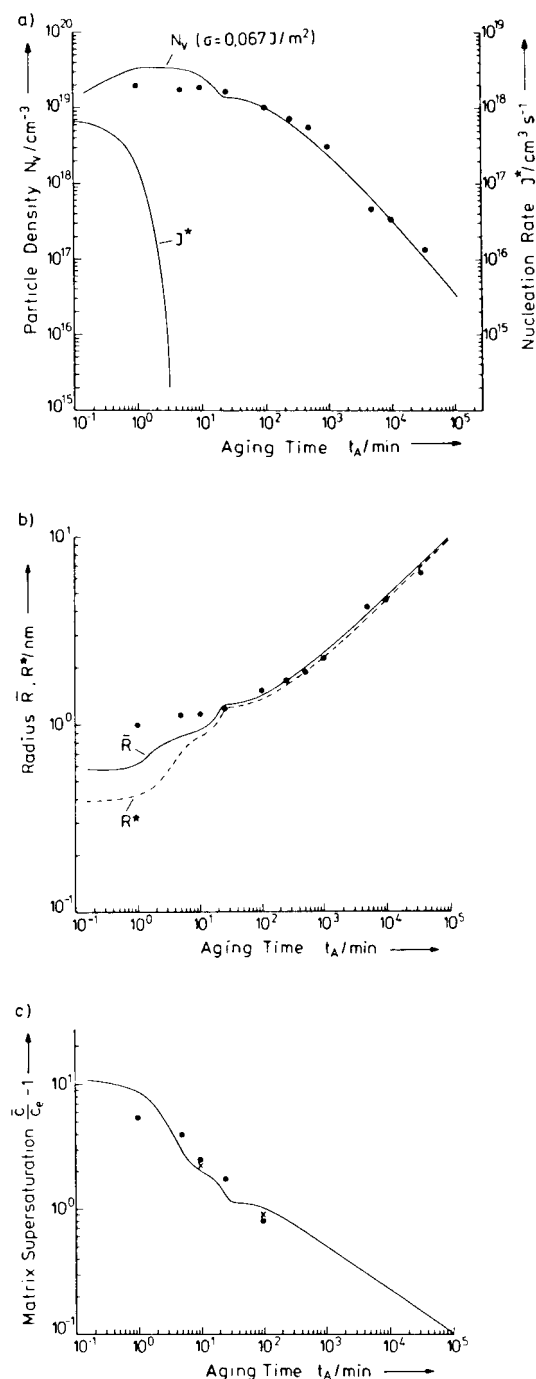


Figure 5-57. Time evolution of (a) the cluster number density N_v and the nucleation rate J^* , (b) of their mean radius \bar{R} and of the critical radius R^* , and (c) of the supersaturations. Experimental SANS results: discrete symbols; computational results: full lines.

cleation is virtually terminated. After about 10 min the critical radius R^* , which is correlated with the momentary supersaturation, reaches the mean value \bar{R} of the global size distribution. At this instant, R^* has grown beyond the mean radius of the smaller, freshly nucleated clusters; these now redissolve leading to a further decrease in N_v . Now the size distribution is again governed by the larger precipitates formed during quenching. After about 500 min, N_v decreases with t as expected from the LSW theory.

With regard to the accuracy of both the SANS experiment and, in particular, the SANS data evaluation, the agreement between the experimental kinetic data and those from the N model is rather good for an interfacial energy $\sigma_{\alpha\beta} = 0.067 \text{ J/m}^2$. This value is identical to that determined for the less concentrated Cu–1.9 at.% Ti alloy (Sec. 5.7.4.4). In the early stages ($t \leq 10$ min) the experimental \bar{R} is considerably larger than the theoretical one. This simply reflects the fact that the scattering power of a particle is weighted with R^6 ; hence, for $t \leq 10$ min, essentially the radius of only the larger particles within the bimodal distribution was determined. The diffusion coefficient ($D = 3 \times 10^{-16} \text{ cm}^2/\text{sec}$) was found to be about one order of magnitude smaller than in the Cu–1.9 at.% Ti alloy (Sec. 5.7.4.4). It was not possible to decide whether this difference in the D values reflects the concentration dependence of D , or whether it was caused by differences in the homogenization temperatures of the two alloys (Cu–2.9 at.% Ti: $T_H = 780^\circ\text{C}$; Cu–1.9 at.% Ti: $T_H = 910^\circ\text{C}$).

5.7.6 Influence of the Loss of Particle Coherency on the Precipitation Kinetics

In many two-phase systems the particles lose coherency once they have grown be-

yond a certain size R_T . The associated increase in the interfacial energy and decrease in the solubility limit (cf. Fig. 5-1) leads to an enhanced driving force and, hence, to accelerated kinetics for further coarsening of the incoherent microstructure with respect to the coherent one. This effect can also be accounted for by the N model. This is shown in Fig. 5-58 for Fe-1.38 at.% Cu aged at 500°C. As inferred from CTEM, the Cu-rich particles transform at $R_T \approx 2.8$ nm from the metastable b.c.c. structure into the f.c.c. equilibrium structure. The associated loss of coherency occurs at particle number densities well beyond the maximum number density $N_{v, \max}$ (Fig. 5-58). Thus, following the procedure outlined in Sec. 5.7.4.4, the coherent interfacial energy could be determined by fitting the N model to the experimental (SANS) kinetic data of the still coherent system. The value $\sigma_{\alpha\beta} \approx 0.27$ J/m² obtained is considerably smaller than the corresponding value $\sigma_{\alpha\beta}^{\text{inc}} \approx 0.50$ J/m² which was derived from a thermodynamical analysis of the Fe-Cu system (Kampmann and Wagner, 1986). As is shown in Fig. 5-58, the loss of coherency in fact leads to a momentary acceleration of the growth kinetics. It is, however, not sufficient to bridge the discrepancy between the experimental kinetic data and the theoretically predicted ones displayed in Fig. 5-58. As the predicted kinetics are much more sluggish than the experimentally determined ones, we might speculate that neglecting particle interaction accounts for the observed discrepancy. Inspection of Fig. 5-43, however, reveals that a consideration of finite volume effects in Fe-1.38 at.% Cu with $f_p \approx 1\%$ would increase the coarsening rate only by less than a factor 1.3 whereas a factor of ≈ 10 is required to match the results from the N model and the SANS experiments at the later stages of

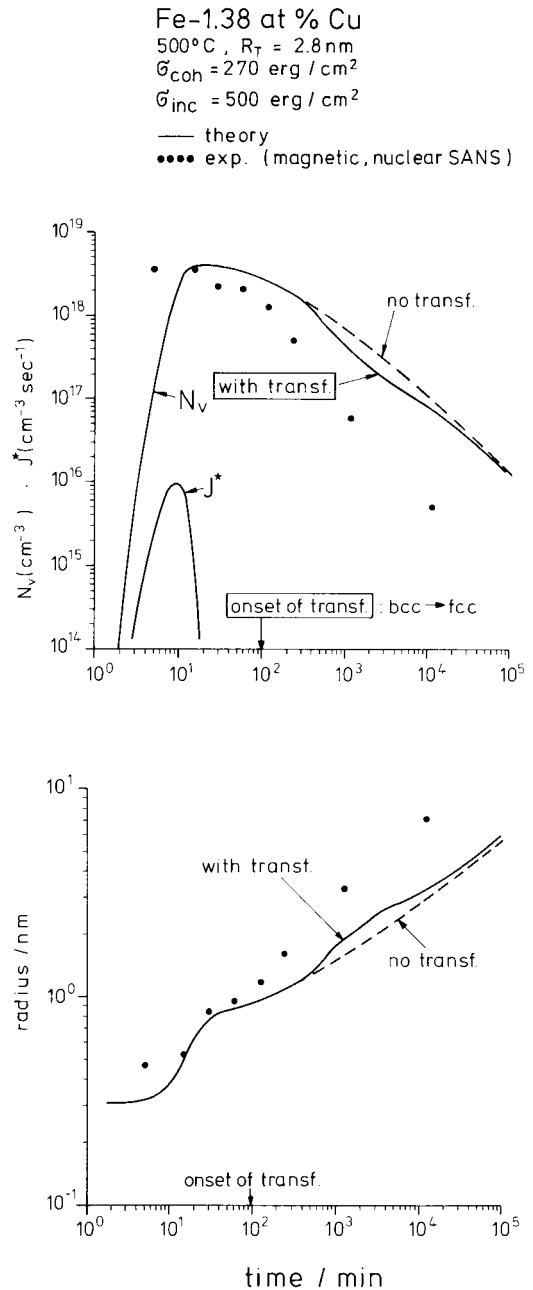


Figure 5-58. Kinetic evolution of the precipitated number density (top) and of the mean radius (bottom) as predicted by the N model for Fe-1.38 at.% Cu. The solid points refer to experimental data derived from nuclear and magnetic SANS experiments. The dashed lines show the kinetic evolution without consideration of the b.c.c. \rightarrow f.c.c. transformation of the copper-rich particles.

precipitation. At present, it is unclear whether the various theories dealing with finite volume effects (Sec. 5.6.3) are still insufficient or whether some heterogeneous precipitation at lattice defects accounts for the observed discrepancy.

At first glance the experimental kinetic data for $\bar{R}(t)$ and $N_v(t)$ in Fig. 5-58 might be seen as being amenable to an LSW analysis in terms of Eq. (5-63). Analyses of the SANS data for $t \gg 10^3$ min, however, showed the width of the particle size distribution to be much broader (standard deviation: $\sigma \approx 0.31$) than expected from the LSW theory or its modification ($\sigma \approx 0.23$). Furthermore, the measured supersaturation was still far from being close to zero. Hence, the conditions for an LSW analysis of the experimental data are not at all fulfilled.

5.7.7 Combined Cluster-Dynamic and Deterministic Description of Decomposition Kinetics

There remain two main shortcomings of the N model outlined in Sec. 5.7.3. Firstly, the stochastic nature of the nucleation process is solely accounted for by using the time- and concentration-dependent nucleation rate (i.e., Eq. (5-29)), whereas the growth (and shrinkage!) is computed in a deterministic manner on the basis of Eq. (5-43). Thus, the stochastic nature of early-stage growth which, in particular, becomes effective in systems with small nucleation energies, is not adequately accounted for in the N model.

Secondly, as in all previous theories, the matrix concentration c_R at the cluster-matrix interface was also calculated on the basis of the Gibbs-Thomson equation, Eq. (5-46). This relation, which describes an equilibrium between the cluster size R and the matrix concentration \bar{c} , is generally not

adequate for describing the growth ($R > R^*$) or dissolution ($R < R^*$) of clusters.

To overcome these shortcomings, Kampmann et al. (Kampmann et al., 1992; Staron and Kampmann, 2000 a, b) extended the N model by a cluster-dynamics (C-D) simulation of the kinetics during the nucleation and growth stages (cf. Sec. 5.5.3). To save computation time, in the later growth and coarsening stages where the stochastic process is no longer relevant, the cluster-dynamics approach is linked to the deterministic description of the original N model. As in the latter, the input parameters entering the extended C-D model are c_0 , c_ω^e , σ and D with variations in D leading only to shifts of the computed curves (e.g., $\bar{R}(t)$ or $J(t)$) parallel to the time scale. Therefore, this C-D simulation can be used in as versatile a manner as the original N model for the interpretation of experimental data (Staron and Kampmann, 2000 b).

The cluster-dynamics algorithm was devised such that its corresponding Helmholtz energy functional approximates closely that of the regular solution model. As proved by CALPHAD studies, this is a rather good approximation for Cu-Co. Fig. 5-59 shows the computed time evolution of the cluster size distribution during the nucleation period and the nucleation rate with input parameters corresponding to a Cu-0.8 at.% Co model alloy aged at 500°C. At $t = 5$ sec all clusters are still below the critical size⁴ and, thus, Fig. 5-59a provides insight into the incubation process.

The nucleation rate J_{B-D}^S calculated according to Eq. (5-27) with $\bar{c} \equiv c_0$ exceeds the maximum computed one (Fig. 5-59b) by more than a factor of 1000. This discrepancy cannot be attributed to incubation

⁴ In the C-D approach the critical radius is defined as that size for which the probabilities of cluster growth and shrinkage are identical.

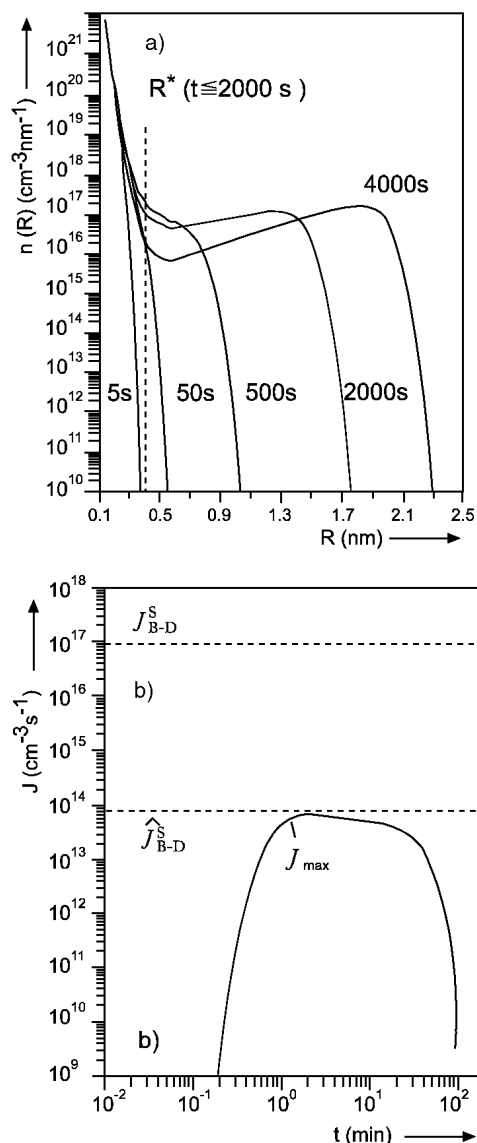


Figure 5-59. a) Evolution of the cluster size distribution during the nucleation stage for a Cu–0.8 at.% Co model alloy aged at $T = 500^\circ\text{C}$, with pair exchange parameter $\Omega = 6.24$, $c_\alpha^e = 0.2$ at.%, $D_{\text{CuCo}} = 1 \times 10^{-19} \text{ m}^2/\text{s}$.

b) Time evolution of the nucleation rate $J(t)$ (solid line) according to the cluster-dynamics calculation. $J_{\text{B-D}}^{\text{S}}$ is based on Eq. (5-27), $\hat{J}_{\text{B-D}}^{\text{S}}$ is the modified Becker–Döring nucleation rate (Eq. (5-80)). (After Kampmann et al., 1992.)

effects; it can only be resolved if – instead of Eq. (5-27) – a more adequate equation is used for calculating the Becker–Döring nucleation rate:

$$\hat{J}_{\text{B-D}}^{\text{S}} = \frac{1}{2} Z \beta^* n_1(t) \times \exp \{ - [\Delta F^*(c_1) - \Delta F^*(1)] / kT \} \quad (5-80)$$

The modified exponent takes into account that no Helmholtz energy $\Delta F^*(1)$ is needed for forming monomers (which are already dissolved in the matrix during the solution treatment).

Accordingly the number of lattice points (N_0) in Eq. (5-28) must be replaced by the number of monomers $n_1(t)$, and for a calculation of ΔF^* the concentration of monomers c_1 (according to Fig. 5-60, $c_1 = 0.7$ at.% rather than the nominal concentration of $c_0 = 0.8$ at.%) must be used. The factor $\frac{1}{2}$ in Eq. (5-80) takes into account that monomers serve both as initial clusters (containing $i = 1$ solute atom) capable of growing, and also as reaction species being able to initiate the growth of “monomer clusters”. As shown in Fig. 5-59b, with these physically justified modifications, excellent agreement is obtained between the maximum nucleation rate (J_{\max}) as obtained from the cluster-dynamics model, and $\hat{J}_{\text{B-D}}^{\text{S}}$ (Eq. (5-80)).

5.8 Self-Similarity, Dynamical Scaling and Power-Law Approximations

5.8.1 Dynamical Scaling

According to the LSW theory and its extensions to finite volume fractions (Sec. 5.6), the distribution of relative particle sizes R/\bar{R} evolves during extended aging ($t \rightarrow \infty$) towards an asymptotic, time-invariant form, the particular shape of which de-

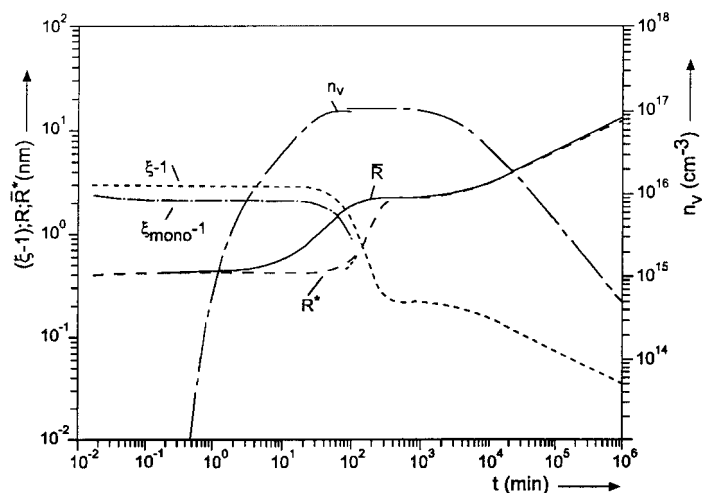


Figure 5-60. Time evolution of the number density (n_v), the mean (dynamical) critical radius (R^*), the mean radius of supercritical clusters (\bar{R}); the conventionally defined supersaturation $\xi - 1 = \bar{c}/c_\alpha^e - 1$ is compared with the supersaturation $\xi_{\text{mono}} - 1 = c_1/c_\alpha^e - 1$ of monomers. For $t \leq 100$ min the computation was performed cluster-dynamically and afterwards continued deterministically on the basis of the N model of Sec. 5.7.3. (After Kampmann et al., 1992.)

depends on the precipitated volume fraction (Fig. 5-44). The final time invariance of $f(R/\bar{R})$ reflects the fact that once the precipitated volume fraction has reached its equilibrium value, consecutive configurations of the precipitate microstructure are geometrically similar in a statistical sense, i.e., all consecutive configurations are statistically uniform on a scale that is considerably larger than some characteristic length such as the mean particle size \bar{R} or the mean center-to-center distance $\bar{L} = N_v^{-1/3}$. The *self-similarity* of the microstructural evolution has found its expression in the *dynamical scaling* of the structure function $S(\kappa, t)$ (Binder and Stauffer, 1974; Binder et al., 1978). Furukawa (1981) proposed $S(\kappa, t)$ to satisfy (after some transient time t_0) a scaling law of the form:

$$S(\kappa, t) = l^3(t) \tilde{F}[\kappa l(t)]; \quad t \geq t_0 \quad (5-81)$$

where $\tilde{F}[\kappa l(t)] \equiv \tilde{F}(x)$ is the time-independent scaling function. As the scaling parameter, $l(t)$ denotes some characteristic length and contains exclusively the time dependence of $S(\kappa, t)$.

Strong theoretical support for the validity of the scaling hypothesis, Eq. (5-81), during the later stages of decomposition

was first provided by Monte Carlo simulations of the time evolution of binary model alloys (Sec. 5.5.6). From these studies it was concluded that there is a small though systematic dependence of $\tilde{F}(x)$ on the initial supersaturation, at least for small x (Lebowitz et al., 1982); for large values of x , the scaling function appears to be universal in that it becomes independent of temperature and precipitated volume fraction and even of the investigated material (Fratzl et al., 1983). By analogy to the Porod law of small-angle scattering, in this regime $\tilde{F}(x)$ decays in proportion to x^{-4} .

In experiments designed to test the validity of the scaling behavior, $l(t)$ is commonly related to either the radius of gyration R_G , the mean particle radius, or to either $\kappa_m^{-1}(t)$ or $\kappa_1^{-1}(t)$ if κ_m and κ_1 denote the maximum and the first moment of $S(\kappa, t)$, respectively. The scaling function $\tilde{F}(x)$ is then simply obtained, for instance, by plotting $\kappa_m^3 S(\kappa, t)$ versus κ/κ_m . If scaling holds, $\tilde{F}(\kappa/\kappa_m)$ is time independent⁵. After

⁵ In order to test whether experimental data satisfy the scaling law, Fratzl et al. (1983) have proposed a direct method by which the evaluation of R_G , \bar{R} , κ_m or κ_1 can be avoided and by means of which $\tilde{F}(x)$ can be determined graphically.

some initial transient time this, in fact, was observed in the glass systems B_2O_3 -PbO- Al_2O_3 (Craievich et al., 1981, 1986) and in several binary alloys such as Mn-Cu (Fig. 5-61), Al-Zn (e.g., Simon et al., 1984; Hoyt and de Fontaine, 1989) or Ni-Si (Polat et al., 1989). Dynamical scaling behavior was also found in some ternary alloys such as Al-Zn-Mg (Blaschko and Fratzl, 1983). For Cu-Ni-Fe, which was studied by means of anomalous SAXS (Lyon and Simon, 1987), the scaling behavior is found to be obeyed only by the partial structure functions, indicating that this system does not behave like a pseudo-binary system. For Fe-Cr the results are controversial. In contrast to Katano and Iizumi (1984) and Furusaka et al. (1986), La Salle and Schwartz (1984) reported that dynamical scaling does *not* hold. The decomposition kinetics in Fe-Cr at about 500°C are fairly sluggish and it may well be that even after the longest chosen aging time (100 h) the system had not yet reached the scaling region where the microstructure displays self-similarity.

In principle, the structure function $S(\kappa, t)$ contains all the information on the various structural parameters of a decomposing solid such as $f(R, t)$, $N_v(t)$, $\bar{R}(t)$, morphology, etc. which, for instance, may control its mechanical properties. In practice, however, commonly only \bar{R} and N_v and neither $f(R, t)$ nor the morphology can be extracted from experimental data. This stems mainly from a lack of knowledge of the interparticle interference function, which contains the spatial correlations of the precipitate microstructure and which manifests itself in the appearance of a maximum in the $S(\kappa, t)$ curves of less dilute systems. Furthermore, both the limited range of κ over which $S(\kappa, t)$ can be measured and the large background in conventional small-angle scattering experiments often render

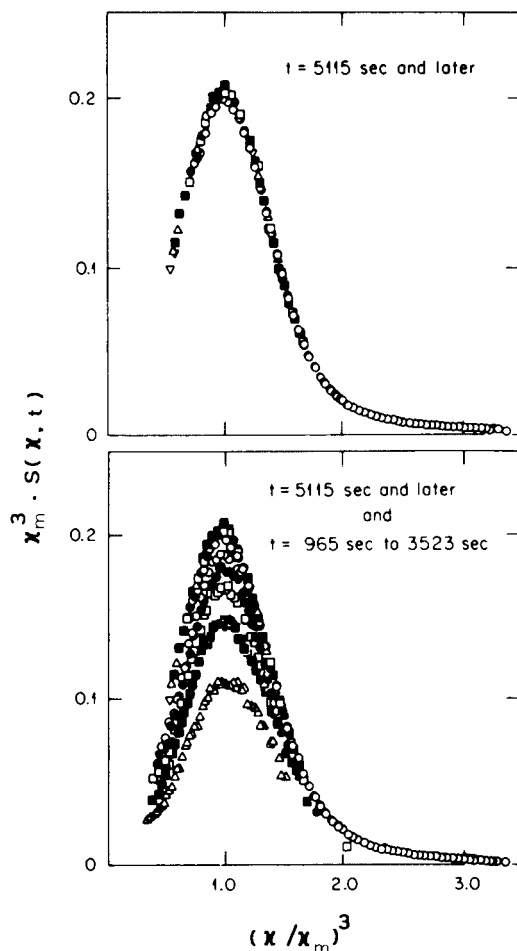


Figure 5-61. Time dependence of the scaling function $\tilde{F}(\kappa/\kappa_m) = \kappa_m^3 S(\kappa, t)$ for Mn-33 at.% Cu at 450°C. For later times ($t > 5115$ s) $\tilde{F}(\kappa/\kappa_m)$ becomes time independent and, hence, dynamic scaling holds (top). The structure functions taken at earlier times (965, 1602, 2239, 2886 and 3532 s) do not yet display scaling behavior (bottom). (After Gaulin et al., 1987.)

the quantitative extraction of information on the precipitate microstructure rather difficult.

From a practical point of view, scaling analyses are sometimes seen to allow *all* information contained in $S(\kappa, t)$ to be deciphered. Provided the explicit form of $\tilde{F}(\kappa)$ could be predicted on grounds of a first-

principles theory, it could be compared with experimental data and employed for a comparison of $S(\kappa, t)$ curves taken from different materials. Up to now, however, this is not feasible. For this reason various *phenomenological theories* for $\tilde{F}(x)$ have been conceived (e.g., Furukawa, 1981; Hennion et al., 1982) amongst which the model of Rikvold and Gunton (1982) may be regarded as the one that is most convenient for a comparison with experimental data as it contains the precipitated volume fraction as the only parameter. This model assumes the two-phase microstructure to consist of a 'gas' of spherical second phase particles (with an identical scattering form factor) each of which is surrounded by a zone depleted of solute atoms. With simple approximations on the probability distribution for pairs of particles with certain inter-particle spacings, the explicit analytical form for $\tilde{F}(x)$ was derived. However, due to the various assumptions invoked, the Rikvold–Gunton model is restricted to smaller precipitated volume fractions. In spite of its simplicity, fair agreement was reported between the theoretical $\tilde{F}(x)$ and the scaling functions obtained from computer simulations and from scaling analyses of $S(\kappa, t)$ curves taken from decomposed Al–Zn and Al–Ag–Zn alloys (Simon et al., 1984). In contrast, in studies of Al–Zn (Forouhi and de Fontaine, 1987) and of Ni–Si (Chen et al., 1988) the predicted $\tilde{F}(x)$ was found to be much broader than the experimental ones; scaling analyses for borate glasses also could not verify the theoretically predicted form of $\tilde{F}(x)$ (Craievich et al., 1986). This may stem from the inadequate assumptions on the chosen probability distribution in which long-range correlations are neglected and/or from precipitate morphologies deviating from spheres, e.g., platelets in Al–Zn.

In contrast to Al–Zn, the small misfit strains between the Al-rich matrix and the spherical δ' -Al₃Li precipitates renders the Al–Li system ideal for an accurate test of scaling in the later stages of coarsening. Using SAXS, Che et al. (1997) found scaling behavior to be obeyed in the coarsening regime of each of the Al–Li alloys with different volume fractions ranging from 0.18 to 0.23. The breadth of the scaled structure function, measured by the full width at half maximum, versus the equilibrium volume fraction, agreed well with the boundary integral-based computer simulation of Akaiwa and Voorhees (1994) (cf. Sec. 5.6.3).

As a concluding remark to this section it is probably fair to state that scaling analyses currently can neither furnish the practical metallurgist with more information on the precipitate microstructure nor on its dynamic evolution than has been possible by conventional analyses of $S(\kappa, t)$ curves prior to the emergence of the scaling hypotheses. It is felt that precise information on the size distribution, the morphology, and the spatial arrangement of precipitates in a two-phase microstructure becomes more readily available from studies employing direct imaging techniques, e.g., CTEM or AFIM, in particular, as dynamical scaling only holds in the later stages of aging where the precipitate microstructure, in general, can be easily imaged and resolved by these techniques. Furthermore, once dynamical scaling is satisfied, the system is close to the asymptotic limit where the LSW theory or its extensions may be applied for a prediction of its dynamic evolution during further aging.

5.8.2 Power-Law Approximations

So far not explicit assumption has been made about the time dependence of the

chosen characteristic length, e.g., $\kappa_m^{-1}(t)$, entering the scaling law, Eq. (5-81). As the self-similarity of a precipitate microstructure and, hence, the scaling law is implicitly contained in the LSW theory of coarsening, the region of validity of dynamical scaling coincides with the LSW regime of coarsening. $\kappa_m^{-1}(t)$ is thus expected to show the simple power-law behavior,

$$\kappa_m^{-1}(t) \sim t^a \quad (5-82)$$

with $a = 1/3$. Accordingly, if scaling holds, the maximum of the structure function must evolve in time as

$$S_m(t) \sim t^b \quad (5-83)$$

with $b = 3a$ (Eq. (5-81)). Such a power-law behavior was frequently corroborated by scattering experiments on materials that were aged in the scaling region, and also by computer simulations (e.g., Lebowitz et al., 1982), which indicated that scaling would hold.

The more recent theoretical developments on the kinetics of phase separation have predicted various other values for the exponent a . On the basis of their cluster-diffusion-coagulation model (Sec. 5.6.4), for *intermediate times* Binder and coworkers predict $a = 1/6$ and $a = 1/5$ or $1/4$ for low and intermediate temperatures, respectively (Binder and Stauffer, 1974; Binder 1977; Binder et al., 1978). As is shown in Fig. 5-31 b, approximation of $S_m(t)$, which displays some curvature, by a power-law (Eq. (5-83)) yields $b = 0.7$ rather than 0.48 as implied by scaling. The LBM theory of spinodal decomposition, which accounts for some coarsening at *earlier* stages (Sec. 5.5.4), yields $a = 0.21$. As outlined in Sec. 5.5.6, these values agree quite well with the corresponding values ($a = 0.16$ to 0.25 and $b = 0.41$ to 0.71 , depending on the supersaturation and ‘aging temperature’) obtained from fitting power laws to the

corresponding data from computer simulations.

Inspired by the theoretical predictions, many scattering experiments on alloys were interpreted in terms of power-law approximations. Frequently the existence of two well-defined kinetic regimes with distinct values of a has been reported (e.g., Fig. 5-32b). At earlier times, a ranges between ≤ 0.1 and ≈ 0.2 , whereas at later stages a and b are found close to the values $1/3$ and 1 predicted by the LSW theory. Sometimes this has been taken as evidence (e.g., Katano and Iizumi, 1984) for the first regime to be dominated by the cluster-diffusion-coagulation mechanism (Sec. 5.6.4), whereas in the second regime, the evolution proceeds according to the LSW mechanism via the evaporation and condensation of single solute atoms.

However, the interpretation of $S_m(t)$ and $\kappa_m(t)$ in terms of two distinct kinetic regimes, each of which is well described by a power law, seems rather debatable. A closer examination of the $S_m(t)$ and κ_m curves (e.g., Fig. 5-32b) always reveals some curvature prior to reaching the scaling region. This clearly shows that the exponents a and b are time dependent; thus, apart from the LSW regime, a power-law approximation must be seen as a rather poor description of the dynamic evolution of a decomposing solid and commonly does not disclose the specific growth mechanism dominating at a certain aging regime. This becomes particularly evident by employing the Numerical Model (Sec. 5.7.3) for a derivation of the exponent $a(t) = \partial \log \bar{R} / \partial \log t$. As the N model comprises nucleation, growth and coarsening as concomitant processes on the basis of just *one* growth mechanism – single-atom evaporation or condensation in the LSW sense – a plot of $a(t)$ versus t allows a closer examination to be made of the valid-

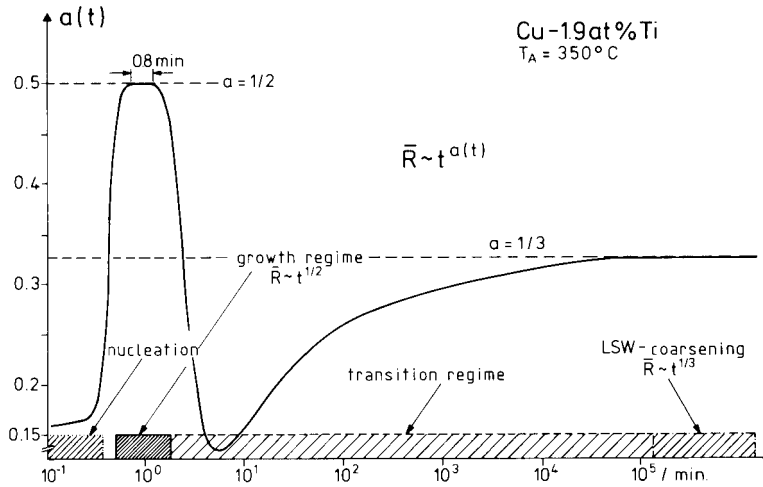


Figure 5-62. Variation of the time exponent a with aging time as evaluated for Cu-1.9 at.% Ti by means of the N model.

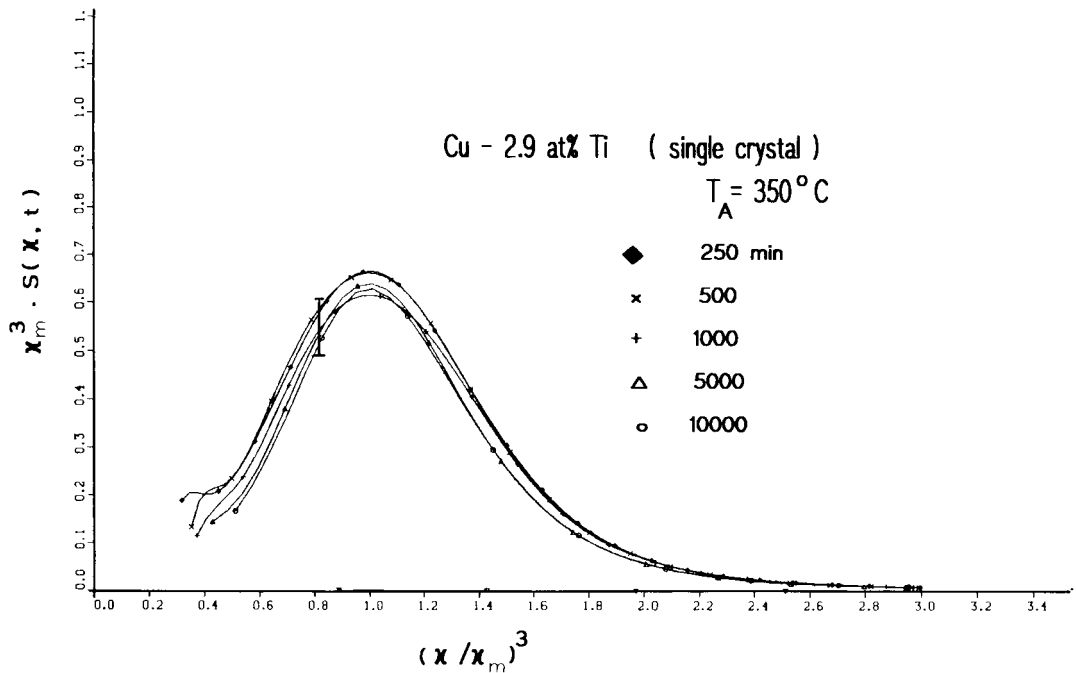


Figure 5-63. Dynamical scaling of the structure function of Cu-2.9 at.% Ti beyond $t = 250$ min; SANS results

ity of power-law approximations at any instant. This is shown in Fig. 5-62 for Cu-1.9 at.% Ti, the experimental kinetic data of which are well described by the N model (cf. Figs. 5-53 and 5-55). Towards the end of the nucleation regime, $a(t)$ increases

sharply from ≈ 0.15 to its maximum value $a = 0.5^6$ which is indicative of a diffusion-controlled growth of the particles. The du-

⁶ Accounting for modified boundary conditions, the cluster-dynamics approach even yields a maximum value $a = 0.7$ (Kampmann et al., 1992).

ration of the growth regime where \bar{R} evolves according to the parabolic power law $\bar{R} \sim t^{1/2}$ is rather short for this alloy (cf. Sec. 5.7.4.3). At the end of the growth regime, where the particle number density has reached its maximum value (Fig. 5-55), $a(t)$ drops within about 250 s to a value of less than 0.1. In the subsequent transition regime at intermediate times, $a(t)$ increases continuously and approaches only slowly the LSW-coarsening regime where dynamical scaling holds. Evidently, there is no time regime between the appearance of the growth regime and the LSW region where power-law behavior is observed. On the other hand, it may be inferred from Fig. 5-62 that the kinetic evolution of \bar{R} during intermediate aging stages might be artificially interpreted in terms of power laws if the time window covered by the experiment was too short; in this case any exponent between 0.15 and 0.33 may be derived. Thus, if the time window for the kinetic experiment is not properly chosen, $a \approx 0.2$ may be obtained, but *without* the cluster–diffusion–coagulation mechanism being operative. As has been pointed out in Sec. 5.6.4.3, with increasing supersaturation, the growth regime with $\bar{R} \propto t^{1/2}$ disappears completely and $a(t)$ takes values only between zero and 1/3. Furthermore, the transition period (where $a < 1/3$) becomes shorter. In this case, LSW coarsening and dynamical scaling are observed after rather short aging times. This is illustrated in Fig. 5-63 for Cu–2.9 at.% Ti which satisfies dynamical scaling after aging for ≈ 250 min at 350°C, whereas for the less concentrated Cu–1.9 at.% Ti alloy scaling only holds after about 5×10^4 min.

5.9 Non-Isothermal Precipitation Reactions

For many age-hardening commercial alloys, the microstructure is established during continuous cooling from the processing temperature, i.e., the solidification or hot-working temperature in cast or wrought alloys, respectively, or during cooling after laser surface treatments or welding (Bratland et al., 1997, and references therein). The resulting non-isothermal transformation usually involves nucleation and growth of the precipitates as concomitant processes. Modeling of non-isothermal transformation rates thus ought to account for the independent variations of the nucleation and the growth rates with temperature and with the temperature-dependent solubilities in the matrix and the precipitated phase. Furthermore, heterogeneous nucleation at lattice defects often must also be taken into account, as usually the driving force for homogeneous nucleation becomes sufficient only once the alloy has been cooled sufficiently deep into the miscibility gap.

Whereas previous models, which have been based on isokinetic behavior and the additivity concept, are limited to a description of only diffusional growth (or dissolution during reheating) (e.g., Shercliff and Ashby, 1990a, b; Myhr and Grong, 1991a, b; Onsoien et al., 1999), Grong and Myhr (2000) considered the non-isothermal precipitation reaction as a coupled nucleation and growth process in terms of a numerical solution and two analytical models. As validated through a comparison with the numerical results, both analytical models, i.e., a simplified state variable solution and a solution based on the Avrami equation, yielded an adequate description of the overall non-isothermal transformation behavior comprising the variation of

the nucleation and growth rates as well as the precipitated volume fraction with temperature and cooling rate.

5.10 Acknowledgements

The authors would like to thank Prof. R. Bormann and Dr H. Mertins for their critical comments on this chapter and Mrs E. Schröder, A. Conrad-Wienands and B. Feldmann for their kind endurance and assistance in preparing the manuscript. The support of this work by the Deutsche Forschungsgemeinschaft (Leibniz-Programm) is also gratefully acknowledged.

5.11 References

- Aalders, C., Van Dijk, S., Radelaar, S. (1984), in: *Decomposition of Alloys: The Early Stages*: Haasen, P., Gerold, V., Wagner, R., Ashby, M. F. (Eds.). Oxford: Pergamon Press, pp. 149–155.
- Aaron, H. B., Fainstain, D., Kotler, G. R. (1970), *J. Appl. Phys.* 41, 4404.
- Aaronson, H. I., Russell, K. C. (1982), in: *Solid-State Phase Transformations*: Aaronson, H. I., Laughlin, D. E., Sekerka, D. F., Wayman, C. M. (Eds.). Warrendale: The Metallurgical Society of AIME, pp. 371–399.
- Aaronson, H. I., Kinsman, K. R., Russell, K. C. (1970a), *Scripta Metall.* 4, 101.
- Aaronson, H. I., Laird, C., Kinsman, K. R. (1970b), in: *Phase Transformations*: Aaronson, H. I. (Ed.). Metals Park, Ohio: Am. Soc. of Metals, pp. 313–396.
- Acuna, R., Craievich, A. F. (1979), *J. Non-Cryst. Solids* 34, 13.
- Agarwal, S. C., Herman, H. (1973), in: *Phase Transformations and Their Application in Materials Science*: Heinisch, H. K., Roy, R. (Eds.). New York: Pergamon, pp. 207–222.
- Akaiwa, N., Voorhees, P. W. (1994), *Phys. Rev. E* 49, 3860.
- Al-Kassab, T., Wollenberger, H., Blavette, D. (1997), *Z. Metallkd.* 88, 2.
- Alkemper, J., Snyder, V. A., Akaiwa, N., Voorhees, P. W. (1999), *Phys. Rev. Lett.* 82, 2725.
- Ardell, A. J. (1967), *Acta Metall.* 15, 1772.
- Ardell, A. J. (1968), *Acta Metall.* 16, 511.
- Ardell, A. J. (1970), *Met. Trans.* 1, 525.
- Ardell, A. J. (1972), *Acta Metall.* 20, 61.
- Ardell, A. J. (1990), *Scripta Metall. Mater.* 24, 343.
- Ardell, A. J. (1995), *Interface Sci.* 3, 119.
- Ardell, A. J., Nicholson, R. B. (1966), *Acta Metall.* 14, 1793.
- Ardell, A. J., Nicholson, R. B., Eshelby, J. D. (1966), *Acta Metall.* 14, 1295.
- Asta, M. (1996), *Acta Mater.* 44, 4131.
- Asta, M., Hoyt, J. J. (1999), *Acta Mater.* 48, 1089.
- Asta, M., Foiles, S. M., Quong, A. (1998), *Phys. Rev. B* 57, 11265.
- Auger, P., Danoix, F., Menand, A., Bourgoign, J., Guttmann, M. (1990), *Mat. Sci. Techn.* 6, 301.
- Auger, P., Pareige, P., Akamatsu, M., Blavette, D. (1995), *J. Nucl. Mat.* 225, 225.
- Bartel, T. L., Rundman, K. B. (1975), *Metall. Trans.* 6A, 1887.
- Bates, F. S., Wiltzius, P. (1989), *J. Chem. Phys.* 91, 3258.
- Beaven, P. A., Frisius, F., Kampmann, R., Wagner, R. (1986), in: *Atomic Transport and Defects in Metals by Neutron Scattering*: Janot, C., Petry, W., Richter, D., Springer, T. (Eds.). Berlin: Springer Verlag, p. 228.
- Becker, R., Döring, W. (1935), *Ann. Phys.* 24, 719.
- Beddoe, R., Haasen, P., Kosterz, G. (1984), in: *Decomposition of Alloys: the Early Stages*: Haasen, P., Gerold, V., Wagner, R., Ashby, M. F. (Eds.). Oxford: Pergamon Press, pp. 233–238.
- Biehl, K.-E., Wagner, R. (1982), in: *Solid-Solid Phase Transformations*: Aaronson, H. I., Laughlin, D. E., Sekerka, R. F., Wayman, C. M. (Eds.). Warrendale: The Metallurgical Society of AIME, pp. 185–189.
- Bigot, A., Auger, P., Chambrelaud, S., Blavette, D., Reeves, A. (1997), *Microsc. Microanal. Microstr.* 8, 103.
- Binder, K. (1977), *Phys. Rev. B* 15, 4425.
- Binder, K. (1980), *J. Phys. (Paris) C* 4, 51.
- Binder, K. (1983), *J. Chem. Phys.* 79, 6387.
- Binder, K. (1984), *Phys. Rev. A* 29, 341.
- Binder, K. (1987), *Advances on Phase Transitions and Disorder Phenomena*: Busiello, G., De Cesare, L., Mancini, F., Marinaro, M. (Eds.). Singapore: World Scientific, pp. 1–71. (Kinetics of First Order Transitions)
- Binder, K., Heermann, D. W. (1985), in: *Scaling Phenomena in Disordered Systems*: Pynn, R., Skjeltorp, T. (Eds.). New York: Plenum Press, pp. 207–230.
- Binder, K., Stauffer, D. (1974), *Phys. Rev. Lett.* 33, 1006.
- Binder, K., Stauffer, D. (1976), *Adv. Phys.* 25, 343.
- Binder, K., Fratzl, P. (2001), in: *Phase Transformations in Materials*: Kosterz, G. (Ed.). Weinheim: Wiley-VCH, Ch. 6.
- Binder, K., Billotet, C., Mirol, P. (1978), *Z. Physik* B30, 183.
- Binder, K., Kalos, M. H., Lebowitz, J. L., Marro, J. (1979), *Colloid Interface Sci.* 10, 173.
- Blaschko, O., Fratzl, P. (1983), *Phys. Rev. Lett.* 51, 288.

- Blaschko, O., Ernst, G., Fratzl, P., Auger, P. (1982), *Acta Metall.* 30, 547.
- Blavette, D., Bostel, A., Sarran, J. M., Deconihout, B., Menand, A. (1993), *Nature* 363, 432.
- Blavette, D., Deconihout, B., Chambreland, S., Bostel, A. (1998), *Ultramicroscopy* 70, 115.
- Bonfiglioli, A. F., Guinier, A. (1966), *Acta Metall.* 14, 1213.
- Bouchard, M., Thomas, G. (1975), *Acta Metall.* 23, 1485.
- Brailsford, A. D., Wynblatt, P. (1979), *Acta Metall.* 27, 489.
- Bratland, D. H., Grong, O., Shercliff, H., Myhr, O. R., Tjøtta, S. (1997), *Acta Mater.* 45, 1.
- Brenner, S. S., Camus, P. P., Miller, M. K., Soffa, W. A. (1984), *Acta Metall.* 32, 1217.
- Cahn, J. W. (1962), *Acta Metall.* 10, 179, 907.
- Cahn, J. W. (1965), *J. Chem.* 42, 93.
- Cahn, J. W. (1966), *Trans. AIME* 242, 166.
- Cahn, J. W., Charles, R. J. (1965), *Phys. Chem. Glasses* 6, 181.
- Cahn, J. W., Hilliard, J. E. (1958), *J. Chem. Phys.* 28, 258.
- Cahn, J. W., Hilliard, J. E. (1959a), *J. Chem. Phys.* 31, 539.
- Cahn, J. W., Hilliard, J. E. (1959b), *J. Chem. Phys.* 31, 688.
- Calderon, H. A., Voorhees, P. W., Murray, J. L., Kostorz, G. (1994), *Acta Metall. Mater.* 42, 991.
- Cerri, A., Schmelzer, R., Schwander, P., Kostorz, G., Wright, A. F. (1987), in: *Proc. MRS Symp.*, Vol. 82: *Characterization of Defects in Materials*: Siegel, R. W., Weertman, J. R., Sinclair, R. (Eds.). Pittsburgh: Materials Research Society, p. 169.
- Cerri, A., Schönfeld, B., Kostorz, G. (1990), *Phys. Rev. B* 42, 958.
- Chan, K. S., Lee, J. K., Shiflet, G. J., Russell, K. C., Aaronson, H. I. (1978), *Metall. Trans.* 9A, 1016.
- Che, D. Z., Spooner, S., Hoyt, J. J. (1997), *Acta Mater.* 45, 1167.
- Chen, H., Polat, S., Epperson, J. E. (1988), in: *Dynamics of Ordering Processes in Condensed Matter*: Komura, S., Furukawa, H. (Eds.). New York: Plenum Press, pp. 245–250.
- Cho, J. H., Ardell, A. J. (1997), *Acta Mater.* 45, 1393.
- Christian, J. W. (1975), *The Theory of Transformations in Metals and Alloys*, 2nd edn. Oxford: Pergamon Press. (General Diffusive Phase Transformations in Solids)
- Cockayne, D. J. H., Gronsby, R. (1981), *Phil. Mag.* A44, 159.
- Cook, H. E. (1970), *Acta Metall.* 18, 297.
- Craievich, A. (1975), *Phys. Chem. Glasses* 16, 133.
- Craievich, A. F., Olivieri, J. R. (1981), *J. Appl. Cryst.* 14, 444.
- Craievich, A., Sanchez, J. M. (1981), *Phys. Rev. Lett.* 47, 1308.
- Craievich, A. F., Sanchez, J. M., Williams, C. E. (1986), *Phys. Rev. B* 34, 2762.
- Danoix, F., Auger, P., Bostel, A., Blavette, D. (1991), *Surf. Sci.* 246, 260.
- Davies, C. K. L., Nash, P., Stevens, R. N. (1980), *Acta Metall.* 28, 179.
- Davies, D. M., Ralph, B. (1972), *J. Microscopy* 96, 343.
- de Fontaine, D. (1969), *Trans. AIME* 245, 1703.
- de Fontaine, D. (1971), *J. Appl. Crystallogr.* 4, 15.
- de Fontaine, D. (1973), *J. Phys. Chem. Sol.* 34, 1285.
- de Fontaine, D. (1982), in: *Metallurgical Treatises*: Tien, J. K., Elliott, J. F. (Eds.). Warrendale, PA: The Metallurgical Society of AIME, pp. 423–444. (Kinetics of First Order Transitions)
- Doherty, R. D. (1982), *Metal. Science* 16, 1.
- Doherty, R. D. (1983), in: *Physical Metallurgy*: Cahn, R. W., Haasen, P. (Eds.), Vol. 2. Amsterdam: North Holland Physics Publishing, pp. 933–1030.
- Doi, M., Miyazaki, T. (1986), *Mater. Sci. Eng.* 78, 87.
- Doi, M., Miyazaki, T., Wakatsuki, T. (1984), *Mater. Sci. Eng.* 67, 247.
- Doi, M., Fukaya, M., Miyazaki, T. (1988), *Phil. Mag.* A57, 821.
- Dutta, I., Allen, S. M. (1991), *J. Mater. Sci. Lett.* 10, 323.
- Eckerlebe, H., Kampmann, R., Wagner, R. (1986), *Atomic Transport and Defects in Metals by Neutron Scattering*: Janot, C., Petry, W., Richter, D., Springer, T. (Eds.). Berlin: Springer Verlag, pp. 66–72.
- Edwards, G. A., Stiller, K., Dunlop, G. L., Couper, M. J. (1998), *Acta Mater.* 46, 3893.
- Enomoto, Y., Kawasaki, K., Tokuyama, M. (1987), *Acta Metall.* 35, 907, 815.
- Epperson, J. E. (1988), in: *Dynamics of Ordering Processes in Condensed Matter*: Komura, S., Furukawa, H. (Eds.). New York: Plenum Press, pp. 245–250.
- Ernst, F., Haasen, P. (1988), *Phys. Stat. Sol. (a)*, 104, 403.
- Ernst, F., Xiao, S. Q., Haider, F., Wilbrandt, P.-J. (1987), *Scripta Metall.* 21, 1189.
- Eshelby, J. D. (1957), *Proc. R. Soc. A* 241, 376.
- Fährmann, M., Fratzl, P., Paris, P., Fährmann, E., Johnson, W. C. (1995), *Acta Metall. Mater.* 43, 1007.
- Feder, J., Russell, K. C., Lothe, J., Pound, G. M. (1966), *Adv. Phys.* 15, 111.
- Ferguson, P., Jack, K. H. (1984), *Phil. Mag.* A50, 221.
- Ferguson, P., Jack, K. H. (1985), *Phil. Mag.* A52, 509.
- Forouhi, A. R., de Fontaine, D. (1987), *Acta Metall.* 35, 1863.
- Fratzl, P., Penrose, O. (1994), *Phys. Rev. B* 50, 3477.
- Fratzl, P., Penrose, O. (1996), *Acta Metall.* 44, 3025.
- Fratzl, P., Lebowitz, J. L., Marro, J., Kalos, M. H. (1983), *Acta Metall.* 31, 1849.
- Frenkel, J. (1939), *J. Phys. (USSR)* 1, 315.
- Furukawa, H. (1981), *Phys. Rev. A* 23, 1535.

- Furusaka, M., Ishikawa, Y., Yamaguchi, S., Fujino, Y. (1986), *J. Phys. Soc. Japan* 55, 2253.
- Gaskell, D. R. (1983), in: *Physical Metallurgy*, Vol. 1: Cahn, R. W., Haasen, P. (Eds.). Amsterdam: North Holland Physics Publishing, pp. 271–326. (Metallurgical Thermodynamics)
- Gaulin, B. D., Spooner, S., Morii, Y. (1987), *Phys. Rev. Lett.* 59, 668.
- Gerling, R., Schimansky, F.-P., Wagner, R. (1988), *Acta Metall.* 36, 575.
- Gerold, V., Merz, W. (1967), *Scripta Metall.* 1, 33.
- Glatter, O. (1982), in: *Small Angle X-Ray Scattering*: Glatter, O., Kratky, O. (Eds.). London: Academic, p. 167.
- Gleiter, H. (1983), in: *Physical Metallurgy*: Cahn, R. W., Haasen, P. (Eds.), Vol. 1. Amsterdam: North Holland Physics Publishing, pp. 649–713.
- Goldstein, M. (1965), *J. Am. Ceram. Soc.* 48, 126.
- Grong, O., Myhr, O. R. (2000), *Acta Mater.* 48, 445.
- Gronsky, R., Okada, M., Sinclair, R., Thomas, G. (1975), *33rd Ann. Proc. E.M.S.A.*, 22.
- Grüne, R. (1988), *Acta Metall.* 36, 2797.
- Grüne, R., Oehring, M., Wagner, R., Haasen, P. (1985), in: *Rapidly Quenched Metals*, Vol. 1: Steeb, S., Warlimont, H. (Eds.). Amsterdam: North Holland, pp. 761–765.
- Gunton, J. D. (1984), in: *Decomposition of Alloys: the Early Stages*: Haasen, P., Gerold, V., Wagner, R., Ashby, M. F. (Eds.). Oxford: Pergamon Press, pp. 1–10.
- Gunton, J. D., Droz, M. (1984), *Lecture Notes in Physics*, Vol. 183 – *Introduction to the Theory of Metastable and Unstable States*. Berlin: Springer Verlag. (Kinetics of First Order Transitions)
- Gupta, A. K., Lloyd, D. J. (1992), in: *Proc. 3rd Int. Conf. on Aluminium Alloys: Their Physical and Mechanical Properties*, Vol. 2: Arnberg, L. (Ed.). Trondheim: Norwegian Institute of Technology and SINTEF Metallurgy, p. 21.
- Guyot, P., Simon, J. P. (1981), in: *Solid–Solid Phase Transformation*: Aaronson, H. I., Laughlin, D. E., Sekerka, R. F., Wayman, C. M. (Eds.). New York: Metallurgical Society of A.I.M.E., p. 325.
- Haasen, P., Wagner, R. (1985), *Ann. Rev. Mat. Sci.* 15, 43.
- Hardy, S. C., Voorhees, P. W. (1988), *Metall. Trans.* 19A, 2713.
- Hashimoto, T., Itakura, M., Hasegawa, H. (1986a), *J. Chem. Phys.* 85, 6118.
- Hashimoto, T., Itakura, M., Hasegawa, H. (1986b), *J. Chem. Phys.* 85, 6773.
- Hennion, M., Ronzaud, D., Guyot, P. (1982), *Acta Metall.* 30, 599.
- Herring, C. (1953), in: *Structure and Properties of Solid Surfaces*: Gomer, R., Smith, C. S. (Eds.). Chicago, IL: Univ. of Chicago Press, pp. 5–149.
- Hilliard, J. E. (1970), in: *Phase Transformations*: Aaronson, H. I. (Ed.). Metals Park, Ohio: Am. Soc. of Metals, pp. 497–560.
- Hirata, T., Kirkwood, D. H. (1977), *Acta Metall.* 25, 1425.
- Hobbs, L. W., Westmacott, K. W., Williams, D. B. (Eds.) (1986), *Proc. of the Materials Research Society Symposium*, Vol. 62: *Materials Problem Solving with the Transmission Electron Microscope*. (Experimental Techniques; CTEM)
- Horiuchi, S., Izumi, F., Kikuchi, T., Uchida, K. (1984), *Phil. Mag.* A50, L29.
- Hornbogen, E. (1967), *Aluminium* 43, 115.
- Hoyt, J. J. (1989), *Acta Metall.* 37, 2489.
- Hoyt, J. J., de Fontaine, D. (1989), *Acta Metall.* 37, 1611.
- Hoyt, J. J., Sluiter, M., Clark, B., Kraitchman, M., de Fontaine, D. (1987), *Acta Metall.* 35, 2315.
- Hoyt, J. J., Clark, B., de Fontaine, D. (1989), *Acta Metall.* 37, 1597.
- Hütten, A., Haasen, P. (1986), *J. Phys. (Paris)* C7, 205.
- Izumitani, T., Hashimoto, T. (1985), *J. Chem. Phys.* 83, 3694.
- Jantzen, C. M. F., Herman, H. (1978), in: *Phase Diagrams: Materials Science and Technology*, Vol. 5: Alper, A. M. (Ed.). New York: Academic Press, pp. 128–185.
- Johnson, W. C. (1984), *Acta Metall.* 32, 465.
- Johnson, W. C., Cahn, J. W. (1984), *Acta Metall.* 23, 1839.
- Johnson, W. C., Abinandanan, T. A., Voorhees, P. W. (1990), *Acta Metall.* 38, 1349.
- Kalos, M., Lebowitz, J. L., Penrose, O., Sur, A. (1978), *J. Stat. Phys.* 18, 39.
- Kampmann, R., Wagner, R. (1984), in: *Decomposition of Alloys: the Early Stages*: Haasen, P., Gerold, V., Wagner, R., Ashby, M. F. (Eds.). Oxford: Pergamon Press, pp. 91–103.
- Kampmann, R., Wagner, R. (1986), in: *Atomic Transport and Defects in Metals by Neutron Scattering*: Janot, C., Petry, W., Richter, D., Springer, T. (Eds.). Berlin: Springer Verlag, pp. 73–77.
- Kampmann, R., Eckerlebe, H., Wagner, R. (1987), in: *Phase Transitions in Condensed Systems – Experiments and Theory*: Cargill, G. S., Spaepen, F., Tu, K.-N. (Eds.). MRS-Symp. Proceedings, Vol. 57: Materials Research Society, Pittsburgh, PA, pp. 525–542.
- Kampmann, R., Ebel, T., Haese, M., Wagner, R. (1992), *Phys. Stat. Sol. B* 172, 295.
- Katano, S., Iizumi, M. (1982), *J. Phys. Soc. Japan* 51, 347.
- Katano, S., Iizumi, M. (1984), *Phys. Rev. Lett.* 52, 835.
- Kaufman, L. (Ed.) (1977), *CALPHAD*, 1. Oxford: Pergamon Press. (Volumes are published annually, from 1977 onwards.)
- Kaufman, L., Bernstein, H. (1970), *Computer Calculations of Phase Diagrams*. New York: Academic Press.
- Kaufmann, M. J., Voorhees, P. W., Johnson, C., Biancaniello, F. S. (1989), *Metall. Trans.* 20A, 2171.

- Kawasaki, K. (1972), in: *Phase Transitions and Critical Phenomena*, Vol. 2: Domb, C., Green, M. S. (Eds.). New York: Academic Press, p. 2.
- Khachaturyan, A. G. (1983), *Theory of Phase Transformations in Alloys*. New York: John Wiley.
- Khachaturyan, A. G., Airapetyan, V. M. (1974), *Phys. Stat. Sol.* 26, 61.
- Khachaturyan, A. G., Semenovskaya, S. V., Morris, J. W. (1988), *Acta Metall. Mater.* 36, 1563.
- Kirkwood, D. H. (1970), *Acta Metall.* 18, 563.
- Kostorz, G. (Ed.) (1979), *Neutron Scattering*. New York: Academic, p. 227. (Experimental Techniques; SANS)
- Kuo, S. Y., Virkar, A. V. (1987), *J. Am. Ceram. Soc.* 70, C-125.
- Langer, J. S. (1971), *Ann. Phys.* 65, 53.
- Langer, J. S. (1973), *Acta Metall.* 21, 1649.
- Langer, J. S. (1975), in: *Fluctuations, Instabilities, and Phase Transitions*: Riste, T. (Ed.). New York: Plenum Press, pp. 19–42.
- Langer, J. S., Schwartz, A. J. (1980), *Phys. Rev. A* 21, 948.
- Langer, J. S., Bar-On, Miller, H. D. (1975), *Phys. Rev. A* 11, 1417.
- Langmayr, F., Fratzl, P., Vogl, G. (1994), *Phys. Rev. B* 49, 11759.
- La Salle, J. C., Schwartz, L. H. (1984), in: *Decomposition of Alloys: the Early Stages*: Haasen, P., Gerold, V., Wagner, R., Ashby, M. F. (Eds.). Oxford: Pergamon Press, pp. 104–109.
- Laughlin, D. E. (1976), *Acta Metall.* 24, 53.
- Laughlin, D. E., Cahn, J. W. (1975), *Acta Metall.* 23, 329.
- Lê, T. N., Barbu, A., Maury, F. (1992), *Scripta Metall. Mater.* 26, 771.
- Lebowitz, J. L., Kalos, M. H. (1976), *Scripta Metall.* 10, 9.
- Lebowitz, J. L., Marro, J., Kalos, M. H. (1982), *Acta Metall.* 30, 297.
- Lee, J. K. (1997), *Mater. Sci. Eng.* A238, 1.
- Lee, J. K. (2000), *Theor. Appl. Fract. Mech.* 33, 207.
- Lee, J. H., Johnson, W. C. (1982), in: *Solid-State Phase Transformations*: Aaronson, H. I., Laughlin, D. E., Sekerka, D. F., Wayman, C. M. (Eds.). Warrendale: The Metallurgical Society of AIME, pp. 127–150.
- Lee, J. K., Barnett, D. M., Aaronson, H. I. (1977), *Metall. Trans.* 8A, 963.
- Lee, Y. W., Aaronson, H. I. (1980), *Acta Metall.* 28, 539.
- LeGoues, F. K., Aaronson, H. I. (1984), *Acta Metall.* 32, 1855.
- LeGoues, F. K., Aaronson, H. I., Lee, Y. W., Fix, G. J. (1982), in: *Solid-Solid Phase Transformations*: Aaronson, H. I., Laughlin, D. E., Sekerka, R. F., Wayman, C. M. (Eds.). Warrendale: The Metallurgical Society of AIME, pp. 427–431.
- LeGoues, F. K., Lee, Y. W., Aaronson, H. I. (1984a), *Acta Metall.* 32, 1837.
- LeGoues, F. K., Lee, Y. W., Aaronson, H. I. (1984b), *Acta Metall.* 32, 1845.
- LeGoues, F. K., Wright, R. N., Lee, Y. W., Aaronson, H. I. (1984c), *Acta Metall.* 32, 1865.
- Leo, P. H., Mullins, W. W., Sekerka, R. F., Vinals, J. (1990), *Acta Metall. Mater.* 38, 1573.
- Lifshitz, I. M., Slyozov, V. V. (1961), *Phys. Chem. Solids* 19, 35.
- Liu, Z. G., Wagner, R. (1984), *J. Phys. Colloq.* C9, 441.
- Livak, R. J., Thomas, G. (1974), *Acta Metall.* 22, 589.
- Lyon, O., Simon, J. P. (1987), *Phys. Rev. B* 35, 5164.
- Lyon, O., Simon, J. P. (1988), *J. Phys. F, Metal Physics* 18, 1787.
- Maheshwari, A., Ardell, A. J. (1992), *Scripta Metall.* 26, 347.
- Mandyam, H., Glicksman, M. E., Helsing, J., Marsh, S. P. (1998), *Phys. Rev. E* 58, 2119.
- Marder, M. (1987), *Phys. Rev. A* 36, 858.
- Marqusee, J. A., Ross, J. (1984), *J. Chem. Phys.* 79, 373.
- Marqusee, J. A., Ross, J. (1984), *J. Chem. Phys.* 80, 536.
- Marro, J., Bortz, A. B., Kalos, M. H., Lebowitz, J. L. (1975), *Phys. Rev. B* 12, 2000.
- Marro, J., Bortz, A. B., Kalos, M. H., Lebowitz, J. L. (1977), *Phys. Rev. B* 15, 3014.
- Marsh, S. P., Glicksman, M. E. (1996), *Acta Mater.* 44, 3761.
- Martin, G. (1978), in: *Solid State Phase Transformations in Metals and Alloys: Aussois: Les Editions de Physique*, pp. 337–406. (Kinetics of Phase Separation in Solids)
- Martin, J. W., Doherty, R. D. (1976), *Stability of Microstructure in Metallic Systems*. Cambridge: University Press, p. 163.
- Miller, M. K., Brenner, S. S., Burke, M. G., Soffa, W. A. (1984), *Scripta Metall.* 18, 111.
- Miller, M. K., Horton, L. L., Spooner, S. (1986), in: *Proc. 32nd Intl. Field Emission Symp.: J. Phys. (Paris)* 47, *Coloque C2*: Miller, M. K., Brenner, S. S. (Eds.). Paris: Les Editions de Physique, pp. 409–416.
- Miller, M. K., Cerezo, A., Hetherington, M. G., Smith, G. D. W. (1996), *Atom-Probe Field Ion Microscopy*, Oxford: Oxford Science Publications. (Tomographic Atom-Probe)
- Mirolod, P., Binder, K. (1977), *Acta Metall.* 25, 1435.
- Miyazaki, T., Doi, M. (1989), *Mater. Sci. Eng. A* 110, 175.
- Miyazaki, T., Imamura, H., Kozakai, T. (1982), *J. Mater. Sci. Eng.* 54, 9.
- Miyazaki, T., Seki, K., Doi, M., Kozakai, T. (1986), *J. Mater. Sci. Eng.* 77, 125.
- Morrall, J. E., Cahn, J. W. (1971), *Acta Metall.* 19, 1037.
- Mueller, R., Gross, D. (1998), *Comp. Mat. Sci.*, 11, 25.
- Mullins, W. W. (1986), *J. Appl. Phys.* 59, 1341.

- Murata, Y., Iwama, Y. (1981), *Trans. Japan. Inst. of Metals* 22, 433.
- Myhr, O. R., Grong, O. (1991a), *Acta Metall.* 39, 2693.
- Myhr, O. R., Grong, O. (1991b), *Acta Metall.* 39, 2703.
- Neilson, G. F. (1969), *Phys. Chem. Glasses* 10, 54.
- Nishi, T., Wang, T. T., Kwei, T. K. (1975), *Macromolecules* 8, 227.
- Nishimori, H., Onuki, A. (1990), *Phys. Rev.* B42, 980.
- Okada, M., Han, C. C. (1986), *J. Chem. Phys.* 85, 5317.
- Onsoien, M. I., Grong, O., Gundersen, O., Skaland, T. (1999), *Metall. Mater. Trans.* 30A, 1069.
- Onuki, A., Nishimori, H. (1991), *Phys. Rev.* B43, 13649.
- Pareige, P., Soisson, F., Martin, G., Blavette, D. (1999), *Acta Mater.* 47, 1889.
- Paris, O., Langmayr, F., Vogl, G., Fratzl, P. (1995), *Z. Metallkd.* 86, 860.
- Park, M. W., Mitchell, T. E., Heuer, A. H. (1975), *J. Am. Ceram. Soc.* 58, 43.
- Park, M. W., Mitchell, T. E., Heuer, A. H. (1976), *J. Mater. Sci.* 11, 1227.
- Penrose, O. (1978), in: *Lecture Notes in Physics*, Vol. 84: Garrido, L., Seglar, P., Shepherd, P. J. (Eds.). Heidelberg: Springer Verlag, pp. 210–234.
- Penrose, O., Lebowitz, J. L. (1979), in: *Studies in Statistical Mechanics*, Vol. 7: Lebowitz, J. L., Montroll, E. (Eds.). Amsterdam: North Holland, pp. 293–340. (Kinetics of First Order Transitions)
- Penrose, O., Lebowitz, J. L., Marro, J., Kalos, M. H., Sur, A. (1978), *J. Stat. Phys.* 19, 243–267.
- Pike, B. C., Messoloras, S., Stewart, R. J. (1989), *Scripta Metall.* 23, 983.
- Piller, J., Wagner, W., Wollenberger, H., Mertens, P. (1984), in: *Decomposition of Alloys: the Early Stages*: Haasen, P., Gerold, V., Wagner, R., Ashby, M. F. (Eds.). Oxford: Pergamon Press, pp. 156–164.
- Polat, S., Marsh, C., Little, T., Ju, C. P., Epperson, J. E., Haydn Chen (1986), *Scripta Metall.* 20, 1759.
- Polat, S., Haydn Chen, Epperson, J. E. (1989), *Met. Trans.* 20A, 699.
- Purdy, G., Bréchet, Y. J. M. (2001), in: *Phase Transformations in Materials*: Kosterz, G. (Ed.). Weinheim: Wiley-VCH, Chap. 7.
- Radmilovic, V., Fox, A. G., Thomas, G. (1989), *Acta Metall.* 37, 2385.
- Rikvold, P. A., Gunton, J. D. (1982), *Phys. Rev. Lett.* 49, 286.
- Rindone, G. E. (1975), *Bull. Cent. Glass Ceram. Research Inst. Calcutta* 22, 119.
- Rioja, R. J., Laughlin, D. A. (1977), *Metall. Trans.* 8A, 1257.
- Rundman, K. B., Hilliard, J. E. (1967), *Acta Metall.* 15, 1025.
- Russell, K. C. (1980), *Adv. Colloid Interface Sci.* 13, 205.
- Sato, R., Han, C. C. (1988), *J. Chem. Phys.* 88, 2057.
- Sato, K., Tagawa, K., Inoue, Y. (1989), *Mater. Sci. Engin. A111*, 45.
- Sauthoff, G., Pitsch, W. (1987), *Phil. Mag.* B56, 471.
- Schmidt, I., Gross, D. (1997), *J. Mech. Phys. Solids* 45, 1521.
- Schmidt, I., Mueller, R., Gross, D. (1998), *Mech. Mater.* 30, 181.
- Schmitz, G., Haasen, P. (1992), *Acta Metall. Mater.* 40, 2209.
- Sequeira, A. D., Calderon, H. A., Kosterz, G., Pedersen, J. S. (1995), *Acta Metall. Mater.* 43, 3427.
- Servi, I. S., Turnbull, D. (1966), *Acta Metall.* 14, 161.
- Shercliff, H. R., Grong, O., Myhr, O. R., Ashby, M. F. (1992), in: *Proc. 3rd Int. Conf. on Aluminium Alloys – Their Physical, Mechanical Properties*, Vol. 3: Arnberg, L. (Ed.). Trondheim: Norwegian Institute of Technology and SINTEF Metallurgy, p. 357.
- Shercliff, H. R., Ashby, M. F. (1990a), *Acta Metall.* 38, 1789.
- Shercliff, H. R., Ashby, M. F. (1990b), *Acta Metall.* 38, 1803.
- Shewmon, P. G. (1965), *Trans. TMS-AIME* 233, 736.
- Shiflet, G. J., Lee, Y. W., Aaronson, H. I., Russell, K. C. (1981), *Scripta Metall.* 15, 719.
- Si-Qun Xiao, Haasen, P. (1991), *Acta Metall.* 39, 65.
- Simon, J. P., Lyon, O. (1989), *Acta Metall.* 37, 1727.
- Simon, J. P., Guyot, P., DeSalva, A. G. (1984), *Phil. Mag.* A49, 151.
- Sinclair, R., Thomas, G. (1974), *32nd Ann. Proc. E.M.S.A.*, 500.
- Singh, J., Lele, S., Ranganathan, S. (1980), *J. Mater. Sci.* 15, 2010.
- Singhai, S. P., Herman, H., Kosterz, G. (1978), *J. Appl. Cryst.* 11, 572.
- Skipov, V. P., Skipov, A. V. (1979), *Sov. Phys. Usp.* 22, 389.
- Sluiter, M., Kawazoe, Y. (1996), *Phys. Rev.* B54, 10381.
- Smith, D. J. (1983), *Helv. Phys. Acta* 56, 463. (Experimental Techniques; HREM)
- Snyder, H. L., Meakin, P. (1983a), *J. Chem. Phys. Soc.* 79, 5588.
- Snyder, H. L., Meakin, P. (1983b), *Macromolecules* 16, 757.
- Snyder, H. L., Meakin, P. (1985), *J. Polym. Sci.* 73, 217.
- Soisson, F., Barbu, A., Martin, G. (1996), *Acta Mater.* 44, 3789.
- Staron, P., Kampmann, R. (2000a), *Acta Mater.* 48, 701.
- Staron, P., Kampmann, R. (2000b), *Acta Mater.* 48, 713.
- Stauffer, D. (1979), *Phys. Rep.* 54, 1.
- Steiner, D., Beddoe, R., Gerold, V., Kosterz, G., Schmelzger, R. (1983), *Scripta Metall.* 17, 733.
- Stubican, V. S., Schultz, A. H. (1970), *J. Am. Ceram. Soc.* 53, 211.
- Su, C. H., Voorhees, P. W. (1996), *Acta Metall. Mater.* 44, 1987.

- Sur, A., Lebowitz, J. L., Marro, J., Kalos, M. H. (1977), *Phys. Rev. B* 15, 3014.
- Taylor, K. A. (1985), Sc.D. Thesis *Aging Phenomena in Ferrous Martensites*. MIT, Cambridge, MA.
- Thompson, M. E., Voorhees, P. W. (1999), *Acta Mater.* 47, 983.
- Thompson, M. E., Su, C. S., Voorhees, P. W. (1994), *Acta Metall.* 42, 2107.
- Tien, J. K., Shewmon, P. G., Foster, J. S. (1973), *Scripta Metall.* 7, 1171.
- Tokuyama, M., Kawasaki, K. (1984), *Physica A* 123, 386.
- Tsumuraya, K., Miyata, Y. (1983), *Acta Metall.* 31, 437.
- Ujihara, T., Osamura, K. (2000), *Acta Mater.* 48, 1629.
- Vintaikin, Y. E., Dmitriyev, V. B., Udovenko, V. A. (1979), *Phys. Met. Metall.* 46, 97.
- Volmer, M., Weber, A. (1926), *Z. Phys. Chem.* 119, 277.
- von Alvensleben, L., Wagner, R. (1984), in: *Decomposition of Alloys: the Early Stages*: Haasen, P., Gerold, V., Wagner, R., Ashby, M. F. (Eds.). Oxford: Pergamon Press, pp. 143–148.
- Voorhees, P. W., Glicksman, M. E. (1984), *Acta Metall.* 32, 2001, 2013.
- Voorhees, P. W., Johnson, W. C. (1988), *Phys. Rev. Lett.* 61, 225.
- Voorhees, P. W., Schaefer, R. J. (1987), *Acta Metall.* 35, 327.
- Wagner, C. (1961), *Z. Elektrochem.* 65, 581.
- Wagner, R. (1982), *Field Ion Microscopy in Materials Science*, Vol. 6, *Crystals–Growth, Properties and Applications*: Freyhardt, H. C. (Ed.). Berlin: Springer Verlag. (Experimental Techniques; AFIM)
- Wagner, R., Brenner, S. S. (1978), *Acta Metall.* 26, 197.
- Wagner, W., Poerschke, R., Wollenberger, H. (1984), in: *Decomposition of Alloys: the Early Stages*: Haasen, P., Gerold, V., Wagner, R., Ashby, M. F. (Eds.). Oxford: Pergamon Press, pp. 170–179.
- Wagner, R., Kampmann, R., Jiang, B., Beaven, P. A. (1988), in: *Proc. Int. Conf. Cu '86 – Copper Tomorrow – Technology, Products, Research*: Ceresara, S. (Ed.). Barga die Lucca, pp. 119–127.
- Wahi, R. P., Stajer, J. (1984), in: *Decomposition of Alloys: the Early Stages*: Haasen, P., Gerold, V., Wagner, R., Ashby, M. F. (Eds.). Oxford: Pergamon Press, pp. 165–169.
- Wang, Y., Khachaturyan, A. G. (1995), *Acta Metall. Mater.* 43, 1837.
- Wang, Y., Chen, L.-Q., Khachaturyan, A. G. (1991), *Scripta Metall. Mater.* 25, 1387.
- Wang, Y., Chen, L.-Q., Khachaturyan, A. G. (1992), *Phys. Rev. B* 46, 11194.
- Weins, J. J., Cahn, J. W. (1973), in: *Sintering and Related Phenomena*, Kuczynski, G. C. (Ed.). London: Plenum, p. 151.
- Wendt, H., Haasen, P. (1983), *Acta Metall.* 31, 1649.
- West, A. W., Kirkwood, D. H. (1976), *Scripta Metall.* 10, 681.
- Williams, D. B., Carter, C. B. (1996), *Transmission Electron Microscopy*. New York and London: Plenum Press, p. 683.
- Wiltzius, P., Bates, F. S., Dierker, S. B., Wignall, G. D. (1987), *Phys. Rev. A* 36, 2991.
- Wiltzius, P., Bates, F. S., Heffner, W. R. (1988), *Phys. Rev. Lett.* 60, 1538.
- Wood, J. V., Mills, P. F., Bingham, J. K., Bee, J. V. (1979), *Metall. Trans.* 10A, 525.
- Yaldram, K., Binder, K. (1991 a), *Z. Phys.* B82, 405.
- Yaldram, K., Binder, K. (1991 b), *Acta Metall. Mater.* 39, 707.
- Yao, J. H., Elder, K. R., Guo, H., Grant, M. (1993), *Phys. Rev. B* 47, 14110.
- Yin, F., Oksawa, Y., Sato, A., Kawakara, K. (2000), *Acta Mater.* 48, 1273.
- Yoo, Y. S., Yoon, D. Y., Henry, M. F. (1995), *Metals and Mater.* 1, 47.
- Yoshida, S., Fukaya, M., Miyazaki, T. (1987), *J. Japan. Inst. Metals* 51, 18.
- Zeldovich, J. B. (1943), *Acta Physicochim. (USSR)* 18, 1.
- Zener, C. (1949), *J. Appl. Phys.* 20, 950.
- Zhu, F., Haasen, P., Wagner, R. (1986), *Acta Metall.* 34, 457.

6 Spinodal Decomposition

Kurt Binder

Institut für Physik, Johannes Gutenberg-Universität Mainz,
Mainz, Federal Republic of Germany

Peter Fratzl

Erich-Schmid-Institut der Österreichischen Akademie der Wissenschaften
und Montan-Universität Leoben, Leoben, Austria

List of Symbols and Abbreviations	411
6.1 Introduction	414
6.2 General Concepts	416
6.2.1 Phenomenological Thermodynamics of Binary Mixtures and the Basic Ideas of Phase Separation Kinetics	416
6.2.2 The Cahn–Hilliard–Cook Nonlinear Diffusion Equation	420
6.2.3 Linearized Theory of Spinodal Decomposition	421
6.2.4 Spinodal Decomposition of Polymer Mixtures	426
6.2.5 Significance of the Spinodal Curve	428
6.2.6 Towards a Nonlinear Theory of Spinodal Decomposition in Solids and Fluids	437
6.2.7 Effects of Finite Quench Rate	441
6.2.8 Interconnected Precipitated Structure Versus Isolated Droplets, and the Percolation Transition	442
6.2.9 Coarsening and Late Stage Scaling	445
6.2.10 Effects of Coherent Elastic Misfit	447
6.3 Survey of Experimental Results	450
6.3.1 Metallic Alloys	451
6.3.2 Glasses, Ceramics, and Other Solid Materials	454
6.3.3 Fluid Mixtures	455
6.3.4 Polymer Mixtures	457
6.4 Extensions	460
6.4.1 Systems Near a Tricritical Point	460
6.4.2 Spontaneous Growth of Ordered Domains out of Initially Disordered Configurations	462
6.4.3 Phase Separation in Reduced Geometry and near Surfaces	467
6.4.4 Effects of Quenched Impurities; Vacancies; Electrical Resistivity of Metallic Alloys Undergoing Phase Changes	468
6.4.5 Further Related Phenomena	470

6.5	Discussion	471
6.6	Acknowledgements	473
6.7	References	474

List of Symbols and Abbreviations

a	lattice spacing
A, B, \dots	symbols for chemical elements
$a(t)$	structural relaxation variable
A, B	symbols for Landau expansion coefficients or other constants
a_0, \dots, a_3	constants
\hat{B}	critical amplitude of the order parameter
$c(\mathbf{x}), c_i$	local concentration, concentration of site i
\hat{C}	critical amplitude of the scattering function
$c_B^s, c_{sp}(T)$	concentration at the spinodal curve
c_{coex}	concentration at the coexistence curve
\bar{c}	average concentration
c_{crit}	critical concentration
d	spatial dimensionality
D_0	diffusion constant
D_2	damping coefficient of second sound
D_t	tracer diffusion coefficient
e	electron charge
e_{ij}	elastic strain tensor
e_{ij}^0	elastic misfit tensor
E_{act}	activation energy
F	thermodynamic free energy
$\Delta \mathcal{F}$	free energy function
ΔF^*	nucleation free-energy barrier
F_{MF}^*	mean-field result for the nucleation barrier
f_0	parameter or universal constant of order unity
f_{cg}	free energy density (coarse-grained)
f_D	Debye function
g	cooling rate
\mathcal{H}	Hamiltonian
\hbar	Planck constant
J	concentration current density
J	interaction strength of the Ising model
K	elastic modulus
\mathbf{k}	wavevector, scattering vector in diffraction experiments
k	modulus of \mathbf{k}
k_B	Boltzmann constant
k_c	critical wavenumber in Cahn's theory
k_F	radius of Fermi sphere
k_m	wavenumber of maximal growth
L	length scale of coarse-graining cell
l	number of atoms within a cluster
\mathcal{L}	Liouville operator
M	mobility

m_{eff}	effective mass of an electron
N	chain length of a polymer
N	number of atoms per cm^3
n_L	concentration of a cluster containing L atoms
$P_L(M)$	magnetization distribution function
q	rescaled wavenumber
Q_B	superstructure Bragg spot
r	range of effective interaction
r	radius of the grain
$\langle R^2 \rangle$	mean-square end-to-end distance of a polymer chain
$\langle R_{\text{gyr}}^2 \rangle$	gyration radius of a polymer chain
$R(k)$	rate factor
r_0	phenomenological coefficient
$S(k, t)$	equal-time structure factor
$s(\mathbf{x}, t)$	entropy density
\tilde{S}	rescaled structure factor
T	temperature
t	time
T_0	temperature at which a quench is started at $t=0$
$T_{\alpha\beta}$	Oseen tensor (component)
T_c	critical temperature
T_i, T_f	initial, final temperature
t_{ij}	elastic stress tensor
T_t	tricritical point
u	phenomenological coefficient of the Landau expansion
u_2	second sound velocity
V	volume
v	phenomenological coefficient of the Landau expansion
w	elastic energy density
$W(l, l')$	cluster reaction matrix
W_A, W_B	time constant of element A, B
x	Lifshitz–Slyozov exponent
\mathbf{x}	position vector
x, y, z	spatial coordinates
X_A, X_B	degree of polymerization of a polymer chain of type A, B
δ	scaling variable
Z-A %, Z-B %	atomic numbers of constituents A, B
α	phenomenological coupling constant
β	critical exponent of the order parameter
γ	critical exponent of the structure factor
γ	phenomenological coefficient
Γ, γ	rate factors
η	viscosity
η_a	change of lattice constant with alloy composition

η_T	random force
Θ	temperature at which behavior of polymer in solution is ideal
κ	factor describing screening of Coulomb interaction
λ	wavelength
λ_c	critical wavelength in Cahn's theory
λ_{ijmn}	elastic stiffness tensor
Λ	generalized Onsager coefficient
μ	chemical potential difference
μ	elastic modulus
ν	critical exponent of the correlation length
ν_P	Poisson coefficient in elasticity theory
ξ	interfacial width; correlation length
ξ_c	critical amplitude of the correlation length
ξ_{coex}	correlation length at the coexistence curve
Q_1, Q_2, \dots	probability distributions
σ	subunit length of a polymer
σ_{ij}	elastic stress tensor
τ	rescaled coordinate (time)
τ	time constant
φ	pair interaction energy
Φ	volume fraction
Φ_c	volume fraction at the critical point
χ	Flory–Huggins parameter
χ_s	Flory–Huggins parameter at the spinodal curve
χ_n^{-1}	phenomenological coefficient
ψ	complex order parameter
ABV	element-A–element-B–vacancy model
CHC	Cahn–Hilliard–Cook (method)
ESA	European Space Association
LBM	Langer–Baron–Miller (method)
LSW	Lifshitz–Slyozov–Wagner (method)
m	(index) maximum
MF	mean field
p	(index) polarization
V	vacancy (also as index)

6.1 Introduction

This chapter deals with the dynamics of phase changes in materials, which are caused by transferring the material into an initial state that is not thermodynamically stable (e.g. by rapid cooling (“quenching”) or, occasionally, rapid heating; in fluids the system may also be prepared by a rapid pressure change). It is generally believed (Gunton et al., 1983; Binder, 1984a, 1987a, 1989; Kosterz, 1991; Wagner and Kampmann, 2000) that in *homogeneous* materials such phase changes may be initiated by two different types of mechanism, corresponding to two different types of statistical fluctuations, namely “homophase fluctuations” and “heterophase fluctuations”. Fig. 6-1 illustrates these fluctuations qualitatively for the example of a binary mixture, where the variable to consider is a local concentration variable $c(\mathbf{x})$. By “local” we do not mean the scale of a lattice site i (in a crystalline solid), since then the associated concentration variable c_i could take

only two values: $c_i=1$, if the site is taken by a B atom, and $c_i=0$, if it is taken by an A atom in an AB mixture. Instead here we are interested in an averaged concentration field obtained by “coarse graining” over a cell of size L^3 (or L^2 if we consider a two-dimensional layer):

$$c(\mathbf{x}) = L^{-3} \sum_{i \in \text{cell}} c_i \quad (6-1)$$

where \mathbf{x} is the center of gravity of the cell over which c_i is averaged. This intermediate length scale L must be large in comparison with the lattice spacing, since only if the cell contains many lattice sites is a continuum description as anticipated in Fig. 6-1 warranted. On the other hand, L must be small in comparison with the length scales of the statistical fluctuations that we wish to consider, i.e., the wavelength λ of the concentration wave in Fig. 6-1 a, or the width ξ of the interface between a droplet of the new phase and its environment in Fig. 6-1 b. As we shall see, the existence of this intermediate length scale L severely re-

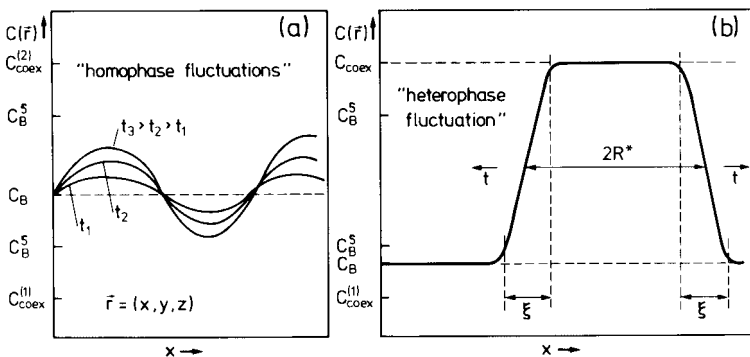


Figure 6-1. Schematic diagram of unstable thermodynamic fluctuations in the two-phase regime of a binary mixture AB at a concentration c_B (a) in the unstable regime inside two branches c_B^S of the spinodal curve and (b) in the metastable regime between the spinodal curve c_B^S and the coexistence curve $c_{\text{coex}}^{(1)}$. The local concentration $c(\mathbf{r})$ at a point $\mathbf{r} = (x, y, z)$ in space is schematically plotted against the spatial coordinate x at some time t after the quench. In case (a), the concentration variation at three distinct times t_1 , t_2 , and t_3 is indicated. The diameter of the critical droplet, whose cross-section is shown in case (b), is denoted by $2R^*$, and the width of the interfacial region by ξ . Note that the concentration profile of the droplet reaches the other branch of the coexistence curve $c_{\text{coex}}^{(2)}$ in the droplet center only for weak “supersaturations” of the mixture, where $c_B - c_{\text{coex}}^{(1)} \ll c_B^S - c_B$ and $R^* \gg \xi$; for the sake of clarity, the figure is therefore not drawn to scale (Binder, 1981).

stricts the quantitative validity of the theoretical concepts developed in the present chapter (see also Binder, 2000). This chapter will exclusively consider the mechanism of Fig. 6-1a, where in a thermodynamically unstable initial state long-wavelength delocalized small-amplitude statistical fluctuations grow spontaneously in amplitude as the time after the quench increases. For a binary mixture, this mechanism is called *spinodal decomposition* (Cahn, 1961, 1965, 1966, 1968); the relevant fluctuations can then be considered as a wavepacket of “concentration waves”, and one such wave is shown in Fig. 6-1a. As will be discussed below, this mechanism should not occur inside the whole two-phase coexistence region of the phase diagram of the mixture, but rather only inside a smaller region, the boundary of which is given by the spinodal curve (Cahn and Hilliard, 1958, 1959). Between the *spinodal curve* c_B^S and the coexistence curve $c_{\text{coex}}^{(1)}$ (or in between the other branch of the spinodal and $c_{\text{coex}}^{(2)}$) the mechanism of droplet nucleation and growth is involved (Fig. 6-1a). This latter mechanism is discussed in the chapter by Wagner et al., 2001). Apart from these phase transformation mechanisms triggered by spontaneous thermal fluctuations, heterogeneous nucleation processes must also be considered (Zettlemoyer, 1969); near inhomogeneities in solids such as grain boundaries, dislocations, external surfaces, or point defects such as substitutional or interstitial impurities or clusters thereof, microdomains of the new phase may already be formed before the quench, or at least their formation after the quench is greatly facilitated. General theoretical statements about these heterogeneous mechanisms, however, are hardly possible without a detailed discussion of the nature of such defects. Such problems will not be discussed in this

chapter, and the spontaneous growth of thermal fluctuations dominating phase changes of unstable but nearly ideal (i.e., defect-free) systems will be emphasized. Although most of the discussion refers to binary mixtures, an extension to ternary mixtures is often possible.

Unmixing of binary or ternary mixtures is not the only phase change where spontaneous growth of statistical fluctuations occurs. Consider, for example, an alloy A–B, which in thermal equilibrium undergoes an order–disorder phase transition from a disordered state, where the two species of atoms A and B are distributed at random over the available lattice sites, to an ordered arrangement. There A and B atoms preferentially occupy sites on sublattices (e.g., β -CuZn, Cu₃Au, CuAu, Fe₃Al, and FeAl). If we quench such an alloy from the disordered regime to a state which in equilibrium should be ordered, the unstable disordered initial state may also decay by spontaneous growth of fluctuations. The distinction from Fig. 6-1a is that the wavelength of the growing concentration wave is not large but coincides with the lattice spacing of the superstructure. Nevertheless, the theoretical treatment of this *spinodal ordering* (De Fontaine, 1979) is similar to the theory of spinodal decomposition, and will also be discussed in this chapter, which emphasizes the theoretical aspects (see Wagner and Kampmann (2000) for a complementary treatment emphasizing the point of view of the experimentalist).

One of the basic questions in the applications of materials is to understand the precipitated microstructure that forms in the late stages of a phase separation process. One of the main characteristics of this microstructure concerns its morphology: the minority phase may either form compact islands well separated from each other or it may form an irregular interconnected net-

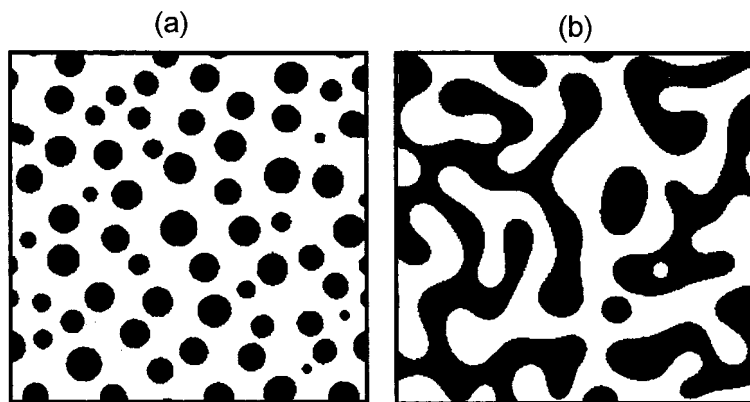


Figure 6-2. Snapshot pictures of a two-dimensional system undergoing phase separation with a volume fraction of (a) $\Phi = 0.21$ and (b) $\Phi = 0.5$. The pictures were obtained by numerical solution of the non-linear Cahn–Hilliard equation, Eq. (6-14) (Rogers and Desai, 1989).

work-like structure (Fig. 6-2). Obviously, a critical volume fraction exists where this interconnected net first appears, a so-called *percolation threshold* (Stauffer, 1985). Often it is assumed that the morphology of well separated islands must have formed by nucleation and growth, while the percolating morphology is taken as the signature of the spinodal curve. However, such an identification is misleading, as will be discussed in detail in this chapter: the spinodal curve at best has a meaning for the initial stages of phase separation; in the late stages, however, a generally universal coarsening behavior occurs (which is sensitively affected by defects!), irrespective of whether the morphology is interconnected or not. Since a closely related universal coarsening behavior also occurs in fluid mixtures and can be studied fairly well in these systems, we include a discussion of phase separation in fluid mixtures throughout this chapter. Moreover, “polymer alloys” can be conveniently produced by quenching from the fluid phase of polymer mixtures, and have become a practically important class of materials (Hashimoto, 1993).

6.2 General Concepts

6.2.1 Phenomenological Thermodynamics of Binary Mixtures and the Basic Ideas of Phase Separation Kinetics

We first consider the dynamics of phase transformations induced by an instantaneous quench from the initial temperature T_0 to a final temperature T (the idealization of this infinitely rapid cooling will be relaxed in Sec. 6.2.7). The simplest case where such a sudden change of external parameters causes a phase transition is a system undergoing an order–disorder phase transition at a critical temperature T_c with $T < T_c < T_0$ (Fig. 6-3a). The initially disordered system is then unstable, and immediately, small ordered domains form. As the time t after the quench passes, the order parameter in these domains must reach its equilibrium value ($\pm \psi$), and the domain size must ultimately grow to macroscopic size.

Alternatively, we consider a solid or liquid mixture A–B with a miscibility gap (Fig. 6-3b). Quenching the system at time $t = 0$ from an equilibrium state in the single phase region to a state underneath the coexistence curve leads to phase separation; in thermal equilibrium, macroscopic regions of both phases with concentrations $c_{\text{coex}}^{(1)}$ and $c_{\text{coex}}^{(2)}$ coexist.

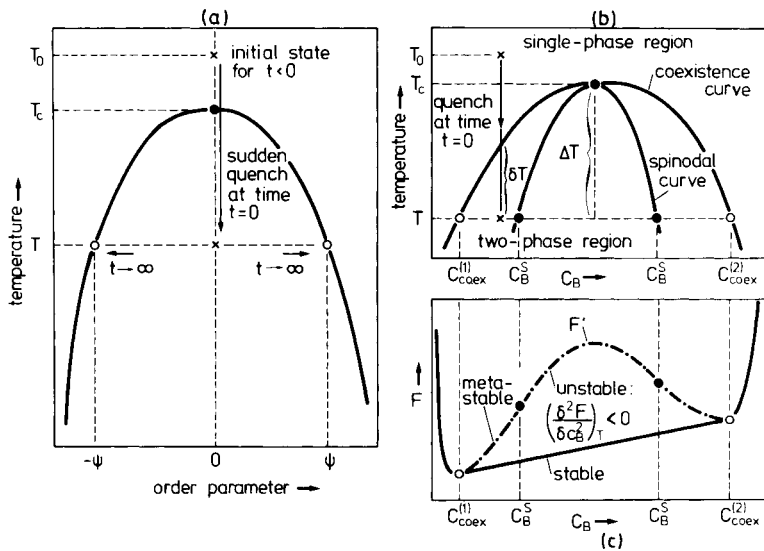


Figure 6-3. (a) Order parameter ψ of a second-order phase transition vs. temperature, assuming a two-fold degeneracy of the ordered state (described by the plus and minus signs of the order parameter). The quenching experiment is indicated. (b) Phase diagram of a binary mixture with a miscibility gap ending in a critical point (T_c , c_B^{crit}) of unmixing, in the temperature–concentration plane. Again the quenching experiment is indicated, and the quenching distances from the coexistence curve (δT) and from the critical point (ΔT) are indicated. (c) Free energy plotted versus composition at temperature T (schematic). For further explanations, see text (Binder, 1981).

Of course, phase transformations combining an ordering process (such as in Fig. 6-3a) with an unmixing process (such as in Fig. 6-3b) also occur; as we are interested mainly in the basic concepts of these processes, we will not consider these more complex phenomena here, but will return to this problem in Sec. 6.4.1.

The basic concepts of the kinetic mechanisms of the processes indicated in Fig. 6-3a and b invoke the idea of extending the concept of the thermodynamic Helmholtz free energy F to states out of equilibrium (Gunton et al., 1983; Binder, 1987a). In the single-phase region of the A-rich alloy, F first decreases with increasing concentration of B atoms c_B , owing to the entropy of mixing. Similarly, in the B-rich single-phase region, F decreases with increasing concentration of A atoms, $c_A = 1 - c_B$. In the two-phase coexistence region in equilib-

rium, we have a linear variation of F with composition; this reflects the fact that the amounts of the two coexisting phases (with concentrations $c_{\text{coex}}^{(1)}$, $c_{\text{coex}}^{(2)}$) change linearly with c_B according to the lever rule.

Mean-field type theories (Gunton et al., 1983; Binder, 1987a) suggest that a free energy $F' \leq F$ can also be introduced describing single-phase states within the two-phase region. Since F' must coincide with F for $c_{\text{coex}}^{(1)}$ and $c_{\text{coex}}^{(2)}$, inevitably a double-well structure results, as indicated by the dash-dotted curve in Fig. 6-3c. This hypothetical free energy F' now allows a further distinction to be made: states where $(\partial^2 F' / \partial c_B^2)_T > 0$ are called *meta-stable*, and states where $(\partial^2 F' / \partial c_B^2)_T < 0$ are called *un-stable*. The locus of inflection points in the (T, c_B) plane,

$$(\partial^2 F' / \partial c_B^2)_T = 0 \quad (6-2)$$

defines the spinodal curve $c = c_B^s(T)$. This distinction is now linked to the two transformation mechanisms shown in Fig. 6-1; it is the unstable regime inside the two branches of the spinodal curve, where long-wavelength fluctuations spontaneously grow rather than decay. At a later stage, the inhomogeneous concentration distribution thus generated will coarsen. In the metastable regime, the system is stable against such weak (small-amplitude) fluctuations, and localized large-amplitude fluctuations (“droplets” of the new phase) must form in order to start the transformation.

This idea implies, as will be explained below, a *singular transition in the kinetic transformation mechanism* at the spinodal curve. However, this spinodal singularity is really only an artefact of an over-simplified theoretical picture: apart from the very special limit of infinitely weak, infinitely long-ranged forces in which mean-field theory becomes correct (Penrose and Lebowitz, 1971; Lebowitz and Penrose, 1966; Binder, 1984b), the transition from the nucleation mechanism to the spinodal decomposition mechanism is completely gradual

(Binder et al., 1978). As will be discussed in more detail in Sec. 6.2.5, the spinodal curve cannot be unambiguously defined. At this point, we recall that the “weak delocalized long-wavelength fluctuations” cannot be identified in terms of the atomic concentration variable c_i , which undergoes rapid large-amplitude ($c_i = 0$ to $c_i = 1$) variations from one lattice site to the next, but implies the introduction of the coarse-grained concentration field $c(\mathbf{r})$, Eq. (6-1).

The free energy F' of “homogeneous” states in the two-phase region depends on the length scale L over which short-wavelength concentration fluctuations have been integrated (Fig. 6-4). This “coarse-grained” free-energy density f_{cg} is not precisely identical to the true free-energy density f in the single-phase region, since concentration variations with wavelengths exceeding L contribute to f but are excluded from f_{cg} . However, this difference is minor, and in the single-phase region we may consider the limit $L \rightarrow \infty$ and then f_{cg} tends towards f uniformly. This is not possible in the two-phase region, however, where f_{cg} describes homogeneous states only if $L \lesssim \xi$, the interfacial width; if $L \gg \xi$ then

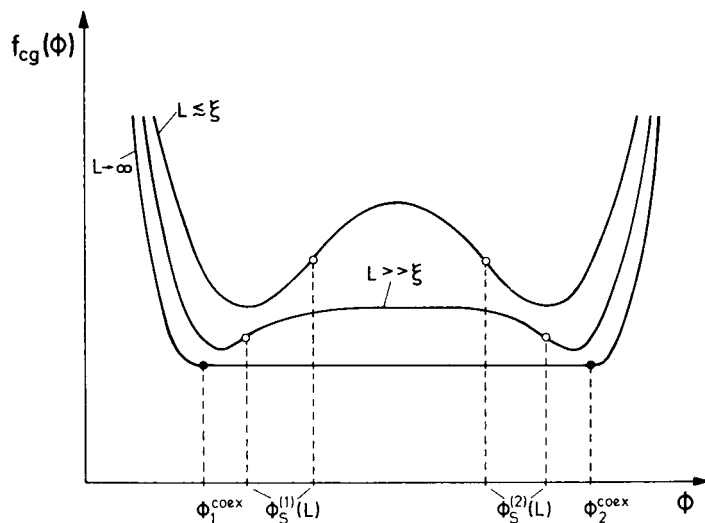


Figure 6-4. Schematic plot of the coarse-grained free-energy density $f_{cg}(\phi)$ as a function of the order parameter $\phi = (c - c_{crit})/c_{crit}$ in a first-order transition from ϕ_1^{coex} to ϕ_2^{coex} , for a “symmetric” situation with $f(\phi_1^{coex}) = f(\phi_2^{coex})$ as in the Ising model. Spinodals $\phi_s^{(1,2)}(L)$ defined from inflection points of $f_{cg}(\phi)$ depend distinctly on the coarse-graining length L and the interfacial width ξ (Binder, 1987a).

the states that yield dominating contributions to f_{cg} are phase separated on a local scale, and therefore f_{cg} tends smoothly towards the double-tangent construction as $L \rightarrow \infty$. Hence there is no unique theoretical method of calculating a spinodal curve; remember that mean-field theories, which yield spinodal curves easily, are only inaccurate descriptions of real systems. Similarly, extrapolation procedures by which spinodal curves are extracted from experimental data also involve related ambiguities, as will be discussed in Sec. 6.2.5.

Hence the coarse-graining alluded to above means that a microscopic Hamiltonian $\mathcal{H}\{c_i\}$ of the binary mixture is replaced by a so-called free-energy function $\Delta\mathcal{F}\{c(\mathbf{x})\}$. For example, the Hamiltonian may correspond to a standard Ising-type pairwise interaction model (Binder, 1986; De Fontaine, 1979):

$$\begin{aligned} \mathcal{H}\{c_i\} = & \frac{1}{2} \sum_{i \neq j} \{ \varphi_{BB}(\mathbf{x}_i - \mathbf{x}_j) c_i c_j \\ & + \varphi_{AB}(\mathbf{x}_i - \mathbf{x}_j) [c_i(1 - c_j) + c_j(1 - c_i)] \\ & + \varphi_{AA}(\mathbf{x}_i - \mathbf{x}_j) (1 - c_i)(1 - c_j) \} \end{aligned} \quad (6-3)$$

where φ is the interaction energy between a pair of atoms.

Carrying out the coarse-graining defined in Eq. (6-1) we expect that $\mathcal{H}\{c_i\}/k_B T$ will be replaced by

$$\begin{aligned} & \frac{\Delta\mathcal{F}\{c(\mathbf{x})\}}{k_B T} \\ & = \int d^d x \{ f_{cg}[c(\mathbf{x})]/k_B T + \frac{1}{2} r^2 [\nabla c(\mathbf{x})]^2 \} \end{aligned} \quad (6-4)$$

where d is the spatial dimensionality of the system and r is the range of the effective interaction in Eq. (6-3) ($\Delta\varphi(\mathbf{x}_i - \mathbf{x}_j) \equiv \varphi_{AA} + \varphi_{BB} - 2\varphi_{AB}$):

$$r^2 = \frac{\sum_j (\mathbf{x}_i - \mathbf{x}_j)^2 \Delta\varphi(\mathbf{x}_i - \mathbf{x}_j)}{2d \sum_j \Delta\varphi(\mathbf{x}_i - \mathbf{x}_j)} \quad (6-5)$$

The term $\frac{1}{2} r^2 [\nabla c]^2$ in Eq. (6-4) accounts for the free energy cost of inhomogeneous concentration distributions. Here the coarse-grained free-energy density $f_{cg}(c)$ resulting from Eqs. (6-3) and (6-1) by carrying out the restricted trace over the $\{c_i\}$ for a fixed concentration field $\{c(\mathbf{x})\}$ is very difficult to obtain in practice; qualitatively the behavior of $f_{cg}(c)$ should be similar to the mean-field (MF) result for the free energy of a binary mixture,

$$\begin{aligned} \frac{1}{k_B T} f_{MF}(c) = & c \ln c + (1 - c) \ln(1 - c) \\ & + 2 \frac{T_c^{MF}}{T} c(1 - c) \end{aligned} \quad (6-6)$$

with

$$k_B T_c^{MF} \equiv \sum_j \Delta\varphi(\mathbf{x}_i - \mathbf{x}_j) \quad (6-7)$$

Near T_c^{MF} we can replace $f_{MF}(c)$ by its Landau expansion,

$$\begin{aligned} f_{MF}(c) = & f_0 + A(c - c_{crit})^2 \\ & + B(c - c_{crit})^4 + \dots \end{aligned} \quad (6-8)$$

where $A \sim (T/T_c^{MF} - 1) < 0$ for $T < T_c^{MF}$ and $B > 0$. It is well known that the actual critical temperature T_c does not coincide with the mean-field prediction. Therefore, it is usually assumed that the parameters appearing in the actual coarse-grained free energy $f_{cg}(c)$ are not the mean-field parameters A, B, \dots , but rather these parameters are “renormalized” due to short-wavelength fluctuations, and also r (Eq. (6-5)) may thus be modified. Therefore, $f_{cg}(c)$ and r are not calculated from microscopic models such as Eq. (6-3), but are treated as phenomenological input parameters of the theory, which are fitted to experiment.

6.2.2 The Cahn–Hilliard–Cook Nonlinear Diffusion Equation

Since in the total volume V the average concentration,

$$\bar{c} = (1/V) \int d\mathbf{x} c(\mathbf{x}, t) \quad (6-9)$$

is conserved, the time-depnt concentration field $c(\mathbf{x}, t)$ satisfies a continuity equation,

$$\frac{\partial c(\mathbf{x}, t)}{\partial t} + \nabla \cdot \mathbf{j}(\mathbf{x}, t) = 0 \quad (6-10)$$

where $\mathbf{j}(\mathbf{x}, t)$ is the concentration current density. Following standard nonequilibrium thermodynamics (de Groot and Mazur, 1962), $\mathbf{j}(\mathbf{x}, t)$ is assumed to be proportional to the gradient of the local chemical potential difference $\mu(\mathbf{x}, t)$:

$$\mathbf{j}(\mathbf{x}, t) = -M \nabla \mu(\mathbf{x}, t) \quad (6-11)$$

where M is a mobility that is discussed below.

In the thermal equilibrium the chemical potential difference is given as a partial derivative of the Helmholtz energy $F(c, T)$:

$$\mu = (\partial F / \partial c)_T; \quad (6-12)$$

remember that the condition for two-phase coexistence, the equality of chemical potential differences

$$\mu_1 = (\partial F / \partial c)_T|_{c_{\text{coex}}^{(1)}} = \mu_2 = (\partial F / \partial c)_T|_{c_{\text{coex}}^{(2)}}$$

is the physical content of the double-tangent construction shown in Fig. 6-3c. Eq. (6-12) is generalized to an inhomogeneous nonstationary situation far from equilibrium, where both $c(\mathbf{x}, t)$ and $\mu(\mathbf{x}, t)$ depend on space and time, by defining $\mu(\mathbf{x}, t)$ as a functional derivative of the Helmholtz energy functional $\Delta \mathcal{F}$ in Eq. (6-4):

$$\mu(\mathbf{x}, t) \equiv \delta (\Delta \mathcal{F} \{c(\mathbf{x}, t)\}) / \delta c(\mathbf{x}, t) \quad (6-13)$$

Inserting Eq. (6-14) into Eq. (6-13) yields

$$\mu(\mathbf{x}, t) = (\partial f_{\text{cg}} / \partial c)_T - r^2 k_B T \nabla^2 c(\mathbf{x}, t)$$

and using this result in the continuity relation, Eq. (6-10), we obtain the Cahn–Hilliard nonlinear diffusion equation (Cahn, 1961):

$$\frac{\partial c(\mathbf{x}, t)}{\partial t} = M \nabla^2 \left\{ \left(\frac{\partial f_{\text{cg}}[c(\mathbf{x}, t)]}{\partial c} \right)_T - r^2 k_B T \nabla^2 c(\mathbf{x}, t) \right\} \quad (6-14)$$

One immediately obvious defect of this equation is its completely deterministic character, which implies that random statistical fluctuations are disregarded (apart from fluctuations included in the initial condition, the state at temperature T_0 where the quench starts). This defect can be remedied, following Cook (1970), by adding a random force term $\eta_T(\mathbf{x}, t)$ to Eq. (6-14):

$$\frac{\partial c(\mathbf{x}, t)}{\partial t} = M \nabla^2 \left\{ \left(\frac{\partial f_{\text{cg}}[c(\mathbf{x}, t)]}{\partial c} \right)_T - r^2 k_B T \nabla^2 c(\mathbf{x}, t) \right\} + \eta_T(\mathbf{x}, t) \quad (6-15)$$

Here $\eta_T(\mathbf{x}, t)$ is assumed to be delta-correlated Gaussian noise, and the mean-square amplitude $\langle \eta_T^2 \rangle_T$ is then linked to the mobility M via a fluctuation-dissipation relation.

$$\langle \eta_T(\mathbf{x}, t) \eta_T(\mathbf{x}', t') \rangle_T = \langle \eta_T^2 \rangle_T \nabla^2 \delta(\mathbf{x} - \mathbf{x}') \delta(t - t') \quad (6-16)$$

$$\langle \eta_T^2 \rangle_T = 2 k_B T M \quad (6-17)$$

Eqs. (6-15)–(6-17) constitute the main results of this section, on which all further treatment presented here is based. At this point we stress the main assumptions that have been made either explicitly or tacitly:

(i) Effects due to the lattice anisotropy of the solid have been ignored. In a crystalline solid the interfacial free energy between co-existing A-rich and B-rich phases will

depend on the orientation of the interface; only in the limit $T \rightarrow T_c$ does this interfacial free energy become isotropic (Wortis, 1985). The isotropic form of Eq. (6-15) outside the critical region would only hold for phase separation in isotropic amorphous solids.

(ii) It is assumed that the local concentration field is the only slowly relaxing variable whose dynamics must be considered explicitly after the quench, while all other variables equilibrate instantaneously. This assumption is not true, of course, if phase-separating fluids are considered where the coupling of hydrodynamic variables and the resulting long-range hydrodynamic interactions need to be taken into account (Kawasaki and Ohta, 1978). However, in solids other slow variables may also occur, particularly near the glass transition (in amorphous solids) or near other phase transformations. A treatment of spinodal decomposition in the presence of a coupling to slowly relaxing structural variables is only possible in very simplified cases (Binder et al., 1986).

(iii) It is assumed that the spatial concentration variations of interest are small, i.e., in Eq. (6-4) terms of the order $[\nabla^2 c(\mathbf{x})]^2$ (and higher) can be neglected in comparison with the lowest-order gradient term, $[\nabla c(\mathbf{x})]^2$. This assumption is true near the critical point of unmixing, where the interfacial width ξ is much larger than the interatomic spacing, but it is not true in the general.

(iv) The concentration dependence of the mobility M is neglected in the derivation yielding Eqs. (6-14) and (6-15). Again, this approximation is valid near T_c , since then the relevant scale for concentration variations becomes small ($(c_{\text{coex}}^{(2)} - c_{\text{coex}}^{(1)})/c_{\text{crit}} \ll 1$), but is not true in general.

(v) The use of a continuum description for a solid (Eqs. (6-1) and (6-4)) requires

that a coarse-graining is performed over a length scale much larger than the lattice spacing, but less than ξ , which again restricts the region of validity of the theory to the critical region. On the other hand, fluctuations and nonlinear phenomena are known to lead to a breakdown of meanfield theory near the critical point, and nontrivial critical phenomena arise (Stanley, 1971; Binder, 2001). As we shall see (Secs. 6.2.5 and 6.2.6) this also restricts the applicability of the theory.

6.2.3 Linearized Theory of Spinodal Decomposition

It may seem unsatisfactory that the basic equation of the theory (Eq. (6-15)) is supposed to hold only under fairly restrictive conditions, but what is even worse is the fact that this equation completely withstands an analytical solution, and brute force numerical approaches where Eq. (6-15) is attacked by large-scale computer simulation are needed (Meakin et al., 1983; Petschek and Metiu, 1985; Milchev et al., 1988; Gawlinski et al., 1989; Rogers et al., 1988; Toral et al., 1988; Oono and Puri, 1988; Puri and Oono, 1988). We shall return to these approaches in Sec. 6.2.6, and also address the complementary approach of Monte Carlo simulations based directly on the microscopic Hamiltonian, Eq. (6-3) (Bortz et al., 1974; Marro et al., 1975, 1979; Rao et al., 1976; Sur et al., 1977; Binder et al., 1979; Lebowitz et al., 1982; Fratzl et al., 1983; Heermann, 1984a, b, 1985; Amar et al., 1988). Here we prefer to discuss the *assumption* that in the initial stages of unmixing the fluctuation

$$\delta c(\mathbf{x}, t) \equiv c(\mathbf{x}, t) - \bar{c}$$

is small everywhere in the system. Since L cannot be made arbitrarily large, *this assumption is not typically true*, as we shall

see below (Secs. 6.2.5 and 6.2.6), but nevertheless it is instructive to study it!

Given this assumption, we may linearize Eq. (6-15) (or Eq. (6-14) if we also neglect the thermal noise) in $\delta c(\mathbf{x}, t)$. Then Eq. (6-14) becomes

$$\frac{\partial}{\partial t} \delta c(\mathbf{x}, t) = M \nabla^2 \times \left\{ \left(\frac{\partial^2 f_{cg}(c)}{\partial c^2} \right)_{T, \bar{c}} - r^2 k_B T \nabla^2 \right\} \delta c(\mathbf{x}, t) \quad (6-18)$$

and, introducing Fourier transformations

$$\delta c_{\mathbf{k}}(t) \equiv \int d^d x \exp(i \mathbf{k} \cdot \mathbf{x}) \delta c(\mathbf{x}, t) \quad (6-19)$$

Eq. (6-18) is solved by a simple exponential relaxation,

$$\delta c_{\mathbf{k}}(t) \equiv \delta c_{\mathbf{k}}(0) \exp[R(k) t] \quad (6-20)$$

with the rate factor $R(k)$:

$$R(k) \equiv M k^2 [(\partial^2 f_{cg}/\partial c^2)_{T, \bar{c}} + r^2 k_B T k^2] \quad (6-21)$$

The equal-time structure factor $S(k, t)$ at time t after the quench:

$$S(k, t) \equiv \langle \delta c_{-\mathbf{k}}(t) \delta c_{\mathbf{k}}(t) \rangle_T \quad (6-22)$$

where $\langle \dots \rangle_T$ denotes a thermal average, then also exhibits a simple exponential relaxation:

$$S(k, t) \equiv S_{T_0}(k) \exp[2R(k) t] \quad (6-23)$$

Here the prefactor

$$S_{T_0}(k) \equiv \langle \delta c_{-\mathbf{k}}(0) \delta c_{\mathbf{k}}(0) \rangle_T \equiv \langle \delta c_{-\mathbf{k}} \delta c_{\mathbf{k}} \rangle_{T_0} \quad (6-24)$$

is simply the equal-time structure factor in thermal equilibrium at temperature T_0 before the quench. Note that $R(k)$ is positive for $0 < k < k_c$, with

$$k_c \equiv 2\pi/\lambda_c = [-(\partial^2 f_{cg}/\partial c^2)_{T, \bar{c}}/(r^2 k_B T)]^{1/2} \quad (6-25)$$

Thus, whereas the structure factor should exhibit exponential growth in this region, for $k = k_c$ it should be time-independent, $S(k_c, t) = S(k_c, 0)$. However, neither in ex-

periment (Fig. 6-5a, b) nor in simulations (Figs. 6-5c, d) is such a time-independent intersection point observed. Also in the Cahn plot, $R(k)/k^2$ plotted versus k^2 , instead of the predicted linear behavior (Fig. 6-6a), $2R(k)/k^2 = 2D_0(1 - k^2/k_c^2)$ with a negative diffusion constant

$$D_0 = -M(\partial^2 f_{cg}/\partial c^2)_{T, \bar{c}} \quad (\text{uphill diffusion})$$

curvature is typically observed (Fig. 6-6b).

There are several possible reasons why the simple linearized theory of spinodal decomposition as it has been outlined so far is invalid:

(i) Fluctuations in the final state at the temperature T must be included (Cook, 1970). This problem will be considered at the end of this subsection.

(ii) Nonlinear effects are important during the early stages of the quench. This problem will be discussed in Secs. 6.2.5 and 6.2.6.

(iii) There is already an appreciable relaxation of the structure factor occurring during the quench from T_0 to T if the cooling rate $g = -dT/dt$ is finite (see Sec. 6.2.7).

(iv) The concentration field is coupled to another slowly relaxing variable (Binder et al., 1986; Jäcke and Pieroth, 1988). Here we only very briefly outline the idea of the approach of Binder et al. (1986). According to Eqs. (6-23) and (6-21), the maximum growth rate of the structure factor occurs at

$$R_m = R(k_m), \quad k_m = k_c/\sqrt{2} \quad (6-26)$$

Suppose now the concentration couples linearly to a non-conserved variable $a(t)$ describing, for example, structural relaxation, whose fluctuations in the absence of any coupling would decay exponentially, proportional to $\exp(-\gamma t)$. The decay of concentration fluctuations will be affected

(i) if the coupling between the variables $a(t)$ and $c(\mathbf{x}, t)$ is sufficiently strong, and

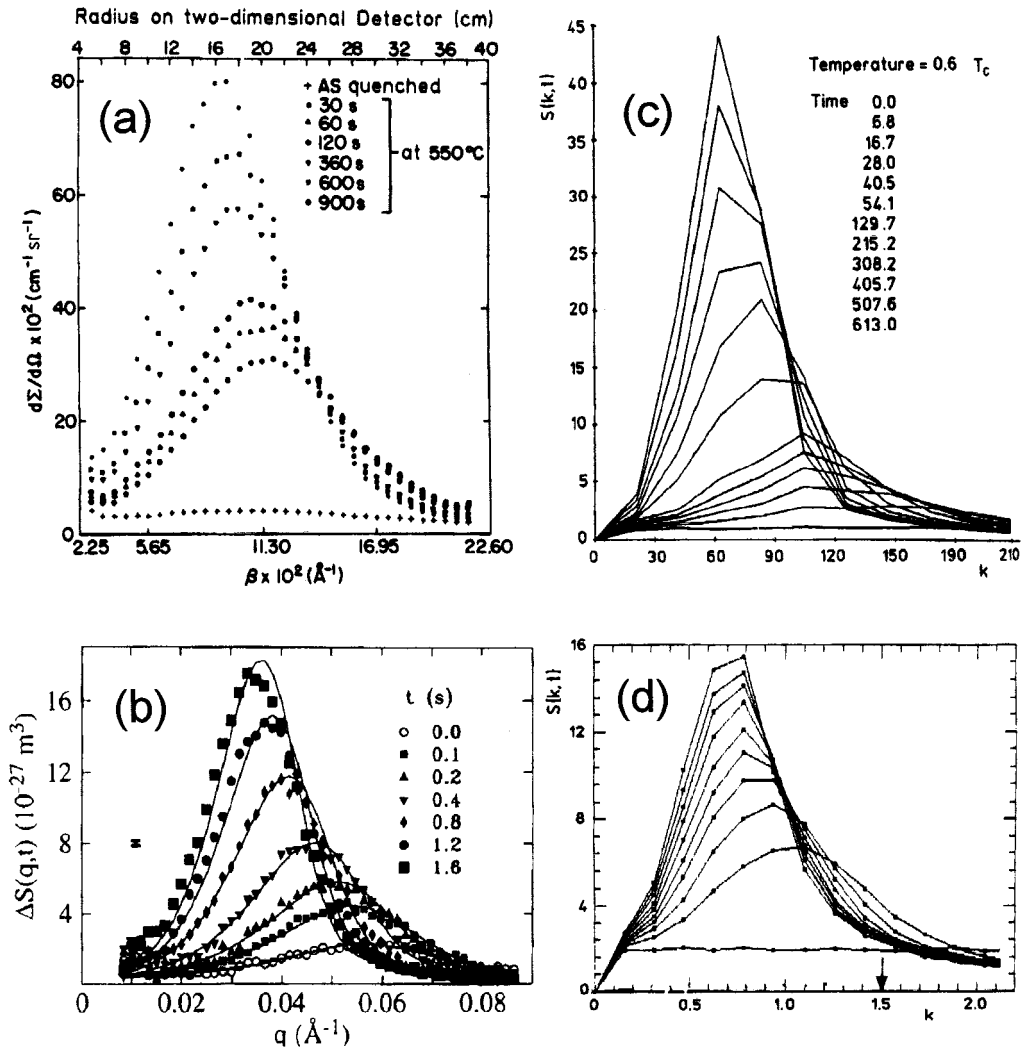


Figure 6-5. (a) Neutron small-angle scattering intensity vs. scattering vector k (β : scattering angle) for an Au-60 at.% Pt alloy quenched to 550°C (Singhal et al., 1978). (b) Time evolution of the structure factor at 541 K in Al-38 at.% Zn after subtraction of the prequench scattering. Solid lines are the best fit to the data using the LBM theory, Eq. (6-60) (Mainville et al., 1997). (c) Time evolution of the structure factor $S(k, t)$ according to a Monte Carlo simulation of a three-dimensional nearest-neighbor Ising model of an alloy at critical concentration and temperature $T = 0.6 T_c$. Due to the periodic boundary condition for the $30 \times 30 \times 30$ lattice, k is only defined for discrete multiples of $(2\pi)/30$; these discrete values of $S(k, t)$ are connected by straight lines (Marro et al., 1975). (d) Time evolution of the normalized structure factor $\tilde{S}(k, t)$ vs. k for the discrete version of the Ginzburg-Landau model (Eq. (6-4)), namely

$$\mathcal{H}/k_B T = \sum_l [A(c_l - c_{\text{crit}})^2 + B(c_l - c_{\text{crit}})^4] + \sum_{\langle lm \rangle} \frac{1}{2} C(c_l - c_m)^2$$

where c_l is a continuous variable representing the average concentration in the l th cell of size $L \times L$, and the phenomenological constants A , B , and C have been chosen as $A/C = -2.292$, $\sqrt{B}/C = 0.972$ (C can be scaled out by redefining the c_l s). Data are for an $N = 40 \times 40$ lattice with periodic boundary conditions at times $t = 0, 10, 20, \dots, 90$ Monte Carlo steps (MCS) per site. The arrow indicates the estimate for the wavenumber of maximum growth, $k_m(0) = k_c/\sqrt{2} = \sqrt{-A/C}$ (Milchev et al., 1988).

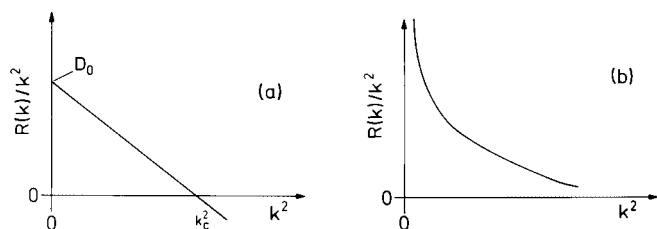


Figure 6-6. Schematic “Cahn plot”, i.e., $R(k)/k^2$ vs. k^2 , (a) as predicted by the linear theory and (b) as it is typically observed. Ideally, the “Cahn plot” should yield a straight line: the intercept with the abscissa occurs at k_c^2 , and the intercept with the ordinate at D_0 (Binder et al., 1986).

(ii) if the rates R_m and γ are of the same order. In the absence of any coupling between these variables their fluctuations would decay independently of each other, with decay rates being given as $\Gamma_+(k) = \gamma$ (relaxation of $a(t)$ is then independent of k) and $\Gamma_-(k) = -|D_0|k^2(1 - k^2/k_c^2)$ (spinodal decomposition). This *mode spectrum* of uncoupled structural and concentration fluctuations is shown by the dashed curves in Fig. 6-7). However, both relaxation rates become strongly modified if these variables are coupled. The strength of this coupling can be related to $1 - D_\infty/D_0$, where D_0 and D_∞ are the low- and high-frequency limits of the diffusion constant. Full curves in Fig. 6-7 show for three (arbitrary) choices of parameters, the relaxation rates $\Gamma_+(k)$ and $\Gamma_-(k)$ for the case of coupled variables. It is seen that a “mixing” of interdiffusion and relaxation occurs; for small k the interdiffusion (or spinodal decomposition) is given by $\Gamma_-(k)$, for large k by $\Gamma_+(k)$, and for intermediate k both exponentials $\exp[-\Gamma_+(k)t]$ and $\exp[-\Gamma_-(k)t]$ contribute to the growth and/or decay of concentration fluctuations. Plotting the mode $\Gamma_-(k)$ which describes spinodal decomposition for small k in the form of a Cahn plot, we encounter pronounced curvature.

Such a coupling where R_m and γ are of comparable size might occur if we study spinodal decomposition in glasses (see for example Yokota, 1978; Acuña and Craievich, 1979; Craievich and Olivieri, 1981)

or in fluid polymer mixtures near their glass transition (e.g., Meier and Strobl, 1988). The slow variables are then expected to relax with a broad spectrum of rates rather than with a single rate γ . Fluc-

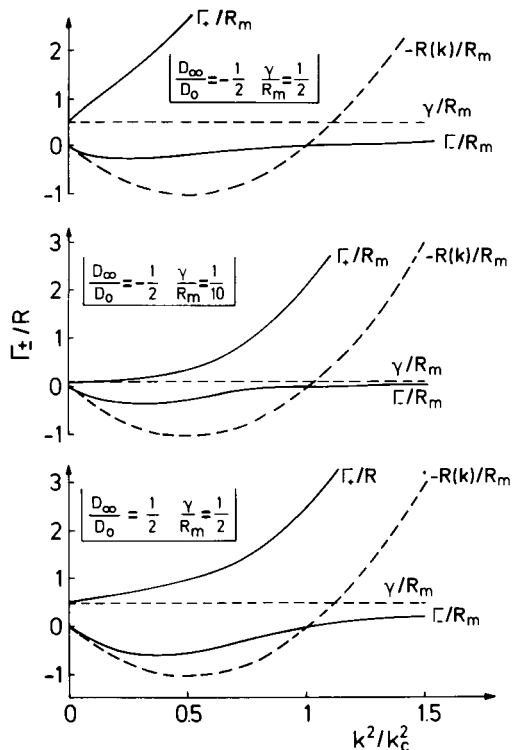


Figure 6-7. Mode spectrum $\{\Gamma_+(k), \Gamma_-(k)\}$ (full curves) of an unmixing system coupled to a slow variable plotted vs. k^2/k_c^2 for three parameter choices. In the absence of any coupling, the slow variable would relax with a rate $\Gamma_+(k) = \gamma$ (broken horizontal straight lines) and the unmixing system would relax with a rate $\Gamma_-(k) = 4R_m(k^2/k_c^2)(1 - k^2/k_c^2)$ (broken curves). All rates are normalized by R_m (Binder et al., 1986).

tuations in the final state also need to be included in this case (Jäckle and Pieroth, 1988).

We now discuss the effect of fluctuations in the final state for the simplest case, Eq. (6-15), treated in the framework of the linearization approximation. After some simple algebra we obtain from Eqs. (6-15) to (6-22) the following equation (Cook, 1970):

$$\frac{d}{dt} S(k, t) = -2Mk^2 \times \left\{ \left[\frac{\partial^2 f_{cg}}{\partial c^2} \right]_{T, \bar{c}} + r^2 k_B T k^2 \right\} S(k, t) - k_B T \quad (6-27)$$

It is seen that an effective diffusion constant for uphill diffusion, defined as

$$D_{\text{eff}}(k, t) \equiv \frac{1}{2k^2} \frac{d}{dt} \ln S(k, t) \quad (6-28)$$

now yields

$$D_{\text{eff}}(k, t) \equiv -D_0 \left(1 - \frac{k^2}{k_c^2} \right) + k_B T M / S(k, t) \quad (6-29)$$

Since in the linear theory $S(k, t \rightarrow \infty) \rightarrow \infty$, $D_{\text{eff}}(k, t \rightarrow \infty)$ reduces to the simple Cahn (1961) result quoted above, but this limit is never reached owing to nonlinear effects. On the other hand, at $t=0$, Eq. (6-29) leads to a linear relation between $D_{\text{eff}}(k, 0)$ and k^2 again, because

$$[S(k, 0)]^{-1} = \left[\frac{\partial^2 f_{cg}}{\partial c^2} \right]_{T_0, \bar{c}} + r^2 k_B T k^2 \Big/ k_B T_0$$

is linear in k^2 also. Here the point where $D_{\text{eff}}(k, 0)$ changes sign is not k_c , but shifts to a larger value. This behavior is illustrated in the upper part of Fig. 6-8 where the (rescaled) structure factor $\tilde{S}(q, \tau)$ and (rescaled) effective diffusion constant

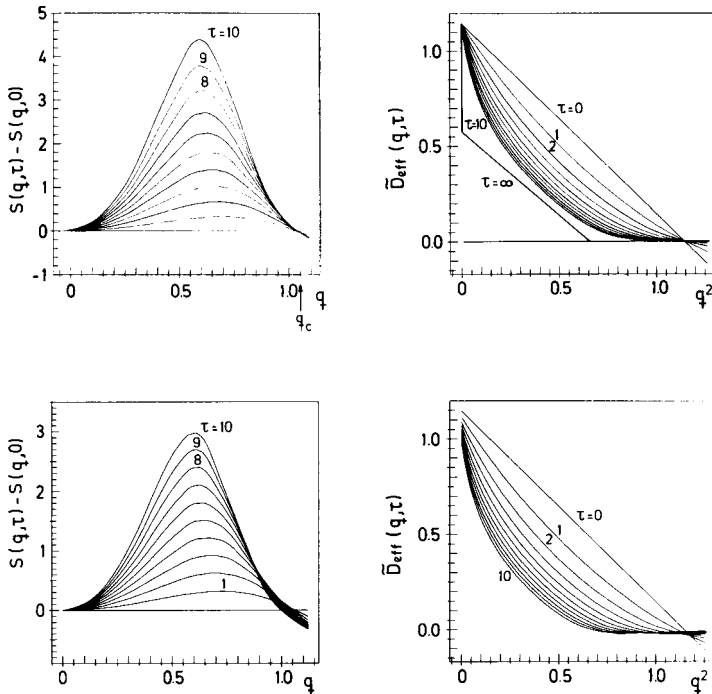


Figure 6-8. Scaled structure function (left) and normalized diffusion constant $\tilde{D}_{\text{eff}}(q, \tau) \equiv q^2 d[\ln \tilde{S}(q, \tau)]/d\tau$ (right) vs. q or q^2 , respectively, for an instantaneous quench from infinite temperature to $T/T_c = 4/9$. Top, Cahn–Hilliard–Cook (CHC) approximation, Eqs. (6-27) and (6-29), bottom based on the Langer–Baron–Miller (LBM) (1975) theory. Ten times $\tau = 1, 2, \dots, 10$ are shown after the quench. Note that in the CHC approximation we use the renormalized value μ_- (Fig. 6-18) of $(\partial^2 f_{cg}/\partial c^2)_{T, \bar{c}}$ instead $(\partial^2 f_{cg}/\partial c^2)_{T, \bar{c}}, \mu_-(T, \tau=0) = 0.65$ in the present units (Carmesin et al., 1986).

$\tilde{D}_{\text{eff}}(q, \tau)$ following from Eqs. (6-27) and (6-29) are plotted against the (rescaled) square of the scattering vector, q^2 (where $q = k/k_c$, $\tau = 2Mr^2 T k_c^4 t$, $\tilde{S} = r^2 k_c^2 S$). It is seen that on the level of the Cahn–Hilliard–Cook (CHC) approximation there is initially some shift in the position at which $S(k, t)$ has its maximum, although this shift is more pronounced when nonlinear effects are taken into account, as is approximated by the theory of Langer et al. (1975), which we shall refer to as the Langer–Baron–Miller (LBM) approximation. It is seen that the main distinction between the CHC and LBM approximations during the early stages is the lack of a common intersection point in the LBM approximation. Also the growth of $\tilde{S}(q, \tau)$ with τ is generally slower (note the difference in the ordinate scales!). Qualitatively, however, the behavior is similar, and this is also true for the behavior of $\tilde{D}_{\text{eff}}(q, \tau)$. Note that $\tilde{D}_{\text{eff}}(q, \tau)$ is distinctly curved in both cases (apart from the limit $\tau \rightarrow 0$).

6.2.4 Spinodal Decomposition of Polymer Mixtures

Here we consider the modifications necessary for describing binary mixtures of long flexible macromolecules. In a dense polymer melt, the configurations of these linear chain molecules (we disregard here star polymers, branched polymers, copolymers, and also interconnected networks, although some aspects of the theory can be extended to these more complex situations, see Binder and Frisch (1984)) are random Gaussian coils interpenetrating each other. In terms of subunits (“Kuhn segments”) of lengths σ_A and σ_B for the two types of polymers A and B, the degree of polymerization X_A and X_B is expressed in terms of chain lengths N_A and N_B as $X_A = N_A g_A$ and $X_B = N_B g_B$, if each subunit contains g_A and g_B monomers. The mean square end-to-end

distance and gyration radius of these coils then is (Flory, 1953; De Gennes, 1979):

$$\begin{aligned} \langle R_A^2 \rangle &= \sigma_A^2 N_A, & \langle R_B^2 \rangle &= \sigma_B^2 N_B, \\ \langle R_{\text{gyr}, A}^2 \rangle &= \frac{1}{6} \sigma_A^2 N_A, & \langle R_{\text{gyr}, B}^2 \rangle &= \frac{1}{6} \sigma_B^2 N_B \end{aligned} \quad (6-31)$$

In the Flory–Huggins (FH) approximation (Flory, 1953; Koningsveld et al., 1987) the expression corresponding to Eq. (6-4) becomes (De Gennes, 1980)

$$\begin{aligned} \frac{\Delta \mathcal{F}\{\Phi(\mathbf{x})\}}{k_B T} &= \int d^d x \left\{ f_{\text{FH}}[\Phi(\mathbf{x})]/k_B T \right. \\ &\quad \left. + \frac{1}{2} a^2 \frac{1}{\Phi(1-\Phi)} [\nabla \Phi(\mathbf{x})]^2 \right\} \end{aligned} \quad (6-32)$$

where $\Phi(\mathbf{x})$ is the volume fraction of A segments, $1 - \Phi(\mathbf{x})$ is the volume fraction of B segments, the mixture is assumed to be incompressible, and the lattice spacing a of the Flory–Huggins lattice model is given by $a^2/[\Phi(1-\Phi)] \equiv \sigma_A^2/\Phi + \sigma_B^2/(1-\Phi)$. Note that unlike Eq. (6-4) the parameter a is not related to the range of interaction, but rather reflects the random coil structure of the polymer chains. Owing to the connectivity of the polymer chains, the entropy of mixing term is much smaller than in Eq. (6-6) (Flory, 1953):

$$\begin{aligned} \frac{1}{k_B T} f_{\text{FH}}(\Phi) &= \frac{\Phi \ln \Phi}{N_A} \\ &\quad + \frac{(1-\Phi) \ln(1-\Phi)}{N_B} + \chi \Phi(1-\Phi) \end{aligned} \quad (6-33)$$

where the Flory–Huggins parameter χ contains all enthalpic contributions that lead to unmixing. If χ does not depend on volume fraction, then the spinodal curve resulting from Eq. (6-33) is given by

$$2\chi_s(\Phi) = (\Phi N_A)^{-1} + [(1-\Phi) N_B]^{-1} \quad (6-34)$$

and the critical point occurs at

$$\begin{aligned} \Phi_c &= (\sqrt{N_A/N_B} + 1)^{-1} \\ \chi_c &= (N_A^{-1/2} + N_B^{-1/2})^2/2 \end{aligned}$$

These results assume well-defined chain lengths ("monodisperse polymers"), but can be generalized to a distribution of chain lengths ("polydispersity"; see Joanny, 1978).

Another modification concerns the constitutive kinetic equation: instead of Eq. (6-11) the connectivity of the chains requires a non-local relationship for the current density $\mathbf{J}_\Phi(\mathbf{x}, t)$ relating to volume fraction Φ (De Gennes, 1980; Pincus, 1981),

$$\mathbf{J}_\Phi(\mathbf{x}, t) = - \int \Lambda(\mathbf{x} - \mathbf{x}') \nabla \mu(\mathbf{x}', t) d\mathbf{x}' \quad (6-35)$$

where $\Lambda(\mathbf{x} - \mathbf{x}')$ is a generalized Onsager coefficient describing polymer-polymer interdiffusion. The rate $R(k)$ in Eq. (6-21) is then expressed in terms of the Fourier transform Λ_k of $\Lambda(\mathbf{x} - \mathbf{x}')$, i.e.,

$$R(k) = k^2 \Lambda_k [S_T^{\text{coll}}(k)]^{-1} \quad (6-36)$$

where the expression for the effective collective structure factor $S_T^{\text{coll}}(k)$ can be expressed in terms of the structure factors $S_A(k)$ and $S_B(k)$ of the single chains as (Binder, 1983, 1984c, 1987b)

$$[S_T^{\text{coll}}(k)]^{-1} = [\Phi S_A(k)]^{-1} + [(1 - \Phi) S_B(k)]^{-1} - 2\chi^{\text{eff}}(\Phi, T, k) \quad (6-37)$$

where $2\chi^{\text{eff}}(\Phi, T, k)$ is a wavevector-dependent generalization of the term resulting from the second derivative of $\partial^2[\chi\Phi(1 - \Phi)]/\partial\phi^2$ in Eq. (6-33). The single-chain structure functions $S_A(k)$ and $S_B(k)$ are expressed for Gaussian chains by the Debye function $f_D(x)$ as

$$\begin{aligned} S_A(k) &= N_A f_D(k^2 \langle R_{\text{gyr}, A}^2 \rangle) \\ S_B(k) &= N_B f_D(k^2 \langle R_{\text{gyr}, B}^2 \rangle) \end{aligned} \quad (6-38)$$

where $f_D(x) \equiv 2[1 - (1 - e^{-x})/x]/x$.

Eqs. (6-36) and (6-37) result (Binder, 1983) from random phase approximations (De Gennes, 1979) and agree with the treatment as given by Eqs. (6-9)–(6-30) (but using Eq. (6-32) instead of Eqs. (6-4)–

(6-6)) only in the long wavelength limit, where $k_c \langle R_{\text{gyr}}^2 \rangle^{1/2} < 1$ (for both types of chains). In this limit Λ_k can be replaced by a constant Λ_0 , and the results are just special cases of Eqs. (6-9)–(6-30); e.g., for a symmetric mixture ($N_A = N_B$, $\sigma_A = \sigma_B = a$) we simply find:

$$\begin{aligned} 2\pi/\lambda_c &= k_c = \left(\frac{18}{Na^2} \right)^{1/2} (1 - \chi_s(\Phi)/\chi)^{1/2}, \\ k_m &= k_c / \sqrt{2} \end{aligned} \quad (6-39)$$

Hence the critical wavelength λ_c is rescaled by a large prefactor, namely the coil gyration radius, similar to the correlation length ξ_{coex} of concentration fluctuations at the coexistence curve,

$$\xi_{\text{coex}} = (Na^2/36)^{1/2} (\chi/\chi_c - 1)^{-1/2} \quad (6-40)$$

Eq. (6-39), however, is only applicable for "shallow" quenches, where χ does not greatly exceed $\chi_s(\Phi)$. A different behavior occurs (Binder, 1983) for deep quenches, where $\chi \gg \chi_s(\Phi)$ (thus describing the unmixing of two incompatible polymers):

$$\begin{aligned} k_c &\approx \left(\frac{6}{Na^2} \right)^{1/2} [2\chi/\chi_s(\Phi)]^{1/2} \\ k_m &\approx \left(\frac{6}{Na^2} \right)^{1/2} [2\chi/\chi_s(\Phi)]^{1/4} \end{aligned} \quad (6-41)$$

Now the initial wavelength of maximum growth is smaller than the coil radius, and $k_m \ll k_c$, since the gradient-square expansion, Eq. (6-32), is no longer applicable.

As is obvious from Eq. (6-36), the relaxation rate $R(k)$ is the product of two factors, a static factor $[S_T^{\text{coll}}(k)]^{-1}$ which contains the thermodynamic singularities at the critical point (and along the spinodal curve; cf Eq. (6-39)), and a kinetic factor $k^2 \Lambda_k$, to which we now turn. Here the factor k^2 simply reflects the conservation law for the concentration, while Λ_k reflects the

complicated dynamics of single polymer chains in an entangled polymer melt. Despite some effort (De Gennes, 1980; Pincus, 1981; Binder, 1983; Akcasu et al., 1986) there is no systematic method that yields information on the k -dependence of Λ_k ; the approximate theories quoted above all lead to a long-wavelength limit called the *slow-mode theory*, which is believed to be an incorrect description of interdiffusion because it disregards bulk flow (Kramer et al., 1984). Remember that Eq. (6-36) for $k \rightarrow 0$ can be interpreted as $R(k) = k^2 D^{\text{coll}}$, where $D^{\text{coll}} = \Lambda_0 / S_T^{\text{coll}}(0)$, i.e., uphill diffusion. In the slow-mode theory, the interdiffusion coefficient of an ideal non-interacting mixture is expressed in terms of tracer diffusion coefficients D_t^A and D_t^B of an A chain (B chain) in a pure B (A) environment as

$$(D^{\text{coll}})^{-1} = (1 - \Phi) / D_t^A + \Phi / D_t^B \quad (6-42)$$

i.e., the slow species controls the interdiffusion coefficients. In contrast, the *fast-mode theory* (Kramer et al., 1984) yields the opposite result, that the fast species controls interdiffusion:

$$D^{\text{coll}} = (1 - \Phi) D_t^A + \Phi D_t^B \quad (6-43)$$

Experimental evidence (for a review of polymer interdiffusion, see Binder and Sillescu, 1989) seems to favor Eq. (6-43) over Eq. (6-42), but we feel that a valid derivation of Eq. (6-43) is still lacking, and moreover neither Eq. (6-43) nor (6-42) describe interdiffusion in lattice gas models correctly, as computer simulations show (Kehr et al., 1989). Both Eqs. (6-42) and (6-43) are based on a description of transport in which in the constitutive equation relating currents and chemical potential differences (cf. Eq. (6-11)) *off-diagonal* Onsager coefficients are neglected; the Monte Carlo simulation shows that this approximation is inaccurate.

If D_t^A and D_t^B are of the same order, then Eqs. (6-42) and (6-43) also yield D^{coll} of the same order, and the order of magnitude of D^{coll} (and hence $R(k)$, Eq. (6-36)) is then predicted correctly from these equations. If the chain length $N_A(N_B)$ is less than the chain length $N_A^e(N_B^e)$ between effective entanglements, the single-chain dynamics are simply given by the Rouse (1953) model, which implies

$$D_t^A \approx \sigma_A W_A / N_A, \quad D_t^B \approx \sigma_B W_B / N_B$$

where $W_A(W_B)$ are time constants for the reorientation of subunits. In contrast, for $N_A \gg N_A^e$, $N_B \gg N_B^e$ the reptation model (Doi and Edwards, 1986; De Gennes, 1979) implies for strongly entangled chains

$$D_t^A \approx \sigma_A W_A N_A^e / N_A^2, \quad D_t^B \approx \sigma_B W_B N_B^e / N_B^2$$

(neglecting prefactors of order unity). A problem which is not completely understood so far is the concentration dependence of the parameters N_A^e and N_B^e in blends. In view of all these uncertainties about the validity of Eqs. (6-42) and (6-43) and the precise values of the constants D_t^A and D_t^B to be used in them, it is better to consider Λ_k in Eq. (6-36) as a phenomenological coefficient, about which only the order of magnitude can roughly be inferred.

An effect disregarded by the theories but seen in computer simulations (Sariban and Binder, 1989a) is the change in the chain linear dimensions (Eq. (6-31)) in quenching experiments. This also means that the parameter a in Eqs. (6-32) and (6-39) to (6-41) should be treated as a χ -dependent quantity, which further complicates the quantitative analysis of experiments.

6.2.5 Significance of the Spinodal Curve

From Eq. (6-25) it is evident that the linear theory predicts a singular behavior

when the concentration \bar{c} approaches the concentration $c_{sp}(T)$ of the spinodal curve, defined by

$$(\partial^2 f_{cg} / \partial c^2)_{T, \bar{c}=c_{sp}(T)} = 0 \quad (6-44)$$

Here the critical wavelength λ_c diverges to infinity. For example, if we adopt Eq. (6-8) with $A \sim (T/T_c^{MF} - 1)$, near the spinodal we obtain, omitting prefactors of order unity,

$$\lambda_c \sim r(1 - T/T_c^{MF})^{-1/2} \left[\frac{\bar{c} - c_{sp}(T)}{c_{crit} - c_{sp}(T)} \right]^{-1/2} \quad (6-45)$$

On the metastable side of the spinodal curve a similar divergence occurs for both the correlation length $\xi(\bar{c})$ of concentration fluctuations and the radius R^* of a critical droplet, namely (Binder, 1984b)

$$\xi(\bar{c}) \sim R^* \sim r(1 - T/T_c^{MF})^{-1/2} \times \left[\frac{c_{sp}(T) - \bar{c}}{c_{coex}^{(2)} - c_{coex}^{(1)}} \right]^{-1/2}, \quad \bar{c} \leq c_{sp}(T) \quad (6-46)$$

Although R^* diverges as \bar{c} approaches $c_{sp}(T)$, the associated free-energy barrier ΔF^* against the formation of a critical droplet vanished there (Fig. 6-9). The maximum growth rate of spinodal decomposition

tion, which according to Eqs. (6-21), (6-25) and (6-26) can be written as

$$R_m = (1/4) M r^2 k_B T (2\pi/\lambda_c)^4 \quad (6-47)$$

vanishes as $\bar{c} \rightarrow c_{sp}(T)$, and a similar “critical slowing down” (Hohenberg and Halperin, 1977) would occur in the growth rate of a supercritical droplet. Thus, within the framework of this theory, the spinodal curve plays the role of a line of critical points. We now wish to investigate whether there is a physical significance to this singular behavior.

In Sec. 6.2.1 we emphasized that the definition of f_{cg} is not unique but really involves a length scale L over which a coarse-graining of short-range fluctuations is performed. This is best seen from the attempts to calculate f_{cg} explicitly, which can be approximated by using renormalization group methods (Kawasaki et al., 1981) or by Monte Carlo simulation (Kaski et al., 1984). These treatments show that the position of $c_{sp}(T)$ depends strongly on the length scale L (see Fig. 6-10a), and therefore for systems with short-range forces, to which these treatments apply, there is no physical significance to the spinodal singularity (Eqs. (6-44) to (6-47)) whatsoever.

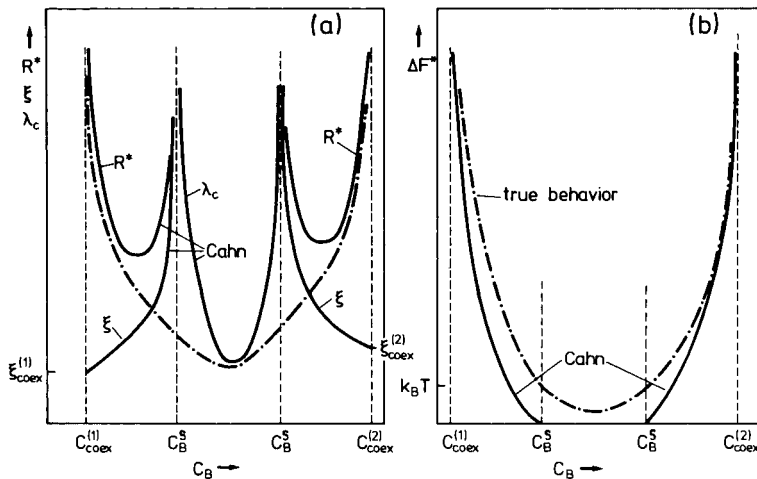


Figure 6-9. (a) Characteristic lengths R^* , ξ , λ_c and (b) nucleation barrier ΔF^* vs. concentration c_B (schematic). Full curves are the predictions of the linearized Cahn–Hilliard mean-field theory of nucleation. Dash-dotted curves show, on a different scale, the conjectured smooth behavior of a system with extremely short-range interaction, for which the spinodal singularity is completely washed out (Binder, 1981).

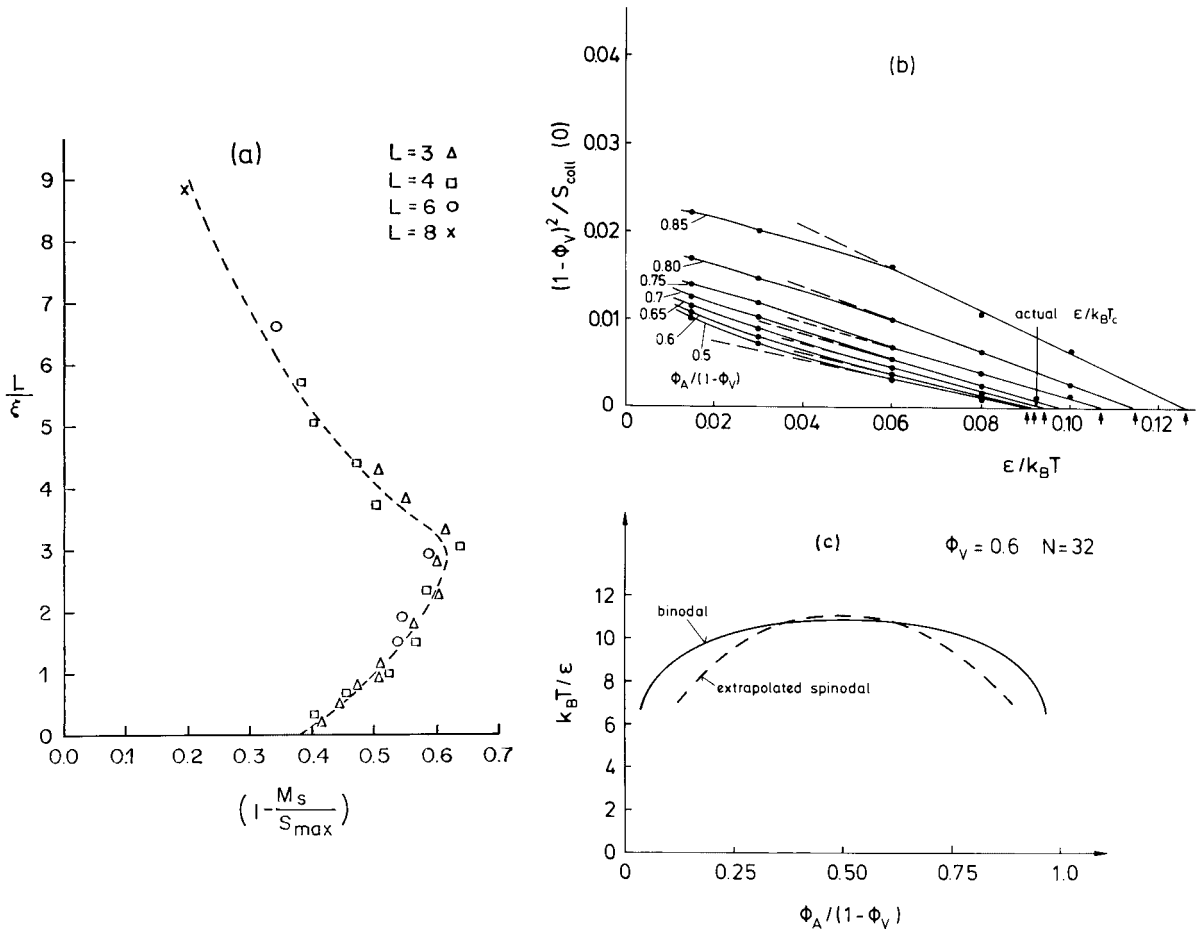


Figure 6-10. (a) Monte Carlo results for the dependence of the relative distance of the “spinodal” from the coexistence curve on the size of the coarse-graining cell L . The results refer to a simple-cubic nearest-neighbor Ising magnet in the critical region, and are obtained from sampling the magnetization distribution function $P_L(M)$ in $L \times L \times L$ sub-blocks of a 24^3 system. Here, S_{\max} is the value at which $\ln P_L(M)$ has its maximum, and corresponds to the coexistence curve if we assume $\ln P_L(M) \sim L^3 f_{cg}/k_B T$, with $c = (1 - M)/2$, and the “spinodal” is estimated as inflection point M_s of $\ln P_L(M)$. By scaling L with the correlation length ξ , all temperatures superimpose on one “scaling function” (Kaski et al., 1984). (b) Extrapolation of the inverse collective structure function versus inverse temperature to locate the spinodal temperatures $T_{sp}(\bar{c})$ or their inverse (arrows). Here Monte Carlo simulation data for a polymer mixture are used, the polymers (A, B) being modelled as self- and mutually avoiding random walks on the simple cubic lattice with $N_A = N_B = N = 32$ steps, at a concentration of vacancies $\phi_v = 0.6$. Values on the curves are the reduced volume fraction $\Phi_A/(1 - \Phi_v)$ of monomers of A chains. If two neighboring lattice sites are taken by monomers of the same kind, an energy ϵ is obtained, and thus an enthalpic driving force for phase separation is created. From Sariban and Binder (1989b). (c) Phase diagram of the model for a polymer mixture as described in (b), displaying both the true coexistence curve (binodal) and the extrapolated spinodal. From Sariban and Binder (1989b).

Another way of showing this comes from a closer examination of the procedures by which experimentalists locate spinodal curves. Eqs. (6-30) and (6-37) imply that

$$[S_T^{\text{coll}}(k \rightarrow 0)]^{-1} \sim (\partial^2 f_{\text{cg}} / \partial c^2)_{T, \bar{c}} \sim T - T_{\text{sp}}(\bar{c})$$

where $T_{\text{sp}}(\bar{c})$ is the inverse function of $c_{\text{sp}}(T)$ in the c - T plane. Thus a plot of $[S_T^{\text{coll}}(k \rightarrow 0)]$ vs. temperature should allow a linear extrapolation to locate $T_{\text{sp}}(\bar{c})$ from the vanishing of $[S_T^{\text{coll}}(k \rightarrow 0)]$ (cf. Fig. 6-10b). However, the extrapolated spinodal determined in this way (e.g., Sariban and Binder, 1989b) (Fig. 6-10c), is not physically meaningful as it crosses the true co-existence curve (binodal) near T_c , which is physically impossible. This happens because, in reality,

$$[S_T^{\text{coll}}(k \rightarrow 0)]_{\bar{c}=c_{\text{crit}}}^{-1} \sim (T - T_c)^\gamma$$

with $\gamma \approx 1.24$, a critical exponent different from the mean-field result $\gamma = 1$. Hence a linear extrapolation fails near $\bar{c} = c_{\text{crit}}$. At strongly off-critical concentrations this extrapolation is also ambiguous, because usually actual data cannot be taken deep in the metastable phase for temperatures close to $T_{\text{sp}}(\bar{c})$.

This situation is different, however, for systems with infinitely weak but infinitely long-range interactions (Penrose and Lebowitz, 1971); then the mean-field theory is correct because statistical fluctuations are suppressed. At the same time, the lifetime of metastable states is infinite because homogeneous nucleation is no longer possible ("heterophase fluctuations" are suppressed at the same times as "homophase fluctuations"). The spinodal curve is the limit of metastability here.

While such a system with infinitely long-range interactions is clearly artificial, it makes sense to consider systems with long but finite range r of the interactions (Heermann et al., 1982; Binder, 1984b;

Heermann, 1984a,b). Although very close to the critical point T_c such systems behave qualitatively like short-range systems (this is to be expected from the so-called "universality principle" (Kadanoff, 1976)), farther from T_c a well-defined mean-field critical region exists. It is this region where both the coarse-graining defined in Eq. (6-1) and the linearization approximation of Sec. 6.2.2 make sense, as we will now discuss.

The argument is simply an extension of the Ginzburg (1960) criterion for the validity of the mean-field theory for critical phenomena to nucleation and spinodal decomposition (Binder, 1984b): nonlinear terms in $\delta c(\mathbf{x}, t)$ can be neglected if their mean-square amplitude in a coarse-graining cell is small in comparison with the concentration difference squares in the system, over which relevant nonlinear effects are felt:

$$\langle [\delta c(\mathbf{x}, t)]^2 \rangle_{T, L} \ll [\bar{c} - c_{\text{sp}}(T)]^2 \quad (6-48)$$

We estimate $\langle [\delta c(\mathbf{x}, t)]^2 \rangle_{T, L}$ as

$$\langle [\delta c(\mathbf{x}, t)]^2 \rangle_{T, L} \approx \langle [\delta c(\mathbf{x}, 0)]^2 \rangle_{T, L} \exp[2R_m t]$$

where R_m is the maximum growth rate defined in Eq. (6-26), and the initial mean-square amplitude is related to the correlation function of concentration fluctuations in the initial state at temperature T_0 . Thus, using Eq. (6-1):

$$\begin{aligned} \langle [\delta c(\mathbf{x}, 0)]^2 \rangle_{T, L} &= \langle [\delta c(\mathbf{x})]^2 \rangle_{T_0, L} \\ &= \frac{1}{L^6} \sum_{i, j} [\langle c_i c_j \rangle_{T_0} - \bar{c}^2] \\ &= \frac{1}{L^3} \int d\mathbf{x} [\langle c(0) c(\mathbf{x}) \rangle_{T_0} - \bar{c}^2] \end{aligned} \quad (6-49)$$

the summations over i and j being restricted to sites within the cell of size L^3 centered at \mathbf{x} and in the last step the sums are converted into integrals (one sum \sum_i is cancelled against a factor L^3 making use of the

translational invariance of the correlation function). For distances $|\mathbf{x}| \ll \xi$ the correlation function is simply given by a power-law decay, $\langle c(0) c(\mathbf{x}) \rangle_{T_0} - \bar{c}^2 \approx r^{-2} x^{-1}$, and therefore the order of magnitude of the integral in Eq. (6-49) is estimated, yielding

$$\langle [\delta c(\mathbf{x}, 0)]^2 \rangle_{T_0, L} \approx r^{-2} L^{-1} \quad (6-50)$$

As expected, the mean-square concentration fluctuation is the smaller the larger is the range of the interactions and the larger is the coarse-graining length L . Since the largest permissible value for L is $L \approx \lambda_c$, Eqs. (6-45), (6-48), and (6-50) readily yield

$$\exp(2R_m t) \ll r^3 (1 - T/T_c)^{1/2} \times [\bar{c}/c_{sp}(T) - 1]^{3/2} \quad (6-51)$$

A similar self-consistency criterion can be formulated in the metastable region, where the largest permissible choice for L in the Ginzburg criterion

$$\langle [\delta c(\mathbf{x})]^2 \rangle_{T, L} \ll (c_{sp}(T) - \bar{c})^2$$

now is $L = \xi(\bar{c})$, as given in Eq. (6-46), and it is found in full analogy with Eqs. (6-48) to (6-51) that

$$1 \ll r^3 (1 - T/T_c)^{1/2} [1 - \bar{c}/c_{sp}(T)]^{3/2} \quad (6-52)$$

It is also interesting that Eq. (6-52) can be derived from a completely different argument, namely requiring that the free energy barrier of nucleation $\Delta \mathcal{F}^* \gg k_B T$ (Binder, 1984b) (for \bar{c} near $c_{sp}(T)$ the Cahn-Hilliard (1959) mean-field theory of nucleation predicts $\Delta \mathcal{F}^*/k_B T \sim r^3 (1 - T/T_c)^{1/2} \times [1 - \bar{c}/c_{sp}(T)]^{3/2}$). From Eqs. (6-51) and (6-52) we draw the following conclusions:

(i) For the linearized theory of spinodal decomposition to be self-consistent, and for the description of a metastable state near the spinodal to be self-consistent (and that it has a long lifetime owing to a large barrier against homogeneous nucleation), the in-

equalities which must be satisfied require that

$$r^3 (1 - T/T_c)^{1/2} \gg 1 \quad (6-53)$$

This condition can be satisfied only for a large range r of interaction, and defines the *mean-field critical region* (Ginzburg, 1960). As long as Eq. (6-53) holds, the Landau mean-field theory of critical phenomena (Stanley, 1971) is quite adequate. However, for systems with rather short-range interactions Eq. (6-53) and hence Eqs. (6-51) and (6-52) can never be fulfilled.

(ii) Even for systems with a long but finite range r of interaction, close enough to T_c (namely for $r^3 (1 - T/T_c)^{1/2} \approx 1$) a cross-over occurs to a non-mean-field critical behavior, described by the same critical behavior as short-range systems. This is expected from the principle of universality of critical behavior (Kadanoff, 1976). Then the nonlinear character of Eq. (6-15) is important during the initial stages of the quench, and the linearization approximation (Eq. (6-18)) is never warranted.

(iii) For mean-field-like systems for which Eq. (6-53) holds, Eqs. (6-51) and (6-52) hold only if we do not come too close to the spinodal. The region excluded by these inequalities scales as

$$|\bar{c}/c_{sp}(T) - 1| \sim r^{-1} (1 - T/T_c)^{-1/3}$$

In this excluded region the singularities described by Eqs. (6-45) to (6-47) are essentially smeared out, and a gradual transition from nucleation and growth to nonlinear spinodal decomposition occurs. This gradual transition can be understood qualitatively from a cluster dynamics treatment of phase separation (Binder and Stauffer, 1976a; Binder, 1977, 1981; Mirolid and Binder, 1977; Binder et al., 1978). Figs. 6-11 and 6-12 summarize the main ideas about this description which is closely

related in spirit to the Langer–Schwartz (1980) and Kampmann–Wagner (1984) treatments of concomitant nucleation, growth, and coarsening (see Wagner et al., 2001). Each state of the system is characterized by a cluster size distribution $\bar{n}_l(t)$, where l is the number of B atoms contained within a cluster (Fig. 6-11 a) and the bar represents an average over other “cluster coordinates” (cluster surface area, shape, etc.) which are not considered explicitly. The time evolution of the cluster size distribution in a quenching experiment is described by a system of kinetic equations:

$$\begin{aligned} \frac{d}{dt} \bar{n}_l(t) = & \sum_{l'=1}^{\infty} S_{l+l',l'} \bar{n}_{l+l'}(t) \\ & - \frac{1}{2} \sum_{l'=1}^{l-1} S_{l,l'} \bar{n}_l(t) \\ & + \frac{1}{2} \sum_{l'=1}^{l-1} c_{l-l',l'} \bar{n}_{l'}(t) \bar{n}_{l-l'}(t) \\ & - \sum_{l'=1}^{\infty} c_{l,l'} \bar{n}_l(t) \bar{n}_{l'}(t) \end{aligned} \quad (6-54)$$

Here $S_{l+l',l'}$ is a rate factor for a splitting reaction of a cluster of size $l+l'$ into two

clusters of size l and l' , and $c_{l,l'}$ is the rate factor for the inverse “coagulation” reaction. These rate factors are assumed to be independent of time t and hence Eq. (6-54) also describes the concentration fluctuations in thermal equilibrium, where detailed balance must hold between splitting and coagulation reactions:

$$S_{l+l',l'} n_{l+l'} = c_{l,l'} n_l n_{l'} \equiv W(l, l') \quad (6-55)$$

where n_l is the cluster concentration in equilibrium and $W(l, l')$ is a cluster reaction matrix in equilibrium. While $n_l(t=0)$ for a random distribution of atoms in the alloy is just the cluster distribution in the well-known percolation problem (Stauffer, 1985), n_l and $W(l, l')$ are not explicitly known, but can be fixed by plausible assumptions (Binder, 1977; Mirolid and Binder, 1977). Then Eqs. (6-54) and (6-55) can be solved numerically (see Fig. 6-11 b). What must happen is that $\bar{n}_l(t)$ for $t \rightarrow \infty$ develops towards n_l , the cluster size distribution in the state at the coexistence curve

$c_{\text{coex}}^{(1)}$, with $c_{\text{coex}}^{(1)} = \sum_{l=1}^{\infty} l n_l$. The excess concentration $\bar{c} - c_{\text{coex}}^{(1)} = \sum_{l=1}^{\infty} l [n_l(0) - n_l]$ is

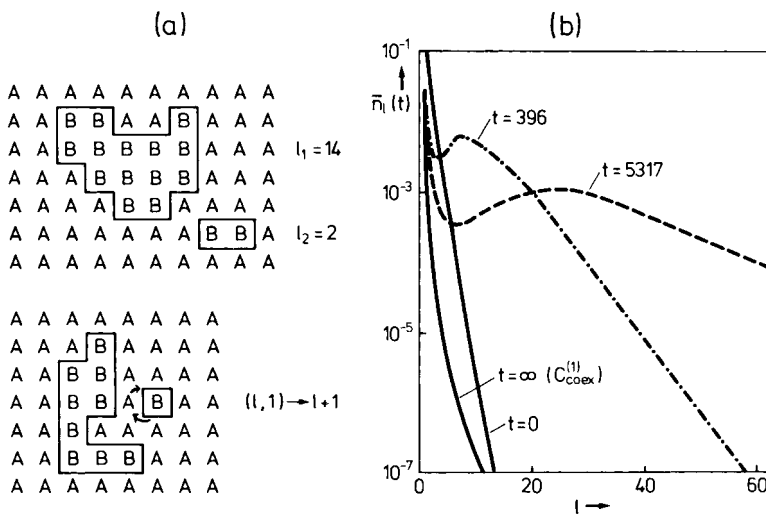


Figure 6-11. (a) “Clusters” of B atoms in a binary AB mixture defined from contours around groups of B atoms and their reactions. (b) Cluster size distribution $\bar{n}_l(t)$ for various times t after a quench from infinite temperature to $T/T_c = 0.6$ at $\bar{c} = 0.1$ for parameters appropriate for a two-dimensional Ising model of a binary alloy. These results were obtained from a numerical solution of Eq. (6-54), where time units are rescaled by an arbitrary rate factor. From Mirolid and Binder (1977).

redistributed into macroscopic B-rich domains (of concentration $c_{\text{coex}}^{(2)}$), i.e., occurs at cluster size $l \rightarrow \infty$ for $t \rightarrow \infty$. For intermediate times, we find a nonmonotonic cluster size distribution (Fig. 6-11b); a minimum occurs at the *critical size* l^* of nucleation theory (Binder and Stauffer, 1976a), while the broad maximum at larger sizes is due to growing supercritical clusters which have already been nucleated. For $l < l^*$ the cluster size distribution is basically the equilibrium size distribution of a slightly supersaturated solid solution. As time goes on, the peak in $\bar{n}_l(t)$, representing the supercritical growing clusters, shifts to larger and larger cluster sizes, and at the same time the supersaturation is diminished, until for $t \rightarrow \infty$ the peak has shifted to $l \rightarrow \infty$. This separation of clusters into two classes – small ones describing concentration fluctuations in the supersaturated A-rich background and large ones describing the growing B-rich domains – can also be shown analytically from Eqs. (6-54) and (6-55) (Binder, 1977). This picture of the phase separation process also emerges very clearly from computer simu-

lations (Marro et al., 1975; Rao et al., 1976; Sur et al., 1977).

The description in terms of Eqs. (6-54) and (6-55) contains both nucleation and growth and coagulation as special cases (Binder, 1977), and it can be used as a basis for understanding the *gradual transition from nucleation to spinodal decomposition* (Binder et al., 1978). In the metastable regime the density of unstable fluctuations (“critical” and “supercritical” clusters with $l < l^*$) is very small (Fig. 6-12a), because the energy barrier $\Delta F^* \gg k_B T$. Near the spinodal curve, on the other hand, $\Delta F^* \approx k_B T$, and hence there is a high density of unstable fluctuations: ΔF^* here no longer limits the growth, but rather the conservation of concentration. Near growing clusters, $c(\mathbf{x}, t)$ locally decreases, and then no other cluster can grow there. Owing to this “excluded volume” interaction of clusters, a quasiperiodic variation of concentration results (Fig. 6-12a, bottom), roughly equivalent to a wavepacket of Cahn’s concentration waves. But the latter are not growing independently, rather they are strongly interacting; hence it is more

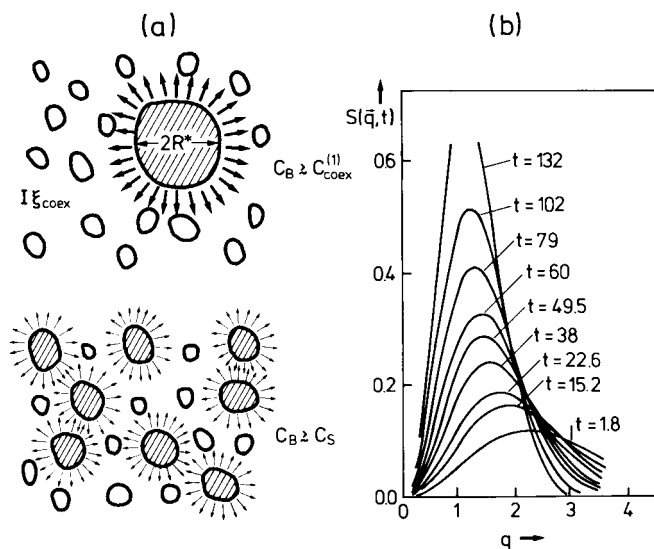


Figure 6-12. (a) Schematic “snapshot pictures” of fluctuations of an unmixing system in the metastable regime (top) and in the unstable regime (bottom). Unstable fluctuations, which steadily grow with increasing time (arrows) are shaded. (b) Structure factor $S(\mathbf{q}, t)$ vs. scaled wavevector q at various times t after a quench from infinite temperature to $T = 0.6 T_c$ for $\bar{c} = 0.1$. Parameters are chosen for a three-dimensional Ising model of a binary alloy. These results were obtained from a numerical solution of Eqs. (6-54) to (6-56). From Binder et al. (1978).

reasonable to consider large clusters as objects nearly independent of each other (apart from the reactions in Eq. (6-54)) rather than as these waves.

The fact that the cluster picture and the concentration picture are simply two dual descriptions of the same physical situation becomes very apparent when the structure factor $S(k, t)$ is calculated from the cluster size distribution $\bar{n}_l(t)$. Introducing the conditional probability $g_l(\mathbf{x})$ that the site $\mathbf{x} + \mathbf{x}'$ is taken by a B atom if \mathbf{x}' is taken by a B atom of an l -cluster, we find (Binder et al., 1978):

$$S(k, t) = \sum_{l=1}^{\infty} l n_l(t) \int d\mathbf{x} \{g_l(\mathbf{x}) - \bar{c}\} \times \exp(i\mathbf{k} \cdot \mathbf{x}) \quad (6-56)$$

Simple assumptions for $g_l(\mathbf{x})$ yield $S(k, t)$ as shown in Fig. (6-12b). The resulting $S(k, t)$ is therefore in qualitative agreement with experimentation (Fig. 6-5a, b), computer simulation of microscopic models (Fig. 6-5c, d) and the approximate non-linear theory of spinodal decomposition of Langer et al. (1975) (see Fig. 6-8, bottom).

This gradual transition between nucleation and spinodal decomposition always appears close to the critical point in the phase diagram (Fig. 6-13); for systems with a large interaction range r a mean-field critical regime exists (Eq. (6-53)) where this gradual transition is confined to a narrow regime adjacent to the spinodal. Outside this transition regime the linearized theory of spinodal decomposition is expected to hold *initially* in the unstable regime, while a nonclassical nucleation theory (where ramified droplets, which must first be compacted before they can grow, are nucleated (Klein and Unger, 1983; Unger and Klein, 1984; Heermann and Klein, 1983a, b)) holds in the metastable regime. This crossover line between clas-

sical and nonclassical "spinodal nucleation" is essentially given by the condition that the free-energy barrier Δf^* to form a critical nucleus is of the order of $r^3(1 - T/T_c)^{1/2} \gg 1$ (Fig. 6-14a). Therefore this regime of "spinodal nucleation" must disappear when the non-mean-field critical region is approached (Fig. 6-14b).

It should be emphasized that the phase diagram in Fig. 6-13 showing these various regimes in the temperature-concentration plane is relevant only in the very early stages of phase separation. This should be obvious from Eq. (6-51). The time range where it is valid is, at best, of the order of $R_m t \approx \ln r$ (r being measured in units of the lattice spacing). Therefore the experimental verification of the linear theory of spinodal decomposition is a difficult problem (see Sec. 6.4). Clear confirmation of the ideas described above has come from computer simulations of medium-range Ising models due to Heermann (1984a) (see Figs. 6-15 and 6-16). Since for the Ising model the result for $R(k)$ is readily worked out, a comparison between theory and simulation is possible without any adjustable parameter whatsoever! Fig. 6-15 shows that there is indeed a regime where initially fluctuations increase exponentially with time (Eq. (6-23)) and the observed rates $R(k)$ do agree with the predictions, if we stay far off the spinodal.

It is not easy to identify physical systems that have a large but finite interaction range. What is really needed is a large prefactor in the mean-field result for the correlation length (Eq. (6-46)), and such a large prefactor has in fact been identified for polymers with high molecular weight (Eq. (6-40)). This happens because for polymers the coefficient of the gradient energy in Eq. (6-32) comes from the random-coil structure, and does not have the meaning of a squared interaction range as in Eq. (6-4).

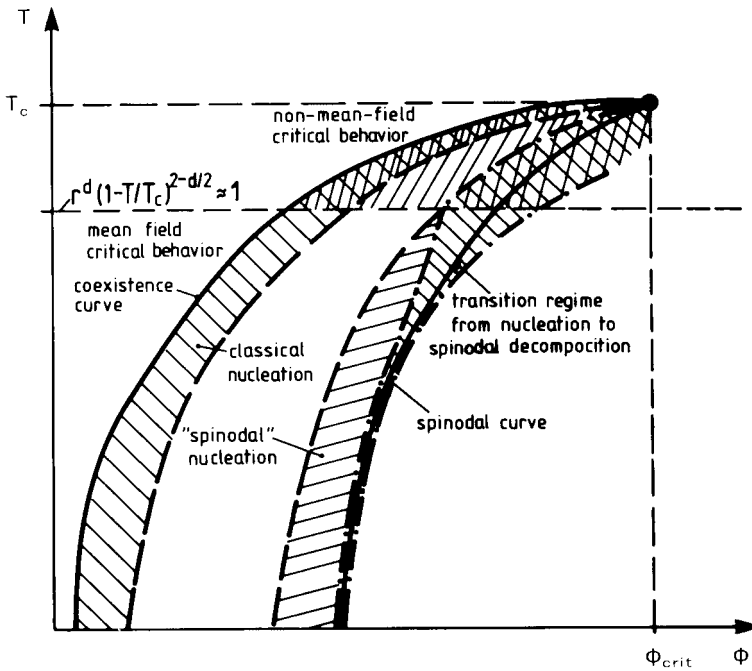


Figure 6-13. Various regimes in the phase diagram of a binary mixture AB, showing part of the plane formed by temperature T and volume fraction Φ of the B component (only volume fractions $\Phi < \Phi_{\text{crit}}$ are shown, since this schematic phase diagram is symmetric around the axis $\Phi = \Phi_{\text{crit}}$). The horizontal broken line separates the non-mean-field critical regime (top) from the mean-field critical regime (bottom). The two solid curves are the coexistence curve (left) and the spinodal curve (right). The two dash-dotted curves on both sides of the spinodal limit represent the regime where a gradual transition from nucleation to spinodal decomposition occurs. The linearized theory of spinodal decomposition (Fig. 6-1 a) should hold to the right of these dash-dotted curves. The regime between the coexistence curve and the left of the two broken curves is described by classical nucleation theory (compact droplets, Fig. 6-1 b). The regime between the right broken curve and the left dash-dotted curve is described by “spinodal nucleation” (ramified droplets). From Binder (1984b).

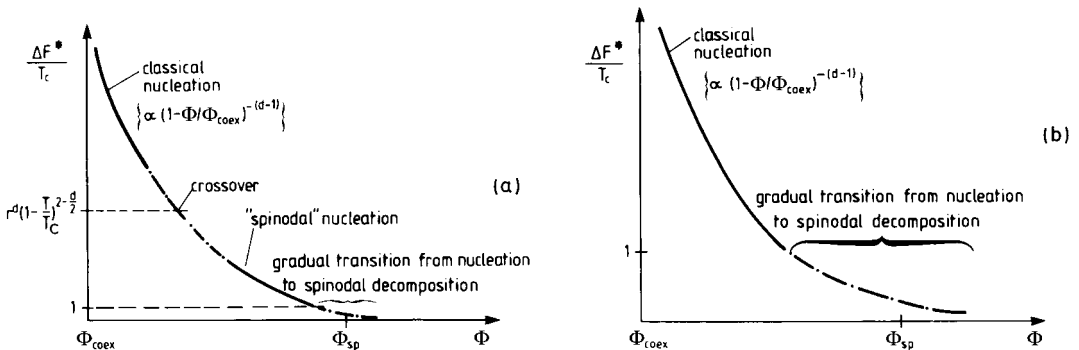


Figure 6-14. Schematic plots of the nucleation free energy barrier for (a) the mean-field critical region of a d -dimensional alloy system, i.e., $r^d(1-T/T_c)^{(4-d)/2} \geq 1$ and (b) the non-mean-field critical region, i.e., $r^d(1-T/T_c)^{(4-d)/2} < 1$. The gradual transition from nucleation to spinodal decomposition occurs for $\Delta F^*/k_B T_c \approx 1$. From Binder (1984b).

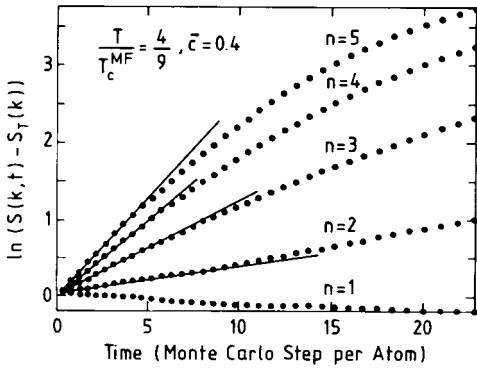


Figure 6-15. Time dependence of the logarithm of spherically averaged structure factors of a 60^3 simple-cubic Ising lattice, where each spin interacts with $q=124$ neighbors with equal interaction strength J , quenched from infinite temperature to

$$T = (4/9) T_c^{\text{MF}} = (4/9) q J / k_B \quad \text{and} \quad \bar{c} = 0.4$$

The five smallest wavenumbers $k_n = 2\pi n/60$ are displayed. Straight lines for short times indicate exponential growth and thus yield $R(k)$. From Heermann (1984a).

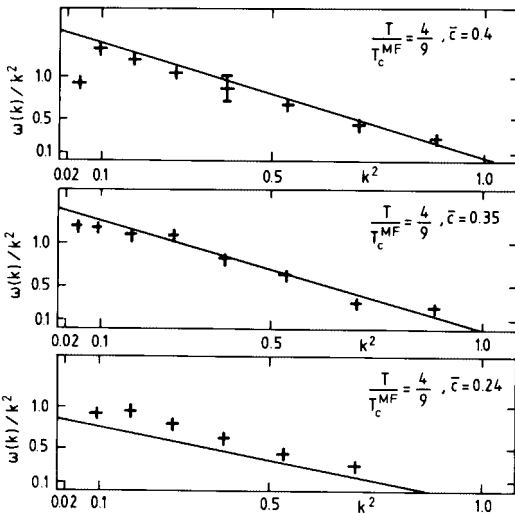


Figure 6-16. Cahn plot $R(k)/k^2$ vs. $k^2(R(k)$ is denoted as $\omega(k)$ in this figure), as extracted from data such as shown in Fig. 6-15. Crosses are the Monte Carlo results, and straight lines are the predictions of the linearized theory. Note that $c_{\text{sp}}(T) \approx 0.127$ in this case. From Heermann (1984b).

However, we note that for $N_A = N_B = N$ we may map Eqs. (6-33) and (6-32) into Eqs. (6-4) and (6-6) with the following identifications (Binder, 1984b):

$$\Delta \mathcal{F}_{\text{polymer}} \equiv \frac{1}{N} \Delta \mathcal{F}_{\text{small molecules}}$$

$$\chi \equiv 2 \frac{T_c}{T} \frac{1}{N}, \quad r^2 \equiv \frac{2}{3} N a^2 \quad (6-57)$$

The condition that the nucleation barrier $\Delta \mathcal{F}^*/k_B T \gg 1$ instead of Eq. (6-52) then yields

$$1 \ll N^{1/2} \left(1 - \frac{\chi_{\text{crit}}}{\chi} \right)^{1/2} |1 - \bar{c}/c_{\text{sp}}(T)|^{3/2} \quad (6-58)$$

and a similar criterion holds on the unstable side of the spinodal (Binder, 1983), with 1 being replaced by $\exp(2R_m t)$ on the left-hand side of Eq. (6-58), as in Eq. (6-51). It follows that for large chain length N the spinodal is smeared out over a region of width $N^{-1/3}$.

In view of these results, it is gratifying to note that for polymers, convincing experimental demonstrations of the validity of Cahn's linearized theory of spinodal decomposition have indeed been presented (see Sec. 6.3.4).

6.2.6 Towards a Nonlinear Theory of Spinodal Decomposition in Solids and Fluids

In the last subsection it was shown that the regime of times for which the linear theory of spinodal decomposition holds is extremely restricted, if it holds at all. Therefore, a treatment of nonlinear effects is necessary. A systematic approach is only possible by an expansion in powers of $1/r$ for large r (Grant et al., 1985). This theory is very complicated and has so far been worked out only for $\bar{c} = c_{\text{crit}}$. It explicitly shows the coupling between concentration waves with different wavevectors.

So far the most popular (if approximate) approach is the decoupling approximation suggested by Langer et al. (1975). Exact equations of motion are derived for the probability distributions $\varrho_1[c(\mathbf{x})]$, $\varrho_2[c(\mathbf{x}_1), c(\mathbf{x}_2)]$, etc. Here ϱ_1 is the probability density that, at point \mathbf{x} , the concentration $c(\mathbf{x})$ occurs, and ϱ_2 is the corresponding two-point function. As expected, the equation of motion for ϱ_1 involves ϱ_2 , and the equation of motion for ϱ_2 involves the three-point function ϱ_3 , etc., so that an infinite hierarchy of equations of motion is generated.

This hierarchy is decoupled by the following approximation for the two-point function $[\delta c(\mathbf{x}) = c(\mathbf{x}) - \bar{c}]$:

$$\begin{aligned} \varrho_2[c(\mathbf{x}_1), c(\mathbf{x}_2)] &= \varrho_1[c(\mathbf{x}_1)] \varrho_1[c(\mathbf{x}_2)] \\ &\times \left\{ 1 + \frac{\langle \delta c(\mathbf{x}_1) \delta c(\mathbf{x}_2) \rangle_T}{\langle (\delta c)^2 \rangle_T} \frac{\delta c(\mathbf{x}_1) \delta c(\mathbf{x}_2)}{\langle (\delta c)^2 \rangle_T} \right\} \end{aligned} \quad (6-59)$$

The motivation for Eq. (6-59) is the following: if there were no correlation between concentrations at points \mathbf{x}_1 and \mathbf{x}_2 , the probability ϱ_2 would just be the product of the one-point probabilities. Therefore, the correction of this factorization approximation is made proportional to the two-point correlation function $\langle \delta c(\mathbf{x}_1) \delta c(\mathbf{x}_2) \rangle_T$. In this way, Eq. (6-59) yields a closed equation of motion for the probability ϱ_1 . This equation is then solved approximately, assuming that the coarse-grained free energy has the Landau form (Eqs. (6-5) and (6-8)). The coefficients A , B and r are adjusted self-consistently such that the resulting state equilibrium is correctly described in the non-mean-field critical region.

This approach has also been worked out for the dynamics of non-conserved order parameters (Billotet and Binder, 1979) and the validity of this approximation has been studied carefully (see also Binder et al., 1978). The final result can be cast in a form

that is similar to Eq. (6-27), namely,

$$\begin{aligned} \frac{d}{dt} S(k, t) &= -2Mk^2 \\ &\times \left\{ \left[\left(\frac{\partial^2 f}{\partial c^2} \right)_{T, \bar{c}} + a(t) + r^2 T k^2 \right] S(k, t) - k_B T \right\} \end{aligned} \quad (6-60)$$

where all nonlinear effects are now contained in a correction term $a(t)$, which itself depends on $S(k, t)$ in a nonlinear way.

As noted above, the coefficients A , B , and r in Eqs. (6-5) and (6-8) are adjusted such that the critical behaviors of the coexistence curve, critical scattering intensity, and correlation length (at the coexistence curve) are reproduced:

$$(c_{\text{coex}}^{(1)} - c_{\text{crit}})/c_{\text{crit}} = \hat{B}(1 - T/T_c)^\beta \quad (6-61 \text{ a})$$

$$\chi_{\text{coex}} = \hat{C}(1 - T/T_c)^{-\gamma} \quad (6-61 \text{ b})$$

$$\xi_{\text{coex}} = \hat{\xi}(1 - T/T_c)^{-\nu} \quad (6-61 \text{ c})$$

where \hat{B} , \hat{C} , and $\hat{\xi}$ are the appropriate *critical amplitudes* and β , γ , and ν the associated *critical exponents* (Stanley, 1971; Binder, 2001). It now turns out that the strength of nonlinear effects is controlled by the inverse of a parameter f_0 which near T_c is expressed as (Billotet and Binder, 1979)

$$f_0 \sim \hat{\xi}^d \hat{B}^2 \hat{C}^{-1} (1 - T/T_c)^{\gamma+2\beta-d\nu} \quad (6-62)$$

for a d -dimensional system. In the non-mean-field critical region, the hyperscaling relation $d\nu = \gamma + 2\beta$ (Kadanoff, 1976) eliminates the temperature dependence from Eq. (6-62). In addition, two-scale factor universality (Stauffer et al., 1972) implies that the critical amplitude ratio $\hat{\xi}^d \hat{B}^2 / \hat{C}$ and hence f_0 is a universal constant of order unity (Billotet and Binder, 1979), i.e., $f_0 \approx 9.45$. On the other hand, if we consider a quench into the mean-field critical region, again adjusting the coefficients A and B in Eq. (6-8) but now using mean-field

results in Eqs. (6-61a-c), namely, $\beta = \frac{1}{2}$, $\gamma = 1$, and $\nu = \frac{1}{2}$, $\xi \sim r$, we obtain

$$f_0 \sim r^d (1 - T/T_c)^{(4-d)/2}$$

for $r^d (1 - T/T_c)^{(4-d)/2} \gg 1$ (6-63)

It is seen that f_0 is now simply proportional to the parameter appearing in the Ginzburg criterion, and hence very large. For $r^d (1 - T/T_c)^{(4-d)/2} \approx 1$ a crossover to the universal constant $f_0 \approx 9.45$ in the non-mean-field critical region occurs.

Fig. 6-17 shows the time evolution for the structure factor for two choices of f_0 . Here again a rescaling of the structure factors $\hat{S} = r^2 k_c^2 S$ and of time $\tau = 2 M r^2 T k_c^4 t$ was used, while $q = 40 k / (2 \pi k_c)$ here. It is seen that for $f_0 \approx 9.45$ the linear theory is indeed invalid from the start, as expected.

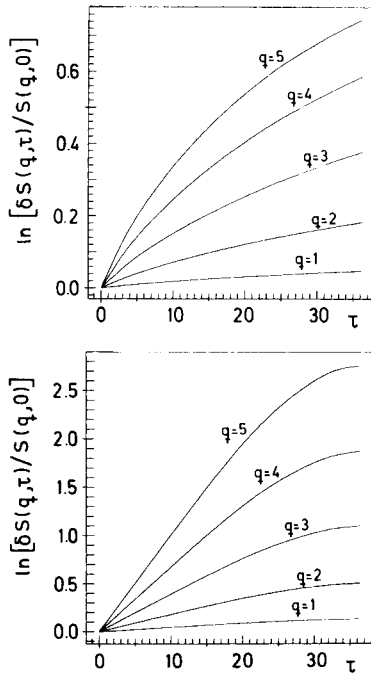


Figure 6-17. Plot of $\ln \{[\tilde{S}(q, \tau) - \tilde{S}_T(q)] / \tilde{S}_{T_0}(q)\}$ vs. scaled time τ for five different values of q , for a quench from infinite temperature at c_{crit} , using $f_0 = 9.45$ (top) and $f_0 = 9450$ (bottom). From Carmesin et al. (1986).

However, for large values of f_0 the linear theory does hold initially, consistent with the simulations (Fig. 6-15). The same conclusion emerges from the time dependence of the rescaled effective second derivative $\mu_-(T, t)$ in Eq. (6-60):

$$\mu_-(T, t) \equiv 1 + a(t) / [\partial^2 f / \partial c^2]_{T, c} \quad (6-64)$$

(see Fig. 6-18). Nonlinear effects are negligible as long as $\mu_- = 1$, while the decrease in μ_- is a signal of nonlinear effects, since $a(t)$ is always negative. The physical significance of $\mu_-(T, t)$ is that it describes the ratio between the actual $k_c^2(t)$, where the growth rate in Eq. (6-60) changes sign, and the corresponding prediction of the Cahn–Hilliard theory. Fig. 6-18 implies that *even if the nonlinear effects are very strong* the Cahn–Hilliard prediction for k_c^2 differs from the actual $k_c^2(t)$ by about a factor of two at most; therefore, the Cahn–Hilliard theory is certainly useful for esti-

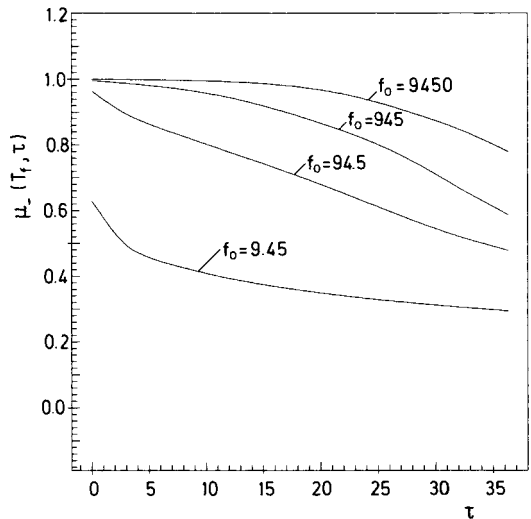


Figure 6-18. Rescaled effective second derivative $\mu_-(T_f, t)$ (Eq. (6-64)) vs. scaled time τ for four choices of f_0 . Only when $\mu_-(T, \tau) \approx 1$ is the Cahn–Hilliard–Cook approximation accurate. For $f_0 = 9.45$ the initial value $\mu_-(T, 0) = 0.65$. From Carmesin et al. (1986).

imating the order of magnitude of the range of wavelengths that is unstable initially.

For systems with short-range forces, where $f_0 \approx 9.45$ applies, the early-time structure factor for critical quenches (Fig. 6-8, bottom) is in reasonable agreement with both experiment (Fig. 6-5a,b) and simulations (Figs. 6-5c,d). However, the Langer–Baron–Miller (LBM) (1975) approximation gets worse for strongly off-critical quenches (Binder et al., 1978). The theory again exhibits a spurious singularity at a spinodal curve, which does not coincide with the mean-field spinodal of the CHC approximation, but occurs at a renormalized concentration closer to the coexistence curve. This shift of the spinodal is not surprising, since the effective second derivative of the potential is also renormalized (Fig. 6-18). This spinodal of the LBM approximation is completely spurious – its precise location depends on details of the coarse-graining procedure. For concentrations between the coexistence curve and this spinodal, i.e., the metastable regime, the structure factor $S(k, t)$ for $T \rightarrow \infty$ saturates at a value $S(k, \infty) = k_B T / [\partial^2 f / \partial x^2]_{T,c} + a(\infty) + r^2 T k^2$, i.e., at the Ornstein–Zernike result for scattering from fluctuations in metastable equilibrium (Binder et al., 1978).

We now consider fluid binary mixtures. Here the theoretical formulation is complicated by another long-range interaction, namely the hydrodynamic backflow interaction. If the Liouville equation is written for the probability distribution $\mathcal{Q}(\{c(\mathbf{x})\}, t)$ that a concentration field $c(\mathbf{x})$ occurs,

$$\frac{\partial}{\partial t} \mathcal{Q}(\{c(\mathbf{x})\}, t) = \mathcal{L} \mathcal{Q}(\{c(\mathbf{x})\}, t) \quad (6-65a)$$

the Liouville operator \mathcal{L} contains a term \mathcal{L}_A also present in solid alloys and another term \mathcal{L}_{HD} containing the Oseen tensor $\mathbf{T} = \{T_{\alpha\beta}\}$ describing the hydrodynamic

interaction:

$$\mathcal{L} = \mathcal{L}_A + \mathcal{L}_{HD} \quad (6-65b)$$

$$\mathcal{L}_A = -M \int d\mathbf{x} \frac{\delta}{\delta c(\mathbf{x})} \nabla^2 \left[\frac{\delta}{\delta c(\mathbf{x})} + \frac{\delta F}{\delta c(\mathbf{x})} \right]$$

$$\begin{aligned} \mathcal{L}_{HD} = 2 \iint d\mathbf{x} d\mathbf{x}' \frac{\delta}{\delta c(\mathbf{x})} \nabla c(\mathbf{x}) \cdot \mathbf{T}(\mathbf{x} - \mathbf{x}') \\ \times \nabla' c(\mathbf{x}') \left[\frac{\delta}{\delta c(\mathbf{x}')} + \frac{\delta F}{\delta c(\mathbf{x}')} \right] \end{aligned} \quad (6-65c)$$

and

$$\begin{aligned} T_{\alpha\beta}(\mathbf{x} - \mathbf{x}') = \frac{1}{8\pi\eta} \left[\frac{1}{|\mathbf{x} - \mathbf{x}'|} \delta_{\alpha\beta} \right. \\ \left. + \frac{1}{|\mathbf{x} - \mathbf{x}'|^3} (x_\alpha - x'_\alpha)(x_\beta - x'_\beta) \right] \end{aligned} \quad (6-65d)$$

where η is the shear viscosity. Kawasaki and Ohta (1978) adapted the LBM decoupling to binary fluids. Their results differ from the original LBM theory mainly where $k_m(t)/k_m(0) \ll 1$; however, at such late times neither of these theories is valid, since they can only account for nonlinearities during the early stages where $k_m(t)/k_m(0) \approx 1$. No theory exists which reliably describes the crossover from these initial time regimes to the late stages, where $k_m^{-1}(t) \sim t$ is presumed to hold.

An interesting extension is to consider spinodal decomposition of fluid mixtures in the presence of flow, e.g., laminar shear flow (Onuki and Kawasaki, 1978, 1979) or turbulent flow (Onuki, 1984, 1989c). In weak shear, the scattering pattern is no longer the ring pattern familiar from standard spinodal decomposition, since concentration fluctuations become anisotropic. In polymer mixtures additional effects arise because the polymer coils become stretched and oriented by the flow (Pistoors and Binder, 1988a, b). No such phenomena are considered here.

6.2.7 Effects of Finite Quench Rate

So far both the theory and the discussed simulations have always assumed instantaneous quenches from an initial temperature T_i to a final temperature T_f . With regard to actual experiments, this is extremely idealized. Often the early stages of spinodal decomposition have already been passed during such a continuous quench where the temperature is gradually lowered. While it is believed that the late stages are not affected by the “quenching history”, the latter can have a drastic effect on both early and intermediate stages of phase separation. Unfortunately, in general, the problem is complicated – the behavior of both the thermodynamic functions and of the mobility $M(T)$ in the full regime from T_i to T_f may affect the phase separation behavior. Thus, relatively little theoretical effort has been devoted to this problem (Houston et

al., 1966; Carmesin et al., 1986). Here we only quote a few results from the model calculation of Carmesin et al. (1986), since the work by Houston et al. (1966) only considers fluctuations in the initial state and not in the intermediate states visited in the quench, which is an approximation that usually cannot be justified.

As an example, Fig. 6-19 shows a situation similar to the quench treated in Fig. 6-8, but here the quench is not carried out instantaneously from infinite temperature to $T/T_c = 4/9$, but takes several steps: at $\tau=0$ the system is cooled instantaneously to $T_1/T_c = 0.75185$, at $\tau=1$ to $T_2/T_c = 0.67667$, at $\tau=2$ to $T_3/T_c = 0.60148$, at $\tau=3$ to $T_4/T_c = 0.5263$, and at $\tau=4$ to $T/T_c = 4/9$, where the system is later maintained. This stepwise quenching is more readily accessible to calculation than a fully continuous quench. A further simplification of the calculation is to neglect any temperature de-

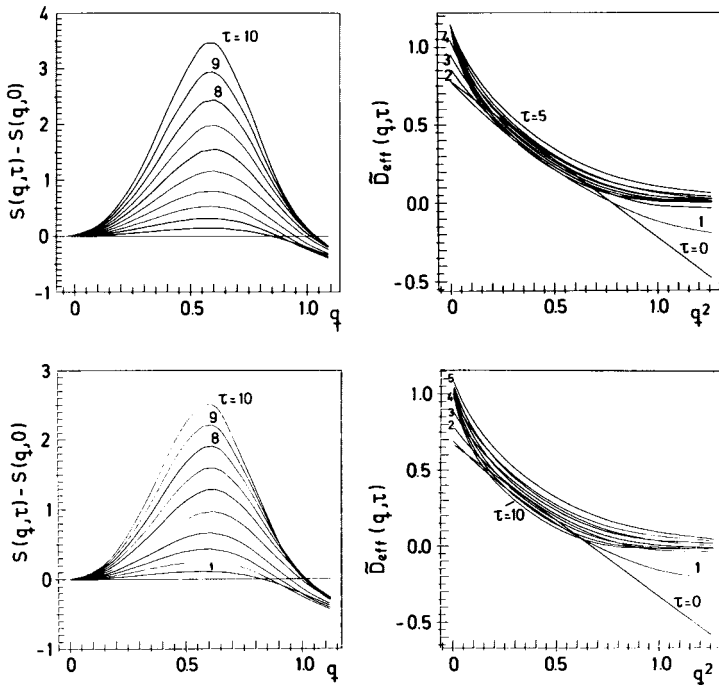


Figure 6-19. Scaled structure function (left) and normalized diffusion constant $\tilde{D}_{\text{eff}}(q, \tau) \equiv q^2 d[\ln \tilde{S}(q, \tau)]/d\tau$ (right) vs. q or q^2 , respectively, for the stepwise quenching procedure described in the text. Top, CHC approximation; bottom, LBM theory. Ten scaled times τ are shown. From Carmesin et al. (1986).

pendence of the mobility. Comparing Fig. 6-19 with Fig. 6-8, characteristic differences are noted: even in the CHC approximation there is no longer a unique intersection point for $S(q, \tau) - S(q, 0)$ at different times τ ; apart from $\tau=0$, $\tilde{D}_{\text{eff}}(q, \tau)$ in the “Cahn plot” exhibits pronounced curvature, although it depends relatively weakly on time. Note that in the LBM approximation we can no longer see any distinct shift of the maximum position of $\tilde{S}(q, \tau)$ for the times shown; this happens because first (at the intermediate temperature steps) smaller- q components become more amplified and later (at the final temperature) amplification occurs at larger values of q . This behavior just happens to offset the coarsening tendency. This example shows that care must be taken in drawing any conclusions about the validity of the CHC approximation from experimental data – the effects of fluctuations in the final state, the gradual onset of nonlinearities, and finite quench rate effects are interwoven in a complicated manner, and very accurate measurements and detailed knowledge of the system parameters are indispensable for disentangling all these effects.

These effects are much more dramatic if the mobility has a thermally activated behavior, $M(T) \sim \exp(-E_{\text{act}}/k_B T)$, with $E_{\text{act}} \gg k_B T_f$. As a second example, we consider a shallow continuous quench from $T_i = 1.01 T_c$ to $T_f = 0.99 T_c$ during $\tau = 0.001$, the temperature being lowered linearly with time (Fig. 6-20). Although this is as good an approximation for an instantaneous quench as is experimentally feasible, nevertheless, for the choice $E_{\text{act}}/k_B T_c = 900$, more relaxation takes place during the quench than in the remaining early time interval ($\tau \leq 1$). The qualitative behavior of the CHC and LBM approximations is identical – only the absolute scales of the structure factors differ significantly.

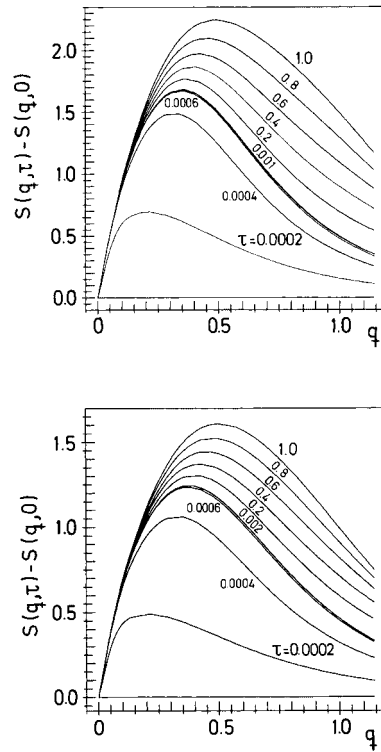


Figure 6-20. Structure function $S(q, \tau)$ vs. scaled wavevector q for scaled times τ as indicated in the figure, for a continuous quench (linear cooling from $T_i = 1.01 T_c$ to $T_f = 0.99 T_c$ during $\tau = 0.001$), using $E_{\text{act}}/k_B T = 900$. Top: CHC approximation; bottom: LBM approximation. From Carmesin et al. (1986).

6.2.8 Interconnected Precipitated Structure Versus Isolated Droplets, and the Percolation Transition

Whereas so far the description of the structures formed by phase separation has focussed on the behavior of the equal-time structure factor $S(k, t)$ at time t after the quench, we now concentrate on the description of these structures in real space. In Fig. 6-2 it was illustrated that during late or intermediate stages two different patterns of behavior are present, depending on the volume fraction Φ of the minority phase. For small Φ , the minority phase is confined to independent clusters well sep-

arated from each other; for larger Φ , we have a percolating interconnected network (in viewing Fig. 6-2 we expect an isotropic system, such as a fluid or glassy mixture; in crystalline solids the shape of the precipitates reflects the anisotropy of the interfacial free energy between the coexisting phases, and elastic interactions may even lead to a regular rather than a random arrangement of these precipitates).

This difference in morphology of the growing structures often – *and erroneously* – is associated with the distinction between nucleation and growth versus spinodal decomposition; it is then claimed that the percolation of the growing structure is the hallmark of spinodal decomposition, while it is assumed that well separated domains must have been formed by nucleation and growth. We maintain, however, that the distinction between nucleation and spinodal decomposition, meaningful only for the earliest stages of phase separation, *must not* be confused with this distinction in morphology of the precipitated structures, which is relevant for intermediate and late stages: even if well separated domains occur, they may result from a spinodal decomposition mechanism, and even if a state decays by nucleation, it may correspond to an interconnected percolating microscopic structure of B atoms in the A-rich matrix. Hence, the transition regime between nucleation and spinodal decomposition and the line of percolation transitions separating the regime of finite B clusters (Fig. 6-11 a) from the regime where a percolating cluster occurs which reaches from one boundary of the system to the opposite one must in fact cross each other (Fig. 6-21). Fig. 6-21 shows both the molecular-field result for the spinodal and the actual regime of gradual transition between nucleation and nonlinear spinodal decomposition of a short-range system, defined approxi-

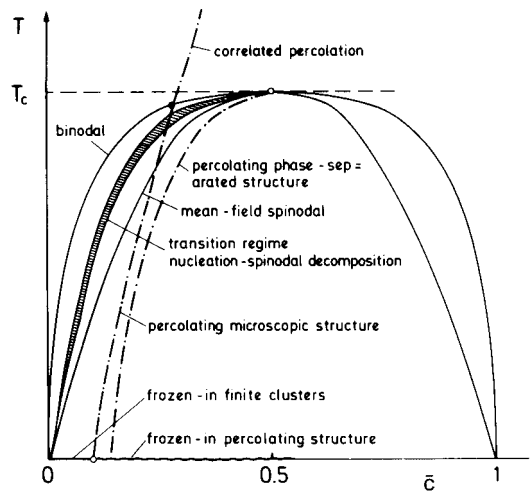


Figure 6-21. Schematic phase diagram (temperature vs. concentration \bar{c}) of a three-dimensional, short-range Ising lattice model of a binary mixture. Since the diagram is symmetric along the line $\bar{c} - c_{\text{crit}} = 0.5$, if the meaning of A and B is exchanged, full information is given only for the regime $\bar{c} \leq 0.5$. Both the coexistence curve (“binodal”) separating the single-phase region from the two-phase region and the mean-field spinodal curve separating metastable from unstable states in mean-field theory are shown. The mean-field spinodal is described here by the equation $(c_{\text{crit}} - c)/c_{\text{crit}} = \pm(1 - T/T_c)^{1/2}$, T_c being the actual critical temperature. The transition regime from nucleation to spinodal decomposition for a short-range system, as discussed in the text, is also indicated. The dash-dotted curves indicate percolation transitions, as discussed in the text. From Hayward et al. (1987).

mately by the region from $\Delta F_{\text{MF}}^* = 10 k_B T$ to $\Delta F_{\text{MF}}^* = k_B T$, where ΔF_{MF}^* is the mean-field result for the nucleation barrier (this shift of the transition region from the molecular-field result towards the binodal was disregarded in Fig. 6-13). Two different percolation transition lines are drawn, which depend on the *resolution* with which the system is observed. Suppose the resolution is very fine, such that individual atoms can be distinguished (this is the situation envisaged in Fig. 6-11 a). Then in the single-phase region we encounter a percola-

tion transition of a correlated percolation problem at $c_p^{(\text{corr})}(T)$. This line starts out for $T \rightarrow \infty$ at the percolation concentration for random percolation ($c_p^{(\text{random})} \approx 0.312$ for the simple cubic lattice (Stauffer, 1985)) and bends over to the left, until it hits the coexistence curve at the point $T/T_c \approx 0.96$, $\bar{c} \approx 0.22$ (Müller-Krumbhaar, 1974). This line continues in the two-phase region as a transient time-dependent phenomenon, $c_p^{(\text{corr})}(T, t)$ (see Fig. 6-22). Hayward et al. (1987) and Lironis et al. (1989) have shown that for certain concentrations the configuration is percolating for a time interval $t_1 < t < t_2$, whereas it does not percolate for $0 \leq t_1$ and for $t \geq t_2$. If the concentration decreases, a critical concentra-

tion is reached where $t_1 = t_2$ (for still lower concentrations there is no percolation at all), whereas for increasing concentration another critical concentration is reached where $t_2 \rightarrow \infty$. For still higher concentrations the system percolates as the time exceeds t_1 and then remains percolating throughout.

A different behavior occurs if a system with a much coarser resolution is studied; at late stages, where the system is phase-separated on a length scale $k_m^{-1}(t)$ into the coexisting phases with concentrations given by the two branches of the coexistence curve, $c_{\text{coex}}^{(1)}$ and $c_{\text{coex}}^{(2)}$, respectively. It now makes sense to consider percolation phenomena on much larger length scales than the lattice spacing a . Suppose we divide our system again into cells of linear dimension L (Eq. (6-1)), with $a \ll L \ll k_m^{-1}(t)$. Most of these cells will then have concentrations close to either $c_{\text{coex}}^{(1)}$ or $c_{\text{coex}}^{(2)}$. We may now define clusters consisting of neighboring cells with concentrations in a given interval $[c_{\text{coex}}^{(2)} - \delta c/2, c_{\text{coex}}^{(2)} + \delta c/2]$ and we may ask whether these clusters are well separated from each other or if they form an infinite percolating network. Since $l(t \rightarrow \infty) \rightarrow \infty$ we may also take $L \rightarrow \infty$ in this limit and therefore $\delta c \rightarrow 0$. Hence there is no longer any ambiguity in this coarse-grained percolation problem. We expect that this “macroscopic percolation” will occur at a critical volume fraction ϕ_p of the minority phase, which does not depend on temperature. Therefore, the line of macroscopic percolation concentrations is simply

$$c_p^{(\text{macro})} = c_{\text{coex}}^{(1)} + (c_{\text{coex}}^{(2)} - c_{\text{coex}}^{(1)}) \phi_p$$

and hence must end in the critical point. This line is also shown schematically in Fig. 6-21. Note that this line will be observed experimentally by techniques which are sensitive to the “contrast” (i.e., difference in refractive index) between the two

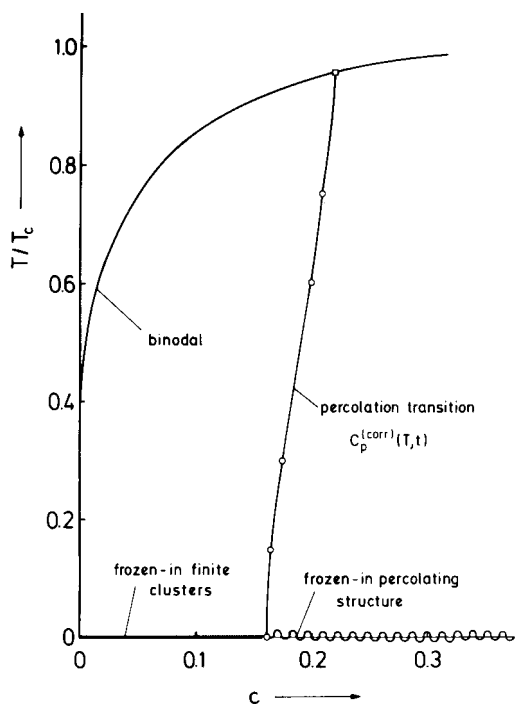


Figure 6-22. Part of the phase diagram of the simple cubic, nearest-neighbor lattice-gas model, showing the percolation transition line $c_p^{(\text{corr})}(T, t)$, where the time t refers to an average over the time interval from $t=80$ to $t=240$ MCS per site during phase separation. From Hayward et al. (1987).

coexisting phases, such as observations with light or electron microscopes.

This phenomenon of “gelation of clusters” at $c_p^{(\text{corr})}(T, t)$ into an infinite percolating net has a pronounced effect on the cluster size distribution $\bar{n}_l(t)$, of course, which was used in the “cluster dynamics” modeling of Eq. (6-54). This is shown in Fig. 6-23 where $\bar{n}_l(t)$ is plotted against l for $\bar{c}=0.156$ in a quench to $T=0$, where the system develops towards a frozen-in cluster size distribution. The curvature of $\bar{n}_l(0)$ on the log-log plot reflects the exponential variation, $\ln \bar{n}_l(0) \sim l$, while the straight-line behavior occurring at later times is characteristic of the power law of percolation, $\bar{n}_l(t) \sim l^{-\tau}$. This percolation problem is usually disregarded in treatments based on Eq. (6-54) or related models (Langer and Schwartz, 1980). Certainly this behavior also makes theories of coarsening, where the growing droplets are modeled as essentially spherical, doubtful at volume fractions Φ close to Φ_p ; note that from Fig. 6-22 and the fact that the critical vol-

ume fraction for continuum percolation is about 0.16 (Scher and Zallen, 1970), we expect all these theories only to be reliable for $\Phi \ll 0.16$. This percolative behavior $\bar{n}_l(t) \sim l^{-\tau}$ is in conflict with the scaling behavior that is described in the next section, namely (Binder, 1977, 1989), $\bar{n}_l(t) = l^{-1} \tilde{n}(lt^{-d/3})$, where $\tilde{n}(z)$ is a scaling function. The extent to which this percolation transition affects $S(k, t)$ is unclear.

6.2.9 Coarsening and Late Stage Scaling

From Figs. 6-5 and 6-12 it is evident that the peak position $k_m(t)$ of the structure factor $S(k, t)$ decreases with increasing time after the quench. This decrease already reflects the onset of a coarsening behavior of the domains of A-rich and B-rich phases that have formed (Fig. 6-2). For large enough times, the domains have grown to a size much larger than all “microscopic” lengths (such as the interfacial width). Then a simple power law should hold,

$$k_m(t) \sim t^{-x}, \quad t \rightarrow \infty \quad (6-66)$$

and the structure factor should satisfy a scaling hypothesis (Binder and Stauffer, 1974, 1976b; Binder et al., 1978; Furukawa, 1978; Marro et al., 1979)

$$S(k, t) - k_B T / [(\partial^2 f / \partial c^2)_{T, c_{\text{coex}}^{(1,2)}} + r^2 T k^2] \sim [k_m(t)]^{-d} \tilde{S}\{k/k_m(t)\} \quad (6-67)$$

The term subtracted on the left-hand side of Eq. (6-67) represents the scattering from concentration fluctuations within the domains, and $\tilde{S}(\zeta)$ is a scaling function which will be discussed later.

Understanding the growth law, Eq. (6-66), and predicting the associated scaling function $\tilde{S}(\zeta)$ has been a longstanding problem that is still not completely solved (see Bray, 1994, for a recent review). It is now thought that for solid mixtures, both in $d=2$ and in $d=3$ dimensions, but in the ab-

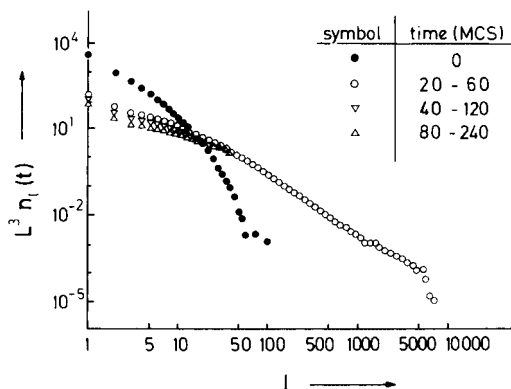


Figure 6-23. Cluster size distribution for a system of L^3 lattice site with $L=40$. Full symbols give the cluster size distribution $\bar{n}_l(0)$ corresponding to the random percolation problem at $\bar{c}=0.156$ at the simple cubic lattice, and open symbols denote the cluster size distribution averaged over the time intervals shown. From Hayward et al. (1987).

sence of any elastic interactions (see Sec. 6.2.10), a result originally derived by Lifshitz and Slyozov (1961) and Wagner (1961) holds

$$x = 1/3 \quad (6-68)$$

This LSW theory is essentially a mean-field theory valid in the limit of zero volume fraction Φ of the new phase [$\Phi \equiv (\bar{c} - c_{\text{coex}}^{(1)}) / (c_{\text{coex}}^{(2)} - c_{\text{coex}}^{(1)})$] and considers the cluster size distribution $\bar{n}_l(t)$ that was discussed in Sec. 6.2.5, showing that for $\Phi=0$ there exists a solution $n_l(t) = l^{-1} \bar{n}(lt^{-d/3})$, which implies that the mean cluster “size” (i.e., volume) $\bar{l}(t)$ scales as $\bar{l}(t) \sim t^{d/3}$ for $t \rightarrow \infty$ (for a more detailed outline of this theory, see Wagner et al., 2001). Thus the cluster linear dimension scales as $[\bar{l}(t)]^{1/d} \sim t^{1/3}$, and if we can extend this result to nonzero Φ we would expect $k_m(t) \sim [\bar{l}(t)]^{1/d}$ and hence Eq. (6-68) results. However, despite numerous attempts (e.g., Tokuyama and Enomoto, 1993; Akaiwa and Voorhees, 1994) even the extension of LSW theory to the case of small Φ is only approximately possible, and the accuracy of these extensions is open to doubt (Mazenko and Wickham, 1995). Different power laws for not so late stages have also been proposed (e.g., Binder, 1977, invoking a cluster diffusion and coagulation mechanism, and Tokuyama and Enomoto, 1993), and observed in computer simulations where atomic diffusion is mediated by a single vacancy moving through the lattice (Fratzl and Penrose, 1994, 1997). Only for deep quenches where we must take into account that the mobility M in Eq. (6-11) is itself concentration-dependent and (almost) vanishing in the pure phases, diffusion along interfaces results in a slower growth law, $x = 1/4$ (Puri et al., 1997).

“Cluster dynamics” approaches such as Eq. (6-54) (see Binder, 1977; Miold and

Binder, 1977; and Binder et al., 1978) and various extensions (e.g., Langer and Schwartz, 1980; Kampmann and Wagner, 1984; Wagner et al., 2001) incorporate the LSW growth law, nucleation and coagulation in a phenomenological way. But they do not take into account the statistical fluctuations and the correlations in the diffusion field around growing clusters.

Eq. (6-68) has now been confirmed by approaches based on scaling ideas (Furukawa, 1978, 1984, 1985a, 1988; Bray, 1998), renormalization group concepts (e.g., Lai et al., 1988; Bray, 1990, 1994), and theories considering fluctuating random interfaces (Mazenko, 1994; Mazenko and Wickham, 1995). However, the most convincing evidence that Eq. (6-68) is true both for critical and for off-critical quenches in $d=2$ and in $d=3$ comes from computer simulations (Amar et al., 1988; Gunton et al., 1988; Gawlinski et al., 1989; Huse, 1986; Rogers et al., 1988; Rogers and Desai, 1989; Chakrabarti et al., 1993).

We emphasize that Eq. (6-68) holds both in $d=2$ and in $d=3$ dimensions. The situation is different for fluid binary mixtures: the droplet diffusion–coagulation mechanism (also called “Brownian coalescence”) predicts (Binder and Stauffer, 1974)

$$k_m(t) \sim t^{-1/d} \quad (6-69)$$

while mechanisms invoking hydrodynamic flow of interconnected structures imply (Siggia, 1979)

$$k_m(t) \sim t^{-1}, \quad d = 3 \quad (6-70)$$

and $k_m(t) \sim t^{-1/2}$, $d=2$ (San Miguel et al., 1985), in the “viscous hydrodynamic regime” (Bray, 1994), while $k_m(t) \sim t^{-2/3}$ in the “inertial hydrodynamic regime” (Furukawa, 1985c).

A theoretical problem that is still outstanding is the calculation of the scaling function $\tilde{S}(\zeta)$ in Eq. (6-67) (see Bray

(1994), Puri et al. (1997) and Mazenko (1994, 1998) for recent discussions). We mention here only a few approaches very briefly. Rikvold and Gunton (1982) used Eq. (6-56), following Binder et al. (1978) but treating the depletion zones around growing clusters more realistically. Clearly, their model is only qualitative. More ambitious early attempts are due to Furukawa (1984, 1985a, b), Ohta (1984), Tomita (1984) and Tokuyama et al. (1987). An equation due to Furukawa (1984) has been extensively compared with experimental data on Al–Zn alloys (Komura et al., 1985)

$$\tilde{S}(\xi) \sim \xi^2/(\tilde{\gamma}^2/2 + \xi^{2+\tilde{\gamma}}) \quad (6-71)$$

where $\tilde{\gamma} = d+1$ for strongly off-critical quenches (cluster regime) and $\tilde{\gamma} = 2d$ for critical quenches (percolative regime). $\tilde{S}(\xi)$ thus exhibits “Porod’s law” (see e.g., Glatter and Kratky (1982))

$$S(k, t) \sim k^{-(d+1)} \quad (6-72)$$

in the cluster regime only. Eq. (6-71) also fails to reproduce the exactly established (Yeung, 1988) behavior for small ξ , $\tilde{S}(\xi) \sim \xi^4$. For systems without hydrodynamics, good empirical forms for $\tilde{S}(\xi)$ describing the limiting behavior both for small ξ and for large ξ correctly and accounting both for simulation and experiment have been constructed by Fratzl et al. (1991), but the derivation of such functions from more fundamental theories is still not fully solved (Mazenko, 1994, 1998; Mazenko and Wickham, 1995; Bray, 1994). Fig. 6-27 shows a comparison of some theoretical predictions for the halfwidth of the scaling function \tilde{S} with corresponding experiments (Kostorz, 1991). It is intriguing to note that the behavior of $\tilde{S}(\xi)$ does not change much when the volume fraction ϕ changes from the “cluster regime” at smaller ϕ through a percolation transition to the interconnected regime at large ϕ . Re-

call that for fluid binary mixtures even the exponent x is different in these two regimes (Eqs. (6-69), (6-70)). For the percolative regime of fluid mixtures, Furukawa (1984) has proposed an approximate relation for q_m vs. τ

$$(q_m^{-1} - 1) [\sqrt{A^*/B^*} \arctan(\sqrt{B^*/A^*} q_m) - \arctan \sqrt{B^*/A^*}] = B^* \tau \quad (6-73)$$

where A^* and B^* are adjustable constants. Again a more precise treatment has to rely on numerical calculations (Koga and Kawasaki, 1991, 1993; Puri and Dünweg, 1992; Valls and Farrell, 1993; Shinozaki and Oono, 1993; Alexander et al., 1993; Bastea and Lebowitz, 1995).

6.2.10 Effects of Coherent Elastic Misfit

When phase separation occurs on a crystalline lattice it is often the case that the two phases differ slightly in their crystal structure or their lattice constants, thus introducing elastic strains in the crystal. The resulting elastic interaction is long-range and typically anisotropic and may considerably change the phase separation process, e.g., in metal alloys (for a recent review, see Fratzl et al., 1999; an extensive treatment of this problem is also given in Khachaturyan, 1983).

The coherent misfit strain tensor e_{ij}^0 is the strain required to transform the (undistorted) lattice of one phase into the (undistorted) lattice of the other. In metals, parts of this strain can be relaxed by misfit dislocations disrupting the continuity of the lattices between the two phases. This process will not be discussed here. In cases of non-zero misfit strain, $e_{ij}^0 \neq 0$, an influence on spinodal decomposition is expected if one of the following conditions is violated:

- (i) both phases have the same elastic stiffness tensor;

- (ii) the misfit strain is purely dilatational;
- (iii) the elastic stiffness tensor is isotropic;
- (iv) the crystal can be considered infinitely large;
- (v) the stress depends linearly on the strains.

If all five conditions are satisfied, then phase separation can proceed independently of the misfit strains (Bitter–Crum theorem, see, for example, Cahn and Larché (1984)). Otherwise, we can expect changes in the shape of the single-phase domains, e.g., from spherical to cuboidal or plate-like shapes but also in their spatial arrangement and coarsening kinetics. Typically the tendency towards shape changes increases when single-phase droplets become larger because the elastic energy (being proportional to the droplet volume) increases faster with the radius than the surface energy.

The introduction of elastic misfit effects into the theory of spinodal decomposition means substituting f_{cg} by $f_{cg} + w$ in Eq. (6-15). The function w is the elastic energy density stored in the lattice

$$w = \frac{1}{2} \sum_{ijmn} \lambda_{ijmn} \Delta e_{ij}(\mathbf{x}) \Delta e_{mn}(\mathbf{x}) \quad (6-74)$$

where λ_{ijmn} is the elasticity tensor or stiffness tensor (which may depend on the alloy composition).

$$\Delta e_{ij}(\mathbf{x}) = e_{ij}(\mathbf{x}) - e_{ij}^0(\mathbf{x}) \quad (6-75)$$

is the difference between the strain at position \mathbf{x} in the elastic equilibrium, $e_{ij}(\mathbf{x})$, and the misfit strain, $e_{ij}^0(\mathbf{x})$. Inserting this into the nonlinear Cahn–Hilliard equation (Eq. (6-14)), we obtain (Larché and Cahn, 1982; Onuki, 1989a–c)

$$\frac{\partial c}{\partial t} = M \nabla^2 \left\{ \frac{\partial f_{cg}}{\partial c} + \frac{\partial w}{\partial c} - r^2 k_B T \nabla^2 c \right\} \quad (6-76)$$

with

$$\begin{aligned} \frac{\partial w}{\partial c} = & \frac{1}{2} \sum_{ijmn} \frac{d\lambda_{ijmn}}{dc} \Delta e_{ij} \Delta e_{mn} \\ & - \sum_{ijmn} \lambda_{ijmn} \Delta e_{ij} \frac{de_{mn}^0}{dc} \end{aligned} \quad (6-77)$$

The first term arises from a dependence of the elastic constants on composition and the second one from the composition dependence of the misfit strain.

The main difficulty in the use of Eq. (6-77) is the determination of Δe_{ij} . Since the strains in the alloy can be assumed to relax much faster to their equilibrium values than the concentration profiles, Δe_{ij} will always be given by the elastic equilibrium condition

$$\sum_j \frac{\partial t_{ij}}{\partial x_j} = 0 \quad (6-78)$$

where the stress tensor is defined by Hooke's law

$$t_{ij} = \lambda_{ijmn} \Delta e_{mn} \quad (6-79)$$

As a consequence, the equilibrium strain at each point in the material is a (non-local) functional of the entire concentration profile $c(\mathbf{x}, t)$. In the special case when the elastic constants λ_{ijmn} are independent of composition, the elastic problem can be solved by Fourier transformation (Khachaturyan, 1966, 1983) to give

$$\begin{aligned} w = & \frac{1}{2} \iint V_{el}(\mathbf{x} - \mathbf{y}) (c(\mathbf{x}, t) - \bar{c}) \\ & \times (c(\mathbf{y}, t) - \bar{c}) d^3 x d^3 y \end{aligned} \quad (6-80)$$

or

$$\frac{\partial w}{\partial c}(\mathbf{x}, t) = \int V_{el}(\mathbf{x} - \mathbf{y}) (c(\mathbf{y}, t) - \bar{c}) d^3 y \quad (6-81)$$

which enters the equations (6-76). $V_{el}(\mathbf{u})$ is an elastic potential that depends on the stiffness constants λ_{ijmn} and the misfit strain e_{ij}^0 (Khachaturyan, 1983). The aver-

age concentration within the specimen is called \bar{c} .

In the case of isotropic elasticity and misfit strain, Eq. (6-81) reduces to (Onuki, 1989a–c)

$$\frac{\partial w}{\partial c} = \frac{2K}{1-\nu_p} \eta_a^2 [c(\mathbf{x}, t) - \bar{c}] \quad (6-82)$$

where η_a is the change of lattice constant with concentration c , that is

$$e_{ij}^0(c) = \eta_a (c - \bar{c}) \delta_{ij} \quad (6-83)$$

K and ν_p are Young's modulus and the Poisson coefficient of the elastic matrix, and $\delta_{ij}=0$ if $i \neq j$, $\delta_{ii}=1$ (Kronecker delta). Eq. (6-82) has been introduced by Cahn (1961). The consequence of this equation is a shift of the spinodal line towards lower temperatures because Eq. (6-44) has to be replaced by

$$\frac{\partial^2 f_{cg}}{\partial c^2} + \frac{\partial^2 w}{\partial c^2} = \frac{\partial^2 f_{cg}}{\partial c^2} + \frac{2K}{1-\nu_p} \eta_a^2 = 0$$

Hence, the coherent elastic misfit between the phases may stabilize the solid solution, even though the demixing into two *incoherently* separated phases would decrease the total energy (Cahn, 1961). The reason is that the coherency condition forces the alloy to store a considerable amount of elastic energy in the lattice, which could be released by creating an incoherent boundary between two regions both having the (undistorted) equilibrium lattice structure.

For anisotropic stiffness constants λ_{ijmn} or anisotropic misfit strains e_{ij}^0 , the chemical potential due to elastic interactions, $\partial w / \partial c$, will depend on the direction in the crystal. This has already been recognized by Cahn (1962) (see also Khachaturyan (1983) and Onuki (1989a–c)). Numerical solutions of Eq. (6-76) combined with Eq. (6-81) have shown the development of strongly anisotropic domains (Nishimori

and Onuki, 1990). A discretized version of similar equations was used by Khachaturyan and coworkers to study the behavior of single precipitates (Wang et al., 1991) or the evolution of precipitate morphologies (Wang et al., 1992, 1993). Moreover, Monte Carlo simulations of phase separation have also been performed, including elastic misfit interactions between unequally sized atoms on a lattice (Fratzl and Penrose, 1995, 1996; Laberge et al., 1995, 1997; Lee, 1997, 1998; Gupta et al., 2001). A further approach is the simulation of the coarsening of particles with sharp interfaces to the matrix, describing the elastic misfit interaction in the framework of macroscopic elasticity theory. Recent examples are the studies by Su and Voorhees (1996), Abinandanan and Johnson (1993, 1996) or Jou et al. (1997) (see also the review by Fratzl et al. (1999)). The common observations in all these approaches are that the domains become very anisotropic and typically orient parallel to crystallographic directions of the alloy crystal (Fig. 6-24d, e). Moreover, the spatial arrangement of the domains becomes progressively more periodic. Despite these enormous changes with respect to the case without elastic misfit interactions, the growth law of a typical domain size is often still described by the result of the LSW theory (Eq. (6-68)). If *external stress* is applied, an additional reorientation of the domains either parallel or perpendicular to the applied stress is observed (Laberge et al., 1995, 1997; Weinkamer et al., 2000). Many of these effects are observed in real alloys, most notably for the technically important nickel-based superalloys (Maheswari and Ardell, 1993; Conley et al., 1989; Sequeira et al., 1995; Paris et al., 1995, 1997; Fährmann et al., 1995).

If the elastic stiffness constants λ_{ijmn} depend on alloy composition (see the first term in Eq. (6-77)), this can result in anom-

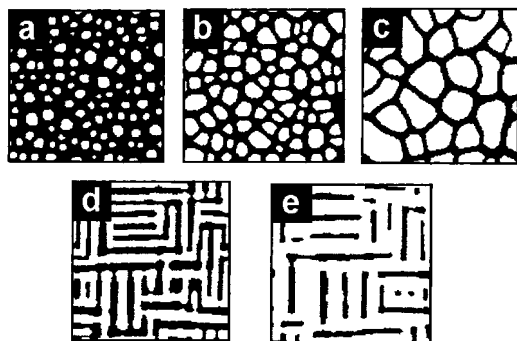


Figure 6-24. Typical snapshot pictures using the Cahn-Hilliard equation with elastic interactions (Eq. (6-77)). (a–c) is the case of isotropic elasticity but where the elastic stiffness depends on composition. The stiffer phase is shown white with volume fractions of 0.3, 0.5 and 0.7, respectively (from Onuki and Nishimori, 1991). Note that the softer phase always “wraps” stiffer particles. (d, e) is the case where the elastic stiffness has cubic anisotropy. The volume fraction of the white phase is 0.5 and 0.7, respectively (from Nishimori and Onuki, 1990).

alously slow precipitate growth. The most spectacular observation, however, is that (at sufficiently late times in the coarsening process) the softer phase always “wraps” precipitates of the harder phase (that is, the phase with the higher stiffness) and, therefore, stays percolated even if it is the minority phase (Onuki and Nishimori, 1991; Sagui et al., 1994; Leo et al., 1998; Orlikowski et al., 1999), see Fig. 6-24 a–c.

Most recently, the possibility of atomic ordering within the precipitates has also been included in the theory outlined in this section (Sagui et al., 1994; Wang and Khachatryan, 1995), as well as in Monte Carlo simulations on an elastic lattice (Nielaba et al., 1999). This amounts to studying decomposition close to a tricritical point, including the effects of elastic misfit interaction. With these features, the theoretical models are now capable of describing a surprising number of details in the evolution of alloy microstructures (e.g., Li and Chen, 1998). An example is shown in Fig. 6-25.

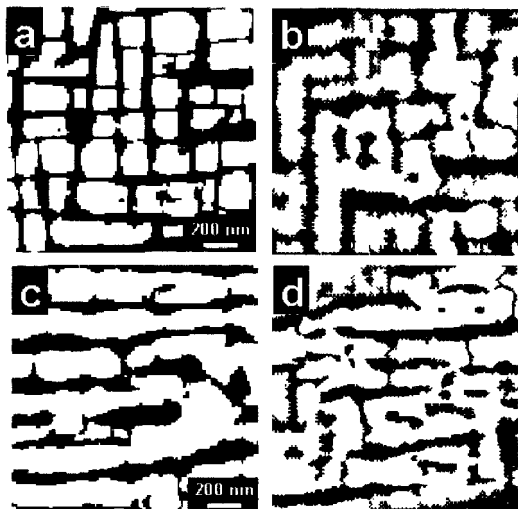


Figure 6-25. Transmission electron micrograph taken in the (001)-plane of a Ni–Al–Mo where the lattice spacing between matrix and precipitates (gamma-prime phase) is different by $\eta_a = -0.5\%$ (aged for 5 h at 1253 K). Cube-like precipitates can be seen, aligned along the elastically soft directions, [010] and [100]. (b) Results from computer simulations of an Ising model with elastic interactions on a simple square lattice and with repulsive interaction of like atoms on nearest-neighbor sites (with interaction energy J) and attractive interaction of like atoms on next-nearest-neighbor sites (energy $J/2$). The disordered phase (containing mostly A atoms) is shown in black and the ordered phase (consisting of about 50% A and 50% B atoms) is shown in white. The overall concentration of B atoms was 0.35 and the run was performed at a temperature of $T = 0.567 J/k_B$ on a 128×128 lattice and stopped after 10^6 Monte Carlo steps. (c) The same alloy and heat treatment as in (a), but now with an external compressive load of 130 MPa applied along the vertical [010]-direction. (d) The same model, temperature and annealing time as in (b), but with an additional external load along the vertical direction. Experimental data (a and c) are from Paris et al. (1997) and simulation data (b and d) from Nielaba et al. (1999).

6.3 Survey of Experimental Results

The number of experimental studies devoted to spinodal decomposition is enormous: first, it is a widespread phenomenon

that occurs in diverse systems; second, there has been much interest from a theoretical point of view in this phenomenon, and therefore many experimental studies have been carried out in an attempt to test some of the theoretical concepts.

This section cannot present a complete overview of all these experiments. More detailed reviews of various aspects of the experimental work can be found in Haasen et al. (1984), De Fontaine (1979), Gerold and Kostorz (1978), Gunton et al. (1983), Goldburg (1981, 1983), Beysens et al. (1988), Kostorz (1988, 1994), Hashimoto (1987, 1988, 1993), and Nose (1987), among others. Here we attempt only to give a few representative examples to illustrate some of the points discussed in the theoretical section, and at the same time show similarities – as well as differences – between different systems.

6.3.1 Metallic Alloys

Some systems in which spinodal decomposition has been very extensively studied are Al–Zn alloys (e.g., Hennion et al., 1982; Guyot and Simon, 1982, 1988; Simon et al., 1984; Osamura, 1988; Komura et al., 1985, 1988; Mainville et al., 1997), ternary Al–Zn–Mg alloys (Komura et al., 1988; Fratzl and Blaschko, 1988), Ni-based alloys such as Ni–Al, Ni–Ti, Ni–Cr, and Ni–Mo (Kostorz, 1988; see also Kampmann and Wagner, 1984), Al–Li alloys (Furusaka et al., 1985, 1986, 1988; Livet and Bloch, 1985; Tomokiyo et al., 1988; Che et al., 1997; Schmitz et al., 1994; Hono et al., 1992), Mn–Cu alloys (Gaulin et al., 1987), Ni–Si alloys (Chen et al., 1988; Cho and Ardell, 1997), Fe–Cr alloys (Katano and Iizumi, 1984), and various other ternary alloys, e.g., Cu–Ni–Fe (Lyon and Simon, 1987; Lopez et al., 1993) or Ni–Al–Mo (Fährmann et al., 1995;

Paris et al., 1995, 1997; Sequeira et al., 1995). In all these systems, the structure factor looks very similar to the early data on Au–Pt alloys (Singhal et al., 1978) and those of Al–Zn (Mainville et al., 1997) reproduced in Fig. 6-5. These results are in qualitative agreement with the nonlinear LBM theory and the computer simulations. The hallmarks of the linearized Cahn theory (exponential increase in intensity with time, time-independent intersection point of $S(k, t)$, maximum position k_m of $S(k, t)$ independent of time) are never found. In a few cases it has been found that at early times $k_m(t)$ is nearly independent of time, e.g., in Mn₆₇Cu₃₃ (Morii et al., 1988), and this fact has been taken as evidence for the validity of the Cahn–Hilliard–Cook (CHC) approximation. In view of the fact that $k_m(t)$ almost independent of t can also result as an effect of continuous rather than instantaneous quenching (Sec. 6.2.7) from a nonlinear theory, we feel that the question of whether the CHC theory applies to any of the metallic systems quantitatively is still unanswered. Certainly we expect that the CHC theory gives a useful order of magnitude estimate of $k_m(0)$ and the initial growth rate R_m , as it does for the theoretical models (Fig. 6-5d), provided a spinodal curve is not close. Experiments by Guyot and Simon (1982) and Hennion et al. (1982) were deliberately carried out choosing temperatures both above and below the spinodal curve of Al–Zn, for several concentrations. The structure factor in both cases is qualitatively the same, as was predicted (see Sec. 6.2.5). This classical set of experiments in our view definitely shows that the spinodal singularity does not play any role in the unmixing kinetics of Al–Zn alloys. Note that it is clear that the effective potential in this alloy is predominantly short range; however, this alloy does have a significant misfit of atomic radii between

Al and Zn, and thus the “coherent phase diagram” (where elastic strain fields are not released) is depressed by about 30 K below the thermodynamic (incoherent) miscibility gap, and the spinodal curves are then similarly shifted, providing an example of the effects of elastic interactions (Sec. 6.2.10). Despite these significant long-range elastic forces, the data for Al–Zn spinodal decomposition are surprisingly similar to the Monte Carlo results on simple nearest-neighbor Ising models of alloys, where all such elastic effects are not included. In other cases, such as many binary and ternary Ni alloys (see, for example, Fig. 6-25) elastic misfit interactions lead to highly anisotropic precipitate morphologies and to ordered arrangements of precipitates (see Sec. 6.2.10).

There is ample experimental evidence for the scaling of the structure factor at late stages (Eq. (6-67)), and the validity of the Lifshitz–Slyozov exponent $x=1/3$ (Eq. (6-68)). Sometimes smaller exponents are found, e.g., $k_m^{-1}(t) \sim t^x$ with $x \approx 0.13$ to $x \approx 0.2$ (see, for example, Furusaka et al., 1986; Osamura, 1988), but typically data extending over only 1.5 decades in time are available. A general problem is that some misfit between matrix and precipitates is present in many real alloys. Moreover, vacancy concentrations may be larger than the equilibrium value after the quench and then decrease gradually. Both effects could affect the exponent in real alloys. Katano and Iizumi (1984), Furusaka et al. (1988) and Forouhi and De Fontaine (1987) found a regime of 1.5 decades in time where $x=1/6$ whereas after a rather sharp crossover $x=1/3$ at later times. Other experiments (e.g., Morii et al., 1988) where the $k_m^{-1}(t)$ vs. t relationship is also measured over about three decades in time find a much smoother crossover from the initial stages, where the log–log plot of $k_m^{-1}(t)$ vs.

t is curved and a well-defined exponent x cannot be identified, to the final Lifshitz–Slyozov behavior, $x=1/3$. Katano and Iizumi (1984) interpret the result $x=1/6$ in terms of the mechanism (Binder and Stauffer, 1974) that B-rich clusters in a solid solution show a random diffusive motion since B atoms evaporate randomly from the cluster and re-impinge at another boundary position, thus leading to a small shift in the cluster center of gravity. The resulting cluster diffusivity decreases strongly with increasing cluster size. Assuming then that two clusters coalesce when they meet in their random motions, we arrive at $k_m(t) \sim t^{-1/(d+3)}$ in d dimensions. Although such a mechanism certainly exists, it is not clear whether it ever dominates during a well-defined time interval, since the Lifshitz–Slyozov–Wagner (1961) mechanism competes with it and should dominate, at least for long times. Monte Carlo simulations considering diffusion via vacancies indicate that cluster–diffusion–coagulation could be important at low temperatures (Fratzl and Penrose, 1997). This cluster–diffusion–coagulation mechanism was originally proposed to explain the corresponding small values of the exponent x seen in Monte Carlo simulations (Bortz et al., 1974; Marro et al., 1975). However, more accurate simulations (Huse, 1986; Amar et al., 1988) are rather consistent with a gradual approach to the asymptotic Lifshitz–Slyozov–Wagner (1961) law without an intermediate regime characterized by a well-defined different exponent x . In fact, the data can usually be fitted to an equation derived by Huse (1986):

$$k_m^{-1}(t) = A + B t^{1/3} \quad (6-84a)$$

while the original treatment of Lifshitz and Slyozov (1961) yielded

$$k_m^{-3}(t) = A' + B' t \quad (6-84b)$$

where A , B , A' , and B' are constants. Eq. (6-84a) can also be interpreted by an effective exponent in the growth law,

$$X_{\text{eff}}(t) \equiv d \{ \log k_m^{-1}(t) \} / d(\log t) \\ = \frac{1}{3} [1 - A k_m(t)]$$

Evidence for this law is found in various simulations (Amar et al., 1988; Gunton et al., 1988) and some experiments (Morii et al., 1988; Chen et al., 1988; Alkemper et al., 1999).

There have also been numerous attempts to characterize experimentally the scaling function $\tilde{S}(\beta)$ in Eq. (6-67). Typical data for Al-Zn alloys are shown in Fig. 6-26. Although the agreement with Eq. (6-71) looks impressive, the theory (Furukawa, 1984) neglects anisotropy, and so does the data analysis on polycrystalline samples of Komura et al. (1985). Single-crystal work (Simon et al., 1984), however, shows pronounced anisotropy. Anisotropy was also seen, for example, in scattering from Ni-based alloys as a result of the coherent elastic misfit (Kostorz, 1988; Fährmann et al., 1995; Sequeira et al., 1995). In early stages of phase separation, the anisotropy increases roughly linearly with the mean radius of precipitates, $R \propto l^{1/3}$ (Paris et al., 1995). The reason is that the elastic misfit energy (which favors anisotropy) is proportional to the volume of the precipitate, l , while the surface energy (which favors round shapes) depends on $l^{2/3}$.

The scaling function has been determined experimentally for a number of alloys and there is a general trend that the width of the scaling function decreases with increasing volume fraction of precipitate phase. A large collection of data is shown in Fig. 6-27, mostly taken from the review by Kostorz (1991). This decrease can be understood qualitative as follows: if L is a typical period in the spatial arrange-

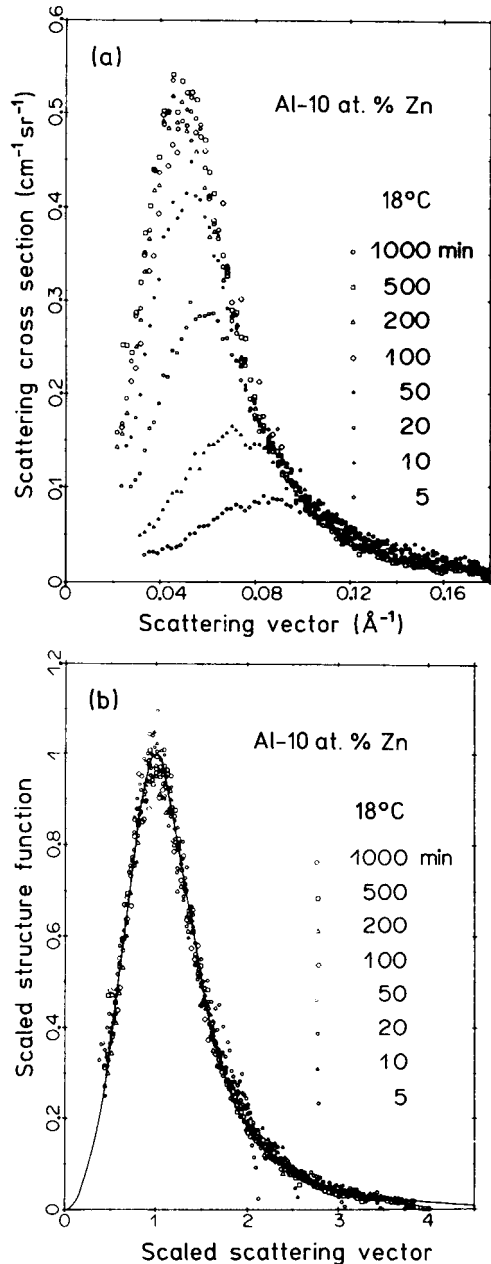


Figure 6-26. (a) Scattering cross-section measured for neutron small-angle scattering from Al-10 at. % Zn polycrystals at 18 °C (Komura et al., 1985). (b) Scaling plot of the data shown in (a). Full curve is a fit to Furukawa's (1984) function, Eq. (6-71). From Komura et al. (1985).

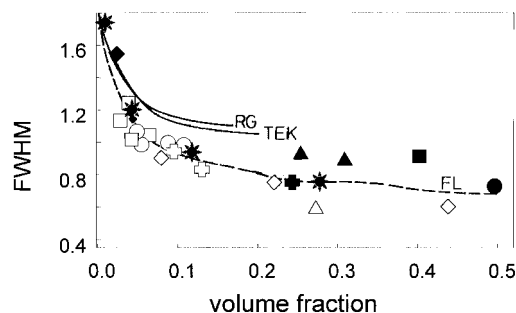


Figure 6-27. Full width at half maximum (FWHM) of the scaling function normalized such that the position of the maximum is located at 1. Black stars are for Al–Ag alloys (Langmayr et al., 1992), all other data points are taken from the review by Kostorz (1991) and correspond to Al–Zn, Pt–Au, Cu–Mn, Fe–Cr and Al–Li. Full and broken lines indicate predictions from various models (RG: Rikvold and Gunton (1982), TEK: Tokuyama et al., (1987), FL: Fratzl and Lebowitz (1989)).

ment of the precipitates, the maximum position of the structure function varies as L^{-1} . For spherical precipitates of radius R , the width of the structure function varies roughly as R^{-1} . Hence, the width of the scaling function behaves approximately as $R/L \propto \Phi^{-1/3}$ for small volume fractions Φ . A similar argument may also be developed for larger volume fractions, where the microstructure corresponds to percolated domains instead of isolated droplets (Fratzl, 1991), leading to the prediction shown in Fig. 6-27 (broken line).

6.3.2 Glasses, Ceramics, and Other Solid Materials

Early experimental data on glassy systems such as the $\text{Na}_2\text{O}-\text{SiO}_2$ system have been reviewed by Jantzen and Herman (1978). Some data have been interpreted in the framework of the linearized theory of spinodal decomposition (e.g., Yokota, 1978; Acuna and Craievich, 1979; Craievich and Olivieri, 1981), but not all

features of the linear theory can be demonstrated quantitatively in these materials, and thus no real evidence for the significance of a spinodal curve is present. While the isotropy of these systems is clearly a simplifying feature, coupling to structural relaxation sometimes needs to be considered (Yokota, 1978), which implies a significant complication (Binder et al., 1986).

An investigation of late stages was carried out by Craievich and Sanchez (1981) for the $\text{B}_2\text{O}_3-\text{PbO}(\text{A}_2\text{O}_3)$ glass at $T = 0.65 T_c$ where the critical point of unmixing is $T_c \approx 657^\circ\text{C}$. The structure factor $\tilde{S}(k, t)$ was obtained in a time range of about 12 to 400 min, and Eq. (6-66) was found to be obeyed with $k_m^{-1}(t) \sim t^x$, $x \approx 0.23$. The early stages were studied by Stephenson et al. (1991) and were found to qualitatively agree with the Cahn–Hilliard–Cook theory (Eq. 6-27). Qualitatively, the behavior is very similar to the results for metallic alloys (Sec. 6.3.1) and to computer simulations.

At this point, we also mention the application of spinodal decomposition of borosilicate glass-forming melts to produce porous Vycor glass; on cooling the melt below its demixing temperature it decomposes into an SiO_2 -rich phase and a B_2O_3 -alkali-oxide-rich phase. The latter is acid soluble and can be leached out with suitable solvents leaving a fully penetrable microporous glass. The small-angle scattering from such materials has been examined and interpreted in the framework of the theory of spinodal decomposition (Wiltzius et al., 1987).

Qualitative observations of phase separation on a local scale attributed to spinodal decomposition have been reported for a variety of glassy materials and ceramics. Examples include rapidly quenched $\text{Al}_2\text{O}_3-\text{SiO}_2-\text{ZrO}_8$ (McPherson, 1987), La–Ni–Al amorphous alloys (Okamura et al., 1993),

and SiC–AlN ceramics (Kuo et al., 1987). The crystallization behavior of bulk metallic glasses, such as Zr–Ti–Cu–Ni–Be, has been found to be strongly influenced by decomposition (e.g., Wang et al., 1998b).

Of course, spinodal decomposition is also expected to occur in various nonmetallic mixed crystals, e.g., oxides such as the TiO_2 – SnO_2 system (Flevaris, 1987; Takahashi et al., 1988) and semiconducting GaInAsP epitaxial layers (Cherns et al., 1988; Mcdevitt et al., 1992). Often these situations are difficult because of lower crystal symmetry (the SnO_2 – TiO_2 system is tetragonal) and strong elastic lattice misfit effects (Flevaris, 1987).

6.3.3 Fluid Mixtures

Binary fluids containing small molecules such as lutidine–water (Goldburg et al., 1978; Goldburg, 1981, 1983; Chou and Goldburg, 1979, 1981) and isobutyric acid–water (Wong and Knobler, 1978, 1979, 1981; Chou and Goldburg, 1979, 1981) are classic systems where nonlinear spinodal decomposition was observed via light scattering techniques. Since the inter-

diffusion in fluid mixtures proceeds much faster than in solids, we must consider quenches in a narrow region just below T_c , in order to take advantage of critical slowing down. This implies that we must always work in the non-mean-field critical region (in the phase diagram in Fig. 6-13), i.e., nonlinear effects are very strong, and so it is not expected that the linearized theory of spinodal decomposition will account for these systems. In addition, very early stages are not observable because the unmixing proceeds too fast. This is best seen when working with rescaled variables (Chou and Goldburg, 1979, 1981), defining

$$q_m(\tau) \equiv k_m \xi(t=0)$$

and

$$\tau = t D(t=0) / \xi^2(t=0)$$

where $\xi(t=0)$ and $D(t=0)$ are the correlation length and the interdiffusion constant in the initial state, respectively. Early times then mean a τ of the order of unity. Fig. 6-28 shows that only scaled times $\tau \geq 6$ are accessible, whereas earlier times are accessible for fluid polymer mixtures (see Sec. 6.3.4). The growth rate exponent x

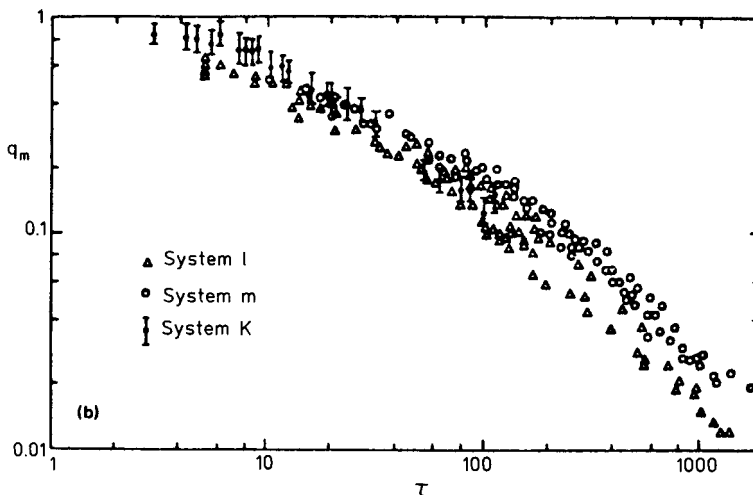


Figure 6-28. Log–log plot of q_m vs. τ found in the polymer mixture polystyrene (PS)–poly(vinyl methyl ether) (PVME) (data labelled system K), compared with isobutyric acid–water (l) and 2,6-lutidine–water mixtures (m). Systems (K, m) are data from Chou and Goldburg (1979). From Snyder and Meakin (1983).

$(q_m^{-1}(\tau) \sim \tau^x)$ crosses over from x near $x \approx 1/3$ for $\tau = 10$ to $x \approx 1$ at very late times, as expected (Siggia, 1979) (see Eq. (6-70)). The behavior $q_m^{-1}(\tau) \sim \tau^{-1/3}$, which for off-critical quenches where the structure corresponds to well separated clusters is believed to be the true asymptotic behavior for $\tau \rightarrow \infty$ (Siggia, 1979), is attributed to a cluster diffusion and coagulation mechanism (Binder and Stauffer, 1974; Siggia, 1979). Note that for fluid droplets the diffusion constants decrease in proportion to their radii with increasing droplet size, due to Stokes' law, and hence the cluster diffusion-coagulation mechanism never becomes negligible in comparison with the Lifshitz-Slyozov (1961) evaporation-condensation mechanism.

Fig. 6-28 shows, however, that the crossover to the asymptotic power law is gradual. This smooth behavior is approximately described by the nonlinear theory of spinodal decomposition of Kawasaki and Ohta (1978). However, this theory can give only a poor account of the full structure function. This is not surprising, since it is only expected to be accurate for $\tau \leq 10$ (see Sec. 6.2.6). Again, the problem of calculating the scaled structure function $\tilde{S}(\beta)$ (Eq. (6-67)) arises and is as difficult as in the case of solids (Furukawa, 1985a).

A problem for binary fluids is the effect of gravity. Since the two coexisting phases usually differ in density, one phase must go to the top and the other to the bottom of the container. This effect (for a more detailed discussion see Beysens et al., (1988)) implies a smearing of the critical region for the unmixing critical point of a sample of finite height, and also affects the late stages of phase separation (where even hydrodynamic instabilities may set in; see Chan and Goldburg (1987)). The effect of gravity, however, can be strongly reduced if isodensity systems are used (using mixtures of

methanol and partially deuterated cyclohexane, a perfect density matching at T_c is possible; see Houessou et al., (1985)) or space experiments are performed, where the gravitational effect can be reduced by a factor of 10^4 . Beysens et al. (1988) showed that such experiments agree with the results obtained from isodensity systems. By such means not only can the accuracy of data of the sort shown in Fig. 6-28 be substantially improved, but several decades can be added to a plot of q_m vs. τ (Fig. 6-29). The full curve in this plot is the function (Eq. (6-73)) proposed by Furukawa (1984), which reduces to Eq. (6-70) for large τ , i.e., the result of Siggia (1979). More recently, a growth of the mean droplet size with the power-law exponent $1/3$ could be followed over more than seven decades in a microgravity experiment (Perrot et al., 1994).

Interesting extensions involve spinodal decomposition in fluid mixtures under weak steady-state shear (Chan et al., 1988; Krall et al., 1992; Lauger et al., 1995; Hashimoto et al., 1995; Hobbie et al., 1996) or periodically applied shear (Beysens and Perrot, 1984; Joshua et al., 1985), as well as in strongly stirred mixtures where a turbulent suppression of spinodal decomposition occurs (Pine et al., 1984; Chan et al., 1987; Easwar, 1992). Many of these observations can be explained on the basis of the theoretical considerations of Onuki (1984, 1986a, 1989c).

Finally, we draw attention to phase separation phenomena in more exotic fluids such as surfactant micellar solutions (Wilcoxon et al., 1988, 1995), polymer solutions near their Θ -point, e.g., polystyrene in methyl acetate (Chu, 1988), gel-gel transitions (such a transition occurs, for example, in N-isopropylacrylamide gel with water as a solvent, where this system phase separates into two states with different sol-

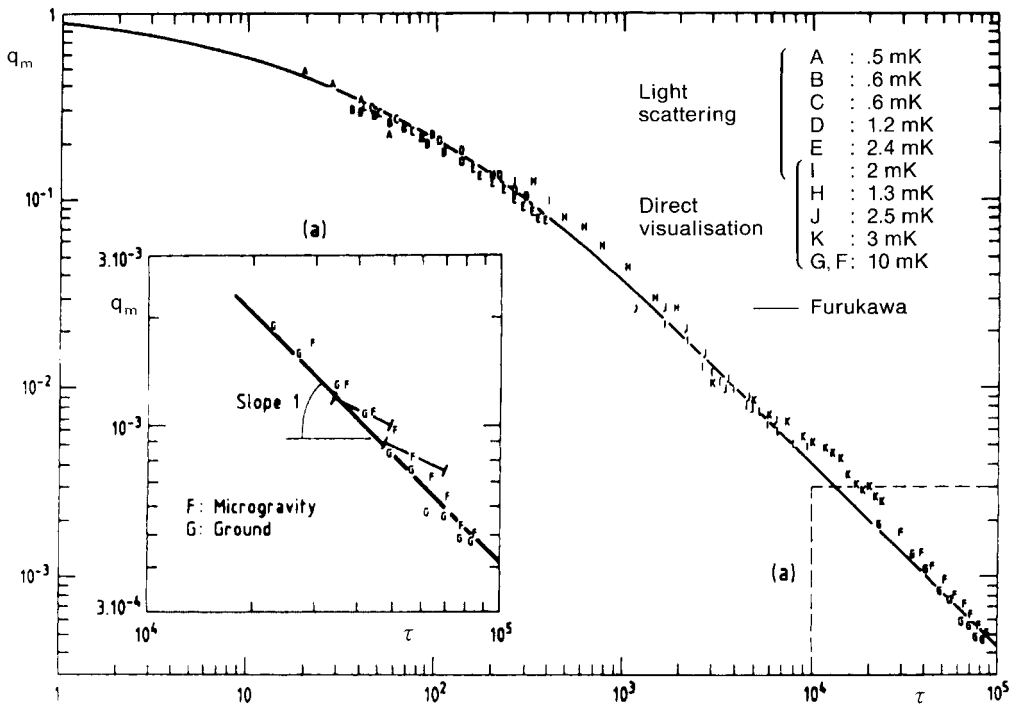


Figure 6-29. Behavior of the scaled wavevector $q_m(\tau)$ versus scaled time τ . Full curve is from Furukawa (1985), data points refer to mixtures of methanol and cyclohexane in space-flight experiments (F) or to isodensity mixtures of methanol and partially deuterated cyclohexane for various quench depths, as indicated. The late-time behavior, where $q_m(\tau) \sim \tau^{-1}$ is observed, is magnified in the inset. From Beysens et al. (1988).

vent concentrations and hence a different swelling ratio of the gel; see Hirotsu and Kaneki (1988)), and lipid membranes with dissolved protein.

6.3.4 Polymer Mixtures

As pointed out in Secs. 6.2.4 and 6.2.5, mixtures of long flexible macromolecules are particularly well suited model systems for the study of phase separation kinetics: (i) owing to the mutual entanglement of the random polymer coils, their interdiffusion is very slow for high molecular weights, so the early stages can be studied; (ii) polymer mixtures exhibit a well-defined mean-field critical regime, where the linear theory of spinodal decomposition should hold, and a

spinodal curve can be defined; (iii) changing the molecular weights while other parameters (in particular, intermolecular forces!) remain constant allows a more stringent test of theories than for other systems. For example, it has been possible recently to obtain by laser scanning confocal microscopy (Jinnai et al., 1997) three-dimensional images of phase-separated polymer blends that look very similar to pictures obtained from theory (Fig. 6.30).

Therefore, it is gratifying that quantitative agreement with the linear theory of spinodal decomposition was obtained in careful experiments with various polymer blends, e.g., polystyrene–poly(vinyl methyl ether) (Okada and Han, 1986; Han et al., 1988; Sato and Han, 1988), polybu-

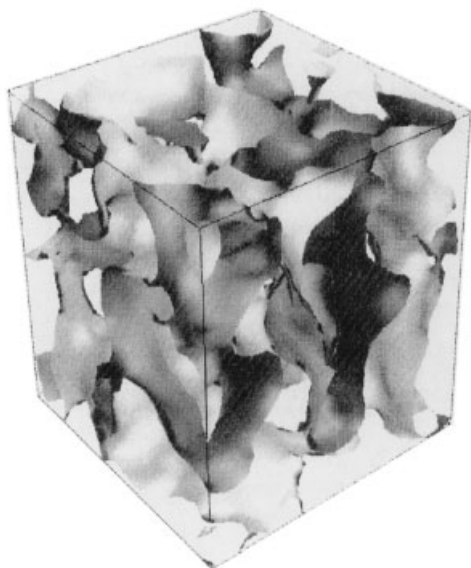


Figure 6-30. Three-dimensional representation of a bicontinuous phase-separated polymer blend. Investigation of the blend by laser scanning confocal microscopy gives results very similar to numerical solutions of the nonlinear theory of spinodal decomposition (Jinnai et al., 1997).

tadiene and styrene–butadiene random copolymer mixtures (Hashimoto and Izumitani, 1985), and mixtures of deuterated and protonated polybuta-1,4-diene (Bates and Wiltzius, 1989), among others. As an example, Fig. 6-31 now provides an experimental counterpart to Figs. 6-15, 6-16, which were obtained from simulation. Note that here Eq. (6-23) is used, i.e., fluctuations in the final state are neglected – therefore the Cahn plot bends over for large wavevectors, and $R(q)/q^2$ never becomes negative, owing to the second term on the right-hand side of Eq. (6-29). Moreover, by carrying out quenches to different temperatures it is shown that both $q_m^2(0)$ and the effective diffusion constant D_0 vary linearly with $(1 - T/T_c)$, as expected from Sec. 6.2.5. The onset of nonlinear effects can be identified, but it is not accurately described by LBM-type theories (Sato and Han, 1988).

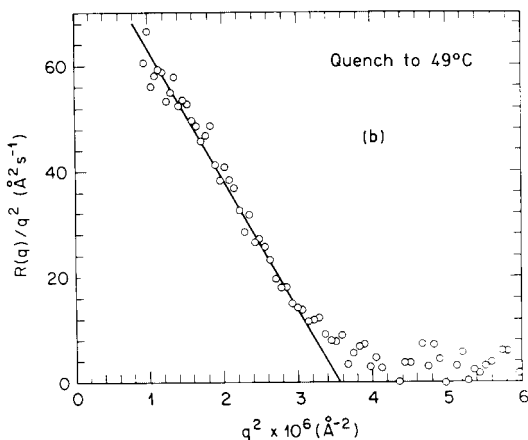
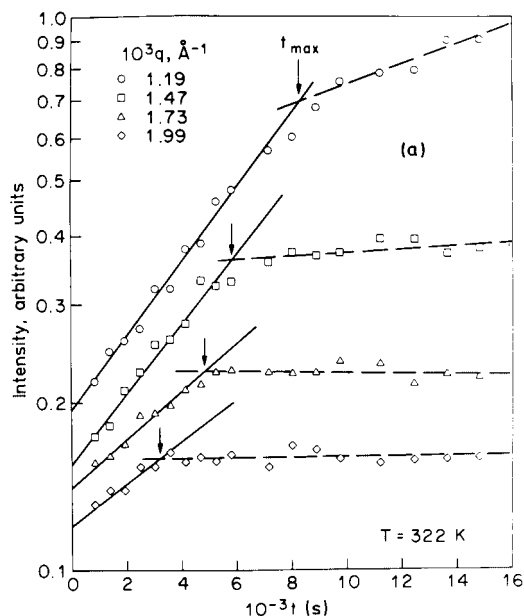


Figure 6-31. (a) Early stage growth of concentration fluctuations in a mixture of protonated and deuterated polybuta-1,4-diene, with polymerization index $N_H=3180$, $N_D=3550$, at critical volume fraction $\phi_D=0.486$ and $T=322$ K ($T_c=334.5$ K). Four representative scattering vectors are shown. From the straight-line fits to these semi-logarithmic plots the amplification factor $R(q)$ is extracted, which is shown as a Cahn plot in (b). From Bates and Wiltzius (1989).

At intermediate time a behavior $k_m^{-1}(t) \sim t^x$ is observed, where x varies with quench depth. This behavior is not understood theoretically. In this regime of times, nonlinear effects gradually become important. A transition stage then occurs, before the full scaling behavior of the structure factor is observed in the final stage. The scaling plot for $q_m(\tau)$ vs. τ is presented in Fig. 6-32, and the scaling function for the structure factor is shown in Fig. 6-33. It is seen that Furukawa's (1984) function gives a reasonable overall account of the data. The fact that the curves for cyclohexane methanol and for poly(vinyl methyl ether)–polystyrene (PVME–PS) mixtures are offset is not considered to be very serious, because there are some uncertainties involved in the rescaling of k and t in order to obtain the scaled variables q and τ ; only in terms of the scaled variables does it make sense to compare different materials with each other and to discuss whether a truly universal behavior exists.

A possible interpretation of the deviations from universality in the “intermediate” and “transition” stage in Fig. 6-32 is the fact that Bates and Wiltzius (1989) consider deep quenches, for which $1 - T/T_c$ is no longer very small. Only for $1 - T/T_c \ll 1$ can we expect a truly universal behavior. In any case, comparison of Fig. 6-29 and Fig. 6-32 with Fig. 6-28 clearly demonstrates the experimental progress made during less than a decade; the accuracy of the data in Fig. 6-32 is substantially better and the range of τ is nearly one decade larger.

Figure 6-33 shows the behavior of the scaling function at small and at large β for a polymer blend (a) and for a metal alloy (b). This behavior is of the form β^x with $x = -4$ at large β . At small β , x is close to 4 in both polymers and metal alloys. The decay at large β follows directly from Porod's law (Porod, 1951) which is a consequence of

sharp interfaces between the single-phase domains. The exponent $x = 4$ at small β has been proposed by Yeung (1988) from an analysis of the Cahn–Hilliard equation. Up to now, there is no theoretical expression for the scaling function that is capable of reproducing all the features in Fig. 6-33. The model of Fratzl and Lebowitz (1989) uses the correct exponents at low β and at large β and predicts a volume fraction de-

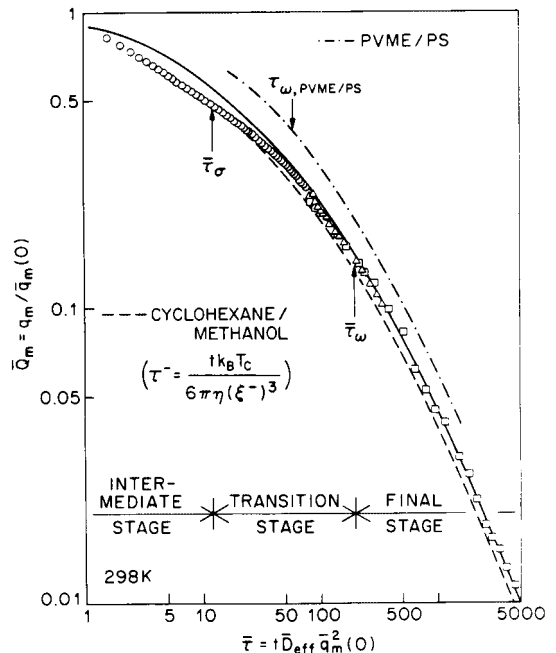


Figure 6-32. Log-log plot of $q_m(\bar{\tau})$ versus scaled time $\bar{\tau}$ for the polymer mixtures in Fig. 6-28 (different symbols represent different samples) at $T = 298$ K. Solid curve is a fit of Furukawa's (1984) function, Eq. (6-73), to the data in the “final stage region”. The poly(vinyl methyl ether)–polystyrene (PVME–PS) curve represents results of Hashimoto et al. (1986), and the curve for the cyclohexane–methanol small-molecule mixture is taken from data of Guenoun et al. (1987). The crossover time from the intermediate stage to the transition stage is denoted as $\bar{\tau}_\sigma$, from the transition stage to the final stage $\bar{\tau}_w$. Note that the scaled time $\bar{\tau}$ for the small-molecule mixtures is defined differently, since $\bar{D}_{\text{eff}} = D_0$ is not well defined. From Bates and Wiltzius (1989).

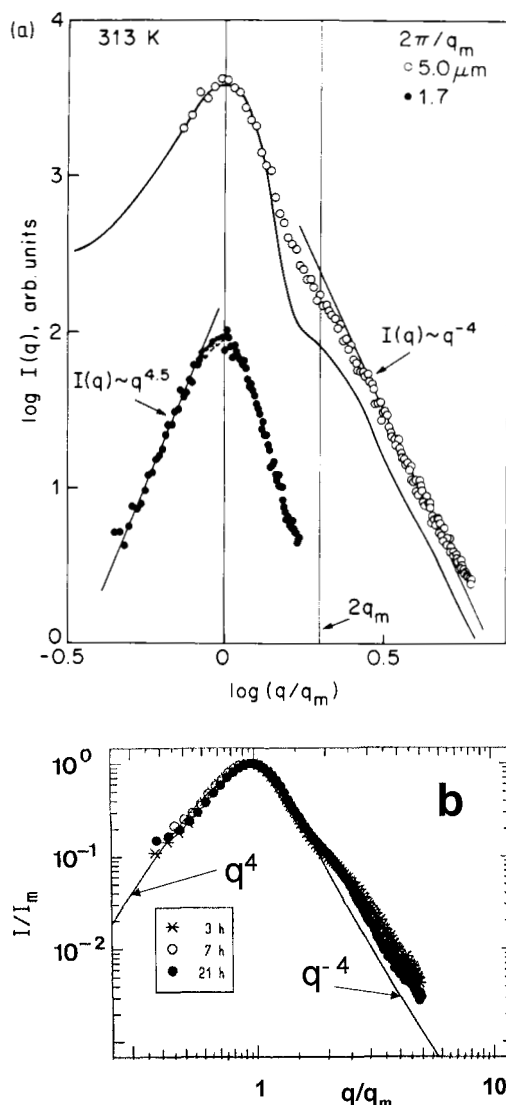


Figure 6-33. (a) Log-log plot for the structure-factor scaling function in the late stages of a quench to 313 K for the polymer mixture in Fig. 6-31. The solid curve is the theoretical prediction of Ohta and Nozaki (1989). The straight line $I(q) \sim q^{-4}$ demonstrates the validity of Porod's law. The inset shows low- q behavior, as measured in the intermediate stage, where a power law $I(q) \sim q^{4.5}$ is found. From Bates and Wiltzius (1989). (b) Similar plot for the scaling function in the metallic alloy Al-15 at.% Ag (Langmayr et al., 1992). The full line corresponds to the model function of Fratzl and Lebowitz (1989) for a volume fraction of $\Phi = 0.27$. This function $\bar{S}(\beta)$ increases with β^4 at small β and decreases with β^{-4} at large β (Porod's law).

pendence in reasonable agreement with experiments (Fig. 6-27), but it fails to reproduce the shoulder in the scaling function appearing on the right side of the maximum for polymers (Fig. 6-33a) and even some metal alloys (Fig. 6-33b). Earlier theories also fail to produce this shoulder, except for the approach by Ohta and Nozaki (1989), which predicts a function qualitatively similar to the data in Fig. 6-33a, but is still quantitatively off.

6.4 Extensions

Basic aspects of the theory of spinodal decomposition were treated in Sec. 6.2. Only the generic phase diagram (Figs. 6-3b, 6-13, and 6-21) of a binary mixture with a miscibility gap has been considered. In this section, we briefly mention the related phenomenon of ordering kinetics (Fig. 6-3a) and also discuss cases where formation of order and unmixing compete. The effects of certain complications (impurities, effects of finite size and free surfaces) are briefly assessed.

6.4.1 Systems Near a Tricritical Point

If a binary system exhibits a line of critical points $T_c(\bar{c})$ for an order-disorder transition, a tricritical point $T_t(\bar{c}_t)$ may occur where this critical line stops, and below this tricritical point both ordering and phase separations occur simultaneously (Griffiths, 1970; Lawrie and Sarbach, 1984). Two order parameters, $\psi(\mathbf{x})$ and $c(\mathbf{x})$, are simultaneously needed to describe such phenomena. Examples of this situation occur in some magnetic alloys where the order-disorder transition describes a magnetic ordering, $^3\text{He}-^4\text{He}$ mixtures (here ψ describes the superfluid order parameter and hence must be taken as a

complex variable), and also crystallographic order–disorder phase transitions in alloys and in adsorbed layers at surfaces are known to exhibit such tricritical points. In alloys, the first discussions of phase separation in tricritical systems come from Allen and Cahn (1976, 1979a, b) in the context of Fe–Al alloys. An elegant extension of the linearized theory of spinodal decomposition to tricritical ^3He – ^4He mixtures was given by Hohenberg and Nelson (1979). Nonlinear effects have mostly been studied for the model with simple relaxational dynamics of the order parameter (Dee et al., 1981; San Miguel et al., 1981). Here we briefly mention the case of ^3He – ^4He mixtures, since the most detailed experiments exist for these systems (Hoffer et al., 1980; Sinha and Hoffer, 1981; Benda et al. 1981, 1982; Alpern et al., 1982). ^3He – ^4He mixtures have no practical applications in materials science, but we mention them here as a model system for the study of phase separation near a tricritical point. The concepts developed (and checked experimentally) for this model system can be carried over to more complex materials such as ternary mixtures, magnetic alloys, etc. Instead of Eqs. (6-4) and (6-8), the expression for the free energy functional is now

$$\begin{aligned} \frac{\Delta\mathcal{F}}{k_B T} = \int d\mathbf{x} \left\{ \frac{1}{2} r_0 |\psi|^2 + \frac{1}{4} u |\psi|^4 \right. \\ + \frac{1}{6} v |\psi|^6 + \frac{1}{2} r^2 |\nabla\psi(\mathbf{x})|^2 \\ + \frac{1}{2} \chi_n^{-1} c^2 + \gamma c |\psi|^2 - (\mu_3 - \mu_4 + \Delta_0) c \\ \left. + \frac{1}{2} l_0^2 |\nabla c(\mathbf{x})|^2 \right\} \quad (6-85) \end{aligned}$$

where r_0 , u , v , χ_n^{-1} , l_0 , and γ are phenomenological coefficients that should depend only on temperature and not on the local ^3He concentration c , which is measured

from some reference value that fixes the constant Δ_0 , and μ_3 and μ_4 are the chemical potentials of ^3He and ^4He , respectively. For fixed c , T , and $\Delta = \mu_3 - \mu_4 + \Delta_0$ the static equilibrium follows from seeking the minimum of

(6-86)

$$F = \frac{1}{2} \tilde{r} |\psi|^2 + \frac{1}{4} \tilde{u} |\psi|^4 + \frac{1}{6} v |\psi|^6 + \frac{1}{2} \chi_n \Delta^2$$

where $\tilde{r} = r_0 + 2\gamma\chi_n$, $\tilde{u} = u - 2\chi_n\gamma^2$, and $c = \chi_n[\Delta - \gamma|\psi|^2]$ was eliminated from the equation. For $\tilde{u} > 0$ there is a second-order transition from normal fluid to superfluid at $\tilde{r} = 0$, whereas for $\tilde{u} < 0$ the transition is of first order. The critical point occurs for $\tilde{u} = 0$.

Whereas for the binary mixture a single Langevin equation for the concentration field $c(\mathbf{x}, t)$ and $\psi(\mathbf{x}, t)$ had to be derived (Eq. (6-15)), here we need two equations. In fact, the entropy density $S(\mathbf{x}, t)$ must also be added (Hohenberg and Nelson, 1979), and thus the calculation becomes complicated. However, since ψ is not a conserved quantity, it relaxes much more rapidly, hence the assumption is made that it always adjusts to the local equilibrium corresponding to the local concentration $c(\mathbf{x}, t)$. Instead of the simple exponential function in Eq. (6-23), additional oscillating terms due to the “second-sound” mode are found:

$$\begin{aligned} S(k, t) = a_1 e^{2R(k)t} + a_2 e^{[R(k) - D_2 k^2]t} \quad (6-87) \\ \times \cos(u_2 k t) + a_3 e^{-2D_2 k^2 t} \cos(2u_2 k t) + a_0 \end{aligned}$$

where a_0 , a_1 , a_2 , and a_3 are constants, u_2 is the second-sound velocity and D_2 its damping coefficient. In the spinodal region, $R(k)$ is positive, and not too close to the tricritical point for small k , $R(k) - D_2 k^2$ should also be positive. Therefore in addition to the first term on the right-hand side of Eq. (6-87), which is the analog of Eq. (6-23), there is another exponentially growing term oscillating in time. This would imply

a “flickering” component in the scattering. However, the linearized theory of spinodal decomposition is not expected to hold for ^3He – ^4He mixtures, since neither of the interaction ranges r and l_0 in Eq. (6-85) are expected to be large. Note, however, that the Ginzburg (1960) criterion for tricritical systems shows that mean-field theory is essentially correct for tricritical points; hence nonlinear effects do not become worse when $T \rightarrow T_i$, and unlike in Eqs. (6-51) and (6-52), we expect no factor depending on the temperature distance from T_i under the conditions of validity of the linear theory.

For tricritical systems, both experiments and simulations (Sahni and Gunton, 1980; Sahni et al., 1982; Ohta et al., 1988; Sagui et al., 1994; Wang et al., 1998a; Goretsveig et al., 1997; Nielaba et al., 1999) have shown a nonlinear behavior for all times accessible to study, and a scaling behavior of the structure factor as in Eq. (6-67) again applies to the late stages.

6.4.2 Spontaneous Growth of Ordered Domains out of Initially Disordered Configurations

There are many examples where the dynamics of a phase change involve the spontaneous formation of ordered structures. Suppose an alloy such as β -CuZn, which is a prototype realization of Ising-model type ordering (Als-Nielsen, 1976), is quenched from $T_0 > T_c$ to $T < T_c$ (Fig. 6-3a). Then again the initial homogeneously disordered state is thermodynamically unstable, and we expect that ordered domains will form. Since no sign of the order parameter is preferred, and there is no symmetry-breaking field, the average order parameter $\bar{\psi}$ in the system, $\bar{\psi} = (1/V) \int d\mathbf{x} \psi(\mathbf{x}, t)$, will remain $\bar{\psi} = 0$: domains with both signs of the order parameter form equally often. Again, the (unfavorable) domain wall energy acts as a

driving force leading to coarsening of the domain structure, similar to the coarsening discussed for spinodal decomposition (Sec. 6.2.9).

The description of the initial stages of this domain growth process closely parallels the treatment presented in Eqs. (6-4) to (6-26). Let us assume a free energy functional similar to Eq. (6-85), with phenomenological constants r_0 , u , v , and r :

$$\frac{\Delta \mathcal{F}}{k_B T} = \int d\mathbf{x} \left\{ \frac{1}{2} r_0 \psi^2 + \frac{1}{4} u \psi^4 + \frac{1}{6} v \psi^6 + \frac{1}{2} r^2 [\nabla \psi(\mathbf{x})]^2 \right\} \quad (6-88)$$

and we emphasize that the order parameter ψ is not a conserved quantity. Thus instead of Eqs. (6-10) and (6-11) we write:

$$\frac{\partial \psi(\mathbf{x}, t)}{\partial t} = -\Gamma \tilde{\mu}(\mathbf{x}, t) \quad (6-89)$$

$$\tilde{\mu}(\mathbf{x}, t) = \delta \Delta \mathcal{F}(\psi(\mathbf{x}, t)) / \delta \psi(\mathbf{x}, t)$$

describing a simple relaxational approach towards equilibrium, with Γ being an appropriate rate constant. Again, fluctuations must be added to this equation as in Eqs. (6-14) to (6-17), so that the final result is

$$\frac{\partial \psi(\mathbf{x}, t)}{\partial t} = \Gamma \left\{ \left[\frac{\partial f_{cg}[\psi(\mathbf{x}, t)]}{\partial \psi} \right]_T - r^2 k_B T \nabla^2 \psi(\mathbf{x}, t) \right\} + \eta_T(\mathbf{x}, t) \quad (6-90)$$

where the random force $\eta_T(\mathbf{x}, t)$ now satisfies the relationship

$$\begin{aligned} & \langle \eta_T(\mathbf{x}, t) \eta_T(\mathbf{x}', t') \rangle \\ &= \langle \eta_T^2 \rangle_T \delta(\mathbf{x} - \mathbf{x}') \delta(t - t') \\ & \langle \eta_T^2 \rangle_T = 2 k_B T \Gamma \end{aligned} \quad (6-91)$$

Again the first step of the analysis is a linearization approximation, similar to Eqs. (6-18) to (6-26). For the structure factor, which we now define as follows,

$$S(k, t) = \langle \delta \psi_{-k}(t) \delta \psi_k(t) \rangle$$

$$\delta \psi_k(t) \equiv \int d\mathbf{x} [\exp(i\mathbf{k} \cdot \mathbf{x})] \psi(\mathbf{x}, t) \quad (6-92)$$

the result is analogous to Eq. (6-23) (De Fontaine and Cook, 1971):

$$S(k, t) = S_{T_0}(k) \exp[2R(k)t] \quad (6-93)$$

with

$$R(k) \equiv -\Gamma \left[\left(\frac{\partial^2 f_{cg}}{\partial \psi^2} \right)_{T, \bar{\psi}=0} + r^2 k_B T k^2 \right] \quad (6-94)$$

Note that k in Eqs. (6-92) to (6-94) describes the distance in reciprocal space from the superstructure Bragg spot \mathbf{Q}_B corresponding to the considered ordering. Suppose now f_{cg} has the form assumed in Eq. (6-88), with $u > 0$, $v > 0$, and $r_0 = r'(T - T_0)$ changes sign at T_0 (this is the standard Landau description of a second-order transition; see Stanley (1971) or Binder (2000)). Then

$$(\partial^2 f_{cg} / \partial \psi^2)_{\bar{\psi}} = r_0 + 12u \bar{\psi}^2 + 30v \bar{\psi}^4$$

is equal to $r_0 < 0$ for $\bar{\psi} = 0$, i.e., the initial configuration is always unstable, and all modes $\psi_k(t)$ grow in the interval from $0 < k < k_c$, with k_c still being given by Eq. (6-25). However, Eq. (6-26) does not hold here and the maximum growth rate occurs for $k = 0$, as is obvious from Eq. (6-94).

In a case where $u < 0$, however, the phase transition does not occur for $T = T_0$ where r_0 changes sign, but rather at a higher temperature $T_c = T_0 + 3u^2/32r'v$ (Binder, 1987a). For $T_0 < T < T_c$ the state with $\bar{\psi} = 0$ is metastable, and the ordering reaction again needs a nucleation process (Chan, 1977; Fredrickson and Binder, 1989). The temperature T_0 hence again plays the role of a spinodal point ("ordering spinodal"; De Fontaine, 1979). Such spinodals for thermally driven first-order transitions have been calculated for diverse systems, from alloys such as Cu–Au systems (De

Fontaine and Kikuchi, 1978) to the meso-phase separation transition of block copolymers (Fredrickson and Binder, 1989). It is important to realize, however, that the "ordering spinodal" is also a mean-field concept, suffering from the same "ill-definedness" as the unmixing spinodal. Taking into account both statistical fluctuations and nonlinear effects, as they are both contained in Eqs. (6-90) and (6-91), we again expect to find a smooth transition between the nucleation of order and the "spinodal ordering" mechanism (Cook et al., 1969), as described by Eqs. (6-93) and (6-94). In addition, nonlinear effects will limit the predicted exponential growth, as they do in the case of spinodal decomposition.

This similarity of the behavior also carries over to the late stages of growth, where a scaling similar to Eq. (6-67) applies: but now $k_m(t)$ denotes the half-width of the peak (unlike spinodal decomposition, the maximum growth always occurs at the Bragg position \mathbf{Q}_B describing the order, i.e., $\mathbf{k} \equiv 0$). Since the order parameter ψ in Eq. (6-90) is not conserved, a faster growth law than Eq. (6-68) is predicted (Lifshitz, 1962; Allen and Cahn, 1979b; Ohta et al., 1982; Bray, 1994):

$$k_m^{-1}(t) \sim t^{1/2} \quad (6-95)$$

In a binary alloy undergoing an order–disorder transition, or in a layer adsorbed at a surface at constant coverage, the conservation of concentration (or density, respectively) may change the growth law (Eq. (6-95)): Sadiq and Binder (1984) suggested that the excess concentration (or excess density, respectively) contained in certain types of domain walls could again lead to a mechanism of the Lifshitz–Slyozov type, i.e., Eq. (6-68). The validity of this suggestion is not yet confirmed (Binder and Heermann, 1985; Binder et al., 1987). Figs. 6-34 and 6-35 give some examples of the

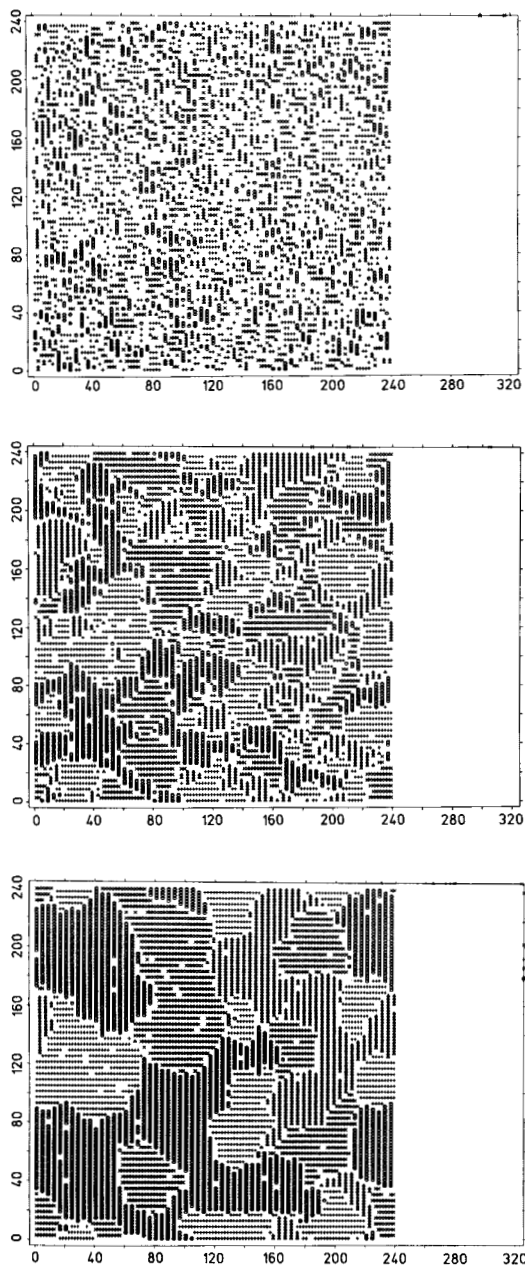


Figure 6-34. “Snapshot pictures” of the computer simulation of the ordering process of a 120×120 square lattice model of an alloy with repulsive interactions between A–B pairs on nearest- and next-nearest-neighbor sites, $\varepsilon_{nn} = \varepsilon_{nnn}$. A quench from a disordered configuration at infinite temperature to $k_B T / \varepsilon_{nn} = 1.33$ is performed for $\bar{c} = 0.5$ (a second-order transition to the (2×1) structure occurs in equilibrium at $k_B T_c / \varepsilon_{nn} \approx 2.1$). Time evolution occurs via random nearest-neighbor A–B exchanges (i.e., the model of Kawasaki (1972)). Times shown refer to 10 MCS after the quench (upper part), 200 MCS (middle) and 1700 MCS (bottom). Only B atoms are shown (using four different symbols to indicate whether a B atom belongs to a domain of type 1, 2, 3, or 4, see Fig. 6-35a), A atoms are not shown. From Sadiq and Binder (1984).

behavior found in computer simulations of a square lattice model of a two-dimensional alloy, where there is a repulsive interaction between AB pairs on both nearest- and next-nearest-neighbor sites. For $\bar{c} = 0.5$ the ordering is the two-component (2×1) structure: there are four kinds of domains, where in the ground state full rows of A atoms alternate with full rows of B atoms, and these rows may be oriented in either the x -direction or y -direction for a square lattice. Fig. 6-34 shows the growth of these ordered domains in the simulation of a quenching experiment for this model, and Fig. 6-35 the resulting growth of the superstructure Bragg intensity. The scaling behavior of Eq. (6-67) is well verified. Similar results have also been found for simulations of various other models (see Binder et al., (1987), Furukawa (1985a), Bray (1994), for review.

Experiments on the kinetics of the formation of ordered superstructures have been carried out both for two-dimensional monolayers adsorbed at surfaces (Wang and Lu, 1983; Wu et al., 1983; 1989; Tringides et al., 1986, 1987; Henzler and Busch, 1990), three-dimensional metallic alloys (e.g., Hashimoto et al., 1978; Nishihara et al., 1982; Noda et al., 1984; Takeda et al., 1987; Katano and Iizumi, 1988; Konishi and Noda, 1988), dielectric materials such as $K_2Ba(NO_2)_4$ (Noda, 1988) or K_2ZnCl_4 (Mashiyama, 1988), martensitic materials such as $KD_3(SeO_3)_2$ (Yagi and Lu,

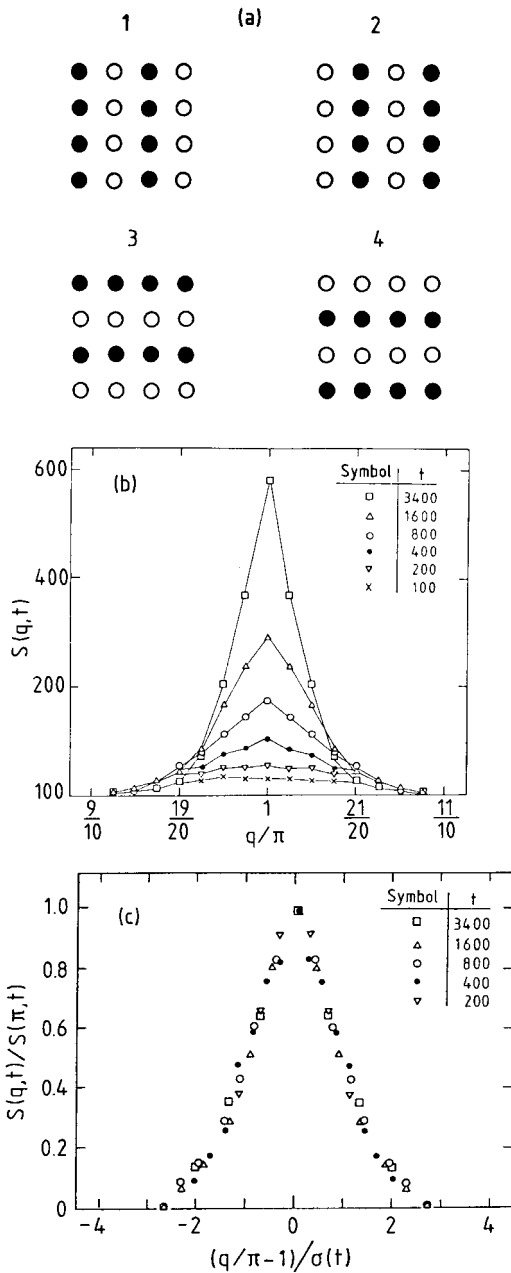


Figure 6-35. (a) Four types of domains (1, 2, 3, and 4) in the (2×1) structure of a binary alloy AB on the square lattice (B atoms are indicated by black circles and A atoms by white circles). (b) Structure factor $S(q, t)$ of superlattice Bragg scattering, at times t after the quench. Since the lattice spacing is set to unity, the Bragg positions of the (2×1) structure are $(\pm\pi, 0)$ and $(0, \pm\pi)$. Only the variation with q_x near $q_x = \pi$ is shown. Times are measured in units of Monte Carlo steps per site. Data are for a computer simulation of a quench from $T = \infty$ to $k_B T/\varepsilon_{nn} = 1.33$ as in Fig. 6-34. (c) Scaling plot of the data shown in (b), with the structure factor $S(q, t)$ being rescaled with the maximum intensity $S(\pi, t)$ and the relative distance $q/\pi - 1$ from the Bragg position being rescaled with the half-widths $\sigma(t)$ of the peaks in (b). From Sadiq and Binder (1984).

1988), graphite intercalation compounds such as transition metal chlorides in graphite (Matsuura, 1988), molecular crystals such as $\text{CN}_{1-x}\text{Cl}_x$ -adamantane (Descamps and Caucheteux, 1988), etc. Of course, there are also cases where phase separation and ordering occur simultaneously, a classic example being Fe–Al alloys where Fe_3Al domains precipitate (Allen, 1977; Oki et al., 1973; Eguchi et al., 1984). Again, no attempt at completeness is made here, we simply quote a number of examples to emphasize the universality of the phenomenon.

As expected from the above discussion, we must distinguish the cases where the “parent phase” from which the ordered structure forms is metastable or unstable; in the latter case, the structure forms by “spinodal ordering” (De Fontaine, 1979) whereas in the former case it forms by nucleation and growth, although again this distinction is not very sharp. An example of the latter case is Mg_3In , where the order is of Cu_3Au type but the transition is very strongly of first order (Konishi and Noda, 1988). The volume fraction of the ordered phase is then found to obey the well-known Avrami (1939), Johnson–Mehl (1939) equation

$$\Phi(t) = 1 - \exp[-(t/\tau)^n] \quad (6-96)$$

where n is a constant characteristic of the type of nucleation process and τ a time constant that depends on the degree of

undercooling of the transition. Here we are more interested in the “spinodal ordering” as occurs in Cu_3Pd (Takeda et al., 1987), Ni_3Mn (Katano and Iizumi, 1988), Cu_3Au (Hashimoto et al., 1978; Nishihara et al., 1982; Noda et al., 1984), and $\text{K}_2\text{Ba}(\text{NO}_2)_4$ (Noda, 1988).

Fig. 6-36 shows examples of growing Bragg peaks, i.e. the experimental counterparts to simulation data such as shown in Fig. 6-35. Whereas for $\text{K}_2\text{Ba}(\text{NO}_2)_4$ we

find a law $k_m^{-1}(t) \sim t^{1/4}$ (Noda, 1988), for Ni_3Mn a crossover from $k_m^{-1}(t) \sim t^{1/4}$ at short times to $k_m^{-1}(t) \sim t^{1/2}$ at later times is found (Katano and Iizumi, 1988), and for AuCu_3 a law $k_m^{-1}(t) \sim t^{1/2}$ (i.e., Eq. (6-95)) is established (Noda et al., 1984). Whereas the $t^{1/2}$ law is expected from various theories (Lifshitz, 1962; Allen and Cahn, 1979b; Ohta et al., 1982), a $t^{1/4}$ law occurring over a transient period of time can perhaps be attributed to the “softness” of the domain walls between the growing ordered regions (Mouritsen, 1986; Mouritsen and Praestgaard, 1988). An interesting observation of Lifshitz–Slyozov type coarsening of the structure factor is also reported for colloid crystallization (Schätzel and Ackerson, 1993).

In the two dimensional case, Wu et al. (1989) measured a growth exponent $x = 0.28 \pm 0.05$ for O on W (110). Since the $p(2 \times 1)$ phase is believed to have an eight-fold ground-state degeneracy in this system, whereas the theories mentioned above refer to a two-fold degenerate ordering only, the interpretation of this result is not obvious. We note, however, that reasonable scaling of the structure factor is observed (Fig. 6-37). For the system silver on Ge (111), a growth exponent $x = 1/2$ is found (Henzler and Busch, 1990) and also good scaling of the structure factor is seen. In this system, on the other hand, a crossover to slower growth occurs at later times; the reason for this behavior is not clear – perhaps it is due to pinning of domain walls at defects (see Sec. 6.4.4). At this point, we note that a similar slowing down of the growth where $k_m^{-1}(t)$ basically stops growing further, has also been seen in Ni_3Mn (Katano and Iizumi, 1988) and in the phase separation of mixtures of flexible and semi-rigid polymers (Hasegawa et al., 1988). In neither of these systems is the very slow growth at late stages understood.

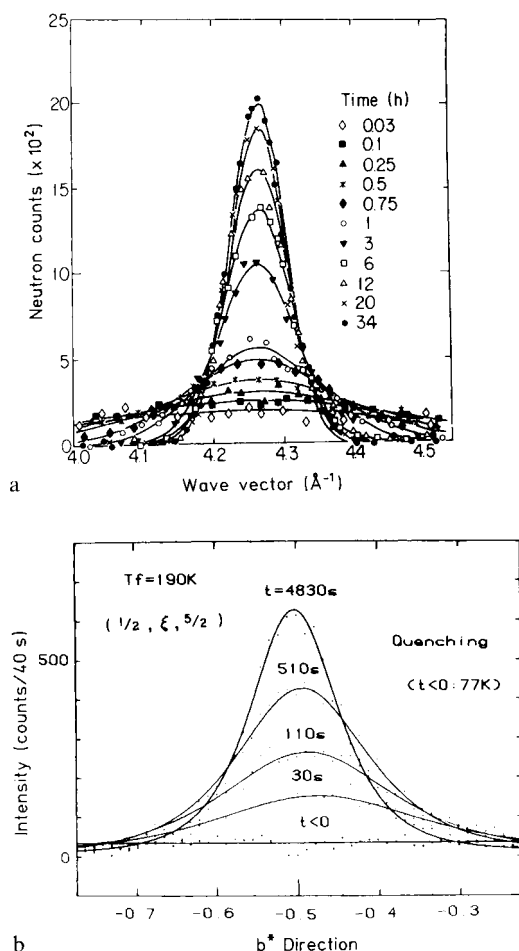


Figure 6-36. (a) Time evolution of the 211 superlattice peak of Ni_3Mn annealed at 470°C for times up to 34 h. From Katano and Iizumi (1988). (b) Time evolution of the $(\frac{1}{2}, \xi, \frac{5}{2})$ superlattice peak of $\text{K}_2\text{Ba}(\text{NO}_2)_4$ annealed at 190 K. From Noda (1988).

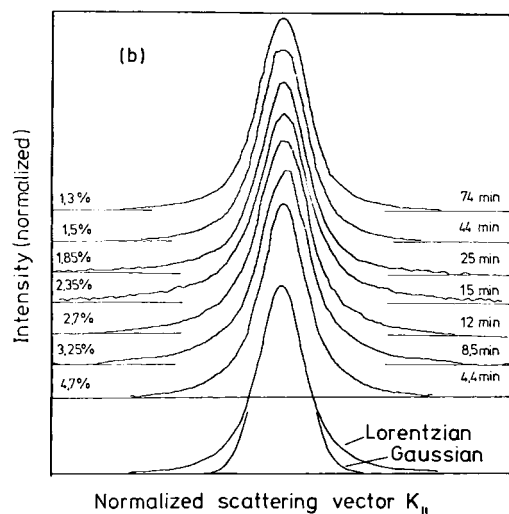
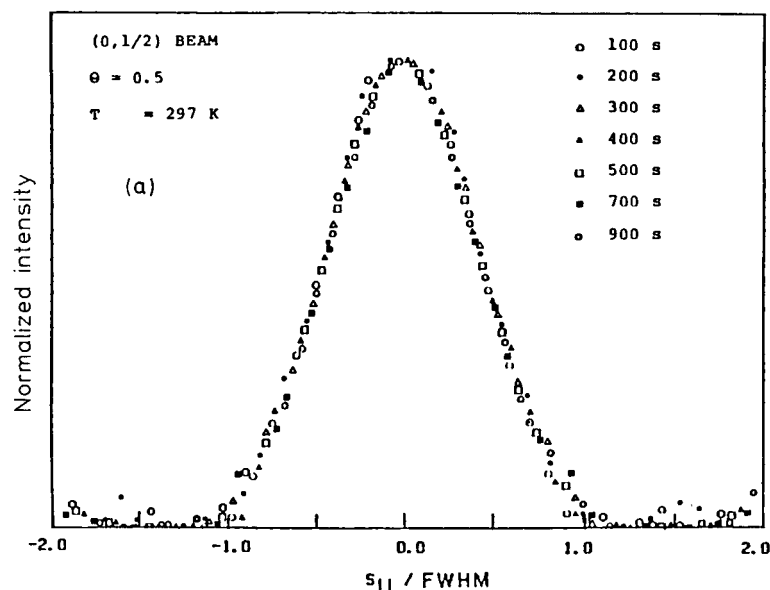


Figure 6-37. (a) Dynamic scaling in the growth of Bragg peaks for W (110) $p(2 \times 1)$ -O at coverage $\Phi = 0.5$ and $T = 297 \text{ K}$. From Wu et al. (1989). (b) Scaled LEED intensities of the $\sqrt{3}$ peak of Ag adsorbed on Ge (111) at $T = 111^\circ \text{C}$. From Henzler and Busch (1990).

In domain growth studies of O on W (112) Zuo et al. (1989) also found scaling behavior at early times but slowing of domain growth attributed to random field effects at later times.

6.4.3 Phase Separation in Reduced Geometry and Near Surfaces

Various cases of reduced geometry may be of interest; for example, spinodal decomposition of fluid mixtures confined to pores in porous media like Vycor glass, or spinodal decomposition or ordering of thin films or adsorbed monolayers at surfaces, and phase separation in small particles or grains in inhomogeneous materials. All these problems have seen much recent activity, and lack of space allows us to give only a very brief introduction.

In a porous medium (or gel), a binary mixture at critical composition experiences a random chemical potential difference (De Gennes, 1984). Using concepts from the random field Ising model (Villain, 1985; Huse, 1987) we expect both a change in the phase diagram and slow relaxation (Goldburg, 1988; Goldburg et al., 1995; Falicov and Berker, 1995). However, there is also the view that we must rather focus on the wetting behavior on the walls inside a straight cylindrical pore (Liu et al., 1990; Monette et al., 1992; Tanaka, 1993; Zhang

and Chakrabarti, 1994, 1995). Of course, ultimately we should combine this single-pore behavior with effects due to the random structure of the pore network.

From Sec. 6.2 it should be clear that the behavior in bulk two and bulk three dimensions is qualitatively similar, although non-linear phenomena are usually more important for $d=2$ than for $d=3$. In particular, for polymer mixtures different coils can interpenetrate each other for $d=3$ but not for $d=2$; therefore a mean-field critical regime does not exist for two-dimensional polymer mixtures.

For thin films that are many atomic diameters thick, there is an interesting interplay between finite size effects (Binder et al., 1987) and surface effects. Usually already in equilibrium at the surface of a mixture, the concentration of one component of a mixture will be enhanced in comparison with the bulk concentration ("surface enrichment" occurs because the interactions between a wall and the two components A and B differ from each other). At the coexistence curve, this preference of the surface for, say, the B component may lead to the formation of a wetting layer at the surface (Dietrich, 1988). Inside the two-phase coexistence region, surfaces may hence have a profound effect on the kinetics of phase separation: surface-directed concentration waves (with wavevector normal to the surface plane) dominate the initial growth in the region near the surface (first observed by Jones et al. (1991) for a polymer mixture). In later stages of the coarsening, we have an interesting competition between the domain growth in the bulk and the possible propagation of a wetting layer from the surface into the bulk (see Krausch, 1995; Puri and Frisch, 1997; and Binder, 1998, for recent reviews).

6.4.4 Effects of Quenched Impurities; Vacancies; and Electrical Resistivity of Metallic Alloys Undergoing Phase Changes

In this subsection, we draw attention to a variety of topics that cannot be discussed here in any depth, owing to lack of space.

(i) *Quenched Impurities*

Throughout this chapter, only ideal systems have been considered where phase separation is triggered by spontaneous fluctuations. However, real materials always contain impurities, whereas in fluids these impurities are mobile ("annealed defects") and hence act like a dilute additional component of a multi-component mixture, in solids such impurities are often immobile ("quenched defects") at the temperatures of interest. This frozen-in disorder may have two effects: in a metastable region, free energy barriers for nucleation are reduced and hence *heterogeneous nucleation* is facilitated (Zettlemoyer, 1969). In the late stages of spinodal decomposition or domain growth, there is an important interaction between such defects and domain walls. Whereas so far it has been assumed that domain walls may diffuse freely owing to their capillary wave excitations, the randomly spaced defects act like a random potential in which the interface moves. Since thermal activation is now required to overcome the barriers of this potential, at low temperatures the domain wall motion is dramatically slowed owing to such impurities. Simulations of this problem have been carried out by Grest and Srolovitz (1985) and Srolovitz and Grest (1985). More work has been devoted to the related problem of the dynamics of the random field Ising model (see Villain, 1985; and Nattermann, 1998, for reviews). In all these systems, we expect that the growth law of the ideal system (Eqs. (6-68) or

(6-95)) will hold until some characteristic length l_c is reached, which depends on the concentration c_i of the quenched impurities ($l_c \sim c_i^{-1/d}$ in d dimensions). At times t significantly exceeding the time given by the condition $k_m^{-1}(t)l_c \approx 1$, a logarithmic growth law (Villain, 1985) is expected:

$$k_m^{-1}(t) \sim \ln t \quad (6-97)$$

A similar crossover in the relaxation from a fast to a slow growth law may also be caused by interface pinning at extended defects (e.g., dislocations, grain boundaries) rather than point defects.

(ii) Vacancies

In solid mixtures, vacancies V are crucial for a microscopic description of interdiffusion, which occurs via a vacancy mechanism rather than by direct A–B exchange (Flynn, 1972; Manning, 1986). Microscopically we therefore need concentrations $c_i^A(t)$, $c_i^B(t)$, and $c_i^V(t)$ for A atoms, B atoms, and vacancies as dynamic variables, respectively, rather than the single concentration variable c_i or concentration field $c(x, t)$ (Eq. (6-1)). Since $c_i^V(t) \ll 1$, it may be possible to reduce the problem to Eq. (6-15), where the mobility M then needs to be related to the jump rates Γ_A and Γ_B of A and B atoms to vacant sites (and the vacancy concentration). However, owing to correlation effects in the vacancy motion, this is a difficult problem even in the non-interacting case (Kehr et al., 1989). There Eqs. (6-6) and (6-14) would yield an interdiffusion coefficient $D_{\text{int}} = M/[c(1-c)]$, i.e., M can be found if D_{int} can be simply related to Γ_A and Γ_B and the average vacancy concentration \bar{c}^V . Although M obviously is proportional to \bar{c}^V for small \bar{c}^V , computer simulations (Kehr et al., 1989) show that the simple relationships proposed in the literature to relate M to Γ_A and Γ_B are inaccurate.

A simulation of the early stages of spinodal decomposition in such an ABV model (Yaldram and Binder, 1991) shows that the general features of the structure factor $S(k, t)$ are almost the same as those of the direct-exchange AB model (Fig. 6-5), and the two models can be approximately mapped onto each other by adjusting the time scales. In real systems, however, the behavior may be more complicated; the vacancy concentration does not need to remain constant, and it may be that many vacancies are created during the quench which later are annealed out by migration to surfaces or recombination with interstitials. If this happens, the effective mobility M would itself depend on the time t after the quench. Also the vacancy concentrations in equilibrium may be different in A-rich and B-rich domains, or may become preferentially enriched in domain boundaries. This did not occur in the simulation of Yaldram and Binder (1991), since there the static properties were assumed with perfect symmetry between A and B and there was no energy parameter associated with the vacancies, but this model is still a gross over-simplification of reality. Fratzl and Penrose (1994, 1997) found that vacancies may speed up the coarsening by changing the mechanism. Note that for very low vacancy content but very late stages a faster growth law ($x = 1/2$) due to cluster–cluster aggregation has been suggested (Mukherjee and Cooper, 1998). These problems may confuse the proper interpretation of real experiments.

(iii) Electrical Resistivity of Metallic Alloys Undergoing Phase Changes

In metallic alloys the quasi-free electrons responsible for electrical conduction are scattered from the atomic disorder. In the framework of the Born approximation, treating the scattering as elastic, the excess

resistivity $\Delta\varrho$ due to concentration fluctuations can be represented as a convolution of the structure factor $\langle\delta\psi_{-\mathbf{k}}(t)\delta\psi_{\mathbf{k}}(t)\rangle$ and the Fourier transform of the effective potential that the quasi-free electrons feel, namely (Binder and Stauffer, 1976b),

$$\Delta\varrho = N \frac{e^2 (Z_B - Z_A)^2 m_{\text{eff}}^2}{(4\pi)^2 \hbar^3 n_{\text{eff}} \alpha^4 k_F^3} \times \int_{0 < k < 2k_F} d\mathbf{k} \frac{k}{(1 + k^2/\kappa^2)^2} \times [\langle\delta c_{-\mathbf{k}}(t)\delta c_{\mathbf{k}}(t)\rangle - \bar{c}^2 \delta(\mathbf{k})] \quad (6-98)$$

where e is the charge of an electron, m_{eff} its effective mass, N is the number of atoms per cm^3 , Z_A and Z_B are the atomic numbers of the two constituents, \hbar is Planck's constant, and κ describes the screening of the Coulomb interaction. In Eq. (6-98) it is assumed that the Fermi sphere (whose radius is k_F) lies completely within the first Brillouin zone, and that there is no sublattice ordering.

Using the structure factor from the computer simulations of Marro et al. (1975), Binder and Stauffer (1976b) showed that during spinodal decomposition a resistivity maximum occurs. This can be understood since in Eq. (6-98) the main contribution comes from the large k (k of order κ or of order k_F). As the coarsening proceeds, however, the structure factor is large only at much smaller values of k . Scaling considerations (Eq. (6-67)) suggest that

$$\Delta\varrho(t) - \Delta\varrho(\infty) \sim k_m(t) \sim t^{-1/3}$$

This treatment can again be generalized for the kinetics of ordering alloys. We refer to Binder and Stauffer (1976a) for a discussion of this problem, and of previous theories and related early experiments.

Just as an alternative description for concentration inhomogeneities in terms of "concentration waves" and their mean-square amplitude $S(k, t)$ in terms of the

time-dependent cluster distribution function (see Sec. 6.2.5), the problem of the electrical resistivity can be rephrased in terms of electron scattering from clusters (Hillel et al., 1975; Edwards and Hillel, 1977). Experimental resistivity data for Al–Zn alloys can be interpreted qualitatively along such lines (Luigi et al., 1980).

At this point, we also mention that electrical currents have been found to affect the phase separation behavior of Al–Si alloys (Onodera and Hirano, 1986, 1988) and other alloys. At present, the explanation of these phenomena is unclear.

6.4.5 Further Related Phenomena

As a first point of this subsection, we draw attention to peculiar morphologies of structures that may form via phase separation in fluid mixtures with very strong dynamic asymmetry, e.g., solution of polymers which are frozen into a glass-like structure at high density. The resulting viscoelastic phase separation leads to the formation of sponge-like patterns (Tanaka, 1994, 1996; Taniguchi and Onuki, 1996) or rigid foams (Hikmet et al., 1988).

Another recent topic of interest is phase separation induced by temperature gradients (Kumaki et al., 1996) and velocity gradients, i.e. shear (Onuki et al., 1997). The effect of shear flow on the unmixing of fluids is in fact three-fold, as recently reviewed by Onuki (1997): the phase diagram is modified (shear-induced mixing due to a depression of the critical temperature may occur), the rheology of the unmixed two-phase states is profoundly altered, and the morphology of the patterns that form is changed.

Finally we mention the interplay of phase separation and chemical reactions (Huberman, 1976; Glotzer et al., 1995; Leffever et al., 1995). Chemical reactions may

terminate the coarsening process and thus freeze in an inhomogeneous pattern.

6.5 Discussion

The understanding of the dynamics of phase changes of materials has advanced considerably in recent years; the theoretical results now present a fairly clear picture of at least some basic questions, and also quantitatively reliable experiments are available for many systems. This chapter has emphasized the theoretical aspects; its main conclusions can be summarized as follows:

(i) The linearized theory of spinodal decomposition holds only for mean-field type systems (with long ranges of interactions) or in systems that are equivalent to them, such as polymer mixtures.

(ii) Whereas a spinodal curve is well defined in the mean-field limit or for polymer mixtures in the limit of chain length $N \rightarrow \infty$, in all other cases the spinodal is an ill-defined concept. This implies that the transition from nucleation to spinodal decomposition is gradual. For polymer mixtures, the width of this transition region may be narrow, as estimations from Ginzburg criteria show. Experiments are still needed to check the latter point, whereas the gradual transition from nucleation to spinodal decomposition in metallic alloys over a broad temperature region has been established experimentally.

(iii) Nonlinear spinodal decomposition during the early stages can be successfully described qualitatively by the Langer–Baron–Miller theory (for solid mixtures) and the Kawasaki–Ohta theory (for fluid mixtures). Recent experiments, however, show that these theories are not quantitatively accurate. More work is required to

understand the crossover from these early stages to the late stage of phase separation where the structure factor develops towards a scaling limit. It is not clear under which conditions power-law behavior $k_m(t) \sim t^{-x}$ can be observed at intermediate stages, and what the appropriate interpretation of the exponent x is.

(iv) In the late stages the structure factor obeys the scaling behavior first suggested by Binder and Stauffer (1974, 1976b),

$$S(k, t) \sim [k_m(t)]^{-d} \tilde{S}\{k/k_m(t)\}$$

While the scaling function $\tilde{S}(\zeta)$ proposed by Furukawa (1984) seems to account well for the general shape of experimental data on solid or polymer mixtures, several details are not reproduced correctly. Good evidence for Porod's law, $\tilde{S}(\zeta) \sim \zeta^{-(d+1)}$ for $\zeta \ll 1$, has been provided. The width of $\tilde{S}(\zeta)$ increases when the volume fraction ϕ of precipitate phase decreases from that of the critical mixture (Fratzl and Lebowitz, 1989). There we find, as a function of temperature and ϕ , both morphologies, interconnected domains and well separated droplets. Such a transition can also be observed as a function of time in computer simulations (Hayward et al., 1987; Lironis et al., 1989) and experiments on polymer mixtures (Hasegawa et al., 1988) (see Fig. 6-38).

(v) There is now agreement that in solid mixtures the behavior at late times is given by the Lifshitz–Slyozov law, $k_m^{-1}(t) \sim t^{1/3}$, even in the percolative regime (Amar et al., 1988). This has recently also been verified in a solid–liquid system that satisfies all assumptions of the LSW theory (Alkemper et al., 1999). For critical quenches of fluid mixtures at late times, Siggia's (1979) result $k_m^{-1}(t) \sim t$ holds, but further research is needed to achieve an understanding of the exponents for the growth of ordered structures in cases with a higher degeneracy of

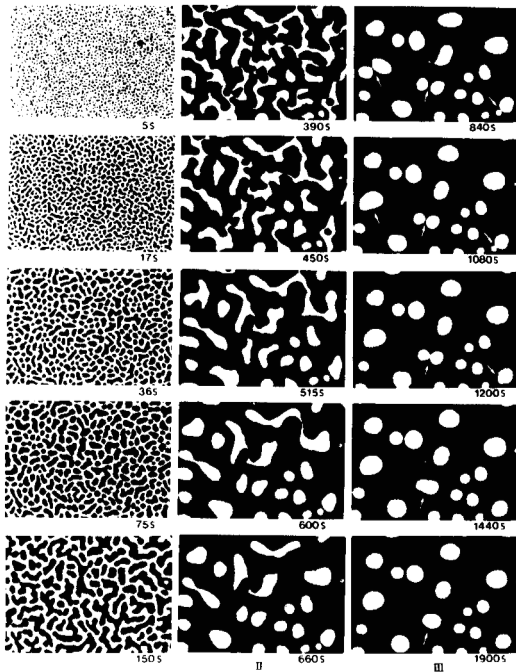


Figure 6-38. Polarizing optical microscope images obtained from the same area of a cast film of a binary mixture of poly(ethylene terephthalate) and a copolyester composed of 60 mol% p-oxybenzoate and 40 mol% ethylene terephthalate at 50% relative concentration during isothermal heat treatment at 270 °C. Times at which the images are taken are indicated (in seconds). From Hasegawa et al. (1988).

the ordered phase, and to understand how these growth laws are affected by defects. Other questions concern the suggestion (Langer et al., 1975; Binder, 1977) that by expressing k_m and t as suitably scaled quantities q_m and τ , e.g., $q_m(\tau) = k_m(t) \xi$ and $\tau = D_0 t / \xi^2$, where ξ is the correlation length at phase coexistence and D_0 the interdiffusion constant, a material-independent universal function should be obtained (which must depend, however, on the volume fraction of the phases coexisting in the final equilibrium state). A counter-example for this universality seems to be the “ N branching” found for polymer mixtures (Onuki, 1986b; Hashimoto, 1988), and more work is needed to understand this problem. Clearly such a universality, if it exists, would be useful as it allows the phase separation behavior of other materials to be predicted if properties such as ξ and D_0 are known. Of course, we must distinguish between different “universality classes” (Binder, 1977) for solids and fluid mixtures (cf. Figs. 6-28 and 6-39).

(vi) Apart from crude “cluster dynamics” models, there is no theoretical ap-

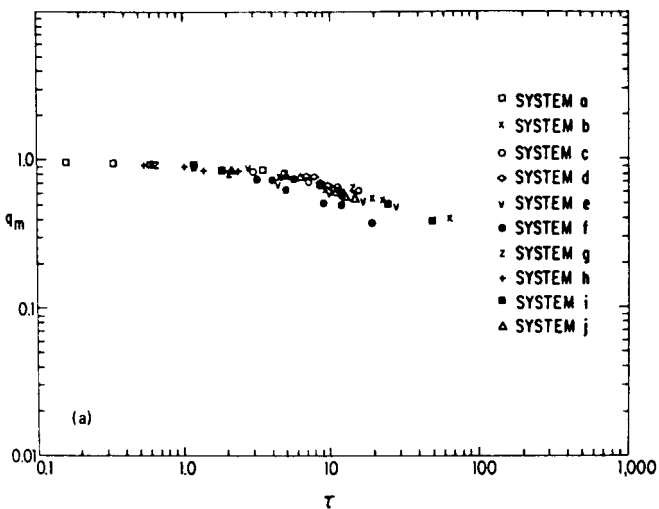


Figure 6-39. Comparison of q_m vs. τ behavior found in metallic alloys (a)–(h) and in organic glasses (i), (j). Here the scaling is done differently to that in the text, namely $q_m = k_m(t)/k_m(0)$ and $\tau = -2t R[k_m(0)]$. Systems used are Au–60 at.% Pt at 550 °C (a) (Singhal et al., 1978), Al–6.8 at.% Zn at $T = 108$ °C (b), 116 °C (c), 129 °C (d) (Laslaz et al., 1977), Al–5.3 at.% Zn at $T = 20$ °C (e), Al–6.8 at.% Zn at 20 °C (f), 90 °C (g), 110 °C (h) (Hennion et al., 1982), 76B₂O₃–19PbO–5Al₂O₃ at 450 °C (i) (Zarzycki and Naudin, 1969), and 13.2Na₂O–SiO₂ at 560 °C (j) (Tomozawa et al., 1970). From Synder and Meakin (1983).

proach to describe the behavior in the transition region from spinodal decomposition to nucleation. This problem, and theories connecting consistently the early-time spinodal decomposition to the scaling behavior at late stages, still needs more research. So far much progress has been due to large-scale computer simulation, e.g., Amar et al. (1988) (see Figs. 6-40 and 6-41); it is still a challenge to explain quantitatively simulation data such as shown in these figures or experimental data as shown in Fig. 6-32 by analytical theories.

(vii) Finally, we draw attention to the fact that the concepts developed in the present context can also be extended to very different physical phenomena. For example, the Lifshitz–Slyozov mechanism can be identified to describe processes such as the healing of rough surfaces at low temperature (Villain, 1986; Selke, 1987).

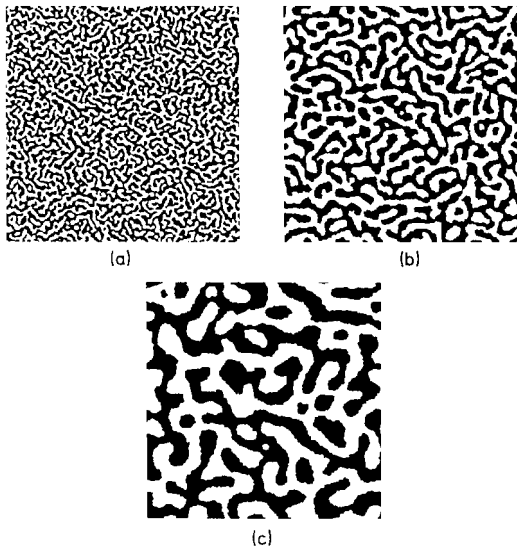


Figure 6-40. “Snapshot pictures” of the two-dimensional nearest-neighbor Ising model of a phase-separating mixture evolving after a critical quench to $T=0.5 T_c$ at times $t=5000$ MCS (a), $t=10^5$ MCS (b) and $t=9.8 \times 10^5$ MCS (c). B atoms are shown in black, A atoms are not shown. Data are for a 512×512 lattice. From Amar et al. (1988).

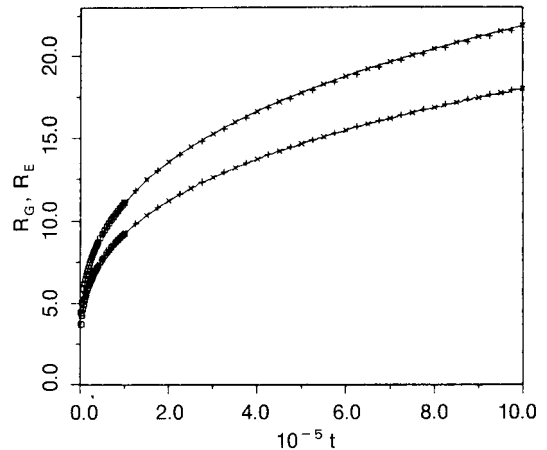


Figure 6-41. Log–log plot of the characteristic linear dimensions $R_G(t)$ and $R_E(t)$ at time t after the quench, for the simulation shown in Fig. 6-40. $R_G(t)$ is extracted from the correlation function and $R_E(t)$ from the energy relaxation. The full curve is a fit to Eq. (6-84a). From Amar et al. (1988).

6.6 Acknowledgements

This work has profited considerably from a longstanding and stimulating interaction of K. B. with D. Stauffer and D. W. Heermann. This author thanks them and also other co-workers, namely C. Billotet, H.-O. Carmesin, H. L. Frisch, J. D. Gunton, S. Hayward, J. Jäckle, M. H. Kalos, K. Kaski, K. W. Kehr, J. L. Lebowitz, G. Lironis, A. Milchev, P. Mirolid, S. Reulein, A. Sariban, and K. Yaldram, for fruitful collaboration.

The other author (P. F.) is particularly indebted to O. Penrose and J. L. Lebowitz for a longstanding and fruitful collaboration. Furthermore he is indebted to H. Gupta, C. A. Laberge, F. Langmayr, P. Nielaba, O. Paris, G. Vogl, and R. Weinkamer for fruitful interactions.

6.7 References

- Abinandanan T. A., Johnson W. C. (1993), *Acta Metall. Mater.* 41, 17; 27.
- Abinandanan T. A., Johnson W. C. (1995), *Mat. Sci. Eng. B* 32, 169.
- Acuña, R. J., Craievich, A. F. (1979), *J. Non-Cryst. Solids* 34, 13.
- Akaiwa, N., Voorhees, P. W. (1994), *Phys. Rev. E* 49, 3860.
- Akcasu, A. Z., Benmouna, M., Benoit, H. (1986), *Polymer* 27, 1935.
- Alexander, F. J., Chen, S., Grunau, D. W. (1993), *Phys. Rev. B* 48, 634.
- Alkemper, J., Snyder, V. A., Akaiwa, N., Voorhees, P. W. (1999), *Phys. Rev. Lett.* 82, 2725.
- Allen, S. M. (1977), *Philos. Mag.* 36, 181.
- Allen, S. M., Cahn, J. W. (1976), *Acta Metall.* 24, 425.
- Allen, S. M., Cahn, J. W. (1979a), *Acta Metall.* 27, 1017.
- Allen, S. M., Cahn, J. W. (1979b), *Acta Metall.* 27, 1085.
- Alpern, P., Benda, Th., Leiderer, P. (1982), *Phys. Rev. Lett.* 49, 1267.
- Als-Nielsen, J. (1976), in: *Phase Transitions and Critical Phenomena*, Vol. 5a: Domb, C., Green, M. S. (Eds.). New York: Academic Press, p. 88.
- Amar, J. G., Sullivan, F. E., Mountain, R. D. (1988), *Phys. Rev. B* 37, 196.
- Avrami, M. (1939), *J. Chem. Phys.* 7, 1103.
- Bastea, S., Lebowitz, J. L. (1995), *Phys. Rev. E* 52, 3821.
- Bates, F. S., Wiltzius, P. (1989), *J. Chem. Phys.* 91, 3258.
- Benda, Th., Alpern, P., Leiderer, P. (1981), *Physica* 107B, 157.
- Benda, Th., Alpern, P., Leiderer, P. (1982), *Phys. Rev. B* 26, 1450.
- Beysens, D., Perrot, F. (1984), *J. Phys. (Paris) Lett.* 45, L-31.
- Beysens, D., Guenoun, P., Perrot, F. (1988), in: *Dynamic of Ordering Process in Condensed Matter*: Komura, S., Furukawa, H. (Eds.). New York: Plenum Press, p. 373.
- Billotet, C., Binder, K. (1979), *Z. Phys.* B32, 195.
- Binder, K. (1977), *Phys. Rev. B* 15, 4425.
- Binder, K. (1981), in *Stochastic Nonlinear Systems in Physics, Chemistry and Biology*: Arnold, L., Lefever, R. (Eds.). Berlin: Springer, p. 62.
- Binder, K. (1983), *J. Chem. Phys.* 79, 6387.
- Binder, K. (1984a), in: *Condensed Matter Research Using Neutrons*: Lovesey, S. W., Scherm, R. (Eds.). New York: Plenum Press, p. 1.
- Binder, K. (1984b), *Phys. Rev. A* 29, 341.
- Binder, K. (1984c), in: *Kinetics of Aggregation and Gelation*: Family, F., Landau, D. P. (Eds.). Amsterdam: Elsevier, p. 209.
- Binder, K. (1986), in: *Festkörperprobleme – Advances in Solid State Physics*, Vol. 26: Grosse, P. (Ed.) Braunschweig: Vieweg, p. 133.
- Binder, K. (1987a), *Rep. Prog. Phys.* 50, 783.
- Binder, K. (1987b), *Colloid Polym. Sci.* 265, 273.
- Binder, K. (1989), in: *Alloy Phase Stability*: Gonis, A., Stocks, L. M. (Eds.). Dordrecht: Kluwer, p. 232.
- Binder, K. (1998), *J. Non-Equilib. Thermodyn.* 23, 114.
- Binder, K. (2001), in: *Phase Transformations in Materials*: Kosterz, G. (Ed.). Weinheim: Wiley-VCH, Chap. 4.
- Binder, K., Frisch, H. L. (1984), *J. Chem. Phys.* 81, 2126.
- Binder, K., Heermann, D. W. (1985), in: *Scaling Phenomena in Disordered Systems*: Pynn, R., Skjeltorp, T. (Eds.). New York: Plenum Press, p. 207.
- Binder, K., Sillescu, H. (1989), in: *Encyclopedia of Polymer Science*, Vol. 2: Kroschwitz, J. (Ed.). New York: Wiley, p. 297.
- Binder, K., Stauffer, D. (1974), *Phys. Rev. Lett.* 33, 1006.
- Binder, K., Stauffer, D. (1976a), *Adv. Phys.* 25, 343.
- Binder, K., Stauffer, D. (1976b), *Z. Phys.* B24, 407.
- Binder, K., Billotet, C., Mirol, P. (1978), *Z. Phys.* B30, 183.
- Binder, K., Kalos, M. H., Lebowitz, J. L., Marro, J. (1979), *Adv. Colloid Interface Sci.* 10, 173.
- Binder, K., Frisch, H. L., Jäckle, J. (1986), *J. Chem. Phys.* 85, 1505.
- Binder, K., Heermann, D. W., Milchev, A., Sadiq, A. (1987), in: *Proceedings of Heidelberg Colloquium on Glassy Dynamics*: Van Hemmen, L., Morgenstern, I. (Eds.). Berlin: Springer, p. 154.
- Bortz, A. B., Kalos, M. H., Lebowitz, J. L., Zendejas, M. A. (1974), *Phys. Rev. B* 10, 535.
- Bray, A. J. (1990), *Phys. Rev. B* 41, 6274.
- Bray, A. J. (1994), *Adv. Phys.* 43, 357.
- Bray, A. J. (1998), *Phys. Rev. E* 58, 1508.
- Cahn, J. W. (1961), *Acta Metall.* 9, 795.
- Cahn, J. W. (1962), *Acta Metall.* 10, 179.
- Cahn, J. W. (1965), *J. Chem. Phys.* 42, 93.
- Cahn, J. W. (1966), *Acta Metall.* 14, 1685.
- Cahn, J. W. (1968), *Trans. Metall. Soc. AIME* 242, 166.
- Cahn, J. W., Hilliard, J. E. (1958), *J. Chem. Phys.* 28, 258.
- Cahn, J. W., Hilliard, J. E. (1959), *J. Chem. Phys.* 31, 688.
- Cahn, J. W., Larché, F. C. (1984), *Acta Metall.* 32, 1915.
- Carmesin, H.-O., Heermann, D. W., Binder, K. (1986), *Z. Phys.* B65, 89.
- Chakrabarti, A., Toral, R., Gunton, J. D. (1993), *Phys. Rev. E* 47, 3025.
- Chan, S. K. (1977), *J. Chem. Phys.* 67, 5755.
- Chan, C. K., Goldburg, W. I. (1987), *Phys. Rev. Lett.* 48, 674.
- Chan, C. K., Goldburg, W. I., Maher, J. V. (1987), *Phys. Rev. A* 35, 1756.
- Chan, C. K., Perrot, F., Beysens, D. (1988), *Phys. Rev. Lett.* 61, 412.

- Che, D. Z., Spooner, S., Hoyt, J. J. (1997), *Acta Mater.* 45, 1167.
- Chen, H., Rolat, S., Epperson, J. E. (1988), in: *Dynamics of Ordering Processes in Condensed Matter*: Komura, S., Furukawa, H. (Eds.). New York: Plenum Press, p. 245.
- Cherns, D., Greene, P. D., Hainsworth, A., Preston, A. R. (1988), in: *Microscopy of Semiconducting Materials*. Bristol: Institute of Physics, p. 83.
- Cho, J. H., Ardell, A. J. (1997), *Acta Mater.* 45, 1393.
- Chou, Y. C., Goldburg, W. I. (1979), *Phys. Rev. A* 20, 2105.
- Chou, Y. C., Goldburg, W. I. (1981), *Phys. Rev. A* 23, 858.
- Chu, B. (1988), in: *Dynamics of Ordering Processes in Condensed Matter*: Komura, S., Furukawa, H. (Eds.). New York: Plenum Press, p. 463.
- Conley, J. G., Fine, M. E., Weertmann, J. R. (1989), *Acta Metall.* 37, 1251.
- Cook, H. E. (1970), *Acta Metall.* 18, 297.
- Cook, H. E., De Fontaine, D., Hilliard, J. E. (1969), *Acta Metall.* 17, 765.
- Craievich, A. F., Olivieri, J. R. (1981), *J. Appl. Crystallogr.* 14, 444.
- Craievich, A. F., Sanchez, J. M. (1981), *Phys. Rev. Lett.* 47, 1308.
- Dee, G., Gunton, J. D., Kawasaki, K. (1981), *Prog. Theor. Phys.* 65, 365.
- De Fontaine, D. (1979), in: *Solid State Physics*, Vol. 34: Ehrenreich, H., Seitz, F., Thurnbull, D. (Eds.). London: Academic Press, p. 73.
- De Fontaine, D., Cook, H. E. (1971), in: *Critical Phenomena in Alloys, Magnets and Superconductors*: Miller, R. E., Ascher, E., Jaffee, I. (Eds.). New York: McGraw-Hill, p. 257.
- De Fontaine, D., Kikuchi, R. (1978), *NBS Spec. Publ. No.* 496, 976.
- De Gennes, P. G. (1979), *Scaling Concepts in Polymer Physics*. Ithaca: Cornell University Press.
- De Gennes, P. G. (1980), *J. Chem. Phys.* 72, 4756.
- De Gennes, P. G. (1984), *Phys. Chem.* 88, 6469.
- De Groot, S. R., Mazur, P. (1962), *Non-Equilibrium Thermodynamics*. Amsterdam: North-Holland.
- Descamps, M., Caucheteux, C. (1988), in: *Dynamics of Ordering Processes in Condensed Matter*: Komura, S., Furukawa, H. (Eds.). New York: Plenum Press, p. 257.
- Dietrich, S. (1988), in: *Phase Transitions and Critical Phenomena*, Vol. 12: Domb, C., Lebowitz, S. L. (Eds.). New York: Academic Press, p. 1.
- Doi, M., Edwards, S. F. (1986), *The Theory of Polymer Dynamics*. Oxford: Clarendon Press.
- Easwar, N. (1992), *Phys. Rev. Lett.* 68, 186.
- Edwards, J. T., Hillel, A. J. (1977), *Philos. Mag.* 35, 1231.
- Eguchi, T., Oki, K., Matsumura, S. (1984), *Mater. Res. Soc. Symp. Proc.* 21, 589.
- Fährmann, M., Fratzl, P., Paris, O., Fährmann, E., Johnson, W. C. (1995), *Acta Metall. Mater.* 43, 1007.
- Falicov, A., Berker, A. N. (1995), *Phys. Rev. Lett.* 74, 426.
- Flevaris, N. K. (1987), *J. Am. Ceram. Soc.* 70, 301.
- Flory, P. J. (1953), *Principles of Polymer Chemistry*. Ithaca: Cornell University Press.
- Flynn, C. P. (1972), *Point Defects and Diffusion*. Oxford: Clarendon Press.
- Forouhi, A. R., De Fontaine, D. (1987), *Acta Metall.* 35, 1863.
- Fratzl, P. (1991), *J. Appl. Cryst.* 24, 593.
- Fratzl, P., Blaschko, O. (1988), in: *Dynamics of Ordering Processes in Condensed Matter*: Komura, S., Furukawa, H. (Eds.). New York: Plenum Press, p. 223.
- Fratzl, P., Lebowitz, J. L. (1989), *Acta Metall.* 12, 3245.
- Fratzl, P., Penrose, O. (1994), *Phys. Rev. B* 50, 3477.
- Fratzl, P., Penrose, O. (1995), *Acta Metall. Mater.* 43, 2921.
- Fratzl, P., Penrose, O. (1996), *Acta Metall. Mater.* 44, 3227.
- Fratzl, P., Penrose, O. (1997), *Phys. Rev. B* 55, R6101.
- Fratzl, P., Lebowitz, J. L., Marro, J., Kalos, M. H. (1983), *Acta Metall.* 31, 1849.
- Fratzl, P., Lebowitz, J. L., Penrose, O., Amar, J. (1991), *Phys. Rev. B* 44, 4794.
- Fratzl, P., Penrose, O., Lebowitz, J. L. (1999), *J. Stat. Phys.* 95, 1429.
- Fredrickson, G. H., Binder, K. (1989), *J. Chem. Phys.* 91, 7265.
- Furukawa, H. (1978), *Prog. Theor. Phys.* 59, 1072.
- Furukawa, H. (1984), *Physica* 123 A, 497.
- Furukawa, H. (1985a), *Adv. Phys.* 34, 703.
- Furukawa, H. (1985b), *Prog. Theor. Phys.* 74, 174.
- Furukawa, H. (1985c), *Phys. Rev. A* 31, 1103.
- Furukawa, H. (1988), in: *Dynamics of Ordering Processes in Condensed Matter*: Komura, S., Furukawa, H. (Eds.). New York: Plenum Press, p. 35.
- Furusaka, M., Ishikawa, Y., Mera, M. (1985), *Phys. Rev. Lett.* 54, 2611.
- Furusaka, M., Ishikawa, Y., Yamaguchi, S., Fujino, Y. (1986), *J. Phys. Soc. Jpn.* 55, 2253.
- Furusaka, M., Fujikawa, S., Sakauchi, M., Hirano, K. (1988), in: *Dynamics of Ordering Processes in Condensed Matter*: Komura, S., Furukawa, H. (Eds.). New York: Plenum Press, p. 281.
- Gaulin, B. D., Spooner, S., Morii, Y. (1987), *Phys. Rev. Lett.* 59, 668.
- Gawlinks, E. T., Gunton, J. D., Vināls, J. (1989), *Phys. Rev. B* 39, 7266.
- Gerold, V., Kosterz, G. (1978), *J. Appl. Crystallogr.* 11, 376.
- Ginzburg, V. L. (1960), *Sov. Phys. Solid State* 2, 1824.
- Glatter, O., Kratky, O. (1982), *Small Angle X-Ray Scattering*. London: Academic Press.
- Glotzer, S. C., Di Marzio, E. A., Muthukumar, M. (1995), *Phys. Rev. Lett.* 74, 2034.

- Goldburg, W. I. (1981), in: *Scattering Technique Applied to Supramolecular and Nonequilibrium Systems*: Chen, S. H., Chu, B., Nossal, R. (Eds.). New York: Plenum Press, p. 383.
- Goldburg, W. I. (1983), in: *Light Scattering Near the Phase Transition*: Cummins, H. Z., Levanyuk, A. P. (Eds.). Amsterdam: North-Holland, p. 531.
- Goldburg, W. I. (1988), *Dynamics of Ordering Processes in Condensed Matter*: Komura, S., Furukawa, H. (Eds.). New York: Plenum Press, p. 361.
- Goldburg, W. I., Shaw, C. H., Huang, J. S., Pilant, M. S. (1978), *J. Chem. Phys.* 68, 484.
- Goldburg, W. I., Aliev, F., Wu, X. L. (1995), *Physica A* 213, 61.
- Goretsveig, V. I., Fratzl, P., Lebowitz, J. L. (1997), *Phys. Rev. B* 55, 2912.
- Grant, M., San Miguel, M., Vinals, S., Gunton, J. D. (1985), *Phys. Rev. B* 31, 302.
- Grest, G. S., Srolovitz, D. J. (1985), *Phys. Rev. B* 32, 3014.
- Griffiths, R. B. (1970), *Phys. Rev. Lett.* 24, 715.
- Guenoun, P., Gastand, R., Perrot, F., Beysens, D. (1987), *Phys. Rev. A* 36, 4876.
- Gunton, J. D., San Miguel, M., Sahni, P. S. (1983), in: *Phase Transition and Critical Phenomena*, Vol. 8: Domb, C., Lebowitz, J. L. (Eds.). London: Academic Press, p. 267.
- Gunton, J. D., Gawlinski, E. T., Kaski, K. (1988), in: *Dynamics of Ordering Processes in Condensed Matter*: Komura, S., Furukawa, H. (Eds.). New York: Plenum Press, p. 101.
- Gupta, H., Weinkamer, R., Fratzl, P., Lebowitz, J. L. (2001), *Acta Mater.* 49, 53.
- Guyot, P., Simon, J. P. (1982), in: *Solid State Phase Transformations*: Aaronsen, H. I., Laughlin, D. E., Schuka, R. F., Wayman, C. M. (Eds.). New York: AIME, p. 325.
- Guyot, P., Simon, J. P. (1988), in: *Dynamics of Ordering Processes in Condensed Matter*: Komura, S., Furukawa, H. (Eds.). New York: Plenum Press, p. 211.
- Haasen, P., Gerold, V., Wagner, R., Ashby, M. F. (Eds.) (1984), *Decomposition of Alloys: The Early Stages*. Oxford: Pergamon Press.
- Han, C. C., Okada, M., Sato, T. (1988), in: *Dynamics of Ordering Processes in Condensed Matter*: Komura, S., Furukawa, H. (Eds.). New York: Plenum Press, p. 433.
- Hasegawa, H., Shiawaku, T., Nakai, A., Hashimoto, T. (1988), in: *Dynamics of Ordering Processes in Condensed Matter*: Komura, S., Furukawa, H. (Eds.). New York: Plenum Press, p. 457.
- Hashimoto, T. (1987), in: *Current Topics in Polymer Science*, Vol. 2: Ottenbrite, R. M., Itracki, L. A., Inoue, S. (Eds.). Munich: Hanser, p. 199.
- Hashimoto, T. (1988), in: *Dynamics of Ordering Processes in Condensed Matter*: Komura, S., Furukawa, H. (Eds.). New York: Plenum Press, p. 421.
- Hashimoto, T. (1993), in: *Materials Science and Technology*, Vol. 12: Cahn, R. W., Haasen, P., Kramer, E. J. (Eds.). Weinheim: VCH, p. 251.
- Hashimoto, T., Izumitani, T. (1985), *J. Chem. Phys.* 83, 3694.
- Hashimoto, T., Nishimura, K., Takeuchi, Y. (1978), *J. Phys. Soc. Jpn.* 45, 1127.
- Hashimoto, T., Itakuri, M., Shimidzu, N. (1986), *J. Chem. Phys.* 85, 6773.
- Hashimoto, T., Matsuzaka, K., Moses, E., Onuki, A. (1995), *Phys. Rev. Lett.* 74, 126.
- Hayward, S., Heermann, D. W., Binder, K. (1987), *J. Stat. Phys.* 49, 1053.
- Heermann, D. W. (1984a), *Phys. Rev. Lett.* 52, 1126.
- Heermann, D. W. (1984b), *Z. Phys. B* 55, 309.
- Heermann, D. W. (1985), *Z. Phys. B* 61, 311.
- Heermann, D. W., Klein, W. (1983a), *Phys. Rev. Lett.* 50, 1962.
- Heermann, D. W., Klein, W. (1983b), *Phys. Rev. Lett.* 50, 1732.
- Heermann, D. W., Klein, W., Stauffer, D. (1982), *Phys. Rev. Lett.* 49, 1262.
- Hennion, M., Ronzaud, D., Guyot, P. (1982), *Acta Metall.* 30, 599.
- Henzler, M., Busch, H. (1990), *Phys. Rev. B* 41, 4891.
- Hikmet, R. M., Callister, S., Keller, A. (1988), *Polymer* 29, 1378.
- Hillel, A. J., Edwards, J. T., Wilkes, P. (1975), *Philos. Mag.* 32, 189.
- Hirotsu, S., Kaneki, A. (1988), in: *Dynamics of Ordering Processes in Condensed Matter*: Komura, S., Furukawa, H. (Eds.). New York: Plenum Press, p. 481.
- Hobbie, E. K., Kim, S. H., Han, C. C. (1996), *Phys. Rev. E* 54, R5909.
- Hoffer, J. K., Campbell, L. J., Bartlett, R. J. (1980), *Phys. Rev. Lett.* 45, 912.
- Hohenberg, P. C., Halperin, B. I. (1977), *Rev. Mod. Phys.* 49, 435.
- Hohenberg, P. C., Nelson, D. (1979), *Phys. Rev. B* 20, 2665.
- Hono, K., Babu, S. S., Hiraga, K., Okano, R., Sakurai, T. (1992), *Acta Mater.* 40, 3027.
- Houessou, C., Guenoun, P., Gastaud, R., Perrot, F., Beysens, D. (1985), *Phys. Rev. A* 32, 1818.
- Houston, E. L., Cahn, J. W., Hilliard, J. E. (1966), *Acta Metall.* 14, 1685.
- Huberman, B. A. (1976), *J. Chem. Phys.* 65, 2023.
- Huse, D. A. (1986), *Phys. Rev. B* 34, 7845.
- Huse, D. A. (1987), *Phys. Rev. B* 36, 5383.
- Izumitani, T., Takanaka, M., Hashimoto, T. (1989), *J. Chem. Phys.* 92, 3213.
- Jäckle, J., Pieroth, M. (1988), *Z. Phys. B* 72, 25.
- Jantzen, C. M. F., Herman, H. (1978), in: *Phase Diagrams: Material Science and Technology*, Vol. 5: Alper, A. A. (Ed.). New York: Academic Press, p. 127.
- Jinnai, H., Hashimoto, T., Lee, D., Chen, S.-H. (1997), *Macromolecules* 30, 130.
- Joanny, J. F. (1978), *C. R. Acad. Sci. Ser. B* 286, 89.

- Johnson, W. A., Mehl, R. F. (1939), *Trans. AIME* 135, 416.
- Jones, R. A. L., Norton, L. J., Kramer, E. J., Bates, F. S., Wiltzius, P. (1991), *Phys. Rev. Lett.* 66, 1326.
- Joshua, M., Goldberg, W. I., Onuki, A. (1985), *Phys. Rev. Lett.* 54, 1175.
- Jou, H. J., Leo, P. H., Lowengrub, J. S. (1997), *J. Comp. Phys.* 131, 109.
- Kadanoff, L. P. (1976), in: *Phase Transitions and Critical Phenomena*, Vol. 5a: Domb, D., Green, M. S. (Eds.). London: Academic Press, Ch. 1.
- Kampmann, R., Wagner, R. (1984), in: *Decomposition of Alloys: the Early Stages*: Haasen, P., Gerard, V., Wagner, R., Ashby, M. F. (Eds.). Oxford: Pergamon Press, p. 91.
- Kaski, K., Binder, K., Gunton, J. D. (1984), *Phys. Rev. B* 29, 3996.
- Katano, S., Iizumi, M. (1984), *Phys. Rev. Lett.* 52, 835.
- Katano, S., Iizumi, M. (1988), in: *Dynamics of Ordering Processes in Condensed Matter*: Komura, S., Furukawa, H. (Eds.). New York: Plenum Press, p. 321.
- Kawasaki, K. (1972), in: *Phase Transitions and Critical Phenomena*. Vol. 2: Domb, C., Green, M. S. (Eds.). New Academic Press, Ch. 11.
- Kawasaki, K., Ohta, T. (1978), *Prog. Theor. Phys.* 59, 362.
- Kawasaki, K., Imeada, T., Gunton, J. D. (1981), in: *Perspectives in Statistical Physics*: Raveché, H. J. (Ed.). Amsterdam: North-Holland, p. 203.
- Kehr, K. W., Binder, K., Reulein, S. M. (1989), *Phys. Rev. B* 39, 4891.
- Khachaturyan, A. G. (1966), *Sov. Phys. Solid State* 8, 2163.
- Khachaturyan, A. G. (1983), *Theory of Structural Transformations in Solids*. New York: Wiley.
- Klein, W., Unger, C. (1983), *Phys. Rev. B* 28, 445.
- Koga, T., Kawasaki, K. (1991), *Phys. Rev. A* 44, R 817.
- Koga, T., Kawasaki, K. (1993), *Physica A* 196, 389.
- Komura, S., Osamura, K., Fujii, H., Takeda, T. (1985), *Phys. Rev. Lett.* B11, 1278.
- Komura, S., Takeda, T., Osamura, K., Okuda, K. (1988), in: *Dynamics of Ordering Processes in Condensed Matter*: Komura, S., Furukawa, H. (Eds.). New York: Plenum Press, p. 251.
- Konigsveld, R. Kleintjens, L. A., Nies, E. (1987), *Croat. Chem. Acta* 60, 53.
- Konishi, H., Noda, Y. (1988), in: *Dynamics of Ordering Processes in Condensed Matter*: Komura, S., Furukawa, H. (Eds.). New York: Plenum Press, p. 309.
- Kostorz, G. (1988), in: *Dynamics of Ordering Processes in Condensed Matter*: Komura, S., Furukawa, H. (Eds.). New York: Plenum Press, p. 199.
- Kostorz, G. (1991), *J. Appl. Cryst.* 24, 444.
- Kostorz, G. (1994), *Solid-Solid Phase Transformations, PTM'94*: Johnson, W. C., Howe, J. M., Laughlin, D. E., Soffa, W. A. (Eds.). The Metals, Minerals and Materials Society: Warrendale, p. 133.
- Krall, A. H., Sengers, J. V., Hamano, K. (1992), *Phys. Rev. Lett.* 69, 1963.
- Kramer, E. J., Green, P., Palmstrom, C. (1984), *Polymer* 25, 473.
- Krausch, G. (1995), *Mat. Sci. Eng. Rep.* 14, 1.
- Kumaki, J., Hashimoto, T., Granick, S. (1996), *Phys. Rev. Lett.* 77, 1990.
- Kuo, S. Y., Viskar, A. V. (1987), *J. Am. Ceram. Soc.* 70, C125.
- Laberge, C., Fratzl, P., Lebowitz, J. L. (1995), *Phys. Rev. Lett.* 75, 4448.
- Laberge, C., Fratzl, P., Lebowitz, J. L. (1997), *Acta Mater.* 45, 3946.
- Lai, Z. W., Mazenko, G. F., Valls, O. T. (1988), in: *Dynamics of Ordering Processes in Condensed Matter*: Komura, S., Furukawa, H. (Eds.). New York: Plenum Press, p. 45.
- Langer, J. S., Schwartz, A. J. (1980), *Phys. Rev. A* 21, 948.
- Langer, J. S., Baron, M., Miller, H. D. (1975), *Phys. Rev. A* 11, 1417.
- Langmayr, F., Fratzl, P., Vogl, G. (1992), *Acta Metall. Mater.* 40, 3381.
- Larché, F. C., Cahn, J. W. (1982), *Acta Metall.* 30, 1835.
- Laslaz, G., Guyot, P., Kostorz, G. (1977), *J. Phys. (Paris) C* 7, 406.
- Lauger, J., Laubner, C., Gronski, W. (1995), *Phys. Rev. Lett.* 75, 3576.
- Lawrie, I. D., Sarbach, S. (1984), in: *Phase Transitions and Critical Phenomena*, Vol. 9: Domb, C., Lebowitz, J. L. (Eds.). New York: Academic Press, p. 1.
- Lebowitz, J. L. Penrose, O. (1966), *J. Math. Phys.* 7, 98.
- Lebowitz, J. L. Marro, J., Kalos, M. H. (1982), *Acta Metall.* 30, 297.
- Lee, S. K. (1997), *Mater. Sci. Eng. A* 238, 1.
- Lee, S. K. (1998), *Trans. JIM* 39, 114.
- Lefever, R., Carati, D., Hassani, N. (1995), *Phys. Rev. Lett.* 75, 1674.
- Leo, P. H., Lowengrub, J. S., Jou, H. J. (1998), *Acta Mater.* 46, 2113.
- Li, D. Y., Chen, L. Q. (1998), *Acta Mater.* 46, 639.
- Lifshitz, I. M. (1962), *Sov. Phys. JETP* 15, 939.
- Lifshitz, I. M., Slyozov, V. V. (1961), *J. Phys. Chem. Solids* 19, 35.
- Lironis, G., Heermann, D. W., Binder, K. (1989), *J. Phys. A: Math. Gen.* 23, L329.
- Liu, A. J., Durian, D. J., Herbolzheimer, E., Safran, S. A. (1990), *Phys. Rev. Lett.* 65, 1897.
- Livet, F., Bloch, D. (1985), *Scr. Metall.* 10, 19.
- Lopez, V. M., Sano, N., Sakurai, T., Hirano, K. (1993), *Acta Metall. Mater.* 41, 265.
- Luiggi, N., Simon, J. P., Guyot, P. (1980), *Acta Metall.* 28, 1115.
- Lyon, O., Simon, J. P. (1987), *Phys. Rev. B* 35, 5164.
- Maheswari, A., Ardell, A. J. (1993), *Phys. Rev. Lett.* 70, 2305.

- Mainville, J., Yang, Y. S., Elder, K. R., Sutton, M., Ludwig Jr., K. F., Stephenson, G. B. (1997), *Phys. Rev. Lett.* 78, 2787.
- Manning, J. R. (1986), *Diffusion Kinetics for Atoms in Crystals*. Princeton: Van Nostrand.
- Marro, J., Bortz, A. B., Kalos, M. H., Lebowitz, J. L. (1975), *Phys. Rev. B* 12, 2000.
- Marro, J., Lebowitz, J. L., Kalos, M. H. (1979), *Phys. Rev. Lett.* 43, 282.
- Mashiyama, H. (1988), in: *Dynamics of Ordering Processes in Condensed Matter*: Komura, S., Furukawa, H. (Eds.). New York: Plenum Press, p. 355.
- Matsuura, M. (1988), in: *Dynamics of Ordering Processes in Condensed Matter*: Komura, S., Furukawa, H. (Eds.). New York: Plenum Press, p. 349.
- Mazenko, G. F. (1994), *Phys. Rev. E* 50, 3485.
- Mazenko, G. F. (1998), *Phys. Rev. E* 58, 1543.
- Mazenko, G. F., Wickham, E. (1995), *Phys. Rev. E* 51, 2886.
- Mcdevitt, T. L., Mahajan, S., Laughlin, D. E., Bonner, W. A., Keramidas, V. G. (1992), *Phys. Rev. B* 45, 6614.
- McPherson, R. (1987), *J. Mater. Sci. Lett.* 6, 795.
- Meakin, P., Metiu, H., Petschek, R. G., Scalapino, D. J. (1983), *J. Chem. Phys.* 69, 1948.
- Meier, H., Strobl, G. R. (1988), *Macromolecules* 20, 649.
- Milchev, A., Heermann, D. W., Binder, K. (1988), *Acta Metall.* 36, 377.
- Mirolid, P., Binder, K. (1977), *Acta Metall.* 25, 1435.
- Monette, L., Liu, A. J., Grest, G. S. (1992), *Phys. Rev. A* 46, 7664.
- Morii, Y., Gaulin, B. D., Spooner, S. (1988), in: *Dynamics of Ordering Processes in Condensed Matter*: Komura, S., Furukawa, H. (Eds.). New York: Plenum Press, p. 239.
- Mouritsen, O. G. (1986), *Phys. Rev. Lett.* 56, 850.
- Mouritsen, O. G., Praestgaard, E. (1988), *Phys. Rev. B* 38, 2703.
- Mukherjee, S., Cooper, B. R. (1998), *Mat. Sci. Eng.* A 248, 101.
- Müller-Krumbhaar, H. (1974), *Phys. Lett.* 50A, 27.
- Nattermann, T. (1998), in: *Spin Glasses and Random Fields*: Young, A. P. (Ed.). Singapore: World Scientific, p. 277.
- Nielaba, P., Fratzl, P., Lebowitz, P. (1999), *J. Stat. Phys.* 95, 23.
- Nishihara, S., Noda, Y., Yamada, Y. (1982), *Solid State Commun.* 44, 1487.
- Nishimori, H., Onuki, A. (1990), *Phys. Rev. B* 42, 980.
- Noda, Y. (1988), in: *Dynamics of Ordering Processes in Condensed Matter*: Komura, S., Furukawa, H. (Eds.). New York: Plenum Press, p. 373.
- Noda, Y., Nishihara, S., Yamada, Y. (1984), *J. Phys. Soc. Jpn.* 53, 4241.
- Nose, T. (1987), *Phase Transit.* 8, 245.
- Ohta, T. (1984), *Prog. Theor. Phys.* 71, 1409.
- Ohta, T., Nozaki, H. (1989), preprint referred to by Bates and Wiltzius (1989).
- Ohta, T., Enomoto, Y., Kawasaki, K., Sato, A. (1988), in: *Dynamics of Ordering Processes in Condensed Matter*: Komura, S., Furukawa, H. (Eds.). New York: Plenum Press, p. 127.
- Ohta, T., Jasnow, D., Kawasaki, K. (1982), *Phys. Rev. Lett.* 49, 1223.
- Okada, M., Han, C. C. (1986), *J. Chem. Phys.* 85, 5317.
- Oki, K., Hasaka, M., Eguchi, T. (1973), *Jpn. J. Appl. Phys.* 12, 1522.
- Okumura, H., Inoue, A., Masumoto, T. (1993), *Acta Metall. Mater.* 41, 915.
- Onodera, Y., Hirano, K. (1986), *J. Mater. Sci. Lett.* 5, 1048.
- Onodera, Y., Hirano, K. (1988), in: *Dynamics of Ordering Processes in Condensed Matter*: Komura, S., Furukawa, H. (Eds.). New York: Plenum Press, p. 293.
- Onuki, A. (1984), *Phys. Lett. A* 101, 286.
- Onuki, A. (1986a), *Phys. Rev. A* 34, 3528.
- Onuki, A. (1986b), *J. Chem. Phys.* 85, 1122.
- Onuki, A. (1989a), *J. Phys. Soc. Japan* 58, 3065.
- Onuki, A. (1989b), *J. Phys. Soc. Japan* 58, 3069.
- Onuki, A. (1989c), *Int. J. Thermophys.* 10, 293.
- Onuki, A. (1997), *J. Phys.: Condens Matter* 9, 6119.
- Onuki, A., Kawasaki, K. (1978), *Prog. Theor. Phys. Suppl.* 64, 436.
- Onuki, A., Kawasaki, K. (1979), *Ann. Phys.* 121, 456.
- Onuki, A., Nishimori, H. (1991), *Phys. Rev. B* 43, 13649.
- Onuki, A., Yamamoto, R., Taniguchi, T. (1997), *Phys. II (France)* 7, 295.
- Oono, Y., Puri, S. (1988), *Phys. Rev. A* 38, 434.
- Orlikowski, D., Sagui, C., Somoza, A., Roland, C. (1999), *Phys. Rev. B* 59, 8646.
- Osamura, K. (1988), in: *Dynamics of Ordering Processes in Condensed Matter*: Komura, S., Furukawa, H. (Eds.). New York: Plenum Press, p. 187.
- Paris, O., Fährmann, M., Fratzl, P. (1995), *Phys. Rev. Lett.* 75, 3458.
- Paris, O., Fährmann, M., Fährmann, E., Pollock, T. E., Fratzl, P. (1997), *Acta Mater.* 45, 1085.
- Penrose, O., Lebowitz, J. L. (1971), *J. Stat. Phys.* 3, 211.
- Perrot, F., Guenoun, P., Baumberger, T., Beysens, D., Garrabos, Y., Lenemdre, B. (1994), *Phys. Rev. Lett.* 73, 688.
- Pincus, P. (1981), *J. Chem. Phys.* 75, 1996.
- Pine, D. J., Easwer, N., Maher, J. V., Goldburg, W. I. (1984), *Phys. Rev. A* 29, 308.
- Pistoor, N., Binder, K. (1988a), *Colloid Polym. Sci.* 266, 132.
- Pistoor, N., Binder, K. (1988b), in: *Polymer Motion in Dense Systems*: Richter, D., Springer, T. (Eds.). Berlin: Springer, p. 285.
- Porod, G. (1951), *Kolloid Z.* 124, 83; 125, 51.
- Puri, S., Dünweg, B. (1992), *Phys. Rev. A* 45, R6977.
- Puri, S., Frisch, H. L. (1997), *J. Phys.: Cond. Matt.* 9, 2109.

- Puri, S., Oono, Y. (1988), *Phys. Rev. A* 38, 1542.
- Puri, S., Bray, A. J., Lebowitz, J. L. (1997), *Phys. Rev. E* 56, 758.
- Rao, M., Marro, J., Kalos, M. H., Lebowitz, J. L. (1976), *Phys. Rev. B* 13, 2000.
- Rikvold, P. A., Gunton, J. D. (1982), *Phys. Rev. Lett.* 49, 226.
- Rogers, T. M., Desai, R. C. (1989), *Phys. Rev. B* 39, 11956.
- Rogers, T. M., Elder, K. R., Desai, R. C. (1988), *Phys. Rev. B* 37, 9638.
- Rouse, P. E. (1953), *J. Chem. Phys.* 21, 1273.
- Sadiq, A., Binder, K. (1984), *J. Stat. Phys.* 35, 517.
- Sagui C., Somoza, A. M., Desai, R. (1994), *Phys. Rev. E* 50, 4865.
- Sahni, P. S., Gunton, J. D. (1980), *Phys. Rev. Lett.* 45, 369.
- Sahni, P. S., Gunton, J. D., Katz, S., Timpe, R. (1982), *Phys. Rev. B* 25, 389.
- San Miguel, M., Gunton, J. D., Dee, G., Sahni, P. S. (1981), *Phys. Rev. B* 23, 2334.
- San Miguel, M., Grant, M., Gunton, J. D. (1985), *Phys. Rev. A* 31, 1001.
- Sariban, A., Binder, K. (1989a), *Polym. Commun.* 30, 205.
- Sariban, A., Binder, K. (1989b), *Colloid Polym. Sci.* 267, 469.
- Sato, R., Han, C. C. (1988), *J. Chem. Phys.* 88, 2057.
- Schätzle, K., Ackerson, B. J. (1993), *Phys. Rev. E* 48, 3766.
- Scher, M., Zallen, R. (1970), *J. Chem. Phys.* 53, 3759.
- Schmitz, G., Hono, K., Haasen, P. (1994), *Acta Metall. Mater.* 42, 201.
- Selke, W. (1987), *J. Phys. B* 20, L455.
- Sequeira, A. D., Calderon, M. A., Kosterz, G., Pedersen, J. S. (1995), *Acta Metall. Mater.* 43, 3427; 3441.
- Shinozaki, A., Oono, J. (1993), *Phys. Rev. E* 48, 2622.
- Sigga, E. (1979), *Phys. Rev. A* 20, 595.
- Simon, J. P., Guyot, P., Ghilarducca de Silva (1984), *Philos. Mag.* A49, 151.
- Singhal, S. P., Herman, H., Kosterz, G. (1978), *J. Appl. Crystallogr.* 11, 572.
- Sinha, D. N., Hoffer, J. K. (1981), *Physica* 107B, 157.
- Snyder, H. L., Meakin, P. (1983), *J. Chem. Phys.* 79, 5588.
- Srolovitz, D. J., Grest, G. S. (1985), *Phys. Rev. B* 32, 3021.
- Stanley, H. E. (1971), *An Introduction to Phase Transitions and Critical Phenomena*. Oxford: Oxford University Press.
- Stauffer, D. (1985), *An Introduction to Percolation Theory*. London: Taylor and Francis.
- Stauffer, D., Ferer, M., Wortis, M. (1972), *Phys. Rev. Lett.* 29, 245.
- Stephenson, G. B., Warburton, W. K., Haller, W., Bienenstock, A. (1991), *Phys. Rev. B* 43, 3417.
- Su, C. H., Voorhees, P. W. (1996), *Acta Mater.* 44, 1987; 2001.
- Sur, A., Marro, J., Lebowitz, J. L., Kalos, M. H. (1977), *Phys. Rev. B* 15, 535.
- Takahashi, J., Kuwayama, M., Kamiya, H., Takatsu, M. (1988), *Mater. Sci.* 23, 337.
- Takeda, S., Kulik, J., De Fontaine, D. (1987), *Acta Metall.* 35, 2243.
- Tanaka, H. (1993), *Phys. Rev. Lett.* 70, 53.
- Tanaka, H. (1994), *J. Chem. Phys.* 100, 5323.
- Tanaka, H. (1996), *Phys. Rev. Lett.* 76, 787.
- Taniguchi, T., Onuki, A. (1996), *Phys. Rev. Lett.* 77, 4910.
- Tokuyama, M., Enomoto, Y. (1993), *Phys. Rev. E* 47, 1156.
- Tokuyama, M., Enomoto, Y., Kawasaki, K. (1987), *Physica A* 143, 187.
- Tomita, H. (1984), *Prog. Theor. Phys.* 71, 1405.
- Tomokiyoy, Y., Yahiro, K., Matsumura, S., Oki, K., Epudi, T. (1988), in: *Dynamics of Ordering Processes in Condensed Matter*: Komura, S., Furukawa, H. (Eds.). New York: Plenum Press, p. 233.
- Tomozawa, M., MacCrone, R. K., Herman, H. (1970), *Phys. Chem. Glasses* 11, 136.
- Toral, R., Chakrabarti, A., Gunton, J. D. (1988), *Phys. Rev. Lett.* 60, 2311.
- Tringides, M. C., Wu, P. K., Moritz, W., Lagally, M. G. (1986), *Ber. Bunsenges. Phys. Chem.* 90, 277.
- Tringides, M. C., Wu, P. K., Lagally, M. G. (1987), *Phys. Rev. Lett.* 59, 315.
- Unger, C., Klein, W. (1984), *Phys. Rev. Lett.* B29, 2698.
- Valls, O. T., Farrell, J. E. (1993), *Phys. Rev. E* 47, R36.
- Villain, J. (1985), in: *Scaling Phenomena in Disordered Systems*: Pynn, R., Skjeltorp, A. (Eds.). New York: Plenum, p. 423.
- Villain, S. (1986), *Europhys. Lett.* 2, 531.
- Wagner, C. (1961), *Z. Elektrochem.* 65, 243.
- Wagner, R., Kampmann, R., Voorhees, P. W. (2001), in: *Phase Transformations in Materials*: Kosterz, G. (Ed.). Weinheim: Wiley-VCH, Chap. 5.
- Wang, Y., Khachaturyan, A. G. (1995), *Acta Metall. Mater.* 43, 1837.
- Wang, G. C., Lu, T. M. (1983), *Phys. Rev. Lett.* 50, 2014.
- Wang, Y., Chen, L. A., Khachaturyan, A. G. (1992), *Phys. Rev.* 46, 11194.
- Wang, Y., Chen, L. A., Khachaturyan, A. G. (1993), *Acta Metall. Mater.* 41, 279.
- Wang, Y., Banarjee, D., Su, C. C., Khachaturyan, A. G. (1998a), *Acta Mater.* 46, 2983.
- Wang, W. H., Wei, Q., Friedrich, S. (1998b), *Phys. Rev. B* 57, 8211.
- Weinkamer, R., Gupta, H., Fratzl, P., Lebowitz, J. L. (2000), *Europhys. Lett.* 52, 224.
- Wilcoxon, J. P., Schaefer, D. W., Kaler, E. W. (1988), *Phys. Rev. Lett.* 60, 333.
- Wilcoxon, J. P., Martin, J. E., Odinek, J. (1995), *Phys. Rev. Lett.* 75, 1558.
- Wiltzius, P., Bates, F. S., Dierker, S. B., Wignall, G. D. (1987), *Phys. Rev. A* 36, 2991.

- Wong, N. C., Knobler, C. M. (1978), *J. Chem. Phys.* 69, 725.
- Wong, N. C., Knobler, C. M. (1979), *Phys. Rev. Lett.* 43, 1733.
- Wong, N. C., Knobler, C. M. (1981), *Phys. Rev. A* 24, 3205.
- Wortis, M. (1985), in: *Fundamental Problems in Statistical Physics*, Vol. VI: Cohen, E. G. D. (Ed.). Amsterdam: North-Holland, p. 87.
- Wu, P. K., Perepezko, J. H., McKinney, J. T., Lagally, M. G. (1983), *Phys. Rev. Lett.* 51, 1577.
- Wu, P. K., Tringides, M. C., Lagally, M. G. (1989), *Phys. Rev. B* 39, 7595.
- Yagi, T., Lu, Z.-L. (1988), in: *Dynamics of Ordering Processes in Condensed Matter*: Komura, S., Furukawa, H. (Eds.). New York: Plenum Press, p. 343.
- Yaldram, K., Binder, K. (1991), *J. Stat. Phys.* 63, 161.
- Yeung, C. (1988), *Phys. Rev. Lett.* 61, 1135.
- Yokota, H. (1978), *J. Phys. Soc. Jpn.* 45, 29.
- Zarzycki, J., Naudin, F. (1969), *J. Non-Cryst. Solids.* 1, 215.
- Zettlemoyer, A. C. (1969), *Nucleation*. New York: Dekker.
- Zhang, Z., Chakrabarti, A. (1994), *Phys. Rev. E* 50, R4290.
- Zhang, Z., Chakrabarti, A. (1995), *Phys. Rev. E* 52, 2736.
- Zuo, J.-K., Wang, G.-C., Lu, T. M. (1989), *Phys. Rev. B* 40, 524.

7 Transformations Involving Interfacial Diffusion

Gary R. Purdy

Department of Materials Science and Engineering, McMaster University, Hamilton,
Ontario, Canada

Yves J. M. Bréchet

Laboratoire de Thermodynamique et Physico-Chimie Métallurgiques, E.N.S.E.E.G.,
Institut National Polytechnique de Grenoble, France

List of Symbols and Abbreviations	482
7.1 Introduction	484
7.2 Equilibrium Properties of Solid–Solid Interfaces	484
7.2.1 Structures of Grain Boundaries	484
7.2.2 Structures of Interphase Boundaries	486
7.2.3 Segregation to an Interface	489
7.3 Interfacial Diffusion	490
7.4 Forces for Interface Migration	492
7.4.1 Capillary Forces	492
7.4.2 Chemical Forces	493
7.4.3 Mechanical Forces	493
7.4.3.1 Elastic Strain Energy	493
7.4.3.2 Plastic Response	494
7.4.4 Frictional Forces	496
7.4.4.1 Solute Drag	496
7.4.4.2 Particle Pinning	498
7.5 Examples	498
7.5.1 The Massive Transformation	498
7.5.2 Chemically-Induced Grain Boundary Migration	503
7.5.3 Discontinuous Precipitation	504
7.5.3.1 Initiation of Discontinuous Precipitation	505
7.5.3.2 Theories of Steady Cooperative Growth	507
7.5.3.3 Experimental Observations	510
7.5.4 Interface Migration in Multilayers	514
7.6 Conclusions	516
7.7 References	516

List of Symbols and Abbreviations

A	interfacial area
b	magnitude of the Burgers vector
C_0	average concentration
C_α	concentration
ΔC	local difference from the average concentration C
D	diffusion constant
D_V/v	ratio of the volume diffusion constant and the interfacial velocity
\bar{D}^b	average grain boundary diffusion coefficient
dE/dx	measure of force between solute atoms and boundary
ΔF_{ch}	molar Helmholtz energy change accompanying complete transformation
$\Delta F'_{ch}$	molar Helmholtz energy difference across an interface
ΔF^0_{ch}	fraction of the total available Helmholtz energy dissipated in volume diffusion
$f(C)$	Helmholtz energy density functional
f_0	measure of curvature of Helmholtz energy–composition relationship
g_B	shear modulus
H	$3\kappa_\alpha/(3\kappa_\alpha + 4g_B)$
J_B	flux of solute atoms
$K = dA/dV$	interface curvature
L	half-thickness of a foil specimen
L_0^α, L_0^β	regular solution parameters for the crystal and boundary phases
l	correlation length
M	mobility
N_V	number of atoms per unit volume
n_A^α	mole number
p_{ch}	interfacial driving force/chemical force
p_η	residual chemical force derived from coherency strain
p_i	solute drag force
p_w	virtual mechanical force
r_1, r_2	radii of curvature
r_i	radius of facet
S	spacing between precipitate lamellae
s	equilibrium ratio of solute concentration in a grain boundary and that in adjacent crystal
T/T_m	reduced temperature
T_m	melting temperature
v	boundary velocity
V_f	volume fraction of a precipitate
V_m	molar volume
V_m^b	molar volume of the boundary phase
W	applied load per unit area
x, y, z	coordinates
Y	elastic constant
Z	applied tensile stress

α	crystalline phase
α, β	included, external phase
γ_α	activity coefficient
Γ_B	surface excess concentration of solute B per unit area
δ	boundary thickness
ε	misfit
ε_α	interaction parameter; a measure of the non-ideality of the α solid solution
η	coefficient of lattice parameter change with composition
θ	angle of tilt
κ	gradient energy coefficient
κ_α	bulk modulus of precipitate
λ	spacing of parallel edge dislocations
μ_A, μ_B	solvent, solute chemical potentials
Ω	alignment parameter
σ	specific interfacial Helmholtz energy
σ_A, σ_B	specific grain boundary Helmholtz energy in pure A, B
$\sigma_{\alpha\beta}$	specific interfacial Helmholtz energy of α/β interface
ϕ	phase field parameter
ψ	order parameter
b.c.c.	body-centered cubic
CIGM	chemically induced grain boundary migration
DP	discontinuous precipitation
DC	discontinuous coarsening
f.c.c.	face-centered cubic
h.c.p.	hexagonal close-packed
STEM	scanning transmission electron microscopy

7.1 Introduction

Many microstructure-determining reactions in solids are similar in the sense that they occur primarily at an interface, which traverses a volume of solid material, and leaves that volume altered structurally or chemically, or both. Indeed, most solid–solid transformations fall into this set; in this chapter, we will restrict discussion in the following ways:

1) We will consider only those processes whose main characteristics are determined by diffusion within the transformation front, which may be a grain boundary or an interphase boundary.

2) We will further restrict attention to processes that begin mainly at crystal boundaries, and that lead to heterogeneously transformed regions. This restriction implies that the transformation interface will be of relatively high energy, and therefore that the transformation will often be initiated with some difficulty.

The subset defined above excludes those homogeneous transformations which are initiated everywhere within a parent crystal (Chap. 5; Wagner et al., 2001), and truly diffusionless transformations (Chap. 9; Delaey, 2001). However, the massive transformation survives, as do the processes of peritectoid precipitation, chemically induced grain boundary migration, and discontinuous precipitation. The latter two (and similar diffusional processes) are the subject of an excellent monograph by Pawlowski and Zięba (1991), which is, unfortunately, not widely available. It has recently been observed that the study of these and similar phenomena may be advanced through the use of artificially prepared multilayered structures (Klinger et al., 1997b, c, 1998), which may be subject, for example, to discontinuous homogenization

or to interfacial precipitation. Before discussing these processes, a brief review will be given of the equilibrium properties of transformation interfaces and of the dynamics of interfacial diffusion and interface migration.

7.2 Equilibrium Properties of Solid–Solid Interfaces

7.2.1 Structures of Grain Boundaries

Grain boundaries constitute a well studied class of solid state defects which are structural in nature, and which depend for their existence on a misorientation between otherwise identical crystals. If we restrict attention to macroscopic variables only, the properties of a planar boundary are expected to depend on five geometric variables, three of which define the relative orientations of the two crystals, and a further two are required to specify the orientation of the boundary plane. Three additional degrees of freedom, associated with sublattice translations, exist on the microscopic scale appropriate to the modeling of grain boundary structure.

Much of what is known or inferred about grain boundary structure is obtained from simulations using molecular statics or molecular dynamics, supported in some cases by high resolution microscopic techniques (Smith, 1986).

The three main modeling techniques that have been used for surfaces, grain boundaries and (to a lesser extent) interphase boundaries, are energy relaxation methods, molecular dynamics, and Monte Carlo simulations (Sutton and Balluffi, 1995). The information expected from these simulations concerns both the structural aspects (molecular relaxation, molecular dynamics), chemical aspects such as segregation

(Monte Carlo), and dynamic aspects such as diffusion (molecular dynamics). The structural information stemming from these methods is very much dependent on the interatomic potential chosen, and especially on the anharmonic part, since the structure of the interface is usually rather distorted. The dynamic aspects of interfaces include the interface diffusivity and the interface mobility. While the diffusivity is accessible to these simulations (via molecular dynamics), the mobility is more of a problem, because the system size is typically constrained by available computational resources. This imposes, for example, very large curvatures as driving forces, and results in high interface velocities which might not be realistic reflections of experimental situations (Sutton, 1995).

The chemical aspects accessible to Monte Carlo simulation also possess two facets: the thermodynamic equilibrium to be attained and the kinetics required to reach it. Provided that the interatomic potential is reliable, the Monte Carlo method gives an accurate description of chemical segregation (Treglia and Legrand, 1998). However, the simulation of the kinetics needed to reach this state encounters a new problem of coupling the bulk diffusion to the diffusion close to the interface. Monte Carlo simulations with time residence algorithms (Martin et al., 1998) have allowed the inclusion of the role of vacancies in bulk diffusion, but the treatment of vacancies in solids with free surfaces or internal interfaces remains a source of problems (Delage, 1998).

The whole field of surface and interface thermodynamics and kinetics of metallic alloys with tendencies to ordering or unmixing has profited from Monte Carlo simulations. The next step (to introduce simultaneous structural relaxations and chemical aspects, e.g., via off-lattice

Monte Carlo methods) still requires further development.

A surprisingly large amount of our information relates to a rather special kind of interface, the symmetric tilt grain boundary. As suggested by Fig. 7-1, low angle boundaries are made up of arrays of dislocations, and the low angle symmetric tilt boundary is composed of parallel edge dislocations, whose spacing λ is given by

$$\lambda = b/2 \sin(\theta/2) \quad (7-1)$$

where b is the magnitude of the Burgers vector, and θ the angle of tilt. Studies by Krakow et al. (1986) suggest that this description in terms of individual dislocations can be extrapolated, with some modification, to high angles, e.g., to 26.5° . More generally, the grain boundary region is expected to possess the following characteristics:

a) The high angle grain boundary is thin, perhaps two or three atomic diameters in width. To a first approximation, it may be considered a high energy “phase”, constrained to have constant volume.

b) The high angle grain boundary is periodic in structure, like its low angle counterpart. The geometric repeating units are not

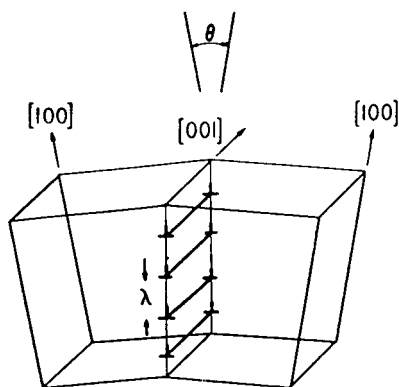


Figure 7-1. A symmetric low angle tilt grain boundary. The tilt angle θ and the edge dislocation spacing λ are related by Eq. (7-1).

lattice dislocations, but are capable of description in terms of nearly perfect compact polyhedra (Ashby et al., 1979). Departures from symmetric orientations are often accommodated by mixing two or more types of structural units within the boundary. It is the view of Sutton and Balluffi (1987) that no general criterion for low grain boundary energy can be developed on the basis of simple geometry.

c) Metastable states, and even degenerate states of different structure but identical energy, may be formed by the relative microscopic translation of one of the crystals (Vitek, 1984).

The computed structures are of great conceptual value, yielding information that is inaccessible or accessible only with difficulty through experiment; they should be treated with a measure of caution however, as the computed results depend to some extent on the choice of potential. Further, many (but not all) of these simulations are performed for a temperature of 0 K. Nevertheless, in combination with experiment, they form a valuable tool in the study of this complex field.

7.2.2 Structures of Interphase Boundaries

These internal surfaces, unlike grain boundaries, are necessary elements of an equilibrium multiphase system; they are not defects. They separate phases which in general may differ both chemically and structurally from one another.

The description of an interface using continuum concepts dates from the seminal papers by Cahn and Hilliard (1958) and Allen and Cahn (1977). The Cahn–Hilliard model of a stationary coherent interphase boundary is illustrated in Fig. 7-2. The Cahn–Hilliard and Allen–Cahn treatments deal with two broad cases involving conserved and non-conserved order param-

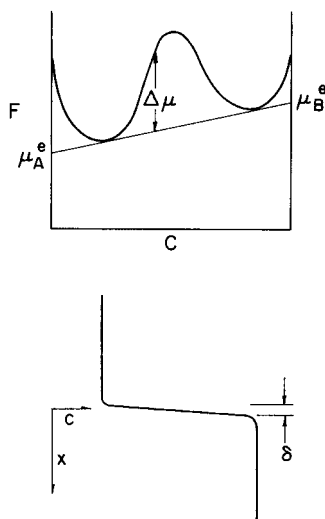


Figure 7-2. Top: A schematic concentration (C) profile through a diffuse coherent interface (components A and B) in which excess chemical Helmholtz energy, represented by the quantity $\Delta\mu$, is everywhere balanced against gradient Helmholtz energy (F : Helmholtz energy, μ_A^e and μ_B^e : equilibrium chemical potentials). Bottom: Finite thickness δ of equilibrium interface, corresponding to concentration profile.

ters. The first applies to chemically heterogeneous solids, and the second to structurally heterogeneous materials. The first allows us to derive a diffusion equation for the evolution of concentrations, and the other an equation for the evolution of order parameters. These two classes of problems, coupled with intermediate situations, cover the range of problems involving relaxed interfaces.

The overall method is to write a Helmholtz energy functional involving not only the dependence of the local composition C or order parameter ψ , labeled $f(C, \psi)$, but also those gradient terms compatible with the symmetry of the problem. This leads to terms in $(\nabla C)^2$ or $(\nabla \psi)^2$. The interfacial energy between the two regions of different prescribed order parameter or composition is then computed in two steps: the concentration or order parameter which minimizes

the excess Helmholtz energy is computed, and this excess energy is then taken as the interfacial energy. In a single model we therefore get both a “continuum structure” for the interface, and the specific interfacial Helmholtz energy.

The time-dependent version of these equations allows us to treat the motion of the interface under a prescribed driving force, provided that a relation is assumed between the fluxes and the driving forces.

For a conserved order parameter C (such as concentration), the kinetic equation takes the form:

$$\frac{\partial C}{\partial t} = M [\nabla^2 f(C) - \kappa^2 \nabla^4 C] \quad (7-2)$$

where κ is a gradient energy coefficient, and for a non-conserved order parameter (such as a long-range order parameter, or a crystal orientation), we obtain:

$$\frac{\partial \psi}{\partial t} = M [\kappa^2 \nabla^2 \psi - f'(\psi)] \quad (7-3)$$

The interfacial Helmholtz energy for a diffuse interface between two concentrations C_1 and C_2 is given by

$$\sigma = 2 N_v \int_{C_1}^{C_2} \kappa^2 f(C) dC \quad (7-4)$$

Similarly, assuming a quadratic expansion of the Helmholtz energy with two minima for order parameters $\psi = 1$ and $\psi = -1$ gives the following expression for the interfacial Helmholtz energy of an antiphase boundary:

$$\sigma = \frac{8}{3} N_v \sqrt{\kappa^2 f''} \quad (7-5)$$

In each case, the width of the interface scales as $\kappa/f^{1/2}$: the stronger the gradient term compared with the local chemical Helmholtz energy contribution, the more diffuse will be the interface. The “structural width” of

the interfaces is thus related to the coupling term weighting the square gradients.

These continuum descriptions are in principle well suited for application to diffuse interfaces. Their facility of implementation in computer simulations (since they do not involve front tracing methods) has triggered much interest under the name of “phase field approaches” (Carter et al., 1997). They have recently been applied to various problems involving sharp interfaces using the following systematics: the interface is artificially made diffuse with respect to a “phase field parameter” ϕ . (For instance, this parameter can be taken equal to 1 in a solid and to 0 in a liquid if we wish to address a solidification problem involving both solute and heat flow (Wheeler et al., 1992). It can be taken to vary continuously from +1 to –1 through a grain boundary, mimicking the orientation change across the boundary for application to a problem in grain growth (Chen et al., 1998).) A Helmholtz energy equation is proposed which involves both the concentration and the phase field parameter and their spatial derivatives. The dynamic equations for the concentrations and the phase fields are solved using continuum methods and the coupling term containing the phase field gradient is set equal to zero so that the sharp interface can be recovered.

These methods have been applied to solidification, phase transformations, grain growth, and chemically induced grain boundary migration. They possess the advantage of relative ease of implementation using classical numerical techniques, and a great flexibility in terms of the introduction of such features as anisotropy. They share the drawback of all Ginzburg–Landau type phenomenological equations, i.e., that the precise atomistic interpretation of both the mobility and the coupling terms is not always clear.

When a structural difference coexists with the chemical difference, the situation becomes more complex. However, if the difference between phases is small, as is the case for structurally similar phases with similar orientations and lattice parameters, the differences may be accommodated by an elastic component or by an array of misfit dislocations. In the case of γ precipitates in β brass, the interfacial energy has been taken as the sum of structural (dislocation) and chemical energies. This approach permits the prediction of weak anisotropies, for example those in Fig. 7-3, after Stephens and Purdy (1975).

More complex systems, e.g., interfaces joining f.c.c. and b.c.c. phases, are generally discussed with respect to a particular

orientation relationship or set of orientation relations, considered to be established at nucleation. In these cases, we search for a reason for the strong anisotropy of interfacial Helmholtz energy commonly observed in such systems. The most plausible approach involves the search for optimum matching of atomic positions at the interface, that is a maximum in coherency, corresponding to a minimum in the structural component of the energy. A particularly simple example is found in the f.c.c./h.c.p. system Al–Ag, where the (111) f.c.c. habit plane corresponds to the structurally similar (001) h.c.p.

Figure 7-4 illustrates a model of the f.c.c./b.c.c. interface due to Rigsbee and Aaronson (1979), in which a macroscopically irrational habit plane interface is made up of rational areas with a high degree of coherency, separated by “structural ledges” which serve to displace the interface plane by a few atomic dimensions, thereby to increase the degree of coherency. Aaronson and his co-workers emphasize that these structural ledges are considered intrinsic to the structure of the interface, and do not provide a mechanism for interface motion. Other studies have utilized a more formal geometrical approach (Bollman, 1970; Dahmen, 1981; Zhang and Purdy, 1993 a, b) to seek interfaces of optimal matching, with similar conclusions. Based on evidence from high resolution electron microscopy (e.g., Zhang et al., 1998), it has become apparent that the typical interface between phases of dissimilar structure is often faceted on a microscopic scale, and that invariant planes or invariant lines of the transformation, when they exist, are clearly important in the selection of precipitate habits.

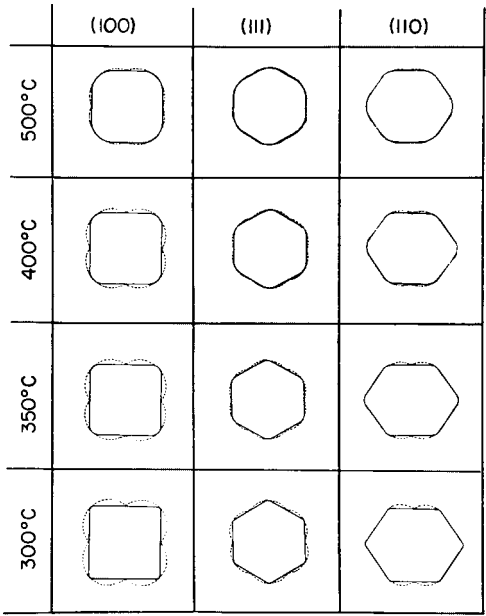


Figure 7-3. The morphologies of equilibrated γ precipitates (solid curves) formed in β brass, and the corresponding Wulff plots (dashed), for the temperatures indicated. The anisotropies are consistent with a model that treats the interfacial Helmholtz energy as a sum of structural (dislocation) and chemical terms (Stephens and Purdy, 1975).

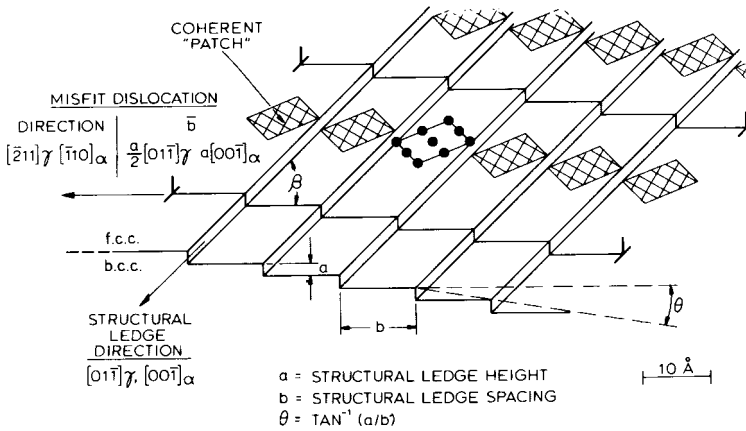


Figure 7-4. Rigsbee and Aaronson's model for the f.c.c./b.c.c. interface, in which structural ledges are introduced which maximize the degree of coherence within the interface. Reprinted with permission from Rigsbee and Aaronson (1979), copyright Pergamon Press.

7.2.3 Segregation to an Interface

In system of two or more components, it is often found that the equilibrium composition at an internal surface is different from that of the surrounding phase(s). As before, it is necessary to distinguish between grain and interphase boundaries; for the case of a grain boundary in a two-component solid solution, we may consider that the high energy defect has its own thermodynamic solution properties. A constrained equilibrium is then possible between the boundary “phase”, which must have an approximately fixed volume, and the adjacent crystalline phase (α). The constant volume condition requires, for a virtual change in mole number n_A^α ,

$$\begin{aligned} \delta n_A^\alpha &= -\delta n_A^b; & \delta n_A^b &= -\delta n_B^b; \\ \delta n_B^b &= -\delta n_B^\alpha \end{aligned} \quad (7-6)$$

and the constrained equilibrium is defined by a line tangential to the α Helmholtz-energy curve at the bulk composition C_0 , and a parallel line tangential to the boundary Helmholtz-energy curve (Hillert, 1975a). This is illustrated in Fig. 7-5. We then obtain for the distribution coefficient

$$s = \frac{C_B^b}{C_B^\alpha} \quad (7-7)$$

$$\ln s = \frac{(\sigma_B - \sigma_A) V_m^b}{RT\delta} + \frac{L^\alpha - L^b}{RT} \quad (7-8)$$

where σ_A and σ_B are the specific grain boundary Helmholtz energies in pure A and B, V_m^b the molar volume of the boundary “phase”, and L^α and L^b the regular solution parameters for the crystal and boundary phases, respectively.

A more comprehensive treatment of phase equilibria of grain boundary structures is given by Cahn (1982). The possibility of faceting transitions is highlighted in this work and supported experimentally by the studies of Ferrence and Balluffi (1988) and Hsieh and Balluffi (1989).

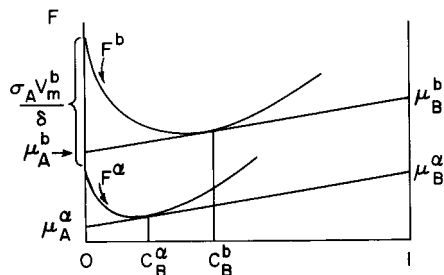


Figure 7-5. Graphical interpretation of the constrained equilibrium between a crystalline solid solution, α , and a grain boundary phase, b . (For details see text.)

For interphase boundaries, segregation is also expected, as first shown by Gibbs (1906). His expression for the relationship between the rate of change of interfacial Helmholtz energy with bulk composition and the interface excess solute concentration, Γ_B , the Gibbs absorption isotherm, may be written as

$$d\sigma = -\Gamma_B d\mu_B \quad (7-9)$$

where Γ_B is the surface excess concentration of solute B per unit area of interface. (The solvent surface excess is zero by definition.)

A growing body of experimental evidence demonstrates that both grain boundaries and interphase boundaries are generally sites for complex interactions among chemical species. Guttman (1995) has reviewed the elementary mechanisms of intergranular segregation in multi-component systems, and concludes that site competition, as well as attractive and repulsive chemical interactions, are all important in determining the degree of interfacial segregation.

7.3 Interfacial Diffusion

Solid–solid interfaces often provide exceptionally rapid paths for diffusion. Provided that there is a significant structural difference, so that there is a disordered region linking nearly perfect crystalline regions, this is easy to understand in broad terms. The mechanisms and the details of grain and interphase boundary diffusion are not fully understood at present, although there exists a wealth of experimental information on the former. The reviews by Peterson (1983) and Kaur and Gust (1988) for grain boundary diffusion, and that of LeClaire (1986) for the related problem of diffusion along dislocations are recommended.

Grain boundary diffusion is commonly investigated experimentally in one of two ways:

a) “Random” polycrystalline specimens are exposed to a source of diffusant (e.g., a planar plated or implanted layer), annealed, then serially sectioned. If the diffusant is a tracer, the technique can be used to give a sensitive evaluation of the product $\bar{D}^b \delta$, where \bar{D}^b is the average grain boundary diffusion coefficient, and δ the boundary thickness, assumed to represent a region of uniformly enhanced diffusivity. If a solute is diffused into the polycrystal, the usual experimentally accessible quantity is the product $\{s \bar{D}^b \delta\}$ (Levine and MacCallum, 1960). It is only in exceptional cases, where the volume diffusion contribution to some part of the penetration profile is negligible (type “C” behavior) that we can obtain in principle a more direct evaluation of the boundary diffusivity.

b) Bicrystals of controlled misorientation are sectioned such that the grain boundary plane is perpendicular to a source of diffusant, which may be of constant composition, or finite. In most cases, as above, both volume diffusion and boundary diffusion will contribute to the penetration profile, as schematized in Fig. 7-6. In this more controlled case, the mathematical solutions of Whipple (1954) or Suzuoka (1964) (depending on whether the source is fixed in composition or finite) are used to unfold the grain boundary transport coefficient from serial sectioning data. The difference here lies in the opportunity to correlate misorientation (and, by inference, structure) with diffusion rates. Again, a large amount of precise data has been acquired, mainly for the special case of the symmetric tilt boundary. This was reviewed by Peterson (1983).

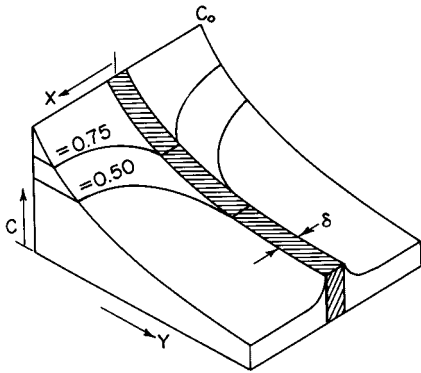


Figure 7-6. Schematic composition (C) distribution in the neighborhood of a grain boundary, normal to a surface of fixed composition, C_0 . δ : boundary thickness.

From the consideration of grain boundary diffusion data for metals, we can draw a few general conclusions:

a) The activation enthalpy for grain boundary self-diffusion is of the order of half that for volume diffusion. Indeed, a good empirical correlation exists between grain boundary diffusivity and reduced temperature T/T_m for different metal structures. For f.c.c. metals, Gust et al. (1985) obtained

$$\delta \bar{D}^b = 9.7 \times 10^{-15} \exp(-9.07 T_m/T) \text{ m}^3/\text{s} \quad (7-10)$$

b) For the low angle symmetric tilt boundary, rates of diffusion are anisotropic, with faster diffusion occurring parallel to the dislocation lines. Undissociated dislocations have higher diffusivities than dissociated ones; the diffusivity increases linearly with dislocation density (and therefore with tilt angle θ) for angles up to about 10° .

c) Anisotropic behavior is also obtained for higher angle symmetric tilt boundaries.

d) Low angle twist boundaries, composed of screw dislocations, are less efficient in transporting material than their tilt counterparts.

e) The mechanism of grain boundary diffusion in close-packed metallic systems is thought to involve vacancy exchange. This is a tentative conclusion based on the experimental evidence of Martin et al. (1967), who studied the pressure dependence of grain boundary diffusion and deduced activation volumes from their data, and of Robinson and Peterson (1973), who studied isotope effects in silver polycrystals and bicrystals, and demonstrated that their results were consistent with a vacancy mechanism. In their computer simulation studies, Balluffi et al. (1981) and Faridi and Crocker (1980) have provided support for this idea by showing that the formation and migration energies for vacancies and interstitials in the grain boundary favored a vacancy exchange process.

Having summarized briefly the present level of understanding of grain boundary diffusion, it is perhaps worth emphasizing that the correlation of structure with diffusivity remains incomplete, and that much remains to be learned about the fundamental processes of interfacial diffusion in solids.

Interphase boundary diffusion is less well studied, to the extent that very few reliable data are available in the literature. Kaur and Gust (1988) cite only one system for which extensive measurements have been reported, the Sn-Ge/In system (Straumal et al., 1981). One reason for the lack of direct information about this important aspect of interfacial diffusion may lie in the fact that, unlike grain boundaries, interphase boundaries can support local equilibrium concentration gradients only in the presence of gradients of curvature, temperature or stress. The isothermal planar interphase boundary is normally isoconcentrate.

Mullins (1957) has considered a number of important cases of interfacial diffusion in response to variations in curvature. For

the case of substitutional diffusion, and under the simplifying assumptions of constancy of composition of the two phases α and β and site conservation at the interface, we may write for the interfacial flux:

$$\begin{aligned} J_{\alpha\beta}^A &= -J_{\alpha\beta}^B = -L_{\alpha\beta} \nabla(\mu_{\alpha\beta}^A - \mu_{\alpha\beta}^B) \\ &= -\frac{L_{\alpha\beta} V_m \sigma_{\alpha\beta}}{c_\alpha - c_\beta} \nabla K_{\alpha\beta} \end{aligned} \quad (7-11)$$

Here, L represents the mobility of atoms along the interface, V_m is a molar volume, the μ 's are chemical potentials within the interface, $\sigma_{\alpha\beta}$ is the specific interfacial Helmholtz energy and $K_{\alpha\beta}$ is the interfacial curvature.

7.4 Forces for Interface Migration

It is useful to define and classify a set of generalized "forces" for interface migration. In most cases, the driving and retarding forces are expressed in terms of a normal force per unit area of interface, and therefore have the units of pressure.

It is conventional to separate the various forces according to their origin (e.g., surface Helmholtz energy, elastic energy, chemical Helmholtz energy) and to some extent the division is arbitrary. Its utility lies in the ability to visualize the interplay of different forces on a moving transformation interface.

It is also true that the definition of the "force" for boundary migration is only a part of the solution to the migration problem. The response function (or mobility) of the interface must also be known, and this function is expected to differ greatly from one interface type to the next.

7.4.1 Capillary Forces

These forces originate from the system's tendency to reduce its total interfacial

Helmholtz energy σA , where σ is the specific interfacial Helmholtz energy and A the interfacial area. For constant σ , the force can be expressed as

$$p_\sigma = K \sigma \quad (7-12)$$

which is the product of the surface Helmholtz energy and the interface curvature $K = dA/dV$.

For smoothly curved interfaces the curvature is the sum of the reciprocals of the two principal radii of curvature $[(1/r_1) + (1/r_2)]$. For strongly anisotropic or faceted interfaces, an effective capillary force may still be defined, through the derivative dA/dV , although care must be taken in its formulation.

For the special case of an equilibrium particle, the capillary force gives rise to a variation of the specific Helmholtz energy of the included phase: the resulting relation between the zero-curvature equilibria (C_0) and the equilibrium compositions in the presence of curvature is summarized in the Gibbs–Thompson relationship. For two components we obtain the linearized expressions (Purdy, 1971)

$$\Delta C^\alpha = \frac{C_0^\alpha (1 - C_0^\beta) V_m}{(C_0^\alpha - C_0^\beta)} \left(\frac{K \sigma}{RT \varepsilon_\beta} \right) \quad (7-13a)$$

$$\Delta C^\beta = \frac{C_0^\beta (1 - C_0^\beta) V'_m}{(C_0^\alpha - C_0^\beta)} \left(\frac{K \sigma}{RT \varepsilon_\beta} \right) \quad (7-13b)$$

where α is the included phase and β the external phase, V_m is the molar volume of the α phase, V'_m the molar volume of the α phase extrapolated to the composition of

the β phase and $\varepsilon_\beta = \left(1 + \frac{\partial \ln \gamma_\beta}{\partial \ln C_\beta} \right)$, where

γ_β is an activity coefficient. This last term is a measure of the departure of the parent phase from ideal solution behavior.

An equivalent graphical construction due to Hillert (1975a) is shown in Fig. 7-7.

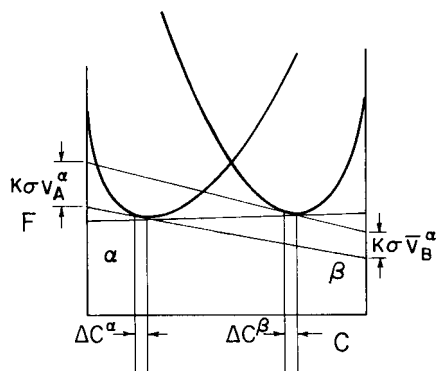


Figure 7-7. Effect of interfacial curvature, K , on the two-phase equilibrium in a binary system; the common tangent line, which generates equilibrium compositions at its points of tangency for the planar phase interface, is replaced by two nonparallel tangent lines, whose intercepts differ by the amounts shown.

The construction is of great conceptual value, and permits the straightforward extension to the case of three components with different partial molar volumes. Morral and Purdy (1995) have also developed compact expressions for the general multi-component case. For example, the solubility change of the included α phase (a column vector $|\Delta C_j^\beta|$) with curvature can be written in terms of second derivatives

of the Gibbs energy, $\left| \frac{\partial^2 G_j}{\partial C_k^2} \right|$, of the parent β phase, the molar volume of the α phase, V_m , and the equilibrium concentration differences between the α and β phases, the row vector $|\Delta C_j^{\alpha\beta}|$:

$$|\Delta C_j^{\alpha\beta}| \left| \frac{\partial^2 G_j}{\partial C_k^2} \right| |\Delta C_j^\beta| = K \sigma V_m \quad (7-14)$$

For faceted equilibrium shapes, the curvature may be replaced by a constant term σ_i/r_i , where the subscript indicates facet i , and r_i is the minimum radial distance to the i th facet.

7.4.2 Chemical Forces

The chemical force for interface migration should be distinguished from the chemical driving force for the transformation ΔF_{ch} , defined by Eq. (5-9) in the chapter by Wagner et al. (2001). In this section the case where the chemical force acts directly across the transformation interface is considered. Its magnitude is given by

$$p_{ch} = \frac{\Delta F'_{ch}}{V_m} \quad (7-15)$$

where $\Delta F'_{ch}$ is the molar Helmholtz energy difference acting directly across the interface, and is generally less than ΔF_{ch} , the Helmholtz energy difference accompanying the complete transformation. The force is derived through a virtual work argument, in which the energy change in displacing the interface through unit normal distance is equated to a work term.

The distinction between total and local chemical driving forces is best seen in the composition-invariant transformation illustrated in Fig. 7-8. Here, the Helmholtz energy difference for interface migration is given by $\Delta F'$, and some fraction ΔF^0 of the total available Helmholtz energy is dissipated in the volume diffusion field. In the often assumed limit of local equilibrium, $\Delta F'$ is implicitly set equal to zero, and all of the Helmholtz energy difference for the transformation is used in the volume diffusion field.

7.4.3 Mechanical Forces

These forces fall into two categories: those that may simply be treated as part of the chemical Helmholtz energy of the strained phase(s) and those that cannot.

7.4.3.1 Elastic Strain Energy

As noted by Wagner et al. (2001, Chap. 5 of this volume), elastic strain energy is an

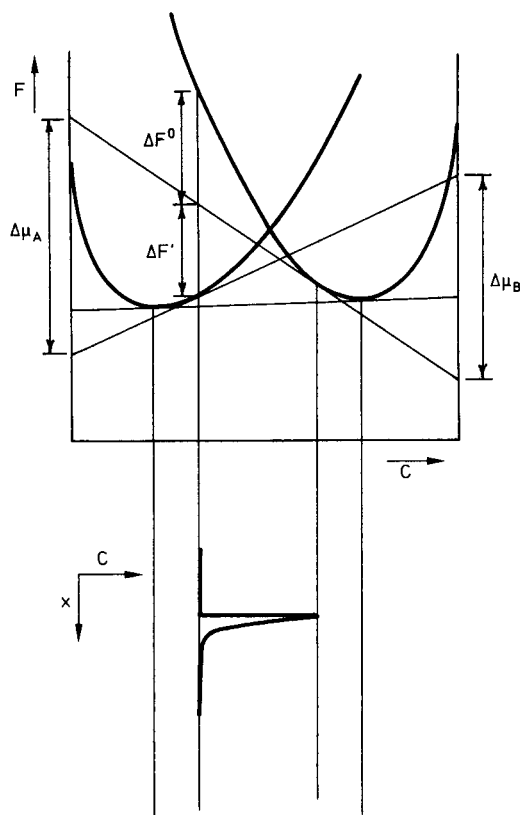


Figure 7-8. Helmholtz energy and interfacial composition relationships for a composition-invariant phase transformation. The available Helmholtz energy for the transformation is used in part to drive the interface, $\Delta F'$, and the balance, ΔF^0 , is dissipated in the volume-diffusion field.

additive term in the Helmholtz energy of a phase. Thus, for homophase variations, the local elastic energy density is given by $\eta^2 \Delta C^2 Y$ as indicated in Eq. (5-12).

This term generally reduces the total driving force for a phase transformation. In Eq. (5-12), ΔC is the local difference from the average concentration C_0 . The equation therefore has application to any case where a gradient of misfitting solute exists in an otherwise perfect crystal, and in particular to the case where a thin layer of altered composition is in coherent contact with an infinite bulk phase of composition C_0 .

The strain energy density in a coherent solute profile will be given as an intensive variable by Eq. (5-12), which therefore has application to the diffusional growth of a precipitate in a binary solid solution, and also to the problem of the stability of thin epitaxial deposited layers.

For the more complex case of the strain energy associated with the formation of a second phase inclusion, Eq. (5-14) holds, independently of inclusion shape, when the transformation strain is a pure dilation and the elastic constants of the two phases are similar. For spherical coherent transformed regions, the combined effects of surface energy and (dilatational) transformation strain may be incorporated in the Gibbs–Thomson equation by adding $6H\varepsilon^2 g_B$ to the numerator of the term in braces in Eqs. (7-13). Here $H = 3\kappa_\alpha / (3\kappa_\alpha + 4g_B)$ where κ_α is the bulk modulus of the precipitate, g_B is the shear modulus of the matrix, and ε is the misfit (Rottman et al., 1988).

7.4.3.2 Plastic Response

It is important to distinguish between mechanically derived forces which originate from elastic strain energy, and those which result in the plastic relaxation of the loaded specimen. In the latter case, the elastic energy may remain approximately constant during the course of the transformation, but the interfaces can experience virtual forces, in the sense that the Helmholtz energy of the loading system is reduced by interface motion.

As an example, consider the symmetric tilt boundary of Fig. 7-9, which is capable of motion in response to the applied load. Studies of this type of boundary have shown that the dislocation boundary undergoes normal migration, that is, synchronous glide, under an appropriate load. We can consider that there is a virtual mechan-

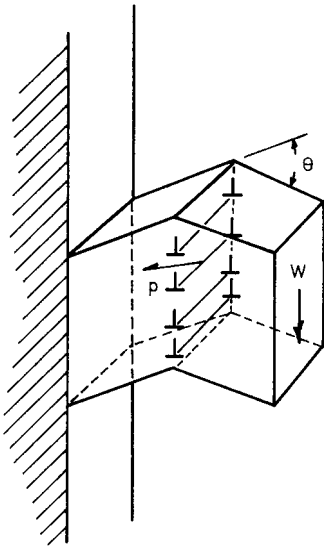


Figure 7-9. A tilt wall (tilt angle θ) is subject to a virtual force, p , derived from the work done on the specimen by the loading system.

ical force on the interface equal to $p_w = W \tan \theta$ where W is the applied load per unit area and θ is the angle of tilt. In this example, the applied stress can be thought of as acting directly on the interface. The experimental response of the symmetric tilt boundary is linear, and a simple statement of the mobility of the boundary summarizes the kinetics of boundary motion.

If a coherent twin boundary were to replace the symmetric tilt boundary in Fig. 7-9, the transformation strain would again be a shear. It is clear, however, that the synchronous glide process would not occur. The propagation of the twin will require the lateral motion of twinning dislocations, and the interface response function will be fundamentally different. This simple example illustrates the general principle that a knowledge of the force for boundary migration is only part of the empirical description of boundary motion; evidently the response characteristics of the boundary must also be known.

Another class of strain energy stored in bulk material is that associated with structural defects such as dislocations. These defects may be generated and stored during plastic deformation, and their effect on the Helmholtz energy of the solid provides the basis for the driving force for recrystallization. Dislocations may also occur due to plastic relaxation of misfit stresses (as seen in some cases of discontinuous precipitation or in some transformations in steels).

The excess Helmholtz energy is traditionally taken to be proportional to the total dislocation density and is added as a bulk driving force in the overall thermodynamic balance. This is probably acceptable for misfit-generated dislocations but, for the case of dislocations stored during plastic deformation, this approximation neglects the formation of dislocation substructures such as subgrains. This relaxation phenomenon decreases the stored Helmholtz energy and renders its increase with dislocation density less than linear due to self-screening effects (Verdier et al., 1997). Again the question of the contribution of this stored energy to the overall kinetics of microstructure development is two-fold: we may consider the nucleation step from an initially homogeneous situation, or the growth regime for which the stored energy is different on either side of the moving interface. A simple approximation for the growth process would be the addition of an extra driving force when the stored energies differ on either side of the interface (e.g. due to different stages of deformation in two neighboring grains). However, this approach is unlikely to be sufficient to explain the nucleation of recrystallization, which is known to occur at grain boundaries, and at localized shear or transition bands (Humphreys and Hatherly, 1995). As proposed initially by Bailey and Hirsch (1962), nucleation seems to be a random

event associated with local fluctuations in subgrain configuration; it is unlikely to be successfully modeled either by a standard nucleation theory or by an averaging approach for the stored energies. Information on local misorientations (leading to differences in local mobilities and local driving forces) may be crucial, as has been suggested using vertex-based numerical simulations (Weygand, 1998).

7.4.4 Frictional Forces

7.4.4.1 Solute Drag

Each type of mobile interface will possess its own characteristic response function. For the simple tilt wall subject to a mechanical force, we have noted that the force–velocity relationship is linear over a range of forces. If a considerable reconstruction of the crystal structure is required for the motion of an interface, as in the motion of a high-angle boundary in a single-component system, we expect that cross-boundary diffusive motion will play a significant role. Turnbull's (1951) expression for the intrinsic mobility, M , of a grain boundary

$$M = \frac{\delta D^b V_m}{b^2 RT} \quad (7-16)$$

is based on a model in which atom jumps across the boundary are independent of one another. This relation has not been confirmed by experiment, and this is taken to suggest that more complex, cooperative movements of atoms are generally involved in interface migration. Again referring to experiment, there exists a considerable database drawn from measurements of grain boundary motion in high purity metals. Thus the intrinsic response of high-angle grain boundaries is rather well documented, even if the mechanisms of

boundary migration are not fully understood.

When two or more components are involved, this picture must be extended. Superimposed on the intrinsic response of the interface, and frequently masking it, we find the effects of solutes which are preferentially attracted to or repelled from the interface. The experiments of Aust and Rutter (1959) first demonstrated conclusively the powerful retarding effects of trace amounts of solute on grain boundary migration.

The idea of a “solute drag” perhaps originated with Cottrell (1953), who noted that solute atoms would be attracted to dislocations, and would therefore be required to diffuse along with the dislocations, or to be left behind by dislocations that had broken free of their solute atmospheres. Similar ideas were put forward by Lücke and his co-workers (1957) for application to the case where a solute is preferentially segregated to grain boundaries. The most complete and informative theoretical treatments of this effect are those of Cahn (1962) and Hillert and Sundman (1976). The latter is based on a treatment put forward earlier by Hillert (1969). The basic reason for the solute drag force is simple: if solute is attracted to the boundary, it will tend to diffuse along with the moving boundary. Depending on the relative rates of boundary motion and solute diffusion, the solute distribution may become asymmetric, with more solute trailing the boundary than leading it. Because of the mutual attraction between the boundary and the solute, the asymmetric solute distribution leads to a retarding force of the form

$$p_i = N_V \int (C - C_0) (dE/dx) dx \quad (7-17)$$

where N_V is the number of atoms per unit volume, and dE/dx is a measure of the

force between the solute atoms and the boundary. The effects of small amounts of solute can be profound. The profiles in Fig. 7-10 are due to Cahn (1962). They are based on a triangular interaction potential between solute and boundary, and correspond (a) to a slowly moving boundary, (b) to a boundary experiencing maximum solute drag, and (c) to a fast-moving boundary. That is, the drag force goes through a maximum as the velocity is increased. If an initial intrinsic force-velocity relationship is assumed linear, and the solute drag term is added, the total response function is quickly rendered nonlinear. Under more severe conditions, the system can even become unstable, displaying a region of velocities where $\frac{\partial p}{\partial v}$ is negative.

Hillert's formulation uses a different interaction potential, initially square (rather than triangular), and later a square-topped potential with ramps at the edges. The drag is evaluated as a rate of dissipation of Helmholtz energy due to diffusion in and in front of the moving interface. The model lends itself to numerical analysis; it

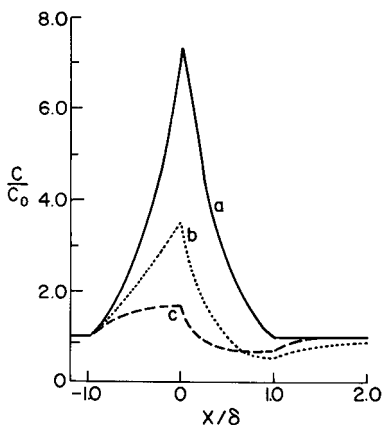


Figure 7-10. Computed solute profile in the vicinity of a moving grain boundary: a) at equilibrium, b) at a velocity corresponding to maximum solute drag, and c) at higher velocity. After Cahn (1962).

is not restricted to dilute solutions, nor is it restricted to grain boundaries. Figure 7-11 uses the simple square well to illustrate the effect of cross-boundary diffusion in setting the degree of asymmetry of the solute profile. The drag term may be written in several ways. Among the most convenient, Hillert and Sundman (1976) find:

$$p_i = \frac{RTv}{V_m} \int \frac{(c - c_0)^2}{Dc(1 - c)} dx \quad (7-18)$$

In their approach, the ramps (zones 1 and 3 in Fig. 7-12), as well as the centre of the boundary (zone 2) and the parent phase region (zone 4), contribute to the drag. Indeed, it is possible to separate out the con-

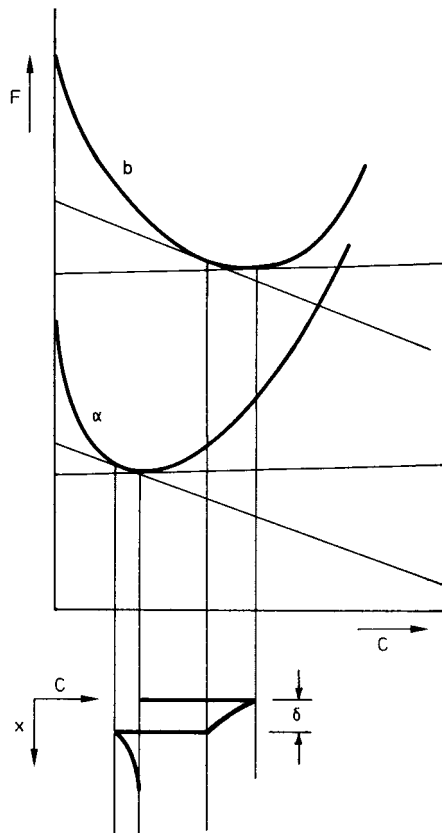


Figure 7-11. A square-well model for the moving grain boundary. After Hillert (1969).

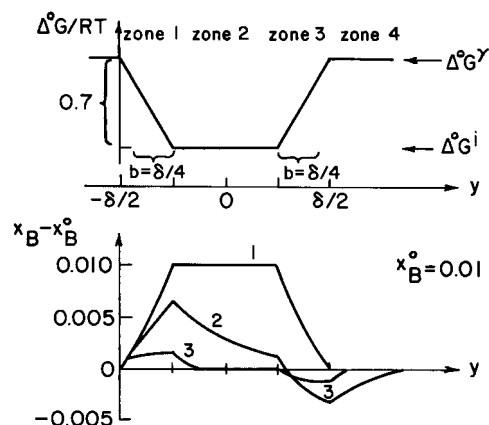


Figure 7-12. The Hillert–Sundman (1976) model of a moving boundary, showing the interaction profile, and some computed solute profiles for $\nu\delta/2D=0.001$ (1), 1.61 (2), and 10 (3).

tribution of any slice taken parallel to the interface, and Sundman and Hillert have presented their results in this way, as components of the total solute drag. They find, as we might expect, that the drag is reduced for given velocity by increasing the cross-boundary diffusion coefficient, or by reducing the depth of the potential well seen by the solute. The model is capable of generating a variety of informative results. It is not restricted to grain boundary motion, but also finds application to steady state phase transformations, as will be seen later.

It is interesting to note that solute drag effects have been (in some sense) better studied and quantified than intrinsic boundary friction forces. The solute effects are thought to be additive, and to dominate and even to mask the intrinsic properties of grain boundaries for many cases of practical interest.

7.4.4.2 Particle Pinning

Whereas the contribution of solute drag as a retarding force is by definition of a viscous nature, another term may prevent the

interface from moving: a pinning force. The idea of pinning a grain boundary with foreign particles was put forward initially by Zener (Smith, 1948). The grain boundary will be able to move only if the gradient of bulk stored energy across the interface is sufficient to move the interface to an untrapped configuration. Zener assumed a purely geometrical distribution of particles along the grain boundary; this led to a friction force to be overcome that scales as V_f/r , where V_f is the volume fraction of particles and r their radius. A more refined approach due to Hazzledine and Oldershaw (1990) allows us to treat the collective pinning problem in a consistent manner (i.e., to treat both the flexibility of the interface and the number of particles along the interface). Hazzledine's result, recently confirmed by computer simulations (Weygand, 1998), indicates that a scaling law in $V_f^{1/2}/r$ might be more appropriate.

The consequence of these pinning forces on the overall kinetics of interface migration can be two-fold: on the one hand, the particles will impose a threshold driving force for boundary migration; and on the other hand, they will impose a constant retarding force to be subtracted from the available Helmholtz energy. The standard method is to equate the retarding force with the threshold force, but this identification is by no means obvious. Numerical experiments on grain growth kinetics do however indicate that this simple approach gives a good description of the overall kinetic behavior (Weygand, 1998).

7.5 Examples

7.5.1 The Massive Transformation

Massive transformations are considered to include all inhomogeneous, noncoherent, thermally activated, composition-in-

variant, solid–solid transformations (Masalski, 1958). Massive solidification reactions are excluded by this definition, but their literature is relevant, in part because of advances in understanding of the rapid solidification of silicon-based alloys (Aziz and Kaplan, 1988).

The massive transformation generally involves a major structural change; it normally begins with the heterogeneous nucleation of a thermodynamically stable or metastable daughter phase, at imperfections or grain boundaries in a supercooled parent, and proceeds by the thermally activated migration of a mobile transformation interface.

Plichta et al. (1984) reviewed the available information on massive transformation nucleation, and concluded that the nucleation event is structurally identical with that expected for diffusional transformations among dissimilar phases; grain boundary and triple junction sites are energetically preferred, and an orientation relationship between the nucleus and at least one parent grain is generally set on nucleation. Since interfacial torques are likely to be present during the nucleation event, the construction of Hoffman and Cahn (1972) may be expected to provide guidance in the modeling of the critical nucleus. Experience has shown, however, that the search for plausible nucleus shapes in such heterogeneous systems seldom leads to unambiguous results.

The chemical Helmholtz energy change, ΔF_{ch} , for nucleation in a single-component system that undergoes an allotropic transformation is obtained directly from the undercooling below the equilibrium temperature, as suggested by Fig. 7-13. For small undercoolings, ΔT , this may be expressed as

$$\Delta F_{ch} = \Delta H \Delta T / T_0 \quad (7-19)$$

with ΔH as the change of enthalpy.

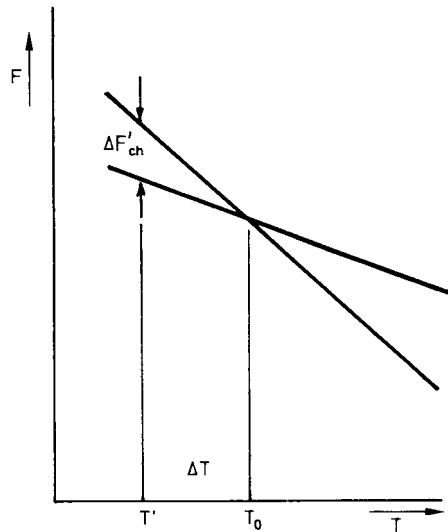


Figure 7-13. Helmholtz energy relationships for the allotropic transformation of a pure element.

For two components, the composition-invariant condition need not apply to massive nucleation (although it must hold overall for massive growth). In the example in Fig. 7-14, drawn for a temperature below T_0 , the temperature for which the α and β phases of the bulk composition C_0 have the same molar Helmholtz energy, it is clear that the formation of a nucleus of composition C_0 would be accompanied by a volume Helmholtz energy change $\Delta F_1/V_m$. However, the volume Helmholtz energy change is maximized ($\Delta F_2/V_m$) if the nucleus takes composition C' . Even in the single-phase supersaturated region, a similar argument shows that the volume Helmholtz energy change will be maximized for a composition other than C_0 .

Turning to the process of massive product growth, if we again consider the allotropic transformation of pure element, it is clear that the rate of transformation is determined by the undercooling (which sets the interfacial driving force p_{ch}), and by the migration characteristics of the transforma-

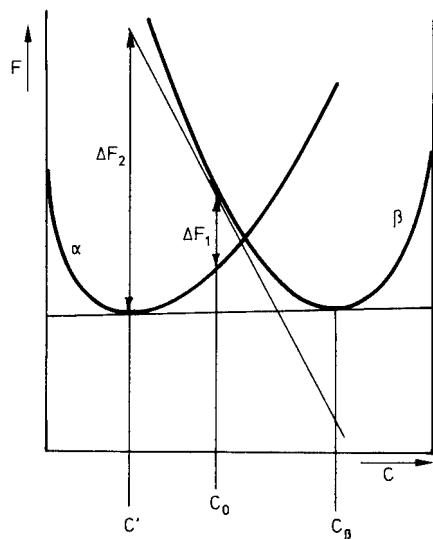


Figure 7-14. Helmholtz energy relationship for the isothermal nucleation of a massive product in a binary system.

tion interface. As in the case of the high angle grain boundary, the details of the cross-boundary atomic transfer process are not well understood. As in the grain boundary case, it has proved difficult to separate the effects of trace impurities from the intrinsic migration properties of the noncoherent interphase boundary. Hillert (1975b) has estimated the mobility of grain boundaries in pure iron from a series of limiting arguments as

$$M = 0.035 \exp(-17700/T) \text{ m}^4/(\text{Js}) \quad (7-20)$$

He then used this expression in his analysis of the rates of the α/γ transformation of iron with very low carbon contents, as investigated experimentally by Bibby and Parr (1964) and Ackert and Parr (1971). Using a model in which a fraction of the chemical force is dissipated by solute diffusion ahead of the interface, Hillert was able to predict a number of characteristics of the massive transformation in pure and nearly pure iron, as summarized in Fig. 7-15.

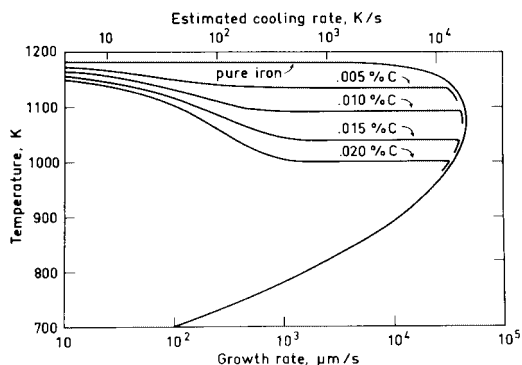


Figure 7-15. Diffusional and diffusionless growth of α from γ iron, calculated assuming that carbon diffusion is negligible at high growth rates. Reprinted with permission from Hillert (1975b), p. 12.

For richer alloys, massive growth could, in principle, be entirely composition-invariant. However, some results (Singh et al., 1985) suggest that solute diffusion ahead of the interface can play a major role in steady interface migration. Referring to Fig. 7-16, which is based on the simple model of an infinitely thin interface, it is clear that a solute build-up in front of the interface will result in a reduction of the chemical force on the interface. Having conceptually released the concentration in the interface region from its value far from the interface (C_0), the description of two-component massive growth becomes a free boundary problem, in which the interfacial driving force and the velocity must be simultaneously determined. It is likely that this type of approach to local equilibrium occurs at higher relative temperatures, where the possibility of volume-diffusion loss is strongest, and where, for example, Widmanstätten growth competes with the massive reaction.

Much of our current knowledge of massive growth derives from the pioneering work of Massalski and co-workers (Massalski, 1958; Barrett and Massalski, 1966).

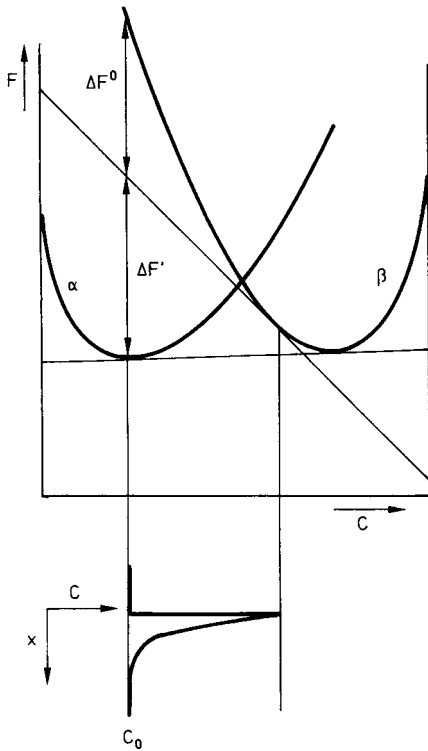


Figure 7-16. Solute build-up in front of the massive interface will result in a reduction of the chemical force for interface migration.

In early papers, it was implicitly assumed that a pseudo-unary cross-boundary diffusion process controlled the rate of massive growth; later (Massalski, 1984) it was noted that local changes of composition in the region of the interface, consistent with overall composition invariance, are possible, even probable, under certain conditions.

Because of the speed of transformation, massive reactions are often studied under conditions of continuous cooling. The most informative kinetic studies, however, are those that yield rates of isothermal transformation, as exemplified by the work of Karlyn et al. (1969); they used pulse-heating and rapid quenching to evaluate the rates of formation of massive α in a Cu–

38 at.% Zn alloy, which had previously been quenched to retain the β phase. They found:

- i) that the transformation occurred only within the single phase α region of the phase diagram and
- ii) that steady massive growth (at constant isothermal velocity of order 1 cm/s) developed after a delay time of several milliseconds.

Both the limited temperature range for growth and the delay time were attributed to the pre-existence of solute fields around small α particles. Only in the single-phase α region would such solute fields be consumed during initial growth, thereby permitting the development of composition-invariant (massive) growth. They noted that massive growth in the two-phase $\alpha + \beta$ region (below T_0) is possible, provided that some massive α has first been formed by pulsing into the single-phase region. With further heating these massive regions continued to grow into the $\alpha + \beta$ region, thus reinforcing the idea that the inhibition of such growth lies in the initiation stage.

In the analysis of growth rates, it was assumed that massive growth occurred without local composition change. However, in discussion, impurity drag effects and parent-phase solute fields were admitted as possibilities.

A comprehensive theoretical treatment of the two-component massive transformation, which applies to a range of transformation conditions, will deal with solute diffusion within the interface and also in the thin region ahead of it. The model of Hillert and Sundman (1976), an extension of their treatment of solute drag at grain boundaries, finds application here. Their formulation of the solute drag involves the computation of the dissipation of Helmholtz energy due to diffusion within the

interface region (Eq. (7-18)). The solute field is schematized in Fig. 7-17(a) for a solute that is attracted to the interphase boundary. The cross-boundary diffusion of solute introduces a component of drag (regions 1, 2 and 3), and diffusion ahead of the boundary provides a further contribution (region 4), which dominates the total drag as the velocity approaches zero. The total drag is optimized for $\frac{v\delta}{2D} \approx 1$, and it may be that the optimum of dissipation of

Helmholtz energy defines the most probable velocity. A second treatment of the solute drag in massive growth (Bréchet and Purdy, 1992) extended Cahn's (1962) analysis, and demonstrated that a finite drag term will always be present, however small the velocity. This analysis, like that of Hillert and Sundman, therefore suggests that a threshold driving force is a natural characteristic of such transformations. However, if the solute field in front of the interface is accompanied by a misfit, in the sense of Eq. (5-12), we expect an additional term in the force balance, a "pulling" force due to the elastic energy contained in the coherent composition gradient.

The above discussion is based on the premise that the migration characteristics of the massive front are those of a non-coherent interface. This is borne out by numerous observations (Massalski, 1984) which indicate, for example, that the transformation interface is able to cross grain boundaries in the parent phase without a change in velocity or morphology. Dynamic observations indicate, however, that the motion of the front is irregular, and often accomplished by a lateral process, in which diffuse steps move parallel to the interface plane (Perepezko, 1984). In the view of Menon et al. (1988), lateral processes are the rule in massive growth. Hence models based solely on diffusion normal to the boundary may need to be modified. However, it is interesting that Perepezko (1984) demonstrated a scaling relationship for a wide range of alloy systems, which yields a composite enthalpy of activation for massive propagation of $94 T_m$ J/mol. This value is similar to that for grain boundary diffusion, which suggests that diffusion within the interface is a common rate-determining feature for all such transformations.

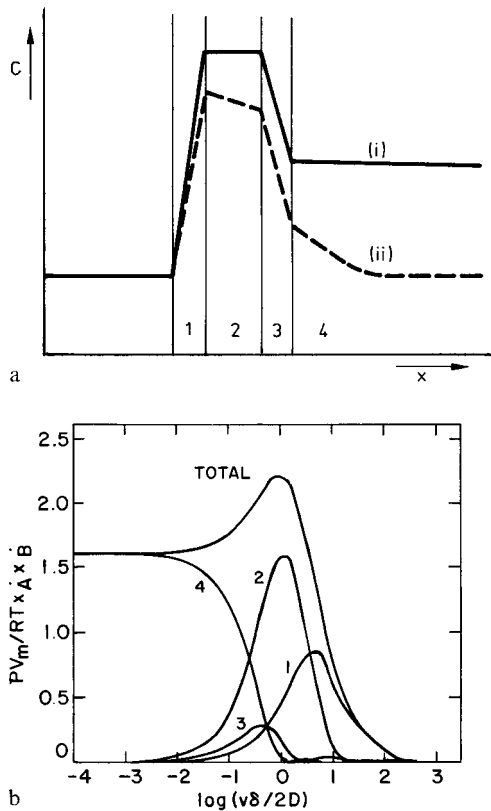


Figure 7-17. a) Schematic concentration profile through a massive transformation interface, i) at equilibrium, and ii) in motion. b) Computed solute drag for the massive transformation in part a, for a constant value of D . X_A^0 and X_B^0 represent the initial composition of the parent phase expressed as mole fractions of the two components A and B. After Hillert and Sundman (1976).

7.5.2 Chemically-Induced Grain Boundary Migration

Chemically-induced grain boundary migration (CIGM), or diffusion-induced grain boundary migration, is a rather recently recognized phenomenon (den Broeder, 1972; Hillert and Purdy, 1978). The process is one in which diffusion along a grain boundary, to or from a sink or source of solute, causes the boundary to move. The source may be in the solid, liquid or gas state. A composition change results (Fig. 7-18).

The process is widespread in binary metallic systems. King (1987) lists 30 systems in which it has been detected. The process is capable of generating substantial intermixing where little or none might be expected in the absence of grain boundary motion.

A variation on the conditions in Fig. 7-18 is obtained for a supersaturated solid solution: an initially planar boundary bows out between grain boundary precipitates, and simultaneously sweeps solute to the precipitates (Fig. 7-19). This type of microstructural development was reported by Hillert and Lagneborg (1971), and was recently supported by microanalytical evidence for solute depletion in the volume swept by the moving boundary by Solorzano et al. (1984).

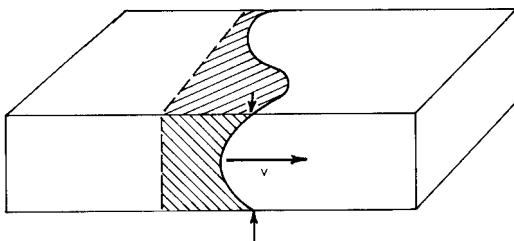


Figure 7-18. Schematic representation of chemically-induced grain boundary migration in a thin sample exposed to a vapor source of solute. The front is often observed to bow against its curvature.

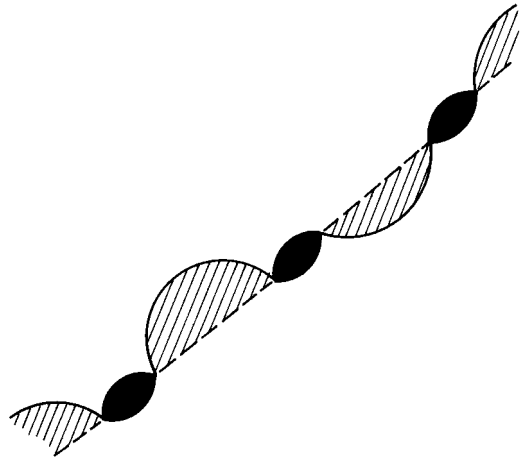


Figure 7-19. Grain boundary bowing between precipitates, which act as solute sinks, and serve to pin the grain boundary.

CIGM is often seen as symmetry breaking. The initiation process is not well documented or understood. It is clear that diffusion along an initially stationary boundary will lead to symmetric diffusion profiles, as illustrated in Fig. 7-6, and this has led to the suggestion that the region next to the boundary will become one of increased elastic strain energy, provided that a solute misfit exists, and provided that the solute-enriched or solute-depleted regions remain coherently connected with their respective grains. The strain energy density will then be given by Eq. (5-12). Because the elastic constant Y is a function of orientation, the strain energy density will in general be different on the two sides of the boundary, and this may lead to boundary displacement. Tashiro and Purdy (1987), in a survey of binary metallic systems, found only one system in which CIGM could not be induced; this was the system with the lowest misfit, Ag–Mn.

Further evidence for the importance of solute misfit in the initiation of CIGM is found in the work of Rhee and Yoon

(1989), who systematically varied the misfit parameter in a ternary system, and showed that the phenomenon is suppressed when the misfit is brought to zero. An approximate parabolic dependence of velocity on misfit was also found, consistent with Eq. (5-12). This suggests that elastic strain energy also plays a role in propagation of the grain boundary.

In practice it is difficult to distinguish the possible driving forces for the process. At the highest temperatures, it is likely that solute field stresses will be dominant. This appears to be the case for the study of Rhee and Yoon (1989). In the early work of Hillert and Purdy (1978), in which thin polycrystalline iron films were exposed to zinc vapor, it was evident that the volume diffusion penetration of the parent grains, indexed by D_V/v , was of atomic dimensions. Hence, it was assumed that the driving force was entirely chemical. A comprehensive model should take into account all possible sources of the driving force.

The moving grain boundary is subject to a set of forces, which may in general include chemical, elastic, frictional and capillary forces. As in the massive transformation, there exists in principle a degree of freedom corresponding to the concentration in the parent phase immediately adjacent to the boundary. In the conceptual limit where no volume-diffusion penetration exists in advance of the boundary, the concentration profile will be a step, and the full chemical force p_{ch} will act across the interface. In a second limiting case, a concentration gradient exists in front of the boundary and an elastically-derived residual force is determined by the coherency field. Intermediate cases would then correspond to a higher or lower degree of relaxation of the concentration at the leading edge of the boundary towards a constrained equilibrium between strained parent crystal

and unstrained product crystal. These considerations are contained in the phenomenological treatment due to Bréchet and Purdy (1992), in which the driving force is evaluated over a correlation length (l) on either side of the boundary. The steady concentration profile is $C(z)$. The force then becomes:

(7-21)

$$\frac{1}{l} \int_0^l \left[\frac{1}{2} \frac{\partial^2 F}{\partial C^2} (C(z) - C_0)^2 + Y \eta^2 C(z)^2 \right] dz$$

where the second derivative is a measure of the Helmholtz energy composition relation. This approach has the virtue of including both possible contributions to the driving force; it results in the conclusion that, as in the massive transformation, a threshold exists, below which no motion is possible.

An ambitious treatment of the problem has been put forward by Cahn et al. (1998). Their analysis is based on a phase-field treatment of the grain boundary. They look for travelling-wave solutions of the equations of motion, and treat their existence as a requirement for forces capable of coupling with the boundary motion. They find that coupling with the elastic field is indeed possible. However, their treatment gives no indication that a purely chemical force is effective in moving the boundary.

7.5.3 Discontinuous Precipitation

Discontinuous precipitation, like chemically-induced grain boundary migration, involves the lateral diffusion of solute within a sweeping grain boundary. The difference lies in the nature and spacing of the solute sources/sinks. In the case of discontinuous precipitation, these are members of a regular array of precipitates, whose spacing is a free variable, capable of internal adjustment. The reaction is found in a wide variety of precipitation systems, often at

low homologous temperatures where grain boundary diffusion is expected to be a dominant mechanism of material transport. Like CIGM, discontinuous precipitation can in principle occur in the absence of volume diffusion. The reaction is capable of destabilizing microstructure at relatively low temperatures, and it is therefore of practical interest.

Unlike eutectoid reactions, which yield morphologically similar products, discontinuous precipitation reactions are not associated with a particular feature of the phase diagram, although supersaturation is an obvious prerequisite. The question of which systems will give rise to discontinuous precipitation, and which will not, will perhaps be answered by reference to and detailed understanding of the initiation and growth processes.

7.5.3.1 Initiation of Discontinuous Precipitation

A nucleation event, in the classical sense, is not required. As in CIGM, a pre-existing grain boundary is caused to move, and eventually to become the steady reaction front, as suggested by Fig. 7-20. The mechanisms proposed for the initial stages of grain boundary displacement fall into two broad classes: free-boundary mechanisms and precipitate-assisted mechanisms. Baumann et al. (1981) have indicated that free-boundary initiation is dominant at higher homologous temperatures, leading eventually to “single-seam” morphologies. At lower temperatures, it is expected that boundary motion is initiated by precipitate–boundary interactions, and that these lead to a preponderance of double-seam morphologies. The correlation between temperature and morphology appears to be quite general, with the break occurring at half the absolute melting temper-

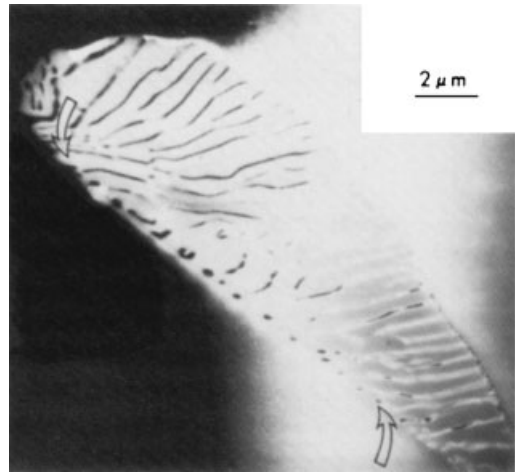


Figure 7-20. Scanning electron micrograph of a discontinuous precipitation colony formed in Al–22% Zn at 478 K. The original grain boundary positions are indicated by arrows. After Solorzano et al. (1984).

ature. Gust (1984) found a correlation with the solvus temperature rather than the melting temperature. Duly and Bréchet (1994) determined that the proportion of double-seam morphologies decreased from more than 1/2 to 0 as the temperature was increased.

In free-boundary initiation, the initial grain boundary displacement is thought to be caused by ordinary recrystallization or grain growth forces (Fournelle and Clark, 1972), or by forces derived from solute segregation (Meyrick, 1976). The subsequent stages must then include the nucleation of precipitates at the moving boundary and the evolution of a steady state in which the precipitates acquire a uniform spacing, as depicted in Fig. 7-21. Cu–Co alloys seem to require this type of initiation, and readily undergo discontinuous precipitation only when cold-worked or when treated to give a small parent grain size (Perovic and Purdy, 1981).

Precipitate–boundary interactions were first studied in detail by Tu and Turnbull (1969), who showed that boundary torques,

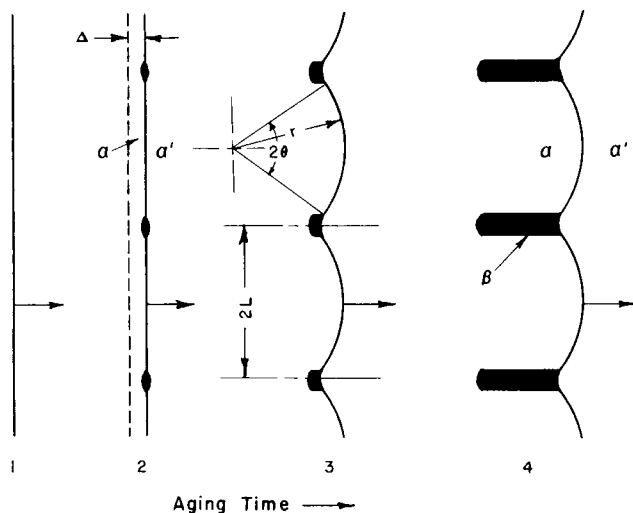


Figure 7-21. Free-boundary initiation and early development of discontinuous precipitation. Reprinted with permission from Fournelle and Clark (1972), p. 2762.

developed when a regular array of precipitates, formed on the boundaries in Pb–Sn bicrystals, were responsible for the initial displacement of the boundary (Fig. 7-22). Eventually, boundary breakaway was envisaged, with the subsequent embedding of the precipitates in the advancing grain. Aaronson and Aaron (1972) extended these ideas to include a range of possible geometries, each of which resulted in an initial boundary displacement due to capillary forces associated with the formation of equilibrium precipitate nuclei at the grain boundaries.

A further class of precipitate–boundary interactions, based on CIGM, was proposed by Purdy and Lange (1984). In this case, initial displacement can occur against capillary forces, in response to chemical forces. If the initial precipitates are closely spaced, the initial displacement may be preceded by a period of precipitate coarsening. The process is suggested by Fig. 7-19. Several reports of grain boundaries bowing between fixed precipitates can be found in the literature (Hillert and Lagneborg, 1971; Solorzano et al., 1984). Michael and Williams (1986) found that so-

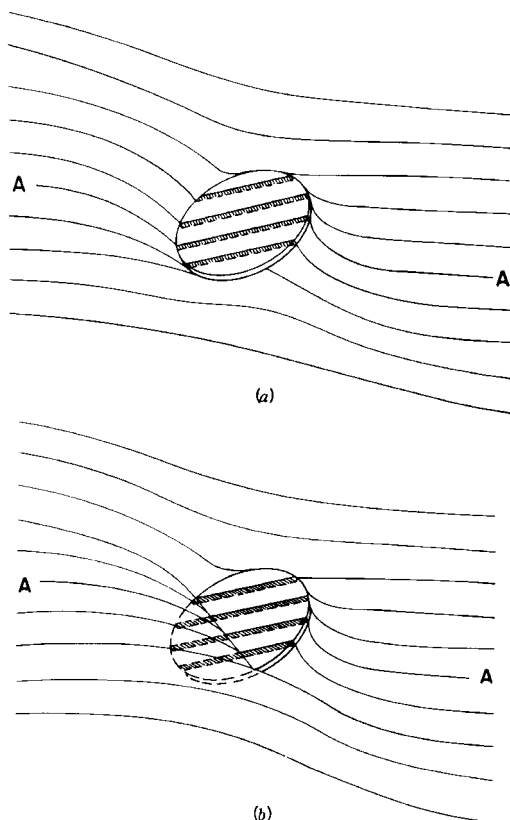


Figure 7-22. Formation of grain boundary precipitates at an initially static boundary (a), and boundary displacements in response to capillary forces (b). Reprinted with permission from Tu (1972), p. 2773.

lute-depleted volumes were left in the wake of bulging grain boundaries in super-saturated Al–4.7 wt.% Cu. Fonda et al. (1998) and Mangan and Shiflet (1997) studied the initiation of discontinuous precipitation in Cu–3% Ti alloys, and demonstrated that, at low supercooling, the initial boundary motion is due to the presence of Widmanstätten precipitates, which grow into one grain, and cause boundary displacement into the other. Duly and Bréchet (1994) examined the initiation of discontinuous precipitation over a wide range of temperatures, initial grain sizes and compositions in Mg–Al alloys. They conclude that the Tu–Turnbull and Fournelle–Clark mechanisms dominate at low and high temperatures respectively, and that the Purdy–Lange mechanism may be important at intermediate temperatures.

It is now clear that a range of mechanisms exist, each mechanism capable of initiating boundary motion. At lower temperatures, precipitation on the static boundary is a common precursor of discontinuous precipitation; the initial precipitates are capable of acting either directly, to pull the boundary from its initial location, or indirectly through CIGM to accomplish a similar result. We conclude that, for most situations where the supersaturation is significant, there will be no difficulty in initiating grain boundary motion.

7.5.3.2 Theories of Steady Cooperative Growth

The development of a steady or near-steady growth front, characterized by a regular spacing between precipitate lamellae (or rods), S , and a constant velocity, v , is not immediate upon initiation, but is preceded by extended transient growth regions. However, steady or near-steady conditions appear eventually to prevail, and

the steady state has attracted the attention of successive generations of theorists. In this section, we review only the more advanced theories, while acknowledging their genealogy.

Before proceeding, the question of the steady state should be pursued in more detail. It appears that the steady state can be achieved fairly generally, and that it can be approached from higher or lower supersaturation, such that the system has little or no memory, and the steady state is characteristic of the isothermal reaction conditions only. Nevertheless, the constancy of reaction front velocity has recently been questioned by a number of authors, including Kaur and Gust (1988), Mangan and Shiflet (1997), and Fonda et al. (1998). This point is discussed in Sec. 7.5.3.3.

It is convenient to divide the theoretical treatments into two classes depending on whether the details of the transformation front are predicted as part of the development. In the “global” approach of Cahn (1959), which builds on the ideas implicit in Turnbull’s (1951) and Zener’s (1946) treatments, the reaction front is treated as a planar high-diffusivity path whose mobility is rate determining. Thus the important input quantities to the theory include the overall Helmholtz energy change accompanying the passage of the front and the interface mobility. Cahn (1959) first emphasized the importance of storage of Helmholtz energy in the product phase, and showed how to estimate it from a knowledge of the interphase boundary energy $\sigma_{\alpha,\beta}$, the grain boundary diffusivity and distribution coefficient, s , and the interlamellar spacing S and velocity v . The Helmholtz energy balance is written

$$\Delta F'' = \Delta F_{\text{ch}} - 2\sigma_{\alpha\beta} V_{\text{m}}/S \quad (7-22)$$

Here ΔF_{ch} is the total chemical Helmholtz energy difference between the parent

and product phases, evaluated some distance from the interface. In determining this quantity, the stored Helmholtz energy in the product α phase must be calculated from a knowledge of the composition profile in the α lamellae. This is determined in theory from a knowledge of the grain boundary transport properties and the velocity and spacing through

$$\frac{C_0 - C(z)}{C_0 - C_3} = \frac{\cosh(z \sqrt{a/S_\alpha})}{\cosh(\sqrt{a/2})} \quad (7-23)$$

where C_0 is the initial concentration in the parent phase, $C(z)$ is the local concentration in the α phase behind the transformation front, C_3 is the concentration in the α phase in contact with the β lamellae and

$$a = \frac{\nu S^2}{s D^b \delta} \quad (7-24)$$

Eq. (7-23) is a solution of the moving-boundary diffusion equation, for constant ν , S , and boundary concentration C_3 ; the solution reduces in approximation to a sine function when the centerline composition $C(z=0)$ is closer to C_3 than to C_0 .

Cahn (1959) next chose $C_3 = C_{\alpha\beta}^e$, the equilibrium composition of α in contact with β at a planar interface. He was then able to evaluate the stored chemical Helmholtz energy in the product phases from Eq. (7-23). To complete the description, he assumed a relationship between the total Helmholtz energy change $\Delta F''$ and the velocity of the form

$$\nu = M'' \Delta F'' \quad (7-25)$$

Here, M'' is a "global" mobility that differs from the intrinsic grain-boundary mobility, e.g., of Eq. (7-16).

The theory described above has been modified by others, for example by Aaronson and Liu (1968), to take partial account of capillary forces acting on the β lamellae.

Certain aspects of the theory are amenable to experimental verification, for example, the concentration profiles left in the α product lamellae have been measured by Porter and Edington (1977) and by Solorzano and Purdy (1984) using high resolution elemental analysis, to give the transport properties of the reaction front, $\{s D^b \delta\}$, through Eq. (7-23). These same measurements allow the evaluation of the amount of the total available Helmholtz energy for the transformation retained as segregation in the product; this latter quantity is also available, albeit in averaged form, through X-ray measurements of the lattice parameter of the product phase.

A heuristic description of discontinuous precipitation, after Petermann and Hornbogen (1968), utilizes a rate equation of the type of Eq. (7-25) coupled with an approximate evaluation of the relaxation time for grain boundary diffusion to the β lamellae, to give a velocity expression which is dimensionally similar to that of Cahn.

A second class of theoretical description has been developed by Hillert (1969, 1972, 1982). This approach has been termed "detailed", in the sense that a much deeper knowledge of the transformation front is implicit, even required, for its application. The basis for this treatment is the application of a local force balance at every point along the interface. Thus the possibility is raised of determining the interface shape for steady growth, as a consequence of the interplay of capillary, chemical, elastic, and frictional forces, as defined in Sec. 7.4.

In simplified form, for application to the case where the composition profile (step), ΔC , measured normal to the interface is not relaxed by volume diffusion, and where elastic and solute drag effects are negligible, the interfacial force balance becomes

$$\nu/M = p_{ch} - p_\sigma \quad (7-26)$$

which holds at every point. The solute profile in the boundary will be given by Eq. (7-23), and the concentration step (ΔC) at the interface will take a minimum value at the centres of the lamellae, varying continuously to a maximum value at the α/α_0 interface immediately adjacent to the β lamellae. Hillert has chosen the limiting value of the solute concentration at this point, C_3 in Eq. (7-23), as the capillary-modified solubility in α in equilibrium with β under curvature $2/S_\beta$.

For a steady transformation, the right-hand side of Eq. (7-26) is constant along the interface, and the curvature must vary to match the chemical force, indexed by the composition step ΔC .

A further local force balance is required at the $\alpha_0/\alpha/\beta$ junction. This is depicted by a vectorial balance of surface energies in Fig. 7-23. Thus the angles of intersection and local curvatures are set at the junction, and the variation of the grain boundary curvature is required to match the variation of chemical force along the boundary. The theory therefore allows the self-consistent calculation of the interface shape for given values of the spacing S , the velocity v , and the interfacial transport property $sD^b\delta$.

Sundquist (1973) extended Hillert's treatment to include the possibility of

solute drag forces and severely nonplanar shapes, thus allowing for consideration of morphological stability of the transformation front.

Neither of the approaches described above is sufficient to predict the transformation state that will occur at given supersaturation in a particular system. Each is capable of generating a unique relationship between v and S , however.

In considering the spacing problem for lamellar eutectoids, Zener (1964) set a thermodynamic limit, a minimum spacing for which all of the available Helmholtz energy for the transformation is stored as interfacial Helmholtz energy in the product. This minimum also exists for discontinuous products:

$$S_{\min} = \frac{2\sigma_{\alpha\beta} V_m}{\Delta F_{\text{ch}}} \quad (7-27)$$

At this (virtual) state, the system is in equilibrium and no growth is possible.

Larger spacings corresponds to finite rates of growth. It has been suggested that the steady spacing is one which maximizes the growth rate (Hillert, 1972) or the integral rate of dissipation of Helmholtz energy (Cahn, 1959). Solorzano and Purdy (1984) put this latter hypothesis to the test, and found a reasonable level of confirma-

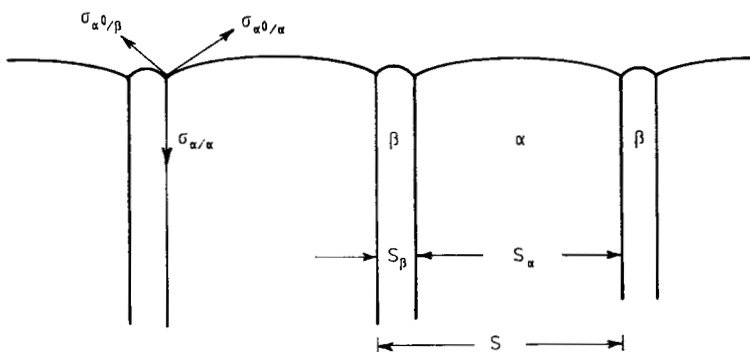


Figure 7-23. Schematic (plan) view of a steady discontinuous growth front, defining the spacings, S , S_α , S_β , relevant to the problem, and indicating the vectorial balance of interfacial energies, $\sigma_{\alpha/\beta}$, $\sigma_{\alpha_0/\alpha}$, $\sigma_{\alpha_0/\beta}$, at the three-grain junction.

tion for two well-characterized systems, Al–22 at. % Zn and Mg–9 at. % Al.

Building upon the local approach of Hillert and co-workers, Klinger et al. (1996) have proposed a solution which leads to a selection of the growth velocity without the need for an optimization principle. This treatment relies on the cooperative nature of the growth of the α and β lamellae, and on the different characters of the interfaces between the α and β phases and the parent α phase: one is a grain boundary and the other is an interphase boundary. Assuming a definite composition for the β phase leads to a Mullins (1957) equation for transport along the α^0/β interface determined by gradients of curvature. Transport along the α^0/α is considered to be driven by concentration gradients, according to Cahn's (1959) formulation. The condition at the triple junction is taken as a local equilibrium, corrected for Gibbs–Thompson effects. The requirement that the α and β growth velocities match in order to have a cooperative growth process is sufficient to select the spacing and velocity of the front. This approach has the advantage of avoiding the introduction of optimization principles, and it has been shown to accurately describe some experimental results for the Al–Zn system. It also predicts that steady-state solutions with invariant front shapes are possible within a limited range of driving forces, suggesting the possibility of morphological instabilities outside this range.

All of these theories of steady growth assume that the motion of the interface is continuous. This assumption is probably acceptable when the growth front is well-rounded, but there is substantial evidence for faceted interfaces at low supersaturations, as discussed in detail in the next section. In the high-supersaturation regime, the continuum models seem to apply with-

out modification; however, the theories need to take into account the possibility of lateral migration of the growth interface for lower supersaturation. A recent treatment by Klinger et al. (1997a) takes this into account by describing the motion of the interface as intermittent.

7.5.3.3 Experimental Observations

The majority of experimental studies have focused on microstructures developed through steady isothermal growth. They are therefore capable of description in terms of the theoretical treatments of the previous section. The types of information accessible to experiment are:

- a) quantities that may be derived from conventional metallographic methods: average velocity v and spacing S ;
- b) chemical information obtained either from averaging processes such as X-ray diffraction measurements of lattice parameters of product lamellae or from high resolution microanalyses of the product;
- c) structural information relating to the growth interface, as obtained for example by transmission electron microscopy.

In addition, for the test of theory we require solution thermodynamic data, interfacial energies and interfacial diffusion coefficients. Many alloy systems have been investigated. In this section we will focus on the systems Al–Zn and Mg–Al, for which much of the necessary data are available (e.g., Rundman and Hilliard, 1967; Cheetham and Sale, 1974; Hassner, 1974).

Yang et al. (1988) collected velocity and spacing data for Al–Zn alloys, and for a range of reaction temperatures and spacings, as summarized in Figs. 7-24 and 7-25. Figure 7-26 gives the average composition of the α lamellae superimposed on the Al-rich portion of the phase diagram. These

composite figures include results from the work of Ju and Fournelle (1985), Suresh and Gupta (1986), Cheetham and Sale (1974), Razik and Maksoud (1979), Watanabe and Koda (1965), Gust et al. (1984) and Yang et al. (1988). Perhaps the most striking feature of these data is the extent of residual supersaturation left in the α phase behind the transformation front; a significant amount of the total Helmholtz energy for the transformation is stored in the product phase.

This stored Helmholtz energy, first emphasized by Cahn (1959), must be estimated in order to evaluate the driving force for the transformation. This estimation is

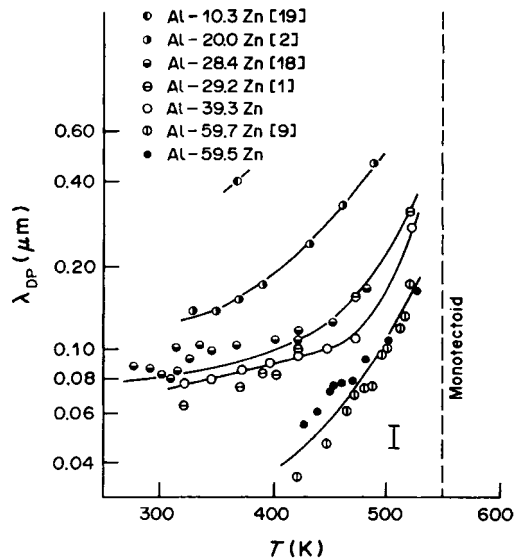


Figure 7-25. Interlamellar spacing measurements for discontinuous precipitation (DP) products, from the same sources as for Fig. 7-24. Reprinted with permission from Yang et al. (1988).

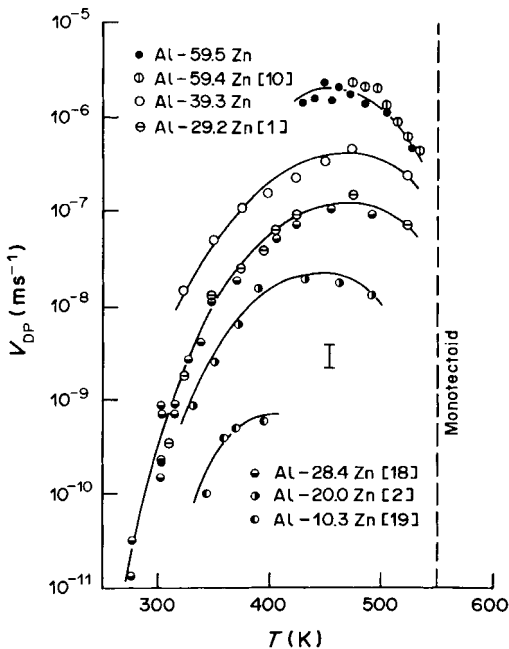


Figure 7-24. Grain-boundary velocities for a range of reaction temperatures and for several Al-Zn alloys (index DP denotes discontinuous precipitation). The data are from studies by Yang et al. (1988), Ju and Fournelle (1985) [1], Suresh and Gupta (1986) [2], Cheetham and Sale (1974) [9], Razik and Maksoud (1979) [10], Gust et al. (1984) [18], and Watanabe and Koda (1965) [19]. Reprinted with permission from Yang et al. (1988).

readily performed using data of the type shown in Fig. 7-26. This stored Helmholtz energy provides a portion of the driving force for subsequent discontinuous coarsening processes, which generally increase the interlamellar spacing and deplete the product α to (near) the solubility limit (Yang et al., 1988).

High resolution microanalysis is capable of providing further insights into the stored Helmholtz energy term (Zięba and Gust, 1998). The elemental trace of Fig. 7-27 was obtained from a STEM (scanning transmission electron microscope) X-ray microanalysis of a thin foil of Al-22 at.% Zn transformed at 428 K. Measurements of this type give both local and integral values of the stored Helmholtz energy. In addition to the information concerning the solute concentration distribution in the α phase, these profiles can be analyzed to yield rather directly the product $\{sD^b\delta\}$ via Eq. (7-23), (Porter and Edington, 1977; Solor-

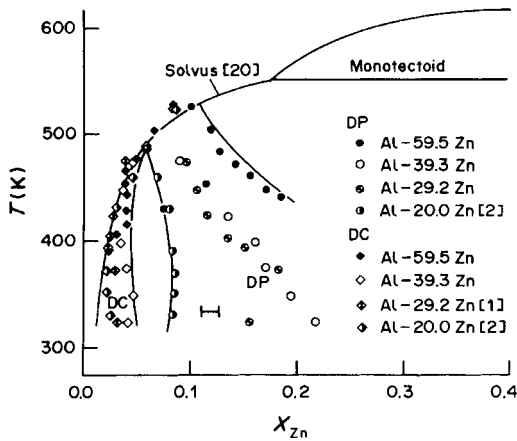


Figure 7-26. Average zinc concentrations in the α phase for discontinuous precipitation (DP) and for discontinuous coarsening (DC) reactions in various Al-Zn alloys. Reprinted with permission from Yang et al. (1988).

zano et al., 1984; Duly et al., 1994a, b). However, in their studies of regular growth in Mg-Al alloys, Duly et al. determined that:

a) In certain cases, the concentration profiles between parallel lamellae (similar to Fig. 7-27) were well described by

Cahn's equation with constant values of $C_{\alpha\beta}^*$ and \sqrt{a} .

b) However, within a given nodule, the value of (a/S_α^2) was generally not constant, varying by more than an order of magnitude. This quantity is proportional to the instantaneous interfacial velocity, and its variation is taken to mean that, on an atomic length scale, the interface velocity is irregular. On a larger length scale, typically 0.1 μm , an average velocity can be defined that is consistent with the steady diffusion analysis of Cahn.

A major implication of these findings is that the transformation interface moves by a lateral growth mechanism, resulting in an average velocity much less than the instantaneous velocity accompanying the passage of a growth step. It is here that the recent studies of Shiflet and his co-workers (Fonda and Shiflet, 1990; Fonda et al., 1998) on Cu-Ti alloys are relevant. Their results indicate a strong and consistent tendency for the transformation front to facet, particularly at low undercoolings, and this implies a lateral displacement process, consistent with the findings of Duly et al.

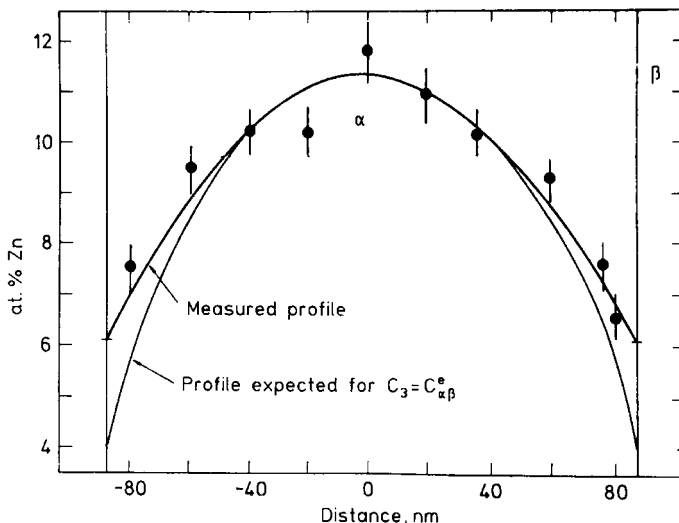


Figure 7-27. STEM microanalysis of an α lamella in Al-22 at.% Zn, formed at 428 K. After Solorzano and Purdy (1984).

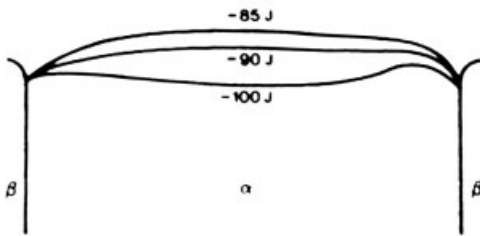
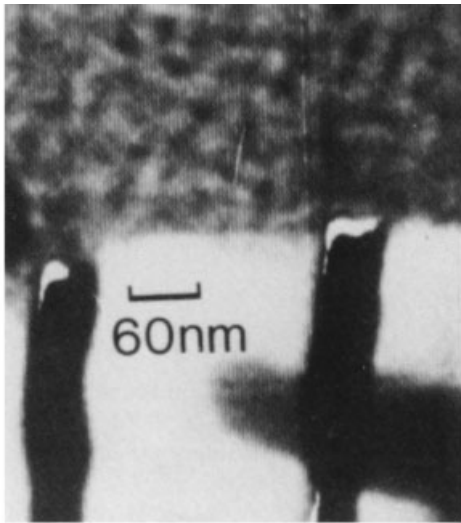


Figure 7-28. Observed and calculated interface shapes for an α lamella formed at 400 K in Al-22 at.% Zn. The numbers on the curves represent different amounts of Helmholtz energy lost owing to continuous precipitation in the parent phase.

(1994 a, b). At lower reaction temperatures, the growth interfaces in Cu-Ti become smoothly curved. This is attributed to the rapid accumulation of growth ledges with increasing undercooling.

The smoothly curved interfaces and steady migration rates seen in high resolution *in situ* studies of discontinuous precipitation in Al-Zn (see Fig. 7-28, Tashiro and Purdy, 1989) suggest that, at lower temperatures, the interface can be considered to move continuously. Indeed, the interface shapes observed could be rationalized in terms of a local balance between

chemical (evaluated from microanalyses), capillary and friction forces, realized at every point on the transformation front. It therefore appears that at some stage an effective transition occurs where the accumulation of growth ledges is sufficient to mimic the normal migration of the front, and the classical theories of Cahn and Hillert then hold to a good approximation.

There is a further set of experimental data on discontinuous precipitation that relates to the effect of an applied stress on the transforming system. Sulonen (1964 a, b) showed that in some alloy systems, fronts with normals parallel to the tensile axis moved more slowly, and those with normals perpendicular to the stress axis more quickly than those in unstressed alloys. In other alloy systems, the opposite behavior was found. The effect for Cu-Cd alloys is shown in Fig. 7-29. Sulonen proposed an

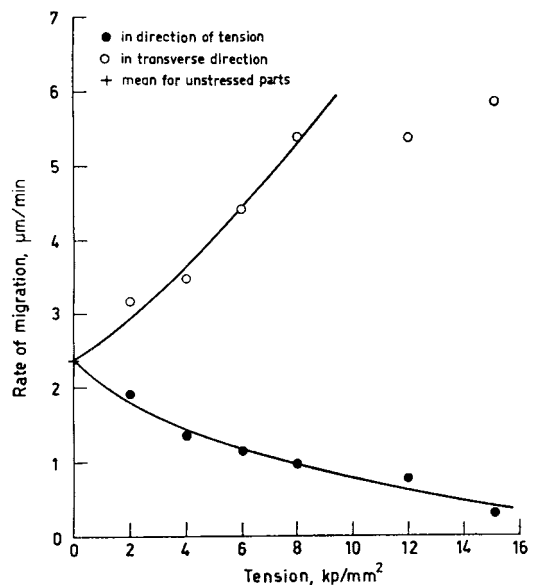


Figure 7-29. Effect of an applied tensile stress on the rates of growth of the discontinuous product in Cu-Cd alloys ($1 \text{ kp/mm}^2 \approx 9.81 \times 10^6 \text{ N/m}^2$). Reprinted with permission from Sulonen (1964b), copyright Pergamon Press.

explanation based on the elastic interaction between the applied and coherency (solute) stress fields. Hillert (1972) indicated how a quantitative treatment of such an effect could be formulated. Sulonen's result and Hillert's analysis have been widely quoted in support of the existence of a solute (coherency) field in front of the discontinuous transformation front, even at temperatures where the calculated diffusion distance is negligible.

Dryden and Purdy (1990) reconsidered the problem, and included the possible effect of a volume misfit in the transformed region. It was found, in agreement with Hillert, that the sign of the effect could be predicted on the basis of an elastic solute field interaction; however, the predicted effects on interface velocities are too small by four orders of magnitude. The more likely cause of the coupling is found in the plastic response of the dead-loaded specimen. The reduction in Helmholtz energy of the loading device results in a virtual force on the transformation interface, as discussed in Sec. 7.4.3.2. For the case of interfaces with normals parallel to the x , y , and z (tensile) axes, these virtual forces are related by

$$p_x = p_y = -\left(\frac{1+3\Omega}{2}\right)p_z = \frac{Z\varepsilon}{2}(1+3\Omega) \quad (7-28)$$

where p_x , p_y , and p_z are forces per unit area, Z is the applied tensile stress, ε is the stress-free strain in the transformed volume, and Ω is an alignment parameter which accounts for the possibility that the lamellae in transformed regions bounded by x and y interfaces are aligned with respect to the z axis.

It is found that the virtual forces so derived, in conjunction with independently derived grain-boundary mobilities, are capable of explaining the sign and magnitude of Sulonen's data for Cu–Cd alloys (Fig.

7-29), and give the correct sign of the effect for the other five systems investigated, for which no quantitative data were obtained. We conclude that it is the plastic (or creep) response of the specimen which is more plausibly coupled to the migration rates of differently oriented transformation interfaces.

7.5.4 Interface Migration in Multilayers

Multilayers have been utilized for critical experiments since the seminal work of Hilliard and his co-workers (1954). They provide an ideal tool for the investigation of the thermodynamics and kinetics of heterogeneous systems far from equilibrium. Much of the work to date has been concerned with the approach to equilibrium via bulk diffusion. The recently developed techniques for precisely controlled growth (e.g., molecular beam epitaxy) prompt the exploration of the approach to equilibrium via interfacial diffusion and migration. The theoretical investigations summarized in this section deal with possible effects, many of which are still to be observed.

Several classes of problems can be developed, beginning with an A–B multilayer grown on a bicrystalline substrate such that a grain boundary penetrates the whole structure and provides a possible fast diffusion path. The simplest case occurs when A and B are fully miscible. Homogenization can then occur by grain boundary motion, either via a cooperative mechanism, or by a “fingering solution” at the former A/B interfaces as illustrated in Figure 7-30 (Klinger et al., 1997a). In each case, the shape of the moving boundary, as well as its velocity and the concentration profile left in its wake, can be computed in terms of driving forces, interface energies and diffusion coefficients.

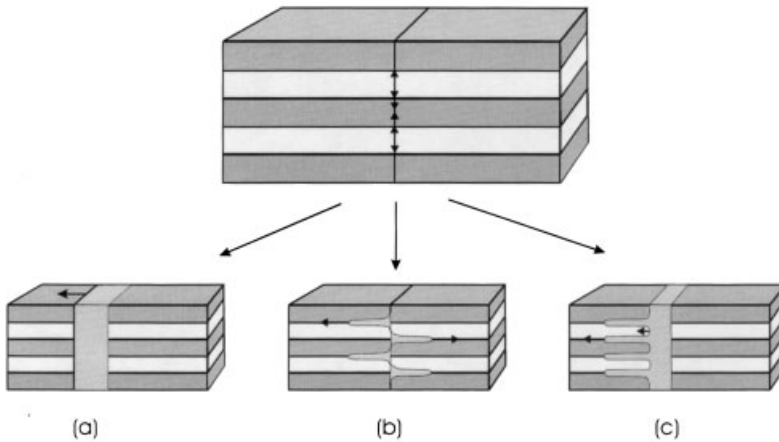


Figure 7-30. Illustrating three different possibilities for the discontinuous homogenization of a monophase multilayer containing a mobile grain boundary, assumed initially to bisect the multilayer. Situations corresponding to (a) the steady state motion of the boundary; (b) an initially sinusoidal instability of the grain boundary, and (c) a “fingering” instability of the moving boundary, after Klinger et al. (1997b).

The next situation to be considered is when A and B are reactive, and form a stoichiometric compound ω (or, conversely, when such a compound decomposes to form A and B). Again, for this case, the velocity of the cooperative moving front for reaction (or dissolution) can be computed as a function of the energies and mobilities involved (Klinger et al., 1997c). A solution involving a reaction product layer at the interface rather than a cooperative growth front can also be considered (Fig. 7-31), and this may help to explain certain peculiarities found in kinetics in reactive multilayers, in terms of diffusion barrier effects (Klinger et al., 1998; Emeric, 1998).

These theoretical investigations, many still awaiting experimental confirmation, suggest a wide variety of possible kinetic paths toward thermodynamic equilibrium (involving pattern and velocity selection as well as morphological instabilities) in well-controlled systems. In these systems, a number of classical hypotheses such as that of local equilibrium could be checked quantitatively. It is suggested that the

search for such interface-mediated structural evolution in controlled multilayered structures can play a key role in the deeper understanding of the more frequently encountered phenomena described in the rest of this chapter.

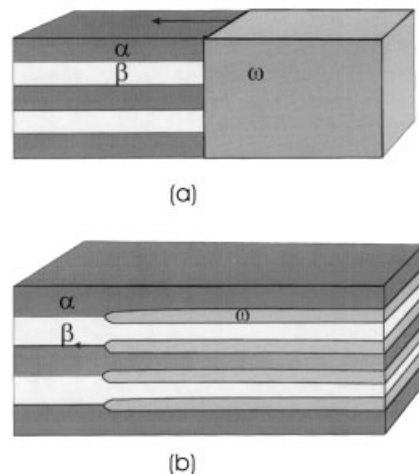


Figure 7-31. Schematic representation of the possible reactions of A and B to form a stoichiometric product phase ω . (a) A cooperative reaction at a single front; (b) the growth of a product layer at the interface (after Klinger et al., 1997c).

7.6 Conclusions

In this chapter we have been concerned with those phase transformations that depend on diffusion within a transformation front. The massive transformation, chemically-induced grain boundary migration, discontinuous precipitation and transformations in multilayers represent different and distinct facets of the general class of interface-diffusion controlled transformations.

In each case, the description of the transformation in terms of a balance of forces on the moving interface has proved a unifying concept. For the massive transformation, it is believed that the major forces at play are the chemical driving force and the opposing frictional forces. In the description of chemically-induced grain boundary migration, especially at higher temperatures, an elastic (coherency) term due to a gradient of misfitting solute atoms in the parent grain must be added to the other two types of force. For discontinuous precipitation, capillary forces must be introduced to oppose the chemical driving force. We have also considered transformations in multilayer heterostructures, where capillary terms must be accounted, and where interfacial diffusion is often driven by interfacial curvature.

The description offered has been predominantly thermodynamic, rather than deeply mechanistic. Much remains to be learned about the mechanisms of accommodation of diffusing atoms within the transformation interface, about the coupling of the driving forces with interface response, and about the interrelationships between interfacial structure and kinetics. It has become increasingly clear that many transformation interfaces are faceted, and remain faceted during migration. In such cases, the classical models for diffusional

transformations will need to be reformulated, and this is only beginning to take place.

The thermodynamic structure remains a valuable synthetic framework within which to place advances in the understanding of this fascinating field.

7.7 References

- Aaronson, H. I., Aaron, H. B. (1972), *Metall. Trans.* A3, 2743.
- Aaronson, H. I., Liu, Y. L. (1968), *Scripta Metall.* 2, 1.
- Ackert, R. J., Parr, J. G. (1971), *J. Iron Steel Inst.* 209, 912.
- Ashby, M. F., Spaepen, F., Williams, S. (1979), *Acta Metall.* 26, 235.
- Aust, K. J., Rutter, J. W. (1959), *Trans. AIME* 215, 119.
- Aziz, M. J., Kaplan, T. (1988), *Acta Metall.* 36, 2335.
- Bailey, J., Hirsch, P. B. (1962), *Proc. Roy. Soc. A287*, 11.
- Balluffi, R. W., Kwok, T., Bristowe, P. S., Brokman, A., Ho, P. S., Yip, S. (1981), *Scripta Metall.* 15, 951.
- Barrett, C. S., Massalski, T. B. (1966), in: *Structure of Metals*, 3rd ed. New York: McGraw-Hill.
- Baumann, S. F., Michael, J., Williams, D. B. (1981), *Acta Metall.* 29, 1343.
- Bibby, M. J., Parr, J. G. (1964), *J. Iron Steel Inst.* 202, 100.
- Bollmann, W. (1970), *Crystal Defects and Crystal-line Interfaces*, Berlin: Springer-Verlag.
- Bréchet, Y. J. M., Purdy, G. R. (1989), *Acta Metall.* 37, 2253.
- Bréchet, Y., Purdy, G. R. (1992), *Scripta Metall.* 27, 1753.
- Cahn, J. W. (1959), *Acta Metall.* 7, 8.
- Cahn, J. W. (1962), *Acta Metall.* 10, 789.
- Cahn, J. W. (1982), *J. Physique* 43, Suppl. 12, C6.
- Cahn, J. W., Allen, S. (1977), *J. Phys.* C7, 12; 57.
- Cahn, J. W., Fife, P., Penrose, O. (1998), *Acta Mater.* 45, 4397.
- Cahn, J. W., Hilliard, J. E. (1958), *J. Chem. Phys.* 28, 258.
- Carter, W. C., Taylor, J. E., Cahn, J. W. (1997), *J. O. M.*, December, 30.
- Cheetham, D., Sale, F. R. (1974), *Acta Metall.* 33, 71.
- Chen, L.-Q., Fan, D. N., Tikare, V. (1998), in: *Grain Growth in Polycrystalline Materials*, Weiland, H., Adams, B., Rollett, T. (Eds.), Warrendale, PA, USA: TMS, p. 137.
- Chen, J. K., Purdy, G. R., Weatherly, G. C., Kroupa, A. (1998), *Metall. Mater. Trans. A* 29, 2049.

- Cottrell, A. H. (1953), *Dislocations and Plastic Flow in Crystals*, Oxford: Oxford University Press.
- Dahmen, U. (1981), *Scripta Metall.* 15, 77.
- Delacy, L. (2001), in: *Phase Transformations in Materials*: Kosterz, G. (Ed.). Weinheim: Wiley-VCH, Chap. 9.
- Delage, S. (1998), Ph.D. thesis, University of Paris V.
- den Broeder, F. J. A. (1972), *Acta Metall.* 20, 319.
- Dryden, J. R., Purdy, G. R. (1990), *Acta Metall.* 38, 1255.
- Duly, D., Bréchet, Y. (1994), *Acta Metall. Mater.* 42, 3035.
- Duly, D., Cheynet, M. C., Bréchet, Y. (1994a) *Acta Metall. Mater.* 42, 3843.
- Duly, D., Cheynet, M. C., Bréchet, Y. (1994b) *Acta Metall. Mater.* 42, 3855.
- Emeric, E. (1998), Ph.D. thesis, Marseille.
- Faridi, B. A., Crocker, A. G. (1980), *Phil. Mag.* A41, 137.
- Ferrence, T. G., Balluffi, R. W. (1988), *Scripta Metall.* 22, 1929.
- Fonda, R. W., Mangan, M. A., Shiflet, G. J. (1998), *Metall. Mater. Trans. A* 29, 2101.
- Fournelle, R. A., Clark, J. B. (1972), *Metall. Trans.* A3, 2757.
- Gibbs, J. W. (1906), *Scientific Papers, Vol. 1, Thermodynamic*. New York: Dover Publications.
- Gust, W. (1984), in: *Decomposition of Alloys, The Early Stages*: Haasen, P., Gerold, V., Wagner, R., Ashby, M. F. (Eds.). Oxford: Pergamon, p. 221.
- Gust, W., Hintz, B. B., Lucic, R., Predel, B. (1984), in: *Phase Transitions in Solids*: Tsakalakos, T. (Ed.). New York: Elsevier, p. 513.
- Gust, W., Mayer, S., Bogel, A., Predel, B. (1985), *J. Physique C* 46, 537.
- Guttman, M. (1995), *J. Phys.* C7, 85.
- Hassner, A. (1974), *Kristall. Tech.* 9, 1371.
- Hazzledine, P. M., Oldershaw, R. D. (1990), *Phil. Mag.* A 61, 579.
- Hillert, M. (1969), in: *The Mechanism of Phase Transformations in Crystalline Solids*. London: Institute of Metals, Monograph No. 33, p. 231.
- Hillert, M. (1972), *Metall. Trans.* 3 A, 2729.
- Hillert, M. (1975a), in: *Lectures on the Theory of Phase Transformations*: Aaronson, H. I. (Ed.), New York: AIME, p. 1.
- Hillert, M. (1975b), *Metall. Trans.* 6 A, 5.
- Hillert, M. (1982), *Acta Metall.* 30, 1689.
- Hillert, M., Lagneborg, R. (1971), *J. Mater. Sci.* 6, 208.
- Hillert, M., Purdy, G. R. (1978), *Acta Metall.* 26, 333.
- Hillert, M., Sundman, B. (1976), *Acta Metall.* 24, 731.
- Hilliard, J. E., Averbach, B. L., Cohen, M. (1954), *Acta Metall.* 2, 621.
- Hoffman, D. W., Cahn, J. W. (1972), *Surface Science* 31, 368.
- Hsieh, T. E., Balluffi, R. W. (1989), *Acta Metall.* 37, 2133.
- Humphreys, F. J., Hatherly, M. (1995), *Recrystallization and Related Annealing Phenomena*. Oxford: Pergamon, Elsevier Science Ltd., p. 212.
- Ju, C. P., Fournelle, R. A. (1985), *Acta Metall.* 33, 71.
- Karlyn, D. A., Cahn, J. W., Cohen, M. (1969), *Trans. TMS-AIME.* 245, 197.
- Kaur, I., Gust, W. (1988), *Fundamentals of Grain and Interphase Boundary Diffusion*. Stuttgart: Ziegler Press.
- King, A. H. (1987), *Internat. Mater. Rev.* 32, 173.
- Klinger, L., Bréchet, Y., Purdy, G. R. (1996), *Acta Mater.* 45, 5005.
- Klinger, L., Bréchet, Y., Duly, D. (1997a), *Scripta Mater.* 37, 1237.
- Klinger, L., Bréchet, Y., Purdy, G. R. (1997b), *Acta Mater.* 45, 325.
- Klinger, L., Bréchet, Y., Purdy, G. R. (1997c), *Acta Mater.* 45, 4667.
- Klinger, L., Bréchet, Y., Purdy, G. R. (1998), *Acta Mater.* 46, 2617.
- Krakow, W., Wetzel, J. T., Smith, D. A. (1986), *Phil. Mag.* A53, 739.
- LeClaire, A. D. (1986), in: *Solute-Defect Interactions*: Saimoto, S., Purdy, G. R., Kidson, G. V. (Eds.). Oxford: Pergamon, p. 251.
- Levine, H. S., MacCallum, C. J. (1960), *J. Appl. Phys.* 31, 595.
- Lücke, K., Detert, K. (1957), *Acta Metall.* 5, 517.
- Mangan, M. A., Shiflet, G. J. (1997), *Scripta Mater.* 37, 517.
- Martin, G., Blackburn, D. A., Adda, Y. (1967), *Phys. Stat. Sol.* 23, 223.
- Martin, G., Athenes, M., Desgranges, C., Nasbur, M., Soissons, F. (1998), in: *Diffusion Mechanisms in Crystalline Solids*, Mishin, Y., Cowern, N. E. B., Catlow, C. R. N., Farkas, D., Vogl, G. (Eds.). MRS Symposium Proceedings, vol. 527, Warrendale, PA, USA: MRS, p. 35.
- Massalski, T. B. (1958), *Acta Metall.* 6, 243.
- Massalski, T. B. (1984), *Metall. Trans.* 15A, 421.
- Menon, E. S. K., Plichta, M. R., Aaronson, H. I. (1988), *Acta Metall.* 36, 321.
- Meyrick, G. (1976), *Scripta Metall.* 10, 649.
- Michael, J. R., Williams, D. B. (1986), in: *Interface Migration and Control of Microstructure*: Pande, C. S., Smith, D. A., King, A. H., Walter, J. (Eds.). Metals Park, OH, USA: ASM, p. 73.
- Morral, J. E., Purdy, G. R. (1995), *J. Alloys and Compounds* 220, 132.
- Mullins, W. W. (1957), *J. Appl. Phys.* 28, 333.
- Pawlowski, A., Zięba, P. (1991), *Phase Transformations Controlled by Diffusion at Moving Boundaries*, Krakow, Poland: Polish Academy of Sciences.
- Perepezko, J. H. (1984), *Metall. Trans.* 15A, 437.
- Perovic, A., Purdy, G. R. (1981), *Acta Metall.* 29, 53.
- Petermann, J., Hornbogen, E. (1968), *Z. Metallk.* 59, 814.
- Peterson, N. L. (1983), *Internat. Met. Rev.* 28, 65.

- Plichta, M. R., Clark, W. A. T., Aaronson, H. I. (1984), *Metall. Trans. A* 15, 42.
- Porter, D. A., Edington, J. W. (1977), *Proc. Roy. Soc. A* 358, 335.
- Purdy, G. R. (1971), *Met. Sci. J.* 5, 81.
- Purdy, G. R., Lange, N. (1984), in: *Decomposition of Alloys, The Early Stages*: Haasen, P., Gerold, V., Wagner, R., Ashby, M. F. (Eds.). Oxford: Pergamon, p. 214.
- Razik, N. A., Maksoud, S. A. (1979), *Appl. Phys.* 19, 331.
- Rhee, W.-H., Yoon, D. K. (1989), *Acta Metall.* 37, 221.
- Rigsbee, J. M., Aaronson, H. I. (1979), *Acta Metall.* 27, 351, 365.
- Robinson, J. T., Peterson, N. L. (1973), *Acta Metall.* 21, 1181.
- Rottman, C., Voorhees, D. W., Johnson, W. C. (1988), *Scripta Metall.* 22, 293.
- Rundman, K. B., Hilliard, J. E. (1967), *Acta Metall.* 15, 1025.
- Singh, J., Purdy, G. R., Weatherly, G. C. (1985), *Metall. Trans. A* 16, 1363.
- Smith, C. S. (1948), *TMS-AIME* 175, 15.
- Smith, D. A. (1986), *Proc. Int. Conf. on Solute-Defect Interactions*: Saimoto, S., Purdy, G. R., Kidson, G. V. (Eds.). Oxford: Pergamon, p. 128.
- Solorzano, I. G., Purdy, G. R. (1984), *Metall. Trans. A* 15, 1055.
- Solorzano, I. G., Purdy, G. R., Weatherly, G. C. (1984), *Acta Metall.* 32, 1709.
- Stephens, D. E., Purdy, G. R. (1975), *Acta Metall.* 23, 1343.
- Straumal, B. B., Bokshtein, B. S., Klinger, L. M., Shvindlerman, L. S. (1981), *Scripta Metall.* 15, 1197.
- Sulonen, M. S. (1964a), *Acta Polytechnica Scandinavica* 28, 5.
- Sulonen, M. S. (1964b), *Acta Metall.* 12, 749.
- Sundquist, B. F. (1973), *Metall. Trans. A* 4, 1919.
- Suresh, V., Gupta, S. (1986), *Z. Metallk.* 77, 529.
- Sutton, A. (1995), in: *Computer Simulation in Materials Science*, NATO ASI vol. 308, Pontikis, V., Kirchner, H., Kubin, L. (Eds.), Dordrecht (Netherlands): Kluwer, p. 163.
- Sutton, A. P., Balluffi, R. W. (1987), *Acta Metall.* 35, 2177.
- Sutton, A., Balluffi, R. W. (1995), *Interfaces in Crystalline Metals*, Oxford: Oxford University Press.
- Suzuoka, T. (1964), *J. Phys. Soc. (Japan)* 19, 839.
- Tashiro, K., Purdy, G. R. (1983), *Scripta Metall.* 17, 455.
- Tashiro, K., Purdy, G. R. (1987), *Scripta Metall.* 21, 361.
- Tashiro, K., Purdy, G. R. (1989), *Metall. Trans. A* 20, 1593.
- Treglia, G., Legrand, B. (1998), in: *Tight Binding Approach to Computational Materials Science*: Turchi, P. E., Gonis, A., Columbo, L. (Eds.). MRS Symposium Proceedings, vol. 491, Warrendale, PA, USA: MRS, p. 275.
- Tu, K. N. (1972), *Metall. Trans. A* 3, 2769.
- Tu, K. N., Turnbull, D. (1969), *Acta Metall.* 17, 1263.
- Turnbull, D. (1951), *Trans. AIME* 191, 661.
- Verdier, M., Groma, I., Flandin, L., Lendvaii, J., Bréchet, Y., Guyot, P. (1997), *Scripta Mater.* 37, 449.
- Vitek, V. (1984), in: *Dislocations 1984*: Veyssiere, P., Kubin, L., Castaing, J. (Eds.). Paris: Editions du CNRS, p. 435.
- Wagner, R., Kampmann, R., Voorhees, P. W. (2001), in: *Phase Transformations in Materials*: Kostorz, G. (Ed.). Weinheim: Wiley-VCH, Chap. 5.
- Wanatabe, R., Koda, S. (1965), *Trans. Natl. Res. Inst. Metals (Japan)* 7, 87.
- Weygand, D. (1998), Ph.D. thesis, Grenoble, INPG.
- Weygand, D., Bréchet, Y., Lepinoux, J. (1999), *Acta Mater.* 47, 961.
- Wheeler, A., Boettinger, W. J., McFadden, G. B. (1992), *Phys. Rev. A* 45, 7425.
- Whipple, R. (1954), *Phil. Mag.* 45, 1225.
- Yang, C. F., Sarker, G., Fournelle, R. A. (1988), *Acta Metall.* 36, 1511.
- Zener, C. (1946), *Trans. AIME* 167, 550.
- Zhang, W.-Z., Purdy, G. R. (1993a), *Phil. Mag. A* 68, 279.
- Zhang, W.-Z., Purdy, G. R. (1993b), *Phil. Mag. A* 68, 291.
- Zhang, W.-Z., Perovic, V., Perovic, A., Weatherly, G. C., Purdy, G. R. (1998), *Acta Mater.* 46, 3443.
- Zigba, P., Gust, W. (1998), *Internat. Mater. Rev.* 43, 70.

8 Atomic Ordering

Gerhard Inden

Max-Planck-Institut für Eisenforschung GmbH, Düsseldorf, Federal Republic of Germany

List of Symbols and Abbreviations	521
8.1 Introduction	523
8.2 Definition of Atomic Configurations	523
8.2.1 Configurational Variables	523
8.2.2 Point Variables	525
8.2.3 Point Correlation Functions and Point Probabilities	526
8.2.4 Pair Variables, Correlation Functions, and Probabilities	527
8.2.5 Generalized Cluster Variables, Correlation Functions, and Probabilities	529
8.2.6 Short-Range-Order (sro) Configurations – Long-Range-Order (lro) Configurations	529
8.3 The Existence Domain and Configuration Polyhedron	531
8.3.1 F.C.C. Structure, First Neighbor Interactions	532
8.3.2 F.C.C. Structure, First and Second Neighbor Interactions	535
8.3.3 B.C.C. Structure, First and Second Neighbor Interactions	537
8.4 Ground States	538
8.4.1 Pair Interactions	538
8.4.1.1 Ground State Energies	540
8.4.1.2 F.C.C. Structure, First Neighbor Interactions	540
8.4.1.3 F.C.C. Structure, First and Second Neighbor Interactions	543
8.4.1.4 B.C.C. Structure, First and Second Neighbor Interactions	544
8.4.1.5 Energy Minimum at Constant Composition	544
8.4.1.6 Canonical Energy of lro States	546
8.4.1.7 Relevant Literature	547
8.4.2 Effective Cluster Interactions (ECIs)	548
8.5 Phase Equilibria at Finite Temperatures	551
8.5.1 Cluster Variation Method	551
8.5.2 Calculation of Phase Diagrams with the CVM	554
8.5.3 Phase Diagram Calculation with the Monte Carlo Method	554
8.5.4 Examples of Prototype Diagrams	555
8.5.4.1 F.C.C. Structure, First Neighbor Interactions	555
8.5.4.2 F.C.C. Structure, First and Second Neighbor Interactions	557
8.5.4.3 B.C.C. Structure, First and Second Neighbor Interactions	558
8.5.4.4 Hexagonal Lattice, Anisotropic Nearest-Neighbor Interactions	558
8.5.5 The Cluster Site Approximation (CSA)	560
8.6 Application to Real Systems	561
8.6.1 The Au–Ni System	563

8.6.2 The Thermodynamic Factor of Ordered Phases 565

8.6.2.1 The B.C.C. Fe–Al System 565

8.6.2.2 The F.C.C. Ni–Al System 567

8.6.3 Ternary Systems 569

8.6.3.1 B.C.C. Fe–Ti–Al 569

8.6.3.2 B.C.C. Ferromagnetic Fe–Co–Al 570

8.6.4 H.C.P. Cd–Mg 573

8.6.5 Concluding Remarks 574

8.7 **Appendix** 575

8.8 **Acknowledgements** 578

8.9 **References** 578

List of Symbols and Abbreviations

$\mathbf{a}, \mathbf{a}_1, \dots$	basic vectors of the structure
a_α	CVM exponents
$\mathbf{b}, \mathbf{b}_1, \dots$	basic vectors of the structure
$\mathbf{c}, \mathbf{c}_1, \dots$	basic vectors of the structure
d	distance of hyperplane to the origin
\tilde{E}	part of internal energy that depends only on the configurational variables
F	Helmholtz energy
i	number identifying the type of atom
k	number identifying a neighbor distance
K	number of constituents
k_B	Boltzmann constant
m_α	number of α -clusters per point
N	number of lattice sites
n, m	number identifying a lattice site
\mathbf{n}	normal vector
N_i	number of atoms i
$N(\sigma_r)$	number of r -clusters with occupation σ_r
N_r	number of equivalent r -site clusters
$p_n^{(i)}$	site-occupation operator for atom i on site n
p_{nm}^{ij}	occupation operator for atom pair i, j on sites n, m
r	number of lattice points within a cluster
S	entropy
T	temperature
U, \tilde{U}	internal energy, grand canonical internal energy
V	volume
V_{ij}^{nm}	pair energy of atoms i, j on sites n, m
W	number of possible arrangements of clusters formed for given values of the correlation functions
$W_{ij}^{(k)}$	pair exchange energy of k -th neighbor atoms I and J
$W^{(k)}$	binary case: indices ij omitted
$W_{ij\dots l}^{12\dots r}$	r -site cluster exchange energy correction term
V_n	cluster expansion coefficient
$w_n^{i \rightarrow j}$	transition probabilities
\mathbf{x}	hyperplane position vector
\mathbf{x}_v	vertex vector
x_i	mole fraction of atom of type i
$z^{(1\dots r)}$	coordination number of r -site clusters
α	number identifying a cluster
α_{n-m}^{ij}	Cowley–Warren sro parameters
μ_i	chemical potential of atoms i
v	dimension of configurational space

ν_{tot}, ν_p	total number of configurational probabilities, number of configurational probabilities related by partial summations
ξ_1, ξ_2, ξ_3	lro parameters
$Q(\sigma_r)$	$N(\sigma_r)/N_r$
Q_{nm}^{ij}	probability of having atoms i, j on sites n, m
σ	vector with site operators as components
σ_n	site operator or spin variable
τ_k	values of the site operator
φ	arbitrary function
Φ_i, Φ	energy variables, defining dual space of the configurational variables, their vector hyperplane
Ω	grand potential
CVM	cluster variation method
CSA	cluster site approximation
EC	cluster expansion
ECI	effective cluster interaction
lro	long-range order
$n-m$	neighbor distance between sites n, m (equivalent to number k)
MC	Monte Carlo simulation
sro	short-range order

$$1 \text{ } k_{\text{B}}\text{-unit} = 1 \text{ } k_{\text{B}} \text{ K} = 13.8 \times 10^{-24} \text{ J} = 8.6 \times 10^{-2} \text{ meV}$$

8.1 Introduction

Ordered structures occur frequently in solid solutions and exhibit interesting physical and mechanical properties. This explains the continuous interest in ordering reactions by theoreticians and experimentalists over recent decades. There are some excellent overview articles and books (e.g., Ducastelle, 1991; Turchi and Gonis, 1994; de Fontaine, 1979, 1994; Khachaturyan, 1978) on the theoretical aspects of this subject, while the experimental and materials science aspects can be found in articles by Kear et al. (1970), Warlimont (1974), Koch et al. (1985), Stoloff et al. (1987), Liu et al. (1989, 1992), and Whang et al. (1990).

The ordered phases can be classified under the family of intermetallic phases. As such they have attracted interest in the development of materials for special applications (e.g., materials for use at high temperatures). Thus there is an increasing demand for quantitative descriptions of the variations in their properties. Furthermore, materials with practical relevance rarely consist of binary systems. Treatments of multicomponent systems are thus especially needed. The most fundamental problems that need to be solved at the start of any optimization of materials involve the type of ordered structure, the variation of the atomic distribution with temperature and composition, and the phase equilibria. This chapter is an updated version of the previous contribution by Inden and Pitsch (1991). The tutorial aspects have been maintained as much as possible. It is for this reason that the basic ideas are still presented in terms of a pair interaction scheme, which can only provide prototype results. An up-to-date treatment of real systems requires more sophisticated approaches that take into account previously neglected but very important physical ef-

fects. First-principles calculations of total energies, of lattice relaxations and of local relaxations were still in their infancy ten years ago, but such theoretical calculations are now available. They will be discussed in relation to the treatment of real alloys.

The variety of materials exhibiting ordering is too great to be dealt with completely. The present chapter will therefore be limited to metallic substitutional alloys, despite the fact that the techniques discussed have also been used extensively in the field of interstitial alloys, carbides, nitrides, oxides, and semiconductor systems.

The chapter is organized as follows. In Sec. 8.2, a general formalism for describing and characterizing atomic configurations in multicomponent substitutional alloys is presented. The concept of correlation functions as independent variables for the definition of the configurations is introduced and used in Sec. 8.3 to derive existence domains; they limit the range of numerical values that can be scanned by the correlation functions for topologically existing configurations. These existence domains are used in Sec. 8.4 to determine the ground states. In Sec. 8.5, equilibrium at finite temperatures is discussed in terms of the cluster variation method (CVM) and the Monte Carlo simulation (MC). Finally, in Sec. 8.6, the application to real systems is discussed.

8.2 Definition of Atomic Configurations

8.2.1 Configurational Variables

Let us consider a crystalline system with N lattice sites and K constituents $i = A, B, \dots$. Defining the number of atoms of type i by N_i gives $\sum_i N_i = N$ and the mole fractions $x_i = N_i/N$. The distribution of the

atoms on the lattice sites defines the configuration.

In order to specify a configuration, we need an operator which identifies unequivocally the atomic species on an arbitrary site n . A convenient means of identification is to associate an integral number with each constituent and to define a site operator σ_n , which takes these integral values corresponding to the constituent on site n . Different choices are possible, e.g.,

$$\sigma_n = \begin{cases} 0 \\ 1 \\ 2 \\ \vdots \\ K-1 \end{cases} \quad \text{or} \quad \begin{cases} 1 \\ 2 \\ 3 \\ \vdots \\ K \end{cases} \quad \text{or} \quad \begin{cases} \frac{K}{2} & \left(\frac{K-1}{2} \right) \\ \vdots \\ 1 \\ -1 \\ \vdots \\ -\frac{K}{2} & \left(\frac{-K+1}{2} \right) \end{cases} \quad (0)$$

$$\text{or generally } \begin{cases} \tau_1 & \text{for } i = A \\ \tau_2 & \text{for } i = B \\ \vdots \\ \tau_K & \text{for } i = K \end{cases}$$

Any configuration is then specified by the vector $\sigma = (\sigma_1, \sigma_2, \dots, \sigma_N)$. In total, there are K^N different configurations. For binary alloys, the choice $\sigma_n = \begin{cases} x_B \\ -x_A \end{cases}$ was first suggested by Flinn (1956). The operator σ_n is sometimes called the *spin variable* because of its correspondence with the Ising model for binary alloys if we take $\sigma_n = \pm 1$. Any function of σ_n including σ_n itself is called a *configurational variable*.

Because N is a very large number, it is not possible to handle such a large amount of information. Therefore, we are forced to work with a reduced amount of information by considering the configurations of much smaller units called *clusters*. A cluster is defined by a set of lattice points $1, 2, \dots, r$, and a configuration on this cluster is given

by $\sigma_r = (\sigma_1, \sigma_2, \dots, \sigma_r)$. The smallest cluster is a point, the next one a pair, then a triplet, and so on. On an r -site cluster there are K^r configurations, a much smaller number than K^N . The configurations of the N -point system can then be classified into groups with the same number of clusters $N(\sigma_r)$ with the configuration σ_r . Instead of $N(\sigma_r)$, it is preferable to work with the reduced number $\varrho(\sigma_r) = N(\sigma_r)/N_r$, where N_r is the number of equivalent r -site clusters contained in the system. These fractions are called *cluster probabilities*. They specify the configuration in the r -point cluster approximation and constitute the most important configurational variables. The approximation depends on the size of the largest cluster taken into account. For a three-dimensional (3-dim.) lattice, it is necessary to include at least one 3-dim. cluster, otherwise the topological connection of the clusters for space filling cannot be taken into account correctly. For instance, if only pairs are considered, it is not possible to distinguish a 3-dim. configuration from a 2-dim. Bethe lattice with the same coordination number.

So far r defines a particular set of points $1, 2, \dots, r$, and N_r is the number of clusters having the same orientation in space, thus differing from this particular set by a translation in the lattice, or $N_r = N$. In this instance, we speak of *oriented clusters* and oriented-cluster probabilities. The N -point system usually exhibits more symmetry elements than translation, and clusters of different orientation then become equivalent. Bringing these clusters together gives $N_r > N$.

Suppose that an r -point cluster has been selected for the description of the configurations. Then the thermodynamic functions derived, for example, with CVM, depend on the probabilities of this cluster and also on the probabilities of all subclusters.

Therefore, the total number of configurational probabilities v_{tot} adds up to

$$v_{\text{tot}} = \binom{r}{1} K + \binom{r}{2} K^2 + \dots + \binom{r}{r} K^r \\ = (K+1)^r - 1$$

because for a point, there are K choices of an element and $\binom{r}{1}$ choices of a point in the cluster, for a pair, there are K^2 choices of two elements and $\binom{r}{2}$ choices of a pair of points in this cluster, and so on. However, these v_{tot} probabilities are not all independent: if the probabilities of the largest cluster are given, then the probabilities of all subclusters can be derived by partial summation, e.g., for a 3-point cluster

$$\varrho(\sigma_1, \sigma_2, \sigma_3) \\ = \sum_{\sigma_4 \dots \sigma_r} \varrho(\sigma_1, \sigma_2, \sigma_3, \sigma_4, \dots, \sigma_r) \quad (8-1)$$

The number of these partial summations in

$$v_p = \binom{r}{1} K + \binom{r}{2} K^2 + \dots + \binom{r}{r-1} K^{r-1}$$

Moreover, the sum of the probabilities of the largest cluster is equal to 1 by definition. Therefore the number of independent probabilities is

$$v = v_{\text{tot}} - v_p - 1 = K^r - 1$$

that is, v is the dimension of the configurational space. When r and K increase, the difference $v_{\text{tot}} - v_p$ becomes very large.

Of course any choice of v probabilities out of the whole set v_{tot} may serve as a set of independent configurational variables. A convenient choice is any selection of v probabilities out of the K^r probabilities of the largest cluster. This is usually done in Kikuchi's natural iteration method (Kikuchi and Sato, 1974). It is necessary, how-

ever, to introduce Lagrange parameters in the minimization of Gibbs energy in order to take account of the v_p consistency relations of Eq. (8-1), and it is not straightforward to make use of efficient minimization algorithms. Therefore, effort has been concentrated in defining a set of independent variables (or a basis) in the v -dim. space such that all the configurational variables can be expressed in terms of this basis. For binary alloys, Sanchez and de Fontaine (1978) used multisite correlation functions as an extension of the pair correlation functions introduced by Clapp and Moss (1966). An extension to multicomponent systems was first proposed by Taggart (1973) using the spin concept, after which Sanchez et al. (1984) suggested Chebychev polynomials as a basis of the configurational space. In the following another basis is developed by a method that is equivalent to the one by Taggart. This basis is simpler and better suited to numerical applications than that by Sanchez et al. (1984).

The procedure is as follows. First, we define a basis in the space of point variables. This yields $(K-1)$ functions of σ_n . Then, we consider the (K^2-1) -dim. space of the two-point variables and define a basis by taking products of the $(K-1)$ basic point variables, and so on. This explains why the most important step is an appropriate choice of the basis for point variables.

8.2.2 Point Variables

In the case of point variables, r corresponds to one point, and the vector σ reduces to one element σ_n . In order to define a basis of configurational point variables, in particular for the point probabilities $\varrho(\sigma_n)$, it is helpful to introduce a second operator $p_n^{(i)}$ which allows us to count the number of sites n with the same type of atom i for taking averages. This operator

$p_n^{(i)}$ is called the *site-occupation operator* (Clapp and Moss, 1966) and is defined as follows:

$$p_n^{(i)} = \begin{cases} 1 & \text{if an atom of type } i \text{ occupies site } n \\ 0 & \text{otherwise} \end{cases}$$

Because i goes from 1 to K we have K operators. Using this definition we can immediately write the following equations:

$$\left\{ \begin{array}{l} 1 = \sum_{i=1}^K p_n^{(i)} \\ \sigma_n = \sum_{i=1}^K \tau_i p_n^{(i)} \\ \sigma_n^2 = \sum_{i=1}^K \tau_i^2 p_n^{(i)} \\ \vdots \\ \sigma_n^{K-1} = \sum_{i=1}^K \tau_i^{K-1} p_n^{(i)} \end{array} \right\} \quad \text{or} \quad \left(\begin{array}{c} 1 \\ \sigma_n \\ \sigma_n^2 \\ \vdots \\ \sigma_n^{K-1} \end{array} \right) \quad (8-2)$$

$$= \left(\begin{array}{ccccc} 1 & 1 & 1 & \dots & 1 \\ \tau_1 & \tau_2 & \tau_3 & \dots & \tau_K \\ \tau_1^2 & \tau_2^2 & \tau_3^2 & \dots & \tau_K^2 \\ \vdots & \vdots & \vdots & \dots & \vdots \\ \tau_1^{K-1} & \tau_2^{K-1} & \tau_3^{K-1} & \dots & \tau_K^{K-1} \end{array} \right) \left(\begin{array}{c} p_n^{(1)} \\ p_n^{(2)} \\ p_n^{(3)} \\ \vdots \\ p_n^{(K)} \end{array} \right)$$

where the upper indices signify powers of σ_n or τ_i . This notation will be used throughout this chapter. To distinguish an upper index from a power, the index will be put in parentheses, except if it is a double or multiple index, which cannot be confused with a power. Let us call \mathbf{M} the matrix of this system of equations. Its determinant is the van der Monde determinant, which is given by

$$\text{Det } \mathbf{M} = \prod_{j=i+1}^K \prod_{i=1}^r (\tau_j - \tau_i)$$

Because all the τ_i are different numbers, this determinant is different from zero, and the equations are linearly independent. This confirms that the $K-1$ functions $\{\sigma_n, \sigma_n^2, \dots, \sigma_n^{K-1}\}$ are linearly independent.

Det $\mathbf{M} \neq 0$ and so we can invert the matrix \mathbf{M} and define $\mathbf{R} = (\mathbf{R}_{ik}) = \mathbf{M}^{-1}$. From Eq. (8-2) we arrive at

$$\begin{aligned} p_n^{(1)} &= \sum_{k=1}^K R_{1k} \sigma_n^{k-1} \\ p_n^{(2)} &= \sum_{k=1}^K R_{2k} \sigma_n^{k-1} \\ &\vdots \\ p_n^{(K)} &= \sum_{k=1}^K R_{Kk} \sigma_n^{k-1} \end{aligned} \quad (8-3)$$

$$\text{or} \quad \left(\begin{array}{c} p_n^{(1)} \\ p_n^{(2)} \\ p_n^{(3)} \\ \vdots \\ p_n^{(K)} \end{array} \right) = \mathbf{R} \left(\begin{array}{c} 1 \\ \sigma_n \\ \sigma_n^2 \\ \vdots \\ \sigma_n^{K-1} \end{array} \right)$$

This is the relation that connects the *site-occupation operators* with the site operators. Because all the elements of the first row of \mathbf{M} are unity, the inverse matrix \mathbf{R} exhibits the following properties: the elements of the first column of \mathbf{R} add up to unity and the elements of all other columns

add up to zero, i.e., $\sum_{i=1}^K R_{ik} = \delta_{1k}$.

8.2.3 Point Correlation Functions and Point Probabilities

So far we have considered the point variables for one arbitrary point n out of the N lattice points of the crystal. As mentioned before, we want to reduce the number of parameters describing an atomic configuration by considering averages over equivalent clusters, or in this case, points. The space group of the structure will define the equivalence of points. We may enumerate the classes of equivalent points by 1, 2, ... and define the number of lattice points in each class by $N^{(1)}, N^{(2)}, \dots, N^{(L)}$. The average of an arbitrary function $\varphi(\sigma_n, \sigma_n^2, \dots)$

of the point variables $\sigma_n, \sigma_n^2, \dots$ is defined by

$$\langle \varphi(\sigma_n, \sigma_n^2, \dots) \rangle = \frac{1}{N^{(n)}} \sum_{s=1}^{N^{(n)}} \varphi(\sigma_s, \sigma_s^2, \dots)$$

The index n now stands for one representative point out of the corresponding class. The averages of the site-occupation operators $p_n^{(i)}$ yield the probabilities of finding an atom A, B, ..., K on a point n :

$$\varrho(\sigma_n = \tau_i) = \langle p_n^{(i)} \rangle = \sum_{k=1}^K R_{ik} \langle \sigma_n^{k-1} \rangle \quad i = 1, \dots, K \quad (8-4)$$

In the limit of $N \rightarrow \infty$, this average corresponds to the thermodynamic site-occupation probability. The $(K-1)$ functions $\langle \sigma_n^{K-1} \rangle$ are called *point correlation functions*. These functions constitute the basis of the configurational space of point variables, and Eq. (8-4) yields the components of the point probabilities with respect to this basis.

8.2.4 Pair Variables, Correlation Functions, and Probabilities

Consider a two-point cluster $r = n, m$. We can immediately introduce a pair-occupation operator that takes the value 1 if an atom of type i occupies site n , and if type j occupies site m . This operator is simply the product of the two previously introduced site-occupation operators $p_{nm}^{ij} = p_n^{(i)} p_m^{(j)}$. Using the expressions of the site operators, Eq. (8-3), we obtain

$$p_{nm}^{ij} = \sum_{k=1}^K \sum_{h=1}^K R_{ih} R_{jk} \sigma_n^{h-1} \sigma_m^{k-1}$$

The pair probabilities ϱ_{nm}^{ij} are obtained by taking the average of the operator p_{nm}^{ij} over all equivalent pairs in the crystal. It is worth mentioning that the pairs may be non-equivalent if they differ by their orien-

tation, i.e., if n and m are non-equivalent points. In this instance, we speak of *oriented* pair probabilities. In the opposite case, we speak of *isotropic* pair probabilities:

$$\varrho_{nm}^{ij} = \langle p_n^{(i)} p_m^{(j)} \rangle = \sum_{k=1}^K \sum_{h=1}^K R_{ih} R_{jk} \times \langle \sigma_n^{h-1} \sigma_m^{k-1} \rangle \quad (8-5)$$

The pair probabilities can thus be expressed in terms of the already introduced point correlation functions, written here in the form $\langle \sigma_n^{h-1} \sigma_m^{k-1} \rangle$ with $h=1$ and $k=2, 3, \dots, K$ (or $k=1$ and $h=2, 3, \dots, K$) together with a second set of functions, $\langle \sigma_n^{h-1} \sigma_m^{k-1} \rangle$, with $h, k=2, \dots, K$ called *pair correlation functions*. The number of pair correlation functions is $(K-1)^2$ if n and m are non-equivalent sites. The total number of point and pair correlation functions adds up to $2(K-1) + (K-1)^2 = K^2 - 1$. This is exactly the dimension of the configurational space if we assume the pair to be the basic cluster. Point and pair correlation functions together constitute a basis in this instance.

By virtue of the relation $\sum_j p_n^{(i)} p_m^{(j)} = p_n^{(i)}$

the pair probabilities are consistent with the point probabilities.

For the purposes of illustration, let us consider two examples:

Binary alloy

For a binary alloy, $K=2$ and $\tau_1=1$ for the first element A, and $\tau_2=-1$ for the second element B. The point probabilities follow from

$$\mathbf{M} = \begin{pmatrix} 1 & 1 \\ 1 & -1 \end{pmatrix} \quad \text{and} \quad \mathbf{R} = -\frac{1}{2} \begin{pmatrix} -1 & -1 \\ -1 & 1 \end{pmatrix}$$

which yields

$$\begin{pmatrix} 1 \\ \sigma_n \end{pmatrix} = \begin{pmatrix} 1 & 1 \\ 1 & -1 \end{pmatrix} \begin{pmatrix} p_n^{(1)} \\ p_n^{(2)} \end{pmatrix}$$

and

$$\begin{pmatrix} p_n^A \\ p_n^B \end{pmatrix} = \begin{pmatrix} p_n^{(1)} \\ p_n^{(2)} \end{pmatrix} = \frac{1}{2} \begin{pmatrix} 1 & 1 \\ 1 & -1 \end{pmatrix} \begin{pmatrix} 1 \\ \sigma_n \end{pmatrix}$$

and consequently

$$\begin{cases} \varrho_n^{(1)} = \frac{1}{2} (1 + \langle \sigma_n \rangle) \\ \varrho_n^{(2)} = \frac{1}{2} (1 - \langle \sigma_n \rangle) \end{cases} \text{ and } \langle \sigma_n \rangle = \varrho_n^{(1)} - \varrho_n^{(2)} \quad (8-6)$$

For the pair probabilities, we obtain, according to Eq. (8-5),

$$\varrho_{nm}^{ij} = \sum_{k=1}^2 \sum_{h=1}^2 R_{ih} R_{jk} \langle \sigma_n^{h-1} \sigma_m^{k-1} \rangle$$

or

$$\begin{pmatrix} \varrho_{nm}^{AA} \\ \varrho_{nm}^{AB} \\ \varrho_{nm}^{BA} \\ \varrho_{nm}^{BB} \end{pmatrix} = \begin{pmatrix} \varrho_{nm}^{11} \\ \varrho_{nm}^{12} \\ \varrho_{nm}^{21} \\ \varrho_{nm}^{22} \end{pmatrix} \quad (8-7)$$

$$= \frac{1}{4} \begin{pmatrix} 1 & 1 & 1 & 1 \\ 1 & 1 & -1 & -1 \\ 1 & -1 & 1 & -1 \\ 1 & -1 & -1 & 1 \end{pmatrix} \begin{pmatrix} 1 \\ \langle \sigma_n \rangle \\ \langle \sigma_m \rangle \\ \langle \sigma_n \sigma_m \rangle \end{pmatrix}$$

Ternary alloy

For a ternary alloy, $K=3$ and $\tau_1=1$ for element A, $\tau_2=0$ for B, and $\tau_3=-1$ for C. In this instance, the point variables follow from

$$\mathbf{M} = \begin{pmatrix} 1 & 1 & 1 \\ 1 & 0 & -1 \\ 1 & 0 & 1 \end{pmatrix}$$

and

$$\mathbf{R} = \frac{1}{2} \begin{pmatrix} 0 & 1 & 1 \\ 2 & 0 & -2 \\ 0 & -1 & 1 \end{pmatrix}$$

According to Eqs. (8-2) and (8-5), we obtain

$$\begin{aligned} \langle \sigma_n \rangle &= \varrho_n^{(1)} - \varrho_n^{(3)} \\ \langle \sigma_n^2 \rangle &= \varrho_n^{(1)} + \varrho_n^{(3)} \\ \varrho_n^A &= \varrho_n^{(1)} = \frac{1}{2} (\langle \sigma_n \rangle + \langle \sigma_n^2 \rangle) \\ \varrho_n^B &= \varrho_n^{(2)} = \frac{1}{2} (2 - 2 \langle \sigma_n^2 \rangle) \\ \varrho_n^C &= \varrho_n^{(3)} = \frac{1}{2} (-\langle \sigma_n \rangle + \langle \sigma_n^2 \rangle) \end{aligned} \quad (8-8)$$

For the pair probabilities, we obtain, according to Eq. (8-5),

$$\begin{pmatrix} \varrho_{nm}^{AA} \\ \varrho_{nm}^{AB} \\ \varrho_{nm}^{AC} \\ \varrho_{nm}^{BA} \\ \varrho_{nm}^{BB} \\ \varrho_{nm}^{BC} \\ \varrho_{nm}^{CA} \\ \varrho_{nm}^{CB} \\ \varrho_{nm}^{CC} \end{pmatrix} = \begin{pmatrix} \varrho_{nm}^{11} \\ \varrho_{nm}^{12} \\ \varrho_{nm}^{13} \\ \varrho_{nm}^{21} \\ \varrho_{nm}^{22} \\ \varrho_{nm}^{23} \\ \varrho_{nm}^{31} \\ \varrho_{nm}^{32} \\ \varrho_{nm}^{33} \end{pmatrix} = \frac{1}{4} \begin{pmatrix} 0 & 0 & 0 & 0 & 1 & 1 & 0 & 1 & 1 \\ 0 & 2 & 2 & 0 & 0 & 0 & 0 & -2 & -2 \\ 0 & 0 & 0 & 0 & -1 & -1 & 0 & 1 & 1 \\ 0 & 0 & 0 & 2 & 0 & -2 & 2 & 0 & -2 \\ 4 & 0 & -4 & 0 & 0 & 0 & -4 & 0 & 4 \\ 0 & 0 & 0 & -2 & 0 & 2 & 2 & 0 & -2 \\ 0 & 0 & 0 & 0 & -1 & 1 & 0 & -1 & 1 \\ 0 & -2 & 2 & 0 & 0 & 0 & 0 & 2 & -2 \\ 0 & 0 & 0 & 0 & 1 & -1 & 0 & -1 & 1 \end{pmatrix} \begin{pmatrix} 1 \\ \langle \sigma_n \rangle \\ \langle \sigma_n^2 \rangle \\ \langle \sigma_m \rangle \\ \langle \sigma_n \sigma_m \rangle \\ \langle \sigma_n^2 \sigma_m \rangle \\ \langle \sigma_m^2 \rangle \\ \langle \sigma_n \sigma_m^2 \rangle \\ \langle \sigma_n^2 \sigma_m^2 \rangle \end{pmatrix} \quad (8-9)$$

8.2.5 Generalized Cluster Variables, Correlation Functions, and Probabilities

The point and pair variables are the simplest examples of the general cluster variables. Consider an oriented cluster defined by r points. As before, we introduce a cluster-occupation operator by the product of site-occupation operators $p_1^{(i_1)} p_2^{(i_2)} \dots p_r^{(i_r)}$. The cluster correlation functions are the averages over all equivalent clusters in the crystal. Thus the result for the cluster probabilities is

$$\begin{aligned} \mathcal{Q}_{12\dots r}^{i_1 i_2 \dots i_r} &= \langle p_1^{(i_1)} p_2^{(i_2)} \dots p_r^{(i_r)} \rangle \\ &= \sum_{k_1=1}^K \sum_{k_2=1}^K \dots \sum_{k_r=1}^K R_{i_1 k_1} R_{i_2 k_2} \dots R_{i_r k_r} \\ &\quad \times \langle \sigma_1^{k_1-1} \sigma_2^{k_2-1} \dots \sigma_r^{k_r-1} \rangle \end{aligned} \quad (8-10)$$

The parameters $\left\langle \prod_{n=1}^r \sigma_n^{k_n-1} \right\rangle$ include the r -point correlation functions (point, pair, etc.) which provide the characterization of the configuration by means of r -site clusters, for example, the point correlation functions are coded in the form $\langle \sigma_m \rangle = \langle \sigma_1^0 \dots \sigma_m^1 \dots \sigma_r^0 \rangle$, $\langle \sigma_m^2 \rangle = \langle \sigma_1^0 \dots \sigma_m^2 \dots \sigma_r^0 \rangle$, etc. and, correspondingly, for the pair correlation functions, they are coded $\langle \sigma_m \sigma_n \rangle = \langle \sigma_1^0 \dots \sigma_m^1 \sigma_n^1 \dots \sigma_r^0 \rangle$, etc. The r -site cluster correlation functions are obtained when $k_n \neq 1$ for all values of k_n . If all the r sites are not equivalent, the total number of r -point correlation functions is $(K-1)^r$. The total number of correlation functions N_c required for an r -point cluster treatment, including all the subcluster correlation functions, is

$$\begin{aligned} N_c &= \binom{r}{1} (K-1) + \binom{r}{2} (K-1)^2 + \dots \\ &\quad + \binom{r}{r} (K-1)^r = (K-1+1)^r - 1 = K^r - 1 \end{aligned}$$

This is the dimension of the configurational space, and the whole set of cluster

correlation functions constitutes a basis of this configurational space. If all sites are equivalent, the number of correlation functions is much smaller.

8.2.6 Short-Range Order (sro) Configurations – Long-Range Order (lro) Configurations

A configuration is called *short-range ordered* if the whole lattice constitutes one class of lattice points (i.e., $N^{(1)}=N$). As a consequence, all the cluster correlation functions are isotropic. A configuration is called *long-range ordered* if at least two classes of points are to be distinguished by their different average occupation. These classes of lattice points are usually called *sublattices*. In Fig. 8-1, the face-centered cubic unit cell is shown with a subdivision of the lattice sites into four simple cubic sublattices labeled 1 to 4 with $N/4$ points each. With these sublattices, the superstructures $L1_2$, $L1_0$ and $P4/mmm$ can be described. Each point on a sublattice is surrounded in its first-neighbor shell by four points corresponding to each of the other

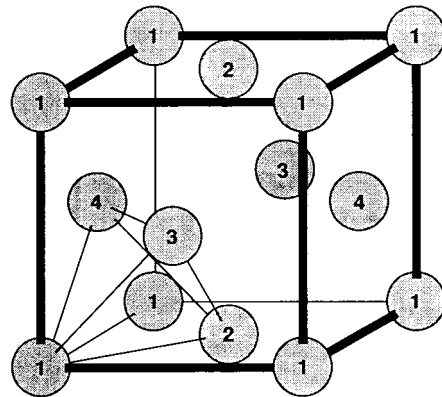


Figure 8-1. Subdivision of the face-centered cubic (f.c.c.) unit cell into four simple cubic sublattices for a characterization of the superstructures $L1_2$, $L1_0$ and $P4/mmm$. The occupations of the sublattices for these structures are given in Table 8-1.

Table 8-1. F.c.c. and b.c.c. superstructures and values of their lro parameters.

Designation/Spacegroup		Point probabilities	lro parameter	Values for maximum lro (binary)
A1 (Cu)	A2 (Fe)	$q_1^{(i)} = q_2^{(i)} = q_3^{(i)} = q_4^{(i)}$	$\xi_1 = \xi_2 = \xi_3 = 0$	$q_1^A = 1 - x_B$
L1 ₀ (CuAu)	B2 (CsCl)	$q_1^{(i)} = q_2^{(i)} \neq q_3^{(i)} = q_4^{(i)}$	$\xi_1 \neq 0, \xi_2 = \xi_3 = 0$	$q_1^A = 1, q_3^A = 1 - 2x_B$
L1 ₂ (Cu ₃ Au)		$q_1^{(i)} \neq q_2^{(i)} = q_3^{(i)} = q_4^{(i)}$	$\xi_1 \neq \xi_2 \neq 0, \xi_3 = 0$	$q_1^A = 1 - 4x_B, q_2^A = 1$
	D0 ₃ (Fe ₃ Al) $x_B \leq 0.25$	$q_1^{(i)} \neq q_2^{(i)} \neq q_3^{(i)} = q_4^{(i)}$	$\xi_1 \neq \xi_2 \neq 0, \xi_3 = 0$	$q_1^A = 1 - 4x_B, q_2^A = 1, q_3^A = 1$
P4/mmm $0.25 \leq x_B \leq 0.5$	D0 ₃ (Fe ₃ Al) $0.25 \leq x_B \leq 0.5$	$q_1^{(i)} \neq q_2^{(i)} \neq q_3^{(i)} = q_4^{(i)}$	$\xi_1 \neq \xi_2 \neq 0, \xi_3 = 0$	$q_1^A = 0, q_2^A = 2 - 4x_B, q_3^A = 1$
	B32 (NaTl)	$q_1^{(i)} = q_3^{(i)} \neq q_2^{(i)} = q_4^{(i)}$	$\xi_1 = 0, \xi_2 \neq \xi_3 \neq 0$	$q_1^A = 1, q_2^A = 1 - 2x_B$
	F $\bar{4}$ 3m $0.25 \leq x_B \leq 0.5$	$q_1^{(i)} \neq q_2^{(i)} \neq q_3^{(i)} \neq q_4^{(i)}$	$\xi_1 \neq \xi_2 \neq \xi_3 \neq 0$	

sublattices. Therefore these structures are called ordered in the first shell. The sublattice occupation for these structures is given in Table 8-1.

In the body-centered cubic structure, four face-centered cubic sublattices with a parameter $a = 2a_0$ can be defined as shown in Fig. 8-2. With these sublattices, the superstructures B2, D0₃, F $\bar{4}$ 3m, and B32 can be described. These structures are ordered in the first two neighbor shells. The occupation of the sublattices is again given in Table 8-1. The complete crystallographic specification of these superstructures is given in Sec. 8.7, Table 8-13.

We must therefore consider the following variables: the points $\langle \sigma_1 \rangle, \langle \sigma_2 \rangle, \langle \sigma_3 \rangle, \langle \sigma_4 \rangle$; the pairs $\langle \sigma_1 \sigma_3 \rangle, \langle \sigma_1 \sigma_4 \rangle, \langle \sigma_2 \sigma_3 \rangle, \langle \sigma_2 \sigma_4 \rangle, \langle \sigma_1 \sigma_2 \rangle, \langle \sigma_3 \sigma_4 \rangle$; the triplets $\langle \sigma_1 \sigma_2 \sigma_3 \rangle$, etc.; and, finally, the tetrahedron $\langle \sigma_1 \sigma_2 \sigma_3 \sigma_4 \rangle$ – in total, $(2^4 - 1) = 15$ variables. Of course, the variables have different meanings in the two structures. In the f.c.c. lattice, all the pairs are nearest neighbors, while in the b.c.c. structure, the pairs of type 1–2 and 3–4 are second-nearest-neighbor pairs. A corresponding distinction among the triplets also has to be made.

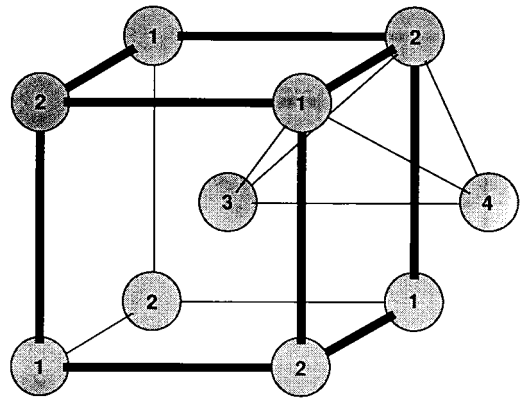


Figure 8-2. Subdivision of the body-centered cubic (b.c.c.) unit cell into four f.c.c. sublattices with twice the lattice constant, $2a_0$, for a characterization of the superstructures B2, D0₃ and B32. The occupation of the sublattices for these structures are given in Table 8-1. The (irregular) tetrahedron cluster 1234 used in the CVM calculations is also shown.

Among these variables, we need four variables to define the isotropic f.c.c. sro state: $\langle \sigma_1 \rangle, \langle \sigma_1 \sigma_2 \rangle, \langle \sigma_1 \sigma_2 \sigma_3 \rangle$, and $\langle \sigma_1 \sigma_2 \sigma_3 \sigma_4 \rangle$; one more variable, $\langle \sigma_1 \sigma_3 \rangle$, is needed to characterize the isotropic b.c.c. sro state. The remaining variables characterize the lro state. For many applications, it is sufficient to identify the existence of lro by the

difference between the point correlation functions or linear combinations between them (e.g., the same combinations as those entering the structure factor for X-ray diffraction). These linear combinations of the point correlation functions are called *lro parameters*. In the case of the b.c.c. structure, we usually define the lro parameters

$$\xi_1 = \langle \sigma_1 \rangle + \langle \sigma_2 \rangle - \langle \sigma_3 \rangle - \langle \sigma_4 \rangle$$

$$\xi_2 = \langle \sigma_1 \rangle - \langle \sigma_2 \rangle$$

$$\xi_3 = \langle \sigma_3 \rangle - \langle \sigma_4 \rangle$$

Table 8-1 lists the b.c.c. superstructures, together with the values of the parameters.

If there is no long-range order, then all the positions are equivalent and the point probability takes one value $Q_n^{(i)} = x_i$. Taking

In practice, the values of the pair correlation functions for the sro states are obtained from diffraction experiments. For this purpose, we usually introduce the *Cowley–Warren sro parameters* α_{n-m}^{ij} (Cowley, 1950), which are directly related to the measured intensities. They are defined as the deviation from the random state:

$$\begin{aligned} Q_{n-m}^{ij} &= Q_{nm}^{ij} + Q_{nm}^{ji} \\ &= [Q_n^{(i)} Q_m^{(j)} + Q_n^{(j)} Q_m^{(i)}] (1 - \alpha_{n-m}^{ij}) \end{aligned}$$

The index $n-m$ stands for the neighbor distance between the positions n and m . Taking again the τ_i values as before (i.e., ± 1 for the binary case and 1, 0, -1 for the ternary case), we obtain the isotropic Cowley–Warren sro parameters:

$$\text{binary alloys: } \alpha_{n-m} = \frac{\langle \sigma_n \sigma_m \rangle - \langle \sigma_n \rangle \langle \sigma_m \rangle}{1 - \langle \sigma_n \rangle \langle \sigma_m \rangle}$$

$$\text{ternary alloys: } \alpha_{n-m}^{\text{AB}} = \frac{\langle \sigma_n \sigma_m^2 \rangle + \langle \sigma_n^2 \sigma_m \rangle + 2 \langle \sigma_n^2 \sigma_m^2 \rangle - 4 x_A (1 - x_B)}{4 x_A x_B}$$

$$\alpha_{n-m}^{\text{AC}} = \frac{-\langle \sigma_n^2 \sigma_m^2 \rangle + \langle \sigma_n \sigma_m \rangle + 4 x_A x_C}{4 x_A x_C}$$

$$\alpha_{n-m}^{\text{BC}} = \frac{-\langle \sigma_n^2 \sigma_m \rangle - \langle \sigma_n \sigma_m^2 \rangle + 2 \langle \sigma_n^2 \sigma_m^2 \rangle - 4 x_C (1 - x_B)}{4 x_B x_C}$$

the same τ_i values as in the examples treated previously in Sec. 8.2.3, we can use Eq. (8-6) and obtain the following values for the point correlation functions: $\langle \sigma_n \rangle = \langle \sigma_1 \rangle = x_A - x_B$ in the case of a binary alloy and $\langle \sigma_1 \rangle = x_A - x_C$, $\langle \sigma_1^2 \rangle = x_A + x_C$ in the case of a ternary alloy.

If there is not even any short-range order, we consider the completely disordered state. All the n -point correlation functions then take a limiting value; for example, in a binary alloy, $\langle \sigma_1 \dots \sigma_r \rangle$ takes the value $(x_A - x_B)^r$.

8.3 The Existence Domain and Configuration Polyhedron

In the preceding section, we developed a set of correlation functions (point, pair, triplet, etc.) for characterizing atomic configurations in multicomponent systems. These correlation functions are independent variables that define the configurational space, but they can only vary within a restricted range of numerical values due to certain consistency conditions, which will now be discussed. Outside this restricted

range, the numerical values do not define actually existing atomic configurations. Therefore, this restricted range of values has been called the *existence domain*, or *configuration polyhedron* (Kudo and Katsura, 1976). The dimension of the configurational space depends either on the number of correlations which are taken into account or, equivalently, on the size of the largest cluster. In the following sections the existence domains will be investigated for some simple examples. The method applied closely follows the procedure developed by Finel (1987). For the sake of simplicity, the analysis will be restricted to binary alloys. For multicomponent systems, the procedure is analogous but has to be carried out on a computer.

Existence domains are most useful for an analysis of ground states. This will be shown in Sec. 8.4. The ground-state analysis will be limited to a finite range of interactions (e.g. pair interactions between first and second nearest neighbors). Therefore, we are particularly interested in the part of the existence domain that is the subspace of correlation functions required for a treatment with finite-range interactions. This existence domain in the configurational subspace will be investigated in detail in this section.

8.3.1 F.C.C. Structure, First-Neighbor Interactions

The first step in this analysis is to make a choice for the basic cluster. This choice then determines the dimension of the configurational space to be dealt with. It is natural to start with the simplest possible basic cluster, the nearest-neighbor pair. The configurational variables are then the point correlation function $x_1 = \langle \sigma_1 \rangle = x_A - x_B$, which defines the composition, and the nearest-neighbor pair correlation function $x_2 = \langle \sigma_1 \sigma_2 \rangle = 1 - 4 \rho_{12}^{AB}$ (see Eq. (8-7)).

Adopting again the values $\tau_i = \pm 1$, which were already used in the examples of Sec. 8.2, the variables can both vary in the interval $[-1, 1]$ (see Fig. 8-3): x_1 takes the value 1 for pure A and -1 for pure B, x_2 takes 1 for each pure component and -1 for an alloy composed only of A-B pairs. These ranges, however, are not fully accessible, for example because of the obvious constraints

$$\rho_{12}^{AA} \geq 0, \quad \rho_{12}^{BB} \geq 0, \quad \rho_{12}^{AB} \geq 0 \quad (8-11)$$

The constraints in Eq. (8-11) yield the following inequalities:

$$\begin{aligned} \rho_{12}^{AA} \geq 0 &\Rightarrow 1 + 2x_1 + x_2 \geq 0 \\ \rho_{12}^{AB} \geq 0 &\Rightarrow 1 - x_2 \geq 0 \\ \rho_{12}^{BB} \geq 0 &\Rightarrow 1 - 2x_1 + x_2 \geq 0 \end{aligned} \quad (8-12)$$

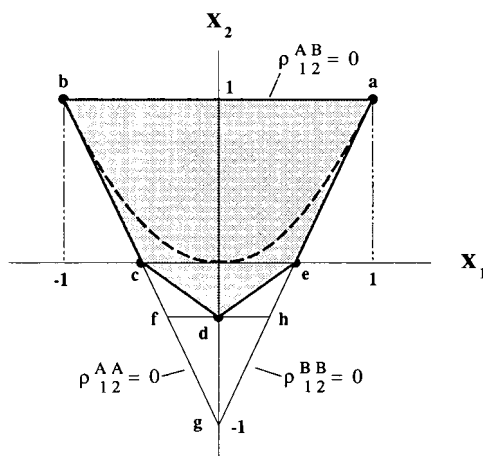


Figure 8-3. Projection of the configuration polyhedron of a regular tetrahedron into the plane of correlation functions $x_1 = \langle \sigma_1 \rangle = x_A - x_B$ and $x_2 = \langle \sigma_1 \sigma_2 \rangle$ for different choices of clusters: (1) domain abg: nearest-neighbor pair; (2) domain abfh: nearest-neighbor triangle; (3) shaded area abcde: nearest-neighbor tetrahedron. The vertices a and b correspond to the pure components A and B, c and e correspond to L_{12} with compositions B_3A and A_3B , and d to L_{10} , composition AB. The dashed line indicates the random configurations. This line separates the existence domain into regions of (ordered) configurations with preferential formation of unlike pairs (lower part) and configurations with preferential formation of like pairs (upper part).

If the relations in Eq. (8-12) are taken as equalities, they define a triangle in the space (x_1, x_2) , as shown in Fig. 8-3. Any point inside the triangle abg fulfills these relations. However, these relations are not sufficient to define the existence domain. In fact, the vertex g, for instance, corresponds to $\varrho_{12}^{AA} = \varrho_{12}^{BB} = 0$ (introduce $x_1 = \langle \sigma_1 \rangle = 0$ and $x_2 = \langle \sigma_1 \sigma_2 \rangle = -1$ into Eq. (8-7)), which defines a configuration built up with A–B pairs only. Such a structure cannot be formed in the f.c.c. lattice. In this structure, the nearest-neighbor bonds form a triangular network, and it is not possible to form a triangle with only A–B pairs. Point g in Fig. 8-3 thus corresponds to a physically impossible state. Obviously, there must be further restricting relations.

The conditions $\varrho_{12}^{ij} \leq 1$ do not introduce new constraints because they are automatically fulfilled together with the inequalities in Eq. (8-11). For the present choice of τ_i values, this is immediately seen from the definition in Eq. (8-7). The general case follows from Eq. (8-2), which yields the relation:

$$\varrho_{12}^{AA} + \varrho_{12}^{BB} + \varrho_{12}^{AB} + \varrho_{12}^{BA} = 1 \quad (8-13)$$

If the constraints in Eq. (8-11) are fulfilled, then Eq. (8-13) is a sum of positive terms which can only be equal to one if each term is less than or equal to one.

Hence, we have to deduce further inequalities from higher-order clusters. Let us consider the nearest-neighbor triangle 123 as the next cluster, see Fig. 8-1. The

new variable $x_3 = \langle \sigma_1 \sigma_2 \sigma_3 \rangle$ must be introduced, and the configurational space is now three-dimensional. The constraints for the triplet probabilities are

$$\begin{aligned} \varrho_{123}^{AAA} &\geq 0 \Rightarrow \left(\begin{array}{cccc} 1 & 3 & 3 & 1 \end{array} \right) \left(\begin{array}{c} 1 \\ x_1 \\ x_2 \\ x_3 \end{array} \right) \geq 0 \\ \varrho_{123}^{AAB} &\geq 0 \Rightarrow \left(\begin{array}{cccc} 1 & 1 & -1 & -1 \end{array} \right) \left(\begin{array}{c} 1 \\ x_1 \\ x_2 \\ x_3 \end{array} \right) \geq 0 \\ \varrho_{123}^{ABB} &\geq 0 \Rightarrow \left(\begin{array}{cccc} 1 & -1 & -1 & 1 \end{array} \right) \left(\begin{array}{c} 1 \\ x_1 \\ x_2 \\ x_3 \end{array} \right) \geq 0 \\ \varrho_{123}^{BBB} &\geq 0 \Rightarrow \left(\begin{array}{cccc} 1 & -3 & 3 & -1 \end{array} \right) \left(\begin{array}{c} 1 \\ x_1 \\ x_2 \\ x_3 \end{array} \right) \geq 0 \end{aligned} \quad (8-14)$$

Because we are only interested in the domain spanned in the subspace (x_1, x_2) , we have to eliminate the variable x_3 . In order to converse the positive value of all the expressions, this elimination can only be performed by additive combinations of the inequalities. This yields the three expressions in Eq. (8-12) already obtained from the pairs, plus one more inequality:

$$1 + 3x_2 \geq 0$$

Taken as an equality, this equation defines the line f–h in Fig. 8-3, and we have to verify again if the new vertices f and h correspond to physically accessible states. Point f corresponds to a state with no triangle of type AAA, AAB, BBB (i.e., a state built up only with triangles of type ABB). It is easy to see that this is impossible in the f.c.c. structure. Thus this procedure has to be continued in order to find further restricting conditions.

The next higher cluster that may be considered is the nearest-neighbor tetrahedron $r = 1234$, see Fig. 8-1. In this case, the new variable $x_4 = \langle \sigma_1 \sigma_2 \sigma_3 \sigma_4 \rangle$ needs to be introduced. The tetrahedron probabilities result in the following consistency relations:

$$\begin{aligned} \varrho_{1234}^{AAAA} &\geq 0 \Rightarrow \left(\begin{array}{cccccc} 1 & 4 & 6 & 4 & 1 \end{array} \right) \left(\begin{array}{c} 1 \\ x_1 \\ x_2 \\ x_3 \\ x_4 \end{array} \right) \geq 0 \\ \varrho_{1234}^{AAAB} &\geq 0 \Rightarrow \left(\begin{array}{cccccc} 1 & 2 & 0 & -2 & -1 \end{array} \right) \left(\begin{array}{c} 1 \\ x_1 \\ x_2 \\ x_3 \\ x_4 \end{array} \right) \geq 0 \\ \varrho_{1234}^{AABB} &\geq 0 \Rightarrow \left(\begin{array}{cccccc} 1 & 0 & -2 & 0 & 1 \end{array} \right) \left(\begin{array}{c} 1 \\ x_1 \\ x_2 \\ x_3 \\ x_4 \end{array} \right) \geq 0 \\ \varrho_{1234}^{ABBB} &\geq 0 \Rightarrow \left(\begin{array}{cccccc} 1 & -2 & 0 & 2 & -1 \end{array} \right) \left(\begin{array}{c} 1 \\ x_1 \\ x_2 \\ x_3 \\ x_4 \end{array} \right) \geq 0 \\ \varrho_{1234}^{BBBB} &\geq 0 \Rightarrow \left(\begin{array}{cccccc} 1 & -4 & 6 & -4 & 1 \end{array} \right) \left(\begin{array}{c} 1 \\ x_1 \\ x_2 \\ x_3 \\ x_4 \end{array} \right) \geq 0 \end{aligned} \quad (8-15)$$

Taken as equalities, these equations define a closed polyhedron in the space (x_1, \dots, x_4) . Because we are still interested in the subspace (x_1, x_2) we have to eliminate x_3 and x_4 . This is done by taking suitable additive combinations of the inequalities in Eq. (8-15). The result is the polygon *abcde* in Fig. 8-3, which differs from the previous one in that the vertices *f* and *h* are removed, and the vertices *c*, *d*, *e* are added. It is easy to see that all these vertices correspond to possible atomic configurations in the f.c.c. structure; *c* and *e* correspond to the $L1_2$ structure with stoichiometric compositions B_3A and A_3B , respectively, and *d* corresponds to the $L1_0$ structure with composition AB . The existence domain is given by the shaded area in Fig. 8-3.

The regular tetrahedron is thus the smallest basic cluster that allows us to define the existence domain in the configuration space of an f.c.c. lattice with nearest-neighbor interactions. Consequently, this tetrahedron is also the smallest basic cluster upon which a statistical treatment should be based. It is possible, of course, to take a higher cluster containing the tetrahedron as a subcluster. In such a case, the dimension of the configurational space is increased but the projection of the domain into the subspace of point correlations and nearest-neighbor pair correlations remains the same. If we had considered a basic cluster that does not contain the tetrahedron, we would have obtained a polygon with some vertices, which again would not correspond to accessible states. The procedure would have to be continued until a cluster containing the tetrahedron were finally selected.

The procedure of obtaining the vertices of the configuration polyhedron outlined above becomes more and more inconvenient with increasing cluster size, i.e., with

an increasing number of correlation functions and, consequently, with more inequalities that have to be taken into account in order to define the existence domain. Therefore we look for a simplification. At first we notice that each one of the consistency relations, when taken as an equality, defines a face of a polyhedron. In the cases studied before (see, for example, Eq. (8-14) or (8-15)), the number of consistency relations was one more than the dimension of the configurational space. The polyhedron was thus built by $d+1$ faces. Therefore, the polyhedron is a *simplex*, which is necessarily closed and convex. Generally, if d is the dimension of the space, a *simplex* is a polyhedron with $d+1$ faces. The intersection of d faces defines a vertex, a simplex thus has $d-1$ vertices. The coordinates of the vertices are obtained by solving the systems of d equations which can be chosen out of the whole set of $d+1$. The simplification comes from a very convenient way of obtaining these coordinates: Finel (1987) showed that the values obtained from these solutions are the same as those obtained simply by dividing the elements in each column of the matrix by the corresponding values of the first row. The coordinates of the vertices are the elements in each row following the first column, which always contains unity and does not define a coordinate. Performing this procedure with the matrix of Eq. (8-14), we directly obtain the coordinates given in Table 8-2. Taking the projection into the subspace (x_1, x_2) means we conserve only the first two coordinates. This exactly defines the polygon *abfh*, which was found before by means of the elimination procedure.

Applying the same procedure to Eq. (8-15) immediately yields the coordinates of the configuration polyhedron in the

Table 8-2. Coordinates of the vertices shown in Fig. 8-3.

Vertex	x_1	x_2	x_3
a	1	1	1
h	1/3	-1/3	-1
f	-1/3	-1/3	1
b	-1	1	-1

Table 8-3. Coordinates of the vertices of the configuration polyhedron shown in Fig. 8-3.

Configuration	Correlation functions				
	Vertex	x_1	x_2	x_3	x_4
Pure A	a	1	1	1	1
$L1_2 (A_3B)$	e	1/2	0	-1/2	-1
$L1_0 (AB)$	d	0	-1/3	0	1
$L1_2 (AB_3)$	c	-1/2	0	1/2	-1
Pure B	b	-1	1	-1	1

four-dimensional space (x_1, \dots, x_4) , see Table 8-3. The vertices abcde in Fig. 8-3 of the two-dimensional polygon in the subspace (x_1, x_2) can immediately be taken from Table 8-3.

8.3.2 F.C.C. Structure, First and Second Neighbor Interactions

First and second neighbor interactions correspond more closely to the situation encountered in real alloys (Inden, 1977a) than the previous case does. The internal energy contains one more term, the second-nearest neighbor interaction. Consequently we will finally be interested in the existence domain within the subspace of point and first and second neighbor pair correlation functions. The interesting part of the existence domain will be a polyhedron in this three-dimensional space.

The analysis begins with the octahedron $r = 234567$ in Fig. 8-4, which is defined as a basic cluster because it includes both types of interaction. For this cluster, nine correlation functions have to be introduced:

$$\begin{aligned}
 x_1 &= \langle \sigma_2 \rangle & x_6 &= \langle \sigma_2 \sigma_3 \sigma_4 \sigma_7 \rangle \\
 x_2 &= \langle \sigma_2 \sigma_3 \rangle & x_7 &= \langle \sigma_3 \sigma_4 \sigma_5 \sigma_6 \rangle \\
 x_3 &= \langle \sigma_2 \sigma_7 \rangle & x_8 &= \langle \sigma_2 \sigma_3 \sigma_4 \sigma_5 \sigma_7 \rangle \\
 x_4 &= \langle \sigma_2 \sigma_3 \sigma_4 \rangle & x_9 &= \langle \sigma_2 \sigma_3 \sigma_4 \sigma_5 \sigma_6 \sigma_7 \rangle \\
 x_5 &= \langle \sigma_2 \sigma_3 \sigma_7 \rangle
 \end{aligned}$$

x_1 again corresponds to $x_A - x_B$. The existence domain will be a polyhedron in 9-dim. space (x_1, \dots, x_9) , which is defined by the consistency relations for the various configurations on the octahedron cluster:

$ij \dots k$

$$\begin{aligned}
 &AAAAAA: \\
 &BAAAAA: \\
 &BBAAAA: \\
 &BAAAAB: \\
 &BBBAAA: \\
 &BBBAAAB: \\
 &BBBBAAB: \\
 &ABBBBA: \\
 &BBBBBBA: \\
 &BBBBBB:
 \end{aligned}
 \mathcal{Q}_{23\dots 7}^{ij\dots k} = \frac{1}{2^6}
 \begin{pmatrix}
 1 & 6 & 12 & 3 & 8 & 12 & 12 & 3 & 6 & 1 \\
 1 & 4 & 4 & 1 & 0 & 0 & -4 & -1 & -4 & -1 \\
 1 & 2 & 0 & -1 & 0 & -4 & 0 & -1 & 2 & 1 \\
 1 & 2 & -4 & 3 & -8 & 4 & -4 & 3 & 2 & 1 \\
 1 & 0 & 0 & -3 & 0 & 0 & 0 & 3 & 0 & -1 \\
 1 & 0 & -4 & 1 & 0 & 0 & 4 & -1 & 0 & -1 \\
 1 & -2 & -4 & 3 & 8 & -4 & -4 & 3 & -2 & 1 \\
 1 & -2 & 0 & -1 & 0 & 4 & 0 & -1 & -2 & 1 \\
 1 & -4 & 4 & 1 & 0 & 0 & -4 & -1 & 4 & -1 \\
 1 & -6 & 12 & 3 & -8 & -12 & 12 & 3 & -6 & 1
 \end{pmatrix}
 \begin{pmatrix}
 1 \\
 x_1 \\
 x_2 \\
 x_3 \\
 x_4 \\
 x_5 \\
 x_6 \\
 x_7 \\
 x_8 \\
 x_9
 \end{pmatrix}
 \geq 0$$

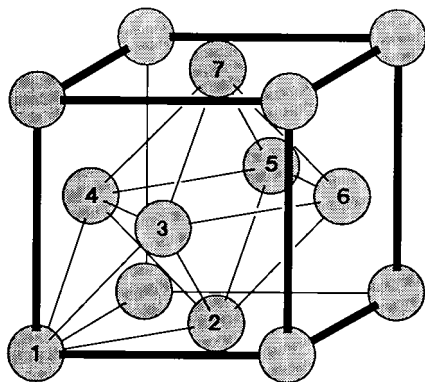


Figure 8-4. Tetrahedron and octahedron clusters in the face-centered-cubic unit cell.

Taken as equalities, these 10 equations define a simplex in the 9-dim. configurational space. From these equations, the vertices of the simplex can be calculated either by solving nine selected equations out of the whole set of 10 or obtained directly by Finel's method outlined above.

Let us consider the projection of this simplex into the subspace (x_1, x_2, x_3) . This projection is obtained from columns 2–4 of the matrix. The result is shown in Fig. 8-5. A verification of whether or not all the vertices correspond to possible atomic arrangements is necessary. For example, vertex $(1/3, -1/3, 1)$ does not correspond to an existing state because it would be built only with octahedra of type BAAAAB. This is topologically impossible in the f.c.c. structure. Therefore, we have to consider further constraints, for instance those resulting from the nearest-neighbor tetrahedron, analyzed before. We can thus use the previous results. In the space (x_1, x_2, x_3) , the previously obtained existence domain would be the rectangular prism built on the basis given by the shaded area in Fig. 8-3 (see also Fig. 8-6). If we now take into account the constraints imposed by both the tetrahedron and the octa-

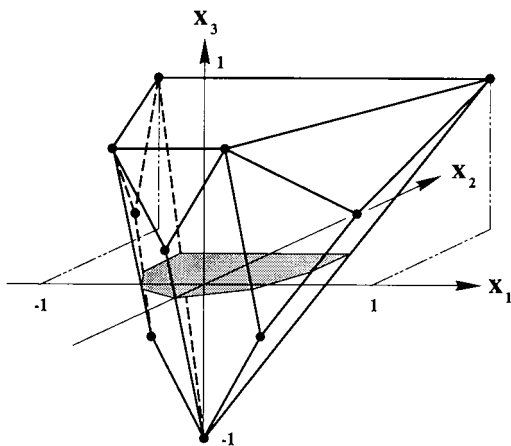


Figure 8-5. Projection of the configuration polyhedron of an octahedron cluster $r=234567$ (see Fig. 8-4) into the subspace of point and first and second neighbor pair correlation functions: $x_1 = \langle \sigma_2 \rangle$, $x_2 = \langle \sigma_2 \sigma_3 \rangle$, $x_3 = \langle \sigma_2 \sigma_7 \rangle$, respectively. Not all the vertices correspond to existing states. The shaded area represents the section for $x_3=0$, i.e. plane (x_1, x_2) . Comparison with Fig. 8-3 reveals that this section defines a larger domain. This shows that the octahedron does not impose the same constraints as the tetrahedron cluster.

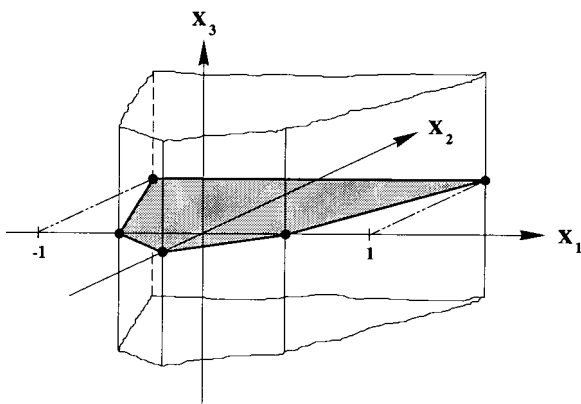


Figure 8-6. Configuration polyhedron of a nearest-neighbor tetrahedron cluster 1234 (Fig. 8-4) in the space (x_1, x_2, x_3) . This cluster does not contain second-nearest neighbor pairs. The polyhedron is thus a rectangular prism built with the existence domain in Fig. 8-3 as basis.

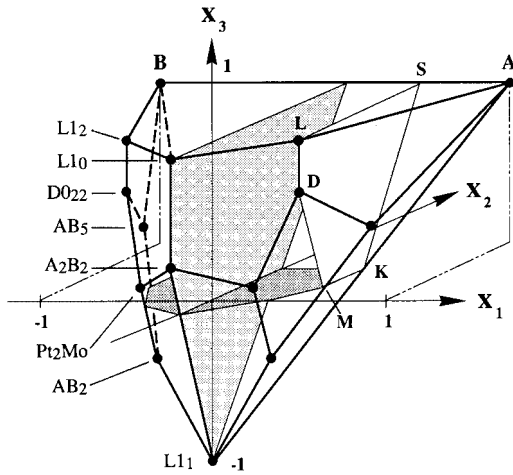


Figure 8-7. Intersection of the two configuration polyhedra corresponding to the tetrahedron and the octahedron, Fig. 8-4 and Fig. 8-5. All vertices of this polyhedron correspond to existing configurations on the f.c.c. lattice. The corresponding superstructures are indicated. Notice the symmetry with respect to the stoichiometric composition AB. The vertical sections represent the existence domains for a fixed alloy composition, here AB and A_3B .

hedron, we will have to intersect the two polyhedra. The result of the intersection of Fig. 8-5 and Fig. 8-6 is shown in Fig. 8-7, and the coordinates of the vertices are given in Table 8-4. It is easy to show that all the vertices of this polyhedron correspond to existing atomic configurations. Consequently, in the f.c.c. structure with first and second nearest-neighbor interactions, we have to introduce at least the regular tetrahedron and the octahedron as basic clusters. Fig. 8-7 also illustrates the

Table 8-4. Coordinates of the vertices of the configuration polyhedron shown in Fig. 8-7.

Configuration	Correlation functions		
	x_1	x_2	x_3
Pure A (A_1)	1	1	1
A_5B , AB_5	$\pm 2/3$	$1/3$	$1/3$
A_3B , AB_3 (L_{12})	$\pm 1/2$	0	1
A_3B , AB_3 (D_{022})	$\pm 1/2$	0	$2/3$
A_2B , AB_2 (Pt_2Mo)	$\pm 1/3$	$-1/9$	$1/9$
A_2B , AB_2	$\pm 1/3$	0	$-1/3$
AB (L_{10})	0	$-1/3$	1
AB (L_{11})	0	0	-1
A_2B_2	0	$-1/3$	$1/3$
Pure B (A_1)	-1	1	1

statement made in the previous paragraph that if we reduce the interaction range to nearest neighbors and keep the two basic clusters, the projected existence domain in the space (x_1, x_2) does not change due to the introduction of the octahedron, a larger cluster than the tetrahedron.

8.3.3 B.C.C. Structure, First and Second Neighbor Interactions

The treatment of the b.c.c. structure is much simpler than that of the f.c.c. structure because an irregular tetrahedron as a basic cluster already contains first and second neighbor distances, as shown in Fig. 8-2. With this cluster, we must introduce the variable $x_1 = \langle \sigma_1 \rangle$, $x_2 = \langle \sigma_1 \sigma_3 \rangle$, $x_3 = \langle \sigma_1 \sigma_2 \rangle$, $x_4 = \langle \sigma_1 \sigma_2 \sigma_3 \rangle$, $x_5 = \langle \sigma_1 \sigma_2 \sigma_3 \sigma_4 \rangle$. This consistency relations are

$$ijkl$$

$$AAAA:$$

$$BAAA:$$

$$BABA:$$

$$BBAA:$$

$$BBBA:$$

$$BBBB:$$

$$Q_{1234}^{ijkl} = \frac{1}{2^4} \begin{pmatrix} 1 & 4 & 4 & 2 & 4 & 1 \\ 1 & 2 & 0 & 0 & -2 & -1 \\ 1 & 0 & 0 & -2 & 0 & 1 \\ 1 & 0 & -4 & 2 & 0 & 1 \\ 1 & -2 & 0 & 0 & 2 & -1 \\ 1 & -4 & 4 & 2 & -4 & 1 \end{pmatrix} \begin{pmatrix} 1 \\ x_1 \\ x_2 \\ x_3 \\ x_4 \\ x_5 \end{pmatrix} \geq 0$$

Taken as equalities, these equations define a simplex in the 5-dim. configurational space. All the vertices correspond to existing atomic configurations. Its projection into the subspace (x_1, x_2, x_3) defines the configuration polyhedron shown in Fig. 8-8. The coordinates of the vertices are given in Table 8-5.

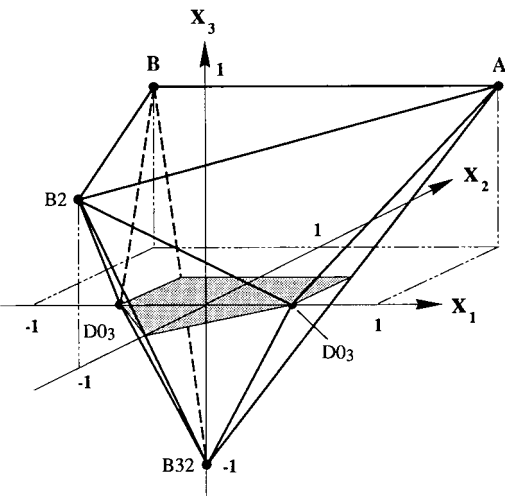


Figure 8-8. Projection of the configuration polyhedron corresponding to the irregular tetrahedron $r=1234$ of the b.c.c. lattice (see Fig. 8-2) into the subspace of point and first and second neighbor pair correlation functions $x_1=\langle\sigma_1\rangle=x_A-x_B$, $x_2=\langle\sigma_1\sigma_3\rangle$, $x_3=\langle\sigma_1\sigma_2\rangle$, respectively. All vertices correspond to existing ordered atomic configurations.

Table 8-5. Coordinates of the vertices of the configuration polyhedron shown in Fig. 8-8.

Configuration	Correlation functions				
	x_1	x_2	x_3	x_4	x_5
Pure A (A2)	1	1	1	1	1
A ₃ B, AB ₃ (D0 ₃)	$\pm 1/2$	0	0	$\mp 1/2$	-1
AB (B2)	0	-1	1	0	1
AB (B32)	0	0	-1	0	1
Pure B (A2)	-1	1	1	-1	1

8.4 Ground States

The description of the configurations will now be used to derive the stability of the configurations at $T=0$ K. The most stable state, the ground state, is given by the minimum of the (grand canonical) internal energy $\tilde{U}(V, T, \mu_A, \mu_B, \dots)$ for given values T, V, μ_i obtained by variation of the internal configurational variables, i.e. point, pair, triplet, etc. correlation functions. In practice it is preferred to consider the (canonical) internal energy $U(T, V, N_A, N_B, \dots)$ with the particle numbers N_i as variables. The grand canonical energy is then obtained by the Legendre transformation of U :

$$\tilde{U} = U + \sum_{i=1}^K \mu_i N_i$$

The general expression for \tilde{U} can be written

(8-16)

$$\begin{aligned} \tilde{U} = & \sum_{(nm)} \sum_{i,j} p_n^{(i)} p_m^{(j)} V_{ij}^{nm} + \sum_{(nmq)} \sum_{i,j,k} p_n^{(i)} \\ & \times p_m^{(j)} p_q^{(k)} V_{ijk}^{nmq} + \dots + \sum_n \sum_i p_n^{(i)} \mu_i \end{aligned}$$

The summations have to be taken over all equivalent points, pairs, etc. In this formulation the higher-order cluster interactions (beyond pairs) are not the total energies of these clusters, but correction terms. Depending on the structure, the clusters of a given class may share subclusters. This sharing of subclusters has to be taken into account if total energies are used.

8.4.1 Pair Interactions

The concept of pair interactions has a long tradition and has been supported by the theoretical work of Gautier (1984), Bieber and Gautier (1984 a, b, 1986, 1987), and Turchi et al. (1991a, b), who came to the conclusion that pair interactions play a

dominant role in alloys, while higher-order cluster interactions are of minor importance. This appears to be a good approximation for the class of alloys with negligible relaxation effects. Furthermore, pair correlations can be determined by diffraction experiments (see, e.g., Schönfeld, 1999).

Grouping together all the energy contributions from positions nm with the same distance k , we obtain the following results for the internal energy:

$$\begin{aligned}\tilde{U} &= \sum_{v=1}^L \sum_k \left\{ \frac{1}{2} z^{(k)} N^{(v)} \sum_{i,j} \langle p_v^{(i)} p_{v_k}^{(j)} \rangle V_{ij}^{(k)} \right. \\ &\quad \left. + N^{(v)} \sum_i \langle p_v^{(i)} \rangle \mu_i \right\} \\ &= \frac{1}{2} \sum_k \sum_{i,j} V_{ij}^{(k)} \sum_{v=1}^L z_v^{(k)} N^{(v)} \varrho_{vv_k}^{ij} \\ &\quad + \sum_i \mu_i \sum_{v=1}^L N^{(v)} \varrho_v^{(i)}\end{aligned}$$

where v_k defines a point in the k -th neighbor shell of an arbitrary position in sublattice v taken as the origin, and $z_v^{(k)}$ is the corresponding coordination number. We obtain

$$\sum_{v=1}^L z_v^{(k)} N^{(v)} \varrho_{vv_k}^{ij} = z^{(k)} N \varrho_{0k}^{ij}$$

and

$$\sum_{v=1}^L N^{(v)} \varrho_v^i = N \varrho_0^{(i)}$$

where position 0 stands for any position in the crystal taken as the origin. Therefore, the energy is

$$\tilde{U} = \frac{1}{2} N \sum_k \sum_{i,j} z^{(k)} V_{ij}^{(k)} \varrho_{0k}^{ij} + N \sum_i \mu_i \varrho_0^{(i)} \quad (8-17)$$

This expression contains only the isotropic pair probabilities because we assumed isotropy for the pair interactions. Consequently, it is not possible to distinguish lro

from sro by energetic arguments. In fact, lro results from a topological constraint. Beyond a critical number of unlike bonds, it is no longer possible to arrange these bonds on a lattice with the constraint to maintain the equivalence of all lattice points.

In Eq. (8-17), no reference state is specified. We will refer the energy to the mechanical mixture of the pure components in the same crystal structure as the alloys and obtain the following expression from Eq. (8-17):

$$\begin{aligned}\Delta \tilde{U} &= \tilde{U} - \frac{1}{2} N \sum_k z^{(k)} \\ &\quad \times (x_A V_{AA}^{(k)} + x_B V_{BB}^{(k)}) - N \sum_{i=A,B} \mu_i^0 \varrho_0^{(i)} \\ &= \frac{N}{2} (\Delta \mu_A + \Delta \mu_B) + \frac{N}{8} (\Delta \mu_A - \Delta \mu_B) \langle \sigma_0 \rangle \\ &\quad - \frac{N}{8} \sum_k z^{(k)} W^{(k)} + \frac{N}{8} \sum_k z^{(k)} W^{(k)} \langle \sigma_0 \sigma_k \rangle\end{aligned} \quad (8-18)$$

where $\Delta \mu_i = \mu_i - \mu_i^0$ and $W^{(k)} = -2 V_{AB}^{(k)} + V_{AA}^{(k)} + V_{BB}^{(k)}$. The $W^{(k)}$ are called *exchange-energy* parameters. They take positive values for an ordering tendency in the k -th shell and negative values for a separation tendency. In order/disorder problems, we are not usually interested in the size of the system, and the quantity $\Delta \tilde{U}/N$ can then be treated. If we fix temperature and pressure and consider only equilibrium states, the number of independent chemical potentials is reduced by one. For convenience we often take $\Delta \mu_A + \Delta \mu_B = 0$ and define an effective chemical potential $\mu^* = \frac{1}{2} (\Delta \mu_A - \Delta \mu_B)$.

Finding the ground states is equivalent to finding the minimum of \tilde{E} , which is defined as the part of the internal energy that depends only on the configurational variables:

$$\tilde{E} = \frac{\Delta \tilde{U}}{N} + \frac{1}{8} \sum_k z^{(k)} W^{(k)} = \sum_{s=1}^{k+1} x_s \Phi_s \quad (8-19)$$

with $x_s = \langle \sigma_0 \rangle, \langle \sigma_0 \sigma_1 \rangle, \dots, \langle \sigma_0 \sigma_k \rangle$ and $\Phi_s = \mu^*, \frac{1}{8} z^{(1)} W^{(1)}, \dots, \frac{1}{8} z^{(k)} W^{(k)}$.

8.4.1.1 Ground State Energies

Eq. (8-19) shows how the energy \tilde{E} depends on the configurational variables x_s , that is, on the composition by $x_1 = \langle \sigma_0 \rangle = x_A - x_B$, and on the pair correlation functions by x_2, x_3, \dots . Among the variety of possible states, there are also those with the lowest energy \tilde{E}_{\min} . These states will now be determined using a geometrical interpretation of Eq. (8-19).

Firstly, Eq. (8-19) is a linear relation. This implies that all those values x_s which fulfill Eq. (8-19) define a (hyper)plane in the configurational space. It will now be shown that the energy \tilde{E} is proportional to the distance of this (hyper)plane from the origin.

To demonstrate this, we introduce the vector $\mathbf{x} = (x_1, x_2, \dots, x_{k-1})$ and a unit vector $\mathbf{n} = \Phi/|\Phi| = |\Phi|^{-1} (\mu^*, z^{(1)} W^{(1)}/8, \dots, z^{(k)} W^{(k)}/8)$. Eq. (8-19) can then be written in vector form:

$$(\mathbf{x}|\mathbf{n}) = \frac{\tilde{E}}{|\Phi|} = d \quad (8-20)$$

where d is the distance of the hyperplane from the origin. This distance takes positive or negative values depending on the directions of the two vectors \mathbf{n} and \mathbf{x} . The factor $|\Phi|$ depends only on the chemical potential, the exchange energies and the coordination numbers, that is, it defines the alloy under consideration. If we change the chemical potential (which controls the composition) and/or the energy parameters, then the direction of \mathbf{n} changes (except if we change all the components Φ_i by a common factor), as does the value of d .

If, on the other hand, we consider a given alloy, which means we keep vector Φ fixed but vary the values of \mathbf{x} , then the normal vector \mathbf{n} does not change. This means

that in this instance the planes of constant \tilde{E} are parallel to each other, and it follows immediately from Eq. (8-20) that the extrema of \tilde{E} must correspond to extreme values of \mathbf{x} . Because the origin is inside the existence domain for the present choice of $\tau_i = \pm 1$, the value \tilde{E}_{\min} must be negative. Searching the ground state thus becomes equivalent to finding, for a given alloy (i.e., for a given $\mathbf{n} = \Phi/|\Phi|$), the values of \mathbf{x} that yield the most negative value for the distance d from the origin. If we recall that the existence domain is a closed polyhedron, it follows that the ground states must correspond to vertices of the polyhedron. This will now be illustrated with some examples that have already been considered in previous sections.

8.4.1.2 F.C.C. Structure, First-Neighbor Interactions

With first-neighbor interactions in the f.c.c. structure, the energy \tilde{E} depends only on the compositional parameter $x_1 = x_A - x_B$, and on one configurational parameter, the correlation function of nearest-neighbor pairs $x_2 = \langle \sigma_0 \sigma_1 \rangle = 1 - 4 \varrho_{01}^{AB}$ (see Eq. (8-7)), where position 1 is a nearest-neighbor site to a central site 0. Therefore, the existence domain in Fig. 8-3 is relevant to this case. It follows from the foregoing discussion that the ground states are given by the vertices in Fig. 8-3 (i.e., pure A, pure B, L1₂ with compositions A₃B and AB₃, and L1₀ with composition AB). Fig. 8-9 illustrates this point with some examples.

If, for example, $\Phi_1 = \mu^*/|\Phi| = 0$, then the vector $\Phi = (0, \Phi_2)$ and, consequently, \mathbf{n} is parallel or antiparallel to the x_2 -axis, depending on the sign of $\Phi_2 = \frac{1}{8} W^{(1)}$. The lines $\tilde{E} = \text{const.}$ are then parallel to the x_1 -axis. This can also be seen from Eq. (8-20), which reduces to

$$\Phi_2 x_2 = \tilde{E}$$

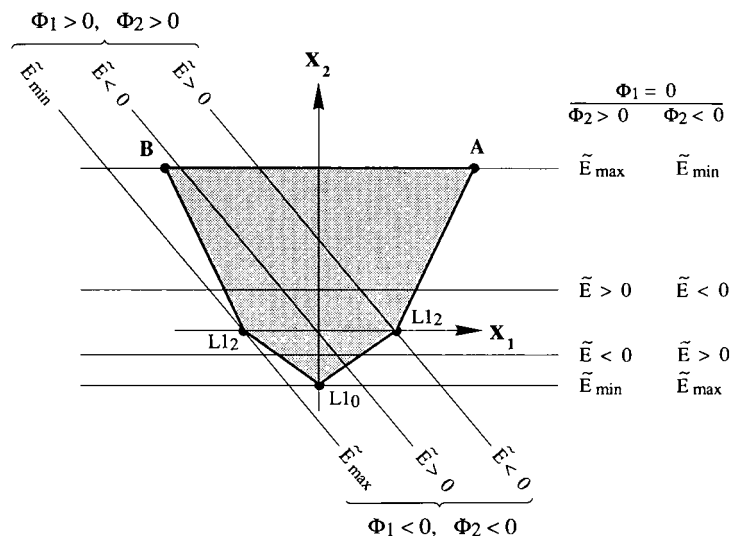


Figure 8-9. Lines of constant grand canonical energy \tilde{E} (Eq. (8-20)) for given sets of values $\Phi_1 = \mu^* = \frac{1}{2}(\mu_A - \mu_B)$ and $\Phi_2 = \frac{3}{4}W^{(1)}$ in the case of the f.c.c. lattice and nearest-neighbor interactions. The configuration polygon is that of Fig. 8-3. Extrema of the energy correspond to lines passing through the vertices of the polygon. Depending on the sign of Φ_1 and Φ_2 the line through a vertex corresponds to a minimum or a maximum. The vertices thus define the ground states. For particular Φ_1, Φ_2 values the lines coincide with the sides of the polygon. For these values, the ground state is degenerate.

These lines are shown in Fig. 8-9. If we consider an alloy with ordering tendency ($W^{(1)} > 0 \Leftrightarrow \Phi_2 > 0$), the value \tilde{E}_{\min} is reached for the most negative x_2 value, which is $x_2 = -1/3$. This point corresponds to the $L1_0$ structure AB. If we consider an alloy with separation tendency ($W^{(1)} < 0 \Leftrightarrow \Phi_2 < 0$), the value \tilde{E}_{\min} is reached for the most positive x_2 value, which is $x_2 = 1$. In this case, the line $\tilde{E} = \tilde{E}_{\min}$ coincides with a side of the configuration polygon. This line joins the vertices corresponding to the pure components A and B. The ground state is degenerate: it could be pure A and pure B in any proportion juxtaposed to each other, or any other arrangement of A and B which, in the limit of $N \rightarrow \infty$, does not form A-B bonds (e.g., constant number of 2-dim. boundaries).

Next, we may consider the case $\Phi_2 = \frac{12}{8}W^{(1)} = 0$, which corresponds to an

ideal solution. The lines $\tilde{E} = \text{const.}$ are parallel to the x_2 -axis in this case, because \mathbf{n} is parallel to the x_1 -axis. Eq. (8-20) now reduces to

$$\Phi_1 x_1 = \tilde{E}$$

For a positive value of $\Phi_1 = \mu^* = \frac{1}{2}(\Delta\mu_A - \Delta\mu_B)$, the most negative value of \tilde{E} is obtained for $x_1 = (x_A - x_B) = -1$, i.e., corresponding to pure B, and a negative value of Φ_1 corresponds to pure A.

The procedure outlined above can be repeated for any direction of the vector Φ , see Fig. 8-9. As long as the lines of constant \tilde{E} pass through a vertex of the polygon, a unique ground state can be defined. If these lines coincide with the sides of the polygon, the ground state is degenerate. It could then be any mixture of the two states corresponding to the two vertices defining the side of the polygon. It was mentioned

before that the proportion of the two states differing in composition is not defined because in these cases of degeneracy the overall composition of the system is not defined by a fixed value of the chemical potential. We can say, however, that the state is two-phase.

Finally, we can determine a so-called *ground-state diagram*, which is shown in Fig. 8-10. It is worth noting that the single-phase fields are sectors in the (Φ_1, Φ_2) plane limited by lines originating from the origin. It is thus sufficient to know the directions of those lines. Furthermore, the diagram is symmetric with respect to $\Phi_1 = 0$.

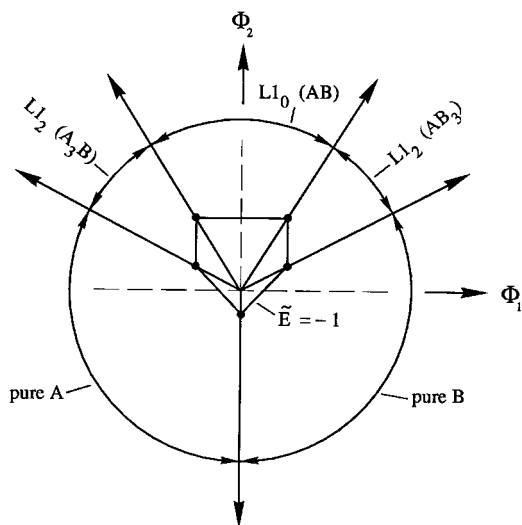


Figure 8-10. Ground-state diagram and dual polygon (to Fig. 8-9) for the case of an f.c.c. lattice with nearest-neighbor interactions. The axes are $\Phi_1 = \mu^* = \frac{1}{2}(\mu_A - \mu_B)$ and $\Phi_2 = \frac{3}{4}W^{(1)}$. The solid lines are radius vectors which subdivide the plane into regions with a defined ground state. The directions of these vectors are defined by the vertices of the dual polygon to Fig. 8-3. It corresponds to a fixed value of the energy, here $\tilde{E} = -1$ (energy units), and is obtained from Eq. (8-21). The dual polygon already contains complete information on the ground-state diagram. For Φ_1, Φ_2 values corresponding to these lines, the ground state is degenerate.

When higher-order interactions are involved, as in the next paragraph, the determination of the ground-state diagram is not that simple, and it is useful to have a more analytical method for its determination. Such a method will now be introduced and, for the purpose of illustration, will be applied to the present very simple case.

The ground-state diagram displays the ranges of Φ_1 and Φ_2 values for which a given state, e.g., $L1_0$, is stable. We thus interpret Eq. (8-19) inversely to that of Eq. (8-20): given a vertex in the configurational space, e.g., vertex $x_v = (-1 \ 3 \ 0)$ corresponding to $L1_0$, we define a unit vector $n^* = x_v/|x_v|$. Eq. (8-19) can then be rewritten as

$$(\Phi|n^*) = \tilde{E}/|x_v| = d^* \quad (8-21)$$

In a method similar to that used with Eq. (8-20), we interpret Eq. (8-21) as the equation of a line in the space (Φ_1, Φ_2) with a distance $d^* = \tilde{E}/|x_v|$ from the origin. If we fix the value of \tilde{E} , then all vectors Φ fulfilling Eq. (8-21) must end in the line with the normal n^* and with distance d^* . In Fig. 8-10, the result is shown for $\tilde{E} = -1$ (energy units). It shows that the vectors fulfilling Eq. (8-21) describe a polygon. The coordinates of the vertices of this polygon are given in Table 8-6. This polygon is the *dual* polygon to the configuration polygon (Finel, 1987), and the space (Φ_1, Φ_2) is called the dual space. A face of the dual polygon corresponds to each vertex of the configuration polygon in the direct space (x_1, x_2) . All vectors Φ pointing to the same face of the polygon define alloys that exhibit the same ground state given by the associated vertex of the configuration polygon. If we vary \tilde{E} , then the polygon shrinks or blows up, respectively, and the vertices of the dual polygon vary along the lines that define the two-phase states in Fig. 8-10. It is easy to verify that these lines are

vertical to the faces of the configuration polygon in Fig. 8-3.

The generalization of these results to higher dimensions is straightforward. A dual polyhedron defined by Eq. (8-21) is associated with the (direct) configuration polyhedron in such a way that each vertex of the direct polyhedron corresponds to a face of the dual polyhedron, and vice versa. In order to get the vertices of the dual polyhedron, we have to solve Eq. (8-21) simultaneously for the number of vertices of the direct polyhedron required to define the (hyper)plane. The application of this in three dimensions will be shown in the next two paragraphs.

8.4.1.3 F.C.C. Structure, First and Second Neighbor Interactions

With first and second neighbor interactions in the f.c.c. structure, the energy \tilde{E} depends on one more configurational parameter, the second neighbor pair correlation function $x_3 = \langle \sigma_0 \sigma_2 \rangle = 1 - 4\varrho_{02}^{AB}$ (see Eq. (8-7)). The relevant existence domain is now that shown in Fig. 8-7. We can again proceed as previously.

Let us first consider $\Phi_3 = \frac{12}{8}W^{(2)} = 0$. The normal vector \mathbf{n} corresponding to the planes of constant energy \tilde{E} is perpendicular to the axis x_3 in this case. If we consider an alloy with an ordering tendency in the first shell, $\Phi_2 = \frac{12}{8}W^{(1)} > 0$, then \mathbf{n} is oriented in the half space $x_2 > 0$, and the planes corresponding to \tilde{E}_{\min} are those passing through the vertices pure A, L1₂ with compositions A₃B or AB₃, L1₀ with composition AB, and pure B, depending on the value of $x_1 = \mu^* = \frac{1}{2}(\Delta\mu_A - \Delta\mu_B)$. This is in accordance with the results already obtained in Sec. 8.4.3 (see Fig. 8-10). However, an additional result can be deduced from Fig. 8-7: the energy planes pass simultaneously through the vertices corresponding to the structures D0₂₂ and L1₂ (both either A₃B or AB₃), as well as L1₀ and A₂B₂. The ground states are thus degenerate in these instances.

The complete ground-state diagram is obtained from the determination of the dual polyhedron associated with the existence domain of Fig. 8-7. This dual polyhedron is shown in Fig. 8-11. All Φ vectors pointing to (or piercing) a given face of the dual

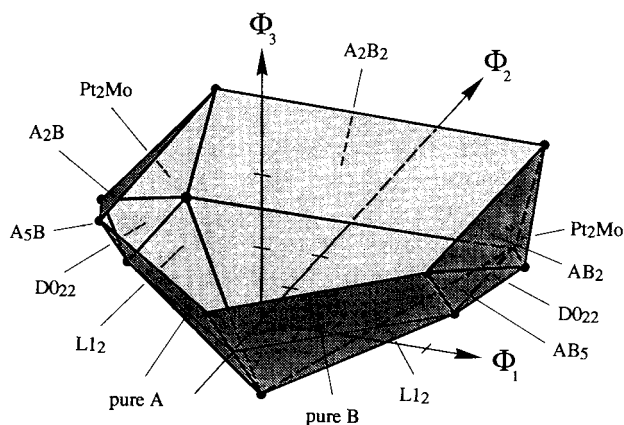


Figure 8-11. Dual polyhedron (to Fig. 8-7) for the case of an f.c.c. lattice with first and second neighbor interactions. The axes are $\Phi_1 = \mu^* = \frac{1}{2}(\mu_A - \mu_B)$, $\Phi_2 = \frac{3}{4}W^{(1)}$, and $\Phi_3 = \frac{3}{4}W^{(2)}$. The dual polyhedron defines the ground-state diagram and corresponds to a constant energy $\tilde{E} = -1$ (energy units). All radius vectors pointing to the same face correspond to the same ground state, which is labeled the top, which is L1₁. Vectors coinciding with the boundaries of the faces correspond to degenerate ground states.

polyhedron define alloys with the same ground state, which is defined by the corresponding vertex of the configuration polyhedron. The ground-state diagram thus divides the dual space into (hyper)cones formed by the vectors from the origin to the borderlines of the faces. Each cone defines a ground state. Due to graphical limitations, those cones are not shown in Fig. 8-11, but the ground states are labeled at each face of the dual polyhedron. The

Table 8-6. Coordinates of the dual polyhedra shown in Figs. 8-10, 8-11 and 8-12.

Tetra- hedron f.c.c.		Tetrahedron– Octahedron f.c.c.			Tetrahedron b.c.c.		
Φ_1	Φ_2	Φ_1	Φ_2	Φ_3	Φ_1	Φ_2	Φ_3
2	1	± 2	1	0	0	0	-1
2	3	± 2	3	0	± 2	1	0
-2	3	$\pm 18/7$	$12/7$	$3/7$	± 2	2	1
-2	1	± 2	0	1	± 2	0	1
0	-1	± 2	4	1	0	-2	1
		0	-2	1			
		0	0	-1			

coordinates of the dual vertices are given in Table 8-6. They have been derived by inserting the vertices in Table 8-3 into Eq. (8-21) for $\tilde{E}_{\min} = -1$.

8.4.1.4 B.C.C. Structure, First and Second Neighbor Interactions

In the first and second neighbor interactions of the b.c.c. structure, the energy \tilde{E} depends on the same variables (x_1, x_2, x_3) as in the preceding example, and the relevant existence domain is that shown in Fig. 8-8. We can now construct the dual polyhedron, solving Eq. (8-21) for $\tilde{E} = -1$ and using the vertex coordinates in Table 8-4. The coordinates of the dual vertices are given in Table 8-6, and the dual polyhedron is shown in Fig. 8-12.

8.4.1.5 Energy Minimum at Constant Composition

From a metallurgical point of view it seems more natural to consider the composition of a system an independent variable which we can control, rather than the

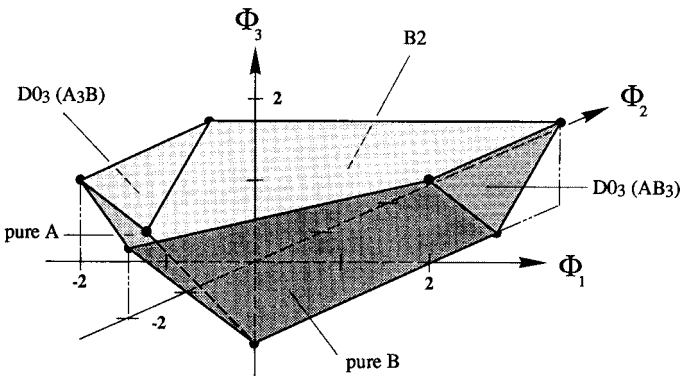


Figure 8-12. Dual polyhedron (to Fig. 8-8) for the case of an b.c.c. lattice with first and second neighbor interactions. The axes are $\Phi_1 = \mu^* = \frac{1}{2}(\mu_A - \mu_B)$, $\Phi_2 = W^{(1)}$, and $\Phi_3 = \frac{3}{4}W^{(2)}$. The dual polyhedron defines the ground-state diagram and corresponds to a constant energy $\tilde{E} = -1$ (energy units). All radius vectors pointing to the same face of the polyhedron correspond to the same ground state, which is labeled for each face, except the top one, which is B32.

chemical potential. However, this is not possible. We can, of course, control the overall composition of our system by taking the appropriate amounts of the pure substances, closing the system against materials exchange, and producing a certain configuration (e.g., by heat treatment). If we thereby equilibrate the system at a given temperature, the system will attain its energy minimum by internal reactions. These reactions can be the formation of ordered atomic arrangements (homogeneous single-phase state) or the formation of heterogeneous microstructures. In the latter case, we have to introduce new variables in addition to the configurational variables, for example, the volume of produced phases, describing the advance of these reactions. At equilibrium, the driving force for the reactions must be zero, that is, the chemical potentials of all the reaction products must be the same. Because the overall composition is fixed, the amount of the phases present is also fixed. This is different from a grand canonical treatment. The energy in this case is given by the canonical energy E , which is given by the expression

$$E = \tilde{E} - x_1 \Phi_1 = \sum_{s=2}^{k+1} x_s \Phi_s \quad (8-22)$$

This equation is similar to Eq. (8-19), except that the number of variables is reduced by one. The geometrical considerations can be applied as before. In Fig. 8-7, two sections corresponding to the compositions $x_1 = x_A - x_B = 0$ and 0.5 (AB and A_3B) are shown as shaded areas. Since in this instance we are confined to a planar section, the loci of constant energy are lines, and the minimum energy corresponds to the lines passing through the vertices of the polygon. We will consider the case $x_1 = 0.5$ in detail, and we thus have to consider the polygon SLDMK in Fig. 8-7.

The states corresponding to L and D ($L1_2$ and $D0_{22}$) are ground states because they are vertices of the configuration polyhedron. S is not a vertex in this figure, but lies on the line joining the states pure A and pure B. This line corresponds to configurations that do not contain any A–B pairs. There is no other configuration possible except for pure A and pure B taken together in the proportion A_3B . Of course, the planar interface, which is necessarily formed, contains A–B pairs. In the thermodynamic limit of $N \rightarrow \infty$, however, the relative number of these pairs approaches zero and can be neglected.

The point K lies on the line joining the vertices pure A and $L1_1$ (AB). Here again the two limiting phases can be taken together in the right proportion to build up a two-phase configuration at point K. The possibility of another homogeneous arrangement needs to be verified, though. But K is not a vertex of the configuration polyhedron in Fig. 8-7. Hence, an additional configuration cannot be characterized within the configurational space created by the basic clusters of the octahedron and tetrahedron.

The point M is on the line joining the vertices A_2B and A_5B . Hence, at first, a mixture of the two limiting phases can be attributed to this point. But a homogeneous configuration also lies here, the structure classified Amm2 in the appendix, which has been observed in Monte Carlo simulations performed at fixed composition (Gahn, 1982). This structure is built up with alternating cube planes which are occupied either by pure A or by an equal amount of A and B in an arrangement identical to the cube planes in the $L1_1$ structure, see Fig. 8-13. It is interesting to notice the structural relationship between this Amm2 structure at point M and the arrangement at K (pure A plus $L1_1$ (AB)): at M the stack-

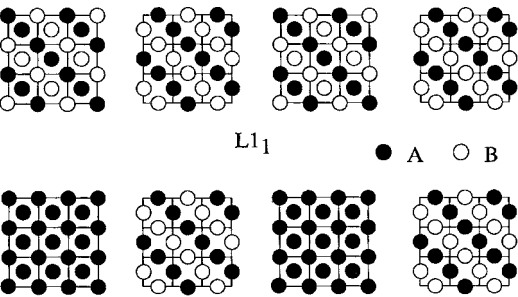


Figure 8-13. Atomic distribution on four subsequent (0 0 1) planes of the superstructures $L1_1$ (AB) and Amm2 (A_3B). The structure Amm2 is composed of alternating (0 0 1) planes of pure A and $L1_1$.

ing sequence is one cube plane of pure A followed by one cube plane of $L1_1$. If we increase the stacking distance (i.e., the number of cube planes of each phase), the corresponding configurational point moves from M toward K. At K, the thickness of each package of cube planes approaches infinity. The displacement of the configurational point is caused by the decreasing number of AB pairs that cross the “interfaces” between the two structural units.

8.4.1.6 Canonical Energy of lro States

Instead of imposing a given composition, we may also impose the state of order (e.g., the most perfect lro) and calculate the canonical energy for these states as a function of composition. These are most stable states under the constraint of homogeneity. Consider the f.c.c. structure with nearest-neighbor interactions and the b.c.c. structure with first and second neighbor interactions as simple examples. In Table 8-1, the point probabilities for most perfect lro (at off-stoichiometric composition) are given. From these probabilities, the numerical values of the correlation functions for the different superstructures in their most perfect lro state can be derived directly using

Table 8-7. Numerical values of the correlation functions for the b.c.c. superstructures in their most perfect lro state.

	B2 ($x_B \leq 0.5$)	D0 ₃ ($x_B \leq 0.25$)	D0 ₃ ($0.25 \leq x_B \leq 0.5$)	B32 ($x_B \leq 0.5$)
$\langle \sigma_1 \rangle$	1	1	1	1
$\langle \sigma_2 \rangle$	1	1	1	$1-4x_B$
$\langle \sigma_3 \rangle$	$1-4x_B$	1	$3-8x_B$	1
$\langle \sigma_4 \rangle$	$1-4x_B$	$1-8x_B$	-1	$1-4x_B$
$\langle \sigma_1 \sigma_3 \rangle$	$1-4x_B$	1	$3-8x_B$	1
$\langle \sigma_1 \sigma_4 \rangle$	$1-4x_B$	$1-8x_B$	-1	$1-4x_B$
$\langle \sigma_2 \sigma_3 \rangle$	$1-4x_B$	1	$3-8x_B$	$1-4x_B$
$\langle \sigma_2 \sigma_4 \rangle$	$1-4x_B$	$1-8x_B$	-1	$(1-4x_B)^2$
$\langle \sigma_1 \sigma_2 \rangle$	1	1	1	$1-4x_B$
$\langle \sigma_3 \sigma_4 \rangle$	$(1-4x_B)^2$	$1-8x_B$	$-(3-8x_B)$	$1-4x_B$

Eq. (8-5). These values are given in Table 8-7 for the b.c.c. structures. Introducing these values into the expression for the canonical energy

$$\begin{aligned} \Delta U &= \Delta \tilde{U} - N x_1 \Phi_1 \\ &= -\frac{N}{8} [8 W^{(1)} + 6 W^{(2)}] \\ &\quad + \frac{N}{4} W^{(1)} [\langle \sigma_1 \sigma_3 \rangle + \langle \sigma_1 \sigma_4 \rangle \\ &\quad \quad + \langle \sigma_2 \sigma_3 \rangle + \langle \sigma_2 \sigma_4 \rangle] \\ &\quad + \frac{3N}{8} W^{(2)} [\langle \sigma_1 \sigma_2 \rangle + \langle \sigma_3 \sigma_4 \rangle] \end{aligned} \tag{8-23}$$

yields the energies of formation of the various lro phases. In Fig. 8-14a, b, the energies of formation of b.c.c. structures are shown for two particular choices of interchange energies. It can be seen in Fig. 8-14a that the canonical energy of the most stable lro phase for an interchange energy ratio $W^{(2)}/W^{(1)} = 0.5$, namely off-stoichiometric $D0_3$, is a polygon. This means that all the homogeneous ordered states that can be formed at every composition are degenerate with the two-phase mixtures A + $D0_3$ and $D0_3$ + B2. This is different from Fig. 8-14b where $W^{(2)}/W^{(1)} = -1$. The canonical energy of the most stable lro phase, off-

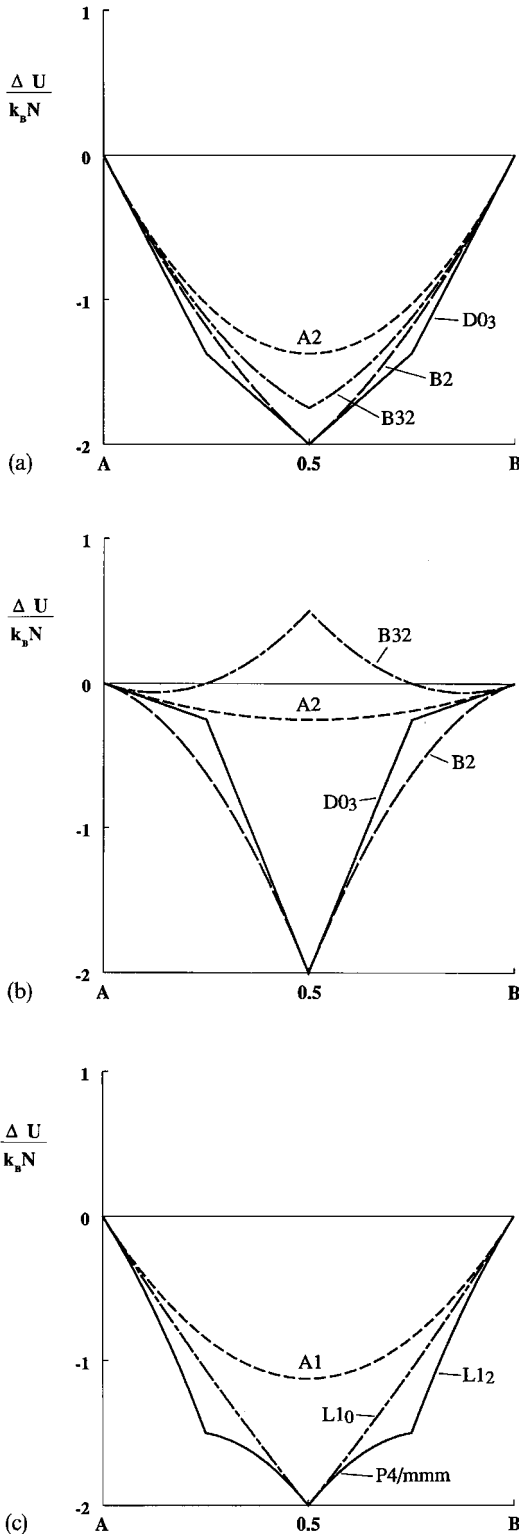


Figure 8-14. Canonical energy ΔU of different b.c.c. and f.c.c. long-range ordered structures as a function of composition for fixed values of the interchange energies. (a) b.c.c., ordering tendency between first and second neighbors: $W^{(1)} = 2W^{(2)} > 0$. (b) b.c.c., ordering tendency between first neighbors and separation tendency between second neighbors: $W^{(1)} = -W^{(2)} \geq 0$. (c) f.c.c. ordering tendency between nearest neighbors: $W^{(1)} > 0, W^{(2)} = 0$.

stoichiometric B2, is a concave curve. In this instance, the most stable state is a two-phase mixture of A + B2. From the canonical energy, we are thus given a hint of whether the ground state will be two-phase, or if there is a degeneracy with single-phase states. The canonical energy for the f.c.c. lro structures $L1_2$ and $L1_0$ can be derived in a similar way. The result is shown in Fig. 8-14c for the ratio $W^{(2)}/W^{(1)} = -1$. Here again, the canonical energy of the most stable lro phase is concave, and only the two-phase mixtures A + $L1_2$ and $L1_2 + L1_0$ are ground states.

8.4.1.7 Relevant Literature

The ground state analysis of f.c.c. and b.c.c. alloys with first and second neighbors was done by Kanamori (1966), Richards and Cahn (1971), Allen and Cahn (1972, 1973), and de Ridder et al. (1980). Multiplet interactions were included by Cahn and Kikuchi (1979), Sanchez and de Fontaine (1981). The ground states of the f.c.c. lattice with up to fourth neighbor interactions were determined by Kanamori and Kakehashi (1977), fifth neighbor interactions were treated by Kanamori (1979), Finel and Ducastelle (1984) and Finel (1984, 1987). The ground states of the hexagonal lattice with anisotropic interactions have been deduced by Crusius and Inden (1988) and Bichara et al. (1992a) from the known ground states of the planar hexagonal lattice with up to third neighbor interactions.

tions (Kudo and Katsura, 1976; Kanamori, 1984).

8.4.2 Effective Cluster Interactions (ECIs)

Up to this point only pair interactions have been considered with the exchange energies $W^{(k)}$ as dummy parameters. The internal energy $\Delta\tilde{U}$, with reference to the pure components in the same crystal structure, has been written in terms of an expansion of these $W^{(k)}$ (Eq. (8-19)). This is a special case of the more general cluster expansion (CE) of the internal energy $\Delta\tilde{U}$ in terms of the correlation functions:

$$\frac{\Delta\tilde{U}}{N} = \sum_0^{\alpha} V_n x_n \quad (8-24)$$

where n refers to subclusters of the basic cluster α ($n=1$ for point, $n=2$ for pair clusters, etc.) (Sanchez et al., 1984). This equation is exact if α represents the entire system. It is expected, however, that Eq. (8-24) converges rapidly such that the series can be truncated. For a general discussion of the method see Laks et al. (1992), de Fontaine (1994) and Sanchez (1996).

The parameters V_n are supposed to embrace all possible energy sources that depend on configuration, including all ground-state features like electronic energy, long-range elastic and Coulombic interactions. But they might also contain configuration-dependent excitation energies such as those arising from vibrational and electronic excitations when finite temperatures are considered, making the model interaction energies temperature dependent. It should be appreciated that the parameters V_n represent energy contributions, not only from direct interactions within the cluster, but also from the interactions of much longer range outside the cluster range. They are thus called effective cluster interactions (ECIs).

It may be useful to spell out explicitly the pure configurational part of the V_n . In the case of pair interactions the V_n with $n \geq 2$ are equivalent to the pair exchange

energies, i.e., $V_n = \frac{z^{(n)}}{8} W^{(n)}$. In this case the specific lattice type is only introduced in terms of the coordination numbers.

In the case of higher-order cluster interactions the lattice type is not only specified by the coordination numbers of the basic cluster and its subclusters, but most importantly by the type of clusters they share with each other. Subclusters which are not shared define no new correlations. They are already taken into account by those of their parent cluster. We could thus expect that the V_n of such clusters do not show up in the expansion, for example triplet correlations in the tetrahedron expansion of the f.c.c. lattice. This, however, is not true because the V_k in the expansion, Eq. (8-24), not only contain terms from the k -point clusters, but also terms from higher clusters ($n > k$).

This becomes transparent if the V_n are expressed in terms of the cluster exchange energies, defined as

$$W_{ij\dots l}^{12\dots r} = -r V_{ij\dots l} + \sum_{k=i}^l V_{kk\dots k}$$

(for example, $W_{ABBB}^{1234} = -4V_{ABBB} + V_{AAAA} + 3V_{BBBB}$). It should be noted that, unlike the pairs, these cluster-exchange energies do not represent the total energy of the clusters, only successive corrections to the cluster energies. If total energies were considered, the sharing of subclusters would have to be taken into account.

Considering the f.c.c. lattice and a truncation at the regular tetrahedron cluster ($\alpha=4$), Eq. (8-24) gives:

$$\frac{\Delta\tilde{U}(\varphi)}{N} = V_0 + V_1(x_A - x_B) + V_2 x_2^{(\varphi)} + V_3 x_3^{(\varphi)} + V_4 x_4^{(\varphi)} \quad (8-25)$$

where ϕ indicates specific states, e.g. the five vertices a–e of the configuration polyhedron in Table 8-3. The V_n expressed in terms of the cluster exchange energies are given by

$$\begin{aligned}
 V_0 &= \frac{1}{2} (\Delta\mu_A + \Delta\mu_B) - \frac{z^{(1)}}{8} W^{(1)} \\
 &\quad - \frac{z^{\text{triplet}}}{24} (W_{BAA} + W_{BBA}) \\
 &\quad - \frac{z^{\text{tetra}}}{64} \left(W_{BAAA} + \frac{3}{2} W_{BBAA} + W_{BBBA} \right) \\
 V_1 &= \frac{1}{2} (\Delta\mu_A - \Delta\mu_B) - \frac{z^{\text{triplet}}}{24} (W_{BAA} - W_{BBA}) \\
 &\quad - \frac{z^{\text{tetra}}}{64} (2 W_{BAAA} - 2 W_{BBBA}) \\
 V_2 &= \frac{1}{8} z^{(1)} W^{(1)} + \frac{z^{\text{triplet}}}{24} (W_{BAA} + W_{BBA}) \\
 &\quad + \frac{z^{\text{tetra}}}{64} (3 W_{BBAA}) \\
 V_3 &= \frac{z^{\text{triplet}}}{24} (W_{BAA} - W_{BBA}) \\
 &\quad + \frac{z^{\text{tetra}}}{64} (2 W_{BAAA} - 2 W_{BBBA}) \quad (8-26) \\
 V_4 &= \frac{z^{\text{tetra}}}{64} \left(W_{BAAA} - \frac{3}{2} W_{BBAA} + W_{BBBA} \right)
 \end{aligned}$$

Taking for example all the triplet terms $W_{ijk}=0$ does not mean $V_3=0$, because there remain tetrahedron terms.

In the irregular tetrahedron approximation of the b.c.c. lattice, the cluster expansion of the internal energy is written as:

$$\begin{aligned}
 \frac{\Delta \tilde{U}(\phi)}{N} &= V_0 + V_1 (x_A - x_B) + V_2 x_2^{(\phi)} \\
 &\quad + V_3 x_3^{(\phi)} + V_4 x_4^{(\phi)} + V_5 x_5^{(\phi)} \quad (8-27)
 \end{aligned}$$

where the CE parameters V_n correspond to:

$$\begin{aligned}
 V_0 &= \frac{1}{2} (\Delta\mu_A + \Delta\mu_B) \\
 &\quad - \frac{z^{(1)}}{8} W_{AB}^{(1)} - \frac{z^{(2)}}{8} W_{AB}^{(2)}
 \end{aligned}$$

$$\begin{aligned}
 &- \frac{z^{\text{triplet}}}{72} (2 W_{ABA} + W_{AAB} \\
 &\quad + W_{BBA} + 2 W_{BAB}) \\
 &- \frac{z^{\text{tetra}}}{256} (4 W_{BAAA} + 4 W_{BABA} \\
 &\quad + 2 W_{BBAA} + 4 W_{BBBA})
 \end{aligned}$$

$$\begin{aligned}
 V_1 &= \frac{1}{2} (\Delta\mu_A - \Delta\mu_B) - \frac{z^{\text{triplet}}}{72} \\
 &\quad \cdot (2 W_{ABA} + W_{AAB} - W_{BBA} - 2 W_{ABB}) \\
 &\quad - \frac{z^{\text{tetra}}}{256} (8 W_{BAAA} - 8 W_{BBBA})
 \end{aligned}$$

$$\begin{aligned}
 V_2 &= \frac{z^{(1)}}{8} W_{AB}^{(1)} + \frac{z^{\text{triplet}}}{72} (2 W_{AAB} + 2 W_{BBA}) \\
 &\quad + \frac{z^{\text{tetra}}}{256} (8 W_{BBAA})
 \end{aligned}$$

$$\begin{aligned}
 V_3 &= \frac{z^{(2)}}{8} W_{AB}^{(2)} + \frac{z^{\text{triplet}}}{72} \\
 &\quad \cdot (2 W_{ABA} - W_{AAB} - W_{BBA} + 2 W_{BAB}) \\
 &\quad + \frac{z^{\text{tetra}}}{256} (8 W_{BABA} - 4 W_{BBAA})
 \end{aligned}$$

$$\begin{aligned}
 V_4 &= \frac{z^{\text{triplet}}}{72} \\
 &\quad \cdot (2 W_{ABA} + W_{AAB} - W_{BBA} - 2 W_{ABB}) \\
 &\quad + \frac{z^{\text{tetra}}}{256} (8 W_{BAAA} - 8 W_{BBBA})
 \end{aligned}$$

$$\begin{aligned}
 V_5 &= \frac{z^{\text{tetra}}}{256} (4 W_{BAAA} - 4 W_{BABA} \\
 &\quad - 2 W_{BBAA} + 4 W_{BBBA}) \quad (8-28)
 \end{aligned}$$

These relations show that cluster interactions not only influence the correlations of their own cluster but also those of the sub-clusters. The system of equations, Eq. (8-24), can be solved for the different V_n . The idea is that the ECIs derived from the energies of ordered configurations are applicable to any configuration, i.e. for lro, sro and for the disordered state. This is equivalent

lent to saying, in the pair approximation, that the $W^{(k)}$ can be used for all configurations. Since the only source of error in Eq. (8-24) is the truncation, it is imperative to carefully select the truncation.

The ingredients for the determination of the ECIs are values of $\Delta\tilde{U}(\varphi)$, which may be obtained from various sources (see e.g. Zunger, 1994). The simplest approach is to take experimental data of the corresponding quantities (e.g. Inden (1975a, b, 1977a, b; Oates et al., 1996)). This requires a truncation at a level imposed by the availability of data and in most cases does not provide satisfactory results.

The second approach is to derive $\Delta\tilde{U}(\varphi)$ from first principles calculations, treating the random alloy by the Coherent Potential Approximation (CPA) and the electronic band structure with the Tight-Binding method (Gautier et al., 1975; Ducastelle and Gautier, 1976; Treglia and Ducastelle, 1980; de Fontaine, 1984; Sigli and Sanchez, 1988; Sluiter and Turchi, 1989a, b) or with the Korringa, Kohn and Rostoker method (Gyorffy and Stocks, 1983; Johnson et al., 1990). The approaches include the Generalized Perturbation Method and the Concentration Wave Method. The ordering contributions are treated as perturbations of the disordered states. The perturbation method is limited to alloys with similar atomic species and provides essentially pair interactions.

The third approach is the inversion method of Connolly and Williams (1983) (Ferreira et al., 1988, 1989; Wei et al., 1990, 1992; Terakura et al., 1987). In this approach special atomic configurations like in ordered compounds are selected and their total energy is obtained from direct electronic structure calculations.

It has been pointed out by Zunger (1994) that it is necessary to account for two types of relaxation, "volume relaxation" when

molar volumes are not constant, and "local relaxation" when atoms deviate from their ideal lattice positions. Ferreira et al. (1987, 1988) and Wei et al. (1990) have shown that, if the volumes depend on composition but only weakly upon configuration, the energy of formation can be split into two additive terms, the elastic energy required to hydrostatically deform the pure constituents from their equilibrium volumes to the alloy volume, and the pure configurational or "chemical" term. The ECIs can be determined either from a set of as many ordered compounds as there are unknowns, or from a larger set, in which case the ECIs are obtained by a fitting procedure (Lu et al., 1991, 1995). It must be emphasized that the ECIs are "effective" and their values depend on the level of truncation.

Cluster expansions for systems with strong lattice relaxations converge slowly in real space. This has led to an alternative route, treating the CE in the reciprocal space (e.g. Laks et al., 1992).

Finally, it should be mentioned that pair interactions may also be obtained from the diffuse scattering of X-rays or neutrons (for a recent review, see Schönfeld, 1999). The procedure is the inverse of the CVM (see Sec. 8.5.1) or the MC technique (see Sec. 8.5.3). Instead of calculating equilibrium configurations using given energy parameters, experimental data of sro are taken as input in order to obtain the interaction parameters. The methods have been presented by Priem et al. (1989a, b) for CVM, and Gerold and Kern (1987) and Livet (1987) for MC.

8.5 Phase Equilibria at Finite Temperatures

Two ways of determining the equilibria at finite temperatures have proven to be most useful (see also the chapter by Binder, 2001), CVM introduced by Kikuchi (1950, 1951) and the MC technique (Binder, 1979, 1986; Binder and Stauffer, 1984; Mouritsen, 1984; Binder and Heermann, 1988).

The CVM is based on an analytical calculation of the configurational entropy S . The equilibrium states at constant volume and temperature are obtained by a minimization of the Helmholtz energy

$$F(V, T, N_i) = U - TS$$

for the equilibrium at fixed composition, or by minimization of the grand potential

$$\Omega(V, T, \mu_i) = U - TS - \sum_i \mu_i N_i$$

for the equilibrium with exchange of atoms, i.e., for given values of the chemical potentials.

The MC method simulates the configurations in a computer crystal. At a given temperature and fixed chemical potentials, atoms are exchanged with a reservoir of atoms with a probability defined in such a way that the equilibrium state is reached after a sufficient number of atomic replacements. In the case of fixed composition, atoms are selected pairwise and interchanged with each other according to an equivalent probability. This method yields the equilibrium configuration but not the thermodynamic functions. On the other hand, we obtain complete and fine-scale information about the atomic configurations and the correlations at large distances, the limitation being imposed only by the size of the computer crystal. Both methods will be applied in this section.

8.5.1 Cluster Variation Method

In the CVM, the entropy is evaluated according to $S = k_B \ln W$, where W is the number of arrangements that can be formed for given values of the correlation functions. The CVM develops an approximate expression for W , taking into account only the correlations up to the basic cluster size. Therefore, the basic clusters are considered to be uncorrelated independent species. The first step in determining the entropy is to write W as the number of possible arrangements of this basic cluster:

$$W = \frac{N_\alpha!}{\prod_\sigma [N_\alpha(\sigma)]!} \stackrel{\text{def}}{=} \{\alpha\}_{N_\alpha} \quad (8-29)$$

where N_α is the total number of α -clusters in a system with N points, and $N_\alpha(\sigma)$ is the number of α -clusters with a given configuration specified by σ ; the term $\{\alpha\}_{N_\alpha}$ is a short notation which will be used hereafter for abbreviation. The ratio $N_\alpha(\sigma)/N_\alpha$ will be indicated by $\varrho_\alpha^{(\sigma)}$.

Eq. (8-29) overestimates the number of arrangements: two overlapping α -clusters cannot be permuted independently because they must fit together with their overlapping units. This becomes obvious if we look at the high temperature limit of Eq. (8-29), which is $W_\infty = \{1\}_{N_\alpha}$, while the exact expression of the limit of W is given by the number of configurations of N points: $W_\infty = \{1\}_N$. Therefore, a correction is needed in order to obtain the correct high-temperature limit. Correcting for the points would correspond to the generalized quasi-chemical approximation (Yang, 1945; Yang and Li, 1947, 1949). Based on geometrical considerations, Kikuchi (1950, 1951) introduced a correction in such a way that the high temperature limit is not only obtained for the point cluster but also for all subclusters of α . A short time later Barker (1953)

arrived at the same result by a more mathematical treatment, and the continued interest in the derivation of the entropy formula is manifested in a number of papers, e.g., Hijmanns and de Boer (1955), Burley (1972), Sanchez and de Fontaine (1978), Gratias et al. (1982) and Finel (1987). For a discussion of the hierarchy of the cluster approximations, see Schlijper (1983, 1984, 1985).

Following Barker, we define m_α as the number of α -clusters per point: $N_\alpha = m_\alpha N$. Then we can write (in Stirling's approximation):

$$\{\alpha\}_N = \frac{(m_\alpha N)!}{\prod_{\sigma} (\varrho_\alpha^{(\sigma)} m_\alpha N)!} = \frac{(N!)^{m_\alpha}}{\prod_{\sigma} ((\varrho_\alpha^{(\sigma)} N!)^{m_\alpha}} \\ = (\{\alpha\}_N)^{m_\alpha}$$

We now want to correct for the overlap with the first subcluster $\alpha-1$, which has one point less than α . Due to the independent variation of the α -clusters, the overlapping cluster $\alpha-1$ has also been counted $(\{\alpha-1\}_N)^{m_\alpha n_\alpha^{\alpha-1}}$ times, where $n_\alpha^{\alpha-1}$ is the number of times the $\alpha-1$ cluster is contained in α . The correct number of times the $\alpha-1$ cluster should be counted, presuming it were an independent species, is $(\{\alpha-1\}_N)^{m_{\alpha-1}}$. Therefore, we must correct Eq. (8-29) as follows:

$$W = (\{\alpha\}_N)^{m_\alpha} \frac{(\{\alpha-1\}_N)^{m_{\alpha-1}}}{(\{\alpha-1\}_N)^{m_\alpha n_\alpha^{\alpha-1}}} \\ = (\{\alpha\}_N)^{m_\alpha} (\{\alpha-1\}_N)^{m_{\alpha-1} - m_\alpha n_\alpha^{\alpha-1}}$$

Using the identity $a_\alpha = 1$, which is valid for the basic cluster, and $a_{\alpha-1}$ determined from the equation

$$m_{\alpha-1} a_{\alpha-1} = m_{\alpha-1} - m_\alpha n_\alpha^{\alpha-1}$$

W can be written as

$$W = (\{\alpha\}_N)^{m_\alpha a_\alpha} (\{\alpha-1\}_N)^{m_{\alpha-1} a_{\alpha-1}}$$

The same reasoning now needs to be followed with the next subcluster $\alpha-2$. For this cluster, the number of arrangements of the basic cluster α , as well as the correction term for $\alpha-1$, have already been counted. We can therefore write

$$W = (\{\alpha\}_N)^{m_\alpha a_\alpha} (\{\alpha-1\}_N)^{m_{\alpha-1} a_{\alpha-1}} \\ \times (\{\alpha-2\}_N)^{m_{\alpha-2} a_{\alpha-2}}$$

with $a_{\alpha-2}$ determined from the equation

$$m_{\alpha-2} = m_\alpha n_\alpha^{\alpha-2} a_\alpha + m_{\alpha-1} n_{\alpha-1}^{\alpha-2} a_{\alpha-1} \\ + m_{\alpha-2} a_{\alpha-2}$$

Continuing this reasoning leads to

$$W = \prod_{v=1}^{\alpha} (\{v\}_N)^{m_v a_v} \quad (8-30)$$

and to the following recursion scheme for the exponent a_v , using the identities $n_v^v = 1$ and $a_\alpha = 1$:

(basic) cluster α : $m_\alpha = m_\alpha n_\alpha^\alpha a_\alpha$

$$\alpha-1: m_{\alpha-1} = m_{\alpha-1} n_{\alpha-1}^{\alpha-1} a_{\alpha-1} \\ + m_\alpha n_\alpha^{\alpha-1} a_\alpha$$

$$\alpha-2: m_{\alpha-2} = m_{\alpha-2} n_{\alpha-2}^{\alpha-2} a_{\alpha-2} \\ + m_{\alpha-1} n_{\alpha-1}^{\alpha-2} a_{\alpha-1} + m_\alpha n_\alpha^{\alpha-1} a_\alpha$$

$$v: m_v = \sum_{\mu=0}^{\alpha-v} m_{\alpha-v} n_{\alpha-v-\mu}^v a_{\alpha-v-\mu} \quad \text{with } 1 \leq v \leq \alpha$$

We thus obtain for the entropy in Stirling's approximation

$$S = -k_B N \sum_{v=1}^{\alpha} m_v a_v \sum_{\sigma} \varrho_v^{(\sigma)} \ln \varrho_v^{(\sigma)} \quad (8-31)$$

The values of m_α and $n_{\alpha-\mu}^{\alpha-v}$ are to be derived by geometrical considerations of the lattice. This procedure is straightforward even for large clusters. For the purpose of illustration, the full set of these values and the "CVM exponents" a_v are given in Table 8-8 both for the f.c.c. structure in the tetrahedron-octahedron approximation and for the b.c.c. structure in the irregular tetra-

Table 8-8. Numerical values of m_α , $n_{\alpha-\nu}^{\alpha-\nu}$, and the CVM exponents a_ν , for the f.c.c. structure in the tetrahedron–octahedron approximation and for the b.c.c. structure in the irregular tetrahedron approximation.

F.C.C. Tetrahedron–Octahedron Fig. 8-4										
Cluster $\alpha =$	23 ... 7 6	23456 5	3456 4a	2347 4b	1234 4c	237 3a	123 3b	27 2a	12 2b	1 1
$m_\alpha =$	1	6	3	12	2	12	8	3	6	1
$n_\alpha^6 =$	1									
$n_\alpha^5 =$	6	1								
$n_\alpha^{4a} =$	3	1	1							
$n_\alpha^{4b} =$	12	4	0	1						
$n_\alpha^{4c} =$	0	0	0	0	1					
$n_\alpha^{3a} =$	12	6	4	2	0	1				
$n_\alpha^{3b} =$	8	4	0	2	4	0	1			
$n_\alpha^{2a} =$	3	2	2	1	0	1	0	1		
$n_\alpha^{2b} =$	12	8	4	5	6	2	3	0	1	
$n_\alpha^1 =$	6	5	4	4	4	3	3	2	2	1
$a_\alpha =$	1	0	0	0	1	0	–1	0	1	–1

B.C.C. Irregular Tetrahedron Fig. 8-2					
Cluster $\alpha =$	1234 4	123 3	12 2a	13 2b	1 1
$m_\alpha =$	6	12	3	4	1
$a_\alpha =$	1	–1	1	1	–1

hedron approximation. In the latter case, the $n_{\alpha-\mu}^{\alpha-\nu}$ have been omitted for the sake of brevity.

For the entropy, we thus obtain the following:

f.c.c.

$$\begin{aligned}
 S &= k_B \ln \frac{\{23 \dots 7\}_N^1 \{1234\}_N^2 \{12\}_N^6}{\{123\}_N^8 \{1\}_N^1} \\
 &= -k_B N \left[\sum_{\{ij \dots k\}} \varrho_{23 \dots 7}^{ij \dots k} \ln \varrho_{23 \dots 7}^{ij \dots k} \right. \\
 &\quad + 2 \sum_{\{ijkl\}} \varrho_{1234}^{ijkl} \ln \varrho_{1234}^{ijkl} \quad (8-32) \\
 &\quad - 8 \sum_{\{ijk\}} \varrho_{123}^{ijk} \ln \varrho_{123}^{ijk} \\
 &\quad \left. + 6 \sum_{\{ij\}} \varrho_{12}^{ij} \ln \varrho_{12}^{ij} - \sum_{\{i\}} \varrho_1^i \ln \varrho_1^i \right]
 \end{aligned}$$

b.c.c.

$$\begin{aligned}
 S &= k_B \ln \frac{\{1234\}_N^6 \{12\}_N^3 \{13\}_N^4}{\{123\}_N^{12} \{1\}_N^1} \\
 &= -k_B N \left[6 \sum_{\{ijkl\}} \varrho_{1234}^{ijkl} \ln \varrho_{1234}^{ijkl} \right. \\
 &\quad - 12 \sum_{\{ijk\}} \varrho_{123}^{ijk} \ln \varrho_{123}^{ijk} \quad (8-33) \\
 &\quad + 3 \sum_{\{ij\}} \varrho_{12}^{ij} \ln \varrho_{12}^{ij} \\
 &\quad \left. + 4 \sum_{\{ik\}} \varrho_{13}^{ik} \ln \varrho_{13}^{ik} - \sum_{\{i\}} \varrho_1^i \ln \varrho_1^i \right]
 \end{aligned}$$

The entropy equations (8-32) and (8-33) are valid for the sro state. In the lro state, the equivalence of certain clusters is broken. For example, Eq. (8-33) has to be written in the lro state with four sublattices (Fig. 8-2):

$$S = k_B \ln \frac{\{1234\}_N^6 \{12\}_N^{3/2} \{34\}_N^{3/2} \{13\}_N^1 \{14\}_N^1 \{23\}_N^1 \{24\}_N^1}{\{123\}_N^3 \{124\}_N^3 \{134\}_N^3 \{234\}_N^3 \{1\}_N^{1/4} \{2\}_N^{1/4} \{3\}_N^{1/4} \{4\}_N^{1/4}} \quad (8-34)$$

8.5.2 Calculation of Phase Diagrams with the CVM

Once the grand canonical energy \tilde{U} , Eq. (8-18), and the entropy, Eq. (8-31) have been derived, the equilibrium at any temperature and the chemical potentials can be determined by minimizing the grand potential $\Omega = \tilde{U} - TS$ with respect to the configurational variables. Two different techniques of minimization can be found in the literature: the natural iteration method, introduced by Kikuchi (1974), in which minimization is achieved with respect to the occupation probabilities of the largest cluster; and minimization by means of the Newton–Raphson and steepest-descent techniques with respect to the correlation functions as independent variables (e.g. Sanchez and de Fontaine, 1978; Mohri et al., 1985; Finel, 1987). The natural iteration method converges even with starting values that are far from the equilibrium values, but it is slow. The second method is more sensitive to the quality of the starting values, but it is much faster.

A phase diagram is determined by calculating the equilibrium state for two phases and comparing the values of the corresponding grand potentials. In this way, the most stable phase is obtained. The transition between different lro states of from lro to sro can be of first order or higher (usually second) order. A first-order transition is detected by the intersection of the grand potentials of two phases for a certain value of the chemical potentials (e.g. Kikuchi, 1977b, 1987). This value yields a different composition for each phase which defines the tie-line of the two-phase equilibria. Three-phase equilibria are recognized af-

terwards by the superposition of all the two-phase equilibria. More sophisticated techniques have not yet been applied because phase diagrams of multicomponent systems beyond ternary have not yet been analyzed. A second-order transition is more difficult to define. In this instance, there is no metastable extension of the existence range of the most-ordered phase beyond the transition point, and the grand potentials meet at this point with a continuous slope. In such a case, the second Hessian of the grand potential has to be analyzed (Kikuchi, 1987). Often this is circumvented by showing that there is no metastable extension of the most-ordered phase within given accuracy limits.

8.5.3 Phase Diagram Calculation with the Monte Carlo Method

In the MC method the configuration of a crystal with a limited number of points (typically several 10^4 to 10^5) is stored in a computer. In order to minimize the boundary effects of the finite size of this crystal, periodic boundary conditions are usually applied. These boundary conditions must be consistent with the superstructures we want to treat so that an integer number of unit cells fits into the crystal. This determines both the shape we have to give to the computer crystal as well as the number of points. In the b.c.c. structure with first and second neighbors, the superstructures are cubic, and there is no difficulty. In the f.c.c. structure, the superstructures have different symmetries and the unit cells have different extensions in different crystal directions, as shown in the appendix. The phase diagram calculation with the MC method is

usually carried out in the grand canonical scheme, i.e., for a given value of the chemical potentials. This ensures a homogeneous single-phase equilibrium state. For this single-phase state, the configuration can be analyzed, and a composition determined. Even in this simple case, problems may appear due to defects such as antiphase boundaries (APBs), which are produced in the equilibration process in the same manner as in real alloys (see, e.g., Gahn, 1986; Ackermann et al., 1986; Crusius and Inden, 1988).

The Monte Carlo process can be started from any configuration and composition, even from the pure components. An arbitrary site n is selected at random and the atom i on this position is replaced by an atom j according to a transition probability $w_n^{i \rightarrow j}$ which has to fulfill certain criteria in order to guarantee the convergence toward the equilibrium state from any initial configuration (Chesnut and Salsburg, 1963; Fosdick, 1963; Binder, 1976). A sufficient condition for this convergence is the fulfillment of the detailed balance equation and of normalization of the transition probability:

$$Q_n^i w_n^{i \rightarrow j} = Q_n^j w_n^{j \rightarrow i} \quad (8-35a)$$

$$\sum_{j=1}^K w_n^{i \rightarrow j} = 1 \quad (8-35b)$$

Different expressions for the transition probability which fulfill this criterion have been suggested. The choice is made according to the most efficient expression in terms of computer time. The following expression fulfills the conditions of Eq. (8-35):

$$w_n^{i \rightarrow j} = \frac{\exp \left[-\frac{1}{k_B T} \left(\Omega \left\{ \begin{smallmatrix} j \\ n \end{smallmatrix} \right\} - \Omega \left\{ \begin{smallmatrix} i \\ n \end{smallmatrix} \right\} \right) \right]}{\sum_{j=1}^K \exp \left[-\frac{1}{k_B T} \left(\Omega \left\{ \begin{smallmatrix} j \\ n \end{smallmatrix} \right\} - \Omega \left\{ \begin{smallmatrix} i \\ n \end{smallmatrix} \right\} \right) \right]} \quad (8-36)$$

where $\Omega \left\{ \begin{smallmatrix} i \\ n \end{smallmatrix} \right\}$ is the grand canonical energy

when an atom of kind i occupies site n . Because the sum of the probabilities over all components adds up to 1, the interval $[0, 1]$ can be subdivided into corresponding intervals. The atom i on site n is then replaced by the atom j , which corresponds to the interval selected by a random number between 0 and 1. If the random number selects the interval corresponding to i , no exchange is made. In a Monte Carlo simulation, the above-mentioned steps have to be performed many times, and it is necessary to use efficient programming techniques for data storage and saving of computer time (for general aspects see Binder (1976, 1979, 1985), Binder and Stauffer (1984); for multispin coding see Jacobs and Rebhi (1981), Zorn et al. (1981) and Kalle and Winkelmann (1982)).

8.5.4 Examples of Prototype Diagrams

The following examples represent prototype diagrams. The interchange energies $W^{(k)}$ used in the calculations are selected in such a way that the phase diagrams display typical features. Calculations for real alloys will be presented in the next section. We will start with the systems treated in the previous sections.

8.5.4.1 F.C.C. Structure, First Neighbor Interactions

In this instance we take the case of an ordering tendency in the first shell, i.e., $W^{(1)} > 0$, $W^{(2)} = 0$. The phase diagram, as obtained by CVM in the tetrahedron–octahedron approximation (Finel and Ducastelle, 1986), together with the results from the MC method (Ackermann et al., 1986; Diep et al., 1986; Gahn, 1986), are shown in Fig. 8-15. The two diagrams do not coin-

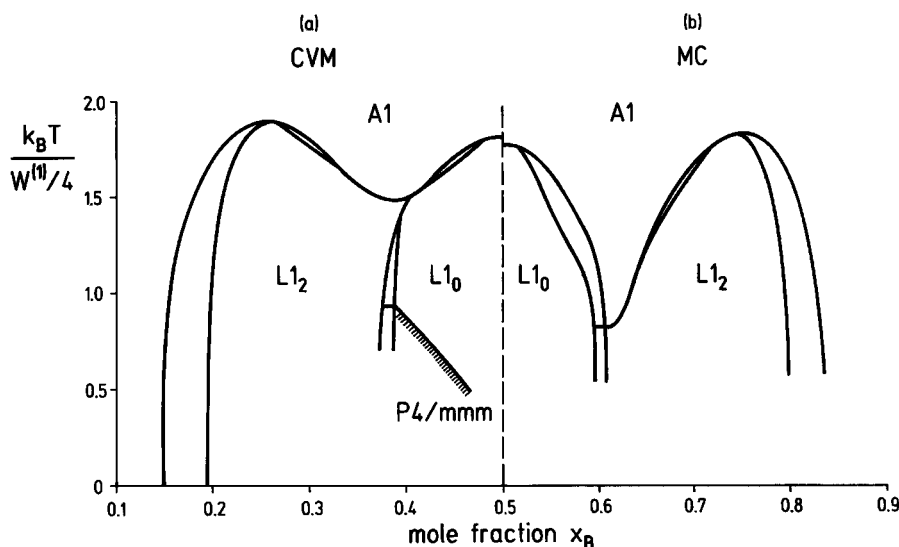


Figure 8-15. F.c.c. structure: calculated prototype phase diagrams for the case of nearest-neighbor interactions, $W^{(1)} > 0$, $W^{(2)} = 0$. (a) CVM calculation in the tetrahedron–octahedron approximation (Finel and Ducastelle, 1986), (b) Monte Carlo simulation (Ackermann et al., 1986).

cide quantitatively, but their main features agree qualitatively. In particular, they agree as to the existence of a triple point at finite temperature, i.e. at

$$\tau_{\text{tri}}^{\text{CVM}} = k_B T_{\text{tri}}^{\text{CVM}} / (W^{(1)}/4) \approx 1.5$$

(Finel and Ducastelle, 1986) and at $\tau_{\text{tri}}^{\text{MC}} \approx 0.8$ (Ackermann et al., 1986) and 0.9 (Diep et al., 1986). This point gave rise to some controversy (discussed by Kikuchi, 1986), caused by an earlier MC study (Binder, 1980; Binder et al., 1981) which indicated that the phase boundaries extrapolate to 0 K, and that a triple point does not exist. The existence of this triple point is now well confirmed and has been further corroborated by the studies of Lebowitz et al. (1985) and Finel (1994). The diagram in Fig. 8-15 replaces that of the earlier MC by Binder. The MCs were not performed at sufficiently low temperatures to detect the P4/mmm phase obtained in the CVM (called L' by Finel, 1984).

The CVM diagram in the tetrahedron–octahedron approximation, Fig. 8-15, differs only slightly from that previously calculated in the tetrahedron approximation (van Baal, 1973; Kikuchi, 1974), which gave a triple point at $\tau_{\text{tri}}^{\text{CVM}} \approx 1.6$. The higher-order cluster approximation does not lead to a strong shift of the triple point to lower temperatures, contrary to an earlier result by Sanchez et al. (1982) who found $\tau_{\text{tri}}^{\text{CVM}} \approx 1.2$. The difference results only from certain approximations in the numerical treatment made by Sanchez et al., which were avoided by Finel (1987). In Finel's work, a more sophisticated CVM calculation was also made using the tetrahedron–octahedron for the ordered phases and the quadrupole tetrahedron for the sro states. In that approximation. Finel obtained complete agreement with the MC work.

8.5.4.2 F.C.C. Structure, First and Second Neighbor Interactions

In this section, the case of an ordering tendency in both shells will be treated first, namely, $W^{(1)} > 0$ and $W^{(2)}/W^{(1)} = 0.25$. The results of the tetrahedron–octahedron CVM (Sanchez and de Fontaine, 1980) and of MC simulations (Bond and Ross, 1982) are shown in Fig. 8-16. The two diagrams

agree fairly closely. Phase diagrams for other values of the ratio $W^{(2)}/W^{(1)}$ are given by Mohri et al. (1985) and Binder et al. (1983).

Fig. 8-17 shows the results for an ordering tendency between first neighbors and a separation tendency between second neighbors, $W^{(1)} > 0$, $W^{(2)} = -W^{(1)}$. This situation corresponds to the calculation presented previously, in Fig. 8-14c. As expected

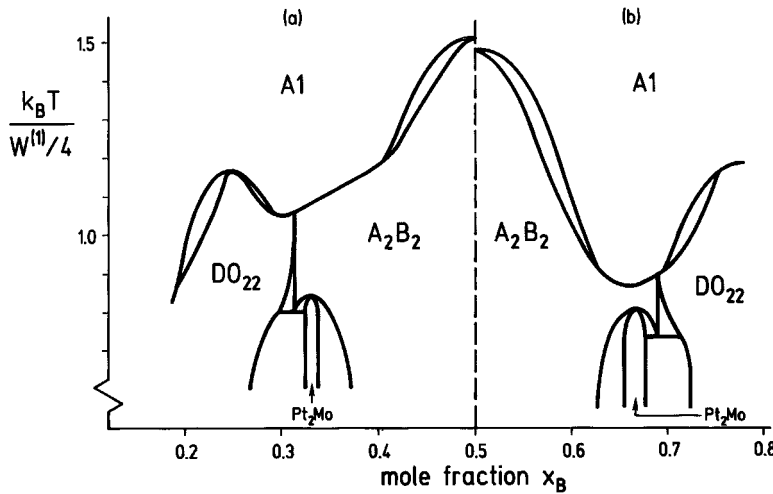


Figure 8-16. F.c.c. structure: calculated prototype phase diagrams for the case of first and second neighbor ordering interactions, $W^{(1)} = 4 W^{(2)} > 0$. (a) CVM calculation in the tetrahedron–octahedron approximation (Sanchez and de Fontaine, 1980). (b) Monte Carlo simulation (Bond and Ross, 1982).

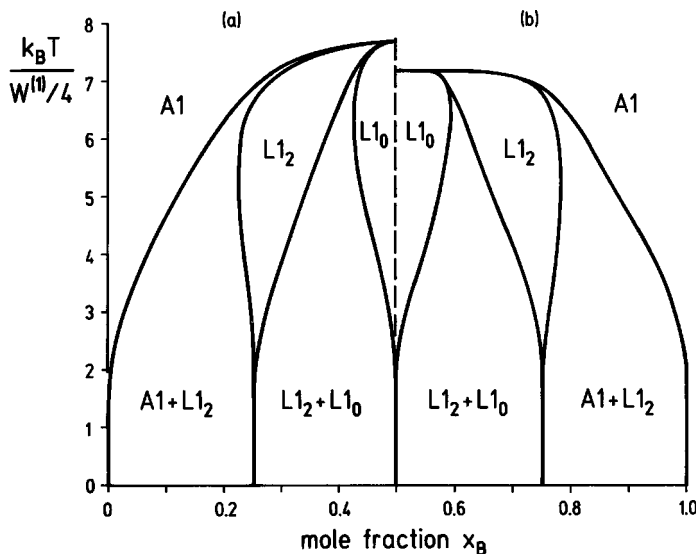


Figure 8-17. F.c.c. structure: calculated prototype phase diagrams for the case of an ordering tendency between first neighbors and a separation tendency between second neighbors, $W^{(1)} = -W^{(2)} > 0$. (a) CVM calculation in the tetrahedron–octahedron approximation (Mohri et al., 1985). (b) Monte Carlo simulation (Binder et al., 1983).

from this diagram the low temperature states are two-phase states and the phase boundaries extrapolate to the pure components and to the stoichiometric ordered phases. A complete series of prototype diagrams calculated with the tetrahedron-octahedron CVM is presented by Mohri et al. (1985).

The case of a separation tendency between first and second neighbors has been analyzed with the MC technique: Kutner et al. (1982) analyzed the case $W^{(1)} < 0$, $W^{(2)} = 0$ with the grand canonical simulation, while Gahn et al. (1984) analyzed the cases $W^{(2)} = 0$ and $W^{(2)} \neq 0$ with a special canonical simulation. The results for $W^{(2)} = 0$ are identical in both treatments. The resulting miscibility gaps are shown in Fig. 8-18 (on a reduced scale in order to show the variation in shape). It is found that the effect of second neighbor interac-

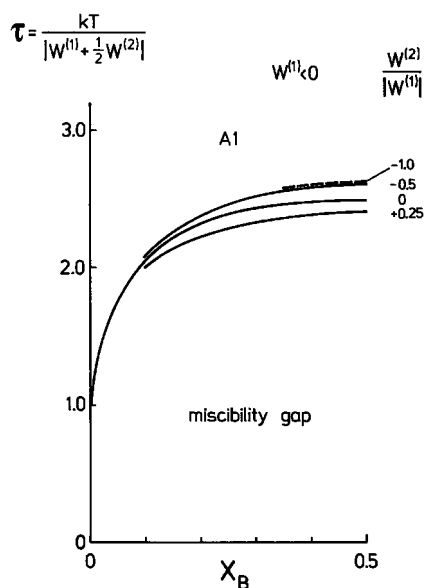


Figure 8-18. Miscibility gaps according to MC calculations for various values of the interchange energies between first and second neighbors. The diagram is symmetric with respect to the equiatomic composition, $W^{(1)} < 0$, $W^{(2)} = 0$ (Kutner et al., 1982). $W^{(2)} = 0$ and $W^{(2)} \neq 0$ (Gahn et al., 1984).

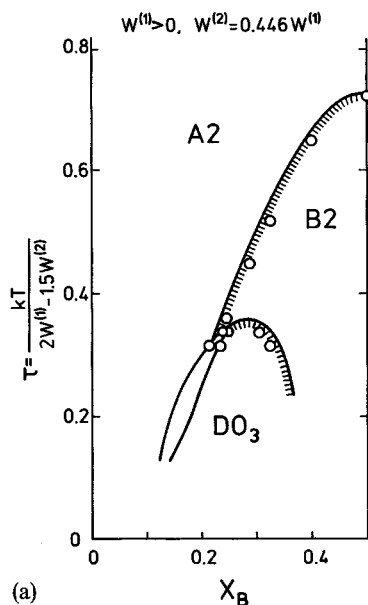
tions on the shape of the miscibility gap is small. The shape obtained differs significantly from the miscibility gap which is usually calculated with the regular solution (i.e., point approx.) model.

8.5.4.3 B.C.C. Structure, First and Second Neighbor Interactions

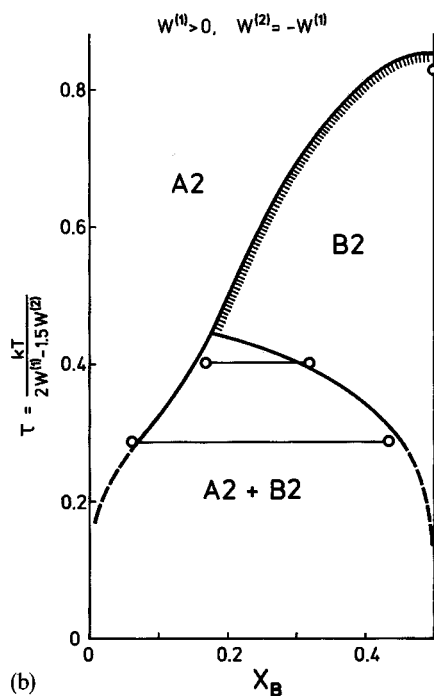
A series of prototype phase diagrams, calculated with the tetrahedron CVM for varying strengths of ordering tendency in both neighbor shells, was first presented by Golosov and Tolstick (1974, 1975, 1976). Simultaneously, Kikuchi and van Baal (1974) presented a diagram corresponding to the ratio $W^{(2)}/W^{(1)} = 0.5$, which is close to the situation encountered in Fe-Si and Fe-Al. Figs. 8-19a, b and c display a series of diagrams calculated with the tetrahedron CVM and with the MC method (Ackermann et al., 1989) for different strengths and signs of the interchange energies. The results of both methods are in good agreement. In these diagrams, second-order transitions are indicated by a hachure. These second-order transitions turn into first-order transitions at tricritical points, and the topology of the phase boundaries close to these points exhibit the characteristics derived by Allen and Cahn (1982).

8.5.4.4 Hexagonal Lattice, Anisotropic Nearest-Neighbor Interactions

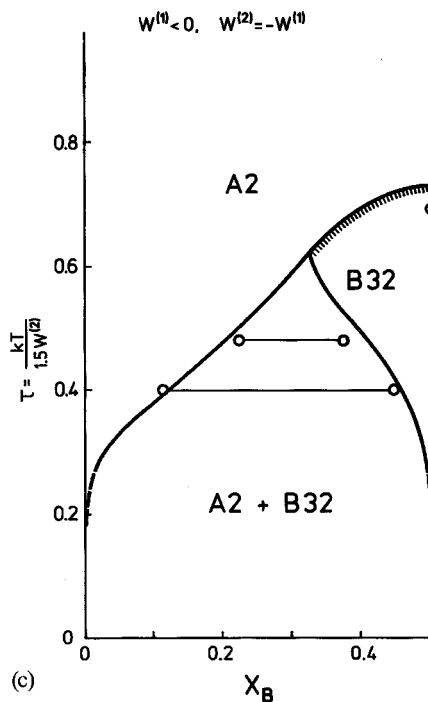
The ordering reactions in the hexagonal crystal structure have been studied with the MC method (Crusius and Inden, 1988; Bichara et al., 1992b). In order to simulate the situation for $c/a \neq 1.633$, i.e., for non-close packing, the interchange energies between nearest neighbors within a basal plane, $W^{(11)}$, and between two such planes, $W^{(12)}$, were given different values. The resulting phase diagrams for two sets of interchange energies are shown in Figs.



(a)



(b)



(c)

8-20a and b. The phase A_2B is a two-dimensional structure built with three subsequently ordered planes, but with no correlation between them. Therefore a two-dimensional characterization has been given in Sec. 8.7 in addition to the three-dimensional one that is to be considered for cases with $W^{(12)} \neq 0$ (see Appendix, Table 8-13).

In the case $W^{(12)} = 0$, the phase A_2B is the only stable superstructure. The transition $A_2B \leftrightarrow A3$ is second order in this instance. For $\mu^* = 0$ ($x_B = 0.5$), no phase transition has been observed down to the reduced temperature $\tau = k_B T / (W^{(11)}/4) = 0.6$. The extrapolation of the transition temperature goes to 0 K at this composition. This is consistent with the exact solution which

Figure 8-19. B.c.c. structure: calculated prototype phase diagrams for ordering or separation tendencies between first or second neighbors. The lines correspond to the CVM calculation in the tetrahedron approximation, the points correspond to the Monte Carlo simulation (Ackermann et al., 1989). The hachure indicates a second-order transition. (a) $W^{(1)} = 2W^{(2)} > 0$, (b) $W^{(1)} = -W^{(2)} > 0$, (c) $W^{(1)} = -W^{(2)} < 0$.

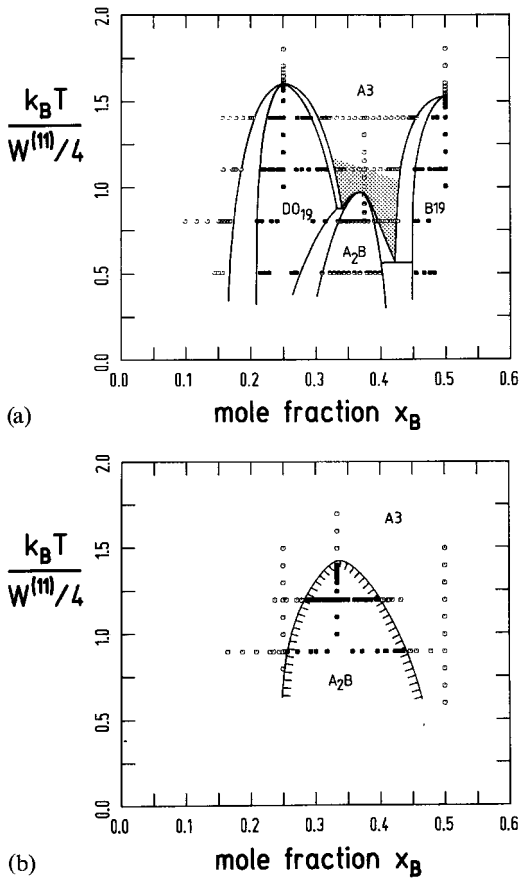


Figure 8-20. Hexagonal structure: calculated prototype phase diagrams for the case of anisotropic nearest-neighbor interactions, $W^{(11)}$ within the basal plane and $W^{(12)}$ between basal planes. Monte Carlo calculations (Crusius and Inden, 1988). The hachure indicates a second-order transition. (a) $W^{(12)}/W^{(11)} = 0.8$, (b) $W^{(12)} = 0$.

is known for $\mu^* = 0$ (Houtappel, 1950; Newell, 1950; Wannier, 1950). The diagram for $W^{(12)} = W^{(11)}$ corresponds to the hexagonal close-packed structure, see Bichara et al. (1992b). This diagram is not shown because it is exactly the same as the one in Fig. 8-15, except that the phases L1₂ and L1₀ have to be replaced by the phases D0₁₉ and B19, respectively. The reason for this is that the f.c.c. and hexagonal close packings cannot be distinguished by nearest-neighbor interactions only.

8.5.5 The Cluster Site Approximation (CSA)

Notwithstanding the successes of the CVM in the calculation of phase diagrams and thermodynamic properties, a major disadvantage is the large number of configurational variables, and thus of non-linear equations, to be solved in order to minimize the Helmholtz energy. The number of independent variables in a K -component system and an r -site CVM is $K^r - 1$. This high number increases strongly with the size of the basic cluster, even for binary systems. Real systems, however, may involve many more than three components.

The CSA suggested by Oates and Wenzl (1996) is a revival of the quasi-chemical tetrahedron approximation (Yang and Li, 1947). A system with N points is decomposed into N_α clusters of type α in such a way that the clusters share only points. The important result of this assumption is that only point correlation functions are used in the Helmholtz energy minimization. The α cluster probabilities are obtained after the calculation from the quasi-chemical equilibrium between the atoms (points) and molecules (clusters). If α contains r points, the number of independent variables is $(K-1)(r-1)$. Thus with increasing cluster size or number of components the number of independent variables in the CSA is significantly smaller than in the case of CVM. This is the main advantage.

Following the concept of the CVM, the entropy of the CSA in the r -site cluster approximation can be written

$$\begin{aligned}
 S &= k_B \ln \frac{(\{12\dots r\}_N)^\gamma \prod_{v=1}^r \{v\}_N}{\prod_{v=1}^r (\{v\}_N)^\gamma} \\
 &= \gamma S_\gamma - (\gamma r - 1) S_1
 \end{aligned} \quad (8-37)$$

where γ is the coordination number of tetrahedra per lattice point. In the case of the f.c.c. lattice and tetrahedron cluster this number is $\gamma=1$, i.e. half the value used in the CVM.

The principal reason for the lack of attention to the CSA is its inability to obtain the correct topology of prototype phase diagrams as obtained from CVM or MC calculations. The tetrahedron approximation of the f.c.c. lattice is a prominent example. The CSA with $\gamma=1$ gives two regions $L1_2$ and $L1_0$ around the stoichiometric compositions, but between these regions the disordered phase is predicted to be stable down to 0 K. Oates et al. (1999) have shown that a simple correction of the value of γ allows us to compensate for this. The authors were able to reproduce the f.c.c. prototype phase diagram of the tetrahedron CVM by taking $\gamma=1.42$.

Several successful results have been obtained with the CSA; those for the Cu–Au system will be mentioned here. Using the value $\gamma=1.42$ as a constant entropy correction term for the tetrahedron treatment of f.c.c. alloys, Oates et al. (1999) applied the CSA to the Cu–Au system using the tetrahedron interactions from Kikuchi et al. (1980). They obtained exactly the same phase diagram as Kikuchi with the CVM. The diagram is shown in Fig. 8-21 a. Furthermore, taking the many-body interactions and also the elastic energy arising from atomic size mismatch from Ferreira et al. (1987), Oates et al. obtained again the same phase diagram as Ferreira with the CVM, see Fig. 8-21 b. This diagram also shows the effect of the elastic terms: they contribute positive corrections to the configurational energy, thus removing the degeneracy of the ground states. Therefore, at 0 K, the phase boundaries meet at the stoichiometric compositions and go to the pure components, contrary to the prototype dia-

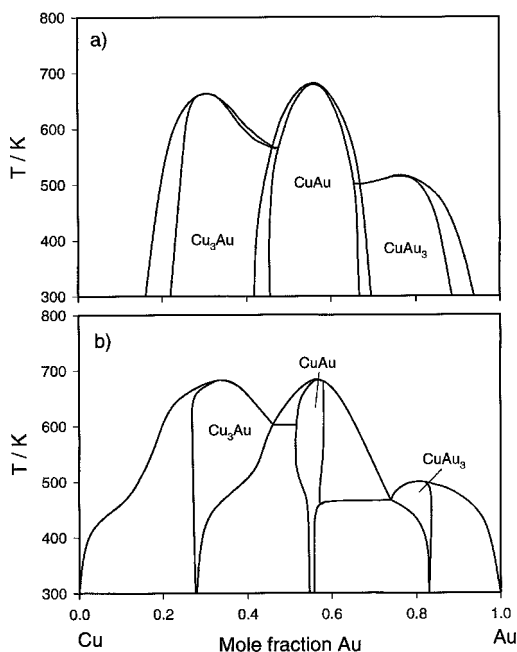


Figure 8-21. Cu–Au phase diagrams calculated with the CSA using the constant entropy correction factor $\gamma=1.42$ (Oates et al., 1999). a) Calculated without any size mismatch using the pair and CuCu–CuAu and CuAuAuAu tetrahedron interactions derived by Kikuchi et al. (1980) using the tetrahedron CVM. The phase diagram is the same as that of the CVM. b) Calculated with size mismatch using the many body interactions and the elastic energy terms derived by Ferreira et al. (1987) using the tetrahedron CVM. The phase diagram is the same as that of the CVM.

grams in Figs. 8-15, 8-16 and 8-19 a where such effects were not included.

These results indicate that the CSA may be a very useful tool when it comes to technological problems. It remains to be seen whether the CSA can be applied as successfully to other structures and to larger clusters.

8.6 Application to Real Systems

In contrast to prototype systems, real systems exhibit very complex properties

even at $T = 0$ K. With the progress made in first-principles calculations, it has become obvious that higher-order pair and multisite cluster interactions have to be used in the configurational part of enthalpy, and that it is mandatory to take lattice and local relaxations into account. This will be illustrated using the Au–Ni system as an example. When it comes to $T > 0$ K the cluster interactions have to embrace all configuration-dependent excitation energies such as arise from thermal vibrations and electronic excitations. The inclusion of these effects means that the cluster interactions become temperature dependent. There is still some disagreement as to whether vibrational contributions can (Ozoliņš et al., 1998b; van de Walle et al., 1998) or cannot (Craievich and Sanchez, 1997; Craievich et al., 1997a, b) be included in the cluster expansion.

However, even the apparently most careful first-principles calculations (Ozoliņš et al., 1998a) remain insufficiently accurate for technological purposes. For the foreseeable future it seems clear that simpler approaches will continue to be important, e.g. for technological phase diagram calculations and also for other applications related to the thermodynamic properties. The systems Fe–Al and Ni–Al will be taken here as examples for calculations of phase diagrams and of the thermodynamic factor for diffusion.

Surveys of the abundant literature describing applications to mainly binary alloy systems can be found in the reviews by Inden and Pitsch (1991) and by de Fontaine (1994).

At this stage multicomponent systems present apparently insurmountable problems for first-principles calculations. This even holds for ternary systems. Rubin and Finel (1993) studied ternary Ti–Al–X ($X = \text{W, Nb, Mo}$) systems with first and sec-

ond neighbor pair interactions and used a power series expansion in composition for the disordered state. No ternary interactions were included. The agreement of the results for the limitrophe binary systems with experimental data is satisfying only in a few of the cases studied, and very little is presented with respect to ternary isothermal sections. McCormack et al. (1996, 1997) studied the systems Cd–Ag–Au (1996) and Cu–Al–Mn (1997) using first and second neighbor pair interactions, but failed to present phase equilibria for ternary and limitrophe binary systems that could be checked by experiments. In the following the two ternary systems Fe–Ti–Al and Fe–Co–Al will be discussed. The Fe–Co–Al system will be treated as a magnetic system with spin 1/2 given to Fe, Co and Al. This leads in fact to a six-component system.

In multicomponent systems the number of points within a chosen basic cluster may not be large enough to accommodate all components. Then the question arises as to what extent this is detrimental to the quality of the approximation. In order to give some idea of this effect, a magnetic spin 7/2 system with f.c.c. structure has been analyzed by Schön and Inden (2001) using the tetrahedron CVM and Monte Carlo simulations. This spin problem is equivalent to an eight-component alloy problem.

The calculation of phase equilibria and thermodynamic properties of multicomponent systems is of paramount importance for technological design and materials development. The use of both a cluster expansion for the energy and the CVM for configurational entropy introduces severe computational problems because of the large number of cluster types that must be considered in both formalisms. It also has to be emphasized that in practical applications with coexisting phases of different

crystal structures, the calculation of the atomic configurations has to be performed for each of the structures, and within each structure with the same level of approximation for all subsystems in order to achieve consistency. That is to say, isolated sophisticated treatments of particular systems will provide deep insight into the physics, but they are only of limited use for solving technological problems.

Recently, the quasi-chemical tetrahedron approximation has been adapted to overcome the problems of obtaining the correct topology of order–disorder phase diagrams for f.c.c. systems and to treat lattice relaxations and excitations. This method seems to offer the possibility of handling order–disorder effects with sufficient quality within a format that can be used in thermodynamic databases of multicomponent systems. The Cd–Mg system will be taken as an example for illustration, because it has been extensively analyzed: all possible contributions to the ground states have been treated by first-principles calculation, and the phase diagram has been calculated by CVM (Asta et al., 1993).

8.6.1 The Au–Ni System

This system has been analyzed intensively over the last decade (Renaud et al., 1987; Eymery et al., 1993; Wolverton and Zunger, 1997; Wolverton et al., 1998; Ozoliņš et al., 1998; Colinet and Pasturel, 2000). It has attracted much interest because of a phase separation tendency and positive enthalpies of mixing at low temperatures, ordering type of short-range order at high temperatures, and a large lattice mismatch of about 15% between the constituents. It may be considered a key system for checking the quality of the theoretical methods.

EXAFS experiments (Renaud et al., 1987) have shown that the atoms are strongly displaced relative to the regular undistorted lattice. The distribution of Au–Au distances was found to be narrow and weakly asymmetric, while those for Ni–Ni were found to be widely distributed and highly asymmetric. Eymery et al. (1993) came to the same conclusion on the basis of their theoretical work. From the calculated average nearest-neighbor distances, partial tetrahedral volumes were calculated as a function of composition. The results are shown in Fig. 8-22. The size

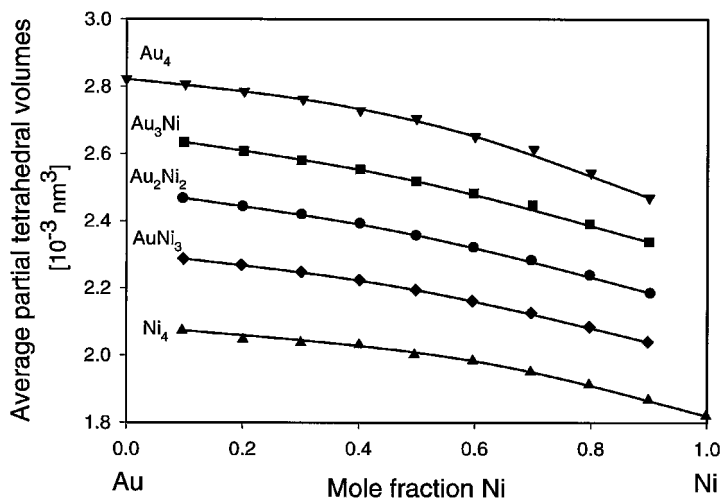


Figure 8-22. Variation of the average tetrahedral volumes Au_4 , Au_3Ni , $AuNi$, $AuNi_3$ and Ni_4 in random $Au_{1-x}Ni_x$ solid solutions at $T = 0$ K versus Ni concentration [redrawn from Eymery et al. (1993)]. The volumes were calculated from the calculated average nearest-neighbor distances. The difference between the various volumes and their variation with composition reflects the lattice relaxations. The calculations were based on a tight-binding second moment approximation.

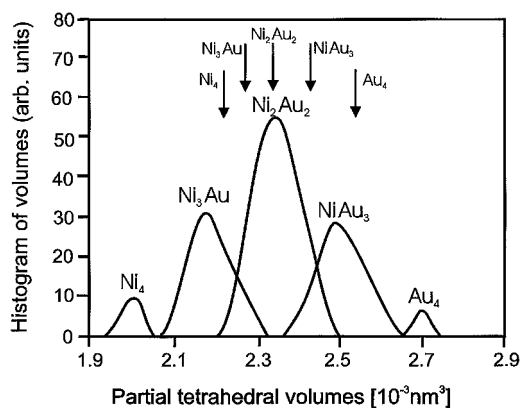


Figure 8-23. Histogram of the calculated partial tetrahedral volumes Au_4 , Au_3Ni , AuNi , AuNi_3 and Ni_4 in a random alloy at $T=0$ K with $x_{\text{Ni}}=0.5$ [redrawn from Eymery et al. (1993)]. The volume distributions are broad and partially asymmetric. The average volumes, taken from Fig. 8-22, are shown by the arrows. The difference between these average values and the centers of gravity of the distributions is remarkable showing the importance of local relaxations.

distribution of the tetrahedral volumes was also calculated. The results for the equi-atomic composition are shown in Fig. 8-23. The local relaxations become evident by the deviation of the average positions of these distributions from the corresponding average volumes in Fig. 8-22, which are shown in Fig. 8-23 by the arrows. These results clearly indicate that both lattice and local relaxations must not be ignored. This fact becomes also visible in the enthalpy of formation of the random alloys differing by a factor of two between unrelaxed and relaxed states.

Wolverton et al. (1997, 1998) considered the Au–Ni system and analyzed the question of up to what order the pair interaction scheme has to be driven in order to reproduce experimental findings. The CE was separated into three parts: the pair interactions with arbitrary distance summed in the reciprocal space representation (Laks et al., 1992), the multi-atom interactions in real-

space representation, and the constituent strain energy. The authors concluded that pair interactions up to about the 15th shell are needed. Ozoliņš et al. (1998a, b) examined the same question for the series of noble metal alloys Cu–Au, Ag–Au, Cu–Ag and Au–Ni. While in Ag–Au and Ag–Cu the first three neighbor pair interactions are dominant, the same is not true for the other systems, particularly not for Au–Ni, where not only pair interactions up to the 10th shell, but also triplet and four-point cluster interactions in increasing distances have to be taken into account.

Most recently, Colinet et al. (2000) took up to fourth neighbor pair and triplet interactions into account, the tetrahedron interactions turning out to be almost negligible in their treatment. They achieved good agreement in the entropy of mixing, fairly good agreement in the enthalpy and Gibbs energy of mixing and calculated the phase diagram by means of the tetrahedron–octahedron CVM. The comparison between the calculated and experimental miscibility gap is shown in Fig. 8-24.

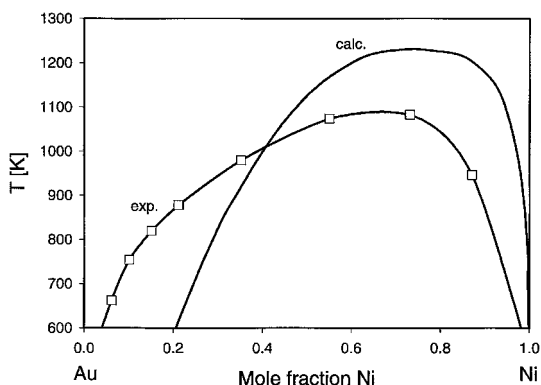


Figure 8-24. Miscibility gap of the Au–Ni system. Experiments from Bienzle et al. (1995). The calculations were performed using pair and triplet interactions in the tetrahedron–octahedron CVM (Colinet et al., 2000).

8.6.2 The Thermodynamic Factor of Ordered Phases

8.6.2.1 The B.C.C. Fe–Al System

Iron aluminides such as Fe_3Al and FeAl have received considerable attention as candidates for high temperature structural materials due to their low cost, high strength and good oxidation resistance. Schön and Inden (1998) assessed the system in order to derive ECIs from experimental enthalpies of formation, corrected for b.c.c reference states and converted into the paramagnetic state:

ϕ	ΔH^ϕ [J/mol of atoms]
$\text{Fe}_3\text{Al} (\text{D0}_3)$	–18 650
$\text{FeAl} (\text{B2})$	–27 940
$\text{FeAl}(\text{B32})$	–21 570
$\text{FeAl}_3(\text{D0}_3)$	–18 650

Introducing these enthalpies and the values of the correlation functions of the configurations (see Table 8-5) into Eq. (8-24), the

following parameters are obtained (in units of $k_B \text{K}$)

$$V_0 = -2190, \quad V_1 = 0, \quad V_2 = 1680, \\ V_3 = 457, \quad V_4 = 0, \quad V_5 = 52.5$$

or equivalently (8-38)

$$W^{(1)} = 1680, \quad W^{(2)} = 740, \quad W_{\text{FeAlFeAl}}^{1234} = -140$$

With these parameters the irregular tetrahedron CVM yields the b.c.c. phase diagram shown in Fig. 8-25. The calculated critical temperatures match the high temperature experimental data. However, at lower temperatures, the tricritical point and the two-phase region $\text{A2} + \text{B2}$ are not obtained and the agreement with the experimental phase boundaries $\text{A2} + \text{D0}_3$ is poor. This is not surprising in view of the large relaxation effects, which are to be expected in this system as seen from the variation of lattice parameter as a function of composition and of state of order, Fig. 8-26. On the other hand, recent experimental data on chemical potential measurements at 1000 K (Kleykamp and Glasbrenner, 1997) are very well

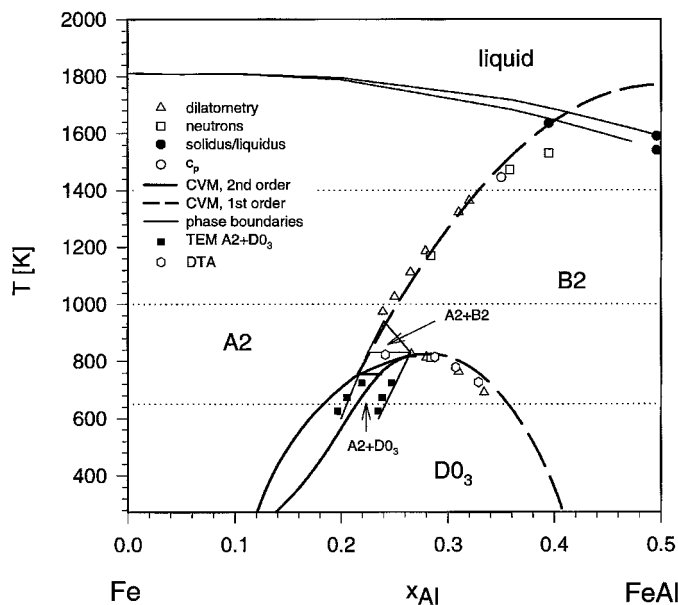


Figure 8-25. The b.c.c. phase diagram of Fe–Al calculated with the irregular tetrahedron CVM using the parameters given in Eq. (8-38) (Schön and Inden, 1998). Second-order transitions are indicated by broken lines. Three temperatures are indicated at which the thermodynamic factor of diffusion is shown below in Fig. 8-28. Experimental points: neutron diffraction and c_p from Inden and Pepperhoff (1990), dilatometry from Köster and Gödecke (1980), TEM and DTA from Ohnuma et al. (1998a).

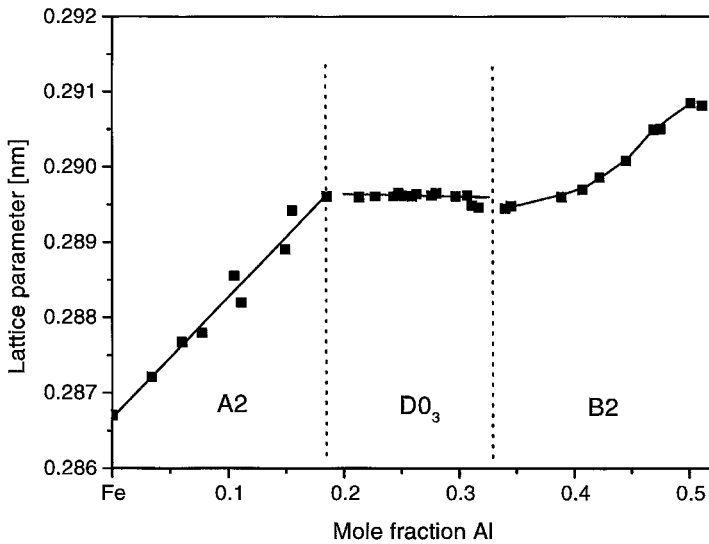


Figure 8-26. Variation of the lattice parameter of Fe–Al alloys as a function of composition and state of order. Experiments: Lihl and Ebel (1961).

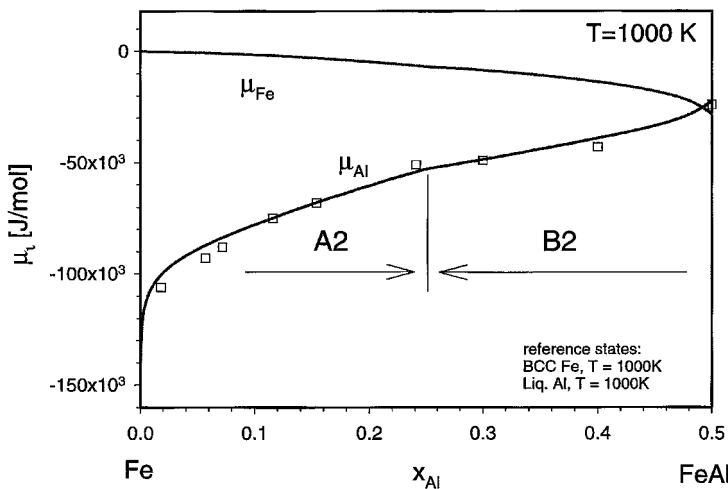


Figure 8-27. Chemical potential of Fe and Al at 1000 K in b.c.c. Fe–Al alloys calculated with the tetrahedron CVM using the parameters given in Eq. (8-38) (Schön and Inden, 1998). Experimental data from Kleykamp and Glasbrenner (1997).

reproduced by the calculations, see Fig. 8-27.

A very important quantity for the treatment of diffusion is the thermodynamic factor defined for a binary system A–B as

$$\Phi = \frac{x_B d\mu_B}{dx_B}$$

This quantity is smooth in a random solid solution, but shows a complicated variation

in ordered alloys. Fig. 8-28 shows this variation at three different temperatures. Close to stoichiometric compositions of ordered phases, Φ varies dramatically. The amount of variation depends on the degree of Iro, reaching up to an order of magnitude at least in almost fully Iro states, as observed at $T = 650$ K for B2 at the composition $x_{Al} = 0.5$. At second-order transition points Φ changes discontinuously.

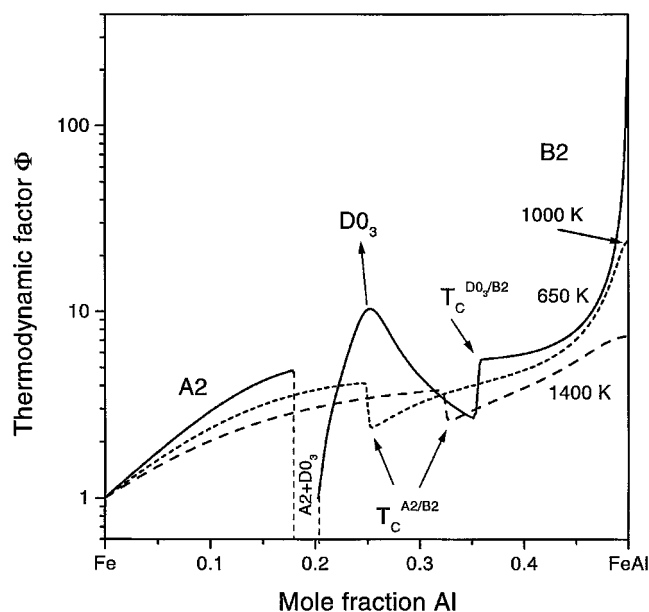


Figure 8-28. Thermodynamic factor of diffusion in b.c.c. Fe–Al alloys, calculated as a function of composition at three temperatures, 650 K, 1000 K and 1400 K. The calculations were performed with the irregular tetrahedron CVM using the parameters given in Eq. (8-38) (Schön and Inden, 1998). At second-order transitions, Φ changes by a step. Close to the stoichiometric compositions $x_{\text{Al}} = 0.25$ and 0.5 the value of Φ increases as a function of the degree of lro. For example, the temperature of $T = 650\text{K}$ is only slightly below the $\text{D0}_3/\text{B2}$ transition temperature, see Fig. 8-25. Therefore, at $x_{\text{Al}} = 0.25$ the increase is small compared to $x_{\text{Al}} = 0.5$ where Φ increases by more than an order of magnitude because the distance from the $\text{B2}/\text{A2}$ transition temperature is large and the degree of lro almost maximum. With increasing temperature this effect becomes smaller.

8.6.2.2 The F.C.C. Ni–Al System

The variation of the thermodynamic factor is even more pronounced in the Ni–Al system because there the order–disorder transitions occur at much higher temperatures than in Fe–Al, as shown in the calculated f.c.c. phase diagram in Fig. 8-29 (Schön and Inden, 1998). The ECIs were derived from the ground-state energies of $\text{L1}_2\text{–Ni}_3\text{Al}$, $\text{L1}_2\text{–NiAl}_3$, and $\text{L1}_0\text{–NiAl}$, obtained by Pasturel et al. (1992) from first-principles calculations:

ϕ	ΔH^ϕ [J/mol of atoms]
$\text{Ni}_3\text{Al (L1}_2\text{)}$	–48 000
$\text{NiAl (L1}_0\text{)}$	–56 000
$\text{NiAl}_3(\text{L1}_2)$	–22 000

Introducing these enthalpies and the values of the correlation functions of the configurations (see Table 8-3) into Eq. (8-24), the following parameters are obtained (in units of $k_B\text{K}$)

$$V_0 = -4630, \quad V_1 = -1563, \quad V_2 = 5051, \\ V_3 = 1563, \quad V_4 = -421$$

or equivalently

$$W^{(1)} = 3370, \quad W_{\text{NiAlAlAl}}^{1234} = -4810, \\ W_{\text{NiNiNiAl}}^{1234} = 1440 \quad (8-39)$$

The calculated thermodynamic factor of diffusion is shown in Fig. 8-30 for the two temperatures indicated in Fig. 8-29. Due to the high degree of lro, the variation of Φ in the range of stoichiometric composition is

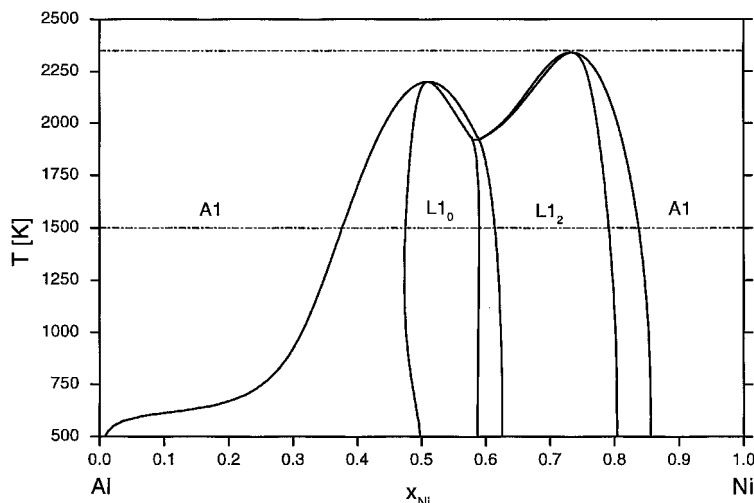


Figure 8-29. Phase diagram of the f.c.c. Ni–Al system calculated with the regular tetrahedron CVM (Schön and Inden, 1998) using the parameters given in Eq. (8-39). Two temperatures are indicated for which the thermodynamic factor has been calculated, Fig. 8-30.

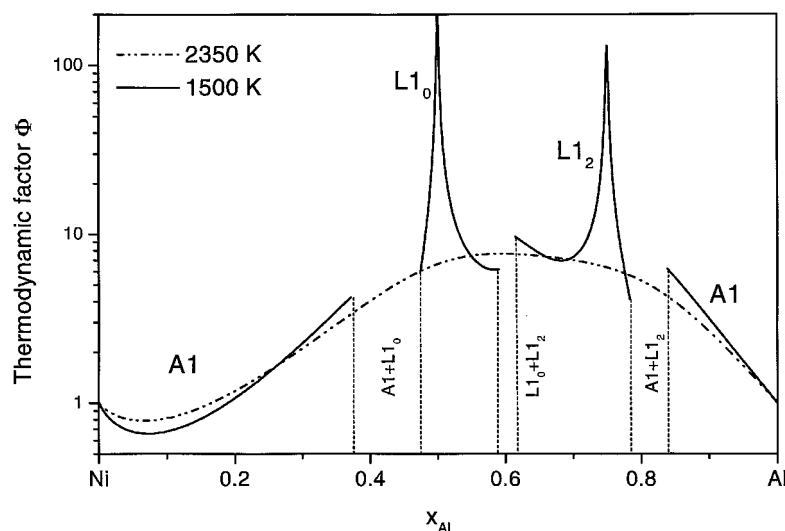


Figure 8-30. Thermodynamic factor of diffusion in f.c.c. Ni–Al alloys, calculated as a function of composition at two temperatures, 1500 K and 2350 K (Schön and Inden, 1998). The calculations were performed with the regular tetrahedron CVM using the parameters given in Eq. (8-39). At the stoichiometric compositions, Φ increases by more than an order of magnitude.

particularly pronounced. Variations of the same order of magnitude are obtained for the B2 phase.

It is worth mentioning that these dramatic variations have repercussions in the composition profiles of diffusion couples. An example is shown in Fig. 8-31, where a contrast has been observed in the micrograph within the B2 phase region as it is

usually observed at phase boundaries. The electron microprobe analysis reveals a steep change of composition at this boundary, which again could be misinterpreted as a tie-line. This is an important fact to be realized, because phase diagram determinations in multicomponent systems are most conveniently performed by means of diffusion couple experiments.

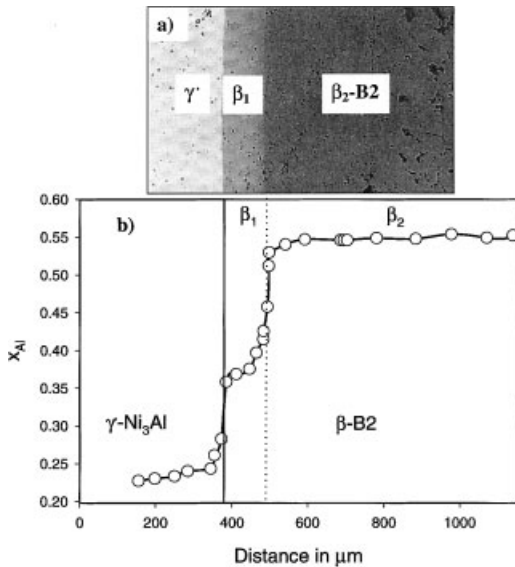


Figure 8-31. Diffusion couple $\text{Ni}_{77}\text{Al}_{23}/\text{Ni}_{40}\text{Al}_{60}$ annealed at 1273 K for 100 h (Kainuma et al., 1997). a) Microstructure showing a change in contrast within the B2 phase field. The regions labelled β_1 and β_2 do not represent two different phases. The pseudo-boundary between β_1 and β_2 comes from a steep change in composition. b) Composition profile measured by electron probe microanalysis.

8.6.3 Ternary Systems

The b.c.c. states of the two systems Fe–Ti–Al and Fe–Co–Al will now be treated by taking the energy description from the limitrophe binaries in order to see what can be obtained by extrapolating from the binaries into the ternary system without ternary interaction terms.

8.6.3.1 B.C.C. Fe–Ti–Al

Ohnuma et al. (1998b) studied ordering and phase separation in the b.c.c. phase of the ternary system, with particular emphasis on ternary miscibility gaps between disordered and ordered phases. The theoretical analysis was based on the irregular tetrahedron CVM. The analysis of the Fe–Ti and Ti–Al binary systems led to the energy

parameters given in Table 8-9. The parameters for Fe–Al were taken as given in Eq. (8-38).

The calculated isothermal sections at 1173 and 1073 K are shown in Figs. 8-32 and 8-33. From the metallurgical point of

Table 8-9. Atomic exchange energy parameters in units of $k_B K$ (Ohnuma et al., 1998b).

A–B	$W_{AB}^{(1)}$	$W_{AB}^{(2)}$	W_{ABAB}^{1234}
Ti–Fe	1580	–1050	1800
Al–Ti	2420	1200	0

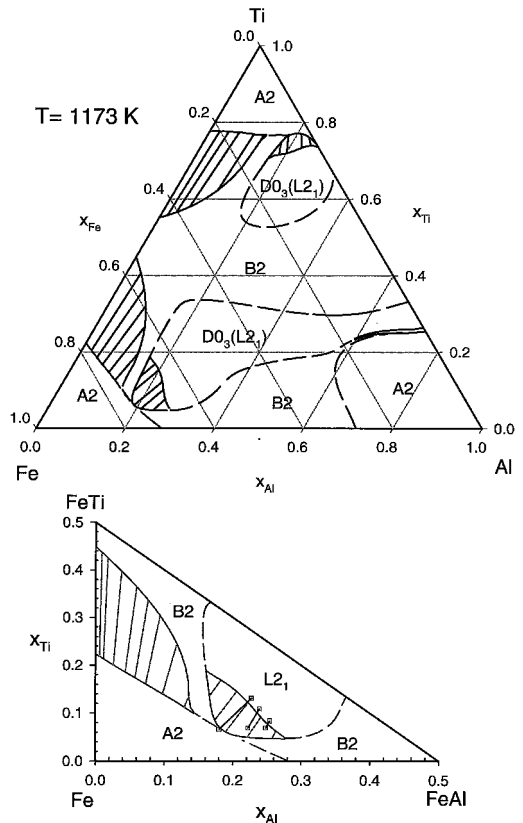


Figure 8-32. Calculated isothermal section of the b.c.c. Fe–Ti–Al system at 1173 K using the energy parameters in Table 8-9. Second-order transitions are shown as broken lines. The enlarged part of the section shows the good agreement obtained between experiments and calculation (Ohnuma et al., 1998b).

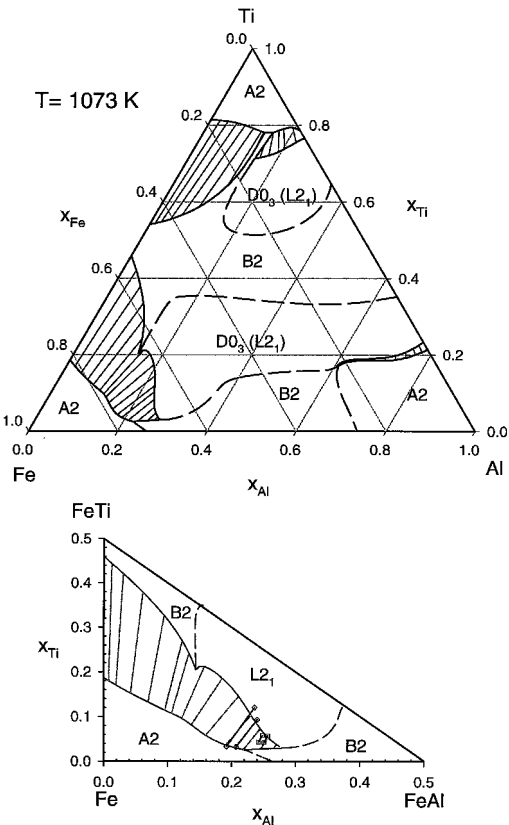


Figure 8-33. Calculated isothermal section of the b.c.c. Fe-Ti-Al system at 1073 K using the energy parameters given in Table 8-9. Second-order transitions are shown as broken lines. The enlarged part of the section shows the good agreement obtained between experiments and calculation (Ohnuma et al., 1998b).

view it is interesting to see the opening of ternary miscibility gaps between ordered and disordered phases. This allows us to produce coherent two-phase equilibria with interesting mechanical properties. Guided by the calculations, Ohnuma et al. (1998b) also performed experiments in order to confirm the existence of the two-phase fields experimentally. The results are shown in the enlarged parts of the sections of Figs. 8-32 and 8-33. The calculated tie-lines agree very well with the experimental results.

8.6.3.2 B.C.C. Ferromagnetic Fe-Co-Al
(six-component system with spin 1/2 for Fe, Co and Al)

This system has been studied by Colinet et al. (1993) in the irregular tetrahedron approximation. The binary system Fe-Al was discussed in Sec. 8.6.2.1, but without taking magnetic effects into account. Because the Curie temperature of metastable b.c.c. Fe-Co alloys goes up to about 1500 K, the magnetic effects cannot be disregarded in this ternary system. A spin 1/2 treatment has been taken in this instance. The magnetic exchange energies are defined in the same way as the atomic equivalents: $J_{AB} = -2J_{AB}^{\uparrow\downarrow} + J_{AB}^{\uparrow\uparrow} + J_{AB}^{\downarrow\downarrow}$, with $A, B \in \{\text{Fe, Co, Al}\}$ and the $J_{AB}^{\uparrow\downarrow}$ etc. being proportional to the corresponding exchange integrals. The energy parameters are given in Table 8-10.

The phase diagram of the b.c.c. Fe-Co system calculated with the energy parameters given in Table 8-10 is shown in Fig. 8-34. All transitions are of second order and have been obtained with the second Hessian method. The calculation without magnetic interactions is also shown. In this non-magnetic case the critical temperature of the B2/A2 transition is lower than in the ferromagnetic case. The magnetic interactions strengthen the atomic ordering in this instance.

In the Co-Al system, the b.c.c. phase is stable only around the equiatomic composition, and there the B2 structure is stable

Table 8-10. Atomic and magnetic exchange energy parameters in units of $k_B K$ (Colinet et al., 1993).

A-B	$W_{AB}^{(1)}$	$W_{AB}^{(2)}$	$J_{AA}^{(1)}$	$J_{BB}^{(2)}$	$J_{AB}^{(1)}$
Fe-Co	500	0	-163	-218	-24
Fe-Al	1680	740	-163	0	-38
Co-Al	3600	1500	-218	0	-38

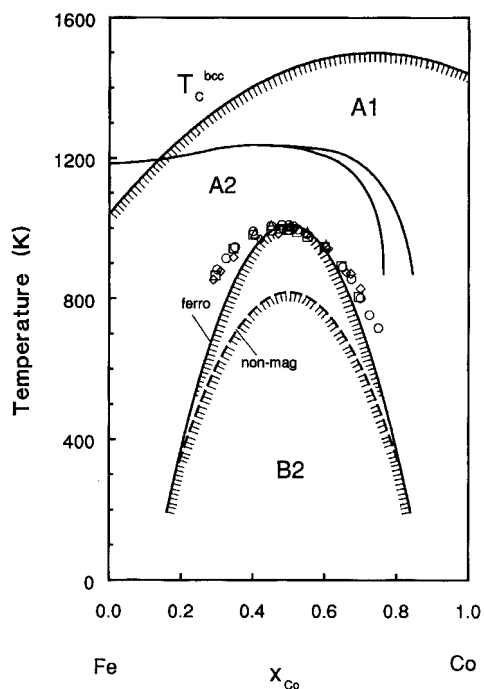


Figure 8-34. Phase diagram of the Fe–Co system. Second-order transitions are indicated by a hachure. Heavy lines: CVM calculation in the (irregular) tetrahedron approximation using the interchange energies given in Table 8-10 (Colinet et al., 1993); lower curve: no magnetic interactions, upper curve: with magnetic interactions. Experiments: (\diamond) Masumoto et al. (1954), (\circ) Eguchi et al. (1968), (\square) Oyedele and Collins (1977).

up to the melting point. The $D0_3$ structure has not been observed within the b.c.c. phase field. This imposes an upper bound as to the value of $W_{\text{CoAl}}^{(2)}$ that controls the value of the critical temperature $D0_3/B2$. Based on these considerations and on experimental values for the critical temperature $B2/A2$ in some ternary Fe–Co–Al alloys, the values in Table 8-10 have been derived by Ackermann (1988).

The b.c.c. phase diagram calculated in the tetrahedron approximation (Colinet et al., 1993) is shown in Fig. 8-35, superposed to the stable diagram. This includes the equilibria with the liquid phase, the

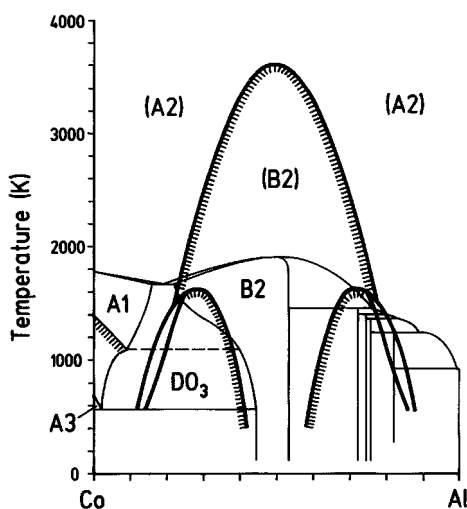


Figure 8-35. Phase diagram of the Co–Al system. Second-order transitions are indicated by a hachure. Heavy lines: CVM calculation in the (irregular) tetrahedron approximation using the interchange energies in Table 8-10 (Colinet et al., 1993). Light lines: Phase diagram according to Hansen and Anderko (1958).

f.c.c. phase, and intermetallic compounds. The B2 phase exists up to very high temperatures in a metastable state, far within the liquid phase. This tendency is consistent with the trend obtained experimentally from data on ternary alloys (Ackermann, 1988).

Figs. 8-36 and 8-37 show the isothermal sections of the ternary system Fe–Co–Al at 1000 K and at 600 K. The ordered regions are separated by first-order and second-order transitions. At 600 K the magnetic interactions become important, but they are still small compared with the chemical interactions. Prior to these calculations, Ackermann (1988) performed an MC calculation of the isothermal section at 700 K using the same chemical interaction parameters as those in Table 8-10. Her diagram and the corresponding CVM diagram agree very well (see Inden and Pitsch, 1991).

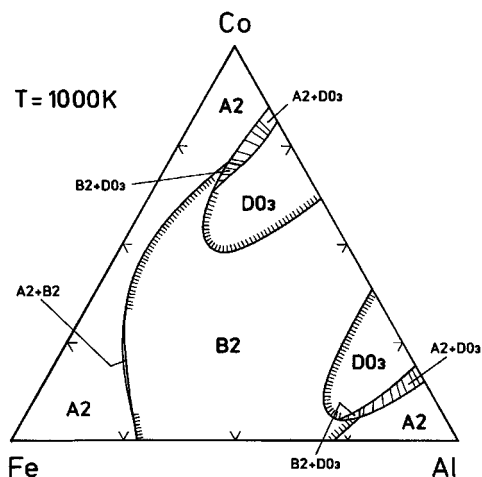


Figure 8-36. Isothermal section of the phase equilibria of ternary b.c.c. Fe-Co-Al alloy at $T = 1000$ K, calculated with the CVM in the (irregular) tetrahedron approximation using the energy parameters given in Table 8-10 (Colinet et al., 1993). Second-order transitions are indicated by a hachure.

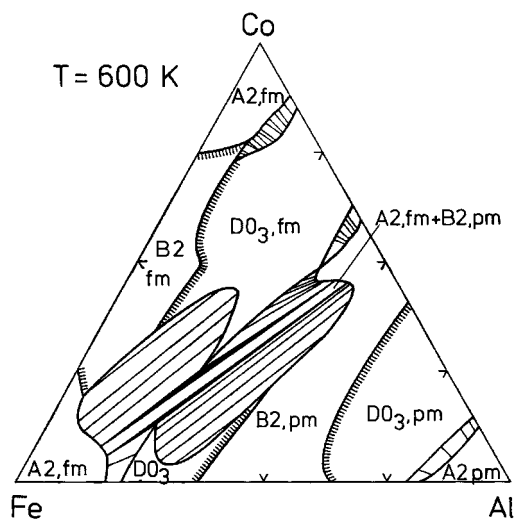


Figure 8-37. Isothermal section of the phase equilibria of ternary b.c.c. Fe-Co-Al alloys at $T = 700$ K, calculated with the CVM in the (irregular) tetrahedron approximation using the energy parameters given in Table 8-10 (Colinet et al., 1993). Second-order transitions are indicated by a hachure. At this temperature ferromagnetic (fm) and paramagnetic (pm) states have to be distinguished.

Ackermann (1988) also analyzed the Fe-Co-Al system experimentally. Here only one comparison will be shown. Fig. 8-38 shows the calculated and experimental miscibility gap in a vertical section which happened to be quasibinary (the tie-lines are within the section).

The agreement between experiment and calculation is surprisingly good, though not really satisfactory. The calculated miscibility gap ends with a “horn” at the tricritical point. This is not obtained in the experiments. However, we should recall that the two coexisting phases A2 and B2 are coherent with different lattice parameters. It has been shown by Williams (1980, 1984) and Cahn and Larché (1984) that the boundary of so-called “coherent” miscibility gaps (with elastic contributions) is lower than the so-called “incoherent” gaps (no elastic contributions). Therefore, elastic effects due to the precipitation of coherent particles depress the phase boundary. This is only one of the effects to be taken into account. A second one is due to the lattice and local relaxations within both of these phases, as already pointed out in Sec. 8.6.2.1 for Fe-Al. The arguments presented for Fe-Al are also valid for the Fe-Co-Al system with Fe and Co being very similar. These relaxation effects tend to shift the miscibility gap to higher temperatures, opposite to the first effect. A full calculation is needed to evaluate the combined result.

Simultaneously with the work by Ackermann (1988) the miscibility gap was experimentally observed by Miyazaki et al. (1987) using transmission electron microscopy (TEM). These authors, however, speculated that the miscibility gap was due to magnetic effects and assumed the tie-lines to be oriented towards the Fe-Co binary system, i.e. perpendicular to those shown in Fig. 8-37. The contradiction be-

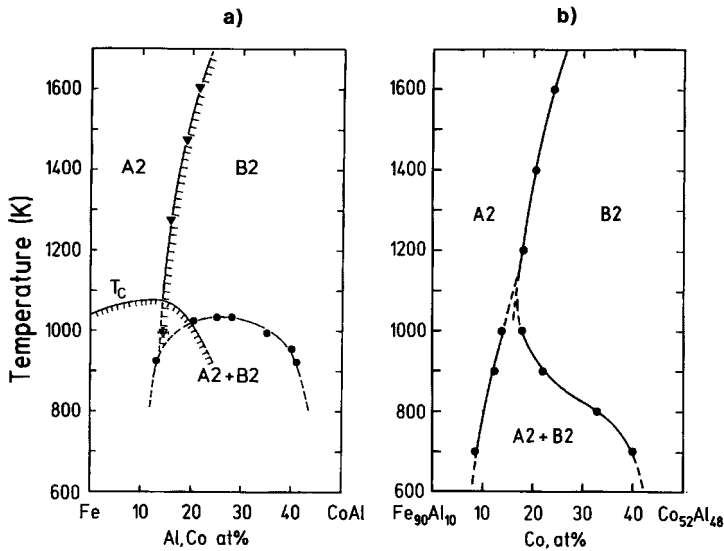


Figure 8-38. Vertical section of the phase diagram showing the ternary miscibility gap as a function of composition according to experiment and MC (Ackermann, 1988), (a) Experiments (●) miscibility gap, (▼) critical temperature of Iro. (b) Calculation with the MC method: (●) miscibility gap and critical temperature of Iro.

tween the results of Miyazaki et al. and those from the CVM and MC pointed out by Inden and Pitsch (1991) was removed by the TEM-EDS analysis of Kozakai and Miyazaki (1994) confirming the calculated direction of the tie-lines.

8.6.4 H.C.P. Cd-Mg

The Cd-Mg system is a prototype ordering system for h.c.p. alloys in the same way as Cu-Au plays this role for f.c.c. alloys. This system has been studied using first-principles methods by Asta et al. (1993). The configurational energy was evaluated by a cluster expansion up to seven-point clusters, as required for a treatment with the octahedron-tetrahedron CVM. Lattice relaxation and vibrational energy were taken into account, but no local relaxations. The lattice relaxation cluster expansion was based on experimental results for disordered alloys, and the other ECIs were obtained from total-energy calculations on ordered phases. In total 32 energy terms were used. The ECIs were then used in the tetra-

hedron-octahedron CVM to calculate the phase diagram, which is shown in Fig. 8-39 a. The topology of the diagram is correct but it does not have the accuracy necessary for technological purposes.

Zhang et al. (2000) tried the CSA in the tetrahedron approximation. Because the c/a ratio is not ideal (f.c.c. and h.c.p. lattices become equivalent in the ideal case), two irregular tetrahedra should be considered (Onodera et al., 1994). Zhang et al. (2000) tried the irregular tetrahedra, but found that the regular tetrahedron CSA gave an equally good description. The value of γ was varied in such a way that the two congruent maxima which appear at the compositions A_3B and AB_3 for $\gamma=1.42$ (valid for the ideal h.c.p. and f.c.c., see Sec. 8.5.5) moved towards the mid-composition until, at $\gamma=1.8$, the maxima disappeared, just as observed in the Cd-Mg system. Starting with energies taken from Asta et al. (1993), which proved to be excellent, only slight changes were applied in order to get an optimum description of all the properties that can be checked with avail-

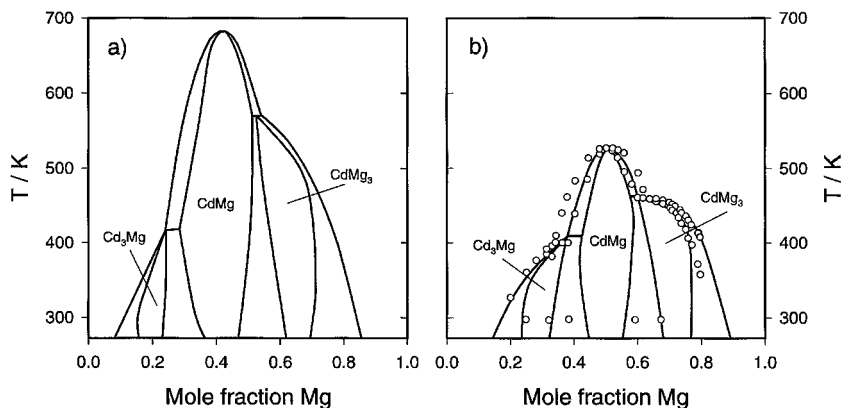


Figure 8-39. Calculated phase diagrams of the hexagonal Cd–Mg system. a) Phase diagram calculated from “first principles” (redrawn from Asta et al., 1993). b) Phase diagram calculated with the CSA using almost the same parameters as in a) and a value $\gamma = 1.8$. Experimental data from Frantz and Gantois (1971).

able experimental data: the phase diagram, the enthalpy of mixing of the disordered state, the enthalpies of formation of ordered phases and the chemical potentials of Cd and Mg. The cluster energies used were (the values of Asta et al. are given in brackets):

Cd_3Mg : -9.3 (-10.3); CdMg : -13.7 (-13.5);
 CdMg_3 : -9.95 (-9.5) in kJ/(mol of atoms).

The calculated phase diagram is shown in Fig. 8-39b. The agreement between calculation and experiment is very good, not only for the phase diagram but also for all the other properties mentioned above.

8.6.5 Concluding Remarks

The examples treated above represent the large group of real systems that can be analyzed using these techniques. Similar findings were obtained for oxide systems, e.g., by Burton (1984, 1985), Burton and Kikuchi (1984), Kikuchi and Burton (1988), Burton and Cohen (1995), Tepesch et al. (1995, 1996), Kohan and Ceder (1996).

At present, it can be concluded that the CVM and MC techniques supply a treatment of sufficient sophistication to correctly handle the statistical aspects of the equilibria in solid solutions.

Much progress has been made in the field of first-principles calculations of total energies, including lattice and local relaxations, and sometimes including excitations. From this the energy parameters of the statistical models can be calculated. The results for binary systems are numerous, but the field of multicomponent systems is still to be explored. With increasing numbers of components the cluster size also has to be increased.

For the solution of metallurgical problems, the phase equilibria between all phases have to be considered. The order–disorder equilibria within a given crystal structure are only one part of this task. Other phases, such as the liquid phase or intermetallic compounds, have to be included. These aspects have been discussed at recent workshops on the thermodynamic modeling of solutions and alloys (e.g. Cacciamani et al., 1997).

8.7 Appendix

Table 8-11. Superstructures of the f.c.c. lattice.¹

Designation ²	Spacegroup	Basis ³	Equivalent positions	Occupation
			Positions	
A1 (Cu)	Fm3m	$a = a_0 \{1\ 0\ 0\}$	(0 0 0; 1/2 1/2 0; 1/2 0 1/2; 0 1/2 1/2)	A/B
A ₅ B Fig. 8-40	B2/m	$a = a_0/2 [1\ \bar{1}\ 2]$	(0 0 0; 1/2 0 1/2)+	
		$b = a_0/2 [2\ \bar{2}\ 2]$	(0 0 0)	2 B
		$c = a_0/2 [3\ 3\ 0]$	(0 1/2 0)	2 A
			(0 0 ± 1/3)	4 A
			(0 1/2 ± 1/3)	4 A
D1a (Ni ₄ Mo) Fig. 8-41	I4/m	$a_1 = a_0/2 [3\ \bar{1}\ 0]$	(0 0 0; 1/2 0 1/2)+	
		$a_2 = a_0/2 [1\ 3\ 0]$	(0 0 0)	2 B
		$c = a_0/2 [0\ 0\ 2]$	(x y 0; $\bar{x}\ \bar{y}\ 0$; $\bar{y}\ x\ 0$; y $\bar{x}\ 0$)	8 A
			$x = a_0 \sqrt{2/5}$ $y = a_0 / \sqrt{10}$	
L1 ₂ (Cu ₃ Au)	Pm3m	$a = a_0 \{1\ 0\ 0\}$	—	
			(0 0 0)	B
			(1/2 1/2 0; 1/2 0 1/2; 0 1/2 1/2)	3 A
—	P4/mmm	$a_1 = a_0 [1\ 0\ 0]$	—	
		$a_2 = a_0 [0\ 1\ 0]$	(0 0 0)	B
		$c = a_0 [0\ 0\ 1]$	(1/2 1/2 0)	A B
			(1/2 0 1/2; 0 1/2 1/2)	A
D0 ₂₂ (Ti ₃ Al) Fig. 8-42	I4/mmm	$a_1 = a_0/2 [0\ 1\ 0]$	(0 0 0; 1/2 1/2 1/2)+	
		$a_2 = a_0/2 [0\ 0\ 1]$	(0 0 0)	2 B
		$c = a_0 [2\ 0\ 0]$	(0 0 1/2)	2 A
			(0 1/2 1/4; 1/2 0 1/4)	4 A
A ₃ B	Amm2	$a = a_0/2 [0\ 2\ 2]$	(0 0 0; 1/2 0 1/2)+	
		$b = a_0/2 [0\ \bar{1}\ 1]$	(0 0 0)	2 B
		$c = a_0/2 [0\ 0\ 2]$	(0 0 1/2)	2 A
			(1/4 1/2 1/4; 1/4 1/2 3/4)	4 A
A ₂ B (Pt ₂ Mo) Fig. 8-43	Immm	$a = a_0/2 [1\ \bar{1}\ 0]$	(0 0 0; 1/2 1/2 1/2)+	
		$b = a_0 [1\ 0\ 0]$	(0 0 0)	2 B
		$c = a_0/2 [3\ 3\ 0]$	(0 0 ± 1/3)	4 A
L1 ₀ (CuAu)	P4/mmm	$a_1 = a_0/2 [1\ 1\ 0]$	—	
		$a_2 = a_0/2 [1\ \bar{1}\ 0]$	(0 0 0)	B
		$c = a_0 [0\ 0\ 1]$	(1/2 1/2 1/2)	A
L1 ₁ (CuPt) Fig. 8-44	R $\bar{3}m$	$a_1 = a_0/2 [2\ 1\ 1]$	—	
		$a_2 = a_0/2 [1\ 2\ 1]$	(0 0 0)	B
		$a_3 = a_0/2 [1\ 1\ 2]$	(1/2 1/2 1/2)	A
A ₂ B ₂ Fig. 8-45	I41/amd	$a_1 = a_0 [0\ 1\ 0]$	(0 0 0; 1/2 1/2 1/2)+	
		$a_2 = a_0 [0\ 0\ 1]$	(0 0 0; 0 1/2 1/4)	B
		$c = a_0 [2\ 0\ 0]$	(0 0 1/2; 0 1/2 3/4)	A

1 Figures 8-40 to 8-45 represent the original f.c.c. unit cell and the unit cells of the superstructures; 2 “Strukturbericht” designation; 3 In terms of vectors of the f.c.c. structure.

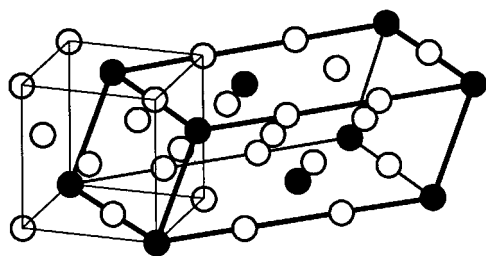
A₅B (B2/m)

Figure 8-40. Original f.c.c. unit cell and unit cell of the superstructure A₅B (B2/m), indicated by bold lines.

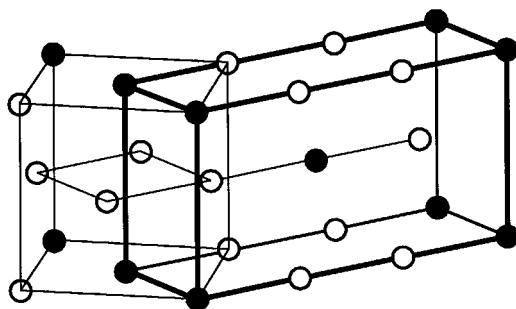


Figure 8-43. Original f.c.c. unit cell and unit cell of the superstructure A₂B (Pt₂Mo), indicated by bold lines.

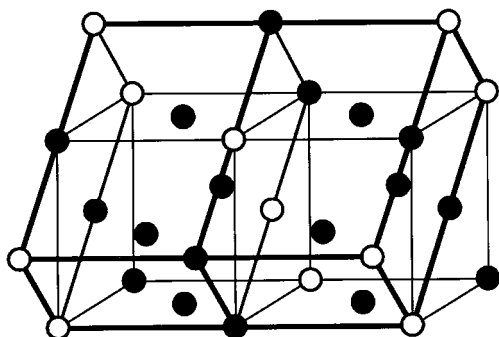


Figure 8-41. Original f.c.c. unit cell and unit cell of the superstructure D1a (Ni₄Mo), indicated by bold lines.

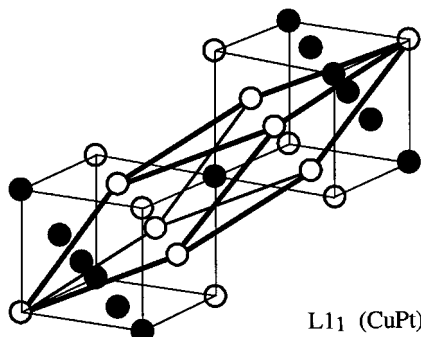
L₁₁ (CuPt)

Figure 8-44. Original f.c.c. unit cell and unit cell of the superstructure L₁₁ (CuPt), indicated by bold lines.

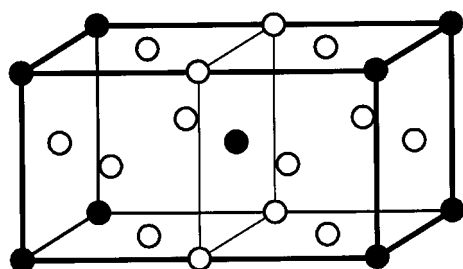
D0₂₂ (Ti₃Al)

Figure 8-42. Original f.c.c. unit cell and unit cell of the superstructure D0₂₂ (Ti₃Al), indicated by bold lines.

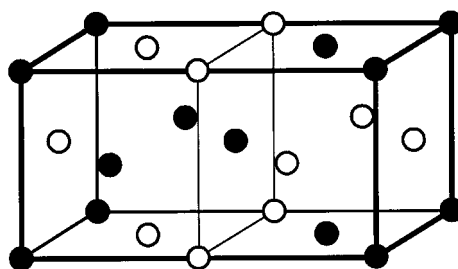
A₂B₂ (I4₁/amd)

Figure 8-45. Original f.c.c. unit cell and unit cell of the superstructure A₂B₂ (I4₁/amd), indicated by bold lines.

Table 8-12. Superstructures of the b.c.c. lattice.

Designation ¹	Spacegroup	Basis ²	Equivalent positions	Occupation
			Positions	
A2 (Fe)	Fd3c	$a = a_0 \{1\ 0\ 0\}$	—	A/B
D0 ₃ (Fe ₃ Al)	Fm3m	$a_1 = a_0 [2\ 0\ 0]$	—	4 B
		$a_2 = a_0 [0\ 2\ 0]$	(0 0 0)	4 A
		$a_3 = a_0 [0\ 0\ 2]$	(1/2 1/2 1/2)	8 A
	$F\bar{4}3m$		(1/4 1/4 1/4; 3/4 3/4 3/4)	
		$a_1 = a_0 [2\ 0\ 0]$	—	4 B
		$a_2 = a_0 [0\ 2\ 0]$	(0 0 0)	4 A
		$a_3 = a_0 [0\ 0\ 2]$	(1/2 1/2 1/2)	4 A/B
			(1/4 1/4 1/4)	4 A
			(3/4 3/4 3/4)	
B2 (CsCl)	Pm3m	$a = a_0 \{1\ 0\ 0\}$	—	A
			(0 0 0)	B
			(1/2 1/2 1/2)	
B32 (NaTl)	Fd3m	$a_1 = a_0 [2\ 0\ 0]$	(0 0 0; 0 1/2 1/2; 1/2 0 1/2; 0 1/2 1/2)+	
		$a_2 = a_0 [0\ 2\ 0]$	(0 0 0; 1/4 1/4 1/4)	8 A
		$a_3 = a_0 [0\ 0\ 2]$	(1/2 1/2 1/2; 3/4 3/4 3/4)	8 B

1 “Strukturbericht” designation; 2 In terms of vectors of the b.c.c. structure.

Table 8-13. Superstructures of the hexagonal lattice.

Designation ¹	Spacegroup	Basis ²	Equivalent positions	Occupation
			Positions	
A3	F6 ₃ /mmc	$a = a_0 [1\ 0\ 0]$ $b = a_0 [0\ 1\ 0]$ $c = a_0 [0\ 0\ 1]$	— (1/3 2/3 3/4)	2 (A/B)
D0 ₁₉ (A ₃ B)	P6 ₃ /mmc	$a = a_0 [2\ 0\ 0]$	—	6 A
		$b = a_0 [0\ 2\ 0]$	6 h (5/6 2/3 1/4)	2 B
		$c = c_0 [1\ 0\ 0]$	2 c (1/3 2/3 1/4)	
B19	Pmma	$a = c_0 [0\ 0\ \bar{1}]$	—	2 A
		$b = a_0 [0\ 1\ 0]$	2 f (1/4 1/2 5/6)	2 B
		$c = a_0 [2\ 1\ 0]$	2 e (1/4 0 1/3)	
A ₂ B	P2 ₁ /m	$a = a_0 [1\ \bar{1}\ 0]$	2 e (1/2 1/6 1/4)	A
		$b = a_0 [1\ 2\ 0]$	2 e (1/6 1/2 1/4)	A
		$c = c_0 [0\ 0\ 1]$	2 e (5/6 5/6 1/4)	B
A ₂ B (2-dim.)	p6m	$a = a_0 [1\ \bar{1}]$	2 b (1/3 2/3)	A
		$b = a_0 [1\ 2]$	1 a (0 0)	B

1 “Strukturbericht” designation; 2 In terms of vectors of the h.c.p. structure.

8.8 Acknowledgements

In writing this chapter the author has benefited from the work of past students, Claudio G. Schön, Sabine Crusius and Helen Ackermann, and from intense co-operation with colleagues, Ryoichi Kikuchi, Catherine Colinet and Christophe Bichara. This is gratefully acknowledged. The concept of multicomponent correlation functions was worked out in co-operation with Alphonse Finel when writing the version for the first edition of this volume (Inden and Pitsch, 1991). Thanks are due to Alan Oates for very helpful and enlightening discussions.

8.9 References

- Ackermann, H. (1988), Thesis, RWTH Aachen, Germany.
- Ackermann, H., Crusius, S., Inden, G. (1986), *Acta Metall.* 34, 2311.
- Ackermann, H., Inden, G., Kikuchi, R. (1989), *Acta Metall.* 37, 1.
- Allen, S. M., Cahn, J. W. (1972), *Acta Metall.* 20, 423.
- Allen, S. M., Cahn, J. W. (1973), *Scripta Metall.* 7, 1261.
- Allen, S. M., Cahn, J. W. (1982), *Bulletin Alloy Phase Diagrams* 3, 287.
- Asta, M., McCormack, R., de Fontaine, D. (1993), *Phys. Rev. B* 48, 748.
- van Baal, C. M. (1973), *Physica* 64, 571.
- Barker, J. A. (1953), *Proc. Roy. Soc. A* 216, 45.
- Bichara, C., Crusius, S., Inden, G. (1992a), *Physica B* 182, 42.
- Bichara, C., Crusius, S., Inden, G. (1992b), *Physica B* 179, 221.
- Bieber, A., Gautier, F. (1984a), *Z. Physik B* 57, 335.
- Bieber, A., Gautier, F. (1984b), *J. Phys. Chem. Soc. Japan* 53, 2061.
- Bieber, A., Gautier, F. (1986), *Acta Metall.* 34, 2291.
- Bieber, A., Gautier, F. (1987), *Acta Metall.* 35, 1839.
- Bienzle, M., Oishi, T., Sommer, F. (1995), *J. Alloys Comp.* 220, 182.
- Binder, K. (1976), in: *Phase Transitions and Critical Phenomena*, Vol. 5b: Domb, C., Green, M. S. (Eds.). New York: Academic Press, p. 2.
- Binder, K. (1979), in: *Monte Carlo Methods in Statistical Physics*: Binder, K. (Ed.). Berlin: Springer, p. 1.
- Binder, K. (1980), *Phys. Rev. Lett.* 45, 811.
- Binder, K. (1981), *Z. Physik B* 45, 61.
- Binder, K. (1985), *J. Comput. Phys.* 59, 1.
- Binder, K. (1986), in: *Advances in Solid State Physics*, Vol. 26: Braunschweig: Vieweg, p. 133.
- Binder, K. (2001), in: *Phase Transformations in Materials*: Kostorz, G. (Ed.). Weinheim: Wiley-VCH, Ch. 4.
- Binder, K., Heermann, D. W. (1988), *Monte Carlo Simulations in Statistical Physics, Springer Series Solid State Sci.*, Fulde, P. (Ed.), Vol. 80. Heidelberg: Springer.
- Binder, K., Stauffer, D. (1984), in: *Applications of the Monte Carlo Method in Statistical Physics*: Binder, K. (Ed.). Berlin: Springer, p. 1.
- Binder, K., Kinzel, W., Selke, W. (1983), *J. Magn. Magn. Mater.* 31–34, 1445.
- Binder, K., Lebowitz, J. L., Phani, M. K., Kalos, M. H. (1981), *Acta Metall.* 29, 1655.
- Bond, R. A., Ross, D. K. (1982), *J. Phys. F* 12, 597.
- Burley, D. M. (1972), in: *Phase Transitions and Critical Phenomena*, Vol. 2: Domb, C., Green, M. S. (Eds.). New York: Academic Press, p. 329.
- Burton, B. (1984), *Phys. Chem. Minerals* 11, 132.
- Burton, B. (1985), *Am. Mineralogist* 70, 1027.
- Burton, P. B., Cohen, R. E. (1995), *Phys. Rev. B* 52, 792.
- Burton, B., Kikuchi, R. (1984), *Am. Mineralogist* 69, 165.
- Cacciamani, G., Chang, Y. A., Grimvall, G., Franke, P., Kaufman, L., Miodownik, P., Sanchez, J. M., Schalin, M., Sigli, C. (1997), *Calphad* 21, 219.
- Cahn, J. W., Kikuchi, R. (1979), *Acta Metall.* 27, 1329.
- Cahn, J. W., Larché, F. (1984), *Acta Metall.* 32, 1915.
- Chesnut, D. A., Salsburg, Z. W. (1963), *J. Chem. Phys.* 38, 2861.
- Clapp, P. C., Moss, S. (1966), *Phys. Rev.* 142, 418.
- Clapp, P. C., Moss, S. (1968), *Phys. Rev.* 171, 754.
- Colinet, C., Pasturel, A. (2000), *J. Alloys Comp.* 296, 6.
- Colinet, C., Inden, G., Kikuchi, R. (1993), *Acta Metall. Mater.* 41, 1109.
- Connolly, J. W. D., Williams, A. R. (1983), *Phys. Rev. B* 27, 5169.
- Cowley, J. M. (1950), *Phys. Rev.* 77, 669.
- Craievich, P. J., Sanchez, J. M. (1997), *Comp. Mater. Sci.* 8, 82.
- Craievich, P. J., Sanchez, J. M., Watson, R. E., Weinert, M. (1997), *Phys. Rev. B* 55, 787.
- Crusius, S., Inden, G. (1988), in: *Proc. Int. Symp. Dynamics of Ordering Processes in Condensed Matter, Kyoto 1987*: Komura, S., Furukawa, H. (Eds.). New York: Plenum, p. 138.
- Diep, H. T., Ghazali, A., Berge, B., Lallemand, P. (1986), *Europhys. Lett.* 2, 603.
- Ducastelle, F. (1991), in: *Cohesion and Structure*, Vol. 3: de Boer, F. R., Pettifor, D. G. (Eds.). Amsterdam: North-Holland, p. 1.

- Ducastelle, F., Gautier, F. (1976), *J. Phys. F* 6, 2039.
- Eymery, J., Lançon, F., Billard, L. (1993), *J. Physique I France* 3, 787.
- Ferreira, L. G., Mbaye, A. A., Zunger, A. (1987), *Phys. Rev. B* 35, 6475.
- Ferreira, L. G., Mbaye, A. A., Zunger, A. (1988), *Phys. Rev. B* 37, 10547.
- Ferreira, L. G., Wei, S.-H., Zunger, A. (1989), *Phys. Rev. B* 40, 3197.
- Finel, A. (1987), Thesis, University Pierre et Marie Curie, Paris.
- Finel, A. (1994), in: *Statics and Dynamics of Alloy Phase Transformations*: Turchi, P. E. A., Gonis, A. (Eds.). NATO ASI Series B, Physics, Vol. 319. Dordrecht: Kluwer, p. 495.
- Finel, A., Ducastelle, F. (1984), in: *Mat. Res. Soc. Symp. Proc. 21: Phase Transformations in Solids, Maleme (Crete) 1983*. Amsterdam: North-Holland Publ., p. 293.
- Finel, A., Ducastelle, F. (1986), *Europhys. Lett.* 1, 135 and Erratum p. 543.
- Finel, A., Gratias, D., Portier, R. (1984), in: *L'ordre et le Desordre dans les Matériaux*, Reynaud, F., Clément, N., Couderc, J. J. (Eds.). Ecole d'Hiver Aussois 1984. Les Ulis: Editions de Physique, p. 9.
- Flinn, P. A. (1956), *Phys. Rev.* 104, 350.
- de Fontaine, D. (1979), in: *Solid State Physics*, Vol. 34: Ehrenreich, H., Seitz, F., Turnbull, D. (Eds.). London: Academic Press, p. 73.
- de Fontaine, D. (1984), in: *High Temperature Ordered Intermetallic Alloys*, *Mat. Res. Soc. Proc.*, Vol. 39: Koch, Liu, Stoloff (Eds.). Pittsburgh: Materials Res. Soc., p. 43.
- de Fontaine, D. (1994), *Solid State Phys.* 47, 33.
- Fosdick, L. D. (1963), *Methods Comp. Phys.* 1, 245.
- Frantz, C., Gantois, M. (1971), *J. Appl. Cryst.* 4, 387.
- Gahn, U. (1982), *J. Phys. Chem. Solids* 43, 977.
- Gahn, U. (1986), *J. Phys. Chem. Solids* 47, 1153.
- Gahn, U., Sauthoff, G., Pitsch, W. (1984), in: *Decomposition of Alloys, the Early Stages*, *Acta-Scripta Metallurgica Conf. Proc.*: Haasen, P., Gerold, V., Wagner, R., Ashby, M. F. (Eds.). New York: Pergamon Press, p. 16.
- Gautier, F. (1984), in: *High Temperature Alloys: Theory and Design*: Stieglar, P. O. (Ed.). New York: Am. Inst. Min. Engrs., p. 163.
- Gautier, F., Ducastelle, F., Giner, J. (1975), *Philos. Mag.* 31, 1373.
- Gerold, V., Kern, J. (1987), *Acta Metall.* 35, 393.
- Golosov, N. S., Tolstick, A. M. (1974), *J. Phys. Chem. Solids* 36, 899.
- Golosov, N. S., Tolstick, A. M. (1975), *J. Phys. Chem. Solids* 36, 903.
- Golosov, N. S., Tolstick, A. M. (1976), *J. Phys. Chem. Solids* 37, 273.
- Gratias, D., Sanchez, J. M., de Fontaine, D. (1982), *Physica A* 113, 315.
- Gyorffy, B. L., Stocks, G. M. (1983), *Phys. Rev. Lett.* 50, 374.
- Hansen, M., Anderko, K. (1958), *Constitution of Binary Alloys*. New York: McGraw-Hill.
- Hijmans, J., de Boer, J. (1955), *Physica* 21, 471.
- Houtappel, R. M. F. (1950), *Physica* 16, 425.
- Inden, G. (1975a), *Z. Metallkde.* 66, 577.
- Inden, G. (1975b), *Z. Metallkde.* 66, 648.
- Inden, G. (1977a), *Z. Metallkde.* 68, 529.
- Inden, G. (1977b), *J. de Physique* 38, C7, 373.
- Inden, G., Pepperhoff, W. (1990), *Z. Metallkde.* 81, 770.
- Inden, G., Pitsch, W. (1991), in: *Materials Science and Technology*, Vol. 5: *Phase Transformation in Materials*: Haasen, P. (Ed.). New York: VCH Press, p. 497.
- Jacobs, L., Rebbi, C. (1981), *J. Comput. Physics* 41, 203.
- Kainuma, R., Ikenoya, H., Ohnuma, I., Ishida, K. (1997), *Defect and Diffusion Forum Vols. 143-147*, 425.
- Kalle, C., Winkelmann, V. (1982), *J. Stat. Phys.* 28, 639.
- Kanamori, J. (1966), *Prog. Theor. Phys.* 35, 16.
- Kanamori, J. (1979), in: *Int. Conf. on Modulated Structures*: Cowley, J. M., Cohen, J. B., Salomon, M. B., Wuensch, B. J. (Eds.). *AIP Conf. Proc.* 53, p. 117.
- Kanamori, J. (1984), *J. Phys. Soc. Jpn.* 53, 250.
- Kanamori, J., Kakehashi, Y. (1977), *J. de Physique* 38, C-7, 274.
- Kear, B. H., Sims, C. T., Stoloff, N. S., Westbrook, J. H. (Eds.) (1970), *Ordered Alloys. Proc. 3rd. Bolton Landing Conf.* Baton Rouge: Claitors Publ.
- Khachatryan, A. G. (1978), in: *Progress in Materials Science*, Vol. 22. New York: Pergamon Press, p. 1.
- Kikuchi, R. (1950), *Phys. Rev.* 79, 718.
- Kikuchi, R. (1951), *Phys. Rev.* 81, 988.
- Kikuchi, R. (1974), *J. Chem. Phys.* 60, 1071.
- Kikuchi, R. (1977a), *Acta Metall.* 25, 195.
- Kikuchi, R. (1977b), *J. de Physique* 38, C7-307.
- Kikuchi, R. (1986), *Progr. Theor. Phys. Suppl.* 87, 69.
- Kikuchi, R. (1987), *Physica* 142A, 321.
- Kikuchi, R., van Baal, C. M. (1974), *Scripta Metall.* 8, 425.
- Kikuchi, R., Burton, B. (1988), *Physica B* 150, 132.
- Kikuchi, R., Sato, H. (1974), *Acta Metall.* 22, 1099.
- Kikuchi, R., de Fontaine, D., Murakami, M., Nakamura, T. (1977), *Acta Metall.* 25, 207.
- Kikuchi, R., Sanchez, J. M., de Fontaine, D., Yamachi, H. (1980), *Acta Metall.* 28, 651.
- Kleykamp, H., Glasbrenner, H. (1997), *Z. Metallkde.* 88, 230.
- Koch, C. C., Liu, C. T., Stoloff, N. S. (Eds.) (1985), *High Temperature Ordered Intermetallic Alloys I*, *Mat. Res. Soc. Symp. Proc.*, Vol. 39. Pittsburgh: Materials Res. Soc.

- Köster, W., Gödecke, T. (1980), *Z. Metallkde.* 81, 770.
- Kohan, A. F., Ceder, G. (1996), *Phys. Rev. B* 53, 8993.
- Kozakai, T., Miyazaki, T. (1994), *J. Mater. Sci.* 29, 652.
- Kudo, T., Katsura, S. (1976), *Prog. Theor. Phys.* 56, 435.
- Kutner, R., Binder, K., Kehr, K. W. (1982), *Phys. Rev. B* 26, 2967.
- Laks, D. B., Ferreira, L. G., Froyen, S., Zunger, A. (1992), *Phys. Rev. B* 46, 12587.
- Lebowitz, J. L., Phani, M. K., Styer, D. F. (1985), *J. Stat. Phys.* 38, 413.
- Li, Y. Y. (1949), *Phys. Rev.* 76, 972.
- Li, Y. Y. (1949), *J. Chem. Phys.* 17, 447.
- Lihl, F., Ebel, H. (1961), *Arch. Eisenhüttenwes.* 32, 483.
- Liu, C. T., Taub, A. I., Stoloff, N. S., Koch, C. C. (Eds.) (1989), *High Temperature Ordered Intermetallic Alloys III*, *Mat. Res. Soc. Symp. Proc.*, Vol. 133, Pittsburgh: Materials Res. Soc.
- Liu, C. T., Cahn, R. W., Sauthoff, G. (Eds.) (1992), *Ordered Intermetallics – Physical Metallurgy and Mechanical Behaviour*, *Nato ASI Series Vol.* 213. Dordrecht: Kluwer, p. 525.
- Livet, F. (1987), *Acta Metall.* 35, 2915.
- Lu, Z. W., Wei, S. H., Zunger, A., Frota-Pessoa, S., Ferreira, L. G. (1991), *Phys. Rev. B* 44, 512.
- Lu, Z. W., Klein, B. M., Zunger, A. (1995), *Model. Sim. Mater. Sci. Eng.* 3, 753.
- McCormack, R., de Fontaine, D. (1996), *Phys. Rev. B* 54, 9746.
- McCormack, R., Asta, M., Hoyt, J. J., Chakoumakos, B. C., Misture, S. T., Althoff, J. D., Johnsson, D. D. (1997), *Comp. Mater. Sci.* 8, 39.
- Miyazaki, T., Isobe, K., Kozakai, T., Doi, M. (1987), *Acta Metall.* 35, 317.
- Mohri, T., Sanchez, J. M., de Fontaine, D. (1985), *Acta Metall.* 33, 1171.
- Mouritsen, O. G. (1984), *Computer Studies of Phase Transitions and Critical Phenomena*. Berlin: Springer.
- Newell, G. F. (1950), *Phys. Rev.* 79, 876.
- Oates, W. A., Wenzl, H. (1996), *Scripta Mater.* 35, 623.
- Oates, W. A., Spencer, P. J., Fries, S. G. (1996), *CALPHAD* 20, 481.
- Oates, W. A., Zhang, F., Chen, S.-L., Chang, Y. A. (1999), *Phys. Rev. B* 59, 11221.
- Ohnuma, I., Ikeda, O., Kainuma, R., Sundman, B., Ishida, K. (1998a), presented at the CALPHAD Meeting, Beijing.
- Ohnuma, I., Schön, C. G., Kainuma, R., Inden, G., Ishida, K. (1998b), *Acta Mater.* 46, 2083.
- Onodera, H., Abe, T., Yokokawa, T. (1994), *Acta Metall.* 42, 887.
- Ozoliņš, V., Wolverton, C., Zunger, A. (1998a), *Phys. Rev. B* 57, 6427.
- Ozoliņš, V., Wolverton, C., Zunger, A. (1998b), *Phys. Rev. B* 57, 5897.
- Pasturel, A., Colinet, C., Paxton, A. T., van Schilf-gaarde, M. (1992), *J. Phys.: Condens. Matter* 4, 945.
- Priem, T., Beuneu, B., Finel, A., Livet, F., de Novion, C. H. (1989a), *J. de Physique* 50, 2217.
- Priem, T., Beuneu, B., de Novion, C. H., Chevrier, J., Livet, F., Finel, A., Lefevbre, S. (1989b), *Physica B* 156+157, 47.
- Renaud, G., Motta, N., Belakhovsky, M., Lançon, F., Billard, L. (1987), *Solid State Comm.* 63, 569.
- Richards, M. J., Cahn, J. W. (1971), *Acta Metall.* 19, 1263.
- de Ridder, R., van Dyck, D., Amelinckx, S. (1980), *Phys. Stat. Solidi A* 61, 231.
- Rubin, G., Finel, A. (1993), *J. Phys.: Condens. Matter* 5, 9105.
- Sanchez, J. M. (1996), in: *Theory and Applications of the Cluster Variation and Path Probability Methods*: Moran-Lopez, J. L., Sanchez, J. M. (Eds.). New York: Plenum Press, p. 175.
- Sanchez, J. M., de Fontaine, D. (1978), *Phys. Rev. B* 17, 2926.
- Sanchez, J. M., de Fontaine, D. (1980), *Phys. Rev. B* 21, 216.
- Sanchez, J. M., de Fontaine, D. (1981), in: *Structure and Bonding in Crystals*, Vol. II: O'Keefe, M., Navrotsky, A. (Eds.). New York: Academic Press, p. 917.
- Sanchez, J. M., de Fontaine, D. (1982), *Phys. Rev. B* 25, 1759.
- Sanchez, J. M., de Fontaine, D., Teitler, W. (1982), *Phys. Rev. B* 26, 1465.
- Sanchez, J. M., Ducastelle, F., Gratias, D. (1984), *Physica A* 128, 334.
- Schlijper, A. G. (1983), *Phys. Rev. B* 27, 6841.
- Schlijper, A. G. (1984), *J. Stat. Phys.* 35, 285.
- Schlijper, A. G. (1985), *Phys. Rev. B* 31, 609.
- Schön, C. G., Inden, G. (2001), *Comp. Mater. Sci.*, 20, 98.
- Schön, C. G., Inden, G. (1998), *Acta Mater.* 46, 4219.
- Schönfeld, B. (1999), in: *Progress in Materials Science*, Vol. 44. New York: Pergamon Press, p. 435.
- Sigli, C., Sanchez, J. M. (1988), *Acta Metall.* 36, 367.
- Sluiter, M., Turchi, P. E. A. (1989a), in: *Alloy Phase Stability*: Stocks, G. M., Gonis, A. (Eds.). Dordrecht: Kluwer Acad. Publ., p. 521.
- Sluiter, M., Turchi, P. E. A. (1989b), *Phys. Rev. B* 40, 215.
- Sluiter, M., Turchi, P. E. A., Fu, Zezhong, de Fontaine, D. (1986), *Phys. Rev. Lett.* 60, 716.
- Stoloff, N. S., Koch, C. C., Liu, C. T., Izumi, O. (Eds.) (1987), *High Temperature Ordered Intermetallic Alloys III*, *Mat. Res. Soc. Symp. Proc.*, Vol. 81.
- Taggart, G. B. (1973), *J. Phys. Chem. Solids* 34, 1917.

- Tepesch, P. D., Garbulski, G. D., Ceder, G. (1995), *Phys. Rev. Lett.* 74, 2274.
- Tepesch, P. D. (1996), *J. Am. Ceram. Soc.* 79, 2033.
- Terakura, K., Oguchi, T., Mohri, T., Watanabe, K. (1987), *Phys. Rev. B* 35, 2169.
- Treglia, G., Ducastelle, F. (1980), *J. Phys. F* 10, 2137.
- Turchi, P. E. A., Gonis, A. (Eds.) (1994), *Statics and Dynamics of Alloy Phase Transformations*: NATO ASI Series B, Physics, Vol. 319. Dordrecht: Kluwer, p. 361.
- Turchi, P. E. A., Sluiter, M., Pinski, F. J., Johnson, D. D. (1991a), in: *Mat. Res. Soc. Symp. Proc.*, Vol. 186: Stocks, G. M., Giamei, A. F., Pope, D. P. (Eds.). Pittsburgh: Materials Res. Soc., p. 59.
- Turchi, P. E. A., Sluiter, M., Pinski, F. J., Howell, R. H., Wachs, A. L., Fluss, M. L., Johnson, D. D., Stocks, G. M., Nicholson, D. M., Schweika, W. (1991b), in: *Mat. Res. Soc. Symp. Proc.*, Vol. 166, Shapiro, S. M., Moss, S. C., Jorgensen, J. D. (Eds.). Pittsburgh: Materials Res. Soc., p. 231.
- Vaks, V. G., Samolyuk, G. D. (1999), *J. Exp. Theor. Phys.* 88, 89.
- van de Walle, A., Ceder, G., Waghmare, U. V. (1998), *Phys. Rev. Lett.* 80, 4911.
- Wannier, G. H. (1950), *Phys. Rev.* 79, 357.
- Warlimont, H. (Ed.) (1974), *Order-Disorder Transformations in Alloys*. Berlin: Springer.
- Wei, S.-H., Ferreira, L. G., Zunger, A. (1990), *Phys. Rev. B* 41, 8240.
- Wei, S.-H., Ferreira, L. G., Zunger, A. (1992), *Phys. Rev. B* 45, 2533.
- Whang, S. H., Liu, C. T., Pope, D. P., Stiegler, J. O. (Eds.) (1990), *High Temperature Aluminides and Intermetallics*. Warrendale: The Minerals Metals and Materials Soc.
- Williams, R. O. (1980), *Metall. Trans. A* 11, 247.
- Williams, R. O. (1984), *CALPHAD* 8, 1.
- Wolverton, C., Zunger, A. (1997), *Comp. Mater. Sci.* 8, 107.
- Wolverton, C., Ozoliņš, V., Zunger, A. (1998), *Phys. Rev. B* 57, 4332.
- Yang, C. N. (1945), *J. Phys. Chem.* 13, 66.
- Yang, C. N., Li, Y. Y. (1947), *Chin. J. Phys.* 7, 59.
- Zhang, J., Oates, W. A., Zhang, F., Chen, S.-L., Chou, K.-C., Chang, Y. A. (2001), *Intermetallics* 9, in print.
- Zorn, R., Heermann, H. J., Rebbi, C. (1981), *J. Comp. Phys.* 23, 337.
- Zunger, A. (1994), in: *Statics and Dynamics of Alloy Phase Transformations*: Turchi, P. E. A., Gonis, A. (Eds.), NATO ASI Series B, Physics, Vol. 319. Dordrecht: Kluwer, p. 361.

9 Diffusionless Transformations

Luc Delaey

Departement Metaalkunde en Toegepaste Materiaalkunde,
Katholieke Universiteit Leuven, Heverlee-Leuven, Belgium

List of Symbols and Abbreviations	585
9.1 Introduction	587
9.2 Classification and Definitions	590
9.3 General Aspects of the Transformation	593
9.3.1 Structural Relations	593
9.3.2 Pre-transformation State	597
9.3.3 Transformation Mechanisms	599
9.3.4 Microstructures	600
9.3.5 Shape Changes	600
9.3.6 Transformation Thermodynamics and Kinetics	604
9.4 Shuffle Transformations	607
9.4.1 Ferroic Transformations	609
9.4.2 Omega Transformations	610
9.5 Dilatation-Dominant Transformations	610
9.6 Quasi-Martensitic Transformations	611
9.7 Shear Transformations	613
9.8 Martensitic Transformations	615
9.8.1 Crystallography of the Martensitic Transformation	615
9.8.1.1 Shape Deformation and Habit Plane	615
9.8.1.2 Orientation Relationship	616
9.8.1.3 Morphology, Microstructure and Substructure	618
9.8.1.4 Crystallographic Phenomenological Theory	620
9.8.1.5 Structure of the Habit Plane	623
9.8.2 Thermodynamics and Kinetics of the Martensitic Transformation	624
9.8.2.1 Critical Driving Force and Transformation Temperatures	624
9.8.2.2 Nucleation	630
9.8.2.3 Growth and Kinetics	632
9.8.2.4 Transformation Hysteresis	634
9.9 Materials	634
9.9.1 Metallic Materials	634
9.9.1.1 Ferrous Alloys	635
9.9.1.2 Non-Ferrous Alloys	637
9.9.2 Non-Metals	639
9.10 Special Properties and Applications	641
9.10.1 Hardening of Steel	641

9.10.2 The Shape-Memory Effect 641

9.10.3 High Damping Capacity 647

9.10.4 TRIP Effect 647

9.11 **Recent Progress in the Understanding of Martensitic Transformations** 649

9.12 **Acknowledgements** 651

9.13 **References** 652

List of Symbols and Abbreviations

a	length
A	factor (containing elastic terms)
a, b, c	constants
A_d	retransformation temperature (deformation induced)
A_j	amplitude of perturbation with polarization j
A_s	starting temperature for austenite formation
B	pure strains associated with lattice correspondence
C	lattice correspondence
C	cubic sequence
C'	elastic shear constant
c^*	size of critical nucleus
C_{ij}	eigenvalues of elasticity tensor
c/a	axial ratio
c/r	thickness/radius ratio of nucleus
e	order parameter
E	electric field
e_1, e_2, e_3	principal strains
E_e	strain energy
F	applied force
ΔG	difference in chemical Gibbs energy
ΔG^*	Gibbs energy of nucleation
Δg_s	surface Gibbs energy per unit volume
G^*	elastic state function
$G^\alpha, G^\beta, G^\gamma$	Gibbs energy of phases α, β, γ
G_c, G_{chem}	chemical Gibbs energy
G_{elast}	elastic Gibbs energy
G_{surf}	surface Gibbs energy
G_{tot}	total Gibbs energy
G_d	defect Gibbs energy
G_i	interaction Gibbs energy
H	magnetic field
H^*	elastic state function
$\Delta H, \Delta H^*$	enthalpy change
l	molar length
M_d	deformation-induced martensitic temperature
M_f	martensite finishing temperature
M_s	martensite starting temperature
P	inhomogeneous lattice-invariant deformation
q	wave vector
r	radius of a plate
r	lattice vector
R	rigid body rotation
R	rhombohedral sequence

r^*	size of critical nucleus
S	strain matrix
ΔS	entropy change
T	temperature
T_0	equilibrium temperature
T_c	critical transition temperature
T_N	Neel temperature
T_{TW}	temperature at which twins appear
v	volume of a plate
V_m	molar volume
x	atomic fraction of elements
\mathbf{x}, \mathbf{y}	lattice vectors
α	name of phase
β	name of phase
γ	name of phase
Γ	interfacial energy
δ_0	shear strain
ε	name of phase
ε_0	strain associated with the transformation
ϕ	surface to volume ratio
σ	stress
σ_a	applied stress
ASM	American Society for Materials
b.c.c.	body-centered cubic
b.c.t.	body-centered tetragonal
f.c.c.	face-centered cubic
f.c.t.	face-centered tetragonal
G–T	Greninger–Troiano
h.c.p.	hexagonal close packed
HIDAMETS	high-damping metals
HP	habit plane
HRTEM	high-resolution transmission electron microscopy
IPS	invariant plane strain
K–S	Kurdjurnov–Sachs
LOM	light optical microscopy
N–W	Nishiyama–Wassermann
PTFE	polytetrafluoroethylene
SMA	shape-memory alloys
SME	shape-memory effect
TRIP	transformation-induced plasticity

9.1 Introduction

Diffusionless solid-state phase transformations, as the name suggests, do not require long-range diffusion during the phase change; only small atomic movements over usually less than the interatomic distances are needed. The atoms maintain their relative relationships during the phase change. Diffusionless phase transformations therefore show characteristics (such as crystallographic, thermodynamic, kinetic and microstructural) very different from those of diffusive phase transformations.

Martensitic transformations, because some of the properties associated with them sometimes lead to specialized applications, are considered to be an extreme class of diffusionless phase transformation and we therefore in this chapter concentrate on martensite. Because of the similarity of some of the transformation characteristics, a number of other diffusionless solid-state phase transformations have sometimes been designated erroneously as martensitic. To avoid misinterpretations, Cohen et al. (1979) proposed a classification scheme that identifies broad categories of displacive transformations showing features in common with martensitic transformations, but distinct from them. Their classification scheme, reproduced in Fig. 9-1, will largely be followed here. Martensitic transformations are here only a subclass of the broader class of displacive/diffusionless phase transformations.

The classification proposed by Cohen et al. (1979) is discussed first, and subsequent sections deal with general aspects of the crystallography, thermodynamics and kinetics of the different displacive transformations. Although it is not the purpose to give full details of all materials that exhibit this type of transformation, the most important material systems in which such

transformations have been observed are presented.

A martensitic transformation can be detected by a number of techniques; some are *in situ* methods, whereas others are step-by-step measurements. The results are usually plotted as a change in a physical property versus temperature (see the schematic representation in Fig. 9-2), from which the transformation temperatures can be determined. Some of these plots can be translated into the volume fraction of martensite formed versus the temperature. Such curves allow us to determine the transformation temperatures as indicated in these figures.

In situ detection becomes limited if the transformation temperature is above room temperature, and dilatometry then seems to be the most appropriate technique provided that quenching – which is needed to avoid alterations in the sample due to diffusion – is possible inside the dilatometer. There are far more ways of following the transformation when the transformation temperature is below room temperature – preparing the sample and carrying out the measurements can take some time and at room temperature diffusion is then almost negligible. During slow cooling after water quenching, the techniques frequently used include dilatometry, electrical resistivity and magnetic measurements, calorimetry, *in situ* microscopy, acoustic emission, elastic and internal friction measurements, positron annihilation, and Mössbauer spectroscopy. Some of the less common techniques used to study martensitic transformations were reviewed by Fujita (1982).

If crystallographic information is required, X-ray and electron or neutron diffraction are used. X-ray diffraction measurements by Fink and Cambell in 1926 (lattice parameter of C-steel martensite), by Kurdjurnov and Sachs in 1930, by Ni-

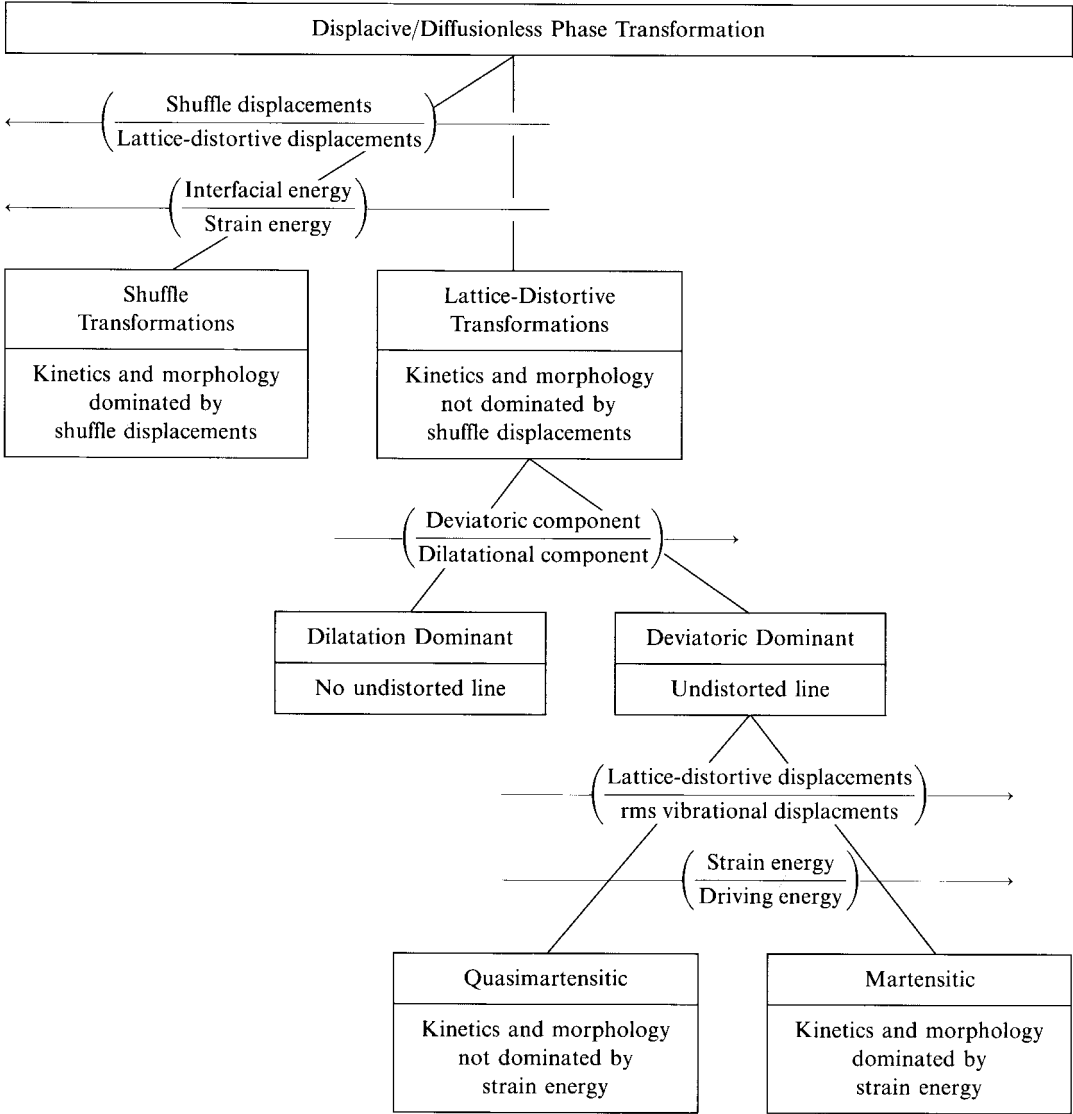


Figure 9-1. Classification scheme for the displacive/diffusionless phase transformations as proposed by Cohen et al. (1979).

shiyama in 1934 and by Greninger and Troiano in 1949 (orientation relationship between austenite – the parent phase – and martensite) represent breakthroughs in the study of martensitic transformations.

The most frequently used techniques will now be briefly discussed and illustrated.

If a sample is polished into the martensite (= parent phase), a surface relief appears. An edge-on section of such a sample is shown in Fig. 9-2a (see Hsu, 1980). The origin of the surface relief is indicated by the white arrows. Owing to the macroscopic martensite shear (the two thinner arrows), a surface relief is obtained. This is

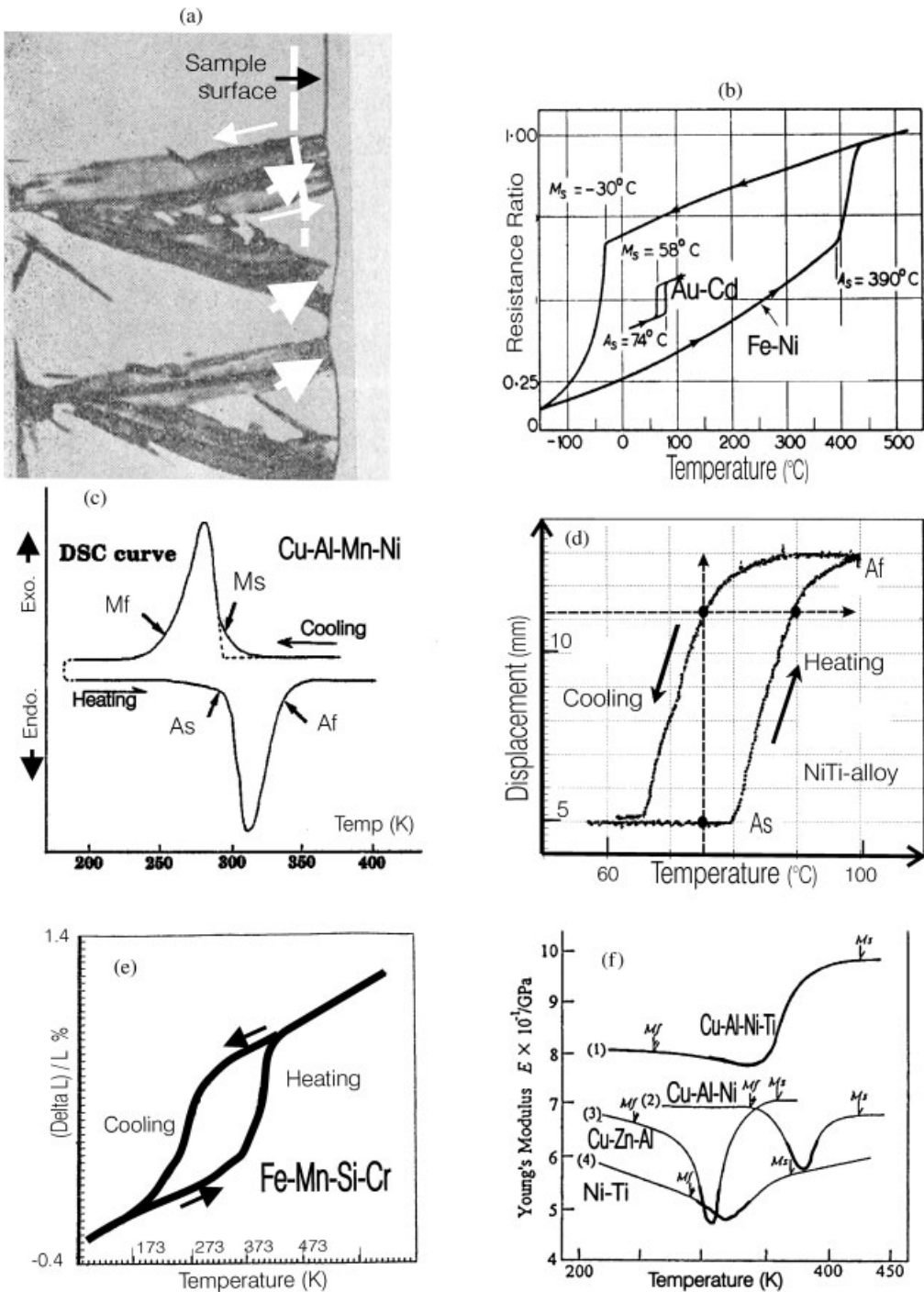


Figure 9-2. Some examples of how to see or measure the presence and growth of martensite (see text for details).

explained further in Sec. 9.8.1.1 (Fig. 9-19).

The electrical resistance shows at the transformation temperatures a deviation from linearity *versus* temperature. This is shown in Fig. 9-2b for the martensitic transformation in an Fe–Ni alloy and a Au–Cd alloy. The difference in the resistance ratio for the two different materials is obvious and remarkable (see Otsuka and Wayman, 1977). Measuring the electrical resistance while cooling or heating a sample is a very convenient and relatively easy and accurate technique of determining the transformation temperatures M_s , M_f , A_s and A_f .

The heat exchanged with the surroundings is becoming a more popular method of determining the transformation temperatures. An example is shown in Fig. 9-2c (Nakanishi et al., 1993). A DSC (differential scanning calorimetry) curve allows any particular behavior of the martensitic sample to be detected (for example, effects occurring during heat treatments and/or deformation steps).

A number of martensitic transformations and materials are characterized by a so-called shape-memory effect (see Sec. 9.11.2). Figure 9-2d (courtesy of Memory Europe) shows the displacement of a spring made of a NiTi shape-memory alloy. The spring controls a small valve in a coffee-making machine. At the temperature A_s the hot water starts to drop onto the coffee powder. This valve is completely open as soon as the temperature A_f is reached. The temperature range between A_s and A_f seems to be most suitable for making the best cup of coffee. On cooling, the valve closes again. The “displacement–temperature” curve measured on cooling does not coincide with the heating curve.

During a martensitic transformation, not only is the shape of the sample changed but

also the specific volume, which allows the transformation temperatures to be determined by dilatometry (Fig. 9-2e, from Yang and Wayman, 1993).

Changes in mechanical properties are also measured while the sample is transforming. The Young’s modulus exhibits a dip between the two transformation temperatures M_s and M_f , as clearly visible in Fig. 9-2f for four different alloys (see Sugimoto and Nakaniwa, 2000).

9.2 Classification and Definitions

A structural change in the solid state is termed “displacive” if it occurs by coordinated shifts of individual atoms or groups of atoms in organized ways relative to their neighbors. In general, this type of transformation can be described as a combination of “homogeneous lattice-distortive strain” and “shuffles”.

A lattice-distortive deformation is a homogeneous strain that transforms one lattice into another; examples are shown in Fig. 9-3. The homogeneous strain can be represented by a matrix according to

$$\mathbf{y} = \mathbf{S} \mathbf{x} \quad (9-1)$$

where the strain \mathbf{S} deforms the lattice vector \mathbf{x} into a lattice vector \mathbf{y} . This strain is homogeneous because it transforms straight lines into other straight lines. A spherical body of the parent phase will thus be transformed into another sphere or into an ellipsoidal body. The actual shape of the ellipsoid depends on the deformation in the three principal directions. If a spherical body is completely embedded inside the matrix phase and is undergoing the strain \mathbf{S} , the volume and shape change associated with this deformation will cause elastic and, sometimes, plastic strains in the parent

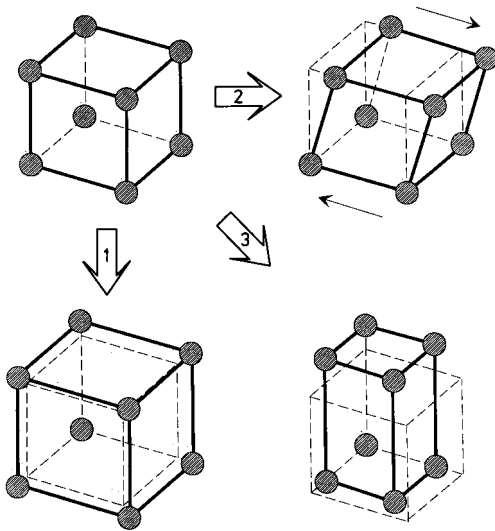


Figure 9-3. Examples of the lattice-distortive deformations of a cubic lattice: (1) a dilatation in the three principal directions transforms the lattice into another cubic lattice with larger lattice parameters; (2) a shear along the (001) plane leads to a monoclinic lattice, and (3) an extension along the [001] axis combined with a contraction along the [100] and [010] axis results in an orthorhombic lattice.

and/or product phases. The lattice-distortive displacements therefore give rise to elastic strain energy. In addition, an interface separating the phases is created, generating an interfacial energy. As is obvious from Fig. 9-1, the relative values of these energies play an important role in the classification scheme.

A shuffle is a coordinated movement of atoms that produces, in itself, no lattice-distortive deformations but alters only the symmetry or structure of the crystal; a sphere before the transformation remains the same sphere after the transformation. Shuffle deformations produce, in the ideal case, no strain energy and thus only interfacial energy. Two examples of the shuffle displacement are given in Fig. 9-4. Shuffle deformations can be expressed by “lattice

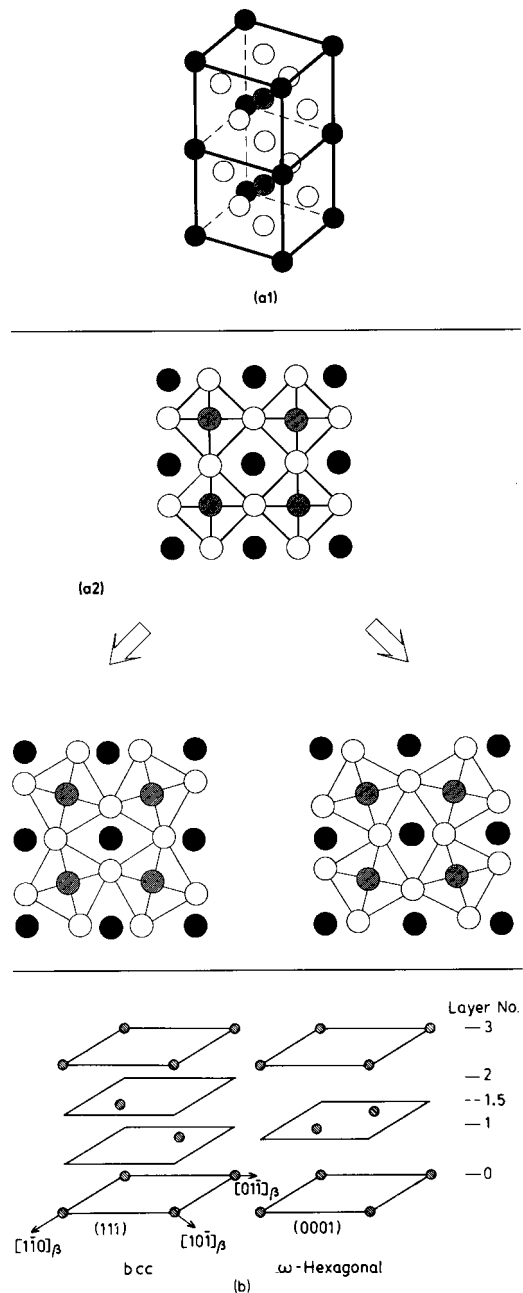


Figure 9-4. Examples of shuffle displacements in: (a1) strontium titanate; ● oxygen, ○ strontium, ⊗ titanium; (a2) the displacement of some of the oxygen atoms can be represented by an alternating clockwise and anti-clockwise rotation around the titanium atoms; and (b) the (111) planes in a β (b.c.c.) lattice and the collapsed (0001) planes in the hexagonal ω lattice (Sikka et al., 1982).

wave modulations" as

$$\Delta \mathbf{x} = A_j(\mathbf{q}) \exp(i \mathbf{q} \cdot \mathbf{r}) \quad (9-2)$$

where \mathbf{r} is a lattice vector, \mathbf{q} is the wave vector giving the direction and inverse wavelength of the modulation, A is the amplitude of the perturbation, and j denotes the polarization of the wave. An alternative description is represented by relative displacements of the various atomic sub-lattices that specify the structures of the two phases in terms of corresponding unit cells, which are not necessarily primitive.

Cohen et al. (1979) subdivided the displacive transformations into two main groups, according to the relative contribution of the two above-mentioned atom displacements and hence the ratio of the interfacial/strain energy. In this context, they distinguish between "shuffle transformations" and "lattice-distortive transformations". Since the latter give rise to elastic strain energy and the former only to interfacial energy, major differences are found in the kinetic and morphological aspects of the transformation, which justifies the distinction. Shuffle transformations are not necessarily pure; small distortive deformations may additionally occur. They therefore also include those transformations involving dilatational displacements, in addition to the pure shuffle displacements, provided that they are small enough not to alter significantly the kinetics and morphology of the transformation.

The lattice-distortive transformations themselves are subdivided according to the relative magnitudes of the two components of the homogeneous lattice deformation, i.e., the dilatational and the deviatoric (shear) components (see Fig. 9-3). The initial and the isotropically dilated spheres have no intersection and it is therefore not possible to find a vector whose length has not been changed by the transformation.

On the other hand, the ellipsoid obtained after a pure shear intersects the original sphere; hence a set of vectors exist, whose lengths remain unchanged. Such a deformation is said to be characterized by an "undistorted line". An undistorted line can only result from a homogeneous lattice deformation if the deviatoric or shear component sufficiently exceeds the dilatational component.

Cohen et al. (1979) thus consider a transformation as deviatoric-dominant if an invariant line exists. A further subdivision was made between phase transformations with and without an invariant line, or between "dilatation-dominant" and "deviatoric-dominant" transformations.

If the magnitude of the lattice-distortive displacements is large in relation to that of the lattice vibrational displacements, high elastic strain energies are involved. However, if they are comparable, the strain energies will be small and hence will not dominate the kinetics and morphology of the transformation. In the latter case we deal with "quasi-martensitic transformations". The former, i.e., the "martensitic transformations", are therefore those displacive or diffusionless phase transformations where the lattice-distortive displacements are large enough to dominate the kinetics and the morphology of the transformation. "Martensite" is the name now given to the product phase resulting from a martensitic transformation. Because of the volume change and the strain energy involved with the transformation, martensitic transformation requires heterogeneous nucleation and passes through a two-phase mixture of parent and product; it is a first-order diffusionless phase transformation. Consequently, the forward and reverse transformations are accompanied by an exothermic and endothermic heat effect, respectively, and forward and reverse trans-

formation paths are separated by a hysteresis.

Among the various diffusionless phase transformations which exist in solid-to-solid phase transformations, martensitic transformations have received much attention in the past. Historically, the term “martensite” was suggested by Osmond in 1895, in honor of the well-known German metallurgist Adolph Martens, as the name for the hard product obtained during the quenching of carbon steels. It was found that the transformation to martensite in steel was associated with a number of distinctive characteristic structural and microstructural features. During the last few decades it was recognized that martensite also forms in numerous other materials, such as superconductors, non-ferrous copper-based alloys, zirconia, which recently became a popular research subject for ceramists, physicists, chemists and polymeric and biological scientists.

Martensitic transformations have been the subject of a series of international conferences held in various places throughout the world. A list is given at the end of this chapter.

This increasing interest not only has academic origins but can to a large extent also be attributed to a number of industrial applications such as maraging, TRIP (**t**ransformation-induced **p**lasticity) and dual-phase steels, applications involving the shape-memory effect, the high damping capacity, and the achievement of transformation toughening in ceramics.

It may also be of interest to draw attention here to the “massive phase transformations”. Although this type of phase transformation, which occurs upon fast cooling, is composition-invariant and the transformation interface has a relatively rapid movement, it does not fall into the present category. Massalski (1984) defines mas-

sive transformation as a non-martensitic composition-invariant reaction involving diffusion at the interfaces (see also the chapter by Purdy and Bréchet (2001)).

“Bainite transformations” are also not treated in this chapter, although they do show some martensitic characteristics, but combined with diffusional processes. For further information, the reader is referred to Aaronson and Reynolds (1988) for an introductory review and to Krauss (1992).

9.3 General Aspects of the Transformation

The various diffusionless phase transformations have a number of features in common, such as the crystallographic aspects of the structural changes, the pretransformation state, the transformation mechanisms, the microstructure and the shape changes that result from the transformation, and the thermodynamic and kinetic aspects. The more general aspects are treated in the following section before discussing separately each subclass of transformation.

9.3.1 Structural Relations

This section is concerned with some crystallographic aspects of the structural changes. It is always useful to first determine a unique relationship – a lattice correspondence (*C*) – between any vector in the initial lattice and the vector that it becomes in the product lattice. A lattice correspondence thus defines a structural unit in the parent phase that, under the action of a homogeneous deformation, is transformed into a unit of the product phase. Such a correspondence therefore tells us which vectors, planes and unit cells of the product phase are derived from particular vectors,

planes and cells of the parent phase, without regard to their mutual orientation. For every structural change there exist many ways of producing a lattice correspondence; the one that involves minimal atomic displacements and which reflects the experimentally observed orientation relationships most closely should be selected.

The actual relationship between labelled vectors, planes, etc., before and after transformation (including their mutual orientation) is given by the lattice deformation. Mathematically this lattice deformation is factorized into a pure strain and a pure rotation, so the correspondence indicates what is the pure strain. Knowing the principal axes of the strain ellipsoid, the directions of undistorted lines, if any exist, can then easily be found. In 1924, Bain proposed such a lattice correspondence for the f.c.c.-to-b.c.c. (or b.c.t.) transformation in iron alloys; it is referred to in the literature as the prototype Bain correspondence and/or Bain strain. Since then, lattice correspondence values (C) and their associated pure strains (B) have been published for a number of other structural changes; some examples are given in Fig. 9-5.

In the original Bain strain, a tetragonal cell is delineated into two adjacent f.c.c. unit cells. Then, it is contracted along z by about 20% and is expanded along x' and y' by about 12%. In another example, the transformation from a NaCl-type structure into a CsCl-type structure, a contraction of 40% along the $[111]$ body diagonal and a 19% isotropic expansion in the perpendicular (111) plane is needed; the volume change is about 17%.

Homogeneous strains alone, however, do not always describe the structural transformation completely. Additional shuffles may be needed to obtain the exact atom arrangements inside the deformed unit cell.

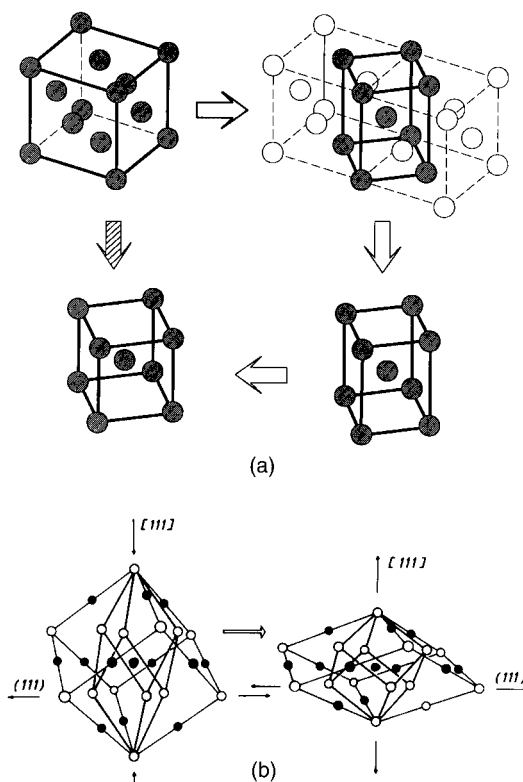


Figure 9-5. Some examples of lattice correspondence and homogeneous deformation (expansions and contractions) for (a) f.c.c. to b.c.c. or b.c.t. (after Bain, 1924) and (b) NaCl- to CsCl-type structures (the Shōji-Buerger lattice deformation) (Kriven, 1982).

A special situation arises for some materials, when the structural change can be achieved by a pure deformation that leaves one of the principal directions unaltered. Such a situation is found in some polymers. It occurs, for example, in polyethylene, which has an orthorhombic and a monoclinic polymorph with chains parallel to the z -axis; these strong covalently bonded chains are unlikely to be distorted by the transformation; consequently, the pure deformation along the z -axis ($e_3=0$) is zero. During transformation the chains are displaced transversely in such a way that one

of the remaining principal strains becomes positive ($e_2 > 0$) and the other negative ($e_1 > 0$) (Bevis and Allan, 1974).

The strain ellipsoid for the above example has a special shape. The cone of undistorted vectors of the product phase degenerates into a pair of planes, which rotate in opposite directions in the pure strain. Hence either of them may be invariant if the total deformation of the lattice includes a suitable rotation. Because all the vectors in this plane are undistorted, the transformation is said to be an “invariant plane strain (IPS)” type. The pure Bain strain is then equivalent to a simple shear on that invariant plane. Because this invariant plane is also a matching plane between the matrix and the product phase and both phases have to be present at the same time, a rigid body rotation (R) over an angle θ is required in order to bring the product and the parent phases in contact along that plane, the habit plane.

A similar situation is found in structurally less sophisticated systems, namely the f.c.c. to h.c.p. transformation in cobalt. Both phases are close packed and a simple shear on the basal plane transforms the cubic stacking into a hexagonal stacking. Because the atomic distances in the basal plane do not change significantly during the transformation, the plane of simple shear is the plane of contact or the habit plane (HP). This is the case, however, only if there is zero volume change in the transformation, i.e., in the case quoted above if the h.c.p. phase has an ideal axial ratio of 1.633.

The situation becomes more complicated if none of the principal strains is zero, but of mixed sign. To achieve matching along the plane of contact in cases where the two phases coexist, a deformation is needed additional to the pure Bain strain in order to have an invariant plane. Because the final

lattice has already been generated by the Bain strain, this additional strain should be a “lattice-invariant strain”. Slip and twinning in the product phase or in both phases are typical lattice-invariant strains; both deformation modes are shown schematically in Fig. 9-6. The diffusionless phase transformation can in this case be represented by an analog consisting of a pure lattice strain (B), a rigid lattice rotation (R) and an inhomogeneous lattice-invariant deformation (P). The last factor is also associated with a shape change, which macroscopically can be considered as homogeneous. Such a combination is typical of martensite and is discussed in Sec. 9.8.1.4.

In cases where the lattice-invariant shear is twinning (as opposed to faulting or slip), type I twinning, where the twin plane originates from a mirror plane in the parent phase, has been assumed. Otsuka (1986) carefully analyzed for a number of systems the possibility of a type II twinning as an alternative inhomogeneous shear. In type II twinning, the shear direction stems from a two-fold symmetry direction of the parent phase. In a table, Otsuka (1986) compiled all the twinning modes observed in marten-

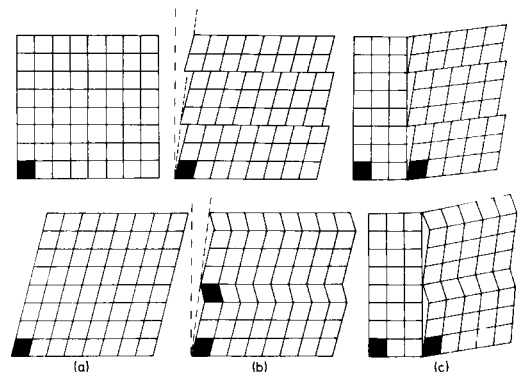


Figure 9-6. Schematic representation of (a) the homogeneous lattice deformation, (b) the inhomogeneous lattice-invariant deformation (slip and twinning), and (c) the lattice rotation.

site and found that most of them are type I or compound but that type II twinning had only recently been observed. According to Nishida and Li (2000), five different twinning modes exist in TiNi and other shape memory alloys such as Cu-Al-Ni, Cu-Sn etc., namely the $\{111\}$ type I, the $\{011\}$ type I, the $\langle 011 \rangle$ type II, the (100)-compound and the (001)-compound twins. Type II twinning has recently received much attention as a mechanism for lattice invariant shear in some alloys. Since type II twins have irrational twin boundaries, the physical meaning of an irrational boundary is still a controversial problem. It has proposed that an irrational boundary consists of rational ledges and steps, the average being irrational. Thereafter, Hara et al. (1998) carried out a careful study to observe $\langle 111 \rangle$ type II twin boundaries in a Cu-Al-Ni alloy by HRTEM, but they could not observe any ledges or steps. The boundary is always associated with dark strain contrast, and the lattice is continuous through the irrational boundary. Nishida and Li (2000) also made extensive studies on $\langle 011 \rangle$ type II twin boundaries in TiNi by HRTEM, but they did not observe ledges or steps either. Based on these experimental results, it is thus most likely that the type II thin boundary is irrational even on a microscopic scale, and the strains at the boundary are elastically relaxed with wide twin width. To confirm this interpretation, Hara

et al. (1998) carried out computer simulations by using the molecular dynamics method. The result showed that the irrational thin boundary did not show any steps. Thus, the above interpretation for an irrational twin boundary is justified. Otsuka and Ren (1999) have pointed out again the importance of type II twinning in the crystallographic aspects of martensite. They also stress the role that martensite aging has on the rubber-like behaviour of martensite, a point that has been a long-standing unsolved problem. They showed that the point defects play a primordial role. The deformation mechanisms of the cold deformation of NiTi martensite have been thoroughly analyzed by Liu et al. (1999a, b). They also found an interplay between type I and type II twinning.

The cubic to tetragonal transformations, which occur in a number of metallic and non-metallic systems, need some special attention. The volume change with these transformations is sometimes very small or even absent, and the c/a ratio does not change abruptly but progressively (Fig. 9-7); the transformation is then said to be “continuous”. The c/a ratio can be smaller or larger than unity, depending on composition and temperature. The shape change associated with the transformation is small enough in many systems, especially in those belonging to the quasi-martensites, for elastic accommodation alone to be suf-

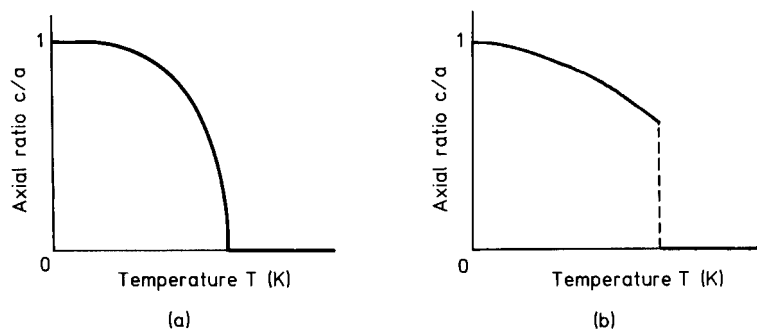


Figure 9-7. Temperature dependence of c/a as measured during the cubic to tetragonal transformation; (a) second and (b) first-order phase transformation.

Table 9-1. A schematic overview of some characteristics typical of the various types of diffusionless phase transformations.

Type of diffusionless transformation	Structural change		Pure lattice deformation		
			Principal strains		Volume change
	type *	order **	Sign	Value	
Shuffle	C or D	F	All zero	Zero	Zero up to 10^{-5}
Dilatational	D	F	All positive or All negative	Large	Large: 10^{-1}
Quasi-martensitic	C or D	F	Mixed sign	Small	Small: $10^{-4} - 10^{-3}$
Martensitic	D	F	Mixed sign or Zero and +, -	Large	Small or large: $10^{-2} - 10^{-1}$

* C: continuous, D: discontinuous

** F: first order, S: second order

ficient for lattice matching. It is, however, possible for c and a to change abruptly with zero volume change.

Based on the crystallographic aspects discussed above, a list of the most typical characteristics of the diffusionless phase transformations can be compiled (Table 9-1).

9.3.2 Pre-transformation State

Diffusionless structural changes are achieved by atom displacements, such as shuffles and shears. The new atomic configuration is already prepared in some material systems at temperatures above the transition temperature. Atoms in the parent phase then become displaced more easily towards their positions in the new phase because the restoring force that is felt by the displaced atoms diminishes on cooling. In certain cases the restoring force even vanishes at the phase transition temperature.

Certain shuffle transformations result from a vibrational instability of the parent phase and are therefore called “softmode”

phase transformations. A soft mode is, in simple terms, a vibrational mode, the square of whose frequency tends toward zero as the temperature approaches that of the phase transition. The average static atom displacements resemble the frozen-in pattern of the vibrational displacements of a certain vibrational mode. According to Vallade (1982), “the crystal lattice vibrations can within the harmonic approximation be separated into independent plane waves (phonons) characterized by a set of collective atomic displacements corresponding to a well defined frequency. The energy involved is a function of the squares of the momentum and of the eigenfrequencies of the mode. The eigenfrequencies depend only on the mass of the atoms and on the force constants. It is clear that the vanishing of one eigenfrequency corresponds to the lack of restoring force for the mode: the amplitude can then grow without any limit and the lattice is mechanically unstable. Stability can be recovered only by changing atomic equilibrium positions which, in turn, changes the force constants”.

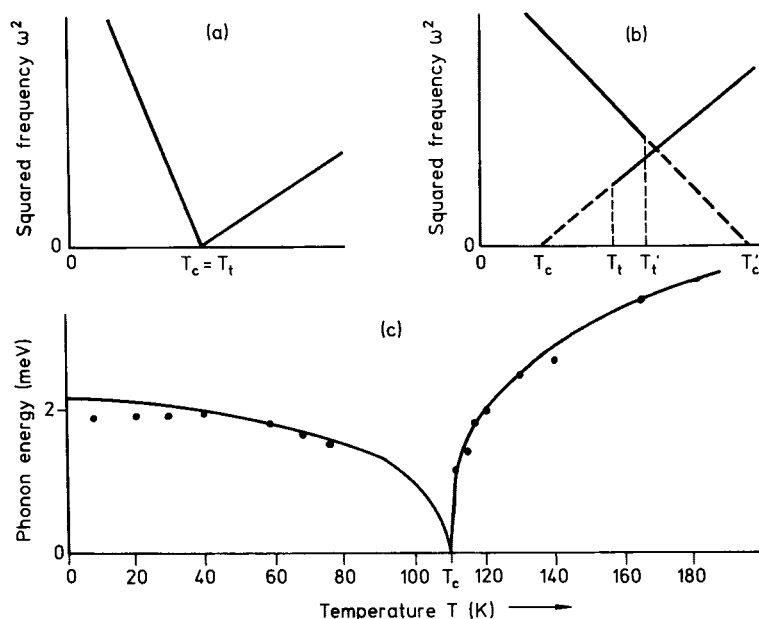


Figure 9-8. Temperature dependence of the squared frequency of the softening mode for (a) a second-order and (b) a first-order transformation, T_c and T_t being the critical and the transformation temperatures, respectively. (c) Phonon energy of SrTiO_3 measured below and above T_c (after Rao and Rao, 1978).

As regards SrTiO_3 , the rotation-vibrational modes of the oxygen atoms are frozen into the low-temperature positions below 110 K. The temperature dependence of the softening, expressed by the square of the eigenfrequency of the mode, is represented schematically in Fig. 9-8 for a second- and first-order phase transformation. Usually, the low-temperature phase also shows a soft mode as the temperature is raised towards T_c .

Lattice softening can also be treated in terms of a static approach in which the stability of the lattice is examined when submitted to small static or quasi-static homogeneous strains. The free energy is then expressed as a function of the elastic constants; for a lattice to be stable when submitted to small homogeneous strains, the free elastic energy must increase for all possible strains. For a cubic crystal this is mathematically expressed by saying that all the eigenvalues of the elasticity tensor must be positive, in other words $C_{44} > 0$, $(C_{11} - C_{12}) > 0$, and $(C_{11} + 2C_{12}) > 0$.

The tendency toward mechanical instability can also be studied through examination of the phonon dispersion curves, which gives the relationship between the wavevector \mathbf{q} of the vibrational mode and its eigenfrequency. The lattice instability can correspond to uniform ($\mathbf{q} = 0$) or modulated ($\mathbf{q} = \text{non-zero}$) atom displacements and the soft phonon may belong to an optic or an acoustic branch; an example of a measured dispersion curve is given in Fig. 9-9. The longitudinal acoustic branch in zirconium shows a dip at about $2/3$ [111], which is the mode needed to transform the high-temperature b.c.c. structure of Zr into the omega structure. The slope of the transverse acoustic branch of Nb_3Sn is very flat at the origin on approaching the transition temperature of 46 K (Shapiro, 1981). This corresponds fairly well with the experimental observation of a vanishing value of the elastic shear constant $C' = (C_{11} - C_{12})/2$. The atom displacements induced by this soft mode coincide exactly with those associated with the deformation from cubic

to tetragonal structure. For Cu–Zn–Al no soft mode is present at $2/3$ $[111]$, although the LA branch shows an anomalous dip; the branch measured perpendicular to it proves that the point in the reciprocal space is a saddle point and not a minimum. The branch TA2 $[110]$ (polarization $[1\bar{1}0]$), however, shows a small slope corresponding to a low value of C' (Guénin 1982). Transformation models have been proposed for Cu–Zn–Al taking into account both the anomalous dip and the small slope.

In a number of materials undergoing a cubic to tetragonal transformation, a tweed-like pattern is observed in the parent phase by transmission electron microscopy. This tweed contrast is characterized by a $\langle 100 \rangle$ direction of the modulation, a type of $\{110\}$ $\langle 1\bar{1}0 \rangle$ shear strain and a modulation which is incommensurate with the parent phase. It is still debated whether all the pre-transformational or precursor effects are evidence of stable or metastable modulated phases or whether they are well-defined artefacts determined by the kinetics of nucleation and the growth process.

A long-standing issue with β Cu-, Ag- and Au-base alloys that has now been resolved is the appearance of extra maxima in the electron diffraction patterns of the parent phase from quenched alloys. Over the years these maxima have been given various interpretations, often with an over-emphasis as possible pre-martensitic effects. Systematic investigation, however, established that these effects are in fact obtained in martensitic structures located on the surface of the thin foil and extending inwards to a depth of 1 μm .

When considering martensitic transformations, the role played by the combination of lattice defects and of lattice instabilities is of particular interest; the large deformations present around the defects may in-

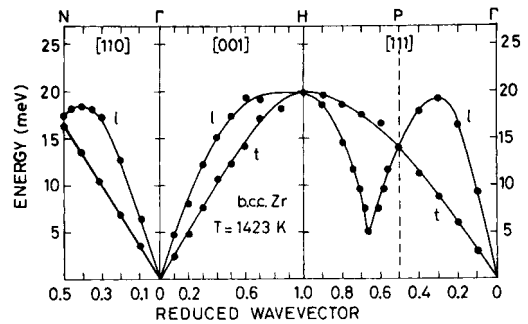


Figure 9-9. Phonon dispersion curves for b.c.c. Zr. A pronounced dip occurs in the longitudinal (l) phonon dispersion curve in the vicinity of $q = 2/3$ $[111]$ (Sikka et al., 1982).

duce a localized lattice instability (Guénin and Gobin, 1982), which may trigger the nucleation of martensite on further cooling or stressing.

Pre-transformational lattice instabilities and soft modes and their relation to diffusionless phase transformations have been reviewed by Delaey et al. (1979), Nakaniishi (1979), Vallade (1982), Nakanishi et al. (1982), and Barsch and Krumhansl (1988). The validity of the soft phonon or soft elastic stiffness approach to martensite is a difficult and somewhat controversial subject.

9.3.3 Transformation Mechanisms

It should be emphasized that the pure lattice distortions considered above do not necessarily imply the actual path the atoms follow during the transformation. For second-order phase transformations, there is a continuous change throughout the crystal with decreasing temperature starting at T_c . Following the soft-mode concept, the appearance of the new phase is considered as the freezing of a particular wavelength vibration. The Bain-type strain for a second-order cubic to tetragonal transformation, for example, is equivalent to two $\{110\}$ $\langle 1\bar{1}0 \rangle$ shear strains whose corresponding C'

shear constant vanishes at T_c . The transformation mechanism is therefore not a combination of expanding and contracting atom movements, but a lock-in of long-wavelength shear-type movements on $\{110\}$ planes in the $\langle 1\bar{1}0 \rangle$ directions in this scheme.

As for the martensitic transformations, the situation is not so straightforward. The Bain-type strains are concerned only with the correspondence between initial and final lattices; they do not give the actual observed crystal orientation relationships between them. Based on the experimentally determined orientation relationships, different transformation mechanisms have been proposed, such as shears on the planes and along the directions involved in the orientation relationship. However, these shear mechanisms have been found to be too simple to be consistent with the experimental facts. More recently, a transformation mechanism has been proposed for martensitic transformations of b.c.c. to close-packed structures; a condensing state of some soft phonon modes combined with a homogeneous shear explains the variety of structures that are found. For the same transformations, Ahlers (1974) proposed a two-shear mechanism; the first shear creates the close-packed planes, whereas the close-packed structure is obtained by the second shear.

Martensitic transformations are first-order phase transformations that occur by nucleation and growth. The growth stage generally takes place by the motion of interfaces converting the parent phase to the fully formed product phase. Two types of paths have to be considered for the case of nucleation, the “classical” and the “non-classical” nucleation paths (Olson and Cohen, 1982). The latter involves a continuous change in structure whereas the former involves a nucleus of the same structure as

the fully formed product. The exact mechanisms for the various types of martensitic transformations are still under debate.

9.3.4 Microstructures

The microstructures that result from diffusionless phase transformations show typical features, which are related to the crystallograph of the transformation. The transformation is associated with a reduction in symmetry; consequently, different equivalent orientational states of the product phase are formed. A single crystal of the parent phase thus transforms to a collection of the product-phase crystals, called variants, that are separated by interfaces. The higher the symmetry of the parent phase and the lower the symmetry of the product phase, the greater is the number of equivalent paths of transformation. The number of equivalent orientations or variants is also determined by the symmetry elements that are maintained or broken due to the Bain strain. The collection of variants constitutes the microstructure.

The order of the transformation (whether first or second order) also determines the microstructure: in the former case parent/product or heterophase interfaces in addition to product/product or homophase interfaces are created, whereas in the latter only product/product interfaces are formed. In the former case the first plates formed can grow to a larger extent than those formed later, which can lead, for example, to microstructures with fractal characteristics.

Fig. 9-10 shows a selection of characteristic microstructures obtained through diffusionless phase transformations.

9.3.5 Shape Changes

If we could transform a single crystal of the parent phase into a single crystal of the

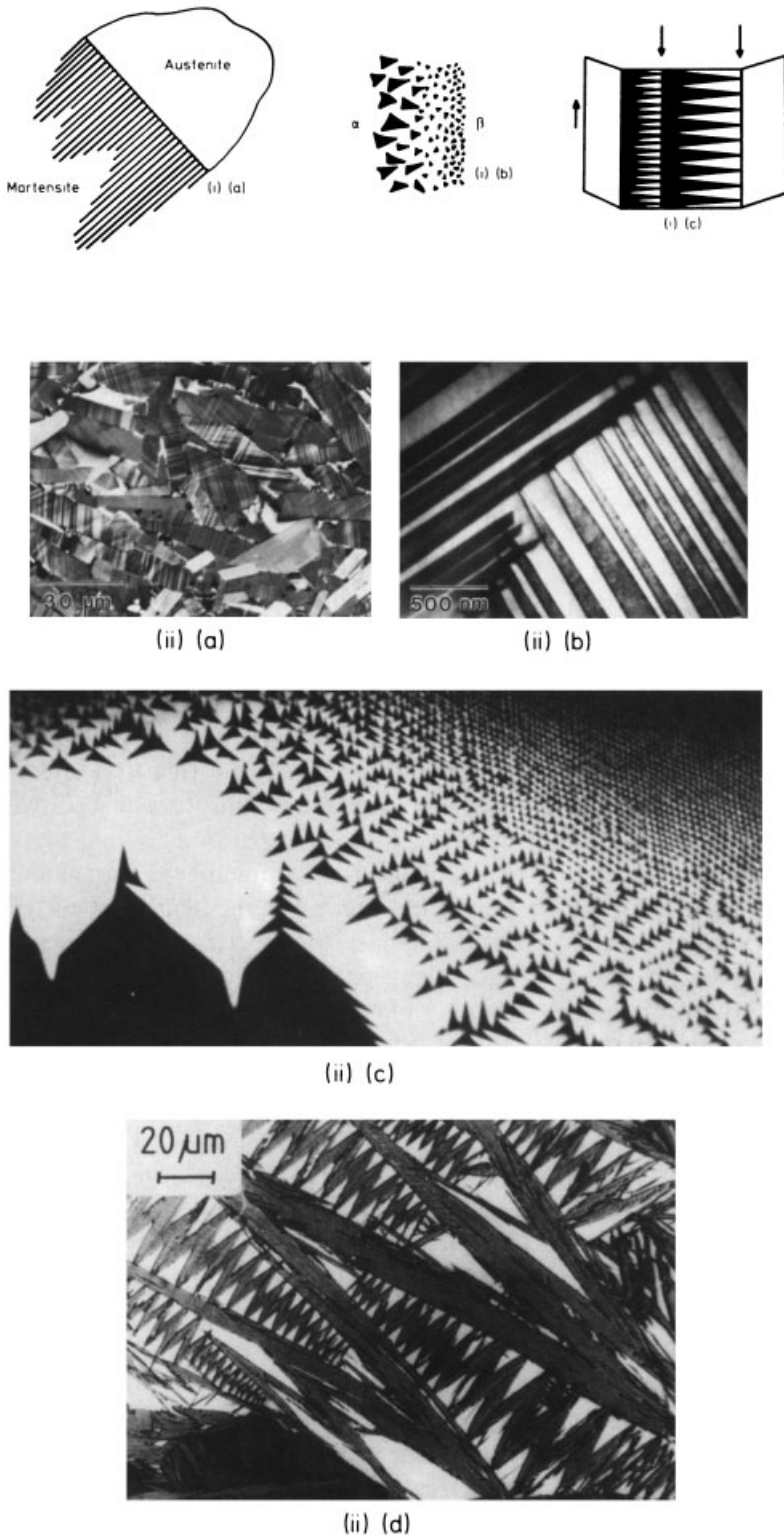


Figure 9-10. A selection of microstructures obtained by diffusionless phase transformations: (i) schematic representation of the microstructure of (a) martensite and austenite, (b) the Dauphiné twins between the low temperature α - and the high temperature β -phase of quartz, and (c) the zig-zag domain structure in neodymium pentaphosphate which undergoes an orthorhombic to monoclinic transformation (after James, 1988); (ii) optical and transmission electron micrographs of (a, b) the twinned orthorhombic $\text{YBa}_2\text{Cu}_3\text{O}_x$ high-temperature superconductor (courtesy H. Warlimont, 1989), (c) the domain in SiO_2 at the transition temperature α to β (846 K) (courtesy Van Tendeloo, 1989), and (d) the fractal nature of the martensite microstructure in steel (courtesy Hornbogen, 1989).

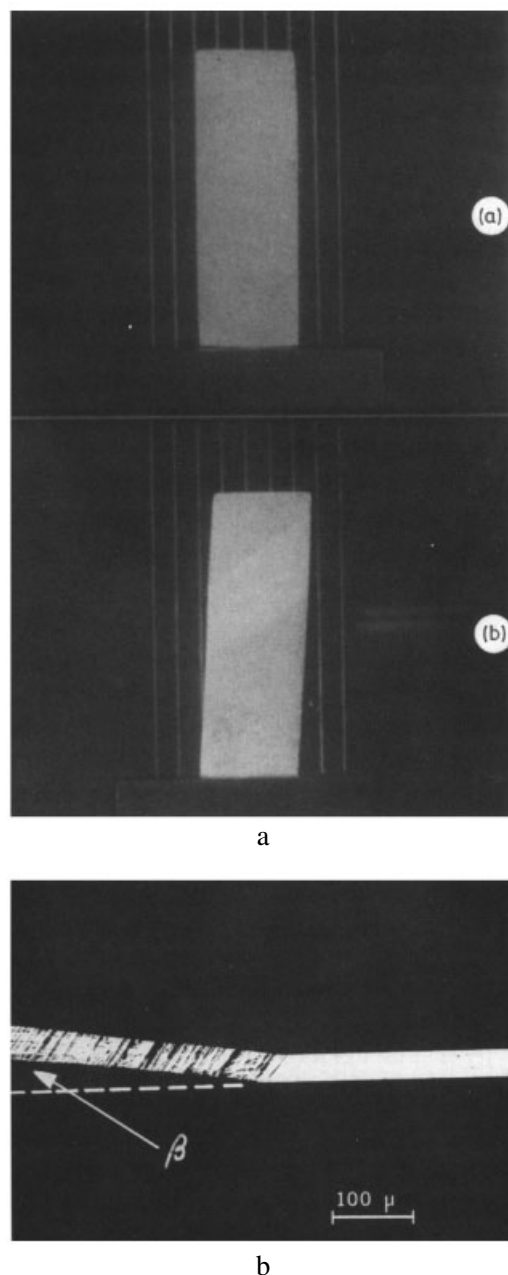


Figure 9-11. Macroscopic shape change associated with martensite: (a) a Cu–Zn–Al single crystal before and after transforming to martensite and (b) a partially transformed Fe whisker (courtesy Wayman, 1989).

product phase, the macroscopically visible shape change would clearly reflect the Bain-type strain; it is then the maximum transformation-induced shape change that can be achieved. Depending on the symmetry relationship, this deformation can be obtained in as many orientations as product variants exist.

In a martensitic transformation, the macroscopic shape change associated with the formation of a single martensite plate is not only the result of the Bain strain but also of a lattice-invariant deformation. The total macroscopic shape change is mainly a shear deformation along the habit plane of the martensite variant. The martensite plate contains either a large number of stacking faults or has twins inside. It is therefore not a single crystal. If the single martensite plate has twins inside and is subjected after the transformation to an externally applied stress, an additional shape change is obtained by detwinning. Only then is the final product a single crystal of the product phase. Fig. 9-11a shows the changes in shape after transforming a β -Cu–Zn–Al single crystal into a single martensite variant and Fig. 9-11b shows the shape change after partially transforming an iron whisker.

The transformed sample usually contains a very large number of single-product domains arranged in a special configuration. In some systems the domains are arranged such that the shape changes are mutually accommodated. Because each product variant is associated with a differently oriented shape change, applying a mechanical stress during the transformation will promote the formation of those variants that accommodate the applied stress. This provides a resolved shape change in the direction of the applied stress. This is the fundamental concept of the shape-memory effect, as will be explained further in Sec. 9.10.2.

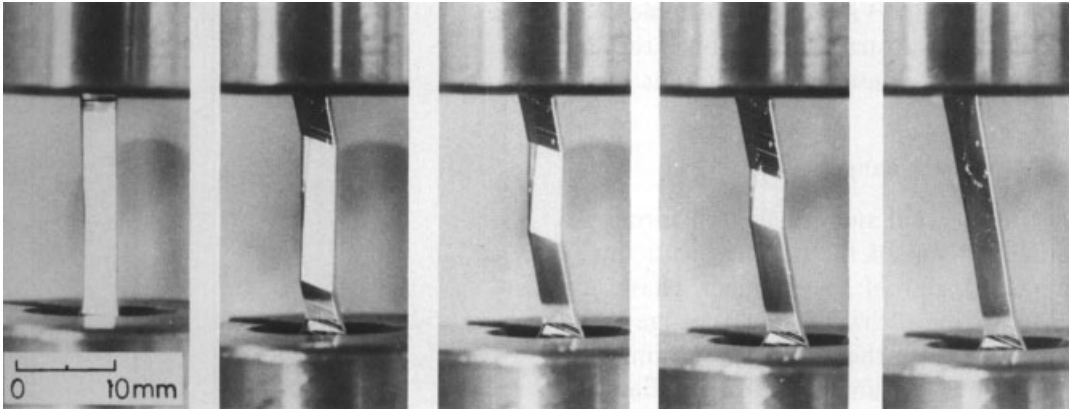


Figure 9-12. A series of macrographs representing the shape change while mechanically straining a Cu–Al–Ni martensite single crystal; (a) to (e) increasing with time (Ichinose et al., 1985).

If a single crystal of the product phase is mechanically strained it can either be transformed to another or be deformed to a differently oriented single crystal of the product phase (Fig. 9-12). Similar behaviour is also typical of a number of ferroelastic materials; the reorientation is there referred to as “switching” (Wadhawan, 1982). The switching force in these materials is not only a mechanical stress but can also be an electric or magnetic field, the domains being either electrically or magnetically polarized.

In first-order phase transformations, as shown above, the full transformation shape change is induced locally and is gradually spread over the whole sample within a small temperature interval, whereas in a second-order phase transformation the sample changes its shape homogeneously and continuously as soon as the critical transition temperature T_c is reached.

Until now, shape changes have been discussed that are induced by the forward transformation. It is evident that if a sample of the low-temperature phase, a single crystal or a polyvariant, is heated to temperatures above the reverse transformation

temperature, similar shape changes are observed, provided that the reverse transformation is also diffusionless. The situation for second-order phase transformations is straightforward; the sample whose shape is changed during the forward transformation and possibly after deformation below T_c reverts back to its original shape above T_c in a homogeneous and continuous way. For first-order transformations, the reverse transformation is more complex and not yet well understood. Much depends on whether the forward transformation is completed or not, and whether the growth of the martensite plate occurs by bursts or under thermoelastic conditions (see below). Occurrence of the reverse transformation does not necessarily imply that the original shape is restored. Depending on the crystal symmetry of the product phase, more than one crystallographically equivalent path can be followed for the reverse transformation. The shape changes that occur during the reverse transformation are at the origin of the shape-memory effect and are discussed in Sec. 9.10.2.

9.3.6 Transformation Thermodynamics and Kinetics

A diffusionless phase transformation may be of second or first order. The former is generally dealt with in the phenomenological Landau theory, while the latter is treated by classical thermodynamics (Kaufman and Cohen, 1958). The Landau theory has, however, been extended to also cover first-order phase transformations (the Devonshire–Ginzburg–Landau theory) and has been applied by Falk (1982) to martensitic transformations. The reader is referred to the chapter by Binder (2001) for an introduction to those theories.

The chemical driving force occupies a key position in the classical thermodynamics of first-order diffusionless phase transformations, a subject that is introduced in the first chapter of this volume (Pelton, 2001). In the following section, therefore, only those aspects directly relevant to diffusionless phase transformations will be dealt with.

Because no chemical composition change is associated with a diffusionless phase transformation, the parent and product phases have the same homogeneous chemical composition and hence they are treated as a single-component system. For those phase transformations whose structural change is easily described by a displacement parameter, a phenomenological description of the free energy as a function of the order parameter in terms of the Landau theory leads to some interesting conclusions. In the following, the free energy is discussed as a function of temperature and composition. Other possible intensive thermodynamic state variables include external pressure, mechanical stress, and magnetic and electrical field strength.

The changes in chemical Gibbs energy, ΔG , as a function of temperature and composition are shown schematically in Fig.

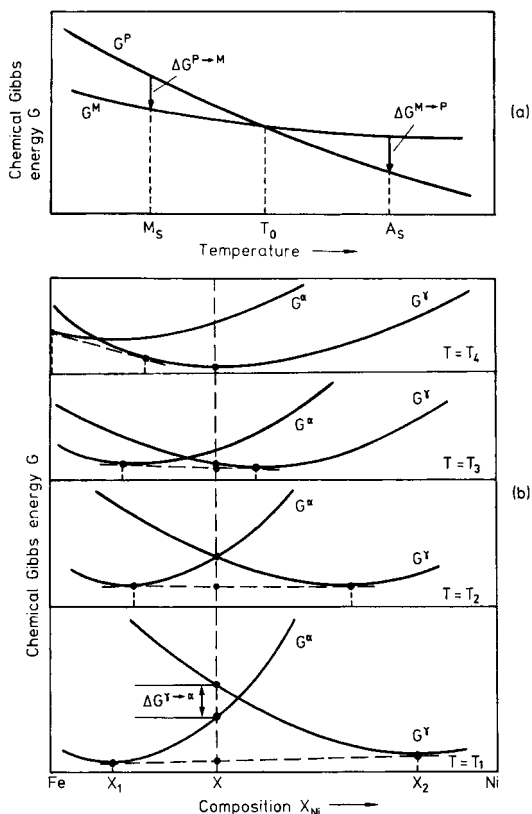


Figure 9-13. Schematic representation of the molar Gibbs energy (a) as a function of temperature but constant composition and (b) as a function of composition for an Fe–Ni alloy with $T_4 > T_3 > T_2 > T_1$ and $T_2 = T_0$ for $X_{Ni} = X$ (after Mukherjee, 1982).

9-13 for first-order diffusionless phase transformations between a parent phase, denoted P, and a product phase, denoted M. The product phase may be one of the low-temperature equilibrium phases or a metastable phase.

Taking again the martensitic transformation as an example, the transformation starts at M_s , which is lower than T_0 , and finishes at M_f . This means that a higher driving force is needed to complete the transformation. On heating a fully martensitic stress-free single crystal, the reverse transformation sets in at a temperature A_s ,

which is higher than T_0 . The difference between the forward and the reverse transformation temperatures is the transformation hysteresis. The true first-order equilibrium temperature, T_0 , which is calculated from $\Delta G = 0$, can thus only be bracketed from experimental data for the forward and the reverse transformation temperatures, and is not necessarily halfway between M_s and A_s .

Strain energy resulting from the transformational shape change and interfacial energy have been omitted from the free-energy curves in Fig. 9-13. These two non-chemical-energy terms have to be considered, however, in the overall free-energy balance. The strain energy associated with the formation of a single domain of the product phase is proportional to the volume of that domain. The interfacial energy is not directly related to the volume of the transformed domain but merely to its surface-to-volume ratio, and, in the case of an anisotropic interfacial energy, also to the orientation of the interface. Both quantities are positive and thus consume part of the chemical driving force for a forward transformation. Both terms will, however, increase the driving force for the reverse transformation, provided that the interfacial coherence is not lost. The reverse transformation might start below T_0 if a negligible net driving force is required for nucleation.

Considering the Gibbs energy per unit molar volume, the total Gibbs energy change per unit molar volume for the formation of a single domain of the product phase embedded in the matrix phase is given by

$$\Delta G_{\text{tot}} = \Delta G_{\text{chem}} + (\Delta G_{\text{elast}} + \phi \Delta G_{\text{surf}}) \quad (9-3)$$

where ϕ is the surface-to-volume ratio of the single domain. The two terms in parentheses are then the non-chemical con-

tributions to the Gibbs energy change, $\Delta G_{\text{non-chem}}$, and Eq. (9-3) then becomes

$$\Delta G_{\text{tot}} = \Delta G_{\text{chem}} + \Delta G_{\text{non-chem}} \quad (9-4)$$

The transformation then proceeds until ΔG_{tot} becomes minimum or, if the phase boundary is mobile, until the total force at the parent-to-product interface is zero. If the advancing direction of the interface is x , we can write

$$[\partial (\Delta G_{\text{tot}}) / \partial x] dx = 0 \quad (9-5)$$

or

$$[\partial \Delta G_{\text{chem}} / \partial x] dx + [\partial \Delta G_{\text{non-chem}} / \partial x] dx = 0$$

The sum of the non-chemical restoring forces is then identical with the chemical driving forces. The difficult task now is to find expressions representing the non-chemical terms. Three thermodynamic approaches have been worked out, dealing essentially with the influence of the two non-chemical contributions on the transformation behavior (Roitburd, 1988; Ball and James, 1988; Shibata and Ono, 1975, 1977).

According to Roitburd (1988), the strain energy, which arises in crystals owing to a diffusionless phase transformation, can decrease if the crystals are subdivided into domains arranged such that a maximum compensation of the individual strain fields is achieved. In order to determine which arrangements are energetically most favorable, Roitburd calculates the strain energy for arbitrary domain arrangements, and then minimizes this energy. The formulation of this problem is complex and can hardly be solved in general, but he succeeded for some specific cases.

Ball and James (1988) do not assume any geometric restrictions on the shape or arrangements of the domains; they found this necessary to determine microstructures occurring in complex stress fields, or to explore new and unusual domain arrange-

ments. The general aim of their work was to develop mathematical models, using calculus of variations, capable of predicting the microstructure, especially the microstructural details at the interface between the parent and the product phases. Attempts have been made to predict the possible interfaces between austenite and martensite from a minimization of a Gibbs energy function, which depends on the deformation gradients of all possible domain variants and on temperature. A deformation or domain is then termed stable if it minimizes the total energy. They show, among others, that a martensite–austenite interface can exist as an energy-minimizing sequence of very fine twins. A further example of an intriguing application is the formation of triangular Dauphiné twins in quartz, which become finer and finer in the direction of increasing temperature. A Gibbs energy function accounting for this behaviour could be constructed.

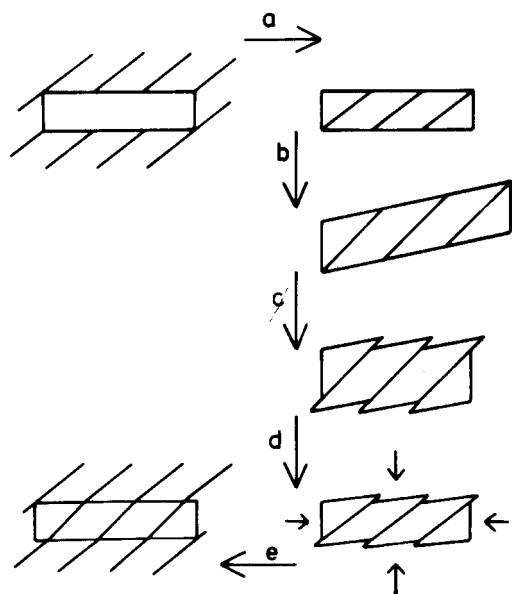


Figure 9-14. The necessary steps in calculating the elastic stresses induced by a transforming ellipsoid (Christian, 1976). (For details see text.)

Shibata and One (1975, 1977) use the Eshelby theory; the principle of their calculation is in a corrected version (Christian, 1976) illustrated schematically in Fig. 9-14. An embedded part of the parent phase is cut out (step a) and is allowed to transform stress-free into the product phase (step b). A lattice-invariant deformation is applied (step c) and the transformed crystal is subjected to forces along its surface such that it is deformed to the original shape (step d). The thus deformed part of the product phase is introduced in the empty space of the parent phase (step e), and the forces are removed, creating internal stresses in both the product and the parent phase. The total energy is then calculated as a function of all possible lattice orientations, taking into account the actual elastic constants and the modes of lattice-invariant deformation, twinning or slip.

The total Gibbs energy of the system is therefore a function not only of the intrinsic energies of the stress- and defect-free parent and product phases, but also of the arrangement of the domains. The non-chemical component of the total Gibbs energy of the transforming system is lowered by an appropriate rearrangement of the microstructure and/or by irreversible plastic deformation.

If the structural change can be represented by an order parameter e , the Gibbs energy of the system can then, according to the theory of Landau–Devonshire, be represented by

$$G = G_0 + a(T - T_1)e^2 - Be^4 + Ce^6 \quad (9-6)$$

where a , B and C are constants and $T_1 > 0$. It can be shown that the high-temperature phase becomes unstable with respect to any fluctuation of e , as soon as the temperature reaches T_1 on cooling, and hence is thermodynamically metastable between T_0 and T_1 . Accordingly, the low-temperature

phase cannot exist at temperatures higher than T_2 , which is the temperature above which the low-temperature phase becomes unstable with respect to any fluctuation in e .

That additional undercooling is needed for further transformation below M_s is due (in part) to the non-chemical contributions, which increase with increasing volume fraction of transformed product.

An interesting aspect of the diffusionless phase transformations that are accompanied by a volume and shape change is the role played by external stresses, e.g., hydrostatic or uniaxial. Both thermodynamics and experiments show that the transformation temperatures are affected by the application of stresses. According to Wollants et al. (1979), the relationship between a uniaxially applied stress σ and the transformation temperature T depends on the transformation entropy and the transformational strain in the direction of the applied stress. This relationship, the Clausius–Clapeyron equation for uniaxially stressed diffusionless first-order phase transformations, is

$$d\sigma/dT = -\Delta S/\varepsilon = -\Delta H^*/[T_0(\sigma)\varepsilon] \quad (9-7)$$

where $\Delta H^* = \Delta H - F\Delta l = \Delta H - \sigma\varepsilon V_m = T_0(\sigma)\Delta S$ is itself a function of the applied load, $\varepsilon = \Delta l/l$, l is the total “molar length” of the sample, and F is the applied load ($\sigma = F/A$). This equation is similar to that relating the equilibrium temperature to the hydrostatic pressure, except for the negative sign on the right-hand side of Eq. (9-7). This relationship between $d\sigma$ and dT is experimentally constant for most of the diffusionless transformations, which means that the thermodynamic quantity ΔS is, within the experimental scatter, independent of temperature and stress. Knowing the transformation strain, uniaxial tensile tests are very useful for determining the transformation entropy.

The most relevant thermodynamic data for the various diffusionless phase transformations are presented in Table 9-2.

9.4 Shuffle Transformations

Shuffle transformations from a distinct class of diffusionless phase transitions. At the unit-cell level the atom displacements are intercellular with little or no pure strain of the lattice. The role of elastic strain energy in shuffle-phase transformations is sufficiently small that the transformation can either occur continuously from the parent to the product phase or that it is completely controlled by interfacial energy. In the former case the transformation is second order whereas in the latter it is a first-order phase transformation.

Cohen et al. (1979) gave three examples which clearly illustrate the shuffle transformations. The displacive transformation in strontium titanate is the prototype example of a pure shuffle transformation. The associated strain energy is so small that the transformation occurs continuously. The β -to- ω transformation in some Ti and Zr alloys shows, in addition to the shuffle displacements, small homogeneous lattice distortions. These distortions are small enough for the transformation mechanism and the resulting microstructure to be dominated only by shuffling. In ferroelectric transformations, which are accomplished by shuffling, the interfacial energy is constituted largely by electrostatic interaction energies and is therefore dependent on the orientation of the domain interfaces. The interfacial energy in those materials is strongly anisotropic and controls the poly-domain structure.

Phase transformations that can be entirely described by shuffle displacements are often found where the change in crystal

Table 9-2. The elastic shear constant and some thermodynamic data characterizing the diffusionless phase transformation (Delaey et al., 1982b).

	Elastic shear constant C' near the M_s temperature		Trans- formation strain	Thermodynamic quantities			
	C' (10^{10} Pa)	$(1/C') (dC'/dT)$ (10^{-4} K $^{-1}$)		Heat of transformation (J/mol)	Change in entropy (J/(K · mol))	Chemical driving force (J/mol)	Transformation temperature hys- teresis (K)
Ferrous $\gamma \rightarrow \alpha'$ $\gamma \rightarrow \epsilon$	2–3	negative 3–10 (positive for Ni > 30%)	$\approx 10^{-1}$	$\approx 2000\text{--}300$	5.8	150–450 600–1800	200–400
Co alloys rare-earth alloys		negative	$\approx 10^{-3}$	$\approx 400\text{--}500$	≈ 0.2	4–16	40–80
Ti and Zr alloys	0.1	negative	$\approx 2 \times 10^{-2}$	≈ 4000	≈ 1.0	≈ 25	–
β Cu–Ag–Au alloys	0.5–1	4–20 (positive)	$\approx 10^{-2}$	$\approx 160\text{--}800$	0.2–3.0	$\approx 8\text{--}20$	10–50
In alloys	0.05–01	≈ 1000 (positive)	$\approx 10^{-3}$	≈ 0	–	≈ 1.5	1–10
Mn alloys		positive (strongly)	$\approx 10^{-3}$				
A 15 com- pounds	0.5	$\approx 1000\text{--}3000$ (positive)	$\approx 10^{-4}$				
Fe–Pt				≈ 320 (ordered)	–	≈ 16 (ordered)	$\approx 20\text{--}200$
Fe–Pd alloys	≈ 1	≈ 100 (positive)	$\approx 10^{-3}$ $\text{--}10^{-2}$	≈ 1200 (disordered)		≈ 1200 (disordered)	

structure is such that the point group to which the crystal structure of the product phase belongs is a subgroup of that of the parent phase. In other words, some symmetry elements of the high-temperature phase are lost on cooling below the transition temperature T_c . Because of this group/subgroup relationship, the product phase possesses two or more equally stable orientational states in the absence of any external field. The change in crystal structure can easily be described by an order parameter which itself is related to the shuffle dis-

placement. For strontium titanate, the order parameter would then simply be the rotation angle that describes the displacement of the oxygen atoms around the titanium atoms (see Fig. 9-4). For convenience, the order parameter is taken as zero for the high-temperature configuration and as non-zero for the low-temperature phase. The majority of such transitions are found in chemical compounds (e.g., Rao and Rao, 1978). As soon as the critical temperature T_c is reached on cooling, the order parameter changes continuously. The thermody-

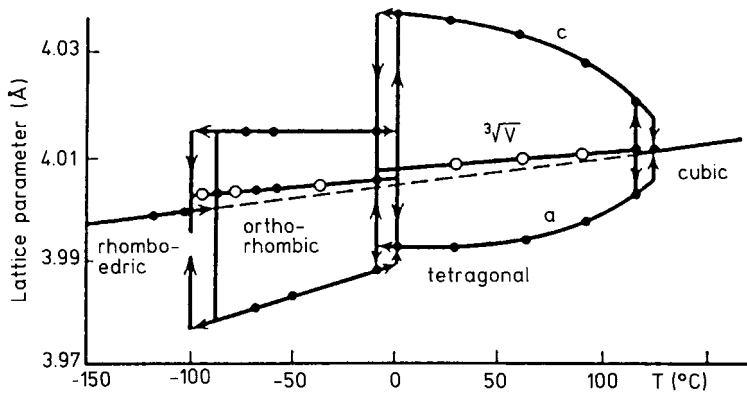


Figure 9-15. Temperature dependences of the lattice parameters of the different phases of BaTiO_3 .

namics of such transformations are then in the temperature range close to T_c , which is dealt with by a Landau approach.

9.4.1 Ferroic Transformations

Usually a phase transition that is dominated by shuffling is associated with a change in some physical properties, such as spontaneous electrical polarization, strain and magnetization. Because the crystal symmetry of the parent phase decreases during the phase transition, two or more equivalent configurations of the product phase are formed. In the absence of any external field, the average polarization of the product phase is zero. However, under a suitably chosen driving force, which may be an electrical field (E), a mechanical stress (σ), or a magnetic field (H), the domain walls of the product phase move, switching the crystal from one domain orientation to the other. Owing to the application of a uniaxial stress, for example, one orientation state can be transformed reproducibly into the other, and the crystal is then said to be “ferroelastic”. The materials exhibiting this property are called ferroelastic materials. Similarly, we can define ferroelectric and ferromagnetic materials. According to Wadhawan (1982), “phase transitions accompanied by a change of the

point-group symmetry are called *ferroic* phase transitions. We refer to a crystal as being in a ferroic phase if that phase results from a symmetry-lowering ferroic phase transition”.

Not all ferroelastic phase transitions belong to shuffle transformations as defined in Fig. 9-1. Indeed, in addition to shuffle displacements, as for example those involved in the cubic to tetragonal transition in barium titanate, the lattice may become homogeneously distorted. For the example considered here, the lattice distortion occurs discontinuously at the transition temperature; the lattice parameters change abruptly (Fig. 9-15). Even below this transition temperature, the lattice continues to be homogeneously distorted. In cases where this lattice is tetragonal, the c/a ratio steadily increases. For barium titanate the change in c/a continues until the temperature for another first-order phase transition is reached. Many such phase transformations are encountered in chemical compounds. In some cases the amount of spontaneous strain is not large enough to control the microstructure. In others, the strain energy associated with the transformation will be dominant. The transformation is then, according to Fig. 9-1, quasi-martensitic or martensitic. In ferroelectric materials, the interfacial energy also has to be

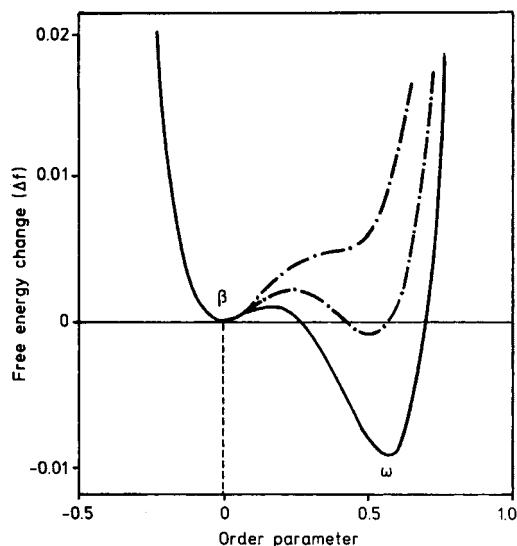


Figure 9-16. Gibbs energy change for the b.c.c. to ω transformation as a function of the order parameter for various reduced temperatures (after de Fontaine, 1973).

taken into account and may even become the dominant parameter controlling the microstructure. A ferroic ferroelastic phase transformation can thus be a shuffle, a quasi-martensitic, or a martensitic phase transformation, a clear discrimination is only possible by analyzing all the transformation characteristics, and this not after but during the transformation.

9.4.2 Omega Transformations

The omega transformation is known to occur as a metastable hexagonal or trigonal phase in certain Ti, Zr and Hf alloys on cooling from the high-temperature b.c.c β -phase solid solution or as a stable phase under the influence of high hydrostatic pressures or shock waves. The ω -phase cannot be suppressed by quenching and forms as small cuboidal or ellipsoidal particles with a diameter of 10–20 nm. Its lattice is obtained by collapse of one pair of (111) planes of the parent b.c.c. β -phase,

leaving the two adjacent planes unaltered (Fig. 9-4b). The collapse can be represented as a short-wavelength displacement of atoms. The displacement of the atoms occurs over a distance approximately equal to $2/3 \langle 111 \rangle$. Each lattice site can thus be associated with a forward, zero or backward displacement that can be represented by a sinusoidal wave dividing the repeat distance along a [111] direction into six parts. The collapse is not always complete, and then results in a “rumpled” plane. If the collapse is incomplete the crystal structure of the ω -phase is trigonal; if the collapse is complete, it is hexagonal. The figure also shows that reversing the direction of the displacement will not lead to a collapse of the {111} planes. Moreover, it can be shown that a $2/3$ [111] displacement wave is equivalent to a $1/3$ $[\bar{1}12]$ displacement wave.

If the displacement is taken as the order parameter in a Landau-type approach, the transformation is seen to be first order and the Gibbs energy as a function of this order parameter has an asymmetric shape. Consequently, no negative values of the order parameter are then allowed (Fig. 9-16). The β -to- ω transformation can also be paraphrased in terms of a soft mode. The lattice tends to a mechanical instability for a $2/3 \langle 111 \rangle$ longitudinal mode. This tendency can be shown when measuring the phonon dispersion curves by inelastic neutron scattering. Such curves are reproduced in Fig. 9-9a for zirconium; a clear dip is visible at the $2/3$ [111] position.

The omega transformation has been reviewed by Sikka et al. (1982).

9.5 Dilatation-Dominant Transformations

A transformation is regarded by Cohen et al. (1979) as dilatation dominant if no

undistorted line can be found in the lattice-distortive deformation. The f.c.c.-to-f.c.c.' transformation in cerium is considered as the prototype for a dilatational dominant transformation. Below 100 K cerium undergoes a pure volume contraction of about 16%; the ellipsoid of the f.c.c.' phase thus falls completely inside that of the high-temperature f.c.c. phase. The low-temperature cubic to tetragonal transformation in tin also appears to be dominated by dilatation, although some deviatoric components are present; the volume expansion is about 27%. The deviatoric component is not large enough to let the original sphere intersect with the dilated ellipsoid.

The name "dilatational diffusionless phase transformation" has been used by Buerger (1951) but with a different meaning. In the systems he considers, for example the CsCl-to-NaCl transitions in many alkali metal halides, he defines the term dilatational as follows: "the transformation can be achieved by a differential dilatation in which the structure expands along the trigonal axis and contracts at right-angles to the axis". Although the volume change in these and other related inorganic systems may be very large (up to 17%), the transformation is, in the context of Fig. 9-1, clearly not dilatation dominant but deviatoric dominant. See Kriven (1982) for a more detailed review of these dilatational dominant transformations.

9.6 Quasi-Martensitic Transformations

The quasi-martensitic and the martensitic transformation are both deviatoric dominant and are characterized by an undistorted line. The morphologies of the product phases of the two transformations

are very similar (large plates, occurrence of variants and twins). A distinction between the two transformations cannot be made by simply judging only the product morphology, but rather a knowledge is required of the morphological relationships between parent and product phases during the transformation itself. It may be adequate to say first what a quasi-martensitic transformation is: a quasi-martensitic transformation is not a martensitic transformation, which itself is "a first-order phase transformation, that undergoes nucleation, passes through a two-phase mixture of the parent and product phases, and which product grows with a transformation front in a plate-like or lath-like shape being indicative of a tendency toward an invariant-plane interface" (Cohen et al., 1979). If a deviatoric dominant transformation does not satisfy the above criterion, it should not be designated as martensitic but as quasi-martensitic.

Three aspects are common to most of the materials that transform quasi-martensitically: (1) the lattice distortion is small and deviatoric dominant and the change in lattice distortion is continuous or nearly continuous; (2) a banded internally twinned microstructure gradually builds up on cooling below T_c ; and (3) a mechanical lattice softening is expressed by elastic shear constants approaching zero as T_c is approached. Because of the small lattice distortion at the transformation, the ratio of the strain energy to the driving energy for transformation is small; this ratio has been used by Cohen et al. (1979) as an alternative index to differentiate quasi-martensitic transformations from martensitic.

The three aspects are now illustrated by taking the manganese-based magnetostrictive antiferromagnetic alloys as an example (see Delaey et al., 1982a). One of the four polymorphic states of manganese is the gamma f.c.c. phase which is stable only at

high temperatures. Alloying with elements such as Cu, Ni, Fe, Ge, Pd and Au stabilizes the f.c.c phase and the latter can be retained by quenching. However, owing to the antiferromagnetic ordering, the lattices become homogeneously distorted. This ordering to the Mn atoms starts at a temperature T_N , which is the Néel temperature for the paramagnetic to antiferromagnetic transition. The transformed product phase has a banded microstructure containing fine twins. The temperature at which this banded microstructure is formed does not always coincide with the transformation temperature T_N . Vintaikin et al. (1979) divide these antiferromagnetic alloys into three classes according to the relative positions of the temperature T_N and the temperature T_{TW} . The latter is the temperature at which the banded microstructure sets in. Depending on the type of lattice distortion, the alloys are grouped into three classes, each class being characterized by the relative positions of the two temperatures. A

schematic representation of the phase diagram of the Mn-based alloys is given in Fig. 9-17a, showing the temperature–composition areas in which the various crystal structures and microstructures are observed. The accompanying variation in the lattice parameters as a function of temperature for the three classes of Mn-based alloys is given in Fig. 9-17b.

The changes in lattice parameters show that the transformation is almost second order, except for some alloys of class I and III where the transformation is weakly first order. A phase transformation is called “weakly first order” whenever the height of the discontinuous jump in the corresponding thermodynamic property is very small. The formation of the twinned banded microstructure extends over the entire volume of the sample quasi-instantaneously and is visible in polarized light because of the non-cubic structure of the product phase. Similar microstructures are observed in other quasi-martensitic product phases such as $V_{54-x}Ru_{46}Os_x$ (Oota and Müller, 1987). The microstructure, if properly oriented with respect to the prepolished surface, exhibits a surface relief effect that is enhanced as the temperature decreases below T_{TW} . This surface relief proves that the transformation is accompanied by a shape change associated with each domain. Because of the continuously changing lattice parameters, accommodation stresses are built up as the temperature decreases. An appropriate arrangement of these domains reduces the overall stored elastic energy; further changes in microstructure are therefore expected to occur even below the transition temperature.

Class II alloys do not exhibit the twinned banded microstructure immediately below T_N . In the temperature region between T_N and T_{TW} , broadening of some of the X-ray diffraction peaks is observed, which is

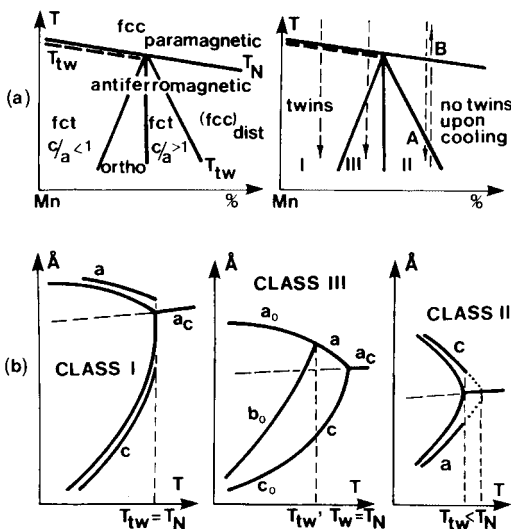


Figure 9-17. Schematic representation of (a) the phase diagram and (b) the variation of the lattice parameters for the three classes of Mn-based alloys (Delaey et al., 1982a).

attributable to a chaotic distribution of the a and c axes with small undercooling. At T_{TW} the banded structure becomes visible (point A in Fig. 9-17) and a tetragonal structure can now be clearly detected by X-ray diffraction. If the sample is now heated, only the banded microstructure disappears, not at A but at a temperature B that coincides with the Néel temperature. This proves that on cooling, very small, submicroscopic tetragonal regions are first formed as soon as T_N is reached. Hocke and Warlimont (1977) have shown that when the distortion $|c/a - 1|$ becomes greater than 0.005, a critical value is obtained at which the elastic strain is relaxed through coalescence of the small distorted regions into large banded twinned regions. Thus, at T_{TW} there is not a phase transformation but a stress relaxation in the microstructure, which results in a twinned microstructure. The lattice distortive phase transformation itself occurs at T_N , followed immediately (class I) or after some undercooling (class II) by a domain rearrangement and macroscopic twinning.

Similar conclusions can be drawn for other quasi-martensitic transformations, as for example in the iron–palladium alloys; the Pd-rich f.c.c. phase transforms on cooling first to an f.c.t phase and at lower temperatures to a b.c.t. phase. The f.c.c.-to-f.c.t. transformation, although sometimes regarded as martensitic, shows all the characteristics of a quasi-martensitic transformation.

Because the formation of each single domain is associated with a shape change and thus with accommodation stresses, the application of an external stress to the transformed product will result in a macroscopic shape change. As the domain boundaries, which for the Mn-based alloys coincide with the antiferromagnetic boundaries, are mobile, the banded structure will

gradually disappear and the product phase becomes a single domain maximizing the shape change. The shape change thus obtained is gradually recovered on heating the sample and is completely recovered at T_N and not (as in the case of Mn-based alloys of class II) at T_{TW} , but at the point B in Fig. 9-17. The quasi-martensitic alloys thus also exhibit the shape-memory effect.

Some of the materials characterized by shuffle displacements during the phase transition may develop elastic strains as transformation proceeds. As in ferroelectrics, for example, in addition to the elastic strain energy, the dipole interaction energy also contributes to the polydomain formation. If the elastic strain energies are only slightly dominating, the transformation is quasi-martensitic; if, however, the elastic strain energy is largely dominating, the transformation can be martensitic.

Sometimes it becomes difficult to differentiate between martensite and quasi-martensite, as for example in In-based alloys. In particular, if quasi-martensitic samples are cooled in such a way that a temperature gradient is created across the sample, the product phase and the parent phase then coexist and apparently the transformation goes through a two-phase region, the two regions being separated by a blurred or planar interface. Such observations do not, of course, facilitate the distinction between quasi-martensite and true martensite.

9.7 Shear Transformations

In this section we discuss a special group of phase transformations, the so-called shear transformations or polytypic transitions, which strictly belong to the martensitic transformations. According to Verma and Krishna (1966), “polytypism may be defined, in general, as the ability of a sub-

stance to crystallize into a number of different modifications, in all of which two dimensions of the unit cell are the same while the third is a variable integral multiple of a common unit. The different polytypic modifications can be regarded as built-up of atom layers stacked parallel to each other at constant intervals along the variable dimension. The two unit-cell dimensions parallel to these layers are the same for all the modifications. The third dimension depends on the stacking sequence, but is always an integral multiple of the layer spacing. Different manners of stacking these layers may result in structures having not only different morphologies but even different lattice types and space groups". Some random disorder of layers (faulted sequences) is almost always present. Polytypic transitions are then transitions among different polytypes; the movement of partial dislocations along the basal plane constitutes the transition mechanism, thereafter the name shear transformations. Polytypic transformations are found in a variety of inorganic compounds and also in metals and alloys.

Polytypic phases are constructed by stacking basic units in a cubic, hexagonal or rhombohedral sequence. The stacking sequences are described by three key layer positions, X, Y and Z; a cubic sequence (C) is represented by the sequence XYZXYZ ..., a hexagonal (H) by, for example, XYXZ ... or XYXZXYXZ ..., and a rhombohedral (R) by, for example, XYZYZXZXYXZYZXZXY Many other stacking variants are possible and unit cells containing as many as 126 or 144 layers have been reported. Each unit itself can contain a single layer, as in cobalt and its alloys, or two as in silicon carbide.

Transitions between different modifications can be achieved either by a simple shear, a shear combined with shuffle dis-

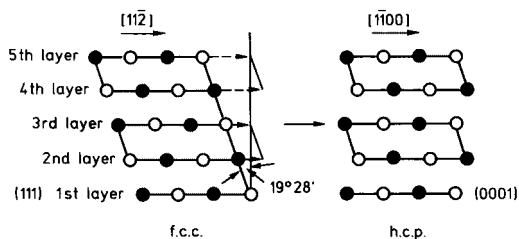


Figure 9-18. Mechanism of the f.c.c.-to-h.c.p. transformation (Nishiyama, 1978).

placements or the movement of partial dislocations along the basal plane. For example, the transition between a 2H and a 3C stacking is easily performed by a shear, whereby the basic units are kept together in pairs (Fig. 9-18). This shear results in a large deviatoric shape change. It should be kept in mind that the interlayer spacing need not be constant, as is observed in the f.c.c.-h.c.p. changes in metals; the transformation may involve small changes and thus be IPS (invariant plane strain) rather than simple shear transitions.

The same transitions can be achieved by the generation and movement of closely spaced and repeatedly arranged partial dislocations. The passage of a positive partial dislocation shifts the crystal in the direction $X \rightarrow Y \rightarrow Z \rightarrow X$ and negative partial dislocations shifts the crystal in the direction $X \rightarrow Z \rightarrow Y \rightarrow X$. The following distribution of partial dislocations on the unit layers in the direction perpendicular to the layers is proposed by Liao and Allen (1982) (a layer without a partial dislocation is denoted by a dot):

- - + · for 2H \rightarrow 4H
- - - - · for 6H \rightarrow 3C

The polytypic shear transformation from one modification to the other is thus accomplished by a coordinated propagation of groups of partials along the interface between the two phases. The lateral dis-

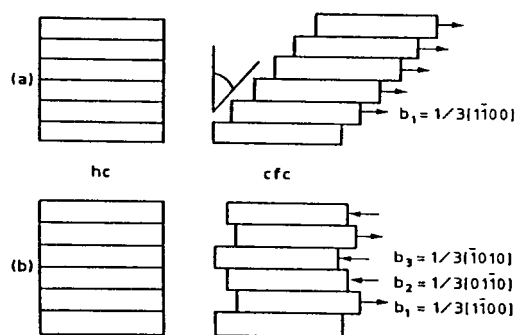


Figure 9-19. Two different mechanisms, (a) and (b), to transform an h.c.p. to an f.c.c. structure (Bidaux, 1988).

placement of the interface, which is the thickening of the new phase generated by the movement of those partials, is then due to the formation of partial dislocations and their outward movement. During the transition from a cubic to a hexagonal 2H sequence, it has been implicitly assumed above that the glide of the layers would always occur in the same direction. There exist, however, three different directions for transforming an X stacked unit into a Z stacked unit. If the glide occurs alternately in these three directions, no shape change results from such a mechanism, as shown in Fig. 9-19 (Bidaux, 1988).

9.8 Martensitic Transformations

The characteristics necessary and sufficient for defining a martensitic transformation are (a) displaciveness of the lattice-distortive type involving a shear-dominant shape change, (b) diffusion not required for the transformation, and (c) sufficiently high shear-strain energy in the process to dominate the kinetics and morphology during the transformation (Cohen, 1982). The definition is thus not based on the identity of the transformation product itself (its

structure, specific morphology or properties), but rather on how it forms.

The crystallographic and thermodynamic aspects are fully discussed in the literature and have already been introduced in a more general context in the above sections; only a brief overview is given here.

9.8.1 Crystallography of the Martensitic Transformation

The relevant experimental observable parameters of the martensitic transformation are the shape deformation, the habit plane, the crystallographic orientation relationships, and the characteristic microstructures.

9.8.1.1 Shape Deformation and Habit Plane

When a sample of the parent phase is cooled to below M_s , a relief gradually appears on a prepolished surface of the parent-phase crystal. The surface relief disappears on heating to temperatures above A_s , provided that no diffusion-controlled transformation interferes.

The martensite phase usually takes the form of plates; the plane of contact between the parent and the martensite phases is called the “habit plane”. A schematic representation of such a martensite plate embedded in the matrix is shown in Fig. 9-20. During the formation of martensite, straight lines (for example, scratches on the prepolished surface) are transformed into other straight lines and planes are transformed into other planes. No discontinuities are observed at the points of deflection. This distortion can thus be represented as a “linear homogeneous transformation” of vectors and can be expressed by a matrix formulation. The macroscopic shape deformation can be decomposed into

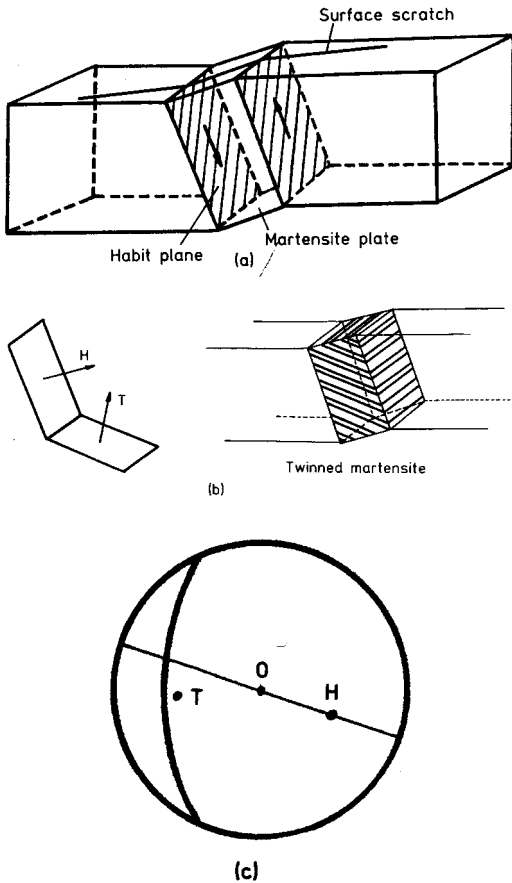


Figure 9-20. Schematic representation of (a) a single martensite plate embedded in a single crystal of the matrix phase, (b) a twinned plate and the position of habit and twin plane, and (c) their stereographic representation.

a component normal to the habit plane and a shear component parallel to a shear direction located in this interface. The latter is called “macroscopic shear” and quantifies the shape deformation, whereas the former represents the volume change associated with the transformation. A careful analysis of the surface relief reveals that the habit plane itself is unrotated and that any vector in this interface is also left unrotated and undistorted by the shape change. The habit plane is thus essentially “undistorted” and the macroscopic shape change associated

with the formation of martensite is thus an “invariant plane strain” deformation, abbreviated to IPS. The most general invariant plane strain deformation, as observed in most martensitic transformations, can be achieved by combining an extension and a simple shear.

The habit plane and the direction of macroscopic shear are, with few exceptions, not simple low-indexed crystallographic planes or directions of the parent or product phase. They are usually represented in a stereographic projection as shown schematically in Fig. 9-20.

9.8.1.2 Orientation Relationship

The next most important observable parameter is the crystallographically well-defined “orientation relationship” that exists between the lattices of the parent and the martensite phases. It is described either by the angles between certain crystallographic directions in both phases or by specifying the parallelism between certain planes and directions. This parallelism does not need to be rigorous, however, experimental results usually deviate slightly. Nevertheless, the fact that such crystallographic parallelism is observed yields important information concerning the possible mechanisms explaining the change in crystal structure. Some of those relationships observed in steels received great attention in the early martensite literature. Depending on the alloy composition, the f.c.c. austenite in steels transforms either to a b.c.c. or b.c.t. martensite or to an h.c.p. martensite, which itself may further transform into b.c.c. martensite. As regards the transformation of f.c.c. austenite to b.c.c. or b.c.t. martensite, the orientation relationships are as follows:

– the Kurdjumov–Sachs (K–S) relations:

$$(111)_P // (011)_{\alpha'} \text{ and } [0\bar{1}1]_P // (1\bar{1}1)_{\alpha'}$$

Table 9-3. The crystallographic observables of the martensitic transformations in some metals and alloys (courtesy G. Guénin et al. 1979*).

Alloy system	Structural change	Composition wt. %	Orientation relationship	Habit plane
Fe–C	f.c.c.	0–0.4% C	$(111)_P \parallel (101)_M$	$(111)_P$
	↓	0.55–1.4% C	$[1\bar{1}0]_P \parallel [1\bar{1}1]_M$	
	b.c.tetr.	1.4–1.8% C	K–S relationship K–S relationship Idem	$(225)_P$
Fe–Ni	f.c.c.	27–34% Ni	$(111)_P \parallel [101]_M$	$\approx (259)_P$
	↓ b.c.c.		$[1\bar{2}1]_P \parallel [10\bar{1}]_M$ N-relationship	
Fe–C–Ni	f.c.c.	0.8% C–22% Ni	$(111)_P \approx 1^\circ$ of $(101)_M$	$(3, 10, 15)_P$
	↓ b.c.tetr.		$[1\bar{2}1]_P \approx 2^\circ$ of $[10\bar{1}]_M$ G–T relationship	
Fe–Mn	f.c.c. ↓ h.c.p. (ϵ -phase)	13 to 25% Mn	$(111)_P \parallel (0001)_\epsilon$ $[1\bar{1}0]_P \parallel [1\bar{2}10]_\epsilon$	$(111)_P$
Fe–Cr–Ni	f.c.c.	18% Cr, 8% Ni	$(111)_P \parallel (0001)_\epsilon \parallel (101)_{\alpha'}$	$\epsilon (111)_P$
	↓ h.c.p. (ϵ), b.c.c. (α')		$[1\bar{1}0]_P \parallel [1\bar{2}10]_\epsilon \parallel [1\bar{1}1]_{\alpha'}$	$\alpha' (111)_P$
Cu–Zn β Cu–Sn	b.c.c. \rightarrow 9 R	40% Zn	$(011)_P \parallel ?(\bar{1}\bar{1}4)_M$	$\approx (2, 11, 12)_P$
	idem	25.6% Sn	$[1\bar{1}1]_P \parallel [\bar{1}10]_M$	$\approx (133)_P$
Cu–Al	b.c.c.	11.0 to 13.1% Al	$(101)_P$ at 4° of $(0001)_M$	2° of $(133)_P$
	↓ h.c.p. distorted	12.9 to 14.7% Al	$[111]_P \parallel [10\bar{1}0]_M$ $(10\bar{1})_P \parallel (10\bar{1})_M$ $[111]_P \parallel [10\bar{1}0]_M$	3° of $(122)_P$
Pure Co	f.c.c.		$(111)_P \parallel (0001)_M$	$(111)_P$
	↓ h.c.p.		$\langle 110 \rangle_P \parallel [11\bar{2}0]_M$	
Pure Zr	b.c.c.		$(101)_P \parallel (0001)_M$	$(596)_P$
Pure Ti	↓		$[111]_P \parallel [11\bar{2}0]_M$	$(8, 12, 9)_P$
	h.c.p.			$(334)_P$
Pure Li			Burgers relations	$(441)_P$

* Gobin, P. F., Guénin, G., Morin, M., Robin, M. (1979), in *Transformations de Phases à l'État Solide-Transformations Martensitiques*. Lyon: Dep. Génie Phys. Mat., INSA

– the Nishiyama–Wassermann (N–W) relations:

$$(111)_P \parallel (101)_{\alpha'} \text{ and } [1\bar{2}1]_P \parallel (10\bar{1})_{\alpha'}$$

– the Greninger–Troiano (G–T) relations (here the planes and directions are no longer exactly parallel):

$$(111)_P \approx (011)_{\alpha'} \text{ and } [\bar{1}01]_P \approx [\bar{1}\bar{1}1]_{\alpha'}$$

Concerning the transformation of f.c.c. to h.c.p. austenite and that of h.c.p. to b.c.c. martensite (the b.c.c. to h.c.p. relation is known as the Burgers relation), the following relations apply:

$$(111)_P // (0001)_E // (101)_{\alpha'}$$

and

$$[\bar{1}\bar{1}0]_P // [\bar{1}\bar{2}10]_E // [11\bar{1}]_{\alpha'}$$

Taking the N–W relations as an example, any one of the four crystallographically equivalent $\{111\}$ austenite planes, (111) , $(\bar{1}\bar{1}1)$, $(1\bar{1}\bar{1})$ and $(11\bar{1})$, can be the plane of parallelism. In each such plane any one of the three $\langle 1\bar{2}1 \rangle$ directions, which happen to be directions of the Burgers vectors, can be chosen. This therefore results in 12 different orientations of an α' -crystal in one austenite crystal. These differently oriented martensite crystals are called “variants”. It can easily be shown that the K–S relations lead to 24 variants.

Orientation relationships and the orientation of the habit plane change from one alloy system to another, and within a given alloy system from one composition to another. The observable crystallographic parameters are summarized in Table 9-3 for a large number of alloy systems; a more complete list of these and other crystallographic characteristics of various martensites is given by Nishiyama (1978).

9.8.1.3 Morphology, Microstructure and Substructure

Because the martensitic transformation is a first-order phase transformation, both phases, the parent and the martensite phase, coexist on cooling in a temperature range between M_s and M_f and on heating between A_s and A_f . Martensite thus occurs in physically isolated regions, the morphology of which is typical of the transforma-

tion. This morphology is easily observed by light optical microscopy (LOM) and the mutual arrangement of these regions constitutes the microstructure at the LOM level. Electron microscopic analysis reveals that also at the submicroscopic level martensite is characterized by a typical substructure. The morphological, microstructural and substructural aspects of martensite are briefly discussed below.

The martensite regions are generally plate-shaped, i.e. one lateral dimension is much smaller than the other two. If the two larger dimensions are nearly equal they are called “plates”, and if they are very unequal “laths”. A typical lath in low-carbon steel (with a carbon content less than 0.4%) has dimensions $0.3 \times 4 \times 200 \mu\text{m}^3$. However, martensite formed into the parent phase does not always appear as a geometrically well-shaped plate. Martensite plates that form near a free surface or in a single crystal as a result of a single-interface transformation may show the idealized plate-like shape. In such a single-interface transformation the habit plane extends from one side of the crystal to the other (see Fig. 9-11). Because of the shape change and the high elastic stresses that are created, a thick plate cannot terminate inside a parent crystal. As is frequently observed, lenticular shapes or groupings of differently oriented martensite plates will reduce these elastic stresses.

In the case of lenticular martensite, the habit plane is no longer a plane but a curved surface and the normal average of the lenticular plate is then taken as the orientation of the habit plane. Sometimes this orientation is visible as a “midrib” in some martensites (Fig. 9-21). It is believed that the martensite could grow to a certain extent as a plate, but that lenticular shapes are formed owing to the high elastic stresses that are building up. The high stresses may

trigger other plates to form in the vicinity of the plate formed earlier, giving rise to an “autocatalytic growth” of martensite.

A multivariant martensite arrangement is the most commonly observed microstructure. Often variants are arranged in some recognizable patterns and at times numerous variants present in a regular array give the impression of a martensite colony. The latter is typical of the “massive” microstructure, consisting of a packet of parallel martensite “laths” separated by more or less wavy interfaces. Each lath in the packet maintains the same variant or orientation relationship with the parent crystal. A single grain of the parent phase can transform into one or more such packets. The “plate” martensite arrangement which is observed in the same alloys differs from the lath configuration, because adjacent martensite plates are generally not parallel to each other.

Diagrams have been constructed for cases where there is a variety in morphology, as for example for Fe–Ni–C alloys. Maki and Tamura (1987) showed that the morphology of the α' -martensite in these alloys is related to the transformation temperature and the carbon content (Fig. 9-22).

Distinct martensite plate arrangements can also be recognized in alloys pertaining to the β -Hume–Rothery alloys. Schroeder and Wayman (1977) classified these arrangements into spear, fork, wedge and diamond forms. Each representation carries with it a definite crystallographic relationship between the variants constituting the arrangement. Grouping of martensite plates in such arrangements will lead to a serious reduction in the elastic stresses. By analysis of the crystallography of the plates in a single group, it can be shown that the respective macroscopic shape changes annihilate each other (Tas et al., 1973). Such

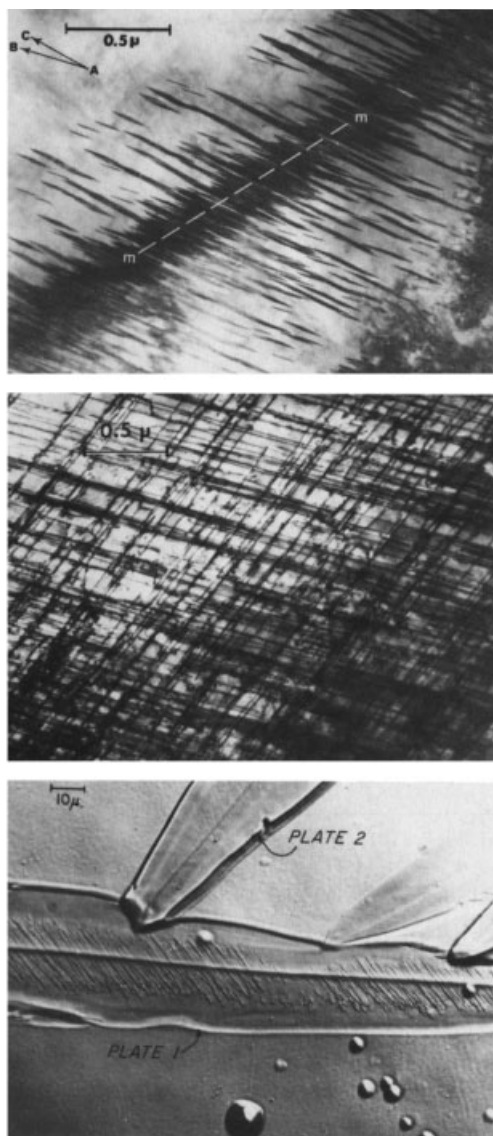


Figure 9-21. Transmission electron micrograph of a martensite in steel showing the twinned midrib (courtesy C. M. Wayman, 1989, University of Illinois, Urbana (IL)).

group formation is then called “self-accommodation”.

In these β -Hume–Rothery alloys, three types of martensite form, the 3R-, 9R- and 2H-types. A detailed analysis of the microstructure reveals that the martensite vari-

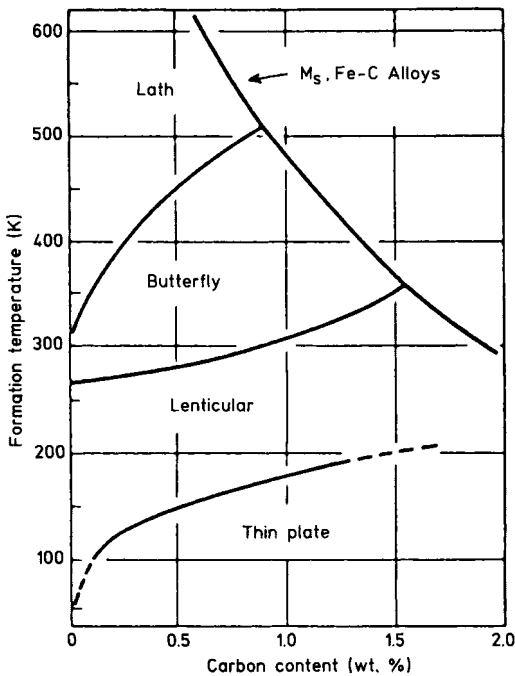


Figure 9-22. Relationship between α' -martensite morphology and M_s temperature as a function of carbon content in Fe-Ni-C alloys (Maki and Tamura, 1987).

ants form in six different groups, each group consisting of four variants. The habit planes of these four variants are located around the same $\{110\}_\beta$ pole, whereas each basal plane is located close to one of four other $\{110\}_\beta$ poles. The total macroscopic deformation of such a group is to a first approximation completely compensated. A more complete reduction in the three-dimensional strain is obtained if the total transformation strain is calculated for the six groups as an entity. As the martensite transformation involves a very small volume change in all β -Hume-Rothery alloys, the strain accommodation is thus almost complete.

The shape change associated with a martensite plate creates stresses in both the parent and the martensite phases. If these stresses exceed the flow stress for plastic

deformation, strain accommodation is then accomplished not only by elastic but also by plastic deformation in one or both phases.

Partitioning of the parent crystal, with finer plates forming subsequently in the partitioned region, frequently occurs and illustrates the fractal nature of the transformation (Fig. 9-10). It should be mentioned, however, that not all martensite microstructures show fractal characteristics (Hornbogen, 1988).

Until now only the more macroscopic observable features of the microstructure of martensite have been discussed. Transmission electron microscopy reveals that the substructure of martensite is also characteristic. It consists, depending on the alloy system and alloy composition, of regularly spaced stacking faults (e.g. Cu-base β' -type martensite), twins with a constant thickness ratio (e.g. Fe-30% Ni), dislocations (e.g. Fe-20% Ni-5% Mn), stacking faults and twins in the same martensite plate (e.g. Cu-Ga), or twins in the midrib region surrounded by dislocations.

9.8.1.4 Crystallographic Phenomenological Theory

The formal phenomenological theories of martensite formation predict the crystallographic characteristics, such as the shape deformation, the orientation of the habit plane, the orientation relationship between parent and product phase, and the amplitude of lattice invariant deformation. This prediction is obtained from the sole knowledge of the structures and lattice parameters of the two phases and with the basic assumption that the interface between parent phase and martensite is undistorted on a macroscopic scale.

The observation of the K-S and N-W orientation relationships led us to originally believe that a martensite was formed

by shear on those planes and directions specified in the orientation relationships. However, it was found that the shear mechanisms proposed by the K–S and N–W relations are not consistent with these experimental observations. The observations made by Greninger and Troiano (1949) on Fe–22%–Ni–0.8% C martensite were the key to the mathematical development of the crystallographic theory of martensite. They found that martensite plates exhibited a surface relief that can be described by a homogeneous shear along the habit plane, but this homogeneous shear could not transform the f.c.c. lattice of the parent phase into the b.c.t. lattice of the martensite. If the f.c.c. lattice had undergone the same homogeneous deformation, the structure of the martensite would have been trigonal. They therefore suggested that two types of shear are involved in the martensitic transformation: a “first” simple shear which is responsible for the macroscopic shape change, and a “second” shear which needs to be added to obtain the structural change but which should produce no observable macroscopic change in shape. Two years later, Bowles (1951) showed that the shape deformation may be any invariant plane strain. This opened the way to the formulation of the general theory of the crystallography by Wechsler et al. (1953) and, independently, by Bowles and Mackenzie (1954). Almost equivalent theories were later developed by Bullough and Bilby (1956) and Bilby and Frank (1960). The reader may consult the following more elaborate reviews of these theories: Wayman (1964), Christian (1965), Nishiyama (1978) and Ahlers (1982).

The basic assumption in the crystallographic theories is that the interface between the product and the parent phases is undistorted, which means that any vector that lies in this interface on the side of the

martensite would be a vector of the same size and the same orientation in the parent phase before transformation. As indicated in Sec. 9.3.1, the macroscopic shape change of an invariant-plane transformation can be represented by a combination of a pure lattice deformation (**B**), the so-called Bain strain, a rigid lattice rotation (**R**), and an inhomogeneous lattice-invariant deformation (**P**). The pure lattice deformation either increases or decreases some vectors in length. According to Wayman (1964), “the essence of the crystallographic theory of martensitic transformations is to find a simple shear (of a unique amount, on a certain plane, and in a certain direction) such that vectors which are increased in length due to the lattice deformation are correspondingly decreased in length due to the simple shear, and vice versa. Such vectors which remain invariant in length to these operations define the potential habit plane. Physically speaking, the ellipsoid generated from the initial sphere by the lattice deformation is distorted by the simple shear into another ellipsoid which becomes tangential to the initial sphere, the points of tangency being related along a diameter.” This is clearly illustrated in Fig. 9-23, where the problem becomes two-dimensional, because one of the principal axes of the lattice deformation is taken as normal to the plane of shear.

Some complementary remarks concerning the crystallographic theory should be made. The input data for the calculations are (i) the lattice parameters of the parent and martensite phases, (ii) the lattice correspondence, and (iii) the lattice-invariant shear. The output of the calculations is then the amount of inhomogeneous shear required to obtain the invariant plane condition, the macroscopic shape change, and the orientation relationship. Because of the lattice symmetries, differently oriented

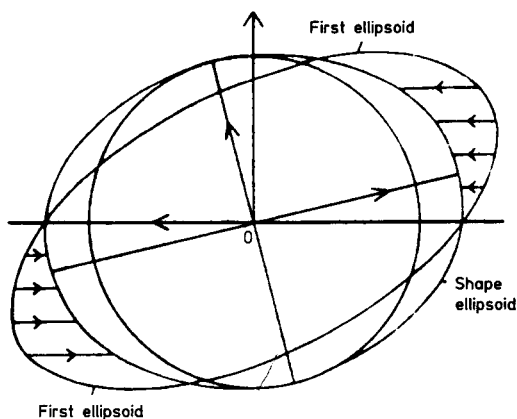


Figure 9-23. Production of an undistorted plane by shear such that the shape ellipsoid touches the unit sphere along one of its principal axes (Christian, 1965).

Brain relations and inhomogeneous shear systems lead to a number of crystallographically equivalent solutions. Because of the observed orientation relationships, the Bain relationship is fixed for most cases. However, larger unit cells are sometimes chosen, especially for those martensites where the crystal structure has a large unit cell compared with that of the parent phase. The only variable in these calculations is the choice of the inhomogeneous shear system. The orientation of the habit plane is found to be very sensitive to the choice that is made. For the f.c.c. to b.c.c. or b.c.t. transformation, the twin shear $(112)_M[11\bar{1}]_M$ gives a $(3\ 15\ 10)_P$ habit plane, whereas a $(011)_M[\bar{1}\bar{1}1]_M$ shear results in a $(111)_P$ habit plane.

The phenomenological theory as explained above is based on one active shear system. However, for some alloy systems this is not adequate. For example, a single $(112)_M$ twinning system is not able to explain the $\{225\}_P$ habit plane in some steels, and even two inhomogeneous shear systems do not give agreement with the experimental observations. Similar disagree-

ments have been observed in other alloy systems. To test critically the validity of the crystallographic theories, all crystallographic parameters should be measured and compared with the theoretical predictions. Agreement should be obtained for the complete set of parameters. For the martensites that are twinned, this includes a careful determination of the normal to the twinning plane K_1 relative to the parent lattice. In Cu–Al–Ni, for example, inconsistencies up to 12.5° have been found.

In cases where the lattice-invariant shear is twinning (as opposed to faulting or slip), type I twinning, where the twin plane originates from a mirror plane in the parent phase, has been assumed. Otsuka (1986) carefully analyzed for a number of systems the possibility of a type II twinning as an alternative inhomogeneous shear. In type II twinning, the shear direction stems from a two-fold symmetry direction of the parent phase. Otsuka (1986) compiled all the twinning modes observed in martensite into a table and found that most of them are type I or compound but that type II twinning had only recently been observed. According to Nishida and Li (2000), five different twinning modes exist in TiNi and other shape-memory alloys such as Cu–Al–Ni, Cu–Sn etc., namely the $\{111\}$ type I, the $\{011\}$ type I, the $\langle 011 \rangle$ type II, the (100) -compound and the (001) -compound twins. Type II twinning has recently received much attention as a mechanism for lattice-invariant shear in some alloys. Because type II twins have irrational twin boundaries, the physical meaning of an irrational boundary is still a controversial problem. It has been proposed that an irrational boundary consists of rational ledges and steps, the average being irrational. Thereafter, Hara et al. (1998) carried out a careful study using HRTEM, to try and observe $\langle 111 \rangle$ type II twin boundaries in a

Cu–Al–Ni alloy, but they were unable to observe any ledges or steps. The boundary is always associated with dark strain contrast, and the lattice is continuous through the irrational boundary. Nishida and Li (2000) also carried out extensive studies on $\langle 011 \rangle$ type II twin boundaries in TiNi using HRTEM, but they did not observe ledges or steps either. Based on these experimental results, it is thus most likely that the type II thin boundary is irrational even on a microscopic scale, and the strains at the boundary are elastically relaxed with wide twin width. To confirm this interpretation, Hara et al. (1998) carried out computer simulations by using the molecular dynamics method. The result showed that the irrational thin boundary did not show any steps. Thus, the above interpretation for an irrational twin boundary is justified. Otsuka and Ren (1999) have pointed out again the importance of type II twinning in the crystallographic aspects of martensite. They also stress the role that martensite aging has on the rubber-like behavior of martensite, a point that has been a long-standing unsolved problem. They showed that the point defects play a fundamental role. The deformation mechanisms of the cold deformation of NiTi martensite have been thoroughly analyzed by Liu et al. (1999a, b). They also found an interplay between type I and type II twinning.

As already mentioned in Sec. 9.3.6, a better and more complete agreement can be achieved when the strain energy terms, both bulk and interfacial, are included in the calculation.

9.8.1.5 Structure of the Habit Plane

In a number of alloys, especially those in which the so-called thermoelastic martensites are formed, the interface between martensite and the parent phase is mobile,

even at very low temperatures. This observation shows that the interface migration must be accomplished without appreciable thermal activation. The interface is thus “glissile”. In searching for models to explain the structure and mobility of the interface, we are concerned with the ideal and the actual interface morphology. A careful experimental analysis of the interface structure is therefore required if we want to verify the various models that have been proposed. As the models treat the interface on an atomistic scale, the substructure of the interface should be studied by conventional and by high-resolution transmission electron microscopy. The same holds for martensite-to-martensite interfaces, which in some alloys are also mobile. Recently, atomistic imaging of the martensite/austenite and martensite/martensite interfaces have been obtained. It is therefore not surprising that both aspects, the observation of interface substructures and the atomistic models, are treated jointly in the literature. For further reading concerning the interface structures and the growth mechanism of martensite we refer to the review papers by Christian (1982), Christian and Knowles (1982), and Olson and Cohen (1986). A summary of these papers is given below.

Let us first introduce the kinds of martensite interfaces concerned: glissile and non-glissile martensitic interfaces, with the latter subdivided into the coherent and semi-coherent interfaces. The two structures, martensite and the parent phase, are said to be “fully coherent” if both lattices have a matching plane parallel to the interface. If a fully coherent interface is displayed, the crystal undergoes a shape deformation leaving all vectors in the interface invariant. In general, the two phases do not have a plane of atomic fit, so that fully coherent martensite interfaces are ex-

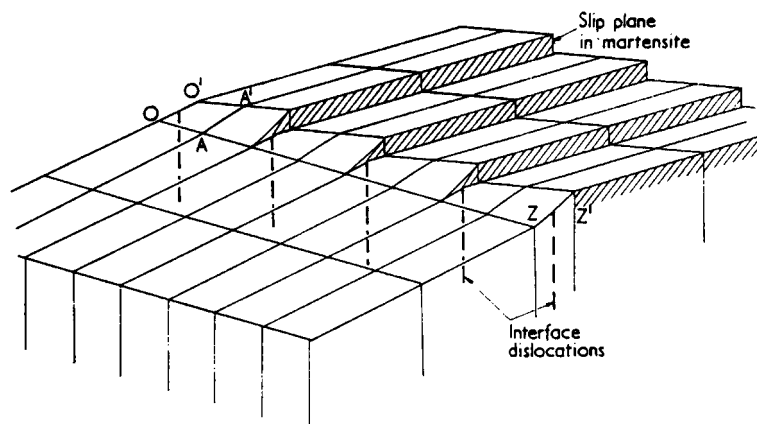


Figure 9-24. Three-dimensional representation of a semi-coherent martensite interface; the vectors OA are distorted into $O'A'$ but the large vectors $OZ = O'Z'$ are invariant (Christian, 1982).

ceptional. A fully coherent martensitic interface is, for example, that between f.c.c. and h.c.p. structures with lattice parameters such that $a(\text{f.c.c.}) = \sqrt{2}a(\text{h.c.p.})$; the atomic arrangement in the basal planes, which constitute the interface between the two structures, are identical. Such transformations are found in Co and its alloys and in some Fe-based alloys. The situation at semi-coherent interfaces becomes more complex. The models predict the presence of dislocations to correct the mismatch along the interface. If this coherent interface moves, it is suggested that not all vectors are left invariant and that the movement of dislocations causes shear in the product phase. Fig. 9-24 shows the slip associated with the interface dislocations.

Internally twinned martensite has been reported to show a zig-zag parent–martensite interface, as observed by conventional electron microscopy in, for example, Ti–Mn and Cu–Al–Ni. Fine parallel striations have been observed in the interface between austenite and both the β' -type and the γ' -type Cu–Al–Ni-martensite. These striations have been accounted for in terms of interfacial dislocations resulting from random faulting on the basal plane of the β' -type martensite and the twinning planes of the γ' -type martensite. High-resolution

electron micrographs show that the interface between martensite and the parent phase and also the intervariant interfaces and the interfaces between the internal twins in one martensite plate contain discontinuities (“steps”) on an atomic scale, the nature of which has not yet been completely unravelled. These steps can be considered as resulting from a small deviation of the ideal habit plane, and would then be comparable to those observed along the interfaces of tapered twins.

An exact understanding of the structure of the interfaces involved in the martensitic transformation (the parent–martensite, the intervariant, and the twin/twin interfaces) is therefore essential in determining the mechanism of transformation and the mobility of the interfaces.

9.8.2 Thermodynamics and Kinetics of the Martensitic Transformation

9.8.2.1 Critical Driving Force and Transformation Temperatures

A quantitative thermodynamic treatment of the martensitic transformation requires a precise knowledge of the thermodynamic equilibrium temperature T_0 and of the change in Gibbs energy at the transforma-

tion temperature M_s . Both can be calculated and/or derived from measured data, as is shown here for two examples: the martensitic transformation in Fe-X (X=Ni, Ru, ...) and in Cu-Zn-Al alloys. In the former example, both the parent and the martensite phases have the same structure as the equilibrium phases and hence the data for the equilibrium phases can be taken. In the latter example, both structures differ from that of the equilibrium phases, which requires a more elaborate calculation.

For the Fe-X alloys, the Gibbs energy per mole of the parent austenite phase γ and of the martensite phase α are G^γ and G^α , respectively. The change in Gibbs energy per mole, $\Delta G^{\gamma \rightarrow \alpha}$, which for a martensitic transformation $\gamma \rightarrow \alpha$ is available to the system at any temperature T , is then

$$\Delta G^{\gamma \rightarrow \alpha}|_T = G^\alpha - G^\gamma \quad (9-8)$$

This quantity is negative for temperatures at which the α -phase is the more stable and positive for temperatures at which the γ -phase is the more stable. There is a characteristic temperature T_0 corresponding to the thermodynamic equilibrium between both phases, such that

$$\Delta G^{\gamma \rightarrow \alpha}|_{T=T_0} = 0 \quad (9-9)$$

Because the transformation creates interfacial and elastic energies, the martensitic transformation $\gamma \rightarrow \alpha$ or $\alpha \rightarrow \gamma$ does not start at T_0 , but at a temperature below or above T_0 , respectively. It is therefore necessary to undercool or overheat, respectively, until M_s or A_s is reached. At these temperatures the Gibbs energy change $\Delta G^{\gamma \rightarrow \alpha}$ is sufficiently large to induce the forward or reverse transformation, respectively. $\Delta G^{\gamma \rightarrow \alpha}$ (at M_s) is then the critical chemical driving force.

The martensite phase, represented by M, is to be regarded as the α -phase embedded

in the γ -phase. Because of the shape and volume changes associated with the transformation, elastic strain energy also has to be considered. The Gibbs energy is thus composed of chemical Gibbs energy, G_c , and strain energy, E_e , so that the Gibbs energy change accompanying the transformation may be written as

$$G^{\gamma \rightarrow M} = \Delta G_c^{\gamma \rightarrow \alpha} + \Delta E_e^{\alpha \rightarrow M} \quad (9-10)$$

At temperatures below M_s , where both phases coexist and thus are in equilibrium, $\Delta G^{\gamma \rightarrow M}|_{T=0} = 0$. $\Delta G_c^{\gamma \rightarrow \alpha}|_T$ is then exactly equal, but opposite in sign, to the sum of all non-chemical energies $\Delta G_{nc}^{\alpha \rightarrow M}|_T$. If the surface energies are neglected in comparison with the high strain energies, the non-chemical energy equals $\Delta E_e^{\alpha \rightarrow M}|_T$, and approaches zero at $T=M_s$. The strain energy stored in the material is the sum of that produced by shearing and by volume change. The former depends on the strength of the parent phase and thus also on the grain size, hence M_s also depends on the grain size, as shown by Hsu and Xiaowang (1989).

The necessary undercooling ($T_0 - M_s$) and superheating ($A_s - T_0$) vary for different alloy systems, and for certain materials even with composition. A precise thermodynamic definition of M_s and A_s cannot be given, however, if the non-chemical energies, $\Delta G_{nc}^{\alpha \rightarrow M}$, are not known. We can then only say that M_s or A_s is the temperature at which the quantity $\Delta G^{\gamma \rightarrow \alpha}$ (at $T=M_s$ or $T=A_s$, respectively) is sufficiently negative or positive, respectively, to have a reasonable chance of nucleation.

Two approaches are found in the literature for calculating the critical chemical driving force. The first is based on the experimentally determined M_s temperatures (Kaufman, 1965) and the other on a theoretical model for the non-chemical energies (Hsu, 1985).

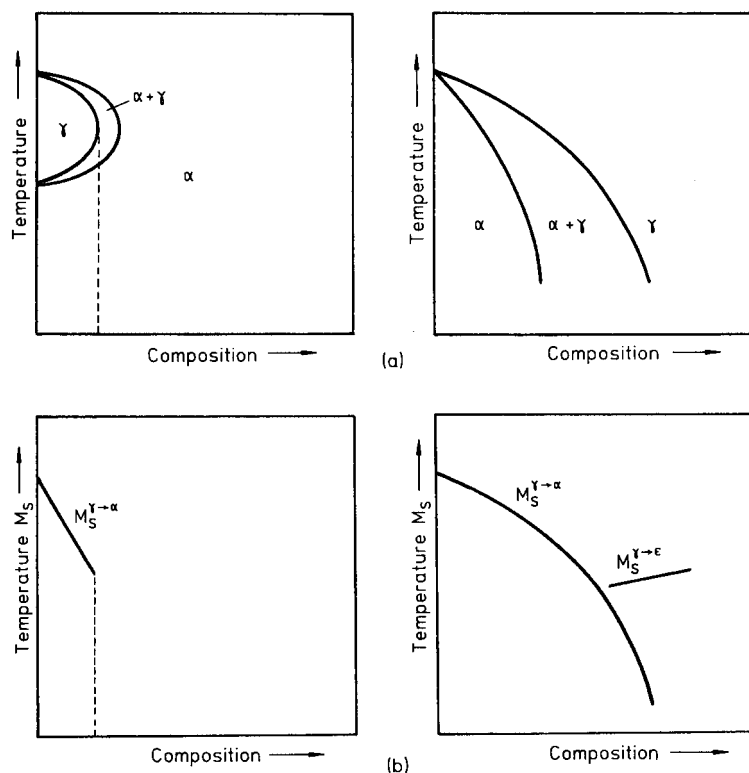


Figure 9-25. Schematic diagrams for ferrous alloys that form a γ -loop (Fe–Cu, Cr, Mo, Sn, V, W) and that γ -loop forms a stabilized austenite phase (Fe–C, Ir, Mn, N, Ni, Pt, Ru); (a) equilibrium diagrams; (b) M_s temperature diagrams (Krauss and Marder, 1971).

The first approach has been used for ferrous alloys, which can be classified into two systems: those with γ -loops and those with stabilized γ -phases (see Fig. 9-25). Figure 9-25 also gives the M_s temperatures for the α - and ϵ -martensite. If A is the alloying element for iron, the molar chemical Gibbs energy for the austenite phase (G^γ) can be written as

$$G^\gamma = (1-x)G_{\text{Fe}}^\gamma + xG_A^\gamma + G_m^\gamma \quad (9-11)$$

where x represents the atomic fraction of the element A in solid solution in the γ -austenite, $(1-x)$ the atomic fraction of iron, G_{Fe}^γ the chemical Gibbs energy of pure iron as f.c.c. γ -phase, G_A^γ the chemical Gibbs energy of element A as f.c.c. phase, and G_m^γ the Gibbs energy of mixing of the γ -phase. Similarly, the Gibbs energy of the α -phase can be given as

$$G^\alpha = (1-x)G_{\text{Fe}}^\alpha + xG_A^\alpha + G_m^\alpha \quad (9-12)$$

where G_{Fe}^α and G_A^α are the Gibbs energies of pure iron and pure element A as a b.c.c. α -phase, respectively, and G_m^α is the Gibbs energy of mixing of the martensite phase. The change in chemical Gibbs energy accompanying the martensitic transformation $\gamma \rightarrow \alpha$ then becomes

$$\Delta G^{\gamma \rightarrow \alpha} = (1-x)\Delta G_{\text{Fe}}^{\gamma \rightarrow \alpha} + x\Delta G_A^{\gamma \rightarrow \alpha} + \Delta G_m^{\gamma \rightarrow \alpha} \quad (9-13)$$

The quantity $\Delta G_{\text{Fe}}^{\gamma \rightarrow \alpha}$ represents the Gibbs energy change for transformation $\gamma \rightarrow \alpha$ of pure iron and can be assessed experimentally from the measured heat of transformation and the specific heat of both phases. The quantity $\Delta G_A^{\gamma \rightarrow \alpha}$ cannot usually be obtained from experiments because the element A does not always exist in the two modifications γ and α ; it must therefore be estimated from thermodynamic models for solid solutions. The quantity $\Delta G_m^{\gamma \rightarrow \alpha}$ is the

Gibbs energy can, according to Hsu and Zhou (1989), be described as

$$\Delta G^{\beta'-M} = \Delta G^{\beta'-\beta} + \Delta G^{\beta-\alpha} + \Delta G^{\alpha-\alpha'} + \Delta G^{\alpha'-M} \quad (9-14)$$

where $\beta'-M$ represents the transformation from the the ordered b.c.c. phase to the ordered 9R-type of martensite, $\beta'-\beta$ the order-disorder transition, $\beta-\alpha$ the transformation from the disordered b.c.c. to the disordered f.c.c. phase having the same composition, $\alpha-\alpha'$ the disorder-order transformation in the f.c.c. phase, and $\alpha'-M$ the transition from the ordered f.c.c. phase to the ordered martensite phase. Assuming a simplified relationship between the degree of ordering and temperature, Hsu and Zhou found good agreement between the calculated and observed M_s . Their calculations show that ordering of the parent phase, which cannot be suppressed even by severe quenching, strongly influences T_0 .

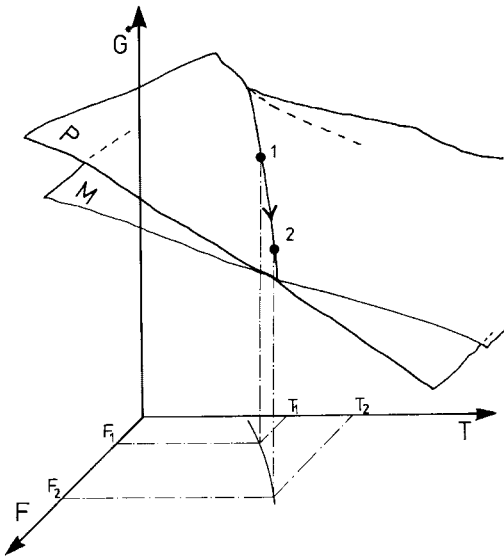


Figure 9-27. Gibbs energy G^* versus temperature and force for stressed samples: P and M represent free energy surfaces for parent and martensite, respectively (Wollants et al., 1979).

It is known that martensite may also be induced by an external stress at temperatures above M_s . The problem now is to calculate the change in T_0 due to changes in stress. As a first approximation, it is assumed that the driving force $\Delta G_m^{P \rightarrow M}|_{T=M_s}$ required for nucleation remains constant with temperature and thus independent of stress. Patel and Cohen (1953) calculated the work done on the stressed specimen; their treatment provides a good understanding of how an applied stress that is decomposed into a shear stress along the habit plane and a normal stress perpendicular to it, affects the transformation temperature. At M_s^σ , which is the martensite start temperature when cooling under an applied stress σ , the chemical Gibbs energy change equals the transformation work of the external stress:

$$\Delta G_\sigma^{P \rightarrow M} = 1/2 \sigma_a \times [\delta_0 \sin 2\theta \pm \varepsilon_0 (1 + \cos 2\theta)] V_m \quad (9-15)$$

where δ_0 is the shear strain, σ_a the applied stress, θ the angle between the stress axis and the normal to the operative shear plane, ε_0 the corresponding strain associated with the transformation, and V_m the molar volume. The quantity $\Delta H^{P \rightarrow M}$ can be measured by calorimetry and $\Delta S^{P \rightarrow M}$ can be evaluated from stress-induced transformation experiments or calculated from Eq. (9-16). The temperature T_0 can be calculated thermodynamically or obtained more or less accurately from the relationships

$$\begin{aligned} \Delta G^{P \rightarrow M} &= \Delta H^{P \rightarrow M} - T \Delta S^{P \rightarrow M} \\ \Delta H^{P \rightarrow M} &= T_0 \Delta S^{P \rightarrow M} \end{aligned} \quad (9-16)$$

and

$$T_0 = (A_s - M_s)/2 = (A_f - M_f)/2 \quad (9-17)$$

However, it should be noted that the determination of T_0 does not always obey these simple relationships and that the calorimet-

rically measured heats do not always reflect the exact heats of transformation.

As stress itself is also a state variable independent of temperature, it should be considered in the thermodynamic treatment as explained by Wollants et al. (1979). To describe the thermodynamic state of a uniaxially stressed crystal, they introduced the “elastic” state functions H^* and G^* , which incorporate the effect of stress as follows:

$$\begin{aligned} H^* &= U + PV - Fl = H - Fl \\ &= H - \sigma \varepsilon V_m \end{aligned} \quad (9-18)$$

$$\begin{aligned} G^* &= U + PV - TS - Fl = G - Fl \\ &= G - \sigma \varepsilon V_m \end{aligned} \quad (9-19)$$

where F is the applied force and l the “molar length” of the crystal. Fig. 9-27 illustrates how the equilibrium temperature and force change when one of the variables is changed; P and M represent the Gibbs energy surfaces of the parent phase and of martensite, respectively. At the two-phase equilibrium $G^{*P} = G^{*M}$ and if, at constant hydrostatic pressure, the intensive variables F (or σ) and T are changed in such a way that there is thermodynamic equilibrium between martensite and the parent phase, then $dG^{*P} = dG^{*M}$, or

$$-S^P dT - l^P dF = -S^M dT - l^M dF$$

so that $dF/dT = -[\Delta S/\Delta l]^{P \rightarrow M}$, or, since the molar work $F \Delta l^{P \rightarrow M} = \sigma \varepsilon^{P \rightarrow M} V_m$ and $\Delta S^{P \rightarrow M} = \Delta H^*(\sigma)/T_0(\sigma)$, it also follows that

$$d\sigma/dT = -[\Delta H^*(\sigma)]/[T_0(\sigma) \varepsilon^{P \rightarrow M} V_m] \quad (9-20)$$

where V_m is the molar volume ($V_m = V^P = V^M$). Eq. (9-20) is the Clausius–Clapeyron equation for a uniaxial stress, which is similar in form to that for hydrostatic pressure, except for the negative sign.

The change in critical stress necessary to induce martensite can be obtained from tensile tests carried out at different temper-

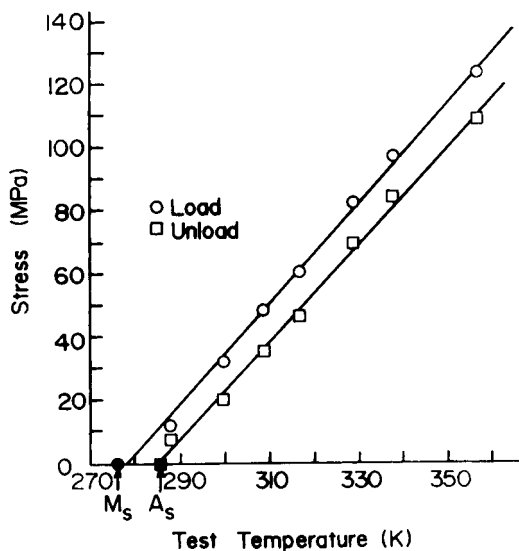


Figure 9-28. Results of tensile tests for inducing martensite in a Cu–34.1 Zn–1.8 Sn (at.%) alloy (Pops, 1970).

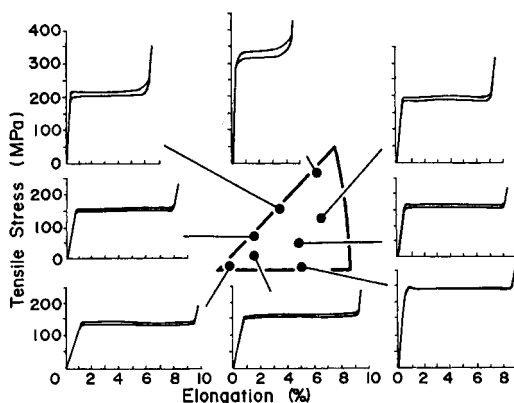


Figure 9-29. Orientation dependence of stress–strain curves for martensite formation in a Cu–Al–Ni alloy (Horikawa et al., 1988).

atures (see Fig. 9-28). The elongation resulting from the transformation is orientation dependent (Fig. 9-29). From data such as those shown in Figs. 9-28 and 9-29, we can calculate $\Delta S^{P \rightarrow M}$. It is evident that for each crystal orientation the slope $d\sigma/dT$ is different.

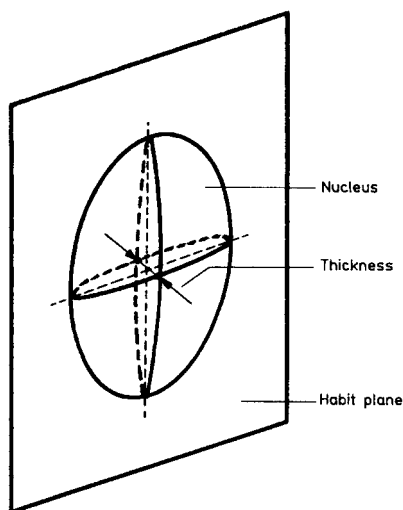


Figure 9-30. Shape of a nucleus of a martensite plate.

Similarly, martensite can be induced by magnetic fields. By taking into account the composition, the influence of grain boundaries, and crystal orientation, the magnetic invar effect and the austenite magnetism, Shimizu and Kakeshita (1989) proposed an equation that describes the shift of M_s as a function of the magnetic field.

9.8.2.2 Nucleation

Martensitic transformations are first-order phase transformations and hence occur by nucleation and growth. In most instances, except in the case of thermoelasticity (see below), the growth of a martensite plate proceeds so rapidly that the transformation kinetics are dominated by the nucleation event. Various mechanisms of martensite nucleation have in the past been proposed and can be considered under two subheadings. In the first group of models, the so-called localized nucleation models, concepts of diffusional nucleation kinetics are applied; the second group of models is based on lattice instability considerations

concerning both static and dynamic lattice instability. All nucleation models can further be divided into classical and non-classical. The former model involves lattice perturbations of fixed amplitude and varying size, whereas the latter considers perturbations of varying size (Olson and Cohen, 1982b).

In the classical nucleation theory; martensite nuclei form along a path of constant composition and structure and the state of the nucleus is given by its size. Because the martensitic transformation involves shear strains, it can be shown that the strain energy is minimized for a disc-like nucleus, but then the surface energy becomes very large. The critical nucleus, assuming an oblate spheroidal shape (Fig. 9-30), will then have an aspect ratio (c/r) such that for any change in shape, the decrease in strain energy will be exactly balanced by an increase in interfacial energy. The interfacial Gibbs energy per plate is

$$v \Delta g_s = 2 \pi r^2 \Gamma \quad (9-21)$$

where v is the volume of the plate, Δg_s the surface Gibbs energy per unit volume, and Γ the interfacial energy. The strain energy per plate is

$$v \Delta g_e = (4/3) \pi r^2 c (A c/r) \quad (9-22)$$

where $\Delta g_e (= A c/r)$ is the strain energy per unit volume and A is a factor to be deduced from linear elasticity and thus a function of the elastic constants and of the shear and dilatational strains. The chemical Gibbs energy change per plate is

$$v \Delta g_c \quad \text{or} \quad (4/3) \pi r^2 c \Delta g_c \quad (9-23)$$

If the nucleation occurs at a lattice defect, we have to consider also the Gibbs energy G_d due to the defect and the nucleus-defect interaction energy G_i . According to Olson and Cohen (1982), the total Gibbs energy describing the formation of a classi-

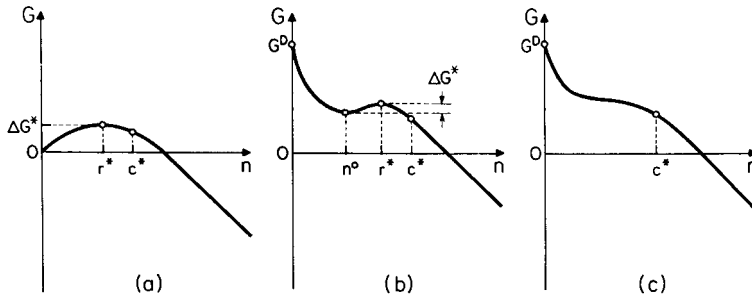


Figure 9-31. Schematic nucleus Gibbs energy (G) curves for nucleation via a classical path: (a) homogeneous, (b) heterogeneous, and (c) barrierless nucleation (Olson and Cohen, 1982b).

cal martensitic nucleus becomes (9-24)

$$G(r, c) = G_d + G_i + v(\Delta g_c + \Delta g_e + \Delta g_s)$$

and is given schematically in Fig. 9-31. Three cases are considered in calculating the critical free energy for nucleation ΔG^* and the critical nucleus size r^* and c^* .

In the case of homogeneous nucleation, G_d and G_i are zero, and on inserting the necessary quantities into Eq. (9-24) we find that the barrier ΔG^* is too high by several orders of magnitude. Even assuming local compositional fluctuations or the existence of pre-existing embryos does not give full satisfaction. It was therefore soon

recognized that homogeneous nucleation of martensite is impossible. Recently, much progress has been made in the understanding of nucleus formation at lattice defects. ΔG^* and therefore also the critical size of the nucleus can be reduced by assuming the nucleation at a defect. Under certain special conditions, this heterogeneous nucleation may even be barrierless. Such a case applies to the f.c.c.-to-h.c.p. transformation, which may take place by dissociation of a number of properly spaced total dislocations present in the matrix phase into partial dislocations separated by stacking faults. The stacking-fault

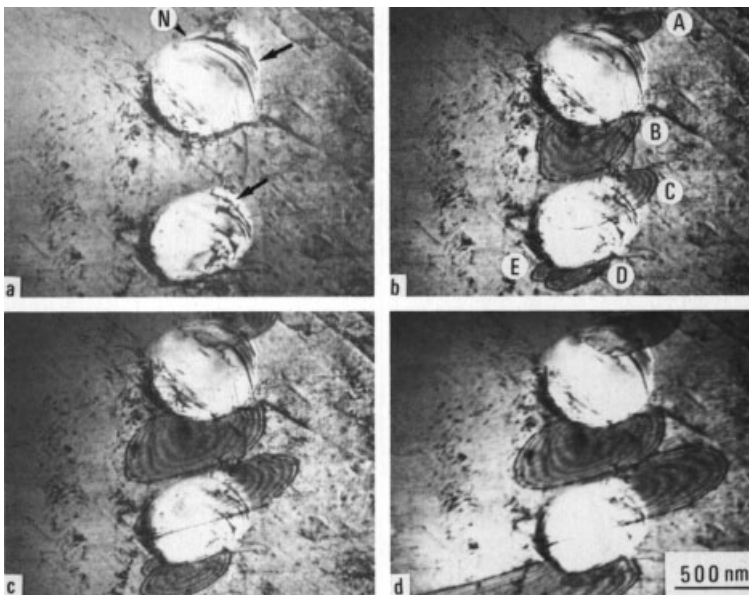


Figure 9-32. Electron micrographs of the nucleation and early growth stage around inclusion particles in a Ti-Ni-Cu alloy (Saburi and Nenno, 1987).

energy is temperature dependent and becomes positive below T_0 , which results in a barrierless nucleation.

In a number of alloy systems, softening of certain elastic constants is observed and it is then argued that, although the homogeneous soft-mode concept is definitely not adequate to describe the nucleation of martensite, stresses and strains present around defects of the lattice can induce a local mechanical instability. Such a model is called “the localized soft-mode concept” (Guénin and Clapp, 1986). In this model the lattice Gibbs energy is a function of pure strains and therefore of second- and third-order elastic constants. The third-order constants (which relate the strain energy to the amount of strain) introduce anharmonic terms into the strain energy and may lead to mechanical instability. The region of mechanical instability, or the “strain spinodal”, is so defined that any further increase in strain will make the lattice unstable with respect to a decomposition into strained regions. In these zones a nucleus can develop without generating any strain energy, and the only resisting term remains the surface energy. This results in a reduced critical size of the nucleus, which is further decreased as the temperature is lowered owing to the increase in chemical driving force.

In situ electron microscope observations have been made on the nucleation and early stages of growth of martensite, as shown in Fig. 9-32. Martensite nucleates at stress concentrations, the nucleation takes place repeatedly at the same place, and the strain contrast disappears as nucleation and growth proceed and reappears when martensite disappears.

At present, the nucleation models are being further refined by molecular dynamic calculations.

9.8.2.3 Growth and Kinetics

A distinction is made between the kinetics of a single martensite plate and the global kinetics, which expresses the volume fraction of the parent phase that is transformed. According to the observed kinetics, martensitic transformations can be divided into two distinct classes: athermal and isothermal martensite. In athermal martensite, the transformation progresses with decreasing temperature, whereas in isothermal martensite, the transformation progresses with time at a constant temperature.

The growth may be “thermoelastic” or of the “burst” type. The latter is the more common mode. It consists of the formation of comparatively large amounts of martensite (typically 10–30 vol.%) in “bursts” that are caused by autocatalytic nucleation and rapid growth of numerous plates. Each individual martensite plate is completely formed with a speed higher than 10^5 cm/s and the transformation progresses by the formation of new plates. The global kinetics of the transformation are therefore essentially controlled by the nucleation frequency. The thermoelastic growth mode is characterized by the formation of thin, parallel-sided plates or wedge-shaped pairs of plates (Fig. 9-33), which form and grow progressively as the temperature is lowered below M_s and which shrink and disappear on reversing the temperature change. This behavior arises because the matrix accommodates the shape deformation of the martensite plate elastically, so that at a specified temperature the transformation front of the plate and the matrix are in thermodynamic equilibrium. Any change in temperature displaces this equilibrium and, therefore, the plate grows or shrinks. A complete mechanical analog of this thermoelastic behavior is the pseudoelastic behavior. The growth or shrinkage of individual mar-

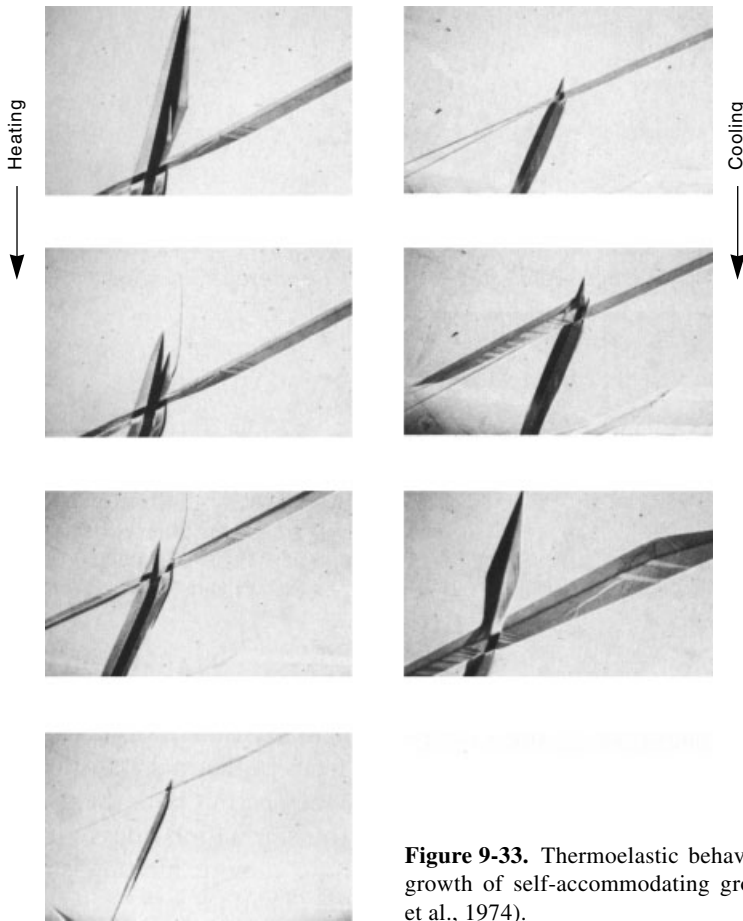


Figure 9-33. Thermoelastic behavior in Ag–Cd alloys showing the growth of self-accommodating groups of martensite plates (Delaey et al., 1974).

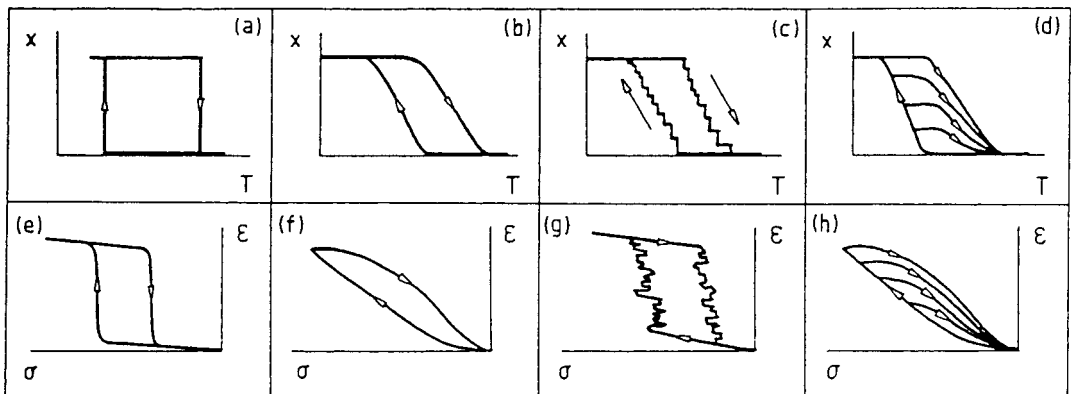


Figure 9-34. Schematic representation of some relevant features (volume-transformed product or transformation strain) experimentally observed in hysteresis curves corresponding to thermally induced and stress-induced thermoelastic transformations: (a, e) single interface transformation in a single crystal; (b, f) multiple interface transformation; (c, g) discontinuous jumps (bursts); (d, h) partial cycling behavior.

tensite plates is then a direct function of the increase or decrease in stress. More elaborate thermodynamic treatments of thermoelasticity can be found in the papers by Delaey et al. (1974), Salzbrenner and Cohen (1979), Ling and Owen (1981) and Ortin and Planes (1989).

The best quantitative understanding of the kinetics of the martensitic transformation is obtained from isothermal transformations, because they permit both the nucleation and the transformation rates to be determined. In those alloys exhibiting isothermal martensite (Thadhani and Meyers, 1986), it is shown that at each temperature the transformation starts in the austenite and proceeds as a function of time. The transformation exhibits a C-curve behavior. Isothermal martensitic transformation kinetics consist of two effects: an initial increase in the total volume fraction of martensite, which is attributed to an autocatalytic nucleation of new martensite plates, followed by a decrease due to the compartmentalization of the austenite into smaller and smaller areas.

9.8.2.4 Transformation Hysteresis

Hysteresis behavior is one of the peculiar characteristics of both the thermal and stress-induced martensitic transformations. In several studies the origin of the frictional resistance opposing the interfacial motion of martensite plates has been investigated and described. From a practical point of view, the hysteresis phenomenon is an important problem in the application of shape-memory alloys. In general hysteresis appears when, on passing through a local extreme value (maximum or minimum) of any control parameter such as temperature or stress, one or more state variables do not follow the original path in state space. When all the state variables, includ-

ing the control parameter, return to their original values, a closed loop is formed (Fig. 9-34). The loop is always contoured in such a sense that it encloses a positive area, representing the energy lost in the cyclic process. Therefore, hysteretic behavior is always related to an energy-dissipative process. The dissipated energy is much smaller in thermoelastic martensitic transformations than in burst-type transformations.

9.9 Materials

9.9.1 Metallic Materials

A classification of the diffusionless displacive transformations in metallic materials is given in Table 9-4, where the alloy systems are subdivided into three groups. The origin of the martensitic transformation in the first group lies in the allotropic transformation of the pure solvent. The parent phase of the alloys of this group thus does not show any remarkable mechanical instability. The second group consists of the β b.c.c. Hume-Rothery alloys, which are characterized by a moderate lattice instability in the temperature range above M_s . The third group is characterized by a drastic mechanical instability of the parent phase. Because the transformation is only weakly first order (by this we mean a discontinuous jump in the corresponding thermodynamic property whose height, however, is very small) or even second order, it is in this group of alloy systems that we find, in addition to the martensitic, the quasi-martensitic transformations.

Traditionally, the ferrous and non-ferrous martensites have been treated separately in the literature. Before going into detail it will be an advantage to first compare and contrast ferrous and non-ferrous martensites and to do it in such a way that we

Table 9-4. Classification of metallic alloy systems showing diffusionless displacive transformations (Delaey et al., (1982).**1. Martensite based on allotropic transformation of solvent atom**

1. Iron and iron-based alloys		
2. Shear transformation, close packed to close packed		
1. Cobalt and alloys	f.c.c. \rightarrow h.c.p., 126 R	SF*
2. Rare earth and alloys	f.c.c., h.c.p., d.h.c.p., 9 R	
(3. MnSi, TiCr ₂)	NaCl \rightarrow NiAs, Laves)	
3. Body centered cubic to close packed		
1. Titanium, zirconium and alloys	b.c.c. \rightarrow h.c.p., orth. f.c.c	tw, d*
2. Alkali and alloys (Li)	b.c.c. \rightarrow h.c.p.	
3. Thallium	b.c.c. \rightarrow h.c.p.	
4. Others: plutonium, uranium, mercury, etc. and alloys	Complex structures	

2. β -b.c.c. Hume–Rothery and Ni-based martensitic shape-memory alloys

1. Copper-, silver-, gold-, β -alloys (disord., ord.) b.c.c.	AB, ABABCBCAC, ABAC	
2. Ni–Ti–X β -alloys	b.c.c. \rightarrow 9 R, AB	tw, SF*
Nickel β -alloys (Ni–Al)	b.c.c. \rightarrow ABC	tw, SF*
Ni _{3–x} M _x Sn (M = Cu, Mn)	b.c.c. \rightarrow AB	tw*
(Cobalt β -alloys, Ni–Co–X)		

3. Cubic to tetragonal, stress-relaxation twinning or martensite

1. Indium-based alloys	f.c.c. \rightarrow f.c.t., orth.	tw, tw ^{σ*}
2. Manganese-based alloys	f.c.c. \rightarrow f.c.t., orth.	tw ^{σ*}
3. A 15 compounds, LaAg _x In _{1–x}	β -W. \rightarrow tetr.	
4. Others: Ru–Ta, Ru–Nb, YCu, LaCd		

* SF: stacking faults; tw^σ: (stress relaxation) twins; d: dislocated

can establish criteria to differentiate the two groups. Although not every detail of transformation behavior will be discussed, a set of criteria have been chosen as shown in Table 9-5. A more detailed review of martensite in metallic systems is given by Nishiyama (1978).

9.9.1.1 Ferrous Alloys

Martensitic transformations in ferrous alloys have been studied extensively, especially the crystallography and morphology which have been reviewed by Muddle

(1982). Depending on alloy composition, a distinction is made among the various martensites, based either on the crystallography, morphology or growth characteristics.

Essentially, three different crystal structures appear: the b.c.c. or b.c.t. α' -martensite, the h.c.p. ϵ -martensite, and the long-range ordered f.c.t. martensite. In plain carbon steels martensite is regarded as a supersaturated, interstitial solid solution of carbon in b.c.c. iron (ferrite), with a crystal structure that is a tetragonally distorted version of the ferrite structure. The tetragonality is linearly dependent on the carbon

Table 9-5. A qualitative comparison between ferrous and non-ferrous martensites (Delaey et al., 1982b).

Ferrous martensite		Non-ferrous martensite	
Interstitial and/or substitutional	Nature of alloying	Substitutional	
Martensitic state in interstitial ferrous alloys is much harder than the austenite state	Hardness	Martensitic state is not much harder and may even be softer than the austenite state	
Large	Transformation hysteresis	Small to very small	
Relatively large	Transformation strain	Relatively small	
High values near the M_s	Elastic constants of the parent phase	Low values near the M_s	
Negative near the M_s in most cases	Temperature coefficient of elastic shear constant	Positive near the M_s in many cases	
High	Transformation enthalpy	Low to very low	
Large	Transformation entropy	Small	
Large	Chemical driving force	Small	
Self-accommodation is not obvious	Growth character	Well developed self-accommodating variants	
High rate, "burst", athermal and/or isothermal transformation	Kinetics	Slower rate, no "burst", no isothermal transformation, thermoelastic balance	
No single interface transformation observed	Growth front	Single interface possible	
Low and non-reversible	Interface mobility	High and reversible	
Low	Damping capacity of martensite	High	

content. This α' -martensite is also found in a number of substitutional ferrous alloys, the martensite being either b.c.c. or b.c.t. In certain alloy systems with an austenite phase of low stacking fault energy, a martensitic transformation to a fully coherent h.c.p. product (ϵ -martensite) is observed.

In some long-range ordered alloys, as in Fe–Pt and Fe–Pd, f.c.t. in addition to b.c.t. martensite is observed.

As far as the morphology is concerned, plate, lath, butterfly, lenticular, banded, thin-plate and needle-like martensite can be distinguished.

Table 9-6. Summary of substructure, habit plane (H.P.) and orientation relationship (O.R.) for the four types of α' -martensite (Maki and Tamura, 1987).

Morphology	Substructure	H.P.	O.R.*	M_s
Lath	(Tangled) dislocations	(111) _A	K-S	<div>High</div> <div>↑</div> <div>↓</div> <div>Low</div>
Butterfly	(Straight) dislocations and twins	(225) _A	K-S	
Lenticular	(Straight) dislocations and twins (Mid-rib)	(259) _A or (3 10 15) _A	N or G-T	
Thin-plate	Twins	(2 10 15) _A	G-T	

* K-S: Kurdjumow–Sachs relationship, N: Nishiyama relationship, G-T: Greninger–Troiano relationship

A distinct substructure, crystallographic orientation of the habit plane and austenite to martensite orientation relationship are associated with each morphology, as summarized in Table 9-6.

Because the carbon atom occupies octahedral interstices in the austenite f.c.c. lattice, special attention is drawn to the Fe–X–C martensite. In the martensite lattice, those interstitial positions are defined by the Bain correspondence (Fig. 9-35). Only those at the midpoints of cell edges parallel to $[001]_B$ and at the centers of the faces normal to $[001]_B$ are permitted. This preferred occupancy affords an explanation of the observed tetragonality c/a , the degree of which is a function of the carbon content:

$$c/a = 1 + 0.045 (\text{wt.}\% \text{ C}) \quad (9-25)$$

Careful X-ray diffraction of martensite, freshly quenched and maintained at liquid nitrogen temperature, has shown signifi-

cant deviations from the above equation. The tetragonality is abnormally lower for $X=\text{Mn}$ or Re and abnormally higher for $X=\text{Al}$ or Ni . Heating to room temperature of the latter martensite results in a lowering of the tetragonality. The formation of domains or microtwinning in the former alloys and ordering of the Al atoms in the latter have been put forward as the origin of the abnormal c/a ratio. This behavior has moreover been related to the martensite plate morphology (Kajiwara et al., 1986, 1991). Kajiwara and Kikuchi found that in Fe–Ni–C alloys the tetragonality is abnormally large and depends on the microstructure. It is very large for a plate martensite, while it is normal or not so large for a lenticular martensite. They conclude that “the martensite tetragonality is dependent on the mode of the lattice deformation in the martensitic transformation. If the lattice deformation is twinning, the resulting $c:a$ is large, while in the case of slip it is small” (Kajiwara and Kikuchi, 1991).

9.9.1.2 Non-Ferrous Alloys

A classification base of the non-ferrous alloy systems exhibiting martensite is

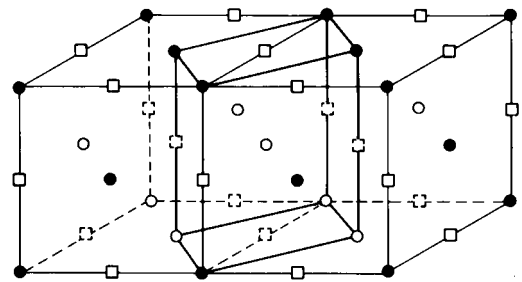


Figure 9-35. Schematic representation of the Bain correspondence for the f.c.c. to b.c.t. transformation. The square symbols represent the possible occupied positions of the interstitial carbon atoms (Muddle, 1982).

the $\gamma'_1 - \beta''_1$, and finally the $\beta''_1 - \alpha'_1$ martensite.

The other typical example of the second group is the Ni–Ti-based alloy system; both prototype alloy systems constitute the shape-memory alloys (SMA). The occurrence of a so-called “pre-martensitic” R-shape has long obscured the observations. The review by Wayman (1987), illustrates the complexity of the transformation behavior. During cooling, the high-temperature ordered b.c.c. phase (P) transforms first to an incommensurate phase (I) and on further cooling to a commensurate phase (C), and finally to martensite. The P-to-I transformation is second order, whereas the I-to-C transformation is a first-order phase transformation involving a cubic-to-rhom-

bohedral (the so-called R-phase) structural change. At still lower temperatures the rhombohedral R-phase transforms into a monoclinically distorted martensite. The R-phase also forms displacively and can be stress-induced, and shows all the characteristics of a reversible transformation.

Concerning the third group, in only a few cases, as in In–Ti, has definite proof been provided to justify the conclusion that the transformation is martensitic. Most of the transformations in these systems have to be classified as quasi-martensitic.

9.9.2 Non-Metals

Inorganic compounds exhibit a variety of crystal structures owing to their diverse

Table 9-8. Non-metals with lattice deformational transformations (Kriven, 1982).

Inorganic compounds		
Alkali and ammonium halides	MX, NH ₄ X	(NaCl-cubic \Leftrightarrow CsCl-cubic)
Nitrates	RbNO ₃ KNO ₃ , TiNO ₃ , AgNO ₃	(NaCl-cubic \Leftrightarrow rhombohedral \Leftrightarrow CsCl-cubic) (Orthorhombic \Leftrightarrow rhombohedral)
Sulfides	MnS ZnS BaS	(Zinc-blende-type \Leftrightarrow NaCl-cubic) (Wurtzite-type \Leftrightarrow NaCl-cubic) (Zinc-blende-type \Leftrightarrow wurtzite-type) (NaCl-type \Leftrightarrow CsCl-type)
Minerals		
Pyroxene chain silicates	Enstatite (MgSiO ₃) Wollastonite (CaSiO ₃) Ferrosilite (FeSiO ₃)	(Orthorhombic \Leftrightarrow monoclinic) (Monoclinic \Leftrightarrow triclinic) (Orthorhombic \Leftrightarrow monoclinic)
Silica	Quartz Tridymite Cristobalite	(Trigonal \Leftrightarrow hexagonal) (Hexagonal, wurtzite-related) (Cubic \Leftrightarrow tetragonal, zinc blende-related)
Ceramics		
Boron nitride	BN	(Wurtzite type \Leftrightarrow graphite-type)
Carbon	C	(Wurtzite type \Leftrightarrow graphite)
Zirconia	ZrO ₂	(Tetragonal \Leftrightarrow monoclinic)
Organics		
Chain polymers	Polyethylene (CH ₂ –CH ₂) _n	(Orthorhombic \Leftrightarrow monoclinic)
Cement		
Belite	2 CaO · SiO ₂	(Trigonal \Leftrightarrow orthorhombic \Leftrightarrow monoclinic)

chemistry and bonding. Compared with metals, the relatively low-symmetry parent structures have fewer degrees of freedom on transforming to even lower symmetry product structures, or vice versa. Many of these transformations involve changes in electronic states with relatively small volume changes. They tend to proceed by shuffle-dominated mechanisms. However, shear transformations involving large structural changes in terms of coordination number or volume changes have also been reported in inorganic and organic compounds, minerals, ceramics, organic compounds, and some crystalline compounds of cement. Some of the most prominent examples are given in Table 9-8 (Kriven, 1982, 1988).

Because of its technological interest as a toughener for brittle ceramic materials, zirconia is considered as the prototype of martensite in ceramic materials. On cooling, the high-temperature cubic phase of zirconia transforms at 2370 °C to a tetragonal phase. On further cooling, bulk zirconia transforms at 950 °C to a monoclinic phase with a volume increase of 3%. The latter transforms on heating at about 1170 °C. The monoclinic to tetragonal phase transformation is considered to be martensitic. The M_s temperature can be lowered substantially even below room temperature by alloying or by reducing the powder size. Small particles of zirconia, embedded in a single-crystal matrix of alumina, remain metastable (=tetragonal) at room temperature for particle diameters less than a critical diameter (Rühle and Kriven, 1982). These metastable particles can transform to the monoclinic phase under the action of an applied stress, and it is this property that is exploited in toughening brittle ceramics (see Becher and Rose (1994)).

Polymorphism is known to occur in several crystalline polymeric materials. In most of these systems the transformation

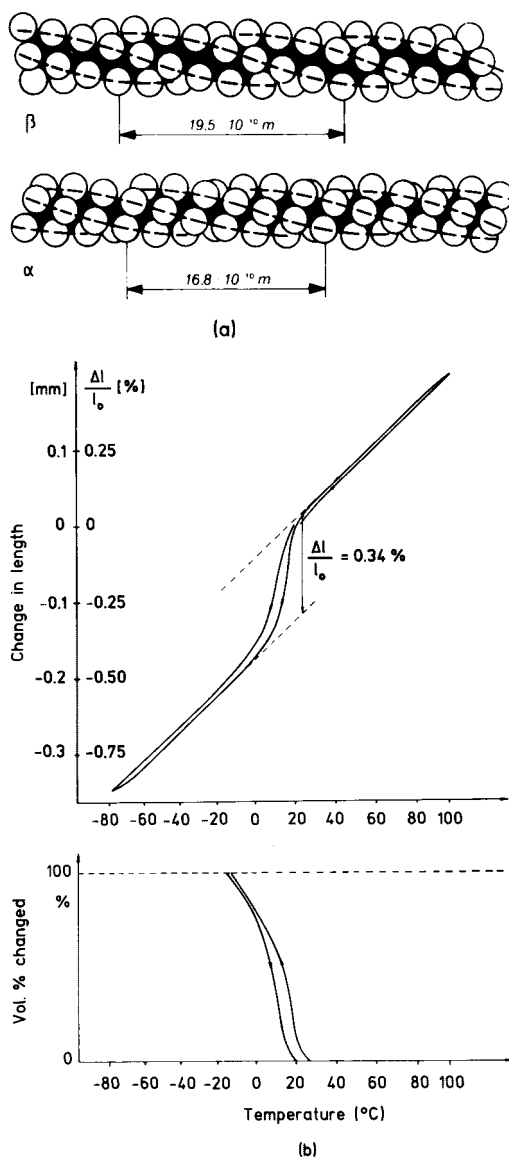


Figure 9-37. (a) Helix structure of the α - and β -modification of PTFE, and (b) dilatometric determination of relative volume changes and temperature range of transformations of PTFE (Hornbogen, 1978).

depends strongly on thermal activation. However, in PTFE (polytetrafluoroethylene) the conditions for no or weak thermal activation are fulfilled, and the transformation can then be regarded as a diffusionless

or martensitic transformation (Hornbogen, 1978). This polymer crystallizes as parallel arrangements of molecular chains parallel to the c -axis. The atoms along the chains are arranged as helices; the period along the c -axis in the α -modification is $13\text{C}_2\text{F}_4$ units while it is 15 units in the β -modification. The transformation from the α - to the β -helix occurs at about 19°C (Fig. 9-37). Relaxation of the helix during this transformation does not lead to an extension of the specific length of the molecules in the c -direction. The diameters of the molecule and thus the lattice parameters in the a -direction increase, which leads to an increase of about 1% in the specific volume. The observed shape change can be increased if the molecules have been aligned by plastic deformation. An analysis of the shape changes leads to the conclusion that the PTFE transformation is diffusionless by a free volume shear, a type of transformation not yet known in metallic and inorganic materials.

Biological materials consisting of crystalline proteins also undergo martensitic transformations in performing their life functions. In a review entitled "Martensite and Life", Olson and Hartman (1982) discuss some examples. The tail-sheath contraction in T4 bacteriophages can be described as an irreversible strain-induced martensitic transformation, while polymorphic transformations in bacterial flagellae appear to be stress-assisted and exhibit a shape-memory effect.

9.10 Special Properties and Applications

9.10.1 Hardening of Steel

Much of the technological interest concerns martensite in steels. In a review on strengthening of metals and alloys, Wil-

Table 9-9. Contribution to as-quenched martensite strength in 0.4 wt.% C steel (Williams and Thompson, 1981).

Boundary strengthening	620 MPa
Dislocation density	270 MPa
Solid solution of carbon	400 MPa
Rearrangement of C in quench	750 MPa
Other effects	200 MPa
<hr/>	
0.2% yield strength	2240 MPa

liams and Thompson (1981) consider martensite as one of the most complex cases of combined strengthening. The hardness of martensite in as-quenched carbon steel depends very much on the carbon content. Up to about 0.4 wt.% C the hardening is linear; retained austenite is present in steel containing more carbon, which reduces the rate of hardening. Solute solution hardening by the interstitial carbon atoms is very substantial, whereas substitutional solid solution hardening is low. For example, Fe-30 wt.% Ni martensites, where the carbon content is very low, are not very hard. The hardening of martensite is not due only to interstitial solute solution hardening, however. The martensite contains a large number of boundaries and dislocations, and the carbon atoms may rearrange during the quench forming clusters that cause extra dislocation pinning. The various contributions to the strength of a typical C-containing martensite are given in Table 9-9, from which it becomes evident that interstitial solid solution hardening is not the most important cause. Because many martensitic steels are used after tempering, lower strengths than those shown in Table 9-9 are found.

9.10.2 The Shape-Memory Effect

A number of remarkable properties have their origin in a martensitic phase trans-

formation, such as the shape-memory effect, superelasticity, rubber-like behavior and pseudoelasticity. The most fascinating property is undoubtedly the shape-memory effect. Review articles were published by Delaey et al. (1974), Otsuka and Shimizu (1986), Schetky (1979), and Junakubo (1987). Recently, Van Humbeeck (1997) prepared a review on Shape Memory Materials: "State of the Art and Requirements for Future Applications". His review contains 104 references to recent articles on the topic.

A metallic sample made of a common material (low-carbon steel, 70/30 brass, aluminum, etc.) can be plastically deformed at room temperature. The macroscopic shape change resulting from this deformation will remain unchanged if the sample is heated to higher temperatures. The only observable change in property may be its hardness, provided that the temperature to which the sample has been heated is above the recrystallization temperature. Its shape, however, remains as it was after plastic deformation. If the sample is made of a martensitic shape-memory material and is plastically deformed (bent, twisted, etc.) at any temperature below M_f and subsequently heated to temperatures above A_f , we observe that the shape that the specimen had prior to the deformation starts to recover as soon as the A_s temperature is reached and that this restoration is completed at A_f . This behavior is called the "shape-memory effect", abbreviated to SME.

If the SME sample is subsequently cooled to a temperature below M_s and its shape remains unchanged on cooling, we talk about the "one-way shape-memory effect". If it spontaneously deforms on cooling to temperatures below M_s into a shape approaching the shape that it had after the initial plastic deformation, the effect is called the "two-way shape-memory ef-

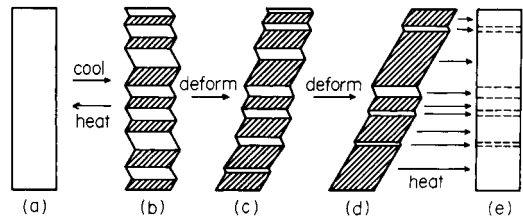


Figure 9-38. Schematic illustration of the shape-memory effect: (a) and (e) parent phase; (b), (c) and (d) martensite phase (Otsuka and Shimizu, 1986).

fect". A more visual description of these two effects is given in Fig. 9-38 and a clarifying example is shown in Fig. 9-39, where the applicability of the one-way shape-memory effect is given for a spacecraft antenna.

The shape that has to be remembered must, first of course, be given to the specimen. This is done by classical plastic deformation by either cold or hot working. This process, however, may not involve any martensite formation. The material must therefore be in a special metallurgical condition, which may require additional thermal treatments. In Fig. 9-40, for example, depicting a temperature-actuated shape-memory switch, two different "remembering" shapes are used. The initial shape may be obtained by hot extrusion or wire drawing and may or may not receive an additional cold or hot working in order to obtain the required shape. The shapes formed must receive a heat treatment, consisting of a high-temperature annealing, followed by water quenching. The specimen is now martensitic, provided that the composition is such that M_f is above room temperature. In order to induce the shape memory, the martensitic specimens are bent either to be curved or to be straight and are placed into the actuator at room temperature. If the temperature of the actuator exceeds the reverse transformation

temperature of the shape-memory material, the specimens recover towards their “remembered” position. The electrical contacts are either closed or opened.

Special procedures for handling of the shape-memory device are needed if we want to induce the two-way memory effect. This can be explained by again taking the temperature-actuated switch as an example. If the specimen taken in its remembered position is cooled back to room tem-

perature, we do not expect further shape changes to occur. In order to reuse the specimens after having performed the shape-memory effect, they must be bent to be either curved or straight again. Reheating these deformed specimens for a second time to temperatures above A_f will result in shape memory. If this cycle, bending–heating–cooling, is repeated several times, gradually a two-way memory sets in. During cooling the specimen reverts spontane-

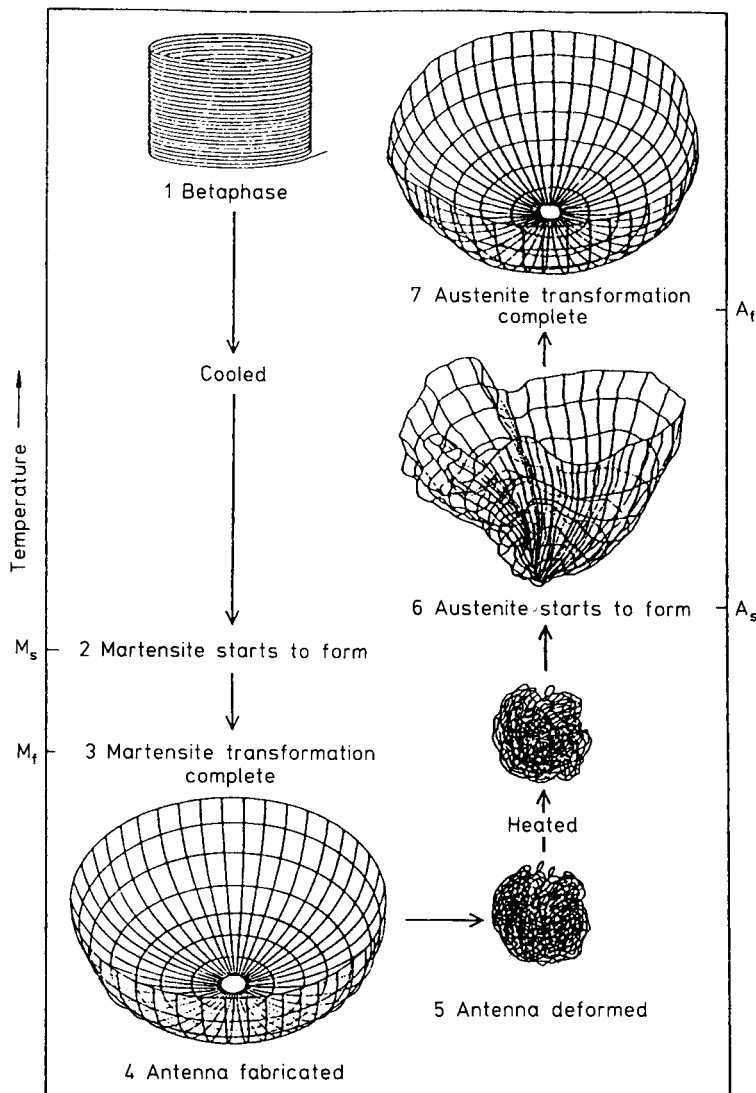


Figure 9-39. Application of Nitinol for a shape-memory spacecraft antenna. From “Shape Memory Alloys” by L. McDonald Shetky. Copyright (1979) by Scientific American, Inc. All rights reserved.



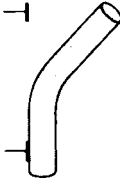
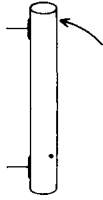

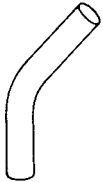
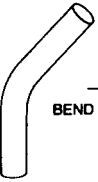

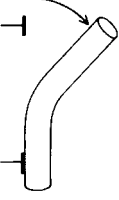
INITIAL SHAPE	ADDITIONAL COLD OR HOT SHAPING	SHAPE AFTER BETATIZING AND QUENCHING	POSITION AT ROOM TEMPERATURE	"REMEMBERED" POSITION (ABOVE A_1)
	NO MARTENSITE	NOW CONTAINS MARTENSITE	MARTENSITE UNDER STRESS	NO MARTENSITE
	NONE	 BEND TO CURVE		
		 BEND STRAIGHT		

Figure 9-40. Temperature-actuated switch designed so that it opens or closes above a particular temperature. From “Shape Memory Alloys” by L. McDonald Shetky. Copyright (1979) by Scientific American, Inc. All rights reserved.

ously to its “deformed” positions, thus opening or closing the electrical contacts on cooling. This repeated cycling, deformation in martensitic condition followed by a heating–cooling, is called “training”. We can thus induce two-way memory by using a training procedure.

A further comment should be made here concerning the shapes that can be remembered. We have to distinguish three shaping procedures: the fabrication step from raw material towards, for example, a coiled wire such as for the antenna, the fabrication of the “to be remembered position”, such as the additional shaping for the actuator, and the final deformation in the martensitic condition, such as the bending of the actuator. The first two fabrication steps involve only classical plastic deformation and, therefore, the type and degree of deformation are in principle not limited, provided that the material does not fail. The degree of deformation, however, is limited

in the third deformation step, because it may not exceed the maximum strain that can be recovered by the phase transformation itself. Because these strains are associated with the martensitic transformation, the maximum amount of recoverable strain is bound to the crystallography of the transformation. Exceeding this amount of deformation in the third fabrication step will automatically result in unrecoverable deformation.

Many examples of shapes that can be remembered are possible. A flat SME specimen can elongate or shorten during heating, can twist clockwise or counter-clockwise, and can bend upwards or downwards. An SME spring can expand or contract during heating. All this depends on the second and third fabrication steps.

What happens now if, for one reason or another, the specimen is restrained to exhibit the shape-memory effect? For example, what happens if an expanded ring is

fitted as a sleeve over a tube with an outer diameter slightly smaller than the inner diameter of the expanded ring but larger than the inner diameter of the ring in the remembered position? On heating, the ring will start to shrink as soon as the temperature A_s is reached. While shrinking it will touch the tube wall and further shrinking will be hindered. From this moment, a compressive stress will be built up, clamping the shrinking ring around the tube. Obviously, the composition of the alloy should be such that the M_s temperature is below the value at which clamping is required; in many cases, this is below room temperature. For clamping rings it is therefore important that on cooling back to room temperature the clamping stress is still present. This means that two-way memory must be avoided, which is easily achieved by choosing a shape-memory alloy that exhibits a large temperature hysteresis.

On heating a shape-memory device, stresses can thus be built up and mechanical work can be done. The latter would be the case if a compressed shape-memory spring has to lift a weight as in a shape-memory actuated window opener (Fig. 9-41). A very useful device is realized when a shape-memory device is used, as shown in Fig. 9-42, in combination with a bias spring made of a conventional linear elastic material, both being clamped between two fixed walls and attached to each other with a plate. At temperatures below M_f , the shape-memory spring is closed and compressed by the bias spring. The SME spring had to be deformed, in this case compressed, in order to fit into the clamping unit. The clamping unit with the two springs installed is now heated to temperatures above A_f ; as soon as A_s is reached, the SME spring will start to expand and try to push back the bias spring. At A_f , the shape-memory spring will not yet have regained

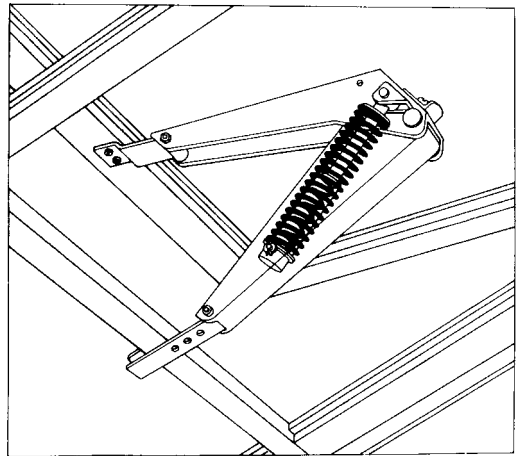


Figure 9-41. A simple shape-memory window opener made from a copper-based shape-memory alloy. From "Shape Memory Alloys" by L. McDonald Shetky. Copyright (1979) by Scientific American, Inc. All rights reserved.

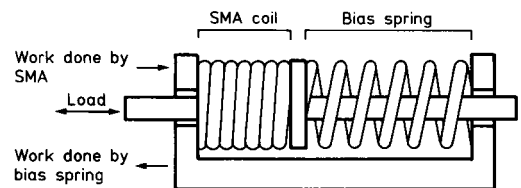


Figure 9-42. A mechanism in which a shape-memory alloy (SMA) spring is used in conjunction with a bias spring. From "Shape Memory Alloys" by L. McDonald Shetky. Copyright (1979) by Scientific American, Inc. All rights reserved.

its original length, and further heating is required to overcome the force exerted by the bias spring. At a certain temperature higher than A_f the shape-memory spring will be fully recovered. This temperature will depend on the strength of the bias spring. During this temperature excursion, the plate that is fixed between the two springs will have moved and can, if an "engine" is attached to it, deliver work. If the clamping unit is now cooled, the bias spring will try to compress the shape-memory spring into

its deformed position. The elastic energy that has been stored in the bias spring during the heating cycle is now released, allowing the plate to perform work also during the cooling cycle. To describe fully such a working performing cycle, a thermodynamic treatment is needed (Wollants et al., 1979). The working performing cycle can best be illustrated by taking a shape-memory spring that expands or contracts during heating or cooling and that carries a load. The working performing cycle can then be represented in a displacement–temperature, a stress–temperature, or an entropy–temperature diagram.

Although the shape-memory effect has been observed in many alloy systems, only three systems are commercially available,

mainly because of economic factors and the reliability of the material. The three alloy systems are Ni–Ti, Cu–Zn–Al and Cu–Al–Ni. Generally, other elements are added in small amounts (of the order of a few weight %) in order to modify the transformation temperatures or to improve the mechanical properties or the phase stability. In all three cases the martensite is thermoelastic. Maki and Tamura (1987) reviewed the shape-memory effect in ferrous alloys, where a non-thermoelastic Fe–Mn–Si alloy has also been found to show a shape-memory effect, and commercialization is being considered. The most important properties of shape-memory alloys are summarized in Fig. 9-43, in which the working temperatures, the width of the

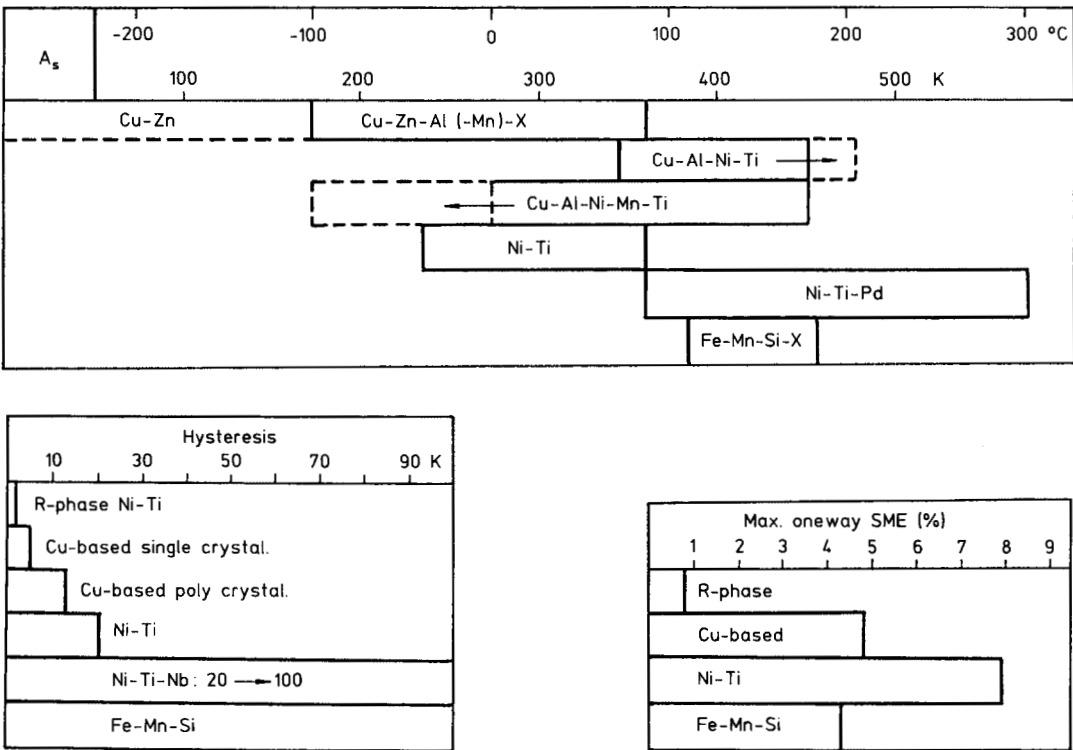


Figure 9-43. Schematic representation of the most relevant shape-memory properties (courtesy Van Humbeeck, 1989).

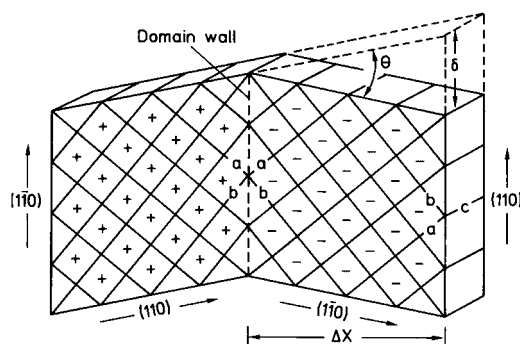


Figure 9-44. Schematic illustration of the mechanism for an electronic micro-positioning (Lemons and Coldren, 1978).

hysteresis, and the maximum recoverable strain are given. Because of the superior mechanical, chemical and shape-memory properties of Ni–Ti alloys, this alloy system has been applied most successfully; about 90% of the present applications use these alloys. Owing to the continuous improvement of the properties of Cu-based alloys, together with their lower price, Cu SME alloys have been successfully used in several applications.

The commercial applications of shape-memory devices can be divided into four groups:

1. motion: by free recovery during heating and/or cooling;
2. stress: by constrained recovery during heating and/or cooling;
3. work: by displacing a force, e.g., in actuators;
4. energy storage: by pseudoelastic loading of the specimen.

Shape-memory effects have also been reported in non-martensitic system, e.g., in ferroelectric ceramics (Kimura et al., 1981), and have found applications as micro-positioning elements (Lemons and Coldren, 1978). The shape change is attrib-

uted here to domain-wall motion, as shown in Fig. 9-44.

9.10.3 High Damping Capacity

The hysteresis exhibited during a pseudoelastic loading and unloading cycle is a measure of the damping capacity of a vibrating device fabricated from a shape-memory material, which is cycling under extreme stress conditions exceeding the critical stress needed to induce martensite by stress. Vibrating fully martensitic samples also exhibit high damping. A fully martensitic sample consists of a large number of differently crystallographically oriented domains whose domain boundaries are mobile. Under the action of an applied stress these boundaries move but, because of friction, energy is lost during this movement. If a cyclic stress is applied, this forward and backward boundary movement will lead to damping of the vibration. Comparing the amount of this damping with the damping that we observe in other non-SME alloy systems, it is found that the damping capacity of martensitic shape-memory alloys is one of the highest. The shape-memory alloys are said to belong to the high-damping materials, the so-called HIDAMETS.

9.10.4 TRIP Effect

TRIP is the acronym for TRansformation-Induced Plasticity and occurs in some high-strength metastable austenitic steels exhibiting enhanced uniform ductility when plastically deformed. This uniform macroscopic strain, up to 100% elongation, accompanies the deformation-induced martensitic transformation and arises from a plastic accommodation process around the martensite plates. This macroscopic strain thus contrasts with that occurring in

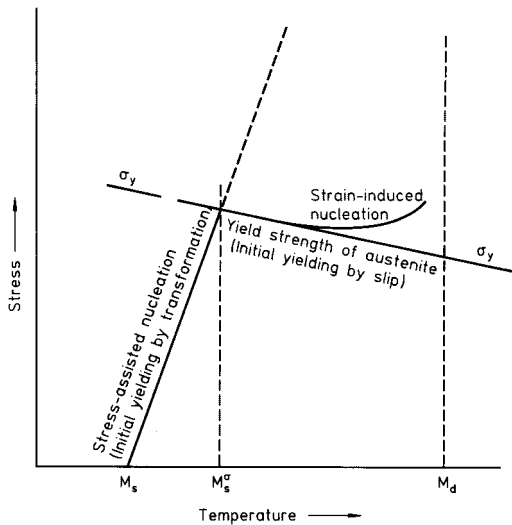


Figure 9-45. Idealized stress-assisted and strain-induced regimes for mechanically-induced nucleation (Olson and Cohen, 1982a).

shape-memory alloys in being unrecoverable.

TRIP has been extensively studied by Olson and Cohen (1982a) and we will follow their approach here. They distinguish two modes of deformation-induced transformation, according to the origin of the nucleation sites for the martensite plates: “stress-assisted” and “strain-induced” transformation. The condition under which each mode can operate is indicated in a temperature–stress diagram as shown in Fig. 9-45. At temperatures slightly higher than M_s^σ , the stress required for stress-assisted nucleation on the same nucleation sites follows the line AB. At B, the yield point for slip in the parent phase is reached, defining the highest temperature M_s^σ for which the transformation can be induced solely by elastic stresses. Above this temperature, plastic flow occurs before martensite can be induced by stress. New strain-induced nucleation sites are formed, contributing to the kinetics of the transformation. The

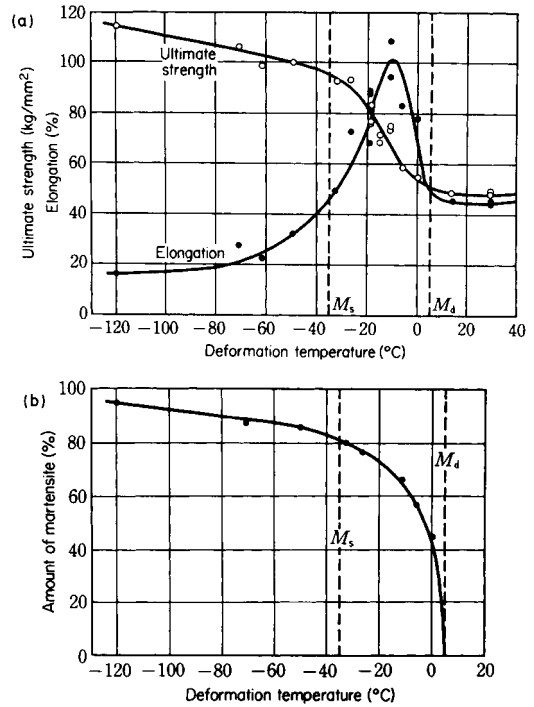


Figure 9-46. Transformation-induced plasticity in tensile tests at various temperatures (Fe–29 wt.% Ni–0.26 wt.% C) (Tamura et al., 1969).

stresses at which this strain-induced martensite is first detected follows the curve BD. At point D, fracture occurs and thus determines the highest temperature M_d at which martensite can be mechanically induced.

When the transformation occurs at temperatures below M_s^σ , the plastic strain is due entirely to transformation plasticity resulting from the formation of preferential martensite variants. The volume of the induced martensite is therefore linearly related to the strain. The existing nucleation sites are aided mechanically by the thermodynamic contribution of the applied stress, reducing the chemical driving force for nucleation. Above M_s^σ , the relationship between strain and volume of martensite becomes more complex, because strain is

then a result of plastic deformation of the parent phase and of transformation plasticity. Strain hardening and enhancement of nucleation of martensite also play an essential role. When martensite is formed during tensile deformation, the strain hardening becomes large. Necking is then expected to be suppressed, explaining the enhanced uniform elongation. Fig. 9-46 shows, as an example, the amount of martensite, the elongation and the ultimate strength measured after tensile tests of a TRIP steel as a function of temperature, clearly illustrating the enhanced elongation, especially in the temperature range between M_s^σ and M_d . Such a large elongation (sometimes over 200%) can also be produced by subjecting a TRIP steel specimen under constant load to thermal cycles through the transformation temperature.

9.11 Recent Progress in the Understanding of Martensitic Transformations

We draw attention here to some recent papers that illustrate recent progress in the understanding of martensite, and in which

some new approaches are also explained. Most of the information referred to in this section was presented at the most recent ICOMAT international conference on martensitic transformations held in 1998 at Bariloche (Ahlers et al., 1999).

New directions in martensite theory are presented by Olson (1999). The nucleation of martensite, the growth of a single martensite plate, the formation of, for example, self-accommodating groups of martensite plates, and this within single crystals of the parent phase as well as in polycrystalline material, and the constraints dictated by the components where martensitic materials are only one (maybe the most important) functional element of the component, are all influenced by different interactive levels of structures (ranging from solute atoms to components). Nucleation is the first step in martensite life, and a component whose functional properties are attributed to those of martensite, can be considered the final step. Olson (1999) constructed a flow-block diagram in which the martensitic transformation is situated in a multilevel dynamic system. This new system, shown in Fig. 9-47, and the one given in Fig. 9-1, offer powerful tools for a better under-

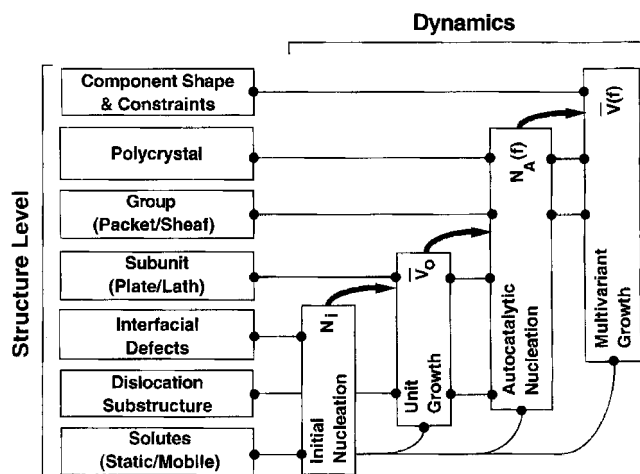


Figure 9-47. The flow-block diagram of martensitic transformation as a multilevel dynamic system (Olson, 1999).

standing of diffusionless phase transformations. Its use should lead to a better design of martensitic and bainitic alloys meeting specific requirements. Close analysis of the papers presented at ICOMAT 98 shows that such an approach can already be found in many papers.

Special attention is given to the influence of external constraints, such as hydrostatic pressure, the application of a magnetic field, and to martensite formed in thin films prepared by either sputtering or rapid solidification. Kakeshita et al. (1999) studied the influence of hydrostatic pressure instead of uniaxial stress, in order to formulate a thermodynamic approach for a better understanding of the nucleation of martensite. The strengthening mechanisms in steel due to martensite are reviewed, the diffusion of carbon in the various states (according to the dynamic system of Fig. 9-47) of martensite is highlighted. In this context, the fracture mechanism is related to the tempering temperature and the carbon diffusion.

As is commonly known, the mechanism of bainite transformation is a subject with many unresolved issues. Bhadeshia (1999) gives an overview of the transformation mechanisms proposed to explain “among others” the growth of bainite. The development of bainite at both high temperatures (upper bainite) and low temperatures (lower bainite) is discussed and is illustrated in Fig. 9-48. According to Bhadeshia, the unresolved issues are:

the growth rate of an individual bainite plate

a theory explaining the kinetics to estimate the volume fraction of bainite in austenite obtained during an isothermal transformation

the modeling describing quantitatively the formation of carbides

and a number of features associated with the interaction between plastic deformation and bainite formation.

The influence of carbon on the bainitic transformation is treated in great detail and is shown to be a controlling factor of the mechanical properties of different multi-phase TRIP-assisted steels (Girault et al., 1999; Jacques et al., 1999).

The martensitic transformation in Fe–Mn-based alloys is treated in various papers, showing the increasing interest in developing ferrous shape-memory alloys. In these alloys, austenite transforms either into a h.c.p. ϵ -phase ($\gamma \rightleftharpoons \epsilon$) or/and into α' -martensite ($\gamma \rightleftharpoons \alpha'$).

New approaches and strategies are discussed for the application of shape-memory alloys in non-medical (Van Humbeeck, 1999) as well as in medical applications (Duerig et al., 1999). Only two examples are shown here. The first example (Fig. 9-49) shows that Ni–Ti superelastic alloys improve significantly the cavitation erosion resistance if compared with marten-

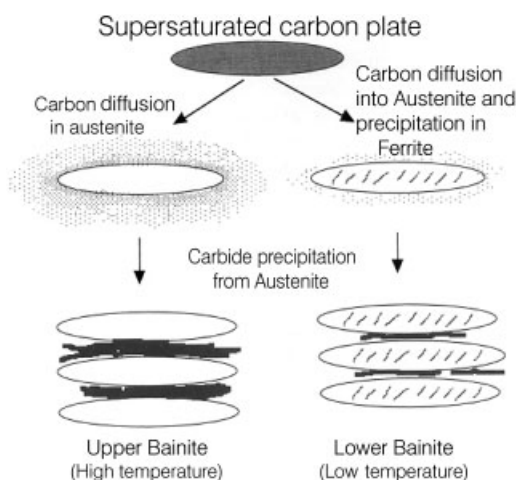


Figure 9-48. A schematic representation of the mechanism explaining the growth and development of bainite (Bhadeshia, 1999).

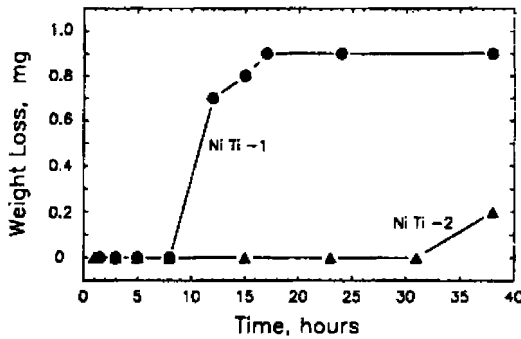


Figure 9-49. The weight loss of a martensitic (Ni Ti-1) and a pseudoelastic (Ni Ti-2) Ni-Ti shape-memory alloy (Richman et al., 1994).

stic Ni-Ti. But it should be remarked that this figure is only an enlargement of a figure giving an overall view of the cavitation resistance of other common alloys. For example, the weight loss after 10 h is already 20–30 mg for the “common” alloys in comparison with the negligible weight loss of both Ni-Ti shape-memory alloys after 10 h tested under the same conditions. A very impressive example of the application of Ni-Ti shape-memory alloys is given in Fig. 9-50. This figure shows an atrial septal occlusion device with Nitinol (Ni-Ti shape-memory alloy) wires incorporated in a sheet of polyurethane. This device allows holes in the atrial wall of the heart to be closed without surgery. The two umbrella-like devices are folded in two catheters, which are placed on either side of the hole. Once the two folded umbrellas are withdrawn from their catheters, they are screwed together in such a way that the hole is closed. Because of the flexibility of both materials, the heart can again beat normally. This device illustrates the concept of the elastic development capacity of shape-memory alloys. Because Ni-Ti shape-memory alloys have proposed to be biocompatible (see Van Humbeeck, 1977), many applications of these Ni-Ti alloys

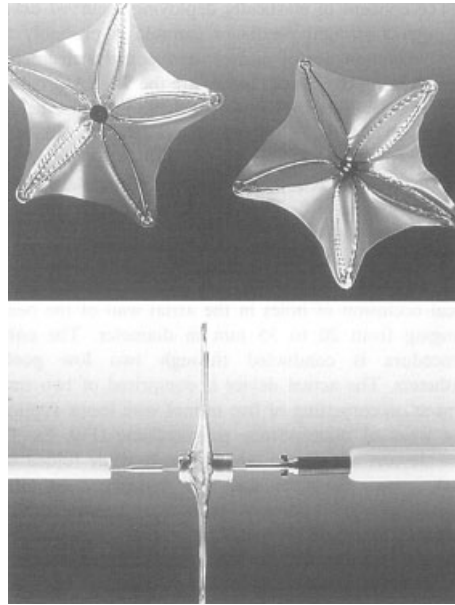


Figure 9-50. A shape-memory device for repairing defects in the heart wall (Duerig et al., 1999).

are currently being developed and marketed.

9.12 Acknowledgements

The author would like to thank M. Ahlers, J. W. Christian, M. De Graef, R. Gotthardt, P. Haasen, H. S. Hsu, J. Ortín, K. Otsuka, J. Van Humbeeck and P. Wollants for support and advice while preparing the manuscript, and M. Van Eylen, M. Nolmans, H. Schmidt and K. Delaey for their assistance. The “Nationaal Fonds voor Wetenschappelijk Onderzoek” of Belgium is acknowledged for financial support (project No. 2.00.86.87). The author especially acknowledges the continuing interest and encouragement he received from A. Deruyttere. For help in preparing the revised version, I would like to thank M. Chandrasekaran.

9.13 References

- Aaronson, H. I., Reynolds, W. T. Jr (1988), in: *Phase Transformations '87*: Lorimer, G. W. (Ed.). London: The Institute of Metals, p. 301.
- Ahlers, M. (1974), *Z. Metallkd.* 65, 636.
- Ahlers, M. (1982), in: *International Summer Course on Martensitic Transformations*. Leuven: Dep. Met. & Mat. Eng., KV Leuven, p. 2.1.
- Ahlers, M., Kosterz, G., Sade, M. (1999), *ICOMAT '98, International Conference on Martensitic Transformations, 7–11 December 1998, S. C. de Bariloche, Argentine Mater. Sci. Eng.* A273–275.
- Bain, E. C. (1924), *Trans. AIME* 70, 25.
- Ball, J. M., James, R. D. (1988), in: *Phase Transformations '87*: Lorimer, G. W. (Ed.). London: The Inst. of Metals, p. 425.
- Barsch, G. R., Krumhansl, J. A. (1988), *Metall. Trans.* 19A, 761.
- Becher, P. F., Rose, L. R. F. (1994), in: *Materials Science and Technology*, Vol. 11: Swain, M. (Ed.). Weinheim: VCH, p. 409.
- Bevis, M. J., Allan, P. S. (1974), *Surface and Defect Properties of Solids* 3, 93.
- Bhadeshia, H. K. D. H. (1999), *Mater. Sci. Eng.* A273–275, 58.
- Bidaux, J. E. (1988), Ph.D. Thesis. Lausanne: EPFL.
- Bilby, B. A., Christian, J. W. (1961), *J. Iron Steel Inst.* 197, 122.
- Bilby, B. A., Frank, F. C. (1960), *Acta Metall.* 8, 239.
- Binder, K. (2001), in: *Phase Transformations in Materials*: Kosterz, G. (Ed.). Weinheim: Wiley-VCH, Chap. 4.
- Bowles, J. S. (1951), *Trans. AIME* 191, 44.
- Bowles, J. S., Mackenzie, J. K. (1954), *Acta Metall.* 2, 158; 224.
- Buerger, M. J. (1951), in: *Phase Transformations in Solids*: Smoluchowski et al. (Eds.). New York: Wiley.
- Bullough, R., Bilby, B. A. (1956), *Proc. Phys. Soc. B*, LXIX, 1276.
- Christian, J. W. (1965), *The Theory of Transformations in Metals and Alloys*. Oxford: Pergamon Press.
- Christian, J. W. (1976), *Suppl. Trans. JIM.* 17, 21.
- Christian, J. W. (1982), in: *International Summer Course on Martensitic Transformations*. Leuven: University of Leuven, p. 5.1.
- Christian, J. W., Knowles, K. M. (1982), in: *Proceedings of Solid to Solid Transformations*. New York: AIME, p. 1185.
- Cohen, M. (1982), in: *International Summer Course on Martensitic Transformations*. Leuven: Dep. Met. & Mat. Eng., KV Leuven, p. 1.1.
- Cohen, M., Olson, G. B., Clapp, P. C. (1979), in: *Proc. ICOMAT '79*. Cambridge (MA): MIT, p. 1.
- de Fontaine, D. (1973), in: *Phase Transitions 1973*. New York: Pergamon Press, p. 169.
- Delaey, L., Krishnan, R. V., Tas, H., Warlimont, H. (1974), *J. Mat. Sci.* 9, p. 1521; 1536; 1545.
- Delaey, L., Deruyttere, A., Aermant, E., Roos, J. R. (1978), *MTM Internal. INCRA Report*. Report 78 R1. Leuven: Dep. Met. & Mat. Eng., KV Leuven.
- Delaey, L., Gobin, P. F., Guénin, G., Warlimont, H. (1979), in: *Proc. ICOMAT '79*. Cambridge (MA): MIT, p. 400.
- Delaey, L., Chandrasekaran, M., Andrade, M., Van Humbeeck, J. (1982a), in: *Proceedings of Solid to Solid Transformations*. New York: AIME, p. 1429.
- Delaey, L., Mukherjee, K., Chandrasekaran, M. (1982b), in: *International Summer Course on Martensitic Transformations*. Leuven: Dep. Met. & Mat. Eng., KV Leuven, p. 7.1.
- Duerig, T., Pelton, A., Stöckel, D. (1999), *Mater. Sci. Eng.* A273–275, 149.
- Falk, F. (1982), in: *ICOMAT '82*: Editions de Physique C4, p. 3.
- Fujita, F. E. (1982), in: *International Summer Course on Martensitic Transformations*. Leuven: Dep. Met. & Mat. Eng., KV Leuven, p. 10.1.
- Funakubo, H. (1987), *Shape Memory Alloys*. New York: Gordon and Breach.
- Girault, E., Jacques, P., Ratchev, P., Van Humbeeck, J., Verlinden, B., Aernoudt, E. (1999), *Mater. Sci. Eng.* A273–275, 471.
- Greninger, A. B., Troiano, A. R. (1949), *Metall. Trans.* 185, 590.
- Guénin, G., Clapp, P. C. (1986), *Proc. ICOMAT '86*. Sendai: Japanese Institute of Metals, p. 171.
- Guénin, G., Gobin, P. F. (1982), in: *ICOMAT '82*: Editions de Physique C4, p. 57.
- Hara, T., Ohba, T., Otsuka, K. (1998), *Proc. PRIM-3, Hawaii, TMS*, p. 1199.
- Hocke, U., Warlimont, H. (1977), *J. Phys.* F7, 1145.
- Horikawa, H., Ichinose, S., Morii, K., Miyazaki, S., Otsuka, K. (1988), *Metall. Trans.* 19A, 915.
- Hornbogen, E. (1978), *Progr. Colloid Polymer Sci.* 64, 125.
- Hornbogen, E. (1988), *Pract. Metall.* 25, 157.
- Hsu, T. Y. (1980), in: *Martensitic Transformation and Martensite*: Hsu, T. Y. (Xu Zuyao) (Ed.). Shanghai: Science Press, p. 10.
- Hsu, T. Y. (1985), *J. Mat. Sci.* 20, 23.
- Hsu, T. Q., Zhou Xiaowang (1989), *Acta Metall.* 37, 3091.
- Ichinose, S., Funatsu, Y., Otsuka, K. (1985), *Acta Metall.* 33, 1613.
- James, R. D. (1988), in: *Materials Instabilities in Continuum Mechanics and Related Mathematical Problems*: Ball, J. M. (Ed.). Oxford: Univ. Press, p. 175.
- Jacques, P., Girault, P., Catlin, T., Geerlofs, N., Kop, T., Van der Zwaag, S., Delannay, F. (1999), *Mater. Sci. Eng.* A273–275, 475.
- Kajiwar, S., Kikuchi, T., Uehara, S. (1986), *Proc. ICOMAT '86*. Sendai: Japanese Institute of Metals, p. 301.

- Kakeshita, T., Saburi, T., Shimizu, K. (1999), *Mater. Sci. Eng. A* 273–275, 21.
- Kaufman, L. (1965), in: *Physical Properties of Martensite and Bainite*: Special Report 93. London: The Iron & Steel Inst., p. 48.
- Kaufman, L., Cohen, M. (1958), *Progr. Metal Phys.* 7, 165.
- Krauss, G. (1992), in: *Materials Science and Technology*, Vol. 7: Pickering, F. B. (Ed.). Weinheim: VCH, p. 1.
- Krauss, G., Marder, A. R. (1971), *Metall. Trans.* 2, 2343.
- Kriven, W. M. (1982), in: *Proceedings of Solid to Solid Transformations*. New York: AIME, p. 1502; and in: *International Summer Course on Martensitic Transformations*. Leuven: Dep. Met. & Mat. Eng., KV Leuven, p. 9.1.
- Kriven, W. M. (1988), *J. Am. Ceram. Soc.* 71, 1021.
- Kurdjurnov, G. V. Sachs, G. (1930), *Z. Phys.* 64, 325.
- Lemons, R. A., Coldren, L. a. (1978), *Rev. Sci. Instrum.* 49, 1650.
- Liao, K. C., Allen, C. W. (1982), in: *Solid-State Phase Transformations*: Aaronson, H. I., Laughlin, D. E., Sekerka, D. F., Wayman, C. M. (Eds.). Warrendale: Met. Soc. AIME, p. 1493.
- Ling, H. C., Owen, W. s. (1981), *Acta Metall.* 29, 1721.
- Liu, Y., Xia, Z., Van Humbeeck, J. (1999a), *Mater. Sci. Eng. A* 273–275, 673.
- Liu, Y., Xia, Z., Van Humbeeck, J., Delaey, L. (1999b), *Mater. Sci. Eng. A* 273–275, 679.
- Maki, T., Tamura, I. (1987), *Proc. ICOMAT '86*. Sendai: Japanese Institute of Metals, p. 963.
- Massalski, T. B. (1984), *Metall. Trans.* 15A, 421.
- Muddle, B. C. (1982), in: *Proceedings of Solid to Solid Transformations*. New York: AIME, p. 1347.
- Mukherjee, K. (1982), in: *International Summer Course on Martensitic Transformations*. Leuven: Dep. Met. & Mat. Eng., KV Leuven, p. 4.1.
- Nakanishi, N. (1979), *Progr. Mat. Sci.* 24, 143.
- Nakanishi, N., Nagasawa, A., Murakami, Y. (1982), in: *ICOMAT '82*: Editions de Physique C4, p. 35.
- Nakanishi, N., Shigematsu, T., Machida, N., Ueda, K., Tanaka, H., Inaba, T., Iwatsu, O. (1993), in: *International Conference on Martensitic Transformation ICOMAT '92*: Wayman, C. M., Perkins, J. (Eds.). Carmel, CA, USA: Monterey Institute of Advanced Studies, p. 977.
- Nishida, M., Li, S. (2000), *Mat. Sci. Forum* 327/328, 103.
- Nishiyama, Z. (1934), *Sci. Rept. Tohoku Univ.* 23, p. 325.
- Nishiyama, Z. (1978), *Martensitic Transformations*. New York: Academic Press.
- Olson, G. B. (1999), *Mater. Sci. Eng. A* 273–275, 11.
- Olson, G. B., Cohen, M. (1982a), *Metall. Trans.* A6, 791.
- Olson, G. B., Cohen, M. (1982b), in: *Solid-State Phase Transformations*: Aaronson, H. I., Laughlin, D. E., Sekerka, D. F., Wayman, C. M. (Eds.). Warrendale: Met. Soc. AIME, p. 1145.
- Olson, G. B., Cohen, M. (1986), in: *Dislocations in Solids*: Nabarro, F. R. N. (Ed.). New York: Elsevier Science Publishers, p. 295.
- Olson, G. B., Hartman, H. (1982), *Proc. ICOMAT '82, J. de Physique* 43, 855.
- Oota, A., Muller, J. (1987), *Proc. ICOMAT '86*. Sendai: Japanese Institute of Metals, p. 1121.
- Ortin, J., Planes, A. (1989), *Acta Metall.* 37, 1433.
- Osmond, M. F. (1895), *Arts Chimiques* 94, 480.
- Otsuka, K. (1986), *Proc. ICOMAT '86*. Sendai: Japanese Institute of Metals, p. 35.
- Otsuka, K., Shimizu, K. (1986), *Int. Metals. Rev.* 31, 93.
- Otsuka, K., Wayman, C. M. (1977), in: *Reviews on the Deformation Behavior of Materials*, Feltham, P. (Ed.). Intl. Quarterly Scient. Reviews Journal II, 81.
- Otsuka, T., Ren, X. (1999), *Mater. Sci. Eng. A* 273–275, 89.
- Patel, J. R., Cohen, M. (1953), *Acta Metall.* 1, 531.
- Pops, H. (1970), *Metall. Trans.* 1, 251.
- Pelton, A. (2001) in: *Phase Transformations in Materials*: Kostorz, G. (Ed.). Weinheim: Wiley-VCH, Chap. 1.
- Purdy, G. R., Bréchet, Y. J. M. (2001), in: *Phase Transformations in Materials*: Kostorz, G. (Ed.). Weinheim: Wiley-VCH, Chap. 7.
- Rao, C. N. R., Rao, K. J. (1978), *Phase Transitions in Solids*. New York: McGraw-Hill.
- Richman, R. H., Zimmerly, C. A., Inal, O. T., Hodgson, D. E., Rao, A. S. (1994), in: *Proceedings International Conference on Shape Memory Alloys and Superplastic Technologies SMST '94*, Pelton, A., Hodgson, D., Duerig, T. (Eds.). Pacific Grove, CA, USA: SMTS Proceedings, p. 175.
- Roitburd, A. L. (1988), in: *Phase Transformations '87*: Lorimer, G. W. (Ed.). Institute of Metals, p. 414.
- Rühle, M., Kriven, S. (1982), *Proc. Phase Transf. Confer.* AIME, p. 1569.
- Saburi, T., Nenno, S. (1987), *Proc. ICOMAT '86*. Sendai: Japanese Institute of Metals, p. 671.
- Salzbrenner, R. J., Cohen, M. (1979), *Acta Metall.* 27, 739.
- Schetky McDonald, L. (1979), *Sci. Am.* 241, 74.
- Schroeder, T. A., Wayman, C. M. (1977), *Acta Metall.* 25, 1375.
- Shapiro, S. M. (1981), *Metall. Trans.* 12A, 567.
- Shibata, M., Ono, K. (1975), *Acta Metall.* 23, 587.
- Shibata, M., Ono, K. (1977), *Acta Metall.* 25, 35.
- Shimizu, K., Kakeshita, T. (1989), *ISIJ Int.* 2, 97.
- Sikka, S. K., Vohra, Y. K., Chidambaram, R. (1982), *Progr. Mat. Sci.* 27, 245.
- Sugimoto, K., Nakaniwa, M. (2000), *Mat. Sci. Forum* 327/328, 363.
- Tamura, I., Maki, T., Hato, H., Aburai, K. (1969), *J. Jpn Inst. Met.* 33, 1383.
- Tas, H., Delaey, L., Deruyttere, A. (1973), *Metall. Trans.* 4, 2833.

- Thadhani, N. N., Meyers, M. A. (1986), *Progr. Mat. Sci.* 30, 1.
- Vallade, M. (1982), in: *International Summer Course on Martensitic Transformations*. Leuven: Dep. Met. & Mat. Eng., KV Leuven, p. 3.1.
- Van Humbeeck, J. (1977), *J. Phys. (Paris) IV*, 7-C5, 3.
- Van Humbeeck, J. (1989), Dep. Met. & Mat. Eng., University of Leuven, Leuven, unpublished.
- Van Humbeeck, J. (1999), *Mater. Sci. Eng. A* 273–275, 134.
- Van Tendeloo, G. (1989), University of Antwerp, Antwerp, unpublished.
- Verma, A. R., Krishna, P. (1966), *Polymorphism and Polytypism*. New York: Wiley.
- Vintaikin, E. Z., Litvin, D. F., Udovenko, V. A., Schcherebinskij, G. V. (1979), in: *Proc. of ICOMAT '79*. Cambridge: MIT-Press, p. 673.
- Wadhawan, V. K. (1982), *Phase Transitions* 3, 3.
- Warlimont, H. (1989), *Vacuumschmelze GmbH*, Hanau.
- Warlimont, H., Delaey, L. (1974), *Progr. Mat. Sci.* 18, p. 1.
- Wayman, C. M. (1964), *Introduction to the Crystallography of Martensitic Transformations*. New York: MacMillan Comp.
- Wayman, C. M. (1983), in: *Physical Metallurgy*: Cahn, R. W., Haasen, P. (Eds.). New York: Elsevier Scientific Publishers, p. 1031.
- Wayman, C. M. (1987), *Proc. ICOMAT '86*. Sendai: Japanese Institute of Metals, p. 645.
- Wechsler, M. S., Lieberman, D. S., Renard, T. A. (1953), *Trans. AIME* 197, 1503.
- Williams, J. C., Thompson, A. w. (1981), in: *Metalurgical Treatises*: Tien, J. K., Elliott, J. F. (Eds.). Warrendale: Met. Soc. AIME, p. 487.
- Wollants, P., De Bonte, M., Roos, J. R. (1979), *Z. Metallkd.* 70, 113.
- Yang, J., Wayman, C. M. (1993), in: *International Conference on Martensitic Transformation ICOMAT '92*, Wayman, C. M., Perkins, J. (Eds.). Carmel, CA, USA: Monterey Institute of Advanced Studies, p. 1187.
- “International Conference on Martensitic Transformations ICOMAT '79” (1979), Cambridge (MA): Dep. of Mat. Science and Techn., M.I.T.
- “International Conference on Martensitic Transformations ICOMAT '82” (1982), Delaey, L., Chandrasekaran, M. (Eds.), *Journal de Physique* 43, Conf. C-4.
- “International Conference on Shape Memory Alloys” (1986), Youyi Chu, Hsu, T. Y., Ko. T. (Eds.). Beijing: China Academic Publishers.
- “International Conference on Martensitic Transformations ICOMAT '86” (1987), Tamura, I. (Ed.). Sendai: The Japan Inst. of Metals.
- “The Martensitic Transformation in Science and Technology” (1989), Hornbogen, E., Jost, N. (Eds.). Oberursel: DGM-Informationsgesellschaft Verlag.
- “Shape Memory Materials” (1989), Otsuka, K., Shimizu, K. (Eds.), Proceedings of the MRS International Meeting on Advanced Materials, vol. 9. Pittsburgh: Mat. Research Soc.
- “International Conference on Martensitic Transformations ICOMAT '89” (1990), Morton, A. J., Dunne, B., Kelly, P. M., Kennon, N. (Eds.) to be published.
- “International Conference on Martensitic Transformations ICOMAT '92” (1993), Wayman, C. M., Perkins, J. (Eds.). Carmel, CA, USA: Monterey Institute of Advanced Studies.
- “International Symposium and Exhibition on Shape Memory Materials (SME '99)” (2000). Zurich: Trans. Tech. Publications.
- “International Conference on Shape Memory and Superelastic Technologies (SMST '97)” (1997), Pelton, A., Hodgson, D., Russell, S., Duerig, T. (Eds.). Santa Clara, CA, USA: SMST Proceedings.
- “Displacive Phase Transformations and Their Applications in Materials Engineering” (1998), Inoue, K., Mukherjee, K., Otsuka, K., Chen, H. (Eds.). Warrendale, OH, USA: TMS Publications.
- “European Symposium on Martensitic Transformations ESOMAT '97” (1997), Beyer, J., Böttger, A., Mulder, J. H. (Eds.). EDP-Sciences Press.
- “European Symposium on Martensitic Transformations ESOMAT '94” (1995), Planes, A., Ortin, J., Lluís Manosa. Les Ulis, France: Les Editions de Physique.
- “International Conference on Martensitic Transformations ICOMAT '98” (1999), Ahlers, M., Kostorz, G., Sade, M. (Eds.). Amsterdam: Elsevier.
- “Martensitic Transformation and Martensite” (1980), Hsu, T. Y. (Xu Zuyao) (Ed.). Shanghai: Science Press (in Chinese).
- “Pseudoelasticity and Stress-Induced Martensitic Transformations” (1977), Otsuka, K., Wayman, C. M. (Eds.), in: “Reviews on the Deformation Behavior of Materials”.
- “Physical Properties of Martensite and Bainite” (1965), Special Report 93. London: The Iron and Steel Institute.
- “Shape Memory Effects in Alloys” (1975), Perkins, J. (Ed.). New York: Plenum Press.
- “New Aspects of Martensitic Transformations” (1976), Suppl. to *Trans. Jap. Inst. Met.* 17.
- “Martensitic Transformations ICOMAT '77” (1978), Kiev: Academy of Science.

Proceedings of International Conferences on Martensitic Transformations

Index

- Aaronson–Aaron model 506
- absolute stability limit, directional dendritic growth 148
- acetone, dendritic growth 115
- acoustic phonons 258
- activation energy, diffusion 201, 491
- activity coefficient
 - decomposition 351
 - Henrian 30
 - phase diagrams 14, 70
- adjoining phase regions law 47 f, 56 f
- Ag–Au system 564
- Ag-based alloys 598 f
- Ag–Cd system 632
- Ag–Cu system 150
- Ag–Mg system 30
- age hardening alloys, microstructure 401 ff
- aggregation
 - clusters 469
 - diffusion 191
- aging parameters 314 ff, 321 ff, 325 ff
- Akaiwa–Voorhees model 373
- Al–Ag–Zn system 398
- Al–Ag system 488
- Al–Cu system
 - directional dendritic growth 150
 - precipitation 325
- Al–CuAl₂ alloys 161
- Al–Fe system 150
- Al–Li alloys, coarsening 375
- Al–Mg–Si alloys 325
- Al–Ni–Co system 377
- Al–Zn–Ag system 329
- Al–Zn–Mg system
 - phase diagram 45
 - precipitation 397
- Al–Zn system
 - dynamic fluctuations 277
 - interfacial diffusion 510
 - precipitation 397, 505, 510
 - spinodal decomposition 451 ff
- alkali alloys 634
- alkali halides 639
- Allen–Cahn concept 486 f
- allotropic transformations
 - interfacial diffusion 499
 - martensites 634
- alloys
 - atomic ordering 523 ff
 - dendritic growth 119
 - diffusion 199, 221 ff
 - diffusionless transformations 583 ff
 - eutectic growth 158
 - order–disorder phenomena 283 ff
 - precipitation 314 ff
 - spinodal decomposition 451
 - spinodal 363 ff
- amorphization, pressure-induced 661
- amorphous alloys 366, 454
- amplification factor, decomposition 357
- analytical electron microscopy (AEM) 327
- analytical field ion microscopy (AFIM) 328, 360, 366
- angle dispersive X-ray powder diffraction (ADX) 678, 680
- anharmonic terms, phase transitions 292
- anion–anion distances, high-pressure transformations 663
- anisotropic attachment kinetics, dendritic growth 115
- anisotropic interactions, atomic ordering 558
- anisotropy, phase transitions 268, 280
- annealed defects 468
- annealed disorder 279
- annealing, shape memory 643
- antiferromagnets 273, 297
- antiphase boundaries 487
- anvils 670 ff
- Arrhenius behavior, diffusion 191, 199 ff, 216 ff
- associative jumps, vacancies 197
- athermal transformations 583–654
- atom–vacancy exchange 218
- atomic jumps 189
- atomic ordering 519–581
- attachment kinetics, anisotropic 115
- Au–Cd alloys 590
- Au–Cu system, atomic ordering 561, 564
- Au–Ni system
 - atomic ordering 563 f
 - phase diagram 21
- Au-based alloys, martensite 599 f
- austenite 588, 600, 617
- austenite stabilizing, martensitic transformations 625
- autocatalytic growth, martensite 618 f

- average jump frequencies 199
- averaging, phase transitions 279
- Avrami equation 401, 465
-
- B–C–N system, high pressure 683 ff
- B–C system, high pressure 686
- B–N system, high pressure 685
- b.c.c. structures 537, 558 f, 577
- bacterial flagellae, martensitic transformation 640
- Bain strain 594 f, 601 f, 620
- bainite 650
- band–dendrites transitions 150
- banded structure, diffusionless transformations 611 f
- Be–Cu alloys 677
- Becker–Döring theory
 - decomposition 342 ff, 352 f
 - precipitation 320 ff, 395
- belite, diffusionless transformations 639
- belt apparatus, high-pressure transformations 669
- bending–heating–cooling cycles 644
- beta alumina, diffusion 209
- Bethe approximation
 - atomic ordering 524
 - phase transitions 287
- Bi–Sn–Cd system 40, 44 ff
- bicritical points, phase transitions 275
- bicrystals
 - discontinuous precipitation 506
 - interfacial diffusion 490
- bifurcation
 - directional solidification 127 f
 - precipitation 337
- bilinear coupling 280
- binary alloys
 - diffusion 200
 - phase transitions 285, 296
 - point variables 527
 - precipitation 314, 317 f, 397
 - substitutional, diffusion 226
- binary fluids, spinodal decomposition 455
- binary mixtures
 - Ising model 443
 - spinodal decomposition 414 ff
- binary monotectic reaction 26
- binary systems
 - atomic ordering 523 ff
 - diffusion 208 f
 - eutectic 23
 - liquid 246
 - metallic 503
 - phase diagrams 14 ff, 42, 314
- Binder model *see*: cluster dynamics/model
- biological materials, martensitic transformations 640
- Bitter–Crum theorem 448
- bivariant phase regions 31
- block copolymer melts 259, 271
- body-centered cubic *see*: b.c.c.
- Boltzmann–Matano analysis 177 ff, 223
- bond model, diffusion 200, 227
- bonding energy, phase diagrams 12
-
- Born approximation, electrical resistivity 469
- boron nitride, displacive transformation 639
- boundary conditions
 - dendritic growth 102 f, 108
 - diffusion 176 ff
 - interfacial diffusion 484 ff, 503
 - LBM theory 423
 - solidification 91 ff, 122
- boundary motion 495 f
- Bragg–Williams approximation 255, 287
- Bragg peak
 - ordering 463 ff
 - phase transitions 250, 258, 293
 - solidification 87
- Bridgman solidification 96 f, 668 ff
- Brillouin scattering 675
- Brown's bond valence approach 664
- Buerger deformations 611
- bursts, martensitic transformations 633, 636
-
- C–N system, high pressure 686
- Cahn–Hilliard–Cook approximation
 - 358 f, 420 ff, 438 ff, 448
- Cahn–Hilliard model
 - decomposition 346 ff
 - interfacial diffusion 486 ff
- see also*: continuum model
- Cahn treatment
 - interface migration 496 ff, 507
 - spinodal decomposition 437
- calcite–argonite transition 259
- calculation models, ternary from binary data 72 ff
- see also*: Monte Carlo
- CALPHAD method
 - coarsening 373
 - concomitant processes 394
 - phase separation 323 ff
- CaO–Fe₂O₃ system, phase diagram 53
- CaO–MnO system, phase diagram 14
- CaO–SiO₂ system, phase diagram 27
- capillarity
 - decomposition 340
 - directional solidification 124
- capillary-corrected diffusion 158
- capillary forces, interface migration 492
- capillary length, dendritic growth 108, 125, 131
- carbides
 - atomic ordering 523
 - diffusionless transformations 650
- carbon
 - diffusionless transformations 639
 - high-pressure transformations 684
- carbon nitrides, high pressure 686
- CASCADE computer code 219
- cast duplex steels, phase separation 366
- casting
 - eutectic growth 158
 - solidification 96, 120
- catastrophic nucleation 344
- catatectic invariants 32

- cation diffusion 231
- Cd–Al–Mn system 562
- Cd–Mg system 563, 573
- Cd–Na system 36 f
- cell spacing, directional solidification 130 ff
- cellular growth
 - dendrites 140 ff, 146
 - solidification 85, 126 f
- cements, displacive transformation 639
- ceramic solutions, phase diagrams 64
- ceramics
 - diffusionless transformations 639
 - spinodal decomposition 454 f
- chain polymers, diffusionless transformations 639
- charge carrier distribution, high-pressure transformations 666
- charge diffusion coefficient 212
- chemical composition gradient 178
- chemical diffusion 184 ff, 232
 - binary system 209
 - dendritic growth 108
 - directional solidification 124
- chemical equilibrium 6
- chemical forces
 - interface migration 493, 503
 - phase separation 322
- chemical interdiffusion 178 f
- chemical potential 10
- chemically induced grain boundary migration (CIGM) 503 ff
- Chemla experiment 181
- chill plate directional solidification 98
- classification, displacive transformations 587 f, 634
- Clausius–Clapeyron equation
 - diffusionless transformations 607
 - directional solidification 126
 - martensitic transformations 629
- cluster–cluster aggregation 469
- cluster–diffusion–coagulation mechanism
 - coarsening 377, 399
 - spinodal decomposition 452, 456 f
- cluster correlation functions 529 ff
- cluster dynamics approach
 - concomitant processes 394 f
 - nucleation 352
 - spinodal decomposition 432, 472
- cluster interactions, atomic ordering 548
- cluster kinetics 340 f
- cluster probabilities
 - atomic ordering 529 f
 - phase transitions 289
- cluster site approximation (CSA) 560
- cluster variation method (CVM)
 - atomic ordering 551, 556 f, 573
 - decomposition 345
 - phase transitions 288 f
- clusters
 - atomic ordering 524 ff, 529 ff
 - concomitant processes 381, 391
 - decomposition 340 ff
 - ionic crystals 230
 - precipitation 315 ff
 - spinodal decomposition 415 ff, 444
- Co–Al system, ordering 570
- Co–Ni–O system 51
- coagulation
 - clusters 352
 - coarsening 377
 - spinodal decomposition 433, 446 f, 452
- coarse graining
 - decomposition 347
 - phase transitions 255, 263, 300
 - spinodal decomposition 414 f, 418 ff, 438 ff
- coarsening
 - concomitant processes 381 ff
 - decomposition 326, 365
 - precipitation 315, 321 ff, 336, 370 ff
 - spinodal decomposition 416, 445
- coarsening stages, experimental identification 387
- cobalt alloys, diffusionless transformations 608, 617, 634 ff
- coexistence curve 414
- coherency strains 377
- coherent elastic misfit 447
- coherent interfacial energies 390
- coherent miscibility gaps 571
- coherent phases, precipitation 324
- coherent potential approximation (CPA), effective cluster interactions 550
- coherent solvus lines 316
- collective correlation factors, diffusion 206
- collective diffusion coefficients 179
- colloid crystallization 466
- columnar growth 95
- composition triangle, ternary 39
- compositions
 - atomic ordering 544, 566
 - eutectic 23
 - phase transitions 246
- see also*: stoichiometric compositions
- compounds
 - phase diagrams 9, 65
 - stoichiometric 29
- compressibility 662
- computer simulation techniques, phase transitions 283, 293
- concentrated alloy systems 199, 226
- concentration–depth profile 231
- concentration fluctuations 339
- concentration gradients 15, 175
- concentration profile
 - diffusion coefficients 235
 - interfacial diffusion 502
- concentration waves
 - interfacial diffusion 486
 - spinodal decomposition 415 f, 434
- concomitant nucleation, spinodal decomposition 433
- concomitant processes, precipitation 381 ff, 401
- configuration polyhedron, atomic ordering 531 ff
- configurations, atomic 523 ff
- congruent compounds 29
- conjugate phases 336

- conjugate thermodynamic variables 60, 247
- conode 15
- conservation laws, phase transitions 277
- consolute temperature 21
- constant composition sections, phase diagrams 46
- constrained growth 95
- continuity equation, solidification 92 ff
- continuous casting 96
- continuous cooling 501
- continuum model
 - decomposition 346
 - diffusion 175
 - interfacial diffusion 486 f
 - spinodal decomposition 356 f, 421
- conventional transmission electron microscopy (CTEM), decomposition 326, 393
- cooling
 - diffusionless transformations 587
 - interfacial diffusion 501
 - phase diagrams 15
 - precipitation 314 f, 401
 - shape memory effect 644
- coordination number
 - atomic ordering 524, 539
 - high-pressure transformations 663
- copper, alloying elements, diffusionless transformations 611, 634
- correlation factor, diffusion 178, 193
- correlation functions
 - atomic ordering 526 ff, 567
 - phase transitions 262
 - solidification 87
 - spinodal decomposition 430
- correlation length
 - intrinsic 85
 - phase transitions 249
- corresponding pairs, phase diagrams 60
- Cottrell solute drag 496
- Coulomb potentials
 - colloidal suspensions 24
 - pair interactions 294
- coumarin-succinonitrile, solidification 141
- coupling mechanisms, defects–order parameter 280
- Cowley–Warren short-range order parameters 531
- cristobalite, diffusionless transformation 639
- critical amplitude, spinodal decomposition 438
- critical clusters 434
- critical exponents 260 f
- critical nucleus 341
- critical phenomena, phase transitions 260 f
- critical radius, nucleation 88, 381, 392
- critical temperature
 - phase diagrams 21
 - spinodal decomposition 416
- cross-boundary diffusion 497 f
- crystal growth, solidification 91
- crystallization
 - colloid 466
 - primary 41
- crystallographic relations 593 f, 614 f, 620
- Cu–Ag–Au alloys, diffusionless transformations 607
- Cu–Ag system, diffusionless transformations 564
- Cu–Al–Mn system, diffusionless transformations 562
- Cu–Al–Ni system
 - diffusionless transformations 602, 621 f
 - shape memory effect 645
- Cu-based alloys, diffusionless transformations 598 f
- Cu–Bi–Fe system, decomposition 397
- Cu–Cd alloys, discontinuous precipitation 513
- Cu–Co system
 - decomposition 345, 350
 - discontinuous precipitation 505
- Cu–Mn system, phase separation 397
- Cu–Ni–Fe system, decomposition 329, 334, 365
- Cu–S–O system 7
- Cu–Sn system, martensitic transformations 617, 622
- Cu–Ti system
 - decomposition 317, 325, 331, 350, 388
 - interfacial energies 390, 512
- Cu–Zn–Al system
 - diffusionless transformations 598 ff
 - shape memory effect 645
- Cu–Zn system, martensitic transformations 617
- Curie–Weiss law, phase transitions 261
- cycle procedures, shape memory effect 644
- cycling behavior, martensitic transformations 633
- cyclohexanol, dendrites 117
- damping capacity, diffusionless transformations 593, 636, 647
- Darken–Manning relation 185 ff, 209
- Datye–Langer theory 155, 157
- Dauphiné twins 601, 606
- decomposition
 - experimental techniques 326 ff
 - precipitation 309–408
 - spinodal 409–480
- defects
 - diffusion 193, 201, 213
 - eutectic growth 161
 - interfacial diffusion 484 f
 - ionic crystals 227, 231
 - phase transitions 280 f
 - precipitation 401
 - spinodal decomposition 415, 468
- deformation, diffusionless transformations 592, 615
- degeneracy, solidification 92
- dendrites 97
- dendritic growth 85 ff, 100 ff
- density differences, phase transitions 246
- deviatoric components, diffusionless transformations 588
- DEVIL computer code 219
- devil's staircase 274
- Devonshire–Ginzburg–Landau theory 603 f
- diamond, high-pressure transformations 683
- diamond anvil cells (DAC) 668 f, 671, 678
- diblock copolymers, phase separation 272
- dielectric solid systems, phase transitions 246

- differential scanning calorimetry, diffusionless transformations 590
- diffraction techniques
 - decomposition 334
 - diffusionless transformations 587, 611
 - high-pressure transformations 671, 678 ff
- diffuse interface model 347 f
- diffusion–coagulation mechanism 446
- diffusion
 - coarsening 377
 - dendritic growth 108
 - directional solidification 124
 - in crystals 171–238
 - interfacial 481–518
 - solidification 91
- diffusion constants
 - definitions 175 ff
 - effective, short circuits 187
 - spinodal decomposition 422
- diffusion-controlled growth
 - precipitation 350, 370 f, 374, 381
 - solidification 94
 - supersaturated matrix 350
- diffusion couples 568
- diffusion kinetics
 - Cahn–Hilliard 420 ff
 - solids 171–238
- diffusion length
 - directional solidification 126
 - eutectic growth 153
- diffusion-limited aggregation (DLA) 101
- diffusionless transformations 583–654
- diffusivity 175, 485 f
- dilatation dominant transformations 587 f, 610
- dilute alloys, diffusion 221, 226
- dimensionality
 - critical 268
 - order parameters 250
- direct imaging techniques 326 f
- directional dendritic growth 131 ff
- directional solidification 86, 95, 98, 120 ff
- discontinuous precipitation 484 f, 504 f
- discrete lattice point model 346 f
- dislocations
 - diffusion 186
 - diffusionless transformations 620
 - interfacial diffusion 485, 495
 - spinodal decomposition 415
- displacement temperature, shape memory effect 645
- displacive transformations 292, 587–651
- disruptive phase transitions 259
- dissipation, spinodal decomposition 420
- dissociative mechanism, diffusion 191, 197
- distortions
 - high-pressure transformations 659
 - phase transitions 283
- divacancies, diffusion 219
- domain structures
 - diffusionless transformations 600
 - phase transitions 259, 274
- doublons, solidification 114, 144
- drift terms, diffusion 175, 183
- driving forces
 - interface migration 492
 - martensitic transformations 624
 - phase separation 322
- droplets
 - decomposition 340
 - phase transitions 300
 - spinodal decomposition 415, 418, 442 f
- Dufour effect 181
- dumbbell split configuration, diffusion 190
- duplex stainless steel, phase separation 364
- dynamic pressure generation 667
- dynamic scaling
 - phase transitions 277 f
 - precipitation 395 ff
 - *see also*: scaling
- dynamics, phase changes 414 f
- E–pH diagrams 9
- early stage decomposition
 - concomitant processes 381 f
 - kinetics 339 ff
- Eckhaus band instability, solidification 128 f, 135 f
- effective cluster interactions (ECIs) 548
- effective diffusion coefficients 187
- Einstein equation 185, 192
- elastic constants
 - diffusionless transformations 608
 - precipitation 336
- elastic interaction, decomposition 447 f
- elastic phase transitions 257
- elastic strain
 - diffusionless transformations 606 f, 636
 - interface migration 493
 - precipitation 324
 - spinodal decomposition 447 f
- electric fields, phase transitions 246
- electrical resistivity
 - diffusionless transformations 587
 - spinodal decomposition 468
- electron back-scattered diffraction (EBSD), solidification 144
- electron energy loss spectroscopy (EELS), phase separation 327
- electronic defects, ionic crystals 231
- electronic properties, high-pressure transformations 659
- Ellingham diagrams 8 f
- energy dispersive X-ray diffraction (EDX)
 - decomposition 327
 - high-pressure transformations 680
- enstatite, diffusionless transformations 639
- enthalpy
 - diffusion 217
 - diffusionless transformations 636
 - phase diagrams 5, 11, 34
 - precipitation 318
- entropy
 - diffusionless transformations 607, 636

- directional dendritic growth 149
- directional solidification 121
- high-pressure transformations 660
- phase diagrams 5, 11, 34
- phase transitions 247
- entropy–temperature diagram, shape memory effect 645
- equiaxed growth, solidification 95
- equilibrium cooling 15
- equilibrium properties, solid–solid interfaces 484 ff
- Eshelby theory, displacive transformations 606
- Euler–Lagrange equation, second order transitions 261
- eutectic growth 86, 99, 151 ff
- eutectic invariants 31 f, 41
- eutectic systems 22
- eutectic temperature 23
- eutectoid invariants 32
- eutectoid reactions, interfacial diffusion 505
- eutectoids 159
- eutectular invariants 52
- evaporation–condensation mechanism, spinodal decomposition 456
- evaporation, phase transitions 246
- excess properties
 - phase diagrams 13 ff
 - polynomial representation 34
- exchange mechanism
 - atomic ordering 539, 569
 - diffusion 191, 217 f
 - phase transitions 284
- existence domains, atomic ordering 531 ff
- extended X-ray absorption fine structure (EXAFS)
 - atomic ordering 563
 - high-pressure transformations 676
- extension rules, phase diagrams 32
- extrinsic defects, diffusion 230

- f.c.c.–b.c.c. transformations 594
- f.c.c. structures, atomic ordering 532 ff, 540 ff, 555 f
- faceted systems, eutectic growth 158
- faceting transitions 489
- FACT (Facility for the Analysis of Chemical Thermodynamics), expert system 75
- fast growth rates, solidification 98
- fast-mode theory, spinodal decomposition 428
- faulting, diffusionless transformations 622
- faults, eutectic growth 161
- Fe–Al system
 - atomic ordering 562, 565
 - order parameters 250
 - phase diagram 276
- Fe–C–Ni system, martensitic transformations 617
- Fe–C system, martensitic transformations 617
- Fe–Co–Al system, martensitic transformations 562, 569 f
- Fe–Cr–Co system
 - coarsening 377
 - decomposition 329, 332
- Fe–Cr–Ni system, martensitic transformations 617
- Fe–Cr–O system, phase diagram 52
- Fe–Cr–V–C system, phase diagram 48
- Fe–Cr system, phase separation 397
- Fe–Cu system, phase separation 350, 390
- Fe–Mn–Si system, shape memory effect 644
- Fe–Mn system
 - martensitic transformation 617
 - shape memory effect 650
- Fe–Ni system, martensite 590, 617
- Fe–Ni–C alloys 619
- Fe–Ni–Cr system, precipitation 364
- Fe–Pd alloys, diffusionless transformation 608, 613
- Fe–Pt alloys, diffusionless transformation 607
- Fe–Ru system, martensitic transformation 627
- Fe–S–O system, phase diagram 8
- Fe–Ti–Al system, ordering 562, 569
- feldspar frameworks, high pressure 665
- ferroelectric transitions 246
- ferroic transformations 608
- ferromagnetic systems, atomic ordering 570
- ferrous martensite 366
- ferrous systems, diffusionless transformation 607, 635
- fibers, solidification 152
- fibrous systems, eutectic growth 158
- Fick's laws of diffusion 175–235
- field ion microscopy (FIM), phase separation 326
- finite precipitate volume fractions 373
- first neighbor interactions 532, 540, 555 f
- first-order phase transitions 249, 271
 - martensites 599
 - solidification 86 ff
- Fisher renormalization 269, 279
- five-frequency model, impurity diffusion 197, 207, 215
- flat interfaces, crystal growth 91
- Flory–Huggins approximation 426 f
- fluctuations
 - dendritic growth 113
 - heterophases 302
 - phase transitions 261, 271, 277
 - precipitation 319
 - solidification 87
 - spinodal decomposition 414 f
- fluid–suprafluid transition 246
- fluid magnet analogy, phase transformations 247
- fluids, spinodal decomposition 437 f, 455 f
- fluorescence line, high pressure 672
- flux balance, eutectic growth 153
- force–velocity relationship, interface migration 492, 496
- formation energies, phase diagrams 29
- fractal structure 266
- framework flexion, high-pressure transformations 661
- free growth
 - dendritic 100 ff, 118
 - solidification 96
- freezing 91 ff, 120
- Frenkel defects 213, 220, 228

- frictional forces, interface migration 496
- frozen-in clusters 444
- frozen-in disorder 468
- frozen-in impurities 279
- frozen phonons 259
- Furukawa function 447, 453
- fusion temperature, phase diagrams 15
- gallium arsenide, high pressure 681
- gaseous compounds, phase diagrams 9
- gasketing system, high pressure 670
- Gaussian noise, phase separation 420
- Ge–Si system, phase diagram 17
- gel–gel transitions 456
- germanium, high pressure 680
- Gibbs–Duhem equation 11 ff, 30, 61
- Gibbs–Thomson equation
 - decomposition 351, 370 f, 382 ff, 394
 - eutectic growth 154
 - interfacial diffusion 492, 510
- Gibbs absorption isotherm 490
- Gibbs energy 5 ff
 - minimization 73, 6 f
- Gibbs phase rule 7 f
- Ginzburg–Landau equation
 - diffusionless transformations 603
 - interfacial diffusion 487
 - solidification 89
- Ginzburg criterion
 - phase transitions 263 ff, 300 ff
 - spinodal decomposition 423, 431, 462, 471
- girdle-type press 669
- glasses, phase separation 361, 367, 454 f
- glissile interfaces, martensitic transformations 622
- gold alloys, displacive transformations 635
- Gorsky effect, diffusion 233
- grain boundaries
 - diffusion 186
 - migration 503 ff
 - phase transitions 282
 - precipitation 317, 325
 - spinodal decomposition 415
- grain refinement 119
- graphical integration analysis, diffusion 233
- graphite, transformations 6, 683
- gravity effects, spinodal decomposition 456
- Greninger–Troiano relations 616, 637 f
- ground states, atomic ordering 538 ff
- group formation, diffusionless transformations 619
- group theoretical techniques 255
- growth
 - bainite 650
 - decomposition kinetics 332
 - dendritic 116, 148
 - diffusion-controlled 350
 - diffusionless transformations 636
 - interface migration 495
 - martensites 599, 632
 - precipitation 319 ff, 370
 - solidification 93 ff
- spinodal decomposition 415
- Gruzin method, diffusion 232
- Guggenheim model 68
- Guinier–Preston zones 325, 360
- Guinier approximation, small-angle scattering 391
- gyration radius 426
- habit plane 595 ff, 615 f, 622, 637
- halides, diffusionless transformations 639
- Hamiltonians, phase transitions 247 ff, 255 ff, 262 f, 271, 281 ff, 419
- hardening
 - diffusionless transformations 648
 - steel 641
- Hart equation 187
- Haven ratio 183 ff, 190, 196, 211 f
- heat flow, solidification 181
- heat sinks, solidification 120
- heating–cooling cycles, shape memory effect 644
- heating, diffusionless transformations 590, 607
- heating rate, decomposition 330
- Heisenberg antiferromagnet 297
- Heisenberg model 267
- Hele–Shaw flow 106
- helimagnetic structures 273
- Helmholtz energy
 - decomposition 347
 - minimization 560
 - precipitation 318 ff, 337 ff
 - spinodal decomposition 417
 - vacancies 218
- Henry's law 21, 29 ff
- Hess' law 660
- heterodiffusion 180, 235
- heterogeneous nucleation, precipitation 315, 319, 468
- heterogeneous regions, interfacial diffusion 484
- heterophase fluctuations 414 f, 431 f
- heterophases 302
- high-angle grain boundaries 485
- high damping materials (HIDAMETS) 647
- high-pressure generation 666 ff
- high-pressure phase transformations 655–695
- high-resolution microanalysis 511
- high-resolution transmission electron microscopy (HRTEM) 326, 620
- Hillert–Sundman treatment 496 ff
- hole hopping, diffusion 205
- homogeneity range, phase diagrams 28
- homogeneous lattice distortive strain 590
- homogeneous second phase precipitation 309–407
- homophase fluctuations, spinodal decomposition 414 f, 431 f
- Hopf solution 92
- Hugoniot elastic limit (HEL) 667
- Hume–Rothery alloys 619 f, 634
- hydraulic presses 668 ff
- hydrodynamics, spinodal decomposition 446
- hydrogen bonds, high-pressure transformations 687 f
- hydrostatic pressure 649

- hyperscaling relation, phase transitions 267
- hysteresis behavior, martensitic transformations 633 f
- ice amorphization 662, 687 ff
- ideal solutions
 - Henrian 29
 - Raoultian 12 f
- immiscibility 26
- impurities
 - diffusion 176 ff, 213
 - directional solidification 120
 - interfacial diffusion 500
 - ionic crystals 231
 - metals diffusion 220
 - phase transitions 279
 - spinodal decomposition 415, 468 f
- impurity–vacancy interaction 198, 221
- impurity correlation factors 196, 208
- incoherent miscibility gaps 570
- incommensurate superstructures 273
- incubation time, precipitation 319, 343
- indirect interstitial mechanism, diffusion 190
- indium-based alloys, diffusionless transformations 607, 634
- inertial hydrodynamics, spinodal decomposition 446
- infrared spectroscopy, high pressure 674
- inoculants, solidification 95
- inorganic compounds, diffusionless transformations 639
- InSb, high-pressure transformations 682
- instabilities
 - dendritic growth 106, 136 ff
 - eutectic growth 157
 - solidification 93
- integral molar enthalpy 12
- interatomic interactions 659
- intercalation compounds 205
- intercluster spacing 336
- interconnected microstructures 377
- interconnected structures 364
- interdiffusion
 - chemical 178 ff
 - metals 227
 - spinodal decomposition 424, 472
- interdiffusion coefficients 233, 357
- interfaces
 - decomposition 340, 347
 - diffusionless transformations 622
 - solidification 85 ff, 89 f, 99
- interfacial diffusion 481–518
- interfacial energies 389 ff
- interlamellar spacing 511
- intermediate phases 26
 - silicon 681
- intermetallic phases 26
 - ordering 523
 - precipitation 314 f
- internal friction, diffusionless transformations 587
- interphase boundaries 484 ff
- interstitial alloys
 - atomic ordering 523
 - diffusion 224
- interstitial ferrous martensites 636
- interstitial jumps 213
- interstitial mechanism, diffusion 189 f, 216
- interstitial solid solutions, diffusion 205
- interstitial solutions, phase diagrams 64
- interstitials, metal diffusion 231
- interstitial-substitutional mechanism, diffusion 191
- intrinsic correlation length, solidification 85
- intrinsic defects, diffusion 227
- intrinsic diffusion 179 f, 184 f
- invariants, binary phase diagrams 31
- invariant plane strain (IPS) 595, 613 ff
- invariant reactions, nomenclature 49
- inverse cluster variation method 550
- inverse coarsening 380
- inverse Monte Carlo technique 550
- ionic conductivity, diffusion 183, 189, 204 f, 208 ff
- ionic crystals, diffusion 227
- ionic solutions, phase diagrams 62
- ionic valence, diffusion 181
- iron
 - alloying elements 611
 - massive transformation 500*see also:* Fe
- iron aluminides, ordering 565
- iron-based alloys, martensitic transformations 635
- iron whiskers, martensitic transformations 601
- irregular structures, eutectic growth 161
- irregular tetrahedron approximation, atomic ordering 553
- irreversible thermodynamics, diffusion 181 ff
- Ising model
 - antiferromagnet 200
 - atomic ordering 524
 - coarsening 380
 - decomposition 367 ff
 - ferromagnets 303
 - phase transitions 264, 275, 285, 293
 - spinodal decomposition 419 ff, 435 ff, 462
- isobaric temperature–composition diagrams 51
- isopleths, ternary 46
- isopropylacrylamide gel 456
- isothermal precipitation 315 f
- isothermal sections, ternary systems 43, 569 ff
- isotope effect, diffusion 196, 213
- isotropic pair probabilities, atomic ordering 527
- Ivantsov–marginal stability, solidification 118
- Ivantsov solution 102 ff, 111, 131
- Jänecke coordinates 51
- Johnson–Mehl equation 465
- jump discontinuity, interface 89
- jump frequency
 - decomposition 343
 - diffusion 194, 216 f
 - metal diffusion 226
- jump singularities 247, 262

- Kampmann–Wagner approach
 - precipitation 382 ff
 - spinodal decomposition 433
- Kawasaki model 367
- kickout mechanism, diffusion 191
- Kikuchi natural iteration 525, 554
- kinetic coefficients
 - dendritic growth 115, 134
 - eutectic growth 155
 - solidification 87
- kinetics
 - diffusionless transformations 588, 603
 - martensitic transformations 624 f, 632 f
 - precipitation 314 f
 - spinodal decomposition 416 f
- Kirkendall effect 179 f, 233
- Kittler–Falikov theory 288
- Koch–Cohen cluster 230
- Kosterlitz–Thoules phase transitions 268
- Kröger–Vink defect notation 228 f
- Kurdjumov–Sachs relations 616, 620 f, 637 f

- La–Ni–Al system, phase separation 454
- lamellar modulations 361 ff
- lamellar systems 152, 158
- Landau coefficient 127
- Landau symmetry classification 246 f
- Landau theory
 - diffusionless transformations 603
 - omega transformations 609
 - phase transitions 250 ff, 262 f, 269, 290
 - spinodal decomposition 419, 438, 463
- Langer–Baron–Miller approximation 359, 423 ff, 440 ff, 471
- Langer–Schwartz model
 - concomitant processes 382 ff
 - spinodal decomposition 433, 445
- Langer theory 321 ff
- large-amplitude fluctuations 418
- large-volume presses 668
- laser trace, dendritic growth 101
- laser treatment, solidification 96
- lasers, high-pressure transformations 667
- laths, diffusionless transformations 617
- lattice anisotropy, decomposition 420
- lattice deformations, diffusionless transformations 620, 639
- lattice diffusion length 187
- lattice distortive displacements 588
- lattice-gas model
 - diffusion 201
 - spinodal decomposition 428, 444 f
- lattice relaxation, ordering 523, 573
- lattice softening, diffusionless transformations 597
- lattice structures
 - atomic ordering 529 ff, 558
 - diffusion 194, 223
 - order parameters 251 f
 - phase transitions 271

see also: structures
- lattice wave modulations 592, 597
- ledges, structural 488
- Legendre polynomials, thermodynamics 34
- Legendre transformation 538, 660
- length scales, solidification 85
- Lennard–Jones interaction 294
- lens-shaped two phase regions 20
- lenticular martensite 618
- lever rule
 - binary systems 15
 - phase diagrams 41, 248
 - spinodal decomposition 417
- LiF–NaF system, phase diagram 35, 67
- Lifshitz–Slyozov–Wagner model 370 ff, 382 f, 452, 456, 463, 471
- Lifshitz invariants 273 ff
- Lifshitz point 275
- light scattering, precipitation 328, 361
- limiting slopes, phase boundaries 66
- linearized theory, spinodal decomposition 421 f
- Liouville equation 440
- liquid–gas transitions 246 ff
- liquid–liquid miscibility 26
- liquid–solid phase transitions 81–170, 246
- liquid compounds, phase diagrams 9
- liquidus 39 f, 74, 279
- lithium alloys, diffusionless transformations 617, 635
- local relaxation, atomic ordering 550
- localized nucleation models, martensitic transformations 629
- long-range order (lro) configurations
 - atomic ordering 529 ff, 539, 546, 566
 - phase transitions 71, 288
- low-angle tilt boundaries 485
- lutidine–water system, decomposition 455

- macroscopic diffusion 175 ff
- magnetic exchange energy, atomic ordering 570
- magnetic ordering, spinodal decomposition 460
- magnetic properties, high-pressure transformations 659
- magnetic solid systems, phase transitions 246
- magnetization, precipitates 339
- magnetostrictive couplings 271
- magnon modes 277
- manganese-based alloys, diffusionless transformations 608, 612, 635
- Manning model 185 f, 199, 209, 215 f, 226
- marginal stability hypothesis, dendritic growth 110, 118
- Marqusee–Ross model 373
- Marsh–Glicksman model 373
- martensitic transformations 260, 587–651
- mass action law, ionic crystals 230
- mass transfer, diffusion 180
- massive transformations, interfacial diffusion 498 ff
- mean field approximation (MFA)
 - decomposition 359
 - phase transitions 255, 259 f, 287 ff

- precipitation 318 ff
- spinodal decomposition 417 ff, 431 f
- mechanical forces, interface migration 493
- mechanical properties, diffusionless transformations 590
- melting
 - congruent 29
 - phase transitions 283
- melting entropy 149
- melting point
 - atomic ordering 571
 - phase diagrams 8, 18
- melting temperature
 - discontinuous precipitation 505
 - solidification 91 ff
- mesophases, block-copolymer melts 259, 271
- metallic glasses, decomposition 455
- metallic substitutional alloys 523 ff
- metallic systems
 - decomposition 360, 366
 - diffusionless transformations 634
 - interfacial diffusion 491, 503
 - phase separation 322 f
 - spinodal decomposition 451 f
 - substitutional ordering 523 ff
- metals
 - dendritic growth 119
 - diffusion 220 ff
- metastability
 - interfacial diffusion 486
 - phase transitions 298 ff
 - precipitation 316
 - spinodal decomposition 417
- metastable phase boundaries 39
- methanol–cyclohexane mixture, decomposition 457
- MgO–CaO system, phase diagram 22
- Mg–Zn system 19, 45
- microanalytical techniques 326 ff, 511
- microclusters 340
- microscopic diffusion 189 ff
- microscopy, high-pressure transformations 674
- microsegregation 131
- microstructures
 - coarsening 377
 - diffusionless transformations 618 ff
 - polydispersed 382
 - precipitation 314 f
- midribs, diffusionless transformations 618 f
- migration
 - atomic 175
 - coarsening 379
 - diffusion 186
 - interfacial diffusion 484 f, 503 ff, 514
 - ionic crystals 228
- minerals, diffusionless transformations 639
- minimization algorithm
 - atomic ordering 525, 554
 - Gibbs energy 73
- miscibility gap
 - atomic ordering 558, 564, 572 f
 - binary systems 21
 - decomposition 333, 339 ff, 390, 416 f, 460
 - phase diagrams 14
 - precipitation 314 ff, 401
- misfit strain, precipitates 447
- mixed alkali effect 209
- mixing energies, phase diagrams 9 ff
- mobilities
 - diffusion 183, 205, 211
 - interface migration 485 f, 496, 508
 - solidification 89
 - spinodal decomposition 421
- modified Langer–Schwartz model 382 ff
- modulated phases 273
- modulated structures, decomposition 360, 364
- molar enthalpy, phase diagrams 12
- molecular crystal systems 246
- molecular dynamics
 - interfacial diffusion 484
 - phase transitions 293
- molecular field approximation 288
- molecular field theory 288 ff
- monoclinic transformations 600
- monodisperse polymers, spinodal decomposition 427
- monolayers, absorbed, order-disorder 288
- monotectic invariants, phase diagrams 26, 32
- Monte Carlo simulations
 - atomic ordering 551, 556 f
 - decomposition 367
 - diffusion 200, 215
 - interfacial diffusion 484 ff
 - phase transitions 287
 - precipitation 321, 396 f
 - spinodal decomposition 428 ff, 437 f
- morphological instabilities, directional dendritic growth 139 f
- morphology
 - decomposition 360 ff
 - diffusionless transformations 588, 616, 636
 - interfacial diffusion 488
 - precipitation 334 ff
 - spinodal decomposition 415, 470
- Mössbauer spectroscopy (MBS)
 - diffusion coefficients 234
 - diffusionless transformations 587
 - high-pressure transformations 675
- mottled microstructure 364
- moving boundaries 503
- Mullins–Sekerka instability
 - dendritic growth 106, 136 ff
 - solidification 93, 120, 126 ff
- Mullins equation 491 f, 510
- mullite, formation 5
- multicomponent phase diagrams 14, 39 ff, 47
- multicomponent systems, atomic ordering 523
- multicritical phenomena, phase transitions 269
- multilayers 514
- multiple interface transformations, martensitic 633
- multisoliton lattice 274
- mutual solubility, limited 29 f

- Na–K–F–Cl salt system, phase diagram 49
- natrolite frameworks, high pressure 662
- nearest neighbors model
 - atomic ordering 532, 558
 - decomposition 367
 - high-pressure transformations 663
 - phase diagrams 63, 268, 288, 295
 - spinodal decomposition 444 f, 450
- needle crystal solution, solidification 101, 113
- neighbor interactions 531 f
- nematic liquid systems, phase transitions 246
- neodymium pentaphosphate, displacive transformations 600
- Nernst–Einstein equation 183 f, 211
- neutral stability, directional solidification 126
- neutron diffraction, phase transformations 587, 678
- Newton–Raphson technique 554
- Ni–Al–Mo system, phase separation 381, 450
- Ni–Al system
 - decomposition 346, 354 f
 - interfacial energies 390
- Ni–Cu–Al system, precipitation 315 f, 332, 390
- Ni–Si system, precipitation 397
- Ni–Ti system, displacive transformations 645, 651
- nickel-based alloys, displacive transformations 635
- Nishiyama–Wassermann relations 616, 620 f, 637 f
- nitinol, shape memory effect 642 f
- nitrate, displacive transformations 639
- nitrides, ordering 523
- noble metal-based alloys
 - atomic ordering 564
 - diffusionless transformations 599 f
- noble metals, diffusion 221
- nonfaceted systems, eutectic growth 158
- nonferrous alloys, diffusionless transformations 637
- nonisothermal precipitation 401
- nonlinear theories, spinodal decomposition 437 f
- nonmetals, diffusionless transformations 638 f
- nonstoichiometric compounds, phase diagrams 65
- nuclear magnetic resonance (NMR)
 - diffusion coefficients 234
 - high-pressure transformations 676
- nuclear methods, diffusion 231, 234
- nucleation
 - concomitant processes 381 ff
 - decomposition kinetics 332, 340 ff
 - eutectic growth 155
 - interface migration 495
 - martensitic transformations 598, 630
 - phase transitions 300
 - precipitation 315 ff
 - solidification 87 f
 - spinodal decomposition 415, 468
- numerical modeling, precipitation 381 ff, 399 f
- octahedron cluster 535, 573
- Olsen–Cohen model 629
- omega transformation 609
- Onsager coefficients 428
- Onsager theorem 181 f, 184, 206
- optimization techniques, phase diagrams 34 f
- orbital overlaps, high pressure 666
- order–disorder transitions
 - atomic ordering 567
 - high-pressure transformations 664
 - kinetics 462
 - phase diagrams 71
 - solidification 87
 - spinodal decomposition 415 f, 460
 - symmetry breaking 247 f
- order parameters
 - interfacial diffusion 486 f
 - phase transitions 71, 246 f
 - solidification 87
- ordering
 - atomic 519–581
 - pressure-induced 664
 - short/long range 68 ff, 529 ff
 - spinodal 415
- organics, diffusionless transformations 639
- orientation relationship, diffusionless transformations 616
- orientational glasses 281 f
- oriented clusters, atomic ordering 524
- Ornstein–Zernike type susceptibility 264
- orthorhombic transformations 600
- oscillations, eutectic growth 162
- Oseen tensor 440
- Ostwald ripening 370
 - see also*: coarsening
- outgassing 224
- oxidation resistance 565
- oxides
 - atomic ordering 523
 - decomposition 361, 367
- oxygen partial pressure, ionic crystals 230
- oxygen self-diffusion 178
- pair interactions, atomic ordering 527 f, 538
- pair variables 527 ff
- parabolic directional dendrites 134
- parabolic growth, precipitates 351
- parabolic Ivantsov solution 104 f, 113
- paraboloid symmetry, dendritic growth 115
- paramagnetic states, ordered phases 565
- Paris–Edinburgh cells 670, 676
- partial diffusion coefficients 179 f
- partial properties, phase diagrams 11 f
- particle (precipitate) coherency 392
- particle (precipitate) pinning 498
- particle (precipitate) splitting 377
- path probability method (PPM) 200, 209
- Pb–Sn bicrystals, boundary displacement 506
- Péclet number 103 ff, 110, 132
- percolation
 - diffusion 209
 - phase transitions 281
 - spinodal decomposition 416, 433, 442 ff
- peritectic invariants, phase diagrams 26 f, 31 f
- peritectics 163

- peritectoid precipitation 484
- perovskites, high pressure 663
- perturbations
 - dendritic growth 111, 139
 - directional solidification 127 f
- phase boundaries, phase diagrams 66
- phase diagrams 1–80
 - CVM/MC methods 554
- phase equilibria, atomic ordering 551 ff
- phase field models
 - directional dendritic growth 151 f
 - interfacial diffusion 487
- phase rule, Gibbs 7 f
- phase separation
 - precipitation 314 f, 320 f
 - spinodal decomposition 416
- phase transformations
 - high pressure 655–695
 - solidification 85
- phase transitions, statistical theories 239–308
- phase/microstructure selection, eutectic growth 164
- phenomenological theories
 - diffusionless transformations 620
 - phase transitions 246 ff
 - precipitation 398
 - spinodal decomposition 416 f
 - interfacial diffusion 487
- phonons
 - diffusionless transformations 597 f
 - phase transitions 258, 277, 282, 291
- physical correlation factor, diffusion 184, 204
- pinning, interfaces 498
- piston–cylinder systems 668
- pivalic acid (PVA), dendrites 115
- plastic crystals
 - dendritic growth 116
 - phase transitions 258
 - solidification 96
- plastic deformation, diffusionless transformations 606
- plastic response, interface migration 494
- plate-shaped martensitic regions 617
- point clusters, atomic ordering 524
- point defects
 - diffusion 193
 - phase transitions 280
 - spinodal decomposition 415
- point variables, atomic ordering 525 f
- polarization, phase transitions 246, 258
- polydispersity, polymers 427
- polygons, atomic ordering 534, 541
- polyhedral joints, high-pressure transformations 661
- polyhedron, atomic ordering 531 ff
- polymer alloys, decomposition 416
- polymer mixtures, decomposition 361, 426 f, 455 ff
- polymer solutions, phase diagrams 66
- polymers, diffusionless transformations 639 f
- polymorphic states 611, 640
- polynomial representation, excess properties 34
- polystyrene–poly(vinyl methyl ether) system, decomposition 328, 455 ff
- polytetrafluoroethylene (PTFE), diffusionless transformations 640 f
- polythermal projections, liquidus surfaces 41
- polytypic transitions, shear transformations 613
- Porod law 447, 460
- positron annihilation diffusionless transformations 587
- potassium, diffusion 232
- potential–composition diagrams 5 ff
- potential axes, phase diagrams 51
- Potts model 255, 259 f, 270 f, 285, 293
- Pourbaix diagrams 9 f
- power law approximation, precipitation 395 ff
- precipitate–growth stages, experimental identification 387
- precipitation
 - discontinuous 504 f
 - homogeneous 309–407
 - interfacial diffusion 484 ff
 - spinodal decomposition 442
- precursor effects
 - diffusionless transformations 598 f
 - phase transitions 282
- predominance diagrams 5 ff
- preexponential factor, diffusion 220
- preloading, high-pressure transformations 669
- premartensitic phase 639
- pressure–composition phase diagrams 19
- pressure, phase diagrams 6
- pressure–temperature diagram, water 54
- pressure-driven phase transitions 246, 655–695
- pretransformation states, diffusionless 595 f
- primary cell spacing, directional dendritic growth 135 f
- primary crystallization, phase diagrams 41
- primary order parameters, phase transitions 252
- pseudo time averages, phase transitions 294
- pseudobinary alloys 332
- pseudocomponents, phase diagrams 64
- pulse transmission/echo method, high-pressure phase transformations 677
- pulsed field gradient NMR, diffusion 234
- Purdy–Lange model 506
- purity, dendritic growth 116
- PVA–ethanol, solidification 115
- pyroxene chain silicates, diffusionless transformation 639
- quadrupolar glasses, ordering 282
- quadrupole moments 252, 258
- quantum liquid systems, order parameters 246
- quartz, high-pressure phase transformations 661
- quasibinary phase diagrams 47
- quasichemical model 68
- quasieleastic neutron scattering (QNS), diffusion 234
- quasiharmonic approximation 292
- quasimartensitic transformations 588, 611 ff
- quasistationary approximation
 - directional dendritic growth 144

- eutectic growth 157
- solidification 92, 125
- quenched disorder 279 f
- quenched impurities 468 f
- quenched-in nuclei 95
- quenching
 - decomposition 330 f, 339
 - diffusionless transformations 587 ff, 643
 - precipitation 314 ff
 - predecomposition 391
 - spinodal decomposition 414 ff, 427
- R-phase 639
- radioisotopes, diffusion coefficients 232
- Raman spectroscopy, high pressure 674
- random alloy model 185 ff, 199, 226
- random bond, phase transitions 280
- random phase approximation 427
- random walk theory 189
- Rankine–Hugoniot relations 667
- Raoultian solutions, ideal 12
- rapid diffusion 191
- rapid solidification 499, 649
- rare-earth alloys, diffusionless transformations 608, 635
- rate-determining mechanism, directional solidification 120
- Rayleigh–Benard systems 127
- Rayleigh number 124
- reaction stoichiometry 5 ff
- real-system applications, atomic ordering 561
- reciprocal ternary phase diagrams 49
- reconstructive phase transitions 260
- recrystallization 495, 505
- Redlich–Kister form, phase diagrams 34
- reduced geometry, phase separation 467
- regular solution theory 23
- regular structures, eutectic growth 158
- relative partial properties, phase diagrams 11 f
- relaxation
 - atomic ordering 523, 550, 573
 - diffusionless transformations 635
 - interface migration 495
 - spinodal decomposition 424, 467
- relaxation methods
 - diffusion coefficients 233
 - interfacial diffusion 484
 - metal diffusion 224
- renormalization group methods
 - phase transitions 266 ff, 271, 279
 - spinodal decomposition 419 f, 429 f
- reptation, spinodal decomposition 428
- residual activity, diffusion coefficients 232
- resistivity, electrical, diffusionless transformations 587
- retarding forces, interface migration 492
- Reynolds number 124
- Rigsbee–Aaronson model 488
- Rikvold–Gunton model 398
- rotational jumps 197
- rotational symmetry, dendritic growth 115
- roughening transition 268
- Rouse model 428
- Saffmann–Taylor limit 130
- salt system, reciprocal ternary 49 f
- salts, transparent, solidification 115
- scaling
 - dendritic growth 110 f, 114, 135
 - directional solidification 124
 - interfacial diffusion 502
 - solidification 94 f
 - spinodal decomposition 425, 430, 445 f, 453 f
- scaling laws
 - eutectic growth 156
 - phase transitions 260 f, 266, 277
 - precipitation 395 ff
- scanning transmission electron microscope (STEM), microanalysis 511
- scattering data, phase transitions 250, 260, 287
- scattering techniques, precipitates 328 f, 423
- Schottky defects 227
- Schreinemaker rule 46, 57
- second-neighbor interactions 535, 543 ff, 557 f
- second-order transitions 249, 252, 258, 260 f
- second-phase precipitation, homogeneous 309–407
- secondary ion mass spectroscopy (SIMS), diffusion 232
- segregation, interfacial 484, 489 f
- segregation coefficients 125
- self-accommodation, diffusionless transformations 619, 636
- self-averaging, phase transitions 280
- self-diffusion 176 ff
 - grain boundaries 491
 - isotope effect 215
 - metals 202
- self-similarity, precipitation 395 ff
- semiconductors
 - atomic ordering 523
 - dendritic growth 119
 - zincblende-type, high pressure 679
- shallow quenching 427
- shape deformations, diffusionless transformations 600 f, 615
- shape-memory alloys (SMA) 590 ff, 633 ff, 638, 641 f
- sharp interface model 340
- shear transformations 606, 613, 636
- shock wave techniques, high-pressure transformations 667
- Shoji–Buerger lattice deformations 594
- short-circuit diffusion 186 ff
- short-range order (sro) configurations
 - atomic ordering 529 ff, 539
 - phase transitions 68, 288
- short-wavelength distortions, phase transitions 283
- shuffles, diffusionless transformations 588 ff, 596 ff, 606 ff
- Si–O–Si angles 661

- SiC–AlN ceramics, decomposition 454
- side branching, dendrites 108 ff, 143, 151
- silica, phase transformations 639, 661
- silicate slags 69
- silicon, high-pressure phase transformations 680
- silicon-based alloys, rapid solidification 499
- silver alloys, diffusionless transformations 634
- simplex, atomic ordering 534
- simulation techniques, phase transitions 293
- single chain dynamics 428
- single-phase solid solutions 15
- single sites, phase transitions 289
- singularities, critical 260
- SiO₂–MgO–MnO system, phase diagram 74
- site cluster approximation 560
- site occupation operator 526
- slip, diffusionless transformations 590, 605, 622
- slow growth rates, solidification 96
- slow mode theory 428
- slowing down, phase transitions 277
- small-amplitude fluctuations, spinodal decomposition 418
- small-angle neutron scattering (SANS), precipitates 328, 391
- small-angle X-ray scattering (SAXS), precipitates 328, 360
- Snoek effect, diffusion 233
- snow flakes, dendritic growth 100
- soft phonons 277, 282, 291
- softmode phase transitions
 - diffusionless 596
 - martensitic transformations 631
- solid compounds, phase diagrams 9
- solid binary mixture systems 246
- solid–liquid equilibria 18
- solid–liquid interface, directional solidification 120
- solid–liquid miscibility, phase diagrams 14
- solid–solid transformations 484, 490
- solid solutions
 - decomposition 314 f, 385
 - diffusionless transformations 635
 - phase diagrams 15
- solid-state diffusion 189
- solidification 81–170
- solidus line 279
- soliton staircase 274
- solubility
 - mutual 29
 - precipitation 316, 370, 393
- solutal dendrites 117
- solute–solute binding 225
- solute–vacancy binding 222
- solute drag, interfacial motion 496
- solute enhancements factors 221
- solution models, phase diagrams 62 ff
- solvability theory, dendritic growth 106, 116
- solvent enhancement factors, diffusion 221
- solvus lines 23, 314 f
- Soret effect 181
- sound velocity, high-temperature transformations 677
- space groups, atomic ordering 526 f575
- space model, ternary 39
- spacing
 - dendritic growth 111, 117
 - directional solidification 130 ff
 - eutectic growth 159
 - interfacial diffusion 485, 509
 - solidification 99
 - spinodal decomposition 426, 450
- see also*: lattice spacing, interface spacing, cell spacing
- spectroscopic techniques, high-temperature transformations 674
- sphere crystal growth 92
- spin glass 281
- spin representation, Ising 286
- spin variables 524, 570
- spinodal alloys 363 ff
- spinodal decomposition 332, 354 ff, 409–480
 - precipitation 319 ff
- spinodal point, phase transitions 22, 299
- spins, phase transitions 255, 259 f
- split sphere anvil technology 670
- splitting
 - clusters 352 f
 - coarsening 377 f
 - spinodal decomposition 433
- sponge-like microstructure 364
- spontaneous growth, ordered domains 462
- spontaneous magnetization 246
- stability
 - dendritic growth 118
 - nucleation 350
 - spinodal decomposition 417
- stability domains, phase diagrams 8
- stability length
 - dendritic growth 106, 111
 - solidification 93
- stability limit, phase transitions 254
- stabilizing, diffusionless transformations 611, 625
- stable pair, exchange reaction 63
- stacking faults, diffusionless transformations 601, 634
- stacking sequences, diffusionless transformations 595, 613
- staggered fields, ordering 248
- standard model, directional solidification 125
- standard molar Gibbs energy 6
- standard states, phase diagrams 11 f
- static pressure devices 668
- statistical theories, phase transitions 239–308
- steady cooperative growth 507
- steady-state nucleation rate 342
- steels, precipitation 366
- steepest descent technique, atomic ordering 554
- stiffness tensor 447
- Stirling approximation
 - atomic ordering 552
 - diffusion 219
 - phase diagrams 13
- stoichiometric compositions 566
- stoichiometric crystals 227
- stoichiometric product phase 515

- stoichiometry, phase diagrams 5 ff, 28
- Stokes' law, cluster diffusion 456
- strain
 - diffusionless transformations 588, 606, 647 f
 - interface migration 493
 - precipitation 324, 337
- strain spinodals 631
- strengthening, martensite 649
- stress–temperature diagramm 645
- stress induced transformations
 - martensitic 633
 - diffusionless 647
- stress relaxation, diffusionless transformations 635
- strontium titanate, displacive transformations 591, 607
- structural distortions, high-pressure transformations 659, 665 f
- structural models 5
- structure functions, spinodal decomposition 442
- structure modulation 360, 364
- structures
 - diffusionless transformations 593 f
 - eutectic growth 158 f
 - grain boundaries 484 f
 - ordered 523 f
 - precipitation 314 f
- styrene–butadiene mixture, phase separation 457
- subcluster probabilities, atomic ordering 529
- subgrains, stored energy 495
- sublattice magnetization 246
- sublattices
 - atomic ordering 529
 - interfacial diffusion 484
 - phase transitions 62, 251
 - spinodal decomposition 415
- substitutional alloys
 - atomic ordering 523 ff
 - diffusion 221, 226
- substitutional ferrous martensite 636
- substitutional impurities, spinodal decomposition 415
- substitutional solution model, ideal 12
- substructures, diffusionless transformations 616, 637
- succinonitrile (SCN)
 - dendritic growth 109, 114 f, 139 f
 - solidification 96 ff
- sulfides, diffusionless transformations 639
- superconductivity, pressure dependence 666
- supercooling
 - dendritic growth 109, 131, 135
 - eutectic growth 154
 - solidification 88 ff, 92
- supercritical clusters 434
- superelastic alloys 650
- superhard materials, high-pressure transformations 659
- superheated melts 95
- supersaturated matrix, precipitation 350
- supersaturation
 - coarsening 377
 - decomposition 330, 345, 359, 414 f
 - diffusionless transformations 635
 - interfacial diffusion 499
 - precipitation 314 f, 323 ff, 396 ff
 - spinodal decomposition 414 f
- superstructures
 - atomic ordering 529, 546
 - b.c.c. lattice 577
 - f.c.c. lattice 575
 - phase transitions 271 ff
- surface diffusion 180 f, 192
 - coefficient measurements 234
- surface effects
 - disorder 283
 - phase transitions 279 f
 - spinodal decomposition 467 f
- surface melting 283
- surface tension 88, 124 ff
- surfactant micellar solutions 456
- symmetry, dendritic growth 115
- symmetry breaking, order parameters 247
- symmetry lowering, ferroic phase transitions 608
- symmetry properties, phase transitions 256, 270
- synchrotron radiation, high-pressure studies 667, 670
- syntectic invariants, phase diagrams 32
- tail instability, solidification 137
- tangent constructions 11 f, 16
- temperature–composition phase diagrams 5 ff, 14
- temperature–concentration plane, spinodal decomposition 435
- temperature–stress diagram, diffusionless transformations 647
- temperature gradients
 - atomic ordering 551 ff
 - diffusion 181
 - spinodal decomposition 470
- temperature ranges
 - decomposition 340
 - diffusionless transformations 587, 590 f, 607
 - interfacial diffusion 501
- ternary alloys
 - pair variables 528
 - phase transitions 285
 - precipitation 334, 397
- ternary mixtures, spinodal decomposition 415
- ternary systems 5, 39 ff
 - atomic ordering 569 f
- tetrahedral framework, high-pressure transformations 661
- tetrahedron, atomic ordering 573
- tetrahedron approximation, phase transitions 288
- tetrahedron clusters, atomic ordering 536 f, 544 f
- tetrahedron–octahedron approximation 553 ff, 560
- thallium alloys, diffusionless transformations 634
- thermal dendrites 116
- thermal diffusion
 - dendritic growth 108
 - solidification 91
- thermal fluctuations
 - dendritic growth 113

- solidification 87
- spinodal decomposition 414 f
- thermal gradients, directional solidification 126
- thermally induced martensitic transformations 633
- thermodynamic compilations, phase diagrams 77
- thermodynamic factor
 - atomic ordering 565
 - diffusion 205
- thermodynamic variables, conjugate 247
- thermodynamics 1–80
 - diffusionless transformations 603 ff
 - irreversible 181 f
 - martensitic transformations 624 f
 - phase separation 322
 - precipitation 317 f
 - spinodal decomposition 416 f
 - two-component systems 121
- thermoelastic behavior, martensitic transformations 622, 632 f
- thin layer methods, diffusion coefficients 231
- three phase stability 9
- Ti–Al–X systems, atomic ordering 562
- Ti–Ni–Cu alloys, martensite 631
- tie lines 15, 41, 60
- tilt grain boundaries 485 ff, 495 f
- tilted domains 156
- tilted lamellar arrays 151
- time-dependent nucleation rate 343
- time residence algorithms, Monte Carlo simulations 485
- tip radius
 - dendritic growth 110 ff, 116 f, 120
 - directional dendritic growth 133, 143
- titanium alloys, diffusionless transformations 607, 617, 623, 634 ff
- tomographic atom probe (TAP), precipitates 328
- topology
 - phase diagrams 45
 - phase transitions 25, 296
- torques
 - discontinuous precipitation 506
 - interfacial diffusion 499
- trace impurities, interfacial diffusion 500
- tracer correlation factor
 - defective systems 204
 - microscopic diffusion 193
- tracer diffusion 178 ff, 182 ff
 - interfacial 490
 - metals 226
 - methods 231
- training, shape memory effect 643
- transformation hysteresis, martensitic 633 f
- transformation-induced plasticity (TRIP) 593, 647
- transformations, interfacial diffusion 481–518
- transmission electron micrographs
 - decomposition 360, 366
 - diffusionless transformations 600
 - directional dendritic growth 149
- transparent salts, dendritic growth 115
- tricritical point
 - atomic ordering 565
 - phase transitions 269, 272
 - spinodal decomposition 460
- triple points, phase diagrams 8, 55
- true phase diagram sections 56 f
- trunk spacing, dendrites 144 ff
- twinning 595, 600, 605, 615, 618, 622, 634
- twist boundaries 491, 495
- two-component systems, directional solidification 121
- two-phase stability 9
- two-phase regions 20
- two sided model, dendritic growth 102
- two-way shape memory effect, diffusionless transformations 644
- ultrasonic sound velocity, high-pressure transformations 677
- undercooling
 - dendritic growth 118, 146
 - diffusionless transformations 612
 - martensitic transformations 625
 - precipitation 325
 - solidification 95 ff
- undistorted lines, diffusionless transformations 592
- univariant lines 41
- univariant phase regions 31
- universality principle
 - phase transitions 266, 293
 - spinodal decomposition 431 f
- unstable states, spinodal decomposition 417
- uphill diffusion 357, 422
- vacancies
 - interfacial diffusion 485
 - spinodal decomposition 468 f
- vacancy–impurity complexes, diffusion 223
- vacancy concentration
 - diffusion 218
 - ionic crystals 230
- vacancy mechanism, diffusion 191
- vacancy-wind effect 182 f, 185 f, 208 ff
- van der Waals forces 24, 255
- vapor–liquid equilibrium 18
- variance, phase diagrams 31
- vector model, order parameters 251
- vibrational displacements 588, 597
- vibrational energy, atomic ordering 573
- vibrational modes, high-pressure transformations 674
- viscoelastic phase separation 470
- viscous hydrodynamics, phase separation 446
- Volmer–Weber theory 342 ff
- volume fractions
 - diffusionless transformations 587
 - eutectic growth 158
 - precipitation 373 f, 395
 - spinodal decomposition 427
- volume relaxation, atomic ordering 550
- volumetric pressure techniques, phase transformations 674

- water
 - high-pressure transformations 687 ff
 - phase diagram 54, 688
- wave modulations, diffusionless transformations 592
- weak fluctuations, spinodal decomposition 418 ff
- wetting phase transitions 283
- whiskers, martensitic transformations 601
- Widmanstätten precipitates 507
- Willis cluster 230
- wollastonite, diffusionless transformations 639
- Wulff construction
 - decomposition 344 f
 - interfacial diffusion 488
 - solidification 90
- wurtzite
 - diffusionless transformations 639
 - high-pressure transformations 680, 688
- X-ray absorption spectroscopy (XAS), transformations 676
- X-ray diffraction, phase transformations 587, 612, 678
- X-ray microanalysis 326, 511
- Young's modulus, diffusionless transformations 590
- Zeldovich factor 341 ff
- zeolite frameworks, high-pressure transformations 662
- zero-phase fraction (ZPF) lines 58
- zincblende type semiconductors, high-pressure transformations 679
- zirconium, diffusionless transformations 598 ff, 639
- zirconium alloys, diffusionless transformations 607, 617, 634
- zone melting 98
- Zr–Ti–Cu–Ni–Be glass, phase separation 455